Advances in Geophysical and Environmental Mechanics and Mathematics

AGEM²

Oscar Castro-Orgaz
Willi H. Hager

Non-Hydrostatic Free Surface Flows

Springer

Advances in Geophysical and Environmental Mechanics and Mathematics

Series editors

Kolumban Hutter, Zürich, Switzerland
Holger Steeb, Stuttgart, Germany

More information about this series at http://www.springer.com/series/7540

Oscar Castro-Orgaz · Willi H. Hager

Non-Hydrostatic Free Surface Flows

Springer

Oscar Castro-Orgaz
University of Cordoba
Cordoba
Spain

Willi H. Hager
ETH Zurich
Zürich
Switzerland

ISSN 1866-8348 ISSN 1866-8356 (electronic)
Advances in Geophysical and Environmental Mechanics and Mathematics
ISBN 978-3-319-47969-9 ISBN 978-3-319-47971-2 (eBook)
DOI 10.1007/978-3-319-47971-2

Library of Congress Control Number: 2016954540

© Springer International Publishing AG 2017
This work is subject to copyright. All rights are reserved by the Publisher, whether the whole or part of the material is concerned, specifically the rights of translation, reprinting, reuse of illustrations, recitation, broadcasting, reproduction on microfilms or in any other physical way, and transmission or information storage and retrieval, electronic adaptation, computer software, or by similar or dissimilar methodology now known or hereafter developed.
The use of general descriptive names, registered names, trademarks, service marks, etc. in this publication does not imply, even in the absence of a specific statement, that such names are exempt from the relevant protective laws and regulations and therefore free for general use.
The publisher, the authors and the editors are safe to assume that the advice and information in this book are believed to be true and accurate at the date of publication. Neither the publisher nor the authors or the editors give a warranty, express or implied, with respect to the material contained herein or for any errors or omissions that may have been made.

Printed on acid-free paper

This Springer imprint is published by Springer Nature
The registered company is Springer International Publishing AG
The registered company address is: Gewerbestrasse 11, 6330 Cham, Switzerland

We would like to dedicate this work to:

Oscar's wife Elena, and his sons Jaime (7 years), Matias (6 years) and Pablo (1 year). Their lovely support, and steady smiles to Oscar every morning when all the family wakes up, constantly gave him the fresh energy to successfully convey this project.

Willi's wife Susanna and their three daughters Olivia, Mirjam, and Caren, who have contributed to this work by their support and constant encouragement.

Oscar Castro-Orgaz and Willi H. Hager

Preface

The computation of unsteady free surface flows has an important place in disciplines such as civil, environmental, and coastal engineering, given the need to solve real-life problems associated with this fascinating type of hydraulic motion. During the past decades, their three-dimensional (3D) computation using RANS and LES models gained impulse, permitting an accurate numerical solution of complex hydraulic flows. These numerical solutions are usually coupled in a hybrid way with physical laboratory experimentation. Given that 3D numerical solutions are still time-consuming and computationally costly, the common mathematical tool for simulating unsteady free surface flows still relies on the use of depth-averaged 2D models. This approach is popular among water scientists and hydraulic engineers, given that the 2D depth-averaged mathematical formulation and numerical implementation are simpler. The standard 2D approach is based on the Saint–Venant hydrostatic theory for flows in a horizontal plane, which is by now powerfully solved using modern shock-capturing methods like the finite volume method or the discontinuous method of Galerkin. However, there are a number of important real-life hydraulic flows that are not suitable for modelling based on the hydrostatic pressure approach, including flows over control structures, such as a dam crest, the bed-form evolution in alluvial rivers, the drainage of recharge in aquifers, or the avalanche mass flows down a steep mountain.

Furthermore, the teaching of free surface flows all over the world strongly relies on the seminal books of Ven Te Chow (published in 1959) and Francis M. Henderson (published in 1966), in which the Saint–Venant theory is lucidly explained and applied. Most of the (few) open-channel books written since expanded and presented in detail the theory of Saint–Venant. However, non-hydrostatic flow problems are often only mentioned without details on the procedures available. They are in most cases referred to papers or explained based on dimensional analysis and experimentation. Advanced depth-averaged modeling approximations, and the power of their possibilities in engineering, are hardly available in open-channel flow books.

Despite the interest of the non-hydrostatic theory for teaching, research, and practice, the only book so far written on that topic is Boussinesq's "*Essai sur la théorie des eaux courantes*," published in 1877. This is indeed the original book in which Boussinesq masterly presented his depth-averaged theory. Today, almost 140 years since, the purpose of this new book is to fill in the gap by presenting the higher mathematical level of approximation over the Saint–Venant hydrostatic theory, also referred to as the Boussinesq theory, and the advances since Boussinesq's book. The theory and computation of non-hydrostatic free surface flow problems using depth-averaged models are developed, including problems in open channels (inviscid and viscous), groundwater with a phreatic surface, and granular material. The application of the theory to coastal engineering problems is beyond the scope of the book. However, the main advances on the use of Boussinesq-type models in this discipline are considered at adequate places by using the theoretical developments presented here.

The book topic coverage originates from the collaborative work of the authors, working toward the solution of these problems during the past ten years. The book was designed to be as complete as possible, with a detailed source of literature references and adequate technical information, so that any interested reader will be ready to deepen into the problems. Worked problems are not presented. Rather, detailed solutions are produced and compared with experimental data to show the performance of the theory. A comparison with other theories is presented when considered adequate and illustrative. Short biographies of pioneers in non-hydrostatic free surface hydraulics are further presented to keep the interest on what others did in the past. A special feature of the book is that mathematical developments are presented step-by-step in great detail. The development of Boussinesq-type equations is sometimes tedious, and algebraic manipulations are difficult to reproduce. This level of detail is usually lacking in papers, and it is fully covered in this work to help young researchers. In addition to the detailed developments included within the text, ten appendices were prepared to further help readers. We envision this book to be of use for Ph.D. students and researchers conducting work on this fascinating field. The material is also adequate for teaching purposes in courses on advanced open-channel flow for master students in civil and environmental engineering.

Cordoba, Spain — Oscar Castro-Orgaz
Zürich, Switzerland — Willi H. Hager
April 2017

Acknowledgements

This project was finished thanks to the support of many persons to our research activities for years. Oscar Castro would like to deeply thank Profs. Juan V. Giraldez and Jose Luis Ayuso, University of Cordoba, Spain, and Dr. Luciano Mateos, IAS-CSIC, for their continuous interest in his research work, and their advice and support. The discussions on the book topic with Prof. Subhasish Dey, IIT Kharagpur, India, Prof. Sergio Montes, University of Hobart, Tasmania, and Prof. Hubert Chanson, the University of Queensland, Australia, were a valuable source of knowledge and inspiration. He would like to cordially thank Dr. Roger Denlinger, US Geological Survey, for his kind support providing with details for the implementation of his numerical algorithm to include vertical accelerations in unsteady non-hydrostatic flow over 3D terrain. As to Willi Hager, he would like to acknowledge his colleague Prof. Robert M. Boes, Director VAW, for his continuous support and the constructive collaboration in the Institute at ETH Zurich.

Last but not least, our warmest thanks are conveyed to the book editor, Prof. Kolumban Hutter. We thank him for his invitation to prepare this book and for his non-static role, supporting all the stages of the book with his deep knowledge of fluid mechanics. He deeply supported the authors double-checking all the mathematical work and contributed to a great extent to the improvement of the original version of the manuscript, with his good suggestions and corrections.

Oscar Castro-Orgaz
Willi H. Hager

Contents

Chapter 1
Introduction

Roman Symbols

D Still water depth (m)
E Specific energy head (m)
$\mathbf{F}$ Flux vector (m^2/s, m^3/s^2)
g Gravity acceleration (m/s^2)
h Flow depth measured vertically (m)
H Energy head (m)
K Parameter in curvature law (–)
N Flow depth measured on normal to channel bottom (m)
p Pressure (N/m^2)
p_b Bottom pressure (N/m^2)
q Unit discharge (m^2/s)
r Radius of bottom curvature (m)
r_z Radius of streamline curvature at elevation z (m)
R Radius of free surface curvature (m)
S Momentum function (m^2/s)
S_o Bottom slope (–)
S_f Friction slope (–)
$\mathbf{S}$ Source term vector (m/s, m^2/s^2)
t Time (s) also flow depth measured as vertical projection of equipotential curve (m)
u Velocity in x-direction (m/s)
U Mean flow velocity (m/s) = q/h
$\mathbf{U}$ Vector of conserved variables (m, m^2/s)
w Velocity in z-direction (m/s)
x Streamwise coordinate (m)
z Vertical elevation (m)
z_b Elevation of channel bottom (m)

© Springer International Publishing AG 2017

O. Castro-Orgaz and W.H. Hager, *Non-Hydrostatic Free Surface Flows*,
Advances in Geophysical and Environmental Mechanics and Mathematics
DOI 10.1007/978-3-319-47971-2_1

Greek Symbols

β Boussinesq velocity correction coefficient (–)
γ Specific weight (N/m^3)

1.1 Aim and Scope

Water resources' engineering requires a solid knowledge of free surface flows for both the mathematical and physical simulations of real flows. The non-hydrostatic pressure distribution is a typical feature of such flows, thereby invalidating the application of the standard (hydrostatic) Saint-Venant equations, including weir and gate flows, undular bores, groundwater flows with a phreatic surface, water-sediment flows and dispersive water waves. Following Liggett (1994), the errors made in open-channel flow computations stem mainly from the lack of knowledge of friction and from the hydrostatic pressure assumption. While the gradually varied flow theory is routinely presented in the open-channel flow books, the issue of non-hydrostatic pressure is not commonly addressed. The aim of this book is to fill this gap by presenting the higher mathematical level of approximation over the gradually varied flow theory, also referred to as the Boussinesq theory, leading to the so-called Boussinesq-type models. Essentially, this theory relates to the inclusion of non-hydrostatic pressure in depth-averaged free surface flow modeling. The higher order Boussinesq-type flow equations and their solutions are presented in this book for its beneficial use in a wide range of pertinent engineering and environmental problems, including open-channel, groundwater, and granular material flows. There is a plethora of "Boussinesq-type" models in the literature. Rather than focus on exploiting a specific model, the main purpose of this book was to highlight how the Boussinesq theory applies to produce models suitable for a particular given problem. Coastal engineering applications are beyond the scope of the book, but the use of Boussinesq-type models in this area is considered at several places. For a detailed account of Boussinesq-type equations in coastal engineering, consult Dingemans (1994) and Brocchini (2013). Gradually varied flow problems are not considered in the book, given the vast amount of books already dealing with the topic, but reference is then made for comparative purposes with higher order equations. In this chapter, non-hydrostatic free surface flows are defined and a historical note on the works is presented from which the current knowledge and theory of this book originates.

1.2 Hydrostatic and Non-hydrostatic Free Surface Flows

Consider free surface flow over a side weir (Castro-Orgaz and Hager 2011a) (Fig. 1.1a) involving the longitudinal free surface profile $h(x)$ along the streamwise x-axis (Fig. 1.1b), where the velocity components in the (x, z) directions are (u, w). If the vertical velocity is nonzero, then the pressure distribution p is non-hydrostatic (Fig. 1.1b), as can be inferred from a vertical momentum balance (Liggett 1994; Montes 1998). Modeling non-hydrostatic free surface flows thus requires consideration of w, or better its variation with x. These flows have been traditionally classified as *gradually varied* flows and *rapidly varied* flows (Bakhmeteff 1912, 1932; Chow 1959; Henderson 1966; Montes 1998; Jain 2001; Sturm 2001; Chanson 2004; Chaudhry 2008; Hager 2010). The first group refers to flow problems of which the local changes in flow depth are small, including backwater curves upstream of a dam extending for kilometers, so that w is close to zero everywhere. In turn, flow problems in which the flow depth varies abruptly over a

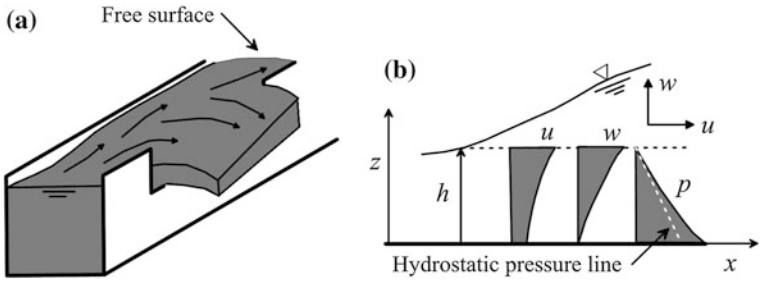

Fig. 1.1 **a** Scheme of a free surface flow over a side weir (adapted from Castro-Orgaz and Hager 2011a), **b** definition of flow variables

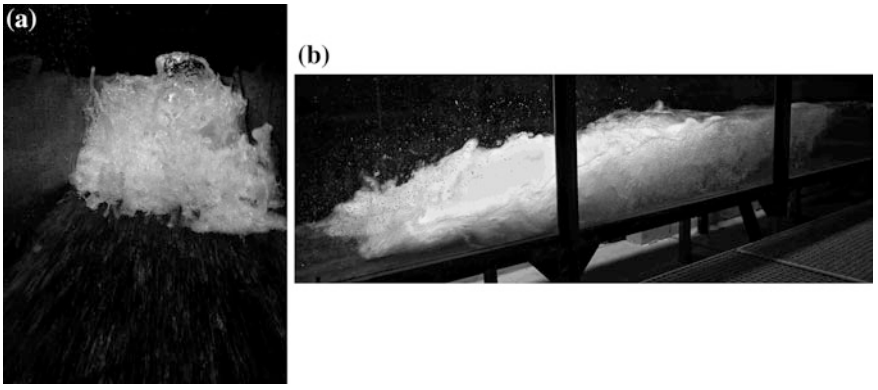

Fig. 1.2 Classical hydraulic jump **a** looking in flow direction, **b** side view (*photograph* VAW, ETH Zurich)

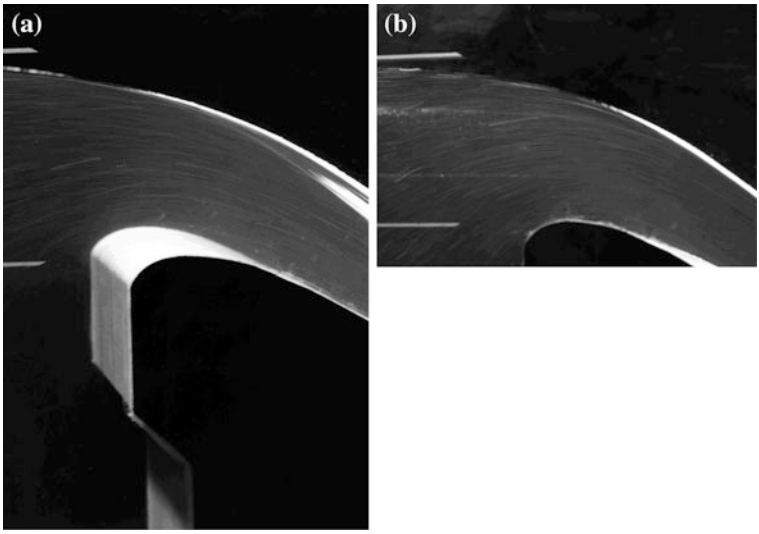

Fig. 1.3 Flow over spillway **a** general view, **b** detail of curved flow near the weir crest. Note the presence of air bubbles by which approximate streamline geometry is highlighted (*photograph* VAW, ETH Zurich)

short distance belong to the second group, including hydraulic jumps (Fig. 1.2) or flows over spillways (Fig. 1.3).

It is usually argued that the vertical (convective) acceleration terms (related to $\partial w/\partial x$) are negligibly small in gradually varied flows so that the pressure distribution is close to hydrostatic, whereas they are kept for rapidly varied flows. It is also generally accepted that in gradually varied flows the pressure is hydrostatic; however, not all rapidly varied flows involve a non-hydrostatic pressure. A prominent example is the hydraulic jump (Fig. 1.2). Detailed pressure measurements within it reveal a non-hydrostatic pressure induced by entrainment of air (Castro-Orgaz and Hager 2009). However, this air–water flow effect on the streamwise momentum balance is so small that the pressure distribution is nearly hydrostatic so that no effects of non-hydrostatic pressure originating from air–water flows must be accounted for. In a classical hydraulic jump, the streamlines in the jet flow are only weakly curved and sloped so that vertical accelerations remain equally small. This flow thus allows for hydrostatic modeling if the effect of the recirculating fluid in the roller is properly accounted for. By contrast, for flows over spillways (Fig. 1.3), streamlines are highly curvilinear so that vertical accelerations induce a markedly non-hydrostatic pressure (Castro-Orgaz 2008). If non-hydrostatic pressure is accounted for in the model equations, such flow problems are adequately approximated as potential flows.

Therefore, the classification of free surface flows includes rather hydrostatic and non-hydrostatic flows, which is a better typification than the terminology "gradually varied" versus "rapidly varied" flows. In what follows, this first classification is

generally adopted, allowing for an improved description of the physical background and the mathematical concept underlying this procedure.

1.3 Historical Background

The teaching and practice of free surface flows strongly rely on the seminal, still widely used books of Chow (1959) and Henderson (1966). These presented, among others, the theory of hydrostatic flows founded by the Frenchmen Bresse, Saint Venant, Dupuit, and Boussinesq, including the computation of backwater profiles (Bélanger 1828). However, few books include the next degree of sophistication in free surface flows, namely the so-called Boussinesq theory, developed by J.V. Boussinesq, C. Fawer, F. Serre, and D.H. Peregrine (Fig. 1.4).

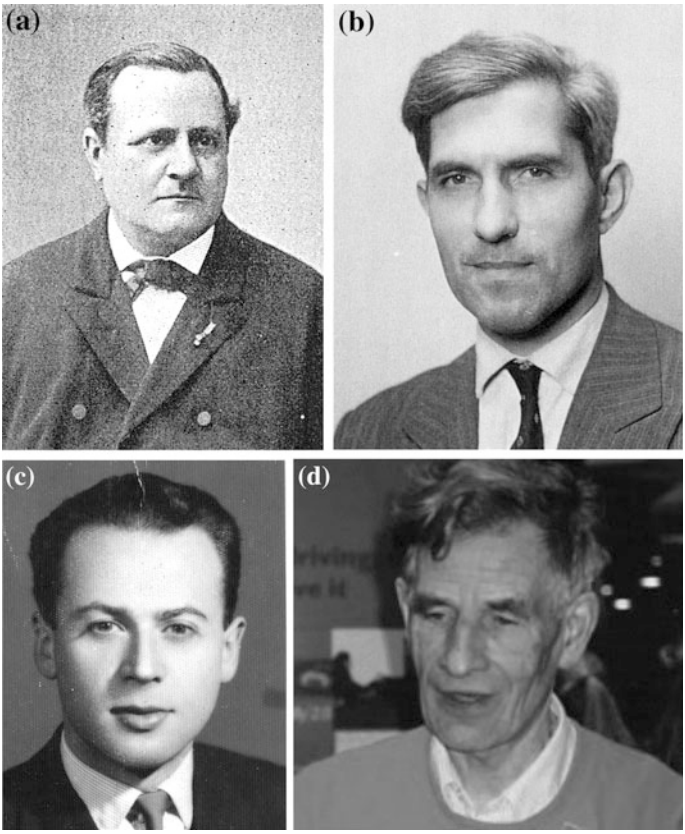

Fig. 1.4 Fathers of non-hydrostatic channel flow modeling **a** Joseph V. Boussinesq (adapted from Castro-Orgaz and Hager 2011b), **b** Carlos Fawer (adapted from Castro-Orgaz 2010a), **c** Francois Serre (adapted from Castro-Orgaz and Hager 2011c), **d** D. Howell Peregrine (*photograph* by Liz Green at http://www.bristol.ac.uk)

This approach deals with cases in which the standard backwater equations fail due to the non-inclusion of the non-hydrostatic pressure originating from streamline curvature, or from other sources, such as spatially varied water discharge in the channel or the existence of bed-load sediment motion. Consequently, this improved approach was hardly transmitted to the engineering profession despite it is a common tool in disciplines as coastal engineering. Joseph Valentin Boussinesq (1842–1929) (Fig. 1.4a) is known in open-channel hydraulics for his outstanding theory bearing his name to deal with non-hydrostatic flows.

John Scott Russell was born on May 8, 1808, at Parkhead, east of Glasgow, UK, and passed away on June 8, 1882, at Ventnor on the Isle of Wight, UK. He made studies at the Universities of St. Andrews and Glasgow graduating in 1824. He was then appointed lecturer in natural sciences in 1832 at the University of Edinburgh, starting his famous wave observations in 1833. He investigated the practicability of steam navigation in canals based on a request by the Scottish Canal Company. This led him to study the resistance of floating bodies due to wave presence. After 10 years of research, he was awarded the Large Gold Medal by the Royal Society of Edinburgh. Russell moved in 1844 to London to take over important positions in the shipbuilding industry, of which the *Great Eastern* was the largest design of his era, which was successfully launched by Isambard K. Brunel (1806–1859). William Froude (1810–1879) was also involved in various early designs of Russell. The *Great Eastern* was a triumph for the future naval development although it was a commercial failure. Russell was thus an outstanding naval engineer and experimenter, changing shipbuilding from an art to a science.

Russell was the first who observed and described in 1837 the solitary wave, corresponding to a local bell-shaped free surface elevation, whose celerity is equal to the square root of gravity acceleration times the still water depth. The solitary wave is thus made up by only one single wave hump whose body is above the undisturbed water elevation, without any wave trough presence. This peculiar feature puzzled scientists, and it was only Joseph V. Boussinesq (1842–1929) who was able to explain it by accounting for streamline curvature effects in 1872. Note that Adhémar Barré de Saint-Venant (1797–1886) one year before introduced the shallow water equations, by which the solitary wave may not be explained, essentially because Saint-Venant theory relies on the hydrostatic pressure assumption. Currently, solitary waves are explored because of their relevance in tsunami generation and propagation.

Boussinesq (1877), motivated by the fascinating experimental findings of Russell (1845) on water waves (Fig. 1.5), investigated the non-hydrostatic pressure modeling in free surface flows, dealing with both water wave motions and steady free surface flow problems. He assumed a linear velocity distribution normal to the channel bottom and used this approach to include streamline curvature effects in a steady version of the momentum equation. Integration of the equation of motion in the transverse direction resulted in an extended third order differential equation for open-channel flows in the streamwise x-direction of the form (Boussinesq 1877; Castro-Orgaz and Hager 2011b)

$$\frac{U^2h^2}{g}\left(\frac{1}{3}\frac{\mathrm{d}^3h}{\mathrm{d}x^3}-\frac{1}{2}\frac{\mathrm{d}^2S_o}{\mathrm{d}x^2}\right)+\left(h-\beta\frac{U^2}{g}\right)\frac{\mathrm{d}h}{\mathrm{d}x}=h\left(S_o-S_f\right). \tag{1.1}$$

Here, U is the depth-averaged velocity, β the Boussinesq velocity correction coefficient, h the flow depth, S_o the bottom slope, and S_f the friction slope.

Based on Eq. (1.1), Boussinesq proposed a systematic classification of non-hydrostatic free surface profiles. While he was the first suggesting the momentum approach, his work was followed by Carlos Fawer (1910–1996) (Fig. 1.4b), who proposed an extended energy equation, which includes streamline curvature effects (Fawer 1937; Castro-Orgaz 2010b) to study irrotational steady flow in hydraulic structures. The work of Boussinesq was further expanded by François Serre (1923–2009) (Fig. 1.4c) (Serre 1953; Castro-Orgaz and Hager 2011c), who developed a turbulent Boussinesq model that was theoretically discussed for steady and unsteady flows, and by D. Howell Peregrine (1938–2007) (Fig. 1.4d), who contributed numerically to the undular bore propagation in coastal engineering problems (Peregrine 1966).

Fawer (1937) considered flows over curved bottom surfaces combining the Bernoulli equation with a law of variation of the streamline curvature radius R_z with the vertical distance z from the channel bottom to the free surface as (Fig. 1.6a)

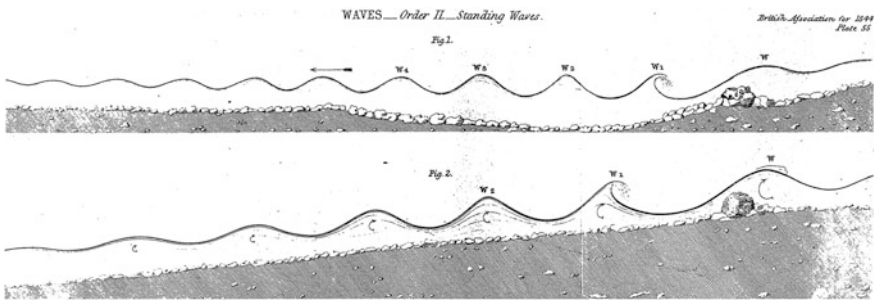

Fig. 1.5 Standing waves (including wave breaking) after Russell (1845), a fascinating example of non-hydrostatic open-channel flow (flow from right to left)

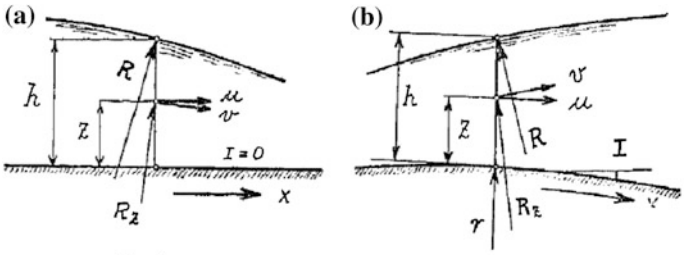

Fig. 2. Fig. 3.

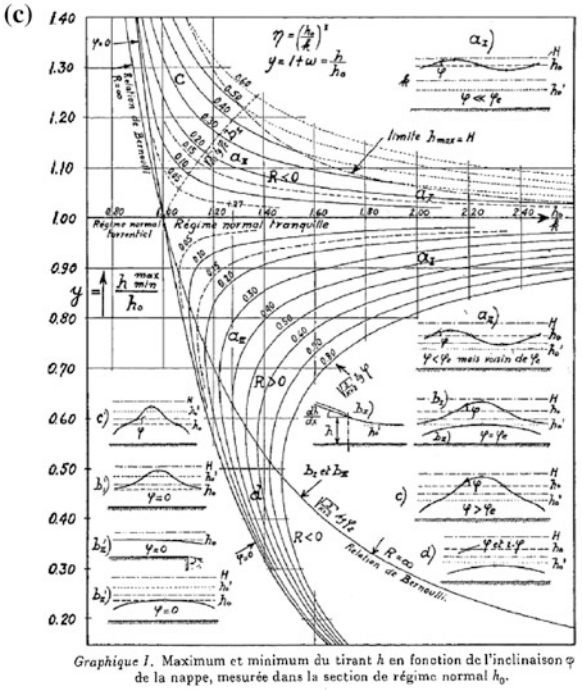

Graphique I. Maximum et minimum du tirant h en fonction de l'inclinaison φ de la nappe, mesurée dans la section de régime normal h_0.

Fig. 1.6 Theory of curvilinear flows (Fawer 1937). Definition of flows over **a** horizontal and **b** curved beds, **c** classification of possible curvilinear free surface profiles on horizontal bottom

$$\frac{1}{R_z} = \frac{1}{r} + \left(\frac{1}{R} - \frac{1}{r}\right)\left(\frac{z}{h}\right)^K. \tag{1.2}$$

Here, R is the radius of curvature at the free surface and r is the radius of curvature at the channel bottom, whereas K is a parameter. Moreover, z is the distance measured from the bottom (curved or flat) (Fig. 1.6a, b). Using Eq. (1.2), Fawer obtained, with z_b denoting the channel bottom elevation, H the total energy head, $h_{xx} = \mathrm{d}^2h/\mathrm{d}x^2$ and $z_{bxx} = \mathrm{d}^2z_b/\mathrm{d}x^2$ the extended Bernoulli equation for flows over curved beds (Fig. 1.6b)

$$H = z_b + h + \frac{U^2}{2g}\left(1 + \frac{2hh_{xx}}{K+2} + hz_{bxx}\right). \tag{1.3}$$

The specific energy E in Fawer's theory is $H - z_b$. In his model, the energy loss is accounted for by the balance $\mathrm{d}H/\mathrm{d}x = -S_f$. Fawer is sometimes cited, using Jaeger (1949) as cross-reference, and it is erroneously believed that his work relates exclusively to horizontal channel bottoms (Castro-Orgaz 2010a). Chow (1959) correctly noted that Fawer's theory is different from Boussinesq's. Curvilinear streamline flows including the undular hydraulic jump or critical flow over round-crested weirs were first considered by Fawer (1937), who further classified curved flows over horizontal bottoms (Fig. 1.6c).

To compare Eq. (1.3) with Boussinesq's Eq. (1.1), the latter is written as two equations, namely

$$\frac{\mathrm{d}S}{\mathrm{d}x} = h\left(S_o - S_f\right), \tag{1.4a}$$

$$\begin{aligned}\frac{\mathrm{d}S}{\mathrm{d}x} &= \frac{U^2h^2}{g}\left(\frac{1}{3}\frac{\mathrm{d}^3h}{\mathrm{d}x^3} - \frac{1}{2}\frac{\mathrm{d}^2S_o}{\mathrm{d}x^2}\right) + \left(h - \beta\frac{U^2}{g}\right)\frac{\mathrm{d}h}{\mathrm{d}x} \\ &= \frac{q^2}{g}\left[\frac{\mathrm{d}}{\mathrm{d}x}\left(\frac{1}{3}\frac{\mathrm{d}^2h}{\mathrm{d}x^2}\right) - \frac{1}{2}\frac{\mathrm{d}}{\mathrm{d}x}\left(\frac{\mathrm{d}S_o}{\mathrm{d}x}\right)\right] + \underbrace{h\frac{\mathrm{d}h}{\mathrm{d}x}}_{\frac{1}{2}\frac{\mathrm{d}}{\mathrm{d}x}(h^2)} - \underbrace{\beta\frac{U^2}{g}\frac{\mathrm{d}h}{\mathrm{d}x}}_{-\beta\frac{q^2}{g}\frac{\mathrm{d}}{\mathrm{d}x}\left(\frac{1}{h}\right)} \\ &= \frac{\mathrm{d}}{\mathrm{d}x}\left\{\frac{q^2}{g}\left[\frac{1}{3}\frac{\mathrm{d}^2h}{\mathrm{d}x^2} - \frac{1}{2}\left(\frac{\mathrm{d}S_o}{\mathrm{d}x}\right) + \beta\left(\frac{1}{h}\right)\right] + \frac{h^2}{2}\right\}\end{aligned} \tag{1.4b}$$

in which $q = Uh = \text{const}$ has been used. Integration of this last equation is now trivial; setting $\beta = 1$, and identifying S_o with $-\partial z_b/\partial x$, one obtains

$$S = \frac{h^2}{2} + \frac{U^2h}{g}\left(1 + \frac{hh_{xx}}{3} + \frac{hz_{bxx}}{2}\right), \tag{1.5}$$

in which the subscript notation has now been used and the constant of integration has been set to zero.

Fawer first noted that the momentum and energy approaches generally yield different solutions for the free surface profile. He further considered the case $S_o = S_f = 0$ and obtained momentum conservation results using the Boussinesq approach, as is evident from Eq. (1.5), in contrast to his energy conservation solution. He also noted that zones of rapidly varied flows of high-energy dissipation, as, e.g., in the classical hydraulic jump, require a momentum conservation approach rather than his potential flow procedure. However, potential flows are correctly treated with the extended energy approach, in which the slope of the energy line is not accounted for. Equation (1.3) corresponds to the first extended

energy equation for free surface flows over curved bottoms. Matthew (1963) and Hager and Hutter (1984), in turn, obtained with a similar approach

$$H = z_b + h + \frac{U^2}{2g}\left(1 + \frac{2hh_{xx} - h_x^2}{3} + hz_{bxx} - z_{bx}h_x - z_{bx}^2\right). \tag{1.6}$$

Comparing Eqs. (1.6) and (1.3) reveals that Matthew's approach implies a linear variation of the streamline curvature ($K = 1$) but a nonzero variation of streamline inclination (accounted for by h_x and z_{bx}), which were not considered by Fawer. Equation (1.6) permits to study a variety of open-channel flows involving non-hydrostatic pressure, including solitary and cnoidal waves (Fig. 1.7), of which the existence is not explained based on the hydrostatic flow theory.

Consideration of the asymptotic behavior of a free surface flow to the normal depth requires inclusion of turbulent friction. Potential flow methods for the analysis of near-critical flows are limited to short reaches (Fawer 1937; Castro-Orgaz 2010b) in order for the horizontal energy-grade line assumption not to falsify the results unduly; yet in some cases, including the undular hydraulic jump, a potential flow solution is not adequate. The backwater approach of hydrostatic flows is well known to break down at the critical depth of a prismatic channel, where the singular point method does not apply (Montes 1998). Thus, a non-hydrostatic model allowing for turbulent friction simultaneously includes the computation of the transition of the field variables across the critical section and the asymptotic conditions at uniform flow. The original model developed by Serre (1953; Castro-Orgaz and Hager 2011b) following Boussinesq (1877) satisfies these requirements. Serre considered curvilinear, turbulent flows over constant bottom slope channels. He obtained for S and E, with E as the specific energy, the expressions

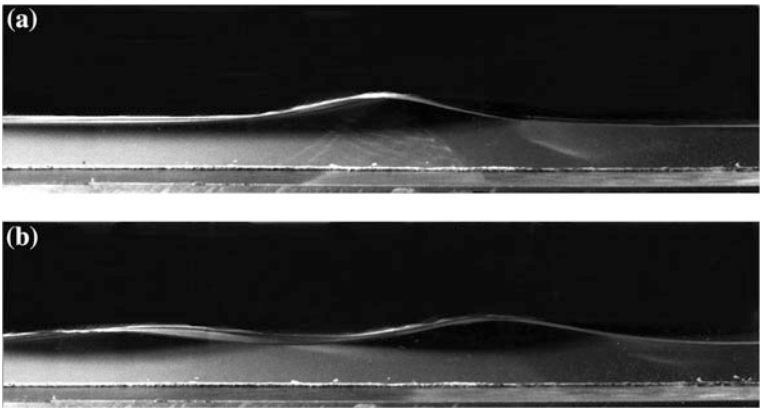

Fig. 1.7 **a** Solitary wave, **b** cnoidal wave, in a rectangular laboratory channel (*photograph* VAW, ETH Zurich)

$$S = \frac{h^2}{2} + \frac{U^2 h}{g}\left(1 + \frac{h h_{xx} - h_x^2}{3}\right), \tag{1.7}$$

$$E = h + \frac{U^2}{2g}\left(1 + \frac{2h h_{xx} - h_x^2}{3}\right). \tag{1.8}$$

The streamwise balances complement these by the statements

$$\frac{\mathrm{d}S}{\mathrm{d}x} = h\left(S_o - S_f\right), \tag{1.9}$$

$$\frac{\mathrm{d}E}{\mathrm{d}x} = \left(S_o - S_f\right). \tag{1.10}$$

Comparing Eqs. (1.8) and (1.3) for the horizontal channel bottom (z_b = 0), Serre's approach implies a linear variation of streamline curvature (K = 1), whereas the effect of streamline inclination (not accounted for by Fawer) was included by a linear relation. The same applies for S by comparing Eq. (1.7) with Eq. (1.5). Thus, Boussinesq (1877), Fawer (1937), and Serre (1953) set up energy and momentum approaches for steady curved flows. A special feature of Serre's work is his study of unsteady flow problems. His 1D unsteady equations for inviscid flows in horizontal channels are written in conservative form as (e.g., Serre 1953; Castro-Orgaz and Hager 2014)

$$\frac{\partial \mathbf{U}}{\partial t} + \frac{\partial \mathbf{F}}{\partial x} = 0. \tag{1.11}$$

Here, t is the time, $\mathbf{U}$ the vector of conserved variables, and $\mathbf{F}$ the flux vector, given by

$$\mathbf{U} = \begin{pmatrix} h \\ hU \end{pmatrix}, \quad \mathbf{F} = \begin{pmatrix} hU \\ gS \end{pmatrix}. \tag{1.12}$$

The momentum function for unsteady curvilinear flows (Serre 1953; Castro-Orgaz and Hager 2014) then takes the form

$$S = \frac{h^2}{2} + \frac{U^2 h}{g} + \left(U_x^2 - U U_{xx} - U_{xt}\right)\frac{h^3}{3g}. \tag{1.13}$$

A special feature of Serre's equations is their full nonlinearity. Peregrine (1966) obtained their simplified version for weak nonlinearity, written in non-conservative form, or primitive variables, as

$$\frac{\partial h}{\partial t} + \frac{\partial}{\partial x}(hU) = 0, \tag{1.14}$$

$$\frac{\partial U}{\partial t} + U\frac{\partial U}{\partial x} + g\frac{\partial h}{\partial x} = \frac{D^2}{3}\frac{\partial^3 U}{\partial x^2 \partial t}, \tag{1.15}$$

in which D is the still water depth. He was the first to integrate numerically Eqs. (1.14)–(1.15) using a finite-difference method for the undular bore, thereby producing a pioneering numerical solution of unsteady Boussinesq-type equations.

1.4 Non-hydrostatic Flows and Environmental Mechanics

The question may well be asked, why a non-hydrostatic flow theory is needed in environmental fluid flow problems, given the routinely used hydrostatic flow theory. Curvilinear streamlines frequently occur in geophysical flow processes, and these flows are fundamental at water control structures (Castro-Orgaz 2008) (Fig. 1.8). They are also relevant in weather forecasts, including atmospheric gravity waves resulting from density currents over mountains and valleys (Fig. 1.8b) (Zhu and Lawrence 1998). They further describe groundwater flows over curved bedrocks in hill slope hydrological problems (Chapman and Dressler 1984) (Fig. 1.8c), the development of sand waves (Bose and Dey 2009) (Fig. 1.8d), and solitary wave run-ups (Brocchini 2013) (Fig. 1.8e).

Therefore, the non-hydrostatic free surface flow theory is of wide applicability in geophysical fluid mechanics, and its consideration is of general interest. For all these applications, the non-hydrostatic velocity components (u, w) apply (Castro-Orgaz and Hager 2015). The changes from one application to another are the specific boundary conditions at the free surface and the bottom level. For example, the pressure at the free surface in a channel structure is set to zero, and the bottom is assumed to be rigid, whereas for an atmospheric current the density interface has a prescribed pressure forced by the air above, which is in geostrophic balance or is stagnant air. In bed-form evolution, the bed is erodible and should be coupled with Exner's sediment continuity equation. In groundwater flows, the bed is generally treated as impervious and the water table pressure is prescribed to be zero, but the velocity components are forced to obey Darcy's law as substitutives of the s- and n-momentum equations. For solitary wave run-up, the flow is unsteady so that both local and convective accelerations have to be accounted for.

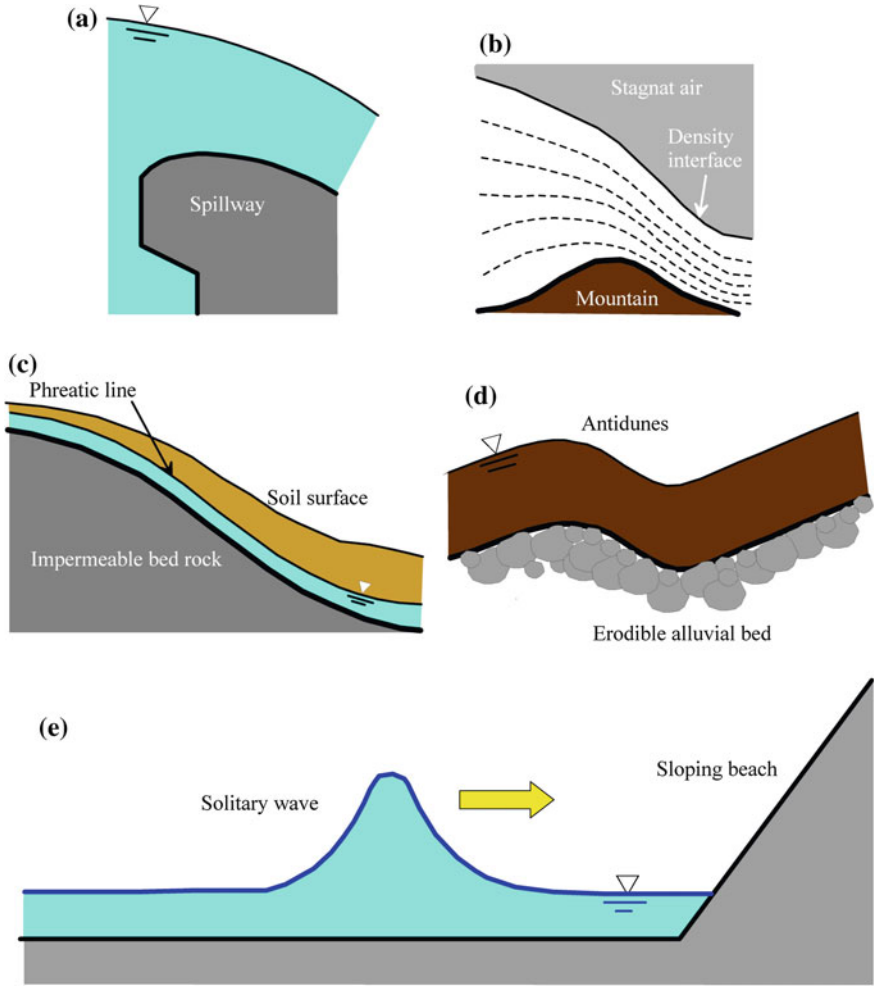

Fig. 1.8 Applications of curvilinear flow theory to **a** flood control structures, **b** atmospheric density currents, **c** groundwater flows over impermeable bedrock, **d** supercritical bed form in alluvial streams, **e** solitary wave run-up (adapted from Castro-Orgaz and Hager 2015)

1.5 Methodology

The purpose of this work is to present the theory and computation of non-hydrostatic free surface flows, including recent developments on irrotational flows, turbulent channel flows, boundary layers, seepage flows, and granular mass flows. The methodology of this book follows a hybrid approach combining experimental–numerical–analytical studies, so that all, or part of these components, are used to elucidate a particular phenomenon. For example, for flows over a

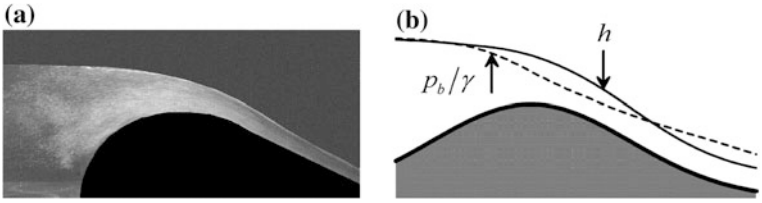

Fig. 1.9 Hybrid approach: **a** physical test of weir flow (*photograph* VAW, ETH Zurich), **b** numerical solution of weir flow, showing flow depth h and bottom pressure head p_b/γ profiles

round-crested weir, velocity and pressure fields are determined using physical experiments (Fig. 1.9a) (Hager 2010) or by a full numerical solution of the Laplace equation (Fig. 1.9b) (Montes 1998). The use of both approaches permits to set limits to 2D potential flow methods and allows for the investigation of the ranges of application of approximate analytical theories, including the approximate Boussinesq-type energy equation for potential flows given by Eq. (1.6) (Matthew 1963).

Further, it is necessary to define the flow depth in each open-channel flow problem. In this introductory chapter, no attempts have been made to accurately define the flow depth. However, in the forthcoming mathematical chapters three different definitions of flow depth arise, usually each associated with the selection of a different coordinate system to formulate the fluid flow equations. The *first* is the flow depth measured vertically, denoted as h (Fig. 1.10a); the *second* is the flow depth measured normally to the channel bottom, denoted as N (Fig. 1.10b); the *third* is the flow depth defined as the vertical projection of an equipotential curve,

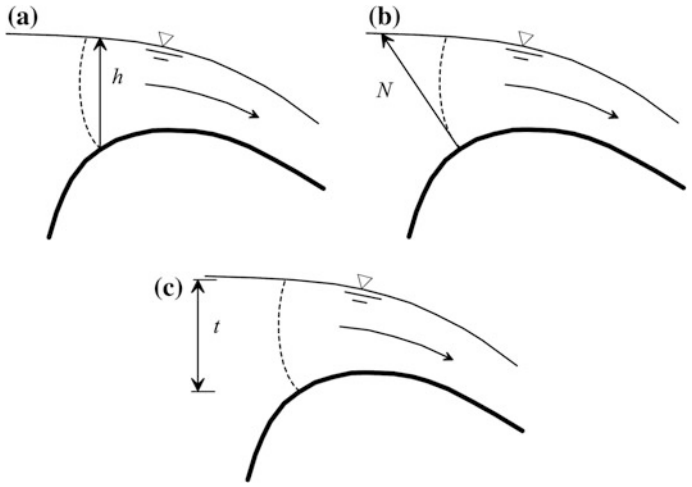

Fig. 1.10 Definition of flow depth in non-hydrostatic flows over curved and sloped bottoms **a** vertical, **b** normal to channel bottom, **c** as vertical projection of equipotential line. *Dashed* are equipotential curves of irrotational motion

t (Fig. 1.10c). This is important for the correct use and understanding of the corresponding theories.

References

Bakhmeteff, B. A. (1912). *O neravnomernom wwijenii jidkosti v otkrytom rusle* (*Varied flow in open channels*). Russia: St Petersburg (in Russian).

Bakhmeteff, B. A. (1932). *Hydraulics of open channels*. New York: McGraw-Hill.

Bélanger, J. B. (1828). *Essai sur la solution numérique de quelques problèmes relatifs au mouvement permanent des eaux courantes* (Essay on the numerical solution of some problems relative to the permanent movement of water flow). Paris: Carilian-Goeury (in French).

Bose, S. K., & Dey, S. (2009). Reynolds averaged theory of turbulent shear flows over undulating beds and formation of sand waves. *Physical Review E*, *80*(3), 036304-1/036304-9.

Boussinesq, J. (1877). *Essai sur la théorie des eaux courantes* (Essay on the theory of water flow). *Mémoires* présentés par divers Savants á l'Académie des Sciences, Paris, 23(1), 1–608 [in French].

Brocchini, M. (2013). A reasoned overview on Boussinesq-type models: The interpaly between physics, mathematics and numerics. *Proceedings of the Royal Society of London, Series A, 469*, 20130496.

Castro-Orgaz, O. (2008). Curvilinear flow over round-crested weirs. *Journal of Hydraulic Research, 46*(4), 543–547.

Castro-Orgaz, O. (2010a). Steady open channel flows with curved streamlines: The Fawer approach revised. *Environmental Fluid Mech., 10*(3), 297–310.

Castro-Orgaz, O. (2010b). Approximate modeling of 2D curvilinear open channel flows. *Journal of Hydraulic Research, 48*(2), 213–224.

Castro-Orgaz, O., & Hager, W. H. (2009). Classical hydraulic jump: Basic flow features. *Journal of Hydraulic Research, 47*(6), 744–754.

Castro-Orgaz, O., & Hager, W. H. (2011a). Spatially-varied open channel flow equations with vertical inertia. *Journal of Hydraulic Research, 49*(5), 667–675.

Castro-Orgaz, O., & Hager, W. H. (2011b). Joseph Boussinesq and his theory of water flow in open channels. *Journal of Hydraulic Research, 49*(5), 569–577.

Castro-Orgaz, O., & Hager, W. H. (2011c). Turbulent near-critical open channel flow: Serre's similarity theory. *Journal of Hydraulic Research, 137*(5), 497–503.

Castro-Orgaz, O., & Hager, W. H. (2014). 1D modelling of curvilinear free surface flow: Generalized Matthew theory. *Journal of Hydraulic Research, 52*(1), 14–23.

Castro-Orgaz, O., & Hager, W. H. (2015). Dressler's theory for curved topography flows: Iterative derivation, transcritical flow solutions and higher-order wave-type equations. *Environmental Fluid Mechanics* (in press).

Chanson, H. (2004). *The hydraulics of open channel flows: An introduction*. Oxford, UK: Butterworth-Heinemann.

Chapman, T. G., & Dressler, R. F. (1984). Unsteady shallow groundwater flow over a curved impermeable boundary. *Water Resources Research, 20*(10), 1427–1434.

Chaudhry, M. H. (2008). *Open-channel flow* (2nd ed.). New York: Springer.

Chow, V. T. (1959). *Open channel hydraulics*. New York: McGraw-Hill.

Dingemans, M. W. (1994). *Water wave propagation over uneven bottoms*. PhD dissertation, Technical University of Delft, Delft, the Netherlands.

Fawer, C. (1937). Etude de quelques écoulements permanents à filets courbes (Study of some steady flows with curved streamlines). *Thesis*, Université de Lausanne. Imprimérie La Concorde, Lausanne, Switzerland (in French).

Henderson, F. M. (1966). *Open channel flow*. New York: MacMillan.

Hager, W. H., & Hutter, K. (1984). Approximate treatment of plane channel flow. *Acta Mechanica, 51*(1–2), 31–48.

Hager, W. H. (2010). *Wastewater hydraulics: Theory and practice* (2nd ed.). New York: Springer.

Jaeger, C. (1949). *Technische Hydraulik* (Technical hydraulics). Birkhäuser, Basel (in German).

Jain, S. C. (2001). *Open channel flow*. New York: Wiley.

Liggett, J. A. (1994). *Fluid mechanics*. New York: McGraw-Hill.

Matthew, G. D. (1963). On the influence of curvature, surface tension and viscosity on flow over round-crested weirs. In *Proceedings of the Institution of Civil Engineers*, *London* 25, 511–524. Discussion: 1964, 28, 557–569.

Montes, J. S. (1998). *Hydraulics of open channel flow*. Reston, VA: ASCE.

Peregrine, D. H. (1966). Calculations of the development of an undular bore. *Journal of Fluid Mechanics, 25*, 321–330.

Russell, J. S. (1845, September). *Report on waves*. 14th Meeting of the British Association for the Advancement of Science, York (Vol. 1844, pp. 311–390).

Serre, F. (1953). Contribution à l'étude des écoulements permanents et variables dans les canaux (Contribution to the study of steady and varied channel flows). *La Houille Blanche*, *8*(6–7), 374–388; *8*(12), 830–887 (in French).

Sturm, T. W. (2001). *Open channel hydraulics*. New York: McGraw-Hill.

Zhu, D. Z., & Lawrence, G. A. (1998). Non-hydrostatic effects in layered shallow water flows. *Journal of Fluid Mechanics, 355*, 1–16.

Chapter 2
Vertically Integrated Non-hydrostatic Free Surface Flow Equations

Roman Symbols

a	Shallow water wave celerity based on enhanced gravity (m/s)
A	Finite volume area (m^2)
CFL	Courant–Friedrichs–Lewy number (–)
D	Representative particle diameter (m)
f	Weighting function (m)
$\mathbf{F}$	Vector of fluxes in x-direction (m^2/s, m^3/s^2)
$\mathbf{F}_{i+1/2}$	Numerical flux in x-direction at cell interface (m^2/s, m^3/s^2)
g	Gravity acceleration (m/s^2)
g'	Enhanced gravity acceleration (m/s^2)
$\mathbf{G}$	Vector of fluxes in y-direction (m^2/s, m^3/s^2)
h	Vertical flow depth (m)
h^*	Flow depth at star region in HLL Riemann solver (m)
H	Vertical length scale (m)
i	x-index for finite volume cell (–)
I	Auxiliary variable (m^2/s)
k	Time index (–)
K	Fawer exponent (–)
L	Horizontal length scale (m)
M	Momentum function (m^2)
n	Curvilinear coordinate normal to channel bottom (m) also bed porosity (–)
N	Flow depth normal to channel bottom (m)
p	Fluid pressure (N/m^2)
p_1	Bottom pressure in excess of hydrostatic pressure (N/m^2)
p_2	Midpressure in excess of pressure average at bottom and surface elevation (N/m^2)
q	Unit discharge (m^2/s)
q_b	Unit bed load (m^2/s)
q_x	Unit discharge in x-direction (m^2/s)
q_y	Unit discharge in y-direction (m^2/s)
q_K	Signal speed factor in HLL solver (–)
R	Submerged specific gravity (–)
R_{ep}	Particle Reynolds number (–)

© Springer International Publishing AG 2017

O. Castro-Orgaz and W.H. Hager, *Non-Hydrostatic Free Surface Flows*,
Advances in Geophysical and Environmental Mechanics and Mathematics
DOI 10.1007/978-3-319-47971-2_2

s Curvilinear coordinate along channel bed (m)
S_o Bottom slope (–)
S_f Friction slope (–)
S_L Speed of left signal in HLL Riemann solver (m/s)
S_R Speed of right signal in HLL Riemann solver (m/s)
$\mathbf{S}$ Vector of source terms (m/s, m^2/s^2)
t Time (s)
T_{ij} Depth-averaged Reynolds stress (N/m^2) with $(i, j) = (x, y)$
$\mathbf{T}$ Stress tensor (N/m^2)
u Velocity in x-direction (m/s)
$\mathbf{u}$ Depth-averaged velocity vector (m/s, m/s)
u_1 Velocity at surface in excess of mean (m/s)
U Depth-averaged flow velocity in x-direction (m/s)
$\mathbf{U}$ Vector of conserved variables (m, m^2/s)
v Velocity in y-direction (m/s)
V Depth-averaged flow velocity in y-direction also modulus of velocity (m/s)
w Velocity in z-direction (m/s)
$\bar{w}$ Depth-averaged flow velocity in z-direction (m/s)
w_2 Middepth vertical velocity in excess of average (m/s)
x Horizontal coordinate (m)
y Horizontal coordinate normal to x (m)
z Vertical coordinate (m)
z_b Bed elevation (m)

Greek Symbols

γ Specific weight of water (N/m^3)
γ_s Specific weight of solids (N/m^3)
ε Shallowness parameter (–)
η Vertical distance above channel bottom (m)
θ Angle of bottom with horizontal (rad)
κ Streamline curvature (m^{-1})
$\bar{\kappa}$ Depth-averaged streamline curvature (m^{-1})
λ Dispersive factor (–)
υ Kinematic viscosity (m^2/s)
ρ Density (kg/m^3)
σ_{ij} Turbulent Reynolds stress, with $(i, j) = (x, y, z)$ (N/m^2)
τ_b Boundary shear stress along bed in s-direction (N/m^2)
τ_{ij} Stress in continuum medium, with $(i, j) = (x, y, z)$ (N/m^2)
ω Weighting parameter (–)
Ω Control volume (m^3)

Subscripts

s Relative to free surface
b Relative to bottom
L Relative to left state in Riemann problem
R Relative to right state in Riemann problem

Superscripts

$*$ Relative to dimensionless quantity

2.1 Introduction

Practically, all gravity-driven flow models constitute the lowest order approximations of shallow flows, in which the horizontal length scales $[L]$ are substantially larger than the vertical length scales $[H]$ (Steffler and Jin 1993). The non-dimensional mass and momentum balance equations based on this anisotropic scaling indicate for basically horizontal flow that the vertical acceleration terms are small, with the aspect ratio $\varepsilon = [H]/[L] \rightarrow 0$, so that the vertical force balance is usually expressed as a hydrostatic pressure balance (Saint-Venant 1871; Friedrichs 1948; Liggett 1994). For a value of ε different from zero, the analogous scale analysis shows that the vertical acceleration term is important (Liggett 1994). In this case, the full vertical momentum equation must be preserved. This type of model is referred to as *Boussinesq-type model*, representing a vertically integrated system of conservation equations based on a finite ε value. It accounts for cases for which non-hydrostatic pressure distributions are relevant, including flows in hydraulic structures, sand waves in water–sediment flows, water wave motions and seepage flows, among others.

The production of a vertically integrated system of non-hydrostatic flow equations can be set up either in Cartesian or curvilinear coordinates following terrain. In a general curvilinear coordinate setting of gravity-driven flows, three types of accelerations may arise affecting the internal stress distribution of free surface flows. The first is the acceleration due to the real forces acting on the flow. The bed-normal component of this acceleration is what makes the key effect of the Boussinesq-type model. The second, actually not a real acceleration, manifests itself as an enhanced pressure due to the Christoffel symbols of the curvilinear coordinate setting and is often simply (but not correctly) referred to as centripetal acceleration. This contribution is accounted for in the well-known Dressler (1978) equations for open-channel flow. The third are the Coriolis, centripetal, and Euler accelerations because the earth-fixed frame is not inertial, routinely neglected in local shallow flow computations, but accounted for in many meteorological applications. The use of curvilinear coordinates increases the mathematical complexities of equations, so

that vertically integrated equations in a Cartesian system are used here to produce a non-hydrostatic system of conservation laws.

In the pioneering works of Boussinesq (1872, 1877) the non-hydrostatic effect was accounted for in a depth-averaged model formulated in a curvilinear setting, but Christoffel symbols were neglected (Castro-Orgaz and Hager 2011a). Serre (1953) and Castro-Orgaz and Hager (2011b) proposed a rigorous depth-averaged turbulent Boussinesq-type model for practical applications to both steady and unsteady water flows on sloping, straight-bottomed channels. Benjamin and Lighthill (1954) proposed a different theoretical treatment based on a third-order expansion of the stream function in a potential flow. The Application of the Boussinesq-type theory to hydraulic engineering[1] was successful in the description of flows over weirs, undular jumps, sand waves, Favre waves, dam breaks, overfalls, and slope breaks.

Castro-Orgaz et al. (2012, 2013) demonstrated that Boussinesq-type equations also describe free surface groundwater flows. The application of the Boussinesq theory to water wave motion was pursued by Peregrine (1966, 1967, 1972), who obtained depth-integrated inviscid Boussinesq equations in two horizontal dimensions presenting thereby the first numerical solution for undular bore propagation. He initiated the use of Boussinesq-type equations in coastal engineering. This work was followed by further improvements of the analysis of the dispersive wave characteristics of the Boussinesq system, developing accurate and robust numerical schemes and including real flow features such as wave breaking, vorticity effects, and turbulence.[2] Nowadays, the governing equations and numerical techniques are in a stage of development involving a large variety of water wave phenomena (Kim et al. 2009; Kim and Lynett 2011; Brocchini 2013). The application of the Boussinesq-theory to granular mass flows and geophysical problems is relatively new and was developed by Denlinger and Iverson (2004), Castro-Orgaz et al. (2015), and Hutter and Castro-Orgaz (2016).

In this chapter, the vertically integrated equations of the continuum mechanical balance laws of mass and momentum are presented as evolution equations for the velocity field and stress tensor following Castro-Orgaz et al. (2015). Boussinesq-type equations are obtained from the vertically integrated equations using Serre's (1953) theory. After suitable approximate representations for the

[1]Fawer (1937), Iwasa (1955, 1956), Iwasa and Kennedy (1968), Mandrup-Andersen (1975, 1978), Marchi (1963, 1992, 1993), Matthew (1963, 1991), Engelund and Hansen (1966), Basco (1983), Hager (1983), Hager and Hutter (1984a, b), Montes (1986), Berger and Carey (1998a, b), Soares-Frazão and Zech (2002), Mohapatra and Chaudhry (2004), Dewals et al. (2006), Bose and Dey (2007, 2009), Chaudhry (2008), Castro-Orgaz and Hager (2009), Denlinger and O'Connel (2008).

[2]Mei (1983), Antunes do Carmo et al. (1993), Nwogu (1993), Chen and Liu (1995), Wei et al. (1995), Wei and Kirby (1995), Madsen et al. (1997), Madsen and Schäffer (1998), Stansby and Zhou (1998), Chen et al. (1999, 2003), Kennedy et al. (2000), Lynett et al. (2002), Stansby (2003), Erduran et al. (2005), Musumeci et al. (2005), Lynett (2006), Chen (2006), Soares-Frazão and Guinot (2008), Mignot and Cienfuegos (2008), Kim et al. (2009), Kim and Lynett (2011), Brocchini (2013).

stress tensor, the emerging equations are applied to turbulent water flows in rivers, flows over steep slopes, water wave propagations, and flows over uneven topography. Movable beds and sediment transport are included, and suitable numerical techniques to solve unsteady and steady flow problems are discussed. Techniques to produce higher-order models are then further presented.

2.2 Vertically Integrated Equations in Continuum Mechanical Description

2.2.1 Basic Conservation Laws

Consider the flow of a continuum material of constant density ρ moving across a 3D terrain (Fig. 2.1), such as a fluidized granular mass. In a horizontal–vertical Cartesian system of reference (x, y, z), the terrain elevation is described by the function $z = z_b(x, y)$, and the velocity components in the (x, y, z) directions are, respectively (u, v, w). The motion is described within the framework of continuum mechanics with mass and momentum conservation equations (Savage and Hutter 1989; Iverson 1997; Andreotti et al. 2013). The mass conservation equation states

$$\frac{\partial u}{\partial x} + \frac{\partial v}{\partial y} + \frac{\partial w}{\partial z} = 0. \tag{2.1}$$

A vector field whose divergence vanishes is called solenoidal. Equation (2.1) is the mass balance for a *density-preserving* medium. This simplification is adopted

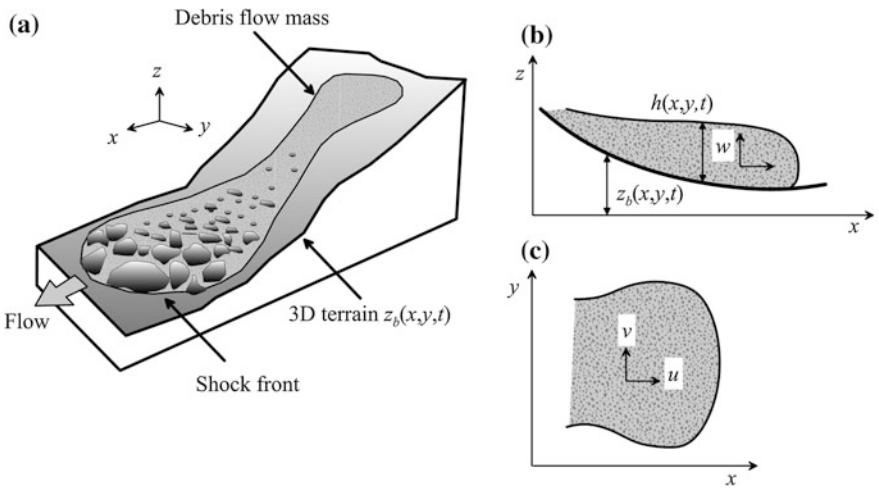

Fig. 2.1 Definition sketch for debris flow over 3D terrain **a** 3D view, **b** profile, **c** plan

here following Castro-Orgaz et al. (2015). The dynamic statement is Newton's second law, according to which the time rate of change of momentum equals the sum of the applied forces, given here by the stress divergence plus the gravity force. In horizontal–vertical Cartesian coordinates, the statement is with g as the acceleration due to gravity

$$\frac{\partial u}{\partial t}+u\frac{\partial u}{\partial x}+v\frac{\partial u}{\partial y}+w\frac{\partial u}{\partial z}=-\frac{1}{\rho}\left(\frac{\partial \tau_{xx}}{\partial x}+\frac{\partial \tau_{xy}}{\partial y}+\frac{\partial \tau_{xz}}{\partial z}\right), \tag{2.2}$$

$$\frac{\partial v}{\partial t}+u\frac{\partial v}{\partial x}+v\frac{\partial v}{\partial y}+w\frac{\partial v}{\partial z}=-\frac{1}{\rho}\left(\frac{\partial \tau_{yx}}{\partial x}+\frac{\partial \tau_{yy}}{\partial y}+\frac{\partial \tau_{yz}}{\partial z}\right), \tag{2.3}$$

$$\frac{\partial w}{\partial t}+u\frac{\partial w}{\partial x}+v\frac{\partial w}{\partial y}+w\frac{\partial w}{\partial z}=-\frac{1}{\rho}\left(\frac{\partial \tau_{zx}}{\partial x}+\frac{\partial \tau_{zy}}{\partial y}+\frac{\partial \tau_{zz}}{\partial z}\right)-g. \tag{2.4}$$

At this point, it should be noted that the stress tensor is symmetric, i.e., $\tau_{ij}=\tau_{ji,}$ $ij=1, 2, 3$, or (x, y, z). Moreover, τ_{ij} is here introduced with the notation used in the environmental contexts (e.g., Iverson 1997, 2005; Andreotti et al. 2013), i.e., it is the negative of the common stress tensor definition used in engineering. Equations (2.1)–(2.4) define mass and momentum conservations for single constituent bodies such as water; they also apply for a dry or fluidized granular mass (Fig. 2.2), under the restricted simplification of density preserving flow.

Equations (2.2)–(2.4) relate the kinematic fields (u, v, w) to an arbitrary stress tensor **T**. If solids are neglected and a time-averaging is performed, then **T** would describe the stress tensor of the Reynolds-Averaged Navier-Stokes (RANS) equations (Rodi 1980), used to model turbulent water flows (Hervouet 2007; Steffler and Jin 1993; Hutter and Jöhnk 2004). Furthermore, if the fluid is absent and the stress tensor is defined based on the Mohr–Coulomb model, the equations describe the motion of a dry granular flow (e.g., Savage and Hutter 1989; Iverson 1997, 2005; Pudasaini and Hutter 2007; Andreotti et al. 2013).

The unsteady three-dimensional (3D) non-hydrostatic numerical solutions of the RANS equations for free surface flows are not a routine matter (Hervouet 2007; Ma et al. 2012). Most of the 3D numerical solutions of non-hydrostatic flows solve a pressure Poisson equation for the dynamic pressure in finite element (Hervouet 2007) or finite volume (Ma et al. 2012) models. A simplified approach to reduce computational work as compared with 3D solutions is to vertically integrate Eqs. (2.1)–(2.4) to obtain vertically averaged variables as functions of only (x, y, t), thereby resulting in a spatially 2D computational scheme. In most practical cases, a depth-averaged computation gives enough information.[3] Thus, Eqs. (2.1)–(2.4)

[3]Examples in hydraulic engineering were studied by Boussinesq (1877), Yen (1973), Steffler and Jin (1993), Liggett (1994), Vreugdenhil (1994), Khan and Steffler (1996a, b), Jain (2001), whereas in rapid gravity-driven mass flows the scene has been set by Hutter and Savage (1988), Savage and Hutter (1989, 1991), Iverson (1997, 2005), Denlinger and Iverson (2004). For a review, see e.g., Pudasaini and Hutter (2007).

Fig. 2.2 Glacier moraines in Tuyk Valley, Alaarcha basin North Tien Shan, Kirgizstan (from unpublished lecture material on granular media by Prof. K. Hutter, Photograph by Prof. Aizen)

provide a general starting point to produce a family of vertically integrated models within the context of continuum mechanics, valid either for water, solid particles, or (solenoidal) mixture flows.

2.2.2 *Depth-Integrated Continuity Equation*

Let the Cartesian coordinates be horizontal (x, y) and vertical (z), against gravity (Fig. 2.1). Then, the mathematical procedure consists in vertically integrating the governing equations at an arbitrary (x, y)-position from z_b to z_s, where subscripts b and s, respectively, refer to the bed and the free surface. After vertical integration, Eq. (2.1) becomes

$$\int_{z_b}^{z_s} \left(\frac{\partial u}{\partial x} + \frac{\partial v}{\partial y} + \frac{\partial w}{\partial z} \right) \mathrm{d}z = 0. \tag{2.5}$$

Using Leibniz's rule (Yen 1973; Hutter and Jőhnk 2004), Eq. (2.5) is converted to

$$\frac{\partial}{\partial x}\int_{z_b}^{z_s} u\mathrm{d}z - u_s\frac{\partial z_s}{\partial x} + u_b\frac{\partial z_b}{\partial x} + \frac{\partial}{\partial y}\int_{z_b}^{z_s} v\mathrm{d}z - v_s\frac{\partial z_s}{\partial y} + v_b\frac{\partial z_b}{\partial y} + w_s - w_b = 0. \quad (2.6)$$

Joseph Valentin Boussinesq was born on March 15, 1842, at St. André-de-Sangonis, France, and passed away on February 19, 1929, in Paris. He was self-taught, starting his scientific writing in 1865. He thereby took into consideration during his long career all branches of mathematical physics except for electromagnetism. After having served as teacher at various colleges of France, he was appointed in 1873 lecturer at the University of Lille. In 1886, Boussinesq was appointed to the chair of mechanics at the famous Sorbonne University, Paris, taking over in 1896 as professor of mathematical physics at *Collège de France*.

Boussinesq's life work in hydraulics is outstanding but extremely hard to follow, given his complicated writing style. His colleagues Alfred A. Flamant (1839–1915) and Auguste Boulanger (1866–1923) were able to present in their books a more popular approach of Boussinesq's ideas. His 1872 paper explains the observations of solitary waves of John Scott Russell (1808–1882) from a physical perspective thereby overcoming the many attempts offered in the past decades. It was noted that many hydraulic phenomena could only be explained by inclusion of the streamline curvature effects. This paper particularly attracted the interest of Adhémar Barré de Saint-Venant (1797–1886), who in 1871 had published his famous paper on the shallow water equations, yet by assuming hydrostatic pressure and uniform velocity distributions. The monumental 1877 *Essay* of Boussinesq made his name definitely known to the hydraulics community given the large number of relevant problems discussed. In the 1880s, he started in addition a close collaboration with Henry Bazin (1829–1917) on weir flow features, for which streamline curvature effects again are significant. In hydraulics, this collaboration between the then best experimenter and scientist marked the start of engineering hydraulics, leading to the close relationship between scientists in mathematical physics and hydraulics in the twentieth century. The outstanding merits of Boussinesq were awarded by his nomination to the mechanics chair at Sorbonne, taking over the chair of his intimate colleague de Saint-Venant.

As to the kinematic boundary conditions, the movement of the material free surface is described by

$$\frac{\partial z_s}{\partial t} + u_s \frac{\partial z_s}{\partial x} + v_s \frac{\partial z_s}{\partial y} - w_s = 0. \tag{2.7}$$

Similarly, the kinematic equation at the movable material bed surface takes the form

$$\frac{\partial z_b}{\partial t} + u_b \frac{\partial z_b}{\partial x} + v_b \frac{\partial z_b}{\partial y} - w_b = 0, \tag{2.8}$$

where a slip velocity at the bed is allowed in depth-averaged modelling. Inserting Eqs. (2.7) and (2.8) into Eq. (2.6) produces with the vertical flow depth given by $h = h(x, y, t) = z_s(x, y, t) - z_b(x, y, t)$ (Fig. 2.1)

$$\frac{\partial h}{\partial t} + \frac{\partial q_x}{\partial x} + \frac{\partial q_y}{\partial y} = 0. \tag{2.9}$$

Equation (2.9) states the general depth-integrated mass (or here volume) conservation subjected to a density preserving body and material free and basal surfaces. The integrals in Eq. (2.9) are the fluxes q_x and q_y in the (x, y) directions given by

$$q_x = \int_{z_b}^{z_s} u \mathrm{d}z, \quad q_y = \int_{z_b}^{z_s} v \mathrm{d}z. \tag{2.10}$$

2.2.3 *Depth-Integrated Momentum Equations in Horizontal Plane*

Integrating Eq. (2.2) over the depth yields

$$\int_{z_b}^{z_s} \left(\frac{\partial u}{\partial t} + u \frac{\partial u}{\partial x} + v \frac{\partial u}{\partial y} + w \frac{\partial u}{\partial z} \right) \mathrm{d}z = \int_{z_b}^{z_s} -\frac{1}{\rho} \left(\frac{\partial \tau_{xx}}{\partial x} + \frac{\partial \tau_{xz}}{\partial z} + \frac{\partial \tau_{xy}}{\partial y} \right) \mathrm{d}z. \tag{2.11}$$

The acceleration term on the left-hand side of Eq. (2.11) is rewritten as

$$\frac{\partial u}{\partial t}+u\frac{\partial u}{\partial x}+v\frac{\partial u}{\partial y}+w\frac{\partial u}{\partial z}=\frac{\partial u}{\partial t}+\frac{1}{2}\frac{\partial u^2}{\partial x}+\frac{\partial (uv)}{\partial y}+\frac{\partial (uw)}{\partial z}-u\left(\frac{\partial w}{\partial z}+\frac{\partial v}{\partial y}\right), \tag{2.12}$$

or with the aid of Eq. (2.1),

$$\frac{\partial u}{\partial t}+u\frac{\partial u}{\partial x}+v\frac{\partial u}{\partial y}+w\frac{\partial u}{\partial z}=\frac{\partial u}{\partial t}+\frac{\partial u^2}{\partial x}+\frac{\partial (uv)}{\partial y}+\frac{\partial (uw)}{\partial z}. \tag{2.13}$$

Inserting Eq. (2.13) into Eq. (2.11), applying the Leibniz rule, and using Eqs. (2.7) and (2.8), the vertically integrated momentum equation in the x-direction takes the form

$$\frac{\partial}{\partial t}\int_{z_b}^{z_s} u\mathrm{d}z+\frac{\partial}{\partial x}\int_{z_b}^{z_s} u^2\mathrm{d}z+\frac{\partial}{\partial y}\int_{z_b}^{z_s} uv\mathrm{d}z=-\frac{1}{\rho}\left[\frac{\partial}{\partial x}\int_{z_b}^{z_s}\tau_{xx}\mathrm{d}z+\frac{\partial}{\partial y}\int_{z_b}^{z_s}\tau_{xy}\mathrm{d}z+(\tau_{xx})_b\frac{\partial z_b}{\partial x}+(\tau_{xy})_b\frac{\partial z_b}{\partial y}-(\tau_{xz})_b\right]. \tag{2.14}$$

Here, all stresses at the free surface have been assumed to vanish, that is, atmospheric pressure and wind shear stress are ignored. Likewise, the depth-integrated momentum equation in the y-direction is written as

$$\frac{\partial}{\partial t}\int_{z_b}^{z_s} v\mathrm{d}z+\frac{\partial}{\partial y}\int_{z_b}^{z_s} v^2\mathrm{d}z+\frac{\partial}{\partial x}\int_{z_b}^{z_s} uv\mathrm{d}z=-\frac{1}{\rho}\left[\frac{\partial}{\partial y}\int_{z_b}^{z_s}\tau_{yy}\mathrm{d}z+\frac{\partial}{\partial x}\int_{z_b}^{z_s}\tau_{xy}\mathrm{d}z+(\tau_{yy})_b\frac{\partial z_b}{\partial y}+(\tau_{xy})_b\frac{\partial z_b}{\partial x}-(\tau_{yz})_b\right]. \tag{2.15}$$

The set of Eqs. (2.14) and (2.15) describes flows with reference to the (x, y) plane. The particular case of 1D turbulent water motion in the x-direction was presented by Steffler and Jin (1993). An approximation to the kinematic field (u, v, w) and parameterizations of the stress tensor $\mathbf{T}$ are required to produce a mathematically closed model.

2.2.4 *Non-hydrostatic Stresses in z-Direction and Vertical Velocity Profile*

The integration of the vertical momentum equation is similar to the deduction of the system (2.14) and (2.15). To be able to account for the non-hydrostatic stress distribution, start with the integral relation between an arbitrary elevation and the free surface; from Eq. (2.4),

$$\int_z^{z_s}\left(\frac{\partial w}{\partial t}+\frac{\partial w^2}{\partial z}+\frac{\partial (wu)}{\partial x}+\frac{\partial (wv)}{\partial y}\right)\mathrm{d}z'=\int_z^{z_s}-\frac{1}{\rho}\left(\frac{\partial \tau_{zz}}{\partial z}+\frac{\partial \tau_{zx}}{\partial x}+\frac{\partial \tau_{zy}}{\partial y}+\rho g\right)\mathrm{d}z'. \tag{2.16}$$

Using the Leibniz rule on the left-hand side (LHS) of Eq. (2.16) yields, after adding the free surface kinematic boundary condition given by Eq. (2.7),

$$\begin{aligned}&\frac{\partial}{\partial t}\int_z^{z_s} w\mathrm{d}z'-w_s\frac{\partial z_s}{\partial t}+\frac{\partial}{\partial x}\int_z^{z_s} wu\mathrm{d}z'-w_s u_s\frac{\partial z_s}{\partial x}+\frac{\partial}{\partial y}\int_z^{z_s} wv\mathrm{d}z'-w_s v_s\frac{\partial z_s}{\partial y}+w_s^2-w^2\\&=\frac{\partial}{\partial t}\int_z^{z_s} w\mathrm{d}z'+\frac{\partial}{\partial x}\int_z^{z_s} wu\mathrm{d}z'+\frac{\partial}{\partial y}\int_z^{z_s} wv\mathrm{d}z'-w^2.\end{aligned} \tag{2.17}$$

Integrating the right-hand side (RHS) of Eq. (2.16) yields

$$\begin{aligned}\int_z^{z_s}-\frac{1}{\rho}\left(\frac{\partial \tau_{zz}}{\partial z}+\frac{\partial \tau_{zx}}{\partial x}+\frac{\partial \tau_{zy}}{\partial y}+\rho g\right)\mathrm{d}z'&=\frac{1}{\rho}\left[\tau_{zz}(z)-\tau_{zz}(z_s)\right]-g(z_s-z)\\&\quad-\frac{1}{\rho}\int_z^{z_s}\left(\frac{\partial \tau_{zx}}{\partial x}+\frac{\partial \tau_{zy}}{\partial y}\right)\mathrm{d}z'.\end{aligned} \tag{2.18}$$

Using the identities given by Eqs. (2.17) and (2.18) generates the general equation for the non-hydrostatic stresses as follows

$$\begin{aligned}\tau_{zz}(z)=\tau_{zz}(z_s)+\rho g(z_s-z)-\rho w^2+\rho\frac{\partial}{\partial t}\int_z^{z_s} w\mathrm{d}z'+\rho\frac{\partial}{\partial x}\int_z^{z_s} wu\mathrm{d}z'+\rho\frac{\partial}{\partial y}\int_z^{z_s} wv\mathrm{d}z'\\+\int_z^{z_s}\left(\frac{\partial \tau_{zy}}{\partial y}+\frac{\partial \tau_{zx}}{\partial x}\right)\mathrm{d}z'.\end{aligned} \tag{2.19}$$

As usual, a vanishing traction on the material surface implies $\tau_{zz}(z_s) = 0$. This equation describes the general distribution of τ_{zz} in the z-direction as a function of the vertical velocity w, the horizontal velocities u and v, and the indicated stresses (last term on the RHS). The equation is general allowing for a systematic development of the depth-averaged equations. By contrast, if Eq. (2.16) is integrated from $z = z_b$ to $z = z_s$, then an equation for the bed vertical normal stress is obtained

$$(\tau_{zz})_b = \rho g h + \rho \frac{\partial}{\partial t}\int_{z_b}^{z_s} w\mathrm{d}z + \rho \frac{\partial}{\partial x}\int_{z_b}^{z_s} wu\mathrm{d}z + \rho \frac{\partial}{\partial y}\int_{z_b}^{z_s} wv\mathrm{d}z + \frac{\partial}{\partial x}\int_{z_b}^{z_s} \tau_{zx}\mathrm{d}z + \frac{\partial}{\partial y}\int_{z_b}^{z_s} \tau_{zy}\mathrm{d}z + (\tau_{zx})_b\frac{\partial z_b}{\partial x} + (\tau_{zy})_b\frac{\partial z_b}{\partial y}, \tag{2.20}$$

in which vanishing surface traction, implying $(\tau_{xz})_s = (\tau_{yz})_s = 0$, has been implemented. Note that the bed stress differs in general from the gravity force term ($\rho g h$). Deviations of $(\tau_{zz})_b$ from the static weight ($\rho g h$) stem from streamline curvature, e.g., convective vertical acceleration terms related to $\partial w/\partial x$ and $\partial w/\partial y$, local vertical acceleration $\partial w/\partial t$, and stress contributions. Therefore, the Saint-Venant theory does not apply for steep and curved terrain.

Knowledge of the vertical velocity profile $w(z)$ is necessary in Eq. (2.20). To this end, integrating Eq. (2.1) between z_b and an arbitrary elevation z yields

$$\int_{z_b}^{z}\left(\frac{\partial u}{\partial x} + \frac{\partial v}{\partial y} + \frac{\partial w}{\partial z}\right)\mathrm{d}z' = 0, \tag{2.21}$$

or

$$w(z) - w(z_b) = -\int_{z_b}^{z}\left(\frac{\partial u}{\partial x} + \frac{\partial v}{\partial y}\right)\mathrm{d}z'. \tag{2.22}$$

Using again the Leibniz rule transforms this into

$$w(z) - w(z_b) = -\left[\frac{\partial}{\partial x}\int_{z_b}^{z} u\mathrm{d}z' + \frac{\partial}{\partial y}\int_{z_b}^{z} v\mathrm{d}z' + u_b\frac{\partial z_b}{\partial x} + v_b\frac{\partial z_b}{\partial y}\right]. \tag{2.23}$$

With the kinematic boundary condition at $z = z_b$, stated by Eq. (2.8), gives

$$w(z) = \frac{\partial z_b}{\partial t} - \left[\frac{\partial}{\partial x}\int_{z_b}^{z} u\mathrm{d}z' + \frac{\partial}{\partial y}\int_{z_b}^{z} v\mathrm{d}z'\right]. \tag{2.24}$$

The result for a rigid basal surface ($\partial z_b/\partial t = 0$) is, therefore,

$$w(z) = -\left[\frac{\partial}{\partial x}\int_{z_b}^{z} u\mathrm{d}z' + \frac{\partial}{\partial y}\int_{z_b}^{z} v\mathrm{d}z'\right]. \tag{2.25}$$

It reveals that once any functional representations for u and v are introduced, w is determined by a simple mass (volume) conservation balance. This avoids the use of an independent function of w, given that it is linked to u and v. Equation (2.25) inserted into Eq. (2.19) mathematically eliminates the dependence of τ_{zz} on w.

2.3 Shallow Flow Approximation and Depth-Averaged Equations

If the vertical thickness $h(x, y, t)$ of a nearly horizontal flow is smaller than the characteristic length in the (x, y) plane, a scaling analysis reveals that, with the exception of the near-bed boundary layer, the velocity components u and v can be assumed to be constant across the depth h, equal to their depth-averaged values U and V (Liggett 1994). Therefore,

$$u(x, y, z, t) \approx U(x, y, t) = \frac{1}{h} \int_{z_b}^{z_s} u \mathrm{d}z, \tag{2.26}$$

$$v(x, y, z, t) \approx V(x, y, t) = \frac{1}{h} \int_{z_b}^{z_s} v \mathrm{d}z. \tag{2.27}$$

This approach permits to obtain the non-hydrostatic equations, first derived by Serre (1953). At the limit, as the aspect ratio $\varepsilon \to 0$, the Saint-Venant hydrostatic theory is regained (Friedrichs 1948). The depth-independent horizontal velocity components imply a slip velocity at the bed, thereby neglecting the high velocity gradient confined to the thin bed boundary layer (Steffler and Jin 1993). This approximation for u and v will also be adopted for flows on steep terrain, given the small contribution of the differential advection originating from the non-uniformity of u and v with depth. Therefore, the Boussinesq velocity correction coefficients in the x- and y-directions are close to unity, so that their impact on the momentum balance projected in the corresponding axis is negligible.

Inserting Eqs. (2.26) and (2.27) into Eqs. (2.14) and (2.15) yields

$$\begin{aligned} &\frac{\partial}{\partial t}(Uh) + \frac{\partial}{\partial x}\left(U^2 h\right) + \frac{\partial}{\partial y}(UVh) \\ &= -\frac{1}{\rho}\left[\frac{\partial}{\partial x}\int_{z_b}^{z_s} \tau_{xx}\mathrm{d}z + \frac{\partial}{\partial y}\int_{z_b}^{z_s} \tau_{xy}\mathrm{d}z + (\tau_{xx})_b \frac{\partial z_b}{\partial x} + (\tau_{xy})_b \frac{\partial z_b}{\partial y} - (\tau_{xz})_b\right], \end{aligned} \tag{2.28}$$

$$\frac{\partial}{\partial t}(Vh)+\frac{\partial}{\partial y}\left(V^2h\right)+\frac{\partial}{\partial x}(VUh)$$
$$=-\frac{1}{\rho}\left[\frac{\partial}{\partial y}\int_{z_b}^{z_s}\tau_{yy}\mathrm{d}z+\frac{\partial}{\partial x}\int_{z_b}^{z_s}\tau_{xy}\mathrm{d}z+\left(\tau_{yy}\right)_b\frac{\partial z_b}{\partial y}+\left(\tau_{xy}\right)_b\frac{\partial z_b}{\partial x}-\left(\tau_{yz}\right)_b\right]. \tag{2.29}$$

The assumption of depth-independent horizontal velocity components automatically yields for the linear vertical velocity profile, from Eq. (2.25),

$$w(x,y,z)=-\left[\frac{\partial}{\partial x}[U(z-z_b)]+\frac{\partial}{\partial y}[V(z-z_b)]\right]. \tag{2.30}$$

With $\eta = z - z_b$ and $h = z_s - z_b$, the vertical stress (pressure) in Eq. (2.19) is then given by

$$\tau_{zz}=\rho g(h-\eta)-\rho w^2+\rho\frac{\partial}{\partial t}\int_z^{z_s}w\mathrm{d}z'+\rho\frac{\partial}{\partial x}\left[U\int_z^{z_s}w\mathrm{d}z'\right]$$
$$+\rho\frac{\partial}{\partial y}\left[V\int_z^{z_s}w\mathrm{d}z'\right]+\int_z^{z_s}\left(\frac{\partial\tau_{zy}}{\partial y}+\frac{\partial\tau_{zx}}{\partial x}\right)\mathrm{d}z'. \tag{2.31}$$

Here, the vertical velocity field w is expressed as $w = w(U, V)$, according to Eq. (2.30).

With the definitions (2.26), (2.27), the depth-integrated mass conservation equation (2.9) takes the form

$$\frac{\partial h}{\partial t}+\frac{\partial(Uh)}{\partial x}+\frac{\partial(Vh)}{\partial y}=0. \tag{2.32}$$

Nothing specific is yet assumed on the stress tensor $\mathbf{T}$, so that the system of equations applies to solids, fluids, and any other material behavior of a continuous body.

Equations (2.28), (2.29), and (2.32) can be expressed in general conservative form as

$$\frac{\partial\mathbf{U}}{\partial t}+\frac{\partial\mathbf{F}}{\partial x}+\frac{\partial\mathbf{G}}{\partial y}=\mathbf{S}, \tag{2.33}$$

in which the vector of dependent variables is $\mathbf{U}$, the vector of fluxes in the x-direction is $\mathbf{F}$, that in the y-direction is $\mathbf{G}$, and $\mathbf{S}$ is the source term vector, defined by

$$\mathbf{U} = \begin{pmatrix} h \\ Uh \\ Vh \end{pmatrix}, \quad \mathbf{F} = \begin{pmatrix} Uh \\ U^2h + \frac{1}{\rho}\int_{z_b}^{z_s} \tau_{xx} \mathrm{d}z \\ UVh + \frac{1}{\rho}\int_{z_b}^{z_s} \tau_{xy} \mathrm{d}z \end{pmatrix}, \quad \mathbf{G} = \begin{pmatrix} Vh \\ VUh + \frac{1}{\rho}\int_{z_b}^{z_s} \tau_{xy} \mathrm{d}z \\ V^2h + \frac{1}{\rho}\int_{z_b}^{z_s} \tau_{yy} \mathrm{d}z \end{pmatrix},$$

$$\mathbf{S} = -\frac{1}{\rho}\begin{pmatrix} 0 \\ (\tau_{xx})_b \frac{\partial z_b}{\partial x} + (\tau_{xy})_b \frac{\partial z_b}{\partial y} - (\tau_{xz})_b \\ (\tau_{yy})_b \frac{\partial z_b}{\partial y} + (\tau_{xy})_b \frac{\partial z_b}{\partial x} - (\tau_{yz})_b \end{pmatrix}. \tag{2.34}$$

Equations (2.30) and (2.31) can also be transformed to a 2D vector notation (Peregrine 1967; Kim et al. 2009). To this end, let I be the auxiliary variable

$$I = \int_z^{z_s} w(x, y, z) \mathrm{d}z', \tag{2.35}$$

and let the depth-averaged velocity vector $\mathbf{U}$ be defined by

$$\mathbf{u} = \begin{pmatrix} U \\ V \end{pmatrix}. \tag{2.36}$$

The vertical velocity, as stated in Eq. (2.30), may then be rewritten as

$$w = -\nabla \cdot [\mathbf{u}(z - z_b)], \tag{2.37}$$

in which ∇ is the 2D Nabla operator defined by

$$\nabla = \left(\frac{\partial}{\partial x}, \frac{\partial}{\partial y}\right). \tag{2.38}$$

Inserting Eq. (2.37) into Eq. (2.35) leads, after integration, to

$$I = -\nabla \cdot \left[\mathbf{u}\frac{(h^2 - \eta^2)}{2}\right] + h[\mathbf{u} \cdot \nabla(h + z_b)]. \tag{2.39}$$

With this, Eq. (2.31) is rewritten as

$$\tau_{zz} = \rho g(h - \eta) + \rho \frac{\partial I}{\partial t} + \rho \nabla \cdot (I\mathbf{u}) - \rho w^2 + \int_z^{z_s} \left(\frac{\partial \tau_{zy}}{\partial y} + \frac{\partial \tau_{zx}}{\partial x}\right) \mathrm{d}z'. \tag{2.40}$$

Equations (2.39) and (2.40) constitute the fundamental relations for modeling non-hydrostatic effects in depth-averaged models.

A scaling analysis reveals the importance of retaining w in vertically integrated models over steep terrain. Let $[x]$, $[y] = L$ and $[z] = H$ be horizontal and vertical scales in the Cartesian system of reference (x, y, z). Similarly, also introducing the velocity scales $[u]$, $[v]$, $[w]$ for the horizontal ($[u]$, $[v]$) and vertical ($[w]$) velocity components, the space and velocity scale ratios are defined as

$$\frac{[w]}{[u]} = \frac{[w]}{[v]} = \varepsilon_{vel}, \quad \frac{[z]}{[x]} = \frac{[z]}{[y]} = \frac{H}{L} = \varepsilon_{spatial}. \tag{2.41}$$

Requesting the perseverance of the solenoidicity of the velocity field $[\mathrm{div}(\mathbf{V}) = 0]$ by scaling then implies

$$\frac{[w]}{[u]} = \frac{[w]}{[v]} = \frac{H}{L} = \varepsilon, \quad \text{or} \quad \varepsilon_{spatial} = \varepsilon_{vel} = \varepsilon. \tag{2.42}$$

With the velocity scaling $[u] = (gL)^{1/2}$ and the time scaling $[t] = (L/g)^{1/2}$, one also readily deduces

$$\frac{[\mathrm{d}w]}{[\mathrm{d}t]} = \varepsilon(Lg)^{1/2}(g/L)^{1/2} = \varepsilon g. \tag{2.43}$$

For $\varepsilon \ll 1$, this result suggests that the vertical acceleration is asymptotically small as compared with g. Else, the hydrostatic pressure assumption is invalid and vertical accelerations must be accounted for. The above expressions for $[u]$ and $[t]$ automatically imply that gravity is important in the dimensionless mathematical description of the processes to be studied. Incidentally, the expressions for $[u]$ and $[t]$ differ from those of the shallow water equations (Friedrichs 1948); $[u]$ and $[t]$ would in those equations be scaled with H and not with L.

If the Cartesian coordinate system is now (s, n), inclined by angle θ, then $[\mathrm{d}w_n/\mathrm{d}t] = g\varepsilon\cos\theta$, and with isotropic scaling ($\varepsilon = 1$) the bed normal acceleration w_n may be ignored for rapid gravity-driven flows on steep mountain slopes (as $\cos\theta$ is small). As an illustrative example, consider the simplest case of uniform flow down a steep slope (Fig. 2.3). In the curvilinear coordinates (s, n) following the terrain, the velocity is $U_s = q/N$, whereas the velocity in the n-direction is zero, with q as the discharge and N the flow thickness measured normal to the bed. Consider now the horizontal–vertical Cartesian coordinates (x, z). The depth-averaged velocity in the x-direction reads $U_s = q/h$, with h as the vertical flow depth. From the bed kinematic boundary condition, the vertical velocity in the z-direction is $w = U\partial z_b/\partial x$.

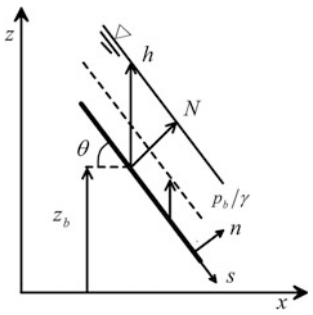

Fig. 2.3 Uniform flow on a steep slope, highlighting differences between free surface flow depth h (gauge-measured, *solid line*), N (perpendicular to bottom), and (*dashed lines*) bottom pressure head p_b/γ (x) where $\gamma = \rho g$

The absolute velocity is then $V = (u^2 + w^2)^{1/2} = U(1 + \tan\theta^2)^{1/2}$. From Fig. 2.3, $N = h\cos\theta$, leading to $V = q/N$, which is identical to U_s. While in (s, n) coordinates, only U_s is non zero, u and w are of similar order of magnitude in horizontal–vertical Cartesian coordinates (x, z). For example, on a steep slope of $\theta = 45°$, $u = w = q/h$.

2.4 Simplified Forms of Non-hydrostatic Extended Flow Equations

2.4.1 RANS Model for River Flow

River flows are usually modeled using a depth-averaged model based on the Reynolds-Averaged Navier–Stokes (RANS) equations. Stresses are then made up of viscous and turbulent contributions. If the vertical velocity is neglected, then the flux vectors reduce to (Rodi 1980; Molls and Chaudhry 1995)

$$\mathbf{F} = \begin{pmatrix} Uh \\ U^2h + \frac{gh^2}{2} + \frac{1}{\rho}hT_{xx} \\ UVh + \frac{1}{\rho}hT_{xy} \end{pmatrix}, \quad \mathbf{G} = \begin{pmatrix} Vh \\ VUh + \frac{1}{\rho}hT_{xy} \\ V^2h + \frac{gh^2}{2} + \frac{1}{\rho}hT_{yy} \end{pmatrix}. \tag{2.44}$$

In these expressions, the hydrostatic pressure term has been substituted and the laminar viscous stress contributions are generally ignored. In that case, T_{xx}, T_{yy}, and T_{xy} are the depth-averaged turbulent stresses. These are determined by coupling an auxiliary turbulence system, e.g., the depth-averaged k-ε model, or simply by using a constant eddy viscosity (Molls and Chaudhry 1995). If turbulent stresses are neglected, the system reduces to the classical 2D Saint-Venant equations (Liggett 1994; Vreugdenhil 1994).

2.4.2 One-Dimensional Water Waves Over Horizontal Topography

Consider the inviscid unsteady water wave propagation in a horizontal channel ($z_b = 0$) (Peregrine 1967, 1972), for which $\tau_{xx} = \tau_{zz} = p$ is the water pressure. Ignoring the last stress term on the RHS, Eq. (2.19) becomes

$$p(z) = \rho g(h-\eta) - \rho w^2 + \rho \frac{\partial}{\partial t}\int_z^{z_s} w\mathrm{d}z' + \rho \frac{\partial}{\partial x}\int_z^{z_s} wu\mathrm{d}z' + \rho \frac{\partial}{\partial y}\int_z^{z_s} wv\mathrm{d}z'. \quad (2.45)$$

This is the general equation as developed by Nwogu (1993) for 2D water waves. Consider the depth-averaged approach for 1D flows, for which Eqs. (2.37) and (2.39) reduce to

$$w = -\eta \frac{\partial U}{\partial x}, \quad I = -\frac{\partial U}{\partial x}\frac{(h^2-\eta^2)}{2}. \quad (2.46)$$

Inserting these expressions into Eq. (2.45) yields a parabolic pressure distribution p consisting of a hydrostatic term plus a quadratic dynamic correction including derivatives U_{xx}, U_x^2, and U_{xt} as

$$\frac{p}{\rho} = g(h-\eta) + \left(U_x^2 - U_{xt} - UU_{xx}\right)\frac{(h^2-\eta^2)}{2}. \quad (2.47)$$

Subscripts indicate, as above, partial differentiations with respect to the indicated variables. Equation (2.33) then simplifies to

$$\frac{\partial \mathbf{U}}{\partial t} + \frac{\partial \mathbf{F}}{\partial x} = \mathbf{0}, \quad \mathbf{U} = \begin{pmatrix} h \\ Uh \end{pmatrix}, \quad \mathbf{F} = \begin{pmatrix} Uh \\ M \end{pmatrix}, \quad M = U^2 h + \frac{1}{\rho}\int_{z_b}^{z_s} p\mathrm{d}z. \quad (2.48)$$

In the free surface hydraulics literature (Montes 1998; Jain 2001), M is referred to as the momentum function, namely

$$M = \underbrace{g\frac{h^2}{2} + U^2 h}_{\text{Saint-Venant term}} + \underbrace{\left(U_x^2 - U_{xt} - UU_{xx}\right)\frac{h^3}{3}}_{\text{non-hydrostatic term}}. \quad (2.49)$$

Dennis Howell Peregrine was born on December 30, 1938, at Birkenhead, UK, and passed away at age 69 on March 29, 2007, at Bristol, UK. He joined the Mathematics Department of Bristol University in 1964, following his undergraduate and postgraduate training at Oxford and Cambridge Universities. He became member of a small but strong group of applied mathematicians in fluid dynamics then headed by Leslie Howarth (1911–2001). Up to his death, Peregrine played a key role in maintaining and promoting the study of fluids thereby ensuring that Bristol University remained one of the British centers of excellence in this discipline.

Peregrine's knowledge in the subject of water waves was encyclopedic. He concerned himself with their generation, propagation, and run-up, including their impact on coastal structures. His contributions are reflected in numerous publications among which his 1966 paper in the Journal of Fluid Mechanics (JFM) on the shallow water wave theory is particularly notable. More results that are recent include extremely high wave impact forces, including tsunami waves. The breaking of water waves is still under intense research, particularly as regards the energy dissipation process, the entrainment of air and sediment, and the generation of turbulence. Peregrine had a well-developed physical insight and skill in mathematical modeling. In addition, he served as associate editor of the JFM, where he processed an average of 50 research papers annually since 1981. He reached the retirement age in 2004 with little apparent change in his work-life balance. A successful event was held in 2005 in Bristol attracting colleagues from around the world to a lecture series in recognition of his contributions.

Thus, M gives rise to higher-order flow equations. The momentum function is composed of the leading order Saint-Venant (hydrostatic) term plus a Boussinesq (non-hydrostatic) correction. Equation (2.49) was originally derived by Serre (1953) and is extensively used in civil and environmental engineering applications (Basco 1983; Soares-Frazão and Zech 2002; Mohapatra and Chaudhry 2004; Chaudhry 2008). Equation (2.49) describes, e.g., the propagation of undular bores (Fig. 2.4), originally investigated by Peregrine (1966) using a finite difference model. Equations (2.48)–(2.49) are the so-called Serre (1953) equations for weakly dispersive, non-linear 1D water waves. The equations were later derived by Su and Gardner (1969) and Green and Naghdi (1976) using alternative theoretical methods. In coastal engineering, the equations are often named the *Serre-Green-Naghdi* equations. Using the irrotational flow theory, it can be demonstrated that the *Serre-*

Fig. 2.4 Undular bore propagating with breaking front (photograph by late Prof. D.H. Peregrine)

Green-Naghdi equations are regained if the variation of u with depth is accounted for (Su and Gardner 1969) (Chap. 3). Cienfuegos et al. (2006) presented finite volume numerical solutions of the extension of this system for variable bathymetry, whereas a detailed analytical investigation of the kinematic velocity field and the stability of solitary and cnoidal wave solutions of Eqs. (2.48)–(2.49) were given by Carter and Cienfuegos (2011). The first investigation of solitary and cnoidal wave solutions of the Serre equations was presented by Iwasa (1955, 1956), who independently derived the system of equations using the same depth-integrated approach of Serre (1953). For reviews of the *Serre-Green-Naghdi* equations and applications to coastal engineering, see Barthelemy (2004), Lannes and Bonneton (2009), Dias and Milewski (2010), and Bonneton et al. (2011).

2.4.3 Turbulent Uniform Flow on Steep Terrain

Consider turbulent water flow in the vertical plane (x, z). Neglecting viscous contributions, the stress tensor is then $\tau_{xx} = p - \sigma_{xx}$, $\tau_{zz} = p - \sigma_{zz}$, and $\tau_{xz} = -\sigma_{xz}$, where σ denotes the turbulent Reynolds stress due to time averaging of the Navier–Stokes equations for fluid flow. The 2D vertically integrated x-momentum equation for turbulent water flows is, from Eq. (2.28),

$$\underbrace{\frac{\partial}{\partial t}(Uh) + \frac{\partial}{\partial x}\left(U^2 h\right)}_{} = -\frac{1}{\rho}\left[\underbrace{\frac{\partial}{\partial x}\int_{z_b}^{z_s}(p-\sigma_{xx})\mathrm{d}z}_{} + (p-\sigma_{xx})_b\frac{\partial z_b}{\partial x} + (\sigma_{xz})_b\right], \tag{2.50}$$

and from Eq. (2.20), the equation describing the bottom pressure is found to be

$$\underbrace{\frac{\partial}{\partial t}(\bar{w}h)+\frac{\partial}{\partial x}(\bar{w}Uh)}=\frac{1}{\rho}\left[(p-\sigma_{zz})_b+\underbrace{\frac{\partial}{\partial x}\int_{z_b}^{z_s}\sigma_{xz}\mathrm{d}z}+(\sigma_{xz})_b\frac{\partial z_b}{\partial x}\right]-gh. \quad (2.51)$$

Here, the depth-averaged vertical velocity is defined as

$$\bar{w}(x,y,t)=\frac{1}{h}\int_{z_b}^{z_s}w\mathrm{d}z. \quad (2.52)$$

Uniform flow is typically defined in hydraulic engineering prescribing a constant flow depth for which the bed shear is in equilibrium with the gravity term of the momentum balance (Chow 1959). However, this definition is not rigorous; here, uniform flow on a slope is defined from a fluid mechanics perspective as an ideal state where the depth is constant and the distributions of velocity, pressure, and Reynolds stresses remain unchanged for any vertical section. Therefore, for uniform flow on a steep slope (Fig. 2.3) the underbraced terms in Eqs. (2.50) and (2.51) are zero by definition, and Eq. (2.50) reduces to the x-force (momentum) balance

$$(p-\sigma_{xx})_b\frac{\partial z_b}{\partial x}+(\sigma_{xz})_b=0, \quad (2.53)$$

whilst the z-momentum balance, Eq. (2.51), collapses to the force balance

$$(p-\sigma_{zz})_b+(\sigma_{xz})_b\frac{\partial z_b}{\partial x}=\rho gh. \quad (2.54)$$

Consider an infinitesimal element at a basal point, subjected to plane strain, once referred to the (x, z)-axes and once inclined by the slope angle θ as shown in Fig. 2.5. The stress states in the (x, z)-coordinates and (s, n)-coordinates are then related to one another based on the equilibrium conditions of triangular elements by the equation (Fig. 2.5)

$$\begin{pmatrix}\sigma_{nn}\\ \sigma_{ss}\\ \tau_{sn}\end{pmatrix}=\begin{pmatrix}\cos^2\theta & \sin^2\theta & 2\cos\theta\,\sin\theta\\ \sin^2\theta & \cos^2\theta & -2\cos\theta\,\sin\theta\\ -\sin\theta\,\cos\theta & \sin\theta\,\cos\theta & \cos^2\theta-\sin^2\theta\end{pmatrix}\begin{pmatrix}\sigma_{xx}\\ \sigma_{zz}\\ \tau_{xz}\end{pmatrix}. \quad (2.55)$$

Simple shear along the bed slope is described by vanishing normal stresses $\sigma_{nn}=\sigma_{ss}=0$ and $\tau_{sn}=\tau_b$. For this choice, the above system of equations is easily inverted with the solution given by

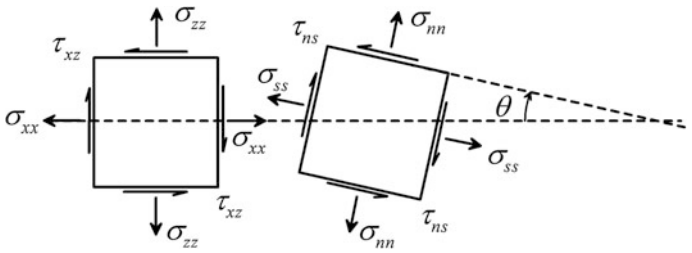

Fig. 2.5 Infinitesimal element subjected to plane stress referred to (x, z)- and (s, n)-coordinates rotated by angle θ

$$\begin{aligned}(\sigma_{zz})_b &= 2\tau_b \cos\theta \sin\theta,\\ (\sigma_{xx})_b &= -2\tau_b \cos\theta \sin\theta,\\ (\sigma_{xz})_b &= \tau_b\left(\cos^2\theta - \sin^2\theta\right).\end{aligned} \tag{2.56}$$

Here, τ_b is the shear stress in the s-direction, measured along the sloping plane (Fig. 2.3), and θ is given by $\partial z_b/\partial x = \tan\theta$. Inserting Eq. (2.56) into Eqs. (2.53) and (2.54) yields, respectively,

$$\tau_b = -p_b \tan\theta, \tag{2.57}$$

$$p_b = \rho g h + \tau_b \tan\theta. \tag{2.58}$$

Combining Eqs. (2.57) and (2.58) results in the non-hydrostatic bottom pressure on a steep slope as

$$\frac{p_b}{\rho g} = \frac{h}{1+\tan^2\theta} = h\cos^2\theta. \tag{2.59}$$

Equation (2.59) indicates that the bottom pressure on a steep slope is non-hydrostatic, which becomes important already for $\theta = 45°$, as in this case a reduction in the bottom pressure of 50 % over the vertical water weight ensues. Equation (2.59) is a classical result obtained in the channel flow literature using gradually varied flow computations in the (s, n) system as shown in Fig. 2.3. Noting that $N = h\cos\theta$, Eq. (2.59) may be written as (e.g., Chow 1959; Henderson 1966)

$$\frac{p_b}{\rho g} = N\cos\theta. \tag{2.60}$$

Equation (2.60) is a particular non-hydrostatic result of the general formulation given by Eq. (2.51), where conditions of gradually varied flows are not assumed. This development demonstrates that non-hydrostatic pressures originate from the turbulent Reynolds stresses and not from the vertical velocity $\bar{w}$, given the fact that the gradient $\partial\bar{w}/\partial x$ is zero.

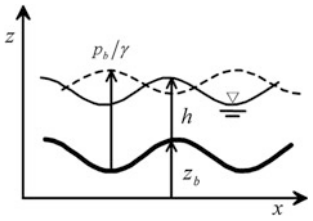

Fig. 2.6 Flow over undular bed $z_b(x)$ with (*thin lines*) free surface profile $h(x)$ and (*dashed lines*) bottom pressure head profile $p_b/\gamma(x)$

2.4.4 Flows Over Curved Beds

Flows over variable topography imply that the source term in Eq. (2.34) is not zero, i.e., resistive forces and bed geometrical source terms must be accounted for. In the geophysical environment, the effect of variable topography on the flow solution of dynamical models by stating conservation of mass and momentum is important. Such problems include atmospheric air currents over variable terrain (Sivakumaran and Dressler 1989) or water flows over fluvial bed forms, such as dunes and anti-dunes (Engelund and Hansen 1966; Dey 2014). Models for 1D flows over curved beds were proposed by Dressler (1978), Hager and Hutter (1984a, b), and Khan and Steffler (1996a, b). For steady 1D flows over a curved bed in the vertical plane given by $z_b = z_b(x)$ (Fig. 2.6), Eq. (2.28) reduces to

$$\frac{\partial}{\partial x}\left(hU^2\right) = -\frac{1}{\rho}\left[\frac{\partial}{\partial x}\int_{z_b}^{z_s}\tau_{xx}\mathrm{d}z + (\tau_{xx})_b\frac{\partial z_b}{\partial x} - (\tau_{xz})_b\right]. \tag{2.61}$$

For frictionless fluids, the stress tensor is the pressure tensor for inviscid flow with $\tau_{xx} = p$ and $\tau_{xz} = 0$. Therefore, Eq. (2.61) can be further simplified to the ODE

$$\frac{\mathrm{d}M}{\mathrm{d}x} = -\frac{p_b}{\rho}\frac{\partial z_b}{\partial x}, \tag{2.62}$$

where

$$M = hU^2 + \int_{z_b}^{z_s}\frac{p}{\rho}\mathrm{d}z. \tag{2.63}$$

Here, p_b is the basal pressure, and the free surface pressure has been set to zero. The vertical velocity for steady 1D flows over curved terrain is obtained from Eq. (2.37), using $q = \text{const} = U(x)h(x)$,

$$w = -\frac{\partial}{\partial x}[U(z-z_b)] = -\frac{\partial}{\partial x}\left[\frac{q}{h}(z-z_b)\right] = -\frac{\partial}{\partial x}\left[-\frac{q}{h^2}\frac{\partial h}{\partial x}(z-z_b) - \frac{q}{h}\frac{\partial z_b}{\partial x}\right]$$
$$= U\left[\frac{\partial z_b}{\partial x} + \frac{\partial h}{\partial x}\frac{(z-z_b)}{h}\right]. \tag{2.64}$$

Similarly, an expression for the pressure results from Eq. (2.40) as

$$p = \tau_{zz} = \rho g(z_s - z) + \rho\frac{\partial I}{\partial t} + \rho\frac{\partial}{\partial x}(IU) - \rho w^2 + \int_z^{z_s}\frac{\partial \tau_{zx}}{\partial x}\mathrm{d}z'$$
$$= \rho g(z_s - z) + \underbrace{\rho\frac{\partial}{\partial t}\left\{\int_z^{z_s} w\mathrm{d}z'\right\}}_{=0\ (\text{steady}-\text{state})} + \rho\frac{\partial}{\partial x}\left\{U\int_z^{z_s} w\mathrm{d}z'\right\} - \rho w^2 + \underbrace{\int_z^{z_s}\frac{\partial \tau_{zx}}{\partial x}\mathrm{d}z'}_{\text{neglected}}, \tag{2.65}$$

or

$$p(z) = \rho g(z_s - z) - \rho w^2 + \rho\frac{\partial}{\partial x}\left(U\int_z^{z_s} w\mathrm{d}z'\right). \tag{2.66}$$

In the above derivation, Eq. (2.40) has been employed in the spatially 1D version and under steady-state conditions. Moreover, the integrated shear stress flux term has been neglected as is common in the pertinent hydraulic literature. Inserting Eq. (2.64) into Eq. (2.66) and performing the relevant integration and differentiations yields

$$\frac{p(z)}{\rho g} = h - \eta + \frac{U^2}{2g}\left[2hz_{bxx}\left(1-\frac{\eta}{h}\right) + \left(hh_{xx} - h_x^2\right)\left(1-\frac{\eta^2}{h^2}\right) - 2h_x z_{bx}\left(1-\frac{\eta}{h}\right)\right]. \tag{2.67}$$

Upon substitution into Eq. (2.63) and performing an additional integration, one obtains

$$M = g\frac{h^2}{2} + hU^2\left(1 + \frac{hh_{xx} - h_x^2}{3} + \frac{hz_{bxx}}{2} - \frac{h_x z_{bx}}{2}\right). \tag{2.68}$$

The analysis to obtain these results is somewhat cumbersome, even though it is not difficult; it is, therefore, deferred to Appendix A.

The bottom pressure, from Eq. (2.67), is of the form

$$\frac{p_b}{\rho g} = h + \frac{U^2}{2g}\left[2hz_{bxx} + hh_{xx} - h_x^2 - 2h_x z_{bx}\right]. \tag{2.69}$$

Equation (2.69) was first derived by Castro-Orgaz and Hager (2009) and solved using a Picard iteration solution of the irrotational flow equations, as described in Chap. 3; it highlights a key ingredient of the Boussinesq theory: Differences between the flow depth h and the bottom pressure head p_b/γ are adequately accounted for. In general, at locations with positive flow curvature (concave bed), one has $p_b/\gamma > h$, whereas $p_b/\gamma < h$ at locations with negative flow curvature (convex bed), see Fig. 2.6. If the same flow is computed using a pure Saint-Venant theory, the free surface is not accurately predicted, because the vertical acceleration is not accounted for, while the bottom pressure can simply not be predicted, given that $p_b/\gamma = h$ is assumed ab initio. This is a strong reason to adopt the Boussinesq theory in geophysical, environmental, civil, and coastal research, given that the increase in computational effort is moderate, but the gain in physical appropriateness is high.

2.4.5 *Enhanced Gravity*

Denlinger and Iverson (2004) and Denlinger and O'Connel (2008) presented a simplified vertically integrated, unsteady non-hydrostatic model in which a key physical element was introduced. They defined a corrected (or "enhanced") gravity acceleration, in which the effect of vertical acceleration is accounted for. Their equation of vertical pressure at the bed level in a turbulent water flow is

$$p_b = \rho g h + \rho\left(\frac{\partial(\bar{w}h)}{\partial t} + \frac{\partial(\bar{w}Uh)}{\partial x} + \frac{\partial(\bar{w}Vh)}{\partial y}\right) = \rho g' h. \tag{2.70}$$

In Eq. (2.70), g' is the enhanced gravity, including a mean vertical acceleration $\mathrm{D}\bar{w}/\mathrm{D}t$ as

$$g' = g + \frac{\mathrm{D}\bar{w}}{\mathrm{D}t} = g + \frac{\partial \bar{w}}{\partial t} + U\frac{\partial \bar{w}}{\partial x} + V\frac{\partial \bar{w}}{\partial y}. \tag{2.71}$$

As to the depth-averaged velocity, these authors used the mean value

$$\bar{w} = \frac{1}{2}(w_s + w_b), \tag{2.72}$$

in which w_s and w_b are determined from Eqs. (2.7) and (2.8), respectively. Equation (2.72) permits the evaluation of p_b from Eq. (2.70). Denlinger and Iverson (2004) further assumed that $p(z)$ is linearly distributed in z as

$$p(z) = \rho g'(h - \eta). \tag{2.73}$$

Steffler and Jin (1993), who also used Eq. (2.73) to produce Boussinesq-type behavior in hydraulic structures, further considered relations that are more complex. Using g', the inclusion of non-hydrostatic effects on vertically integrated models becomes conceptually simple, allowing for their straightforward inclusion into Riemann solvers (Sect. 2.6).

Let us now compare the physical simplifications underlying the enhanced gravity concept with the general mathematical theory presented above. For this purpose, from the general Eq. (2.20) at the bed level, and by neglecting the stress integral, one deduces the equation

$$p_b = \rho g h + \rho \frac{\partial}{\partial t} \int_{z_b}^{z_s} w \mathrm{d}z + \rho \frac{\partial}{\partial x} \int_{z_b}^{z_s} wu \mathrm{d}z + \rho \frac{\partial}{\partial y} \int_{z_b}^{z_s} wv \mathrm{d}z. \tag{2.74}$$

Using Eq. (2.72) for $\bar{w}$, Eq. (2.74) becomes identical to Eq. (2.70). Therefore, the bottom pressure p_b used by Denlinger and Iverson (2004) is an exact depth-averaged value. However, $p(z)$ as given by Eq. (2.73) is assumed to be linearly distributed, whereas a parabolic distribution results from Eq. (2.40) (see Appendix A). Denlinger and Iverson's (2004) approximation to the vertical pressure distribution introduces some error in the momentum computation, despite the exact bed value. The physical significance of the enhanced gravity correction is elucidated using steady 1D flow over curved terrain as a test case. In this case, Eq. (2.71) reduces under steady state to

$$g' = g + \frac{\mathrm{D}\bar{w}}{\mathrm{D}t} = g + U \frac{\partial \bar{w}}{\partial x}. \tag{2.75}$$

From steady, spatially 1D versions of Eqs. (2.7), (2.8) and with Eq. (2.72), as well as for uniform velocity $u(z) = U$, one obtains

$$\bar{w} = \frac{1}{2}(w_s + w_b) = \frac{1}{2}[U(h_x + z_{bx}) + U z_{bx}], \tag{2.76}$$

and after differentiation

$$\frac{\partial \bar{w}}{\partial x} = U_x \left(\frac{h_x}{2} + z_{bx} \right) + U \left(\frac{h_{xx}}{2} + z_{bxx} \right). \tag{2.77}$$

Inserting Eq. (2.77) into Eq. (2.75), using the expression $U_x = -(q/h^2)h_x$ and inserting the resulting g' into Eq. (2.70), yields the bed pressure of the Denlinger and Iverson (2004) theory for this flow problem as

$$p_b = \rho g h + \rho \frac{U^2}{2}\left(h h_{xx} - h_x^2 - 2h_x z_{bx} + 2h z_{bxx}\right). \tag{2.78}$$

This agrees with Eq. (2.69) for the generalized Boussinesq theory. It also corresponds to the bed pressure of Khan and Steffler's (1996a, b) Boussinesq model for 1D steady flow over a curved bed, if turbulent stresses and bed friction forces are neglected. Inserting the linear pressure of Eq. (2.73) into the expression for the flow momentum M, Eq. (2.63), results in

$$M = g\frac{h^2}{2} + hU^2\left(1 + \frac{h h_{xx} - h_x^2}{4} + \frac{h z_{bxx}}{2} - \frac{h_x z_{bx}}{2}\right). \tag{2.79}$$

Comparing Eqs. (2.68) and (2.79), it is noted that the enhanced gravity approach introduces a factor (1/4) in the water-depth derivative-correction term as compared with (1/3) in the exact vertically integrated equations. Therefore, the corrected enhanced gravity in Serre's theory (1953) in a horizontal channel is given by

$$g' = g + \frac{4}{3}\frac{\mathrm{D}\bar{w}}{\mathrm{D}t} = g + \frac{4}{3}U\frac{\partial \bar{w}}{\partial x}. \tag{2.80}$$

In turn, the flow momentum in the x-direction is, therefore, given by

$$M = U^2 h + g'\frac{h^2}{2} = g\frac{h^2}{2} + hU^2\left(1 + \frac{h h_{xx} - h_x^2}{3}\right), \tag{2.81}$$

as shown by Serre (1953) and Benjamin and Lighthill (1954).

2.4.6 *Non-hydrostatic Model Including Friction Effects*

Steffler and Jin (1993) and Khan and Steffler (1996a, b) developed a Boussinesq-type momentum model, in which both acceleration and frictional effects were accounted for in generating non-hydrostatic pressure distributions over steep and curved beds. This model can be deduced from the generalized equations presented in this text. Neglecting depth-averaged turbulent stresses, the full Eqs. (2.50) and (2.51) take the forms

$$\frac{\partial}{\partial t}(Uh) + \frac{\partial}{\partial x}\left(U^2 h + \int_{z_b}^{z_s}\frac{p}{\rho}\mathrm{d}z\right) = -\frac{1}{\rho}\left[(p - \sigma_{xx})_b\frac{\partial z_b}{\partial x} + (\sigma_{xz})_b\right], \tag{2.82}$$

$$\frac{\partial}{\partial t}(\bar{w}h)+\frac{\partial}{\partial x}(\bar{w}Uh)=\frac{1}{\rho}\left[(p-\sigma_{zz})_b+(\sigma_{xz})_b\frac{\partial z_b}{\partial x}\right]-gh. \tag{2.83}$$

Inserting Eq. (2.56) for a pure bed shear into Eqs. (2.82) and (2.83) gives

$$\frac{\partial}{\partial t}(Uh)+\frac{\partial}{\partial x}\left(U^2h+\int_{z_b}^{z_s}\frac{p}{\rho}\mathrm{d}z\right)=-\frac{p_b}{\rho}\frac{\partial z_b}{\partial x}-\frac{\tau_b}{\rho}, \tag{2.84}$$

as well as

$$p_b=\rho gh+\rho\frac{\partial}{\partial t}(\bar{w}h)+\rho\frac{\partial}{\partial x}(\bar{w}Uh)+\tau_b\frac{\partial z_b}{\partial x}. \tag{2.85}$$

In Eq. (2.85) the depth-averaged vertical velocity $\bar{w}$ is given by Eq. (2.72), with w_s and w_b computed from the kinematic boundary conditions, i.e., Eqs (2.7) and (2.8) (Steffler and Jin 1993). A distribution $p = p(z)$ must be introduced into Eq. (2.84) for model closure. A linear distribution was assumed, corresponding to the approximation of Denlinger and Iverson (2004). Equation (2.84) then reduces, after integration, to

$$\frac{\partial}{\partial t}(Uh)+\frac{\partial}{\partial x}\left(U^2h+\frac{h}{2}\frac{p_b}{\rho}\right)=-\frac{p_b}{\rho}\frac{\partial z_b}{\partial x}-\frac{\tau_b}{\rho}. \tag{2.86}$$

This equation is the Boussinesq-type x-momentum equation developed by Khan and Steffler (1996a, b). For steady flow, and after using Eq. (2.72) to eliminate $\bar{w}$ from Eq. (2.85), Eqs. (2.84), and (2.85) reduce to

$$\frac{\mathrm{d}}{\mathrm{d}x}\left(U^2h+\frac{h}{2}\frac{p_b}{\rho}\right)=-\frac{p_b}{\rho}\frac{\partial z_b}{\partial x}-\frac{\tau_b}{\rho}, \tag{2.87}$$

$$p_b=\rho gh+\rho\frac{U^2}{2}\left(hh_{xx}-h_x^2-2h_xz_{bx}+2hz_{bxx}\right)+\tau_b\frac{\partial z_b}{\partial x}. \tag{2.88}$$

From these equations, the flow momentum is

$$M=g\frac{h^2}{2}+hU^2\left(1+\frac{hh_{xx}-h_x^2}{4}+\frac{hz_{bxx}}{2}-\frac{h_xz_{bx}}{2}\right)+\frac{hz_{bx}}{2}\frac{\tau_b}{\rho}. \tag{2.89}$$

A typical non-hydrostatic flow, in which friction effects need to be accounted for, is the undular hydraulic jump (Fawer 1937; Serre 1953; Montes 1986) as shown in Fig. 2.7. Note that upon comparing Eq. (2.89) with Eqs. (2.68) and (2.79), both the theories of Denlinger and Iverson (2004) and of Castro-Orgaz and Hager (2009) do not account for the bed-shear resistance. This is also noted upon comparing Eq. (2.88) with Eqs. (2.69) and (2.78) for the bottom pressure p_b.

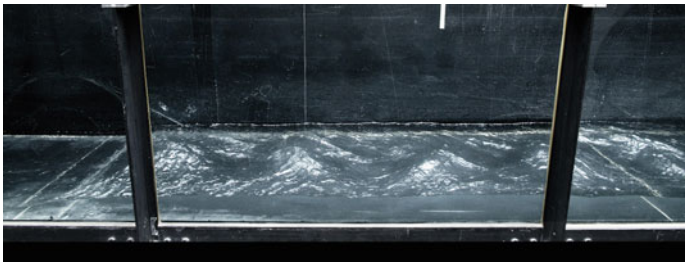

Fig. 2.7 Undular hydraulic jump. Note the highly 3D free surface flow pattern (photograph VAW, ETH Zurich)

The present development, however, allows for inclusion of basal (but not interior) frictional effects in Boussinesq-type computations if large computational domains are considered.

2.5 Sediment Transport and Movable Beds

2.5.1 Introduction

Most of the dynamic models for bed-form evolution are based on the sediment mass conservation equation, also referred to as the Exner equation. It reads (Chaudhry 2008)

$$(1-n)\frac{\partial z_b}{\partial t} = -\frac{\partial q_b}{\partial x}, \tag{2.90}$$

with n as the bed porosity, z_b bed elevation (interface of bed-load layer with clear-water flow), t time, and x longitudinal coordinate. The Saint-Venant equations stating the depth-integrated mass and momentum balances of the water flow are, with the water discharge q and the friction slope S_f,

$$\frac{\partial q}{\partial x} + \frac{\partial h}{\partial t} = 0, \quad \frac{1}{g}\frac{\partial q}{\partial t} + \frac{\partial}{\partial x}\left(\frac{q^2}{gh} + \frac{h^2}{2}\right) = h\left(-\frac{\partial z_b}{\partial x} - S_f\right). \tag{2.91}$$

In this system, the dominant mode of sediment transport is assumed to be bed load, neglecting, e.g., the suspended (so-called wash) load transport. According to Yalin (1977), the unit bed-load transport rate q_b is written in dimensionless form as

$$q_b* = f\left(\tau*, R, \mathsf{R}_{ep}, S_o, \frac{h}{D}\right). \tag{2.92}$$

For the derivation of such formulas, see Hutter and Wang (2016). In Eq. (2.92), $q_b^* = q_b/(RgD^3)^{1/2}$ and $\tau^* = \tau_b/(\gamma RD)$ are dimensionless discharge and basal shear stress variables, g is the gravity acceleration, τ_b the bottom shear stress, $R = (\gamma_s/\gamma) - 1$ the submerged specific gravity, or ratio between the fluid, γ, and sediment-specific weights γ_s; D is a representative particle diameter, $\mathsf{R}_{ep} = (RgD)^{1/2}D/\upsilon$ the particle Reynolds number, that depends on the kinematic viscosity υ, S_o the bed slope, and h the water depth.

Equation (2.92) was principally developed at two institutions to obtain a simplified practical form allowing for a mechanistic interpretation. The *first* school followed the work of Einstein (1950), who considered a bed-load layer disconnected from the upper layer where finer sediment particles were entrained by fluid turbulence. The movement of the solid particles in jumps, or by saltations, was based on its stochastic formulation. The final expression contained coefficients that were fitted to the available experimental data. Einstein considered the saltation of particles as a mode of suspended sediment transport.

The *second* school followed the work of Bagnold (1973), who proposed an alternative method where the bed-load rate is related to the motive power of the moving fluid, i.e., the product of shear stress and fluid velocity, weighted with an efficiency coefficient. Both Einstein and Bagnold's expressions have a theoretical foundation, yet empirical coefficients are used to fit the experimental data. As Garcia (2008) indicated in his review, the current scientific community tends away from Einstein's formulation toward Bagnold's description of bed-load transport. Following the empirical proposals of the early formulas, his model includes a critical or threshold value of the shear stress, τ_c, normalized as τ_c^*, for the inception of the sediment motion, based on the formulation of Shields (Buffington and Montgomery 1997). Using this concept, and assuming uniform flow over gentle slope (S_o in Eq. 2.92 is neglected), Eq. (2.92) simplifies in this case to

$$q_b^* = f\left(\tau^*, \tau_c^*, \text{fitting parameters}\right). \tag{2.93}$$

The main physical insight extracted from this framework is that sediment is entrained by a fluid flow once a critical value of the shear stress is reached. This implies that the moving grains extract momentum from the fluid within the bed-load layer to keep the shear stress at the critical value for motion. This type of bed-load formulation has been widely used to obtain fits in both laboratory and field conditions (Schmocker 2011), and constitutes the basis of open-channel flow models, incorporating sediment transport and movable bed features (Chaudhry 2008). One empirical relation based on Eq. (2.93) of wide acceptance is the expression of Meyer-Peter and Müller (1948). Other mechanistic treatments added more insight to the process of bed-load transport including the saltation model of Wiberg and Smith (1989) or the stochastic model of sediment dynamics of Ancey (2010) and Furbish et al. (2012). However, Eq. (2.93) predominates in open-channel flow models. Table 2.1 shows common expressions of Eq. (2.93).

The Saint-Venant model is based on hydrostatic pressure distributions, so that it is limited to gradually varied flows with almost parallel streamlines. A corollary is

Table 2.1 Dimensionless bed-load transport equations for q_b*, with variables of Eqs. (2.92) and (2.93), f as fitting coefficient and U* as dimensionless average particle horizontal velocity

Author(s)	q_b*
Meyer-Peter and Müller (1948)	$8\left(\tau^* - \tau_c^*\right)^{3/2}$
Einstein (1950)	$12f\left(\tau^* - \tau_c^*\right)^{3/2}$
Bagnold (1973)	$U^*\left(\tau^* - \tau_c^*\right)$
Engelund and Fredsoe (1976)	$18.74\left(\tau^* - \tau_c^*\right)\left(\sqrt{\tau^*} - 0.7\sqrt{\tau_c^*}\right)$
Parker (1979)	$11.2\left(\tau^* - \tau_c^*\right)^{4.5}\tau^{*-3}$

that the application of Eqs. (2.91) and (2.93) requires planar beds, lower-regime flow conditions, i.e., bed forms due to the erosion and deposition processes are not accounted for. However, despite these limitations, the equations listed in Table 2.1 are commonly coupled with Eqs. (2.91)–(2.93) in morphodynamic open-channel flow models (Garcia 2008) with the purpose of predicting the temporal and spatial evolutions of the four variables $q(x, t)$, $h(x, t)$, $q_b(x, t)$, and $z_b(x, t)$. These applications should therefore be restricted to weakly erodible beds under uniform or gradually varied water flows. The models are therefore defined as gradually varied geomorphodynamic models. Despite efforts over the past half century, the prediction of flows and sediment transports over bed forms still presents a major challenge for the solution of sedimentation problems (ASCE 2002). The basic question still needed to be addressed for sediment transport is: "What are the expected flow depths and sediment transport rates for given sediment and fluid characteristics, channel geometry, and discharge?" The answer remains highly uncertain, and much of the uncertainty can be traced to the development of bed forms (ASCE 2002). This source explains that several hydraulic laboratories are currently devoting appreciable experimental efforts to explore, at very small scale, the details of bed-load transport (Ancey 2010; Lajeunesse et al. 2010). Given the limitations stated for the gradually varied geomorphodynamic model, the complex cases of the evolution of bed forms for streams, where both the streamline curvature and bottom slope may affect the bed load, need advanced theoretical approaches.

Figure 2.8 shows some typical bed forms in natural streams, adapted from Engelund and Fredsoe (1982). The undular flow over the bed form may be entirely subcritical (Fig. 2.8a), supercritical (Fig. 2.8b), or involve transcritical flow changing from sub- to supercritical conditions, and vice versa (Fig. 2.8c), forming an undular hydraulic jump (Chanson 2000; Castro-Orgaz and Hager 2011c). Dunes correspond to asymmetrical sand waves appearing beneath subcritical water flows, roughly out of phase with the bed shape. Antidunes are wave-like bed forms appearing beneath a supercritical stream and practically in-phase with the bed geometry. Undular hydraulic jumps are an intermediate configuration where both flow features occur. The sediment motion is induced by the water wave action at wave troughs and crests of the undular flow, respectively, revealing distinctive 3D flow features where friction and inertial forces are predominant.

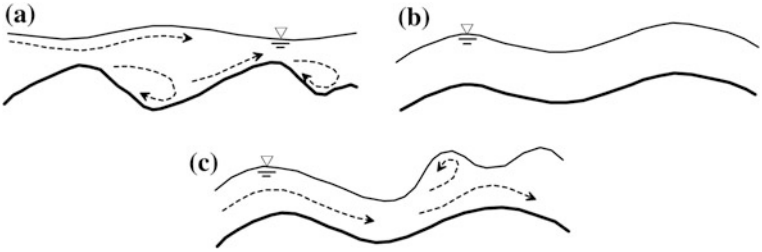

Fig. 2.8 Bed forms **a** dune, **b** antidune, **c** transcritical profile from super- to subcritical flows with undular hydraulic jump and wave breaking (adapted from Engelund and Fredsoe 1982)

The flow over curved bed forms, such as dunes or antidunes, plays a major role in the establishment of flow resistance (Kennedy 1963; Engelund and Hansen 1966; Graf and Altinakar 1996). The curvature on water flows, provoked by the bed forms, causes vertical accelerations of water particles, inducing a non-hydrostatic pressure distribution (Engelund and Hansen 1966; Bose and Dey 2009). Therefore, the gradually varied morphodynamic model described above is inappropriate to study flow over curved bed forms. Figure 2.9 shows water flow over a dune. The streamlines adjust to the shape of the sand wave, and undulations develop at the water surface. Turbulent drag over the sand wave provokes intense erosion at the downstream dune side, and a free streamline separates from the bed sediment surface, trapping a vortex flow zone below. The water surface profile $h = h(x)$ over the curved bed is a function of the local values of $\mathrm{d}h/\mathrm{d}x$, $\mathrm{d}^2h/\mathrm{d}x^2$, $\mathrm{d}z_b/\mathrm{d}x$, and $\mathrm{d}^2z_b/\mathrm{d}x^2$ (Engelund and Hansen 1966; Hager and Hutter 1984a, Bose and Dey 2009; Castro-Orgaz et al. 2015), where $z_b = z_b(x)$ is the longitudinal profile of the bed form. The extended momentum conservation equation for water flow above a sand wave is approximated by a steady-state equation of the form (Engelund and Hansen 1966; Onda and Hosoda 2004)

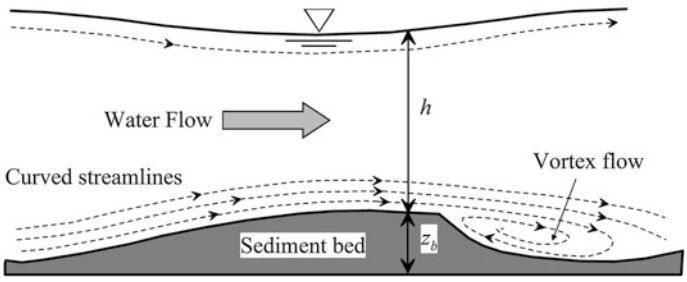

Fig. 2.9 Water flow across a dune with streamline pattern including recirculating flow

$$\frac{\mathrm{d}M}{\mathrm{d}x} = -\frac{p_b}{\rho}\frac{\mathrm{d}z_b}{\mathrm{d}x} - \frac{\tau_b}{\rho},$$
$$M = \frac{h^2}{2} + U^2 h\left(1 + \frac{1}{3}h\frac{\mathrm{d}^2 h}{\mathrm{d}x^2} - \frac{1}{3}\left(\frac{\mathrm{d}h}{\mathrm{d}x}\right)^2 + \frac{1}{2}h\frac{\mathrm{d}^2 z_b}{\mathrm{d}x^2} - \frac{1}{2}\frac{\mathrm{d}h}{\mathrm{d}x}\frac{\mathrm{d}z_b}{\mathrm{d}x}\right). \tag{2.94}$$

Here, M is the specific momentum and p_b the actual (non-hydrostatic) pressure at the curved sediment bed surface. The solution of the system, given by Eq. (2.94) for a given water discharge, bed-form profile, and appropriate boundary conditions produces the local free surface profile $h = h(x)$. The bed profile is updated based on Exner's Eq. (2.90) for the next time cycle. Onda and Hosoda (2004) also parametrized the bed-shear stress using the near-bed velocity and corrected the local skin friction coefficient with a free surface and sediment-bed slope factor. The bed-form profile $z_b(x)$-configuration will affect the profile $h = h(x)$ of the free surface that, in turn, affects the bed-shear stress and then the bed-load transport rate under non-uniform flow conditions, involving curvilinear streamlines and non-hydrostatic pressures. Therefore, non-hydrostatic models are more suitable to account for bed-form processes. At the downstream dune face, erosion results in a vortex-flow zone with recirculation, for which non-hydrostatic 1D models do not account for, unless the momentum of the recirculating bubble is accounted for by a simplified flow model, or an empirical estimator, into the streamwise momentum balance.

2.5.2 *Non-hydrostatic Unsteady Free Surface Flow with Bed-Load Sediment Transport*

Sediment transport problems, such as bed-form migration, involve a vertical length scale of the order of the horizontal length scale, leading to non-hydrostatic flow conditions as pointed out previously. In this section, the non-hydrostatic unsteady sediment transport model over erodible beds is developed by accounting for bed-load motion. The development is shown to be a generalization of the theory by Engelund and Hansen (1966) for flow in alluvial streams. Neglecting depth-averaged turbulent stresses, Eq. (2.50) reduces to

$$\frac{\partial}{\partial t}(Uh) + \frac{\partial}{\partial x}\left(U^2 h\right) = -\frac{1}{\rho}\left[\frac{\partial}{\partial x}\int_{z_b}^{z_s} p\mathrm{d}z + (p - \sigma_{xx})_b\frac{\partial z_b}{\partial x} + (\sigma_{xz})_b\right]. \tag{2.95}$$

Using Eq. (2.56) for a pure bed-shear state one finds

$$-(\sigma_{xx})_b\frac{\partial z_b}{\partial x} + (\sigma_{xz})_b = -\tau_b. \tag{2.96}$$

Assuming a linear pressure distribution

$$p = p_b\left(1-\frac{\eta}{h}\right) = (p_1+\rho g h)\left(1-\frac{\eta}{h}\right), \tag{2.97}$$

where p_1 is the difference between the actual p_b and the hydrostatic bottom pressure ($\rho g h$), the pressure force is

$$\int_{z_b}^{z_s} p\mathrm{d}z = \int_0^h p\mathrm{d}\eta = \rho g\frac{h^2}{2} + \frac{hp_1}{2}. \tag{2.98}$$

Inserting Eqs. (2.96) and (2.98) into Eq. (2.95) results in

$$\frac{\partial}{\partial t}(Uh) + \frac{\partial}{\partial x}\left(U^2 h + g\frac{h^2}{2} + \frac{hp_1}{2\rho}\right) = -\frac{p_b}{\rho}\frac{\partial z_b}{\partial x} - \frac{\tau_b}{\rho}. \tag{2.99}$$

The relation describing bottom pressure is Eq. (2.51); neglecting turbulent stresses, it is simplified to

$$\frac{p_b}{\rho} = gh + \frac{\partial}{\partial t}(\bar{w}h) + \frac{\partial}{\partial x}(\bar{w}Uh), \tag{2.100}$$

with the depth-averaged vertical velocity given by

$$\bar{w} = \frac{w_s + w_b}{2}. \tag{2.101}$$

Moreover, the free surface and bed kinematic boundary conditions are, respectively,

$$w_s = \frac{\partial}{\partial t}(h+z_b) + U\frac{\partial}{\partial x}(h+z_b), \tag{2.102}$$

$$w_b = \frac{\partial z_b}{\partial t} + U\frac{\partial z_b}{\partial x}. \tag{2.103}$$

Here, the bed level z_b is the interface of the bed-load layer with the clear-water flow. With the mean vertical acceleration given by

$$\frac{\mathrm{D}\bar{w}}{\mathrm{D}t} = \frac{\partial \bar{w}}{\partial t} + U\frac{\partial \bar{w}}{\partial x}, \tag{2.104}$$

Equations (2.99) and (2.100) are rewritten as

$$\frac{\partial}{\partial t}(Uh)+\frac{\partial}{\partial x}\left(U^2h+g\frac{h^2}{2}+\frac{\mathrm{D}\bar{w}}{\mathrm{D}t}\frac{h^2}{2}\right)=-\frac{p_b}{\rho}\frac{\partial z_b}{\partial x}-\frac{\tau_b}{\rho}, \tag{2.105}$$

$$\frac{p_b}{\rho}=gh+\frac{p_1}{\rho}=gh+h\frac{\mathrm{D}\bar{w}}{\mathrm{D}t}. \tag{2.106}$$

Note from Eq. (2.106) that the Boussinesq-type theories of Khan and Steffler (1996a) and Denlinger and Iverson (2004) are structurally identical. To find a closed form model, the boundary conditions, Eqs. (2.102) and (2.103), are inserted into Eq. (2.101), so that

$$\bar{w}=\frac{1}{2}\left(\frac{\partial h}{\partial t}+U\frac{\partial h}{\partial x}\right)+\frac{\partial z_b}{\partial t}+U\frac{\partial z_b}{\partial x}. \tag{2.107}$$

Using the depth-averaged continuity equation

$$\frac{\partial h}{\partial t}+\frac{\partial}{\partial x}(Uh)=0 \quad \Rightarrow \quad \frac{\partial h}{\partial t}=-U\frac{\partial h}{\partial x}-h\frac{\partial U}{\partial x}. \tag{2.108}$$

With w_b as the bed contribution, accounting for the spatial and temporal variations of the sediment bed profile $z_b = z_b(x, t)$, Eq. (2.107) reduces to

$$\bar{w}=-\frac{h}{2}\frac{\partial U}{\partial x}+w_b, \quad w_b=\frac{\partial z_b}{\partial t}+U\frac{\partial z_b}{\partial x}. \tag{2.109}$$

Using Eqs. (2.109), Eq. (2.104) is rewritten as

$$\frac{\mathrm{D}\bar{w}}{\mathrm{D}t}=\left(U_x^2-U_{xt}-UU_{xx}\right)\frac{h}{2}+\frac{\mathrm{D}w_b}{\mathrm{D}t}, \tag{2.110}$$

in which the material derivative of w_b is defined as

$$\frac{\mathrm{D}w_b}{\mathrm{D}t}=\frac{\partial w_b}{\partial t}+U\frac{\partial w_b}{\partial x}. \tag{2.111}$$

The flow momentum M, defined by

$$M=U^2h+\int_{z_b}^{z_s}\frac{p(z)}{\rho}\mathrm{d}z, \tag{2.112}$$

is evaluated by using the linear pressure profile

$$p = p_b\left(1 - \frac{\eta}{h}\right). \tag{2.113}$$

It satisfies the vanishing free surface pressure condition and the basal pressure assignment $p(z_b) = p_b$. Substituting Eq. (2.106) yields

$$p = \left(\rho g + \rho \frac{\mathrm{D}\bar{w}}{\mathrm{D}t}\right)(h - \eta). \tag{2.114}$$

The integral of this pressure distribution is

$$\int_{z_b}^{z_s} p\mathrm{d}z = \int_0^h p\mathrm{d}\eta = \rho\left(g + \frac{\mathrm{D}\bar{w}}{\mathrm{D}t}\right)\frac{h^2}{2}, \tag{2.115}$$

which leads to

$$M = U^2 h + \int_{z_b}^{z_s} \frac{p(z)}{\rho}\mathrm{d}z = U^2 h + \left(g + \frac{\mathrm{D}\bar{w}}{\mathrm{D}t}\right)\frac{h^2}{2}. \tag{2.116}$$

When substituting Eq. (2.110), this yields

$$M = U^2 h + \int_{z_b}^{z_s} \frac{p(z)}{\rho}\mathrm{d}z = U^2 h + g\frac{h^2}{2} + \left(U_x^2 - U_{xt} - UU_{xx}\right)\frac{h^3}{4} + \frac{h^2}{2}\frac{\mathrm{D}w_b}{\mathrm{D}t}. \tag{2.117}$$

The total time derivative $\mathrm{D}w_b/\mathrm{D}t$ is determined by using Eqs. $(2.109)_2$ and (2.111), namely

$$\frac{\partial w_b}{\partial t} = \frac{\partial^2 z_b}{\partial t^2} + \frac{\partial U}{\partial t}\frac{\partial z_b}{\partial x} + U\frac{\partial^2 z_b}{\partial x \partial t}, \tag{2.118}$$

$$\frac{\partial w_b}{\partial x} = \frac{\partial^2 z_b}{\partial x \partial t} + \frac{\partial U}{\partial x}\frac{\partial z_b}{\partial x} + U\frac{\partial^2 z_b}{\partial x^2}, \tag{2.119}$$

so that

$$\frac{\mathrm{D}w_b}{\mathrm{D}t} = \underbrace{\frac{\partial^2 z_b}{\partial t}}_{\frac{\partial}{\partial t}\left(-\frac{1}{1-n}\frac{\partial q_b}{\partial x}\right)} + \frac{\partial U}{\partial t}\frac{\partial z_b}{\partial x} + \underbrace{\left(U\frac{\partial^2 z_b}{\partial x \partial t} + U\frac{\partial^2 z_b}{\partial x \partial t}\right)}_{2U\frac{\partial^2 z_b}{\partial x \partial t} = 2U\frac{\partial}{\partial x}\left(-\frac{1}{1-n}\frac{\partial q_b}{\partial x}\right)} + \left[U\left(\frac{\partial U}{\partial x}\frac{\partial z_b}{\partial x} + U\frac{\partial^2 z_b}{\partial x^2}\right)\right]. \tag{2.120}$$

Here, the Exner equation has been used as indicated in the sub-braced terms. For time and space independent porosity, this reduces to

$$\frac{\mathrm{D}w_b}{\mathrm{D}t} = -\frac{1}{(1-n)}\frac{\partial^2 q_b}{\partial x \partial t} - \frac{2U}{(1-n)}\frac{\partial^2 q_b}{\partial x^2} + \frac{\partial U}{\partial t}\frac{\partial z_b}{\partial x} + U\frac{\partial U}{\partial x}\frac{\partial z_b}{\partial x} + U^2\frac{\partial^2 z_b}{\partial x^2}. \tag{2.121}$$

An alternative expression for M is, thus, given by

$$\begin{aligned} M = {} & U^2 h + g\frac{h^2}{2} + \left(U_x^2 - U_{xt} - UU_{xx}\right)\frac{h^3}{4} \\ & + \left(-\frac{1}{(1-n)}\frac{\partial^2 q_b}{\partial x \partial t} - \frac{2U}{(1-n)}\frac{\partial^2 q_b}{\partial x^2} + \frac{\partial U}{\partial t}\frac{\partial z_b}{\partial x} + U\frac{\partial U}{\partial x}\frac{\partial z_b}{\partial x} + U^2\frac{\partial^2 z_b}{\partial x^2}\right)\frac{h^2}{2}. \end{aligned} \tag{2.122}$$

The corresponding bed pressure, Eq. (2.106), is then determined by

$$\begin{aligned} \frac{p_b}{\rho} &= gh + h\frac{\mathrm{D}\bar{w}}{\mathrm{D}t} \\ &= gh + h\left[\left(U_x^2 - U_{xt} - UU_{xx}\right)\frac{h}{2} - \frac{1}{(1-n)}\frac{\partial^2 q_b}{\partial x \partial t} - \frac{2U}{(1-n)}\frac{\partial^2 q_b}{\partial x^2}\right. \\ &\quad \left. + \frac{\partial U}{\partial t}\frac{\partial z_b}{\partial x} + U\frac{\partial U}{\partial x}\frac{\partial z_b}{\partial x} + U^2\frac{\partial^2 z_b}{\partial x^2}\right]. \end{aligned} \tag{2.123}$$

This equation holds only for n = const. Moreover, for vanishing bed transport (q_b = 0), the bed is not eroded and, thus, does not evolve in time [$z_b = z_b(x)$]. The resulting flow momentum is then obtained as

$$M = U^2 h + g\frac{h^2}{2} + \left(U_x^2 - U_{xt} - UU_{xx}\right)\frac{h^3}{4} + \left(\frac{\partial U}{\partial t}\frac{\partial z_b}{\partial x} + U\frac{\partial U}{\partial x}\frac{\partial z_b}{\partial x} + U^2\frac{\partial^2 z_b}{\partial x^2}\right)\frac{h^2}{2}. \tag{2.124}$$

If unsteady flow terms are neglected,

$$M = U^2 h + g\frac{h^2}{2} + \left(U_x^2 - UU_{xx}\right)\frac{h^3}{4} + \left(U\frac{\partial U}{\partial x}\frac{\partial z_b}{\partial x} + U^2\frac{\partial^2 z_b}{\partial x^2}\right)\frac{h^2}{2}, \tag{2.125}$$

or

$$M = g\frac{h^2}{2} + U^2 h\left(1 + \frac{h}{4}\frac{\mathrm{d}^2 h}{\mathrm{d}x^2} - \frac{1}{4}\left(\frac{\mathrm{d}h}{\mathrm{d}x}\right)^2 + \frac{1}{2}h\frac{\mathrm{d}^2 z_b}{\mathrm{d}x^2} - \frac{1}{2}\frac{\mathrm{d}h}{\mathrm{d}x}\frac{\mathrm{d}z_b}{\mathrm{d}x}\right). \tag{2.126}$$

Retaining only curvature terms, one finally arrives at the basic equation used by Engelund and Hansen (1966)

$$M = g\frac{h^2}{2} + U^2 h\left(1 + \frac{h}{4}\frac{\mathrm{d}^2 h}{\mathrm{d}x^2} + \frac{h}{2}\frac{\mathrm{d}^2 z_b}{\mathrm{d}x^2}\right). \tag{2.127}$$

Equation (2.127) is based on a linear pressure distribution with depth. If the parabolic pressure distribution due to Serre (1953) is used instead, the factor (1/4) in the water curvature term must be replaced by (1/3), leading to the theoretical equation used by Engelund and Hansen (1966)

$$M = g\frac{h^2}{2} + U^2 h\left(1 + \frac{h}{3}\frac{\mathrm{d}^2 h}{\mathrm{d}x^2} + \frac{h}{2}\frac{\mathrm{d}^2 z_b}{\mathrm{d}x^2}\right). \tag{2.128}$$

Note that the more general Eq. (2.122) for the momentum flux M is accounting for both unsteadiness and bed-load transport. Although coastal engineering applications are not within the scope of this book, the equations presented are of applicability in this branch of hydraulics too. The propagation of solitary waves over submerged obstacles, e.g., an island, is an application in the realm of coastal engineering; it was so developed by Seabra-Santos et al. (1987). Consider the more general theory by Serre (1953). The 1D unsteady x-momentum equation, in which the stress terms are neglected (potential flow), is, from Eq. (2.28),

$$\frac{\partial}{\partial t}(Uh) + \frac{\partial M}{\partial x} = -\frac{p_b}{\rho}\frac{\partial z_b}{\partial x}, \tag{2.129}$$

where

$$M = hU^2 + \int_{z_b}^{z_s} \frac{p}{\rho}\mathrm{d}z. \tag{2.130}$$

The vertical velocity for unsteady 1D flowing over curved terrain is obtained from Eq. (2.37),

$$\begin{aligned} w &= -\frac{\partial}{\partial x}[U(z - z_b)] = -\frac{\partial}{\partial x}\left[\frac{\partial U}{\partial x}(z - z_b) - U\frac{\partial z_b}{\partial x}\right] \\ &= -\frac{\partial U}{\partial x}(z - z_b) + U\frac{\partial z_b}{\partial x}. \end{aligned} \tag{2.131}$$

Similarly, the expression for the pressure is, from Eq. (2.40),

$$p = \rho g(z_s - z) + \rho \frac{\partial}{\partial t} \int_z^{z_s} w \mathrm{d}z' + \rho \frac{\partial}{\partial x} \left[U \int_z^{z_s} w \mathrm{d}z' \right] - \rho w^2. \tag{2.132}$$

Computing the integral

$$\int_z^{z_s} w \mathrm{d}z' = -\frac{\partial U}{\partial x} \frac{(h^2 - \eta^2)}{2} + U \frac{\partial z_b}{\partial x} (h - \eta), \tag{2.133}$$

and inserting Eqs. (2.131) and (2.133) into Eq. (2.132), the pressure distribution is obtained with similar steps to those used to obtain Eq. (2.67).

For illustrative purposes, an alternative procedure is presented here to obtain the flow momentum M without computing the distribution $p(z)$. The vertical equation of motion for an inviscid fluid is

$$\frac{\mathrm{D}w}{\mathrm{D}t} = \frac{\partial w}{\partial t} + u \frac{\partial w}{\partial x} + v \frac{\partial w}{\partial y} + w \frac{\partial w}{\partial z} = -\frac{1}{\rho} \frac{\partial p}{\partial z} - g. \tag{2.134}$$

Multiplying Eq. (2.134) by $\eta = z - z_b$ gives

$$\eta \frac{\mathrm{D}w}{\mathrm{D}t} = -\frac{1}{\rho} \eta \frac{\partial p}{\partial z} - g\eta, \tag{2.135}$$

or

$$\eta \frac{\mathrm{D}w}{\mathrm{D}t} = -\frac{1}{\rho} \left[\frac{\partial}{\partial z} (p\eta) - p \right] - g\eta. \tag{2.136}$$

Integrating Eq. (2.136) over the flow depth yields

$$\int_{z_b}^{z_s} \eta \frac{\mathrm{D}w}{\mathrm{D}t} \mathrm{d}z = -\frac{1}{\rho} \int_{z_b}^{z_s} \frac{\partial}{\partial z} (p\eta) \mathrm{d}z + \frac{1}{\rho} \int_{z_b}^{z_s} p \mathrm{d}z - \int_{z_b}^{z_s} g\eta \mathrm{d}z, \tag{2.137}$$

or after the evaluation of the integrals

$$\frac{1}{\rho} \int_{z_b}^{z_s} p \mathrm{d}z = g \frac{h^2}{2} + \int_{z_b}^{z_s} \eta \frac{\mathrm{D}w}{\mathrm{D}t} \mathrm{d}z. \tag{2.138}$$

Equation (2.138) is an exact depth-integrated identity, useful for the exact definition of the momentum flux if one does not wish to compute the pressure distribution from Eq. (2.132). Equation (2.130) is rewritten with the aid of Eq. (2.138) as

$$M = hU^2 + g\frac{h^2}{2} + \int_{z_b}^{z_s} \eta \frac{\mathrm{D}w}{\mathrm{D}t}\mathrm{d}z. \tag{2.139}$$

Now, Dw/Dt is for flow in a vertical plane

$$\frac{\mathrm{D}w}{\mathrm{D}t} = \frac{\partial w}{\partial t} + u\frac{\partial w}{\partial x} + w\frac{\partial w}{\partial z}. \tag{2.140}$$

Using Eq. (2.131) one gets

$$\begin{aligned} \frac{\partial w}{\partial t} &= -\frac{\partial^2 U}{\partial x \partial t}(z - z_b) + \frac{\partial U}{\partial t}\frac{\partial z_b}{\partial x}, \\ \frac{\partial w}{\partial z} &= -\frac{\partial U}{\partial x}, \\ \frac{\partial w}{\partial x} &= -\frac{\partial^2 U}{\partial x^2}(z - z_b) + 2\frac{\partial U}{\partial x}\frac{\partial z_b}{\partial x} + U\frac{\partial^2 z_b}{\partial x^2}, \end{aligned} \tag{2.141}$$

from which Eq. (2.140) takes the form

$$\frac{\mathrm{D}w}{\mathrm{D}t} = \left[\left(\frac{\partial U}{\partial x}\right)^2 - \frac{\partial^2 U}{\partial x \partial t} - U\frac{\partial^2 U}{\partial x^2}\right]\eta + \frac{\partial U}{\partial t}\frac{\partial z_b}{\partial x} + U\frac{\partial U}{\partial x}\frac{\partial z_b}{\partial x} + U^2\frac{\partial^2 z_b}{\partial x^2}. \tag{2.142}$$

Inserting Eq. (2.142) into Eq. (2.139) results in the momentum flow function

$$M = U^2 h + g\frac{h^2}{2} + \left(U_x^2 - U_{xt} - UU_{xx}\right)\frac{h^3}{3} + \left(\frac{\partial U}{\partial t}\frac{\partial z_b}{\partial x} + U\frac{\partial U}{\partial x}\frac{\partial z_b}{\partial x} + U^2\frac{\partial^2 z_b}{\partial x^2}\right)\frac{h^2}{2}. \tag{2.143}$$

The bottom pressure is computed by integrating Eq. (2.134) and inserting Eq. (2.142) as

$$\begin{aligned} \frac{p_b}{\rho} &= gh + \int_{z_b}^{z_s} \frac{\mathrm{D}w}{\mathrm{D}t}\mathrm{d}z \\ &= gh + \left(U_x^2 - U_{xt} - UU_{xx}\right)\frac{h^2}{2} + \left(\frac{\partial U}{\partial t}\frac{\partial z_b}{\partial x} + U\frac{\partial U}{\partial x}\frac{\partial z_b}{\partial x} + U^2\frac{\partial^2 z_b}{\partial x^2}\right)h. \end{aligned} \tag{2.144}$$

Seabra-Santos et al. (1987) numerically solved Eqs. (2.129), (2.143), and (2.144) coupled with the continuity equation, finding an accurate description of solitary wave propagation over submerged obstacles. This simplified model is, therefore, a particular case of the general theory developed here.

2.6 Numerical Methods for Boussinesq-Type Models

2.6.1 Unsteady Flow Simulations

Simulation of unsteady flows using depth-averaged models generally requires numerical solutions. The numerical technique used to solve the mathematical equations describing the physical system must be robust and stable. Water flows over irregular topography experiences changes in the flow regimes due to moving shocks (Vreudgenhil 1994; Toro 1997, 2001; Chaudhry 2008; Kim et al. 2009). A key issue for numerical modeling is that the system of equations must be written in conservative form, as done in Eq. (2.33), because shocks are otherwise not captured. The unsteady non-hydrostatic flow equations were solved using finite difference methods for applications involving water wave propagation, in particular by Peregrine (1966, 1967), Seabra-Santos et al. (1987), Antunes do Carmo et al. (1993), Wei et al. (1995), and Mohapatra and Chaudhry (2004), among others. The unsteady non-hydrostatic flow equations were solved using a finite element method by Khan and Steffler (1996a, b) for applications in hydraulic structures. However, the finite volume method appears to be the technique of most frequent use in free surface flow modeling (Le Veque 2002; Toro 2001; Kim et al. 2009; Denlinger and O'Connell 2008), even though it is sometimes coupled in a hybrid way, either with finite difference (Kim et al. 2009), or finite element methods, i.e., the discontinuous method of Galerkin (Khan and Lai 2014). In this section, a practical introduction to finite volume methods for shallow water flows is presented. For fundamental issues or advanced topics, the books of Toro (1997, 2001) or Le Veque (2002) are recommended.

Consider 1D unsteady water flows over a curved and rigid bottom as described for instance by Denlinger and O'Connell (2008). The conservation laws has the form

$$\frac{\partial \mathbf{U}}{\partial t} + \frac{\partial \mathbf{F}}{\partial x} = \mathbf{S}. \tag{2.145}$$

Here, $\mathbf{U}$ is the vector of the conserved variables, $\mathbf{F}$ is the flux vector, and $\mathbf{S}$ the source term vector, given by

$$\mathbf{U} = \begin{pmatrix} h \\ hU \end{pmatrix}, \quad \mathbf{F} = \begin{pmatrix} hU \\ hU^2 + \frac{1}{2}g'h^2 \end{pmatrix}, \quad \mathbf{S} = \begin{pmatrix} 0 \\ -g'h\frac{\partial z_b}{\partial x} - \frac{\tau_b}{\rho} \end{pmatrix}. \tag{2.146}$$

Furthermore, the enhanced gravity for 1D flows is given by

$$g' = g + \frac{\mathrm{D}\bar{w}}{\mathrm{D}t} = g + \frac{\partial \bar{w}}{\partial t} + U\frac{\partial \bar{w}}{\partial x}, \tag{2.147}$$

in which the depth-averaged vertical velocity for flows over a rigid bed is given by

$$\bar{w} = \frac{1}{2}\left(\frac{\partial h}{\partial t} + U\frac{\partial h}{\partial x}\right) + U\frac{\partial z_b}{\partial x} = w_b - h\frac{\partial U}{\partial x}, \quad w_b = U\frac{\partial z_b}{\partial x}. \tag{2.148}$$

The differential Eq. (2.145) is valid in the zones of the computational domain with smooth or continuous solutions, but it does not apply at discontinuous portions like moving shocks. Therefore, Eq. (2.145) is integrated over a control volume in the x-t plane as

$$\iint \left(\frac{\partial \mathbf{U}}{\partial t} + \frac{\partial \mathbf{F}}{\partial x}\right) \mathrm{d}x\mathrm{d}t = \iint \mathbf{S}\mathrm{d}x\mathrm{d}t. \tag{2.149}$$

The integral Eq. (2.149) permits the computation of both continuous and discontinuous solutions as shocks. It is the base of the finite volume method. For a rectangular control volume in the x-t plane (Fig. 2.10), one can write

$$\int_t^{t+\Delta t}\int_{x_{i-1/2}}^{x_{i+1/2}} \left(\frac{\partial \mathbf{U}}{\partial t} + \frac{\partial \mathbf{F}}{\partial x}\right) \mathrm{d}x\mathrm{d}t = \int_{x_{i-1/2}}^{x_{i+1/2}} \mathrm{d}x \int_t^{t+\Delta t} \frac{\partial \mathbf{U}}{\partial t}\mathrm{d}t + \int_t^{t+\Delta t} \mathrm{d}t \int_{x_{i-1/2}}^{x_{i+1/2}} \frac{\partial \mathbf{F}}{\partial x}\mathrm{d}x = \iint \mathbf{S}\mathrm{d}x\mathrm{d}t \tag{2.150}$$

Here, i is the cell index in the x-direction, and $i + 1/2$ the interface between cells i and $i + 1$. The integral of Eq. (2.150) is then exactly given by (Toro 1997, 2001)

$$\int_{x_{i-1/2}}^{x_{i+1/2}} [\mathbf{U}(t+\Delta t) - \mathbf{U}(t)]\mathrm{d}x + \int_t^{t+\Delta t} \left[\mathbf{F}\left(x_{i+1/2}\right) - \mathbf{F}\left(x_{i-1/2}\right)\right]\mathrm{d}t = \iint \mathbf{S}\mathrm{d}x\mathrm{d}t. \tag{2.151}$$

Note that despite the notation is made with reference to the cell index i, and corresponding interfaces, no numerical approximations are invoked in Eq. (2.151).

Let temporal and spatial average values be

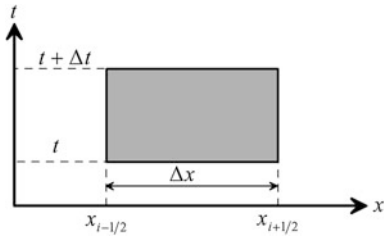

Fig. 2.10 Control volume in x-t plane

$$\mathbf{F}_{i+1/2} = \frac{1}{\Delta t}\int_{t}^{t+\Delta t} \mathbf{F}\left(x_{i+1/2}, t\right)\mathrm{d}t,$$

$$\mathbf{F}_{i-1/2} = \frac{1}{\Delta t}\int_{t}^{t+\Delta t} \mathbf{F}\left(x_{i-1/2}, t\right)\mathrm{d}t,$$

$$\mathbf{U}_i^{n+1} = \frac{1}{\Delta x}\int_{x_{i-1/2}}^{x_{i-1/2}+\Delta x} \mathbf{U}(x, t+\Delta t)\mathrm{d}x, \tag{2.152}$$

$$\mathbf{U}_i^{n} = \frac{1}{\Delta x}\int_{x_{i-1/2}}^{x_{i-1/2}+\Delta x} \mathbf{U}(x, t)\mathrm{d}x,$$

$$\mathbf{S}_i = \frac{1}{\Delta x \Delta t}\iint \mathbf{S}\mathrm{d}x\mathrm{d}t.$$

For the quadrilateral control volume in the x-t plane as shown in Fig. 2.10, the conservative Eq. (2.151) reads exactly, using Eq. (2.152) for time and space averages,

$$\mathbf{U}_i^{n+1} = \mathbf{U}_i^{n} - \frac{\Delta t}{\Delta x}\left(\mathbf{F}_{i+1/2} - \mathbf{F}_{i-1/2}\right) + \Delta t \mathbf{S}_i. \tag{2.153}$$

In the finite volume method, the computational domain is divided into a number of control volumes in the x-t plane (Fig. 2.11), where Eq. (2.153) is applied. Here, $\mathbf{F}_{i+1/2}$ is the numerical flux across the interface between cells i and $i + 1$. Again, no numerical approximations are introduced in Eq. (2.153), but its formulation is presented in the usual form suitable for developing numerical schemes.

In practice, the source terms $\mathbf{S}_i$ and the fluxes $\mathbf{F}_{i+1/2}$ are evaluated at a suitable time level that depends on the specific method applied (Toro 1997, 2001), thereby introducing numerical approximations. Usually, explicit schemes are employed. Shock-capturing finite volume solutions using the Godunov upwind method assisted by robust Riemann solvers (approximate or exact) are well established today as accurate solvers of shallow water flows (Toro 2001; LeVeque 2002;

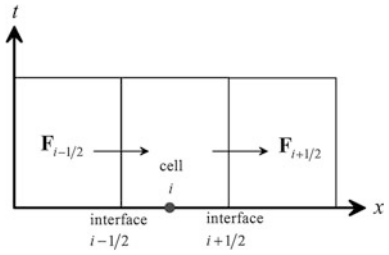

Fig. 2.11 Intercell fluxes

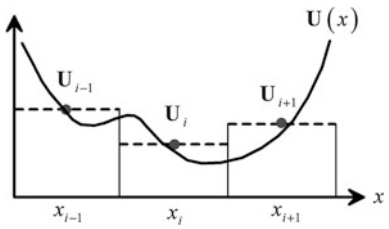

Fig. 2.12 Piecewise approximation using cell-averaged values

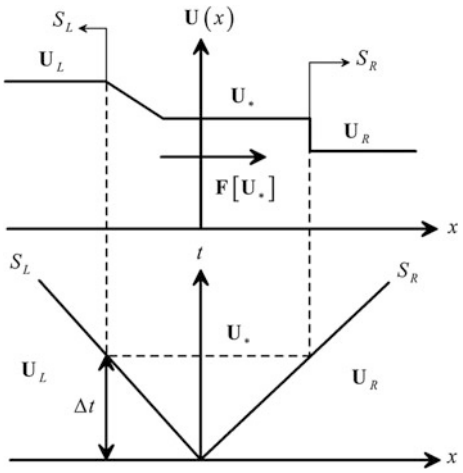

Fig. 2.13 Riemann problem solution structure for left-going rarefaction wave and right going shock front

Denlinger and O'Connell 2008 among others). In the Godunov upwind method, the actual solution $\mathbf{U}(x)$ at time t is approximated by the cell-averaged values within each cell (Fig. 2.12).

Between two adjacent cells, there is a discontinuity in $\mathbf{U}$, giving rise to a number of local Riemann problems at each cell interface. Consider two states $\mathbf{U}_L$ and $\mathbf{U}_R$ separated at the initial time, at a generic interface between two cells. This is by definition a local Riemann problem, and a number of wave patterns may evolve after a time Δt. In Fig. 2.13, the typical case with a left-going rarefaction wave and right-going shock front is presented (note the local system of reference with x-origin at the cell interface). The shock front and rarefaction wave propagate with signal speeds S_R and S_L, respectively.

The constant state region just behind the shock front (star region) is denoted as $\mathbf{U}_*$. The numerical flux crossing the original discontinuity at $x = 0$ is $\mathbf{F}$, which is needed to apply Eq. (2.153). Note that the start region in the Riemann problem is essentially a steady-state zone where the conserved variables are $\mathbf{U}_*$, which is a part of the total (local) Riemann solution $\mathbf{U}(x)$ after time Δt. Therefore, the numerical flux crossing the t-axis ($x = 0$) in the Riemann problem is also a constant, so that the intercell flux is exactly evaluated based on the Riemann solution at $x = 0$ as

$$\mathbf{F}_{i+1/2} = \frac{1}{\Delta t} \underbrace{\int_{t}^{t+\Delta t} \mathbf{F}\left(x_{i+1/2}, t\right) \mathrm{d}t}_{\text{global system of reference}} = \frac{1}{\Delta t} \underbrace{\int_{0}^{\Delta t} \mathbf{F}(0,t) \mathrm{d}t}_{\text{local system of reference}} = \mathbf{F}[\mathbf{U}(x=0)] = \mathbf{F}(\mathbf{U}_*). \tag{2.154}$$

Therefore, the numerical flux at each interface is computed based on the solution of the local Riemann problem $\mathbf{U}(x)$ at this interface, evaluated at $x = 0$.

The solution of the Riemann problem may be conducted exactly, but resort to a numerical method to solve the resulting implicit, nonlinear equation is required. Thus, approximate (explicit) Riemann solvers use a simplified representation of the wave structure as shown in Fig. 2.13. Here, the Harten-Lax-van Leer (HLL) approximate Riemann solver is presented, suitable for 1D depth-averaged water flow equations. It approximates the intercell numerical flux as (Toro 2001)

$$\mathbf{F}_{i+1/2} = \begin{cases} \mathbf{F}_L & \text{if} \quad S_L \geq 0, \\ \frac{S_R \mathbf{F}_L - S_L \mathbf{F}_R + S_R S_L (\mathbf{U}_R - \mathbf{U}_L)}{S_R - S_L}, & \text{if} \quad S_L \leq 0 \leq S_R, \\ \mathbf{F}_R & \text{if} \quad S_R \leq 0. \end{cases} \tag{2.155}$$

Here, $\mathbf{F}_L$ and $\mathbf{F}_R$ are the fluxes computed at states L and R. Basically, the method assumes that the left and right waves are discontinuities, and between them there is a constant-state solution denoted as $\mathbf{U}_{HLL}$. Figure 2.14 illustrates wave propagation cases for the HLL Riemann solver. For a detailed theoretical derivation of the HLL equations, see Toro (1997, 2001). Robust wave speed estimates S_L and S_R are given by (Toro 2001)

$$S_L = U_L - a_L q_L; \quad S_R = U_R + a_R q_R. \tag{2.156}$$

Here $a = (g'h)^{1/2}$, and q_K ($K = L, R$) is

$$q_K = \begin{cases} \left[\frac{1}{2}\left(\frac{h_*(h_* + h_K)}{h_K^2}\right)\right]^{1/2} & h_* > h_K, \\ 1 & h_* \leq h_K. \end{cases} \tag{2.157}$$

Note the use of the enhanced gravity in the Riemann problem (Denlinger and Iverson 2004; Denlinger and O'Connell 2008), and, thus, the inclusion of the non-hydrostatic pressure in the computation of numerical fluxes. The flow depth at the star region of the Riemann problem at each interface h_* is

$$h_* = \frac{1}{g}\left(\frac{1}{2}(a_L + a_R) + \frac{1}{4}(U_L - U_R)\right)^2. \tag{2.158}$$

For a channel reach, discretized into a number of finite volumes, the computation of the intercell numerical flux $\mathbf{F}_{i+1/2}$ amounts to solve several local Riemann problems,

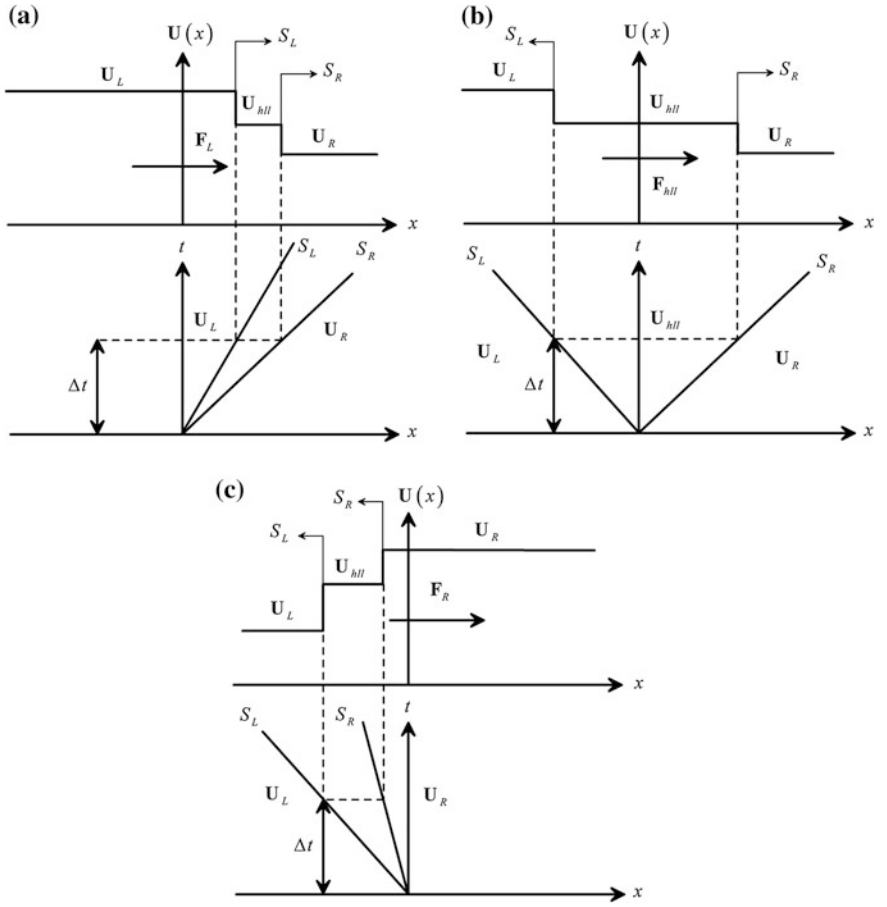

Fig. 2.14 Wave propagation cases of HLL approximate Riemann solver. Cases **a**–**c** represent Eq. (2.155)

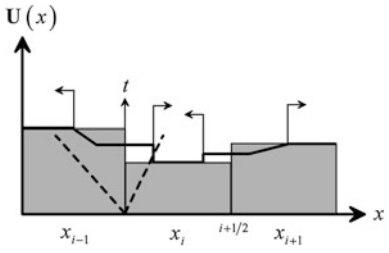

Fig. 2.15 Wave propagation at cell interfaces with (*thick lines*) as instantaneous $\mathbf{U}(x)$ profile and (*dashed lines*) x-t rarefaction wave and shock front paths at interface $i - 1/2$

one between each adjacent cells. As a result, the evolution of $\mathbf{U}$ in the computational domain accounts for the wave propagation conditions at interfaces (Fig. 2.15). Therefore, the method is of upwind type, i.e., the wave propagation

information is used to update the conserved variables in time. This method, first-order accurate in both space and time, is essentially the Godunov first-order upwind method. However, high-order accuracy is sometimes advisable. To obtain second-order accuracy in space, a polynomial reconstruction is made within each cell, sometimes linear. Linear slopes resulting from the reconstructed solution must be limited to avoid spurious oscillations near discontinuities.

For stability in time of the explicit scheme, the Courant–Friedrichs–Lewy number CFL must be less than unity. The time step Δt is then determined at time level n using the equation

$$\Delta t = \frac{\Delta x}{\max\left(|U_i^n| + (gh_i^n)^{1/2}\right)}\mathrm{CFL}. \tag{2.159}$$

Here, Δt and Δx are the step sizes in the x- and t-directions, respectively. Details are found in Toro (1997, 2001).

The computation of shallow water flows over variable topography must be conducted using a well-balanced scheme (Toro 2001). It implies that once a discretization is applied to the source terms $\mathbf{S}_i$, the time evolution of the conserved variables must reach a stable steady state $\mathbf{U}_i^{n+1} = \mathbf{U}_i^n$ if afforded by the boundary conditions. The asymptotic steady-state version of Eq. (2.153) then takes the form

$$\left(\mathbf{F}_{i+1/2} - \mathbf{F}_{i-1/2}\right) + \Delta x \mathbf{S}_i = \mathbf{0}. \tag{2.160}$$

It may be regarded as an identity that is verified only if the discretization of $\mathbf{S}$ is correctly implemented. Consider as example static water over variable topography (Fig. 2.16). The imbalance of intercell fluxes at cell i is then given by the hydrostatic forces as

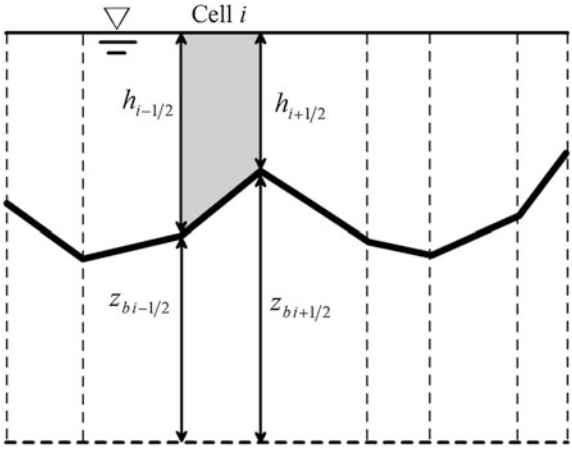

Fig. 2.16 Static water over variable topography

$$\mathrm{F}_{i+1/2} - \mathrm{F}_{i-1/2} = g\frac{\left(h_{i+1/2}^2 - h_{i-1/2}^2\right)}{2} = g\frac{\left(h_{i+1/2} - h_{i-1/2}\right)\left(h_{i+1/2} + h_{i-1/2}\right)}{2}. \tag{2.161}$$

The compatible discretization of the bed slope source term to verify Eq. (2.160) due to the condition $h + z_b = \text{const.}$ is

$$\mathrm{S}_i = gh_i\left(\frac{\partial z_b}{\partial x}\right)_i = g\frac{\left(h_{i+1/2} + h_{i-1/2}\right)}{2}\frac{\left(z_{bi+1/2} - z_{bi-1/2}\right)}{\Delta x}. \tag{2.162}$$

Other discretizations of the bed slope source term will generate unphysical numerical flux.

In general, numerical difficulties are introduced by dispersion terms in non-hydrostatic depth-averaged models. As an illustrative example, consider Eqs. (2.48)–(2.49). Assume that they are discretized using finite difference discretization (Chaudhry 2008). Finite differencing to second-order accuracy of the first-order derivative $\partial U/\partial x = (U_{i+1} - U_{i-1})/(2\Delta x) + \mathrm{O}(\Delta x^2)$ produces in the Saint-Venant terms truncation errors proportional to U_{xxx}. These errors will have mathematically the same form as physical dispersive terms (Abbott 1979; Wei and Kirby 1995), just as those originating from expanding the gradient $\partial(h^3 U U_{xx}/3)/\partial x$. If no counter measures are taken to reduce truncation errors, physical dispersive effects are masked by numerical oscillations. Thus, higher-order differencing of leading order hydrostatic (Saint-Venant) terms is required to guarantee that physical dispersion effects are not masked by spurious numerical oscillations associated with truncation errors (Wei and Kirby 1995). Ideally, these problems disappear with a computational mesh, if $\Delta x \to 0$ and $\Delta y \to 0$. However, this is not practical, so that the control of truncation errors is necessary for usual meshes. Kim et al. (2009) provide a useful reference, given the account of all these issues in a finite volume model. Their modified finite volume method for dispersive systems consists in substituting the Euler time stepping by a fourth-order accurate time stepping method, composed of a predictor step using a third-order Adams–Bashforth formula and an iterative corrector using a fourth-order Adam–Moulton formula. The treatment of the leading order hydrostatic terms was done using a fourth-order accurate MUSCL TVD procedure for reconstruction of interface values and a HLLC Riemann solver to compute fluxes. Prior to the application of the finite volume solution, the vector $\mathbf{U}$ is mathematically replaced by an auxiliary vector that includes terms with spatial derivatives, to eliminate time derivatives (contained in mixed terms such as U_{xt}) from the vectors $\mathbf{F}$ and $\mathbf{G}$. The solution is then performed for auxiliary variables, and the vector $\mathbf{U}$ is determined by discretizing the spatial derivatives to second-order accuracy, leading to tridiagonal systems for determining $\mathbf{U}$. For high-resolution finite volume solutions of non-hydrostatic water wave problems, see Cienfuegos et al. (2006), Kim et al. (2009), and Cantero-Chinchilla et al. (2016a, b).

2.6.2 Steady Flow Simulations

A great variety of non-hydrostatic problems can be considered under steady flow conditions. According to Roache (1976), a steady flow condition may be regained as limiting asymptotic state after a transient flow computation. Khan and Steffler (1996a, b) pursued this approach and computed steady flows in curved bed structures using unsteady flow computations. Another option is to directly solve the steady-state version of the governing equations. Generally, this leads to a system of ordinary differential equations (ODEs), typically reduced to a single third-order ODE, as shown in the next example. Consider based on Eqs. (2.62), (2.68), and (2.69), the flow over a curved bed as given by the ODE

$$\frac{\mathrm{d}}{\mathrm{d}x}\left[\frac{h^2}{2}+\frac{q^2}{gh}\left(1+\frac{hh_{xx}-h_x^2}{3}+\frac{hz_{bxx}}{2}-\frac{h_xz_{bx}}{2}\right)\right] = -\left[h+\frac{q^2}{2g}\left(2hz_{bxx}+hh_{xx}-h_x^2-2h_xz_{bx}\right)\right]z_{bx}. \tag{2.163}$$

Neglecting second-order products of derivatives of h and z_b, Eq. (2.163) is simplified to

$$\frac{q^2}{g}\left(\frac{1}{3}\frac{\mathrm{d}^3h}{\mathrm{d}x^3}+\frac{1}{2}\frac{\mathrm{d}^2z_b}{\mathrm{d}x^2}\right)+\left(h-\frac{q^2}{gh^2}\right)\frac{\mathrm{d}h}{\mathrm{d}x}=-h\frac{\mathrm{d}z_b}{\mathrm{d}x}. \tag{2.164}$$

This closely resembles the original Boussinesq momentum equation for curved beds (Boussinesq 1877). The solution of a steady Boussinesq equation is a boundary-value problem. Equation (2.164) is a third-order ODE, so that three boundary conditions are needed. It can be solved using shooting methods (e.g., by resort to Runge–Kutta solvers), but this approach requires high precision in setting the conditions at the upstream boundary section (Hager and Hager 1985; Fenton 1996). Typically, h, $\mathrm{d}h/\mathrm{d}x$, and $\mathrm{d}^2h/\mathrm{d}x^2$ are prescribed at the shooting boundary section. There, in most cases, $\mathrm{d}^2h/\mathrm{d}x^2 = 0$, but $\mathrm{d}h/\mathrm{d}x$ must be iteratively determined with the shooting method until the downstream boundary condition at the end section of the computational domain is satisfied. This method is simple despite the high accuracy needed in the computation of $\mathrm{d}h/\mathrm{d}x$ at the shooting section. An alternative is to solve the problem using a finite difference approximation of the derivatives in Eq. (2.164). In this case, the values of the flow depth prescribed at the two boundary sections of the computational domain, plus $\mathrm{d}h/\mathrm{d}x$ at one of these sections, are directly incorporated into the mathematical model. The numerical method in this case is more complicated than in the shooting approach, given that a system of nonlinear implicit equations results to be solved iteratively to compute the water depths at the nodes of the finite difference mesh, by any numerical technique, as the Newton–Raphson or Secant methods. This approach was adopted

by Hosoda and Tada (1994), Zerihun and Fenton (2006, 2007), and Castro-Orgaz and Hager (2009). Zhu and Lawrence (1998) solved alternatively the boundary-value problem using a collocation method.

2.7 Higher-Order Equations

2.7.1 Fawer-Type Equations

The theory based on Serre's work (1953) may be regarded as accurate for most open-channel flow problems. However, higher-order models may be needed in some instances. These are obtained by taking higher-order approximations for the velocity and pressure distributions to be used in the general depth-averaged equations. While this may be done using mathematical techniques used in fluid mechanics, such as the expansion of the flow variables using Taylor series (Mei 1983) or a perturbation procedure (Peregrine 1967), the costs involved in the integration of a higher-order model will be payed by an increase in the order of differentiation in the system of PDEs (Madsen and Schäffer 1998). Fawer (1937) produced an interesting approach to increase the resolution details of Boussinesq-type equations in the vertical direction without further increasing the order of differentiation (usually the higher-order spatial derivative is limited to third order). He proposed to use an interpolation equation for the streamline curvature κ in the vertical direction of the form

$$\kappa = \kappa_b + (\kappa_s - \kappa_b)\left(\frac{z}{h}\right)^K. \tag{2.165}$$

Here, κ_s is the radius of curvature at the free surface, κ_b the radius of curvature at the channel bottom, and K is a free parameter to be determined. This theory will extensively be described in Chap. 3; here, only the main aspects are discussed as a means of comparison with Serre's approach (1953).

Su and Gardner (1969) made an interesting development to be used for this purpose. They formulated the momentum function M for unsteady flows as

$$M = \int_0^h u^2 \mathrm{d}z + g\frac{h^2}{2} + \int_0^h \frac{\mathrm{D}w}{\mathrm{D}t} z \mathrm{d}z, \tag{2.166}$$

where $w(x, z, t)$ is the vertical velocity and

$$\frac{\mathrm{D}w}{\mathrm{D}t}(x, z, t) = \frac{\partial w}{\partial t} + u\frac{\partial w}{\partial x} + w\frac{\partial w}{\partial z}. \tag{2.167}$$

Using an irrotational solution of the velocity and pressure fields, they found that the correction for the non-uniformity of u over the depth in Eq. (2.166) is proportional to $[\partial^2 U/\partial x^2]^2$ and thus of higher order. Therefore, the momentum flux is U^2h. Then, they essentially arrived at Serre's equation for 1D flows based on the irrotational flow theory

$$M = hU^2 + g\frac{h^2}{2} + \left(U_x^2 - U_{xt} - UU_{xx}\right)\frac{h^3}{3}. \tag{2.168}$$

If a mean acceleration term over the depth is taken using the depth-averaged vertical velocity $\bar{w}$, then Eq. (2.166) yields

$$M = \int_0^h u^2 \mathrm{d}z + g\frac{h^2}{2} + \int_0^h \frac{\mathrm{D}w}{\mathrm{D}t} z \mathrm{d}z = \int_0^h U^2 \mathrm{d}z + g\frac{h^2}{2} + \int_0^h \frac{\mathrm{D}\bar{w}}{\mathrm{D}t} z \mathrm{d}z = U^2 h + g'\frac{h^2}{2}, \tag{2.169}$$

where

$$\frac{\mathrm{D}\bar{w}}{\mathrm{D}t} = \frac{\partial \bar{w}}{\partial t} + U\frac{\partial \bar{w}}{\partial x}. \tag{2.170}$$

This approach was pursued by Denlinger and Iverson (2004) and may be regarded as a depth-averaged approximation to the integral result of Su and Gardner (1969). Intuitively, Eq. (2.166) reveals that a method to produce higher-order flow equations relies on improving the estimation of the vertical acceleration term of the momentum function. The linear vertical velocity profile of Serre (1953),

$$w = -\frac{\partial U}{\partial x} z, \tag{2.171}$$

is closely related to a linear variation in the streamline curvature, i.e., Eq. (2.165) with $K = 1$,

$$\kappa = \kappa_b + (\kappa_s - \kappa_b)\left(\frac{z}{h}\right), \tag{2.172}$$

which is similar to the theory of Matthew (1963). Therefore, improving the estimation of Dw/Dt amounts to use a value of K different from unity. Fenton (1996) and Fenton and Zerihun (2007) produced such an illustrative Fawer-type theory. For 1D steady flow over a curved bed, they expressed the vertical pressure gradient as

$$\frac{1}{\rho}\frac{\partial p}{\partial z} = -g - \frac{\mathrm{D}w}{\mathrm{D}t}. \tag{2.173}$$

Moreover, they estimated Dw/Dt in a vertical section using an average value, producing an approximation, with $\bar{\kappa}$ as depth-averaged streamline curvature and g' as the corresponding enhanced gravity in the section, as

$$\frac{1}{\rho}\frac{\partial p}{\partial z} = -g - U^2\bar{\kappa} = -g'. \tag{2.174}$$

Therefore, the non-hydrostatic correction in Eq. (2.174) is interpreted as a depth-averaged centrifugal acceleration contribution (Fenton 1996), which essentially corresponds to the use of an enhanced gravity (Denlinger and Iverson 2004). The parameter $\bar{\kappa}$ may be interpolated between the curvature values at the free surface, z_s, and at the channel bed, z_b, as

$$\bar{\kappa} = (1-\omega)\kappa_b + \omega\kappa_s \approx \frac{\partial^2 z_b}{\partial x^2} + \omega\frac{\partial^2 h}{\partial x^2}. \tag{2.175}$$

Here, ω is a weighting factor to distribute the contributions of the bed and free surface curvatures on the depth-averaged centrifugal acceleration; slope contributions are neglected. The corresponding momentum function is then

$$\begin{aligned} M &= \int_0^h \left(u^2 + \frac{p}{\rho}\right)\mathrm{d}z = U^2 h + g\frac{h^2}{2}\left(1 + \frac{U^2}{g}\bar{\kappa}\right) = g\frac{h^2}{2} + U^2 h\left(1 + \frac{\bar{\kappa}h}{2}\right) \\ &= g\frac{h^2}{2} + U^2 h\left(1 + \frac{\omega h h_{xx}}{2} + \frac{h z_{bxx}}{2}\right). \end{aligned} \tag{2.176}$$

In Chap. 3, it will be demonstrated that using Fawer's Eq. (2.165), the momentum function reads, if slope effects are neglected,

$$M = g\frac{h^2}{2} + U^2 h\left(1 + \frac{h h_{xx}}{K+2} + \frac{h z_{bxx}}{2}\right). \tag{2.177}$$

Comparing Eqs. (2.176) and (2.177) gives the identity

$$\omega = \frac{2}{K+2}. \tag{2.178}$$

For ω = 2/3 (Fenton and Zerihun 2007), Eq. (2.176) gives the basic result of the original Boussinesq (1877) theory, namely

$$M = g\frac{h^2}{2} + U^2 h\left(1 + \frac{h h_{xx}}{3} + \frac{h z_{bxx}}{2}\right). \tag{2.179}$$

The compatibility value of Fawer's theory is then $K = 1$ from Eq. (2.178), as used by Matthew (1963). Inserting Eq. (2.179) into the streamwise momentum balance,

$$\frac{\mathrm{d}M}{\mathrm{d}x} = gh\left(S_o - S_f\right), \tag{2.180}$$

produces the ODE (note that the momentum velocity correction coefficient is unity)

$$\frac{U^2h^2}{g}\left(\frac{1}{3}\frac{\mathrm{d}^3h}{\mathrm{d}x^3} - \frac{1}{2}\frac{\mathrm{d}^2S_o}{\mathrm{d}x^2}\right) + \left(h - \frac{U^2}{g}\right)\frac{\mathrm{d}h}{\mathrm{d}x} = h\left(S_o - S_f\right). \tag{2.181}$$

This was originally developed by Boussinesq (1877) and rederived by Fenton and Zerihun (2007), with S_o as the bottom slope and S_f as the friction slope.

Once the main ingredient of Fawer's theory is elucidated, an enhanced 1D unsteady flow model is produced to illustrate how higher-order equations may be formulated. Serre's (1953) theory is based on a parabolic pressure distribution (Castro-Orgaz et al. 2015), whereas Khan and Steffler (1996a, b) and Denlinger and Iverson (2004) prescribed a linear pressure profile to the flow equations. A general interpolation function for the pressure profile follows Fawer (1937) as

$$p = \rho gh\left(1 - \frac{z}{h}\right) + p_1\left[1 - \left(\frac{z}{h}\right)^K\right]. \tag{2.182}$$

Here, the free surface pressure vanishes at $z/h = 1$, and the bed pressure in excess of the hydrostatic pressure is p_1 (Khan and Steffler 1996a, b), namely

$$p_1 = \rho\frac{\partial}{\partial t}(\bar{w}h) + \rho\frac{\partial}{\partial x}(\bar{w}Uh). \tag{2.183}$$

Using Eq. (2.182), the momentum function is then

$$M = \int_0^h \left(u^2 + \frac{p}{\rho}\right)\mathrm{d}z = U^2h + g\frac{h^2}{2} + \frac{K}{K+1}\frac{p_1h}{\rho}. \tag{2.184}$$

For $K = 1$, this expression gives the momentum function of Khan and Steffler's Boussinesq-type model, whereas $K = 2$ results in Serre's theory. For flows over a horizontal bed, Eqs. (2.183)–(2.184) may be combined, using Eq. (2.144), to yield

$$\begin{aligned} M &= U^2h + g\frac{h^2}{2} + \frac{K}{K+1}\frac{p_1h}{\rho} = U^2h + g\frac{h^2}{2} + \frac{K}{K+1}\left[\left(U_x^2 - U_{xt} - UU_{xx}\right)\frac{h^2}{2}\right]h \\ &= U^2h + g\frac{h^2}{2} + \left(U_x^2 - U_{xt} - UU_{xx}\right)\frac{h^3}{3\lambda}, \end{aligned} \tag{2.185}$$

where the auxiliary variable λ, affecting the non-hydrostatic term, is (Castro-Orgaz et al. 2015)

$$\lambda = \frac{2}{3}\frac{K+1}{K}. \tag{2.186}$$

The specific value of K for a given flow problem may be found by fitting the depth-averaged model results to experimental data, or to a 2D solution in a certain range of applications (Fawer 1937).

2.7.2 Moment Equations

Steffler and Jin (1993) devised an important method to better recover vertical resolution details in depth-averaged models. Essentially, they produced general 1D depth-averaged momentum equations in the horizontal and vertical directions, in addition to the well-known continuity equation. If arbitrary distributions of (u, w, p) are set into the depth-averaged equations, a number of free parameters remain undetermined. While for specific cases it may be possible to find approximate predictors based on experimental observations, the idea of the method is to produce an additional set of PDEs, one more for each undetermined free parameter, given that the number of PDEs in the system must be compatible with the number of unknown functions. The standard depth-averaged process described in this chapter may be regarded as a weighted residual method with unit weighting functions (Steffler and Jin 1993). Additional independent depth-averaged equations are determined using weighting functions including collocation, Galerkin, and moment methods. Steffler and Jin (1993) used the weighting function

$$f = 2\frac{z-\bar{z}}{h}, \quad \bar{z} = z_b + \frac{h}{2}. \tag{2.187}$$

The continuity, horizontal, and vertical momentum equations are then multiplied by f and depth-integrated, producing three moment equations. As to the distributions of (u, w, p), Steffler and Jin (1993) used a linear profile for u,

$$u = U + u_1\left(2\frac{\eta}{h} - 1\right), \tag{2.188}$$

and quadratic profiles for w and p,

$$w = w_b\left(1 - \frac{\eta}{h}\right) + 4w_2\frac{\eta}{h}\left(1 - \frac{\eta}{h}\right) + w_s\frac{\eta}{h}, \tag{2.189}$$

$$p = (\rho g h + p_1)\left(1 - \frac{\eta}{h}\right) + 4p_2\frac{\eta}{h}\left(1 - \frac{\eta}{h}\right). \tag{2.190}$$

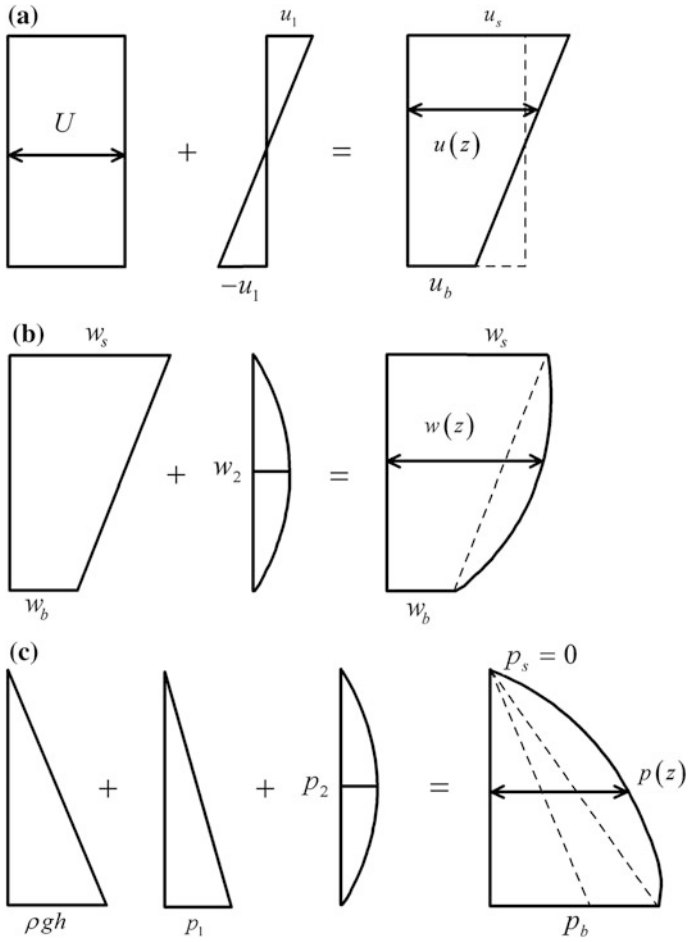

Fig. 2.17 Shape functions used for weighted residual method **a** linear approximation of longitudinal velocity from Eq. (2.188), **b** quadratic distribution of vertical velocity from Eq. (2.189), **c** vertical distribution of pressure from Eq. (2.190)

Here, η is the elevation above the channel bottom, U the vertically averaged horizontal velocity (= q/h), u_1 the linearly distributed surface velocity in excess of the mean, w_2 the middepth vertical velocity in excess of the average, p_1 the bed pressure in excess of hydrostatic, and p_2 the midpressure in excess of the pressure average at the bed and surface (Fig. 2.17).

The kinematic boundary conditions are then

$$w_b = \left(\frac{q}{h} - u_1\right)\frac{\partial z_b}{\partial x}, \tag{2.191}$$

$$w_s = \frac{\partial h}{\partial t} + \left(\frac{q}{h} + u_1\right)\frac{\partial}{\partial x}(z_b + h). \tag{2.192}$$

The governing system of equations based on these particular functions is given by the continuity equation (Steffler and Jin 1993; Khan and Steffler 1996a, b)

$$\frac{\partial q}{\partial x} + \frac{\partial h}{\partial t} = 0. \tag{2.193}$$

The x-momentum equation, in which τ_b is the bed-shear stress and depth-averaged turbulence stresses are neglected, becomes

$$\frac{\partial q}{\partial t} + \frac{\partial}{\partial x}\left(\frac{q^2}{h} + g\frac{h^2}{2} + \frac{1}{3}hu_1^2 + \frac{1}{2\rho}hp_1 + \frac{2}{3\rho}hp_2\right) = -gh\frac{\partial z_b}{\partial x} - \frac{p_1}{\rho}\frac{\partial z_b}{\partial x} - \frac{\tau_b}{\rho}, \tag{2.194}$$

and the z-momentum equation is obtained as

$$\frac{\partial}{\partial t}(h\bar{w}) + \frac{\partial}{\partial x}\left[q\bar{w} - \frac{1}{6}(hu_1\{w_b - w_s\})\right] = \frac{p_1}{\rho} - \frac{\tau_b}{\rho}\frac{\partial z_b}{\partial x}, \tag{2.195}$$

Based on Eq. (2.189), the depth-averaged vertical velocity $\bar{w}$ is

$$\bar{w} = \frac{w_b + w_s}{2} + \frac{2}{3}w_2. \tag{2.196}$$

Khan and Steffler (1996a, b) further derived the moment equations

$$\frac{1}{4}\frac{\partial h^2}{\partial t} + q\frac{\partial \bar{z}}{\partial x} + \frac{\partial}{\partial x}\left(h^2u_1\right) = h\bar{w}, \tag{2.197}$$

$$\frac{\partial u_1}{\partial t} + \frac{\partial}{\partial x}\left(\frac{qu_1}{h}\right) - \frac{1}{2\rho}\left(\frac{\partial p_1}{\partial x} - \frac{p_1}{h}\frac{\partial h}{\partial x}\right) = -\frac{4p_2}{h\rho}\frac{\partial \bar{z}}{\partial x} + \frac{3}{h}\frac{\tau_b}{\rho}, \tag{2.198}$$

$$\begin{aligned}&\frac{\bar{w}}{4}\frac{\partial h^2}{\partial t} - \frac{\partial}{\partial t}\left[\frac{h^2}{12}(w_b - w_s)\right] + \left[q\bar{w} - \frac{hu_1}{6}(w_b - w_s)\right]\frac{\partial \bar{z}}{\partial x}\\ &\quad - \frac{\partial}{\partial x}\left[\frac{hq}{12}(w_b - w_s)\right] + \frac{\partial}{\partial x}\left[\frac{h^2u_1}{10}\left(\frac{w_b + w_s}{3} + \bar{w}\right)\right] - h\overline{w^2}\\ &\quad - \frac{h\tau_b}{2\rho}\frac{\partial z_b}{\partial x} - \frac{2hp_2}{3\rho} = 0,\end{aligned} \tag{2.199}$$

in which, based on Eq. (2.189),

$$\overline{w^2} = \bar{w}^2 + \frac{w_b^2}{12} + \frac{w_s^2}{12} - \frac{w_s w_b}{6} + \frac{1}{20}(2\bar{w} - w_b - w_s)^2. \tag{2.200}$$

Equations (2.191)–(2.195) and (2.197)–(2.199) form a system of eight equations for the eight unknowns (h, q, u_1, w_b, w_s, $\bar{w}$, p_1, and p_2). This system was successfully modeled by Khan and Steffler (1996a, b) using the characteristic dissipative Galerkin finite element scheme for flow in hydraulic structures. It may be regarded as a higher-order Boussinesq-type model with increased order of vertical resolution. If $u_1 = w_2 = p_2 = 0$, then the standard Boussinesq equations are recovered.

References

Abbott, M. B. (1979). *Computational hydraulics: Elements of the theory of free surface flows*. London: Pitman.

Ancey, C. (2010). Stochastic modelling in sediment dynamics: Exner equation for planar incipient bed load transport conditions. *Journal of Geophysical Research, 115*, F00A11. doi:10.1029/2009JF001260

Andreotti, B., Forterre, Y., & Pouliquen, O. (2013). *Granular media: Between fluid and solid*. Cambridge: Cambridge University Press.

Antunes do Carmo, J. S., Santos, F. J., & Almeida, A. B. (1993). Numerical solution of the generalized Serre equations with the MacCormack finite difference scheme. *International Journal for Numerical Methods in Fluids, 16*(8), 725–738.

ASCE Task Committee on flow and transport over dunes. (2002). Flow and transport over dunes. *Journal of Hydraulic Engineering*, *128*(8), 726–728.

Bagnold, R. A. (1973). The nature of saltation and of 'bed-load' transport in water. *Proceedings of the Royal Society of London. Series A, 332*, 473–504.

Barthelemy, E. (2004). Nonlinear shallow water theories for coastal waters. *Surveys In Geophysics, 25*, 315–337.

Basco, D. R. (1983). Computation of rapidly varied, unsteady free surface flow. *Water Resources Investigation Report 83-4284*. Reston VA: US Geological Survey.

Benjamin, T. B., & Lighthill, M. J. (1954). On cnoidal waves and bores. *Proceedings of the Royal Society of London. Series A, 224*, 448–460.

Berger, R. C., & Carey, G. F. (1998a). Free-surface flow over curved surfaces. Part I: Perturbation analysis. *International Journal for Numerical Methods in Fluids, 28*, 191–200.

Berger, R. C., & Carey, G. F. (1998b). Free-surface flow over curved surfaces. Part II: Computational model. *International Journal for Numerical Methods in Fluids, 28*, 201–213.

Bonneton, P., Barthelemy, E., Chazel, F., Cienfuegos, R., Lannes, D., Marche, F., et al. (2011). Recent advances in Serre-Green Naghdi modelling for wave transformation, breaking and runup processes. *The European Journal of Mechanics—B/Fluids, 30*, 589–597.

Bose, S. K., & Dey, S. (2007). Curvilinear flow profiles based on Reynolds averaging. *Journal of Hydraulic Engineering, 133*(9), 1074–1079.

Bose, S. K., & Dey, S. (2009). Reynolds averaged theory of turbulent shear flows over undulating beds and formation of sand waves. *Physical Review E, 80*(3), 036304-1–036304-9.

Boussinesq, J. (1872). Théorie des ondes et des remous qui se propagent le long d'un canal rectangulaire horizontal, en communiquant au liquide contenu dans ce canal des vitesses

sensiblement pareilles de la surface au fond (Theory of waves and disturbances propagating along a rectangular horizontal channel, generating nearly uniform velocities from the surface to the bottom). *Journal de Mathématiques Pures et Appliquées* (Série 2)*, 17*, 55–108 (in French).

Boussinesq, J. (1877). Essai sur la théorie des eaux courantes (Essay on the theory of water flow). *Mémoires présentés par divers savants à l'Académie des Sciences, Paris, 23*, 1–680. (in French).

Brocchini, M. (2013). A reasoned overview on Boussinesq-type models: the interplay between physics, mathematics and numerics. *Proceedings of the Royal Society of London. Series A, 469*, 20130496.

Buffington, J. M., & Montgomery, D. R. (1997). A systematic analysis of eight decades of incipient motion studies, with special reference to gravel-bedded rivers. *Water Resources Research, 33*(8), 1993–2029.

Cantero-Chinchilla, F. N., Castro-Orgaz, O., Dey, S., & Ayuso, J. L. (2016a). Nonhydrostatic dam break flows I: Physical equations and numerical schemes. *Journal of Hydraulic Engineering, 142*(12), 04016068.

Cantero-Chinchilla, F. N., Castro-Orgaz, O., Dey, S., & Ayuso, J. L. (2016b). Nonhydrostatic dam break flows II: One-dimensional depth-averaged modelling for movable bed flows. *Journal of Hydraulic Engineering, 142*(12), 0416069.

Carter, J. D., & Cienfuegos, R. (2011). The kinematics and stability of solitary and cnoidal wave solutions of the Serre equations. *The European Journal of Mechanics—B/Fluids, 30*(5–6), 259–268.

Castro-Orgaz, O., Giráldez, J. V., & Mateos, L. (2013). Second-order shallow flow equation for anisotropic aquifers. *Journal of Hydrology, 501*, 183–185.

Castro-Orgaz, O., Giráldez, J. V., & Robinson, N. (2012). Second order two-dimensional solution for the drainage of recharge based on Picard's iteration technique: A generalized Dupuit-Forchheimer equation. *Water Resources Res*earch*, 48*, W06516. doi:10.1029/2011WR011751

Castro-Orgaz, O., & Hager, W. H. (2009). Curved streamline transitional flow from mild to steep slopes. *Journal of Hydraulic Research, 47*(5), 574–584.

Castro-Orgaz, O., & Hager, W. H. (2011a). Joseph Boussinesq and his theory of water flow in open channels. *Journal of Hydraulic Research, 49*(5), 569–577.

Castro-Orgaz, O., & Hager, W. H. (2011b). Turbulent near-critical open channel flow: Serre's similarity theory. *Journal of Hydraulic Engineering, 137*(5), 497–503.

Castro-Orgaz, O., & Hager, W. H. (2011c). Observations on undular jump in movable bed. *Journal of Hydraulic Engineering, 49*(5), 689–692.

Castro-Orgaz, O., Hutter, K., Giráldez, J. V., & Hager, W. H. (2015). Non-hydrostatic granular flow over 3D terrain: New Boussinesq-type gravity waves? *Journal of Geophysical Research—Earth Surface, 120*(1), 1–28.

Chanson, H. (2000). Boundary shear stress measurements in undular flows: Application to standing wave bed forms. *Water Resources Research, 36*(10), 3063–3076.

Chaudhry, M. H. (2008). *Open-channel flow* (2nd ed.). Berlin: Springer.

Chen, Q. (2006). Fully nonlinear Boussinesq-type equations for waves and currents over porous beds. *The Journal of Engineering Mechanics, 132*(2), 220–230.

Chen, Q., Kirby, J. T., Dalrymple, R. A., Kennedy, A. B., & Haller, C. M. (1999). Boussinesq modeling of a rip current system. *Journal of Geophysical Research, 104*(C9), 20617–20637.

Chen, Q., Kirby, J. T., Dalrymple, R. A., Shi, F., & Thornton, E. B. (2003). Boussinesq modeling of longshore currents. *Journal of Geophysical Research, 108*(C11), 3362–3380.

Chen, Y., & Liu, P. L. F. (1995). Modified Boussinesq equations and associated parabolic models for water wave propagation. *Journal of Fluid Mechanics, 288*, 351–381.

Chow, V. T. (1959). *Open channel hydraulics*. New York: McGraw-Hill.

Cienfuegos, R., Barthélemy, E., & Bonneton, P. (2006). A fourth-order compact finite volume scheme for fully nonlinear and weakly dispersive Boussinesq-type equations. Part I: Model development and analysis. *International Journal for Numerical Methods in Fluids, 51*(11), 1217–1253.

De Saint-Venant, A. B. (1871). Théorie du mouvement non permanent des eaux, avec application aux crues des rivières et à l'introduction des marrées dans leur lit (Theory of unsteady water movement, applied to floods in rivers and the effect of tidal flows). *Comptes Rendus de l'Académie des Sciences, 73*, 147–154; *73*, 237–240 (in French).

Denlinger, R. P., & Iverson, R. M. (2004). Granular avalanches across irregular three-dimensional terrain: 1. Theory and computation. *Journal of Geophysical Research, 109*(F1), F01014. doi:10.1029/2003JF000085

Denlinger, R. P., & O'Connell, D. R. H. (2008). Computing nonhydrostatic shallow-water flow over steep terrain. *Journal of Hydraulic Engineering, 134*(11), 1590–1602.

Dewals, B. J., Erpicum, S., Archambeau, P., Detrembleur, S., & Pirotton, M. (2006). Depth-integrated flow modelling taking into account bottom curvature. *Journal of Hydraulic Research, 44*(6), 785–795.

Dey, S. (2014). *Fluvial hydrodynamics: Hydrodynamic and sediment transport phenomena*. Berlin: Springer.

Dias, F., & Milewski, P. (2010). On the fully non-linear shallow-water generalized Serre equations. *Physics Letters A, 374*, 1049–1053.

Dressler, R. F. (1978). New nonlinear shallow flow equations with curvature. *Journal of Hydraulic Research, 16*(3), 205–222.

Einstein, H. A. (1950). The bed-load function for sediment transportation in open channel flows. *USDA Technical Bulletins, 1026*. Washington D.C.

Engelund, F., & Fredsoe, J. (1976). A sediment transport model for straight alluvial channels. *Nordic Hydrology, 7*(5), 293–306.

Engelund, F., & Fredsoe, J. (1982). Sediment ripples and dunes. *Annual Review of Fluid Mechanics, 14*, 13–37.

Engelund, F., & Hansen, E. (1966). Investigations of flow in alluvial streams. *Hydraulic Laboratory Bulletin* 9. Copenhagen: Technical University of Denmark.

Erduran, K. S., Ilic, S., & Kutija, V. (2005). Hybrid finite-volume finite-difference scheme for the solution of Boussinesq equations. *International Journal for Numerical Methods in Engineering, 49*(11), 1213–1232.

Fawer, C. (1937). Etude de quelques écoulements permanents à filets courbes (Study of some steady flows with curved streamlines). *Thesis*, Université de Lausanne, La Concorde, Lausanne, Switzerland (in French).

Fenton, J. D. (1996). Channel flow over curved boundaries and a new hydraulic theory. *Proceedings of the 10th IAHR APD Congress,* Langkawi, Malaysia (pp. 266–273).

Fenton, J. D., & Zerihun, Y. T. (2007). A Boussinesq approximation for open channel flow. *Proceedings of the 32th IAHR Congress,* Venice, Italy, published on CD.

Friedrichs, K. O. (1948). On the derivation of the shallow water theory. *Communications on Pure and Applied Mathematics, 1*(1), 81–87.

Furbish, D. J., Haff, P. K., Roseberry, J. C., & Schmeeckle, M. W. (2012). A probabilistic description of the bed load sediment flux: 1. Theory. *Journal of Geophysical Research, 117*, F03031. doi:10.1029/2012JF002352

García, M. H. (2008). Sedimentation engineering: Processes, measurements, modeling, and practice. *ASCE Manual of practice, 110*. Reston, VA.

Graf, W. H., & Altinakar, M. S. (1996). Hydraulique fluviale: Écoulement non-permanent et phénomènes de transport (Fluvial hydraulics: Unsteady flow and transport phenomena). Paris: Eyrolles (in French).

Green, A. E., & Naghdi, P. M. (1976). A derivation of equations for wave propagation in water of variable depth. *Journal of Fluid Mechanics, 78*, 237–246.

Guinot, V. (2003). Riemann solvers and boundary conditions for two dimensional shallow water simulations. *International Journal for Numerical Methods in Engineering, 41*(11), 1191–1219.

Hager, W. H. (1983). Hydraulics of plane free overfall. *Journal of Hydraulic Engineering, 109*(12), 1683–1697.

Hager, W. H., & Hager, K. (1985). Streamline curvature effects in distribution channels. *Proceedings of IME, 199*(3), 165–172.

Hager, W. H., & Hutter, K. (1984a). Approximate treatment of plane channel flow. *Acta Mechanica, 51*(3–4), 31–48.

Hager, W. H., & Hutter, K. (1984b). On pseudo-uniform flow in open channel hydraulics. *Acta Mechanica, 53*(3–4), 183–200.

Henderson, F. M. (1966). *Open channel flow*. New York: MacMillan.

Hervouet, J. M. (2007). *Hydrodynamics of free surface flows: Modelling with the finite element method*. New York: Wiley & Sons.

Hosoda, T., & Tada, A. (1994). Free surface profile analysis on open channel flow by means of 1-D basic equations with effect of vertical acceleration. *Annual Journal of Hydraulics Engineering. JSCE, 38*, 457–462 (in Japanese).

Hutter, K., & Castro-Orgaz, O. (2016). Non-hydrostatic free surface flows: Saint Venant versus Boussinesq depth integrated dynamic equations for river and granular flows (Chapter 17). In *Continuous media with microstructure 2* (pp. 245–265). Berlin: Springer.

Hutter, K., & Jőhnk, K. (2004). *Continuum methods of physical modeling: Continuum mechanics, dimensional analysis, turbulence*. Berlin: Springer.

Hutter, K., & Savage, S. B. (1988). Avalanche dynamics: The motion of a finite mass of gravel down a mountain side. *Proceedings of the 5th International Symposium on Landslides,* Lausanne (pp. 691–697).

Hutter, K., & Wang, Y. (2016). *Fluid and thermodynamics* 1: *Basic fluid mechanics*, 2: *Advanced fluid mechanics and thermodynamics*. Berlin: Springer.

Iverson, R. M. (1997). The physics of debris flows. *Reviews of Geophysics, 35*(3), 245–296.

Iverson, R. M. (2005). Debris-flow mechanics. In M. Jakob & O. Hungr (Eds.), *Debris flow hazards and related phenomena* (pp. 105–134). Heidelberg: Springer.

Iwasa, Y. (1955). Undular jump and its limiting conditions for existence. *Proceedings of the 5th Japan national congress in applied mechanics II, 14*, 315–319.

Iwasa, Y. (1956). Analytical considerations on cnoidal and solitary waves. *Transactions of Japan Society of Civil Engineers, 32*, 43–49.

Iwasa, Y., & Kennedy, J. F. (1968). Free surface shear flow over a wavy bed. *Journal of the Hydraulics Division, 94*(HY2), 431–454.

Jain, S. C. (2001). *Open channel flow*. New York: Wiley & Sons.

Kennedy, J. F. (1963). The mechanics of dunes and antidunes in erodible-bed channels. *Journal of Fluid Mechanics, 16*, 521–544.

Kennedy, A. B., Chen, Q., Kirby, J. T., & Dalrymple, R. A. (2000). Boussinesq modeling of wave transformation, breaking, and run-up. Part I: 1D. *Journal of Waterway Port Coastal and Ocean Engineering, 126*(1), 39–47.

Khan, A. A., & Lai, W. (2014). *Modelling shallow water flows using the discontinuous Galerkin method*. London: CRC Press, Taylor and Francis.

Khan, A. A., & Steffler, P. M. (1996a). Modelling overfalls using vertically averaged and moment equations. *Journal of Hydraulic Engineering, 122*(7), 397–402.

Khan, A. A., & Steffler, P. M. (1996b). Vertically averaged and moment equations model for flow over curved beds. *Journal of Hydraulic Engineering, 122*(1), 3–9.

Kim, D.-H., & Lynett, P. J. (2011). Dispersive and nonhydrostatic pressure effects at the front of surge. *Journal of Hydraulic Engineering, 137*(7), 754–765.

Kim, D.-H., Lynett, P. J., & Socolofsky, S. (2009). A depth-integrated model for weakly dispersive, turbulent, and rotational fluid flows. *Ocean Modelling, 27*(3–4), 198–214.

Lajeunesse, E., Malverti, L., & Charru, F. (2010). Bed load transport in turbulent flow at the grain scale: Experiments and modelling. *Journal of Geophysical Research, 115*, F04001. doi:10.1029/2009JF001628

Lannes, D., & Bonneton, P. (2009). Derivation of asymptotic two-dimensional time-dependent equations for surface water wave propagation. *Physics of Fluids, 21*(1), 016601, 9 pp.

LeVeque, R. J. (2002). *Finite volume methods for hyperbolic problems*. Cambridge: Cambridge University Press.

Liggett, J. A. (1994). *Fluid mechanics*. New York: McGraw-Hill.
Lynett, P. J. (2006). Wave breaking effects in depth-integrated models. *Coastal Engineering, 53* (4), 325–333.
Lynett, P., Wu, T. R., & Liu, P. L.-F. (2002). Modeling wave runup with depth-integrated equations. *Coastal Engineering, 46*(2), 89–107.
Ma, G., Fengyang, S., & Kirby, J. T. (2012). Shock-capturing non-hydrostatic model for fully dispersive surface wave processes. *Ocean Modelling, 43–44*, 22–35.
Madsen, P. A., & Schäffer, H. A. (1998). Higher-order Boussinesq-type equations for surface gravity waves: Derivation and analysis. *Philosophical Transactions of the Royal Soceity of London. Series A, 356*, 3123–3184.
Madsen, P. A., Sorensen, O. R., & Schäffer, H. A. (1997). Surf zone dynamics simulated by a Boussinesq type model. I. Model description and cross-shore motion of regular waves. *Coastal Engineering, 32*(4), 255–287.
Mandrup-Andersen, V. (1975). Transition from subcritical to supercritical flow. *Journal of Hydraulic Research, 13*(3), 227–238.
Mandrup-Andersen, V. (1978). Undular hydraulic jump. *Journal of the Hydraulics Division, ASCE 104*(HY8), 1185–1188; *Discussion, 105*(HY9), 1208–1211.
Marchi, E. (1963). Contributo allo studio del risalto ondulato (Contribution to the study of the undular hydraulic jump). *G. Genio Civile, 101*(9), 466–476. (in Italian).
Marchi, E. (1992). The nappe profile of a free overfall. *Rendiconti Lincei Matematica e Applicazioni Serie 9, 3*(2), 131–140.
Marchi, E. (1993). On the free overfall. *Journal of Hydraulic Research, 31*(6), 777–790; *32*(5), 794–796.
Matthew, G. D. (1963). On the influence of curvature, surface tension and viscosity on flow over round-crested weirs. *Proceedings of ICE 25*, 511–524; *28*, 557–569.
Matthew, G. D. (1991). Higher order one-dimensional equations of potential flow in open channels. *Proceedings of ICE, 91*(3), 187–201.
Mei, C. C. (1983). *The applied dynamics of ocean surface waves*. New York: John Wiley.
Meyer-Peter, E., & Müller, R. (1948). Formulas for bed load transport. *Proceedings of the 2nd International IAHR Meeting, Stockholm, 26*, 5–24.
Mignot, E., & Cienfuegos, R. (2008). On the application of a Boussinesq model to river flows including shocks. *Coastal Engineering, 56*(1), 23–31.
Mohapatra, P. K., & Chaudhry, M. H. (2004). Numerical solution of Boussinesq equations to simulate dam-break flows. *Journal of Hydraulic Engineering, 130*(2), 156–159.
Molls, T., & Chaudhry, M. H. (1995). Depth averaged open channel flow model. *Journal of Hydraulic Engineering, 121*(6), 453–465.
Montes, J. S. (1986). A study of the undular jump profile. *Proceedings of the 9th Australasian Fluid Mechanics Conference,* Auckland (pp. 148–151).
Montes, J. S. (1998). *Hydraulics of open channel flow*. Reston, VA: ASCE Press.
Musumeci, R. E., Svendsen, I. A., & Veeramony, J. (2005). The flow in the surf zone: A fully nonlinear Boussinesq-type of approach. *Coastal Engineering, 52*(7), 565–598.
Nwogu, O. (1993). Alternative form of Boussinesq equations for nearshore wave propagation. *Journal of Waterway Port Coastal and Ocean Engineering, 119*(6), 618–638.
Onda, S., & Hosoda, T. (2004). Numerical simulation of the development process of dunes and flow resistance. In *Proceedings of River Flow 2004* (245–252). London: T&F.
Parker, G. (1979). Hydraulic geometry of active gravel rivers. *Journal of Hydraulics Division, ASCE, 105*(9), 1185–1201.
Peregrine, D. H. (1966). Calculations of the development of an undular bore. *Journal of Fluid Mechanics, 25*(2), 321–330.
Peregrine, D. H. (1967). Long waves on a beach. *Journal of Fluid Mechanics, 27*(5), 815–827.

Peregrine, D. H. (1972). Equations for water waves and the approximations behind them. In R. E. Meyer (Ed.), *Waves on beaches and resulting sediment transport* (pp. 95–122). San Diego, CA: Academic Press.

Pudasaini, S. P., & Hutter, K. (2007). *Avalanche dynamics*. Berlin: Springer.

Roache, P. J. (1976). *Computational fluid dynamics*. Albuquerque, NM: Hermosa Publishers.

Rodi, W. (1980). *Turbulence models and their application in hydraulics: A state-of-the-art review*. Dordrecht: IAHR.

Savage, S. B., & Hutter, K. (1989). The motion of a finite mass of granular material down a rough incline. *Journal of Fluid Mechanics, 199*, 177–215.

Savage, S. B., & Hutter, K. (1991). The dynamics of avalanches of granular materials from initiation to runout I: Analysis. *Acta Mechanica, 86*(1–4), 201–223.

Schmocker, L. (2011). Hydraulics of dike breaching. *Dissertation ETH 19983*. Zürich, Switzerland: ETH Zurich.

Seabra-Santos, F. J., Renouard, D. P., & Temperville, A. M. (1987). Numerical and experimental study of the transformation of a solitary wave over a shelf or isolated obstacle. *Journal of Fluid Mechanics, 176*, 117–134.

Serre, F. (1953). Contribution à l'étude des écoulements permanents et variables dans les canaux (Contribution to the study of steady and unsteady channel flows). *La Houille Blanche, 8*(6–7), 374–388; *8*(12), 830–887 (in French).

Sivakumaran, N. S., & Dressler, R. F. (1989). Unsteady density-current equations for highly curved terrain. *Journal of the Atmospheric Sciences, 46*(20), 3192–3201.

Sivakumaran, N. S., Tingsanchali, T., & Hosking, R. J. (1983). Steady shallow flow over curved beds. *Journal of Fluid Mechanics, 128*, 469–487.

Soares-Frazão, S., & Guinot, V. (2008). A second-order semi-implicit hybrid scheme for one-dimensional Boussinesq-type waves in rectangular channels. *The International Journal for Numerical Methods in Fluids, 58*(3), 237–261.

Soares-Frazão, S., & Zech, Y. (2002). Undular bores and secondary waves: Experiments and hybrid finite-volume modelling. *Journal of Hydraulic Research, 40*(1), 33–43.

Stansby, P. K. (2003). Solitary wave run up and overtopping by a semi-implicit finite-volume shallow-water Boussinesq model. *Journal of Hydraulic Research, 41*(6), 639–647.

Stansby, P. K., & Zhou, J. G. (1998). Shallow-water flow solver with non-hydrostatic pressure: 2D vertical plane problems. *The International Journal for Numerical Methods in Fluids, 28*(3), 541–563.

Steffler, P. M., & Jin, Y. C. (1993). Depth-averaged and moment equations for moderately shallow free surface flow. *Journal of Hydraulic Research, 31*(1), 5–17.

Su, C. H., & Gardner, C. S. (1969). KDV equation and generalizations. Part III. Derivation of Korteweg-de Vries equation and Burgers equation. *Journal of Mathematical Physics, 10*(3), 536–539.

Toro, E. F. (1997). *Riemann solvers and numerical methods for fluid dynamics*. Berlin: Springer.

Toro, E. F. (2001). *Shock-capturing methods for free-surface shallow flows*. New York: Wiley.

Vreugdenhil, C. B. (1994). *Numerical methods for shallow water flow*. Dordrecht NL: Kluwer.

Wei, G., & Kirby, J. T. (1995). Time-dependent numerical code for extended Boussinesq equations. Journal of Waterway Port Coastal and Ocean Engineering, *121*(5), 251–261.

Wei, G., Kirby, J. T., Grilli, S. T., & Subramanya, R. (1995). A fully nonlinear Boussinesq model for surface waves 1: Highly nonlinear unsteady waves. *Journal of Fluid Mechanics, 294*, 71–92.

Wiberg, P., & Smith, J. D. (1989). Model for calculating bed load transport of sediment. *Journal of Hydraulic Engineering, 115*(1), 101–123.

Wieland, M., Gray, J. M. N. T., & Hutter, K. (1999). Channelised free surface flow of cohesionless granular avalanche in a chute with shallow lateral curvature. *Journal of Fluid Mechanics, 392*, 73–100.

Yalin, M. S. (1977). *Mechanics of sediment transport*. Oxford: Pergamon.

Yen, B. C. (1973). Open-channel flow equations revisited. *Journal of the Engineering Mechanics Division, ASCE, 99*(EM5), 979–1009.

Zerihun, Y., & Fenton, J. (2006). One-dimensional simulation model for steady transcritical free surface flows at short length transitions. *Advances in Water Resources, 29*(11), 1598–1607.

Zerihun, Y., & Fenton, J. (2007). A Boussinesq-type model for flow over trapezoidal profile weirs. *Journal of Hydraulic Research, 45*(4), 519–528.

Zhu, D. Z., & Lawrence, G. A. (1998). Non-hydrostatic effects in layered shallow water flows. *Journal of Fluid Mechanics, 355*, 1–16.

Chapter 3
Inviscid Channel Flows

Roman Symbols

a	Gate opening (m); also wave amplitude (m/s)
A	Angular momentum function (m^3); wave amplitude (m)
A, B, C, D	Auxiliary variables
B	Boussinesq's mixed term (m^4/s^2)
c	Wave celerity (m/s); also constant of integration (m)
c_o	Celerity of small gravity wave (m/s)
c_w	Celerity of shock front (m/s)
C_d	Weir discharge coefficient (–)
C_D	Spillway discharge coefficient at design head (–)
C_c	Contraction coefficient (–)
CFL	Courant–Friedrichs–Lewy number (–)
d	Still water depth (m)
D	Constant of integration (–)
E	Specific energy head (m)
f	Function (m)
$\mathbf{F}$	Vector of fluxes in the x-direction (m^2/s, m^3/s^2)
F	Froude number (–)
F_o	Froude number of hydrostatic flow (–); also Froude number of undisturbed flow (–)
F_p	Froude number of translating wave over still water (–)
F	Force (N)
g	Gravity acceleration (m/s^2); also function (m/s)
G	Recursion index (–)
h	Flow depth measured vertically (m)
h_c	Critical depth for parallel-streamlined flow (m) = $(q^2/g)^{1/3}$
h_b	Brink depth (m)
h_o	Uniform flow depth (m); also still water depth (m); also terminal jet thickness (m)
h_p	Effective pressure head (m)
h_1	Maximum flow depth of cnoidal wave (m)
h_2	Minimum flow depth of cnoidal wave (m)

© Springer International Publishing AG 2017

O. Castro-Orgaz and W.H. Hager, *Non-Hydrostatic Free Surface Flows*,
Advances in Geophysical and Environmental Mechanics and Mathematics
DOI 10.1007/978-3-319-47971-2_3

h_3	$q^2/(gh_1h_2)$ (m)
$h_{\max}$	Maximum flow depth of solitary wave (m)
H	Total energy head (m)
H_D	Design energy head of spillway profile (m)
i	Relative inclination (–); also node index in the x-direction (–)
j	Node index in the ψ-direction (–)
k	Recursion index (–); also wave number (m^{-1})
k^2	Modulus of incomplete elliptical integral of first kind (–)
K, K_b, K_G	Curvature distribution parameters in Fawer's theory (–)
m	Inclination distribution parameter (–); pressure parameter (–); also parameter of the original Jaeger's theory (–)
m_o	Radius of curvature distribution parameter in Jaeger's theory (–)
m_1	Power-law exponent at inflow section (–)
M	Vertical momentum (m^3); also maximum value of j-index (–), also momentum function (m^4/s^2)
n	Curvilinear coordinate along equipotential (m)
N	Flow depth measured normal to bottom profile (m); also maximum value of j-index (–); also power-law exponent (–)
N_o	Length of equipotential curve (m)
p	Pressure (N/m^2); also auxiliary variable (–)
p_b	Bottom pressure (N/m^2)
p_s	Interface pressure (N/m^2)
p_1	Pressure excess over hydrostatic pressure at channel bottom (N/m^2)
p_{be}	Bottom pressure at brink section of free overfall (N/m^2)
q	Unit discharge (m^2/s)
q_o	Normalized unit discharge in slope break with rounded transition (–)
q_p	Progressive unit discharge (m^2/s)
r	Relative curvature (–); ratio of down- to upstream water depths in dam break problem (–); also roller thickness (m)
R	Radius of streamline curvature (m)
R^*	Radius of circular-shaped equipotential line (m)
R_s	Radius of free surface (m)
R_b	Radius of channel bottom (m); also radius of circular arc transition (m)
s	Curvilinear coordinate along streamline (m); also main stream profile of submerged jet (m)
S	Specific momentum (m^2)
S_o	Bottom slope (–)
t	Vertical flow depth (m); also time (s)
u	Velocity in the x-direction (m/s); also normalized variable (–); also incomplete elliptical integral of first kind (–)
u_ξ	Velocity in the ξ-direction (m/s)
u_α	Velocity at elevation z_α (m/s)
U	Mean flow velocity (m/s) = q/h
U_o	Amplitude of perturbation of flow velocity (m/s)

$\mathbf{U}$	Vector of conserved variables (m, m/s)
U_c	Mean critical flow velocity (m/s) = q/h_c
V	Local velocity (m/s)
w	Velocity in the z-direction (m/s)
w_e	Velocity in the z-direction at gate edge (m/s)
w_ζ	Velocity in the ζ-direction (m/s)
x	Horizontal coordinate (m)
X	X/h_c (–); also longitudinal coordinate in moving system of reference (m); also x/H_D (–)
$\overline{X}$	Modified X-coordinate of sharp-crested weir flow (–)
y	$H/h_{\max}$ (–); also coordinate in the horizontal plane, normal to x (m)
Y	H/h_c (–); also $(y - 1)/(\mathsf{F}_p^2 - 1)$ (–)
z	Vertical elevation (m)
z_s	Free surface elevation (m)
z_b	Elevation of channel bottom (m)
z_α	Reference elevation (m)
Z	Recursion index (–); also normalized variable (–); also z_b/H_D (–)
$\overline{Z}$	Modified Z-coordinate of sharp-crested weir flow (–)

Greek Symbols

α	Dispersion coefficient (–)
α_N	Nwogu-type dispersion coefficient (–)
$\alpha_1, \alpha_2, \alpha_3, \alpha_4$	Coefficients
$\beta_1, \beta_2, \beta_3, \beta_4$	Coefficients
Γ	Incomplete gamma function (–)
γ	Specific weight of water (N/m^3)
Δ	Step in the x-direction (m); also factor in cnoidal wave theory (–)
ε	Lower nappe maximum elevation (m)
$\varepsilon_1, \varepsilon_2$	Curvilinear coefficients (–)
ζ	Coordinate normal to channel bottom profile, normal to ξ (m); also water depth variation around static level (m); also normalized x-coordinate in solitary wave profile (–)
η	Vertical coordinate above channel bottom (m)
θ	Angle of streamline inclination with horizontal (rad)
κ	Curvature of streamline (m^{-1}); also denoted as κ_s
κ_b	Curvature of bottom profile (m^{-1})
κ_n	Curvature of equipotential curve (m^{-1})
Λ	Vorticity factor (–)
λ	Non-hydrostatic correction coefficient in critical flow condition (–); also wavelength (m)
μ	Dimensionless vertical coordinate (–)
ν	Dimensionless curvilinear coordinate along equipotential line (–); also kinematic viscosity (m^2/s)

ξ	Curvilinear coordinate measured along bottom profile (m); also normalized x-coordinate in solitary wave profile (–)
Π	Function (m)
ρ	Density of water (kg/m^3)
τ	R/R_s (–)
ϕ	Potential function (m^2/s)
Φ_1, Φ_2	Functions of water surface profile equation (–)
φ	Non-hydrostatic correction coefficient (–)
χ	E/H_D (–); also curvature parameter (–); also normalized x-coordinate in free jet profile (–); also parameter of cnoidal wave (–)
ψ	Stream function (m^2/s)
Ω	Effective angular momentum function (m^3); also curvilinear function (–); also vorticity (s^{-1}); also normalized variable (–)
ω	Constant in solitary wave profile (–); also recursion index (–); also normalized variable (–); also frequency (s^{-1})

Subscripts

b	Relative to channel bottom
c	Critical flow
crest	Relative to crest section
d	Relative to downstream boundary condition
o	Relative to approach flow conditions
s	Relative to free surface
u	Relative to upstream boundary condition
*	Relative to dimensionless value; also relative to star region in Riemann problem

3.1 Introduction

Open-channel flows in hydraulic structures typically involve large pressure gradients and accelerations with relatively small frictional effects, e.g., as in a free overfall or at a weir crest. In these flow problems, the viscous stresses are not important terms in the Navier–Stokes equations so that the problem can be mathematically solved using the equations of an inviscid fluid, i.e., the Euler's equations. Viscosity effects are typically isolated to thin boundary layers close to solid walls. In this chapter, therefore, the mathematical theory of inviscid fluids is applied to non-hydrostatic conditions within short-channel structures in the vertical plane (x, z). In most cases, the flow may also be assumed to be irrotational so that the potential flow theory applies by defining the corresponding velocity potential and stream functions. Further, a large variety of the fluid processes are steady so that as detailed in the next

section, the energy head is a constant, and changes in the velocity head are linked only to changes in the piezometric pressure. Typical open-channel problems encompassing non-hydrostatic potential conditions were experimentally investigated by Rouse (1932); they include free overfalls (Fig. 3.1a), transitions from mild to steep slopes (Fig. 3.1b, c) and rounded drops (Fig. 3.1d).

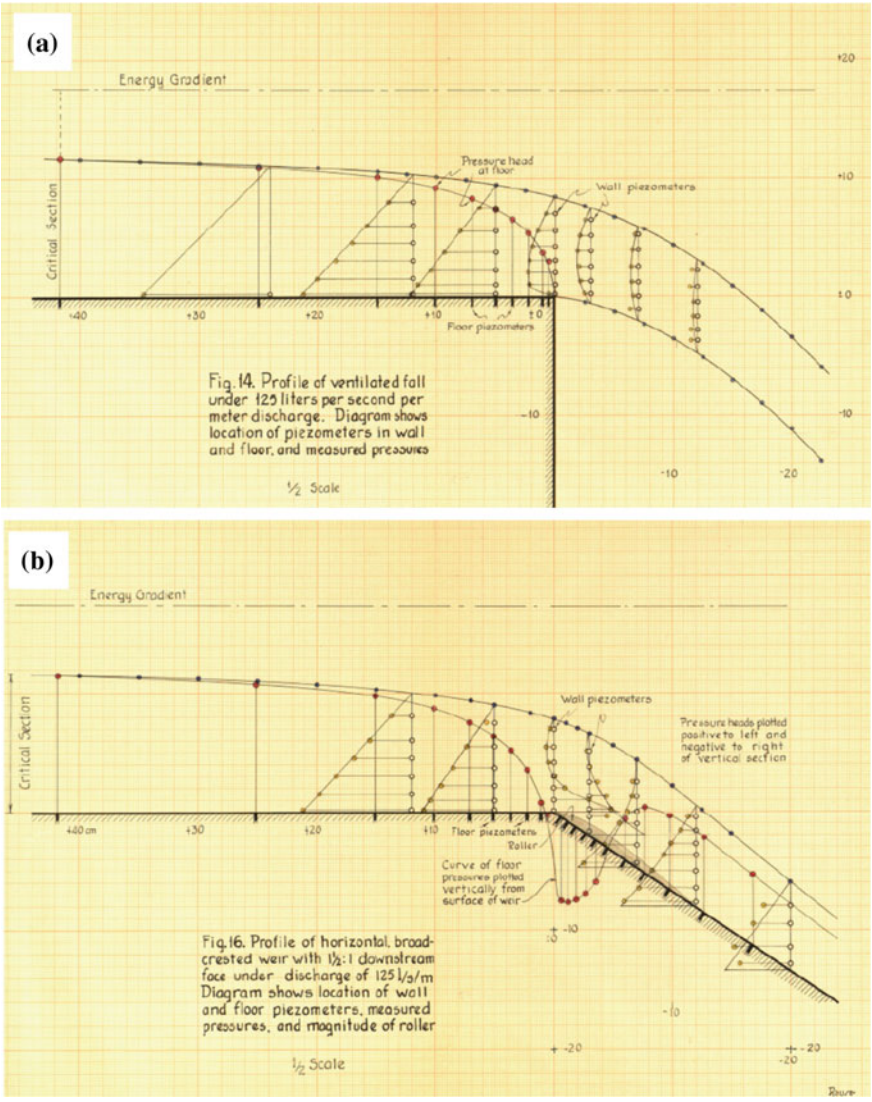

Fig. 3.1 Curvilinear flows at **a** free overfall, **b** transition from mild to steep slopes with small separation bubble (Rouse 1932), **c** transitions from mild to steep slopes with noticeable bottom separation of flow, **d** flow over circular arc drop (Rouse 1932)

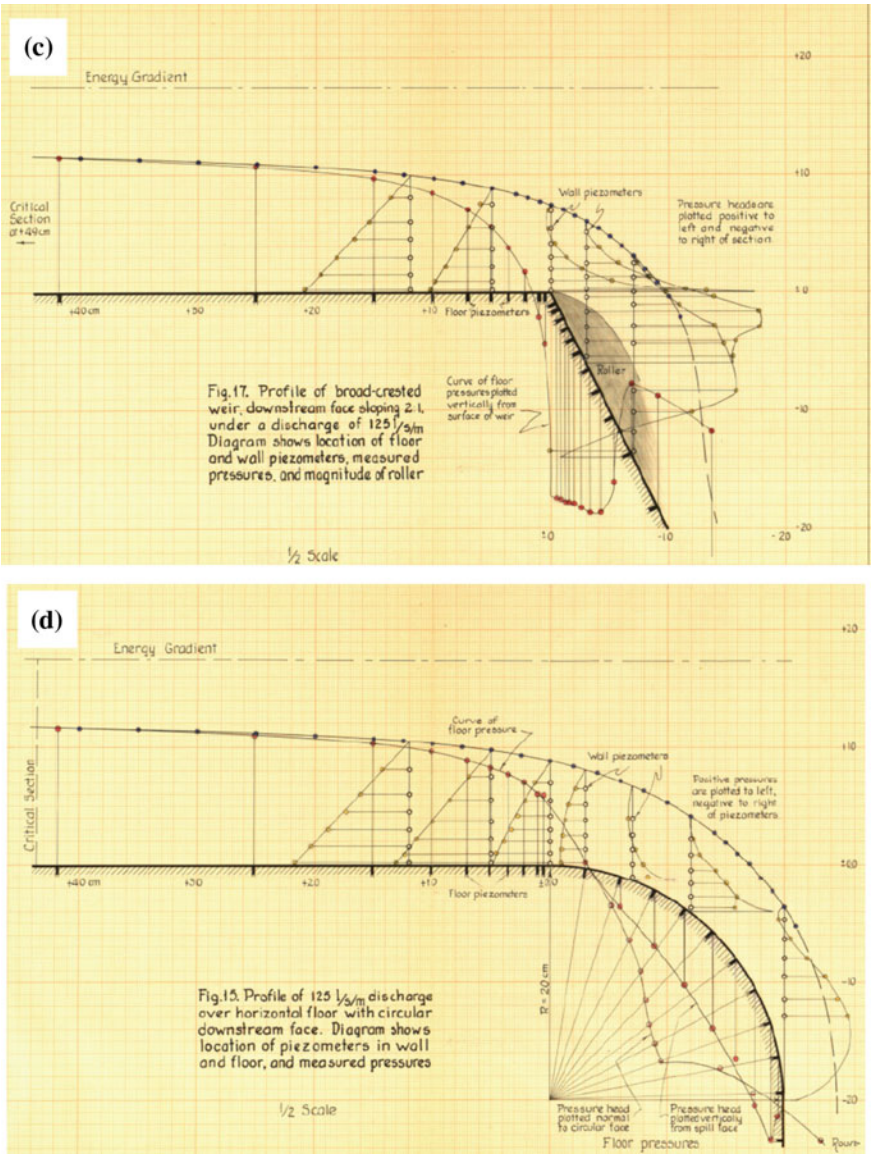

Fig. 3.1 (continued)

In all these situations, the energy headline is essentially horizontal, implying plane potential conditions. In Fig. 3.1, vertical pressure distributions are plotted; note that as the corresponding transition zone is reached, these diverge from the hydrostatic pressure distribution. This is also highlighted when looking at bottom pressure profiles, which are different from the flow depth profile. Whenever these

two characteristic profiles do not overlap in a channel, curvilinear streamlines occur; the diagnosis is that the standard Saint-Venant's theory does not apply. In turn, the potential theory is able to generate in these regions velocity and pressure distributions close to reality. However, care must be taken in analyzing each problem with proper engineering judgment before applying a mathematical theory. For example, the abrupt bottom kink without rounding the slope break of Fig. 3.1b forces a separated streamline to emerge from the kink point, below which a bottom bubble with recirculating fluid is trapped. The flow within this region is rotational, associated with energy losses. In this case, however, the slope break is generally moderate, and the bottom bubble remains small. In contrast, note the extreme separated flow zone in the transition problem of Fig. 3.1c, in which the momentum of the recirculating fluid and associated energy losses have to be accounted for.

As a main lesson, curvilinear potential channel flows need boundary streamlining to avoid flow separation. This technique is well known among dam engineers, who apply this principle to design spillway crests for decades (Hager 1991; Montes 1998). Thus, a streamlined design of a channel structure is iterative; a certain boundary geometry is assumed, and the flow is then visualized to detect whether flow separation occurs. Therefore, boundaries ought to be redefined following the profile of a separation streamline. A fundamental step in the design of efficient short-channel structures (with negligible energy losses) is to visualize the flow in experiments. It is made visible in a model structure by adding particles at the inlet, thereby filming the flow structure with adequate illumination. A typical test of a circular-crested weir is shown in Fig. 3.2, where curvilinear streamlines are noted as the flow passes above the weir crest. The particles are illuminated and the shape of the streamlines is made visible as long as particles are moving in the observation window. These images can be processed to extract the mean steady streamlines.

The two-dimensional (2D) streamline flow pattern of the water along hydraulically short structures, like round-crested weirs or the transition from a mild to a steep slope, encompasses notable spatial changes, where the vertical acceleration is significant and the pressure distribution deviates from the hydrostatic line (Vallentine 1969). Adjustments of streamline slope and curvature occur in response to variations of the boundary shape. Under these conditions, the flow features are described by the equations of inviscid, incompressible, and irrotational flows (Cassidy 1965; Vallentine 1969; Ramamurthy et al. 1994; Montes 1998). The velocity field is, therefore, determined by the existence of potential and stream functions, ϕ and ψ, respectively. The complete 2D potential flow solution provides the velocity field (u, w) at any point of the domain (x, z), with u and w as the velocity components in the x- and z-directions, respectively. Finite-difference solutions for 2D potential flows with a free surface in the gravity field were proposed by Cassidy (1965) and Montes (1992a, b, 1994a), among others. Alternative methods, such as the boundary element method of Cheng et al. (1981), are applied to compute both the free surface and bottom pressure profiles.

A relevant question is: Which conditions of fluid configurations are close to potential flows, in contrast to the conditions under which they are fraught with

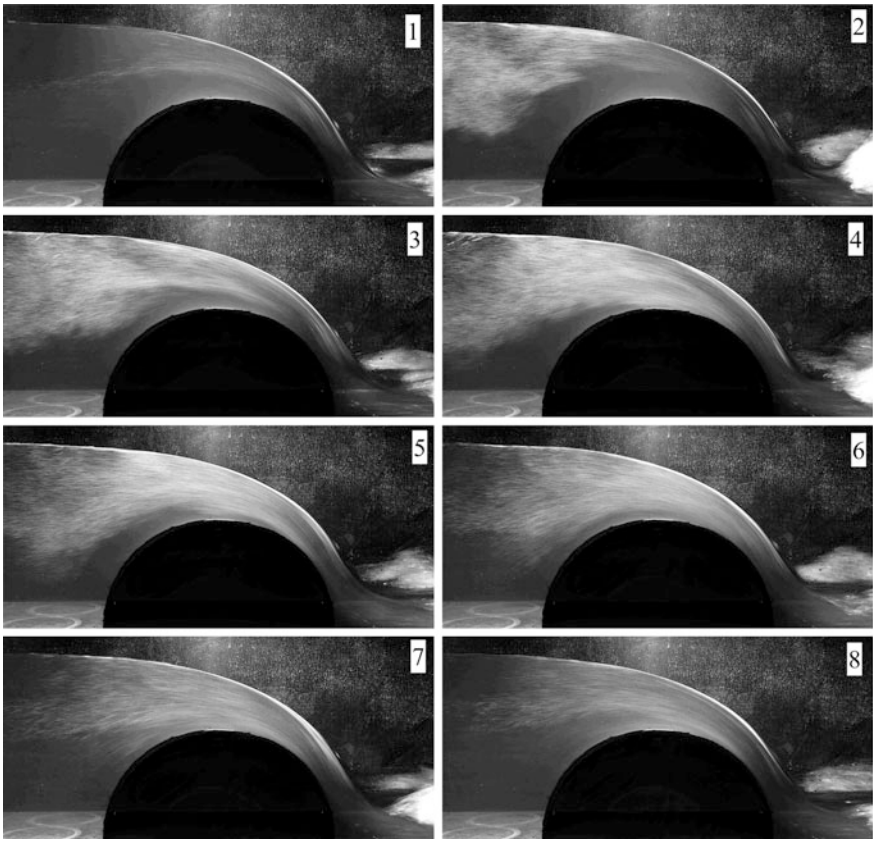

Fig. 3.2 Curvilinear flow over circular-crested weir. Streamlines are made visible by adding particles at the channel inlet. *Numbers* indicate the sequence of photographs during the experiment (Castro-Orgaz 2010a)

rotation? This problem is essential, because potential flows are approximated with the constant energy concept, whereas rotational flows need to be considered using the momentum equation or higher forms of it. As described above, typical potential flows are those over rounded weirs or below gates as the boundary geometry is such that no large flow separation occurs. In contrast, typical rotational flow effects are exhibited in hydraulic jumps, Borda–Carnot expansions in piping systems, or moving bores in the maritime environment. Deciding whether a flow belongs to the first or the second category is essential because their mathematical treatments are different. A simple indication, whether a flow is of potential or of rotational character, is the 2D streamline pattern for smooth variations of the bottom geometry: If the streamlines in 2D converge in the direction of the dominant velocity, the flow has potential character, while flows with diverging streamlines are certainly of the rotational type. This indication may be considered a guide to decide which of the two fundamental categories applies in a specific problem. Note that this

principle is subject to variation for spatially varied flows, as, e.g., flows over side weirs or in side channels.

Numerical solution procedures to determine the complete 2D velocity field are the basis of the development of approximate solutions. The determination of the potential velocity field by successive approximations is achieved using two different methods: perturbation techniques or iteration upon a basic approximate solution (Van Dyke 1975). In both methods, the vertical variation of the velocity components (u, w) is approximated by a 1D approach (Montes 1998), namely Boussinesq's approximation. This model was intensively considered in the 1980s and beyond, given its importance both in theory and in practice. Hager and Hutter (1984a, b) and Hager (1985a) presented one of the first rigorous derivations of a second-order accurate Boussinesq-type potential flow model using intrinsic coordinates, following Matthew (1963). Matthew (1991) and Marchi (1992, 1993) developed identical second-order Boussinesq-type models based on Cartesian coordinates, but using different techniques. Whereas Matthew (1991) used Picard iteration, Marchi (1992, 1993) employed an expansion of the stream function following the work of Benjamin and Lighthill (1954). Matthew's work is unique because he also presented third-order accurate solutions for potential velocity fields. Steady-state, curved open-channel flows were described still with other potential flow approximations, leading essentially to second-order models of a comparable degree of accuracy (Matthew 1963; Hager and Hutter 1984a; Naghdi and Vongsarnpigoon 1986; Ramamurthy et al. 1994), although other alternatives exist, as the moment of momentum method (Steffler and Jin 1993; Khan and Steffler 1995, 1996a, b). However, a generalization of second-order steady-state potential equations to unsteady flows, or to steady-state spatially varied flows, is more feasible by using Picard iteration, originally proposed by Matthew (1991, 1995). Successful applications of Matthew's iterative equations relate to steady flows over curved-bottomed channels, including the round-crested weir (Matthew 1991) and the slope break problem (Castro-Orgaz and Hager 2009). The equations also apply for free jets (Marchi 1992, 1993; Matthew 1995). Despite the success of Boussinesq-type models (Hager 1985a; Matthew 1991; Marchi 1993), this approach was questioned by Montes (1992a, 1994a, b). He argued that as the vertical velocity profile from the Boussinesq's theory is linear, it cannot be used to handle highly curved flows. In contrast, Matthew (1991, 1995) and Marchi (1992, 1993) advocated that the theories apply to highly curved flows, whereas Khan and Steffler (1995) demonstrated that a vertical velocity profile is no reason for the failure of the solution. It is certainly true that the particular assumption of Matthew (1963) or Hager and Hutter (1984a) is that the flow must be weakly curved. In mathematical terms, this assumption requires that $t_x^2, z_{bx}^2, |t\, t_x|$ and $|t\, z_{bxx}| \ll 1$, with t (x) as the flow depth, $z_b(x)$ as the bottom profile, and x as subscript indicating differentiation with respect to x. However, these limitations are not explicitly included in the Picard iteration technique, as proposed by Matthew (1991). Castro-Orgaz and Hager (2013, 2014a) demonstrate that the second-order Boussinesq-type model also applies to highly curved flows.

In this chapter, approximate methods to obtain higher order Boussinesq-type equations are presented, including the theories of Dressler (1978), Hager and Hutter (1984a), and Matthew (1991). The resulting solutions for typical flow problems as the free overfall, the slope break, the round-crested weir, and the vertical gate are then compared with physical and 2D numerical data. Vorticity effects are presented for the free overfall as test case, and the mathematical theory of irrotational, unsteady water waves is introduced.

3.2 Potential Flow Theory

3.2.1 Fundamentals

Consider *steady inviscid* channel flows over a curved bottom (Fig. 3.3). The problem is governed by the steady Euler equations of an inviscid and incompressible fluid as (Rouse 1938; Vallentine 1969; Hutter and Wang 2016)

$$\frac{\partial u}{\partial x} + \frac{\partial w}{\partial z} = 0, \tag{3.1}$$

$$u\frac{\partial u}{\partial x} + w\frac{\partial u}{\partial z} = -\frac{1}{\rho}\frac{\partial p}{\partial x}, \tag{3.2}$$

$$u\frac{\partial w}{\partial x} + w\frac{\partial w}{\partial z} = -\frac{1}{\rho}\frac{\partial p}{\partial z} - g. \tag{3.3}$$

Here, u is the velocity component in the x-direction, w that in the vertical z-direction, p the pressure, g the gravity acceleration and ρ the fluid density.

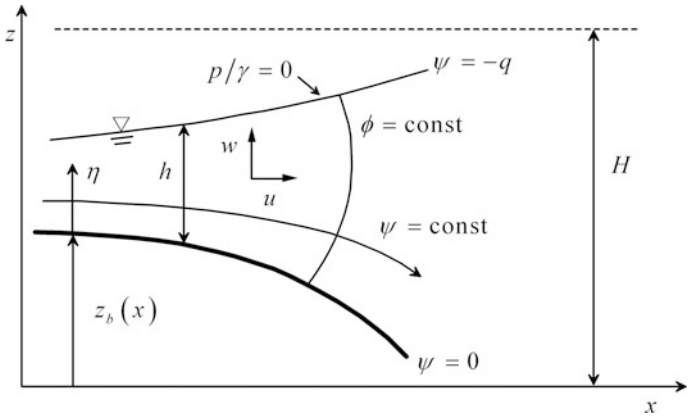

Fig. 3.3 Definition sketch for steady plane potential flow over curved bed

Equation (3.1) is the continuity equation of an incompressible fluid, whereas Eqs. (3.2) and (3.3) state conservation of momentum in the x- and z-directions, respectively. Further, if the fluid particles are free of rotation, the curl of the velocity field in the (x, z) plane is zero, so that

$$\frac{\partial u}{\partial z} - \frac{\partial w}{\partial x} = 0. \tag{3.4}$$

An irrotational and inviscid velocity field (u, w) can be defined using the potential function ϕ such that (Thom and Apelt 1961; Vallentine 1969)[1]

$$u = -\frac{\partial \phi}{\partial x}, \quad w = -\frac{\partial \phi}{\partial z}. \tag{3.5}$$

This irrotational flow field automatically satisfies Eq. (3.4). Using Eqs. (3.5) in (3.1), the flow field obeys the Laplace equation for ϕ

$$\frac{\partial^2 \phi}{\partial x^2} + \frac{\partial^2 \phi}{\partial z^2} = 0. \tag{3.6}$$

For an incompressible fluid, a stream function ψ is defined as (Thom and Apelt 1961; Vallentine 1969) (see Footnote 1)

$$u = -\frac{\partial \psi}{\partial z}, \quad w = +\frac{\partial \psi}{\partial x}. \tag{3.7}$$

Using this in Eq. (3.1) shows that the continuity equation is automatically satisfied. Furthermore, if Eq. (3.7) is used in Eq. (3.4), it is seen that also the stream function satisfies the Laplace equation

$$\frac{\partial^2 \psi}{\partial x^2} + \frac{\partial^2 \psi}{\partial z^2} = 0. \tag{3.8}$$

The lines ψ = const are called streamlines, and the velocity vector, of modulus $V = (u^2 + w^2)^{1/2}$, is tangent to them. The equipotential lines ϕ = const are normal to the streamlines at intersection points, forming the so-called flow net of a potential flow. Thus, a potential flow obeys the Laplacians for both ϕ and ψ, as well as the so-called Cauchy–Riemann equations, derived by equaling the velocity components in Eqs. (3.5) and (3.7) as

$$u = -\frac{\partial \phi}{\partial x} = -\frac{\partial \psi}{\partial z}, \quad w = -\frac{\partial \phi}{\partial z} = +\frac{\partial \psi}{\partial x}. \tag{3.9}$$

[1] In most books on fluid mechanics, ϕ and ψ are defined with the opposite signs.

An additional equation satisfied by potential flows is gained by substituting the irrotational flow condition into the Euler's momentum equations (3.2) and (3.3). These reduce to

$$\frac{1}{2}\frac{\partial}{\partial x}\left(u^2+w^2\right)=-\frac{1}{\rho}\frac{\partial p}{\partial x}, \tag{3.10}$$

$$\frac{1}{2}\frac{\partial}{\partial z}\left(u^2+w^2\right)=-\frac{1}{\rho}\frac{\partial p}{\partial z}-g. \tag{3.11}$$

For density-preserving fluids (ρ = const., i.e., the assumption of incompressibility of water), Eqs. (3.10) and (3.11) are rewritten as

$$\frac{\partial}{\partial x}\left(\frac{u^2+w^2}{2g}+\frac{p}{\rho g}+z\right)=0, \tag{3.12}$$

$$\frac{\partial}{\partial z}\left(\frac{u^2+w^2}{2g}+\frac{p}{\rho g}+z\right)=0. \tag{3.13}$$

Let the total energy head H be defined as

$$H=\frac{u^2+w^2}{2g}+\frac{p}{\rho g}+z. \tag{3.14}$$

Equations (3.12) and (3.13) then state that H is a constant within the flow

$$\mathrm{d}H=\frac{\partial H}{\partial x}\mathrm{d}x+\frac{\partial H}{\partial z}\mathrm{d}z=0. \tag{3.15}$$

Equation (3.15) leads to H = const; coupled with Eq. (3.9) for the velocity components, it allows for solving potential channel flows in the vertical plane. In the next few sections, mathematical techniques (analytical or numerical) are presented to solve these equations.

3.2.2 Conservation Laws

The velocity (u, w) and pressure p of a potential flow can be used in the control volume method for 1D depth-averaged computations. Derivations of the conservation laws of a control volume for steady, plane curvilinear flows are presented. Integration of Eq. (3.2) from the channel bottom to the free surface yields

$$\int_{z_b}^{z_b+h} u\frac{\partial u}{\partial x}\mathrm{d}z + \int_{z_b}^{z_b+h} w\frac{\partial u}{\partial z}\mathrm{d}z = \int_{z_b}^{z_b+h} \frac{\partial u^2}{\partial x}\mathrm{d}z + \int_{z_b}^{z_b+h} \frac{\partial uw}{\partial z}\mathrm{d}z = -\frac{1}{\rho}\int_{z_b}^{z_b+h} \frac{\partial p}{\partial x}\mathrm{d}z. \tag{3.16}$$

Using Leibniz's rule to exchange the order of integration and differentiation where necessary leads to

$$\begin{aligned} &\frac{\mathrm{d}}{\mathrm{d}x}\int_{z_b}^{z_s} u^2\mathrm{d}z - \underbrace{\left[u_s\frac{\partial z_s}{\partial x} - w_s\right]}_{=0} u_s + \underbrace{\left[u_b\frac{\partial z_b}{\partial x} - w_b\right]}_{=0} u_b \\ &= -\frac{1}{\rho}\left(\frac{\mathrm{d}}{\mathrm{d}x}\int_{z_b}^{z_s} p\mathrm{d}z + p_b\frac{\partial z_b}{\partial x} - \underbrace{p_s}_{=0}\frac{\partial z_s}{\partial x}\right) \\ &\Rightarrow \quad \frac{\mathrm{d}}{\mathrm{d}x}\int_{z_b}^{z_b+h}\left(\frac{u^2}{g}+\frac{p}{\gamma}\right)\mathrm{d}z = -\frac{p_b}{\gamma}z_{bx}, \end{aligned} \tag{3.17}$$

in which $\gamma = \rho g$ is the specific weight and where the underbraced terms vanish owing to the kinematic and stress boundary conditions, expressing the tangency of the velocity at the basal and free surfaces and stress-free conditions at the free surface. This is a simplified form of the general Eq. (2.30). The quantity

$$S = \int_{z_b}^{z_b+h}\left(\frac{u^2}{g}+\frac{p}{\gamma}\right)\mathrm{d}z \tag{3.18}$$

is defined in the hydraulic literature as specific momentum (Jaeger 1956; Matthew 1991; Montes 1998). Conservation of the horizontal momentum, from Eq. (3.17), then gives

$$\frac{\mathrm{d}S}{\mathrm{d}x} = -\frac{p_b}{\gamma}z_{bx}. \tag{3.19}$$

Moreover, conservation of energy results in

$$\frac{\mathrm{d}H}{\mathrm{d}x} = 0, \tag{3.20}$$

as implied by Eq. (3.15). The total energy head H is defined in terms of the free surface streamline as

$$H = h + z_b + \frac{u_s^2 + w_s^2}{2g}. \tag{3.21}$$

Integrating the vertical momentum equation (3.3) in the vertical direction yields

$$\int_{z_b}^{z_b+h} u\frac{\partial w}{\partial x}\mathrm{d}z + \int_{z_b}^{z_b+h} w\frac{\partial w}{\partial z}\mathrm{d}z = -\frac{1}{\rho}\int_{z_b}^{z_b+h}\left(\frac{\partial p}{\partial z} + \gamma\right)\mathrm{d}z, \tag{3.22}$$

resulting in the z-momentum balance

$$\frac{\mathrm{d}}{\mathrm{d}x}\int_{z_b}^{z_b+h}\frac{uw}{g}\mathrm{d}z = \frac{p_b}{\gamma} - h. \tag{3.23}$$

Defining the vertical momentum flow per unit mass, M, as

$$M = \int_{z_b}^{z_b+h}\frac{uw}{g}\mathrm{d}z, \tag{3.24}$$

its conservation requires

$$\frac{\mathrm{d}M}{\mathrm{d}x} = \frac{p_b}{\gamma} - h. \tag{3.25}$$

Consider now what is called the moment of an equation for a control volume, here the momentum balance in the x (and later the z)-direction. Adding the term

$$u\left(\frac{\partial u}{\partial x} + \frac{\partial w}{\partial z}\right) = 0 \tag{3.26}$$

to the left-hand side of the horizontal momentum equation (3.2) yields the conservative form of Eq. (3.2), namely

$$\frac{\partial u^2}{\partial x} + \frac{\partial (uw)}{\partial z} = -\frac{1}{\rho}\frac{\partial p}{\partial x}. \tag{3.27}$$

Multiplying this equation on both sides by a weighting function, here simply z, yields

$$z\frac{\partial u^2}{\partial x} + z\frac{\partial (uw)}{\partial z} = -\frac{z}{\rho}\frac{\partial p}{\partial x}. \tag{3.28}$$

Integrating subsequently the resulting equation over the water depth generates

$$\int_{z_b}^{z_b+h} \frac{\partial}{\partial x}\left(u^2 z\right)\mathrm{d}z + \int_{z_b}^{z_b+h} \frac{\partial}{\partial z}(uwz)\mathrm{d}z - \int_{z_b}^{z_b+h} uw\mathrm{d}z = -\frac{1}{\rho}\int_{z_b}^{z_b+h} \frac{\partial}{\partial x}(pz)\mathrm{d}z, \tag{3.29}$$

by using the relation

$$\int_{z_b}^{z_b+h} z\frac{\partial(uw)}{\partial z} = \int_{z_b}^{z_b+h} \frac{\partial}{\partial z}(uwz)\mathrm{d}z - \int_{z_b}^{z_b+h} uw\mathrm{d}z. \tag{3.30}$$

Equation (3.29) is the depth-integrated z-moment of the x-momentum equation. It will be transformed into a more convenient form by interchanging differentiation and integration using the Leibniz rule; with $z_s = z_b + h$, the integrals in Eq. (3.29) are transformed to

$$\begin{aligned}
&\int_{z_b}^{z_s} \frac{\partial(u^2 z)}{\partial x}\mathrm{d}z = \frac{\partial}{\partial x}\int_{z_b}^{z_s} u^2 z\mathrm{d}z - u_s^2 z_s\frac{\partial z_s}{\partial x} + u_b^2 z_b\frac{\partial z_b}{\partial x},\\
&\int_{z_b}^{z_s} \frac{\partial(uwz)}{\partial z}\mathrm{d}z = u_s w_s z_s - u_b w_b z_b,\\
&-\frac{1}{\rho}\int_{z_b}^{z_s} \frac{\partial}{\partial x}(pz)\mathrm{d}z = -\frac{1}{\rho}\frac{\partial}{\partial x}\int_{z_b}^{z_s} pz\mathrm{d}z + \frac{1}{\rho}z_s\underbrace{p_s}_{=0}\frac{\partial z_s}{\partial x} - \frac{1}{\rho}z_b p_b\frac{\partial z_b}{\partial x},
\end{aligned} \tag{3.31}$$

in which the vanishing free surface pressure $p_s = 0$ has been implemented. Inserting Eq. (3.31) in Eq. (3.29) leads to

$$\begin{aligned}
&\frac{\partial}{\partial x}\int_{z_b}^{z_b+h} u^2 z\mathrm{d}z + u_s z_s\underbrace{\left(w_s - u_s\frac{\partial z_s}{\partial x}\right)}_{=0} - u_b z_b\underbrace{\left(w_b - u_b\frac{\partial z_b}{\partial x}\right)}_{=0} - \int_{z_b}^{z_s} uw\mathrm{d}z\\
&\quad = -\frac{1}{\rho}\frac{\partial}{\partial x}\int_{z_b}^{z_b+h} pz\mathrm{d}z - \frac{1}{\rho}z_b p_b\frac{\partial z_b}{\partial x},
\end{aligned} \tag{3.32}$$

in which the underbraced kinematic quantities vanish, since they express the tangency of the basal and free surface velocities to the bed and free surface, respectively. The last equation directly implies

$$\frac{\mathrm{d}}{\mathrm{d}x}\int_{z_b}^{z_b+h}\left(\frac{u^2}{g}+\frac{p}{\gamma}\right)z\mathrm{d}z-\int_{z_b}^{z_b+h}\frac{uw}{g}\mathrm{d}z+z_{bx}\frac{z_b p_b}{\gamma}=0. \tag{3.33}$$

Proceeding analogously with the vertical momentum balance equation, Eq. (3.3), it is written as

$$\frac{\partial}{\partial x}(uw)+\frac{\partial w^2}{\partial z}=-\frac{1}{\rho}\frac{\partial p}{\partial z}-g. \tag{3.34}$$

Multiplying this equation on both sides with x and, subsequently, integrating the emerging equation over the flow depth from $z = z_b$ to $z = z_b + h$ leads to

$$\int_{z_b}^{z_b+h}\frac{\partial}{\partial x}(xuw)\mathrm{d}z+\int_{z_b}^{z_b+h}\frac{\partial}{\partial z}\left(w^2x\right)\mathrm{d}z-\int_{z_b}^{z_b+h}uw\mathrm{d}z=-\frac{1}{\rho}\int_{z_b}^{z_b+h}x\frac{\partial}{\partial z}(p+\rho gz)\mathrm{d}z. \tag{3.35}$$

This is transformed into a more convenient form again by using the Leibniz rule when interchanging differentiations and integrations as above. In this way, one obtains

$$\begin{aligned}&\frac{\mathrm{d}}{\mathrm{d}x}\int_{z_b}^{z_b+h}x\frac{uw}{g}\mathrm{d}z+x\underbrace{\left(w_s-u_s\frac{\partial z_s}{\partial x}\right)}_{=0}\frac{w_s}{g}-x\underbrace{\left(w_b-u_b\frac{\partial z_b}{\partial x}\right)}_{=0}\frac{w_b}{g}-\int_{z_b}^{z_b+h}\frac{uw}{g}\mathrm{d}z\\&=x\left(\frac{p_b}{\gamma}-\underbrace{\frac{p_s}{\gamma}}_{=0}\right)-xh,\end{aligned} \tag{3.36}$$

or

$$\frac{\mathrm{d}}{\mathrm{d}x}\int_{z_b}^{z_b+h}x\frac{uw}{g}\mathrm{d}z-\int_{z_b}^{z_b+h}\frac{uw}{g}\mathrm{d}z-x\left(\frac{p_b}{\gamma}-h\right)=0, \tag{3.37}$$

in which again $p_s = 0$ and the tangency conditions of the streamlines at the bounding surfaces have been applied.

Equations (3.33) and (3.37) are the relevant equations by which a depth-integrated balance of angular momentum is motivated. To this end, let $m_x = 0$ and $m_z = 0$ be the local momentum balances in the above 2D formulation. Then,

$zm_x - xm_z = 0$ is the moment of the x- and z-moments of the momenta with respect to the origin of the coordinates (x, z). Next, let us form

$$\int_{z_b}^{z_s} (zm_x - xm_z) = 0. \tag{3.38}$$

The value of this integral vanishes as an identity if $m_x = 0$ and $m_z = 0$ are satisfied as local identities. However, if the momentum equations are only globally satisfied, e.g., as

$$\int_{z_b}^{z_s} m_x \mathrm{d}z = 0 \quad \text{and} \quad \int_{z_b}^{z_s} m_z \mathrm{d}z = 0, \tag{3.39}$$

then Eq. (3.38) is a genuine statement. Further, it may be stated that Eq. (3.38) is weaker than any one of the two statements

$$\int_{z_b}^{z_s} zm_x \mathrm{d}z = 0 \quad \text{and} \quad \int_{z_b}^{z_s} xm_z \mathrm{d}z = 0, \tag{3.40}$$

and even though from a viewpoint of the principle of weighted residuals, each of them or both are possible candidates of higher order approximation.

Equation (3.38) is obtained by subtracting Eq. (3.37) from (3.33); the result is

$$\frac{\mathrm{d}}{\mathrm{d}x} \int_{z_b}^{z_b+h} \left(\frac{u^2}{g} + \frac{p}{\gamma} \right) z \mathrm{d}z + x \left(\frac{p_b}{\gamma} - h \right) - \frac{\mathrm{d}}{\mathrm{d}x} \int_{z_b}^{z_b+h} x \frac{uw}{g} \mathrm{d}z = -z_{bx} \frac{z_b p_b}{\gamma}. \tag{3.41}$$

Khan and Steffler (1996a, b) and Steffler and Jin (1993) presented moment of momentum equations, where the momentum equations are multiplied by a weighting function, typically related to the vertical coordinate z, e.g., in the first of Eq. (3.40). However, these relations are not conservation equations for angular momentum, but rather additional legitimate depth-averaged mathematical statements based on the residual weighting method, as explained above. Let the angular momentum A due to horizontal forces be

$$A = \int_{z_b}^{z_b+h} \left(\frac{u^2}{g} + \frac{p}{\gamma} \right) z \mathrm{d}z. \tag{3.42}$$

Conservation of angular momentum then requires from Eq. (3.41)

$$\frac{\mathrm{d}A}{\mathrm{d}x} = L - z_{bx}\frac{z_b p_b}{\gamma}, \quad \text{in which} \quad L = -x\left(\frac{p_b}{\gamma} - h\right) + \frac{\mathrm{d}}{\mathrm{d}x}\int_{z_b}^{z_b+h} x\frac{uw}{g}\mathrm{d}z. \tag{3.43}$$

Equations (3.19), (3.20), (3.25), and (3.43) are the conservation laws of horizontal momentum, energy, vertical momentum, and angular momentum, respectively, for an elementary control volume of curvilinear streamlines and vertical sections. For specific applications, the velocity components $u(z)$ and $w(z)$, as well as the pressure distribution $p(z)$ along a vertical section, are needed. If these are computed using a potential flow method, the estimations for velocity and pressure fields should satisfy the conservation equations derived here with a prescribed truncation error. For depth-averaged open-channel flow modeling, it is rather more suitable to use Eq. (3.33), rewritten as

$$\frac{\mathrm{d}A}{\mathrm{d}x} = M - z_{bx}\frac{z_b p_b}{\gamma}. \tag{3.44}$$

3.2.3 *Flow Net*

The family of curves ϕ = const (equipotential lines) and ψ = const (streamlines) forms a flow net, of which the streamline inclination with respect to the x-axis is θ and whose streamline curvature is $\kappa = 1/R$, with R as radius of streamline curvature (Fig. 3.4). For applications to steady curvilinear flows, consider the steady Euler's equations formulated in a curvilinear orthogonal coordinate system with axes along the streamlines (s) and orthogonal to them (n). These are (e.g., Rouse 1938; Milne-Thomson 1962; Montes 1998; Hager and Schleiss 2009)

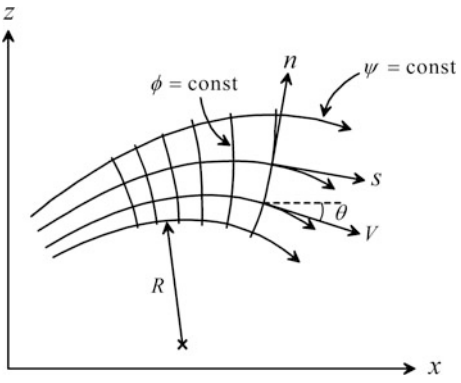

Fig. 3.4 Definition sketch for the flow net in plane open-channel flows (adapted from Rouse 1932)

$$V\frac{\partial V}{\partial s} = -\frac{1}{\rho}\frac{\partial p}{\partial s} - g\frac{\partial z}{\partial s}, \tag{3.45}$$

$$\frac{V^2}{R} = -\frac{1}{\rho}\frac{\partial p}{\partial n} - g\frac{\partial z}{\partial n}. \tag{3.46}$$

Here, $V = (u^2 + w^2)^{1/2}$ is the modulus of the velocity vector and gravity points to the negative z-direction.

For steady irrotational motions, the total energy head is a constant given by

$$H = z + \frac{p}{\gamma} + \frac{V^2}{2g} = \text{const.} \tag{3.47}$$

It permits the computation of $\partial H/\partial n = 0$. Inserting the resulting expression into Eq. (3.46) gives

$$\frac{\partial V}{\partial n} = \frac{V}{R}. \tag{3.48}$$

Equations (3.47) and (3.48) replace the original Euler equations. Note that Eq. (3.48) applies along a curved line $n(x, z)$ characterized by the mathematical condition $\phi(x, z) = \text{const}$. Computing $V(n)$ by the use of $\phi(x, z) = \text{const}$. yields $V(x, z), u = V\cos\theta$ and $w = V\sin\theta$. However, these Cartesian components, (u, w), are determined along the coordinates (x, z) following n measured along the mathematical curve $\phi(x, z) = \text{const}$. In the (s, n) system, the velocity V is related to the stream function by

$$V = \frac{\partial \psi}{\partial n}. \tag{3.49}$$

Substituting this result into Eq. (3.48) yields

$$\frac{\partial^2 \psi}{\partial n^2} - \kappa\frac{\partial \psi}{\partial n} = \nabla^2\psi = 0, \tag{3.50}$$

in which

$$\kappa = \frac{1}{R} = \frac{\partial \theta}{\partial s} \tag{3.51}$$

relates the streamline curvature and the change of the inclination angle θ along the streamlines. Note that the left-hand side of Eq. (3.50) can be reinterpreted as Laplace's equation along an equipotential line.

3.3 Picard Iteration

3.3.1 General Aspects of Iterative Solutions

Van Dyke (1975) discussed two methods to solve the systems of partial differential equations in fluid flow problems by approximations. For 2D potential flows, the existence of stream ψ and potential ϕ functions results in the system of governing equations $\nabla^2\phi = 0$ and $\nabla^2\psi = 0$ obtained from the continuity equation and irrotational flow condition, respectively (Vallentine 1969). These elliptic equations can also be viewed as consequences of the Cauchy–Riemann equations. A *first* method to find a solution is assuming a given power series for ψ, as done by Benjamin and Lighthill (1954) in their study of cnoidal waves and bores. The coefficients of the power series are determined by using the governing equation $\nabla^2\psi = 0$ and the boundary conditions on ψ. This treatment lies in the first class of solutions discussed by Van Dyke (1975).

The *second* kind of approximate solutions of potential flows is to iterate the solution of the equations $\nabla^2\phi = 0$ and $\nabla^2\psi = 0$ starting with an initial solution, without any assumption of the recursion series. Matthew (1991) pursued this idea and iterated the Cauchy–Riemann equations, a process which is equivalent to iteratively finding ϕ and ψ by satisfying $\nabla^2\phi = 0$ and $\nabla^2\psi = 0$. This technique is described below.

3.3.2 Second-Order Velocity Field

Van Dyke (1975) indicated that iterations or perturbations could be used to solve systems of partial differential equations in fluid flow problems, subjected to appropriate initial and boundary conditions. Matthew (1991) pursued this idea in steady open-channel flows and solved the Cauchy–Riemann equations by iteration. This technique permits the reduction of 2D flows in a vertical plane to approximate 1D problems. The resulting 1D equation is solved by suitable numerical techniques. An applied example is, e.g., flow over a weir crest. The application of Picard iteration amounts to applying iterative cycles in a recursive way. Performing an infinite number of iterations would make the method very heavy to produce an algebraically tractable 1D differential equation, given the fact that the development of the third iteration cycle is already tedious (Matthew 1991; Castro-Orgaz and Hager 2013, 2014a).

Consider the free surface flows over an arbitrary bottom geometry $z_b(x)$ (Fig. 3.3). The flow depth $h(x, t)$ and discharge $q(x, t)$ depend in general on the streamwise coordinate x and on time t. The Cartesian velocity components $u(x, z, t)$ and $w(x, z, t)$ of potential flows obey the Cauchy–Riemann equations given by Eq. (3.9) in unsteady potential flows. Equation (3.9) involves only spatial differentiations with respect to the x- and z-coordinates of ϕ and ψ that are also functions of time. Matthew

(1991) used Picard iteration technique to provide the successive approximations of u and w to an arbitrary order of accuracy for steady flows (q = const). The procedure applies, however, also for unsteady flows; one only needs to consider that q is not a constant (Castro-Orgaz and Hager 2014a). For the sake of generality, the velocity field is considered as unsteady; steadiness will be imposed at the end.

The first of Eq. (3.9) is

$$u = -\frac{\partial \psi}{\partial z}. \tag{3.52}$$

Integrating it in the vertical direction, introducing thereby the variable $\eta(x, z) = z - z_b(x)$ as the vertical distance above the channel bottom yields

$$\psi = -\int u \mathrm{d}\eta = -U\eta. \tag{3.53}$$

Note that for vertical integration, the variable z is replaced by η by using a change of variable. The depth-averaged velocity $U = q/h$ has been selected as a starting function in Eq. (3.53). The velocity U is retained as a dependent variable in the mathematical developments rather than expanding it as a function of both q and h, thereby simplifying the algebra. Using the Cauchy–Riemann equations (3.9), and (3.53), gives

$$w = +\frac{\partial \psi}{\partial x} = -U_x\eta - U\eta_x. \tag{3.54}$$

Here and henceforth, subscript notation for differentiation is employed as above. Again from Eq. (3.9),

$$w = -\frac{\partial \phi}{\partial z}, \tag{3.55}$$

which delivers ϕ by depth integration, when w is known from Eq. (3.54). This yields with f as an arbitrary function of x and t

$$-\phi = \int w \mathrm{d}\eta + f(x) = -U_x\frac{\eta^2}{2} - U\eta\eta_x + f(x,t). \tag{3.56}$$

With the aid of Eq. (3.56), and the function f_x not yet determined, the first identity in Eq. (3.9) is

$$u = -\frac{\partial \phi}{\partial x} = -U_{xx}\frac{\eta^2}{2} - (2U_x\eta_x + U\eta_{xx})\eta - U\eta_x^2 + f_x. \tag{3.57}$$

Inserting Eq. (3.57) into Eq. (3.52) and then integrating the emerging equation with respect to η lead to

$$\psi = -\int u \mathrm{d}\eta = U_{xx}\frac{\eta^3}{6} + (2U_x\eta_x + U\eta_{xx})\frac{\eta^2}{2} + U\eta_x^2\eta - f_x\eta. \tag{3.58}$$

Note that the depth-averaged velocity $U(x, t)$ and its spatial derivatives are not functions of z and, thus, neither of η. Furthermore, $\eta_x = -\partial z_b/\partial x$ and $\eta_{xx} = -\partial^2 z_b/\partial x^2$ are also independent of z. Equation (3.58) is now used to obtain f_x subject to the boundary condition of the stream function at the free surface, namely

$$\psi[\eta = h(x,t)] = -q(x,t). \tag{3.59}$$

Inserting Eq. (3.59) into Eq. (3.58) results in

$$f_x = U + U_{xx}\frac{h^2}{6} + (2U_x\eta_x + U\eta_{xx})\frac{h}{2} + U\eta_x^2. \tag{3.60}$$

This result together with Eq. (3.57) yields

$$u = U + (2U_x\eta_x + U\eta_{xx})\left(\frac{h}{2} - \eta\right) + U_{xx}\left(\frac{h^2}{6} - \frac{\eta^2}{2}\right). \tag{3.61}$$

Equation (3.61) is the generalized second-order velocity profile for unsteady potential flow. Note that it accounts for full nonlinearity during the iteration process. The bottom profile contribution in curvilinear flows is given implicitly by the terms η_x and η_{xx}, whereas the free surface profile effects, h_x and h_{xx}, are contained in the terms U_x and U_{xx}. For steady flows over a curved bottom surface, the spatial derivatives of U and η take the form

$$\begin{aligned} U_x &= -\frac{qh_x}{h^2}, \quad U_{xx} = -\frac{qh_{xx}}{h^2} + 2\frac{qh_x^2}{h^3}, \\ \eta_x &= -z_{bx}, \quad \eta_{xx} = -z_{bxx}. \end{aligned} \tag{3.62}$$

Inserting Eq. (3.62) into Eqs. (3.54) and (3.61) results in

$$u = \frac{q}{h}\left[1 + \left(z_{bxx} - \frac{2h_x z_{bx}}{h}\right)\left(\frac{2\eta - h}{2}\right) + \left(\frac{h_{xx}}{2h} - \frac{h_x^2}{h^2}\right)\left(\frac{3\eta^2 - h^2}{3}\right)\right], \tag{3.63}$$

$$w = \frac{q}{h}\left[z_{bx} + \frac{\eta}{h}h_x\right]. \tag{3.64}$$

The pressure distribution follows from the energy conservation law of steady potential flow. From Eqs. (3.14) to (3.15), the total energy head H is a constant in

the entire computational domain for any potential flow; this is so because it is assumed that the flow is free of vorticity at the boundaries. Thus,

$$H = H(x,z) = z + \frac{p}{\gamma}(x,z) + \frac{u^2(x,z) + w^2(x,z)}{2g} = \text{const.} \tag{3.65}$$

The pressure head follows from this as

$$\frac{p}{\gamma} = H - z - \frac{u^2 + w^2}{2g}. \tag{3.66}$$

In steady potential flow, the energy head is a constant for all streamlines; thus, Eq. (3.65) can also be evaluated on the free surface streamline where $p_s = 0$ to obtain

$$H = z_s + \frac{V_s^2}{2g} = \text{const.} \tag{3.67}$$

Moreover, $z_s = z_b + h$ and V_s is the modulus of the velocity vector at the free surface streamline. Using Eqs. (3.63) and (3.64), the velocity at an arbitrary elevation η above the channel bed V is estimated as (Matthew 1995)

$$V^2 = u^2 + w^2 \approx \frac{q^2}{h^2}\left[1 + \left(z_{bxx} - \frac{2h_x z_{bx}}{h}\right)(2\eta - h) + \left(\frac{h_{xx}}{2h} - \frac{h_x^2}{h^2}\right)\left(\frac{6\eta^2 - 2h^2}{3}\right) + z_{bx}^2 + 2\frac{\eta}{h} z_{bx} h_x + \frac{\eta^2}{h^2} h_x^2\right]. \tag{3.68}$$

To account for the terms of similar order of magnitude in Eq. (3.68), u^2 was computed squaring Eq. (3.63) and retaining only the first-order terms, whereas w^2 was determined exactly (Matthew 1995). By evaluating Eq. (3.68) at $\eta = h$, one obtains

$$\begin{aligned} V_s^2 &= \frac{q^2}{h^2}\left[1 + \left(z_{bxx} - \frac{2h_x z_{bx}}{h}\right)(2h - h) + \left(\frac{h_{xx}}{2h} - \frac{h_x^2}{h^2}\right)\left(\frac{6h^2 - 2h^2}{3}\right) + z_{bx}^2 + 2\frac{h}{h} z_{bx} h_x + \frac{h^2}{h^2} h_x^2\right] \\ &= \frac{q^2}{h^2}\left[1 + (h z_{bxx} - 2h_x z_{bx}) + \left(\frac{2h h_{xx}}{3} - \frac{4h_x^2}{3}\right) + z_{bx}^2 + 2 z_{bx} h_x + h_x^2\right]. \end{aligned} \tag{3.69}$$

Inserting Eq. (3.69) in Eq. (3.67), the energy equation at the free surface streamline takes the form (Matthew 1991; Castro-Orgaz and Hager 2014a)

$$H = z_b + h + \frac{V_s^2}{2g} = z_b + h + \frac{q^2}{2gh^2}\left(1 + \frac{2hh_{xx} - h_x^2}{3} + hz_{bxx} + z_{bx}^2\right). \quad (3.70)$$

This is similar to the equations of Fawer (1937), Matthew (1963), Hager and Hutter (1984a), Montes and Chanson (1998), and Montes (1998). Equation (3.70) differs from those of Hager and Hutter (1984a) and Hager (1985a) in the definition of the flow depth, given that intrinsic curvilinear coordinates were used, as explicitly discussed below. However, both results are correct to the same order of accuracy. Equation (3.70) was also obtained by Naghdi and Vongsarnpigoon (1986) using the theory of directed fluid sheets; by Marchi (1992, 1993), by expanding the stream function in power series; and by Zhu and Lawrence (1998), by using a perturbation method. It is a second-order differential equation, from which the free surface profile $h = h(x)$ emerges. For given H = const., and prescribed flow depths at two boundary channel sections, Eq. (3.70) is solved numerically as a two-point boundary-value problem (Castro-Orgaz and Hager 2009).

Equations (3.63) and (3.64) are the steady-state equations of Matthew (1991) for $u^{(2)}$ and $w^{(1)}$, where superscripts indicate the order of the Picard iteration. Marchi (1992, 1993) also independently obtained these results by expanding the steady stream function into a power series, thereby generalizing the results of Benjamin and Lighthill (1954). The pressure distribution results from Eq. (3.66) by inserting Eq. (3.67), given that H is a constant, generating the equation

$$\frac{p}{\gamma} = H - z_b - \eta - \frac{u^2 + w^2}{2g} = h - \eta + \frac{V_s^2}{2g} - \frac{V^2}{2g}. \quad (3.71)$$

Subtracting Eq. (3.68) from (3.69), and inserting the result into Eq. (3.71) gives after some elementary manipulations,

$$\frac{p}{\gamma} = h - \eta + \frac{q^2}{2gh^2}\left[(2hz_{bxx} - 2h_x z_{bx})\left(1 - \frac{\eta}{h}\right) + \left(hh_{xx} - h_x^2\right)\left(1 - \frac{\eta^2}{h^2}\right)\right]. \quad (3.72)$$

Equations (3.63), (3.64), and (3.72) describe a number of ideal fluid flows, such as the cnoidal wave already dealt with by Benjamin and Lighthill (1954). Figure 3.5a sketches the velocity and pressure distributions of a potential, steady cnoidal wave ($z_b = z_{bx} = z_{bxx} = 0$). At a wave crest ($h_x = 0$), the u velocity profile decreases with z ($h_{xx} < 0$), implying a pressure distribution less than hydrostatic. At wave troughs, the trend is reversed; the u velocity profile increases with z ($h_{xx} > 0$), and the pressure is larger than its hydrostatic counterpart.

Another typical non-hydrostatic motion is the flow over a round-crested weir (Fig. 3.5b). Along the weir, streamlines are curved and sloped, and the pressure distribution is non-hydrostatic. Therefore, the flow net is highly curved, leading to significant spatial variations of velocity and pressure. The Picard iteration theory applies to solve this flow problem (Matthew 1991), but the use of natural coordinates based on the equipotential and streamlines is also attractive (Matthew 1963).

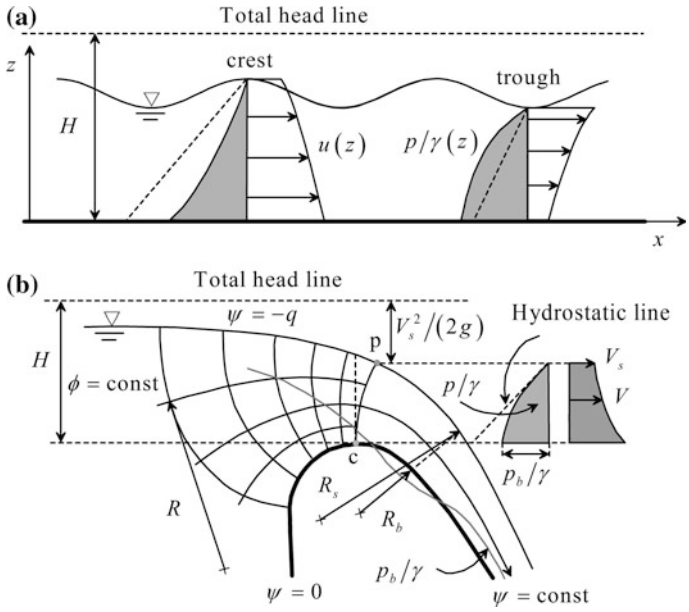

Fig. 3.5 **a** Velocity and pressure distributions at extremes of potential cnoidal wave with (- - -) hydrostatic pressure line, **b** flow net over round-crested weir; bottom pressure head diverges from free surface. Also shown are velocity and pressure distributions at crest section and equipotential line forming the critical point "p"

The equipotential line at the weir crest is important, given that a critical point "p" on the free surface determines the discharge features.

The momentum equation, given by the conservation law, Eq. (3.19), applies also to compute the free surface profile if closures for p_b and S are assigned. Eliminating the pressure with the aid of Eq. (3.65) in the definition of S given by Eq. (3.18) provides the relation

$$S = \left(H - z_b - \frac{h}{2}\right)h + \int_{z_b}^{h+z_b} \left(\frac{u^2 - w^2}{2g}\right) \mathrm{d}z. \tag{3.73}$$

Equation (3.73) was introduced by Matthew (1991) and used by Castro-Orgaz and Hager (2009). It is called the general S–H relation, because it connects S with H. Therefore, to the same order of accuracy, one obtains

$$S = \frac{h^2}{2} + \frac{q^2}{gh}\left(1 + \frac{hh_{xx} - h_x^2}{3} + \frac{hz_{bxx}}{2} - \frac{h_x z_{bx}}{2}\right). \tag{3.74}$$

The bottom pressure profile, $p_b = p(\eta = 0)$, is obtained from Eq. (3.72) as

$$\frac{p_b}{\gamma} = h + \frac{q^2}{2gh^2}\left(2hz_{bxx} + hh_{xx} - h_x^2 - 2z_{bx}h_x\right). \tag{3.75}$$

Note that if $z_{bxx} = z_{bx} = h_{xx} = h_x = 0$, the bottom pressure head p_b/γ is hydrostatic and equal to the vertical flow depth h. Equation (3.75) was introduced by Castro-Orgaz and Hager (2009).

3.3.3 Third-Order Velocity Field

The second iterative cycle parallels the previous steps enclosed in the sequence from Eqs. (3.52) to (3.61), but starts with $u^{(2)}$ [given by Eq. (3.63)] inserted into Eq. (3.53). The algebraic efforts of this new cycle become enormous (Matthew 1991; Castro-Orgaz and Hager 2014a). Appendix B gives the reader an impression of the complexity of the procedure.

In the next iteration, the expression for $w^{(2)}$, a precursor of $w^{(3)}$, was stated by Castro-Orgaz and Hager (2013), resulting in the third-order polynomial representation

$$w^{(2)} = \frac{q}{h}\left(\alpha_1 + \alpha_2\eta + \alpha_3\eta^2 + \alpha_4\eta^3\right), \tag{3.76}$$

with the analytical coefficients

$$\begin{aligned}
\alpha_1 &= z_{bx} - \frac{z_{bxx}z_{bx}h}{2} + h_x z_{bx}^2 - \frac{h_{xx}z_{bx}h}{6} + \frac{z_{bx}h_x^2}{3},\\
\alpha_2 &= \frac{h_x}{h} + \frac{hz_{bxxx}}{2} + \frac{z_{bx}h_x^2}{h} - z_{bx}h_{xx} - z_{bxx}h_x\\
&\quad + \frac{hh_{xxx}}{6} - \frac{2h_xh_{xx}}{3} + \frac{h_x^3}{3h} + z_{bx}z_{bxx} - \frac{2h_xz_{bx}^2}{h},\\
\alpha_3 &= -\frac{z_{bxxx}}{2} + \frac{3z_{bxx}h_x}{2h} - \frac{3z_{bx}h_x^2}{h^2} + \frac{3z_{bx}h_{xx}}{2h},\\
\alpha_4 &= -\frac{h_{xxx}}{6h} + \frac{h_xh_{xx}}{h^2} - \frac{h_x^3}{h^3}.
\end{aligned} \tag{3.77}$$

Using Eq. (3.76), the third-order result for u is

$$u^{(3)} = \frac{q}{h}\left[1 + \beta_1\left(\eta - \frac{h}{2}\right) + \beta_2\left(\eta^2 - \frac{h^2}{3}\right) + \beta_3\left(\eta^3 - \frac{h^3}{4}\right) + \beta_4\left(\eta^4 - \frac{h^4}{5}\right)\right], \tag{3.78}$$

in which the analytical coefficients of the velocity profile are

$$\begin{aligned}
\beta_1 &= z_{bxx} - \frac{2h_x z_{bx}}{h} - z_{bx}z_{bxxx}h - \frac{2h_x^2 z_{bx}^2}{h} - \frac{hz_{bxx}^2}{2} + 2h_{xx}z_{bx}^2 + 3h_x z_{bx}z_{bxx} \\
&\quad - \frac{z_{bx}h_{xxx}h}{3} - \frac{2h_x^3 z_{bx}}{3h} - z_{bx}^2 z_{bxx} + \frac{2h_x z_{bx}^3}{h} + \frac{4h_x z_{bx}h_{xx}}{3} + \frac{h_x^2 z_{bxx}}{3} - \frac{h_{xx}z_{bxx}h}{6}, \\
\beta_2 &= \frac{h_{xx}}{2h} - \frac{h_x^2}{h^2} + \frac{hz_{bxxx}}{4} - \frac{z_{bx}h_x^3}{h^2} + \frac{z_{bxx}h_x^2}{h} + \frac{3z_{bx}h_x h_{xx}}{2h} - \frac{h_{xxx}z_{bx}}{2} \\
&\quad - h_{xx}z_{bxx} - \frac{h_x z_{bxx}}{2} + \frac{hh_{xxx}}{12} + \frac{5h_x^2 h_{xx}}{6h} - \frac{h_{xx}^2}{3} - \frac{h_x h_{xxx}}{3} - \frac{h_x^4}{3h^2} - \frac{4h_x z_{bx}z_{bxx}}{h} \\
&\quad + \frac{z_{bxx}^2}{2} + z_{bx}z_{bxxx} + \frac{5h_x^2 z_{bx}^2}{h^2} - \frac{5h_{xx}z_{bx}^2}{2h}, \\
\beta_3 &= -\frac{z_{bxxx}}{6} + \frac{2z_{bxx}h_x}{3h} - \frac{2h_x^2 z_{bxx}}{h^2} + \frac{4h_x^3 z_{bx}}{h^3} + \frac{z_{bxx}h_{xx}}{h} - \frac{4z_{bx}h_x h_{xx}}{h^2} + \frac{2z_{bx}h_{xxx}}{3h}, \\
\beta_4 &= -\frac{h_{xxx}}{24h} + \frac{h_x^4}{h^4} + \frac{h_{xx}^2}{4h^2} - \frac{3h_x^2 h_{xx}}{h^3} + \frac{h_x h_{xxx}}{3h^2}.
\end{aligned} \tag{3.79}$$

These coefficients for the fourth-order polynomial approximation of u, given by $u^{(3)}$, were first obtained by Matthew (1991). Note that obtaining $w^{(2)}$ is a necessary step to find $u^{(3)}$, although $w^{(2)}$ was not given by Matthew (1991). He tested $u^{(3)}$ and $u^{(2)}$ considering free vortex flow as a hypothetical exact 2D potential flow, while the accuracy of $u^{(3)}$ and $u^{(2)}$ against the full 2D numerical solution of potential flow problems in the gravity field was presented by Castro-Orgaz and Hager (2013). Khan and Steffler (1995) observed that a depth-averaged flow model, based on the momentum and moment of momentum equations (Steffler and Jin 1993), accurately describes the flow over curved beds if the reasonable vertical variations of u and w are considered. They accounted for a linear velocity profile of u and a second-order polynomial for w. Thus, the pairs $[u^{(2)}, w^{(1)}]$ and $[u^{(3)}, w^{(2)}]$ describe the specific polynomial approximations for (u, w) originating from an iterative solution of the potential flow model. The third-order extended energy equation then reads (Matthew 1991)

$$\begin{aligned}
H &= z_b + h + \frac{q^2}{2gh^2}\left(1 + \frac{2hh_{xx} - h_x^2}{3} + hz_{bxx} + z_{bx}^2\right. \\
&\quad + \frac{5}{12}h^2 z_{bxx}^2 - \frac{4}{3}hh_x z_{bx}z_{bxx} + \frac{1}{3}h^2 h_{xx}z_{bxx} + \frac{1}{3}h^2 z_{bx}z_{bxxx} \\
&\quad + \frac{1}{3}h^2 h_x z_{bxxx} + \frac{1}{12}h^3 z_{bxxxx} + \frac{1}{3}h_x^2 z_{bx}^2 - 2hh_x z_{bx}h_{xx} \\
&\quad - hh_x^2 z_{bxx} - \frac{2}{3}hh_{xx}z_{bx}^2 + \frac{2}{3}h_x^3 z_{bx} + \frac{1}{15}h^2 h_{xx}^2 \\
&\quad \left. - \frac{16}{15}hh_x^2 h_{xx} + \frac{4}{45}h^2 h_x h_{xxx} + \frac{4}{15}h_x^4 + \frac{2}{45}h^3 h_{xxxx}\right).
\end{aligned} \tag{3.80}$$

Detailed computations are given in Appendix B, from which the increase in algebra as compared with the second cycle predictor for H becomes evident.

3.4 Approximate Treatment of Flow Net Geometry

3.4.1 Velocity Profile

Consider the steady plane flow over a curved bed (Figs. 3.5b and 3.6a) and the Euler's equations formulated in orthogonal curvilinear coordinates as Eqs. (3.45) and (3.46). At a particular position x, the equipotential line connecting the bottom and free surface has a length N_o, with a projected flow depth t on the vertical line. Integration of Eq. (3.48) along this equipotential curve yields the velocity profile $V(n)$ as (Rouse 1938; Jaeger 1956; Matthew 1963; Hager and Hutter 1984a)

$$V(n) = V_s \exp\left(- \int_n^{N_o} \frac{\mathrm{d}n}{R} \right). \tag{3.81}$$

Here, V_s is the modulus of the velocity at the free surface and $V(n)$ is the velocity at the generic coordinate n of the equipotential line (Fig. 3.6a).

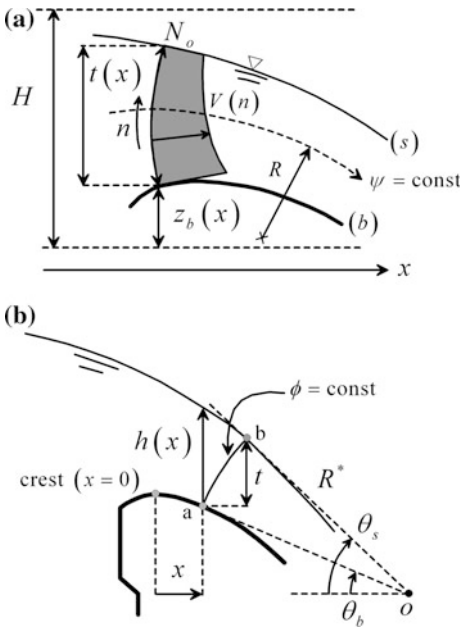

Fig. 3.6 **a** Velocity profile along an equipotential curve in steady flow over curved bottom profile (R is negative in the weir-flow case shown), **b** approximate treatment of flow geometry (slope angles are negative)

The integration in Eq. (3.81) is approximately performed upon an assumption for the variation of $R = R(n)$ (Hager 1985a). An assumption similar to that of Fawer (1937) is used here, relating the curvature radius and the inclination of the streamlines to their corresponding values at the channel bottom (subscript b) and at the free surface (subscript s) as

$$\frac{1}{R} = \frac{1}{R_b} + \left(\frac{1}{R_s} - \frac{1}{R_b}\right) v^K. \tag{3.82}$$

Here, $v = n/N_o$ is the dimensionless curvilinear coordinate along an equipotential line, and K is an empirical exponent, taken by Matthew (1963) as $K = 1$. However, Fawer (1937) and Castro-Orgaz (2010a, b, c) found for K highly different values using flow net computations. Inserting Eq. (3.82) into Eq. (3.81) yields with $r = R_s/R_b$ as the relative curvature of the boundary streamlines

$$V = V_s \exp\left[\frac{N_o}{R_s}\left(r(v-1) + (1-r)\frac{(v^{K+1}-1)}{K+1}\right)\right]. \tag{3.83}$$

Equation (3.83) was originally obtained by Fawer (1937) by neglecting the slope effects, i.e., assuming $N_o \approx t \approx h$. The discharge q across the curved equipotential line between the bottom and free surface lines is, using Eq. (3.49),

$$q = \int_0^{N_o} \frac{\partial \psi}{\partial n} \mathrm{d}n = \int_0^{N_o} V \mathrm{d}n. \tag{3.84}$$

Limitations of this analysis include:

(i) Knowledge of the exponent K, which is routinely assumed as $K = 1$ (Matthew 1963; Hager and Hutter 1984a; Hager 1985a). This restricts the analysis to shallow-water flows, with weakly curved streamlines, as demonstrated by Fawer (1937) and

(ii) Analytical simplifications when integrating Eq. (3.83). No general primitive function is available, so that the exponential function in Eq. (3.83) is developed into a Taylor series, resulting at order one in (Castro-Orgaz et al. 2008a, b, c; Castro-Orgaz 2010b)

$$q = \int_0^{N_o} V \mathrm{d}n \approx N_o V_s \left(1 - \frac{N_o}{R_s}\left(\frac{r}{2} + \frac{1-r}{K+2}\right)\right). \tag{3.85}$$

Matthew (1963) and Hager and Hutter (1984a) proposed this same representation for $K = 1$, from which

$$q = N_o V_s \left(1 - \frac{N_o}{R_s}\left(\frac{r+2}{6}\right)\right). \tag{3.86}$$

Hager (1985a) suggested an empirical approach to improve Eq. (3.86) by assuming that it represents the first-order term of the series development of the more general relation

$$q = N_o V_s \exp\left(-\frac{N_o}{R_s}\left(\frac{r+2}{6}\right)\right). \tag{3.87}$$

However, Eq. (3.87) is equally limited to $K = 1$. Castro-Orgaz et al. (2008c), therefore, implemented this idea in Eq. (3.85) by accounting for $K \neq 1$, namely

$$q = N_o V_s \exp\left(-\frac{N_o}{R_s}\left(\frac{r}{2} + \frac{1-r}{K+2}\right)\right). \tag{3.88}$$

Equation (3.88) is a valid approximation for highly curved open-channel flows, as was demonstrated by Castro-Orgaz (2010b). However, for computations, an empirical function for K is still required, so that the determination of a predictor is detailed in the next sections.

3.4.2 Extended Equations

Extended Boussinesq-type equations for H and S are now developed. At the free surface, Eq. (3.47) states

$$H = z_b + t + \frac{V_s^2}{2g} = \text{const.} \tag{3.89}$$

To find a mathematically closed extended energy equation from Eq. (3.89), Eq. (3.85) is used as the basic q–V_s relation. Note that the connection between t and N_o is given by

$$t = \int_0^{N_o} \cos\theta \mathrm{d}n. \tag{3.90}$$

Next, the variation of the streamline inclination θ relative to the horizontal is prescribed along the equipotential curve as the general power law

$$\theta = \theta_b + (\theta_s - \theta_b)v^m. \tag{3.91}$$

Experience shows that errors made by assuming $m = 1$ are small (Castro-Orgaz 2010a). Using Eq. (3.91) in Eq. (3.90) and expanding the cosine function in a power series, truncated to order 2, give the flow depth t as

$$t = \int_0^{N_o} \cos\theta \mathrm{d}n \approx N_o \int_0^1 \left(1 - \frac{\theta^2}{2}\right)\mathrm{d}v = N_o\left(1 - \frac{\theta_b^2 + \theta_b\theta_s + \theta_s^2}{6}\right). \tag{3.92}$$

Since the streamline inclination angle is assumed small, one may employ the approximations

$$\theta_b = z_{bx}, \quad \theta_s = z_{bx} + t_x, \tag{3.93}$$

so that Eq. (3.92) becomes

$$\frac{t}{N_o} = 1 - \frac{3z_{bx}^2 + 3z_{bx}t_x + t_x^2}{6}. \tag{3.94}$$

Substituting Eq. (3.94) into Eq. (3.86) to eliminate N_o, and only retaining the first-order terms of a Taylor series expansion of the emerging relation, yields

$$q = tV_s\left(1 + \frac{3z_{bx}^2 + 3z_{bx}t_x + t_x^2}{6} - \frac{t}{R_s}\left(\frac{r}{2} + \frac{1-r}{K+2}\right)\right). \tag{3.95}$$

Further assuming that

$$\frac{1}{R_s} \approx (t_{xx} + z_{bxx}), \quad \frac{1}{R_b} \approx z_{bxx}, \tag{3.96}$$

one finds

$$r = \frac{R_s}{R_b} = \frac{z_{bxx}}{t_{xx} + z_{bxx}}. \tag{3.97}$$

Equation (3.95) then simplifies to

$$q = tV_s\left(1 + \frac{3z_{bx}^2 + 3z_{bx}t_x + t_x^2}{6} - \left(\frac{tz_{bxx}}{2} + \frac{tt_{xx}}{K+2}\right)\right). \tag{3.98}$$

As usual in the mathematical developments of Boussinesq's equations, second-order terms are neglected. Equation (3.98) defines V_s versus q, expanded in a Taylor series in the form[2]

$$V_s = \frac{q}{t}\left(1 - \frac{3z_{bx}^2 + 3z_{bx}t_x + t_x^2}{6} + \frac{tt_{xx}}{K+2} + \frac{tz_{bxx}}{2}\right). \tag{3.99}$$

Inserting Eq. (3.99) into Eq. (3.89), and retaining the first-order terms, yields the extended energy equation in the form

$$H = z_b + t + \frac{q^2}{2gt^2}\left(1 + \frac{2tt_{xx}}{K+2} - \frac{t_x^2}{3} + tz_{bxx} - z_{bx}t_x - z_{bx}^2\right). \tag{3.100}$$

A drawback of the second-order Picard iteration equations is that the results are not accurate for high-curvature flow problems in certain cases, including the computation of the discharge coefficient of spillways (Castro-Orgaz et al. 2008a, b, c). To obtain more accurate predictions, third-order results must be considered such as Eq. (3.80) due to Matthew (1991). As noted, the increase of algebraic effort is enormous as compared with the second-order iteration cycle. To overcome these complexities, Boussinesq-type equations in curvilinear natural coordinates as presented in this section are advantageous. In general, $m = 1$ applies, but $K = 1$ is unrealistic for highly curved flows. Equation (3.100) offers a simple tool to model the discharge coefficient of spillway flows by accounting for $K \neq 1$ (Castro-Orgaz et al. 2008a, b, c).

For $K = 1$, Eq. (3.100) reduces to

$$H = z_b + t + \frac{q^2}{2gt^2}\left(1 + \frac{2tt_{xx} - t_x^2}{3} + tz_{bxx} - z_{bx}t_x - z_{bx}^2\right). \tag{3.101}$$

This is the original Boussinesq-type energy equation developed by Matthew (1963). If m in Eq. (3.91) is retained as a general parameter, the result is (Castro-Orgaz 2010a)

$$H = z_b + t + \frac{q^2}{2gt^2}\left(1 + \frac{2tt_{xx}}{K+2} - \frac{t_x^2}{2m+1} + tz_{bxx} - \frac{2z_{bx}t_x}{m+1} - z_{bx}^2\right). \tag{3.102}$$

This Boussinesq-type equation is mathematically valid for weak streamline curvature and small slopes, e.g., $|tt_{xx}|, |tz_{bxx}|, z_{bx}^2, |z_{bx}t_x|$, and $t_x^2 < 0.5$, as stated by Hager and Hutter (1984a). However, consideration of the actual curvature law with

[2]In the processes of the above computations, expressions of the form $(1 + a)^n$ arise, which are approximated as $(1 + na)$ on the basis that $|a| \ll 1$. Another approximation typically used is $\exp(a) = 1 + a$. This is used frequently without explicitly mentioning it.

$K \neq 1$, following Fawer (1937), significantly expands the validity of the model as shown by Castro-Orgaz (2010a).

The specific momentum S, expressed in curvilinear streamline-based coordinates by Hager and Hutter (1984a), is given by

$$S = \int_0^{N_o} \frac{p}{\gamma} \cos\theta \mathrm{d}n + \int_0^{N_o} \frac{V^2}{g} \cos\theta \mathrm{d}n. \tag{3.103}$$

Using Eq. (3.47) to eliminate the pressure, this is written as

$$\begin{aligned} S &= \int_0^{N_o} \left(H - z_b - \eta - \frac{V^2}{2g}\right) \underbrace{\cos\theta \mathrm{d}n}_{=\mathrm{d}\eta} + \int_0^{N_o} \frac{V^2}{g} \cos\theta \mathrm{d}n \\ &= \int_0^{t} (H - z_b - \eta)\mathrm{d}\eta + \int_0^{N_o} \frac{V^2}{2g} \cos\theta \mathrm{d}n = (H - z_b)t - \frac{t^2}{2} + \int_0^{N_o} \frac{V^2}{2g} \cos\theta \mathrm{d}n. \end{aligned} \tag{3.104}$$

To construct the higher order equation of S, the velocity profile $V(n)$ must be inserted into Eq. (3.104). Expanding the exponential function in Eq. (1.83) into power series yields to first order[2]

$$V = V_s \left\{ 1 + \frac{N_o}{R_s} \left(r(v-1) + (1-r) \frac{(v^{K+1} - 1)}{K+1} \right) \right\}. \tag{3.105}$$

This formula allows for the evaluation of the discharge per unit width q as

$$\begin{aligned} q &= \int_0^{N_o} V(n) \mathrm{d}v = N_o \int_0^1 V(n) \mathrm{d}v \\ &= V_s N_o \int_0^1 \left\{ 1 + \frac{N_o}{R_s} \left(r(v-1) + (1-r) \frac{v^{K+1} - 1}{K+1} \right) \right\} \mathrm{d}v \\ &= V_s N_o \left\{ 1 - \frac{N_o}{R_s} \left(\frac{r}{2} + \frac{1-r}{K+2} \right) \right\}. \end{aligned} \tag{3.106}$$

In natural coordinates (s, n) (Fig. 3.4), the vertical water depth h, the vertical distance between the bottom and free surface streamlines t, and the arc length N_o (Fig. 3.6b) are, respectively, given by (Hager and Hutter 1984a)

$$h = -a(\tan\theta_b - \tan\theta_s), \quad t = -R^*(\sin\theta_b - \sin\theta_s), \quad N_o = -R^*(\theta_b - \theta_s), \tag{3.107}$$

assuming that the equipotential lines are circular arcs of radius R^*, with $a = R^*\cos\theta_b$. Therefore, when using second-order approximations (Hager and Hutter 1984a)

$$\begin{aligned}\frac{t}{N_o} &= \frac{\sin\theta_b - \sin\theta_s}{\theta_b - \theta_s} = \frac{\left(\theta_b - \frac{1}{6}\theta_b^2\right) - \left(\theta_s - \frac{1}{6}\theta_s^2\right)}{\theta_b - \theta_s} + \mathrm{O}(3) \\ &= 1 - \frac{\theta_b + \theta_s\theta_b + \theta_s^2}{6} + \mathrm{O}(3),\end{aligned} \tag{3.108}$$

$$\frac{h}{N_o} = \frac{\cos\theta_b(\tan\theta_b - \tan\theta_s)}{\theta_b - \theta_s} = 1 + \frac{2\left(\theta_b\theta_s + \theta_s^2\right) - \theta_b^2}{6} + \mathrm{O}(3). \tag{3.109}$$

Note that from Eq. (3.101) and prescribed boundary conditions at two channel sections, this is a second-order two-point boundary-value problem from which the profile $t = t(x)$ is determined. Physically, this numerical solution is aimed at computing at the x-coordinate of the bottom point of an equipotential line (point "a" in Fig. 3.6a) the vertical distance between this point and the point of this equipotential line at the free surface (point "b" in Fig. 3.6a), t. To plot a free surface profile, therefore, the vertical water depth $h(x)$ at point "a" is needed on the basis of t. Another option is to compute the coordinates of every point "b" on the free surface. Note that the computation of h based on the LHS of Eq. (3.109) is approximate; so is also its expansion on the RHS. Obviously, Eqs. (3.107)–(3.108) imply

$$\frac{t}{h} = \frac{1 - \frac{1}{6}\left(\theta_b^2 + \theta_s\theta_b + \theta_s^2\right)}{1 + \frac{1}{6}\left(2\theta_b\theta_s + 2\theta_s^2 - \theta_b^2\right)} \approx 1 - \frac{1}{2}\left(\theta_s\theta_b + \theta_s^2\right). \tag{3.110}$$

Note that Eq. (3.108) agrees with Eq. (3.92) to the order of expansion used. With the approximations

$$\theta_b \approx z_{bx}, \quad \theta_s \approx z_{bx} + t_x \tag{3.111}$$

Eqs. (3.108) and (3.110) imply, again accurate to second order,

$$\begin{aligned}\frac{t}{N_o} &= 1 - \frac{3z_{bx}^2 + 3z_{bx}t_x + t_x^2}{6} + \mathrm{O}(3), \\ \frac{h}{N_o} &= 1 + \frac{3z_{bx}^2 + 6z_{bx}t_x + 2t_x^2}{6} + \mathrm{O}(3), \\ \frac{t}{h} &= 1 - \frac{2z_{bx}^2 + 3z_{bx}t_x + t_x^2}{2} + \mathrm{O}(3).\end{aligned} \tag{3.112}$$

Solving Eq. (3.95) for V_s yields

$$\begin{aligned} V_s &= \frac{q}{t}\left(1+\frac{3z_{bx}^2+3z_{bx}t_x+t_x^2}{6}-\frac{t}{R_s}\left(\frac{r}{2}+\frac{1-r}{K+2}\right)\right)^{-1} \\ &\approx \frac{q}{t}\left(1-\frac{3z_{bx}^2+3z_{bx}t_x+t_x^2}{6}+\frac{t}{R_s}\left(\frac{r}{2}+\frac{1-r}{K+2}\right)\right), \end{aligned} \tag{3.113}$$

as deduced by Hager and Hutter (1984a) and Montes and Chanson (1998). Inserting this result into Eq. (3.105) permits the elimination of the surface velocity. Retaining first-order terms only, the velocity profile $V(v)$ is found to be after elimination of N_o with Eq. (3.94)

$$V=\frac{q}{t}\left[1-\frac{3z_{bx}^2+3z_{bx}t_x+t_x^2}{6}+\frac{t}{R_s}\left(\frac{r}{2}+\frac{1-r}{K+2}\right)+\frac{t}{R_s}\left(r(v-1)+(1-r)\frac{(v^{K+1}-1)}{K+1}\right)\right]. \tag{3.114}$$

Upon using Eq. (3.97) to eliminate r, this relation transforms to

$$V=\frac{q}{t}\left[1-\frac{3z_{bx}^2+3z_{bx}t_x+t_x^2}{6}+\left(\frac{tz_{bxx}}{2}+\frac{tt_{xx}}{K+2}\right)+tz_{bxx}(v-1)+\frac{tt_{xx}}{K+1}\left(v^{K+1}-1\right)\right]. \tag{3.115}$$

Grouping terms gives

$$V=\frac{q}{t}\left[1-\frac{3z_{bx}^2+3z_{bx}t_x+t_x^2}{6}+tz_{bxx}\left(v-\frac{1}{2}\right)+\frac{tt_{xx}}{K+1}\left(v^{K+1}-\frac{1}{K+2}\right)\right]. \tag{3.116}$$

This velocity profile $V(v)$ applies, with Eq. (3.91) for $\theta(v)$ (m = 1) and Eq. (3.100) for H, to find S from Eq. (3.104). Therefore, the integral of the product $V^2\cos\theta$ is to be computed. The function $\theta(v)$ is from Eqs. (3.91) and (3.93), using m = 1,

$$\theta = z_{bx}+t_x v. \tag{3.117}$$

The function $\cos\theta$ is approximated using Eq. (3.117) as

$$\cos\theta=\left(1-\sin^2\theta\right)^{1/2}\approx 1-\frac{\sin^2\theta}{2}\approx 1-\frac{\theta^2}{2}=1-\frac{(z_{bx}+t_x v)^2}{2}. \tag{3.118}$$

From Eq. (3.116), one produces also the approximate function

$$V^2 \approx \left(\frac{q}{t}\right)^2 \left[1 - \frac{3z_{bx}^2 + 3z_{bx}t_x + t_x^2}{3} + 2tz_{bxx}\left(v - \frac{1}{2}\right) + 2\frac{tt_{xx}}{K+1}\left(v^{K+1} - \frac{1}{K+2}\right)\right]. \tag{3.119}$$

Thus, the product $V^2\cos\theta$ is approximated as

$$\begin{aligned} V^2\cos\theta \approx \left(\frac{q}{t}\right)^2 \Bigg[1 - \frac{3z_{bx}^2 + 3z_{bx}t_x + t_x^2}{3} + 2tz_{bxx}\left(v - \frac{1}{2}\right) \\ + 2\frac{tt_{xx}}{K+1}\left(v^{K+1} - \frac{1}{K+2}\right) - \frac{(z_{bx} + t_x v)^2}{2}\Bigg]. \end{aligned} \tag{3.120}$$

The integral to be determined is then

$$\int_0^{N_o} \frac{V^2}{2g}\cos\theta \mathrm{d}n = \frac{N_o}{2g}\int_0^1 V^2\cos\theta \mathrm{d}v. \tag{3.121}$$

Integrating Eq. (3.120) from the bottom to the free surface yields

$$\begin{aligned} \int_0^1 V^2\cos\theta \mathrm{d}v = \left(\frac{q}{t}\right)^2 \Bigg[1 - \frac{3z_{bx}^2 + 3z_{bx}t_x + t_x^2}{3} - \frac{t_x^2}{6} - \frac{z_{bx}^2}{2} - \frac{z_{bx}t_x}{2} \\ + 2tz_{bxx}\underbrace{\left(\frac{1}{2} - \frac{1}{2}\right)}_{=0} + 2\frac{tt_{xx}}{K+1}\underbrace{\left(\frac{1}{K+2} - \frac{1}{K+2}\right)}_{=0}\Bigg] \\ = \left(\frac{q}{t}\right)^2\left(1 - \frac{3z_{bx}^2 + 3z_{bx}t_x + t_x^2}{2}\right). \end{aligned} \tag{3.122}$$

Using Eq. (3.94), inverted as

$$\frac{N_o}{t} \approx 1 + \frac{3z_{bx}^2 + 3z_{bx}t_x + t_x^2}{6}, \tag{3.123}$$

and inserting Eq. (3.122) into Eq. (3.121), one finds

$$\int_0^{N_o} \frac{V^2}{2g}\cos\theta \mathrm{d}n \approx \frac{N_o}{2g}\left(\frac{q}{t}\right)^2\left(1-\frac{3z_{bx}^2+3z_{bx}t_x+t_x^2}{2}\right)$$
$$\approx \frac{1}{2}\left(\frac{q^2}{gt}\right)\left(1-\frac{3z_{bx}^2+3z_{bx}t_x+t_x^2}{2}+\frac{3z_{bx}^2+3z_{bx}t_x+t_x^2}{6}\right) \quad (3.124)$$
$$= \left(\frac{q^2}{gt}\right)\left(\frac{1}{2}-\frac{3z_{bx}^2+3z_{bx}t_x+t_x^2}{6}\right).$$

Inserting Eqs. (3.124) and (3.100) into Eq. (3.104) leads to the approximate expression

$$S = \frac{t^2}{2}+\frac{q^2}{gt}\left(1+\frac{tt_{xx}}{K+2}-\frac{t_x^2}{3}+\frac{tz_{bxx}}{2}-z_{bx}t_x-z_{bx}^2\right). \quad (3.125)$$

For a Fawer exponent $K = 1$, this reduces to (Hager and Hutter 1984a)

$$S = \frac{t^2}{2}+\frac{q^2}{gt}\left(1+\frac{tt_{xx}-t_x^2}{3}+\frac{tz_{bxx}}{2}-z_{bx}t_x-z_{bx}^2\right). \quad (3.126)$$

If the exponent is $m \neq 1$, the effects of both K and m are included. Castro-Orgaz (2010a) obtained for this case

$$S = \frac{t^2}{2}+\frac{q^2}{gt}\left(1+\frac{tt_{xx}}{K+2}-\frac{t_x^2}{2m+1}+\frac{tz_{bxx}}{2}-\frac{2z_{bx}t_x}{m+1}-z_{bx}^2\right). \quad (3.127)$$

The pressure distribution along the equipotential lines is determined from the conservation of energy in potential flow as

$$H = \frac{p}{\gamma}+z_b+\eta+\frac{V^2}{2g}. \quad (3.128)$$

By using Eqs. (3.100) and (3.119) for H and V^2, respectively, one obtains from Eq. (3.128)

$$\frac{p}{\gamma} = H-z_b-\eta-\frac{V^2}{2g} = t-\eta+\frac{q^2}{2gt^2}\left(1+\frac{2tt_{xx}}{K+2}-\frac{t_x^2}{3}+tz_{bxx}-z_{bx}t_x-z_{bx}^2\right)$$
$$-\frac{q^2}{2gt^2}\left[1-\frac{3z_{bx}^2+3z_{bx}t_x+t_x^2}{3}+2tz_{bxx}\left(v-\frac{1}{2}\right)\right.$$
$$\left.+2\frac{tt_{xx}}{K+1}\left(v^{K+1}-\frac{1}{K+2}\right)\right]$$
$$= t-\eta+\frac{q^2}{2gt^2}\left[2tt_{xx}\left(\frac{1-v^{K+1}}{K+1}\right)+2tz_{bxx}(1-v)\right]. \quad (3.129)$$

To the order of expansion considered, the vertical and curvilinear coordinates along an equipotential line are related by

$$\eta = \int_0^n \cos\theta \mathrm{d}n \approx N_o \int_0^v \left(1 - \frac{[\theta(v)]^2}{2}\right) \mathrm{d}v, \tag{3.130}$$

or using Eq. (3.117) (Hager and Hutter 1984a),

$$\mu = \frac{\eta}{t} = v\left[1 + \frac{z_{bx}t_x}{2}(1-v) + \frac{t_x^2}{6}\left(1-v^2\right)\right], \tag{3.131}$$

and when being inverted (Hager and Hutter 1984a)

$$v = \mu\left[1 - \frac{z_{bx}t_x}{2}(1-\mu) - \frac{t_x^2}{6}\left(1-\mu^2\right)\right]. \tag{3.132}$$

Using Eq. (3.132), the pressure distribution stated in Eq. (3.129) is then expressible as

$$\frac{p}{\gamma} = t - \eta + \frac{q^2}{2gt^2}\left[2tt_{xx}\left(\frac{1-\mu^{K+1}}{K+1}\right) + 2tz_{bxx}(1-\mu)\right], \tag{3.133}$$

where the higher order products have been assumed to be negligible

$$(tt_{xx}) \cdot \left(t_x^2\right) \to 0, \quad (tt_{xx}) \cdot (z_{bx}t_x) \to 0, \quad (tz_{bxx}) \cdot \left(t_x^2\right) \to 0, \quad (tz_{bxx}) \cdot (z_{bx}t_x) \to 0. \tag{3.134}$$

For $K = 1$, the result of Hager and Hutter (1984a) is obtained

$$\frac{p}{\gamma} = t - \eta + \frac{q^2}{2gt^2}\left[tt_{xx}\left(1-\mu^2\right) + 2tz_{bxx}(1-\mu)\right]. \tag{3.135}$$

3.5 Curvilinear Coordinates: Dressler's Theory

3.5.1 Governing Equations for Potential Flow

Dressler (1978) formulated the Euler equations in a Riemann curvilinear system of coordinates, with ξ as the bottom-fitted coordinate and ζ as the coordinate orthogonal to ξ. The continuity equation reads in this case

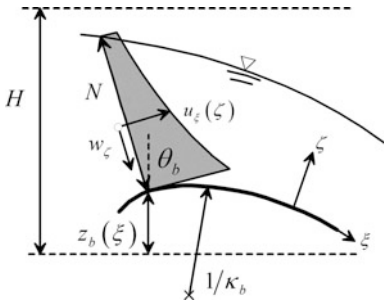

Fig. 3.7 Potential flow over curved bottom profile in curvilinear coordinates following topography

$$\frac{\partial u_\xi}{\partial \xi} + \frac{\partial}{\partial \varsigma}[(1-\kappa_b \varsigma) w_\varsigma] = 0, \tag{3.136}$$

where u_ξ is the physical velocity component in the ξ-direction, $\kappa_b = \kappa_b(\xi)$ the curvature of the bottom profile, and w_ζ the physical velocity component in the ζ-direction (Fig. 3.7).

The irrotational flow condition is then expressed as

$$\frac{\partial w_\varsigma}{\partial \xi} - \frac{\partial}{\partial \varsigma}[(1-\kappa_b \varsigma) u_\xi] = 0, \tag{3.137}$$

and the momentum equations in the ξ- and ζ-directions are, respectively, (Dressler 1978)

$$\frac{u_\xi}{(1-\kappa_b \varsigma)}\frac{u_\xi}{\partial \xi} + w_\varsigma \frac{\partial u_\xi}{\partial \varsigma} - \frac{\kappa_b}{(1-\kappa_b \varsigma)} u_\xi w_\varsigma = -g \sin\theta_b - \frac{1}{\rho(1-\kappa_b \varsigma)}\frac{\partial p}{\partial \xi}, \tag{3.138}$$

$$\frac{u_\xi}{(1-\kappa_b \varsigma)}\frac{w_\varsigma}{\partial \xi} + w_\varsigma \frac{\partial w_\varsigma}{\partial \varsigma} + \frac{\kappa_b}{(1-\kappa_b \varsigma)} u_\xi^2 = -g \cos\theta_b - \frac{1}{\rho}\frac{\partial p}{\partial \varsigma}, \tag{3.139}$$

in which θ_b is the local inclination angle of the bottom profile $z_b(\xi)$ with the horizontal plane.

3.5.2 *Picard Iteration in Curvilinear Coordinates*

Dressler (1978) noted that the use of the Saint-Venant's equations (Saint-Venant 1871) in curved terrain violates kinematic boundary conditions at the free surface and at the terrain surface. Therefore, he emphasized that these equations are valid only for horizontal topography and devised a method to produce improved Saint-Venant-type equations for curved terrain. Dressler then applied the asymptotic stretching method originally developed by Friedrichs (1948) for inviscid and irrotational free surface flows. Asymptotic expansions to the velocity and pressure

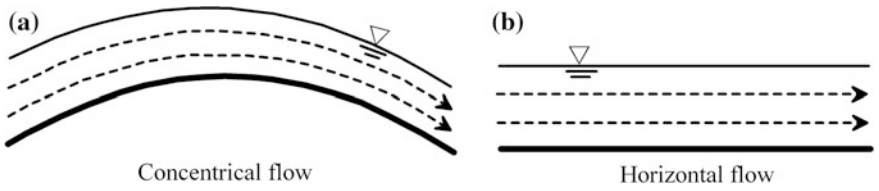

Fig. 3.8 Initial flows of Picard iteration in **a** curvilinear, **b** Cartesian coordinates (adapted from Castro-Orgaz and Hager 2015)

fields were inserted in both the continuity and momentum equations, and the boundary conditions, rendering a system of equations producing a solution to an arbitrary order of expansion in terms of the shallowness parameter. Here, the alternative derivation of Ishiara et al. (1960), Sivakumaran (1981), and Sivakumaran et al. (1981, 1983) is considered, corresponding essentially to a Picard iteration in curvilinear coordinates. First, the irrotational flow condition gives, upon assuming $\partial w_\zeta/\partial\xi = 0$,

$$\frac{\partial}{\partial\varsigma}[(1-\kappa_b\varsigma)u_\xi] = 0. \tag{3.140}$$

After integration, and with $u_{\xi b}$ as the tangential velocity at the bottom level (ζ = 0, Fig. 3.8a), the potential vortex velocity profile is obtained as

$$u_\xi = \frac{u_{\xi b}}{(1-\kappa_b\varsigma)}. \tag{3.141}$$

It is illustrative to compare this step with the germane step of the Picard iteration in Cartesian coordinates. The irrotational flow condition in that system is

$$\frac{\partial w}{\partial x} - \frac{\partial u}{\partial z} = 0. \tag{3.142}$$

Neglecting $|\partial w/\partial x|$ in comparison with $|\partial u/\partial z|$ results in the solution

$$u = U = \text{const.} = \frac{q}{h}. \tag{3.143}$$

This was used as starting velocity profile in Sect. 3.3.1. From a mathematical point of view, this equation expresses uniform flow conditions in a Cartesian system with zero vertical velocity (Fig. 3.8b). This situation is physically possible only over a horizontal bottom. In contrast, the curvilinear counterpart given by Eq. (3.141) indicates "concentric" streamlines to the bottom topography (Fig. 3.8a). Thus, curvilinear coordinates are physically better adjusted to curved bottom problems, given the inclusion of centripetal effects at the lowest order of the Picard iteration. Therefore, to the same order of the Picard iteration, the curvilinear coordinate

formulation is expected to yield improved results from a physical viewpoint than the Cartesian formulation.

In the second step of the iteration cycle, the continuity equation is integrated as

$$\int \frac{\partial u_\xi}{\partial \xi} \mathrm{d}\varsigma + \int \frac{\partial}{\partial \varsigma} [(1 - \kappa_b \varsigma) w_\varsigma] \mathrm{d}\varsigma + g(\xi) = 0. \tag{3.144}$$

Using Eq. (3.141) to evaluate $\partial u_\xi / \partial \xi$, the first approximation to the velocity profile is, after integration of Eq. (3.144) with $g(\xi) = 0$ to satisfy the bottom kinematic boundary condition, $w_\varsigma(\varsigma = 0) = 0$ (Castro-Orgaz and Hager 2016)

$$w_\varsigma = \frac{\ln(1 - \kappa_b \varsigma)}{\kappa_b (1 - \kappa_b \varsigma)} \frac{\partial u_{\xi b}}{\partial \xi} - \frac{1}{\kappa_b^2} \frac{\partial \kappa_b}{\partial \xi} \left[\frac{\ln(1 - \kappa_b \varsigma)}{(1 - \kappa_b \varsigma)} + \frac{\kappa_b \varsigma}{(1 - \kappa_b \varsigma)^2} \right] u_{\xi b}. \tag{3.145}$$

The same result is obtained in the first cycle of a Picard iteration (Appendix C). For a constant curvature (circular) surface, one obtains

$$w_\varsigma = \frac{\ln(1 - \kappa_b \varsigma)}{\kappa_b (1 - \kappa_b \varsigma)} \frac{\partial u_{\xi b}}{\partial \xi}. \tag{3.146}$$

The discharge across a section, owing to Eq. (3.141), is

$$q = \left(\int u_\xi \mathrm{d}\varsigma \right)_{\varsigma = N} = -\frac{u_{\xi b}}{\kappa_b} \ln(1 - \kappa_b N). \tag{3.147}$$

The distance from the channel bottom to the free surface is N, measured orthogonally outward from the bottom curve. Using Eq. (3.147) to compute $\partial u_{\xi b} / \partial \xi$, Eq. (3.146) is rewritten as

$$w_\varsigma = u_\xi \frac{\ln(1 - \kappa_b \varsigma)}{(1 - \kappa_b \varsigma)} \frac{1}{[\ln(1 - \kappa_b N)]} \frac{\partial N}{\partial \xi}. \tag{3.148}$$

Note that the velocity profile is not linear at this iteration step, as in Cartesian coordinates. This equation gives the correct boundary conditions at $\varsigma = 0$, $w_\varsigma = 0$, and at $\varsigma = N$

$$w_\varsigma(\varsigma = N) = u_\xi(\varsigma = N) \frac{1}{(1 - \kappa_b N)} \frac{\partial N}{\partial \xi}. \tag{3.149}$$

The iteration sequence is now clearly established and can be performed to any order. This is essentially a Picard iteration, in which the Cauchy–Riemann equations are formulated as (Castro-Orgaz and Hager 2016)

$$u_\xi = -\frac{1}{(1-\kappa_b\varsigma)}\frac{\partial\phi}{\partial\xi} = -\frac{\partial\psi}{\partial\varsigma}, \quad w_\varsigma = -\frac{\partial\phi}{\partial\varsigma} = +\frac{1}{(1-\kappa_b\varsigma)}\frac{\partial\psi}{\partial\xi}. \tag{3.150}$$

A second cycle of Picard iteration applies for $u_\xi^{(2)}$, obtained by integrating Eq. (3.136)

$$u_\xi^{(2)} = \frac{f(\xi)}{(1-\kappa_b\varsigma)} + \frac{1}{(1-\kappa_b\varsigma)}\int \frac{\partial w_\varsigma^{(1)}}{\partial\xi}\mathrm{d}\varsigma. \tag{3.151}$$

where f is an integration function. The result is

$$u_\xi^{(2)} = u_\xi^{(1)}\left[1 - \frac{\Omega}{2}\left[\frac{1}{3} - \frac{(\ln(1-\kappa_b\varsigma))^2}{(\ln(1-\kappa_b N))^2}\right]\right], \tag{3.152}$$

with

$$\Omega = -\frac{N_{\xi\xi}}{\kappa_b}\frac{\ln(1-\kappa_b N)}{(1-\kappa_b N)} - \frac{N_\xi^2[2+\ln(1-\kappa_b N)]}{(1-\kappa_b N)^2}. \tag{3.153}$$

The use of the Cauchy–Riemann equations (3.150) to obtain Eq. (3.152) is detailed in Appendix C, given that the procedure is tedious.

3.5.3 *Dressler's Theory*

The energy equation of the free surface streamline is

$$H = z_b + N\cos\theta_b + \frac{u_\xi^2 + w_\varsigma^2}{2g} = \text{const.} \tag{3.154}$$

Neglecting the velocity normal to the channel bottom gives

$$H = z_b + N\cos\theta_b + \frac{u_\xi^2}{2g}. \tag{3.155}$$

Using Eq. (3.141), which is the first-order approximation for $u_\xi^{(1)}$, and Eq. (3.147), one finds its value at $\varsigma = N$

$$u_\xi(\varsigma = N) = \frac{-q\kappa_b}{\ln(1-\kappa_b N)(1-\kappa_b N)}. \tag{3.156}$$

If it is inserted into Eq. (3.155), one obtains with E as the specific energy head (Sivakumaran et al. 1981, 1983)

$$H = z_b + N\cos\theta_b + \frac{q^2}{2gN^2}\left[\frac{\kappa_b N}{(1-\kappa_b N)\ln(1-\kappa_b N)}\right]^2 = z_b + E = \text{const.} \quad (3.157)$$

This was originally proposed by Bakhmeteff (1932) using the free vortex velocity profile without any justification. Hager (2010) compared Eq. (3.157) with Eq. (3.101) for weakly curved open-channel flows. Equation (3.157) is numerically solved at every position ξ to compute the free surface profile $N(\xi)$ for the prescribed value of the total head H, as did Sivakumaran et al. (1983). However, this technique does not permit to locate control sections within the flow field. Thus, Eq. (3.157) is differentiated with respect to ξ to produce

$$\begin{aligned}\frac{\mathrm{d}H}{\mathrm{d}\xi} &= \frac{\mathrm{d}z_b}{\mathrm{d}\xi} + \frac{\mathrm{d}N}{\mathrm{d}\xi}\cos\theta_b - N\sin\theta_b\frac{\mathrm{d}\theta_b}{\mathrm{d}\xi} \\ &+ \frac{q^2}{2g}[(1-\kappa_b N)\ln(1-\kappa_b N)]^{-2}2\kappa_b\frac{\mathrm{d}\kappa_b}{\mathrm{d}\xi} + \frac{q^2\kappa_b^2}{2g}[-2(1-\kappa_b N)\ln(1-\kappa_b N)]^{-3} \\ &\cdot\left[\ln(1-\kappa_b N)\left(-N\frac{\mathrm{d}\kappa_b}{\mathrm{d}\xi} - \kappa_b\frac{\mathrm{d}N}{\mathrm{d}\xi}\right) + (1-\kappa_b N)\frac{1}{(1-\kappa_b N)}\left(-N\frac{\mathrm{d}\kappa_b}{\mathrm{d}\xi} - \kappa_b\frac{\mathrm{d}N}{\mathrm{d}\xi}\right)\right] = 0.\end{aligned} \quad (3.158)$$

Using in Eq. (3.158) the differential definitions

$$\frac{\mathrm{d}z_b}{\mathrm{d}\xi} = \sin\theta_b, \quad \kappa_b = \frac{\mathrm{d}\theta_b}{\mathrm{d}\xi}, \quad (3.159)$$

permits to write an ordinary differential equation (ODE) for flow over curved beds (Sivakumaran and Yevjevich 1987; Fenton 1996; Castro-Orgaz and Hager 2016) after rearrangement as

$$\frac{\mathrm{d}N}{\mathrm{d}\xi} = \frac{-\sin\theta_b(1-\kappa_b N) - \frac{q^2}{g}\kappa_b\frac{\mathrm{d}\kappa_b}{\mathrm{d}\xi}\frac{\ln(1-\kappa_b N)+\kappa_b N}{[(1-\kappa_b N)\ln(1-\kappa_b N)]^3}}{\cos\theta_b + \frac{q^2}{g}\kappa_b^3\frac{\ln(1-\kappa_b N)+1}{[(1-\kappa_b N)\ln(1-\kappa_b N)]^3}} = \frac{\Phi_1(N,\xi)}{\Phi_2(N,\xi)}. \quad (3.160)$$

To solve Eq. (3.160), one boundary condition $N_c(\xi_c)$ is needed, corresponding to the flow depth N_c at a prescribed position ξ_c. For transcritical flows passing from sub- to supercritical conditions, the control section is that of minimum specific energy. This is an internal boundary condition, mathematically determined by using the ODE Eq. (3.160). Once N_c and its coordinate of occurrence ξ_c are determined, the flow profile is computed in the up- and downstream directions using Eq. (3.160)

for sub- and supercritical conditions, respectively, by any suitable numerical method to solve ODEs. The bottom Cartesian coordinate x_b is related to ξ by $\mathrm{d}x_b = \cos\theta_b \mathrm{d}\xi$, and the coordinates of the free surface are then given by $z_s = z_b + N\cos\theta_b$ and $x_s = x_b - N\sin\theta_b$. Computing $\partial z_b/\partial x$ from the bottom profile function, one finds by elementary geometry $\cos\theta_b = \left[1 + (\partial z_b/\partial x)^2\right]^{-1/2}$ and $\sin\theta_b = (\partial z_b/\partial x)\cos\theta_b$. Further, $\kappa_b = \partial^2 z_b/\partial x^2 \left[1 + (\partial z_b/\partial x)^2\right]^{-3/2}$ from which $\mathrm{d}\kappa_b/\mathrm{d}\xi$ follows after differentiation with respect to ξ.

Next, N_c and ξ_c are computed. Critical flow is defined by setting to zero the denominator of Eq. (3.160) (Dressler 1978)

$$\Phi_2(N,\xi) = \cos\theta_b + \frac{q^2}{g}\kappa_b^3 \frac{\ln(1-\kappa_b N)+1}{\left[(1-\kappa_b N)\ln(1-\kappa_b N)\right]^3} = 0 \Rightarrow N_c = N_c(\xi). \quad (3.161)$$

This mathematical statement is equivalent to the minimum specific energy condition, obtained by setting $\partial E/\partial N = 0$ in Eq. (3.157). Equation (3.161) defines the critical depth N_c at a given position ξ, where $\theta_b(\xi)$ and $\kappa_b(\xi)$ are determined. However, Eq. (3.161) does not provide a condition to fix the value N_c in a prescribed coordinate. Rather, for every position ξ, Eq. (3.161) produces a different value of N_c, so that this relation actually defines a critical depth profile. Consequently, an additional condition is necessary to locate the real position of the control section for the actual flow conditions. This is given by the pseudo-normal flow condition, mathematically defined in the theory of singular points as $\mathrm{d}N/\mathrm{d}\xi = 0$ (Iwasa 1958; Montes 1998). Thus, setting to zero the numerator of Eq. (3.160), one finds the pseudo-normal depth N_N as (Iwasa 1958; Anh and Hosoda 2007)

$$\Phi_1(N,\xi) = -\sin\theta_b(1-\kappa_b N) - \frac{q^2}{g}\kappa_b \frac{\mathrm{d}\kappa_b}{\mathrm{d}\xi} \frac{\ln(1-\kappa_b N)+\kappa_b N}{\left[(1-\kappa_b N)\ln(1-\kappa_b N)\right]^3} = 0 \Rightarrow N_N = N_N(\xi). \quad (3.162)$$

Likewise, Eq. (3.162) defines the pseudo-normal depth profile. Solving simultaneously the system of equations (3.161) and (3.162) results in the flow depth and position of the control section, corresponding mathematically to a singular point where critical and pseudo-normal depth profiles intersect. At the control section, Eq. (3.160) then yields the indeterminate form

$$\frac{\mathrm{d}N}{\mathrm{d}\xi} = \frac{\Phi_1(N,\xi)}{\Phi_2(N,\xi)} = \frac{0}{0}. \quad (3.163)$$

This indeterminateness is generally removed by differentiating Eq. (3.163),

$$\Phi_2 \frac{\mathrm{d}^2 N}{\mathrm{d}\xi^2} + \frac{\mathrm{d}\Phi_2}{\mathrm{d}\xi}\frac{\mathrm{d}N}{\mathrm{d}\xi} = \frac{\mathrm{d}\Phi_1}{\mathrm{d}\xi}. \tag{3.164}$$

Using the critical flow condition $\Phi_2 = 0$, Eq. (3.164) yields the free surface slope at the critical point from

$$\frac{\mathrm{d}N}{\mathrm{d}\xi} = \frac{\dfrac{\mathrm{d}\Phi_1}{\mathrm{d}\xi}}{\dfrac{\mathrm{d}\Phi_2}{\mathrm{d}\xi}}, \tag{3.165}$$

or

$$\frac{\mathrm{d}N}{\mathrm{d}\xi} = \frac{\dfrac{\partial\Phi_1}{\partial\xi} + \dfrac{\partial\Phi_1}{\partial N}\dfrac{\mathrm{d}N}{\mathrm{d}\xi}}{\dfrac{\partial\Phi_2}{\partial\xi} + \dfrac{\partial\Phi_2}{\partial N}\dfrac{\mathrm{d}N}{\mathrm{d}\xi}}. \tag{3.166}$$

For the simple but fundamental case of symmetrical bottom form at its extreme ($\mathrm{d}\kappa_b/\mathrm{d}\xi = 0$), Eq. (3.160) reduces at the crest (critical; subscript c) section to

$$\left(\frac{\mathrm{d}N}{\mathrm{d}\xi}\right)_c = \frac{-\sin\theta_b(1-\kappa_b N_c)}{\cos\theta_b + \frac{q^2}{g}\kappa_b^3 \frac{\ln(1-\kappa_b N_c)+1}{[(1-\kappa_b N_c)\ln(1-\kappa_b N_c)]^3}} = \frac{\Phi_1(N,\xi)_c}{\Phi_2(N,\xi)_c}. \tag{3.167}$$

Additionally, $\sin\theta_b = 0$ and $\cos\theta_b = 1$ at the crest, corresponding to a control section. Thus, using Eq. (3.161) yields the critical depth N_c from

$$\frac{q^2\kappa_b^3}{g} = -\frac{[(1-\kappa_b N_c)\ln(1-\kappa_b N_c)]^3}{\ln(1-\kappa_b N_c)+1}. \tag{3.168}$$

From Eq. (3.167), the following derivatives are obtained for Φ_1 at the critical point

$$\begin{aligned}
\left(\frac{\partial\Phi_1}{\partial\xi}\right)_c &= \left[\frac{\partial}{\partial\xi}\{-\sin\theta_b(1-\kappa_b N)\}\right]_c \\
&= \left[\left\{-\underbrace{\cos\theta_b}_{=1}\frac{\partial\theta_b}{\partial\xi}(1-\kappa_b N)\right\} - \underbrace{\sin\theta_b}_{=0}\left\{-\frac{\partial\kappa_b}{\partial\xi}N - \frac{\partial N}{\partial\xi}\kappa_b\right\}\right]_c = -\kappa_b(1-\kappa_b N_c), \\
\left(\frac{\partial\Phi_1}{\partial N}\right)_c &= \left[\frac{\partial}{\partial N}\{-\sin\theta_b(1-\kappa_b N)\}\right]_c = \underbrace{-\sin\theta_b}_{=0}\left[\frac{\partial}{\partial N}(1-\kappa_b N)\right]_c = 0,
\end{aligned} \tag{3.169}$$

and for Φ_2

$$\left(\frac{\partial\Phi_2}{\partial\xi}\right)_c = \frac{\partial}{\partial\xi}\left\{\cos\theta_b + \frac{q^2}{g}\kappa_b^3\frac{\ln(1-\kappa_b N_c)+1}{[(1-\kappa_b N_c)\ln(1-\kappa_b N_c)]^3}\right\} = -\underbrace{\sin\theta_b}_{=0}\frac{\partial\theta_b}{\partial\xi}$$
$$+\frac{q^2}{g}\frac{\ln(1-\kappa_b N_c)+1}{[(1-\kappa_b N_c)\ln(1-\kappa_b N_c)]^3}3\kappa_b^2\underbrace{\frac{\partial\kappa_b}{\partial\xi}}_{=0}$$
$$+\frac{q^2}{g}\kappa_b^3\frac{\partial}{\partial\xi}\underbrace{\left\{\frac{\ln(1-\kappa_b N_c)+1}{[(1-\kappa_b N_c)\ln(1-\kappa_b N_c)]^3}\right\}}_{=0,\ \text{given that}\ \frac{\partial\kappa_b}{\partial\xi}=0} = 0,$$

$$\left(\frac{\partial\Phi_2}{\partial N}\right)_c = \frac{\partial}{\partial N}\left\{\cos\theta_b + \frac{q^2}{g}\kappa_b^3\frac{\ln(1-\kappa_b N_c)+1}{[(1-\kappa_b N_c)\ln(1-\kappa_b N_c)]^3}\right\}$$
$$= -3\frac{q^2\kappa_b^4}{g}\frac{\frac{1}{3}\ln(1-\kappa_b N_c) - 1 - [\ln(1-\kappa_b N_c)]^2 - 2\ln(1-\kappa_b N_c)}{[(1-\kappa_b N_c)\ln(1-\kappa_b N_c)]^4}$$
$$= 3\frac{q^2\kappa_b^4}{g}\frac{[\ln(1-\kappa_b N_c)+(5/6)]^2+(11/36)}{[(1-\kappa_b N_c)\ln(1-\kappa_b N_c)]^4}, \tag{3.170}$$

subject to the crest conditions

$$\sin\theta_b = 0, \quad \frac{\mathrm{d}\kappa_b}{\mathrm{d}\xi} = 0. \tag{3.171}$$

Equation (3.166) then yields for the surface gradient at the critical point with the negative sign as the physically correct option for weir flow (Castro-Orgaz and Hager 2016)

$$\frac{\mathrm{d}N}{\mathrm{d}\xi} = \frac{\dfrac{\partial\Phi_1}{\partial\xi} + \dfrac{\partial\Phi_1}{\partial N}\dfrac{\mathrm{d}N}{\mathrm{d}\xi}}{\dfrac{\partial\Phi_2}{\partial\xi} + \dfrac{\partial\Phi_2}{\partial N}\dfrac{\mathrm{d}N}{\mathrm{d}\xi}} = \frac{\dfrac{\partial\Phi_1}{\partial\xi}}{\dfrac{\partial\Phi_2}{\partial N}\dfrac{\mathrm{d}N}{\mathrm{d}\xi}} \quad \Rightarrow \quad \left(\frac{\mathrm{d}N}{\mathrm{d}\xi}\right)_c = -\frac{\left(\dfrac{\partial\Phi_1}{\partial\xi}\right)_c^{1/2}}{\left(\dfrac{\partial\Phi_2}{\partial N}\right)_c^{1/2}}. \tag{3.172}$$

The value of H for prescribed discharge q is computed by evaluating the minimum specific energy E_c at the bottom profile extreme by resorting to Eq. (3.157); incorporating it into Eq. (3.168) and noting that the equation is valid for $N = N_c$, one finds

$$E_c = N_c\left[1 - \frac{1}{2}\frac{(1-\kappa_b N_c)\ln(1-\kappa_b N_c)}{\kappa_b N_c[\ln(1-\kappa_b N_c)+1]}\right]. \tag{3.173}$$

3.5.4 Second-Order Dressler-Type Model

The exact energy equation at the free surface couples Eqs. (3.149) and (3.154) to produce

$$H = z_b + N\cos\theta_b + \frac{u_\xi^2}{2g}\left(1 + \frac{N_\xi^2}{(1-\kappa_b N)^2}\right). \tag{3.174}$$

No approximations are invoked in Eq. (3.174). Therefore, the model accuracy is dictated by the order of expansion of u_ξ. The second-order predictor of u_ξ at the free surface is according to Eq. (3.152) given by

$$u_\xi^{(2)} = u_\xi^{(1)}\left(1 + \frac{\Omega}{3}\right). \tag{3.175}$$

Inserting this result into Eq. (3.174), with Ω given by Eq. (3.153), yields upon the use of Eq. (3.156)

$$H = z_b + N\cos\theta_b + \frac{q^2}{2gN^2}\left[\frac{\kappa_b N}{(1-\kappa_b N)\ln(1-\kappa_b N)}\right]^2\left(1 + \frac{N_\xi^2}{(1-\kappa_b N)^2}\right)\left(1 - \frac{N_{\xi\xi}}{3\kappa_b}\frac{\ln(1-\kappa_b N)}{(1-\kappa_b N)} - \frac{N_\xi^2[2+\ln(1-\kappa_b N)]}{3(1-\kappa_b N)^2}\right)^2. \tag{3.176}$$

This is an extended energy equation for non-hydrostatic flows over curved bottoms in curvilinear coordinates, called here an extended Dressler-type equation. It accounts for bottom curvature effects by the term $\kappa_b N$ as well as for flow depth variations given by N_ξ^2 and $N_{\xi\xi}$. Neither the Saint-Venant equations nor their generalization by Dressler admits wavelike solutions under steady flow. By comparing Eqs. (3.176) and (3.157), note the generalization of the latter as compared to the former, given the inclusion of the terms N_ξ^2 and $N_{\xi\xi}$. These are responsible for the existence of cnoidal type waves (Benjamin and Lighthill 1954; Hager and Hutter 1984b). Given that w is accounted for in Eq. (3.176), streamlines are no longer concentric as in Dressler's (1978) theory. Note that Boussinesq (1877) developed an approximate momentum model in (ξ, ς) coordinates where w was accounted for as well. However, Christoffel symbols were not added to express the Euler equations in the curvilinear orthogonal coordinates. In contrast, Eq. (3.176) originates from a rigorous consideration of the Riemannian metric.

Equation (3.176) is complicated, and the role of the different terms $\kappa_b N$, N_ξ^2, and $N_{\xi\xi}$ is not clearly stated. Thus, Taylor series expansions are used to simplify the model; first,[3] the bottom curvature term is expanded as

$$\left[\frac{\kappa_b N}{(1-\kappa_b N)\ln(1-\kappa_b N)}\right]^2 \approx \left[\frac{1}{(1-\kappa_b N)\left(1+\frac{\kappa_b N}{2}\right)}\right]^2 \approx (1+2\kappa_b N)(1-\kappa_b N) \approx (1+\kappa_b N). \tag{3.177}$$

Second, the free surface streamline inclination effect, originating from the kinematic surface boundary condition, is expanded as

$$1+\frac{N_\xi^2}{(1-\kappa_b N)^2} \approx 1+N_\xi^2(1+2\kappa_b N) \approx 1+N_\xi^2, \tag{3.178}$$

where the condition that second-order Boussinesq-type products are negligible, that is,

$$N_\xi^2 \cdot (\kappa_b N) \approx 0, \tag{3.179}$$

has been implemented. This condition is important and sets a mathematical limit for the validity of the Boussinesq-type approximation used.

Next, the contribution originating from Ω is expanded as

$$\begin{aligned}&\left(1-\frac{N_{\xi\xi}}{3\kappa_b}\frac{\ln(1-\kappa_b N)}{(1-\kappa_b N)}-\frac{N_\xi^2[2+\ln(1-\kappa_b N)]}{3(1-\kappa_b N)^2}\right)^2 \\ &\quad\approx \left(1-\frac{N_{\xi\xi}}{3\kappa_b}\frac{-\kappa_b N\left(1+\frac{\kappa_b N}{2}\right)}{(1-\kappa_b N)}-\frac{N_\xi^2\left[2-\kappa_b N\left(1+\frac{\kappa_b N}{2}\right)\right]}{3(1-\kappa_b N)^2}\right)^2 \\ &\quad\approx \left(1+\frac{NN_{\xi\xi}}{3}-\frac{2N_\xi^2}{3}\right)^2 \approx \left(1+\frac{2NN_{\xi\xi}}{3}-\frac{4N_\xi^2}{3}\right),\end{aligned} \tag{3.180}$$

thereby ignoring the second-order Boussinesq-type products such as

$$N_\xi^2 \cdot (\kappa_b N) \approx 0, \quad NN_{\xi\xi} \cdot (\kappa_b N) \approx 0. \tag{3.181}$$

[3]The expansion $\ln(1-a) = -a - a^2/2 - a^3/3 - \ldots \approx -a(1+a/2)$ is used on the basis that $|a| \ll 1$.

Inserting Eqs. (3.177), (3.178), and (3.180) into Eq. (3.176) produces,

$$H = z_b + N\cos\theta_b + \frac{q^2}{2gN^2}(1+\kappa_b N)\left(1+N_\xi^2\right)\left(1+\frac{2NN_{\xi\xi}}{3}-\frac{4N_\xi^2}{3}\right), \quad (3.182)$$

or by ignoring higher order terms

$$H = z_b + N\cos\theta_b + \frac{q^2}{2gN^2}\left(1+\frac{2NN_{\xi\xi}-N_\xi^2}{3}+\kappa_b N\right). \quad (3.183)$$

This is a cnoidal type extended energy equation generalizing the Benjamin and Lighthill (1954) equation to uneven beds. This equation describes cnoidal waves and bores in horizontal channels. Their theory is embedded in Eq. (3.183) and regained for the flat (κ_b = 0) and horizontal (θ_b = 0) topography as

$$H = N + \frac{q^2}{2gN^2}\left(1+\frac{2NN_{\xi\xi}-N_\xi^2}{3}\right). \quad (3.184)$$

Hager (2010) expanded Eq. (3.157) into a Taylor series as

$$H = z_b + N\cos\theta_b + \frac{q^2}{2gN^2}(1+\kappa_b N). \quad (3.185)$$

This is a particular case for concentric streamlines ($N_\xi^2 = N_{\xi\xi} = 0$) of the general Eq. (3.184), regarded as the cnoidal wavelike second-order equation of the Dressler theory.

3.6 Critical Flow Conditions in Curved Streamline Flows

3.6.1 Critical Irrotational Flows

The problem of critical irrotational flows in open-channel hydraulics is fundamental, given its outstanding role resulting in a unique head-discharge relation used for water discharge measurement structures and allowing for the computation of free surface profiles up- and downstream from the critical point. At the critical point, the streamline curvature and slope are generally significant, so that the velocity distribution is non-uniform and the pressure distribution non-hydrostatic (Hager 1985b; Chanson 2006). These effects must be taken into account to obtain an accurate prediction of critical flow conditions. Consider open-channel flows with a critical point, e.g., spillway flows (Fig. 3.9); note the equipotential curve at the weir crest and the vertical (h) and projected (t) flow depths there. The specific energy head at the weir crest is denoted by E. At the spillway crest, $dz_b/dx = 0$ and

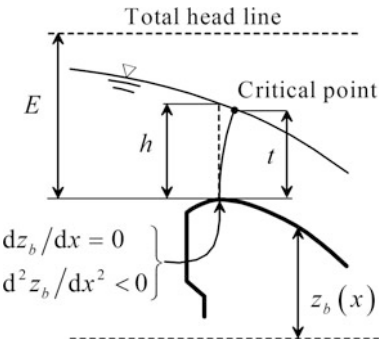

Fig. 3.9 Critical point of irrotational flows over spillways

$d^2z_b/dx^2 < 0$. In potential channel flows, the total energy head H is constant; thus, for all points of the free surface profile (including the weir crest), the energy equation reduces to

$$H = z_b + E = \text{const.} \tag{3.186}$$

Differentiation of Eq. (3.186) with respect to x yields

$$\frac{dH}{dx} = \frac{dE}{dx} + \frac{dz_b}{dx} = \left(\frac{dE}{dt}\right)\left(\frac{dt}{dx}\right) + \frac{dz_b}{dx} = 0. \tag{3.187}$$

From Eq. (3.187), the free surface slope at the spillway crest is

$$\frac{dt}{dx} = -\frac{\left(\frac{dz_b}{dx}\right)}{\left(\frac{dE}{dt}\right)}. \tag{3.188}$$

At the weir crest, $dz_b/dx = 0$, and the flow is passing from sub- to supercritical flow with a finite (negative) free surface slope dt/dx. Therefore, the only physical solution allowing for a transitional flow profile at the weir crest requires the minimum specific energy head condition $dE/dt = 0$ for the actual discharge q. On the basis of this result, the necessary condition for critical flow is a channel bottom extreme given by $dz_b/dx = 0$ (Hager 1985a; Castro-Orgaz et al. 2008a, b, c). This condition fixes the position of the critical flow section at a weir crest. In curved streamline flow, the cross-sectional area is an equipotential curve, which is normal to all streamlines. Thus, the critical flow section is the equipotential, or normal curve, passing through the highest point of the bottom profile (Hager 1985b). The intersection of the equipotential curve with the free surface profile fixes the critical point, with the vertical projection of the normal as the critical flow depth t (Fig. 3.9). In addition to the necessary condition for critical flow, given by the extreme in the channel bottom geometry, a sufficient condition has to be imposed to secure, for a given discharge, a unique relation between the critical depth and the

specific energy. This condition avoids multiple-valued solutions for the specific energy at the weir crest. The sufficient condition for critical flow is $dE/dt = 0$. At the weir crest, there is a singular point of the free surface equation for potential channel flows as

$$\frac{dt}{dx} = -\frac{\left(\frac{dz_b}{dx}\right)}{\left(\frac{dE}{dt}\right)} = \frac{0}{0}. \tag{3.189}$$

This renders the free surface slope finite but indeterminate. Therefore, the critical irrotational flow condition (minimum specific energy) at a spillway crest is equivalent to seek a physical solution where the free surface slope is negative at the critical point.

Critical flow is sometimes defined by using the momentum balance principle (Jaeger 1956). Consider the weir case of Fig. 3.10a involving non-uniform velocity and non-hydrostatic pressure distributions at the crest. At the weir crest, the streamlines are curved and sloped, and the velocity distribution increases from the free surface to the channel bottom. According to the Bernoulli theorem for a streamline, an increase in the velocity head causes a drop in the pressure, which is no longer hydrostatic across the depth. The increase in the velocity causes an increase in discharge for a given head. The figure shows that under critical flow conditions, only a particular streamline has a velocity equal to the water wave

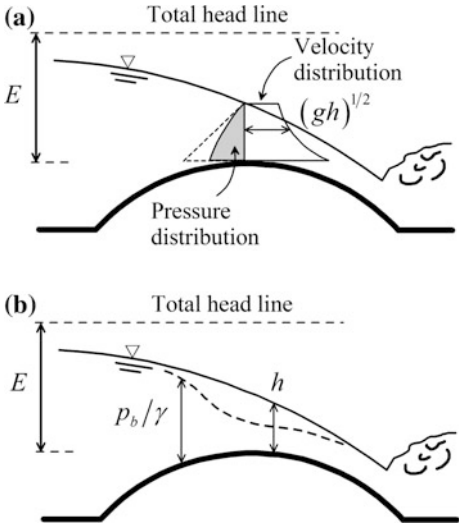

Fig. 3.10 Water wave celerity and minimum specific energy in weir flows: **a** crest velocity and pressure distributions, **b** free surface and bottom pressure head profiles

celerity $(gh)^{1/2}$. As a result, the flow region above the section of minimum specific energy (weir crest) is not isolated from shallow-water waves (Castro-Orgaz and Chanson 2009), highlighting that minimum specific energy considerations are not necessarily in agreement with momentum considerations when defining critical flow conditions. As a result of curved streamlines, the free surface $h(x)$ and the bottom pressure head $p_b/\gamma(x)$ profiles differ (Rouse 1932, 1933) (Fig. 3.10b). A specific advantage of potential flows is the constancy of H; it renders the energy principle advantageous to compute critical flow with curved streamlines. Therefore, this approach is used in the next sections.

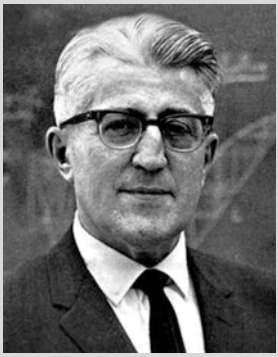

Hunter Rouse was born on March 29, 1906, at Toledo, OH, and he passed away on October 16, 1996, at Sun City, AZ. Educated at the Massachusetts Institute of Technology (MIT), he was a traveling hydraulics fellow receiving in 1933 the Dr.-Ing. title from the Technische Universität Karlsruhe, Germany. He was the instructor then at Columbia University, New York, until 1936, and assistant professor of fluid mechanics at California Institute of Technology, Pasadena, CA, until 1939, when taking over as professor of fluid mechanics at State University of Iowa, Iowa City, IA. From 1944 until his retirement in 1966, he also was the director of the Iowa Institute of Hydraulic Research (IIHR). Rouse was in the 1950s visiting professor to the University of Grenoble, France, among many other similar positions.

Rouse was a man whose name is synonymous with excellence in fluids engineering education, research, and application. His influence on fluids engineering was remarkable, and it continues through his many milestones, still relevant publications, films, and the score of engineers who received advanced degrees under his supervision. He authored a number of successful books in hydraulic engineering and fluid mechanics, notably his fluid mechanics for hydraulic engineers (1938). The book on the history of hydraulics in collaboration with Simon Ince is the far most cited of Rouse's books. Rouse was awarded IAHR honorary membership in 1985. The ASCE Hunter Rouse Annual Lecture was installed in 1979 as an award for distinguished hydraulic engineers. Rouse pursued the application of basic fluid mechanics principles to curvilinear (non-hydrostatic) open-channel flows in his master thesis (1932). He continued with the study of curvilinear free surface flows in his PhD thesis (1933), where he detailed for the first time both theoretically and experimentally the characteristics of the rectangular free overfall under critical approach flow.

3.6.2 Minimum Specific Energy

Consider Eq. (3.70) repeated here for convenience as

$$H = z_b + h + \frac{q^2}{2gh^2}\left(1 + \frac{2hh_{xx} - h_x^2}{3} + hz_{bxx} + z_{bx}^2\right) = \text{const.} \tag{3.190}$$

Based on Eq. (3.186), the computation of $dH/dx = 0$, after imposing $dz_b/dx = 0$ and accepting a physical solution with finite free surface slope, is equivalent to producing the physical statement of the minimum specific energy condition. To regain physical insight into the critical flow condition for irrotational motion with curved streamlines, differentiation of Eq. (3.190) yields

$$\begin{aligned}\frac{dH}{dx} = {} & z_{bx} + h_x - \frac{q^2}{gh^3}h_x\left(1 + \frac{2hh_{xx} - h_x^2}{3} + hz_{bxx} + z_{bx}^2\right) \\ & + \frac{q^2}{2gh^2}\left(\frac{2hh_{xxx}}{3} + hz_{bxxx} + h_x z_{bxx} + 2z_{bx}z_{bxx}\right) = 0.\end{aligned} \tag{3.191}$$

Imposing $dz_b/dx = 0$ in Eq. (3.191) yields, after rearrangement,

$$\frac{q^2}{gh^3}\left(1 + \frac{2hh_{xx} - h_x^2}{3} - \frac{h^2 h_{xxx}}{3h_x} + \frac{hz_{bxx}}{2} - \frac{h^2 z_{bxxx}}{2h_x}\right) = 1. \tag{3.192}$$

This relation is the critical flow condition for curvilinear flows originating from the second-order Picard iteration solution to the potential flow problem; it serves as the mathematical equation to compute the critical depth. Note that in this model, the flow depth is defined vertically, so that the critical flow depth is the vertical flow depth at the crest. Equation (3.192) reveals that for curvilinear flows, the critical flow condition does not depend on the section conditions alone, e.g., the actual value of h, but in addition on the configuration of the flow profile $h = h(x)$ in the vicinity of the critical point and on the local bottom geometry variation $z_b = z_b(x)$. Rouse (1932, 1938) studied curvilinear flows in open channels by using flow nets, thereby highlighting the aspects of the motion including curvilinear streamlines (Fig. 3.11). Note the significant streamline curvature and slope near the spillway crest in Fig. 3.11, as revealed by the added colored tracer. It is elucidating to quote the words by Rouse (1938) on page 326 of his book:

> …Since the ratio of depth to specific energy at the true critical section is so definitely a function of the curvature imposed by the fixed boundaries, it is almost futile to expect that a simple relationship may be found expressing this ratio in terms of boundary geometry. It is to be hoped, nevertheless, that a broader understanding of true critical discharge may soon lead to definite progress in this essential field.

Equation (3.192) reveals this fact; the flow curvature effects imposed by the boundary conditions are included in the critical flow condition. Equation (3.192) is

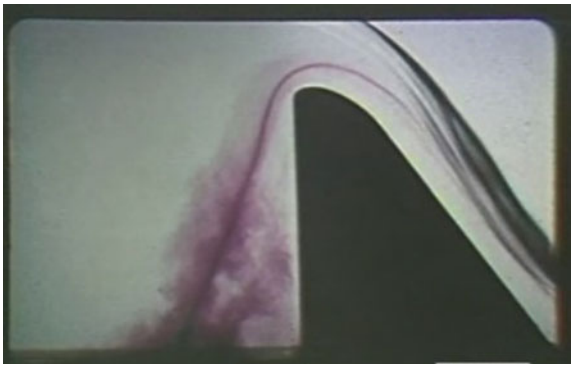

Fig. 3.11 Curvilinear flow over spillway, after Rouse (IIHR movie Fluid motion in a gravitational field)

an approximate solution at the weir crest to the elliptic problem posed by Laplace's equation for irrotational flows. The domain of dependence of an elliptic equation is the entire computational reach, so that the flow condition at a section, like the crest, is determined by the complete solution of the problem. Therefore, it is logical that an approximation to this elliptic problem depends not only on sectional conditions, e.g., the flow depth h, but also on the flow solution in its vicinity, given by the spatial derivatives h_x, h_{xx}, and h_{xxx}. For that reason, consideration of critical flow in 2D motion as given by Laplace's equation results in a mathematical statement for the minimum specific energy that depends not on the sectional conditions, but rather on the flow conditions near the critical point.

It is instructive to study the kind of critical (non-hydrostatic) solutions to be expected from Eq. (3.192). Therefore, the critical depth, the crest bottom pressure head, and the discharge coefficient of spillway flow (Figs. 3.9 and 3.11) are approximated based on this model. At the spillway crest, Eq. (3.190) gives

$$E = h + \frac{q^2}{2gh^2}\left(1 + \frac{2hh_{xx} - h_x^2}{3} + hz_{bxx}\right) = h + \frac{q^2}{2gh^2}(1 + \varepsilon_1), \tag{3.193}$$

where the definition of the small parameter ε_1 is implicitly given in Eq. (3.193). Furthermore, Eq. (3.192) is written as a function of a small parameter ε_2 as

$$\frac{q^2}{gh^3}(1 + \varepsilon_2) = 1. \tag{3.194}$$

The discharge coefficient C_d of spillway flow is defined by Poleni's equation as (Rouse 1938; Montes 1998)

$$q = C_d \left(g E^3\right)^{1/2}. \tag{3.195}$$

Elementary manipulation of Eqs. (3.193)–(3.195) produces

$$C_d = (1+\varepsilon_2)^{-1/2}\left[1+\frac{1}{2}\frac{(1+\varepsilon_1)}{(1+\varepsilon_2)}\right]^{-3/2}. \tag{3.196}$$

Considering that ε_1 and ε_2 are small quantities, an approximation for C_d is developed as follows. The Taylor expansions

$$\begin{aligned}&(1+\varepsilon_2)^{-1/2} \approx \left(1-\frac{\varepsilon_2}{2}\right),\\ &1+\frac{1}{2}\frac{(1+\varepsilon_1)}{(1+\varepsilon_2)} \approx 1+\frac{1}{2}(1+\varepsilon_1)(1-\varepsilon_2) \approx 1+\frac{1}{2}(1+\varepsilon_1-\varepsilon_2) = \frac{3}{2}\left[1+\frac{2}{3}\frac{(\varepsilon_1-\varepsilon_2)}{2}\right],\end{aligned} \tag{3.197}$$

inserted into Eq. (3.196), produce the approximation

$$C_d = \left(\frac{2}{3}\right)^{3/2}\left(1-\frac{\varepsilon_2}{2}\right)\left[1-\frac{(\varepsilon_1-\varepsilon_2)}{2}\right] \approx \left(\frac{2}{3}\right)^{3/2}\left(1-\frac{\varepsilon_1}{2}\right). \tag{3.198}$$

Equations (3.194) and (3.198) give the critical depth h and discharge coefficient C_d once approximations to ε_1 and ε_2 are available. Therefore, approximations to the flow depth derivatives h_x, h_{xx}, and h_{xxx} at the crest (critical) section are needed. Following Matthew (1963) and Hager (1985a), these are determined on the basis of the lower order energy equation for hydrostatic flows

$$H = z_b + h + \frac{q^2}{2gh^2} = \text{const.} \tag{3.199}$$

Differentiation of Eq. (3.199) gives

$$z_{bx} + h_x - \frac{q^2}{gh^3}h_x = 0. \tag{3.200}$$

Setting $\mathrm{d}z_b/\mathrm{d}x = 0$, the critical flow condition for hydrostatic flows requires

$$\frac{q^2}{gh^3} = 1. \tag{3.201}$$

Differentiation of Eq. (3.200) produces

$$z_{bxx} + h_{xx} - \frac{q^2}{gh^3}h_{xx} + 3\frac{q^2}{gh^4}h_x^2 = 0, \tag{3.202}$$

from which, using Eq. (3.201),

$$h_x^2 = -\frac{hz_{bxx}}{3}. \tag{3.203}$$

Note that for a physical solution at the spillway crest (saddle-type singular point), the constraint $d^2z_b/dx^2 < 0$ is required in Eq. (3.203). Otherwise, imaginary free surface slopes are obtained, forming a nodal type singular point (see, e.g., Montes 1998). Now, Eq. (3.202) is differentiated to obtain a predictor for h_{xx} at the spillway crest, resulting in

$$z_{bxxx} + h_{xxx} - \frac{q^2}{gh^3}h_{xxx} + 3\frac{q^2}{gh^4}h_x h_{xx} - 12\frac{q^2}{gh^5}h_x^3 + 6\frac{q^2}{gh^4}h_x h_{xx} = 0. \tag{3.204}$$

Using Eqs. (3.201)–(3.203), and assuming $z_{bxxx} = 0$, thereby approximating the weir crest geometry by a parabolic shape, reduces Eq. (3.204) to

$$h_{xx} = -\frac{4z_{bxx}}{9}. \tag{3.205}$$

The parameter ε_1 is now determined with Eqs. (3.203) and (3.205) as

$$\varepsilon_1 = \frac{2hh_{xx} - h_x^2}{3} + hz_{bxx} = \frac{2}{3}\left(-\frac{4hz_{bxx}}{9}\right) - \frac{1}{3}\left(-\frac{hz_{bxx}}{3}\right) + hz_{bxx} = \frac{22}{27}hz_{bxx}. \tag{3.206}$$

With $R_b = -1/z_{bxx}$ as the crest radius of curvature ($z_{bx} = 0$), and using the hydrostatic identity for critical flow $h = 2E/3$, the discharge coefficient is, from Eq. (3.198) using Eq. (3.206), obtained as

$$C_d = \left(\frac{2}{3}\right)^{3/2}\left(1 + \frac{22}{81}\frac{E}{R_b}\right). \tag{3.207}$$

Equation (3.207) is due to Matthew (1963) using Eq. (3.101), the extended Boussinesq equation using natural, curvilinear coordinates. Here, it was rederived using the Picard iteration, Eq. (3.70). Note that for negligible streamline curvature, Eq. (3.207) yields

$$\frac{E}{R_b} \to 0 \;\Rightarrow\; C_d \to \left(\frac{2}{3}\right)^{3/2}. \tag{3.208}$$

This is the well-known discharge coefficient of a broad-crested weir under ideal fluid flow conditions (Montes 1998, Chanson 2006). Therefore, streamline curvature effects as given by E/R_b increase the discharge capacity.

To compute the curvilinear critical depth using Eq. (3.194), a predictor of h_{xxx} is needed. To this end, Eq. (3.204) is further differentiated, resulting, after imposing Eq. (3.201),

$$\begin{aligned} & z_{bxxxx} + h_{xxxx} - \frac{q^2}{gh^3} h_{xxxx} + 3\frac{q^2}{gh^4} h_x h_{xxx} + 3\frac{q^2}{gh^4}\left(h_x h_{xxx} + h_{xx}^2\right) \\ & - 12\frac{q^2}{gh^5} h_x^2 h_{xx} - 36\frac{q^2}{gh^5} h_x^2 h_{xx} + 12 \times 5\frac{q^2}{gh^6} h_x^4 + 6\frac{q^2}{gh^4}\left(h_{xx}^2 + h_x h_{xxx}\right) \\ & - 24\frac{q^2}{gh^5} h_x^2 h_{xx} = 0, \\ & \xrightarrow{\frac{q^2}{gh^3} = 1,\ z_{bxxxx} = 0} 12\frac{h_x h_{xxx}}{h} + 9\frac{h_{xx}^2}{h} - 72\frac{h_x^2 h_{xx}}{h^2} + 60\frac{h_x^4}{h^3} = 0. \end{aligned} \tag{3.209}$$

Inserting Eqs. (3.203) and (3.205) into Eq. (3.209) results in the desired identity

$$\frac{h^2 h_{xxx}}{h_x} = -\frac{9}{12}\frac{h^2 h_{xx}^2}{h_x^2} + \frac{72}{12}\frac{h h_{xx}}{h} - \frac{60}{12} h_x^2 = \frac{4}{9} h z_{bxx} - \frac{8}{3} h z_{bxx} + \frac{5}{3} h z_{bxx} = -\frac{5}{9} h z_{bxx}. \tag{3.210}$$

Inserting Eqs. (3.203), (3.205), and (3.210) into Eq. (3.192), assuming $z_{bxxx} = 0$, and using $h = 2E/3$, yields the ratio of the critical (crest) curvilinear depth h, and the critical depth of hydrostatic flow $h_c = (q^2/g)^{1/3}$,

$$\frac{q^2}{gh^3}\left(1 - \frac{E}{3R_b}\right) = 1 \ \Rightarrow\ \frac{h}{h_c} = \left(1 - \frac{E}{3R_b}\right)^{1/3} \approx \left(1 - \frac{E}{9R_b}\right). \tag{3.211}$$

Equation (3.211) reveals analytically the well-known experimental result that the depth at a spillway crest is less than the hydrostatic critical depth h_c (Hager 1991; Montes 1998; Chanson 2006). The bottom pressure head $p_b/(\gamma h_c)$ at the crest is computed from Eq. (3.75) for $z_{bx} = 0$ (weir crest), using Eqs. (3.203) and (3.205) as

$$\begin{aligned} \frac{p_b}{\gamma h_c} &= \frac{h}{h_c} + \left(\frac{h}{h_c}\right)^{-2}\left(h z_{bxx} + \frac{h h_{xx} - h_x^2}{2}\right) \approx \frac{h}{h_c} + \left(\frac{h}{h_c}\right)^{-2}\left[-\frac{h}{R_b} + \frac{1}{2}\left(\frac{4}{9}\frac{h}{R_b} - \frac{1}{3}\frac{h}{R_b}\right)\right] \\ &\approx \left(1 - \frac{E}{9R_b}\right) + \left(1 + \frac{2E}{9R_b}\right)\left(-\frac{34E}{54R_b}\right) \approx 1 - \frac{20E}{27R_b}. \end{aligned} \tag{3.212}$$

Equations (3.207), (3.211), and (3.212) are compared in Tables 3.1, 3.2, and 3.3, respectively, with the experimental data of Blau (1963) on a parabolic weir of $R_b = 0.919$ m at the crest. Note that the predictions are close to observations, demonstrating that the weir crest is a non-hydrostatic critical flow section with

Table 3.1 Discharge coefficient of a parabolic weir of R_b = 0.917 m (Blau 1963)

q (m^2/s) measured	E (m) measured	C_d measured	C_d Eq. (3.207)
0.17	0.205	0.5847	0.577
0.51	0.414	0.6112	0.6107
0.574	0.445	0.6173	0.6157
0.96	0.61	0.643	0.6422
0.975	0.61	0.653	0.6422

Table 3.2 Curvilinear flow depth at crest of a parabolic weir of R_b = 0.917 m (Blau 1963)

q (m^2/s) measured	h (m) measured	h/h_c measured	h/h_c Eq. (3.211)
0.17	0.146	1.016	0.975
0.51	0.291	0.975	0.95
0.574	0.314	0.972	0.946
0.96	0.433	0.956	0.926
0.975	0.446	0.97	0.926

Table 3.3 Bottom pressure head at the crest of a parabolic weir of R_b = 0.917 (Blau 1963)

q (m^2/s) measured	p_b/γ (m) measured	$p_b/(\gamma h_c)$ measured	$p_b/(\gamma h_c)$ Eq. (3.212)
0.17	0.121	0.846	0.834
0.51	0.204	0.684	0.665
0.574	0.212	0.658	0.64
0.96	0.25	0.55	0.507
0.975	0.253	0.551	0.507

curved streamlines. The specific energy at the weir crest to this order of approximation is

$$E = h + \frac{q^2}{2gh^2}\left(1 + \frac{22}{27}hz_{bxx}\right) = h + \frac{q^2}{2gh^2}\left(1 - \frac{44}{81}\frac{E}{R_b}\right). \tag{3.213}$$

Owing to Eqs. (3.193), (3.206), and using $h = 2E/3$, the ratio E/h is

$$\frac{E}{h} = 1 + \frac{1}{2}\left(1 + \frac{22}{27}hz_{bxx}\right) = 1 + \frac{1}{2}\frac{\left(1 - \frac{44}{81}\frac{E}{R_b}\right)}{\left(1 - \frac{E}{3R_b}\right)} \approx 1 + \frac{1}{2}\left(1 - \frac{44}{81}\frac{E}{R_b}\right)\left(1 + \frac{E}{3R_b}\right)$$
$$\approx 1 + \frac{1}{2}\left(1 - \frac{44}{81}\frac{E}{R_b} + \frac{E}{3R_b}\right) = 1 + \frac{1}{2}\left(1 - \frac{17}{81}\frac{E}{R_b}\right). \tag{3.214}$$

Equation (3.214) reveals that the ratio E/h in critical curvilinear flow (Bakhmeteff 1932; Montes 1998) is less than 1.5.

A limitation of the above development is that it applies only for low heads, typically for $E/R_b < 0.5$, if a minimum crest radius R_b (typically larger than 5 cm) is used to avoid scale effects (Matthew 1963; Castro-Orgaz and Hager 2014b). In Blau's experiments reported in Tables 3.1, 3.2 and 3.3, R_b is thus sufficiently large to avoid scale effects. The maximum normalized head for these experiments is $E/R_b = 0.665$, roughly in the validity limit of the theory, which implies a linear variation of streamline curvature ($K = 1$). For illustrative purposes on how to obtain higher order models, the non-hydrostatic critical flow model by Castro-Orgaz et al. (2008c) will be presented, but other approximations for the potential velocity profile also apply. Consider steady, plane potential channel flow over a curved bottom. Then, the velocity distribution along an equipotential curve, or normal, is from Eq. (3.81) when performing the integration using the vertical coordinate z (Hager and Hutter 1984a)

$$V = V_s \exp\left(- \int_z^{t+z_b} \frac{\mathrm{d}z}{R\cos\theta} \right). \tag{3.215}$$

The discharge is then given by

$$q = \int_z^{t+z_b} \frac{V}{\cos\theta}\, \mathrm{d}z. \tag{3.216}$$

To integrate Eq. (3.216), an assumption, similar to that of Fawer (1937), is used, relating the vertical projection of the radius of curvature, and the inclination of the streamlines to their corresponding values at the channel bottom (subscript b) and at the free surface (subscript s)

$$\frac{1}{R\cos\theta} = \frac{1}{R_b\cos\theta_b} + \left(\frac{1}{R_s\cos\theta_s} - \frac{1}{R_b\cos\theta_b} \right) \mu^K, \tag{3.217}$$

$$\tan\theta = \tan\theta_b + (\tan\theta_s - \tan\theta_b)\, \mu^K, \tag{3.218}$$

in which $\mu = (z - z_b)/t$ is the dimensionless vertical coordinate (of points on the equipotential) and K is a curvature parameter. Castro-Orgaz et al. (2008c) employed the relations

$$\begin{aligned} \frac{1}{R_b\cos\theta_b} &\approx z_{bxx}, \quad \frac{1}{R_b\cos\theta_b} \approx (t_{xx} + z_{bxx}), \\ \tan\theta_b &= z_{bx}, \quad \tan\theta_s = (t_x + z_{bx}). \end{aligned} \tag{3.219}$$

Carlos Fawer was born on October 10, 1910, at Neuenegg, BE, and passed away at age 86 on December 23, 1996, at Vevey, VD. He entered in 1928 the Lausanne engineering school—today EPFL—graduating in 1932 as a civil engineer. He then made a journey to England, working in the economic crisis during the early 1930s for the Swiss Railways in Berne. Toward 1934, he was a collaborator of Alfred Stucky (1892–1969) at his private engineering company, eventually starting his PhD thesis at the Hydraulic Laboratory of the Engineering School, submitting the work in 1937. Fawer was unable to continue as a hydraulic engineer, his passion, because of the difficult times even in Switzerland shortly before World War II. He thus moved to Nestlé and stayed there during his entire further professional career, with trips to the USA and Argentina as a specialist for constructions in the dairy industry.
Fawer's name is sometimes confused with that of Henry Favre (1901–1966), having nothing in common, however. Fawer submitted an outstanding thesis relating to the effect of streamline curvature, as was earlier developed by Joseph Boussinesq (1842–1929), yet with a direct application to civil engineering structures. The basis of Fawer's approach was a nonlinear assumption of the streamline curvature variation from the channel bottom to the free surface, which was found to be a significant advance over the linear approach by Boussinesq, who adopted the momentum principle. By assuming constant energy for each streamline (potential flow), Fawer formulated the first Boussinesq-type energy equation. He applied this equation to various flows, including undular hydraulic jumps, gate flow, and flow over round-crested weirs. Fawer was the first who investigated the free surface profile, and velocity and pressure distributions of the undular hydraulic jump. He further deduced a classification of non-hydrostatic free surface profiles over flat channels. For round-crested weirs, Fawer was the first who demonstrated that the critical flow theory can be extended to the computation of non-hydrostatic open-channel flows.

Using Eq. (3.217) for the variation of the vertical projection of the radius of curvature, the velocity distribution along an equipotential is

$$V = V_s \exp\left[-tz_{bxx}\,(1-\mu) - tt_{xx}\,\frac{1-\mu^{K+1}}{K+1}\right]. \tag{3.220}$$

With the streamline inclination given by Eq. (3.218), the inverse of the cosine of the angle θ is

$$\frac{1}{\cos\theta} = \left(1 + \tan^2\theta\right)^{1/2} = \left(1 + z_{bx}^2 + \mu^{2K}\, t_x^2 + 2\, z_{bx}\, t_x\, \mu^K\right)^{1/2}. \tag{3.221}$$

Using Eqs. (3.220) and (3.221) permits the computation of V_s from Eq. (3.216); similar steps to those used to find Eq. (3.101) then yield (Castro-Orgaz et al. 2008c)

$$\begin{aligned} H &= z_b + t + \frac{V_s^2}{2g} \\ &= z_b + t + \frac{q^2}{2gt^2}\left(1 + \frac{2tt_{xx}}{K+2} - \frac{t_x^2}{2K+1} + tz_{bxx} - 2\frac{z_{bx}t_x}{K+1} - z_{bx}^2\right). \end{aligned} \tag{3.222}$$

The term in parentheses may be regarded as the first-order term of a Taylor series expansion of an "exp" function, as proposed by Hager (1985a). Therefore, it is tempting to suggest a more general extended energy equation as

$$H = z_b + t + \frac{q^2}{2gt^2}\exp\left(\frac{2tt_{xx}}{K+2} - \frac{t_x^2}{2K+1} + tz_{bxx} - 2\frac{z_{bx}t_x}{K+1} - z_{bx}^2\right). \tag{3.223}$$

If the exponential is expanded in a power series and $K = 1$ for the slope terms, Eq. (3.101) by Hager and Hutter (1984a) is regained. The extended energy Eq. (3.223) is an improvement of the Fawer (1937), Matthew (1963), and Hager (1985a) approaches. The exponential form of Eq. (3.223) applies to flows with a large streamline curvature that is not accounted for by the Matthew (1963) approach. The model is also applicable in regions where streamline curvature and inclination are far from exhibiting a linear variation. Keeping the discharge q constant, and computing $\mathrm{d}H/\mathrm{d}x = 0$ from Eq. (3.223), leads to

$$\frac{\mathrm{d}H}{\mathrm{d}x} = \frac{\mathrm{d}}{\mathrm{d}x}\left[z_b + t + \frac{q^2}{2gt^2}\exp\left(\frac{2tt_{xx}}{K+2} - \frac{t_x^2}{2K+1} + tz_{bxx} - 2\frac{z_{bx}t_x}{K+1} - z_{bx}^2\right)\right] = 0. \tag{3.224}$$

Developing Eq. (3.224), and setting $\mathrm{d}z_b/\mathrm{d}x = 0$ in the resulting expression, the minimum specific energy condition of the extended energy equation takes the form (Castro-Orgaz et al. 2008c)

$$\begin{aligned} &\frac{q^2}{g\,t^3}\left[1 - \frac{t^2\, t_{xxx}}{(K+2)\, t_x} - \left(\frac{K-1}{(K+2)\,(2K+1)}\right) tt_{xx} - \frac{t^2 z_{bxxx}}{2\, t_x} - \left(\frac{K-1}{K+1}\right)\frac{t\, z_{bxx}}{2}\right] \\ &\quad \times \exp\left[\frac{2tt_{xx}}{K+2} - \frac{t_x^2}{2K+1} + tz_{bxx}\right] = 1\,. \end{aligned} \tag{3.225}$$

This is a higher order critical flow condition for curved channel flows. For the transition from sub- to supercritical flow, establishment of critical flow requires $dz_b/dx = 0$ and $dt/dx \neq 0$; thus, $dE/dt = 0$. Equation (3.225) is rewritten as

$$\mathsf{F}^2 = \lambda \frac{q^2}{g\,t^3} = \lambda \mathsf{F}_o^2 = 1. \tag{3.226}$$

Here, F_o is the Froude number of the parallel streamline flows and λ is a correction coefficient accounting for the effects of streamline curvature and inclination in gravity flow problems, given by

$$\lambda = \left[1 - \frac{t^2\,t_{xxx}}{(K+2)\,t_x} - \left(\frac{K-1}{(K+2)\,(2K+1)}\right) t t_{xx} - \frac{t^2 z_{bxxx}}{2\,t_x} - \left(\frac{K-1}{K+1}\right)\frac{t\,z_{bxx}}{2}\right] \times \exp\left[\frac{2 t t_{xx}}{K+2} - \frac{t_x^2}{2K+1} + t z_{bxx}\right]. \tag{3.227}$$

Therefore, the minimum specific energy condition written as a function of the Froude number F for curvilinear flow is

$$\frac{dE}{dt} = 1 - \mathsf{F}^2 = 0. \tag{3.228}$$

For hydrostatic flows, $\lambda = 1$, $t = h$, and the classical critical flow condition is regained from Eq. (3.225). If a linear variation of streamline curvature and slope is assumed ($K = 1$), Eq. (3.225) reduces to

$$\frac{q^2}{g\,t^3}\left(1 - \frac{t^2\,t_{xxx}}{3\,t_x} - \frac{t^2 z_{bxxx}}{2\,t_x}\right)\exp\left(\frac{2 t t_{xx} - t_x^2}{3} + t z_{bxx}\right) = 1. \tag{3.229}$$

Further, if $z_{bxxx} = 0$ (as for parabolic and circular-crested weirs), and the exponential function is expanded in a power series, Eq. (3.229) reduces, by retaining the first-order terms, to

$$\frac{q^2}{g\,t^3}\left(1 - \frac{t^2\,t_{xxx}}{3\,t_x}\right)\exp\left(\frac{2 t t_{xx} - t_x^2}{3} + t z_{bxx}\right) \approx \frac{q^2}{g\,t^3}\left(1 - \frac{t^2\,t_{xxx}}{3\,t_x}\right)\left(1 + \frac{2 t t_{xx} - t_x^2}{3} + t z_{bxx}\right) \approx \frac{q^2}{g\,t^3}\left(1 + \frac{2 t t_{xx} - t_x^2}{3} + t z_{bxx} - \frac{t^2\,t_{xxx}}{3\,t_x}\right) = 1. \tag{3.230}$$

Equation (3.230) was previously developed by Hager (1985b). Note that Eq. (3.192) is similar but not identical to Eq. (3.230), given the different definitions of the flow depth.

3.6.3 Maximum Discharge

According to the Belanger–Böss theorem [see Jaeger (1956) for the mathematical proof], the minimum specific energy E condition for constant discharge q is mathematically equivalent to the relation that is obtained by the maximization of the discharge keeping the specific energy constant. The maximum discharge condition originates from the seminal work of Fawer (1937), who used a velocity distribution similar to Eq. (3.83) for spillway flows (Fig. 3.12a) and imposed the maximum discharge condition for E fixed to find the critical depth at the spillway crest (Fig. 3.12b).

For a given flow depth, the velocity profile was determined by Fawer using Eq. (3.83), neglecting slope effects, and obtaining curvatures from a flow net sketch (Fig. 3.12a); then, the discharge q was computed by graphical integration of the velocity profile. In this method, the flow depth h (Fig. 3.12b) was progressively increased until reaching the maximum discharge. This approach is presented here but following Jaeger (1956), based on an alternative approximation for the flow net geometry at the weir crest and therefore of the velocity distribution. Assume that the

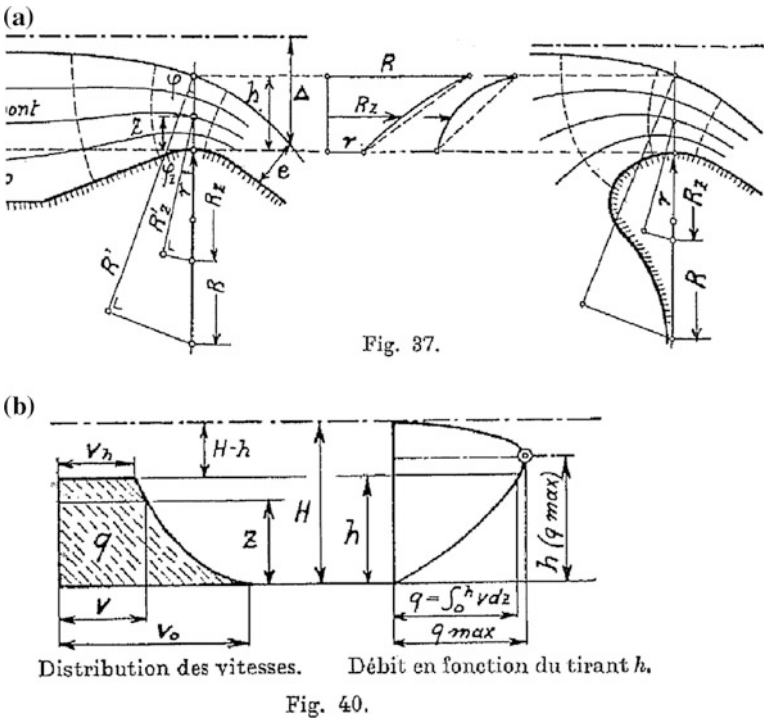

Fig. 3.12 Critical flow at spillway crest after Fawer (1937): **a** flow net, **b** maximum discharge condition with velocity distribution (left) and discharge distribution (right)

radius of streamline curvature along the equipotential crest curve (Fig. 3.9) can be expanded using a Taylor series development about the bed ($n = 0$; subscript b) as

$$R(n) = R_b + \left(\frac{\partial R}{\partial n}\right)_b n + \left(\frac{\partial^2 R}{\partial n^2}\right)_b \frac{n^2}{2} + \cdots. \tag{3.231}$$

Truncation of the series after the linear term gives the approximation to the function $R = R(n)$

$$R(n) \approx R_b + \left(\frac{\partial R}{\partial n}\right)_b n. \tag{3.232}$$

This kind of approximation was pursued by Jaeger (1939, 1956), Montes (1970, 1998), and Castro-Orgaz (2008). A linear variation of R at a weir crest is reasonable based on 2D results by Ramamurthy et al. (1994) and Castro-Orgaz (2010a, 2013a). Generally, Eq. (3.232) diverges from 2D results near the free surface, but it is an excellent approximation otherwise. Thus, the approximation,

$$m_o = \left(\frac{\partial R}{\partial n}\right)_b \approx \frac{(R_s - R_b)}{N_o}, \tag{3.233}$$

is adopted, where the R values at the channel bottom (b) and at the free surface (s) are used. Inserting Eq. (3.233) into Eq. (3.232) produces

$$R = R_b + m_o n = R_b + (R_s - R_b)v, \tag{3.234}$$

which is similar, but not identical, to Jaeger's expression (1956). Inserting Eq. (3.234) into Eq. (3.48) gives

$$\frac{\partial V}{\partial n} = \frac{V}{R_b + m_o n}. \tag{3.235}$$

Integrating between an arbitrary point and the free surface, one finds with V_s as the free surface velocity at the critical point (Fig. 3.9)

$$\ln V_s - \ln V = \frac{1}{m_o}[\ln(R_b + m_o N_o) - \ln(R_b + m_o n)]. \tag{3.236}$$

From Eq. (3.236), the velocity profile along a normal is (Jaeger 1956; Castro-Orgaz 2008)

$$\frac{V}{V_s} = \left[\frac{R_b + m_o n}{R_b + m_o N_o}\right]^{1/m_o} = \left[\frac{1}{r} + \left(1 - \frac{1}{r}\right) v\right]^{1/m_o}. \tag{3.237}$$

Here, $r = R_s/R_b$ is the relative curvature of the boundary streamlines and $R_s = R_b + m_o N_o$. The velocity profile given by Eq. (3.237) is integrated along a normal to obtain unit discharge q as

$$q = \int_0^{N_o} V \, \mathrm{d}n = V_s N_o \int_0^{N_o} \left[\frac{1}{r} + \left(1 - \frac{1}{r}\right) v\right]^{1/m_o} \mathrm{d}v. \tag{3.238}$$

Evaluating the integral gives

$$\begin{aligned} \int_0^{N_o} \left[\frac{1}{r} + \left(1 - \frac{1}{r}\right) v\right]^{1/m_o} \mathrm{d}\, v &= \frac{1}{\left(1 - \frac{1}{r}\right)} \frac{1}{\left(1 + \frac{1}{m_o}\right)} \left\{ \left[\frac{1}{r} + \left(1 - \frac{1}{r}\right) v\right]^{\frac{1}{m_o}+1} \right\}_0^1 \\ &= \frac{r}{(r-1)} \frac{m_o}{(m_o+1)} \left[1 - \left(\frac{1}{r}\right)^{\frac{1}{m_o}+1}\right]. \end{aligned} \tag{3.239}$$

Thus, Eq. (3.238) takes the form

$$q = V_s N_o \frac{r}{(r-1)} \frac{m_o}{(m_o+1)} \left[1 - \left(\frac{1}{r}\right)^{\frac{1}{m_o}+1}\right]. \tag{3.240}$$

The parameter m_o in Eq. (3.234) is rewritten as

$$m_o = \frac{R_s - R_b}{N_o} = \frac{R_b}{N_o}(r-1). \tag{3.241}$$

Inserting Eq. (3.241) into Eq. (3.240) yields

$$q = V_s R_b \frac{r}{(m_o+1)} \left[1 - \left(\frac{1}{r}\right)^{\frac{1}{m_o}+1}\right]. \tag{3.242}$$

With the discharge coefficient C_d of a spillway, defined in Eq. (3.195), that is,

$$q = C_d \left(g E^3\right)^{1/2}, \tag{3.243}$$

and the free streamline velocity at the critical point, given by (Fig. 3.5b)

$$V_s = [2g(E-t)]^{1/2}, \tag{3.244}$$

coupling of Eqs. (3.242), (3.243), and (3.244) yields

$$C_d = \frac{2^{1/2}}{1+m_o}\left(\frac{E}{R_b}\right)^{-1}\left(1-\frac{t}{E}\right)^{1/2} r\left[1-\left(\frac{1}{r}\right)^{1+1/m_o}\right]. \tag{3.245}$$

Here, t is the critical flow depth defined as the vertical projection of the normal at the critical point (Fig. 3.9). For a constant value of the specific energy, the critical depth is obtained by the maximum discharge condition $\partial q/\partial t = 0$ (Montes 1998). Given that both E and R_b have constant values, the critical flow condition is equivalent to the maximum discharge condition (Jaeger 1939)

$$\frac{\partial C_d}{\partial (t/R_b)} = 0. \tag{3.246}$$

Consequently, C_d as given by Eq. (3.245) reaches a maximum for a given value of the specific energy E/R_b corresponding to the critical depth t/R_b. This method is applied in Sects. 3.10 and 3.11 to determine the discharge characteristics of sharp-crested weirs and spillway profiles, respectively. In the parameter m_o, the relative crest curvature r ($z_{bx} = 0$) is given by

$$r = \frac{tz_{bxx}}{tt_{xx} + tz_{bxx}}\left(1+t_x^2\right)^{3/2}. \tag{3.247}$$

3.7 2D Solution of Irrotational Flows: The x-ψ Method

3.7.1 Semi-inverse Mapping

Weirs are structures widely used for water discharge measurements in open channels, in which minimum specific energy or critical flow conditions prevail, as discussed above (Montes 1998; Chanson 2006). Open-channel flows passing from sub- to supercritical flow across a critical point, where the Froude number $\mathsf{F} = 1$ and the specific energy is a minimum, are generally described by inviscid, incompressible, and irrotational flow equations (Rouse 1932, 1938; Jaeger 1956; Vallentine 1969; Hager 1985b; Ramamurthy et al. 1994; Ramamurthy and Vo 1993a, b; Montes 1998; Chanson 2006). The potential flow solutions encompass the determination of the stream and potential functions in any point of the flow domain from which velocity and pressure fields are derived (Rouse 1938; Vallentine 1969). Problem solutions for open-channel flows are especially complex because of the existence of a free surface, which is unspecified in advance (Montes 1998). Flows over round-crested weirs are an important case of open-channel flows with minimum specific energy conditions and curvilinear streamlines (Matthew 1963; Hager 1985b; Montes 1998; Chanson 2006). In the approximate methods

explained above, critical flow conditions were used after assuming the flow geometry in the crest vicinity. The main outcomes are analytical, (approximate) 1D potential flow equations. Limitations of these methods of analysis include specific assumptions about the geometry of the flow, e.g., the variation of the streamline radius of curvature along the crest equipotential curve, and, more importantly, the impossibility to compute the field variables in sections different from the crest. A more general method relies on the full 2D solutions of the potential flow equations. Specific advantages of this method are the lack of assumptions on the potential flow variables and that the solution is determined in the full computational domain. A disadvantage is that 2D numerical computations are needed, given that highlighting analytical solutions is rarely possible.

Early potential open-channel flow models considered problem solutions in the physical plane of Cartesian coordinates (x, z) using the relaxation technique (Southwell and Vaisey 1946; Ganguli and Roy 1952). However, the discretization of Laplace's equation near a curved boundary and the choice of an efficient relaxation pattern are tedious tasks (Thom and Apelt 1961). The solution of Laplace's equation in the physical plane is also considered in the application of both the finite-element method (Dao-Yang and Man-Ling 1979) and the boundary element method (Cheng et al. 1981). An alternative method was discussed by Thom and Apelt (1961), who proposed to transform the role of dependent and independent variables and then solve for the variables (x, z) as functions of (ψ, ϕ), where ψ is the stream function and ϕ is the potential function. This approach was adopted by Cassidy (1965) and Markland (1965) for standard spillway and free overfall problems, respectively. These authors used a finite-difference discretization of Laplace's equation. A pertinent modification of this method was proposed by Boadway (1976) and applied by Montes (1992a, b, 1994a), where the z variable is expressed versus (ψ, x), and only a semi-inverse mapping is used. A characteristic of previous 2D potential flow solutions for weir flows is their focus on free surface and bottom pressure simulations (Cassidy 1965; Cheng et al. 1981; Guo et al. 1998). However, these solutions were not used to analyze the internal flow features of interest, such as vertical velocity, streamline curvature, and streamline inclination. These aspects were analyzed by Castro-Orgaz (2013a, b) given that the vertical variation of these parameters in the crest domain is of engineering interest and forms the basis of approximate 1D potential flow models (Hager and Hutter 1984a, Montes 1998). Boadway's method is appropriate for open-channel flows, given its simplicity as compared to other proposals. The purpose of this section is to apply the model proposed by Boadway (1976) to open-channel flows and weir crest overflows under minimum specific energy. The model applies to the relevant cases of critical flows over a weir, the transitions from mild to steep slopes, and the free overfall (Fawer 1937; Hager 1985b; Ramamurthy et al. 1994; Chanson 2006; Castro-Orgaz 2013a, b; Castro-Orgaz and Hager 2013) as occurring in water discharge measurement structures.

Consider transcritical flow over a round-crested weir (Fig. 3.13a). Laplace's equation in the physical plane states

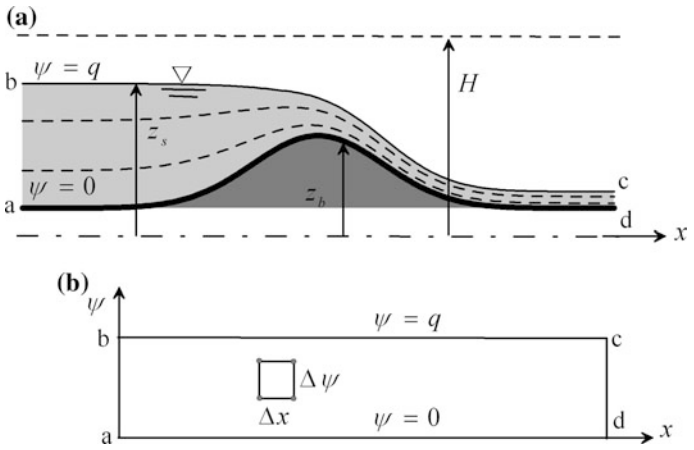

Fig. 3.13 2D potential flow solution in **a** physical plane, **b** x-ψ plane (adapted from Castro-Orgaz 2013a)

$$\nabla^2\psi = \frac{\partial^2\psi}{\partial x^2} + \frac{\partial^2\psi}{\partial z^2} = 0. \tag{3.248}$$

To solve Eq. (3.248) in the (x, z) plane, irregular computational elements near a curved boundary streamline are needed (Thom and Apelt 1961; Vallentine 1969). The alternative method of Thom and Apelt (1961) solves the problem in the plane (ψ, ϕ), where the Laplacians are expressed as

$$\nabla^2 z = \frac{\partial^2 z}{\partial \psi^2} + \frac{\partial^2 z}{\partial \phi^2} = 0, \quad \nabla^2 x = \frac{\partial^2 x}{\partial \psi^2} + \frac{\partial^2 x}{\partial \phi^2} = 0. \tag{3.249}$$

In this plane, the computational domain is a rectangular band requiring no irregular mesh. This mapping was used by Cassidy (1965) and Markland (1965). However, contour integrals are required to iterate for both x and z in their corresponding planes. Boadway (1976) proposed a challenging alternative, especially suitable for open-channel flow. He proposed to solve the Laplacian for z as a function of the pair of variables (ψ, x). The Laplacian of this semi-inverse transformation $z = z(x, \psi)$ is (Boadway 1976)

$$\nabla^2 z = \frac{\partial^2 z}{\partial x^2}\left(\frac{\partial z}{\partial \psi}\right)^2 + \frac{\partial^2 z}{\partial \psi^2}\left[1 + \left(\frac{\partial z}{\partial x}\right)^2\right] - 2\frac{\partial^2 z}{\partial x \partial \psi}\frac{\partial z}{\partial x}\frac{\partial z}{\partial \psi} = 0. \tag{3.250}$$

The derivation of Eq. (3.250) is presented in Appendix D.

Equation (3.250) must be solved subject to suitable boundary conditions. The computation directly yields the equation for each streamline $z = z(x, \psi = \text{const})$, from which velocity and pressure fields of the potential flow ensue. One advantage

of the method is that the flow domain maps into a rectangular strip (Fig. 3.13b) and also that computational efforts are divided into half by considering only ψ. Note that only the function ψ is sought, whereas the function ϕ is no longer considered. In other words, Boadway's mapping achieves to avoid consideration of the entire flow net, because the potential function can be ignored. Note that with the streamline flow pattern, the problem is solved from a hydraulic point of view because the velocity and pressure fields are obtained (Boadway 1976). The problem statement is thus to find the function $z = z(x, \psi)$ instead of both for $x = x(\psi, \phi)$ and $z = z(\psi, \phi)$.

3.7.2 Boundary Conditions at Up- and Downstream Sections

The boundary sections far up- (subscript u) and far downstream (subscript d) are selected where streamlines are parallel to the channel bottom. Under these conditions, the flow depth h for a given energy head H is given, with S_o as the bottom slope, by Montes (1994a)

$$H = z_b + h + \frac{q^2}{2gh^2}\left(1 + S_o^2\right). \tag{3.251}$$

If the section lies at a horizontal channel bottom, there is no slope contribution and Eq. (3.251) reduces to $H = h + q^2/(2gh^2)$. The relation between the stream function ψ and the elevation z in these sections is

$$z = z_b + (z_s - z_b)\frac{\psi}{q}, \tag{3.252}$$

provided ψ is normalized with $\psi = 0$ at $z = z_b$. Equation (3.252) expresses physically that the velocity profile is uniform in the z-direction at the boundary sections.

3.7.3 Free Surface Profile and Energy Head

To start the solution of the Laplace equation (Eq. 3.250), a free surface profile $z_s = z_s(x)$ and energy head H must be prescribed (Fig. 3.13a) for the selected discharge q. Therefore, it is necessary to generate good estimations of the profile $h(x)$ and the energy head H. A simple option is to use Eq. (3.70) obtained using Picard iteration. This equation was presented by Naghdi and Vongsarnpigoon (1986) based on the theory of a Cosserat surface (Green and Naghdi 1976a, b; Naghdi 1979).

3.7.4 Solution of Laplacian Field

The problem statement is the solution of Eq. (3.250) for coordinate z as a function of both x and ψ, once the boundary streamlines $z_s(x)$ and $z_b(x)$, and the relations $z_u = z_u(x_u, \psi)$ and $z_d = z_d(x_d, \psi)$ at boundary sections are prescribed. In the (x, ψ) plane, the computational domain is a rectangular strip where the value of z is known along the entire contour a–b–c–d–a (Fig. 3.13b). Thus, it is not necessary to use an irregular mesh for the flow solution near the curved boundaries, as was done when a solution was directly sought in the physical plane (x, z) (Thom and Apelt 1961; Vallentine 1969). Let i be the node index of the mesh in the x-direction and j that corresponding to the ψ-direction; second-order accurate central discretization of derivatives leads to (Boadway 1976; Montes 1992a, b, 1994a)

$$\frac{\partial z}{\partial x} = \frac{z(i+1,j) - z(i-1,j)}{2\Delta x}, \tag{3.253}$$

$$\frac{\partial z}{\partial \psi} = \frac{z(i,j+1) - z(i,j-1)}{2\Delta \psi}, \tag{3.254}$$

$$\frac{\partial^2 z}{\partial x^2} = \frac{z(i+1,j) - 2z(i,j) + z(i-1,j)}{(\Delta x)^2}, \tag{3.255}$$

$$\frac{\partial^2 z}{\partial \psi^2} = \frac{z(i,j+1) - 2z(i,j) + z(i,j-1)}{(\Delta \psi)^2}, \tag{3.256}$$

$$\frac{\partial^2 z}{\partial x \partial \psi} = \frac{z(i+1,j+1) - z(i-1,j+1) - z(i+1,j-1) + z(i-1,j-1)}{4\Delta x \Delta \psi}. \tag{3.257}$$

Let the auxiliary variables be

$$A = \frac{z(i+1,j) + z(i-1,j)}{(\Delta x)^2} \left(\frac{\partial z}{\partial \psi}\right)^2, \tag{3.258}$$

$$B = \frac{z(i,j+1) + z(i,j-1)}{(\Delta \psi)^2} \left[1 + \left(\frac{\partial z}{\partial x}\right)^2\right], \tag{3.259}$$

$$C = \frac{1}{(\Delta \psi)^2} \left[1 + \left(\frac{\partial z}{\partial x}\right)^2\right] + \frac{1}{(\Delta x)^2} \left(\frac{\partial z}{\partial \psi}\right)^2, \tag{3.260}$$

$$D = 2 \frac{\partial^2 z}{\partial x \partial \psi} \frac{\partial z}{\partial x} \frac{\partial z}{\partial \psi}. \tag{3.261}$$

Substitution of Eqs. (3.253)–(3.261) into Eq. (3.250) leads to an equation for $z(i, j)$ at a generic node inside the mesh as

$$z(i,j) = \left(\frac{A+B-D}{2C}\right). \tag{3.262}$$

Equation (3.262) reveals that $z(i, j)$ is a function of $z(i - 1, j)$, $z(i + 1, j)$, $z(i, j - 1)$, and $z(i, j + 1)$, i.e., the four surrounding mesh points.

It is of interest to recall now the well-known finite-difference approximation to Eq. (3.248), for comparative purposes. Denoting by (i, j) the mesh indexes in the x- and z-directions, the second-order accurate finite differences are defined as

$$\frac{\partial^2\psi}{\partial x^2} = \frac{\psi(i+1,j) - 2\psi(i,j) + \psi(i-1,j)}{(\Delta x)^2}, \tag{3.263}$$

$$\frac{\partial^2\psi}{\partial z^2} = \frac{\psi(i,j+1) - 2\psi(i,j) + \psi(i,j-1)}{(\Delta z)^2}. \tag{3.264}$$

Inserting Eqs. (3.263)–(3.264) into Eq. (3.248), one obtains, for a rectangular mesh in the (x, z) plane $[\Delta x = \Delta z]$ (Thom and Apelt 1961; Vallentine 1969),

$$\psi(i,j) = \frac{\psi(i+1,j) + \psi(i,j+1) + \psi(i,j-1) + \psi(i-1,j)}{4}, \tag{3.265}$$

This is the well-known result expressing that the stream function at a node is an average of the values of this function at the four surrounding points. The solution is known to be iterative, starting with an assumed value of the stream function at all nodes of the computational domain and following with a successive application of Eq. (3.265). Compare now with Eq. (3.262), which indicates that the value of the dependent variable, in this case z, is an average of the values of this function at the four surrounding points. In this case, however, the "average" is defined by a more complex mathematical expression linking the function at a node with the values in its vicinity, given the semi-inverse mapping used to form the field equation.

The process to obtain z at each node is therefore a process of iteration. Thom and Apelt (1961) proposed what they called the "squaring method." Applied to the present equations, this consists of defining inside the mesh initial starting values for $z(i, j)$ and then applying Eq. (3.262) iteratively with G as recursion index as

$$z(i,j)^G = \left(\frac{A+B-D}{2C}\right)^{G-1}. \tag{3.266}$$

For all (i, j) in the computational domain, accordingly, a fresh value of z at any node is obtained from the previous values at the four surrounding points. The solution method is convergent, eliminating the need for a preassumed pattern to reduce

residuals in the Laplace equation. This alternative method is called relaxation technique, and its success depends on the ability of the modeler to reduce the residuals efficiently. To start the iteration using squaring, the values of z inside the mesh are assumed to follow the linear law

$$z(i,j) = z_b(i,0) + [z_s(i,N) - z_b(i,0)]\frac{\psi(i,j)}{q}, \quad \psi(i,j) = j\Delta\psi. \tag{3.267}$$

This is equivalent to assuming that the horizontal velocity profile is uniform in the vertical direction within the entire computational domain, of value $U = q/h$. Repeated application of Eq. (3.266) collocates the streamlines $z = z(x, \psi = \text{const.})$ and, therefore, produces the correct velocity profile at all vertical sections of the mathematical model. The number of streamlines required varies from 10 to 30, depending on the application. The vertical discretization must be successively reduced until no variations in the results occur. The longitudinal discretization is typically of the order of $0.01h_c$, with $h_c = (q^2/g)^{1/3}$. This mathematical model is applied in forthcoming sections to compute flow over free overfalls, transitions from mild to steep slopes, and round-crested weirs.

3.7.5 *Determination of Velocity and Pressure Distributions*

The Cartesian velocity components (u, w) in the directions (x, z) are (Vallentine 1969, Montes 1998)

$$u = \frac{\partial\psi}{\partial z}, \tag{3.268}$$

$$w = u\frac{\partial z}{\partial x}. \tag{3.269}$$

Once the solution for the Laplacian field converges, the values of $z(i, j)$ are known in the entire computational domain. Second-order accurate discretizations of Eqs. (3.268)–(3.269) result in (Boadway 1976; Montes 1994a)

$$u(i,j) = \frac{2\Delta\psi}{z(i,j+1) - z(i,j-1)}, \tag{3.270}$$

$$w(i,j) = u(i,j)\frac{z(i+1,j) - z(i-1,j)}{2\Delta x}, \tag{3.271}$$

from which the velocity fields are easily obtained. Let N be the maximum value of j; at the free surface, the velocity u at boundary streamlines is discretized as (Montes 1994a)

$$u_s = u(i,N) = \frac{2\Delta\psi}{3z(i,N) - 4z(i,N-1) + z(i,N-2)}, \tag{3.272}$$

$$u_b = u(i,0) = \frac{2\Delta\psi}{-3z(i,0) + 4z(i,1) - z(i,2)}. \tag{3.273}$$

Using the condition of energy conservation in potential flow, and once the components (u, w) are computed, the pressure head is given by

$$\frac{p}{\gamma} = H - z - \frac{u^2 + w^2}{2g}. \tag{3.274}$$

3.8 Free Overfall

3.8.1 Picard Iteration

Consider potential flow in a horizontal free overfall with critical flow conditions and hydrostatic pressure distribution upstream of the brink section (Fig. 3.14). The free overfall represents a basic hydraulic structure having attracted numerous experimental and numerical studies in the past 80 years (Mandrup Andersen 1967; Hager 1983; Montes 1992a; Marchi 1993; Khan and Steffler 1996b; Bose and Dey 2007), but it is fair to state that the first rigorous hydraulic analysis of the problem was conducted by Hunter Rouse. Dey (2002) presented a detailed state-of-the-art review. The free overfall results from a sill of zero height, which, under certain conditions, constitutes a flow-measuring device (Rouse 1932, 1933, 1938; Jaeger 1948, 1956; Montes 1992a, 1998; Dey 2002). It is divided into two portions with reference to the brink (subscript b) section: the upstream approach flow and the ventilated free jet (Fig. 3.14).

Matthew (1995) obtained a complete analytical solution for the free overfall problem based on second-order Picard iteration equations by forcing continuity of the free surface slope and the bottom surface slope across the brink section. His development is presented here in detail. The momentum function S is given by Eq. (3.73) as

$$S = \left(H - z_b - \frac{h}{2}\right)h + \int_{z_b}^{h+z_b} \left(\frac{u^2 - w^2}{2g}\right) \mathrm{d}z. \tag{3.275}$$

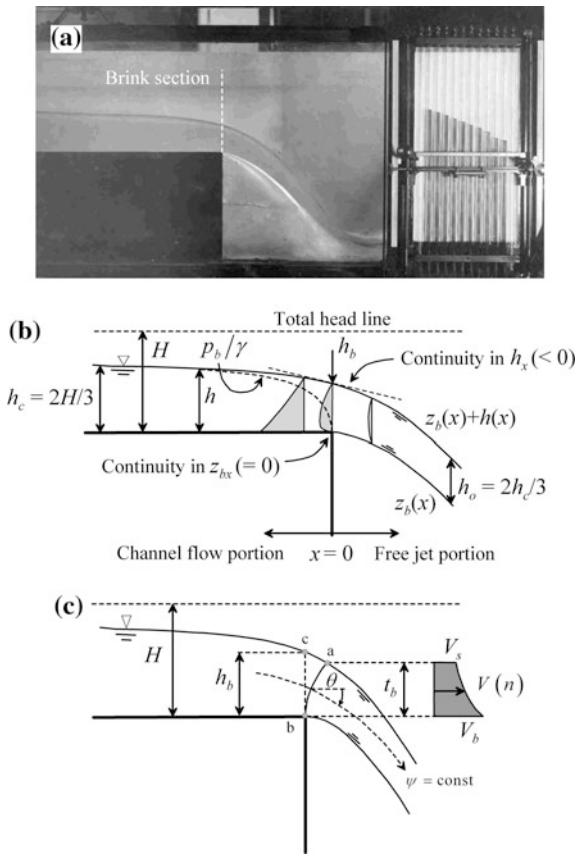

Fig. 3.14 Free overfall with upstream critical flow: **a** laboratory experiment (Rouse 1932), **b** definition sketch for the Picard iteration solution, (c) equipotential line and velocity profile at brink section

The S function is related to the bottom pressure by Eq. (3.19) as

$$\frac{\mathrm{d}S}{\mathrm{d}x} = -\frac{p_b}{\gamma} z_{bx}. \tag{3.276}$$

Along the upstream channel flow portion, $z_{bx} = 0$, and thus, S = const. In the jet flow portion, $p_b = 0$ so that S is equally a constant. As the flow is assumed to be irrotational and thus H = const., this implies that the free overfall is governed by the three invariants already stated by Benjamin and Lighthill (1954) to study cnoidal waves

$$S = \text{const.}, \quad H = \text{const.}, \quad q = \text{const.} \tag{3.277}$$

Inserting Eqs. (3.63) and (3.64) for u and w into Eq. (3.275) gives

$$\begin{aligned} S &= \left(H - z_b - \frac{h}{2}\right)h + \int_{z_b}^{h+z_b} \left(\frac{u^2 - w^2}{2g}\right) \mathrm{d}z \approx \left(H - z_b - \frac{h}{2}\right)h \\ &+ \frac{1}{2g} \int_{z_b}^{h+z_b} \left(\frac{q}{h}\right)^2 \left[1 + 2\left(z_{bxx} - \frac{2h_x z_{bx}}{h}\right)\left(\frac{2\eta - h}{2}\right) + 2\left(\frac{h_{xx}}{2h} - \frac{h_x^2}{h^2}\right)\left(\frac{3\eta^2 - h^2}{3}\right)\right] \mathrm{d}z \\ &- \frac{1}{2g} \int_{z_b}^{h+z_b} \left(\frac{q}{h}\right)^2 \left(z_{bx} + \frac{\eta}{h} h_x\right)^2 \mathrm{d}z \\ &= \left(H - z_b - \frac{h}{2}\right)h + \frac{q^2}{2gh}\left(1 - z_{bx}^2 - h_x z_{bx} - \frac{h_x^2}{3}\right). \end{aligned} \tag{3.278}$$

For critical approach flow ($\mathsf{F} = 1$), the (S, H, q) invariants are (Rouse 1933; Jaeger 1956; Montes 1998)

$$S = \frac{3}{2}h_c^2, \quad H = \frac{3}{2}h_c, \quad q^2 = g h_c^3. \tag{3.279}$$

Inserting Eqs. (3.279) into Eq. (3.278) yields

$$\underbrace{3\left(\frac{h}{h_c}\right)^2 - 3\frac{h}{h_c} - \left(\frac{h}{h_c}\right)^3 - \frac{2h^2 z_b}{h_c^3} + 1 - z_{bx}^2 - h_x z_{bx} - \frac{h_x^2}{3} = 0}_{\text{momentum equation for } \mathsf{F}=1}. \tag{3.280}$$

Equation (3.280) is a form of the momentum equation valid both in the up- and in the downstream portions of the free overfall. Consider first the *upstream channel flow portion*, where $z_b = z_{bx} = z_{bxx} = 0$. Equation (3.280) then simplifies to

$$\underbrace{\frac{h_x^2}{3} = 1 - 3\frac{h}{h_c} + 3\left(\frac{h}{h_c}\right)^2 - \left(\frac{h}{h_c}\right)^3}_{\text{momentum equation of upstream channel flow for } \mathsf{F}=1} = \left(1 - \frac{h}{h_c}\right)^3. \tag{3.281}$$

This equation was previously obtained by Hager (1983) and Marchi (1993) using alternative developments.

Consider now the *free jet portion*, particularly the energy head at the lower nappe[4] (or lower jet surface) of the jet portion. Using Eq. (3.68), evaluated at $\eta = 0$, yields

$$V_b^2(\eta=0) = \frac{q^2}{h^2}\left[1+\left(z_{bxx}-\frac{2h_x z_{bx}}{h}\right)(2\eta-h)+\left(\frac{h_{xx}}{2h}-\frac{h_x^2}{h^2}\right)\left(\frac{6\eta^2-2h^2}{3}\right)\right.$$
$$\left.+z_{bx}^2+2\frac{\eta}{h}z_{bx}h_x+\frac{\eta^2}{h^2}h_x^2\right]_{\eta=0} = \frac{q^2}{h^2}\left(1-\frac{hh_{xx}-2h_x^2}{3}-hz_{bxx}+2h_x z_{bx}+z_{bx}^2\right). \tag{3.282}$$

The energy equation of the lower nappe is, therefore,

$$H = z_b + \underbrace{\frac{p_b}{\rho g}}_{=0} + \frac{V_b^2}{2g} = z_b + \frac{q^2}{2gh^2}\left(1-\frac{hh_{xx}-2h_x^2}{3}-hz_{bxx}+2h_x z_{bx}+z_{bx}^2\right). \tag{3.283}$$

The energy equation of the free surface streamline (upper nappe) of both the channel and the jet portions is given by Eq. (3.70), e.g.,

$$H = z_b + h + \underbrace{\frac{p_s}{\rho g}}_{=0} + \frac{V_s^2}{2g} = z_b + h + \frac{q^2}{2gh^2}\left(1+\frac{2hh_{xx}-h_x^2}{3}+hz_{bxx}+z_{bx}^2\right). \tag{3.284}$$

Adding Eqs. (3.283) and (3.284) and dividing the resulting expression by 2 provides an alternative form of the energy equation of the free jet without the presence of the z_{bxx} term as

$$H = z_b + \frac{h}{2} + \frac{q^2}{2gh^2}\left(1+\frac{hh_{xx}+h_x^2}{6}+h_x z_{bx}+z_{bx}^2\right). \tag{3.285}$$

Imposing the upstream critical flow conditions on Eq. (3.285), as given by Eq. (3.279), results in the energy equation for the free jet portion under critical approach flow

[4]Nappe is a French word used by hydraulic engineers to define the free surface of a jet. Therefore, the free jet is defined by the upper and lower nappe profiles [$z_s = z_s(x)$ and $z_b = z_b(x)$, respectively].

$$\underbrace{-3\left(\frac{h}{h_c}\right)^2+\left(\frac{h}{h_c}\right)^3+\frac{2h^2z_b}{h_c^3}+1+\frac{hh_{xx}}{6}+\frac{h_x^2}{6}+z_{bx}^2+h_xz_{bx}=0}_{\substack{\text{energy equation downstream}\\ \text{free jet flow for } \mathsf{F}=1.}} \tag{3.286}$$

Adding the free jet momentum and energy equations, Eqs. (3.280) and (3.286), eliminates the terms containing z_b, z_{bx}, and z_{bxx}, producing

$$\underbrace{hh_{xx}-h_x^2=6\left(3\frac{h}{h_c}-2\right)}_{\substack{\text{momentum + energy equations of}\\ \text{downstream free jet flow for } \mathsf{F}=1}}. \tag{3.287}$$

An obvious solution of Eq. (3.287) is $h_o = 2h_c/3$, implying $h_{xx} = h_x = 0$. This is the well-known asymptotic jet thickness in a rectangular and ventilated free overfall (Montes 1998). This value is easily regained by formulating a momentum balance between the critical section and the jet section as (Rouse 1932) (Fig. 3.14b)

$$\frac{q^2}{gh_c}+\frac{h_c^2}{2}=\frac{q^2}{gh_o}\Rightarrow\frac{h_o}{h_c}=\frac{\mathsf{F}^2}{\mathsf{F}^2+\frac{1}{2}}=\frac{2}{3}. \tag{3.288}$$

Consider the differential identity

$$\frac{h^3}{2h_x}\frac{\mathrm{d}}{\mathrm{d}x}\left(\frac{h_x^2}{h^2}\right)=hh_{xx}-h_x^2, \tag{3.289}$$

or

$$\frac{h^3}{2}\frac{\mathrm{d}}{\mathrm{d}h}\left(\frac{h_x^2}{h^2}\right)=hh_{xx}-h_x^2. \tag{3.290}$$

Inserting it into Eq. (3.287) yields

$$\frac{h^3}{2}\frac{\mathrm{d}}{\mathrm{d}h}\left(\frac{h_x^2}{h^2}\right)=6\left(3\frac{h}{h_c}-2\right). \tag{3.291}$$

Integration of Eq. (3.291) with respect to h gives with C as an integration constant

$$h_x^2=12-36\frac{h}{h_c}+C\left(\frac{h}{h_c}\right)^2. \tag{3.292}$$

Imposing the boundary condition $h_x \to 0$ as $h \to h_o$ in Eq. (3.292), and $h_o = 2h_c/3$; then, $C = 27$, and thus,

$$h_x^2 = 12 - 36\frac{h}{h_c} + 27\left(\frac{h}{h_c}\right)^2 = 3\left(2 - 3\frac{h}{h_c}\right)^2 . \tag{3.293}$$

Matthew (1995) assumed that there is no discontinuity in slopes at the brink section, neither at the free surface nor at the bottom. Therefore, continuity of the free surface slopes is forced by equating h_x^2 from Eqs. (3.281) and (3.293)

$$h_x^2 = \underbrace{3\left(1 - \frac{h}{h_c}\right)^3}_{\text{channel flow portion}} \equiv \underbrace{3\left(2 - 3\frac{h}{h_c}\right)^2}_{\text{free jet portion}} . \tag{3.294}$$

Of the two roots of Eq. (3.294), $h/h_c = 0.7169$ agrees with the physically observed value of 0.715 (Rouse 1932) and the predicted value 0.714 from 2D potential flow computations (Montes 1992a; Castro-Orgaz 2013b). The continuous slopes at the brink section are, thus,

$$h_x = -\left[3\left(1 - \frac{h}{h_c}\right)^3\right]^{1/2} = -0.261 \ , \quad z_{bx} = 0. \tag{3.295}$$

Return now to the *upstream flow portion* to compute the free surface profile. Equation (3.281) is rewritten as

$$\frac{\mathrm{d}h}{\mathrm{d}x} = -\left[3\left(1 - \frac{h}{h_c}\right)^3\right]^{1/2} , \tag{3.296}$$

or by separation of variables as

$$\mathrm{d}h\left[3\left(1 - \frac{h}{h_c}\right)^3\right]^{-1/2} = -\mathrm{d}x. \tag{3.297}$$

The general solution $h = h(x)$ at a generic position x, with h_b as the brink flow depth at the coordinate origin $x = 0$ (Fig. 3.14b) is (Hager 1983; Marchi 1993)

$$\frac{x}{h_c} = \frac{2}{\sqrt{3}}\left[\left(1 - \frac{h_b}{h_c}\right)^{-1/2} - \left(1 - \frac{h}{h_c}\right)^{-1/2}\right]. \tag{3.298}$$

Elementary manipulation of Eq. (3.298) gives the explicit result

$$\frac{h}{h_c} = \frac{(a^2-1) + 2ab(x/h_c) + b^2(x/h_c)^2}{a^2 + 2ab(x/h_c) + b^2(x/h_c)^2}, \quad a = \left(1 - \frac{h_b}{h_c}\right)^{-1/2}, \quad b = -\frac{\sqrt{3}}{2}. \tag{3.299}$$

Thus,

$$\frac{h}{h_c} = \frac{2.5323 - 3.2553(x/h_c) + 0.75(x/h_c)^2}{3.5323 - 3.2553(x/h_c) + 0.75(x/h_c)^2}, \tag{3.300}$$

reaching the critical flow condition $h = h_c$ for $x \to -\infty$ (Matthew 1995).

The ODE for the free surface profile of the *free jet portion* is given by Eq. (3.294) as

$$h_x = \sqrt{3}\left(2 - 3\frac{h}{h_c}\right). \tag{3.301}$$

Separation of variables gives

$$\frac{\mathrm{d}h}{\left(2 - 3\frac{h}{h_c}\right)} = \sqrt{3}\mathrm{d}x, \tag{3.302}$$

with a general primitive

$$\frac{h}{h_c} = \frac{2}{3} + C\exp\left(-3\sqrt{3}\frac{x}{h_c}\right). \tag{3.303}$$

Using the boundary condition $h(x = 0) = h_b = 0.7169h_c$ results in the integration constant $C = 0.7169 - (2/3) \approx 0.05024$.

George Douglas Matthew was born on April 23, 1931, at Aberdeen, UK, and he passed away there on December 26, 1996. He was educated at Aberdeen University, Aberdeen, UK, obtaining in 1952 the B.Sc. degree in civil engineering. He started his engineering career with Sir Halcrow Consultants, first in London, UK, and then for hydropower developments in Scotland. He returned in 1957 to his Alma Mater, becoming a lecturer below Jack Allen (1905–1984), then professor of hydraulic

engineering. Matthew presented his PhD thesis in 1961 on weir flow, including a fresh mathematical development based on the theory of Joseph V. Boussinesq (1842–1929), and on detailed hydraulic model data. In 1970, Matthew was promoted to Reader at the University of Aberdeen, where he was respected by the students for his excellent teaching activities and his personal relation. He was in addition consulting hydraulic engineer taking both a practical and an aesthetic approach including a fine personal and professional perspective in engineering. Matthew was retired in 1995, but shortly later passed away.
Students loved it when the derivations or proofs would go wrong during a lecture. It meant that he had to depart from the prepared script and "go live." You could see him working and thinking in front of you and just watching this process proved to be entertaining and inspirational. He was remembered for his final lecture during a course in the 1980s, during which he was writing DLTBGYD on the blackboard. Eventually, someone asked him what this meant. He said that this was the most important thing to remember for the examinations. Yes, but what does it mean, was asked, and he replied that it means Don't Let The Buggers Get You Down. He was a member of the Institution of Civil Engineers ICE. His leisure time activities included swimming, badminton, oil painting, aviation history, and dancing. Matthew has written comparably few papers, but many of these contain original and noteworthy ideas. His PhD thesis published in 1963 generalizes the treatment of round-crested weir flow by including the effects of streamline curvature and slope, and the effects of fluid viscosity and surface tension. His approach remained for a long time unnoticed, but from the mid-1970s influenced the further treatment of this classical hydraulic problem. He was the developer of a new technique to produce irrotational, Boussinesq-type equations based on Picard iteration, resulting in an accurate prediction of flow over round-crested weirs and free overfalls. He must be credited for being the first who produced a complete, exact, analytical solution for the free overfall problem based on Boussinesq's equations.

To compute the lower free jet profile, the use is made of the bottom pressure profile function, Eq. (3.75), by imposing $p_b = p(\eta = 0) = 0$, that is,

$$0 = h + \frac{q^2}{2gh^2}\left(2hz_{bxx} + hh_{xx} - h_x^2 - 2z_{bx}h_x\right), \tag{3.304}$$

or

$$2\left(\frac{h}{h_c}\right)^3 + 2hz_{bxx} + hh_{xx} - h_x^2 - 2z_{bx}h_x = 0. \tag{3.305}$$

Inserting Eq. (3.287) for $(hh_{xx} - h_x^2)$ and Eq. (3.301) for h_x yields

$$2\left(\frac{h}{h_c}\right)^3 + 2hz_{bxx} + \underbrace{6\left(3\frac{h}{h_c} - 2\right)}_{=hh_{xx}-h_x^2} - 2z_{bx}\underbrace{\left[\sqrt{3}\left(2 - 3\frac{h}{h_c}\right)\right]}_{=h_x} = 0. \tag{3.306}$$

The following substitutions are introduced, with p as an auxiliary variable,

$$p = z_{bx}, \quad z_{bxx} = p_x = \frac{\mathrm{d}p}{\mathrm{d}h}h_x = \sqrt{3}\left(2 - 3\frac{h}{h_c}\right)p_h. \tag{3.307}$$

This permits to reduce Eq. (3.306) to

$$hp_h - p = \sqrt{3} + \frac{\sqrt{3}}{3[3(h/h_c) - 2]}\left(\frac{h}{h_c}\right)^3. \tag{3.308}$$

Based on the differential identity,

$$hp_h - p = h^2\frac{\mathrm{d}}{\mathrm{d}h}\left(\frac{p}{h}\right), \tag{3.309}$$

Equation (3.308) is rewritten as

$$\frac{\mathrm{d}}{\mathrm{d}h}\left(\frac{p}{h}\right) = \frac{\sqrt{3}}{h^2} + \frac{\sqrt{3}}{3h_c^2[3(h/h_c) - 2]}\left(\frac{h}{h_c}\right). \tag{3.310}$$

Equation (3.310) integrated with respect to h yields

$$\frac{p}{h} = -\frac{\sqrt{3}}{h} + \frac{\sqrt{3}}{3h_c}\int\frac{(h/h_c)}{[3(h/h_c) - 2]}\mathrm{d}(h/h_c) + C. \tag{3.311}$$

The reader can easily deduce that a primitive function of the integral in Eq. (3.311) is

$$\int\frac{(h/h_c)}{[3(h/h_c) - 2]}\mathrm{d}(h/h_c) = \frac{1}{9}\left[\left(3\frac{h}{h_c} - 2\right) + 2\ln\left(3\frac{h}{h_c} - 2\right)\right]. \tag{3.312}$$

Equation (3.311) thus takes with $D/h_c = C$ the form

$$z_{bx} = -\sqrt{3} + \frac{\sqrt{3}}{27}\frac{h}{h_c}\left[\left(3\frac{h}{h_c} - 2\right) + 2\ln\left(3\frac{h}{h_c} - 2\right)\right] + D\frac{h}{h_c}. \tag{3.313}$$

Manipulation of Eq. (3.313) yields

$$z_{bx} = -\sqrt{3} + \left(D - \frac{2\sqrt{3}}{27}\right)\frac{h}{h_c} + \frac{3\sqrt{3}}{27}\left(\frac{h}{h_c}\right)^2 + \frac{\sqrt{3}}{27}\frac{h}{h_c}\left[2\ln\left(3\frac{h}{h_c} - 2\right)\right]. \tag{3.314}$$

Imposing continuity of the bottom free surface slope at $x = 0$, that is, $z_{bx} = 0$ in Eq. (3.314) for $h/h_c = 0.7169$, yields a simple algebraic equation, from which $D = 2.6492$. Inserting this value into Eq. (3.314) yields the final $z_{bx}(h/h_c)$ relation

$$z_{bx} = -\sqrt{3} + 2.5209\left(\frac{h}{h_c}\right) + \frac{\sqrt{3}}{9}\left(\frac{h}{h_c}\right)^2 + \frac{2\sqrt{3}}{27}\left(\frac{h}{h_c}\right)\ln\left(3\frac{h}{h_c} - 2\right). \tag{3.315}$$

The lower nappe profile $z_b(x)$ is computed from this equation by noting the identity

$$z_{bx} = \frac{\mathrm{d}z_b}{\mathrm{d}h}h_x = \sqrt{3}\left(2 - 3\frac{h}{h_c}\right)z_{bh}, \tag{3.316}$$

which allows for the integration of Eq. (3.315) with respect to h, resulting in (Matthew 1995)

$$\frac{z_b}{h_c} = 0.372 - 0.481\left(\frac{h}{h_c}\right) - 0.0185\left(\frac{h}{h_c}\right)^2 + [0.0099 - 0.0247\left(\frac{h}{h_c}\right) - 0.0082 \times \ln\left(3\frac{h}{h_c} - 2\right)\Big]\ln\left(3\frac{h}{h_c} - 2\right). \tag{3.317}$$

Equation (3.317) is expressed in terms of (x/h_c) by resorting to Eq. (3.303), resulting in (Matthew 1995)

$$\frac{z_b}{h_c} = 0.0232 - 0.1271(x/h_c) - 0.2214(x/h_c)^2 - 0.0232\exp\left[-3(3x/h_c)^{1/2}\right] + 0.0064(x/h_c)\exp\left[-3(3x/h_c)^{1/2}\right]. \tag{3.318}$$

The upper free surface profile $z_s(x)$ is determined by adding Eqs. (3.303)–(3.318), resulting in

$$\frac{z_s}{h_c} = 0.6899 - 0.1271(x/h_c) - 0.2214(x/h_c)^2 + 0.027\exp\left[-3(3x/h_c)^{1/2}\right] + 0.0064(x/h_c)\exp\left[-3(3x/h_c)^{1/2}\right]. \tag{3.319}$$

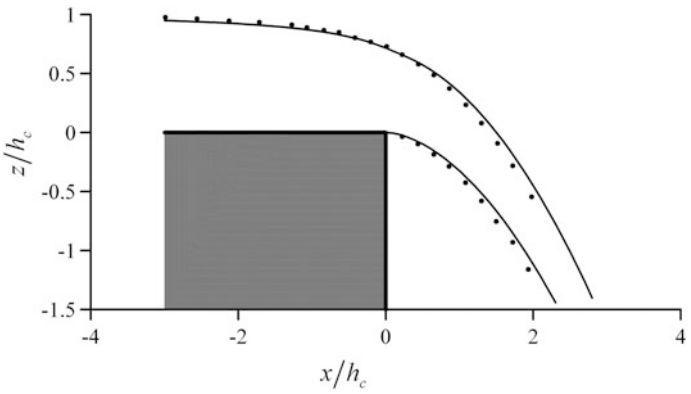

Fig. 3.15 Comparison of Picard iteration solution for free overfall with data of (•) Rouse (1932) (adapted from Castro-Orgaz 2013b)

Equations (3.300), (3.318), and (3.319) are plotted in Fig. 3.15 and compared with the experimental data of Rouse (1932, 1933). The upstream free surface profile is accurately predicted, whereas slight deviations in the jet portion are noted below $z/h_c = -0.5$. The accuracy of the free surface prediction near the brink section is, therefore, excellent. Note that the only assumption of Matthew (1995) to predict the complete analytical solution was to admit discontinuities in the surface and bottom curvatures at the brink section (but not in the slopes). The curvature terms at the brink section are now easily determined to highlight these discontinuities. First, looking to the *jet flow* portion, from Eqs. (3.287) and (3.293)

$$hh_{xx} = h_x^2 + 6\left(3\frac{h}{h_c} - 2\right) = 3\left(2 - 3\frac{h}{h_c}\right)^2 + 6\left(3\frac{h}{h_c} - 2\right) = +0.972, \quad (3.320)$$

with $h_b/h_c = 0.7169$, and from Eq. (3.305), the bottom curvature term at $x = 0$ is

$$hz_{bxx} = -\left(\frac{h}{h_c}\right)^3 - \frac{hh_{xx} - h_x^2}{2} + \underbrace{z_{bx}}_{=0} h_x = -0.820. \quad (3.321)$$

The relative curvature of the free surface is, therefore,

$$hz_{sxx} = hh_{xx} + hz_{bxx} \approx +0.26. \quad (3.322)$$

Obviously, this positive curvature does physically not agree with the convex free surface profile. This is a limitation linked to the degree of expansion used in the analysis.

Consider now the channel flow portion. There, $hz_{bxx} = 0$, from which the bottom curvature term discontinuity is evident. The corresponding free surface curvature term is evaluated by resorting to the energy equation for the upstream free surface profile as [Eq. (3.284) for $z_b = z_{bx} = z_{bxx} = 0$]

$$H = h + \frac{q^2}{2gh^2}\left(1 + \frac{2hh_{xx} - h_x^2}{3}\right). \tag{3.323}$$

The curvature term hh_{xx} at the brink section results from Eq. (3.323) as

$$\begin{aligned} hh_{xx} &= \frac{3}{2}\left\{\left[2\left(\frac{h_b}{h_c}\right)^2\left(\frac{3}{2} - \frac{h_b}{h_c}\right)\right] - 1\right\} + \frac{h_x^2}{2} \\ &= \frac{3}{2}\left\{\left[2\left(\frac{h_b}{h_c}\right)^2\left(\frac{3}{2} - \frac{h_b}{h_c}\right)\right] - 1\right\} + \frac{3}{2}\left(1 - \frac{h_b}{h_c}\right)^3 = -0.258. \end{aligned} \tag{3.324}$$

In Eq. (3.324), the critical flow condition at the upstream section is set equal to $H/h_c = 3/2$. Further, Eq. (3.281) was used to evaluate the slope term as $h_x^2 = 3[(1 - (h_b/h_c)]^3$; then, Eq. (3.324) is evaluated for $h_b/h_c = 0.7169$ (brink depth ratio). The negative sign of this curvature agrees with what is physically expected. However, having admitted curvature discontinuities, velocity and pressure distributions at the brink section depend on which side the second derivative is computed. Marchi (1993) and Matthew (1995) advocated that the correct velocity and pressure distributions are determined based on the equations of the free jet portion and not by the upstream channel flow equations. Thus, they consider the free jet equations, allowing for terms $z_{bx} = \mathrm{d}z_b/\mathrm{d}x$ and $z_{bxx} = \mathrm{d}^2 z_b/\mathrm{d}x^2$ in the pressure distribution, from which the pressure at the lower nappe was set to zero, including the brink section. Montes (1994b) reported the failure of the upstream channel flow equations at the brink section. The failure reason was examined by Castro-Orgaz and Hager (2010) as follows: The free overfall has peculiar free surface and bottom profile features, where both curves separate from each other as the brink section is approached (Fig. 3.14b). Consider Eq. (3.323) originating from Picard iteration for the upstream free surface profile of the free overfall. Note, roughly, that Eq. (3.323) at the brink section assumes a linear variation of streamline curvature in the vertical direction from the channel bottom to the free surface, whereas both Jaeger (1948) and Castro-Orgaz (2010a) obtained $K < 0$ using different arguments from Rouse's (1933) data. Equation (3.323) was integrated numerically using a fourth-order Runge–Kutta method from $x/h_c = -3$ to $x/h_c = 0$ (Serre 1953; Montes 1986) subjected to the boundary condition $h/h_c(x/h_c = -3) = 1$ corresponding to the parallel-streamlined critical approach flow with $\mathsf{F} = 1$. The boundary free surface slope was determined iteratively using a Newton–Raphson algorithm until the downstream boundary condition at the brink section $h/h_c(x/h_c = 0) = 0.715$ was reached. A variation of the shooting section coordinate $x/h_c = -3$ had negligible impact on the results.

As shown in Fig. 3.16, the computational results for $h = h(x)$ are in excellent agreement with the experimental data (Bose and Dey 2007). Note that this potential flow computation is different from the results of Hager (1983), Marchi (1993), and Matthew (1995) because no assumptions regarding the flow conditions at the brink section are invoked. Here, the free surface profile of the upstream flow portion was

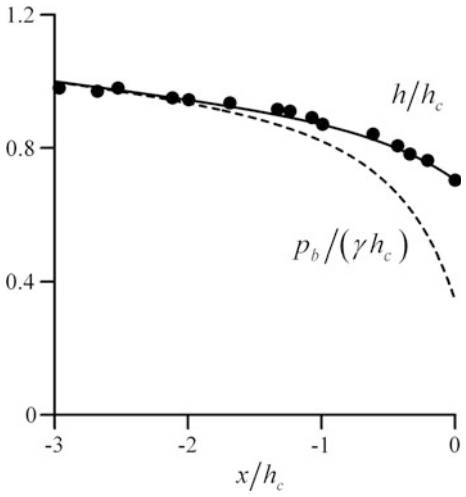

Fig. 3.16 Free surface profile $h/h_c(x/h_c)$ from (—) Eq. (3.323), bottom pressure profile $p_b/(\gamma h_c)(x/h_c)$ from (- - -) Eq. (3.325), data of (•) Bose and Dey (2007) (adapted from Castro-Orgaz and Hager 2010). Brink section is located at $x/h_c = 0$

determined as a two-point boundary-value problem involving the experimental flow depths at the two boundary sections. The present computation is representative of an impartial determination to flow conditions at the brink section. Once the profile $h = h(x)$ is given, the bottom pressure profile results from Eq. (3.75) as

$$\frac{p_b}{\gamma} = h + \frac{q^2}{2gh^2}\left(hh_{xx} - h_x^2\right). \tag{3.325}$$

The bottom pressure at the brink section is $p_b/(\gamma h_c) \approx 0.34 > 0$. Thus, the Picard iteration model results in excellent free surface profile predictions for the channel portion, but the bottom pressure is poorly simulated. This gap is removed by considering a general K value and adding the moment of momentum closure equation for K, as highlighted by Castro-Orgaz and Hager (2010). This is explored in the next section. Despite the limitations of the Boussinesq's equations with $K = 1$ at the brink (discontinuity) section, these equations provide otherwise an excellent solution.

Before developing a more general solution at the brink section using the equations of the upstream channel flow portion, the angular momentum balance is examined from Picard iteration results. The Picard approximations for u, w, and p/γ are from Eqs. (3.63), (3.64), and (3.72) (Matthew 1991; Marchi 1992)

$$u = \frac{q}{h}\left[1 + \left(\frac{h_{xx}}{2h} - \frac{h_x^2}{h^2}\right)\left(\frac{3\eta^2 - h^2}{3}\right)\right], \tag{3.326}$$

$$w = \frac{q}{h}\left(\frac{\eta}{h}h_x\right), \tag{3.327}$$

$$\frac{p}{\gamma} = h - \eta + \frac{q^2}{2gh^2}\left[\left(hh_{xx} - h_x^2\right)\left(1 - \frac{\eta^2}{h^2}\right)\right]. \tag{3.328}$$

The vertical momentum flux M is then, from Eq. (3.24) using Eqs. (3.326)–(3.327),

$$\begin{aligned} M &= \int_{z_b}^{z_b+h} \frac{uw}{g}\mathrm{d}z = \frac{1}{g}\int_0^h \frac{q}{h}\left[1 + \left(\frac{h_{xx}}{2h} - \frac{h_x^2}{h^2}\right)\left(\frac{3\eta^2 - h^2}{3}\right)\right] \times \frac{q}{h}\left(\frac{\eta}{h}h_x\right)\mathrm{d}\eta \\ &\approx \frac{1}{g}\int_0^h \frac{q}{h} \times \frac{q}{h}\left(\frac{\eta}{h}h_x\right)\mathrm{d}\eta = \frac{q^2}{2gh}h_x. \end{aligned} \tag{3.329}$$

The moment of momentum Eq. (3.44) yields the independent equation

$$\frac{\mathrm{d}A}{\mathrm{d}x} = M. \tag{3.330}$$

Using Eqs. (3.329) and (3.330) yields

$$\mathrm{d}A = \frac{q^2}{2gh}h_x\mathrm{d}x. \tag{3.331}$$

Integrating, this yields, with subscript 1 referring to a reference section,

$$A = A_1 + \frac{q^2}{2g}\ln\left(\frac{h}{h_1}\right). \tag{3.332}$$

Consider the definition of A in Eq. (3.42)

$$A = \int_{z_b}^{z_b+h}\left(\frac{u^2}{g} + \frac{p}{\gamma}\right)z\mathrm{d}z = \int_0^h \left(\frac{u^2}{g} + \frac{p}{\gamma}\right)\eta\mathrm{d}\eta. \tag{3.333}$$

Using Eqs. (3.326) and (3.328), the solutions of the integrals are

$$\begin{aligned} \int_0^h \frac{u^2}{g}\eta\mathrm{d}\eta &\approx \int_0^h \left(\frac{q^2}{gh^2}\right)\left[1 + \left(\frac{h_{xx}}{h} - 2\frac{h_x^2}{h^2}\right)\left(\frac{3\eta^2 - h^2}{3}\right)\right]\eta\mathrm{d}\eta \\ &= \left(\frac{q^2}{gh^2}\right)\left[\frac{h^2}{2} + \left(\frac{h_{xx}}{h} - 2\frac{h_x^2}{h^2}\right)\frac{h^4}{12}\right], \end{aligned} \tag{3.334}$$

$$\int_0^h \frac{p}{\gamma}\eta \mathrm{d}\eta = \int_0^h \left[h - \eta + \frac{q^2}{2gh^2}\left(hh_{xx} - h_x^2\right)\left(1 - \frac{\eta^2}{h^2}\right)\right]\eta \mathrm{d}\eta$$
$$= \frac{h^3}{6} + \frac{q^2}{2gh^2}\left(hh_{xx} - h_x^2\right)\frac{h^2}{4}. \tag{3.335}$$

Inserting Eqs. (3.334)–(3.335) into Eq. (3.333) yields

$$A = \int_0^h \left(\frac{u^2}{g} + \frac{p}{\gamma}\right)\eta \mathrm{d}\eta = \left(\frac{q^2}{gh^2}\right)\left[\frac{h^2}{2} + \left(\frac{h_{xx}}{h} - 2\frac{h_x^2}{h^2}\right)\frac{h^4}{12}\right] + \frac{h^3}{6} + \frac{q^2}{2gh^2}\left(hh_{xx} - h_x^2\right)\frac{h^2}{4}$$
$$= \frac{q^2}{2g}\left(1 + \frac{hh_{xx}}{6} - \frac{h_x^2}{3}\right) + \frac{h^3}{6} + \frac{q^2}{2g}\frac{\left(hh_{xx} - h_x^2\right)}{4}$$
$$= \frac{h^3}{6} + \frac{q^2}{2g}\left(1 + \frac{5hh_{xx}}{12} - \frac{7h_x^2}{12}\right). \tag{3.336}$$

Equation (3.332) is rewritten as

$$A - \frac{q^2}{2g}\ln\left(\frac{h}{h_1}\right) = A_1 - \frac{q^2}{2g}\ln\left(\frac{h_1}{h_1}\right). \tag{3.337}$$

Inserting Eq. (3.336) into Eq. (3.332) leads to the moment of momentum equation for the curvilinear flow upstream of the free overfall as (Castro-Orgaz and Hager 2010)

$$\Omega = \frac{h^3}{6} + \frac{q^2}{2g}\left(1 + \frac{5hh_{xx} - 7h_x^2}{12} - \ln\frac{h}{h_1}\right) = \text{const.} \tag{3.338}$$

Here, Ω is defined as the effective angular momentum function. Thus, A is not conserved in curvilinear flow due to the vertical momentum flux contribution, thereby resulting in the effective or conserved angular momentum Ω (Eq. 3.338).

To further investigate the reason of failure of the Picard solution to predict bottom pressure features, as stated in Fig. 3.16, the Ω function and the conservation of angular momentum were investigated. From the computed free surface profile $h = h(x)$, the profile $\Omega = \Omega(x)$ was determined using Eq. (3.338). The results are plotted in Fig. 3.17, showing that the Picard iteration solution of the free surface profile does not satisfy conservation of angular momentum. The higher streamline curvature occurs at the brink section, resulting in the largest deviation of Ω from its upstream value at the critical flow section.

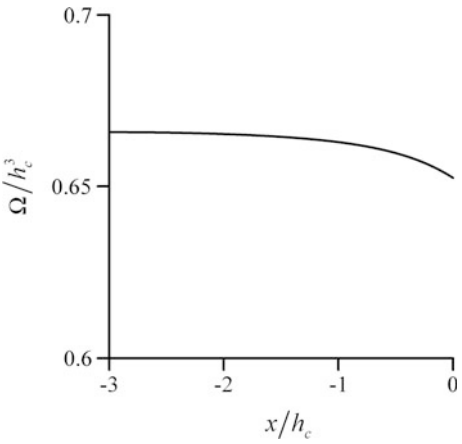

Fig. 3.17 Conservation of angular momentum upstream of free overfall for Picard second-order solution (adapted from Castro-Orgaz and Hager 2010)

3.8.2 Curvilinear Flow at the Brink Section

Recall that the quality of the Picard iteration solution is related to the curvature exponent K introduced in Eq. (3.86). The velocity profile along an equipotential curve is given by Eq. (3.116) as

$$V = \frac{q}{t}\left[1 - \frac{3z_{bx}^2 + 3z_{bx}t_x + t_x^2}{6} + tz_{bxx}\left(v - \frac{1}{2}\right) + \frac{tt_{xx}}{K+1}\left(v^{K+1} - \frac{1}{K+2}\right)\right]. \tag{3.339}$$

To compute the velocity components (u, w) along the equipotential curve, the terms $\sin\theta$ and $\cos\theta$ are, respectively, approximately given by [truncation errors are O(3)]

$$\sin\theta \approx \theta \approx z_{bx} + t_x v, \tag{3.340}$$

$$\cos\theta = \left(1 - \sin^2\theta\right)^{1/2} \approx 1 - \frac{\sin^2\theta}{2} \approx 1 - \frac{(z_{bx} + t_x v)^2}{2}. \tag{3.341}$$

Thus, the velocity components are

$$u = V\cos\theta \approx \left(\frac{q}{t}\right)\left[1 - \frac{3z_{bx}^2 + 3z_{bx}t_x + t_x^2}{6} + tz_{bxx}\left(v - \frac{1}{2}\right) + \frac{tt_{xx}}{K+1}\left(v^{K+1} - \frac{1}{K+2}\right) - \frac{(z_{bx} + t_x v)^2}{2}\right], \tag{3.342}$$

$$w = V\sin\theta \approx \left(\frac{q}{t}\right)\left[1 - \frac{3z_{bx}^2 + 3z_{bx}t_x + t_x^2}{6} + tz_{bxx}\left(v - \frac{1}{2}\right) + \frac{tt_{xx}}{K+1}\left(v^{K+1} - \frac{1}{K+2}\right)\right](z_{bx} + t_x v) \approx \left(\frac{q}{t}\right)(z_{bx} + t_x v). \tag{3.343}$$

To this order of expansion, normalized curvilinear and vertical coordinates are replaced, thus obtaining from Eqs. (3.342) to (3.343)

$$u \approx \left(\frac{q}{t}\right)\left[1 - \frac{3z_{bx}^2 + 3z_{bx}t_x + t_x^2}{6} + tz_{bxx}\left(\mu - \frac{1}{2}\right) + \frac{tt_{xx}}{K+1}\left(\mu^{K+1} - \frac{1}{K+2}\right) - \frac{(z_{bx} + t_x\mu)^2}{2}\right] = \left(\frac{q}{t}\right)\left[1 - z_{bx}^2 - \frac{z_{bx}t_x}{2}(1+2\mu) - \frac{t_x^2}{6}(1+3\mu^2) + \frac{tz_{bxx}}{2}(2\mu - 1) + \frac{tt_{xx}}{K+1}\left(\mu^{K+1} - \frac{1}{K+2}\right)\right], \tag{3.344}$$

$$w \approx \left(\frac{q}{t}\right)(z_{bx} + t_x\mu). \tag{3.345}$$

The u velocity component for $K = 1$ is from Eq. (3.344) (Hager and Hutter 1984a)

$$u = \left(\frac{q}{t}\right)\left[1 - z_{bx}^2 - \frac{z_{bx}t_x}{2}(1+2\mu) - \frac{t_x^2}{6}(1+3\mu^2) + \frac{tz_{bxx}}{2}(2\mu - 1) + \frac{tt_{xx}}{6}(3\mu^2 - 1)\right]. \tag{3.346}$$

For a horizontal bottom, Eq. (3.344) simplifies to (Montes and Chanson 1998)

$$u = \left(\frac{q}{t}\right)\left[1 + \frac{tt_{xx}}{K+1}\left(\mu^{K+1} - \frac{1}{K+2}\right) - \frac{t_x^2}{6}(1+3\mu^2)\right]. \tag{3.347}$$

For $K = 1$, Eq. (3.347) reduces to

$$u = \left(\frac{q}{t}\right)\left[1 + \frac{tt_{xx}}{2}\left(\mu^2 - \frac{1}{3}\right) - \frac{t_x^2}{6}(1+3\mu^2)\right]. \tag{3.348}$$

The u velocity component corresponding to the Picard iteration from Eq. (3.63) reads

$$u = \frac{q}{h}\left[1 + \left(\frac{hh_{xx}}{2} - h_x^2\right)\left(\mu^2 - \frac{1}{3}\right)\right] = \frac{q}{h}\left[1 + \frac{hh_{xx}}{2}\left(\mu^2 - \frac{1}{3}\right) - \frac{h_x^2}{6}(6\mu^2 - 2)\right]. \tag{3.349}$$

Note that the u velocity component given by Eq. (3.348) is given along the coordinates of a equipotential line, whereas Eq. (3.349) refers to points on a vertical. Note, therefore, the difference in the slope term containing t_x and h_x, respectively. To further compare both models, assume, following Fawer (1937), that the slope effects are small as compared with the curvature effects. Fawer (1937) and Montes (1970) demonstrated that this simplification leads to small errors. This amounts to assuming that the equipotential line is a vertical, so that $N_o \approx h \approx t$, for which Eq. (3.347) reduces to

$$u \approx \left(\frac{q}{t}\right)\left[1+\frac{tt_{xx}}{K+1}\left(\mu^{K+1}-\frac{1}{K+2}\right)\right] \approx \left(\frac{q}{h}\right)\left[1+\frac{hh_{xx}}{K+1}\left(\mu^{K+1}-\frac{1}{K+2}\right)\right]. \tag{3.350}$$

Note that for $K = 1$, Eq. (3.350) yields Eq. (3.349) without slope effects. Thus, Eq. (3.350) suggests that the failure in the bottom pressure prediction stems from an unsatisfied angular momentum balance, which, in turn, relies on the assumption $K = 1$ implicit in the Picard iteration results for the order of expansion used.

Jaeger (1948) presented a detailed analysis of the brink flow conditions without assuming $K = 1$. His treatment is presented here to elucidate a physically correct value of K. Jaeger (1948) started with the energy-momentum Eq. (3.104) in streamline coordinates,

$$S = (H - z_b)t - \frac{t^2}{2} + \int_0^{N_o} \frac{V^2}{2g}\cos\theta \mathrm{d}n, \tag{3.351}$$

and with the mass conservation Eq. (3.216),

$$q = \int_z^{t+z_b} \frac{V}{\cos\theta}\,\mathrm{d}z. \tag{3.352}$$

Consider the equipotential line immediately to the right of the brink section connecting points "a" and "b" in Fig. 3.14c. Jaeger (1948) used the potential velocity distribution along this curve as given by Eq. (3.220) with $\mu = z/t$,

$$V = V_s \exp\left[\frac{-tt_{xx}}{K+1}\left(1-\mu^{K+1}\right)\right]. \tag{3.353}$$

The energy equation written at points "a" and "b" provides

$$H = t_b + \frac{V_s^2}{2g}, \quad H = \underbrace{\frac{p_b}{\gamma}}_{=0} + \frac{V_b^2}{2g} = \frac{V_b^2}{2g}. \tag{3.354}$$

Owing to Eq. (3.353), the free surface and bottom velocities are related by

$$V_b = V_s \exp\left(\frac{-tt_{xx}}{K+1}\right) = V_s \exp\chi. \tag{3.355}$$

Using Eq. (3.354), and in view of Fig. 3.14c,

$$\chi = \frac{-tt_{xx}}{K+1} = \ln\left(\frac{V_b}{V_s}\right) = \ln\left(\frac{H}{H-t_b}\right)^{1/2}. \tag{3.356}$$

The parameter χ is, therefore, determined once H and t_b are given. Further, Jaeger (1948) assumed that the equipotential line at the brink section is a vertical, so that $h_b \approx t_b$ and $\cos\theta \to 1$. With these identifications, Eqs. (3.351)–(3.352) reduce to

$$S = Hh_b - \frac{h_b^2}{2} + \int_0^{h_b} \frac{V^2}{2g} \mathrm{d}z, \tag{3.357}$$

$$q = \int_0^{h_b} V \mathrm{d}z \ . \tag{3.358}$$

Obviously, to this order of approximation,

$$\chi \approx \frac{-hh_{xx}}{K+1} = \ln\left(\frac{H}{H-h_b}\right)^{1/2}. \tag{3.359}$$

The velocity distribution, Eq. (3.353), then takes the form

$$V = V_s \exp\left[\chi\left(1-\mu^{K+1}\right)\right], \tag{3.360}$$

and when inserted into Eq. (3.358) produces the integral equation

$$q = V_s \exp\chi \left[\int_0^{h_b} \exp\left(-\chi\mu^{K+1}\right)\mathrm{d}z\right]. \tag{3.361}$$

Using the change of variable

$$\begin{aligned}\omega &= -\chi\left(\frac{z}{h_b}\right)^{K+1},\\ \mathrm{d}\omega &= -\chi(K+1)\left(\frac{z^K}{h_b^{K+1}}\right)\mathrm{d}z = -\chi\frac{(K+1)}{h_b^{K+1}}h_b^K\left(-\frac{\omega}{\chi}\right)^{\frac{K}{K+1}}\mathrm{d}z\\ &= -\chi^{\frac{1}{K+1}}\frac{(K+1)}{h_b}(-\omega)^{\frac{K}{K+1}}\mathrm{d}z,\end{aligned} \tag{3.362}$$

Equation (3.361) is rewritten as

$$\begin{aligned}q &= V_s\exp\chi\,\frac{-h_b}{(K+1)}\,\chi^{-\frac{1}{K+1}}\int_0^{-\chi}\exp\omega\,(-\omega)^{-\frac{K}{K+1}}\mathrm{d}\omega\\ &= V_s\exp\chi\,\frac{h_b}{(K+1)}\,\chi^{-\frac{1}{K+1}}\Gamma\left(1-\frac{K}{K+1},\chi\right).\end{aligned} \tag{3.363}$$

The integral term is given by the incomplete gamma function defined as

$$\int_0^{-\chi}\exp\omega\,(-\omega)^{-\frac{K}{K+1}}\mathrm{d}\omega\ = -\Gamma\left(1-\frac{K}{K+1},\chi\right). \tag{3.364}$$

Inserting Eq. (3.360) into Eq. (3.357) yields

$$S = Hh_b - \frac{h_b^2}{2} + \frac{V_s^2}{2g}\exp(2\chi)\int_0^{h_b}\exp\left(-2\chi\mu^{K+1}\right)\mathrm{d}z. \tag{3.365}$$

Using the change of variables

$$u = -2\chi\left(\frac{z}{h_b}\right)^{K+1},\quad \mathrm{d}u = -2\chi\frac{(K+1)}{h_b^{K+1}}z^K\mathrm{d}z, \tag{3.366}$$

the integral in Eq. (3.365) is rewritten as

$$\int_0^{h_b}\exp\left(-2\chi\mu^{K+1}\right)\mathrm{d}z = \frac{-h_b}{(K+1)}(2\chi)^{-\frac{1}{K+1}}\int_0^{-2\chi}\exp u\,(-u)^{-\frac{K}{K+1}}\mathrm{d}u\ , \tag{3.367}$$

and the gamma function is used with the new arguments as

$$\Gamma\left(1-\frac{K}{K+1},2\chi\right)=-\int_0^{-2\chi}\exp u\,(-u)^{-\frac{K}{K+1}}\mathrm{d}u\ . \tag{3.368}$$

Therefore, Eq. (3.365) is rewritten as

$$S=Hh_b-\frac{h_b^2}{2}+\frac{V_s^2}{2g}\exp(2\chi)\frac{h_b}{(K+1)}(2\chi)^{-\frac{1}{K+1}}\Gamma\left(1-\frac{K}{K+1},2\chi\right). \tag{3.369}$$

Equations (3.363) and (3.369) are now expressed as

$$q=[2g(H-h_b)]^{1/2}\exp\chi\frac{h_b}{(K+1)}\chi^{-\frac{1}{K+1}}\Gamma\left(1-\frac{K}{K+1},\chi\right). \tag{3.370}$$

$$S=Hh_b-\frac{h_b^2}{2}+(H-h_b)\exp(2\chi)\frac{h_b}{(K+1)}(2\chi)^{-\frac{1}{K+1}}\Gamma\left(1-\frac{K}{K+1},2\chi\right). \tag{3.371}$$

The parameter χ is computed from Eq. (3.359). In Eqs. (3.370)–(3.371), the quantities q, S, and H are treated as described. However, h_b and K still remain to be determined. Jaeger (1948) proposed the solution

$$h_b=0.48H,\quad K=-1/2. \tag{3.372}$$

Note that $h_b = 0.48H$ is close to the mean experimental value deduced by Rouse (1933) as $h_b = 0.715h_c = 0.715{\cdot}(2/3)H \approx 0.4767H$. Now, *as worked-out exercise*, the experimental verification done by Jaeger (1948) is repeated here in detail step by step, to demonstrate that predictions are extremely accurate. Therefore, given the experimental quantities measured by Rouse (1933), including the three invariants momentum, energy, and mass conservation in the free overfall

$$S=0.02046\,\mathrm{m}^2,\quad H=0.1738\,\mathrm{m},\quad q=0.125\,\mathrm{m}^2/\mathrm{s}, \tag{3.373}$$

demonstrate that Eq. (3.372) permit the verification of Eqs. (3.370)–(3.371) as identities.

First, compute

$$\begin{aligned} &h_b = 0.48 \times 0.1738 = 0.0842\,\text{m}, \\ &\chi = \ln\left(\frac{H}{H-h_b}\right)^{1/2} = \ln\left(\frac{0.1738}{0.1738-0.0842}\right)^{1/2} \approx \ln(0.52)^{1/2} \approx 0.327, \\ &[2g(H-h_b)]^{1/2} = [2g(0.1738-0.0842)]^{1/2} \approx 1.33\,\text{m/s}, \\ &\exp\chi = \exp(0.327) = 1.385. \end{aligned} \tag{3.374}$$

The gamma function of $K = -1/2$ is, after numerical evaluation,

$$\Gamma\left(1-\frac{K}{K+1},\chi\right) = \Gamma(2, 0.327) = 0.04312. \tag{3.375}$$

Inserting the above values of Eqs. (3.374)–(3.375) into Eq. (3.370), the computed discharge is

$$q = 1.33 \times 1.385 \frac{0.0842}{0.5} 0.327^{-2} \times 0.04312 \approx 0.1249\,\text{m}^2/\text{s}. \tag{3.376}$$

This is extremely close to the measured value (0.125 m^2/s) (Rouse 1933). To highlight the importance of a correct K value, consider the gamma function for $K = 1$,

$$\Gamma\left(1-\frac{K}{K+1},\chi\right) = \Gamma(0.5, 0.327) = 1.0303, \tag{3.377}$$

which gives the discharge estimation

$$q = 1.33 \times 1.385 \frac{0.0842}{0.5} 0.327^{-2} \times 1.0303 \approx 2.9869\,\text{m}^2/\text{s}. \tag{3.378}$$

Obviously, this poor discharge estimation relies on the unrealistic assumption $K = 1$.

Consider next the energy-momentum function. The gamma function needed for $K = -1/2$ is

$$\Gamma\left(1-\frac{K}{K+1},2\chi\right) = \Gamma(2, 0.654) = 0.1399, \tag{3.379}$$

and the integral in Eq. (3.365) then takes the value

$$\int_0^{h_b} \exp\left(-2\chi\mu^{K+1}\right)\mathrm{d}z = \frac{h_b}{(K+1)}(2\chi)^{-\frac{1}{K+1}}\Gamma\left(1-\frac{K}{K+1},2\chi\right) = \frac{0.0842}{0.5}0.654^{-2}\times 0.1399 \approx 0.05507. \tag{3.380}$$

The following computations are now conducted:

$$\begin{aligned} H - h_b &= 0.1738 - 0.0842 = 0.0896\,\mathrm{m},\\ \exp(2\chi) &= 1.385^2 \approx 1.9182,\\ Hh_b &= 0.1738\times 0.0842 = 0.01463\,\mathrm{m}^2,\\ h_b^2/2 &= 0.5\times 0.0842^2 = 0.00354\,\mathrm{m}^2, \end{aligned} \tag{3.381}$$

and using the results of Eqs. (3.380)–(3.381) in Eq. (3.371) gives

$$S = 0.01463 - 0.00354 + 0.0896\times 1.9182\times 0.05507 \approx 0.0205\,\mathrm{m}^2, \tag{3.382}$$

which is again extremely close to the experimental value 0.02046 m^2 (Rouse 1933).

Jaeger (1948) found that for the value $K = -1/2$, the equations of mass, energy, and momentum are satisfied with great accuracy. Thus, in the potential velocity distribution, K cannot take unity at the brink section. Khafagi and Hammad (1954a, b) found $K = -0.56$ for flow over broad-crested weirs, a value in close agreement with Jaeger (1948).

It is of interest to compare these results with those originating from Dressler (1978). For illustrative purposes, consider the general equation for the velocity distribution along an equipotential line, Eq. (3.81),

$$V(n) = V_s \exp\left(-\int_n^{N_o}\frac{\mathrm{d}n}{R}\right). \tag{3.383}$$

Dressler's theory (1978) is derived from Eq. (3.383) and applied to the free overfall section, considering the jet flow portion. Dressler (1978) assumed concentric streamlines (Fig. 3.8a). Therefore, the center of curvature is common to all streamlines intersecting a given equipotential line; noting that the positive n is directed opposite to the curvature center in Eq. (3.383), one has for the free overfall section $\mathrm{d}n = -\mathrm{d}R$. Thus, from Eq. (3.383),

$$V(R) = V_s \exp\left(+\int_R^{R_s}\frac{\mathrm{d}R}{R}\right) = V_s \exp\left[\ln\left(\frac{R_s}{R}\right)\right] = V_s\frac{R_s}{R}. \tag{3.384}$$

This corresponds to the free vortex velocity distribution, as expected. From Eq. (3.147) and with a negative curvature for the convex free surface at the brink section, the bottom velocity V_b and the discharge q are related by

$$V_b = \frac{q}{R_b \ln\left(1 + \frac{h_b}{R_b}\right)}, \tag{3.385}$$

and from the free vortex profile, the surface velocity is

$$V_s = \frac{V_b}{\left(1 + \frac{h_b}{R_b}\right)}. \tag{3.386}$$

Conservation of energy at points "c" and "b" of Fig. 3.14c requires

$$H = h_b + \frac{V_s^2}{2g}, \quad H = \frac{V_b^2}{2g}. \tag{3.387}$$

Combining Eqs. (3.386) and (3.387) gives

$$\frac{V_b}{V_s} = \left(1 + \frac{h_b}{R_b}\right) = \left(\frac{H}{H - h_b}\right)^{1/2}. \tag{3.388}$$

From Eq. (3.385),

$$V_b^2 = \frac{q^2}{R_b^2\left[\ln\left(1 + \frac{h_b}{R_b}\right)\right]^2} \equiv 2gH. \tag{3.389}$$

The critical approach flow condition states

$$q^2 = gh_c^3 = g\left(\frac{2}{3}H\right)^3. \tag{3.390}$$

Inserting Eq. (3.390) into Eq. (3.389) gives

$$\frac{2}{3\sqrt{3}} = \left(\frac{h_b}{H}\right)\frac{\ln\left(1 + \frac{h_b}{R_b}\right)}{(h_b/R_b)}. \tag{3.391}$$

From Eq. (3.388),

$$\frac{h_b}{R_b} = \left(\frac{H}{H - h_b}\right)^{1/2} - 1, \tag{3.392}$$

which, when inserted into Eq. (3.391), produces (Ali and Sykes 1972)

$$\frac{2}{3\sqrt{3}} = \left(\frac{h_b}{H}\right) \frac{\ln\left[\left(\frac{H}{H-h_b}\right)^{1/2}\right]}{\left(\frac{H}{H-h_b}\right)^{1/2} - 1}. \tag{3.393}$$

Solving numerically Eq. (3.393) produces $h_b/H = 0.448$, corresponding to $h_b/h_c = 0.672$. This value is physically reasonable in the sense that a drop of h below h_c at the brink section due to curvilinear streamlines is correctly accounted for. However, the value of the predicted flow depth is inaccurate. This points at the importance of using a general velocity distribution and a correct K value as did Jaeger (1948).

3.8.3 Moment of Momentum Method

Based on Jaeger (1948), improved predictions for the channel flow portion of a free overfall require consideration of general K values. However, the theory and development by Jaeger (1948) does not render a theoretical method to compute K, given the resort to Rouse's (1933) experimental work. A more general treatment is based on Hager and Hutter (1984a) with a general K as given by the Fawer (1937) theory. The distributions $u(z)$, $w(z)$, and $p(z)$ are given along the equipotential lines by Hager and Hutter (1984a), enabling the evaluation of S and H. The unknown parameter K in $u(z)$ and $p(z)$ is determined by imposing conservation of angular momentum. For flat bottoms, conservation of energy and horizontal momentum yields, respectively, from Eqs. (3.100) and (3.125) (Montes and Chanson 1998; Castro-Orgaz 2010a)

$$H = t + \frac{q^2}{2gt^2}\left(1 + \frac{2tt_{xx}}{K+2} - \frac{t_x^2}{3}\right) = \text{const.}, \tag{3.394}$$

$$S = \frac{t^2}{2} + \frac{q^2}{gt}\left(1 + \frac{tt_{xx}}{K+2} - \frac{t_x^2}{3}\right) = \text{const.} \tag{3.395}$$

Equating the slope term $t_x^2/3$ in Eqs. (3.394) and (3.395) results in

$$-\frac{t_x^2}{3} = \left[\frac{2gt^2}{q^2}(H-t)\right] - 1 - \frac{2tt_{xx}}{K+2} = \left[\frac{gt}{q^2}\left(S - \frac{t^2}{2}\right)\right] - 1 - \frac{tt_{xx}}{K+2}, \tag{3.396}$$

or

$$\frac{tt_{xx}}{K+2} = \left[\frac{2gt^2}{q^2}(H-t)\right] - \left[\frac{gt}{q^2}\left(S - \frac{t^2}{2}\right)\right]. \tag{3.397}$$

Assuming, following Jaeger (1948), that $t \approx h$, Eq. (3.397) gives the general ODE for the upstream channel flow portion of a free overfall[5]

$$\frac{hh_{xx}}{K+2} = \left[\frac{2gh^2}{q^2}(H-h)\right] - \left[\frac{gh}{q^2}\left(S - \frac{h^2}{2}\right)\right]. \tag{3.398}$$

Closure for K is, however, needed.

In streamline coordinates, S is defined as (Hager and Hutter 1984a)

$$S = \int_{z_b}^{z_b+t} \left(\frac{u}{g}V + \frac{p}{\gamma}\cos\theta\right) \mathrm{d}n. \tag{3.399}$$

Therefore, the vertical momentum M along the equipotential curve follows from

$$M = \int_{z_b}^{z_b+t} \left(\frac{w}{g}V + \frac{p}{\gamma}\sin\theta\right) \mathrm{d}n, \tag{3.400}$$

and the angular momentum function is

$$A = \int_{z_b}^{z_b+t} \left(\frac{u}{g}V + \frac{p}{\gamma}\cos\theta\right) z\mathrm{d}n. \tag{3.401}$$

Here, it is again assumed that the equipotential lines are vertical, so that $\cos\theta \to 1$ and $\sin\theta \to 0$, simplifying Eqs. (3.400) and (3.401) to

$$M = \int_{z_b}^{z_b+h} \frac{uw}{g}\mathrm{d}z, \tag{3.402}$$

$$A = \int_{z_b}^{z_b+h} \left(\frac{u^2}{g} + \frac{p}{\gamma}\right) z\mathrm{d}z. \tag{3.403}$$

[5]From Appendix E and for flat channels, the approximate integration of the Euler equations along the equipotential lines (Hager and Hutter 1984a) agrees with the first Picard iteration cycle (Matthew 1991).

These are identical with Eqs. (3.24) and (3.42), respectively. Therefore,

$$M = \frac{q^2}{2gh} h_x. \tag{3.404}$$

However, A will be affected by K, which is the interaction sought between the angular momentum balance and the curvature distribution exponent. The velocity and pressure distributions are, from Eqs. (3.350) and (3.133)

$$u = \frac{q}{h}\left[1 - \frac{hh_{xx}}{K+1}\left(\frac{1}{K+2} - \mu^{K+1}\right)\right], \tag{3.405}$$

$$\frac{p}{\gamma} = h - \eta + \frac{q^2}{gh^2}\left(\frac{hh_{xx}}{K+1}\right)\left(1 - \mu^{K+1}\right), \tag{3.406}$$

respectively. Evaluating the integrals gives

$$\begin{aligned}\int_0^h \frac{u^2}{g}\eta \mathrm{d}\eta &\approx h^2 \int_0^1 \left(\frac{q^2}{gh^2}\right)\left[1 - \frac{2hh_{xx}}{K+1}\left(\frac{1}{K+2} - \mu^{K+1}\right)\right]\mu \mathrm{d}\mu \\ &= \left(\frac{q^2}{g}\right)\left[\frac{1}{2} - \frac{hh_{xx}}{K+1}\left(\frac{1}{K+2} - \frac{2}{K+3}\right)\right],\end{aligned} \tag{3.407}$$

$$\begin{aligned}\int_0^h \frac{p}{\gamma}\eta \mathrm{d}\eta &= h^2 \int_0^1 \left[h - \eta + \frac{q^2}{gh^2}\left(\frac{hh_{xx}}{K+1}\right)\left(1 - \mu^{K+1}\right)\right]\mu \mathrm{d}\mu \\ &= \frac{h^3}{6} + \frac{q^2}{g}\left(\frac{hh_{xx}}{K+1}\right)\left(\frac{1}{2} - \frac{1}{K+3}\right).\end{aligned} \tag{3.408}$$

The angular momentum function is obtained by summing Eqs. (3.407) and (3.408) by

$$\begin{aligned}A &= \left(\frac{q^2}{g}\right)\left[\frac{1}{2} - \frac{hh_{xx}}{K+1}\left(\frac{1}{K+2} - \frac{2}{K+3}\right)\right] + \frac{h^3}{6} + \frac{q^2}{g}\left(\frac{hh_{xx}}{K+1}\right)\left(\frac{1}{2} - \frac{1}{K+3}\right) \\ &= \frac{h^3}{6} + \left(\frac{q^2}{2g}\right) + \left(\frac{q^2}{g}\right)\left[\frac{1}{2} - \frac{1}{K+3} - \frac{1}{K+2} + \frac{2}{K+3}\right]\frac{hh_{xx}}{K+1} \\ &= \frac{h^3}{6} + \frac{q^2}{2g}\left(1 + \frac{(K+4)}{(K+3)(K+2)} hh_{xx}\right).\end{aligned} \tag{3.409}$$

Inserting Eq. (3.409) in Eq. (3.332) permits rewriting the moment of momentum balance as

$$\Omega = \frac{h^3}{6} + \frac{q^2}{2g}\left(1 + \frac{(K+4)}{(K+3)(K+2)} h h_{xx} - \ln\frac{h}{h_1}\right) = \text{const.}, \tag{3.410}$$

where h_1 is the flow depth at a reference section. Equation (3.410) is a closure law that may be imposed to compute K. Note that Eq. (3.410) reduces to Eq. (3.338) by letting $K = 1$, if the squared free surface slope h_x^2 term is neglected in the latter. Equation (3.398) is normalized as

$$Y_{XX} = \frac{(K+2)}{Y}\left[2Y^2(H^* - Y) - Y\left(S^* - \frac{Y^2}{2}\right)\right]. \tag{3.411}$$

Here, $Y = h/h_c$, $X = x/h_c$, $h_c = (q^2/g)^{1/3}$ is the critical (subscript c) depth for parallel-streamlined flow, $H^* = H/h_c = 1.5$ and $S^* = S/h_c^2 = 1.5$ for critical flow $\mathsf{F} = 1$ with parallel streamlines upstream of the brink section. This equation satisfies conservation of energy and horizontal momentum. The bottom pressure head is from Eq. (3.406)

$$\frac{p_b}{\gamma} = h + \frac{q^2}{gh^2}\frac{h h_{xx}}{K+1}. \tag{3.412}$$

The zero pressure boundary condition is given, setting $p_b = 0$ in Eq. (3.412), by (Castro-Orgaz 2010a)

$$Y Y_{XX} = -(1+K)Y^3. \tag{3.413}$$

Inserting this boundary condition into Eq. (3.411), the generalized brink depth ratio $Y_b = h_b/h_c$ is given by a cubic equation for Y_b once K is determined

$$2Y_b^2(H^* - Y_b) - Y_b\left(S^* - \frac{Y_b^2}{2}\right) + \frac{(K+1)}{(K+2)}Y_b^3 = 0. \tag{3.414}$$

To obtain the closure condition, Eq. (3.413) is combined with Eq. (3.410) to yield

$$\frac{Y_b^3}{6} + \frac{1}{2}\left(1 - \frac{(K+4)(K+1)}{(K+3)(K+2)}Y_b^3 - \ln Y_b\right) - \Omega^* = 0, \tag{3.415}$$

in which $\Omega^* = \Omega/h_c^3 = 2/3$. Equation (3.415) approximately represents the conservation of angular momentum balance between the critical point and the brink section. Equations (3.414) and (3.415) are plotted in Fig. 3.18. The solution of the system yields $Y_b \approx 0.71$ for $K \approx -0.665$, indicating a significant deviation from $K = 1$. The theoretical value of K is close to $K = -0.5$ as proposed by Jaeger (1948) and $K = -0.4$ by Castro-Orgaz (2010a). Further, $Y_b = 0.71$ is in excellent

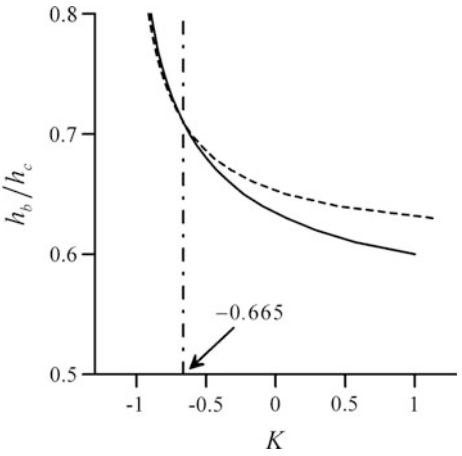

Fig. 3.18 Brink depth ratio $h_b/h_c(K)$ from (—) Eq. (3.414), (- - -) Eq. (3.415) (adapted from Castro-Orgaz and Hager 2010)

agreement with the experimental value 0.715 (Rouse 1932, 1933) and with potential flow methods based on the Laplace equation (Montes 1992a; Castro-Orgaz 2013b). This result is thus a theoretical solution for the brink depth ratio based on the simultaneous conservation of energy, horizontal momentum, vertical momentum, and angular momentum (Castro-Orgaz and Hager 2010). It further demonstrates that the Picard second-order Boussinesq-type solution for the upstream channel portion does not satisfy the angular momentum balance, given the inaccurate value of $K = 1$ at the brink section. The value of the free surface slope at the brink section deduced from Eq. (3.394) or (3.395) for $Y_b = 0.71$ and $K = -0.665$ is $h_x = -0.268$, e.g., close to the experimental value of -0.25 (Rouse 1933; Jaeger 1948; Montes 1992a).

Taking as starting point the brink section, where $Y_b = 0.71$, $K = -0.665$, and $h_x = -0.268$, Eq. (3.411) was numerically solved using the fourth-order Runge–Kutta method. At each computational node, Eq. (3.410) was used to apply K-closure by its evaluation in the previous node, to keep the numerical scheme as simple as possible. The computational step was progressively reduced until no variation in the results was detected. From $h = h(x)$ and $K = K(x)$, the bottom pressure was computed from Eq. (3.412). The computational results are plotted in Fig. 3.19. The computed free surface profile $h/h_c(x/h_c)$ of Fig. 3.19a agrees with the experimental data, yet the degree of improvement over Fig. 3.16 is small. However, the predicted bottom pressure head $p_b/(\gamma h_c)(x/h_c)$ is physically realistic, with zero value at the brink section and a hydrostatic pressure recovery roughly at $x/h_c = -2$. In contrast, the computed bottom pressure head $p_b/(\gamma h_c)(x/h_c)$ in Fig. 3.16 is unrealistic. This is clearly an improvement achieved by considering generalized K values using the moment of momentum conservation equation. Further, note the good comparison of the relative pressure $p_b/(\gamma h)$ from the present method with the results of the Laplace equation and experimental data (Montes 1992a) in Fig. 3.19b. Thus, a complete approach for curvilinear flow involves K as well as angular momentum conservation, thereby relaxing previous failures attributed to the

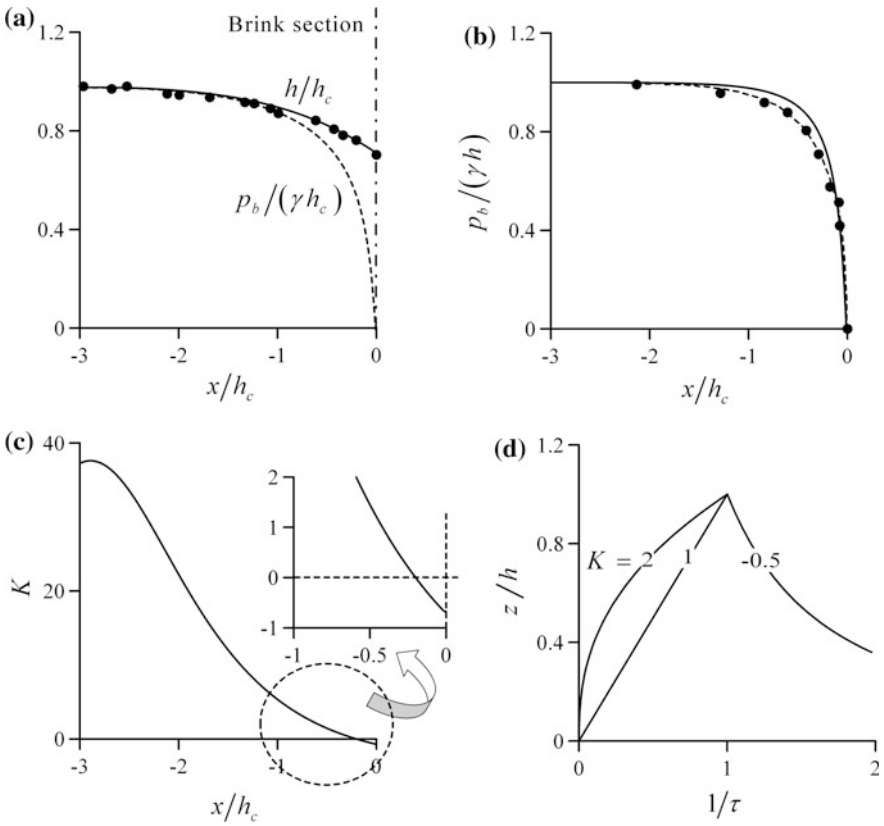

Fig. 3.19 **a** Free surface profile $h/h_c(x/h_c)$ from (—) Eqs. (3.410) and (3.411), bottom pressure profile $p_b/(\gamma h_c)(x/h_c)$ (- - -) from Eq. (3.412), **b** relative bottom pressure $p_b/(\gamma h)(x/h_c)$ from (—) Eq. (3.412), (- - -) Laplace's equation (Montes 1992a), (•) experimental data (Montes 1992a), **c** curvature parameter $K(x/h_c)$ from Eq. (3.410), **d** streamline curvature distribution $1/\tau(\eta, K)$ (adapted from Castro-Orgaz and Hager 2010)

Boussinesq's approach (Montes 1994b). The theoretical results for $K = K(x)$ are plotted in Fig. 3.19c, which increases fast from −0.665 at the brink section up to large values shortly upstream of the brink. The particular value $K = 1$ is reached at $x/h_c \approx -0.4$ (inset of Fig. 3.19c).

In the energy equation $H = h + \varphi q^2/(2gh^2)$, the streamline curvature and slope effects are accounted for by the parameter

$$\varphi = 1 + \frac{2hh_{xx}}{K+2} - \frac{h_x^2}{3}. \tag{3.416}$$

K may therefore be interpreted as a weighting factor in Eq. (3.416). If K is small, a large effect of hh_{xx} results on the free surface profile. This is shown in Fig. 3.19a, b for the domain $-0.4 < x/h_c < 0$, where streamline curvature is large and $p_b/(\gamma h) < 1$. For this zone of high curvilinear effects, $1 < K < -0.668$. However, for $x/h_c < -0.4$, the experimental data in Fig. 3.19b indicate that $p_b \rightarrow \gamma h$, thereby stating that streamline curvature effects are extremely small. In concordance with this experimental evidence, the moment of momentum closure equation results in large theoretical K values, e.g., as for $x/h_c < -1$. Note that the maximum $K = 37$ occurs at $x/h_c = -2.8$, e.g., where streamlines are almost parallel. A large K value in Eq. (3.416) points at a reduction factor, e.g., the effect of streamline curvature hh_{xx} is reduced in the computational results. The curvature law distribution $1/\tau = (z/h)^K$ is plotted in Fig. 3.19d for several K values, with $\tau = R/R_s$. For $K = -0.5$, the curvature distribution is similar to that of round-crested weir flow, indicating a large effect of streamline curvature, as compared to the standard value $K = 1$. Further, a positive value $K = 2$ indicates that streamlines become parallel in a larger portion of the flow depth. The higher the K, the larger the portion of flow depth where the streamlines are straight, i.e., $1/\tau \approx 0$. Thus, the theoretical results obtained for K using the angular momentum balance are in close agreement with physical reasoning based on the curvature law and its modification depending on the degree of streamline curvature. An important consequence is that K and hh_{xx} are related by angular momentum conservation.

The potential velocity distribution at the brink section follows from Eq. (3.339) by inserting Eq. (3.413), and setting $t \approx h$ and $v \approx \mu$; the result is

$$V = \left(\frac{q}{h}\right)\left[1 - Y_b^3\left(\mu^{K+1} - \frac{1}{K+2}\right) - \frac{h_x^2}{6}\right]. \tag{3.417}$$

The free surface slope is computed from any of the two identities of Eq. (3.396) after inserting Eq. (3.413), e.g., from the energy equation, one obtains

$$h_x^2 = 3\left\{1 - \frac{2(K+1)Y_b^3}{(K+2)} - \left[2Y_b^2\left(\frac{3}{2} - Y_b\right)\right]\right\}. \tag{3.418}$$

With the previous results for the brink depth conditions $Y_b \approx 0.71$ and $K \approx -0.665$, Eq. (3.417) is plotted in Fig. 3.20a. The results are in excellent agreement with those from the numerical solution of Laplace's equation (Montes 1992a; Castro-Orgaz 2013b). Further, the computed velocity distribution for $K = 1$ yields an unrealistic velocity profile. Additionally, a value of $K = -0.5$ from Jaeger (1948) is plotted, yet without a significant effect on the velocity profile. From the computed velocity distribution, the pressure distribution was deduced assuming potential flow, with the results plotted in Fig. 3.20b. The shape of the computed curve for $K \approx -0.665$ is qualitatively correct, yet its maximum value is too large as compared to the solution of the Laplace equation and experimental data (Montes 1992a; Castro-Orgaz 2013b). The computed curve for $K = -0.5$ is also included, showing excellent agreement with the solution of the Laplace equation and

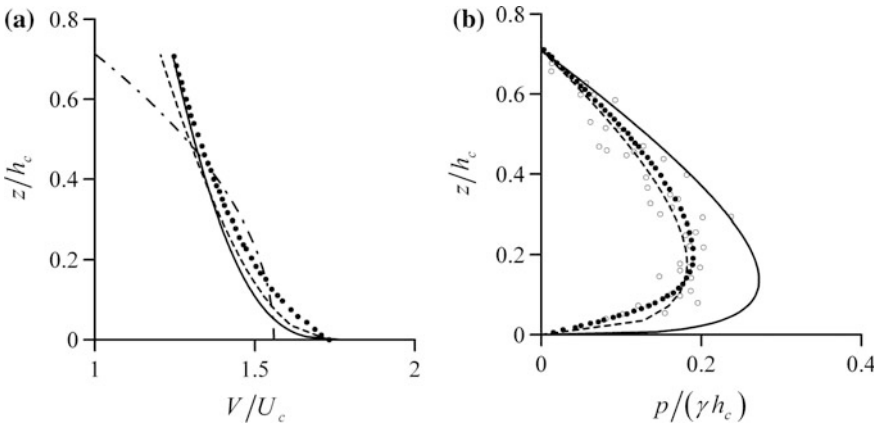

Fig. 3.20 (a) Velocity distribution $V/U_c(z/h_c)$ from Eq. (3.417) for (—) $K = -0.665$, (- - -) $K = -0.5$, (- • -) $K = 1$, (•) Laplace's equation (Montes 1992a, Castro-Orgaz 2013b), **b** pressure distribution $p/(\gamma h_c)(z/h_c)$ for (—) $K = -0.665$, (- - -) $K = -0.5$, (•) Laplace's equation (Montes 1992a, Castro-Orgaz 2013b), (○) Experimental data (Montes 1992a) (adapted from Castro-Orgaz and Hager 2010)

experiments. This comparative result indicates that the velocity distribution is not very sensitive to the small variations of K from −0.665 to −0.5, but such small variations, if squared for energy conservation, result in a larger effect on the pressure distribution. Further refinements are required in the angular momentum balance, if the degree of vertical model definition should be improved. However, the K values computed according to the angular momentum balance reproduce the main features of the free overfall.

3.8.4 Two-Dimensional Solution

The x-ψ method proposed by Boadway (1976) and applied by Montes (1992a) and Castro-Orgaz (2013b) consists in expressing the z variable versus the pair of variables (ψ, x). Boadway's method is suitable for open-channel flows given its simplicity as compared with other proposals. An advantage of the ideal fluid flow theory is that the mathematical jet modeling is simple, and a more advanced turbulent computation (Tayadon and Ramamurthy 2009) may be used at a later stage. Montes (1992a) verified that Boadway's method is accurate for the free overfall. He detailed the velocity and pressure distributions at and upstream of the brink section. Free surface and bottom pressure profiles were also investigated. The jet portion was described by Castro-Orgaz (2013b). The purpose of this section is to detail the model of Boadway (1976) for free overfalls. For this task, a convergent, iterative method is used (Castro-Orgaz 2013b). The proposed potential flow solver determines the shape of the free surfaces using an analytical solution of the Boussinesq equations to initiate the algorithm.

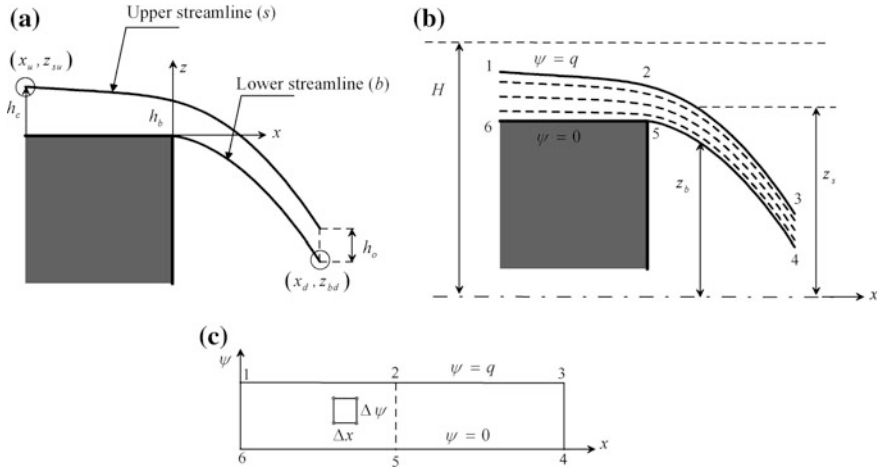

Fig. 3.21 Free overfall with upstream critical flow: **a** coordinate system and boundary conditions, **b** physical plane, **c** x-ψ plane (adapted from Castro-Orgaz 2013b)

At the upstream boundary section (subscript u), the critical flow conditions with parallel streamlines prevail (Rouse 1938), from which $h_c = (q^2/g)^{1/3}$ (Fig. 3.21a) and $H = 3h_c/2$, with H as the total energy head. The downstream section of the flow domain (subscript d) was selected at the terminal jet portion, where the internal pressure is negligible. Therefore, a basic application of the continuity and momentum equations led to $t_o = (2/3)h_c$ for upstream critical flow conditions (Rouse 1938; Montes 1992a). The relation between the stream function ψ and the elevation z at these sections is $z = z_b + (z_s - z_b)\psi/q$, physically expressing that the velocity profile is uniform in the z-direction at boundary sections. The boundary flow sections are selected at $x_u/h_c = -3$ and $x_d/h_c = +3$.

To start the 2D solution, an initial estimate of the free surface profiles (upstream portion of the free overfall as well as upper and lower jet nappes) is necessary (Markland 1965; Montes 1992a). Equations (3.300), (3.318), and (3.319) are an approximate solution of Laplace's equation to be adopted below as initial free surface profiles to find the accurate 2D solution for the free streamlines. The problem statement is the solution of Eq. (3.250) for coordinate z as a function of both x and ψ, once the boundary streamlines $z_s(x)$ and $z_b(x)$ and the relations $z_u = z_u(x_u, \psi)$ and $z_d = z_d(x_d, \psi)$ at boundary sections are prescribed (Fig. 3.21b). In the plane (x, ψ), the computational domain is a rectangular strip, where the value of z is known along the entire contour 1–2–3–4–5–6–1 (Fig. 3.21c). Thus, it is unnecessary to use a non-uniform mesh size for the flow solution near the curved boundaries, as is done if a solution is directly sought in the physical plane (x, z) (Thom and Apelt 1961; Vallentine 1969).

Let i be the node index of the mesh in the x-direction and j corresponding to the ψ-direction; second-order central discretization of derivatives $\partial z/\partial x$, $\partial z/\partial \psi$, $\partial^2 z/\partial x^2$, $\partial^2 z/\partial \psi^2$ and $\partial^2 z/\partial x \partial \psi$ (Boadway 1976; Montes 1992a) as given by

Eqs. (3.253)–(3.257) inserted into Eq. (3.250) permits to obtain an equation for $z(i, j)$ at a generic node inside the mesh as

$$z(i,j) = \frac{\frac{z(i+1,j)+z(i-1,j)}{(\Delta x)^2}\left(\frac{\partial z}{\partial \psi}\right)^2 + \frac{z(i,j+1)+z(i,j-1)}{(\Delta \psi)^2}\left[1+\left(\frac{\partial z}{\partial x}\right)^2\right] - 2\frac{\partial^2 z}{\partial x \partial \psi}\frac{\partial z}{\partial x}\frac{\partial z}{\partial \psi}}{\frac{2}{(\Delta \psi)^2}\left[1+\left(\frac{\partial z}{\partial x}\right)^2\right] + \frac{2}{(\Delta x)^2}\left(\frac{\partial z}{\partial \psi}\right)^2}. \quad (3.419)$$

Note that $\partial z/\partial x$, $\partial z/\partial \psi$ and $\partial^2 z/\partial x \partial \psi$ are not discretized in Eq. (3.419), to produce a simplified expression for illustrative purposes. However, the complete discretization for the numerical solution was conducted using Eqs. (3.253)–(3.257). Equation (3.419) states that $z(i, j)$ is a function of $z(i - 1, j)$, $z(i + 1, j)$, $z(i, j - 1)$, and $z(i, j + 1)$, i.e., the four surrounding mesh points. The process for obtaining z at each node is therefore iterative (Thom and Apelt 1961). It consists of defining initial starting values for $z(i, j)$ inside the mesh and then applying Eq. (3.419) iteratively. Accordingly, a fresh value of z at any node is obtained from the previous values at the four surrounding points. The iteration is applied until the differences in the $z(i, j)$ values between two successive iterations are below a limiting tolerance, typically 10^{-6}. This numerical method is different from the relaxation technique of Southwell and Vaisey (1946) and Montes (1992a), in which a preassumed relaxation pattern to limit the residuals in the finite-difference form of the Laplace equations is necessary. To start the iteration process using the squaring technique, the values of z inside the mesh are assumed to follow the linear law $z = z_b + (z_s - z_b)\psi/q$. This is equivalent to assuming that the initial horizontal velocity profile is uniform in the vertical direction within the entire computational domain. A repeated application of Eq. (3.419) will collocate the streamlines $z = z(x, \psi = \text{const.})$ and, therefore, produce the correct velocity profile at each vertical section of the mathematical model. Once the iteration of the positions of the free streamlines is initiated as described below, the initial values for $z(i, j)$ inside the mesh are taken from the final values in the previous position of the free surfaces. This technique accelerates convergence in the solution of the Laplacian field.

In the present application, 10 streamlines and 60 vertical sections were used to construct the finite-difference mesh. A duplication of the number of streamlines and vertical sections to increase mesh resolution did not alter the results. The Cartesian velocity components (u, w) in the directions (x, z) are determined by resorting to Eqs. (3.270)–(3.273).

The energy head at a section at distance x is obtained for the actual free streamlines $z_s(x)$ and $z_b(x)$ as follows

$$H_s(x) = z_s + \frac{u_s^2}{2g}\left[1+\left(\frac{\partial z_s}{\partial x}\right)^2\right], \quad H_b(x) = z_b + \frac{u_b^2}{2g}\left[1+\left(\frac{\partial z_b}{\partial x}\right)^2\right]. \quad (3.420)$$

Let H be the total energy head of a potential flow. This is a constant value, which must be conserved in any point of the computational domain. However, the free streamlines are generally unknown in advance such that the positions $z_s = z_s(x)$ and

$z_b = z_b(x)$ must be assumed and then corrected iteratively. In general, if a free surface is not in the correct position, energy residuals $[H - H_s(x)]$ and $[H - H_b(x)]$ appear at every position x, so that the pressure head at each free surface is not zero. The free streamline position must therefore be displaced iteratively until the zero pressure condition is satisfied with a prescribed tolerance along the entire free surface. Each time a free surface is moved, internal streamlines must also be relocated, requiring a new solution of Eq. (3.250), as described above. Using the Newton–Raphson technique, a better estimate for the position of each free surface node is

$$\begin{aligned} z_s^k &= z_s^{k-1} + \left[\frac{H - H_s(x)}{\dfrac{\mathrm{d}H_s(x)}{\mathrm{d}z_s}}\right]^{k-1} = z_s^{k-1} + \Delta z_s^{k-1}, \\ z_b^k &= z_b^{k-1} + \left[\frac{H - H_b(x)}{\dfrac{\mathrm{d}H_b(x)}{\mathrm{d}z_b}}\right]^{k-1} = z_b^{k-1} + \Delta z_b^{k-1}, \end{aligned} \tag{3.421}$$

with k as the recursion index (Montes 1994a).

The z_s- and z_b-coordinates at the boundary nodes ($i = 0$ and $i = M$) are fixed during the relocation process of the free surfaces. The derivatives of $H_s(x)$ and $H_b(x)$ for both the upper and lower streamlines are, with u_s and u_b as the x-velocity components at each free streamline, from differentiation of equations (3.420)

$$\begin{aligned} \frac{\mathrm{d}H_s}{\mathrm{d}x} &= \frac{\mathrm{d}z_s}{\mathrm{d}x} + \frac{u_s}{g}\frac{\mathrm{d}u_s}{\mathrm{d}x}\left[1 + \left(\frac{\partial z_s}{\partial x}\right)^2\right] + \frac{\partial z_s}{\partial x}\frac{\partial^2 z_s}{\partial x^2}\frac{u_s^2}{g}, \\ \frac{\mathrm{d}H_b}{\mathrm{d}x} &= \frac{\mathrm{d}z_b}{\mathrm{d}x} + \frac{u_b}{g}\frac{\mathrm{d}u_b}{\mathrm{d}x}\left[1 + \left(\frac{\partial z_b}{\partial x}\right)^2\right] + \frac{\partial z_b}{\partial x}\frac{\partial^2 z_b}{\partial x^2}\frac{u_b^2}{g}, \end{aligned} \tag{3.422}$$

or

$$\begin{aligned} \frac{\mathrm{d}H_s}{\mathrm{d}z_s} &= 1 + \frac{u_s}{g}\frac{\mathrm{d}u_s}{\mathrm{d}z_s}\left[1 + \left(\frac{\partial z_s}{\partial x}\right)^2\right] + \frac{\partial^2 z_s}{\partial x^2}\frac{u_s^2}{g}, \\ \frac{\mathrm{d}H_b}{\mathrm{d}z_b} &= 1 + \frac{u_b}{g}\frac{\mathrm{d}u_b}{\mathrm{d}z_b}\left[1 + \left(\frac{\partial z_b}{\partial x}\right)^2\right] + \frac{\partial^2 z_b}{\partial x^2}\frac{u_b^2}{g}, \end{aligned} \tag{3.423}$$

which are the derivatives needed in Eq. (3.421). Estimates of $\mathrm{d}u_s/\mathrm{d}z_s$ and $\mathrm{d}u_b/\mathrm{d}z_b$ were found using the one-sided second-order differences equations (3.272)–(3.273), rewritten here as

$$u_s = \frac{2\Delta\psi}{3z_s - 4z(i,N-1) + z(i,N-2)}, \tag{3.424}$$

$$u_b = \frac{2\Delta\psi}{-3z_b + 4z(i,1) - z(i,2)}, \tag{3.425}$$

from which

$$\frac{\mathrm{d}u_b}{\mathrm{d}z_b} \approx +\frac{3}{2}\frac{u_b^2}{\Delta\psi} \quad [z_b = z(i,0)], \quad \frac{\mathrm{d}u_s}{\mathrm{d}z_s} \approx -\frac{3}{2}\frac{u_s^2}{\Delta\psi} \quad [z_s = z(i,N)]. \tag{3.426}$$

The corrections for the position of each node at both the upper and lower streamlines are, respectively,

$$\Delta z_s = \frac{H - H_s(x)}{1 - \frac{u_s^2}{gh}\left[\frac{3}{2}\frac{u_s h}{\Delta\psi}\left(1 + (\partial z_s/\partial x)^2\right) - h\partial^2 z_s/\partial x^2\right]}, \tag{3.427}$$

$$\Delta z_b = \frac{H - H_b(x)}{1 - \frac{u_b^2}{gh}\left[-\frac{3}{2}\frac{u_b h}{\Delta\psi}\left(1 + (\partial z_b/\partial x)^2\right) - h\partial^2 z_b/\partial x^2\right]}. \tag{3.428}$$

Therefore, Δz_s was used to correct the ordinates of line 1–2–3 (Fig. 3.21b), whereas Δz_b was employed to correct the ordinates of line 5–4. The use of Eqs. (3.427) and (3.428) in the numerical model was efficient and stable.

During the process of solving Eq. (3.250) by squaring and successive adjustment of the free streamlines by Eqs. (3.427) and (3.428), the boundary nodes of coordinates (−3, 1), [+3, $(z_b)_d$] and [+3, h_o + $(z_b)_d$] were fixed. In the first run of the algorithm, the initial value of $(z_b)_d$ was obtained from Eq. (3.318) (Note that subindex d in $(z_b)_d$ refers to the value of z_b at the downstream node of the computational domain, Fig. 3.21a.). After the numerical solution converges to the zero pressure condition with a prescribed tolerance along both free streamlines, the pressure head at the bottom of the brink section may not be zero, indicating that the position of the boundary jet section is incorrect. Therefore, an iteration method for the boundary section elevation $(z_b)_d$ (Fig. 3.21a) was formulated using the Newton–Raphson technique with ω as the recursion index and p_{be} the pressure at the brink section bottom as

$$\left[(z_b)_d\right]^{\omega} = \left[(z_b)_d\right]^{\omega-1} + \left[\frac{-p_{be}\left[(z_b)_d\right]}{\frac{\mathrm{d}p_{be}\left[(z_b)_d\right]}{\mathrm{d}(z_b)_d}}\right]^{\omega-1} = \left[(z_b)_d\right]^{\omega-1} + \left[\Delta(z_b)_d\right]^{\omega-1}. \tag{3.429}$$

Note that p_{be} = 0 for the correct physical solution. Moreover, note that z_{sd} = t_o + z_{bd} for any iteration. Once the displacement $\Delta(z_b)_d$ to be applied to the boundary node

[+3, $(z_b)_d$] is determined, a new solution as described above must be initiated using squaring for the Laplacian field and the iterative computation of the free streamlines. For this task, it is necessary to define the new initial jet profiles. A linear correction was used to find the jet profiles as

$$z_b^{\omega} = z_b^{\omega-1} + \frac{x}{x_d}\left[\Delta(z_b)_d\right]^{\omega-1}, \quad z_s^{\omega} = z_s^{\omega-1} + \frac{x}{x_d}\left[\Delta(z_s)_d\right]^{\omega-1}. \tag{3.430}$$

These statements close the numerical model for the iterative computation of the 2D problem.

Figure 3.22a compares the final free streamlines obtained by the numerical model and the initial streamlines used from the analytical solution of the Boussinesq equation (Eqs. 3.300, 3.318, 3.319). The Boussinesq equations and the 2D solution agree if $x/h_c < 0$. The brink depth ratio from the 2D results is 0.714 as compared to 0.7169 from the Boussinesq equations. However, deviations

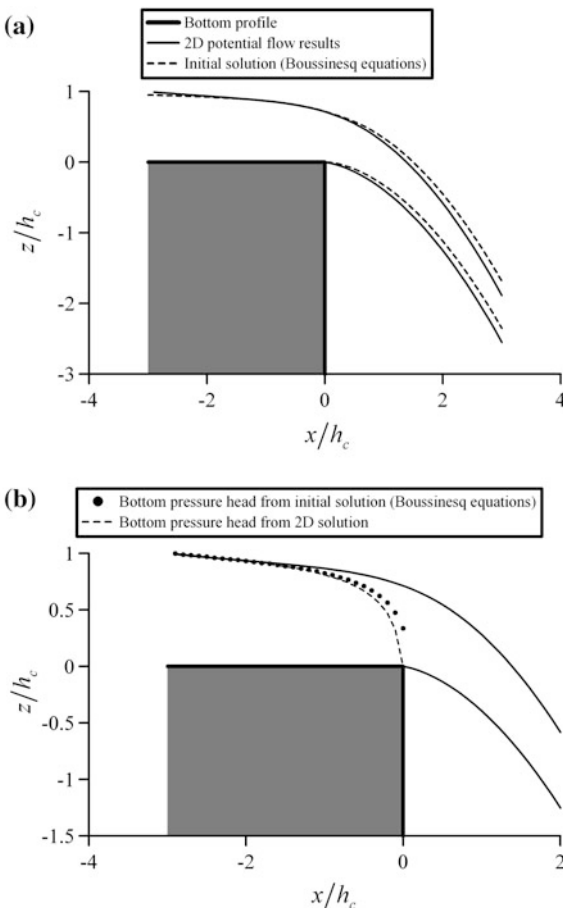

Fig. 3.22 Free overfall with upstream critical flow: **a** comparison of computed streamlines from 2D solution with initial solution using Boussinesq equations, **b** detail of bottom pressure head (adapted from Castro-Orgaz 2013b)

between both solutions in the jet portion are noticeable, rendering the Boussinesq equations questionable in this zone. The computed 2D bottom pressure from the Boussinesq equations as initial free streamlines, without any iteration of the jet terminal section, yields at $x/h_c = 0$ the result $p_{be}/(\gamma h_c) = 0.337$, which is unrealistic (Fig. 3.22b). This was previously discussed with pure 1D computations in Fig. 3.16. Therefore, the numerical model iteratively moved the jet until reaching the correct physical brink condition, namely $p_{be}/(\gamma h_c) = 0$.

The computed free streamlines and bottom pressure distribution are shown in Fig. 3.23a. Comparison of the numerical results with the test data of Rouse (1932) indicates excellent agreement. Figure 3.23b contains the computed streamline flow pattern, which is the direct computation regained from the numerical model and used to derive the velocity and pressure fields.

Montes (1992a) and Matthew (1995) detailed the velocity and pressure distributions for $x/h_c < 0$, whereas the pressure reduction inside the jet was computed by

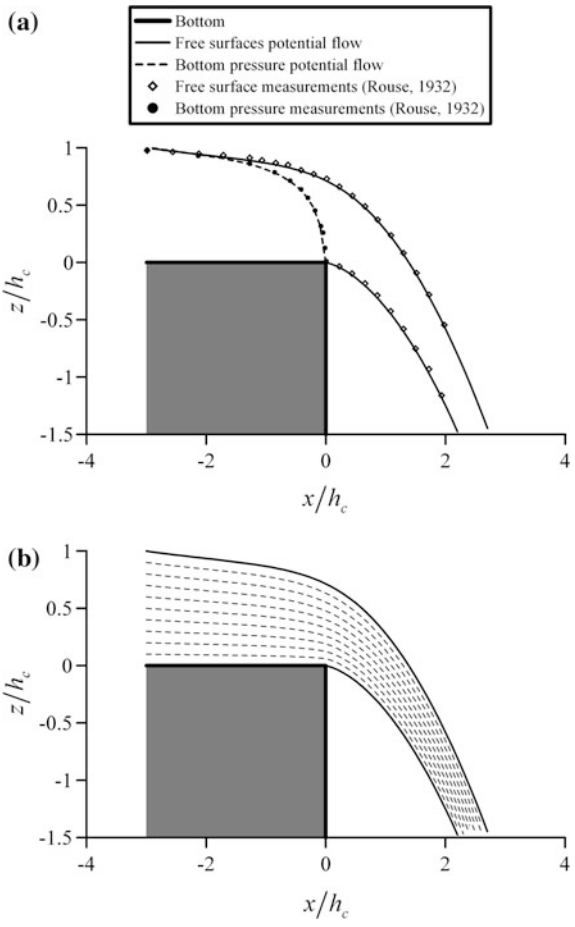

Fig. 3.23 Free overfall with upstream critical flow: **a** comparison of computed 2D solution with the experimental data (Rouse 1932), **b** computed streamline flow pattern (adapted from Castro-Orgaz 2013b)

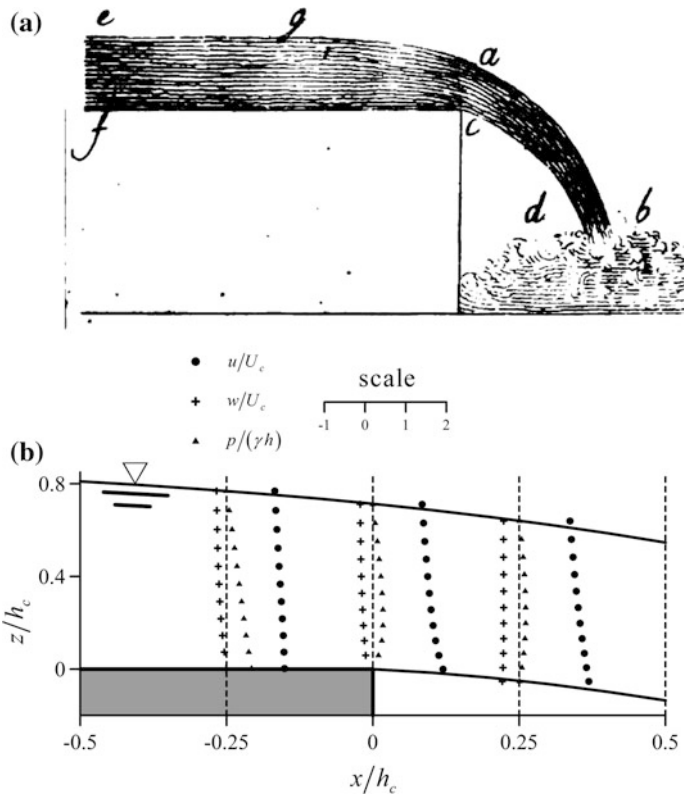

Fig. 3.24 Free overfall with upstream critical flow: **a** sketch of free overfall (Da Vinci re-edited 1828), **b** computed velocity and pressure distributions using irrotational flow model by Castro-Orgaz (2013b)

Castro-Orgaz (2013b). The free overfall is a fascinating hydraulic problem having attracted a number of hydraulic studies, among which the work of Hunter Rouse (1932, 1933) deserves particular credit for the first research based on fluid mechanics. He detailed the main aspects of this problem, and his 1933 flow net may be compared with the beautiful hand drawing of Leonardo da Vinci (1828; year of re-edition) (Fig. 3.24a) in his "Del moto e misura dell' acqua," possibly the first documented "hydraulic" drawing of a free overfall (Rouse and Ince 1957) including motion features by resorting to streamlines. The computed velocity and pressure distributions in the vicinity of the brink section using the 2D irrotational numerical model of Castro-Orgaz (2013b) are displayed in Fig. 3.24b.

Figure 3.25 shows the computed pressure distributions at $x/h_c = 0$, 0.26, and 1. The experimental data in the same three sections obtained by Rouse (1932) are also plotted, indicating good agreement with the potential flow model. For jet flow

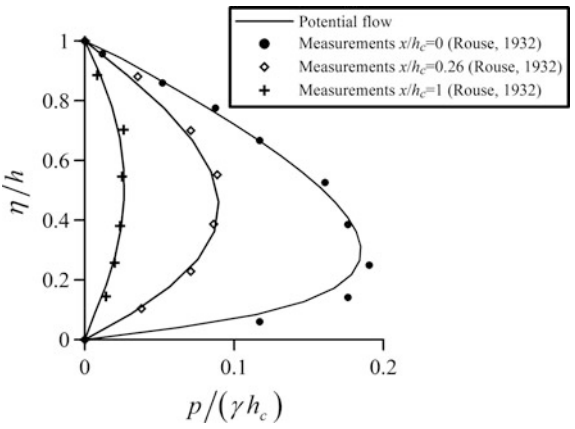

Fig. 3.25 Pressure distribution within jet portion (adapted from Castro-Orgaz 2013b)

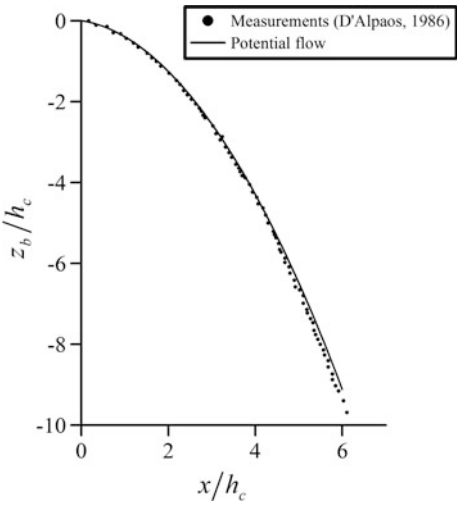

Fig. 3.26 Comparison of computed 2D lower nappe profile solution with the experimental data (D'Alpaos 1986) (adapted from Castro-Orgaz 2013b)

computations, it is desirable to check how accurate an ideal 2D flow model is for larger values of x_d (Rouse's jet data are limited to $0 < x/h_c < 2$). D'Alpaos (1986) made detailed measurements of the lower nappe profile within $0 < x/h_c < 6$ for a jet originating from a free overfall with upstream critical flow conditions. The numerical model was applied using $x_d/h_c = +6$, with the resulting lower free streamline plotted in Fig. 3.26. The potential flow result is compared in this figure with the experimental data by D'Alpaos (1986), showing excellent agreement.

Figure 3.27 shows the computed ratios u_s/U and u_b/U throughout the computational domain of the mathematical model, indicating large deviations from unity. Thus, the velocity can not be assured to be uniform in the free overfall.

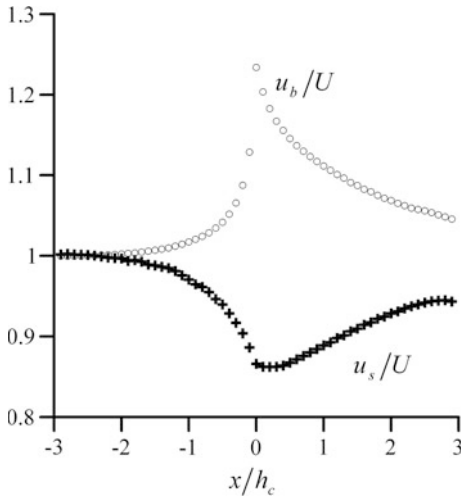

Fig. 3.27 Computed u velocity component along upper and lower streamlines (adapted from Castro-Orgaz 2013b)

3.8.5 *Flow Net*

Equations (3.82) and (3.91) based on Fawer's theory (Fawer 1937) are rewritten with $r = R_s/R_b$ and $i = \theta_b/\theta_s$ as

$$\frac{R_s}{R} = r + (1 - r)v^K, \tag{3.431}$$

$$\frac{\theta}{\theta_s} = i + (1 - i)v^m. \tag{3.432}$$

The classical flow net for the free overfall developed by Rouse (1933) is replotted in Fig. 3.28a. It was analyzed graphically to obtain the approximate 2D distributions of R_s/R and θ/θ_s. These computations intended to test whether the approximation $K = m = 1$ (Matthew 1961, 1963, 1967; Hager 1983) is accurate at the brink section. The results of Jaeger (1948) indicate a dramatic departure from these conditions at the brink section.

The distributions of $R_s/R(v)$ and $\theta/\theta_s(v)$ were determined for the flow net of Rouse (1933), using 8 equipotentials and 8 streamlines (Fig. 3.28a). The results obtained for 3 of these are plotted in Fig. 3.28b–d. The exponents K and m were adjusted to fit Eqs. (3.431) and (3.432) to the 2D distributions obtained from the flow net. The values obtained are indicated in the figure, as well as the resulting distributions. The distributions for $K = m = 1$ (Matthew 1963) are further considered there. The flow net may be divided into two zones, namely the flow zones up- and downstream of the brink section. An analysis of the upstream portion reveals that as $N/R_s \to 0$, away from the brink section, both K and $m \to 1$. As the brink section is approached, N/R_s increases, streamline curvature and slope effects

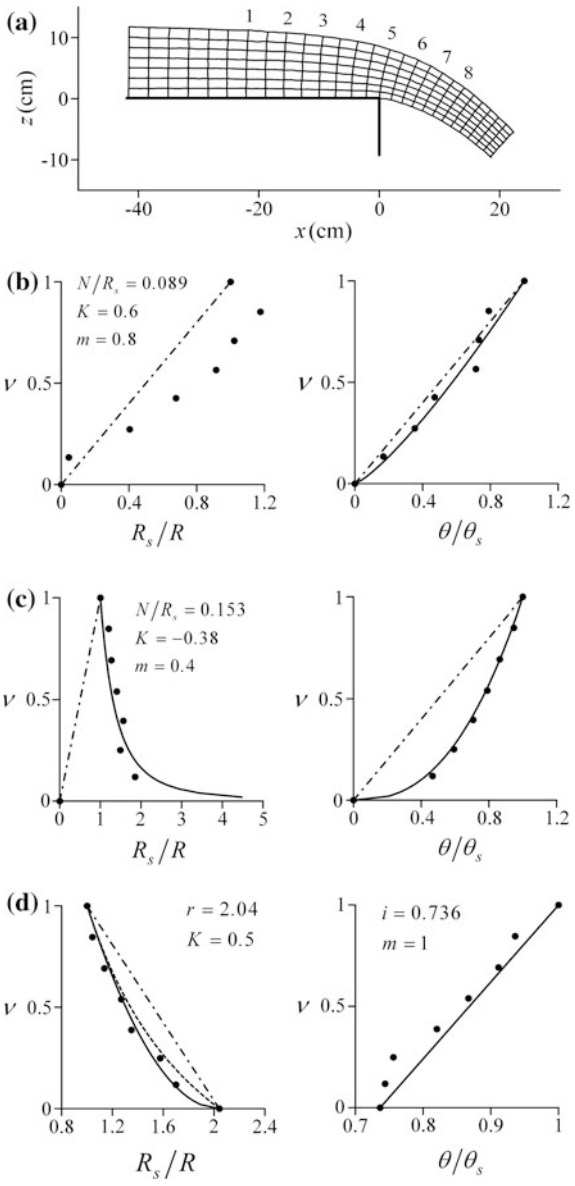

Fig. 3.28 Flow net parameters for free overfall flow: **a** flow net, with 8 equipotential lines labeled (Rouse 1933), (—) $R_s/R(v)$ and $\theta/\theta_s(v)$ from Fawer's theory, Eqs. (3.431) and (3.432), using actual values of K and m fitting flow net data, (– • –) $R_s/R(v)$ and $\theta/\theta_s(v)$ from Matthew's theory, Eqs. (3.431) and (3.432), using $K = m = 1$, (- - -) $R_s/R(v)$ from Jaeger's theory, Eq. (3.433), (•) flow net data for equipotential number (b) 3, (c) 5, (d) 6 (adapted from Castro-Orgaz 2010a)

become important, and K and $m < 1$, resulting in nonlinear relations for $R_s/R(v)$ and $\theta/\theta_s(v)$. The typical curvature distribution in horizontal channels implies $R_s/R(v)$ increasing from the bottom to the free surface. The free jet flow downstream of the brink section may be considered as flow over a curved bottom with the particularity that the bottom pressure is atmospheric. Faraway from the brink, $R_s \to R_b$ and $K \to 1$, corresponding to the concentric streamline flow. In contrast, the typical

curvature distribution over curved channel bottoms implies that $R_s/R(v)$ decreases from the bottom to the free surface. The curvature distribution is therefore inverse as compared to the horizontal and "curved" bottom portions of the free overfall, indicating that the brink section is a hydraulic transition between these two zones. The approximations $K = m = 1$ close to the brink section are generally not accurate.

The equipotential curve at the brink section is considered in Fig. 3.28c. The curvature distribution is seen to be similar to that of a curved bottom, with $R_s/R(v)$ increasing from the free surface to the bottom. At $v = 0$ there is, however, a discontinuity imposed by the horizontal bottom, implying $R_s/R(v) \to 0$. Fitting the flow net results with the distribution law $R_s/R(v) = v^K$ yields $K = -0.38$ (Castro-Orgaz 2010a), thereby implying a dramatic drop below the standard value $K = 1$. Jaeger (1948) proposed $K = -0.5$. These results are in agreement with the findings of Fig. 3.19 using the moment of momentum method. Note from Fig. 3.28b for equipotential number 3 that is just upstream of the brink section, the flow net is transitional from the standard curvature distribution of a horizontal channel to the actual distribution of the free overfall. The first section downstream of the brink section (Fig. 3.28d) gives $K < 1$, resulting from $r > 1$. The distribution $\theta/\theta_s(v)$ also drops from $m = 1$ as the brink section is approached, yet with a linear distribution $\theta/\theta_s(v)$ recovery in the jet zone.

The linear approach for R according to Jaeger (1956) is, from Eq. (3.234),

$$\frac{R_s}{R} = \frac{1}{(1/r) + [1 - (1/r)]v}. \tag{3.433}$$

This distribution is considered for the jet flow portion in Fig. 3.28d, resulting in good agreement with 2D data.

3.9 Transition from Mild to Steep Slopes

3.9.1 Picard Iteration

Transitional flows from mild to steep bottom slopes, where the flow changes from sub- to supercritical conditions, are smooth and curved, involving a continuous free surface profile and a significant departure from the bottom piezometric pressure profile from the free surface (Fig. 3.29). The transitional flow profile $h = h(x)$ from mild to steep slopes was analyzed by Massé (1938) using the singular point method applied to the gradually varied open-channel flow equation. Assuming a hydrostatic pressure distribution, this approach does not predict the detailed 2D flow features in a vertical plane associated with curvilinear streamlines, so that it is only considered an estimate for $h(x)$. The singular point analysis relates to a finite free surface slope at the location of the critical depth, contrary to the unrealistic vertical flow profile of standard gradually varied flows (Chow 1959; Henderson 1966). Although the singular point method approximates weakly curved flows from mild to steep slopes,

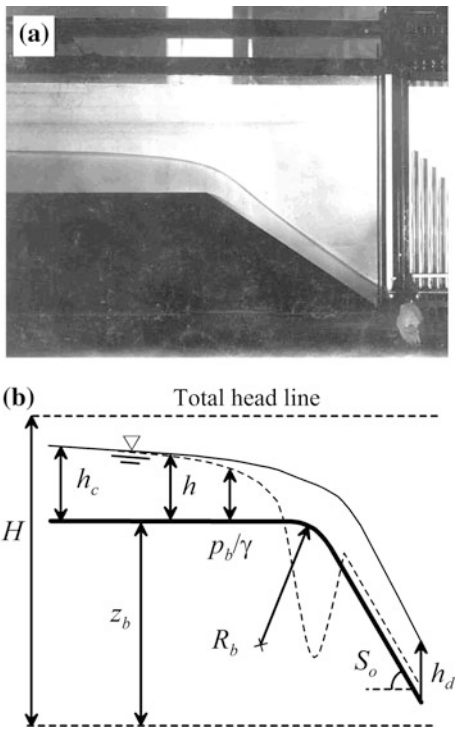

Fig. 3.29 Transitional flow from mild to steep bottom slopes: **a** photograph of experimental test (Rouse 1932), **b** definition sketch (adapted from Castro-Orgaz and Hager 2009)

it does not predict the detailed flow features like the non-hydrostatic bottom pressure (Castro-Orgaz and Hager 2009). At an abrupt slope break (Fig. 3.29a), the flow separates at the bottom kink (Rouse 1932; Weyermuller and Mostafa 1976), a feature beyond the scope of the Boussinesq equations.

The inclusion of streamline curvature effects in the open-channel flow equation due to Boussinesq (1877) assumes a linear velocity distribution normal to the channel bottom, resulting in a pseudo-2D approach. Similar closure hypotheses were advanced, e.g., by Fawer (1937), Matthew (1963, 1991), Mandrup Andersen (1975), or Hager and Hutter (1984a). Mandrup Andersen (1975) used a Boussinesq-type energy equation for slope breaks of less than 5° obtaining fair agreement with his own test data. However, his approximation was not compared with severe slope breaks of, say, larger than 30°, involving strong curvilinear effects, as are typical in hydraulic engineering. The mathematical development of Boussinesq-type equations is commonly subjected to small streamline curvature (Hager and Hutter 1984a). Interestingly, as discussed by Matthew (1995) and Castro-Orgaz and Hager (2009, 2013), their range of application may be much larger than expected from the limited mathematical constraints. In this section, transitions from a horizontal to a steeply sloping rectangular channel reach are studied to analyze the application range of the Boussinesq-type equation, following Castro-Orgaz and Hager (2009). Slope breaks with a rounded transition from the

brink section to the tailwater channel slope are considered and compared with the potential flow solution based on the Laplace equation (Montes 1992a, 1994a). The Boussinesq-type equation is further compared with the test data of Hasumi (1931) and Westernacher (1965) for transitions with a large downstream slope to investigate the strong curvilinear gravity effect.

The Picard iteration technique results in the ODE for the water surface profile (Eq. 3.70)

$$H = z_b + h + \frac{q^2}{2gh^2}\left(1 + \frac{2hh_{xx} - h_x^2}{3} + hz_{bxx} + z_{bx}^2\right) = \text{const.} \tag{3.434}$$

As previously, Eq. (3.434) differs from the earlier results of Hager and Hutter (1984a) and Hager (1985a) in the definition of the flow depth. However, both results are correct to the same order of accuracy (Appendix E). Equation (3.434) is a second-order differential equation from which the free surface profile $h = h(x)$ ensues. For given H and prescribed boundary conditions at the two extreme channel sections, Eq. (3.434) may be solved numerically. The velocity distributions $u(\eta)$ and $w(\eta)$ are then computed from Eqs. (3.63) and (3.64) and the pressure distribution $p(\eta)$ deduced from the Bernoulli equation given by Eq. (3.66). The bottom (subscript b in Fig. 3.29b) pressure profile $p_b = p(\eta = 0)$ is obtained from Eq. (3.72) as

$$\frac{p_b}{\gamma} = h + \frac{q^2}{2gh^2}\left(2hz_{bxx} + hh_{xx} - h_x^2 - 2z_{bx}h_x\right). \tag{3.435}$$

Test data of Hasumi (1931) and Westernacher (1965) indicate that the critical depth $h_c = (q^2/g)^{1/3}$ for parallel-streamlined flows is established on the horizontal slope portion, at a distance of around $3h_c$ upstream of the brink section or more, located at the start of the circular arc transition. At the critical section, a hydrostatic pressure distribution prevails (Westernacher 1965). A Cartesian coordinate system (x, z) is placed at the brink section, with a circular-shaped transition of radius R_b connecting the horizontal and the tailwater reaches (Fig. 3.29b). Thus, the upstream (subscript u) boundary condition $h_u = h(x_u = -3h_c) = h_c$ is used for computational purposes. This critical flow condition at the upstream boundary section fixes the energy line on the horizontal bottom ($z_b = 0$) to $H = 3h_c/2$. The downstream (subscript d) boundary condition is set where the streamlines are assumed to be nearly parallel to the channel bottom. The resulting condition is given by Eq. (3.251) (Montes 1994a; Hager 1999a). The downstream flow depth h_d thus must satisfy Eq. (3.251). Based on the test data of Hasumi (1931) and Westernacher (1965), $x_d \cong +3h_c$.

The computational domain $-3 \leq x/h_c \leq +3$ was divided into 120–180 computational nodes, depending on whether the final selection for x_d was $+3h_c$ or larger, as discussed below. The terms h_{xx} and h_x in Eq. (3.434) were estimated with 5-point central finite differences as (Abramowitz and Stegun 1972)

$$h_x = \frac{-h_{i+2} + 8h_{i+1} - 8h_{i-1} + h_{i-2}}{12\Delta}, \tag{3.436}$$

$$h_{xx} = \frac{-h_{i+2} + 16h_{i+1} - 30h_i + 16h_{i-1} - h_{i-2}}{12\Delta^2}, \tag{3.437}$$

to reduce truncation errors, with i as the computational node index in the x-direction and Δ as the step length, which was successively reduced until the numerical solution converged. The terms h_x and h_{xx} for the computational nodes near the extreme boundary section were estimated with 3-point central finite differences, to avoid imaginary nodes outside the computational domain. Equations (3.436) and (3.437) were substituted in Eq. (3.434), resulting in a system of nonlinear implicit equations for flow depth h_i at each computational node. The system of equations was solved iteratively as an optimization problem (Castro-Orgaz and Hager 2009).

Equation (3.434) is based on the assumption that the boundary streamlines, given by the free surface and the bottom profiles, are continuous at least up to second-order derivatives. The problem treated consists of a horizontal channel followed by a steep chute, connected by a circular arc transition. This bottom geometry is continuous in the bottom slope, but the bottom curvature has discontinuities at both the start and the end of the transition. The bottom profile thus violates the assumptions of Eq. (3.434) at two computational nodes. A first solution of the numerical model of Eq. (3.434) was made, and the discontinuities were removed with a numerical estimation of bottom curvature from a 5-point central finite-difference representation. Once $h = h(x)$ was found, $p_b = p_b(x)$ was computed from Eq. (3.435) using the numerical results. The curvature term at the downstream end of the circular arc generated an abrupt peak with this method. However, this resulted in excellent computed free surface profiles $h = h(x)$. Thus, a smoothed curve for the bottom profile in the circular arc transition was added to provide a continuous transition of bottom curvature and to improve $p_b = p_b(x)$. A fifth-degree polynomial was employed to approximate the circular arc profile $z_b/R_b = -1 + [1 - (x/R_b)^2]$. The free surface profile $h = h(x)$ was numerically determined using the smoothed transitional curve, resulting in almost the same result as computed previously, but significantly improving $p_b = p_b(x)$ (Castro-Orgaz and Hager 2009).

The numerical results of Eq. (3.434) are compared in Fig. 3.30 with the experimental data of Hasumi (1931) for $S_o = 1$ and 1.732, and $R_b/h_c = 1.59$, 1, and 0.76. These compare favorably with observations, even for $R_b/h_c = 0.76$ and $S_o = 1.732$ (60°) corresponding to highly curvilinear flows. The model results are further compared in Fig. 3.31 with the free surface profiles of Westernacher (1965) from potential flow nets for $S_o = 1.5$ and $R/h_c = 1.6$ and 2.57, resulting again in excellent agreement. As mentioned, the downstream boundary condition Eq. (3.251) was generally set at $x_d \cong +3h_c$. However, computational results indicated that the boundary section had to be moved to $x_d \cong +3.5h_c$ in certain simulations. If the downstream boundary section was located too close to the brink section, an abrupt drawdown of the flow profile $h = h(x)$ near x_d resulted in an

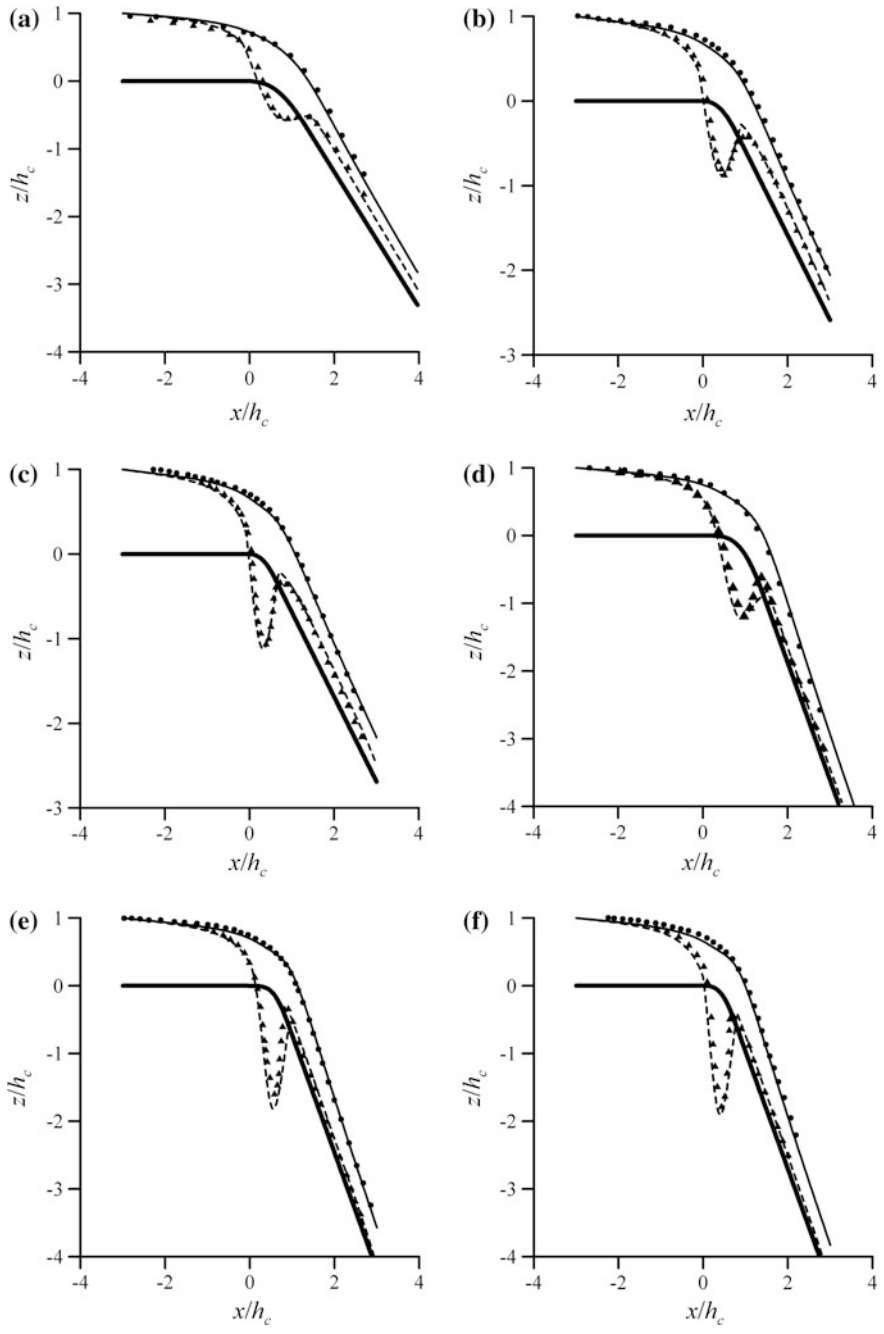

Fig. 3.30 Comparison of computed $(h + z_b)/h_c$ from Eq. (3.434) (—) and $(p_b/(\gamma) + z_b)/h_c$ from Eq. (3.435) (- - -) with measured free surface (•) and bottom pressure head of (▲) Hasumi (1931) for $[R_b/h_c;S_o]$ = **a** [1.59;1], **b** [1;1], **c** [0.76;1], **d** [1.59;1.732], **e** [1;1.732], **f** [0.76;1.732] (adapted from Castro-Orgaz and Hager 2009)

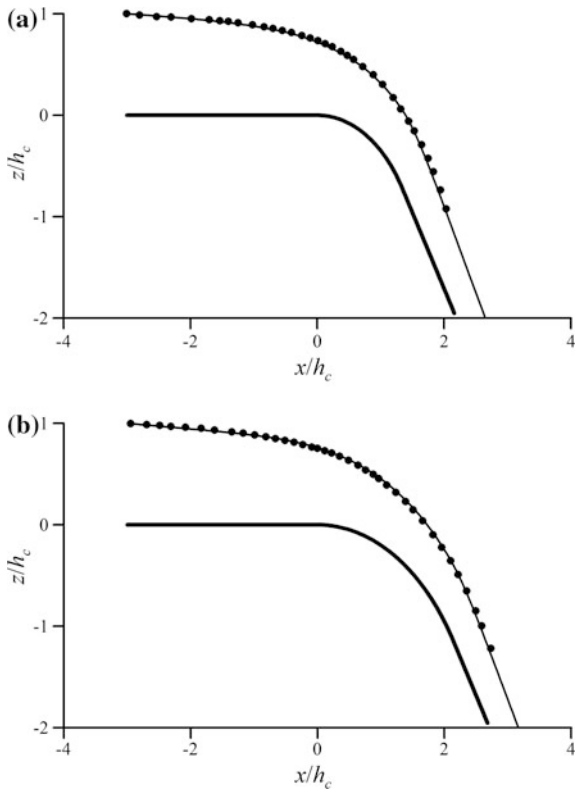

Fig. 3.31 Comparison of (—) computed $(h + z_b)/h_c$ from Eq. (3.434) with (•) measured free surface profiles of Westernacher (1965) for $[R_b/h_c;S_o]$ = **a** [1.6;1.5], **b** [2.57;1.5] (adapted from Castro-Orgaz and Hager 2009)

unrealistic, subatmospheric pressure peak $p_b = p_b(x)$ close to this section x_d, due to the significant effect of the Boussinesq terms h_x and h_{xx} in Eq. (3.435). This mathematical effect was removed simply by increasing x_d until the entire profile $p_b = p_b(x)$ on the steep slope was nearly parallel to the channel bottom. If x_d is located too close to the brink section, the profile $h = h(x)$ of necessity generates an abrupt drawdown to satisfy the parallel flow boundary condition imposed at x_d. This drawdown implies both h_x and $h_{xx} < 0$, so that p_b close to x_d reduces above its correct value for nearly parallel-streamlined flow. The position of the downstream boundary condition has to satisfy the original hypothesis of nearly parallel-streamlined flow, allowing to determine x_d by iteration, until the stable solution is obtained.

There have been few attempts to model curved flow at slope breaks using the Boussinesq equations, among which are Khan and Steffler (1995, 1996a). They obtained vertically averaged momentum and moment of momentum equations starting with RANS 2D equations, solving the resulting system of equations using a finite-element technique. The starting equations and numerical technique are different from Castro-Orgaz and Hager (2009). Therefore, it is of interest to study this alternative technique for steep slope flows. Khan and Steffler (1995) solved their

system of equations by adopting a Boussinesq-type approximation, involving the following specifications:

(i) Velocity profile in the x-direction is uniform and equal to its depth-averaged value U,
(ii) Pressure distribution is non-hydrostatic and linear, with p_1 as difference between the bottom pressure head p_b/γ and the flow depth h,
(iii) Turbulent stresses, including the bed-shear stress, are neglected. Their equation for the vertical momentum is [see Chap. 2, Eq. (2.83) for steady flow and zero bed-shear stress)]

$$\frac{\partial}{\partial x}\left[\frac{hU}{2}(w_s + w_b)\right] - \frac{p_1}{\rho} = 0, \tag{3.438}$$

where

$$w_b = U\frac{\partial z_b}{\partial x}, \quad w_s = U\frac{\partial (z_b + h)}{\partial x}. \tag{3.439}$$

Khan and Steffler (1995) made no assumptions regarding the bottom slope S_o, which therefore can also be steep. They solved their system of equations by the finite-element technique and found good agreement for both free surface and bottom pressure predictions on steep slopes. Khan and Steffler (1996a) expanded their simulations to cover more test cases, with generally good agreement of their Boussinesq model with the data. They found that the inclusion of the moment of momentum equations improved the solutions even though the Boussinesq system had already generated physically satisfactory results. Montes (1995) suggested combining Eqs. (3.438)–(3.439) to produce a single equation for p_1 as

$$\frac{p_1}{\rho} = \frac{q^2}{2}\frac{\mathrm{d}}{\mathrm{d}x}\left[\frac{2z_{bx} + h_x}{h}\right]. \tag{3.440}$$

Thus, by performing the differentiations, it is simple to obtain the bottom pressure equation modeled by Khan and Steffler (1995, 1996a), which is identical to Eq. (3.435).

The computed brink depth $h_b = h(x = 0)$ as a function of S_o for $R_b/h_c = 1$ using Eq. (3.434) is compared in Fig. 3.32a with the solution of the Laplace equation (Montes 1994a), given by Eq. (3.250). The Laplace equation predicts a nearly constant value $h_b \approx 0.70$ for $S_o > 1$, whereas the extended Boussinesq equation yields $h_b \approx 0.68$. Given the high numerical accuracy obtained with the present discretization scheme, this difference appears to be a consequence of the order of expansion in Eq. (3.434). Test data of Mandrup Andersen (1975) and Weyermuller and Mostafa (1976) for small downstream slopes also corroborate the results of the Boussinesq model, with imperceptible differences from the Laplace equation.

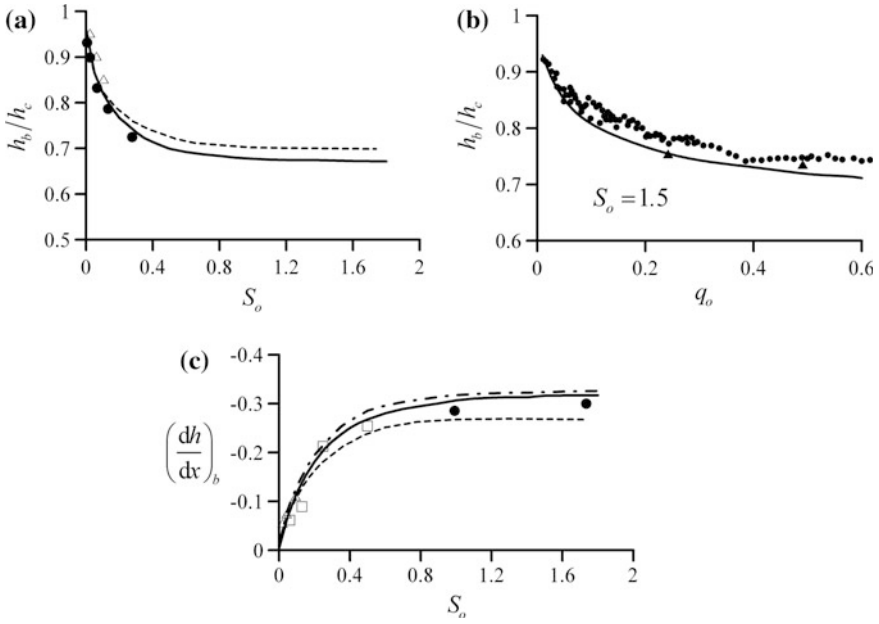

Fig. 3.32 Brink depth results: **a** $h_b/h_c(S_o)$ for $R_b/h_c = 1$ from (—) Eq. (3.434), (- - -) Eq. (3.250), test data of (•) Weyermuller and Mostafa (1976), (▵) Mandrup Andersen (1975), **b** $h_b/h_c(q_o)$ from (—) Eq. (3.434) for $S_o = 1.5$, Westernacher (1965) (▲) 2D potential flow, (•) test data, **c** $dh_b/dx(S_o)$ from (—) Eq. (3.434) for $R_b/h_c = 1$, (- - -) Eq. (3.250), (– – –) Eq. (3.441), test data of (▫) Weyermuller and Mostafa (1976), (▵) Mandrup Andersen (1975), (•) Hasumi (1931) (adapted from Castro-Orgaz and Hager 2009)

The model results for h_b are compared in Fig. 3.32b with the test data of Westernacher (1965) for $S_o = 1.5$ versus the dimensionless discharge $q_o = q/(gR^3)^{1/2}$. The computed curve from Eq. (3.434) is slightly below the test data because of a small viscous effect. The brink depth results based on potential flow nets by Westernacher (1965) are also included, resulting in fair agreement with Eq. (3.434).

Based on Fig. 3.32b, the transition from mild to steep slopes is proposed as a simple and accurate flow-measuring device, similar to a free overfall. As shown in Fig. 3.32b, the brink depth ratio h_b/h_c varies only with R_b/h_c, or $q_o = (R_b/h_c)^{-3/2}$ if $S_o > 1$. Figure 3.32b indicates the general relation $h_b/h_c(q_o)$ ($S_o = 1.5$) without any chute slope effect. Measuring h_b, q is assumed, and $h_c = (q^2/g)^{1/3}$ is determined, resulting in $q_o = (R_b/h_c)^{-3/2}$. Estimating h_b/h_c, q_o is obtained with Fig. 3.32b, to be compared with the value previously assumed. This iterative sequence is repeated until sufficient convergence is achieved. For practical purposes, the curve of Fig. 3.32b is approximated by the empirical equation $h_b/h_c = 0.70q_o^{-0.06}$ for $0.01 < q_o < 0.60$ so that q_0 is directly obtained for a given h_b.

The free surface slope $(dh/dx)_b$ at the brink section is successfully compared with the Laplace equation in Fig. 3.32c, predicting a limiting value of $(dh/dx)_b = -0.27$ (15.1°), whereas the Boussinesq energy equation yields $(dh/dx)_b = -0.31$ (17.22°). Test data of Mandrup Andersen (1975), Weyermuller and Mostafa (1976), and Hasumi (1931) also agree with the results from Eq. (3.434). The equation for the free surface slope at a free overfall (Matthew 1995) (Eq. 3.281),

$$h_x^2 = 3\left(1 - \frac{h_b}{h_c}\right)^3, \tag{3.441}$$

was also inserted in Fig. 3.32c, using the computed values for h_b based on Eq. (3.434), resulting in excellent agreement with the numerical results. Accordingly, there is a strong analogy between the flows over a free overfall and the transition from mild to steep slopes.

The potential flow equations are based on a constant energy head along the entire computational domain. Obviously, this is true near the slope break, but solutions cannot be expected to be valid far downstream on the steep slope portion up to infinity. A potential flow model cannot reach asymptotic uniform flow conditions on a steep slope. Thus, the bottom pressure computation for steep slopes using potential Boussinesq equations, as done here, is limited to a finite portion of the crest–slope domain. The crest is a zone of engineering interest, given the minimum bottom pressure there and the risk of cavitation. Streamline curvature is important at the crest (Fig. 3.30). Further downstream on the chute, the pressure is non-hydrostatic due to slope effects (Fig. 3.30). Consider for illustrative purposes flows away from the crest, on the chute slope. The flow there is gradually varied, so that the variation of h with x is small; this hypothesis is confirmed by the experimental data of Hasumi (1931) plotted in Fig. 3.30. For these flows, it can be assumed that $h_x^2 \approx h_{xx} \approx 0$. Further, on the slope, the bottom is flat, resulting in $z_{bxx} = 0$, whereas the term z_{bx} is finite. Thus, retaining only slope effects, Eq. (3.434) reduces, with $S_o = -z_{bx}$, to

$$H = z_b + h + \frac{q^2}{2gh^2}\left(1 + z_{bx}^2\right) = z_b + h + \frac{q^2}{2gh^2}\left(1 + S_o^2\right) = \text{const.} \tag{3.442}$$

Its differential produces the 1D gradually varied flow equation for potential flow in a sloping channel as

$$\frac{dh}{dx} = \frac{S_o}{1 - \left[\frac{q^2}{gh^3}\left(1 + S_o^2\right)\right]}. \tag{3.443}$$

Uniform flow $dh/dx = 0$ cannot be reached at any point of the slope, as seen from Eq. (3.443). This highlights that the potential flow Eq. (3.443) cannot reach the uniform flow depth at the downstream slope, and therefore, its validity is confined to the slope break domain, as applied by Castro-Orgaz and Hager (2009), to predict

the flow features near the slope break. The computations are in agreement with the ideal 2D solution (Montes 1994a), that is also valid in the slope break domain where transitional flow conditions develop. To set the boundary conditions as uniform flow at $x \to +\infty$, friction should be included as presented in Chap. 2, Sect. 2.4.6, Eqs. (2.82)–(2.85). Close to the crest in the chute slope portion, a hypercritical flow approach as given by the condition $\mathsf{F} = q/(gh^3)^{1/2} > 3$ (Castro-Orgaz 2009; Castro-Orgaz and Hager 2009) simplifies Eq. (3.443) to

$$\frac{\mathrm{d}h}{\mathrm{d}x} = -S_o \left[\frac{q^2}{gh^3}\left(1 + S_o^2\right)\right]^{-1} \Rightarrow \frac{q^2}{gh^3}\mathrm{d}h = -\frac{S_o}{1 + S_o^2}\mathrm{d}x. \tag{3.444}$$

Using the boundary condition $h(x = 0) = h_c$, its general solution is

$$\frac{h}{h_c} = \left(1 + \frac{2S_o}{1 + S_o^2}\frac{x}{h_c}\right)^{-1/2}. \tag{3.445}$$

As previously noted, $x \to +\infty$ implies $h \to 0$, thereby requiring the consideration of real fluid flow features. This is achieved by using a turbulent flow model based on the RANS equations as presented in Chap. 2 or employing a boundary layer approximation (Chap. 5) (Castro-Orgaz 2009). Figure 3.33 shows that Eq. (3.445) yields almost the same result as Eq. (3.434) for $x/h_c > 1$, resulting in an accurate approximation for the chute flow portion. The hypercritical approach derived from the gradually varied flow theory, therefore, applies to the slope reach, along which the term z_{bx} is finite. Therefore, although h_x as given by Eq. (3.444) is small, the product $(h_x\, z_{bx})$ remains finite. Assuming that $h_x^2 \approx h_{xx} \approx 0$, and inserting Eq. (3.444), the bottom pressure head is from Eq. (3.435)

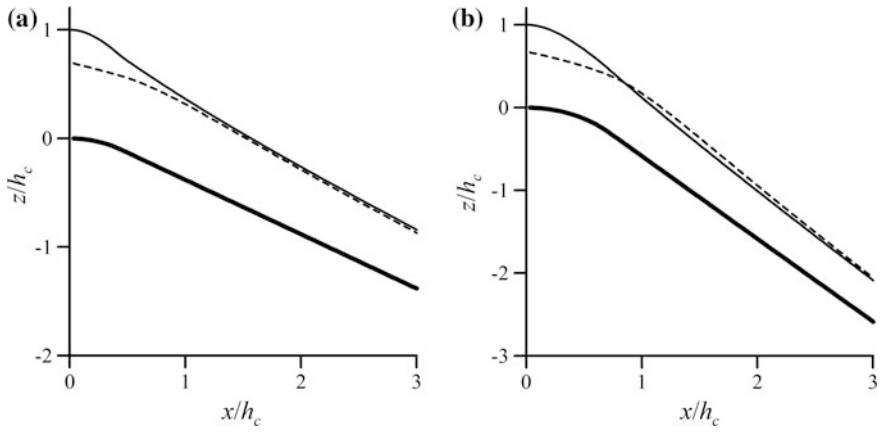

Fig. 3.33 Comparison of computed profiles $(h + z_b)/h_c[x/h_c]$ from (- - -) Eq. (3.434) and (—) Eq. (3.445) for $R_b/h_c = 1$ and $S_o =$ **a** 0.5, **b** 1

$$\frac{p_b}{\gamma} = h - \frac{q^2}{2gh^2}(2z_{bx}h_x) = h\left(1 - \frac{z_{bx}^2}{1+z_{bx}^2}\right) = \frac{h}{1+S_o^2}. \tag{3.446}$$

Equation (3.446) is the 1D, potential, gradually varied flow approximation for the bottom pressure head in a finite slope.

For potential flows over a curved bottom, the momentum equation applies in the form

$$\frac{\mathrm{d}S}{\mathrm{d}x} = -z_{bx}\frac{p_b}{\gamma}, \quad S = \left(H - z_b - \frac{h}{2}\right)h + \int_{z_b}^{h+z_b}\left(\frac{u^2 - w^2}{2g}\right)\mathrm{d}z, \tag{3.447}$$

as used by Naghdi and Vongsarnpigoon (1986) and Matthew (1995). This equation indicates that a model based on the momentum principle depends on the particular function used to model the vertical velocity profile $w = w(z)$. Following Khan and Steffler (1995), a linear vertical velocity profile is no reason for solution failure of the Boussinesq equations; the resulting S function is then (Matthew 1995)

$$S = \left(H - z_b - \frac{h}{2}\right)h + \frac{q^2}{2gh}\left(1 - z_{bx}^2 - z_{bx}h_x - \frac{h_x^2}{3}\right). \tag{3.448}$$

However, a higher order approximation is desirable for accurate results (Khan and Steffler 1996a; Matthew 1991). For potential flow, both the energy and momentum equations are applied to model such flows (Hager and Hutter 1984a). However, as the energy head H remains constant within the entire computational domain, the use of the energy equation is advantageous. By contrast, S is not a conserved quantity, and the corresponding streamwise variation must be determined by resorting to Eq. (3.447). These complications, combined with the necessity of using an accurate predictor of w for higher order modeling, render the use of the energy head equation for potential channel flows advisable and, fortunately, also simple. For potential free surface flows over a curved bottom, the *exact equation* at the free surface with (u_s, w_s) as the velocity components at the free surface is (Eq. 3.67)

$$H = z_s + \frac{V_s^2}{2g} = z_s + \frac{u_s^2 + w_s^2}{2g} = z_b + h + \frac{u_s^2}{2g}\left[1 + (h_x + z_{bx})^2\right]. \tag{3.449}$$

This equation indicates that the extended energy head model depends only on the value of u at the water surface ($z_s = z_b + h$). This result is independent of the vertical velocity profile, as it correctly accounts for the kinematic boundary condition at the free surface. Thus, the accuracy of the 1D potential flow model [i.e., Eq. (3.449)] is directly constrained by the accuracy of u, but is independent of w. Extended energy-type Boussinesq's models for potential flows are, therefore, independent of the vertical velocity profile.

3.9.2 Two-Dimensional Solution

In this section, the functions $u^{(2)}$ and $u^{(3)}$ of the Picard iteration (Eqs. 3.63, 3.78) are scrutinized as predictors of u along the entire computational domain of a slope break. They are investigated by comparison with a detailed 2D flow solution using semi-inverse mapping or the x-ψ method described in Sect. 3.7 (Montes 1992a, b, 1994a). Derivatives of h, h_x, h_{xx}, h_{xxx}, and h_{xxxx} were determined numerically using accurate 5-point central finite differences based on the 2D results. To start the solution of Laplace's equation (Eq. 3.250), an initial free surface profile $h = h(x)$ and the energy head H must be prescribed for the selected discharge q. As initial free surface profile, the numerical solution of Eq. (3.434), previously described, was used. Once the initial free surface profile is set, the free surface position is iteratively corrected with a Newton–Raphson algorithm until reaching the desired tolerance in the zero pressure boundary condition at the free surface. The correction is based on Eq. (3.427), previously applied to the upper free surface of a free overfall (Montes 1994a; Castro-Orgaz 2013b). Figure 3.34 considers one of the test cases of Hasumi (1931) for a slope transition composed by a horizontal reach followed by a circular-shaped transition profile of $R_b = 0.1$ m that finishes in a steep slope reach of 45° inclination. The discharge is 0.987 m^2/s ($h_c = 0.10$ m). The up- and downstream boundary sections were located at $x/h_c = \pm 3$. Twenty streamlines were used to model this flow. The initial free surface profile was determined for $H/h_c = 1.5$ by solving Eq. (3.434). The free surface position was moved iteratively until the mean pressure along the free surface was reduced to 0.25 mm, taking some 50 iterations. The initial [solution of Boussinesq's Eq. (3.434)] and final free surface profiles are plotted in Fig. 3.34a, showing only minor deviations.

The computed water surface and bottom pressure profiles are successfully compared in Fig. 3.34b with the experimental data of Hasumi (1931). The streamline flow pattern obtained from the 2D solution is given in Fig. 3.34c. The computed free surface and piezometric bottom pressure head profiles obtained from the 2D model are compared in Fig. 3.34d with the 1D gradually varied flow approximations for a finite slope, namely Eqs. (3.445) and (3.446). These are plotted for $x/h_c > 1$, as suggested by Castro-Orgaz and Hager (2009). Note the excellent agreement, thereby confirming the leading role of S_o on the non-hydrostatic effects there.

The 2D potential flow data are plotted in Fig. 3.35 at 7 vertical sections representative of the flow domain. The variations of u and w along the computational domain are extreme, given the high operational head of $E/R_b = 1.5$. Note that $u^{(2)}$ agrees well with u at all sections. For this test case, $u^{(3)}$ yields better predictions for $x/h_c > 0$ in the curved bottom portion, whereas this is less evident for the straight bottom portion. Note that $w^{(1)}$ is not a good approximation of w, whereas $w^{(2)}$ improves predictions, especially for $x/h_c < 0$. However, even though $w^{(2)}$ is a better prediction of w than $w^{(1)}$, its accuracy is limited for $x/h_c > 0$, given the strong flow curvature. The pressure distribution computed from the 2D flow model reveals a great departure from hydrostatic conditions (Fig. 3.36).

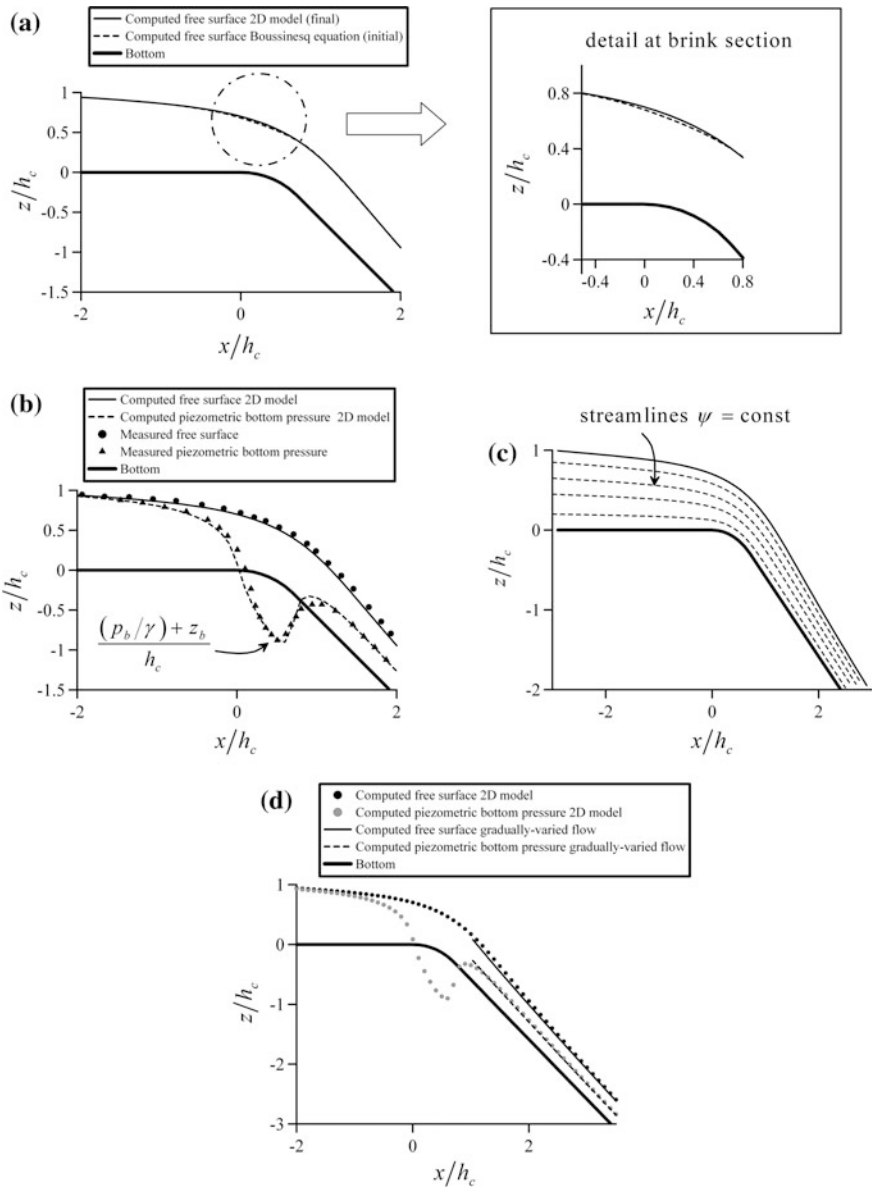

Fig. 3.34 Flow features in slope transition for $R_b/h_c = 1$ and $S_o = 0.5$: **a** initial and final free surfaces, **b** comparison with experiments, **c** potential streamline flow pattern (adapted from Castro-Orgaz and Hager 2013), **d** gradually varied flow solution for $x/h_c > 1$

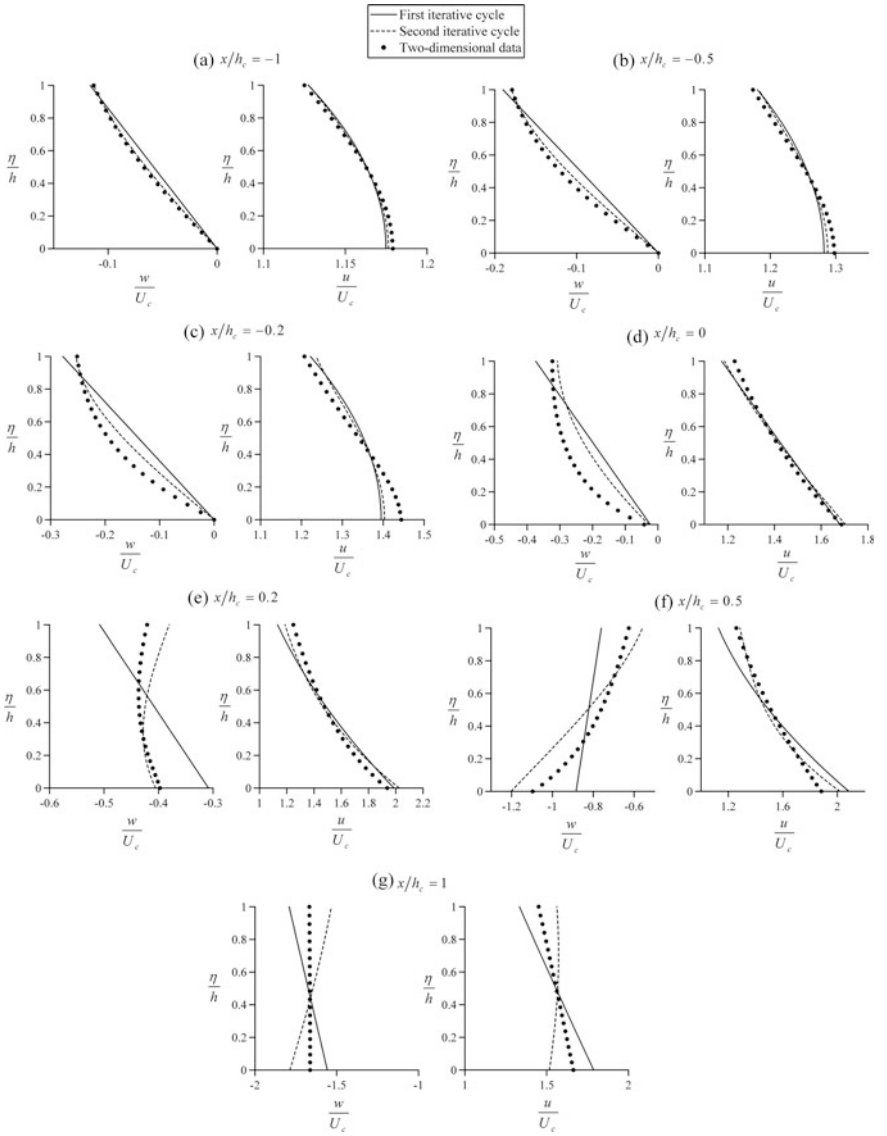

Fig. 3.35 Comparison of (u/U_c, w/U_c) from the 2D solution along the slope transition, with U_c as critical velocity, with predictions from second- and third-order results based on Picard iteration (adapted from Castro-Orgaz and Hager 2013)

The 2D results for u at the brink section of the slope transition are plotted in Fig. 3.37. The Dressler free vortex velocity profile given by Eq. (3.141) may be rewritten as

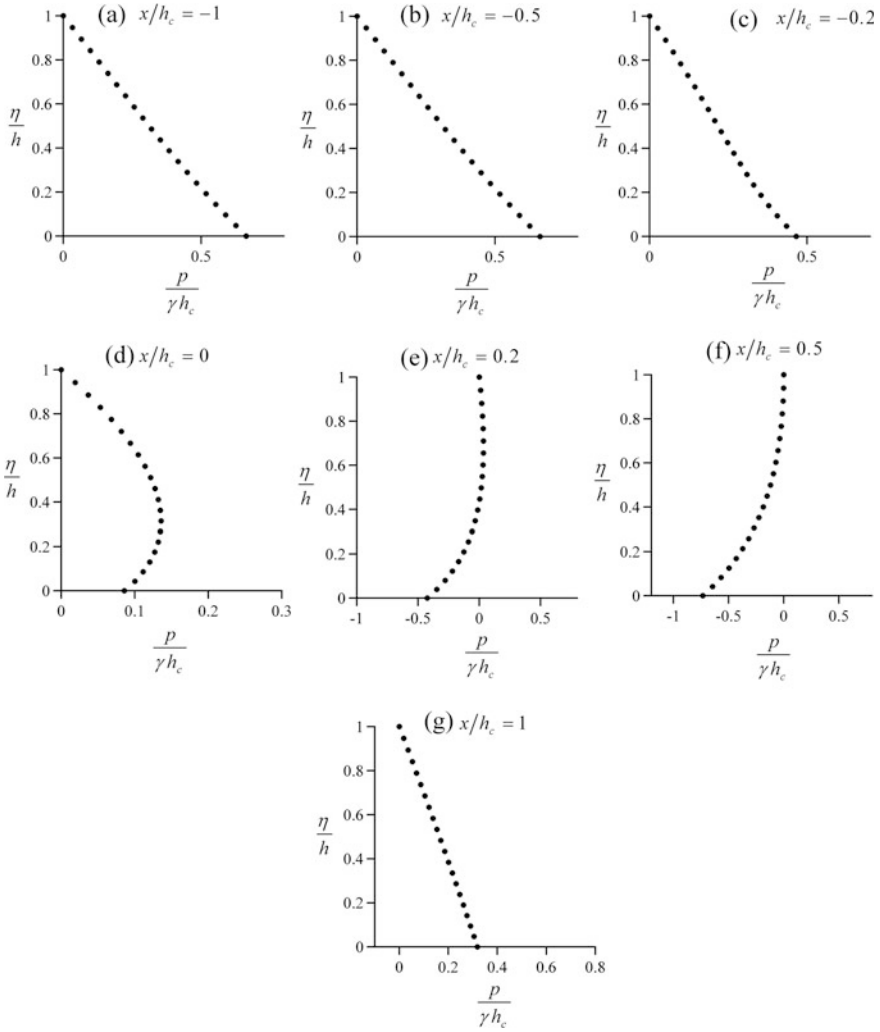

Fig. 3.36 Pressure distributions $p/(\gamma h_c)[\eta/h]$ from the 2D solution along the slope transition for $R_b/h_c = 1$ and $S_o = 0.5$

$$u_\xi = \frac{-q\kappa_b}{(1-\kappa_b\varsigma)\ln(1-\kappa_b N)}. \tag{3.450}$$

Equation (3.450) is plotted in Fig. 3.37 using the computed value of N, comparing excellently with 2D results. Note that at the weir crest, $\varsigma \equiv \eta/h$ and $N \equiv h$. This indicates that the first Picard iteration in curvilinear coordinates gives results comparable to the second iteration in Cartesian coordinates (Castro-Orgaz and Hager 2013).

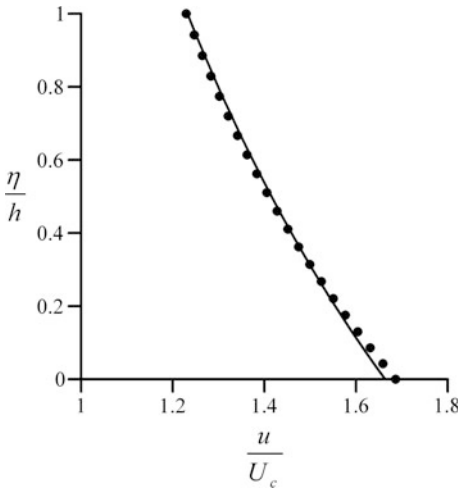

Fig. 3.37 Comparison of results obtained for Dressler's Eq. (3.450) (—) with 2D simulation (•) (adapted from Castro-Orgaz and Hager 2013)

3.9.3 Flow Net

The distributions of $R_s/R(v)$ and $\theta/\theta_s(v)$ were determined for the flow net of Westernacher (1965) for a chute slope of 3:2 (H:V) with a circular arc transition of $R_b = 0.30$ m, considering 10 equipotentials and 7 streamlines (Fig. 3.38a). The results obtained for three of these are plotted in Fig. 3.38b–d similar to the free overfall, this flow net may be divided into two portions, namely up- and downstream from the brink section at the start of the circular arc transition to the downstream chute. Again, the analysis of the upstream portion reveals that as $N/R_s \to 0$ away from the brink section, both $K \to 1$ and $m \to 1$. In the downstream curved portion, $R_s \to R_b$ and $K \to 1$, corresponding to the almost concentric-streamlined flow. Two distribution laws apply for $R_s/R(v)$, relating to the straight and curved bottom portions. The brink section involves, therefore, also a transitional behavior between these distribution types, as shown from Fig. 3.38c, where the streamline curvature distribution changes its shape from the typical law of the horizontal channel (Fig. 3.38b) to that for a curved bottom (Fig. 3.38d). Note the drop to $K = 0.12$ at the brink section. However, this drop is smaller than that for free overfalls because of pressure readjustment as the flow transition is reached. For the free overfall, the bottom pressure vanishes abruptly, whereas for the transition from mild to steep slopes, the pressure remains positive throughout, yet below hydrostatic. Moreover, the distribution of $\theta/\theta_s(v)$ also drops from $m = 1$ as the brink section is approached, with a linear recovery as the tailwater is reached, as for free overfall flow.

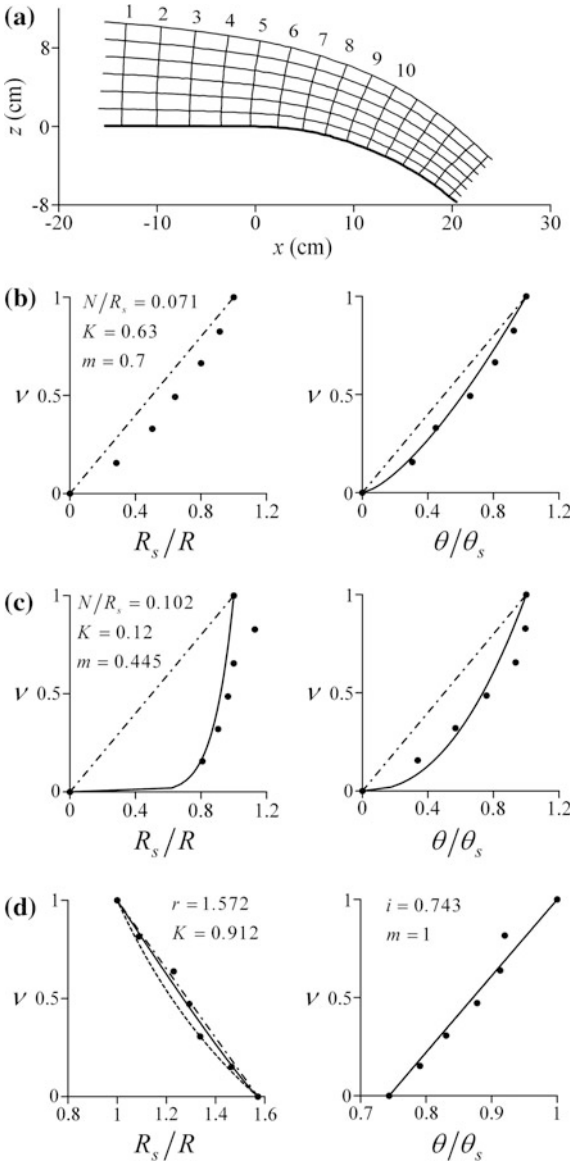

Fig. 3.38 Potential flow at the transition from mild to steep slopes: **a** flow pattern (Rouse 1933), **b** flow net parameters with theory of (—) Fawer, (– • –) Matthew, (- - -) Jaeger, (•) flow net data, for equipotential 2, **c** 5, **d** 9 (adapted from Castro-Orgaz 2010a)

3.10 Flow Over Round-Crested Weirs

3.10.1 Picard Iteration

Open-channel flows passing from sub- to supercritical flow across a critical point F = 1 occur at round-crested weirs if the tailwater level is not drowning the structure (Fig. 3.39). This is an important case of open-channel flow, given its role in discharge measurements structures.

Equation (3.434) also applies to this flow problem. Figure 3.40 displays the experimental data of Sivakumaran et al. (1983) for a symmetrical hump of shape $z_b = 20\exp[-0.5(x/24)^2]$ (cm). The unit discharge is 0.11197 m^2/s ($h_c = 0.1085$ m). The up- and downstream boundary sections were located at $x/h_c = \pm 10$. Equation (3.434) was numerically integrated using the method of Naghdi and Vongsarnpigoon (1986) for flows over an obstacle, using the fourth-order Runge–Kutta method (Press et al. 2007). Equation (3.434) is a second-order differential equation for $h(x)$, so that two boundary conditions, in addition to the total head H, are required for its solution. Following Naghdi and Vongsarnpigoon (1986), a boundary section was taken far upstream of the obstacle, where the bottom is almost horizontal and pressure is essentially hydrostatic. There, the free surface slope was set to $h_x = 0$ and the total head H for an initially assigned value of h_o estimated to $H \approx h_o + q^2/(2gh_o^2)$. With these conditions at the boundary section, Eq. (3.434) was numerically integrated across the weir, transforming it into a system of two first-order ODEs. If the initially assigned value of h_o is too low, the value of H is incorrect, so that the corresponding value of the minimum specific energy at the hump crest is too low and the flow is not able to pass the hump. The computed flow profile thus intersects the bottom profile elsewhere (Naghdi and Vongsarnpigoon 1986; Fenton 1996) (Fig. 3.40a). This indicates that no steady flow solutions are possible. If the initially assigned value of h_o is too high, an

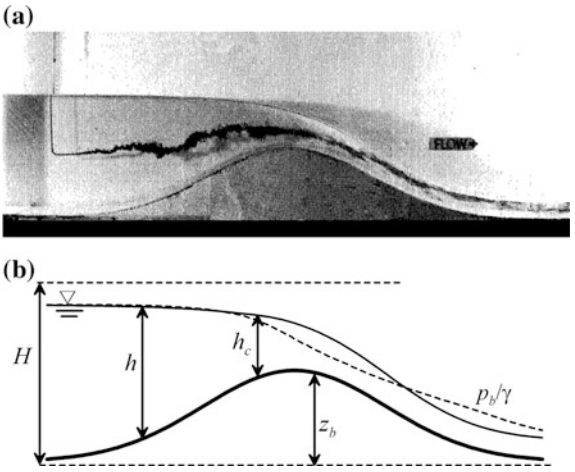

Fig. 3.39 Flow over round-crested weir: (a) experimental image (Sivakumaran 1981), (b) definition sketch

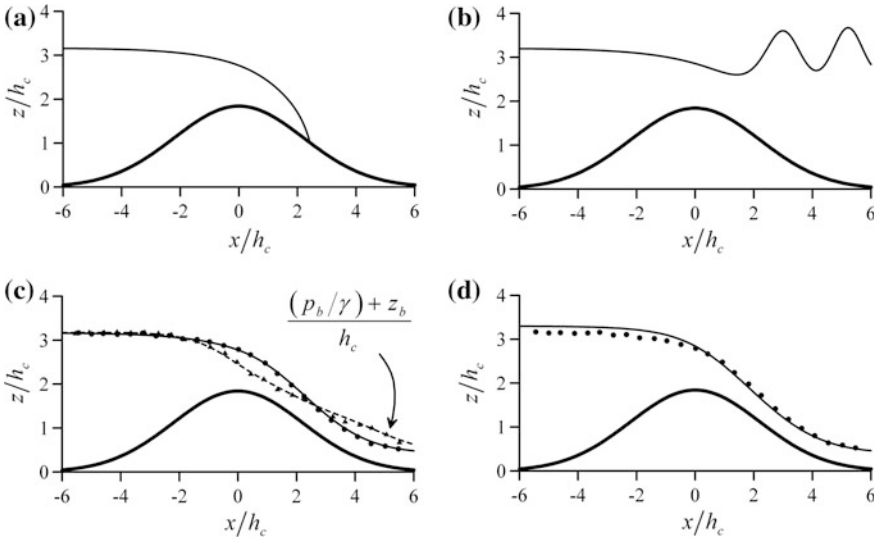

Fig. 3.40 Flow over round-crested weir: **a** (—) computed $(h + z_b)/h_c$ from Eq. (3.434) for a low value of h_o, **b** (—) computed $(h + z_b)/h_c$ from Eq. (3.434) for a high value of h_o, **c** computations using an accurate value of h_o; comparison of (—) computed $(h + z_b)/h_c$ from Eq. (3.434) (Boussinesq's theory) and (- - -) $(p_b/(\gamma) + z_b)/h_c$ from Eq. (3.435), with (•) measured free surface and (▲) bottom pressure head (Sivakumaran et al. 1983), **d** simulation using Eq. (3.451) (Saint-Venant's theory)

undular jump is formed at the tailwater face of the weir (Fig. 3.40b). Thus, h_o was iteratively adjusted as described by Naghdi and Vongsarnpigoon (1986) until a continuous flow profile passing from sub- to supercritical flow resulted. Once the free surface profile was determined, the bottom pressure head was computed using Eq. (3.435). The computed water surface and bottom pressure profiles are compared in Fig. 3.40c with the corresponding test data (Sivakumaran et al. 1983), resulting in excellent agreement.

Shallow-water flows are commonly simulated using the theory of Saint-Venant (1871). For steady flow over a hump, these equations reduce to the ODE (Montes 1998; Hager 1999a)

$$\frac{dh}{dx} = \frac{-\tan\theta_b}{1 - \frac{q^2}{gh^3}}. \tag{3.451}$$

The weir crest flow depth from Eq. (3.451) is the standard critical depth $h_c = (q^2/g)^{1/3}$. The water surface slope at the weir crest is given by (Chen and Dracos 1998; Hager 1999a) (Eq. 3.203)

$$\left(\frac{\mathrm{d}h}{\mathrm{d}x}\right)_c = -\left(-\frac{h_c}{3}\frac{\partial^2 z_b}{\partial x^2}\right)^{1/2}. \tag{3.452}$$

Equation (3.451) was integrated using the fourth-order Runge–Kutta method in the up- and downstream directions. At the weir crest, Eq. (3.452) was used to remove the indetermination. The results are given in Fig. 3.40d. Note that the free surface prediction of Saint-Venant's theory is inaccurate, especially in the upstream subcritical branch, whereas the bottom pressure is only poorly accounted for, given that the water depth is identical to the bottom pressure in this approach.

3.10.2 Dressler's Theory

This theory for flows over curved bottoms is applied here by integrating Eq. (3.167). The boundary condition is given by the critical depth N_c at the hump crest ($\xi = 0$), and N_c was computed by solving Eq. (3.168) using the Newton–Raphson method. Then, Eq. (3.167) was numerically integrated using the fourth-order Runge–Kutta method, employing Eq. (3.172) to remove the singularity of Eq. (3.167) at $\xi = 0$. Computations of sub- and supercritical portions were performed by integrating in the up- and downstream directions, respectively. Once $N(\xi)$ was determined, the bottom pressure profile $p_b(\xi)$ was computed from (Dressler 1978)

$$p_b = \rho g N \cos\theta_b + \rho \frac{q^2 \kappa_b^2}{2[\ln(1-\kappa_b N)]^2}\left[\frac{1}{(1-\kappa_b N)^2} - 1\right]. \tag{3.453}$$

The computed profiles $N(\xi)$ and $p_b(\xi)$ are plotted in Fig. 3.41a, showing good agreement with observations for both the free surface and bottom pressure profiles. The first aspect deserving attention is that Dressler's equations produce a stable and continuous transcritical flow profile over this topography. The previous failure of Sivakumaran et al. (1983) and Fenton (1996) to produce transcritical flow solutions is due to the fact that Eq. (3.167) was solved taking the value of H as given by experiments, whereas H should rather be determined based on the theory itself, respecting the critical flow conditions at the crest of the hump. The minimum specific energy thus fixes the total head H and the flow conditions over the weir. As demonstrated, the free surface and bottom pressure profiles under minimum specific energy at the hump crest are continuous and physically in agreement with observations. Figure 3.41a indicates that the supercritical branch is accurately predicted by Eq. (3.167), given that the flow is essentially concentric. However, the free surface profile computed for the subcritical flow portion is below the experimental data. In this zone of the computational domain, the free surface is roughly horizontal as inferred from the experimental data, but the bottom profile is sloped and

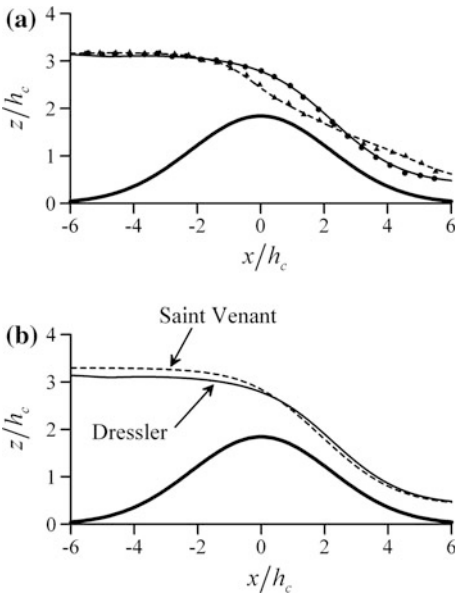

Fig. 3.41 Flow over round-crested weir: **a** comparison of (—) computed $(h + z_b)/h_c$ from Eq. (3.167) and (- - -) $(p_b/(\gamma) + z_b)/h_c$ from Eq. (3.453) with measured (•) free surface and (▲) bottom pressure head (Sivakumaran et al. 1983) (adapted from Castro-Orgaz and Hager 2016), **b** simulation using (—) Eq. (3.167) (Dressler's theory) and (- - -) Eq. (3.451) (Saint-Venant's theory)

curved, so that streamlines are not concentric. It appears that the concentric streamline approximation provokes an excessive drop of the upstream water level as it is fixed by the minimum specific energy over the weir crest based on Eq. (3.167). Saint-Venant's theory is compared with that of Dressler in Fig. 3.41b, indicating relatively large deviations, as previously found in a different experimental setup involving only supercritical flows (Sivakumaran and Yevjevich 1987).

A limitation of this application of Dressler's theory is the potential flow assumption. Specific resistance terms are further available for his theory (Dressler and Yevjevich 1984; Sivakumaran and Dressler 1986).

Robert Franklin Dressler was born on June 04, 1920, in Philadelphia, USA, and passed away at age 79 on August 27, 1999 at Perkiomenville PA/USA. He graduated in 1940 with the BS degree as a mathematician from the University of Pennsylvania. From 1954 to 1958, he was chief of mathematics, the Physics Division, National Bureau of Standards (NBS), Washington DC. Until 1962, he acted as an assistant director of research, *Philco* Corp., Philadelphia PA, moving then until 1966 as a chief of mathematics analysis to the US Federal Aviation Administration, Washington DC. From then until 1968, Dressler was first the chief scientist of the Swedish Government Aerospace Agency,

Stockholm, when joining as a professor of mechanical and civil engineering the City University, New York. From 1976 to 1983, he was the manager of the NASA science program, Washington DC, and from then until 1989, he was the director of engineering research, International Water Resources Institute, George Washington University, Washington DC.
Dressler worked in the 1960s on the sonic boom effect in aerodynamics, after having published excellent theoretical and experimental papers on dam break waves. His 1952 paper is a first account on the effect of bottom friction, which is large at the wave front but reduces toward the upstream direction. Using a perturbation approach, Dressler obtained the leading wave features, thereby generalizing the classical results of Adhémar Barré de Saint-Venant (1797–1886). The theoretical results were compared in the 1954 paper with laboratory tests, in a channel whose size was small, however. The 1959 paper deals with the effect of bottom slope on the dam break wave. The introduction of the bottom slope source term in the Saint-Venant's equations complicates the application of the method of characteristics. Dressler mathematically solved the complex problem by the inclusion of slope effects. Around 1980, Dressler attempted to generalize Saint-Venant's equations for flows over a curved bottom. However, his equations are a partial solution to Boussinesq's problem relating to the inclusion of streamline curvature effects into the 1D open-channel flow equations. Dressler's equations account for the bottom curvature effects, but Boussinesq-type terms relating to the free surface slope and curvature are absent.

3.10.3 Two-Dimensional Solution

To find 2D solutions to flows over round-crested weirs, the x-ψ method was applied (Montes 1992a; Castro-Orgaz 2013a). Twenty streamlines were used to model the flow. The initial free surface profile and energy head H were determined using Eq. (3.434) following the procedure of Naghdi and Vongsarnpigoon (1986), as previously described. For the initial free surface profile, the mean pressure along the free surface was 0.71 mm, so the position of the water surface was considered acceptable. The computed water surface and bottom pressure profiles are compared in Fig. 3.42a with the corresponding test data (Sivakumaran et al. 1983). Note the excellent agreement of the 2D potential flow solution with the experimental data. The streamline flow pattern from the 2D solution is shown in Fig. 3.42b.

Once the stream function was determined from Eq. (3.250) at each point (x, z) using the computed position of the free surface, the velocity components (u, w) were determined in a mesh formed by 20 streamlines at 180 vertical sections in the mathematical model. The number of streamlines and vertical sections was also doubled to check mesh independence of the results. The 2D potential flow results are plotted in Fig. 3.43 at seven representative vertical sections. Note that

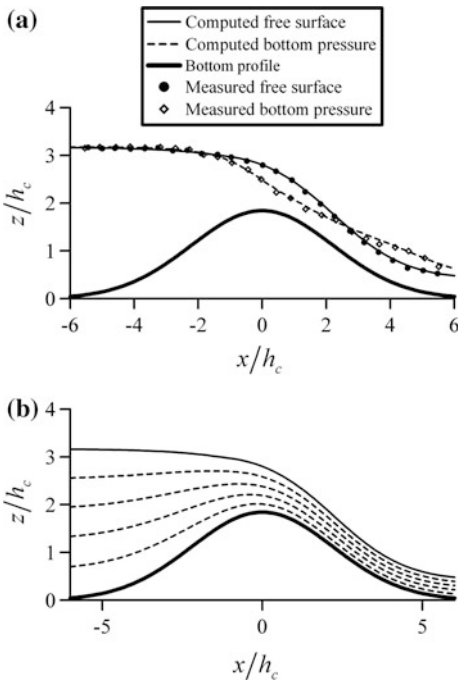

Fig. 3.42 Flow over round-crested weir: **a** comparison of computed $(h + z_b)/h_c$ and $(p_b/(\gamma) + z_b)/h_c$ from the 2D model with data of Sivakumaran et al. (1983), **b** streamline flow pattern (adapted from Castro-Orgaz 2013a)

the shapes of u and w rapidly change within the transitional flow over the weir crest. Using the computed free surface profile, the derivatives of h, h_x, h_{xx}, h_{xxx}, and h_{xxxx} were determined numerically using accurate 5-point central finite differences. The bottom values were computed analytically from the bottom profile equation. The predictions $u^{(2)}$, $w^{(1)}$, $w^{(2)}$, and $u^{(3)}$ were then determined in all vertical sections using Eqs. (3.63), (3.64), (3.76), and (3.78), respectively. Note that no linear vertical velocity profile results, so that $w^{(1)}$ is no accurate approximation. In contrast, the prediction $w^{(2)}$ fits remarkably well with the 2D data along the entire computational domain (e.g., Figure 3.43d for the overflow crest). The prediction of $u^{(2)}$ is in excellent agreement with the 2D results for all sections, whereas $u^{(3)}$ predictions reveal an improved accuracy, providing a precise estimation for u.

The Boussinesq approximation includes not only a refinement of 2D velocity distributions based on irrotational flow but also on the pressure distribution by considering the acceleration term in the vertical direction. The pressure distribution is a quantity of interest in flows over a curved surface (Iwasa and Kennedy 1968). Based on the 2D velocity field (u, w), the vertical pressure distribution for potential flow is $p/\gamma = H - z - (u^2 + w^2)/(2g)$. The effects of streamline curvature on the vertical pressure distribution are shown in Fig. 3.44. The data corresponding to the second- and third-order Boussinesq-type approximations are included as well. At sections $x/h_c = -4$ and -2, the pressure distribution is hydrostatic (Fig. 3.44a, b), indicating that free surface and bottom pressure profiles coincide (Fig. 3.42). As the flow accelerates toward the weir crest, the vertical centrifugal forces provoke

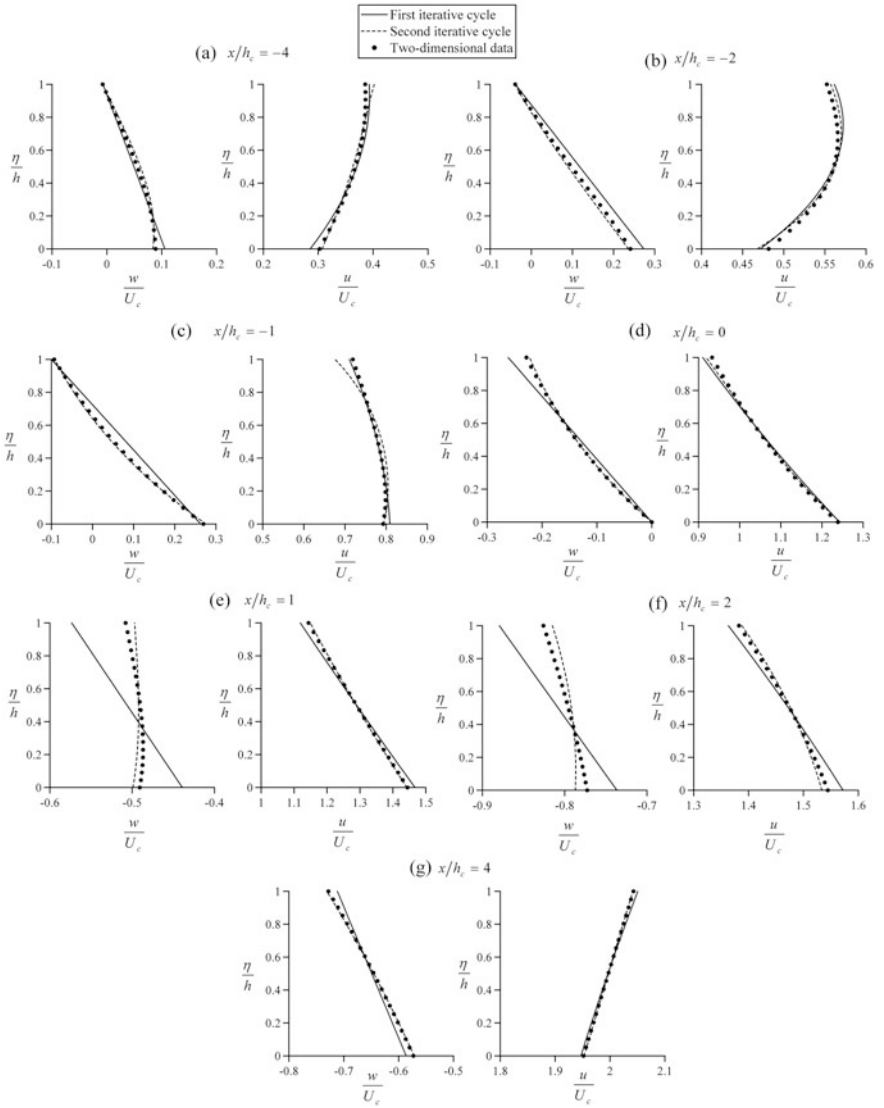

Fig. 3.43 Comparison of (u/U_c, w/U_c) from the 2D solution along a round-crested weir domain, with U_c as critical velocity, with predictions given by second- and third-order results originating from Picard iteration (adapted from Castro-Orgaz and Hager 2013)

vertical pressures below the hydrostatic pressure (convex free surface curvature) (Fig. 3.44c–e). At $x/h_c = +2$, an increase of the pressures associated with supercritical flow approaching the tailwater weir portion is observed. Vertical pressures are then above the hydrostatic pressure at $x/h_c = +4$ (concave free surface curvature), as observed by comparing the free surface with the bottom pressure profile in

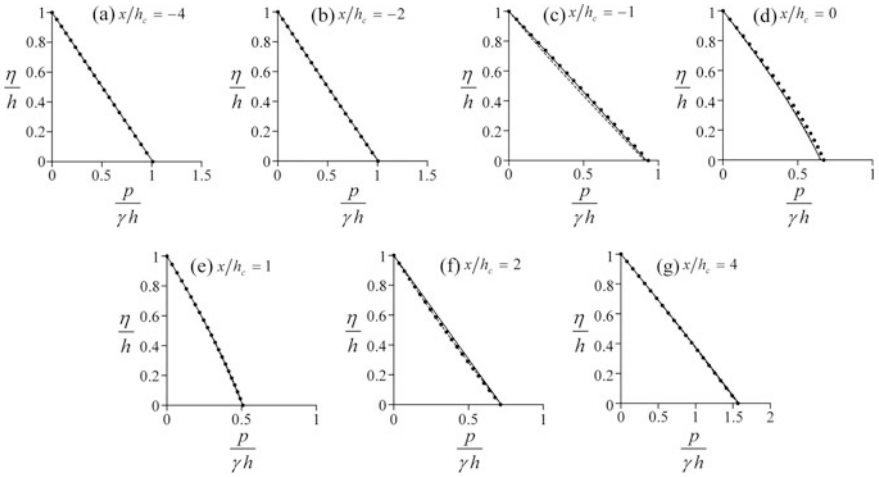

Fig. 3.44 Comparison of $p/(\gamma h)$ from 2D solution along round-crested weir domain of Fig. 3.42, with predictions given by second- and third-order results originating from Picard iteration (symbols as in Fig. 3.43) (adapted from Castro-Orgaz and Hager 2013)

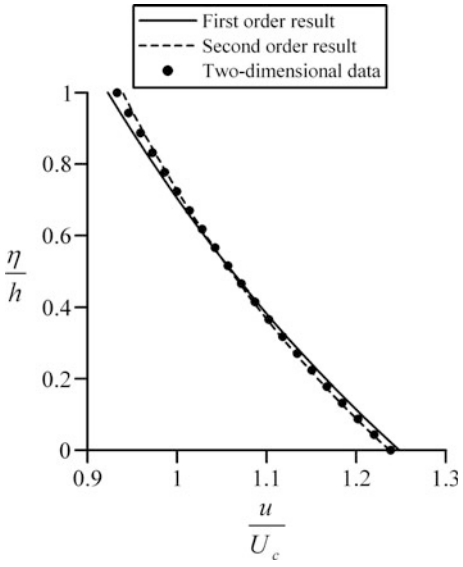

Fig. 3.45 Comparison of Dressler's first- and second-order velocity profiles with 2D simulation at overflow crest (adapted from Castro-Orgaz and Hager 2013)

Fig. 3.42. The second-order Boussinesq approximation agrees excellently with the 2D results, with small differences between the second- and the third-order Boussinesq predictions. These computations account for the effect of the vertical acceleration on the pressure distribution, which, therefore, is no longer hydrostatic.

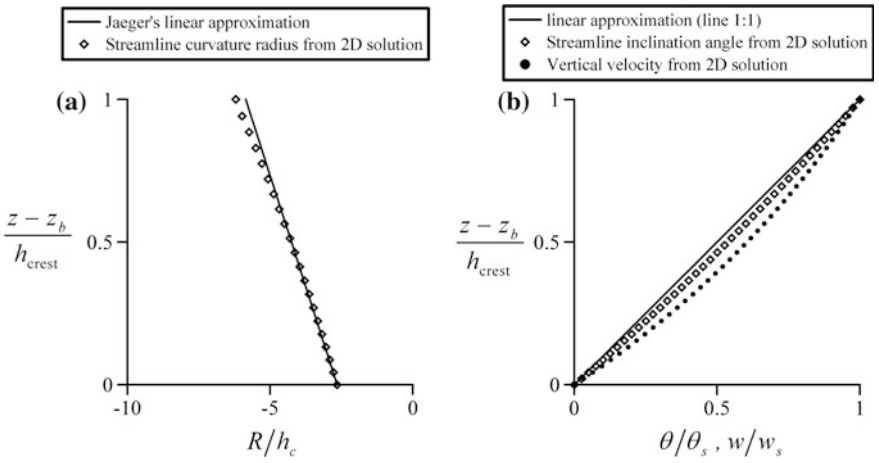

Fig. 3.46 Vertical distributions of **a** R/h_c, **b** θ/θ_s and w/w_s, at overflow crest versus $(z-z_b)/h_{crest}$ adapted from Castro-Orgaz (2013a)

The 2D results for u at the weir crest are plotted in Fig. 3.45, including the prediction of $u_\xi^{(1)}$ given by Eq. (3.450) as an excellent approximation of u. The second-order prediction from Dressler's theory, using Eq. (3.152) for $u_\xi^{(2)}$, is also plotted in Fig. 3.45, indicating improved predictions over $u_\xi^{(1)}$.

In the potential flow equations at the weir crest, the Euler equations depend on the distribution of the radius of streamline curvature along an equipotential curve. Jaeger (1956) and Montes (1970) rather used the $R(z)$ distribution in the vertical direction at the weir crest. The function $R(z)$ is expanded using a Taylor series at the weir crest, retaining only the first term as (Montes 1970)

$$R = R_b + \left(\frac{\partial R}{\partial z}\right)_b (z - z_b) + \left(\frac{\partial^2 R}{\partial z^2}\right)_b \frac{(z - z_b)^2}{2} + \cdots \approx R_b + \left(\frac{\partial R}{\partial z}\right)_b (z - z_b). \tag{3.454}$$

Jaeger (1956) and Montes (1970) suggested[6] $m = (\partial R/\partial z)_b \approx -2$. The 2D distribution of $R(z)$ at the hump crest was investigated for the weir shown in Fig. 3.41 with the result plotted in Fig. 3.46a, with h_{crest} as the flow at the weir crest. The fitting value obtained from Eq. (3.454) against the 2D data is $m = -3.1$, i.e., different from Jaeger's $m = -2$. Note that the linear approximation for R is excellent except for a small region below the free surface, in agreement with LDV

[6]In weir flow, R_b is negative (convex bottom profile), resulting in $m < 0$. In the original developments presented by Jaeger (1939) and Montes (1970), R_b is to be used in absolute value, given that a negative sign was introduced into the governing equations. Therefore, $m = +2$ is the value used in these works.

measurements (Ramamurthy et al. 1994). The vertical velocity distribution obtained from the detailed 2D solution is plotted in Fig. 3.46b. The classical Boussinesq theory (Montes 1998) assumes that this law is linear, a fact not verified in Fig. 3.46b, thus questionable. The streamline inclination $\theta = \arctan(\partial z/\partial x)$ at the weir crest obtained from the 2D solution is plotted in Fig. 3.46b. Matthew (1963), Hager and Hutter (1984a), and Montes and Chanson (1998) assumed it linear for the inviscid Boussinesq equations. The results of Fig. 3.46b corroborate that this approximation is reasonable at the weir crest, although not exact. In contrast, the vertical velocity profile approximation is only a rough hypothesis.

3.10.4 Flow Nets

To investigate the flow net geometry for circular-crested weir flows without a downstream chute slope, tests were conducted at VAW, ETH Zürich (Castro-Orgaz 2010a). The channel was 0.50 m wide and 0.7 m deep, in which a circular weir of radius R_b = 0.30 m was inserted. The channel was covered with a tap in which a longitudinal slot allowed for light passage along the weir to visualize the axial streamline pattern. Particles were added at the channel inflow section to track streamlines over the weir body with high-exposure photographs (Fig. 3.47).

Image distortion was removed using a calibration panel, and the flow nets were digitized from the calibrated plots (Fig. 3.48a). The distributions $R_s/R(v)$ and $\theta/\theta_s(v)$ were determined for 5 equipotentials and 10 streamlines. The results for three equipotentials are plotted in Fig. 3.48b–d. The results for K for equipotential 3 at the weir crest give K = 0.58. However, as the downstream weir side is approached, K increases to $K \to 1$ because of the downstream chute slope effect. Note that R_b is constant, but there is no limitation to $R_s \to \infty$. As a result, the streamlines are almost concentric downstream of the weir crest with $R_s \to R_b$, resulting in $K \to 1$, i.e., as for shallow flows with weakly curved and sloped streamlines.

The flow net of Fawer (1937) for a circular-crested weir of R_b = 0.0325 m and a downstream chute slope of 3:2 (H:V) is considered in Fig. 3.49. The distributions $R_s/R(v)$ and $\theta/\theta_s(v)$ were determined for 8 equipotential lines and 9 streamlines (Fig. 3.49a). The results for 3 of these are plotted in Fig. 3.49b–d. The caption includes the values obtained for K and m, as well as those of r and i for the

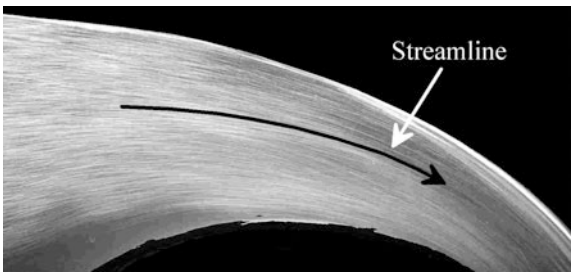

Fig. 3.47 Detail of streamlines at overflow crest from high-exposure photographs (VAW photograph)

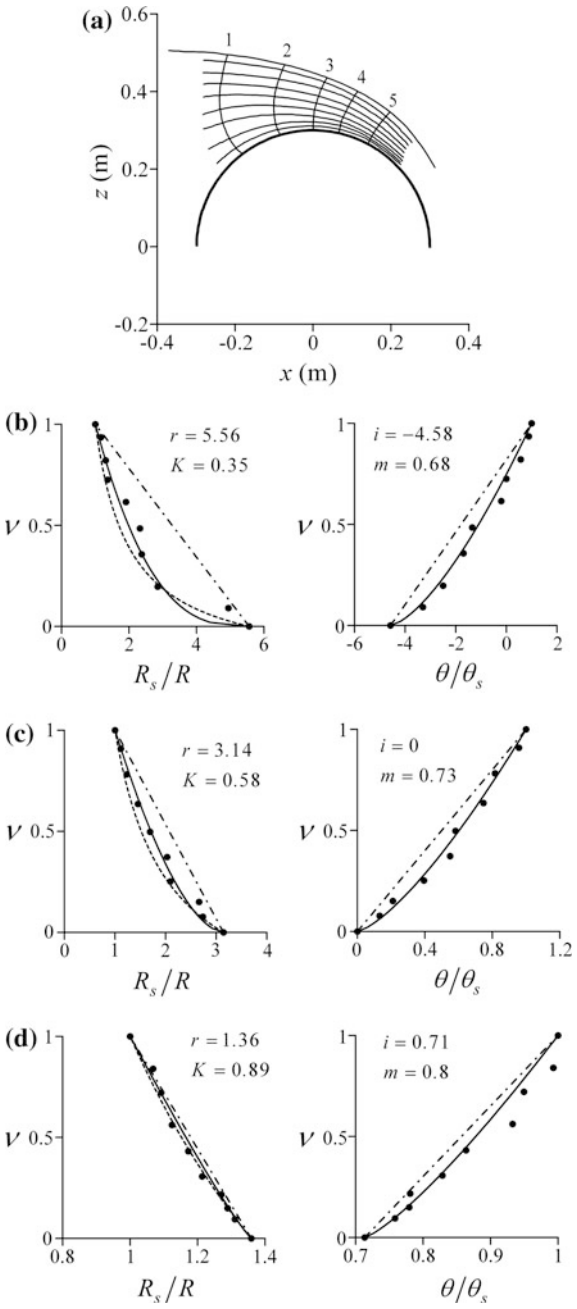

Fig. 3.48 Potential flow over circular-crested weir: **a** flow pattern (Castro-Orgaz 2010a), **b** flow net parameters with (—) Fawer's approach, (– • –) Matthew's approach, (- - -) Jaeger's approach, (•) flow net data, for equipotential line 1, **c** 3, **d** 5 (adapted from Castro-Orgaz 2010a)

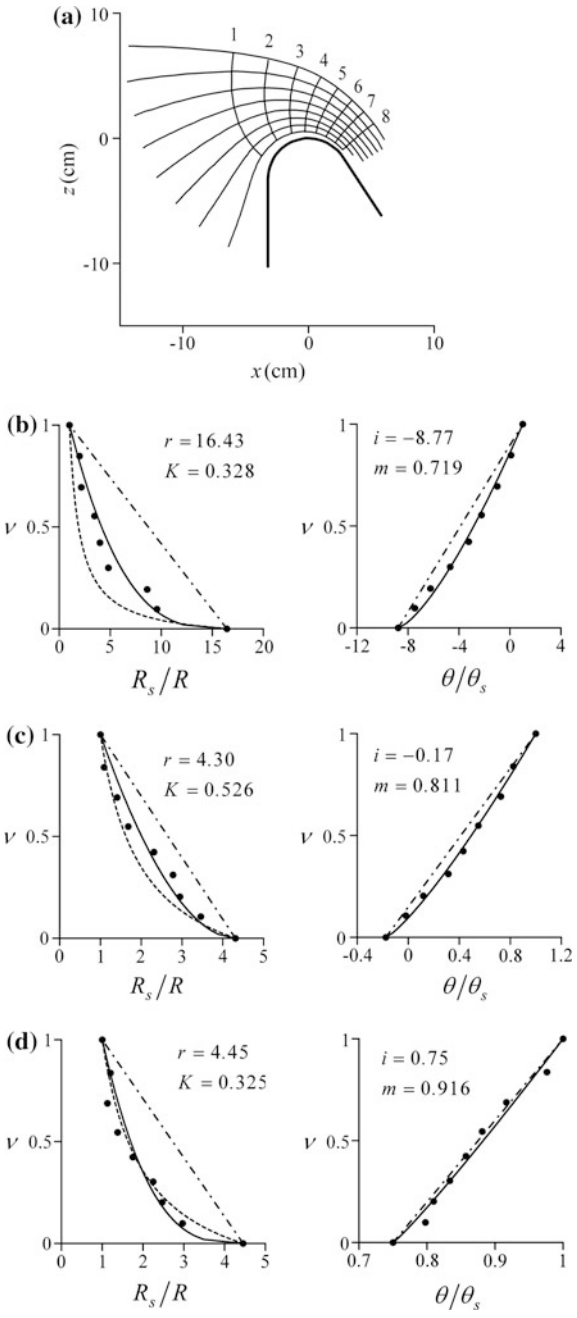

Fig. 3.49 Potential flow over circular-crested weir: **a** flow pattern (Castro-Orgaz 2010a), **b** flow net parameters with (—) Fawer's approach, (– • –) Matthew's approach, (- - -) Jaeger's approach, (•) flow net data, for equipotential line 1, **c** 4, **d** 7 (adapted from Castro-Orgaz 2010a)

equipotential lines considered. The actual values of K and m are compared with $K = m = 1$. The distribution of $R_s/R(v)$ is highly nonlinear, with $K < 1$. The parameter K is small at equipotential line 1 increasing toward the weir crest up to $K \to 0.5$. Beyond the weir crest, K reduces again. The nonlinear distribution of $R_s/R(v)$ closely agrees with Jaeger's approach. Note that R_b is constant for a circular-crested weir and the value of r, that is correlated with K, depends mainly on R_s. Close to equipotential line 1, R_s is large, and the high ratio R_s/R_b at a given equipotential leads to a small K value. In contrast, at the crest vicinity, R_s is still larger than R_b, but the ratio is smaller, resulting in larger K values. Approaching the downstream weir slope, $R_s \to \infty$, with K reducing again. In contrast, the distribution of $\theta/\theta_s(v)$ is weakly nonlinear, even at equipotential line 1, where it has its maximum, as shown in Fig. 3.49b.

The flow over a standard spillway crest is a basic flow problem involving variable bottom curvature, to improve the weir-flow performance (Cassidy 1970; Hager 1987, 1991; Chanson 2006). The flow net of Escande (1933) under the weir design condition is analyzed in Fig. 3.50. The distributions of $R_s/R(v)$ and $\theta/\theta_s(v)$ were determined for eight equipotential lines and ten streamlines (Fig. 3.50a). The results obtained for three equipotential lines are plotted in Fig. 3.50b–d. Similar to circular-crested weir flow, the analysis of equipotential line 1 results in a small K value, corresponding to $R_s \to \infty$. As previously, as the flow approaches the crest zone, $1/R_s$ and K increase. Escande's standard spillway had a downstream angle of 53°. It could be expected that then $R_s \to \infty$, with a corresponding drop in K. However, $1/R_s$ decreases, but concurrently, the bottom profile $1/R_b$ decreases toward the chute point of tangency, resulting in $R_s \to R_b$ and $K \to 1$. The minimum K value is attained at equipotential line 1, and K continuously increases to $K = 1$, where the flow is weakly curved and streamline curvature effects are small. The results for m are similar, with a minimum value at equipotential 1, and increasing to $m = 1$ along the chute zone.

The results for $K = K(r)$ are plotted in Fig. 3.51. Note the strong correlation between K and r, because for a given equipotential in free surface flow both R_s and R_b are fixed, as is then K. According to Fig. 3.51, flows with $r > 1$ are characterized by a strong drop in K as r increases. For $r \to 1$, the limit $K \to 1$ is attained, i.e., the basis of Matthew's theory (1963) as an asymptotic value, because $K(r)$ is generally nonlinear. The results from the flow net analysis follow, for $1 < r < 18$ and $K < 1$, the best-fit equation ($R^2 = 0.915$) (Castro-Orgaz 2010a)

$$K = r^{-0.55}. \tag{3.455}$$

In contrast, flows with $r < 1$ are approximated by $K = 1$. A singularity in the channel bottom geometry with a possible discontinuity in bottom slope or curvature violates the basic derivation of the governing Eq. (3.86), where continuity in the bottom profile is assumed, implying jumps in the flow net parameters. The effect of m is small as compared to the effect of K, so that $m = 1$ is assumed (Castro-Orgaz 2010a).

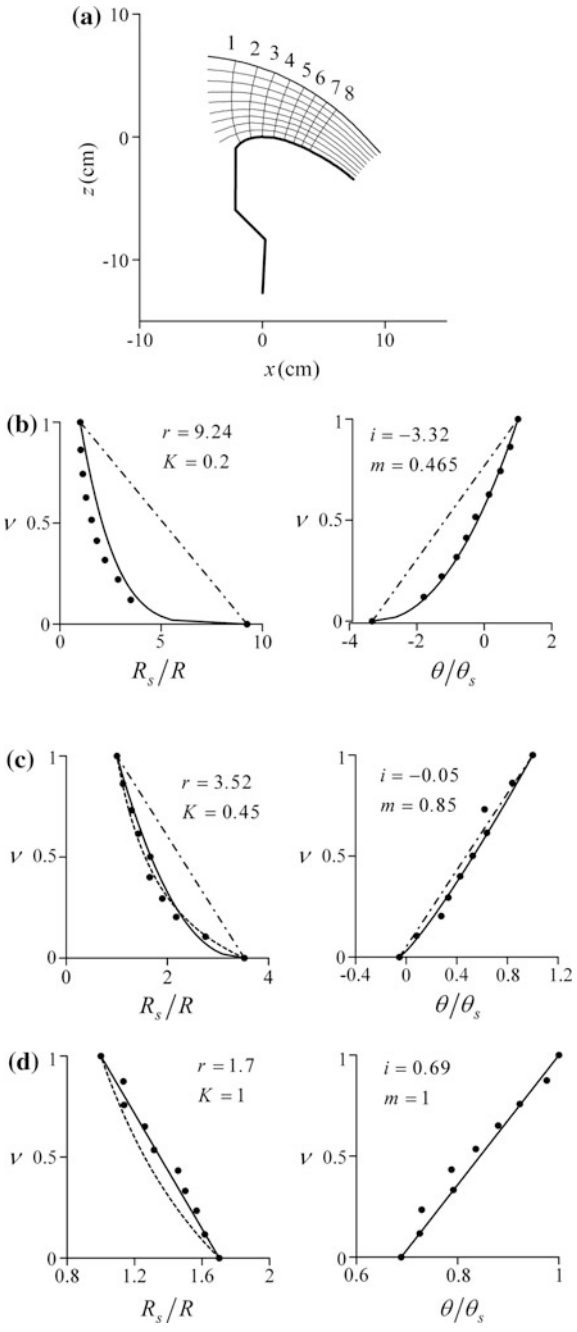

Fig. 3.50 Potential flow over standard spillway: **a** flow pattern (Castro-Orgaz 2010a), **b** flow net parameters with (—) Fawer's approach, (– • –) Matthew's approach, (- - -) Jaeger's approach, (•) flow net data, for equipotential line 1, **c** 3, **d** 6 (adapted from Castro-Orgaz 2010a)

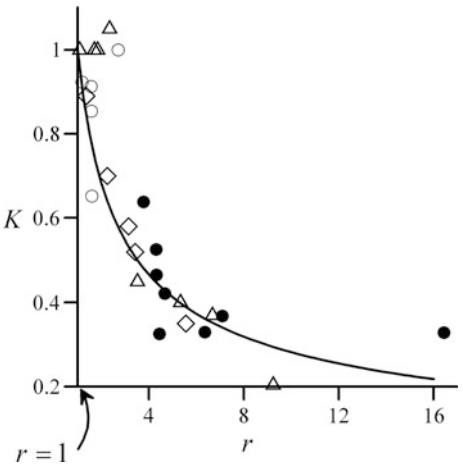

Fig. 3.51 Flow net parameter $K = K(r)$ from (—) Eq. (3.455), (◇) Castro-Orgaz (2010a), (•) Fawer (1937), (○) Westernacher (1965), (△) Escande (1933) (adapted from Castro-Orgaz 2010a)

3.11 Sharp-Crested Weir

3.11.1 Critical Flow

A sharp-crested weir is formed by inserting into a subcritical open-channel flow a thin, standard-crested plate (Fig. 3.52a). If sidewall contractions are absent, the flow is (2D) in the vertical plane and may be mathematically tackled using the equations of inviscid and irrotational flow (Rouse 1932, 1938). A free jet spills from the vertical thin plate, with the upper and lower free surfaces describing the curves depicted by Rouse (1932) in Fig. 3.52a. The flow over a sharp-crested weir was investigated experimentally by Bazin (1888), Creager (1917), Scimemi (1930), and Rouse (1932), among many others. The application of 2D potential flow computations was pursued by Hay and Markland (1958) and Strelkoff (1964), resulting in accurate predictions of the jet surfaces and the velocity and pressure distributions. From a 1D point of view, this flow involves a transition from upstream subcritical channel to downstream free jet flow. Therefore, a critical flow section is formed within the jet. The purpose of this section is to analyze flow over a sharp-crested weir using 1D critical flow computations based on the potential flow model. The theory developed by Jaeger (1956) will be adopted following the presentation by Montes (1998).

The differential equation describing the potential velocity profile V along an equipotential curve is (Eq. 3.48)

$$\frac{\partial V}{\partial z} = -\frac{V}{R\cos\theta}. \tag{3.456}$$

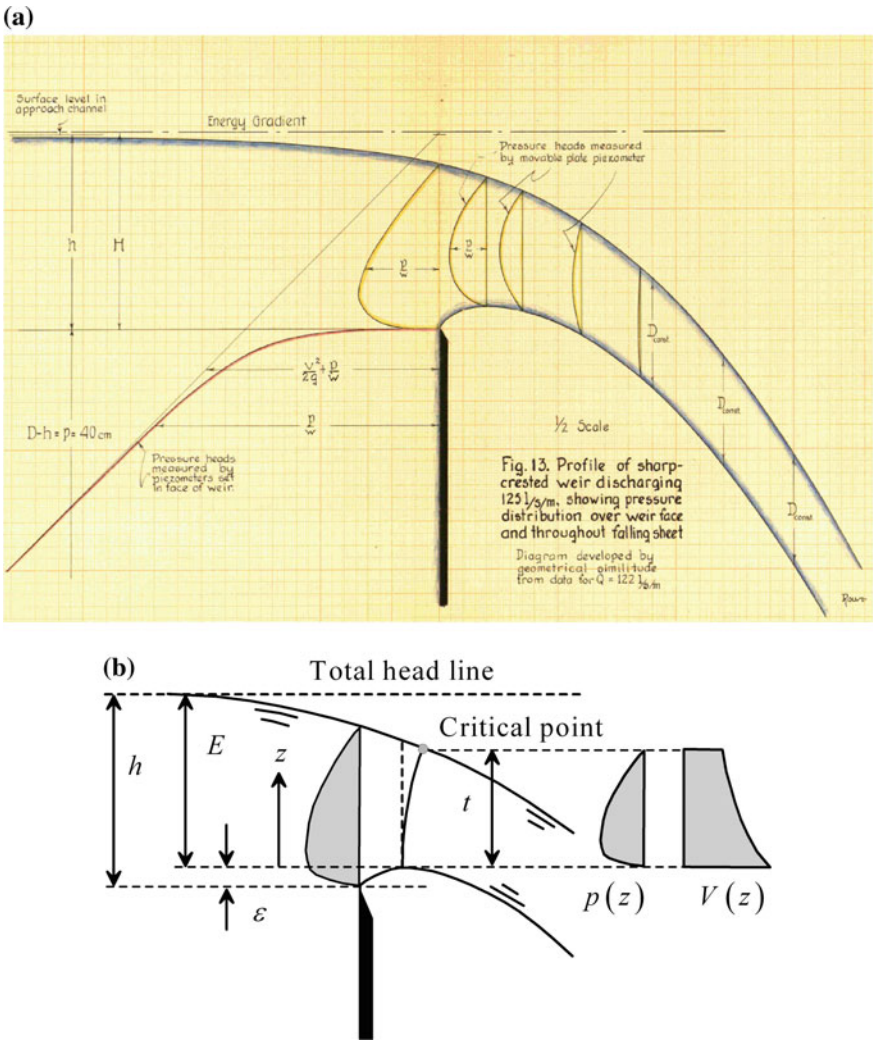

Fig. 3.52 Sharp-crested weir flow: **a** experimental test (Rouse 1932), **b** definition sketch

Here, V is the algebraic velocity tangential to the streamline, R is the radius of the streamline curvature (absolute value) at coordinate z of a point of the equipotential curve, and θ is the streamline inclination. The origin of the z-coordinate, positive upward, is taken at the point of maximum elevation of the lower jet profile. In Eq. (3.456), a Taylor series development truncated at the linear term (Montes 1998)

$$\begin{aligned} R\cos\theta(z) &= R_b + \left[\frac{\mathrm{d}}{\mathrm{d}z}(R\cos\theta)\right]_b z + \left[\frac{\mathrm{d}^2}{\mathrm{d}z^2}(R\cos\theta)\right]_b \frac{z^2}{2} + \cdots \\ &\approx R_b + \left[\frac{\mathrm{d}}{\mathrm{d}z}(R\cos\theta)\right]_b z = R_b + mz, \end{aligned} \tag{3.457}$$

is inserted, producing

$$\frac{\mathrm{d}V}{\mathrm{d}z} = -\frac{V}{R_b + mz}. \tag{3.458}$$

Integration of Eq. (3.458) yields the potential velocity distribution (Jaeger 1956; Montes 1998)

$$\frac{V}{V_s} = \left[\frac{R_b + m\,t}{R_b + mz}\right]^{1/m}. \tag{3.459}$$

The steps to obtain Eq. (3.458) from Eq. (3.459) are identical to those described in detail using Eqs. (3.235)–(3.237). It implies separation of variables in Eq. (3.458), e.g., $\mathrm{d}V/V = \mathrm{d}z/(R_b + mz)$, and integration of the resulting differential equation between the free surface and an arbitrary point. Here, t is the crest flow depth defined as the vertical projection of the crest equipotential curve (Fig. 3.52b), and V_s is the free surface velocity. The discharge per unit width q is computed by integrating Eq. (3.459) across the jet thickness t (Jaeger 1956). Neglecting the effect of $\cos\theta$, so done by Fawer (1937) and Montes (1970), leads, after some intermediate steps, approximately to

$$q = \int_0^t V\cos\theta\,\mathrm{d}z = \frac{V_s R_b}{m-1}\left[\left(1 + \frac{mt}{R_b}\right) - \left(1 + \frac{mt}{R_b}\right)^{\frac{1}{m}}\right]. \tag{3.460}$$

This implies that the flow depth t approximates the vertical flow depth at the crest. The free surface velocity is, with E as the specific energy (Fig. 3.52b),

$$V_s = [2g(E-t)]^{1/2}. \tag{3.461}$$

In the ensuing developments, a sharp-crested weir of infinite height is considered, for which the effect of the approach flow velocity head is neglected (Rouse 1938; Montes 1998). Inserting Eq. (3.461) into Eq. (3.460) produces

$$q = [2g(E-t)]^{1/2}\frac{R_b}{m-1}\left[\left(1 + \frac{mt}{R_b}\right) - \left(1 + \frac{mt}{R_b}\right)^{\frac{1}{m}}\right], \tag{3.462}$$

which is a mathematical statement linking the unit discharge q, the crest water depth t, and the specific energy E. Critical flow appears at the point of maximum elevation of the lower jet profile, where the specific energy E is a minimum. This section is referred to as the contracted section, but it is in fact a critical flow section with a non-hydrostatic pressure distribution. Following Montes (1998), critical flow is determined by maximizing the value of q with respect to t, keeping E constant. The parameters m and R_b are taken as constant in this computation. Therefore, the partial differentiation of Eq. (3.462) with respect to t (note that E is kept constant), and equating the result to zero, produces

$$\begin{aligned}\frac{\partial q}{\partial t} = &-\frac{1}{2}[2g(E-t)]^{-1/2}2g\frac{R_b}{m-1}\left[\left(1+\frac{mt}{R_b}\right)-\left(1+\frac{mt}{R_b}\right)^{\frac{1}{m}}\right]\\ &+[2g(E-t)]^{1/2}\frac{R_b}{m-1}\left[\frac{m}{R_b}-\frac{1}{m}\left(1+\frac{mt}{R_b}\right)^{\frac{1}{m}-1}\frac{m}{R_b}\right]\equiv 0.\end{aligned} \tag{3.463}$$

After rearrangement, this simplifies to

$$\frac{mE}{R_b}=\frac{mt}{R_b}+\frac{1}{2}\frac{\left(1+\frac{mt}{R_b}\right)-\left(1+\frac{mt}{R_b}\right)^{1/m}}{1-\frac{1}{m}\left(1+\frac{mt}{R_b}\right)^{1/m-1}}. \tag{3.464}$$

Equation (3.464) is a critical flow condition invoking that R_b is a constant. Furthermore, the characteristic sharp-crested weir feature, namely atmospheric pressure along the lower jet profile, is so far not included. Therefore, Eq. (3.464) is formally valid for flow over a round-crested weir with a solid bottom profile, where the bottom pressure head does not necessarily vanish. Based on Eq. (3.464), Montes (1970) computed critical flow over circular-crested weirs. The pressure distribution along the crest equipotential curve is determined from (Eq. 3.66)

$$\frac{p}{\gamma}=E-z-\frac{V^2}{2g}. \tag{3.465}$$

Inserting Eqs. (3.459) and (3.461) into Eq. (3.465) produces

$$\frac{p}{\gamma}=E-z-(E-t)\left(\frac{R_b+m\,t}{R_b+mz}\right)^{2/m}, \tag{3.466}$$

or

$$\frac{p}{\gamma E}=1-\frac{z}{E}-\left(1-\frac{t}{E}\right)\left(\frac{1+\frac{m\,t}{R_b}}{1+\frac{m\,z}{R_b}}\right)^{2/m}. \tag{3.467}$$

This is an equation valid for the round-crested, solid bottom weir. For the particular case of the sharp-crested weir, the lower streamline is a free jet surface, for which the bottom pressure head vanishes. Therefore, Eq. (3.467) at $z = 0$ yields

$$0 = 1 - \left(1 - \frac{t}{E}\right)\left(1 + \frac{m\,t}{R_b}\right)^{2/m}, \tag{3.468}$$

or

$$\frac{mt}{R_b} = \left(1 - \frac{t}{E}\right)^{-m/2} - 1\cdot \tag{3.469}$$

The discharge coefficient C_d of the sharp-crested weir is defined by Poleni's equation in the form (Jaeger 1956; Montes 1998)

$$q = \frac{2}{3} C_d h (2gh)^{1/2}\cdot \tag{3.470}$$

Here, h is the approach flow depth, measured from the weir crest (Fig. 3.52b). The detail of the reference level is subtle, but non-trivial, given that E is measured from the point of maximum elevation of the lower jet profile. Therefore, $h = E + \varepsilon$ (Fig. 3.52b). Equating Eqs. (3.462) and (3.470) to one another produces the identity

$$\frac{2}{3} C_d h (2gh)^{1/2} = [2g(E-t)]^{1/2} \frac{R_b}{m-1}\left[\left(1 + \frac{mt}{R_b}\right) - \left(1 + \frac{mt}{R_b}\right)^{\frac{1}{m}}\right], \tag{3.471}$$

or, after elementary manipulation,

$$C_d = \frac{3}{2}\left(\frac{E}{R_b}\right)^{-1}\left(1 - \frac{t}{E}\right)^{1/2}\left(\frac{E}{h}\right)^{3/2} \frac{1}{m-1}\left[\left(1 + \frac{mt}{R_b}\right) - \left(1 + \frac{mt}{R_b}\right)^{\frac{1}{m}}\right]\cdot \tag{3.472}$$

The critical flow problem over a sharp-crested weir is, therefore, mathematically determined once the ratio E/h is computed. Based on the experimental results of Scimemi (1930), the maximum lower jet elevation is $\varepsilon \approx 0.112h$, resulting in $E = h - \varepsilon \approx 0.888h$. The critical flow theory is now compared with the experimental data of Scimemi (1930) as follows. A value of $m = 2$ is adopted based on the former results of Jaeger (1939) and Montes (1970) for flow over circular-crested weirs. Equations (3.464) and (3.469) represent a pair of two nonlinear algebraic equations for the two unknowns t/R_b and t/E. The numerical solution of this system is summarized in Table 3.4, allowing for the prediction of C_d with these numerical values using Eq. (3.472).

Table 3.4 Critical flow over sharp-crested weir assuming R_b = const. and $m = 2$ (Montes 1998)

	mt/R_b	t/E	E/R_b	C_d
Computed	2.2469	0.692	1.6235	0.62
Measured	–	0.7422	–	0.6338

On inspecting Table 3.4, a fair agreement between the predicted and computed values of C_d is noted; however, the computed critical depth ratio t/E unexpectedly deviates from the test value. The conducted computations are constrained by the assumption R_b = const. adopted in the development of Eq. (3.464). This limitation is easily understood from Eq. (3.469), stating essentially that $R_b = R_b(t)$. Therefore, this functional relation must be considered to produce the differential identity $\partial q/\partial t \equiv 0$. Furthermore, the value $m = 2$, adopted for the data in Table 3.4, stems from physical experiments on flows over circular-crested weirs (Montes 1970). This is a questionable choice for sharp-crested weir flows, given that $m = 2$ originates from tests on a circular-crested weir where R_b = const., for which the bottom pressure head is not necessarily atmospheric. Therefore, m for sharp-crested weir flows remains undetermined.

Computations were reconsidered keeping m as an undermined parameter and treating R_b as a function of t in Eq. (3.462). Let the normalized variables $Z = mt/R_b$ and $\Omega = t/E$ be defined, so that Eq. (3.472) can be rewritten as

$$C_d = \frac{3}{2}\left(\frac{E}{h}\right)^{3/2}\frac{m}{m-1}\frac{\Omega}{Z}(1-\Omega)^{1/2}\left[(1+Z)-(1+Z)^{1/m}\right]. \tag{3.473}$$

Critical flow is determined by computing $\partial C_d/\partial\Omega \equiv 0$, given that E = const. Performing the differentiations, Eq. (3.473) yields

$$\frac{\partial C_d}{\partial \Omega} = \frac{3}{2}\left(\frac{E}{h}\right)^{3/2}\frac{m}{m-1}\left[(1-\Omega)^{1/2}\left[(1+Z)-(1+Z)^{1/m}\right]\left(\frac{1}{Z}-\frac{\Omega}{Z^2}\frac{\mathrm{d}Z}{\mathrm{d}\Omega}\right)\right.$$
$$\left.+\frac{\Omega}{Z}\left\{-\frac{1}{2}(1-\Omega)^{-1/2}\left[(1+Z)-(1+Z)^{1/m}\right]+(1-\Omega)^{1/2}\left(\frac{\mathrm{d}Z}{\mathrm{d}\Omega}-\frac{1}{m}(1+Z)^{\frac{1}{m}-1}\frac{\mathrm{d}Z}{\mathrm{d}\Omega}\right)\right\}\right] \equiv 0, \tag{3.474}$$

or,

$$\left[(1+Z)-(1+Z)^{1/m}\right]\left(\frac{1}{Z}-\frac{\Omega}{Z^2}\frac{\mathrm{d}Z}{\mathrm{d}\Omega}\right)$$
$$+\frac{\Omega}{Z}\left\{-\frac{1}{2}(1-\Omega)^{-1}\left[(1+Z)-(1+Z)^{1/m}\right]+\frac{\mathrm{d}Z}{\mathrm{d}\Omega}\left(1-\frac{1}{m}(1+Z)^{\frac{1}{m}-1}\right)\right\} \equiv 0. \tag{3.475}$$

Table 3.5 Critical flow over sharp-crested weir

	mt/R_b	t/E	E/R_b	C_d
Computed $m = 2$	3	0.75	2	0.627
Computed $m = 1.6$	2.1428	0.761	1.76	0.6376
Measured	–	0.7422	–	0.6338

Rewriting Eq. (3.469) as

$$Z = (1 - \Omega)^{-m/2} - 1, \tag{3.476}$$

its differentiation yields

$$\frac{dZ}{d\Omega} = \frac{m}{2}(1 - \Omega)^{-\frac{m}{2}-1}. \tag{3.477}$$

It is evident, by formally substituting Eqs. (3.476) and (3.477) into Eq. (3.475), that a functional relation emerges from Eq. (3.475), which can be written as a nonlinear implicit equation $f(\Omega, m) = 0$. For a selected value of m, this leads to the value of $\Omega = t/E$, and, via Eq. (3.476), for $Z = mt/R_b$, and, consequently, via Eq. (3.473), to the value of C_d. This problem has been numerically solved. Consider Table 3.5, where numerical computations conducted using values $m = 2$ and 1.6 are presented. Note that the two computations produce good estimations of C_d, as well as of the critical depth ratio t/E. A comparison of these results with those in Table 3.4 indicates that the effect of the derivative $\partial R_b/\partial t$ on t/E is important, given the improved accuracy in Table 3.5.

Therefore, the value of m cannot be arbitrarily selected. To determine m, the predicted velocity and pressure distributions using Eqs. (3.459) and (3.467) were compared with the experimental data of Scimemi (1930). Firstly, the velocity and pressure distributions, based on the results of Table 3.4, are plotted in Fig. 3.53a and b, respectively. The relation $E/h = 0.888$ was used to scale the plots. Neither the velocity nor the pressure distributions are accurately predicted, however. Computations based on Table 3.5 for $m = 2$ are plotted in Fig. 3.53c, d. The predicted velocity and pressure distributions are in fair agreement with observations. However, the computed pressures are somewhat overpredicted (Fig. 3.53d), suggesting that the value of m should be lower than 2. Computations based on Table 3.5 for $m = 1.6$ are shown in Fig. 3.53e, f. The effect of m on the computed velocity profile is noted to be small, but noticeable on the pressures, however. This particular value of m produces good estimates of C_d and t/E (Table 3.5) and velocity and pressure distributions that are in good agreement with observations. These results, thus, reveal that a sharp-crested weir is a critical flow device operating with a non-hydrostatic pressure distribution and that the free jet spilling from the vertical plate is a peculiar case of flow over a round-crested weir, for which the bottom pressure head vanishes along the lower streamline.

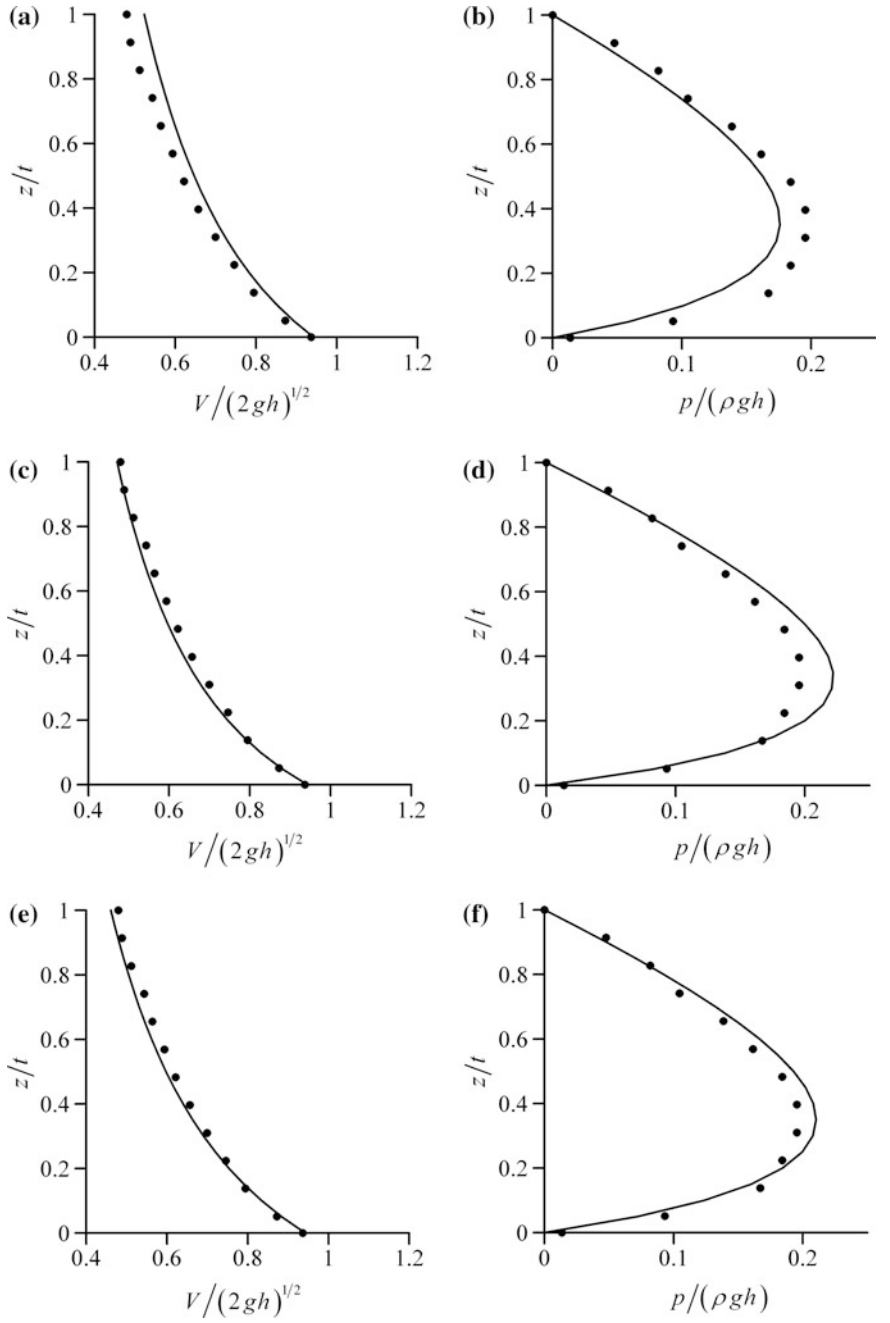

Fig. 3.53 Comparison of sharp-crested weir velocity $V/(2gh)^{1/2}(z/t)$ and pressure $p/(\rho gh)(z/t)$ distributions (—) at the contracted section based on **a**, **b** critical flow computation (Table 3.4), **c**, **d** critical flow computation (Table 3.5) for $m = 2$, **e**, **f** critical flow computation (Table 3.5) for $m = 1.6$, with (•) experimental data by Scimemi (1930)

3.11.2 Profile of High Dams

The spillway crest of a high dam is usually shaped based on the lower trajectory of the sharp-crested weir $z_b = z_b(x)$ for design flow conditions (Fig. 3.54a). Its upstream head is E, which is a minimum specific energy $E_{\min}$ corresponding to the critical flow conditions, as demonstrated in the above section. A spillway designed based on this sharp-crested weir (Fig. 3.54b) is characterized by the design head H_D. Ideally, if the spillway bottom profile is shaped based on the lower nappe trajectory $z_b = z_b(x)$ of the sharp-crested weir of Fig. 3.54a, the bottom pressure head must vanish. This concept is widely used by dam engineers, namely that the absolute bottom pressures over a spillway crest are atmospheric at design conditions (actual head E equal to the design head H_D). In practice, however, these bottom pressures are not exactly zero, given the boundary layer development along the weir face (Montes 1998). A spillway profile based on the lower jet trajectory of a sharp-crested weir is referred to as the "ogee" spillway profile. An "ogee-shaped" spillway profile guarantees that the bottom pressure remains close to atmospheric pressure at design conditions. If the bottom pressure head along the spillway crest profile falls below the vapor pressure, cavitation occurs, leading to severe potential damage on the hydraulic structure. In addition to cavitation-related damage, if the spillway profile is not ogee-shaped, the flow may separate from the bottom, leading to additional operational problems. Specific advantages of ogee spillway profiles are the increase of the discharge coefficient for heads larger than H_D. For $E > H_D$, bottom pressures are below the atmospheric pressure and the actual discharge coefficient is larger than the design discharge coefficient. For $E < H_D$, bottom pressures are above the atmospheric pressure and the discharge coefficient is smaller than the design discharge coefficient. For a high dam, $E = H_D \approx 0.888h$, based on Fig. 3.52.

Consider for illustrative purposes a spillway profile designed based on the data of Scimemi (1930), previously described in Tables 3.4 and 3.5 and in Fig. 3.53.

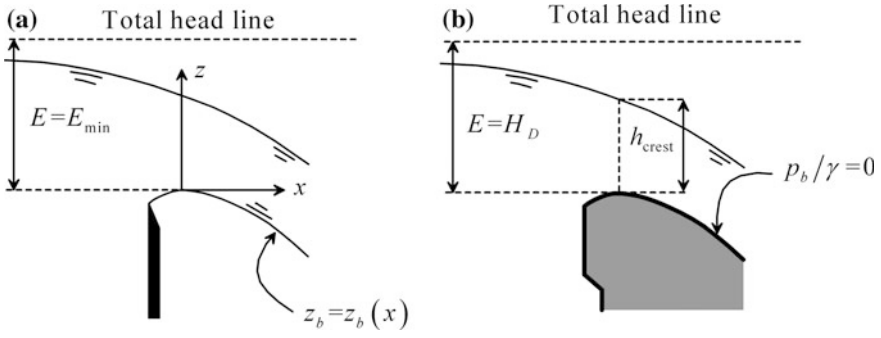

Fig. 3.54 Profile of high dams: **a** sharp-crested weir used to define design conditions, **b** equivalent spillway profile operating at design head, with ideally vanishing pressures along the weir face

The design (subscript D) discharge coefficient C_D of the spillway profile is defined as (Montes 1998)

$$q = C_D\left(gE^3\right)^{1/2}. \tag{3.478}$$

Equating Eqs. (3.478) to (3.470) yields

$$C_D\left(gE^3\right)^{1/2} \equiv \frac{2}{3}C_d h(2gh)^{1/2}, \tag{3.479}$$

and thus,

$$C_D = \frac{2\sqrt{2}}{3}C_d\left(\frac{h}{E}\right)^{3/2} = \frac{2\sqrt{2}}{3} \times 0.6338 \times \left(\frac{1}{0.888}\right)^{3/2} \approx 0.714. \tag{3.480}$$

This corresponds to the discharge coefficient at design conditions based on Scimemi (1930). It is, however, widely accepted to adopt the mean value $C_d = 0.612$, leading to $C_D \approx 0.689$. For shallow free surface flow approaching the limiting operating condition $E \to 0$, the overflow is hydrostatic, with the crest flow depth equal to the hydrostatic critical flow depth $h_{\text{crest}} = h_c = (q^2/g)^{1/3}$. The minimum discharge coefficient of the spillway profile, in the absence of scale effects, originating from fluid surface tension and viscosity, is, thus, $C_D = (2/3)^{3/2} \approx 0.544$.

In practice, several attempts were made to mathematically define the lower nappe trajectory of the sharp-crested weir, to determine analytically a spillway profile for design purposes. The data of the lower jet profile of sharp-crested weirs conducted by Scimemi (1930) are fitted for $X > 0$, with $X = x/H_D$ and $Z = z/H_D$, by the WES (Waterways Experiment Station) profile in dam hydraulics

$$Z = -\frac{1}{2}X^{1.85}. \tag{3.481}$$

The Creager (1917) profile is similar to Eq. (3.481), given by

$$Z = -0.47X^{1.8}, X > 0. \tag{3.482}$$

It corresponds to an empirical fit to the data of Bazin (1888). Knapp (1960) proposed the empirical curve

$$\frac{z}{R_b} = -\frac{x}{R_b} + \ln\left(1 + \frac{x}{R_b}\right), \tag{3.483}$$

corresponding to a continuous crest profile, with $R_b = 0.688h$ as the crest radius of curvature. Therefore, with $H_D = 0.888h$, an alternative form of Eq. (3.483) is

$$Z = -X + 0.7747 \cdot \ln\left(1 + \frac{X}{0.7747}\right), \tag{3.484}$$

in which $X = x/H_D$ and $Z = z/H_D$. Hager (1987, 1991) proposed a continuous profile for the standard spillway defined by the mathematical curve

$$\overline{Z} = -\overline{X} \cdot \ln\overline{X}, \tag{3.485}$$

where

$$\begin{aligned} \overline{Z} &= 2.705(Z + 0.136), \\ \overline{X} &= 1.3055(X + 0.2818). \end{aligned} \tag{3.486}$$

The experimental data of Scimemi (1930), numerically smoothed by Montes (1998), are shown in Fig. 3.55a, including also curves based on Eqs. (3.484) and (3.485). Overall, the accuracy of the Knapp (1960) profile is limited, roughly to $-0.1 < X < 0.4$. In contrast, Eq. (3.485) precisely describes the crest shape for $-0.3 < X < 0.8$ (Fig. 3.55a-c). Hager's profile (1987) also agrees with the numerically generated continuous weir crest profile of Montes (1992c), assuming a gradual transition of bottom curvature along the crest. The profile given by Eq. (3.485) was experimentally verified using model tests and the performance compared to other designs used in dam engineering (Hager 1991). Therefore, the practical design of a spillway profile is adequately addressed with the current state of knowledge. However, from a theoretical point of view, attempts to explain the shape of a spillway profile using hydraulic computations are rare.

The purpose of the following computation is to present a simplified theory explaining approximately the spillway crest shape. The bottom pressure head for flow over a curved bottom profile is given by (Eq. 3.75)

$$\frac{p_b}{\gamma} = h + \frac{q^2}{2gh^2}\left(2hz_{bxx} + hh_{xx} - h_x^2 - 2z_{bx}h_x\right). \tag{3.487}$$

For a free jet, the bottom pressure head is $p_b/\gamma = 0$, so that

$$0 = h + \frac{q^2}{2gh^2}\left(2hz_{bxx} + hh_{xx} - h_x^2 - 2z_{bx}h_x\right). \tag{3.488}$$

Following Hager (1983) and Marchi (1992, 1993), assume that the water depth derivatives in a free jet can be neglected, namely $h_{xx} \approx h_x \approx 0$ as compared with the significant nappe curvature, approximated in Eq. (3.488) by d^2z_b/dx^2. Therefore, Eq. (3.488) simplifies to (Hager 1983)

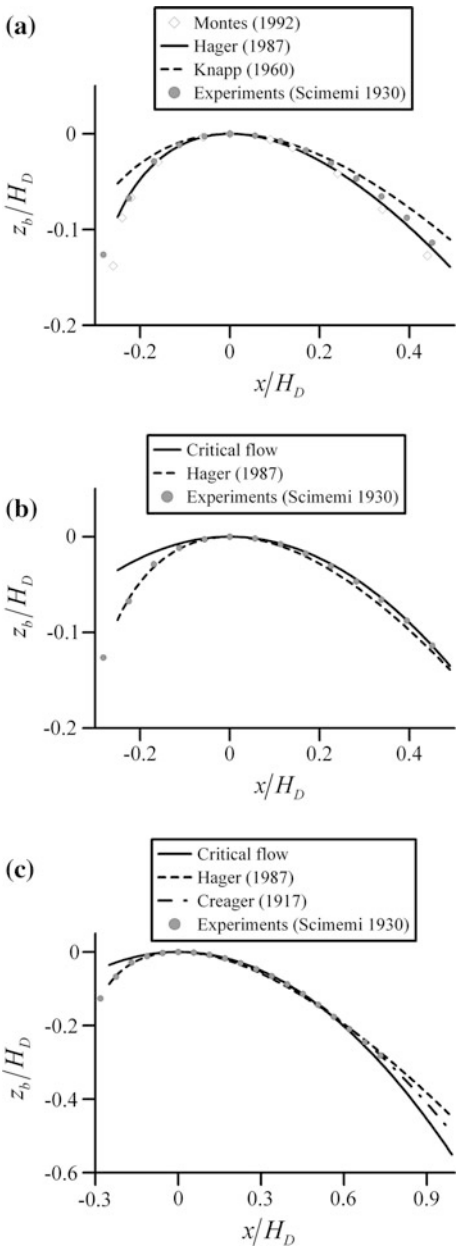

Fig. 3.55 Spillway crest profiles $Z_b(X)$: **a** comparison of approximations, **b** comparison of critical flow profile with Hager's (1987) empirical profile and experimental data (Scimemi 1930), **c** idem as b, but for larger X

$$0 = 1 + \frac{q^2}{gh^2} z_{bxx}, \tag{3.489}$$

or

$$\frac{d^2 z_b}{dx^2} = -\frac{gh^2}{q^2}. \tag{3.490}$$

Equation (3.478) at design conditions is

$$q = C_D \left(g H_D^3\right)^{1/2}. \tag{3.491}$$

Inserting Eq. (3.491) into Eq. (3.490), taking h as the crest flow depth h_{crest}, and defining $X = x/H_D$ and $Z = z/H_D$, yields the ODE describing the spillway crest profile as

$$\frac{d^2 Z}{dX^2} = -\left(\frac{h_{crest}/H_D}{C_D}\right)^2. \tag{3.492}$$

Integrating Eq. (3.492) twice subject to the boundary conditions $Z(X = 0) = Z_X(X = 0) = 0$ produces the solution

$$Z = -\frac{1}{2}\left(\frac{h_{crest}/H_D}{C_D}\right)^2 X^2. \tag{3.493}$$

Based on the results of Table 3.5, flow over a sharp-crested weir is critical, with minimum specific energy conditions at the point of maximum elevation of the lower jet profile. Using the critical flow results for $m = 1.6$, C_D is computed from

$$C_D = \frac{2\sqrt{2}}{3} C_d \left(\frac{h}{E}\right)^{3/2} = \frac{2\sqrt{2}}{3} \times 0.6376 \times \left(\frac{1}{0.888}\right)^{3/2} \approx 0.7184, \tag{3.494}$$

and with the crest critical depth ratio $h_{crest}/H_D = 0.761$, Eq. (3.493) produces the parabolic profile

$$Z = -\frac{1}{2}\left(\frac{h_{crest}/H_D}{C_D}\right)^2 X^2 = -\frac{1}{2}\left(\frac{0.761}{0.7184}\right)^2 X^2 \approx -0.561 X^2. \tag{3.495}$$

The weir crest shape based on critical flow is, therefore, given by Eq. (3.495). Figure 3.55b shows good agreement with the Scimemi data (1930) (Eq. 3.481) is an accurate fit to these data] in the interval $-0.1 < X < 0.7$. Comparison of the Creager (1917) profile given by Eq. (3.482) with Eq. (3.495) indicates good agreement up to $X = 0.7$. Therefore, the weir crest shape in the vicinity of the contracted section can be explained based on the critical flow theory.

The assumption $h_{xx} \approx h_x \approx 0$ used to construct Eq. (3.495) is not accurate for $X < 0$, given the significant drawdown curve, but it provides a good approximation for $X > 0$. The theoretical coefficient 0.561 in Eq. (3.495) is close to 0.5 as used by Scimemi (1930) to produce Eq. (3.481). The exponent 1.85 differs, though, from the theoretical value 2; differences are attributed to the best data-fitting strategy to produce Eq. (3.481). The widely used Eq. (3.481) is, therefore, interpreted as an empirically corrected curve to the theoretical result originating from the critical flow theory with non-hydrostatic pressure.

3.12 Critical Flow Over Weir Profiles

3.12.1 Jaeger's Theory

In the previous sections, 1D and 2D methods to produce the complete solution for flows over a round-crested weir are presented. However, if the main interest focuses on crest conditions, the problem is solved by the computation of the flow depth h_{crest} and the discharge coefficient C_d. These variables are determined by resorting to critical flow computations with curvilinear streamlines as presented in Sect. 3.6. Consider the case of standard spillway flow (Hager 1991; Castro-Orgaz 2008) (Fig. 3.56).

The generalized Jaeger theory presented in Sect. 3.6.3 is well suited for this problem (Jaeger 1956; Montes 1970; Castro-Orgaz 2008). The computation of the head-discharge relation $C_d = C_d(E/H_D)$ is as follows. For a given dimensionless head E/R_b, an arbitrary value of t_{crest}/R_b is selected. The terms t_x and t_{xx} are computed as (Castro-Orgaz 2008)

$$t_x = -\left(\frac{2\,E/R_b}{9+7\,(E/R_b)^2}\right)^{1/2}, \tag{3.496}$$

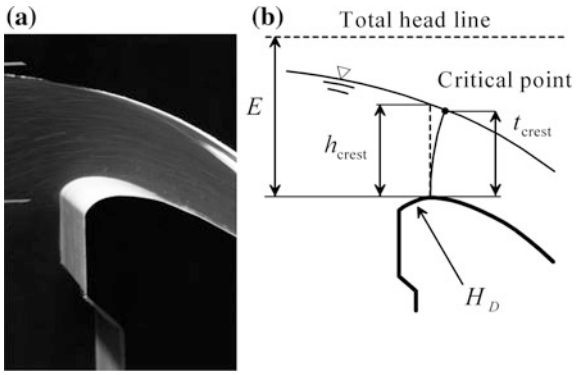

Fig. 3.56 Standard spillway flow: **a** experiment in physical model (Hager 1991), **b** definition sketch for critical flow

$$t_{xx} = \frac{4}{9R_b}\left[1 + \frac{7}{15}\left(\frac{E}{R_b}\right)^{1/2}\right]. \tag{3.497}$$

Equations (3.496) and (3.497) were developed by Castro-Orgaz (2008) making empirical corrections to the basic theoretical results $t_x^2 = 2E/(9R_b)$ and $t_{xx} = 4/(9R_b)$, formally derived using Picard iteration method [see Eqs. (3.203) and (3.205)]. The curvature parameter r is approximated by

$$r = \frac{tz_{bxx}}{tt_{xx} + tz_{bxx}}, \tag{3.498}$$

and m_o computed using Eq. (3.241),

$$m_o = \frac{R_b}{N_o}(r - 1), \tag{3.499}$$

with N_o determined on the basis of t_{crest}, using Eq. $(3.112)_1$ at the spillway crest as

$$\frac{t_{\text{crest}}}{N_o} = 1 - \frac{t_x^2}{6}. \tag{3.500}$$

The value of C_d is then, from Eq. (3.245),

$$C_d = \frac{2^{1/2}}{1 + m_o}\left(\frac{E}{R_b}\right)^{-1}\left(1 - \frac{t_{\text{crest}}}{E}\right)^{1/2} r\left[1 - \left(\frac{1}{r}\right)^{1 + 1/m_o}\right]. \tag{3.501}$$

This sequence is repeated for several t_{crest}/R_b values, until obtaining the maximum discharge coefficient C_d for the prescribed value of E/R_b. The corresponding critical depth for curved flows is, therefore, the value t_{crest} for which C_d reaches a maximum. Figure 3.57a shows the function given by Eq. (3.501) for $E/R_b = 1$ and several values of t_{crest}/R_b. At the point of maximum C_d, the flow is critical and the depth corresponds to the critical flow depth.

The dimensionless parameter governing the flow features at the spillway crest is E/R_b (Matthew 1963, Hager 1991, Castro-Orgaz 2008). However, it is common practice in dam hydraulics to relate spillway flow features to the dimensionless head $\chi = E/H_D$, in which E is the actual head and H_D the design head of the spillway profile. Hence, the relevant critical flow variables at the spillway crest, C_d, h_{crest}, and p_{crest} were determined as functions of χ using $H_D = 1.7R_b$ as scaling (Hager 1987). The discharge coefficient is plotted in Fig. 3.57b together with the experimental data of Hager (1991). Note that the computed C_d curve reasonably agrees with the test data up to $\chi = 2$, an operational head with a markedly high degree of curvature effects. Normal operating conditions of an overflow structure comprise

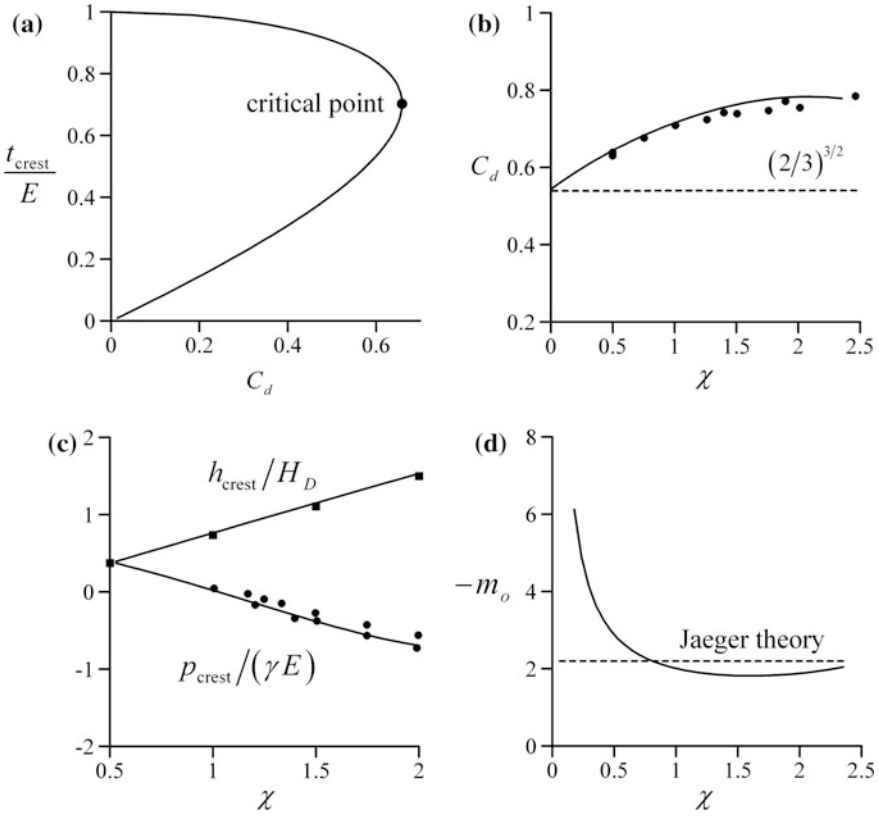

Fig. 3.57 Critical flow over a standard spillway profile: **a** determination of critical flow conditions for $E/R_b = 1$, **b** comparison of (—) computed $C_d(\chi)$ with data of (•) (Hager 1991), **c** comparison of (—) computed $h_{crest}/H_D(\chi)$ and $p_{crest}/(\gamma E)(\chi)$ with data of (•,■) (Hager 1991), **d** comparison of (—) computed $m_o(\chi)$ and (- - -) Jaeger's theory (adapted from Castro-Orgaz 2008)

usually $\chi < 1.33$. Test data concerning the vertical flow depth h_{crest} at the crest presented by Hager (1991) are plotted in Fig. 3.57c. The vertical critical depth h_{crest} is estimated using its equivalent vertical projection of a normal t_{crest} (Fig. 3.56b) as (Hager and Hutter 1984a) (Eq. $3.112)_3$

$$h_{crest} = t_{crest}\left(1 - \frac{t_x^2}{2}\right)^{-1} \cdot \tag{3.502}$$

The prediction given by Eq. (3.502) is plotted in Fig. 3.57c. The curve computed theoretically predicts higher values of h_{crest}/H_D than computed with the hydrostatic pressure approach ($h_{crest}/H_D = 2\chi/3$), in agreement with Hager's data (1991). The dimensionless bottom pressure at the spillway crest is obtained from

conservation of energy of a potential flow as (Castro-Orgaz 2008) [see Eq. (3.467) for $z = 0$]

$$\frac{p_{\text{crest}}}{\gamma E} = 1 - \left(1 - \frac{t_{\text{crest}}}{E}\right) r^{-2/m_o}. \tag{3.503}$$

Charles Jaeger was born on March 26, 1901, in Zurich, Switzerland, and passed away on December 05, 1989, at Pully, VD. He obtained the ETH civil engineering diploma in 1924 and went to an engineering office at Genève for two years to become then private assistant to Eugen Meyer-Peter (1883–1969). He submitted his PhD thesis in 1933 on water hammer analysis and was at a sanatorium because of tuberculosis, returning to the *Versuchsanstalt* in 1938. In 1944, he was appointed ETH Lecturer yet retired because of differences with the director. In 1947, he moved to the UK as an engineer with the English Electric Company at Rugby, became Reader at Imperial College in 1958, and led International Courses until his retirement in 1965. He was awarded the position of special lecturer at Imperial College and received the Gotthilf-Hagen Medal in 1965 and the ETH honorary doctorate in 1983 for outstanding works in hydraulics.

Jaeger contributed significantly to hydraulics and was one of the founders of rock mechanics. His researches are in theoretical hydraulics, mainly in water hammer and surge tanks during his early Zurich period, in the critical flow theory during his second Zurich period and then in hydraulic engineering during his London period. He has written excellent books, including *Technische Hydraulik* later translated into various languages, a book on rock mechanics, and the Hydraulic transients book, which was not so successful though because the methods presented to solve equations were outdated. Yet, Jaeger was a key expert in questions relating to unsteady flows, and he designed these details for various hydropower plants mainly in Scotland. He presented an outstanding theory for curvilinear flow over weirs generalizing previous findings of Boussinesq. He was also the first requiring hydraulic similarity for scour phenomena, with Willy Eggenberger (1916–1994) presenting the corresponding results in his PhD thesis at ETH Zurich.

Equation (3.503) is plotted in Fig. 3.57c with the test data of Hager (1991). The computed curve agrees with these also up to $\chi = 2$. The model predicts $p_{\text{crest}}/(\gamma E) \approx 0$ for design conditions of the spillway crest, namely, $\chi = 1$, as

expected. The crest bottom pressure is of design relevance due to the risk of cavitation damage. It is related to the minimum bottom pressure of the spillway profile by a factor nearly equal to 3/2 (Hager 1991). The parameter $-m_o$ of this theory is plotted in Fig. 3.57d for comparison purposes with the hypothesis of Jaeger, who adopted a constant coefficient of 2.2. Note that $-m_o$ varies considerably with the curvature of the flow, represented by χ. The parameter $-m_o$ is only close to 2.2 if $1 \leq \chi \leq 2$. For $\chi \to 0$, m_o approaches $-\infty$, so that the velocity distribution of Jaeger theory, given by Eq. (3.237), becomes uniform. From energy conservation in potential flow, the pressure distribution then follows the hydrostatic law, and C_d tends to $(2/3)^{3/2}$ for shallow flows.

The extension of Jaeger (1939) theory by Castro-Orgaz (2008) relies on the use of the parameter $m_o(r)$, which, therefore, depends on the actual flow curvature. As previously discussed, the theory is limited to $\chi = 2$, given the empirical approximations used to compute t_{xx} and t_x^2 (Eqs. 3.496–3.497). Furthermore, the parameter m_o is obtained by definition from the slope of the curve $R = R(n)$ at the bottom level ($v = 0$) as

$$m_o = \left[\frac{\partial R(n)}{\partial n}\right]_{v=0}. \tag{3.504}$$

However, it is approximated here as slope of a linear function across the whole equipotential line by

$$m_o = \left(\frac{\partial R}{\partial n}\right)_b \approx \frac{(R_s - R_b)}{N_o}. \tag{3.505}$$

At high heads, the curve $R = R(n)$ is nonlinear near the free surface. Therefore, the bottom-level slope will differ from the mean slope across the equipotential line. Based on the results of Fig. 3.57, Eq. (3.505) is, thus, limited to $\chi < 2$. To simulate standard spillway flow at higher heads, the original theory of Jaeger (1939) was applied, adopting the value $-m_o = m = 2.2$ based on the experimental data of flow over circular-crested weirs (Jaeger 1939, Montes 1970). Given that m is a constant, a simple relation exists between E and the critical flow depth. In the classical Jaeger theory, the critical depth is approximated by the crest flow depth h_{crest}. Equations (3.456)–(3.467) form the mathematical basis; the critical flow condition for standard spillway flow is, thus, from Eq. (3.464), with $m = -m_o = 2.2$

$$\frac{mE}{R_b} = \frac{mh_{\text{crest}}}{R_b} + \frac{1}{2}\frac{\left(1 + \frac{mh_{\text{crest}}}{R_b}\right) - \left(1 + \frac{mh_{\text{crest}}}{R_b}\right)^{1/m}}{1 - \frac{1}{m}\left(1 + \frac{mh_{\text{crest}}}{R_b}\right)^{1/m-1}}, \tag{3.506}$$

The computation of the head-discharge relation $C_d = C_d(E/H_D)$ is as follows. For a given dimensionless head E/R_b, an arbitrary value of h_{crest}/R_b is selected. The

value of E/R_b is then determined from Eq. (3.506), and the discharge coefficient for critical flow is from Eq. (3.462)

$$C_d\left(gE^3\right)^{1/2} = \left[2g(E - h_{\text{crest}})\right]^{1/2} \frac{R_b}{m-1}\left[\left(1 + \frac{mh_{\text{crest}}}{R_b}\right) - \left(1 + \frac{mh_{\text{crest}}}{R_b}\right)^{\frac{1}{m}}\right], \tag{3.507}$$

or,

$$C_d = \left[2\left(1 - \frac{h_{\text{crest}}}{E}\right)\right]^{1/2}\left(\frac{E}{R_b}\right)^{-1}\frac{1}{m-1}\left[\left(1 + \frac{mh_{\text{crest}}}{R_b}\right) - \left(1 + \frac{mh_{\text{crest}}}{R_b}\right)^{\frac{1}{m}}\right]. \tag{3.508}$$

The crest bottom pressure is, from Eq. (3.467) at $z = 0$,

$$\frac{p_{\text{crest}}}{\gamma E} = 1 - \left(1 - \frac{h_{\text{crest}}}{E}\right)\left(1 + \frac{m\,h_{\text{crest}}}{R_b}\right)^{2/m}. \tag{3.509}$$

Predictions based on Eqs. (3.506)–(3.509) are shown in Fig. 3.58, showing good agreement with observations of Hager (1991) up to $\chi = 4$, despite the constant value $m = 2.2$ that was adopted. Jaeger's theory was limited to critical flow computations at a weir crest. However, his theory can also be extended to water surface profile computations with equally good results (Appendix F).

Consider now flow over a circular-crested weir (Fig. 3.59). Velocity and pressure distributions based on Jaeger's theory will be compared with the experimental measurements by Fawer (1937). Applying the generalized Jaeger theory (Castro-Orgaz 2008) to a circular weir test by Fawer (1937), corresponding to a normalized operational head $E/R_b = 2.363$, the results are summarized in Table 3.6. These are based on the computed value $m_o = -1.8318$, resulting in an accurate prediction of C_d. A deviation on the predicted ratio h_{crest}/E from measurements is noted, however.

The velocity distribution given by Eq. (3.237) is compared with Fawer's (1937) data in Fig. 3.60a, resulting in a fair agreement. The pressure distribution was computed based on energy conservation of the potential flow, using the computed velocity profile displayed on Fig. 3.60a. The results are again in fair agreement with observations, yet deviations are noted. Overall, the model results correctly predict the shapes of velocity and pressure distributions, including the negative pressures. For comparative purposes, the classical Jaeger theory previously described was applied to the same test case, using two different values of m, namely $m = 2.2$ and $m = 1.6$. The computed results are stated in Table 3.7. Note that neither C_d, nor h_{crest}/E, are accurately predicted based on $m = 2.2$. In contrast, the computation based on $m = 1.6$ produces excellent agreement between computations and experiments. Computed velocity and pressure distributions using Eqs. (3.459) and

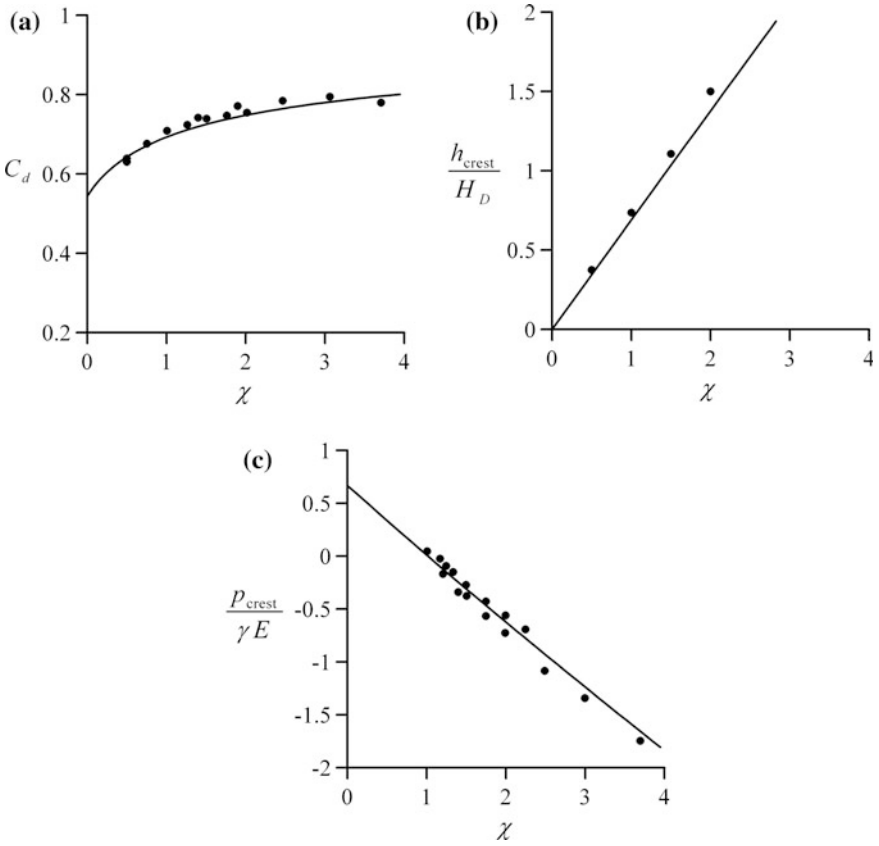

Fig. 3.58 Critical flow over standard spillway profile using Jaeger's (1939) theory ($-m_o = 2.2$). Comparison of (—) computed and (•) measured data (Hager 1991): **a** $C_d(\chi)$, **b** $h_{crest}/H_D(\chi)$, **c** $p_{crest}/(\gamma E)(\chi)$

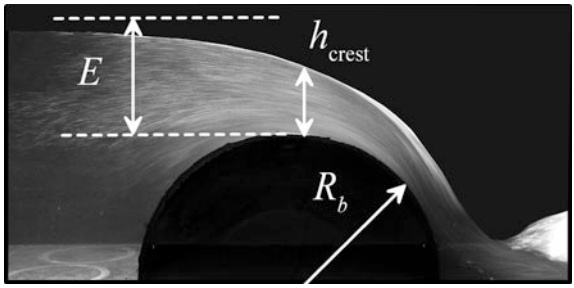

Fig. 3.59 Critical flow over circular-crested weir. Note streamline pattern (photograph VAW)

Table 3.6 Critical flow over circular-crested weir using extended Jaeger's theory (Castro-Orgaz 2008)

	h_{crest}/R_b	h_{crest}/E	E/R_b	C_d
Computed $-m_o = 1.8318$	1.731	0.7326	2.363	0.7545
Measured	1.652	0.6992	2.363	0.755

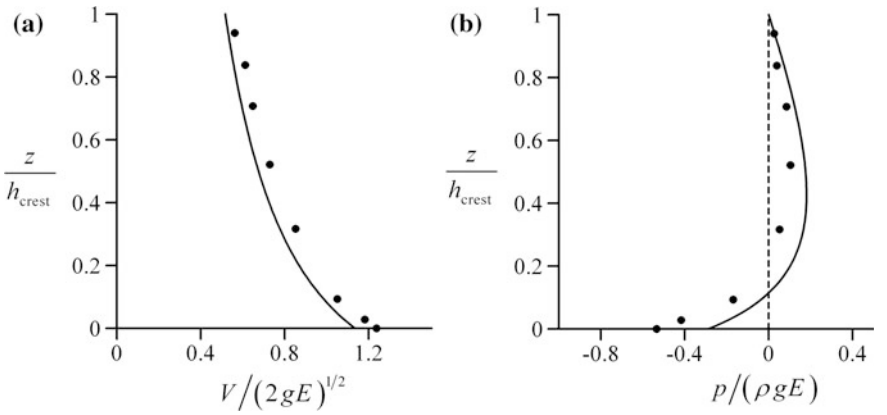

Fig. 3.60 Comparison of velocity $V/(2gE)^{1/2}(z/h_{crest})$ and pressure $p/(\rho gE)(z/h_{crest})$ distributions (—) at circular weir crest based on critical flow computations in Table 3.6, with (•) experimental data of Fawer (1937)

Table 3.7 Critical flow over circular-crested weir using Jaeger's theory (1939)

	mh_{crest}/R_b	h_{crest}/E	E/R_b	C_d
Computed $m = 2.2$	3.585	0.689	2.363	0.718
Computed $m = 1.6$	2.6432	0.6991	2.363	0.7658
Measured	–	0.6992	2.363	0.755

(3.466), respectively, are plotted in Fig. 3.61a,b for $m = 2.2$. The predictions are similar to those depicted previously in Fig. 3.60. The results for $m = 1.6$ are displayed in Fig. 3.61c,d, respectively. Note the improved agreement of both velocity and pressure computations with data. This comparative analysis highlights that the choice of m is important and should not be arbitrary. For $\chi < 2$, the generalized Jaeger theory (Castro-Orgaz 2008) produces good results, and the theory automatically generates an approximate value of m. For $\chi > 2$, resorting to the classical Jaeger theory (1939) is required. However, there is not yet a rational method to compute m for $\chi > 2$, although the present results indicate that a reasonable value must lie in the interval $1.5 < m < 2$.

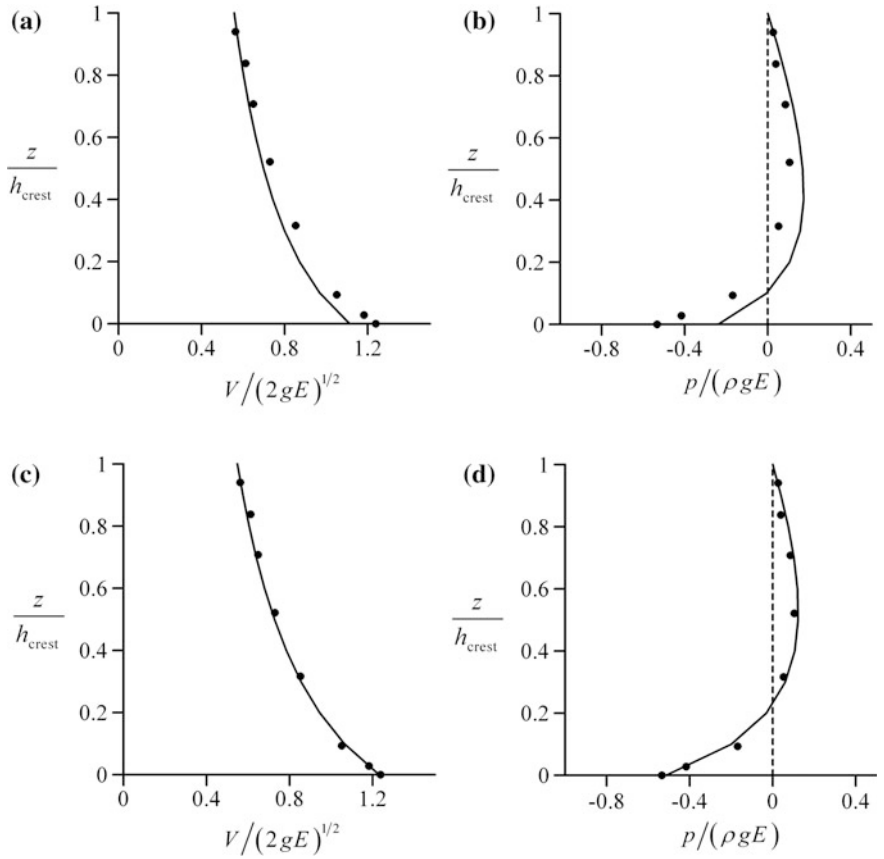

Fig. 3.61 Comparison of velocity $V/(2gE)^{1/2}(z/h_{crest})$ and pressure $p/(\rho gE)(z/h_{crest})$ distributions (—) at circular weir crest based on critical flow computations of Table 3.7 for $m = 2$ (**a**, **b**), 1.6 (**c**, **d**), with (•) experimental data of Fawer (1937)

3.12.2 Fawer's Theory

An alternative approach to compute critical flow over a weir is based on Fawer's theory (Fawer 1937; Khafagi and Hammad 1956; Castro-Orgaz 2010a). Based on an interpolation function for the radius of the streamline curvature (Eq. 3.82), Fawer's velocity distribution at the spillway crest (Fig. 3.56b) is (Eq. 3.83)

$$\frac{V}{V_s} = \exp\left[\frac{N_o}{R_s}\left(r(v-1) + (1-r)\frac{(v^{K+1}-1)}{K+1}\right)\right]. \tag{3.510}$$

A dimensionless discharge $q/(N_o V_s)$, with q = unit discharge, is expressed as

$$\frac{q}{N_o V_s} = \int_0^1 (V/V_s)\mathrm{d}v. \tag{3.511}$$

Inserting Eq. (3.510) into Eq. (3.511), the integral can only be determined numerically, unless simplifications are introduced. Equation (3.510) was developed into a Taylor series by Hager and Hutter (1984a) assuming $K = 1$, resulting in (Matthew 1963; Hager 1985a, b)

$$V = V_s\left[1 + \frac{N}{R_s}\left(r(v-1) + (1-r)\frac{(v^2-1)}{2}\right)\right]. \tag{3.512}$$

Inserting Eq. (3.512) into Eq. (3.511) yields after integration (Eq. 3.86),

$$\frac{q}{N_o V_s} = 1 - \frac{N}{R_s}\left(\frac{r+2}{6}\right). \tag{3.513}$$

This relation is limited to weakly curved flows, e.g., for $r \to 1$, resulting either from the approximation $K = 1$, or from the Taylor series development of the velocity profile. Hager (1985a) proposed an empirical correction to improve Eq. (3.513), assuming that this is the first-order term of the series expansion of the function (Eq. 3.87)

$$\frac{q}{N_o V_s} = \exp\left[-\frac{N}{R_s}\left(\frac{r+2}{6}\right)\right]. \tag{3.514}$$

However, Eq. (3.514) is still limited to $K = 1$. Equation (3.514) was improved by accounting for $K \neq 1$ as (Castro-Orgaz et al. 2008a, b, c, Castro-Orgaz 2010b)

$$\frac{q}{N_o V_s} = \exp\left[-\frac{N}{R_s}\left(\frac{r}{2} + \frac{1-r}{K+2}\right)\right]. \tag{3.515}$$

Equation (3.515) is valid for highly curved open-channel flows. It was applied using $K = 0.5$ to circular weir flows (Castro-Orgaz et al. 2008a, b, c). This K value is, however, not general. In weir flows, the discrete relation $K = K(r)$ obtained from the flow net analysis is fitted by the empirical function (Eq. 3.455), (Castro-Orgaz 2010a, b, c)

$$K = r^{-0.55}. \tag{3.516}$$

The dimensionless discharge $q/(N_o V_s)$ for given values of r and N_o/R_s is obtained by inserting Eq. (3.516) into Eq. (3.510) and then integrating Eq. (3.511) numerically using this velocity profile. Results for $r = 2$, 4, 6, and 8 are plotted in Fig. 3.62 for

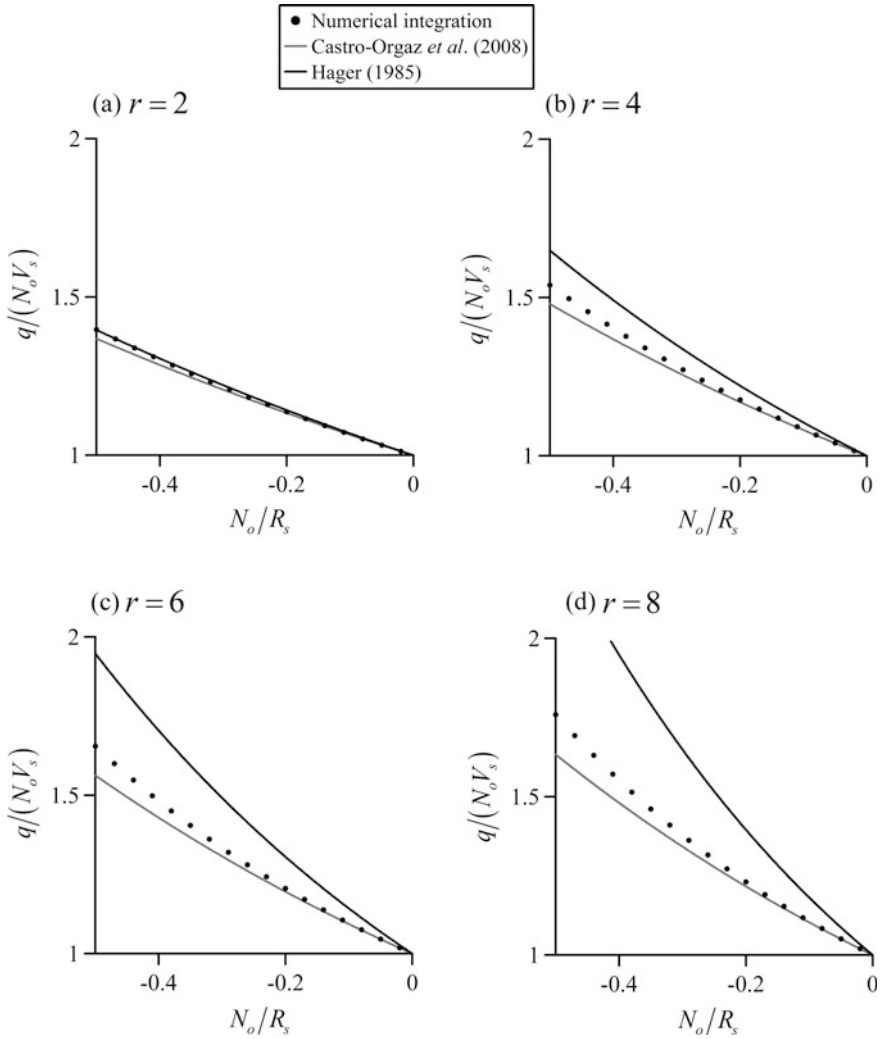

Fig. 3.62 Dimensionless weir-flow discharge $q/(N_o V_s)(N_o/R_s)$ as function of $r = 2$ (**a**), 4 (**b**), 6 (**c**), 8 (**d**)

the weir-flow case ($N_o/R_s < 0$). The results from Eqs. (3.514) and Eq. (3.515) using Eq. (3.516) for $K(r)$ closure are also displayed for comparative purposes. As shown in Fig. 3.62a, Eq. (3.514) is in excellent agreement with the full numerical solution for $r = 2$. The performance is better than that obtained from Eq. (3.515), yet deviations are small. For $r > 2$, Eq. (3.515) matches the numerical results well, indicating that the inclusion of the function $K = K(r)$ is important as the flow curvature increases.

The computation of the head-discharge curve $C_d = C_d(E/R_b)$ based on Fawer's Eq. (3.510) is accomplished by the following steps:

(1) For a value of E/R_b, t_x and t_{xx} are determined from the semi-empirical Eqs. (3.496) and (3.497), respectively. The value of R_b is taken as positive, implying that $E/R_b > 0$, requiring that a negative sign be introduced in computations to account for the weir-flow case.
(2) An arbitrary value for t_{crest}/R_b is selected. Based on hydrostatic critical flow, a reasonable starting value is given by $(t_{crest}/R_b) = 2(E/R_b)/3$.
(3) The relative curvature r is determined from Eq. (3.247) using the available values for t_{xx}, t_x, and $t_{crest}z_{bxx} = -(t_{crest}/R_b)$. Using this value of r, K is estimated from Eq. (3.516).
(4) The value of N_o/R_b is determined from Eq. (3.500), using the available values for t_x and t_{crest}/R_b.
(5) Compute $N_o/R_s = -(N_o/R_b)/r$ based on available values.
(6) Integrate Eq. (3.511) numerically, using Eq. (3.510), for the parametric values $(r, K, N_o/R_s)$ available.
(7) Compute $t_{crest}/E = (t_{crest}/R_b)/(E/R_b)$ and $N_o/t_{crest} = (N_o/R_b)/(t_{crest}/R_b)$, using the available values.
(8) The discharge coefficient is then given, based on Eq. (3.511), by the identity

$$C_d\left(gE^3\right)^{1/2} = \left[\int_0^1 (V/V_s)\mathrm{d}v\right] N_o[2g(E - t_{crest})]^{1/2}, \tag{3.517}$$

or

$$C_d = 2^{1/2}\left(\frac{N_o}{t_{crest}}\right)\left(1 - \frac{t_{crest}}{E}\right)^{1/2}\left(\frac{t_{crest}}{E}\right)\left[\int_0^1 (V/V_s)\mathrm{d}v\right]. \tag{3.518}$$

The sequence of steps (2)–(8) is repeated until the condition $\partial C_d/\partial(t_{crest}/R_b) = 0$ is reached, corresponding to the critical flow at the weir crest (Fawer 1937; Chanson 2006; Castro-Orgaz et al. 2008c; Castro-Orgaz 2010a). Then, a new value of E/R_b is selected, and the entire sequence is repeated. The resulting head-discharge curve $C_d = C_d(E/R_b)$ is plotted in Fig. 3.63a, showing good agreement with the experimental data (Hager 1991) of a standard spillway flow up to $E/R_b = 2.5$ ($\chi \approx 1.5$). The accuracy of this approach is, therefore, slightly smaller as compared with Jaeger's generalized theory. To highlight the effect of the nonlinearity of $K = K(r)$, the identical numerical computation was performed by assuming $K = 1$, i.e., the treatment of Hager (1985a). As shown in Fig. 3.63a, the results of the analysis using Eq. (3.514), based on $K = 1$, agree excellently with the data of Hager (1991) up to $E/R_b = 1$ ($\chi \approx 0.58$), i.e., weakly curved flows. The results based on Eq. (3.515)

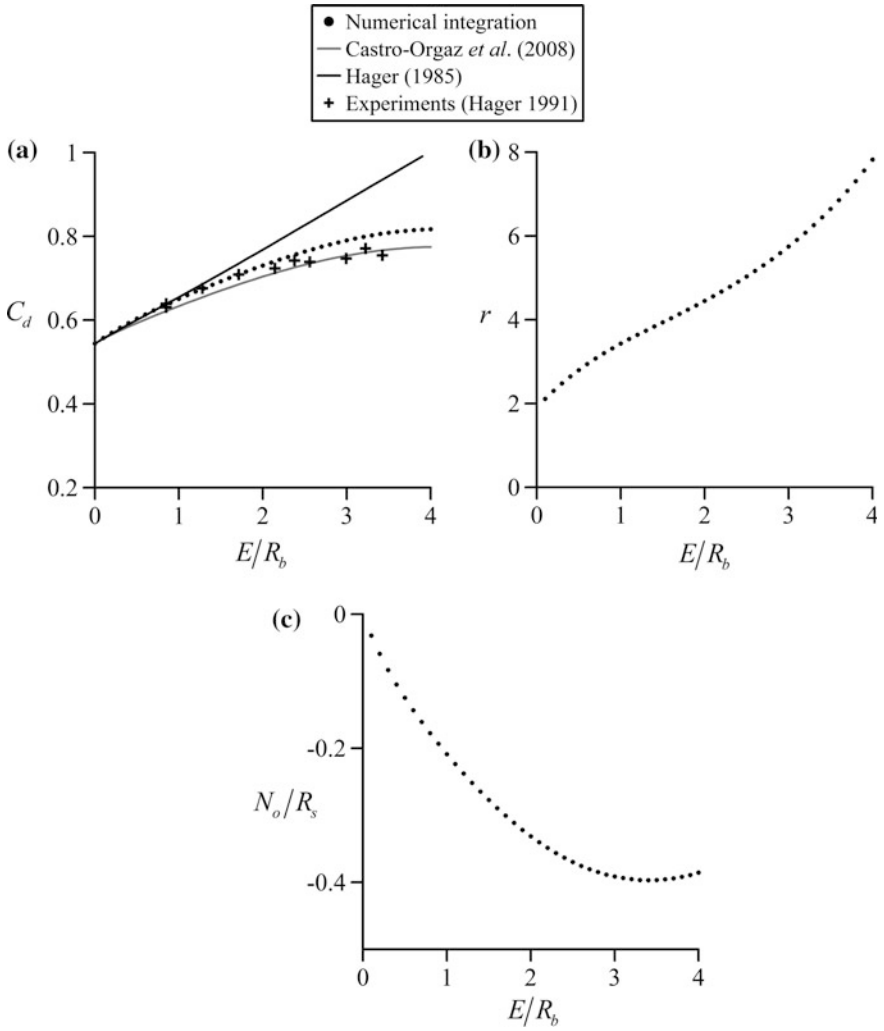

Fig. 3.63 Critical flow computation of standard spillway flow using Fawer's theory **a** $C_d(E/R_b)$, **b** $r(E/R_b)$, **c** $N_o/R_s(E/R_b)$

match the experimental data up to $E/R_b = 3$, i.e., highly curved flows. The computed function $r(E/R_b)$ is displayed in Fig. 3.63b, showing that the maximum value obtained for $E/R_b = 4$ is $r \approx 8$. Further, the computed curve $N_o/R_s(E/R_b)$ in Fig. 3.63c shows that N_o/R_s is below -0.5 for this range of operational heads involving highly curved flows. Values previously generated in Fig. 3.62 correspond, therefore, to these practical limits for both r and N_o/R_s.

Fawer's critical flow theory for curvilinear flow (Castro-Orgaz et al. 2008c) applies to study flow over circular-crested weirs (Fig. 3.55), as investigated by

Fawer (1937), Matthew (1963, 1991), Lenau (1967), Montes (1970, 1998), Hager (1985b, 1993), Ramamurthy and Vo (1993a, b), Ramamurthy et al. (1992), Chanson and Montes (1998), Heidarpour and Chamani (2006), Schmocker et al. (2011), and Castro-Orgaz and Chanson (2014). For a given unit discharge q, the minimum specific energy head defines the critical flow depth t_{crest} as predicted by Eq. (3.225). By using Eq. (3.223) at the weir crest ($z_{bx} = 0$), the specific energy and hence the weir discharge coefficient C_d are determined. The first and second derivatives are approximated as (Matthew 1991; Castro-Orgaz et al. 2008c)

$$t_x = -\frac{2^{1/2}}{3}\left(\frac{E}{R_b}\right)^{1/2}\left(1 - \frac{236}{729}\frac{E}{R_b}\right), \tag{3.519}$$

$$t_{xx} = \frac{4}{9R_b}\left(1 + \frac{4783}{16038}\frac{E}{R_b}\right). \tag{3.520}$$

Equations (3.519) and (3.520) were determined by Matthew (1991) by an iteration procedure using the third-order extended energy equation (Eq. 3.80). The parallel flow relation $t = 2E/3$ was used as an approximation in Eqs. (3.519) and (3.520). The term $t^2 t_{xxx}/t_x$ in Eq. (3.225) follows from the lower order critical flow condition given by Eq. (3.230); there, the required value q^2/gt_{crest}^3 was estimated from $q^2/(gt_{crest}^3)\exp(-t_{crest}/R_b) = 1$, the first-order expansion of which is the weakly curved critical flow condition of Hager (1985b). Once the critical depth t_{crest} is computed, its corresponding vertical flow depth h_{crest} as the variable measured by Chanson and Montes (1998) is given by Eq. (3.502). The mean value of $K = 0.5$ was adopted to compute curved streamline flow over a circular weir, which reasonably reproduces the flow features in the range of practical applications for the circular-crested weir (Castro-Orgaz et al. 2008c).

The results for the critical depth at the weir crest are shown in Fig. 3.64a. The model prediction for the critical depth at the weir crest was tested with the data from a careful set of experiments reported by Chanson and Montes (1998). The predicted critical depth agrees with the data up to $E/R_b = 2$, except for very low heads (i.e., $E/R_b < 0.2$), for which both viscosity and surface tension play a major role (Matthew 1963). For $E/R_b = 0$, the potential curved model yields $h_c = (q^2/g)^{1/3}$. If the boundary layer effect is included in the analysis, the critical depth increases above its value h_c (Montes 1998) due to the boundary layer displacement thickness. This theoretically explains the values $h_{crest}/h_c > 1$ obtained experimentally for low heads. As shown in Fig. 3.64b, the computed discharge coefficient based on the present higher order critical flow theory agrees well with the experimental data (Blau 1963; Heidarpour and Chamani 2006; Castro-Orgaz 2010a) again up to $E/R_b = 2$. For low heads, the differences with the experimental data of Heidarpour and Chamani (2006) are again due to viscous and surface tension effects (Matthew 1963). For low heads, the effect of streamline curvature plays a minor role, whereas scale effects have a notable impact on the discharge characteristics. The inclusion of the boundary layer in the analysis causes a reduction of the discharge coefficient, as

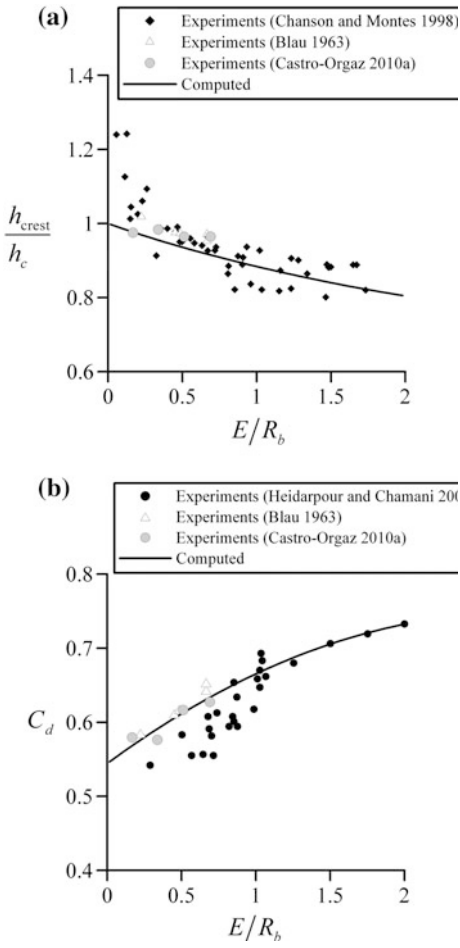

Fig. 3.64 Critical flow over circular-crested weir: comparison of **a** (—) computed $h_{crest}/h_c(E/R_b)$, **b** $C_d(E/R_b)$ with measurements (adapted from Castro-Orgaz et al. 2008c)

found analytically by Matthew (1963), Montes (1970), and Castro-Orgaz and Hager (2014b).

The computation of $C_d(E/R_b)$ shown in Fig. 3.64b based on the higher order critical flow conditions given by Eq. (3.225) is compared in Fig. 3.65 with the theories of Dressler (1978) and Matthew (1991). The third-order extended energy equation from a Picard iteration (Eq. 3.80) gives upon imposing critical flow at the weir crest (Matthew 1991)

$$C_d = \left(\frac{2}{3}\right)^{3/2}\left[1 + \frac{22}{81}\frac{E}{R_b} - 0.045\left(\frac{E}{R_b}\right)^2\right]. \tag{3.521}$$

The results of Eq. (3.521) in Fig. 3.64 are extremely close to those of Eq. (3.225). Therefore, by resorting to $K \neq 1$ in Eq. (3.100), it is possible to find similar results

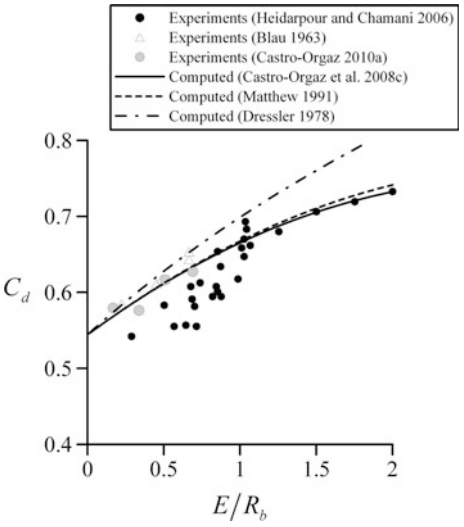

Fig. 3.65 Comparison of critical flow theories for circular-crested weir flow (adapted from Castro-Orgaz et al. 2008b)

to those originating from Eq. (3.80). The prediction of $C_d(E/R_b)$ from Dressler's theory using Eq. (3.161) is, however, far from the experimental data for $E/R_b > 1$. Therefore, the concentric streamline approximation needs to be relaxed for higher heads.

3.13 Standard Sluice Gate

3.13.1 Free Jet Flow

Gates constitute an important hydraulic structure used in irrigation schemes, inland navigation, and dam structures. The standard sluice gate relates to a planar vertical "wall" inserted in a smooth and prismatic, horizontal rectangular channel (Fig. 3.66). Its crest is formed as a sharp-crested weir, made up by a 2-mm horizontal sharp crest bevelled at its tailwater side by 45°. This structure is employed to measure discharge or to set a backwater level. Its basic flow features were investigated by model researches so that detailed results are available (Rajaratnam and Humphries 1982; Othsu and Yasuda 1994; Roth and Hager 1999).

Gate flow is divided into the approach flow portion up to the gate section made up of an internal jet along the channel bottom with a vortex flow zone above it, and the free jet portion in the tailwater (Fig. 3.66b). Detailed computational simulations based on the ideal fluid flow theory are available (Fangmeier and Strelkoff 1968; Montes 1997). Free gate flow is often treated using 1D conservation of energy between the approach flow and the tailwater jet assuming parallel-streamlined flow (Rouse 1950; Montes 1998). Flow features of engineering interest including the

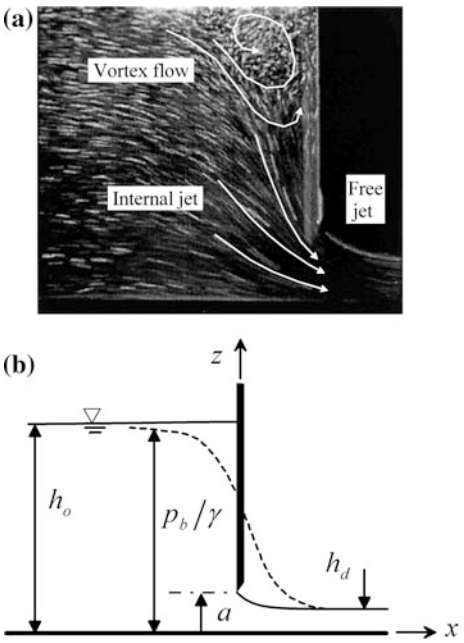

Fig. 3.66 Standard sluice gate flow: **a** typical internal flow structure of upstream flow, **b** definition sketch with (- - -) bottom pressure head distribution (adapted from Castro-Orgaz and Hager 2014c)

free surface profile and the bottom pressure distribution (Montes 1997) are overlooked by this approach.

Standard sluice gate flow exhibits features incompatible with parallel-streamlined flow considerations, originating from the non-hydrostatic pressure distribution (Fangmeier and Strelkoff 1968; Montes 1997). The Boussinesq-type approximation introduces the vertical acceleration effect in the 1D flow equations (Boussinesq 1877; Matthew 1991; Bose and Dey 2007, 2009; Castro-Orgaz and Hager 2009), thereby overcoming the standard 1D hydrostatic pressure limitation. Boussinesq's theory was considered by Serre (1953) for the free jet flow portion of free gate flow, without checking the theoretical results with the experimental data or 2D ideal fluid flow computations. Benjamin (1956) fitted the 2D free surface jet profile to a standard solitary wave profile, without satisfactory results. Both Serre and Benjamin overlooked the effects of the upstream free surface profile and the bottom pressure features. The gate pressure distribution was not considered in these applications of Boussinesq's theory. No notable 1D computations of standard sluice gate flow using the Boussinesq equations were presented since these works, as noted, e.g., in the detailed review of Montes (1997). Therefore, Castro-Orgaz and Hager (2014c) studied the free surface and the bottom pressure features using the 1D Boussinesq's approach, including the pressure distributions both on the gate and on the channel bottom. This approximate treatment is described herein. The computation of the free jet portion in the tailwater of a standard sluice gate has been extensively considered using the full 2D potential

flow model. A solution of the Laplace equation is sought using suitable numerical techniques (Fangmeier and Strelkoff 1968; Montes 1997). Montes (1997) reviewed the relevant 2D solutions from 1860, so that reference to his paper is made for detailed information. On the other hand, the computation of free jets using a 1D model received almost no attention. The first attempt was due to Fawer (1937), who used an extended Boussinesq-type energy equation. His model was, however, only valid for inclined gates and was employed to estimate the contraction coefficient, yet without furnishing jet profile computations. He then proceeded with a 2D hydrodynamic solution without gravity effects for planar sluice gates. The next attempt was made by Serre (1953), who proposed a theoretical model for the free jet surface profile, again without verifying the results with the experimental data or 2D computations. Using a 1D model, Benjamin (1956) tried to fit a standard solitary wave to the 2D free surface profile computed by Southwell and Vaisey (1946). However, the fit was stated to be valid only far from the gate lip. A hybrid method was then proposed using a 2D solution in the vicinity of the gate section. The 1D modeling of free jets is therefore reconsidered starting with the (E, S, q) invariants of Boussinesq-type equations for steady potential flow in a horizontal channel as (Serre 1953; Benjamin and Lighthill 1954; Hager and Hutter 1984b)

$$\begin{aligned} E &= h + \frac{q^2}{2gh^2}\left(1 + \frac{2hh_{xx} - h_x^2}{3}\right) = \text{const.}, \\ S &= \frac{h^2}{2} + \frac{q^2}{gh}\left(1 + \frac{hh_{xx} - h_x^2}{3}\right) = \text{const.}, \quad q = \text{const.} \end{aligned} \tag{3.522}$$

Here, h is the vertical flow depth, E the specific energy head, S the specific momentum, and q the unit discharge; subscripts indicate ordinary differentiation with respect to the horizontal coordinate x. The jet invariants E and S are evaluated, taking the conditions at the downstream jet section, as $E = h_d + q^2/(2gh_d^2)$ and $S = h_d^2/2 + q^2/(gh_d)$, with h_d as the tailwater flow depth (Fig. 3.66b). The first of Eq. (3.522) is expressed in the alternative form

$$\frac{q^2}{6g}\frac{\mathrm{d}}{\mathrm{d}h}\left(\frac{h_x^2}{h}\right) = E - h - \frac{q^2}{2gh^2}. \tag{3.523}$$

This equation straightforwardly integrates to (Serre 1953)

$$\frac{q^2}{6g}h_x^2 = Eh^2 - \frac{h^3}{2} + \frac{q^2}{2g} + Ch = \left(h_d + \frac{q^2}{2gh_d^2}\right)h^2 - \frac{h^3}{2} + \frac{q^2}{2g} + Ch, \tag{3.524}$$

where use of the jet invariant $E = h_d + q^2/(2gh_d^2)$ was made. Setting the boundary condition $h_x \to 0$, for $h \to h_d$, on Eq. (3.524), the integration constant C is given by $C = -[h_d^2/2 + q^2/(gh_d)] \equiv -S$. Thus, Eq. (3.524) is rewritten as

$$\frac{q^2}{3g}h_x^2 = 2\left(h_d + \frac{q^2}{2gh_d^2}\right)h^2 - h^3 + \frac{q^2}{g} - 2\left(\frac{h_d^2}{2} + \frac{q^2}{gh_d}\right)h = (h-h_d)^2\left(\frac{q^2}{gh_d^2} - h\right), \tag{3.525}$$

or in the alternative form,

$$h_x^2 = \frac{3}{\mathsf{F}_d^2}\left(\frac{h}{h_d} - 1\right)^2\left(\mathsf{F}_d^2 - \frac{h}{h_d}\right). \tag{3.526}$$

Here, $\mathsf{F}_d = q/(gh_d^3)^{1/2}$ is the tailwater Froude number. The general integral of Eq. (3.526) is with ω as a constant (Serre 1953)

$$\frac{h}{h_d} = 1 + 4\left(\mathsf{F}_d^2 - 1\right)\frac{\omega \exp\chi}{\left(1+\omega\exp\chi\right)^2}, \tag{3.527}$$

where

$$\chi = \frac{\left(3\mathsf{F}_d^2 - 3\right)^{1/2}}{\mathsf{F}_d}\frac{x}{h_d}. \tag{3.528}$$

F_d is related to E by imposing conservation of energy between the approach and the tailwater sections as $E = h_d + q^2/(2gh_d^2) = h_d(1 + \mathsf{F}_d^2/2)$, resulting in

$$\mathsf{F}_d^2 = 2\left(\frac{E}{C_c a} - 1\right), \quad (0 < C_c < 1) \tag{3.529}$$

with $h_d = C_c a$, a as the gate opening and C_c as the contraction coefficient. The value of ω is determined by imposing the boundary condition $h(x = 0) = a$ at the gate section, from which Eq. (3.527) produces the quadratic equation

$$1 + 4\left(\mathsf{F}_d^2 - 1\right)\frac{\omega}{(1+\omega)^2} - \frac{1}{C_c} = 0. \tag{3.530}$$

For $\omega = 1$, the general Eq. (3.527) degenerates into the standard solitary wave profile deduced by Benjamin (1956)

$$\frac{h}{h_d} = 1 + 4\left(\mathsf{F}_d^2 - 1\right)\frac{\exp\chi}{(1+\exp\chi)^2} = 1 + \left(\mathsf{F}_d^2 - 1\right)\mathrm{sech}^2\left(\frac{\chi}{2}\right). \tag{3.531}$$

Results of Eq. (3.527) are compared in Fig. 3.67a with the 2D computations of Montes (1997) using $C_c = 0.61$. This mean constant value is supported by 2D potential flow computations, indicating only a slight variation down to $a/E = 0.60$ (Montes 1997). The agreement of Eq. (3.527) with 2D results is in general good for this range of E/a, yet with slight deviations near $x = 0$ for the low values of $E/a = 2$

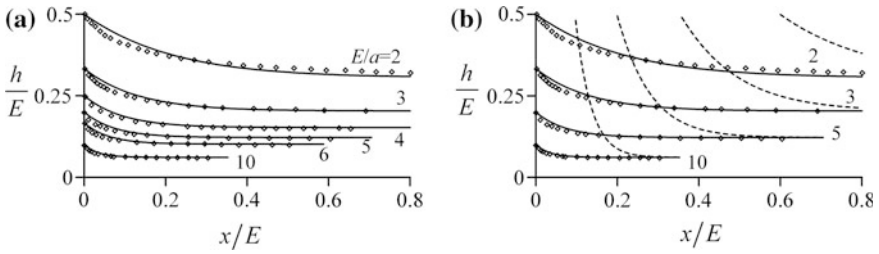

Fig. 3.67 Free jet surface profiles $h/E(x/E)$ for various values of E/a: **a** comparison of (—) Boussinesq-type solution with (◊) 2D potential flow computations (Montes 1997), **b** idem including (- - -) standard solitary wave (Benjamin 1956) (adapted from Castro-Orgaz and Hager 2014c)

and 3. A limitation of 1D models as compared with the full 2D solution relates to the exact boundary conditions at $x = 0$. From Eq. (3.527), $h_x(0) \cong -1$ was obtained for most of the simulations, whereas the surface profile is vertical at the gate lip based on the 2D computations. This effect is local, so that its importance is small for larger values of x.

Equation (3.531) is compared in Fig. 3.67b for selected tests with Eq. (3.527) and the 2D results. Note that the agreement is generally not very good and limited to the tailwater solitary wave portion for large E/a. The solitary wave does not account for correct boundary conditions at $x = 0$, whereas Eq. (3.527) describes a generalized solitary wavelike profile that accounts for correct boundary conditions (Castro-Orgaz and Hager 2014c).

3.13.2 Approach Flow

All previous 1D computations assumed a horizontal upstream free surface. Benjamin and Lighthill (1954) and Hager and Hutter (1984b) demonstrated that the only possible steady-state water wave in a subcritical flow ($\mathsf{F} < 1$) conserving E, S, and q is the cnoidal wave. Thus, the approach flow in the vicinity of the gate is physically better represented by a cnoidal wave train than by a horizontal surface. This is exploited in Fig. 3.68, in which 2D surface profiles of Montes (1997) are compared with the cnoidal wave solution of Eq. (3.522). A numerical solution was determined using the first of Eq. (3.522) imposing the flow depth h_o as boundary condition at $x = -5a$ and $h_x = -0.05$ as arbitrary value there to deviate the flow from uniformity. Results indicate that the upstream approach flow follows indeed the cnoidal wave solution of small wave amplitude and large wavelength. An aspect of 2D potential flow solutions deserving attention relates to the method used to find iteratively the upstream surface profile. In the numerical methods of Cheng et al. (1981) or Montes (1997), the iteration of the free surface involves the specific energy head of parallel-streamlined flows $E = h + q^2/(2gh^2)$, to relocate the nodes

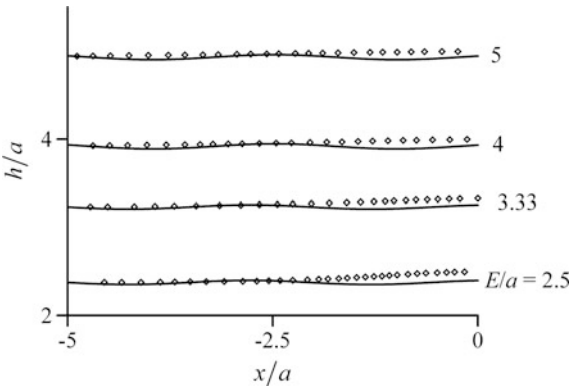

Fig. 3.68 Approach flow profile $h/a(x/a)$ with (—) 1D computation, (◊) 2D computation (Montes 1997) (adapted from Castro-Orgaz and Hager 2014c)

at the free surface. It is known that this equation does not allow for water surface undulations as in cnoidal wave trains (Benjamin and Lighthill 1954). Thus, it remains unexplored to which degree the current numerical searching algorithms for the free surface, based on this equation, artificially smooth the physical oscillations, in the computed free surface position. Therefore, it appears reasonable to assume that a gate inserted in a subcritical stream provokes a slightly non-horizontal free surface exhibiting cnoidal wavelike features.

The existence of irrotational water wave patterns is not trivial and has implications related to the physical features of transitional potential open-channel flows in horizontal, straight channels. The transition from super- ($\mathsf{F} > 1$) to subcritical ($\mathsf{F} < 1$) flows close to the critical depth appears in the form of an undular hydraulic jump. This transition is characterized as a solitary wave connected with a cnoidal wave (Iwasa 1955; Hager and Hutter 1984b). The solitary wave provides a transitional flow from a supercritical approach flow to a wave emerging in a subcritical flow. A local loss of energy permits to connect this solitary wave portion with a cnoidal wave train in the subcritical reach. Standard sluice gate flow provokes a transition from sub- ($\mathsf{F} < 1$) to supercritical ($\mathsf{F} > 1$) flows, involving a cnoidal wave in the upstream portion. A drop in momentum S provoked by the gate reaction permits a generalized solitary wavelike flow to emerge below the gate that asymptotes to the tailwater conditions. Thus, the transitional flow at a standard sluice gate follows Benjamin and Lighthill's (1954) theory, providing with the undular jump a complete image of flow transitions in straight-bottomed channels.

3.13.3 Gate Pressure Distribution

At the gate section, the pressure is markedly non-hydrostatic (Montes 1997; Castro-Orgaz and Hager 2014c). From the ideal fluid flow theory, the horizontal velocity is zero at the vertical gate plane, so that the vertical velocity is large. A standard Boussinesq-type development using the Cartesian system of reference,

taking streamline curvatures and slopes with respect to the x-coordinate into account, is inadequate, because $h_x \to \infty$ at the gate, so that a special solution must be developed along the gate plane. At the gate lip, the exact 2D boundary condition is, with w_e as the vertical velocity at the gate lip,

$$\frac{w_e^2}{2g} = E - a. \tag{3.532}$$

Following the standard Boussinesq equations, the vertical velocity may be assumed to vary linearly along the gate plane as

$$w = w_e\left(1 - \frac{z-a}{E-a}\right). \tag{3.533}$$

The strong vertical acceleration does not render this law accurate. For strongly vertical flows, Fawer's (1937) theory applies, thereby generalizing Eq. (3.533) with K_G as Fawer-type exponent and $\mu = (z - a)/(E - a)$ to

$$w = w_e\left(1 - \mu^{K_G}\right). \tag{3.534}$$

The pressure distribution on the gate is then given by the Bernoulli equation $E = p/\gamma + z + w^2/(2g)$. Inserting in it Eq. (3.534) for w and Eq. (3.532) for w_e yields

$$\begin{aligned} E - a &= \frac{p}{\gamma} + z - a + (E-a)\left(1 - \mu^{K_G}\right) \\ &\Rightarrow \frac{p}{\gamma(E-a)} = 2\mu^{K_G} - \mu^{2K_G} - \mu. \end{aligned} \tag{3.535}$$

A simple check of this equation with 2D data by Montes (1997) indicates that $K_G = 1$ is not accurate, so that a theoretical method is required to compute K_G. The pressure force F at the gate section is given upon integrating Eq. (3.535) by

$$\frac{F}{(E-a)^2} = \int_0^1 \frac{p}{\gamma(E-a)}\mathrm{d}\mu = \frac{2}{K_G+1} - \frac{1}{2K_G+1} - \frac{1}{2}. \tag{3.536}$$

This constitutes the first relation $F(K_G)$. A second identity to be satisfied by F originates from the momentum balance applied between the boundary sections as

$$F = \left(\frac{h_o^2}{2} + \frac{q^2}{gh_o}\right) - \left(\frac{C_c^2 a^2}{2} + \frac{q^2}{gC_c a}\right). \tag{3.537}$$

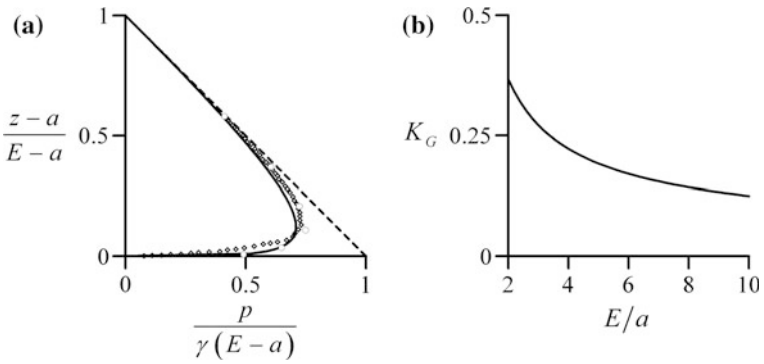

Fig. 3.69 Pressure distribution on gate: **a** E/a = 3.33 (K_G = 0.25), with (—) Eq. (3.263), (◊) 2D computation (Montes 1997), (○) 2D data (Cheng et al. 1981), **b** $K_G = K_G(E/a)$ (adapted from Castro-Orgaz and Hager 2014c)

This equation ignores the shear stress at the bottom boundary. In addition, for given E, the discharge q follows from conservation of energy as

$$q = C_c a[2g(E - C_c a)]^{1/2}. \tag{3.538}$$

The discharge q was computed for the given values of E and a by using Eq. (3.538) and C_c = 0.61. The upstream flow depth h_o was computed using the values of E and q and the force F from Eq. (3.537). With this value of F, the parameter K_G results from Eq. (3.536), and the pressure distribution follows from Eq. (3.535). A test case for E/a = 3.33 is considered in Fig. 3.69a, where the 1D results agree well with 2D data of Montes (1997) and Cheng et al. (1981). The system of Eqs. (3.536)–(3.538) was numerically solved using a Newton–Raphson algorithm, and the variation of K_G with E/a is depicted in Fig. 3.69b.

3.13.4 Bottom Pressure Distribution

The transitional behavior of $h = h(x)$ is discussed and explained in the context of steady water waves. The gate essentially provokes a drop in S permitting the approaching cnoidal wave to pass below the gate, thereby being transformed into a solitary wave, with E kept constant. The flow depth at the gate is discontinuous, therefore, whereas the bottom pressure profile $p_b(x)$ is continuous, approaching asymptotically the up- and downstream flow depths (Fig. 3.66b). This important transitional flow feature was explored by Castro-Orgaz and Hager (2014c). The bottom pressure associated with Eq. (3.522) is (Matthew 1991; Castro-Orgaz and Hager 2009, 2014a)

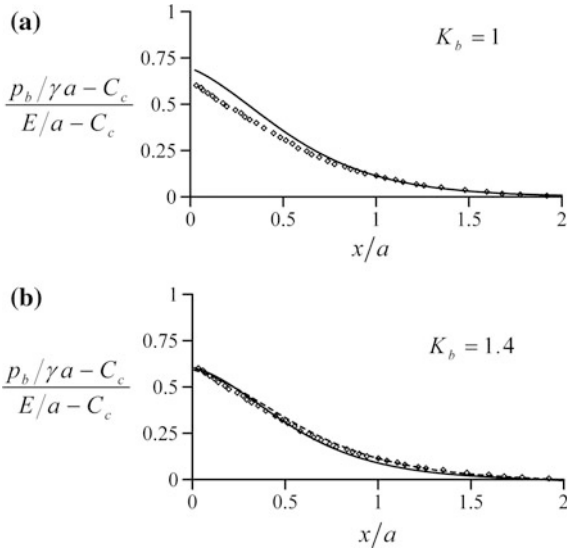

Fig. 3.70 Normalized free jet bottom pressure profile $(p_b/\gamma a - C_c)/(E/a - C_c)$, comparison of Boussinesq-type solution with 2D potential flow results for K_b = **a** 1, **b** 1.4 for (—) E/a = 5, (- - -) E/a = 2, (◊) 2D computation (Montes 1997) (adapted from Castro-Orgaz and Hager 2014c)

$$\frac{p_b}{\gamma} = h + \frac{q^2}{gh^2}\left(\frac{hh_{xx} - h_x^2}{2}\right). \tag{3.539}$$

The flow depth derivatives h_x and h_{xx} and, thus, p_b for the free jet portion are determined by Eq. (3.527). The results are shown in Fig. 3.70a for E/a = 5 and compared with 2D results. Note the perfect agreement for $x/a > 1$ that reduces as the gate section is approached. Deviations are attributed to the weakly curved flow validity of Eq. (3.539). Although the predictions of $h(x)$ are good, the disagreement in $p_b(x)$ indicates that streamline curvature exhibits a nonlinear behavior. Let K_b be a curvature distribution parameter (Fawer 1937), so that Eq. (3.539) is based on K_b = 1. Fawer (1937) indicated that for gate flow, $K_b > 1$. Both the specific energy E and the bottom pressure p_b can be expressed by K_b to account for a nonlinear curvature distribution as (Fawer 1937; Castro-Orgaz and Hager 2014c) (Appendix E)

$$E = h + \frac{q^2}{2gh^2}\left(1 + \frac{2hh_{xx}}{K_b + 2} - \frac{h_x^2}{3}\right), \quad \frac{p_b}{\gamma} = h + \frac{q^2}{gh^2}\left(\frac{hh_{xx}}{K_b + 1} - \frac{h_x^2}{2}\right). \tag{3.540}$$

Equation $(3.540)_1$ for $h = h(x)$ was solved using the fourth-order Runge–Kutta method, subject to the boundary conditions $h(0) = a$ and $h_x(x \to +\infty) \to 0$. The Runge–Kutta method was used to transform Eq. $(3.540)_1$ into a system of two ODEs from which the solutions $[h(x), h_x(x)]$ ensue. As the boundary condition of h_x is prescribed at infinity, the solution is iterative. Using a shooting method, e.g., as the Runge–Kutta algorithm, a value of $h_x(0)$ is first assumed. The system of equations is then solved numerically, and the conditions at the tailwater section are revised. The tailwater section for this computation was fixed at x/a = +6. If $h_x(6)$ is

not close to zero within a prescribed tolerance, then computations restarted with a new value of $h_x(0)$. Once $h(x)$ was determined, the computation of $p_b(x)$ from the numerical results is straightforward. Results are presented in Fig. 3.70b for K_b = 1.4, indicating an excellent reproduction of the bottom pressure distribution. The numerical free surface profile agrees practically perfectly when compared with the results of Eq. (3.527).

The cnoidal wave profile of the approach flow produces a slight deviation of the bottom pressure from the free surface profile, indicating that the quadratic and linear profiles for the horizontal and vertical velocities (u, w) of potential flow [see Eqs. (3.63) and (3.64) for a horizontal bottom] (Matthew 1991) do not reproduce the internal jetlike features. Keutner (1935) stated that the non-hydrostatic bottom pressure of the upstream flow is associated with an internal jet originating at the upstream approach flow section transforming at the gate section into a free jet. To explain the bottom pressure features of the approach flow, Keutner's method will be developed. The flow is assumed to be divided in two layers, an internal jet layer of thickness s transporting the discharge q and a recirculating fluid layer above it. The equations of a classical hydraulic jump with a surface roller of thickness r are given under hydrostatic pressure by (Valiani 1997)

$$S = \frac{(s+r)^2}{2} + \frac{q^2}{gs}, \quad \frac{p_b}{\gamma} = r + s. \tag{3.541}$$

With p_s as the pressure at the jet surface and s as the jet thickness, Eq. (3.541) can be empirically enhanced to account for a non-hydrostatic pressure as

$$S = \frac{(s+p_s/\gamma)^2}{2} + \frac{q^2}{gs}\left(1 + \frac{ss_{xx} - s_x^2}{3}\right), \quad \frac{p_b}{\gamma} = \frac{p_s}{\gamma} + s + \frac{q^2}{gs^2}\left(\frac{ss_{xx} - s_x^2}{2}\right). \tag{3.542}$$

Equation (3.542) is a generalization of the development of Valiani (1997) for hydrostatic submerged jets. In the sluice gate problem, experiments indicate that the vertical velocity component is significant (Roth and Hager 1999), so that this effect needs to be retained. The equations are further enhanced to account for a nonlinear curvature distribution, resulting in

$$S = \frac{(s+p_s/\gamma)^2}{2} + \frac{q^2}{gs}\left(1 + \frac{ss_{xx}}{K_b+2} - \frac{s_x^2}{3}\right), \quad \frac{p_b}{\gamma} = \frac{p_s}{\gamma} + s + \frac{q^2}{gs^2}\left(\frac{ss_{xx}}{K_b+1} - \frac{s_x^2}{2}\right). \tag{3.543}$$

The sum $p_s/\gamma + s = h_p$ is the effective piezometric pressure head at the interface of the jet and the recirculating fluid layer. The function $p_s(x)$ is unknown and difficult to approximate. Note that $p_s(x = 0) = 0$ despite the local water column $(E - a)$ there. Further, it is not reliable to assume that p_s is equal to the local flow depth, given the significant vertical velocities close to the gate and the

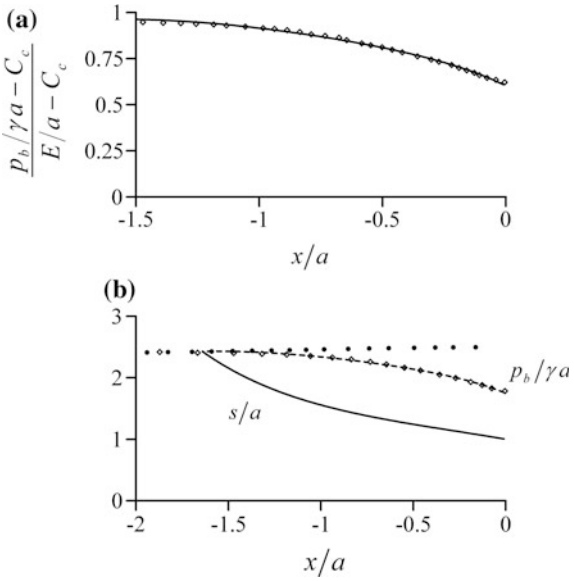

Fig. 3.71 Approach flow portion: **a** bottom pressure $[(p_b/\gamma a - C_c)/(E/a - C_c)](x/a)$ with (—) 1D computation, (◊) 2D computation (Montes 1997), **b** internal jet features with (—) $s/a(x/a)$, (- - -) $p_b/\gamma a$ (x/a), (◊) 2D bottom pressure computation (Montes 1997), (•) 2D free surface computation (Montes 1997) (adapted from Castro-Orgaz and Hager 2014c) $E/a = 2.5$

corresponding non-hydrostatic pressure. Due to the complex flow pattern as the flow approaches the gate, the simplest approximation is to assume h_p = constant for the internal jet. Its value will be determined using as boundary condition the bottom pressure at $x = 0$. Computations with Eq. $(3.543)_1$ used the fourth-order Runge–Kutta method with $s(0) = a$ and $K_b = 1.4$, as previously for the free jet portion. The value of S is taken as an invariant, determined from known values of h_o and q. The value $s_x(0)$ was thereby iteratively adjusted until reaching the asymptotic condition $p_b/\gamma(x \to -1.5a) \to h_o$. Results for $E/a = 2.5$ are shown in Fig. 3.71a. Note that the agreement of the 2D bottom pressure and the two-layer approximation of Keutner (1935) is excellent, thereby justifying that the internal flow features close to the gate are provoked by an internal jet and not by the free surface cnoidal wavelike configuration. The theoretical shape of the internal jet is shown in Fig. 3.71b; note its similarity with the Benjamin-Cola cavity bubble (Hager 1999b).

3.14 Vorticity Effects

3.14.1 Vorticity Equation for Streamline

Fluid flow in hydraulic structures, including flow-measuring devices, is dealt with using approximate potential flow methods (Rouse 1950; Bos 1976). These involve a flow net where energy is conserved in the entire flow domain. Velocity and pressure fields at control sections are determined without considering vorticity or viscous effects near solid boundaries. This approach is often accurate, especially if

accelerations over short-channel reaches are significant, as for spillway and weir flows (Rouse 1932, 1933). However, vorticity and viscous effects result in non-uniformity of the energy distribution and, thus, in the distortion of the velocity and pressure patterns obtained based on the irrotational flow theory. A typical example is the free overfall, studied by Hunter Rouse, who introduced potential flow computations using flow nets (Rouse 1932, 1933, 1938), including the use of intrinsic coordinates for the Euler equations. He measured velocity and pressure distributions and found that the energy head varied within a flow section. Considering inviscid flow, and using intrinsic coordinates, Rouse obtained Bernoulli's equation along a streamline (Fig. 3.72a).

Rouse indicated that the "constant head" for a streamline varies from one streamline to another due to vorticity. He defined an "averaged" cross-sectional energy head and proceeded to its computation using experimental data. This 1D method was discussed by Jaeger (1956), Castro-Orgaz and Chanson (2009), and Castro-Orgaz and Hager (2011). Montes (1992a) presented a detailed irrotational 2D flow solution for the free overfall problem, demonstrating that the free surface and the bottom pressure profiles predicted by this approach excellently agree with the experimental data, including those of Rouse (1933). The inflow velocity profile was assumed uniform, as usual for parallel-streamlined potential flows. Montes further analyzed the internal flow features of the free overfall, namely the streamline

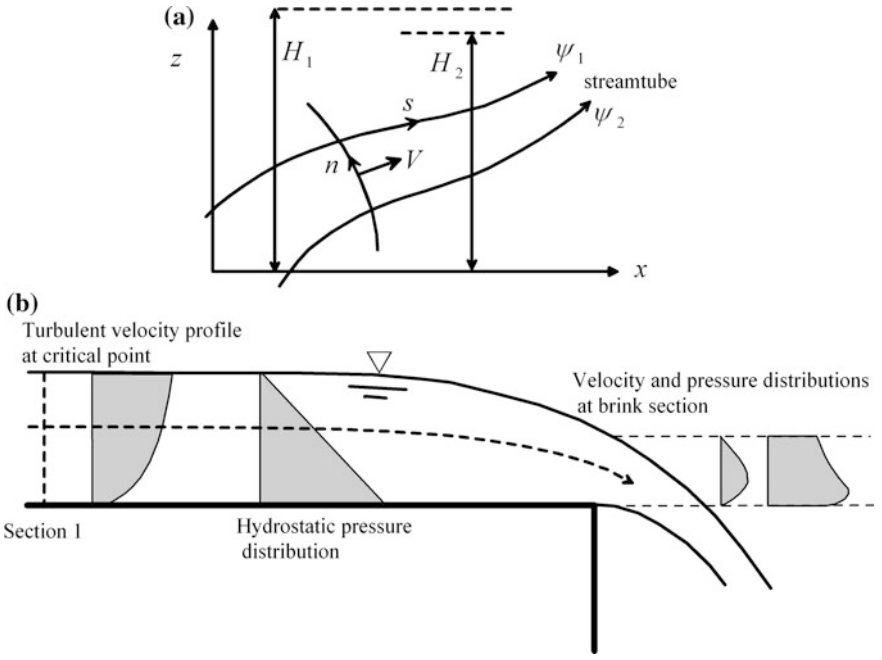

Fig. 3.72 **a** Stream tube in coordinates (s, n) and Bernoulli's relation, **b** free overfall with typical velocity and pressure distributions (Bos 1976) (adapted from Castro-Orgaz and Hager 2011)

inclination, pressure distribution, and velocity profiles. Of all the flow features tested, the velocity profiles predicted by the irrotational flow theory were found to disagree with observations at the brink section. Montes (1992a) attributed this failure to the neglect of the non-uniformity of the inflow velocity profile. This finding is equivalent to state that the inflow velocity profile must account for its non-uniformity or that the inflow vorticity affects the brink velocity distribution. Jaeger (1948) predicted the brink depth ratio and the depth-averaged velocity and pressure coefficients at the free overfall using an irrotational Boussinesq-type equation based on Fawer (1937). Deviations of the velocity profiles at the brink section were later attributed to the inflow velocity profile (Jaeger 1966; Biggiero 1964). Nakagawa (1969) found that the effect of a non-uniform velocity profile due to vorticity was significant at the brink section. In this section, a higher order solution for the velocity profile of inviscid flows is presented using the free overfall as a test case.

Consider the momentum equations in the s- and n-directions of the natural coordinate system (Fig. 3.72a) (Rouse 1959; Milne-Thomson 1962)

$$V\frac{\partial V}{\partial s} = -\frac{1}{\rho}\frac{\partial p}{\partial s} - g\frac{\partial z}{\partial s} + \nu\left[\frac{\partial^2 V}{\partial s^2} + \frac{\partial^2 V}{\partial n^2} - \kappa_s\frac{\partial V}{\partial n} + \kappa_n\frac{\partial V}{\partial s} - V\left(\kappa_s^2 + \kappa_n^2\right)\right], \tag{3.544}$$

$$\kappa_s V^2 = -\frac{1}{\rho}\frac{\partial p}{\partial n} - g\frac{\partial z}{\partial n} + \nu\left[2\kappa_s\frac{\partial V}{\partial s} + 2\kappa_n\frac{\partial V}{\partial n} + V\left(\frac{\partial \kappa_s}{\partial s} + \frac{\partial \kappa_n}{\partial n}\right)\right]. \tag{3.545}$$

Here, V is the velocity in the s-direction, z the elevation above the datum, p the pressure, g the gravity acceleration, κ_s the streamline curvature, κ_n the curvature of the normal curve, ν the kinematic viscosity, and ρ the fluid density. Defining the total head H as

$$H = z + \frac{p}{\gamma} + \frac{V^2}{2g}, \tag{3.546}$$

then Eq. (3.544) reads

$$\frac{\partial H}{\partial s} = \frac{\nu}{g}\left[\frac{\partial^2 V}{\partial s^2} + \frac{\partial^2 V}{\partial n^2} - \kappa_s\frac{\partial V}{\partial n} + \kappa_n\frac{\partial V}{\partial s} - V\left(\kappa_s^2 + \kappa_n^2\right)\right]. \tag{3.547}$$

Differentiation of Eq. (3.546) in the n-direction gives, after substituting $\partial(p/\gamma + z)/\partial n$ from Eq. (3.544),

$$\begin{aligned}\frac{\partial H}{\partial n} &= \frac{\partial}{\partial n}\left[z + \frac{p}{\gamma} + \frac{V^2}{2g}\right] \\ &= \frac{V}{g}\frac{\partial V}{\partial n} - \frac{\kappa_s}{g}V^2 + \frac{\nu}{g}\left[2\kappa_s\frac{\partial V}{\partial s} + 2\kappa_n\frac{\partial V}{\partial n} + V\left(\frac{\partial \kappa_s}{\partial s} + \frac{\partial \kappa_n}{\partial n}\right)\right].\end{aligned} \tag{3.548}$$

Coupling Eqs. (3.548) with (3.547) provides closure for the variation of $H(s, n)$. For a 2D flow, the vorticity vector Ω has only the component (Milne-Thomson 1962; White 1991, 2003)

$$\Omega = \frac{\partial V}{\partial n} - \kappa_s V. \tag{3.549}$$

Integrating Eq. (3.549) along a normal curve with N_o as the total length of the curve and n its arc length yields the general equation for the velocity profile as

$$V = V_s \exp\left(-\int_n^{N_o} \kappa_s \mathrm{d}n\right) \exp\left(-\int_n^{N_o} \frac{1}{V}\Omega \mathrm{d}n\right). \tag{3.550}$$

For irrotational flows (e.g., potential flow), Eq. (3.550) simplifies to Eq. (3.81) used to deal with curvilinear-streamlined flow (Rouse 1933; Fawer 1937; Jaeger 1956; Matthew 1963; Hager and Hutter 1984a; Montes 1998; Montes and Chanson 1998; Castro-Orgaz 2010a). Note that Eq. (3.550) involves a potential flow term affected by the vorticity factor. From Eqs. (3.548) and (3.549) results

$$\Omega = \frac{g}{V}\left(\frac{\partial H}{\partial n} - \frac{v}{g}\left[2\kappa_s \frac{\partial V}{\partial s} + 2\kappa_n \frac{\partial V}{\partial n} + V\left(\frac{\partial \kappa_s}{\partial s} + \frac{\partial \kappa_n}{\partial n}\right)\right]\right). \tag{3.551}$$

Together with Eq. (3.547), this states that vorticity is affected by variations of $H(s, n)$. Consider inviscid flow so that $\partial H/\partial s = 0$ from Eq. (3.547), that is, the total head H is conserved along a streamline, with its magnitude changing from one streamline to another (Rouse 1970; Castro-Orgaz and Chanson 2009; Castro-Orgaz and Hager 2011). This standard form of Bernoulli's equation was misapplied in open-channel hydraulics for decades, given its confusion with the integral energy equation from a control volume derived from the first law of thermodynamics. Liggett (1993, 1994) states that Bernoulli's equation arises from the momentum analysis of a streamline and not from the energy balance equation for a control volume. The vorticity along a streamline is conserved for inviscid flow (Nakagawa 1969; White 1991; Castro-Orgaz and Hager 2011). This result implies that *for modeling inviscid curvilinear flow, vorticity appears as a part of the approach flow conditions. The Euler equations include no vorticity change, so that the approach flow vorticity is transmitted from the inflow section to the curvilinear flow portion*. The free overfall with critical approach flow is a typical example (Fig. 3.72b). At the critical point $\mathsf{F} = 1$, a hydrostatic pressure distribution prevails, but the turbulent velocity profile is governed by the bottom boundary layer. At the brink section, this feature is still present (Biggiero 1964; Jaeger 1966; Nakagawa 1969).

3.14.2 Velocity Profile

Consider the upstream section "1" of a free overfall (Fig. 3.72b) and the brink section with curvilinear streamlines. Applying Bernoulli's theorem

$$H = h_1 + \frac{V_1^2}{2g} = z + \frac{p}{\gamma} + \frac{V^2}{2g} = \text{const.}, \tag{3.552}$$

$$\Omega = \frac{g}{V}\frac{\partial H}{\partial n} = \frac{g}{V_1}\frac{\partial H}{\partial z} = \frac{\partial V_1}{\partial z} = \text{const.} \tag{3.553}$$

Substituting Eq. (3.553) into Eq. (3.550) yields for the velocity profile at the brink section

$$V = V_s \exp\left(-\int_n^{N_o} \kappa_s \mathrm{d}n'\right) \exp\left(-\int_n^{N_o} \frac{1}{V}\frac{\partial V_1}{\partial z}\mathrm{d}n'\right). \tag{3.554}$$

So far, only Bernoulli's theorem is used. The distribution of $\kappa_s(n)$ at the brink section is approximated by the interpolation function using the streamline curvature at the free surface (subscript s) as (Fawer 1937; Montes and Chanson 1998; Castro-Orgaz 2010a)

$$\kappa_s = \kappa_s(n = N_o)\left(\frac{n}{N_o}\right)^K. \tag{3.555}$$

If the normals are circular arcs, then (Hager and Hutter 1984a, b; Montes and Chanson 1998)

$$\exp\left(-\int_n^{N_o} \kappa_s \mathrm{d}n'\right) \approx \exp\left[-hh_{xx}\frac{1-\mu^{K+1}}{K+1}\right], \quad \mu = \frac{z}{h}. \tag{3.556}$$

Consider a power-law model for the upstream turbulent velocity profile with m_1 = power-law exponent at Sect. 1 and $U = q/h$ as the mean flow velocity (Montes 1986; Bose and Dey 2007). Thus,

$$V_1 = U_1(1 + m_1)\mu^{m_1}. \tag{3.557}$$

Inserting Eq. (3.557) into Eq. (3.554), and noting that $\Omega = \partial V_1/\partial z = m_1 V_1/z$, generates

$$\frac{V}{V_s} = \underbrace{\exp\left(-\int_n^{N_o} \kappa_s \mathrm{d}n'\right)}_{\text{Eq.(3.556)}} \underbrace{\exp\left(-\int_n^{N_o} \frac{1}{V}\frac{m_1 V_1}{z'}\mathrm{d}n'\right)}_{\Lambda} = \Lambda \exp\left[-hh_{xx}\frac{1-\mu^{K+1}}{K+1}\right], \tag{3.558}$$

with

$$\Lambda = \exp\left(-\int_n^{N_o} \frac{1}{V}\frac{m_1 V_1}{z'}\mathrm{d}n'\right) = \exp\left(m_1 \frac{h}{h_1}\int_1^{\mu} \frac{V_1}{V\cos\theta}\frac{\mathrm{d}\mu'}{\mu'}\right). \tag{3.559}$$

Here, Λ is a vorticity factor and θ the streamline inclination with the horizontal. Equation (3.558) describes the velocity profile at the brink section, including a correction for the inflow vorticity. Assuming that $\cos\theta \approx 1$, $V \approx q/h$, and $V_1 \approx q/h_1$, Eq. (3.559) simplifies to the power-law vorticity factor

$$\Lambda = \exp\left[m_1\left(\frac{h}{h_1}\right)^2 \int_1^{\mu} \underbrace{\frac{\mathrm{d}\mu'}{\mu'}}_{\mathrm{d}(\ln\mu)}\right] = \exp\left[\ln\mu^{m_1\left(\frac{h}{h_1}\right)^2}\right] = \mu^N, \quad N = m_1\left(\frac{h}{h_1}\right)^2. \tag{3.560}$$

With $C_c(x) = [h(x)/h_1]^2$ as contraction-expansion factor, the exponent N differs from m_1, because

$$N = m_1\left(\frac{h}{h_1}\right)^2 = m_1 C_c. \tag{3.561}$$

For accelerating flows $C_c < 1$, the effect of m_1 originating from the inflow section is reduced. By contrast, for decelerating flows $C_c > 1$, the effect of m_1 is amplified. This does not imply that vorticity varies along a streamline, but that any flow non-uniformity interacts with the power-law exponent of the inflow velocity profile. Therefore, Eq. (3.558) finally reads using Eq. (3.560)

$$V = V_s \mu^N \exp\left[-hh_{xx}\frac{1-\mu^{K+1}}{K+1}\right]. \tag{3.562}$$

Equation (3.562) was obtained analytically by Castro-Orgaz and Hager (2011). Previously, it was proposed as semi-empirical law by Montes and Chanson (1998). The present development demonstrates that Eq. (3.562) is physically justified based

on Bernoulli's equation. Equation (3.550) is general, and solutions depend on the inflow profile, i.e., the log-law or the wall-wake law. Note that the no-slip condition $V(\mu = 0) = 0$ is a typical feature of turbulent, and wall-bounded flows (White 1991) correctly accounted for by Eq. (3.562).

If the normals are circular arcs, then (Hager and Hutter 1984a; Montes and Chanson 1998)

$$\cos\theta^{-1} = 1 + \frac{h_x^2}{2}\mu^2. \tag{3.563}$$

Therefore, [Appendix G, Eq. (G.19); here, the curvature and slope Boussinesq-type parameters are approximated as $\varepsilon_o \approx hh_{xx}$ and $\varepsilon_1 \approx h_x^2$]

$$q = h\int_0^1 \frac{V}{\cos\theta}\mathrm{d}\mu = \frac{hV_s}{N+1}\left[1 - \frac{hh_{xx}}{K+1}\left(1 - \frac{N+1}{2+N+K}\right) + \frac{h_x^2}{2}\left(\frac{N+1}{N+3}\right)\right], \tag{3.564}$$

so that the relation between V_s and U is

$$V_s = (N+1)U\left[1 + \frac{hh_{xx}}{K+1}\left(1 - \frac{N+1}{2+N+K}\right) - \frac{h_x^2}{2}\left(\frac{N+1}{N+3}\right)\right]. \tag{3.565}$$

Using Eq. (3.565) in Eq. (3.562) gives for the velocity components (u, w) in the x- and z-directions (Montes and Chanson 1998) [Appendix G, Eqs. (G22) and (G24)]

$$u = (N+1)U\mu^N\left[1 + \frac{hh_{xx}}{K+1}\left(\mu^{K+1} - \frac{N+1}{2+N+K}\right) - \frac{h_x^2}{2}\left(\frac{N+1}{N+3} + \mu^2\right)\right], \tag{3.566}$$

$$w = (N+1)U\mu^{N+1}h_x\left[1 + \frac{hh_{xx}}{K+1}\left(\mu^{K+1} - \frac{N+1}{2+N+K}\right) - \frac{h_x^2}{2}\left(\frac{N+1}{N+3}\right)\right]. \tag{3.567}$$

Integrating the momentum equation in the n-direction yields for the pressure distribution (Montes and Chanson 1998) [Appendix G, Eq. (G30)]

$$\frac{p}{\gamma h} = 1 - \mu + \frac{hh_{xx}(1+N)^2}{K+2N+1}\frac{U^2}{gh}\left[1 - \mu^{1+2N+K}\right]. \tag{3.568}$$

3.14.3 Free Overfall

Rouse (1932, 1933) studied the free overfall in a horizontal, rectangular and smooth channel for F = 1, which is the most difficult case given the large non-hydrostatic effects. At the critical point, the hydrostatic pressure condition prevails with a turbulent velocity profile (Fig. 3.72b). As the brink section is approached, the bottom pressure profile deviates from the free surface profile (Fig. 3.73a), until reaching the atmospheric pressure at the edge. Using $p = 0$ in Eq. (3.568) gives for the relative curvature at the brink section

$$hh_{xx} = -\frac{K+2N+1}{(1+N)^2} Y_b^3. \tag{3.569}$$

Here, $Y_b = h_b/h_c$ is the brink depth ratio, h_b the brink flow depth, and $h_c = (q^2/g)^{1/3}$ the critical depth. Inserting Eq. (3.569) into Eq. (3.568) yields for the brink pressure distribution

$$\frac{p}{\gamma h_b} = \mu^{1+2N+K} - \mu, \tag{3.570}$$

whereas the brink velocity distribution is, from Eq. (3.562),

$$\frac{V}{U} = (N+1)\mu^m \left[1 - \frac{K+2N+1}{(K+1)(1+N)^2} Y_b^3 \left(\mu^{K+1} - \frac{N+1}{2+N+K}\right) - \frac{h_x^2}{2}\left(\frac{N+1}{N+3}\right)\right]. \tag{3.571}$$

Equations (3.570) and (3.571) allow for the prediction of the brink flow features. A value of $K = -0.665$ resulted for irrotational flow based on conservation of momentum, energy, and angular momentum (Castro-Orgaz and Hager 2010), whereas $K = -0.5$ was obtained by Jaeger (1948). The velocity profile is not greatly affected by K, but the pressure distribution is sensitive to it (Castro-Orgaz and Hager 2010). A mean value of $K \approx -0.6$ is considered here. Figure 3.73b shows the inflow velocity profiles for $m_1 = 0$ (potential flow), $m_1 = 1/5$, and $m_1 = 1/10$. Rouse (1933) found experimentally $Y_b = 0.715$, resulting in $C_c = 0.511$. The corresponding brink velocity and pressure distributions are plotted in Fig. 3.73c, d.

Note that the effect of m_1 is noticeable for the brink velocity profiles, provoking a reduction of V as compared with potential flow if $z/h < 0.3$ and vice versa in the upper flow portion. Overall, the velocity profiles with vorticity tend to be more uniform than predicted by the potential flow computation. The effect of m_1 on the pressure distribution is significant (Fig. 3.73d), so that an inexact selection of m_1 may produce a poor pressure profile prediction, in contrast to the velocity distribution, which is not very sensitive to these variations. This result agrees with previous irrotational flow analyses, indicating that the pressure distribution is more sensitive to K than the velocity profile (Castro-Orgaz and Hager 2010). Biggiero (1964), Jaeger (1966), and Nakagawa (1969) also stated that the inflow velocity

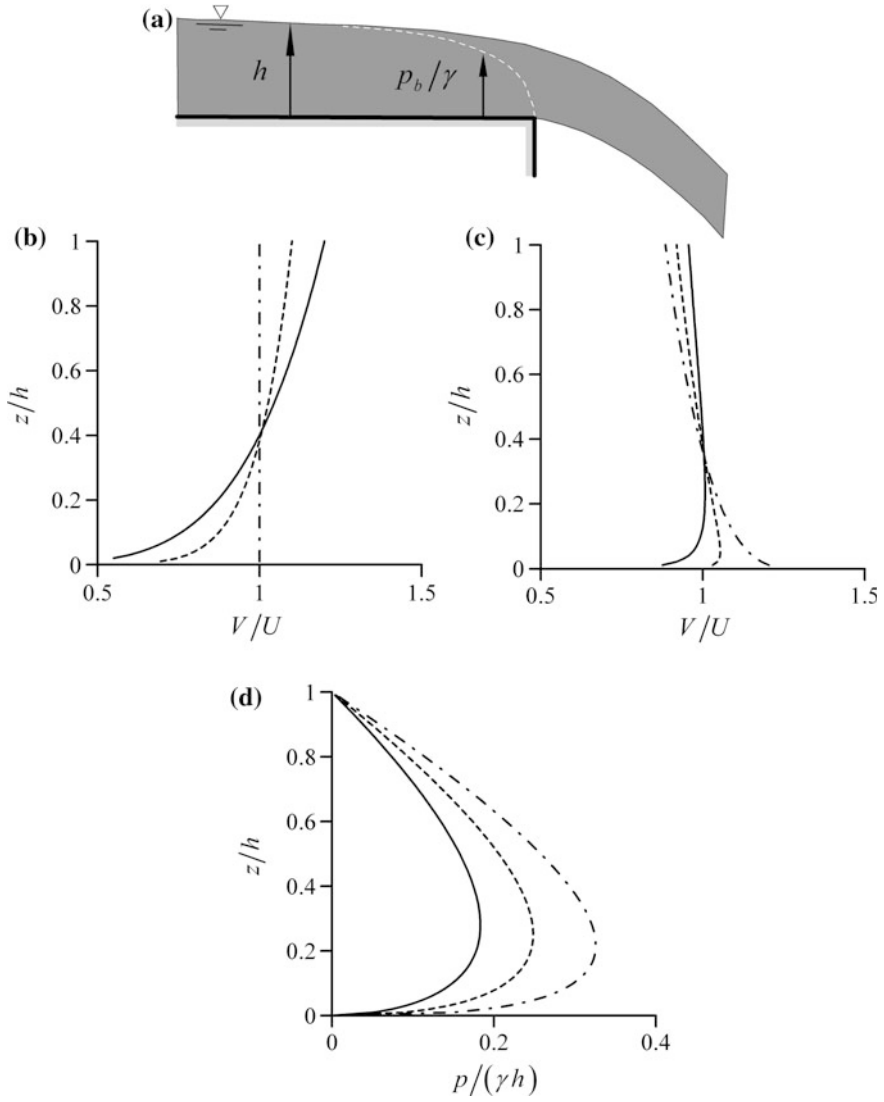

Fig. 3.73 Free overfall features for F = 1: **a** definition sketch, **b** inflow velocity profiles $V/U(z/h)$ for m_1 = (—) 1/5, (- - -) 1/10, (– • –) 0 (irrotational flow), **c** corresponding brink velocity profiles V/U (z/h), **d** brink pressure distributions (adapted from Castro-Orgaz and Hager 2011)

profile of the free overfall affects significantly the internal brink flow features. Free surface profiles and bottom pressures are well predicted by the irrotational flow theory (Montes 1992a), but the corresponding experimental brink velocity profiles deviate from the irrotational flow theory.

Equations (3.570) and (3.571) are functions applied to the flow discontinuity at the brink section bottom. To the left of the brink, at distance $x = 0 - \mathrm{d}x$, the bottom

pressure $p_b \neq 0$ and $V_b = 0$, as dictated by the bottom boundary layer. This is satisfied by Eqs. (3.570) and (3.571). However, to the right of the brink, at distance $x = 0 + dx$, the bottom pressure is $p_b = 0$ and $V_b \neq 0$, as dictated by free jet flows. There is a discontinuity in κ_s as well (Jaeger 1948). Note that exactly at $x = 0$, Eqs. (3.570) and (3.571) involve $p_b = 0$ and $V_b = 0$, i.e., the bottom energy head at that section is $H_b = 0$. At the critical point, however, $H_b = h_c$, indicating that the approach bottom streamline does not satisfy conservation of energy, given the no-slip velocity condition satisfied by Eq. (3.571). This is a limitation of the approximate model presented.

Results of the model composed of Eqs. (3.570) and (3.571) are compared in Fig. 3.74 with data of Rouse (1933) for $\mathsf{F} = 1$. His inflow velocity profiles agree well with Eq. (3.557) using $m_1 = 1/12$ (Fig. 3.74a). Note that the commonly assumed value $m_1 = 1/7$ poorly fits the inflow velocity profile, because the approach flow turbulence given by the Reynolds number dictates a lower value. The brink velocity profile for $N = m_1 C_c = (1/12)\cdot(0.715)^2 \approx (1/23.47)$, $K = -0.60$, $Y_b = 0.715$, and $h_x = -0.25$ is plotted in Fig. 3.74b. Note that the acceleration toward the free overfall generates a power-law exponent at the brink section of (1/23.47), i.e., the acceleration tends to produce vertical velocity profiles with less non-uniformity. The agreement between the prediction and test data is remarkable, resulting in a significant improvement over the irrotational flow theory. The pressure distribution given by Eq. (3.570) is plotted in Fig. 3.74c for $N = (1/23.47)$, $Y_b = 0.715$, and $h_x = -0.25$, using the values $K = -0.665$ and $K = -0.50$ considered above. Using these K values, the predictions are not good. The velocity profile is insensitive to the K value if $-0.665 < K < -0.5$, whereas its effect on the pressure distribution is noticeable. For $K = -0.60$, Eq. (3.570) fits the test data reasonably well (Fig. 3.74d). The computed curve is close to the potential flow solution (Montes 1992a), yet the scatter of the test data is so large that a refined value of K can hardly be determined.

Replogle (1962) repeated Rouse's experiments (Fig. 3.75). His inflow velocity profile (Fig. 3.75a) was identical to that of Rouse ($m_1 = 1/12$). The brink velocity profile is plotted in Fig. 3.75b for $N = m_1 C_c = (1/12)\cdot(0.716)^2 \approx (1/23.38)$, $K = -0.60$, $Y_b = 0.716$, and $h_x = -0.25$. The velocity prediction again agrees well with observations, except at its lowest portion. The pressure distribution is shown in Fig. 3.75c, from which Replogle's data indicate lower pressure values than those measured by Rouse. The theoretical curve has the correct shape, yet the test data suggest a higher K value. With $K = -0.55$, the computations improve as compared with $K = -0.60$, indicating again that within $-0.665 < K < -0.50$, V/U is hardly affected, whereas the pressure distribution is sensitive to these variations in K. Therefore, $K = 1$ (Matthew 1963, 1991, 1995; Marchi 1992, 1993) is a poor selection.

Consider a comparative analysis to highlight the implications of K and N. Figure 3.76a, b shows computations based on Eqs. (3.570) and (3.571) for $N = 0$ and $K = 1$, i.e., irrotational flow with a linear streamline curvature variation. This approach yields excellent free surface predictions (Hager 1983; Matthew 1991, 1995; Marchi 1992, 1993). However, the velocity profile deviates from the test

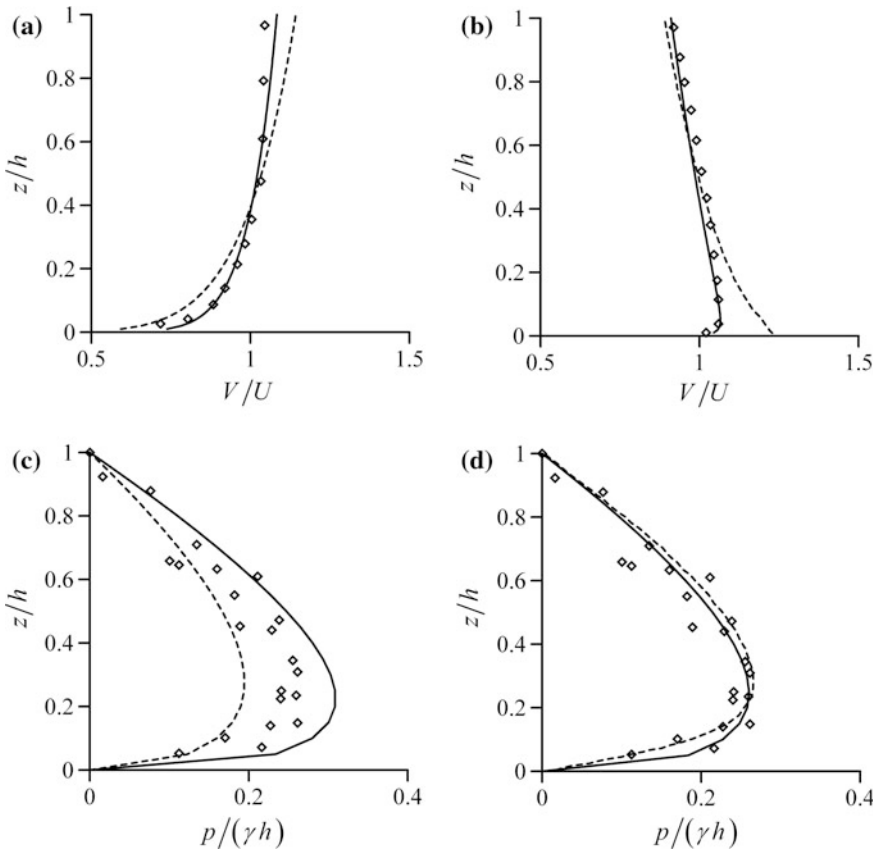

Fig. 3.74 Free overfall for F = 1: **a** Eq. (3.557) with m_1 = (—) 1/12, (- - -) 1/7, **b** (—) Eq. (3.571) with m_1 = 1/12 and $K = -0.6$, (- - -) 2D potential flow (Montes 1992a), (◊) test data of Rouse (1933), **c** (—) Eq. (3.570) with m_1 = 1/12 and $K = -0.665$, (- - -) m_1 = 1/12 and $K = -0.50$, (◊) test data of Montes (1992a), **d** (—) Eq. (3.570) with m_1 = 1/12 and $K = -0.60$, (- - -) 2D potential flow (Montes 1992a), (◊) test data of Montes (1992a) (adapted from Castro-Orgaz and Hager 2011)

data, and the pressure distribution incorrectly reaches negative values over the entire profile. Consider then the irrotational flow but $K = -0.60$ (Jaeger 1948; Castro-Orgaz and Hager 2010, Fig. 3.76c, d), resulting in a significant improvement. This model still deviates from the test data, but agrees well with the 2D potential flow model (Castro-Orgaz and Hager 2010), thereby demonstrating that the irrotational Boussinesq equations at the brink section imply $K < 0$. Bose and Dey (2007) found that for turbulent curvilinear flow, the free surface profiles are well predicted using $N = 1/7$. Consider Fig. 3.76e, f, where Eqs. (3.570) and (3.571) are plotted for $N = 1/7$ and $K = -0.60$. Note that the velocity reduction for $z/h < 0.5$ is too large, and computed pressures are too low, indicating that not only values for K, but also N, are relevant, because both parameters interact.

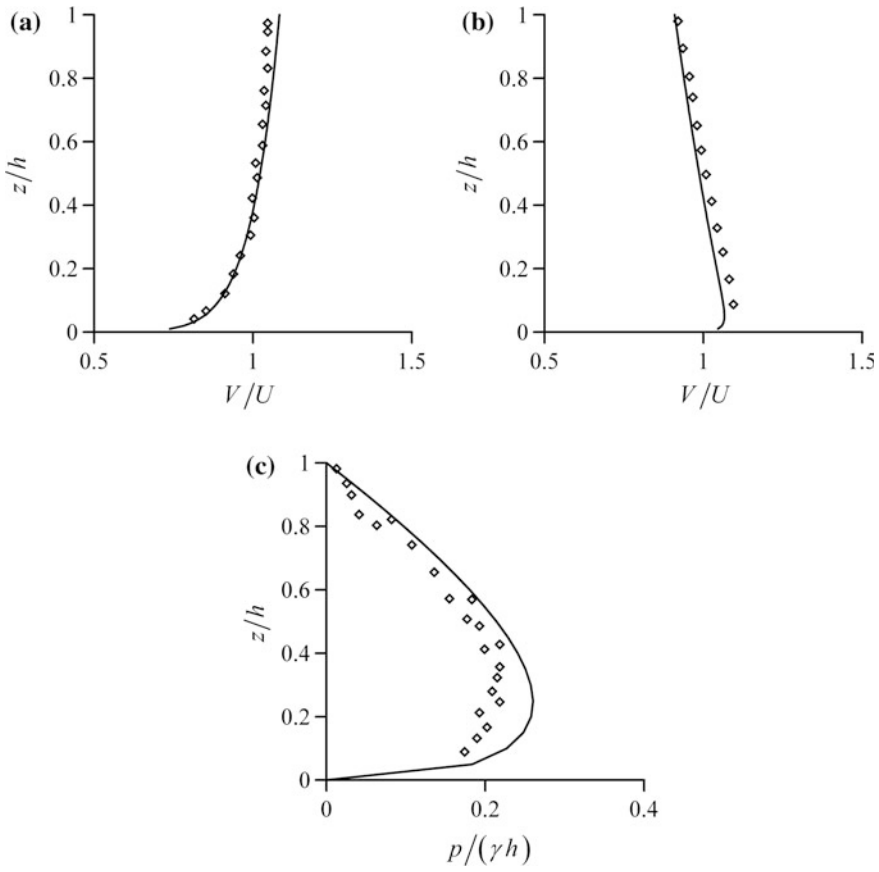

Fig. 3.75 Free overfall for F = 1: **a** (—) Eq. (3.557) with m_1 = 1/12, **b** (—) Eq. (3.571), **c** (—) Eq. (3.570), (◇) data of Replogle (1962) (adapted from Castro-Orgaz and Hager 2011)

3.15 Water Waves

3.15.1 Irrotational Water Waves

In this section, an introduction to the governing equations of irrotational water waves is given, see, e.g., Liggett (1994). The solution of the problem of surface waves consists in solving inside the fluid domain Laplace's equation for the velocity potential $\phi(x, y, z, t)$, originating from the continuity equation

$$\nabla^2\phi = \frac{\partial^2\phi}{\partial x^2} + \frac{\partial^2\phi}{\partial y^2} + \frac{\partial^2\phi}{\partial z^2} = 0. \tag{3.572}$$

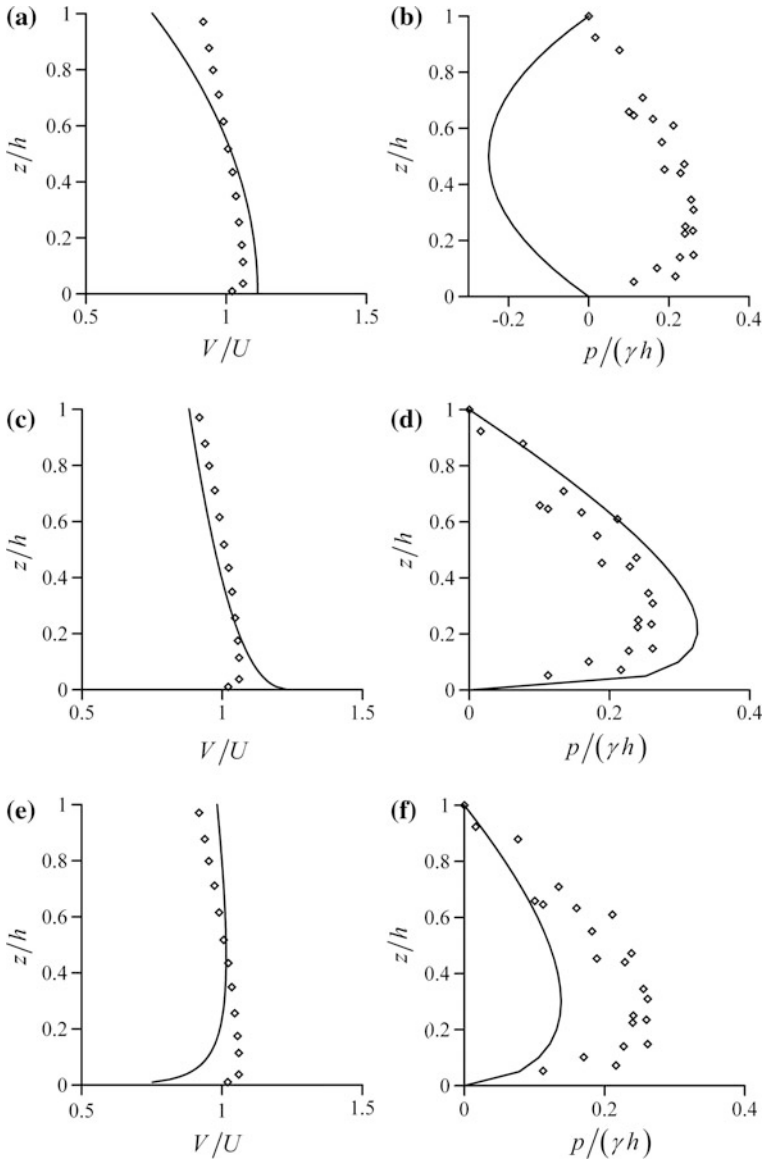

Fig. 3.76 Free overfall for F = 1, (—) Eqs. (3.570) and (3.571) for **a**, **b** $N = 0$ and $K = 1$, **c**, **d** $N = 0$ and $K = -0.60$, **e**, **f** $N = 1/7$ and $K = -0.60$, (◇) test data (adapted from Castro-Orgaz and Hager 2011)

The velocity components (u, v, w) are given by using the positive sign in the potential function

$$u = \frac{\partial \phi}{\partial x}, \quad v = \frac{\partial \phi}{\partial y}, \quad w = \frac{\partial \phi}{\partial z}. \tag{3.573}$$

Two boundary conditions are then set on the unsteady free surface, the first corresponding to the kinematic boundary condition stating that a particle on the free surface $z_s = z_s(x, y, t)$ remains there during the motion

$$\frac{\partial \phi}{\partial z} = \frac{\partial z_s}{\partial t} + \frac{\partial \phi}{\partial x}\frac{\partial z_s}{\partial x} + \frac{\partial \phi}{\partial y}\frac{\partial z_s}{\partial y}; \tag{3.574}$$

the second is the Bernoulli equation for unsteady flow

$$\frac{\partial \phi}{\partial t} + g z_s + \frac{1}{2}\left[\left(\frac{\partial \phi}{\partial x}\right)^2 + \left(\frac{\partial \phi}{\partial y}\right)^2 + \left(\frac{\partial \phi}{\partial z}\right)^2\right] = 0. \tag{3.575}$$

Assuming a rigid surface, the kinematic boundary condition at the bottom $z_b = z_b(x, y)$ is

$$\frac{\partial \phi}{\partial z} = \frac{\partial \phi}{\partial x}\frac{\partial z_b}{\partial x} + \frac{\partial \phi}{\partial y}\frac{\partial z_b}{\partial y}. \tag{3.576}$$

Equations (3.572)–(3.576) form the basis to produce unsteady Boussinesq-type water wave models. The potential function is expanded in power series as

$$\phi = \sum_{n=0}^{\infty} \phi_n z^n. \tag{3.577}$$

Using Eq. (3.577), the velocity components (u, v, w) follow from Eq. (3.573) as functions of the undetermined series coefficients. Inserting these into Eq. (3.572), a recursive formula emerges to compute the coefficients. Using the resulting power series in the kinematic and dynamic boundary conditions, a system of Boussinesq's equations results (see, e.g., Mei (1983) or Liggett (1994) for a detailed derivation).

3.15.2 Serre–Green–Naghdi Equations

This section is limited to unsteady irrotational water waves in the vertical plane. Instead of using the kinematic and dynamic boundary conditions as given by Eqs. (3.574)–(3.576) to produce the Boussinesq equations, an alternative is to resort

to the vertically integrated mass and momentum equations (e.g., Nwogu 1993) as (see Chap. 2)

$$\frac{\partial h}{\partial t} + \frac{\partial}{\partial x}\int_{z_b}^{z_s} u\mathrm{d}z = 0, \tag{3.578}$$

$$\frac{\partial}{\partial t}\int_{z_b}^{z_s} u\mathrm{d}z + \frac{\partial}{\partial x}\int_{z_b}^{z_s}\left(u^2 + \frac{p}{\rho}\right)\mathrm{d}z = -\frac{p_b}{\rho}\frac{\partial z_b}{\partial x}. \tag{3.579}$$

Picard iteration technique is applied to find the potential velocity field (u, w) and pressure p, and then, these distributions are used in Eqs. (3.578)–(3.579) to produce the Boussinesq-type equations. With ψ as the stream function, the propagation of 1D water waves in unsteady potential flow obeys the Cauchy–Riemann conditions (e.g., Liggett 1994; Montes 1998)

$$u = -\frac{\partial \phi}{\partial x} = -\frac{\partial \psi}{\partial z}, \quad w = -\frac{\partial \phi}{\partial z} = +\frac{\partial \psi}{\partial x}. \tag{3.580}$$

Based on Picard iteration, the unsteady irrotational velocity components (u, w) in the vertical plane are, from Eq. (3.54) (Castro-Orgaz and Hager 2014a),

$$w = -U_x\eta - U\eta_x, \tag{3.581}$$

where $\eta = z - z_b$ is the elevation above the bottom, and from Eq. (3.61),

$$u = U + (2U_x\eta_x + U\eta_{xx})\left(\frac{h}{2} - \eta\right) + U_{xx}\left(\frac{h^2}{6} - \frac{\eta^2}{2}\right). \tag{3.582}$$

Equation (3.582) is the fully nonlinear second-order velocity profile for unsteady potential flow. The bottom profile contribution is given by the terms $\eta_x = -\partial z_b/\partial x$ and $\eta_{xx} = -\partial^2 z_b/\partial x^2$, and the free surface inclination and curvature terms h_x and h_{xx} are contained in U_x and U_{xx}. The pressure distribution p is determined using the vertical Euler equation as

$$\frac{p}{\gamma} = h - \eta + \frac{1}{g}\int_{\eta}^{h}\left(\frac{\partial w}{\partial t} + u\frac{\partial w}{\partial x} + w\frac{\partial w}{\partial z}\right)\mathrm{d}\eta'. \tag{3.583}$$

Equation (3.581) yields

$$\frac{\partial w}{\partial t} = -U_{xt}\eta - U_t\eta_x, \tag{3.584}$$

$$\frac{\partial w}{\partial x} = -U_{xx}\eta - 2U_x\eta_x - U\eta_{xx}, \tag{3.585}$$

$$\frac{\partial w}{\partial z} = -U_x. \tag{3.586}$$

When neglecting second-order products of η and its derivatives, the corresponding terms of the convective acceleration are

$$u\frac{\partial w}{\partial x} \approx -UU_{xx}\eta - 2UU_x\eta_x - U^2\eta_{xx}, \tag{3.587}$$

$$w\frac{\partial w}{\partial z} \approx U_x^2\eta + UU_x\eta_x. \tag{3.588}$$

Inserting Eqs. (3.584), (3.587), and (3.588) into Eq. (3.583) yields after integration

$$\begin{aligned}
\frac{p}{\gamma} &= h - \eta + \frac{1}{g}\int_\eta^h \left(\frac{\partial w}{\partial t} + u\frac{\partial w}{\partial x} + w\frac{\partial w}{\partial z}\right)\mathrm{d}\eta' = h - \eta \\
&\quad + \frac{1}{g}\int_\eta^h (-U_{xt}\eta - U_t\eta_x)\mathrm{d}\eta' \\
&\quad + \frac{1}{g}\int_\eta^h \left(-UU_{xx}\eta - 2UU_x\eta_x - U^2\eta_{xx}\right)\mathrm{d}\eta' + \frac{1}{g}\int_\eta^h \left(U_x^2\eta + UU_x\eta_x\right)\mathrm{d}\eta' \\
&= h - \eta + \left[-U_{xt}\left(\frac{h^2-\eta^2}{2g}\right) - U_t\eta_x\left(\frac{h-\eta}{g}\right)\right] \\
&\quad + \left[-UU_{xx}\left(\frac{h^2-\eta^2}{2g}\right) - 2UU_x\eta_x\left(\frac{h-\eta}{g}\right) - U^2\eta_{xx}\left(\frac{h-\eta}{g}\right)\right] \\
&\quad + \left[U_x^2\left(\frac{h^2-\eta^2}{2g}\right) + UU_x\eta_x\left(\frac{h-\eta}{g}\right)\right] \\
&= h - \eta + \left(U_x^2 - UU_{xx} - U_{xt}\right)\left(\frac{h^2-\eta^2}{2g}\right) - \left[U^2\eta_{xx} + (U_t + UU_x)\eta_x\right]\left(\frac{h-\eta}{g}\right).
\end{aligned} \tag{3.589}$$

Consider the basic case of undular bores propagating over a straight horizontal channel, for which $z_b = z_{bx} = z_{bxx} = 0$ (Fig. 3.77). Thus, Eqs. (3.581), (3.582), and (3.589) read

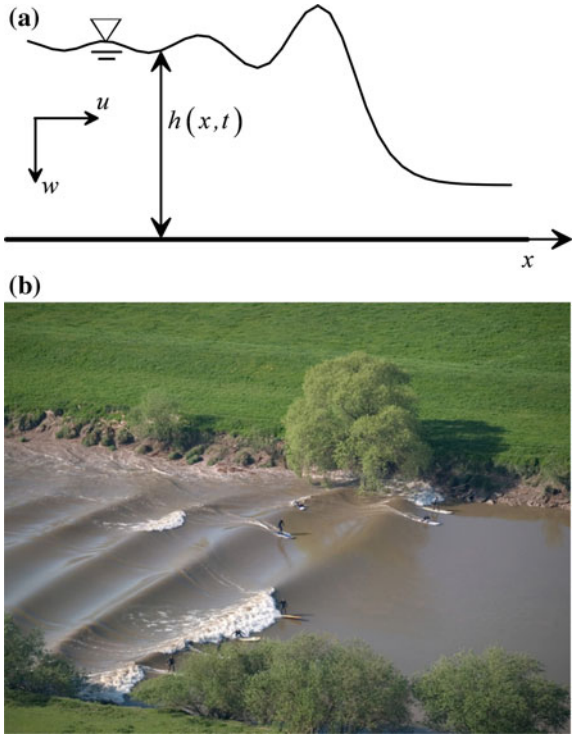

Fig. 3.77 Undular bore: **a** definition sketch, **b** Severn bore (photograph courtesy of Mark Humpage)

$$w = -U_x \eta, \tag{3.590}$$

$$u = U + U_{xx}\left(\frac{h^2}{6} - \frac{\eta^2}{2}\right), \tag{3.591}$$

$$\frac{p}{\gamma} = h - \eta + \left(U_x^2 - UU_{xx} - U_{xt}\right)\left(\frac{h^2 - \eta^2}{2g}\right). \tag{3.592}$$

This result is also obtained by using the perturbation technique (Peregrine 1967, 1972; Cienfuegos et al. 2006; Carter and Cienfuegos 2011), or the expansion of ϕ in power series of z (Mei 1983; Dingemans 1994).

Inserting Eqs. (3.591)–(3.592) into Eq. (3.579) with $\partial z_b/\partial x = 0$ yields, after integration, the x-momentum equation

$$\frac{\partial (Uh)}{\partial t} + \frac{\partial}{\partial x}\left[g\frac{h^2}{2} + U^2 h + \left(U_x^2 - UU_{xx} - U_{xt}\right)\frac{h^3}{3}\right] = 0. \tag{3.593}$$

The mass balance is given by Eq. (3.578), with $U = q/h$ as depth-averaged velocity, as

$$\frac{\partial h}{\partial t} + \frac{\partial (Uh)}{\partial x} = 0. \tag{3.594}$$

Equations (3.593)–(3.594) are the Serre (1953) equations for weakly dispersive, fully nonlinear 1D water waves, written in conservative form. The non-conservative form of Eqs. (3.593)–(3.594) is

$$\begin{aligned} &\frac{\partial h}{\partial t} + h\frac{\partial U}{\partial x} + U\frac{\partial h}{\partial x} = 0, \\ &\frac{\partial U}{\partial t} + U\frac{\partial U}{\partial x} + g\frac{\partial h}{\partial x} + \frac{1}{h}\frac{\partial}{\partial x}\left[\left(U_x^2 - UU_{xx} - U_{xt}\right)\frac{h^3}{3}\right] = 0. \end{aligned} \tag{3.595}$$

Equations (3.593)–(3.594) were obtained by Shu and Gardner (1969) and Green and Naghdi (1976b) by applying the irrotational flow theory. The *Serre–Green–Naghdi* equations for water wave propagation are discussed in depth by Barthelemy (2004), Dias and Milewski (2010), Carter and Cienfuegos (2011), and Bonneton et al. (2011). Based on Eq. (3.593), the momentum function M of the 1D Serre theory is $M = gh^2/2 + U^2h + (U_x^2 - UU_{xx} - U_{xt})h^3/3$ (Serre 1953; Mohapatra and Chaudhry 2004; Chaudhry 2008; Castro-Orgaz and Hager 2014a) [see Eq. (2.49)]. This M function was derived in Chap. 2 using the Serre theory, for which the u velocity component in the x-direction is approximated by its depth-averaged value U. This obviously implies that the vorticity is nonzero in the classical Serre theory. However, Su and Gardner (1969) demonstrated that the Serre equations can also be derived based on the irrotational flow theory, as done here as well. To the order of expansion used to find the irrotational velocity field, the non-uniformity of u with depth contributes to the advection of momentum with a term proportional to $(U_{xx})^2$, which, therefore, is of a higher order small. This is easily demonstrated evaluating the momentum flux by resorting to Eq. (3.591), e.g.,

$$\begin{aligned} \int_0^h u^2 \mathrm{d}z &= \int_0^h \left[U + U_{xx}\left(\frac{h^2}{6} - \frac{\eta^2}{2}\right)\right]^2 \mathrm{d}\eta \\ &= \int_0^h \left[U^2 + U_{xx}^2\left(\frac{h^2}{6} - \frac{\eta^2}{2}\right)^2 + 2UU_{xx}\left(\frac{h^2}{6} - \frac{\eta^2}{2}\right)\right]\mathrm{d}\eta \\ &= \int_0^h \left[U^2 + U_{xx}^2\left(\frac{h^4}{36} + \frac{\eta^4}{4} - \frac{2h^2}{12}\eta^2\right) + 2UU_{xx}\left(\frac{h^2}{6} - \frac{\eta^2}{2}\right)\right]\mathrm{d}\eta \\ &= U^2h + U_{xx}^2\frac{h^5}{45}. \end{aligned} \tag{3.596}$$

The main conclusion to be drawn is that Serre's equations mathematically result from the irrotational flow theory and are, thus, based on a non-uniform velocity profile with depth. This detail may appear subtle, but it is of paramount importance to improve the frequency dispersion features of the Serre equations, as will be discussed in the next section. The application of the irrotational flow theory to translation waves was initiated by Boussinesq (1872) to mathematically prove the existence of solitary waves, a translation wave of permanent form, and significant free surface curvature that remains unexplained based on the Saint-Venant theory. Later, Favre (1935) undertook a significant experimental study where he observed stable undular translation waves. These undular surges are now referred to as Favre waves (Soares-Frazão and Zech 2002; Soares-Frazão and Guinot 2008). Both solitary waves and undular surges were considered by Keulegan and Patterson (1940), who made a detailed analysis of both wave-type motions following the Boussinesq (1872) theory.

3.15.3 Small-Amplitude Waves

A special feature of the Serre equations is that they show frequency dispersion, i.e., waves of different lengths propagating at different celerities. Consider a small-amplitude sinusoidal wave propagating with wave number $k = (2\pi)/\lambda$, wavelength λ, and frequency ω over still water of constant depth d (Fig. 3.78a)

$$U = U_o \exp[i(kx - \omega t)], \quad \varsigma = A\exp[i(kx - \omega t)]. \tag{3.597}$$

Here, $\varsigma = h - d$ is the depth around the static level, and $i^2 = -1$ is the imaginary unit. As the wave amplitude A is small relative to d, the non-conservative Serre equations (3.595) are linearized to investigate wave propagation. Given that the ratio A/d is small, the term $\partial h/\partial x = \partial \varsigma/\partial x$ is neglected in Eq. $(3.595)_1$ compared with $\partial U/\partial x$. For this small-amplitude wave, the local acceleration term $\partial U/\partial t$ will be more important than the convective acceleration term $U\,\partial U/\partial x$; thus, the latter is neglected in Eq. $(3.595)_2$. Further, in the vertical momentum equation, the local acceleration term, represented in Eq. $(3.595)_2$ by the non-hydrostatic term, proportional to U_{xt}, is assumed to be more important than the non-hydrostatic convective term, proportional to $(U_x^2 - UU_{xx})$. The resulting linearized system from Eqs. (3.595) is (Mei 1983; Dingemans 1994)

$$\frac{\partial \varsigma}{\partial t} + d\frac{\partial U}{\partial x} = 0, \tag{3.598}$$

$$\frac{\partial U}{\partial t} + g\frac{\partial \varsigma}{\partial x} = \frac{d^2}{3}\frac{\partial^3 U}{\partial^2 x \partial t}. \tag{3.599}$$

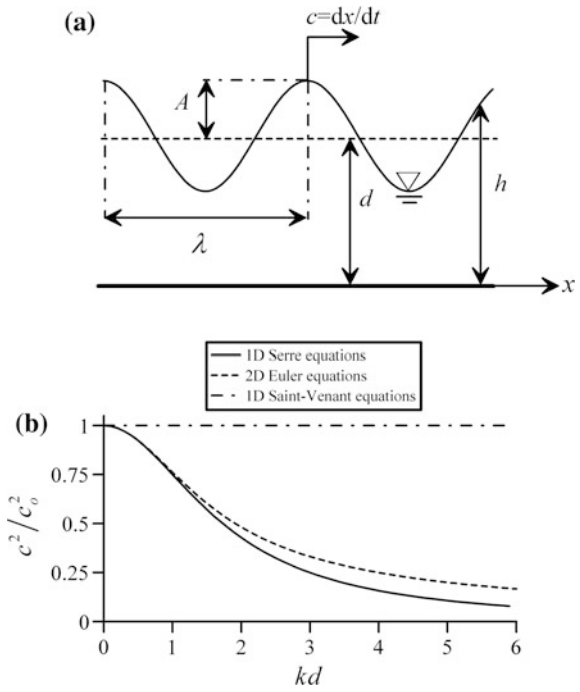

Fig. 3.78 Small-amplitude sinusoidal wave: **a** definition sketch, **b** dispersion relation of Serre's theory, with $c_o = (gd)^{1/2}$ as the propagation speed of hydrostatic waves (Saint-Venant's theory)

Inserting Eq. (3.597) into Eqs. (3.598)–(3.599) leads to a homogeneous system of linear equations, implying a non-trivial solution, provided that

$$\begin{vmatrix} -i\omega & ikd \\ igk & -i\omega\left(1+\frac{k^2d^2}{3}\right) \end{vmatrix} = 0, \tag{3.600}$$

from which the linear dispersion[7] relation with c as phase speed is

$$c^2 = \frac{\omega^2}{k^2} = gd\left[1+\frac{1}{3}(kd)^2\right]^{-1}. \tag{3.601}$$

The exact dispersion relation from the 2D Euler equations is (see, e.g., Mei 1983; Dingemans 1994)

$$c^2 = gd\frac{\tanh(kd)}{kd}. \tag{3.602}$$

Comparing Eqs. (3.601) and (3.602) in Fig. 3.78b shows that the Serre equations have weak dispersion characteristics, e.g., they are invalid at deep- and

[7]If the phase speed c depends on the wave number k, the corresponding wave is called dispersive.

intermediate-water depths. However, they are a good model for $kd < 1$ (shallow flows), e.g., for waves of wavelength of about 6 times the water depth. For shorter waves, the dispersion relation must be enhanced, to propagate the perturbations at the correct celerity (Nwogu 1993; Wei et al. 1995). Frequency dispersion may be improved enhancing the linear dispersion relation by using Nwogu's (1993) approach, selecting the velocity u_α at a prescribed elevation z_α as a dependent variable in the continuity and momentum equations, instead of U. This method was applied by Kim and Lynett (2011), and it is of wide use in coastal engineering, where applications from shallow- to intermediate-water depths are common. The Serre equations (3.593)–(3.594) are derived by assuming that the flow is shallow, i.e., that a typical vertical length scale (water depth) is smaller than a typical horizontal length scale, e.g., the wave amplitude. This leads to a weakly dispersive (long wave) model, shown in Fig. 3.78b. Note that the shallowness parameter must be small, but not asymptotically small, given that otherwise non-hydrostatic contributions are not preserved and the model becomes non-dispersive, as shown in Fig. 3.78b for the Serre equations, using $kd = 0$. In this case, the Saint-Venant (non-dispersive) model is regained.

In civil and environmental engineering, the flows are typically shallow, so the main concern is to retain the full nonlinearity of the model rather than improving the frequency dispersion features. Serre's equations are derived without assuming that the model nonlinearity is small, i.e., the ratio of wave amplitude to water depth is arbitrary. As the flow tends to become shallow, the wave amplitude usually increases, leading to waves for which the ratio of amplitude to depth is not small and nonlinear effects become important. Waves close to breaking imply large wave amplitudes, e.g., A/d may be as high as 0.4, so that nonlinear terms shall be accounted for in the Boussinesq-type model. Frequency dispersion is important to predict the correct celerity of propagation at intermediate- and deep-water depths, given that short waves propagate slower than long waves. However, the accurate prediction of the wave amplitude is important as well, for example, to avoid overtopping in open channels. The classical Boussinesq system for weakly dispersive and weakly nonlinear waves is regained if the terms U_x^2 and U_{xx} are neglected in M, as demonstrated by Peregrine (1966, 1967, 1972)

$$\frac{\partial h}{\partial t} + \frac{\partial (Uh)}{\partial x} = 0, \tag{3.603}$$

$$\frac{\partial (Uh)}{\partial t} + \frac{\partial}{\partial x}\left(g\frac{h^2}{2} + U^2 h\right) = \frac{d^3}{3}\frac{\partial^3 U}{\partial^2 x \partial t}. \tag{3.604}$$

This model is, however, unsuited for shallow flows, so that the Serre equations are generally recommended. Note further that steady-state flows with non-hydrostatic pressure conditions are not preserved by transient simulations based on Eq. (3.604), given that convective acceleration terms are dropped.

To improve the frequency dispersion in Boussinesq-type models, the approach of Nwogu (1993) is recommended. It is based on the fact that the dispersion

features of Boussinesq-type equations are highly sensitive to the choice of the dependent variables. Thus, consider the u component of the irrotational velocity field evaluated at an arbitrary elevation $z_\alpha = \eta = \alpha h/3^{1/2}$. From Eq. (3.591) follows with α as a parameter

$$u_\alpha = U + U_{xx}\left(\frac{h^2}{6} - \frac{z_\alpha^2}{2}\right) = U + U_{xx}\left(\frac{h^2}{6} - \frac{\alpha^2\eta^2}{6}\right) = U + \left(1-\alpha^2\right)\frac{h^2}{6}U_{xx}. \tag{3.605}$$

Inserting Eq. (3.605) into Eqs. (3.593)–(3.594) to obtain Serre's equations expressed as a function of u_α instead of U, neglecting higher order terms by assuming $U_{xx} \approx u_{\alpha xx}$, leads to

$$\frac{\partial h}{\partial t} + \frac{\partial (u_\alpha h)}{\partial x} - \left(1-\alpha^2\right)\frac{\partial}{\partial x}\left(\frac{h^3}{6}u_{\alpha xx}\right) = 0, \tag{3.606}$$

$$\begin{aligned}&\frac{\partial (u_\alpha h)}{\partial t} + \frac{\partial}{\partial x}\left(g\frac{h^2}{2} + u_\alpha^2 h\right) + \frac{\partial}{\partial x}\left[\left(u_{\alpha x}^2 - u_\alpha u_{\alpha xx} - u_{\alpha xt}\right)\frac{h^3}{3}\right] \\ &\quad - \left(1-\alpha^2\right)\left[\frac{\partial}{\partial t}\left(\frac{h^3}{6}u_{\alpha xx}\right) + \frac{\partial}{\partial x}\left(\frac{h^3}{3}u_\alpha u_{\alpha xx}\right)\right] = 0.\end{aligned} \tag{3.607}$$

Equations (3.606)–(3.607) are the generalized Serre equations with improved frequency dispersion developed by Dias and Milewski (2010), obtained here based on a Picard iteration method. The linear system, obtainable from Eqs. (3.606)–(3.607), is

$$\frac{\partial \varsigma}{\partial t} + d\frac{\partial u_\alpha}{\partial x} = \left(1-\alpha^2\right)\frac{d^3}{6}\frac{\partial^3 u_\alpha}{\partial x^3}, \tag{3.608}$$

$$\frac{\partial u_\alpha}{\partial t} + g\frac{\partial \varsigma}{\partial x} = \left(3-\alpha^2\right)\frac{d^2}{6}\frac{\partial^3 u_\alpha}{\partial x^2 \partial t}. \tag{3.609}$$

Inserting Eq. (3.597) into Eqs. (3.608)–(3.609) yields the homogeneous linear system of equations

$$\begin{bmatrix} \omega & -kd\left[1 + \frac{1}{6}(1-\alpha^2)(kd)^2\right] \\ -gk & \omega\left[1 + \frac{1}{6}(3-\alpha^2)(kd)^2\right] \end{bmatrix}\begin{bmatrix} A \\ U_o \end{bmatrix} = \begin{bmatrix} 0 \\ 0 \end{bmatrix}. \tag{3.610}$$

It possesses a non-trivial solution provided its determinant vanishes, resulting in the linear dispersion relation (Dias and Milewski 2010)

$$c^2 = \frac{\omega^2}{k^2} = gd\frac{\left[1 + \frac{1}{6}(1-\alpha^2)(kd)^2\right]}{\left[1 + \frac{1}{6}(3-\alpha^2)(kd)^2\right]}. \tag{3.611}$$

For comparative purposes, consider the weakly nonlinear 1D Boussinesq equations of Nwogu (1993)

$$\frac{\partial \varsigma}{\partial t} + \frac{\partial (hu_\alpha)}{\partial x} + \left(\alpha_N + \frac{1}{3}\right)d^3\frac{\partial^3 u_\alpha}{\partial x^3} = 0, \tag{3.612}$$

$$\frac{\partial u_\alpha}{\partial t} + g\frac{\partial \varsigma}{\partial x} + u_\alpha\frac{\partial u_\alpha}{\partial x} + \alpha_N d^2\frac{\partial^3 u_\alpha}{\partial^2 x \partial t} = 0. \tag{3.613}$$

The arbitrary elevation z_α and coefficient α_N in Nwogu's theory are related by

$$\alpha_N = \frac{1}{2}\left(\frac{z_\alpha}{d}\right)^2 + \left(\frac{z_\alpha}{d}\right). \tag{3.614}$$

The dispersion relation for Eqs. (3.612)–(3.613) is

$$c^2 = \frac{\omega^2}{k^2} = gd\frac{\left[1 - \left(\alpha_N + \frac{1}{3}\right)(kd)^2\right]}{1 - \alpha_N(kd)^2}. \tag{3.615}$$

Comparing Eqs. (3.611) and (3.615) yields the compatibility condition

$$\alpha^2 = 6\alpha_N + 3. \tag{3.616}$$

Therefore, the equations of Nwogu (1993) are equivalent to the enhanced Serre equations by Dias and Milewski (2010) in terms of linear frequency dispersion. The errors predicting the frequency dispersion with Eq. (3.601) as compared with the exact Eq. (3.602) are considered in Fig. 3.79a for reference. Note that these are acceptable up to $kd = 1$, as previously stated. The errors using Eq. (3.615) are inserted in the same figure for the optimized value $\alpha_N = -0.39$ (Nwogu 1993), equivalent to $\alpha^2 = 0.66$ as used by Dias and Milewski (2010), indicating good model performance up to $kd = 3$. This technique leads, thus, to a significant improvement of the prediction of the linear frequency dispersion for intermediate-water depths.

If a more accurate prediction of frequency dispersion is sought, an alternative method is to resort to the moment equations by Steffler and Jin (1993), as presented in Chap. 2. The linear dispersion relation for the momentum and moment of momentum system (Eqs. 2.191–2.200) according to Steffler and Jin (1993) is

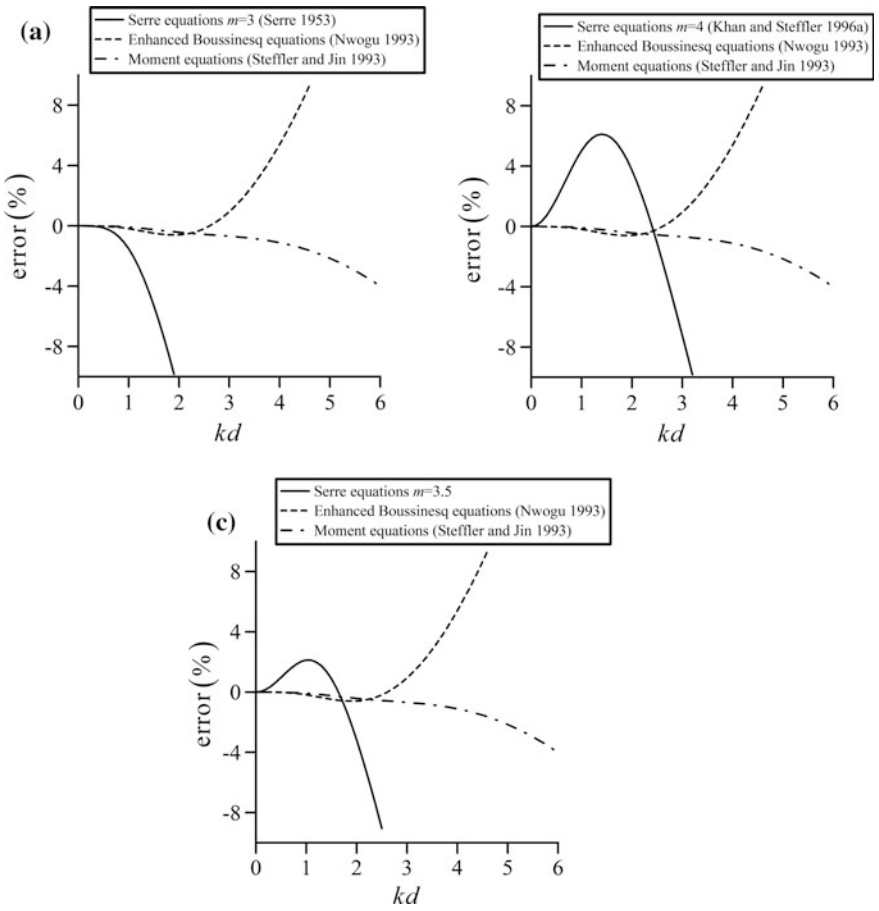

Fig. 3.79 Errors in the frequency dispersion relation for **a** Serre's (1953) theory, **b** Khan and Steffler's Boussinesq-type model (1996a), **c** enhanced Serre's equations with $m = 3.5$. Comparison with Nwogu (1993) and moment method (Steffler and Jin 1993)

$$c^2 = \frac{\omega^2}{k^2} = gd \frac{\left[1 + \frac{(kd)^2}{12}\right]}{\left[1 + \frac{5(kd)^2}{12} + \frac{(kd)^4}{144}\right]}. \tag{3.617}$$

This is also considered in Fig. 3.79a. A comparison reveals that the moment equations are accurate up to $kd = 5$. Obviously, the cost for numerical modeling of water waves is to solve a larger system of PDEs, but the effort appears to be worthy if an accurate dispersion prediction is sought from shallow to deep waters. The Boussinesq equations by Khan and Steffler (1996a) are a simplified momentum and

moment of momentum model, given by the system [see Eqs. (2.105) and (2.110) for a horizontal bed without friction]

$$\frac{\partial h}{\partial t}+\frac{\partial (Uh)}{\partial x}=0, \tag{3.618}$$

$$\frac{\partial (Uh)}{\partial t}+\frac{\partial}{\partial x}\left[g\frac{h^2}{2}+U^2h+\left(U_x^2-UU_{xx}-U_{xt}\right)\frac{h^3}{4}\right]=0. \tag{3.619}$$

Construction of the linear system in the same spirit as done above for Eqs. (3.611) and (3.615) leads to the linear dispersion relation given by (Fig. 3.79b)

$$c^2=\frac{\omega^2}{k^2}=gd\left[1+\frac{1}{4}(kd)^2\right]^{-1}. \tag{3.620}$$

An aspect of interest is that the dispersion features of this approximation (based on a linear vertical pressure profile) are not satisfactory as compared with Serre's theory (parabolic pressure profile) in the interval $0<kd<1$.

The generalized Serre equations for an arbitrary pressure distribution exponent are given by [see Eq. (2.185) for the M function]

$$\frac{\partial h}{\partial t}+\frac{\partial (Uh)}{\partial x}=0, \tag{3.621}$$

$$\frac{\partial (Uh)}{\partial t}+\frac{\partial M}{\partial x}=\frac{\partial (Uh)}{\partial t}+\frac{\partial}{\partial x}\left[g\frac{h^2}{2}+U^2h+\left(U_x^2-UU_{xx}-U_{xt}\right)\frac{h^3}{m}\right]=0. \tag{3.622}$$

The non-hydrostatic term in Eq. (3.622) was obtained using a vertical pressure distribution with an arbitrary exponent [see Eq. (2.182)]. In Eq. (3.622), m is thus a pressure coefficient dependent on the vertical pressure distribution law (=3 for parabolic pressure profile; =4 for linear pressure profile). The corresponding dispersion relation for the Serre equations with a generic pressure profile is

$$c^2=\frac{\omega^2}{k^2}=gd\left[1+\frac{1}{m}(kd)^2\right]^{-1}. \tag{3.623}$$

The error disclosed by Eq. (3.623) is plotted in Fig. 3.79c for m = 3.5; errors keep roughly in the band ±2 % below kd = 2. Therefore, this is an alternative to enhance the prediction of frequency dispersion at a low increase of mathematical complexities as compared with the standard Serre equations. This assessment of the Serre-type equations as function of m reveals that the linear dispersion features are sensitive to the value of m, e.g., for m = 3, the behavior is good for shallow water, whereas the accuracy diminishes for m = 4. This fact is used to improve the

linear dispersion features using $m = 3.5$. However, the accuracy increase is not as high as that when using the Nwogu-type approach.

Consider the coupling of both techniques, by using u_α instead of U as dependent variable and prescribing a generic vertical pressure profile, resulting in a momentum pressure coefficient m. From Steffler and Jin (1993), arbitrary functions for velocity and pressure distributions can be prescribed in the depth-averaged flow equations, so that the irrotational flow assumption is not used. The mathematical limitation is that undetermined parameters should not remain in the system of the PDEs. The use of the following set of predictors for (u, w, p) is investigated

$$u = U + U_{xx}\left(\frac{h^2}{6} - \frac{\eta^2}{2}\right) = u_\alpha + u_{\alpha xx}\left(\frac{z_\alpha^2 - \eta^2}{2}\right), \tag{3.624}$$

$$w = -U_x\eta, \tag{3.625}$$

$$p = \rho g h\left(1 - \frac{z}{h}\right) + p_1\left[1 - \left(\frac{z}{h}\right)^K\right], \tag{3.626}$$

with K as a Fawer-type interpolating exponent and the bed pressure in excess of the hydrostatic pressure given by

$$p_1 = \rho\left(U_x^2 - UU_{xx} - U_{xt}\right)\frac{h^2}{2}. \tag{3.627}$$

The generalized Serre Eqs. (3.621)–(3.622) were obtained using Eq. (3.626)–(3.627) [see chapter 2, Eqs. (2.182)-(2.186)] for the pressure distribution. These are now expressed in terms of u_α instead of U, using Eq. (3.624), producing the enhanced Serre equations

$$\frac{\partial h}{\partial t} + \frac{\partial (u_\alpha h)}{\partial x} - \left(1 - \alpha^2\right)\frac{\partial}{\partial x}\left(\frac{h^3}{6}u_{\alpha xx}\right) = 0, \tag{3.628}$$

$$\begin{aligned}&\frac{\partial (u_\alpha h)}{\partial t} + \frac{\partial}{\partial x}\left(g\frac{h^2}{2} + u_\alpha^2 h\right) + \frac{\partial}{\partial x}\left[\left(u_{\alpha x}^2 - u_\alpha u_{\alpha xx} - u_{\alpha xt}\right)\frac{h^3}{m}\right] \\ &- \left(1 - \alpha^2\right)\left[\frac{\partial}{\partial t}\left(\frac{h^3}{6}u_{\alpha xx}\right) + \frac{\partial}{\partial x}\left(\frac{h^3}{3}u_\alpha u_{\alpha xx}\right)\right] = 0.\end{aligned} \tag{3.629}$$

For $m = 3$, Eqs. (3.628)–(3.629) reduce to Eqs. (3.606)–(3.607). The linear system obtained from Eqs. (3.628)–(3.629) is

$$\frac{\partial \varsigma}{\partial t} + d\frac{\partial u_\alpha}{\partial x} = \left(1 - \alpha^2\right)\frac{d^3}{6}\frac{\partial^3 u_\alpha}{\partial x^3}, \tag{3.630}$$

$$\frac{\partial u_\alpha}{\partial t} + g\frac{\partial \varsigma}{\partial x} = \left(1-\alpha^2\right)\frac{d^2}{6}\frac{\partial^3 u_\alpha}{\partial x^2 \partial t} + \frac{d^2}{m}\frac{\partial^3 u_\alpha}{\partial x^2 \partial t}, \tag{3.631}$$

with the linear dispersion relation

$$c^2 = \frac{\omega^2}{k^2} = gd\frac{\left[1+\frac{1}{6}(1-\alpha^2)(kd)^2\right]}{\left[1+\left\{\frac{1}{6}(1-\alpha^2)+\frac{1}{m}\right\}(kd)^2\right]}. \tag{3.632}$$

For $m = 3$, Eq. (3.632) reduces to Eq. (3.611). The parameters m and α^2 must be determined within the physical limits: 3 (parabolic) < m < 4 (linear pressure profile) and 0 (bottom) < α^2 < $3^{1/2}$ (free surface level). Selection of the bottom or free surface elevations to compute α^2 was found to be a poor choice, as was also the consideration of a value m close to 4.

The frequency dispersion errors using Eq. (3.632) are plotted in Fig. 3.80 for the values $m = 3.2$ and $\alpha^2 = 0.75$ (labeled as enhanced Serre's equations, meaning that both m and α^2 must be determined to improve the dispersion relation). These particular values were found to keep the errors in the band ±2 %. Standard Serre equations and the Nwogu-type equations are plotted in the same figure for comparative purposes. The standard Serre equations apply up to $kd = 1.1$ for this error band, whereas the Nwogu equations are valid up to $kd = 3.3$. The enhanced Serre equations with variable m are valid up to $kd = 4.7$, a considerable increase of their application range. The moment equation remains valid up to $kd = 4.9$, e.g., close to the enhanced Serre equations.

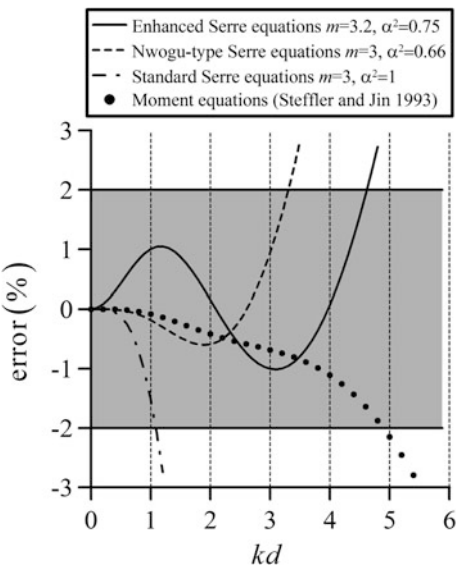

Fig. 3.80 Errors in the frequency dispersion relation for the enhanced Serre equations (error band ±2 %)

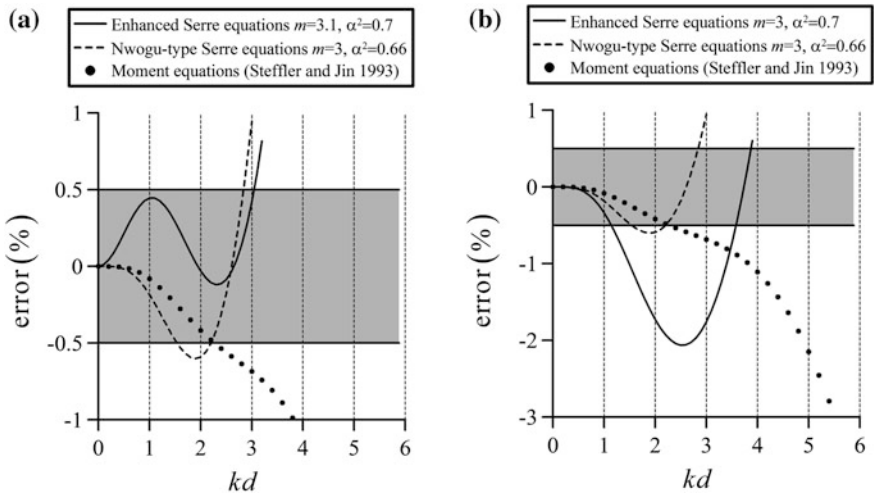

Fig. 3.81 Errors in frequency dispersion for the enhanced Serre equations (error band ±0.5 %)

For the more restrictive error band ±0.5 %, Eq. (3.632) is plotted in Fig. 3.81a for the values $m = 3.1$ and $\alpha^2 = 0.7$. The approach remains valid up to $kd = 3$, whereas the moment method is valid up to $kd = 2.2$, and the Nwogu equations lie outside the error band in a portion of the kd interval. To highlight the model sensitivity in relation to combinations of m and α^2, Eq. (3.632) is plotted in Fig. 3.81b for the values $m = 3$ and $\alpha^2 = 0.7$, showing a limited improvement as compared with the standard Serre equations.

3.15.4 Cnoidal and Solitary Waves

An important nonlinear dispersive long water wave of permanent form is the cnoidal wave. It is a periodic irrotational wave solution of the Euler equations, originally due to Korteweg and de Vries (1895), and masterly reconsidered in the pioneering work of Benjamin and Lighthill (1954). The solutions are given in terms of Jacobi's elliptical function cn, from which the name cnoidal wave originates. This wave type is periodic, characterized by sharp wave crests and flat wave troughs (Fig. 3.82).

For the limiting case of infinite wavelength, the solitary wave is regained from the cnoidal wave theory (Keulegan and Patterson 1940; Iwasa 1956). Here, the cnoidal wave theory is considered following Iwasa (1956). Steady irrotational water waves over a horizontal bottom (or unsteady translation waves of permanent form) are described by the 3 invariants (E, S, and q) as (Benjamin and Lighthill 1954)

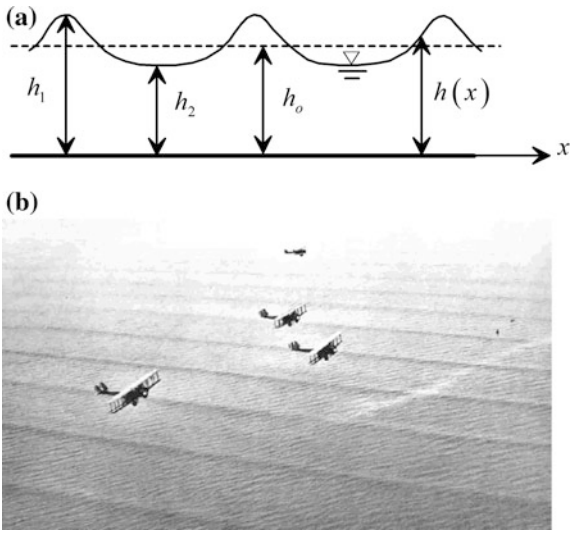

Fig. 3.82 Cnoidal waves: **a** definition sketch, **b** US Army bombers flying over cnoidal waves close to the Panama coast (1933) (photograph of public domain by US Army, taken from https://en.wikipedia.org/)

$$E = h + \frac{q^2}{2gh^2}\left(1 + \frac{2hh_{xx} - h_x^2}{3}\right) = \text{const.}, \tag{3.633}$$

$$S = \frac{h^2}{2} + \frac{q^2}{gh}\left(1 + \frac{hh_{xx} - h_x^2}{3}\right) = \text{const.}, \tag{3.634}$$

$$q = Uh = \text{const.} \tag{3.635}$$

Consider the momentum invariant, Eq. (3.634), rewritten as

$$\frac{q^2}{3g}\left(h_{xx} - \frac{1}{h}h_x^2\right) = S - \frac{h^2}{2} - \frac{q^2}{gh}. \tag{3.636}$$

The left-hand side of Eq. (3.636) is transformed to

$$\frac{q^2}{3g}\left(h_{xx} - \frac{1}{h}h_x^2\right) = \frac{q^2}{6g}\left(2h_{xx} - \frac{2h_x^2}{h}\right) = \frac{q^2}{6g}\left[\frac{\mathrm{d}}{\mathrm{d}h}\left(h_x^2\right) - \frac{2h_x^2}{h}\right], \tag{3.637}$$

based on

$$\frac{\mathrm{d}}{\mathrm{d}x}\left(h_x^2\right) = 2h_x h_{xx} \Rightarrow \frac{\mathrm{d}}{\mathrm{d}h}\left(h_x^2\right)\frac{\mathrm{d}h}{\mathrm{d}x} = 2h_x h_{xx} \Rightarrow \frac{\mathrm{d}}{\mathrm{d}h}\left(h_x^2\right) = 2h_{xx}. \tag{3.638}$$

Moreover, with

$$\frac{\mathrm{d}}{\mathrm{d}h}\left(\frac{h_x^2}{h^2}\right) = \frac{1}{h^2}\frac{\mathrm{d}}{\mathrm{d}h}\left(h_x^2\right) - \frac{2}{h^3}h_x^2, \tag{3.639}$$

Eq. (3.636) is finally rewritten in the alternative form

$$\frac{q^2h^2}{6g}\frac{\mathrm{d}}{\mathrm{d}h}\left(\frac{h_x^2}{h^2}\right) = S - \frac{h^2}{2} - \frac{q^2}{gh}. \tag{3.640}$$

Integration of Eq. (3.640) with c as a constant of integration yields

$$\begin{aligned}\frac{q^2}{6g}\frac{\mathrm{d}}{\mathrm{d}h}\left(\frac{h_x^2}{h^2}\right) = \frac{S}{h^2} - \frac{1}{2} - \frac{q^2}{gh^3} \Rightarrow \frac{q^2}{6g}\frac{h_x^2}{h^2} &= \frac{S}{-2+1}h^{-2+1} - \frac{1}{2}h - \frac{q^2}{g}\frac{h^{-3+1}}{-3+1} + c \\ \Rightarrow \frac{q^2}{6g}h_x^2 &= -\frac{h^3}{2} + ch^2 - Sh + \frac{q^2}{2g} \\ &= -\frac{h^3}{2} + Eh^2 - Sh + \frac{q^2}{2g}.\end{aligned} \tag{3.641}$$

In Eq. (3.641), the constant c is equal to the specific energy E. This can be easily obtained by the integration of Eq. (3.633) [see development from Eqs. (3.522)–(3.524)]. Let $h_1 > h_2 > h_3$ be the 3 real-valued roots of the cubic on the right-hand side of Eq. (3.641); it can be rewritten as (Keulegan and Patterson 1940; Benjamin and Lighthill 1954)

$$\frac{q^2}{3g}h_x^2 = (h_1 - h)(h - h_2)(h - h_3). \tag{3.642}$$

Expanding Eq. (3.642) and comparing the resulting cubic in h with Eq. (3.641), it follows that $E = (h_1 + h_2 + h_3)/2$, $S = h_1h_2 + h_1h_3 + h_2h_3$ and $h_1h_2h_3 = q^2/g$. Here, h_1 and h_2 are the water depths at the wave crest (maximum depth) and trough (minimum depth), respectively (Fig. 3.82a), where $h_x = 0$ (Keulegan and Patterson 1940; Benjamin and Lighthill 1954). Note that in a cnoidal wave, the fluid is disturbed at infinity, i.e., h_x and h_{xx} do not vanish (Fig. 3.82a). The flow depth h must be comprised between h_1 and h_2, given that h_x^2 must be positive for a real-valued solution of $h = h(x)$ [see Eq. (3.642)]. Thus, using the change of variable satisfying these conditions

$$h = h_1\cos^2\chi + h_2\sin^2\chi, \tag{3.643}$$

the following transformations are obtained

$$\begin{aligned}
\frac{\mathrm{d}h}{\mathrm{d}x} &= \frac{\mathrm{d}h}{\mathrm{d}\chi}\frac{\mathrm{d}\chi}{\mathrm{d}x} = (-2h_1\cos\chi\sin\chi + 2h_2\sin\chi\cos\chi)\frac{\mathrm{d}\chi}{\mathrm{d}x} \\
&= -2\cos\chi\sin\chi(h_1 - h_2)\frac{\mathrm{d}\chi}{\mathrm{d}x} = -2\sin 2\chi(h_1 - h_2)\frac{\mathrm{d}\chi}{\mathrm{d}x}, \\
h_1 - h &= h_1 - h_1\cos^2\chi - h_2\sin^2\chi = h_1\left(1 - \cos^2\chi\right) - h_2\sin^2\chi = \sin^2\chi(h_1 - h_2), \\
h - h_2 &= h_1\cos^2\chi + h_2\sin^2\chi - h_2 = h_1\cos^2\chi + h_2\left(\sin^2\chi - 1\right) = \cos^2\chi(h_1 - h_2), \\
h - h_3 &= h_1\cos^2\chi + h_2\sin^2\chi - h_3 = h_1\left(1 - \sin^2\chi\right) + h_2\sin^2\chi - h_3 \\
&= (h_1 - h_3) - \sin^2\chi(h_1 - h_2).
\end{aligned} \tag{3.644}$$

Inserting Eq. (3.644) into Eq. (3.642) yields the modified ODE

$$\frac{4}{3}\frac{q^2}{g}\left(\frac{\mathrm{d}\chi}{\mathrm{d}x}\right)^2 = (h_1 - h_3) - (h_1 - h_2)\sin^2\chi, \tag{3.645}$$

which is rewritten as (Keulegan and Patterson 1940; Benjamin and Lighthill 1954)

$$\begin{aligned}
\frac{\mathrm{d}x}{\mathrm{d}\chi} &= \pm\frac{\Pi}{\left(1 - k^2\sin^2\chi\right)^{1/2}}, \quad \Pi^2 = \frac{4}{3}\frac{q^2}{g}\frac{1}{h_1 - h_3} = \frac{4}{3}\frac{q^2}{g}\left(h_1 - \frac{q^2}{gh_1h_2}\right)^{-1}, \\
k^2 &= \frac{h_1 - h_2}{h_1 - h_3} = (h_1 - h_2)\left(h_1 - \frac{q^2}{gh_1h_2}\right)^{-1} \le 1.
\end{aligned} \tag{3.646}$$

Integration of Eq. (3.646), taking the origin of the x-coordinate at the wave crest, where $\chi = 0$ and thus $h = h_1\cos^2\chi + h_2\sin^2\chi = h_1$, gives (Keulegan and Patterson 1940; Benjamin and Lighthill 1954)

$$x = \Pi\int_0^\chi \left(1 - k^2\sin^2\chi'\right)^{-1/2}\mathrm{d}\chi' = \Pi\cdot u\left(\chi, k^2\right). \tag{3.647}$$

Here, $u(\chi, k^2)$ is the incomplete elliptical integral of the first kind and modulus k^2 (Montes 1998). Equations (3.643) and (3.647) are a parametric representation [$h = h(\chi)$, $x = x(\chi)$] of the free surface profile $h = h(x)$, in terms of the new variable χ (see Abramowitz and Stegun 1972). Since $\mathrm{sn}(u, k^2) = \sin\chi$, $\mathrm{cn}(u, k^2) = \cos\chi$, it follows that $\mathrm{sn}^2(u, k^2) + \mathrm{cn}^2(u, k^2) = 1$. Thus, Eq. (3.643) is rewritten as $h = h_1\cos^2\chi + h_2\sin^2\chi = h_1\mathrm{cn}^2(u, k^2) + h_2[1 - \mathrm{cn}^2(u, k^2)]$. The free surface profile is finally given by

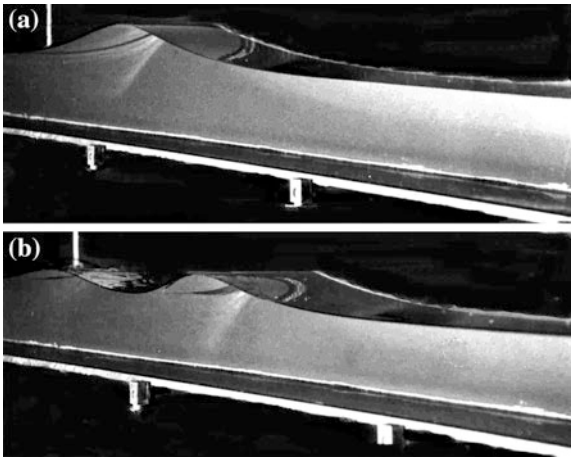

Fig. 3.83 Translation waves in laboratory channel: **a** solitary wave ($k^2 = 1$), **b** cnoidal wave ($k^2 < 1$) (photograph VAW)

$$h = h_2 + (h_1 - h_2)\mathrm{cn}^2\left(u, k^2\right). \tag{3.648}$$

The "cnoidal" surname of this irrotational motion thus becomes evident, given the Jacobi elliptical function cn as the solution. If $k^2 = 0$, a sinusoidal wave is regained, whereas the value $k^2 = 1$ produces the solitary wave (Fig. 3.83), given that $\mathrm{cn}(u, 1) = \mathrm{sech}(u)$ (Iwasa 1956; Montes 1998). Thus, the solitary wave theory is a particular case of the cnoidal wave theory. The solitary wave was first observed by Russell (1837), and it is clearly described with his own words as follows:

> I was observing the motion of a boat which was rapidly drawn along a narrow channel by a pair of horses, when the boat suddenly stopped - not so the mass of water in the channel which it had put in motion; it accumulated round the prow of the vessel in a state of violent agitation, then suddenly leaving it behind, rolled forward with great velocity, assuming the form of a large solitary elevation, a rounded, smooth and well-defined heap of water, which continued its course along the channel apparently without change of form or diminution of speed. I followed it on horseback, and overtook it still rolling on at a rate of some eight or nine miles an hour, preserving its original figure some thirty feet long and a foot to a foot and a half in height. Its height gradually diminished, and after a chase of one or two miles I lost it in the windings of the channel. Such, in the month of August 1834, was my first chance interview with that singular and beautiful phenomenon which I have called the Wave of Translation.

In a cnoidal wave, the fluid is disturbed at infinity. If the fluid is undisturbed there, h_x and h_{xx} vanish and the flow depth remains constant. Setting conditions at $x \to \pm\infty$, namely h_{xx} and $h_x \to 0$ for $h \to h_o$, with h_o as the uniform flow depth (Fig. 3.84a), yields $S = h_o^2/2 + q^2/(gh_o)$. Using this in Eq. (3.641), the constant of integration is found to be $c = h_o + q^2/(2gh_o^2) \equiv E$. Thus, Eq. (3.641) can be rewritten in this case as

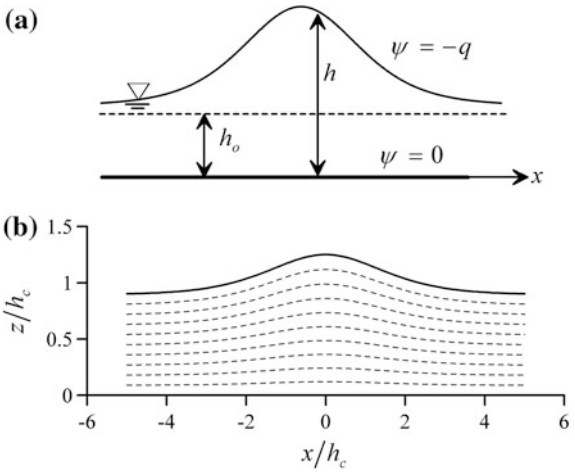

Fig. 3.84 Solitary wave: **a** definition sketch, **b** steady streamline flow pattern for $\mathsf{F}_o^2 = 1.4$, with h_c as critical depth = $(q^2/g)^{1/3}$

$$\frac{q^2}{6g}h_x^2 = -\frac{h^3}{2} + Eh^2 - Sh + \frac{q^2}{2g} = -\frac{h^3}{2} + \left(h_o + \frac{q^2}{2gh_o^2}\right)h^2 - Sh + \frac{q^2}{2g}, \quad (3.649)$$

and, inserting also the invariant S, gives the ODE describing solitary waves

$$\frac{q^2}{3g}h_x^2 = -h^3 + \left(2h_o + \frac{q^2}{gh_o^2}\right)h^2 - \left(h_o^2 + \frac{2q^2}{gh_o}\right)h + \frac{q^2}{g}. \quad (3.650)$$

Equation (3.650) is further manipulated, factorizing the cubic on the right-hand side as (Serre 1953, Iwasa 1956)

$$\frac{q^2}{3g}h_x^2 = (h - h_o)^2\left(\frac{q^2}{gh_o^2} - h\right). \quad (3.651)$$

The general integral of Eq. (3.651), with the boundary condition $h_x \to 0$ for $h \to h_o$, is with $\mathsf{F}_o = q/(gh_o^3)^{1/2}$(Serre 1953; Iwasa 1956)

$$\frac{h}{h_o} = 1 + \left(\mathsf{F}_o^2 - 1\right)\mathrm{sech}^2\left[\frac{\left(3\mathsf{F}_o^2 - 3\right)^{1/2}}{\mathsf{F}_o}\frac{x}{2h_o}\right]. \quad (3.652)$$

Equation (3.652) was originally obtained by Rayleigh (1876) expanding the potential velocity components (u, w) in power series of the elevation z. Bernoulli's equation and the kinematic boundary condition at the free surface were applied to find a differential equation describing the free surface profile. Here, Eq. (3.652) is presented as a solution of the Serre–Green–Naghdi equations, based on a Picard iteration of the stream and potential functions. The solution obtained by Boussinesq (1872), expanding the potential function in power series of z, is

$$\frac{h}{h_o} = 1 + \left(\mathsf{F}_o^2 - 1\right)\mathrm{sech}^2\left[\left(3\mathsf{F}_o^2 - 3\right)^{1/2}\frac{x}{2h_o}\right]. \tag{3.653}$$

It is different from Eq. (3.652) by a factor $1/\mathsf{F}_o$ in the argument of the sech^2 function. This result is based on a weakly nonlinearity (Keulegan and Paterson 1940). Equation (3.652) is more general than Eq. (3.653), given that the former originates from the fully nonlinear Serre equations (Carter and Cienfuegos 2011).

Consider Eq. (3.652) regarded as the second-order Picard iteration solution to the solitary wave profile. The steady irrotational velocity field associated with this wave profile is (Matthew 1991, 1995) [see Eqs. (3.63)–(3.64) for a horizontal bottom]

$$u = \frac{q}{h}\left[1 + \left(\frac{h_{xx}}{2h} - \frac{h_x^2}{h^2}\right)\left(\frac{3z^2 - h^2}{3}\right)\right], \tag{3.654}$$

$$w = q\frac{z}{h^2}h_x. \tag{3.655}$$

To test their accuracies, the full 2D solution of the irrotational velocity field (u, w) of a steady solitary wave (Fig. 3.84a) was determined using the x-ψ method (Montes 1994a). The free surface streamline was prescribed on the basis of Eq. (3.652), and the flow field was numerically determined by solving the Laplace equation of the x-ψ method [see Eq. (3.250)]

$$\nabla^2 z = \frac{\partial^2 z}{\partial x^2}\left(\frac{\partial z}{\partial \psi}\right)^2 + \frac{\partial^2 z}{\partial \psi^2}\left[1 + \left(\frac{\partial z}{\partial x}\right)^2\right] - 2\frac{\partial^2 z}{\partial x \partial \psi}\frac{\partial z}{\partial x}\frac{\partial z}{\partial \psi} = 0. \tag{3.656}$$

The up- and downstream boundary sections were located at $x/h_c = \pm 5$. The energy head of the potential flow is $H = h_d(1 + \mathsf{F}_o^2/2)$, and the flow depth h_d as the boundary sections is given by Eq. (3.652) evaluated at the selected boundary coordinates $x/h_c = \pm 5$. The numerical method of solution for Eq. (3.656) is extensively described in Sect. 3.7. A simulation for $\mathsf{F}_o^2 = 1.4$ is shown in Fig. 3.84b, where the flow was modeled using 11 streamlines.

The computed 2D velocity field (u, w) at selected locations is plotted in Fig. 3.85 and compared with Eqs. (3.654)–(3.655), indicating excellent agreement. At the section $x/h_c = -2$, the free surface is concave, implying a u-velocity profile increasing with the elevation. At section $x/h_c = -1$, and at the solitary wave crest $(x/h_c = 0)$, the free surface is convex, implying that the streamline of maximum velocity is at the bottom. The steady irrotational wave solutions of the Euler equations, namely the solitary and cnoidal waves, are important in steady channel flow problems. An example is the *undular hydraulic jump*, where the surface profile is characterized by connecting a solitary wave to a cnoidal wave (Iwasa 1955; Hager and Hutter 1984b).

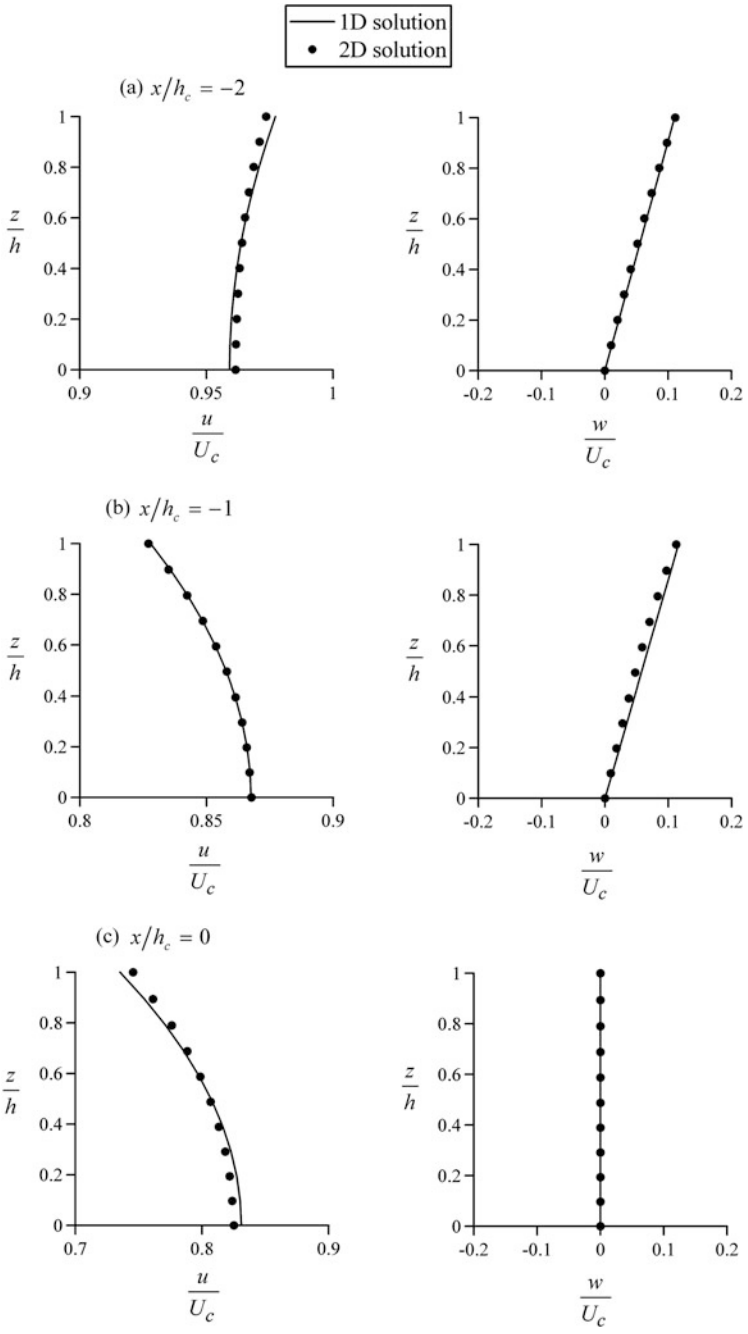

Fig. 3.85 Steady solitary wave velocity field (u/U_c, w/U_c) for $\mathsf{F}_o^2 = 1.4$, with U_c as the critical velocity

Consider now an unsteady solitary wave propagating over still water with celerity c. Using the Galilei transformation $X = x - ct$ for a wave translating in the positive x-direction, the Serre–Green–Naghdi equations, Eqs. (3.593)–(3.594), take the form

$$-c\frac{\partial h}{\partial X} + \frac{\partial Uh}{\partial X} = 0, \tag{3.657}$$

$$-c\frac{\partial Uh}{\partial X} + \frac{\partial}{\partial X}\left[g\frac{h^2}{2} + U^2h + \left(U_X^2 - UU_{XX} + cU_{XX}\right)\frac{h^3}{3}\right] = 0. \tag{3.658}$$

Integration of Eq. (3.657) yields, with q_p as the progressive discharge,

$$q_p = (U - c)h = \text{const.}, \tag{3.659}$$

or

$$U = c + \frac{q_p}{h}. \tag{3.660}$$

Using Eq. (3.657), Eq. (3.658) is rewritten as

$$-c^2\frac{\partial h}{\partial X} + \frac{\partial}{\partial X}\left[g\frac{h^2}{2} + U^2h + \left(U_X^2 - (U - c)U_{XX}\right)\frac{h^3}{3}\right] = 0, \tag{3.661}$$

or,

$$\frac{\partial}{\partial X}\left[g\frac{h^2}{2} + \left(U^2 - c^2\right)h + \left(U_X^2 - (U - c)U_{XX}\right)\frac{h^3}{3}\right] = 0. \tag{3.662}$$

In the moving frame, Eq. (3.662) implies the conservation of the expression

$$g\frac{h^2}{2} + \left(U^2 - c^2\right)h + \left(U_X^2 - (U - c)U_{XX}\right)\frac{h^3}{3} = c_1 = \text{const.} \tag{3.663}$$

Using the identities

$$U_X = -\frac{q_p}{h^2}h_X, \quad U_{XX} = -\frac{q_p}{h^2}h_{XX} + 2\frac{q_p}{h^3}h_X^2, \tag{3.664}$$

the non-hydrostatic term in Eq. (3.663) is

$$\begin{aligned} U_X^2 - (U - c)U_{XX} &= \left(\frac{q_p}{h^2}h_X\right)^2 - \frac{q_p}{h}\left(-\frac{q_p}{h^2}h_{XX} + 2\frac{q_p}{h^3}h_X^2\right) \\ &= \frac{q_p^2}{h^4}h_X^2 + \frac{q_p^2}{h^3}h_{XX} - 2\frac{q_p^2}{h^4}h_X^2 = \frac{q_p^2}{h^3}h_{XX} - \frac{q_p^2}{h^4}h_X^2. \end{aligned} \tag{3.665}$$

Thus, Eq. (3.663) is reduced to

$$\frac{h^2}{2} + \frac{q_p^2}{gh}\left(1 + \frac{hh_{XX} - h_X^2}{3}\right) = c_2 = \text{const.} \tag{3.666}$$

The solitary wave solution of Eq. (3.666) is with h_o as still water depth and $\mathsf{F}_p = q_p/(gh_o^3)^{1/2}$

$$\frac{h(x,t)}{h_o} = 1 + \left(\mathsf{F}_p^2 - 1\right)\text{sech}^2\left[\frac{\left(3\mathsf{F}_p^2 - 3\right)^{1/2}}{\mathsf{F}_p}\frac{(x - ct)}{2h_o}\right]. \tag{3.667}$$

The steps in the development of Eq. (3.667) are identical to those presented in Eqs. (3.649)–(3.652). The maximum flow depth at the solitary wave crest is obtained from Eq. (3.667) at $x - ct = 0$ as $h_{\max} = h_o\mathsf{F}_p^2$; this then yields $c = (gh_{\max})^{1/2}$. Equation (3.667) is mathematically identical to Eq. (3.652), as expected.

A difference between the steady solitary wave used to characterize the first wave of the undular hydraulic jump (Hager and Hutter 1984b) and the solitary wave propagating over still water (Sander and Hutter 1991) relates to the velocity profiles. Consider a solitary wave propagating over still water. Using the conditions $h = h_o$ and $U = 0$ at $\pm\infty$, the progressive discharge verifies the identity

$$q_p = [U(X) - c]h(X) = -ch_o, \tag{3.668}$$

from which the depth-averaged velocity, now interpreted as a function of x and t, follows as

$$U(x,t) = c\left[1 - \frac{h_o}{h(x,t)}\right]. \tag{3.669}$$

Using Eq. (3.591), the unsteady velocity profile in the fixed frame is given by[8]

$$u = U + U_{XX}\left(\frac{h^2}{6} - \frac{z^2}{2}\right), \quad U_{XX} = c\left(\frac{h_o}{h^2}h_{XX} - 2\frac{h_o}{h^3}h_X^2\right). \tag{3.670}$$

Consider the solitary wave crest, where $h_X = 0$, so that the velocity profile for u simplifies to

$$u = U + c\frac{h_o h_{XX}}{2h^2}\left(\frac{h^2 - 3z^2}{3}\right). \tag{3.671}$$

[8]Note, on comparing Eq. $(3.664)_2$ with $(3.670)_2$, the negative sign on the right-hand side of Eq. (3.668).

The steady velocity profile from Eq. (3.654) is rewritten as

$$u = U - U\frac{h_{xx}}{2h}\left(\frac{h^2 - 3z^2}{3}\right). \tag{3.672}$$

At the wave crest $h_{xx} < 0$, implying that the maximum of the steady velocity profile occurs at the bottom, as shown in Fig. 3.85c. In contrast, the maximum of the velocity profile of the unsteady translating solitary wave is at the free surface from Eq. (3.671) (Carter and Cienfuegos 2011). Obviously, in the moving frame, velocities are computed as $u(x, z, t) - c$, and the velocity profile becomes steady. For a detailed study of the irrotational velocity field of an unsteady solitary wave, see Carter and Cienfuegos (2011).

The Serre Eqs. (3.593)–(3.594) were used to describe translation waves of permanent form based on Eqs. (3.657)–(3.658). This system was reduced to a second-order differential equation (Eq. 3.666), with Eq. (3.667) as the particular solution for the solitary wave profile. If the same development is repeated starting with the generalized Serre Eqs. (3.621)-(3.622), the ODE describing translation waves is

$$\frac{h^2}{2} + \frac{q_p^2}{gh}\left(1 + \frac{hh_{XX} - h_X^2}{m}\right) = \text{const.} \tag{3.673}$$

Its first integral follows identical steps to those used to produce Eq. (3.651), resulting in

$$\frac{1}{m}\frac{q_p^2}{g}h_X^2 = (h - h_o)^2\left(\frac{q_p^2}{gh_o^2} - h\right). \tag{3.674}$$

The solitary wave solution of Eq. (3.674) is given by

$$\frac{h}{h_o} = 1 + \left(\mathsf{F}_p^2 - 1\right)\text{sech}^2\left[(m/3)^{1/2}\chi\right], \tag{3.675}$$

where

$$\chi = \frac{\left(3\mathsf{F}_p^2 - 3\right)^{1/2}}{\mathsf{F}_p}\frac{X}{2h_o} = \frac{\zeta}{\mathsf{F}_p}. \tag{3.676}$$

Again, the steps in the development of Eq. (3.675) are identical to those presented in Eqs. (3.649)–(3.652). For $m = 3$, Eq. (3.675) yields the solitary wave of the Serre equations (Eq. 3.667). The Boussinesq (1872, 1877) solution is [see Eq. (3.653)]

$$\frac{h}{h_o} = 1 + \left(\mathsf{F}_p^2 - 1\right)\mathrm{sech}^2\left[\left(3\mathsf{F}_p^2 - 3\right)^{1/2}\frac{X}{2h_o}\right] = 1 + \left(\mathsf{F}_p^2 - 1\right)\mathrm{sech}^2\zeta. \quad (3.677)$$

Equation (3.675) for $m = 3$ and Eq. (3.677) are compared in Fig. 3.86a, with $Y = (y - 1)/(\mathsf{F}_p^2 - 1)$ and $y = h/h_{\max}$, for a test case with $\mathsf{F}_p^2 = 1.65$ of Carter and Cienfuegos (2011). For reference, the exact 2D potential flow solution obtained by the method of Tanaka (1986), based on the simultaneous solution of Bernoulli's equation along the free surface and a boundary integral equation obtained from Cauchy's theorem, is also included. Note that although the Serre (1953) equations accounting for the full nonlinearity are theoretically more general than the Boussinesq (1872) equation, the latter is in better agreement with the Tanaka (1986) 2D solution, as discussed by Carter and Cienfuegos (2011). However, the Serre (1953) equations provide better prediction of other wave features, namely the particle kinematics and celerity of translation, so that they are recommended even though the predicted free surface profile is less accurate than that obtained with the Boussinesq solution. Tursunov (1969) presented a solution for the solitary wave profile based on the expansion in power series of the velocity modulus at the free

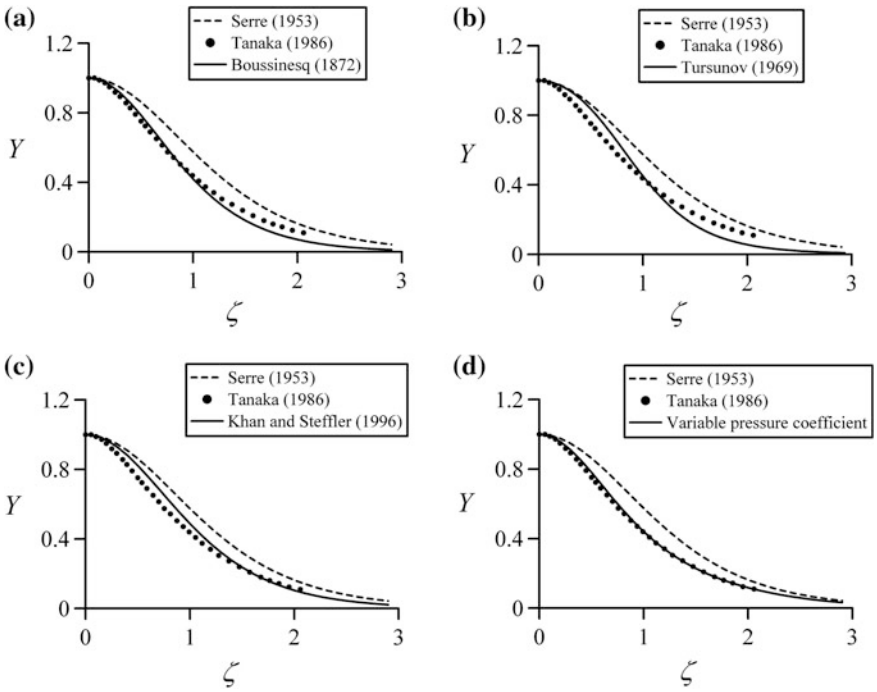

Fig. 3.86 Comparison of solitary wave theories with solitary wave solution of the Serre (1953) equations and the Tanaka (1986) exact 2D numerical profile, for $\mathsf{F}_p^2 = 1.65$ **a** Boussinesq theory (1872), **b** Tursunov (1969) theory, **c** Khan and Steffler (1996a) Boussinesq-type theory, **d** variable pressure coefficient depth-averaged computation

surface and the free surface inclination, in terms of a small parameter depending on F_p. His formula for h/h_o is

$$\frac{h}{h_o} = 1 + \frac{\mathsf{F}_p^2}{2}\left\{1 - \exp\left[-\left(4\ln \mathsf{F}_p\right)\mathrm{sech}^2\xi\left(1 + \frac{3}{2}\ln \mathsf{F}_p\left[3\mathrm{sech}^2\xi - 2\right]\right)\right]\right\}, \tag{3.678}$$

where

$$\xi = \frac{x}{h_o}\left(\frac{3}{2}\ln \mathsf{F}_p\right)^{1/2}. \tag{3.679}$$

The computed wave profile using Eq. (3.678) is plotted in Fig. 3.86b, showing a slight improvement over the Serre (1953) profile. However, Eq. (3.677) is better than Eq. (3.678). The reasons are unclear, given that for small F_p, Eq. (3.678) reduces exactly to Eq. (3.677). Equation (3.675) for $m = 4$, that is, the Boussinesq-type model by Khan and Steffler (1996a) based on a linear non-hydrostatic pressure distribution, is plotted in Fig. 3.86c, showing improvement over the Serre profile based on $m = 3$. Thus, the selection of the pressure coefficient is significant to improve the wave profile prediction. Using a value $m = 6$, the wave profile in the vicinity of the wave crest was accurately predicted, whereas a lower value $m = 4$ produced a good prediction of the descending wave branch. Thus, to investigate the impact of the pressure distribution coefficient, the smooth interpolation function

$$m = 2\left[\mathsf{F}_p^2 + \exp\left[\left(1 - \mathsf{F}_p^2\right)\chi^2\right]\right], \tag{3.680}$$

was used in Eq. (3.675), with the results plotted in Fig. 3.86d. Note that the agreement with the Tanaka (1986) profile is generally good, showing, in turn, that the pressure coefficient m is important not only for the improvement of the frequency dispersion, but also for the nonlinear effects.

3.15.5 *Dam Break Wave*

The computation of dam break flood waves is an important problem in civil and environmental engineering, given the risk associated with this dangerous phenomenon. Dam break waves are usually computed using Saint-Venant's theory (Chaudhry 2008). Despite the non-hydrostatic modeling yields essentially similar arrival times of the flood wave (Mohapatra and Chaudhry 2004), deviations between the Saint-Venant and the Boussinesq modeling approaches are considerable (Kim and Lynett 2011). For example, the water depth at the leading wave of an undular shock front may be significantly larger than the corresponding shock wave

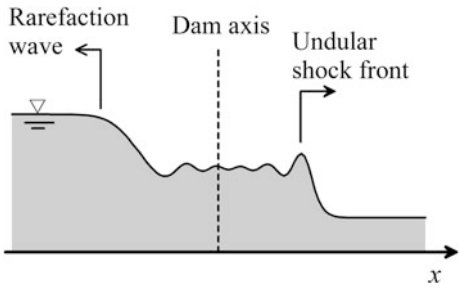

Fig. 3.87 Non-hydrostatic dam break wave including rarefaction wave and undular shock front

height predicted by Saint-Venant's theory, thereby increasing inundation risk. Further, obstacles submerged in the natural watercourse may experience different loads given by the non-hydrostatic flood wave. If the non-hydrostatic effect is weak in a given flow problem, this fact should be automatically detected by the non-hydrostatic computational scheme, rather than by artificially patching hydrostatic and non-hydrostatic solutions (Basco 1983). Therefore, it is preferable to introduce non-hydrostatic modeling effects in the computation of dam break waves (Denlinger and O'Connell 2008, Kim and Lynett 2011). In this section, the mathematical modeling of 1D non-hydrostatic dam break waves is illustrated by using a simple finite-difference scheme.

A non-hydrostatic dam break wave is composed of an undular shock front and a rarefaction wave (Fig. 3.87). Undulations appear between the two wave fronts, originating from non-hydrostatic pressure. Let h_u be the initial flow depth at the dam section, h_d the downstream flow depth, and $r = h_d/h_u$. Free surface undulations of the instantaneous free surface profile were experimentally observed for $r > 0.4$ (Mohapatra and Chaudhry 2004), which are well predicted by Boussinesq-type equations (De Almeida and Franco 1994). For $r < 0.4$, wave breaking occurs and rollers extinguish the non-hydrostatic undulations. These flows are well modeled by the standard Saint-Venant equations (De Almeida and Franco 1994). Below, the standard Serre equations ($m = 3$ and $\alpha^2 = 1$) used in typical civil engineering applications are solved to simulate a non-hydrostatic dam break wave using a finite-difference scheme.

The Serre equations written in conservative form with $\mathbf{U}$ as the vector of unknown variables and $\mathbf{F}$ as the flux vector are given by Eqs. (3.593)–(3.594) (Mohapatra and Chaudhry 2004; Chaudhry 2008)

$$\frac{\partial \mathbf{U}}{\partial t} + \frac{\partial \mathbf{F}}{\partial x} = 0, \quad \mathbf{U} = \begin{pmatrix} h \\ Uh \end{pmatrix}, \quad \mathbf{F} = \begin{pmatrix} Uh \\ g\frac{h^2}{2} + U^2 h + \left(U_x^2 - UU_{xx} - U_{xt}\right)\frac{h^3}{3} \end{pmatrix}. \tag{3.681}$$

Mohapatra and Chaudhry (2004) solved Eqs. (3.681) numerically using the two-four dissipative predictor-corrector finite-difference scheme, to be presented here. It is a scheme fourth-order accurate in space and second-order accurate in time. A scheme of this higher order resolution is necessary to solve unsteady

Boussinesq equations, given that the third-order physical derivatives of the dispersive terms are mathematically similar to the truncation errors of the leading Saint-Venant terms, if these are discretized using second-order accuracy in finite differences. A high-order scheme is needed to avoid that the true physical dispersion added by the Boussinesq terms is swamped by numerically generated frequency dispersion originating from truncation errors (Basco 1983).

The numerical method consists of a predictor step (superscript p) with i as the node index in the x-direction and k referring to the actual time level as

$$\mathbf{U}_i^p = \mathbf{U}_i^k + \frac{1}{6}\frac{\Delta t}{\Delta x}\left(\mathbf{F}_{i+2}^k - 8\mathbf{F}_{i+1}^k + 7\mathbf{F}_i^k\right). \tag{3.682}$$

Here, Δt and Δx are mesh sizes in the t- and x-directions, respectively, and at time level k, the vectors $\mathbf{F}$ and $\mathbf{U}$ are known at each i node. The corrector step (superscript c) is then given by

$$\mathbf{U}_i^c = \mathbf{U}_i^k + \frac{1}{6}\frac{\Delta t}{\Delta x}\left(-\mathbf{F}_{i-2}^p + 8\mathbf{F}_{i-1}^p - 7\mathbf{F}_i^p\right). \tag{3.683}$$

Equations (3.682)–(3.683) are applied by dropping U_{xt} in the M function, approximated by

$$M = g\frac{h^2}{2} + U^2 h + \left(U_x^2 - UU_{xx}\right)\frac{h^3}{3}, \tag{3.684}$$

that is, the computed velocity U at each node i for $k + 1$ lacks from the mixed derivative effect. The spatial derivatives are approximated with a central discretization as

$$U_x = \frac{U_{i+1} - U_{i-1}}{2\Delta x}, \quad U_{xx} = \frac{U_{i+1} - 2U_i + U_{i-1}}{(\Delta x)^2}. \tag{3.685}$$

The vector $\mathbf{U}$ is estimated at time level $k + 1$ for each node i as

$$\tilde{\mathbf{U}}_i = \frac{\mathbf{U}_i^p + \mathbf{U}_i^c}{2}. \tag{3.686}$$

Therefore, this cycle accounts for the convective acceleration effects on the non-hydrostatic dam break wave. However, the local acceleration is important in dam break waves and cannot be dropped in extended non-hydrostatic simulations. The central finite-difference discretization of the mixed derivative

$$U_{xt} = \frac{\tilde{U}_{i+1} - \tilde{U}_{i-1} - U_{i+1}^k + U_{i-1}^k}{2\Delta x \Delta t}, \tag{3.687}$$

is used to recompute velocities at time level $k + 1$ as (Mohapatra and Chaudhry 2004)

$$U_i^{k+1} = \tilde{U}_i - \frac{\Delta t}{\tilde{h}_i}\left(\frac{\partial B}{\partial x}\right)_i, \quad B_i = -\frac{\tilde{h}_i^3}{6\Delta x \Delta t}\left(\tilde{U}_{i+1} - \tilde{U}_{i-1} - U_{i+1}^k + U_{i-1}^k\right). \tag{3.688}$$

The boundary conditions at the 3 first nodes of the mesh are $h_i = h_u$ and $U_i = 0$. At the last 3 downstream nodes, it is $h_i = h_d$ and $U_i = 0$. The initial condition is given by static water depths up- and downstream from the dam axis. The Courant–Friedrichs–Lewy number (CFL) must be less than 2/3 for stability in the two-four dissipative scheme (Chaudhry 2008), and Δt is computed based on

$$\Delta t = \frac{\Delta x}{\max\left[\left|U_i^k\right| + \left(g h_i^k\right)^{1/2}\right]}\mathrm{CFL}. \tag{3.689}$$

At the end of each computational step, the values of h and U are numerically smoothed using artificial viscosity to suppress high-frequency oscillations.

The instantaneous free surface profile for $r = 0.7$ at dimensionless time $t(gh_u)^{0.5}/h_u = 15$ is shown in Fig. 3.88a. The dam axis is located at $x = 0$. In Fig. 3.88, $\Delta x = 0.5h_u$, CFL = 0.5, and a coefficient of artificial viscosity equal to 0.5 were used. The 1D simulation is compared with the 2D free surface profile computed by Mohapatra et al. (1999) solving the full Euler equations. Note that the wave profile is well predicted, including the shock front and the rarefaction wave. An additional simulation for $r = 0.5$ is shown in Fig. 3.88b also for $t(gh_u)^{0.5}/h_u = 15$. The 1D instantaneous flow profile is again compared with the 2D simulation of Mohapatra et al. (1999), resulting in good prediction of the shock front and the rarefaction wave, but the first wave height is slightly underpredicted by the 1D simulation in this case.

A comparison of 1D simulations with experiments (Stansby et al. 1998) at different times for $r = 0.45$ is plotted in Fig. 3.89, using CFL = 0.1, to reduce truncation errors from the time stepping. The computed variables were smoothed using a coefficient of artificial viscosity equal to 0.2. The shock front and rarefaction waves given by the hydrostatic Saint-Venant theory are also plotted for comparative purposes. The rarefaction wave is given by the parabolic free surface profile (Montes 1998)

$$\frac{x}{t} = 2(gh_u)^{1/2} - 3(gh)^{1/2}. \tag{3.690}$$

The mass and momentum conservation equations across the shock front are given by (Liggett 1994; Montes 1998)

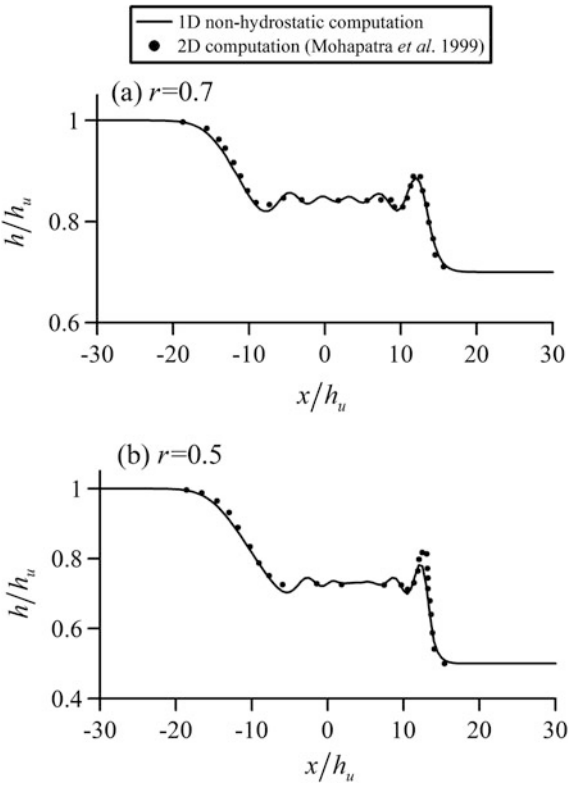

Fig. 3.88 Dam break free surface profile $h/h_u(x/h_u)$ in a horizontal channel for $r = h_d/h_u$ = **a** 0.7, **b** 0.5 (adapted from Castro-Orgaz and Hager 2014a)

$$h_*(c_w - U_*) = h_d c_w, \tag{3.691}$$

$$\frac{h_*^2}{2} + h_* \frac{(c_w - U_*)^2}{g} = \frac{h_d^2}{2} + \frac{h_d c_w^2}{g}. \tag{3.692}$$

Here, c_w is the shock front celerity and subscript * identifies variables at the constant state portion behind the shock front. In Eqs. (3.691) and (3.692), there are three unknowns (h_*, U_*, and c_w). A third equation needed to close the system is given by the conservation of the Riemann invariant along the forward characteristic C^+, applied between the two extreme points of the rarefaction wave as (Liggett 1994; Montes 1998)

$$U_* + 2(gh_*)^{1/2} = 2(gh_u)^{1/2}. \tag{3.693}$$

These three equations are coupled to produce a single equation for the depth h_* as

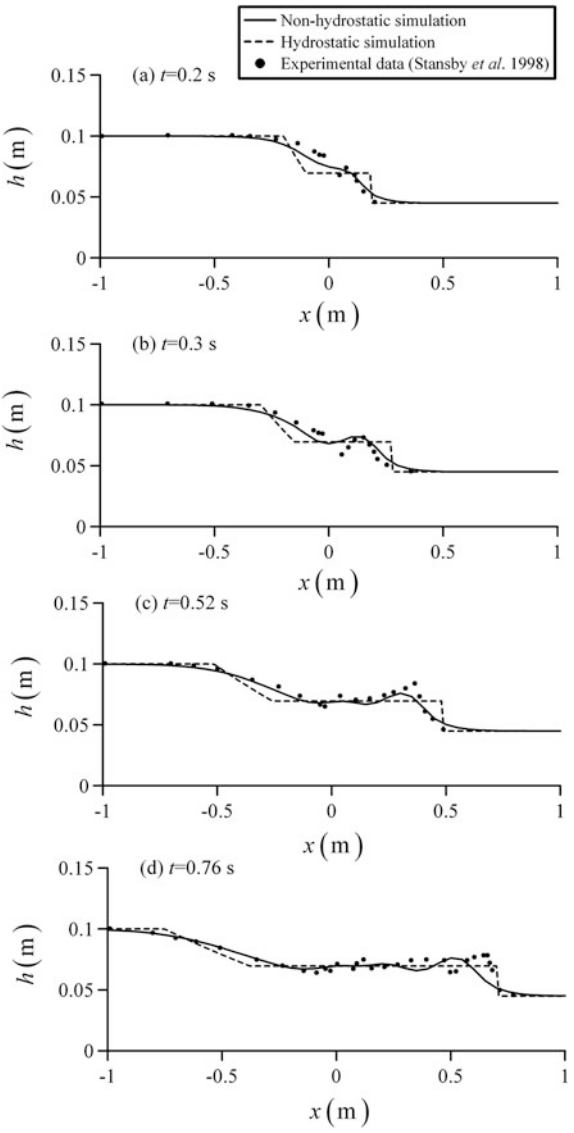

Fig. 3.89 Dam break free surface profile $h(x)$ in a horizontal channel for $r = h_d/h_u = 0.45$ at different times t

$$\left[\frac{g}{2}\frac{h_*}{h_d}(h_* + h_d)\right]^{1/2} = \frac{h_*\left[2(gh_u)^{1/2} - 2(gh_*)^{1/2}\right]}{(h_* - h_d)}. \tag{3.694}$$

Its solution was numerically determined using the Newton–Raphson method. With the value of h_* determined, c_w is computed from the momentum equation as

$$c_w = \left[\frac{g}{2}\frac{h_*}{h_d}(h_* + h_d)\right]^{1/2}, \tag{3.695}$$

and U_* from the Riemann invariant along the C^+ characteristic as

$$U_* = 2(gh_u)^{1/2} - 2(gh_*)^{1/2}. \tag{3.696}$$

The non-hydrostatic computation accurately predicts the rarefaction wave (Figs. 3.89), and a fair agreement also results for the shock front, despite an evident phase lag in Fig. 3.89d. The plot reveals that the non-hydrostatic simulation is a significant physical improvement over the hydrostatic Saint-Venant theory. For more advanced numerical schemes to compute non-hydrostatic dam break waves using the finite-volume method, see Cienfuegos et al. (2006), Kim and Lynett (2011), and Cantero-Chinchilla et al. (2016).

References

Abramowitz, M., & Stegun, I. A. (1972). *Handbook of mathematical functions with formulas, graphs, and mathematical tables* (10th ed.). New York: Wiley.

Ali, K. H. M., & Sykes, A. (1972). Free-vortex theory applied to free overfall. *Journal of the Hydraulics Division ASCE, 98*(HY5), 973–979.

Anh, T., & Hosoda, T. (2007). Depth-averaged model of open-channel flows over an arbitrary 3D surface and its applications to analysis of water surface profile. *Journal of Hydraulic Engineering, 133*(4), 350–360.

Bakhmeteff, B. A. (1932). Discussion of Tests of broad crested weirs. *Transactions of the ASCE, 96*, 423–434.

Barthelemy, E. (2004). Nonlinear shallow water theories for coastal waters. *Surveys In Geophysics, 25*(3), 315–337.

Basco, D. R. (1983). Computation of rapidly varied, unsteady free surface flow. *Water Resources Investigation Report* 83-4284. Reston, VA: US Geological Survey.

Bazin, H. (1888). Expériences nouvelles sur l'écoulement en déversoir (Novel experiments on weir flow). *Annales des Ponts et Chaussées, 58*, 393–488 (in French).

Benjamin, T. B. (1956). On the flow in channels when rigid obstacles are placed in the stream. *Journal of Fluid Mechanics, 1*, 227–248.

Benjamin, T. B., & Lighthill, M. J. (1954). On cnoidal waves and bores. *Proceedings of the Royal Society of London, 224*, 448–460.

Biggiero, V. (1964). Vene libere allo sbocco di canale (Free surfaces at channel brink). *Fondazione Politecnica per il Mezzogiorno d'Italia* 3, 63p (in Italian).

Blau, E. (1963). Der Abfluss und die hydraulische Energieverteilung über einer parabelförmigem Wehrschwelle (Flow and the hydraulic energy distribution over a parabolic weir). *Mitteilung, 7*, 5–72. Forschungsanstalt für Schiffahrt, Wasser und Grundbau, Berlin (in German).

Boadway, J. D. (1976). Transformation of elliptic partial differential equations for solving two dimensional boundary value problems in fluid flow. *International Journal for Numerical Methods in Engineering, 10*(3), 527–533.

Bonneton, P., Barthelemy, E., Chazel, F., Cienfuegos, R., Lannes, D., Marche, F., et al. (2011). Recent advances in Serre-Green-Naghdi modelling for wave transformation, breaking and runup processes. *European Journal of Mechanics B/Fluids, 30*(6), 589–597.

Bos, M. G. (1976). Discharge measurement structures. *Publication*, 20. Wageningen, NL: Intl. Inst. for Land Reclamation (ILRI).

Bose, S. K., & Dey, S. (2007). Curvilinear flow profiles based on Reynolds averaging. *Journal of Hydraulic Engineering, 133*(9), 1074–1079.

Bose, S. K., & Dey, S. (2009). Reynolds averaged theory of turbulent shear flows over undulating beds and formation of sand waves. *Physical Review E*, *80*(3), 036304-1/036304-9.

Boussinesq, J. (1872). Théorie des ondes et des remous qui se propagent le long d'un canal rectangulaire horizontal, en communiquant au liquide contenu dans ce canal des vitesses sensiblement pareilles de la surface au fond (Theory of waves and disturbances propagating along a rectangular horizontal channel, generating nearly uniform velocities from the surface to the bottom). *J. Mathématiques Pures et Appliqués*, Série, *2*(17), 55–108 (in French).

Boussinesq, J. (1877). Essai sur la théorie des eaux courantes (Memoir on the theory of flowing water). *Mémoires* présentés par divers savants à l'Académie des Sciences, Paris, *23*(1), 1–660; *24*(2), 1-60 (in French).

Cantero-Chinchilla, F. N., Castro-Orgaz, O., Dey, S., & Ayuso, J. L. (2016). Nonhydrostatic dam break flows I: Physical equations and numerical schemes. *Journal of Hydraulic Engineering, 142*(12), 04016068.

Carter, J. D., & Cienfuegos, R. (2011). The kinematics and stability of solitary and cnoidal wave solutions of the Serre equations. *European Journal of Mechanics B/Fluids, 30*(3), 259–268.

Cassidy, J. J. (1965). Irrotational flow over spillways of finite height. *Journal of the Engineering Mechanics Division ASCE, 91*(EM6), 155–173.

Cassidy, J. J. (1970). Designing spillway crests for high head operation. *Journal of the Engineering Mechanics Division ASCE, 96*(3), 745–753.

Castro-Orgaz, O. (2008). Curvilinear flow over round-crested weirs. *Journal of Hydraulic Research, 46*(4), 543–547.

Castro-Orgaz, O. (2009). Hydraulics of developing chute flow. *Journal of Hydraulic Research, 47* (2), 185–194.

Castro-Orgaz, O. (2010a). Approximate modeling of 2D curvilinear open channel flows. *Journal of Hydraulic Research, 48*(2), 213–224.

Castro-Orgaz, O. (2010b). Equations for plane, highly-curved open channels flows. *Journal of Hydraulic Research, 48*(3), 405–408.

Castro-Orgaz, O. (2010c). Steady open channel flows with curved streamlines: The Fawer approach revised. *Environmental Fluid Mechanics, 10*(3), 297–310.

Castro-Orgaz, O. (2013a). Potential flow solution for open channel flows and weir-crest overflow. *Journal of Irrigation and Drainage Engineering, 139*(7), 551–559.

Castro-Orgaz, O. (2013b). Iterative solution for ideal fluid jets. *Journal of Hydraulic Engineering, 139*(8), 905–910.

Castro-Orgaz, O., & Chanson, H. (2009). Bernoulli theorem, minimum specific energy and water wave celerity in open channel flow. *Journal of Irrigation and Drainage Engineering, 135*(6), 773–778.

Castro-Orgaz, O., & Chanson, H. (2014). Depth-averaged specific energy in open channel flow and analytical solution for critical irrotational flow over weirs. *Journal of Irrigation and Drainage Engineering, 140*(1), 04013006.

Castro-Orgaz, O., Giraldez, J. V., & Ayuso, J. L. (2008a). Critical flow over spillway profiles. *Journal of Water Management ICE, 161*(2), 89–95.

Castro-Orgaz, O., Giraldez, J. V., & Ayuso, J. L. (2008b). Critical flow over circular crested weirs. *Journal of Hydraulic Engineering, 134*(11), 1661–1664.

Castro-Orgaz, O., Giraldez, J. V., & Ayuso, J. L. (2008c). Higher order critical flow condition in curved streamline flow. *Journal of Hydraulic Research, 46*(6), 849–853.

Castro-Orgaz, O., & Hager, W. H. (2009). Curved streamline transitional flow from mild to steep slopes. *Journal of Hydraulic Research, 47*(5), 574–584.

Castro-Orgaz, O., & Hager, W. H. (2010). Moment of momentum equation for curvilinear free-surface flow. *Journal of Hydraulic Research, 48*(5), 620–631.

Castro-Orgaz, O., & Hager, W. H. (2011). Vorticity equation for the streamline and the velocity profile. *Journal of Hydraulic Research, 49*(6), 775–783.

Castro-Orgaz, O., & Hager, W. H. (2013). Velocity profile approximations for two-dimensional potential channel flow. *Journal of Hydraulic Research, 51*(6), 645–655.

Castro-Orgaz, O., & Hager, W. H. (2014a). 1D modelling of curvilinear free surface flow: Generalized Matthew theory. *Journal of Hydraulic Research, 52*(1), 14–23.

Castro-Orgaz, O., & Hager, W. H. (2014b). Scale effects of round-crested weir flow. *Journal of Hydraulic Research, 52*(5), 653–665.

Castro-Orgaz, O., & Hager, W. H. (2014c). Transitional flow at standard sluice gate. *Journal of Hydraulic Research, 52*(2), 264–273.

Castro-Orgaz, O., & Hager, W. H. (2016). Dressler's theory for curved topography flows: Iterative derivation, transcritical flow solutions and higher-order wave-type equations. *Environmental Fluid Mechanics, 16*(2), 289–311.

Chanson, H. (2006). Minimum specific energy and critical flow conditions in open channels. *Journal of Irrigation and Drainage Engineering, 132*(5), 498–502.

Chanson, H., & Montes, J. S. (1998). Overflow characteristics of circular weirs: Effects of inflow conditions. *Journal of Irrigation and Drainage Engineering, 124*(3), 152–162.

Chaudhry, M. H. (2008). *Open-channel flow* (2nd ed.). Berlin: Springer.

Chen, J., & Dracos, T. (1996). Water surface slope at critical controls in open channel flow. *Journal of Hydraulic Research, 34*(4), 517–536.

Cheng, A. H.-D., Liggett, J. A., & Liu, P. L.-F. (1981). Boundary calculations of sluice and spillway flows. *Journal of the Hydraulics Division ASCE, 107*(HY10), 1163–1178.

Chow, V. T. (1959). *Open channel hydraulics*. New York: McGraw-Hill.

Cienfuegos, R., Barthélemy, E., & Bonneton, P. (2006). A fourth-order compact finite volume scheme for fully nonlinear and weakly dispersive Boussinesq-type equations. Part I: Model development and analysis. *International Journal for Numerical Methods in Fluids, 51*(11), 1217–1253.

Creager, W. P. (1917). *Engineering for masonry dams*. New York: Wiley.

D'Alpaos, L. (1986). Effetti scala nei moti di efflusso fortemente accelerate (Scale effects in highly-accelerated outflows) (pp. 15–23). In *20th Italian Congress of Hydraulics and Hydraulic Structures* Padova (in Italian).

Da Vinci, L. (1828). *Del moto e misura dell' acqua* (On water flow and discharge measurement). Bologna, Italy (in Italian).

Dao-Yang, D., & Man-Ling, L. (1979). Mathematical model of flow over a spillway dam. In *Proceedings of 13th International Congress of Large Dams* New Delhi Q50(R55) (pp. 959–976).

De Almeida, A. B., & Franco, A. B. (1994). Modeling of dam-break flow. In *Computer modeling of free-surface and pressurized flows* (pp. 343–373). Berlin: Springer.

de Saint-Venant, A. B. (1871). Théorie du mouvement non permanent des eaux, avec application aux crues des rivières et à l'introduction des marrées dans leur lit (Theory of unsteady water movement, applied to floods in rivers and the effect of tidal flows). *Comptes Rendus de l'Académie des Sciences*, *73*, 147–154; *73*, 237–240 (in French).

Denlinger, R. P., & O'Connell, D. R. H. (2008). Computing nonhydrostatic shallow-water flow over steep terrain. *Journal of Hydraulic Engineering, 134*(11), 1590–1602.

Dey, S. (2002). Free overfall in open channels: State-of-the-art review. *Flow Measurement and Instrumentation, 13*(5–6), 247–264.

Dias, F., & Milewski, P. (2010). On the fully non-linear shallow-water generalized Serre equations. *Physics Letters A, 374*(8), 1049–1053.

Dingemans, M. W. (1994). Water wave propagation over uneven bottoms. *PhD Dissertation*, Technical University of Delft, Delft, the Netherlands.

Dressler, R. F. (1978). New nonlinear shallow flow equations with curvature. *Journal of Hydraulic Research, 16*(3), 205–222.

Dressler, R. F., & Yevjevich, V. (1984). Hydraulic-resistance terms modified for the Dressler curved-flow equations. *Journal of Hydraulic Research, 22*(3), 145–156.

Escande, L. (1933). Détermination pratique du profile optimum d'un barrage déversoir: Tracé des piles par les méthodes aérodynamiques. Application à un ouvrage déterminé (Practical determination of the optimum weir profile: Pier shape using aerodynamic methods, application to prototype structure). *Science et Industrie*, *17*(9), 467–474 (in French).

Fangmeier, D. D., & Strelkoff, T. S. (1968). Solution for gravity flow under a sluice gate. *Journal of the Engineering Mechanics Division ASCE, 94*(EM1), 153–176.

Favre, H. (1935). *Étude théorique et expérimentale des ondes de translation dans les canaux découverts* (Theoretical and experimental study of translation waves in open channels). Dunod, Paris (in French).

Fawer, C. (1937). Etude de quelques écoulements permanents à filets courbes (Study of some steady flows with curved streamlines). *Thesis*. Université de Lausanne. La Concorde, Lausanne, Switzerland (in French).

Fenton, J. D. (1996). Channel flow over curved boundaries and a new hydraulic theory. In *Proceedings 10th IAHR APD Congress Langkawi, Malaysia* (pp. 266–273).

Friedrichs, K. O. (1948). On the derivation of the shallow water theory. *Communications on Pure and Applied Mathematics, 1*(1), 81–87.

Ganguli, M. K., & Roy, S. K. (1952). On the standardisation of the relaxation treatment of systematic pressure computations for overflow spillway discharge. *Irrigation and Power, 9*(2), 187–204.

Green, A. E., & Naghdi, P. M. (1976a). Directed fluid sheets. *Proceedings of the Royal Society of London A, 347*, 447–473.

Green, A. E., & Naghdi, P. M. (1976b). A derivation of equations for wave propagation in water of variable depth. *Journal of Fluid Mechanics, 78*, 237–246.

Guo, Y., Wen, X., Wu, C., & Fang, D. (1998). Numerical modelling of spillway flow with free drop and initially unknown discharge. *Journal of Hydraulic Research, 36*(5), 785–801.

Hager, W. H. (1983). Hydraulics of the plane free overfall. *Journal of Hydraulic Engineering, 109* (12), 1683–1697.

Hager, W. H. (1985a). Equations for plane, moderately curved open channel flows. *Journal of Hydraulic Engineering, 111*(3), 541–546.

Hager, W. H. (1985b). Critical flow condition in open channel hydraulics. *Acta Mechanica, 54*(3–4), 157–179.

Hager, W. H. (1987). Continuous crest profile for standard spillway. *Journal of Hydraulic Engineering, 113*(11), 1453–1457.

Hager, W. H. (1991). Experiments on standard spillway flow. *Proceedings of the ICE, 91*(2), 399–416.

Hager, W. H. (1993). Abfluss über Zylinderwehr (Flow over cylindrical weirs). *Wasser und Boden, 44*(1), 9–14 (in German).

Hager, W. H. (1999a). *Wastewater hydraulics*: *Theory and practice* (2nd ed.). Berlin: Springer.

Hager, W. H. (1999b). Cavity flow from a nearly horizontal pipe. *International Journal of Multiphase Flow, 25*(2), 349–364.

Hager, W. H. (2010). Comment on Steady open channel flow with curved streamlines: The Fawer approach revised. *Environmental Fluid Mechanics, 10*(4), 491–494.

Hager, W. H., & Hutter, K. (1984a). Approximate treatment of plane channel flow. *Acta Mechanica, 51*(3–4), 31–48.

Hager, W. H., & Hutter, K. (1984b). On pseudo-uniform flow in open channel hydraulics. *Acta Mechanica, 53*(3–4), 183–200.

Hager, W. H., & Schleiss, A. (2009). *Constructions hydrauliques: Ecoulements stationnaires* (Hydraulic structures: Steady flows). *Traité de Génie Civil* 15. Presses Polytechniques Universitaires Romandes, Lausanne (in French).

Hasumi, M. (1931). Untersuchungen über die Verteilung der hydrostatischen Drücke an Wehrkronen und -Rücken von Überfallwehren infolge des abstürzenden Wassers (Studies on the distribution of hydrostatic pressure distributions at overflows due to water flow). *J. Dept. Agriculture*, *3*(4), 1–97 (Kyushu Imperial University) (in German).

Hay, N., & Markland, E. (1958). The determination of the discharge over weirs by the electrolytic tank. *Proceedings of the Institution of Civil Engineers*m, *10*(1), 59–86; *11*(3), 381–382.
Heidarpour, M., & Chamani, M. R. (2006). Velocity distribution over cylindrical weirs. *Journal of Hydraulic Research, 44*(5), 708–711.
Henderson, F. M. (1966). *Open channel flow*. New York: MacMillan.
Hutter, K., & Wang, Y. (2016). *Fluid and thermodynamics* 1: Basic fluid mechanics. Series Advances in Geophysical and Environmental Mechanics and Mathematics. Berlin: Springer.
Ishihara, T., Iwasa, Y., & Ihda, K. (1960). Basic studies on hydraulic performances of overflow spillways and diversion weirs. *Bulletin of the Disaster Prevention Research Institute, 33*, 1–30.
Iwasa, Y. (1955). Undular jump and its limiting conditions for existence. *Proceedings of the Japan National Congress for Applied Mechanics,* II-14, 315–319.
Iwasa, Y. (1956). Analytical considerations on cnoidal and solitary waves. *Memoires Faculty of Engineering, Kyoto University, 17*(4), 264–276.
Iwasa, Y. (1958). Hydraulic significance of transitional behaviours of flows in channel transitions and controls. *Memoires Faculty of Engineering, Kyoto University, 20*(4), 237–276.
Iwasa, Y., & Kennedy, J. F. (1968). Free surface shear flow over a wavy bed. *Journal of the Hydraulics Division ASCE, 94*(2), 431–454.
Jaeger, C. (1939). Remarques sur quelques écoulements le long des lits à pente variant graduellement (Remarks on some flows along bottoms of gradually varied slope). *Schweizerische Bauzeitung, 114*(20), 231–234 (in French).
Jaeger, C. (1948). Hauteur d'eau à l'extrémité d'un long déversoir (Flow depth at the extremity of a long weir). *La Houille Blanche, 3*(6), 518–523 (in French).
Jaeger, C. (1956). *Engineering fluid mechanics*. Edinburgh: Blackie and Son.
Jaeger, C. (1966). Discussion of Calculation of flow at a free overfall by relaxation method. *Proceedings of the ICE, 34*(2), 285–286.
Keulegan, G. H., & Patterson, G. W. (1940). Mathematical theory of irrotational translation waves. *Journal of Research of the National Bureau of Standards, 24*(1), 47–101.
Keutner, C. (1935). Die Strömungsvorgänge an unterströmten Schützentafeln mit scharfen und abgerundeten Unterkanten (The flow features at gates with sharp and rounded crests). *Wasserkraft und Wasserwirtschaft, 30*(2), 16–21 (in German).
Khafagi, A., & Hammad, S. Z. (1954a). Velocity and pressure distributions in curved streamline flow. *Water and Water Engineering, 57*(3), 106–115.
Khafagi, A., & Hammad, S. Z. (1954b). The critical depth, the critical velocity and the Froude number as functions of the non-uniform flow. *Water and Water Engineering, 57*(10), 436–445.
Khafagi, A., & Hammad, S. Z. (1956). The curvilinear flow in open channels. *Bulletin*, *3*, 71–104 (Faculty of Engineering, Cairo University).
Khan, A. A., & Steffler, P. M. (1995). Discussion of Potential flow solution to the 2D transition form mild to steep slope. *Journal of Hydraulic Engineering, 121*(9), 680–681.
Khan, A. A., & Steffler, P. M. (1996a). Vertically averaged and moment equations model for flow over curved beds. *Journal of Hydraulic Engineering, 122*(1), 3–9.
Khan, A. A., & Steffler, P. M. (1996b). Modelling overfalls using vertically averaged and moment equations. *Journal of Hydraulic Engineering, 122*(7), 397–402.
Kim, D.-H., & Lynett, P. J. (2011). Dispersive and nonhydrostatic pressure effects at the front of surge. *Journal of Hydraulic Engineering, 137*(7), 754–765.
Knapp, F. H. (1960). *Ausfluss*, *Überfall und Durchfluss im Wasserbau* (Outflow, overflow and through-flow in hydraulic engineering). Karlsruhe, Braun (in German).
Korteweg, D. J., & de Vries, G. (1895). On the change of form of long waves advancing in a rectangular canal, and on a new type of long stationary waves. *Philosophical Magazine, 39*, 422–443.
Lenau, C. W. (1967). Potential flow over spillways at low heads. *Journal of the Engineering Mechanics Division ASCE, 93*(3), 95–107.
Liggett, J. A. (1993). Critical depth, velocity profile and averaging. *Journal of Irrigation and Drainage Engineering, 119*(2), 416–422.
Liggett, J. A. (1994). *Fluid mechanics*. New York: McGraw-Hill.

Mandrup Andersen, V. (1967). Non-uniform flow in front of a free overfall. *Acta Polytechnica Scandinavica, 42*, 1–24.
Mandrup Andersen, V. (1975). Transition from subcritical to supercritical flow. *Journal of Hydraulic Research, 13*(3), 227–238.
Marchi, E. (1992). The nappe profile of a free overfall. *Rendiconti Lincei Matematica e Applicazioni Serie 9, 3*(2), 131–140.
Marchi, E. (1993). On the free overfall. *Journal of Hydraulic Research*, *31*(6), 777–790; *32*(5), 794–796.
Markland, E. (1965). Calculation of flow at a free overfall by relaxation method. *Proceedings of the ICE*, *31*, Paper 686, 71–78.
Massé, P. (1938). Ressaut et ligne d´eau dans les cours à pente variable (Hydraulic jump and free surface profile in channels of variable bottom slope). *Revue Générale de l'Hydraulique*, *4*(19), 7–11; *4*(20), 61–64 (in French).
Matthew, G. D. (1963). On the influence of curvature, surface tension and viscosity on flow over round-crested weirs. *Proceedings of the ICE*, *25*, 511–524; *28*, 557–569.
Matthew, G. D. (1991). Higher order one-dimensional equations of potential flow in open channels. *Proceedings of the ICE, 91*(3), 187–201.
Matthew, G. D. (1995). Discussion of A potential flow solution for the free overfall. *Proceedings of the ICE, 112*(1), 81–85.
Mei, C. C. (1983). *The applied dynamics of ocean surface waves*. New York: Wiley.
Milne-Thomson, L. M. (1962). *Theoretical hydrodynamics*. London: Macmillan.
Mohapatra, P. K., & Chaudhry, M. H. (2004). Numerical solution of Boussinesq equations to simulate dam-break flows. *Journal of Hydraulic Engineering, 130*(2), 156–159.
Mohapatra, P. K., Eswaran, V., & Murthy Bhallamudi, S. (1999). Two-dimensional analysis of dam-break flow in a vertical plane. *Journal of Hydraulic Engineering, 125*(2), 183–192.
Montes, J. S. (1970). Flow over round crested weirs. *L´Energia Elettrica*, *47*(3), 155–164.
Montes, J.S. (1986). A study of the undular jump profile. In *Proceedings of the 9th Australasian Fluid Mechanics Conference*, *Auckland* (pp. 148–151).
Montes, J. S. (1992a). A potential flow solution for the free overfall. *Proceedings of the ICE*, *96* (6), 259–266; *112*(1), 85–87.
Montes, J. S. (1992b). Potential flow analysis of flow over a curved broad crested weir. In *Proceedings of the 11th Australasian Fluid Mechanics Conference, Auckland* (pp. 1293–1296).
Montes, J. S. (1994a). Potential flow solution to the 2D transition form mild to steep slope. *Journal of Hydraulic Engineering, 120*(5), 601–621.
Montes, J. S. (1994b). Discussion of on the free overfall. *Journal of Hydraulic Research, 32*(5), 792–794.
Montes, J. S. (1995). Closure to Potential flow solution to the 2D transition from mild to steep slope. *Journal of Hydraulic Engineering, 121*(9), 681–682.
Montes, J. S. (1997). Irrotational flow and real fluid effects under planar sluice gates. *Journal of Hydraulic Engineering, 123*(3), 219–232.
Montes, J. S. (1998). *Hydraulics of open channel flow*. Reston, VA: ASCE Press.
Montes, J. S., & Chanson, H. (1998). Characteristics of undular hydraulic jumps: Experiments and analysis. *Journal of Hydraulic Engineering, 124*(2), 192–205.
Naghdi, P. M. (1979). Fluid jets and fluid sheets: A direct formulation. In *Proceedings of the 12th Symposium Naval Hydrodynamics* (pp. 505–515). Washington, D.C.: National Academy of Sciences.
Naghdi, P. M., & Vongsarnpigoon, L. (1986). The downstream flow beyond an obstacle. *Journal of Fluid Mechanics, 162*, 223–236.
Nakagawa, H. (1969). Flow behaviours near the brink of free overfall. *Bulletin of the Disaster Prevention Research Institute, 18*(4), 66–76.
Nwogu, O. (1993). Alternative form of Boussinesq equations for nearshore wave propagation. *Journal of Waterway Port Coastal and Ocean Engineering, 119*(6), 618–638.

Ohtsu, I., & Yasuda, Y. (1994). Characteristics of supercritical flow below sluice gate. *Journal of Hydraulic Engineering, 120*(3), 332–346.
Peregrine, D. H. (1966). Calculations of the development of an undular bore. *Journal of Fluid Mechanics, 25*(2), 321–330.
Peregrine, D. H. (1967). Long waves on a beach. *Journal of Fluid Mechanics, 27*(5), 815–827.
Peregrine, D. H. (1972). Equations for water waves and the approximations behind them. In R. E. Meyer (Ed.), *Waves on beaches and resulting sediment transport* (pp. 95–122). San Diego, CA: Academic Press.
Press, W. H., Teukolsky, S. A., Vetterling, W. T., & Flannery, B. P. (2007). *Numerical recipes: The art of scientific computing* (3rd ed.). Cambridge: Cambridge University Press.
Rajaratnam, N., & Humphries, J. A. (1982). Free flow upstream of vertical sluice gates. *Journal of Hydraulic Research, 20*(5), 427–436.
Ramamurthy, A. S., & Vo, N. D. (1993a). Application of Dressler theory to weir flow. *Journal of Applied Mechanics, 60*(1), 163–166.
Ramamurthy, A. S., & Vo, N. D. (1993b). Characteristics of circular-crested weirs. *Journal of Hydraulic Engineering, 119*(9), 1055–1062.
Ramamurthy, A. S., Vo, N. D., & Balachandar, R. (1994). A note on irrotational curvilinear flow past a weir. *Journal of Fluids Engineering, 116*(2), 378–381.
Ramamurthy, A. S., Vo, N. D., & Vera, G. (1992). Momentum model of flow past a weir. *Journal of Irrigation and Drainage Engineering, 118*(6), 988–994.
Rayleigh, L. (1876). On waves. *Philosophical Magazine and Journal of Science Series 5*, *1*, 257–279.
Replogle, J. A. (1962). Discussion of End depth at drop in trapezoidal channel. *Journal of the Hydraulics Division ASCE, 88*(2), 161–165.
Roth, A., & Hager, W. H. (1999). Underflow of standard sluice gate. *Experiments in Fluids, 27*(4), 339–350.
Rouse, H. (1932). The distribution of hydraulic energy in weir flow in relation to spillway design. *MS Thesis*. MIT, Boston, MA.
Rouse, H. (1933). Verteilung der hydraulischen Energie bei einem lotrechten Absturz (Distribution of hydraulic energy at a vertical drop). *PhD Dissertation*. TU Karlsruhe, Karlsruhe (in German).
Rouse, H. (1938). *Fluid mechanics for hydraulic engineers*. New York: McGraw-Hill.
Rouse, H. (1950). *Engineering hydraulics*. New York: Wiley.
Rouse, H. (1959). *Advanced mechanics of fluids*. New York: Wiley.
Rouse, H. (1970). Work-energy equation for the streamline. *Journal of the Hydraulics Division ASCE, 96*(HY5), 1179–1190.
Rouse, H., & Ince, S. (1957). *History of hydraulics*. New York: Dover Publications.
Russell, J. S. (1837). *Report of the Committee on Waves*. British reports VI, 417–468, plus plates 1–8.
Sander, J., & Hutter, K. (1991). On the development of the theory of the solitary wave: A historical essay. *Acta Mechanica, 86*(1), 111–152.
Schmocker, L., Halldórsdóttir, B., & Hager, W. H. (2011). Effect of weir face angles on circular-crested weir flow. *Journal of Hydraulic Engineering, 137*(6), 637–643.
Scimemi, E. (1930). Sulla forma delle vene tracimanti (On the form of overflow jets). *L'Energia Elettrica, 7*(4), 293–305 (in Italian).
Serre, F. (1953). Contribution à l'étude des écoulements permanents et variables dans les canaux (Contribution to the study of steady and unsteady channel flows). *La Houille Blanche*, *8*(6-7), 374–388; *8*(12), 830–887 (in French).
Sivakumaran, N. S. (1981). Shallow flow over curved beds. *PhD thesis*. Asian Institute of Technology, Bangkok, Thailand.
Sivakumaran, N. S., & Dressler, R. F. (1986). Distribution of resistive body-force in curved free-surface flow. *Mathematical Methods in the Applied Sciences, 8*(4), 492–501.
Sivakumaran, N. S., Hosking, R. J., & Tingsanchali, T. (1981). Steady shallow flow over a spillway. *Journal of Fluid Mechanics, 111*, 411–420.

Sivakumaran, N. S., Tingsanchali, T., & Hosking, R. J. (1983). Steady shallow flow over curved beds. *Journal of Fluid Mechanics, 128*, 469–487.

Sivakumaran, N. S., & Yevjevich, V. (1987). Experimental verification of the Dressler curved-flow equations. *Journal of Hydraulic Research, 25*(3), 373–391.

Soares-Frazão, S., & Guinot, V. (2008). A second-order semi-implicit hybrid scheme for one-dimensional Boussinesq-type waves in rectangular channels. *International Journal for Numerical Methods in Fluids, 58*(3), 237–261.

Soares-Frazão, S., & Zech, Y. (2002). Undular bores and secondary waves: Experiments and hybrid finite-volume modelling. *Journal of Hydraulic Research, 40*(1), 33–43.

Southwell, R. V., & Vaisey, G. (1946). Relaxation methods applied to engineering problems XII: Fluid motions characterized by free streamlines. *Philosophical Transactions of the Royal Society London A, 240*(815), 117–161.

Stansby, P. K., Chegini, A., & Barnes, T. C. D. (1998). The initial stages of dam-break flow. *Journal of Fluid Mechanics, 374*, 407–424.

Steffler, P. M., & Jin, Y. C. (1993). Depth-averaged and moment equations for moderately shallow free surface flow. *Journal of Hydraulic Research, 31*(1), 5–17.

Strelkoff, T. S. (1964). Solution of highly curvilinear gravity flows. *Journal of the Engineering Mechanics Division ASCE*, *90*(EM3), 195–221; *90*(EM5), 467–470; *91*(EM1), 172–178; *92* (EM3), 95–96.

Su, C. H., & Gardner, C. S. (1969). KDV equation and generalizations. Part III. Derivation of Korteweg-de Vries equation and Burgers equation. *Journal of Mathematical Physics, 10*(3), 536–539.

Tadayon, R., & Ramamurthy, A. S. (2009). Turbulence modeling of flows over circular spillways. *Journal of Irrigation and Drainage Engineering, 135*(4), 493–498.

Tanaka, M. (1986). The stability of solitary waves. *Physics of Fluids, 29*, 650–655.

Thom, A., & Apelt, C. (1961). *Field computations in engineering and physics*. London: Van Nostrand.

Tursunov, A. A. (1969). Near-critical state of free surface flows. *Izvestiya Vsesoyuznogo Naucho-Issledovatel'skogo Instituta Gidrotekhniki, 90*, 201–224. (translated from Russian).

Valiani, A. (1997). Linear and angular momentum conservation in hydraulic jump. *Journal of Hydraulic Research, 35*(3), 323–354.

Vallentine, H. R. (1969). *Applied hydrodynamics*. London: Butterworths.

Van Dyke, M. (1975). *Perturbation methods in fluid mechanics*. Stanford, CA: The Parabolic Press.

Wei, G., Kirby, J. T., Grilli, S. T., & Subramanya, R. (1995). A fully nonlinear Boussinesq model for surface waves 1: Highly nonlinear unsteady waves. *Journal of Fluid Mechanics, 294*, 71–92.

Westernacher, A. (1965). Abflussbestimmung an ausgerundeten Abstürzen mit Fliesswechsel (Discharge determination at rounded drops at transitional flow). *Dissertation*, TU Karlsruhe, Karlsruhe, Germany (in German).

Weyermuller, R. G., & Mostafa, M. G. (1976). Flow at grade-break from mild to steep slope flow. *Journal of the Hydraulics Division ASCE, 102*(HY10), 1439–1448.

White, F. M. (1991). *Viscous fluid flow*. New York: McGraw-Hill.

White, F. M. (2003). *Fluid mechanics*. New York: McGraw-Hill.

Zhu, D. Z., & Lawrence, G. A. (1998). Non-hydrostatic effects in layered shallow water flows. *Journal of Fluid Mechanics, 355*, 1–16.

Chapter 4
Seepage Flows

Roman Symbols

A	Coefficient (−)
c, c_1, c_2	Constants
D	Aquifer static saturated thickness (m)
E	Function (m/s)
f	Integration function (m^2/s)
h	Flow depth measured vertically (m)
h_b	Saturated thickness at control point of DODE (m)
h_e	Water depth at upstream section of rectangular dam (m)
h_o	Maximum saturated thickness in drainage of recharge problem (m)
h_s	Seepage face height (m)
h_w	Water depth at tailwater section of rectangular dam (m)
h_D	Water depth at tailwater section in drainage of recharge problem (m)
h_N	Uniform flow saturated thickness on sloping aquifer (m)
i	Node index in x-direction (–)
k	Node index in time integration (–)
K	Hydraulic conductivity (m/s)
K_h	Horizontal hydraulic conductivity (m/s)
K_v	Vertical hydraulic conductivity (m/s)
L	Length of aquifer (m); also length of dam (m)
m	Curvature distribution parameter in Fawer's theory (–)
m_M	Maximum value of m (–)
n	Curvilinear coordinate along equipotential (m); also specific yield (–); also series index (–); also coordinate normal to closed curve (m)
N	Recharge rate (m/s); also number of nodes in x-direction (–)
N_o	Length of equipotential curve (m)
p	Pressure (N/m^2)
p_b	Bottom pressure (N/m^2)
q	Unit discharge (m^2/s)
r	Relative curvature (–); also anisotropy ratio (–)
R	Radius of streamline curvature (m)

© Springer International Publishing AG 2017

O. Castro-Orgaz and W.H. Hager, *Non-Hydrostatic Free Surface Flows*,
Advances in Geophysical and Environmental Mechanics and Mathematics
DOI 10.1007/978-3-319-47971-2_4

R_b Radius of aquifer bed (m)
R_s Radius of free surface (m)
s Curvilinear coordinate along streamline (m); also curvilinear coordinate along closed curve (m)
S Specific yield (–)
t Flow depth defined as vertical projection of equipotential line (m); also time (s)
u Velocity in x-direction (m/s)
U Mean flow velocity = q/h (m/s)
V Local velocity (m/s)
w Velocity in z-direction (m/s)
x Horizontal coordinate (m)
x_b X-coordinate at control point of DODE (m)
X Dimensionless x-coordinate (m)
Y Dimensionless z-coordinate (m); also hh_x/x (–)
z Vertical elevation (m)
z_b Elevation of bed (m)
z_s Elevation of phreatic surface (m)
Z hh_x (m)

Greek Symbols

α Angle (rad)
α_n Series variable (–)
β Angle (rad); also coefficient (–)
γ Coefficient (–); also specific weight of water (N/m^3)
δ Anisotropy and shallowness coefficient (–)
ε Parameter (–)
η Vertical coordinate above bed (m); also flow depth above static level D (m)
θ Angle of streamline inclination with horizontal (rad)
κ_s Curvature of phreatic surface (m^{-1})
λ Parameter (m^2)
μ Dimensionless vertical coordinate (–)
ν Dimensionless curvilinear coordinate along equipotential line (–)
ρ Density of water (kg/m^3)
ϕ Potential function or piezometric head (m)
$\overline{\phi}$ Depth-averaged piezometric head (m)
$\tilde{\phi}$ Dimensionless potential function (–)
Φ Discharge potential (m^3/s)
ψ Stream function (m^2/s)
$\tilde{\psi}$ Dimensionless potential function (–)
ω Auxiliary variable (m)
Ω Error function (–)

Subscripts

b Bed
d Downstream
o Origin
s Free surface
u Upstream
\+ Dimensionless

Acronyms

DF Dupuit–Forchheimer
DODE Dupuit Ordinary Differential Equation

4.1 Introduction

This chapter considers saturated flow in a homogeneous aquifer with a phreatic surface at atmospheric pressure in the vertical plane (x, z), bounded by an impermeable bed rock. Hydraulic models for phreatic aquifers, in which the water table position is a priori unknown, are difficult to solve analytically by complex variables, or numerical methods (Bear 1972). It is therefore not surprising that the Dupuit approximation is still widely used for free surface groundwater flows. Jules Dupuit (1804–1866) was the first to propose an analytical model for groundwater hydraulics, leading to a simplified one-dimensional (1D) approach (Dupuit 1863). Under isotropic, homogeneous conditions, he eliminated the dependence of the groundwater flow equations upon the vertical coordinate by assuming a uniform profile of horizontal velocity with depth, and a near-horizontal water table (Bear 1972; Hager 2004). From this simplification stems Dupuit's parabola for the dam seepage problem, or the widely used Boussinesq equation for transient flow in phreatic aquifers (Bear 1972). The validity of Dupuit's theory is limited to an aquifer with a horizontal length L much larger than its thickness D, say $D/L < 0.1$ (Bear 1972; Serrano 1995; Liu and Wen 1997; Knight 2005; Hunt 2005). Steady-state models proposed by Jaeger (1956), Knight (2005), Castro-Orgaz (2011a, b), or Castro-Orgaz and Giraldez (2012) were applied to the dam seepage problem, indicating an improved accuracy over Dupuit's approach, given the inclusion of curvilinear flow in the governing equations.

The 2D water movement in a saturated porous matrix is a real fluid flow. Under conditions of laminar fluid flow through isotropic and homogeneous porous media, Darcy's empirical law takes the form (e.g., Jaeger 1956; Bear 1972; Raudkivi and Callander 1976) (Fig. 4.1)

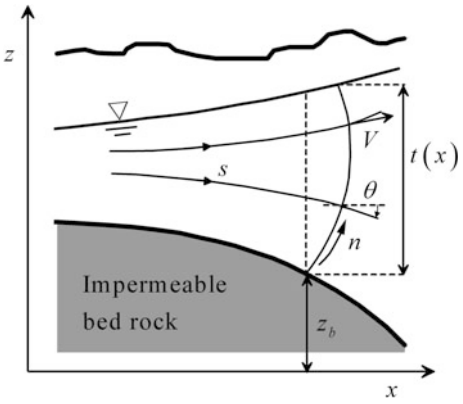

Fig. 4.1 Definition sketch of 2D free surface flow in porous media

$$V = -K\frac{\partial}{\partial s}\left[\frac{p}{\gamma} + z\right] = -K\frac{\partial \phi}{\partial s}. \tag{4.1}$$

Here, V is the groundwater velocity in the streamline direction s, K the hydraulic conductivity, p/γ the pressure head, z the elevation, and $\phi = (p/\gamma + z)$ the potential function. Note that Eq. (4.1) is a head-loss relation, where K is closely related to the friction factor (Raudkivi and Callander 1976). In Cartesian coordinates, Darcy's law reads with u and w as the velocity components in the x- and z-directions, respectively,

$$u = -K\frac{\partial \phi}{\partial x}, \quad w = -K\frac{\partial \phi}{\partial z}. \tag{4.2}$$

A velocity field that obeys Darcy's law is irrotational (Bear 1972). By resort to Darcy's law, the momentum equations in the x- and z-directions are no longer needed for this flow type. Therefore, only 2D Darcy flows in a vertical plane are considered in this chapter.

The continuity equation in the Cartesian x- and z-coordinates is [see Eq. (3.1)]

$$\frac{\partial u}{\partial x} + \frac{\partial w}{\partial z} = 0. \tag{4.3}$$

Inserting Eqs. (4.2) into Eq. (4.3) results in Laplace's equation in terms of ϕ as (Bear 1972; Raudkivi and Callander 1976)

$$\nabla^2 \phi = \frac{\partial^2 \phi}{\partial x^2} + \frac{\partial^2 \phi}{\partial z^2} = 0. \tag{4.4}$$

Further, the Cauchy–Riemann equations expressed in Cartesian coordinates (x, z) are

$$\frac{\partial \psi}{\partial z} = K \frac{\partial \phi}{\partial x}, \quad \frac{\partial \psi}{\partial x} = -K \frac{\partial \phi}{\partial z}. \tag{4.5}$$

Here, ψ is the stream function, also satisfying Laplace's equation, originating from the irrotational flow condition [see Eq. (3.4)] (Thom and Apelt 1961; Vallentine 1969)

$$\nabla^2 \psi = \frac{\partial^2 \psi}{\partial x^2} + \frac{\partial^2 \psi}{\partial z^2} = 0 \tag{4.6}$$

The fact that Eq. (4.4) is satisfied in seepage flows is important, because it enables real flows in a porous medium to be treated as a potential flow. The flow in the porous matrix is composed of a net of streamlines and equipotential lines, as for irrotational flow along channel transitions (see Chap. 3). Methods of potential flow computations were extensively applied to groundwater flows (e.g., Muskat 1942; Polubarinova-Kochina 1962; Bear 1972; Raudkivi and Callander 1976). Among these are analytical methods based on the complex potential theory and numerical solutions of Eq. (4.4), by using finite difference or finite element methods. However, these approaches, although rigorous, are either complicated from the analytical point of view (Polubarinova-Kochina 1962) or computationally involved.

2D flow computations are avoided if streamlines are nearly parallel, for which a hydraulic approach is adequate, similar to the classical gradually varied flow theory in open channels (Montes 1998). With z_s as the phreatic surface elevation, Dupuit proposed (Jaeger 1956; Bear 1972)

$$u = -K \frac{\mathrm{d}z_s}{\mathrm{d}x}. \tag{4.7}$$

The approach implicit in Eq. (4.7) assumes constant u velocity with depth and zero vertical velocity, e.g., as for gradually varied flows (Montes 1998). Equation (4.7) also follows from Eq. (4.1) with $\phi = z_s$ at the free surface and streamlines parallel to x ($s \rightarrow x$). Limitations in terms of small streamline curvature and slope are essentially those of the gradually varied flow theory. Thus, Eq. (4.7) is not accurate if the curvature of the seepage flow is large; of necessity then, the full 2D potential flow approach is required (Muskat 1942; Polubarinova-Kochina 1962; Raudkivi and Callander 1976). The characterization of the flow net requires integration of either Eq. (4.4) or Eq. (4.6) with the corresponding boundary conditions associated with the physical problem (Knight 2005; Rushton and Youngs 2010). These require, therefore, a left and right boundary condition, a seepage condition, and a nonlinear free surface condition. Its integration yields a full 2D numerical solution approximating the exact nonlinear problem, but demands numerical methods, which in many cases are challenging. An alternative to the numerical solution of the

Laplace equation is the adoption of the complex potential theory. Polubarinova-Kochina (1962) developed exact analytical solutions for 2D unconfined flows in porous media. However, her equations were complicated and seldom used in practice (Hornung and Krueger 1985), and did not include the rainfall recharge to the aquifer. Most classical formulations do not give room for hydrologic functions as the recharge. However, the treatment of 2D seepage flows should allow for its for use in practice.

Although 2D models are the most powerful tool, their demanding numerical efforts or implied difficulties of the complex analytical solutions triggered consideration of approximate 1D models for unconfined seepage flow. For example, the decomposition and variation-iteration approaches permit simple analytical, higher-dimensional solutions (Serrano 1995, 2003). The Dupuit–Forchheimer (DF) approximation is widely accepted as the simplest approach to overcome the difficulties. In this 1D model, however, only one boundary condition can be imposed, but the computation is straightforward. The DF theory assumes that the horizontal velocity u is uniform in depth [see Eq. (4.7)], so that streamlines are everywhere horizontal and equipotential curves are vertical lines. This fact, therefore, reduces the validity of the approach to regions of the water table where both the free surface slope and curvature are small. Youngs (1966) indicated that the DF theory is exact for the discharge in the rectangular dam seepage problem, but it ignores the existence of seepage surfaces where the water exits from the soil (Youngs 1990). Youngs and Rushton (2009) found that the DF theory yields good estimates of steady-state water table heights due to accretion. Rushton and Youngs (2010) analyzed the limitations of the Dupuit–Forchheimer theory in the problem of recharge to symmetrically located downstream boundaries. They found that the inclusion of the seepage surface height as the boundary condition to integrate the differential equation of the DF theory is often accurate enough. This simple approach cannot, however, predict the seepage surface. The reduction of Laplace's equation for 2D seepage flows to an Ordinary Differential Equation (ODE) describing the seepage line was discussed by Fenton (1990). Essentially, his method consists of the depth-integrated mass conservation equation coupled with an expansion of ϕ, similar to that of Dagan (1967). The result is a third-order ODE describing the seepage line. A similar approach was later considered by Nielsen et al. (1997) for unsteady groundwater waves in aquifers. Kashef (1965) and Knight (2005) obtained approximate solutions for seepage problems based on a parabolic assumption for the vertical distribution of ϕ. Castro-Orgaz (2011a, b) followed Knight (2005) by proposing an alternative approach, resulting in good agreement for 2D problems.

Dagan (1967) was the first to derive unsteady groundwater flow equations accounting for the vertical velocity distribution, which is responsible for the existence of a non-hydrostatic pressure head within the saturated aquifer zone. He used the perturbation method, and his development constitutes the current reference for

the second-order shallow-water model of unsteady groundwater flow. Nielsen et al. (1997) and Liu and Wen (1997) obtained also Dagan's second-order equation using alternative approximations. Nielsen et al. (1997) estimated the vertical velocity profile using Dupuit's approach in combination with the 2D continuity equation. Liu and Wen (1997) expanded the piezometric head into a power series of the vertical elevation, a technique widely used to model unsteady water waves. Dagan's second-order theory was applied by Nielsen et al. (1997) and Liu and Wen (1997) to oscillatory flow in coastal aquifers, and the theory was tested in steady state for the dam seepage problem by Castro-Orgaz and Dey (2014).

In this chapter, approximate 1D models retaining 2D features, e.g, the inclination and curvature of the streamlines, are presented using two different techniques: First, the Picard iteration is used (Matthew 1991; Castro-Orgaz et al. 2012; Castro-Orgaz and Hager 2014), and thereafter, an approximate integration of the Laplacian in intrinsic natural coordinates is developed (Castro-Orgaz 2011a, b). The models are applied to illustrative flow cases of seepage flows in rectangular and trapezoidal dams, the drainage of flows with recharge, flows in sloping and curved aquifers, and the bank storage problem. The existence of the seepage surface is investigated, and the limitations of the DF theory are discussed by comparison with the full 2D solution, as well as to other approximate models.

Jules Dupuit was born on May 18, 1804, at Fossano, Italy, and passed away at age 62 on October 05, 1866, in Paris, France. He became *Ingénieur des Ponts et Chaussées* in 1829 and was stationed at Mans, France. After having worked on road design, he returned to Paris in 1839. In 1840, he moved to the Maine-et-Loire Department there being overwhelmed by the spectacular and dangerous floods, motivating him to publish two works on flood flows. In 1850, when back to Paris again, he was promoted to chief engineer and asked to advance its water supply and sewer designs. His 1854 book on water distribution had several reeditions. It contains engravings of the major French fountains, an important issue at the time and a rare source to view the beauties of water flow of the past. Dupuit was promoted to *Inspecteur Général* in 1855.

Dupuit was an excellent practitioner in all civil engineering branches. His contributions to hydraulics are in groundwater and pipe flows, and backwater curves. He applied the Bernoulli equation for the hydraulic jump and thus erroneously overlooked the contributions of both Jean-Baptiste Bélanger (1790–1874) and Charles Bresse (1822–1883). Dupuit also conducted early observations on sediment transport and noted that the transport entrainment depends mainly on the sediment grain size. His successors Médéric Lechalas (1820–1904) and Paul Du Boys (1847–1924) worked on bed-load transport. In turn, Dupuit was the main developer of the hydrostatic or gradually varied flow theory for phreatic flow in aquifers, still widely used today.

4.2 Picard Iteration

4.2.1 Generalized Water Table Equation

The particle kinematics in unconfined seepage flows is assumed to follow Darcy's law in isotropic and homogeneous porous media. Thus, real fluid flows of groundwater can be modeled using the potential flow equations. For the sake of generality, consider unsteady phreatic flows over a curved impermeable bedrock stratum (Fig. 4.2). Thus, Eq. (3.56) is rewritten, with h as the vertical saturated thickness, $U = q/h$ as the depth-averaged velocity, $\eta(x, z) = z - z_b(x)$ as the vertical distance above the bed, and f as an integration function, as

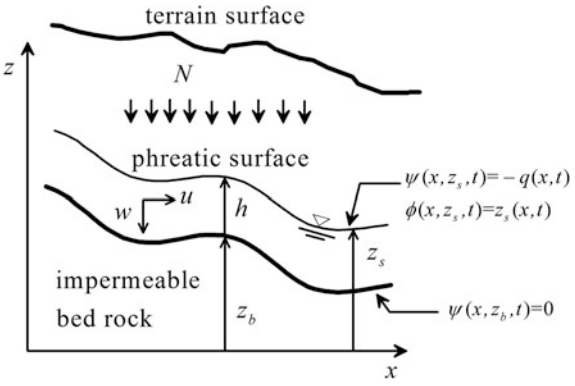

Fig. 4.2 Definition sketch of an unsteady 2D free surface flow in a porous medium over curved bedrock

$$-K\phi = -U_x\frac{\eta^2}{2} - U\eta\eta_x + f(x,t). \tag{4.8}$$

At the phreatic surface, the pressure is atmospheric (Fig. 4.2), so that Eq. (4.8) gives

$$-K(h+z_b) = -U_x\frac{h^2}{2} - Uh\eta_x + f(x,t). \tag{4.9}$$

This equation is solved for f, and then back-substituted into Eq. (4.8), producing

$$-K\phi = \frac{U_x}{2}\left(h^2-\eta^2\right) + U\eta_x(h-\eta) - K(h+z_b). \tag{4.10}$$

Equation (4.10) is differentiated to obtain the horizontal velocity component u as

$$\begin{aligned} u = -K\phi_x = -K(h_x+z_{bx}) + \frac{U_{xx}}{2}\left(h^2-\eta^2\right) + (U\eta_{xx}+U_x\eta_x)(h-\eta) \\ + (h_x-\eta_x)U\eta_x + U_x(hh_x-\eta\eta_x). \end{aligned} \tag{4.11}$$

The boundary condition of the stream function at the phreatic surface is (Fig. 4.2)

$$\psi[\eta = h(x,t)] = -q(x,t), \tag{4.12}$$

from which the velocity profile in the x-direction is obtained as [see Eq. (3.61)]

$$u = U + (2U_x\eta_x + U\eta_{xx})\left(\frac{h}{2}-\eta\right) + U_{xx}\left(\frac{h^2}{6}-\frac{\eta^2}{2}\right). \tag{4.13}$$

Equation (4.13) at the water table ($\eta = h$) yields

$$u_s = U - (2U_x\eta_x + U\eta_{xx})\frac{h}{2} - U_{xx}\frac{h^2}{3}, \tag{4.14}$$

whereas from Eq. (4.11)

$$u_s = -K(h_x+z_{bx}) + (h_x-\eta_x)U\eta_x + U_xh(h_x-\eta_x). \tag{4.15}$$

Equating Eqs. (4.14) and (4.15) yields the general unsteady equation describing the water table, to second-order accuracy, as

$$U - \left[\left(Uh_x\eta_x - U\eta_x^2 + \frac{U\eta_{xx}h}{2}\right) + \left(U_xh_xh + U_{xx}\frac{h^2}{3}\right)\right] + K(h_x+z_{bx}) = 0. \tag{4.16}$$

Expressing U and η as functions of the variables q, h, and z_b produces

$$U_x = \frac{q_x}{h} - \frac{qh_x}{h^2}, \quad U_{xx} = \frac{q_{xx}}{h} - \frac{qh_{xx}}{h^2} + 2\frac{qh_x^2}{h^3} - 2\frac{q_x h_x}{h^2}$$
$$\eta_x = -z_{bx}, \quad \eta_{xx} = -z_{bxx}. \tag{4.17}$$

Inserting Eqs. (4.17) into Eq. (4.16) provides the general water table equation for unsteady groundwater flow to second-order accuracy as (Castro-Orgaz and Hager 2014)

$$\frac{q}{h}\left(1 + h_x z_{bx} + z_{bx}^2 + \frac{hz_{bxx}}{2} + \frac{hh_{xx} + h_x^2}{3} - \frac{q_x h_x h}{3q} - \frac{q_{xx}h^2}{3q}\right) + K(h_x + z_{bx}) = 0. \tag{4.18}$$

Equation (4.18) accounts for streamline curvature effects, so that it is a Boussinesq-type approximation for groundwater hydraulics. At this point, it is pertinent to remark that the Boussinesq approximation in free surface hydraulics relates to the consideration of non-hydrostatic pressure in a depth-averaged model. However, the term "Boussinesq equation" is used in groundwater hydraulics for Dupuit's, linearized, unsteady flow equation in phreatic aquifers (see Sect. 4.8). Note that the quantities q_x and q_{xx} are nonzero for unsteady flows. With $N(x, t)$ as the groundwater accretion rate and S the specific yield, these are related to the water table elevation derivatives by the depth-averaged mass conservation equation as

$$S\frac{\partial h}{\partial t} + \frac{\partial q}{\partial x} = N. \tag{4.19}$$

4.2.2 Particular Cases

For steady flow in a horizontal aquifer ($z_{bx} = z_{bxx} = 0$) with $q_x = N$ from Eq. (4.19), Eq. (4.18) simplifies to

$$\frac{q}{h}\left(1 + \frac{hh_{xx} + h_x^2}{3} - \frac{Nh_x h}{3q} - \frac{N_x h^2}{3q}\right) + Kh_x = 0. \tag{4.20}$$

For spatially uniform recharge $q = Nx$ ($N_x = 0$), Eq. (4.20) reduces to (Castro-Orgaz et al. 2012)

$$\frac{Nx}{h}\left(1 + \frac{hh_{xx} + h_x^2}{3} - \frac{h_x h}{3x}\right) + Kh_x = 0. \tag{4.21}$$

For steady flow over a flat bed without recharge, Eq. (4.20) simplifies to a curvilinear flow equation for flows over earth dams or drainage ditches as (Castro-Orgaz 2011a, b)

$$\frac{q}{h}\left(1+\frac{hh_{xx}+h_x^2}{3}\right)+Kh_x=0. \tag{4.22}$$

Equation (4.18) can be viewed as a non-hydrostatic groundwater flow model reducing to the DF theory, i.e., the theory of gradually varied groundwater flow, if $h_x z_{bx}$, hz_{bxx}, z_{bx}^2, hh_{xx}, h_x^2, $q_x h_x$, and $q_{xx}h^2$ asymptotically tend to zero, resulting in

$$\frac{q}{h}+Kh_x=0. \tag{4.23}$$

The Chapman and Dressler (1984) equations are a curvilinear model of groundwater flows originating from the curvilinear flow model for open-channel flows of Dressler (1978). Matthew (1991) presented a curvilinear model for open channels, expanded by Castro-Orgaz and Hager (2014) to groundwater flows. Comparing the two formulations for groundwater flows in horizontal aquifers, the model of Chapman and Dressler (1984) reduces to the DF model, whereas the more general Matthew model simulates curved flows, as seepage flows across rectangular and trapezoidal dams (Castro-Orgaz and Hager 2014).

4.3 Dupuit–Fawer Equations

4.3.1 Generalized Water Table Equation

Consider the flow net of steady flows in porous media over an arbitrarily curved and sloped impermeable bedrock $z_b = z_b(x)$, with subscript b referring to the bottom boundary surface (Fig. 4.1). In this section, the Dupuit–Fawer equations are developed (Castro-Orgaz 2011a, b), which apply to problems in which the curvature of streamlines is highly nonlinear and the Picard iteration theory only gives accurate solutions using higher-order iteration cycles. The second-order Picard results are related to a linear variation of streamline curvature (Appendix E), an approximation inaccurate in some seepage flow problems involving short horizontal length scales (Castro-Orgaz and Giraldez 2012).

The Euler equations in natural, curvilinear (s, n) (Fig. 4.1) coordinates imply (Eq. 3.48)

$$\frac{\partial V}{\partial n}=\frac{V}{R}. \tag{4.24}$$

Here, R is the radius of streamline curvature and n the distance of a trajectory normal to s. The Cauchy–Riemann equations in these coordinates are

$$V = -\frac{\partial \psi}{\partial n} = -K\frac{\partial \phi}{\partial s}, \quad \frac{\partial \psi}{\partial s} = -K\frac{\partial \phi}{\partial n} = 0. \tag{4.25}$$

The integration of Eq. (4.24) along an equipotential curve yields with V_s as free surface (subscript s) velocity and N_o as length of an equipotential curve, (Eq. 3.81) yields

$$V = V_s \exp\left(-\int_n^{N_o} \frac{\mathrm{d}n'}{R}\right). \tag{4.26}$$

Following Fawer (1937), the radius of curvature and the streamline inclination are related to their corresponding values at the bedrock and free surface as [see Eqs. (3.82) and (3.91)]

$$\frac{1}{R} = \frac{1}{R_b} + \left(\frac{1}{R_s} - \frac{1}{R_b}\right)v^m, \tag{4.27}$$

$$\theta = \theta_b + (\theta_s - \theta_b)v. \tag{4.28}$$

Here, $v = n/N$ is the dimensionless curvilinear coordinate along a normal, m is an exponent, and θ is the streamline inclination. Equations (4.27) and (4.28) are the essential equations for reducing the 2D problem to a 1D problem; i.e., the unknown free surface position is replaced by explicit expressions involving the curvature of the boundary streamlines (Hager and Hutter 1984; Castro-Orgaz 2011a, b). Using Eq. (4.27), Eq. (4.26) is integrated with $r = R_s/R_b$ as the relative curvature to (Eq. 3.83)

$$V = V_s \exp\left[\frac{N_o}{R_s}\left(r(v-1) + (1-r)\frac{(v^{m+1}-1)}{m+1}\right)\right]. \tag{4.29}$$

The discharge q through an equipotential line is then (Eq. 3.85)

$$q = \int_0^{N_o} V\mathrm{d}n \approx N_o V_s\left(1 - \frac{N_o}{R_s}\left(\frac{r}{2} + \frac{1-r}{m+2}\right)\right). \tag{4.30}$$

Here, the velocity distribution given by Eq. (4.29) is approximated by a truncated series expansion of the exponential function to first order. Further, the free surface curvature is

$$\frac{1}{R_s} = [t_{xx} + z_{bxx}]\left[1 + (t_x + z_{bx})^2\right]^{-3/2}, \tag{4.31}$$

in which t is the flow depth defined as the vertical projection of the equipotential length N_o (Fig. 4.1). For the bottom streamline, one obtains

$$\frac{1}{R_b} = z_{bxx}\left[1 + z_{bx}^2\right]^{-3/2}. \tag{4.32}$$

Moreover, N_o and t are related to one another by assuming that the shape of the equipotential line is a circular arc. From a Taylor series expansion for small θ of the function describing the circular arc, one obtains (Eq. 3.94)

$$\frac{t}{N_o} = 1 - \frac{3z_{bx}^2 + 3z_{bx}t_x + t_x^2}{6}. \tag{4.33}$$

From Eq. (4.30), the free surface velocity V_s is approximated as[1]

$$V_s \approx \frac{q}{N_o}\left[1 + \frac{N_o}{R_s}\left(\frac{r}{2} + \frac{1-r}{m+2}\right)\right] = \frac{q}{N_o}\left[1 + N_o\left(\frac{1}{2R_b} + \frac{1}{m+2}\left(\frac{1}{R_s} - \frac{1}{R_b}\right)\right)\right]. \tag{4.34}$$

Inserting Eqs. (4.31) and (4.32) into Eq. (4.34) produces

$$V_s = \frac{q}{N_o}\left[1 + N_o\left(\frac{z_{bxx}}{2}\left[1 + z_{bx}^2\right]^{-3/2} + \frac{\left[t_{xx} + z_{bxx}\right]}{m+2}\left[1 + \left(t_x + z_{bx}\right)^2\right]^{-3/2} - \frac{z_{bxx}}{m+2}\left[1 + z_{bx}^2\right]^{-3/2}\right)\right]. \tag{4.35}$$

Inserting Eq. (4.33) into Eq. (4.35) yields

$$V_s \approx \frac{q}{t}\left[1 + \frac{tz_{bxx}}{2}\left[1 + z_{bx}^2\right]^{-3/2} + \frac{\left[tt_{xx} + tz_{bxx}\right]}{m+2}\left[1 + \left(t_x + z_{bx}\right)^2\right]^{-3/2} - \frac{tz_{bxx}}{m+2}\left[1 + z_{bx}^2\right]^{-3/2} - \frac{t_x^2}{6} - \frac{z_{bx}^2 + z_{bx}t_x}{2}\right]. \tag{4.36}$$

Equation (4.36) is a Boussinesq-type approximation for the velocity at the seepage surface. Boussinesq-type equations are mathematically valid for small streamline curvature and slope, e.g., $\left| tt_{xx} \right|$, $\left| tz_{bxx} \right|$, z_{bx}^2, $\left| z_{bx}t_x \right|$, and $t_x^2 < 0.5$ (Hager and Hutter 1984), corresponding to a mathematical limitation of Eq. (4.36). Using Eq. (4.1), an additional condition for the free surface velocity is obtained from

$$V_s = -K\frac{\partial}{\partial s}\left[\frac{p}{\gamma} + z\right]_s = -K\frac{\partial}{\partial s}(t + z_b) = -K\sin\theta_s. \tag{4.37}$$

[1]The development of the equations of this section parallels the steps described in detail in Sect. 3.4 and is not repeated here.

Furthermore, $\sin\theta_s$ (Fig. 4.1) is expressed in terms of the free surface streamline inclination $\mathrm{d}(t + z_b)/\mathrm{d}x$ by using the trigonometric relation

$$\sin\theta_s = (t_x + z_{bx})\cos\theta_s = (t_x + z_{bx})\left[1 + (t_x + z_{bx})^2\right]^{-3/2}. \tag{4.38}$$

Inserting Eq. (4.38) into Eq. (4.37) produces the relation

$$V_s = -K\sin\theta_s = -K(t_x + z_{bx})\left[1 + (t_x + z_{bx})^2\right]^{-1/2} \tag{4.39}$$

Equating Eqs. (4.36) and (4.39) yields a second-order nonlinear ODE describing 2D flows in porous media over an arbitrary, impervious bottom geometry $z_b = z_b(x)$ as

$$\begin{aligned}\frac{q}{Kt}\Bigg[1 + \frac{tz_{bxx}}{2}\left[1 + z_{bx}^2\right]^{-3/2} + \frac{\left[tt_{xx} + tz_{bxx}\right]}{m+2}\left[1 + (t_x + z_{bx})^2\right]^{-3/2} \\ - \frac{tz_{bxx}}{m+2}\left[1 + (z_{bx})^2\right]^{-3/2} - \frac{t_x^2}{6} - \frac{z_{bx}^2 + z_{bx}t_x}{2}\Bigg] \\ + (t_x + z_{bx})\left[1 + (t_x + z_{bx})^2\right]^{-1/2} = 0.\end{aligned} \tag{4.40}$$

This is the Dupuit–Fawer ODE, developed by Castro-Orgaz (2011a).

4.3.2 Particular Cases

A practical case to apply Eq. (4.40) is the 2D flow across earth dams over a horizontal, impervious bed, for which the bottom geometry is $z_b(x) = 0$ (Fig. 4.3). Equation (4.40) simplifies then to

$$\frac{q}{Kt}\left(1 + \frac{tt_{xx}\left(1 + t_x^2\right)^{-3/2}}{m+2} - \frac{t_x^2}{6}\right) + t_x\left(1 + t_x^2\right)^{-1/2} = 0. \tag{4.41}$$

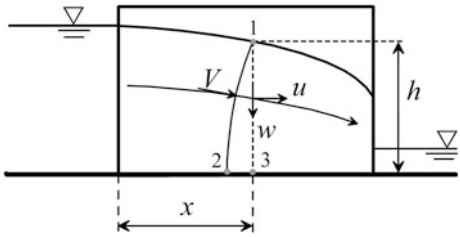

Fig. 4.3 Definition sketch of a 2D flow across an earth dam with vertical faces ($h = t$, see Appendix E)

A physical condition is needed to determine the nonlinear curvature distribution exponent m. From Eq. (4.29), the velocity distribution at the impermeable base $v = 0$ (subscript b) is, with $1/R_b = 0$ (or $r = 0$),

$$V_b = V_s \exp\left[-\frac{1}{m+1}\frac{N_o}{R_s}\right] \approx V_s \exp\left[-\frac{tt_{xx}}{m+1}\right] \approx V_s\left[1 - \frac{tt_{xx}}{m+1}\right]. \tag{4.42}$$

The pressure head at the point of the equipotential line intersecting the bed (point 2 in Fig. 4.3) is $p_b/\gamma = t$, given that along this equipotential curve, connecting the bed and a point at the phreatic surface (point 1 in Fig. 4.3), $\phi = p_b/\gamma + z = \text{const.}$, by definition. Moreover, along the base, $ds = dx$, resulting from Darcy's law,

$$V_b = -K\frac{\mathrm{d}}{\mathrm{d}s}\left[\frac{p}{\gamma}\right]_b = -K\frac{d}{\mathrm{d}x}\left[\frac{p}{\gamma}\right]_b = -Kt_x. \tag{4.43}$$

Using Eq. (4.39),

$$V_s = -Kt_x\left(1 + t_x^2\right)^{-1/2}, \tag{4.44}$$

and eliminating (Kt_x) with the aid of Eqs. (4.43) and (4.44) produces

$$V_b = V_s\left(1 + t_x^2\right)^{1/2}. \tag{4.45}$$

The theoretical condition for the streamline curvature parameter m follows by equaling Eqs. (4.42) and (4.45) as

$$m = \left[tt_{xx}\left[1 - \left(1 + t_x^2\right)^{1/2}\right]^{-1}\right] - 1. \tag{4.46}$$

Equation (4.46) provides closure to Eq. (4.41), so that the water table height t can be computed. Note that the value $m = 1$ is not necessarily accurate. For $m \to \infty$, the effect of streamline curvature disappears from Eq. (4.41). Thus, a high m value physically means that the streamlines are becoming parallel ($\kappa_s \to 0$; with κ_s as the curvature of the phreatic surface), whereas a low m value indicates a highly curved seepage flow. Equation (4.41) is rewritten as

$$\frac{q}{Kt}\left(1 + \frac{tt_{xx}\left(1 + t_x^2\right)^{-3/2}}{m+2} - \frac{t_x^2}{6}\right)\left(1 + t_x^2\right)^{1/2} + t_x = 0. \tag{4.47}$$

Using Taylor series developments, as usual, this expression transforms to

$$\frac{q}{Kt}\left(1 + \frac{tt_{xx}\left(1 - \frac{3}{2}t_x^2\right)}{m+2} - \frac{t_x^2}{6} + \frac{t_x^2}{2}\right) + t_x = 0, \tag{4.48}$$

and neglecting the second-order product $(tt_{xx})t_x^2$ leads to

$$\frac{q}{Kt}\left(1+\frac{tt_{xx}}{m+2}+\frac{t_x^2}{3}\right)+t_x=0. \tag{4.49}$$

Taking $m = 1$, Eq. (4.49) yields

$$\frac{q}{Kt}\left(1+\frac{tt_{xx}+t_x^2}{3}\right)+t_x=0. \tag{4.50}$$

For flows over a horizontal aquifer, x is defined as the position of point 3 at the base of the equipotential line (Fig. 4.3), so that exactly $t = h$, without need for further approximations in computing h as a function of t (Appendix E). Equations (4.22) from the Picard iteration and (4.48) from the Dupuit–Fawer theory are therefore mathematically identical. For parallel-streamlined seepage flows, Eq. (4.50) reduces to the Dupuit equation (Jaeger 1956; Bear 1972)

$$\frac{q}{Kt}+t_x=0. \tag{4.51}$$

4.4 Polubarinova-Kochina's Rectangular Dam Seepage Problem

4.4.1 Picard Iteration

Figure 4.4 displays the Polubarinova-Kochina (PK) rectangular dam seepage problem (Chapman 1957; Polubarinova-Kochina 1962). Several works have indicated that the DF theory leads to an inaccurate free surface prediction for this flow (Muskat 1946; Youngs 1990; Knight 2005), represented by the so-called Dupuit parabola.

In contrast, the discharge predicted by the DF theory is coincident with the exact result (Charny 1952; Huard de la Marre 1956; Polubarinova-Kochina 1962; Khasef 1965; Youngs 1966). Below, following Chapman (1957), an exact derivation of the function for the discharge q of curved seepage flow in a rectangular dam is

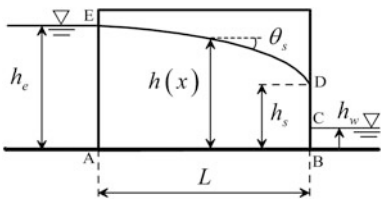

Fig. 4.4 Definition sketch of variables in earth dam with vertical faces

presented. Green's second identity (Courant and Hilbert 1962), for two arbitrary functions ω and ϕ in a 2D flow, reduces to

$$\oint \omega \frac{\partial \phi}{\partial n} \mathrm{d}s = \oint \phi \frac{\partial \omega}{\partial n} \mathrm{d}s, \tag{4.52}$$

provided both are regular harmonic functions (Huard de la Marre 1956; Chapman 1957, 2003).

Pelageya Yakovlevna Kochina (born Polubarinova) was born on May 13, 1899, in Astrakhan, Russia, and passed away at age 100 on July 03, 1999, in Moscow, Russia. She graduated from Petrograd University as a mathematician in 1921, starting work at its Geophysical Observatory already in 1919. From 1927 to 1934, she was both a Lecturer at Leningrad University and a staff member of the Institute of Civil Aviation Engineering. In 1935, she moved to Moscow's Steklov Mathematical Institute, leaving in 1938 for the Institute of Mechanics of the USSR Academy of Sciences. Submitting a doctoral thesis in mathematical and physical sciences in 1940, she was an associate of that institute until 1957. From 1958, she directed the Department of Applied Hydrodynamics at Novosibirsk. In 1970, she returned to Moscow to direct the section of mathematical methods in mechanics at Moscow University.

Kochina is known for her fundamental contributions to the theory of flows in porous media. She in particular developed a general method for solving two-dimensional seepage problems in homogeneous soils. Kochina's research was characterized by a deep and well-organized link with practice, a subtle attention to the physical essence of the phenomena considered, an exact mathematical formulation of the relevant physical problem, and by a brilliant mastery of the mathematics. She was awarded, among many others, the Stalin Prize in 1946; she was a full member of the USSR Academy of Sciences from 1958 and Hero of Socialist Labour from 1969, and received the Order of the Friendship of Nations in 1979.

The derivatives are evaluated in the normal direction n external to the closed surface; s is the curvilinear distance along its perimeter. For the case depicted in

Table 4.1 Evaluation of arguments for Green's second identity, Eq. (4.52). Both sides of Eq. (4.52) are multiplied by the hydraulic conductivity K, for convenience.

Line	ω	$K\frac{\partial\phi}{\partial n}$	$K\phi$	$\frac{\partial\omega}{\partial n}$
AB	x	0	Unknown	0
BC	L	$-u$	Kh_w	1
CD	L	$-u$	Kz	1
DE	x	0 (phreatic surface is a streamline)	Kz	$-\sin\theta_s$
EA	0	0	Kh_e	-1

Fig. 4.4, defining θ_s as the angle between the free surface and the x-axis, Table 4.1 summarizes each term needed to apply Eq. (4.52) (Chapman 1957), using the function $\omega = x$. In Fig. 4.4, h_e is the upstream flow depth, h_w the downstream flow depth, and L the dam length.

The left-hand side of the identity is evaluated as (see Fig. 4.4)

$$\begin{aligned}\oint \omega K\frac{\partial\phi}{\partial n}\mathrm{d}s &= \int_{\mathrm{A}}^{\mathrm{B}} x(0)\mathrm{d}x + \int_{\mathrm{B}}^{\mathrm{C}} L(-u)\mathrm{d}z + \int_{\mathrm{C}}^{\mathrm{D}} L(-u)\mathrm{d}z + \int_{\mathrm{D}}^{\mathrm{E}} xK\underbrace{\frac{\partial\phi}{\partial n}}_{=0}(-\mathrm{d}s) + \int_{\mathrm{E}}^{\mathrm{A}} (0)(0)(-\mathrm{d}z)\\ &= \int_{\mathrm{B}}^{\mathrm{C}} L(-u)\mathrm{d}z + \int_{\mathrm{C}}^{\mathrm{D}} L(-u)\mathrm{d}z = -L\int_{\mathrm{B}}^{\mathrm{D}} u\mathrm{d}z = -qL.\end{aligned} \tag{4.53}$$

The right-hand side of the identity is

$$\begin{aligned}\oint K\phi\frac{\partial\omega}{\partial n}\mathrm{d}s &= \int_{\mathrm{A}}^{\mathrm{B}} K\phi(0)\mathrm{d}x + \int_{\mathrm{B}}^{\mathrm{C}} Kh_w(1)\mathrm{d}z + \int_{\mathrm{C}}^{\mathrm{D}} Kz(1)\mathrm{d}z + \int_{\mathrm{D}}^{\mathrm{E}} Kz(-\sin\theta_s)(-\mathrm{d}s) + \int_{\mathrm{E}}^{\mathrm{A}} Kh_e(-1)(-\mathrm{d}z)\\ &= Kh_w\int_{\mathrm{B}}^{\mathrm{C}}\mathrm{d}z + K\int_{\mathrm{C}}^{\mathrm{D}} z\mathrm{d}z + K\int_{\mathrm{D}}^{\mathrm{E}} z(-\sin\theta_s)\left(-\frac{\mathrm{d}z}{\sin\theta_s}\right) + Kh_e\int_{\mathrm{E}}^{\mathrm{A}}\mathrm{d}z\\ &= Kh_w^2 + K\int_{\mathrm{C}}^{\mathrm{E}} z\mathrm{d}z - Kh_e^2 = Kh_w^2 + K\frac{\left(h_e^2 - h_w^2\right)}{2} - Kh_e^2 = -K\frac{\left(h_e^2 - h_w^2\right)}{2}.\end{aligned} \tag{4.54}$$

Equating Eqs. (4.53) and (4.54) yields the exact 2D result

$$q = \frac{K}{2L}\left(h_e^2 - h_w^2\right). \tag{4.55}$$

There is a fortuitous coincidence with the result obtained if Dupuit's 1D theory is applied (Bear 1972; Strack 1989).

Now, Eq. (4.55) is used to compute q in Eq. (4.22). This ODE is rewritten as

$$\frac{q}{h}\left(1+\frac{hh_{xx}+h_x^2}{3}\right)+Kh_x=\frac{q}{h}\left[1+\frac{1}{3}\frac{\mathrm{d}}{\mathrm{d}x}(hh_x)\right]+Kh_x=0. \tag{4.56}$$

Using the change of variable $Z = hh_x$, Eq. (4.56) produces

$$1+\frac{1}{3}\frac{\mathrm{d}Z}{\mathrm{d}x}=-\frac{K}{q}Z, \tag{4.57}$$

or

$$\frac{\mathrm{d}Z}{\left(1+\frac{K}{q}Z\right)}=-3\mathrm{d}x, \tag{4.58}$$

with the solution, using the boundary condition $Z = Z_o$ at $x = x_o = 0$

$$\ln\left[\frac{\left(1+\frac{K}{q}Z\right)}{\left(1+\frac{K}{q}Z_o\right)}\right]=-3\frac{K}{q}(x-x_o)=-3\frac{K}{q}x, \tag{4.59}$$

or

$$\left(1+\frac{K}{q}Z\right)=\left(1+\frac{K}{q}Z_o\right)\exp\left[-3\frac{K}{q}x\right]. \tag{4.60}$$

Reverting to hh_x by using the definition of Z,

$$hh_x=\left(\frac{q}{K}+(hh_x)_o\right)\exp\left[-3\frac{K}{q}x\right]-\frac{q}{K}. \tag{4.61}$$

Separating variables, Eq. (4.61) takes the form

$$h\mathrm{d}h=\left(\frac{q}{K}+(hh_x)_o\right)\exp\left[-3\frac{K}{q}x\right]\mathrm{d}x-\frac{q}{K}\mathrm{d}x. \tag{4.62}$$

Integrating Eq. (4.62) subject to the boundary condition $h(x = 0) = h_e$ yields (Di Nucci 2011)

$$\frac{h^2}{2}-\frac{h_e^2}{2}=\frac{q}{3K}\left[\frac{q}{K}+(hh_x)_o\right]\left[1-\exp\left(-\frac{3K}{q}x\right)\right]-\frac{q}{K}x. \tag{4.63}$$

If the boundary used to produce 2D solutions, namely $h_x(x = 0) = 0$ (Bear 1972), is substituted in Eq. (4.63), one obtains

$$\frac{h^2}{2} = \underbrace{\frac{h_e^2}{2} - \frac{q}{K}x}_{\text{Dupuit term}} + \underbrace{\frac{1}{3}\left(\frac{q}{K}\right)^2\left[1 - \exp\left(-\frac{3K}{q}x\right)\right]}_{\text{Non-hydrostatic term}}. \tag{4.64}$$

Equation (4.64) is a second-order solution to the Polubarinova-Kochina rectangular dam seepage problem. If the effects of streamline curvature are neglected in Eq. (4.64), it reduces to the classical Dupuit parabola

$$\frac{h^2}{2} = \frac{h_e^2}{2} - \frac{q}{K}x. \tag{4.65}$$

The flow across a rectangular earth dam for $h_e/L = 1$ and $h_w/h_e = 0$ (Knight 2005) is considered in Fig. 4.5. Equation (4.64) is compared in Fig. 4.5a with the numerical solution of Laplace's Eq. (4.4) by Knight (2005), resulting in an overall agreement of Picard's approximate iteration solution with the full 2D potential flow results. In contrast, results obtained by using Eq. (4.65), inserted in the same figure, disagree conspicuously with the 2D results.

Knight (2005) presented an interesting approach assuming a parabolic distribution of ϕ in the vertical direction, from which his differential equation describing the free surface profile is

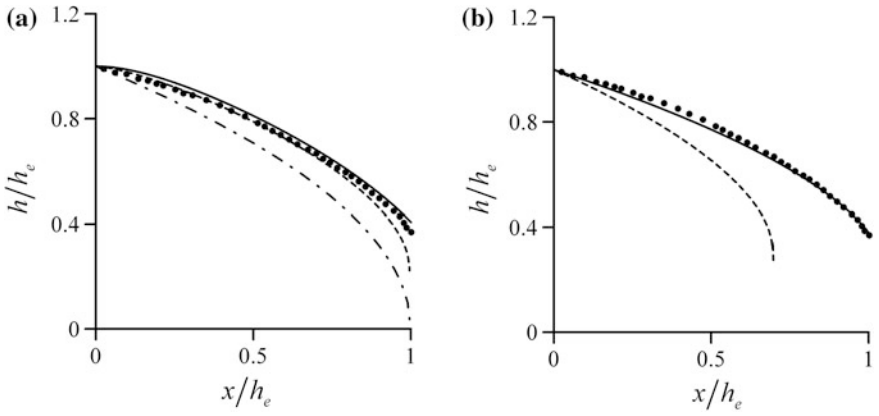

Fig. 4.5 Test case for $h_e/L = 1$ and $h_w/h_e = 0$; **a** (•) numerical solution of Eq. (4.4), (—) Eq. (4.64), (— • —) Eq. (4.65), (- -) numerical solution of Eq. (4.66); **b** (•) numerical solution of Eq. (4.4), (—) Eq. (4.67) with fitted q, (- -) Eq. (4.67) with "exact" q given by Eq. (4.55) (adapted from Castro-Orgaz 2011a)

$$\left(\frac{dh}{dx}\right)^2 = \frac{h^2 - h_e^2 + (x/L)\left(h_e^2 - h_w^2\right)}{h_e^2 - (x/L)\left(h_e^2 - h_w^2\right) - h^2/3}. \tag{4.66}$$

Equation (4.66) was solved numerically using the standard fourth-order Runge–Kutta method subject to the boundary condition $h(x = 0) = h_e$. Note the excellent agreement of Eqs. (4.64) and (4.66) except for $0.9 < x/h_e < 1$; this is the zone of maximum drawdown, where streamline curvature and slope are large. Jaeger (1956) proposed an approximate theory for free surface seepage flow, in which the equipotential curves are assumed to be circular arcs. His differential equation of the free surface profile is

$$\frac{dh}{dx} = -\tan\left(\frac{q}{Kh}\right). \tag{4.67}$$

To solve Eq. (4.67), Jaeger (1956) proposed to start computations using the boundary condition $h(x = 0) = h_e$ and adjusting the value of q until the downstream boundary condition $h(x = L) = h_s$ was reached, with h_s as the height of the surface of seepage (Fig. 4.4). This procedure is analyzed below. Equation (4.67) was solved numerically using the standard fourth-order Runge–Kutta method subject to $h(x = 0) = h_e$. First, q was computed from the exact Eq. (4.55), resulting in the dimensionless discharge $q/(Kh_e) = 0.5$. The results of this computation are included in Fig. 4.5b, showing poor agreement with the numerical solution of Laplace's equation. Following Jaeger (1956), q was successively reduced until the boundary condition $h(x = L) = h_s$ was reached, resulting in a computed normalized discharge after the iterations of $q/(Kh_e) = 0.38$. Results of this computation, displayed in Fig. 4.5b, yield an excellent free surface prediction. However, this method is not physically sound, given that the exact discharge is $q/(Kh_e) = 0.50$, and Jaeger's iteration method indicates a reduction of 24 %. Thus, Eq. (4.67) is unreliable for free surface predictions. This is attributed to the omission of the curvature effects.

Another test case is considered in Fig. 4.6 for $h_e/L = 1$ and $h_w/h_e = 0.25$. Figure 4.6a successfully compares Eq. (4.64) with 2D results of Baiocchi (Knight 2005). Moreover, Eq. (4.65) generates again poor results. Figure 4.6b compares Eq. (4.64) with the numerical solution of Eq. (4.66), resulting in close agreement with both models.

The 2D results of Shaw and Southwell (1941) are considered in Fig. 4.7a. Note that Eq. (4.64) provides a close approximation to the 2D results, in good agreement with Eq. (4.66), except at the downstream end, where Eq. (4.64) appears to provide a more realistic trend. Equation (4.65) does not agree with the 2D results, as expected. The numerical results of the Polubarinova-Kochina (1962) equations are shown in Fig. 4.7b, as presented by Hornung and Krueger (1985), for $h_e/L = 1$ and $h_w/h_e = 0$. The agreement of the Picard iteration Eq. (4.64) with the solution of PK's model by Hornung and Krueger (1985) is excellent, whereas the agreement with Eq. (4.66) is good, but of limited accuracy near $x/h_e \cong 1$.

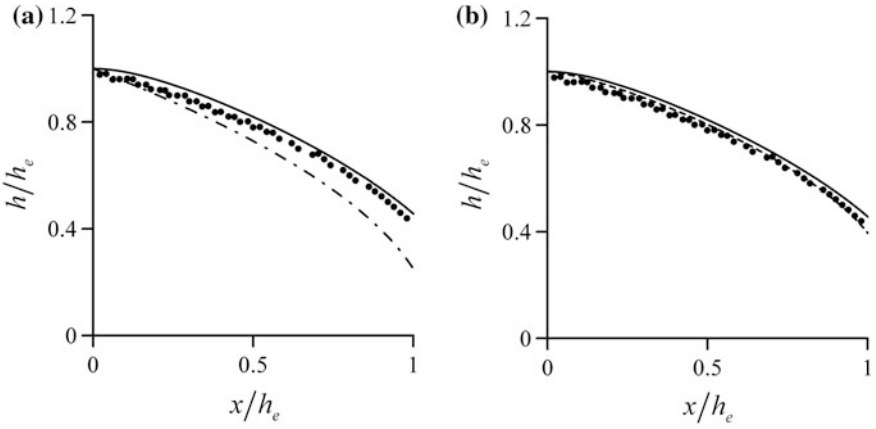

Fig. 4.6 Flow across a rectangular dam for $h_e/L = 1$ and $h_w/h_e = 0.25$ from **a** (•) Baiocchi's 2D results (Knight 2005), (—) Eq. (4.64), (— • —) Eq. (4.65); **b** (—) Eq. (4.64), (- -) numerical solution of Eq. (4.66) (adapted from Castro-Orgaz 2011a)

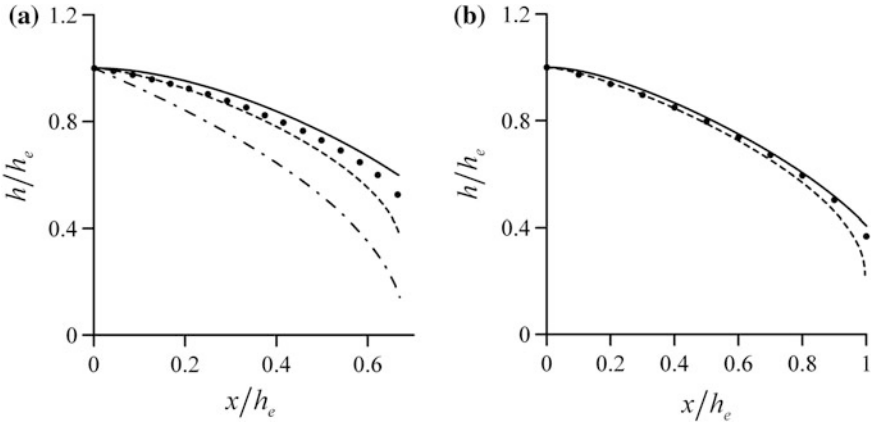

Fig. 4.7 Flow across rectangular dam for **a** $L/h_e = 0.665$ and $h_w/h_e = 0.167$ from (•) 2D results (Shaw and Southwell 1941), (—) Eq. (4.64), (— • —) Eq. (4.65), (- -) numerical solution of Eq. (4.66); **b** $L/h_e = 1$ and $h_w/h_e = 0$ from (•) 2D results (Hornung and Krueger 1985), (—) Eq. (4.64), (- -) numerical solution of Eq. (4.66) (adapted from Castro-Orgaz 2011a)

To further explore the reliability of Picard's iteration model in predicting the downstream flow depth h_s, which is different from h_w (Fig. 4.4), consider a test case for $h_w/h_e = 0$. The drawdown at the downstream end is then a maximum so that deviations of Eq. (4.65) from Eq. (4.64) become evident (Fig. 4.5a). Chapman (1957) presented a graph $h_s/h_e(L/h_e)$ based on a conformal mapping of the hodograph representation of the potential flow equations (Fig. 4.8). Equation (4.64) was used to obtain the function $h_s/h_e(L/h_e)$, and the results are included there, agreeing well with the 2D results.

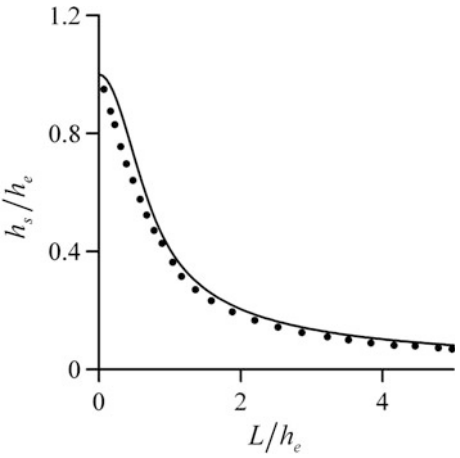

Fig. 4.8 Downstream flow depth $h_s/h_e(L/h_e)$ in a rectangular dam for $h_w/h_e = 0$ from (•) 2D results (Chapman 1957), (—) Eq. (4.64) (adapted from Castro-Orgaz 2011a)

Another pertinent test of Picard's iteration model relates to its comparison with experimental data obtained from Hele-Shaw models (Billstein et al. 1999). A test case for $L/h_e = 1.041$ and $h_w/h_e = 0.5$ is considered in Fig. 4.9, in which the Hele-Shaw data, and the numerical results obtained from the solution of the continuity and momentum equations for flow in porous media (Billstein et al. 1999) are compared with Eq. (4.64), resulting in excellent agreement.

Consider next steady unconfined seepage flows in the drainage ditch of Fig. 4.10, in which h is the saturated aquifer thickness and $\overline{\phi}$ the depth-averaged piezometric head in a vertical section. The streamline curvature and slope effects of the flow net induce a non-hydrostatic pressure distribution that, in turn, leads to depth-averaged piezometric heads differing from the depths h. The mathematical relation linking h with $\overline{\phi}$ is developed as follows. The discharge q across a vertical section is obtained using Eq. $(4.2)_1$

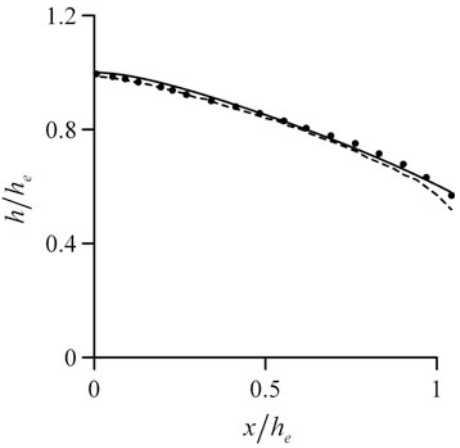

Fig. 4.9 Flow across a rectangular dam for $h_e/L = 1.041$ and $h_w/h_e = 0.5$ from (•) Hele-Shaw data (Billstein et al. 1999), (—) Eq. (4.64), (- -) numerical solution of fluid flow equations (Billstein et al. 1999) (adapted from Castro-Orgaz 2011a)

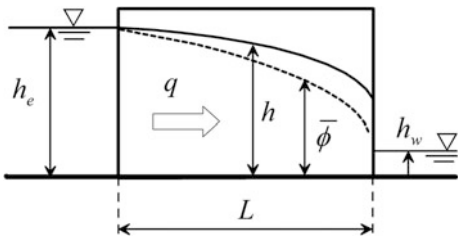

Fig. 4.10 Saturated thickness and depth-averaged piezometric heads in non-hydrostatic seepage flows

$$q = -K \int_0^h \frac{\partial \phi}{\partial x} \mathrm{d}z. \tag{4.68}$$

Using Leibniz's rule, Eq. (4.68) is integrated as

$$q = -K \int_0^h \frac{\partial \phi}{\partial x} \mathrm{d}z = -K \left(\frac{\partial}{\partial x} \int_0^h \phi(x,z) \mathrm{d}z - \phi(x, z=h) \frac{\partial h}{\partial x} \right) = -K \left(\frac{\partial}{\partial x} \int_0^h \phi(x,z) \mathrm{d}z - h(x) \frac{\partial h}{\partial x} \right)$$
$$= -K \frac{\partial}{\partial x} \left(\int_0^h \phi(x,z) \mathrm{d}z - \frac{h^2}{2} \right) = -\frac{\partial \Phi}{\partial x}. \tag{4.69}$$

Therefore, the discharge q is exactly related to the discharge potential by (Zaoui 1964; Youngs 1966; Strack 1989; Knight 2005; Strack et al. 2006)

$$q = -\frac{\partial \Phi}{\partial x}, \tag{4.70}$$

where the discharge potential Φ in groundwater hydraulics is defined as

$$\Phi = K \int_0^h \phi(x,z) \mathrm{d}z - K \frac{h^2}{2}. \tag{4.71}$$

Here, ϕ is the potential function, i.e., the piezometric or hydraulic head, and K is the hydraulic conductivity in x-direction. Depth-averaged regional groundwater flow models are based on Eq. (4.70) combined with the depth-averaged mass conservation equation (Strack 1989)

$$\nabla^2 \Phi = -N. \tag{4.72}$$

Here, N is the net accretion rate and the nabla operator refers to the horizontal plane, e.g., to the x-direction. The depth-averaged piezometric head is, from Eq. (4.71),

$$\overline{\phi} = \frac{1}{h}\int_0^h \phi(x,z)\mathrm{d}z = \frac{h}{2} + \frac{\Phi}{Kh}. \tag{4.73}$$

Equation (4.73) indicates that for a known value of Φ, the computation of h requires the knowledge of $\overline{\phi}$.

Following Strack et al. (2006), the only assumption necessary to regain the DF theory from Eqs. (4.70)–(4.73) is that the depth-averaged piezometric head equals the local saturated thickness, e.g.,

$$\overline{\phi} = h. \tag{4.74}$$

This relation results either by assuming horizontal flow (Polubarinova-Kochina 1962; Bear 1972; Murray and Monkmeyer 1973; Knight 2005) or by neglecting vertical resistance to the flow (Kirkham 1967; Strack 1989; Strack et al. 2006). Inserting Eq. (4.74) into Eq. (4.71) yields the basic result used in DF-type, depth-averaged groundwater flow models (Strack 1989) as

$$\Phi = K\frac{h^2}{2}. \tag{4.75}$$

Strack et al. (2006) indicated that other relations, different from $\overline{\phi} = h$, are possible in Eq. (4.71) to obtain a higher order expression for Φ. This is addressed here using Picard iteration, by quantifying $\overline{\phi}$ versus h. The second-order result for the piezometric head is from Eq. (4.10), for the rectangular dam seepage problem (z_b = 0)

$$-K\phi = \frac{U_x}{2}\left(h^2 - z^2\right) - Kh. \tag{4.76}$$

Using $U_x = -qh_x/h^2$, Eq. (4.76) yields

$$\phi = h - \frac{qh_x}{2K}\left(\frac{z^2}{h^2} - 1\right). \tag{4.77}$$

This expresses a parabolic distribution in the vertical direction, e.g., similar to Knight (2005). Depth-averaging Eq. (4.77) yields

$$\begin{aligned}\overline{\phi} &= \frac{1}{h}\int_0^h \phi(x,z)\mathrm{d}z = \frac{1}{h}\int_0^h \left[h - \frac{qh_x}{2K}\left(\frac{z^2}{h^2} - 1\right)\right]\mathrm{d}z = \frac{1}{h}\left[h^2 - \frac{qhh_x}{6K} + \frac{qhh_x}{2K}\right] \\ &= h + \frac{q}{3K}h_x.\end{aligned} \tag{4.78}$$

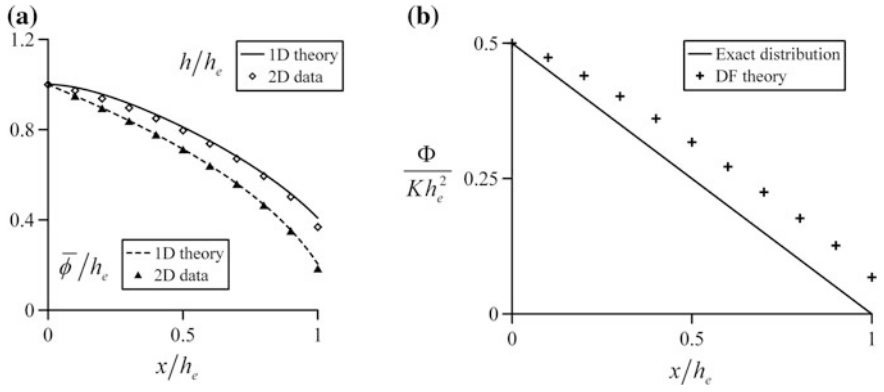

Fig. 4.11 Rectangular dam test case for $h_e/L = 1$ and $h_w/h_e = 0$ **a** saturated thickness from 1D theory (Eq. 4.64), depth-averaged piezometric head from 1D theory [Eq. (4.78) using Eqs. (4.55) and (4.82)] and 2D data, **b** discharge potential from DF theory using exact water depths (Eq. 4.75) and exact 2D result (Eq. 4.81)

Inserting Eq. (4.78) into Eq. (4.71) yields for the discharge potential

$$\Phi = K\overline{\phi}h - K\frac{h^2}{2} = Kh\left(h + \frac{q}{3K}h_x\right) - K\frac{h^2}{2} = K\frac{h^2}{2} + \frac{q}{3}hh_x. \tag{4.79}$$

Note that the term hh_x in Eq. (4.79) is given by Eq. (4.61). The main purpose to present these results is to quantify the differences between $\overline{\phi}$ and h. Consider in Fig. 4.11 the test case $L/h_e = 1$ and $h_w = 0$, previously considered in Fig. 4.5. The 2D free surface data computed by Hornung and Krueger (1985) using the exact Polubarinova-Kochina equations, and the 1D free surface profile from Eq. (4.64), are plotted in Fig. 4.11a. For the rectangular dam seepage problem, the "exact" distribution of Φ is obtained upon integrating Eq. (4.70) as (Youngs 1966; Knight 2005)

$$\Phi = \Phi(x = 0) - qx. \tag{4.80}$$

At the upstream section ($x = 0$), the pressure distribution is hydrostatic and the discharge potential is given by Eq. (4.75). Thus, Eq. (4.80) yields

$$\Phi = K\frac{h_e^2}{2} - qx. \tag{4.81}$$

Using Eq. (4.55) to compute q, Eq. (4.81) permits computation of the exact 2D distribution of Φ at each position x along the dam, as plotted in Fig. 4.11b. The discharge potential from Picard's iteration method, given by Eq. (4.79), will be compared with the exact Eq. (4.81). Using Eq. (4.61) with $h_x = 0$ at $x = 0$, the following identity is obtained

$$\frac{qhh_x}{3} = \frac{q^2}{3K}\exp\left(-\frac{3K}{q}x\right) - \frac{q^2}{3K} = -\frac{q^2}{3K}\left[1 - \exp\left(-\frac{3K}{q}x\right)\right], \tag{4.82}$$

and from Eq. (4.64),

$$\frac{Kh^2}{2} = \frac{Kh_e^2}{2} - qx + \frac{q^2}{3K}\left[1 - \exp\left(-\frac{3K}{q}x\right)\right]. \tag{4.83}$$

Substituting Eqs. (4.82)–(4.83) into Eq. (4.79) yields

$$\begin{aligned}\Phi = K\frac{h^2}{2} + \frac{q}{3}hh_x &= \frac{Kh_e^2}{2} - qx + \frac{q^2}{3K}\left[1 - \exp\left(-\frac{3K}{q}x\right)\right] - \frac{q^2}{3K}\left[1 - \exp\left(-\frac{3K}{q}x\right)\right] \\ &= \frac{Kh_e^2}{2} - qx.\end{aligned} \tag{4.84}$$

This means that Picard's iteration result for Φ is exact. The 2D $\overline{\phi}$ distribution is computed using the exact Eq. (4.73), inserting in it the exact distribution of Φ given by Eq. (4.81), and the 2D $h(x)$ values computed by Hornung and Krueger (1985). This result is plotted in Fig. 4.11a and labeled depth-averaged piezometric head "2D data." Note that $\overline{\phi}$ progressively diverges from h as the seepage face is approached and the free surface slope increases. The 2D results for (h, $\overline{\phi}$) are thus available for comparative purposes with the hydraulic theory given by the Picard iteration. The results $h = h(x)$ from Eq. (4.64) are plotted in Fig. 4.11a, showing good agreement with 2D data, as previously reported. The prediction of $\overline{\phi}$ using Eq. (4.78), with q computed from Eq. (4.55), and h_x from Eq. (4.82) is also included, showing excellent agreement with the 2D data. This confirms that the divergence between $\overline{\phi}$ and h can be predicted using the hydraulic theory.

The DF estimate for Φ is given by Eq. (4.75). This approximate equation was applied by using the 2D data of Hornung and Krueger (1985), to test its accuracy using "exact" data for $h = h(x)$. The results are plotted in Fig. 4.11b (labeled "DF theory"), indicating that the DF computation of Φ is not in agreement with the exact distribution, especially for large x, where h_x is most pronounced. It is in this zone where the differences between h and $\overline{\phi}$ are maximum.

Computations were repeated for a test case $h_e/L = 2/3$ and $h_w/h_e = 1/6$ from the Polubarinova-Kochina book. The results are shown in Fig. 4.12. Note that as L/h_e decreases, the accuracy in aquifer thickness prediction is reduced (Fig. 4.12a), but the piezometric head estimation is less sensitive to these variations.

A third test case under the more extreme conditions $h_e/L = 0.5$ and $h_w/h_e = 0.5$ (Hornung and Krueger 1985) is plotted in Fig. 4.13. The previous trends are essentially confirmed, verifying that Picard's iteration yields good results and permits to overcome some of the limitations of the DF theory implicit in the assumption $\overline{\phi} = h$.

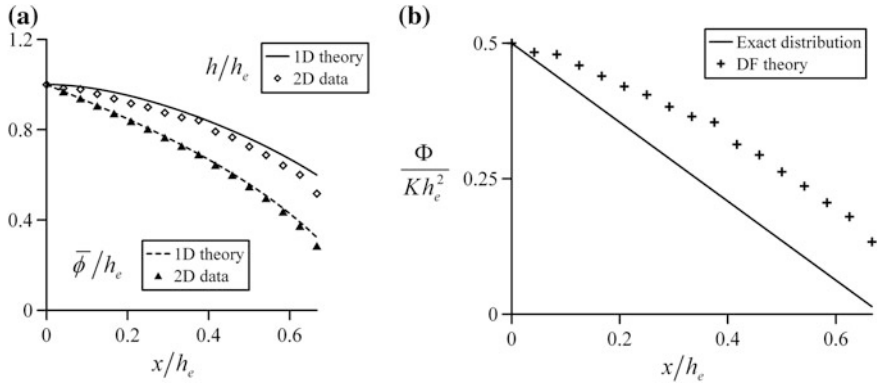

Fig. 4.12 Rectangular dam test case for $h_e/L = 2/3$ and $h_w/h_e = 1/6$ **a** saturated thickness from 1D theory (Eq. 4.64), depth-averaged piezometric head from 1D theory [Eq. (4.78) using Eqs. (4.55) and (4.82)] and 2D data, **b** discharge potential from DF theory using exact water depths (Eq. 4.75) and exact 2D result (Eq. 4.81)

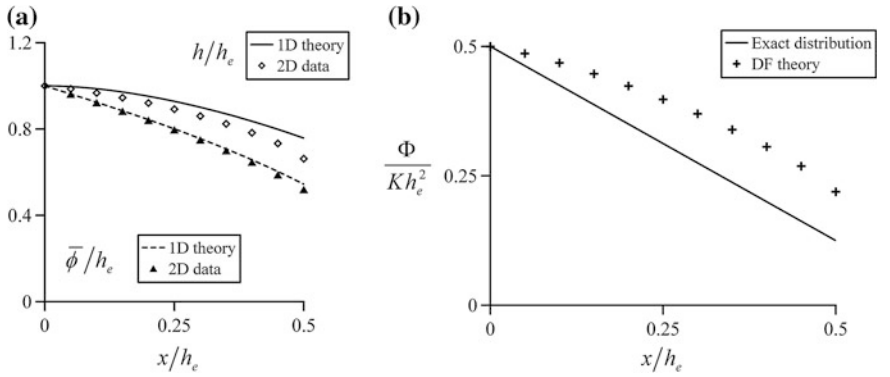

Fig. 4.13 Rectangular dam test case for $h_e/L = 0.5$ and $h_w/h_e = 0.5$ (legend as in Fig. 4.12)

4.4.2 Validity of the Dupuit–Forchheimer Theory

From the above discussion, it was found that by using the exact 2D boundary conditions $h_x = 0$ at $x = 0$, some deviations of the predicted value of h_s by Eq. (4.64) occur (Fig. 4.8). Therefore, Eq. (4.63) was applied with the boundary conditions: $h = h_e$ and $h_x = h_{xe}$ at $x = 0$ (Castro-Orgaz 2011b). The free surface slope at $x = 0$ was determined from Eq. (4.63) by using the downstream boundary condition $h = h_s$ at $x = L$. The results in Fig. 4.14a indicate the improved accuracy of Picard's iteration. This additional degree of freedown in Picard's iteration theory, given by a second-order differential equation, permits to increase the accuracy of the computation.

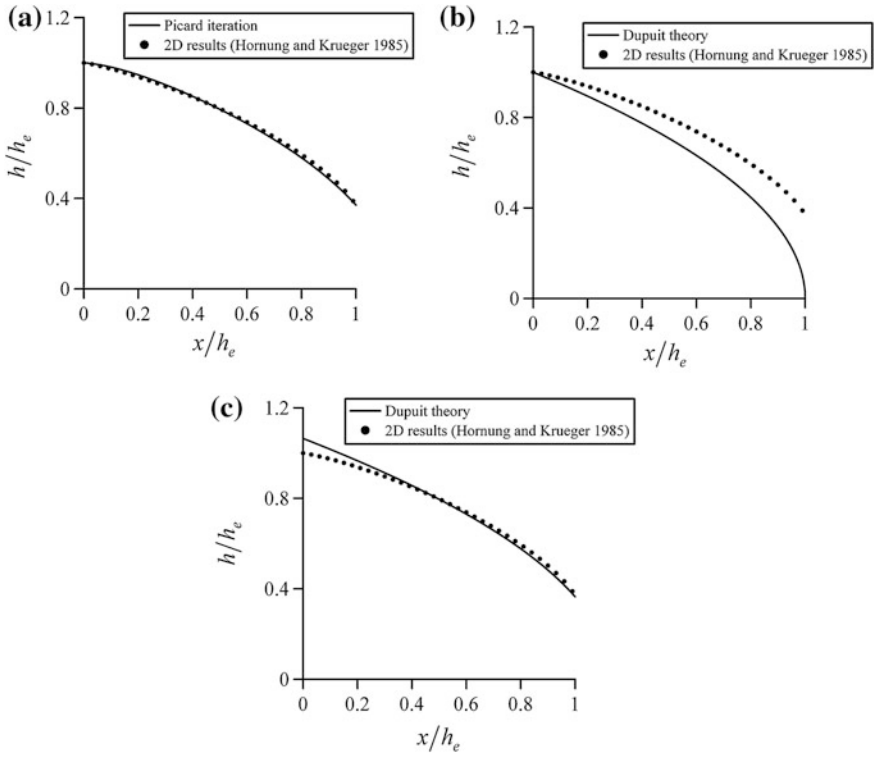

Fig. 4.14 Rectangular dam test case for $h_e/L = 1$ and $h_w/h_e = 0$, comparison of 2D results (Hornung and Krueger 1985) with **a** Picard iteration Eq. (4.63), **b** Dupuit parabola with control point at inlet (Eq. 4.86), **c** Dupuit parabola with control point at outlet (Eq. 4.87) (adapted from Castro-Orgaz and Dey 2014)

However, the Dupuit Ordinary Differential Equation (DODE henceforth) is, from Eq. (4.23),

$$q = -Khh_x. \tag{4.85}$$

This is mathematically a first-order equation subject to only one boundary condition. Taking the boundary condition (or control point) at the upstream section produces the classical result (Muskat 1946; Jaeger 1956; Bear 1972)

$$\frac{h^2}{2} = \frac{h_e^2}{2} - \frac{q}{K}x. \tag{4.86}$$

Results using Eq. (4.86) are plotted in Fig. 4.14b, showing poor agreement with 2D computations, as previously reported. This failure is attributed in the literature to the fact that Dupuit's theory neglects the existence of a vertical velocity component.

Consider the DODE from a mathematical viewpoint. An arbitrary control point (x_b, h_b) leads by integration of Eq. (4.85) to the general parabolic law

$$\frac{h^2}{2} = \frac{h_b^2}{2} + \frac{q}{K}(x_b - x). \tag{4.87}$$

The general Dupuit parabola Eq. (4.87) was considered taking the boundary condition as the seepage face height, i.e., at the point ($x/h_e = 1$, $h/h_e = 0.368$) based on the 2D data plotted in Fig. 4.14b. The results are plotted in Fig. 4.14c, showing good agreement with 2D data along the major portion of the flow profile. This surprising result suggests an excellent accuracy of Dupuit's modified parabola, thereby indicating that the failure of Dupuit's parabola in Fig. 4.14b is not necessarily related to the existence of curvilinear flow (Castro-Orgaz and Dey 2014). This issue is examined in detail below.

The traditional condition stated in the literature for the validity of the DODE is a near-horizontal water table, i.e., $h_x^2 \ll 1$ (Bear 1972; Murray and Monkmeyer 1973). However, the results of Fig. 4.14c are in contradiction with this requirement, given the excellent results of the DODE in the interval $0.4 < x/h_e < 1$, where h_x^2 is large. The condition $h_x^2 \ll 1$ (Bear 1972; Murray and Monkmeyer 1973) was obtained in the literature from a first-order vertical velocity profile, which is only a linear function of h_x. Castro-Orgaz et al. (2012) and Castro-Orgaz and Dey (2014) demonstrated, using Picard's iteration procedure for steady flows, that the vertical velocity is a function of h_x, but the second-order horizontal velocity includes, additionally, the term hh_{xx}. This term has an important effect in the dynamic condition at the water table, as is easily observed by inspecting Eq. (4.22). For a given flow problem, the free surface curvature hh_{xx} contributes to the same order of accuracy in the ODE, despite $h_x^2 \ll 1$. Therefore, in a general problem of curvilinear seepage flows, there is no guarantee that the term hh_{xx} asymptotically tends to zero simultaneously with h_x^2.

Equation (4.22) is rewritten in the alternative form

$$-\frac{hh_x}{q/K} = 1 + \frac{hh_{xx} + h_x^2}{3}. \tag{4.88}$$

The left-hand side ratio provides an assessment of the validity of the DODE, $q = -Khh_x$, so that the DODE is a good water table predictor if it is close to unity. Note that if $h_x^2 = 0$ is substituted into Eq. (4.88), $q = -Khh_x$ is not regained unless simultaneously h_{xx} is close to zero. This indicates that the traditional condition to evaluate the validity of DODE is incomplete. To examine this issue, the terms h_x^2 and hh_{xx} obtained from the computed water table profile using Eq. (4.64) [based on $h_x(x = 0) = 0$] for the test case of Fig. 4.14 are included in Fig. 4.15a, along with those deduced numerically here from the 2D results by Hornung and Krueger (1985), using finite differences. Figure 4.15a indicates that the term h_x^2 is accurately simulated by Eq. (4.64), whereas the agreement of hh_{xx} is in general good, but only fair near the boundaries. Note that the free surface slope term is only large for

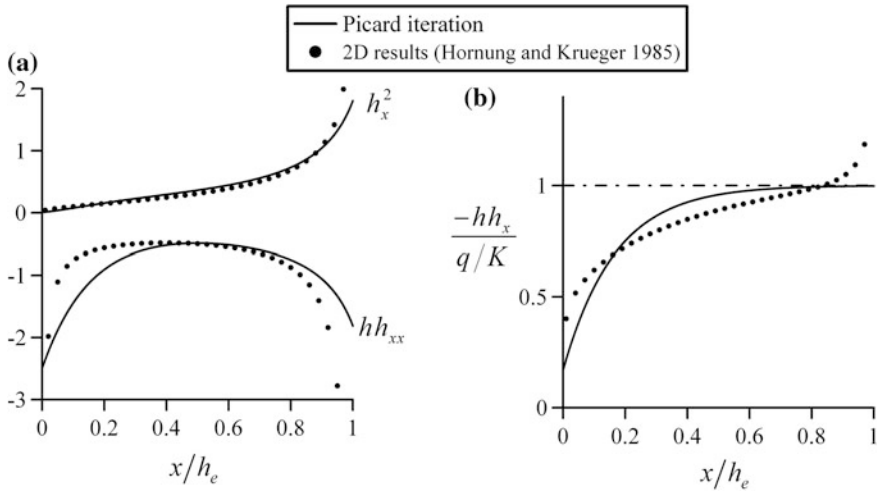

Fig. 4.15 Comparison of 2D and Picard computations for $h_e/L = 1$ and $h_w/h_e = 0$ **a** streamline inclination and curvature terms, **b** index of validity of Dupuit's theory (adapted from Castro-Orgaz and Dey 2014)

$x/h_e > 0.4$, whereas the term hh_{xx} is high along the entire water table, including the section $x = 0$, where $h_x = 0$. The ratio $(-Khh_x/q)$ is plotted in Fig. 4.15b using both methods, indicating that the equation $q = -Khh_x$ is poorly satisfied within the interval $0 \leq x/h_e \leq 0.4$, but it is an excellent approximation for $x/h_e > 0.4$. This result is unexpected and contradicts the literature, where it is systematically stated that the DODE is valid in regions of small water table inclination. The results of Fig. 4.15b indicate that the DODE, in this test, is not valid where the streamline inclination is small, but it is a good model in the portion of the water table where the free surface slope is large, thus confirming the surprising results of Fig. 4.14c. Figure 4.15a reveals the large magnitude of both terms h_x^2 and hh_{xx} for $x/h_e > 0.4$. Further, Fig. 4.15a indicates that $(hh_{xx} + h_x^2) \approx 0$ for $x/h_e > 0.4$, implying that $q \approx -Khh_x$ [Fig. 4.15b and Eq. (4.88)].

The main conclusion of the former computations is that the DODE applies to curvilinear groundwater flow if the curvature term is canceled by the slope term, i.e., if $h_x^2 \approx -hh_{xx}$ (Fig. 4.16a). For $0 \leq x/h_e < 0.4$, the results shown in Fig. 4.15a indicate that $(hh_{xx} + h_x^2) \ll 0$, thereby invalidating the use of $q = -Khh_x$ despite $h_x^2 \approx 0$, which is the validity condition of Murray and Monkmeyer (1973). As shown in Fig. 4.15b, the DODE cannot be applied for $0 \leq x/h_e \leq 0.4$. Therefore, the failure of Eq. (4.86) in Fig. 4.14b is due to an incorrectly placed control point condition in the flow zone where the DODE does not apply. The traditional condition for the validity of the DODE, $h_x^2 \approx 0$, must be supplemented with the additional constraint $hh_{xx} \approx 0$ that relates to portions of the water table where it is almost horizontal but also straight (Fig. 4.16b). This means that the control point (x_b, h_b) of Eq. (4.87) cannot be arbitrary; rather, it should lie along a portion of the

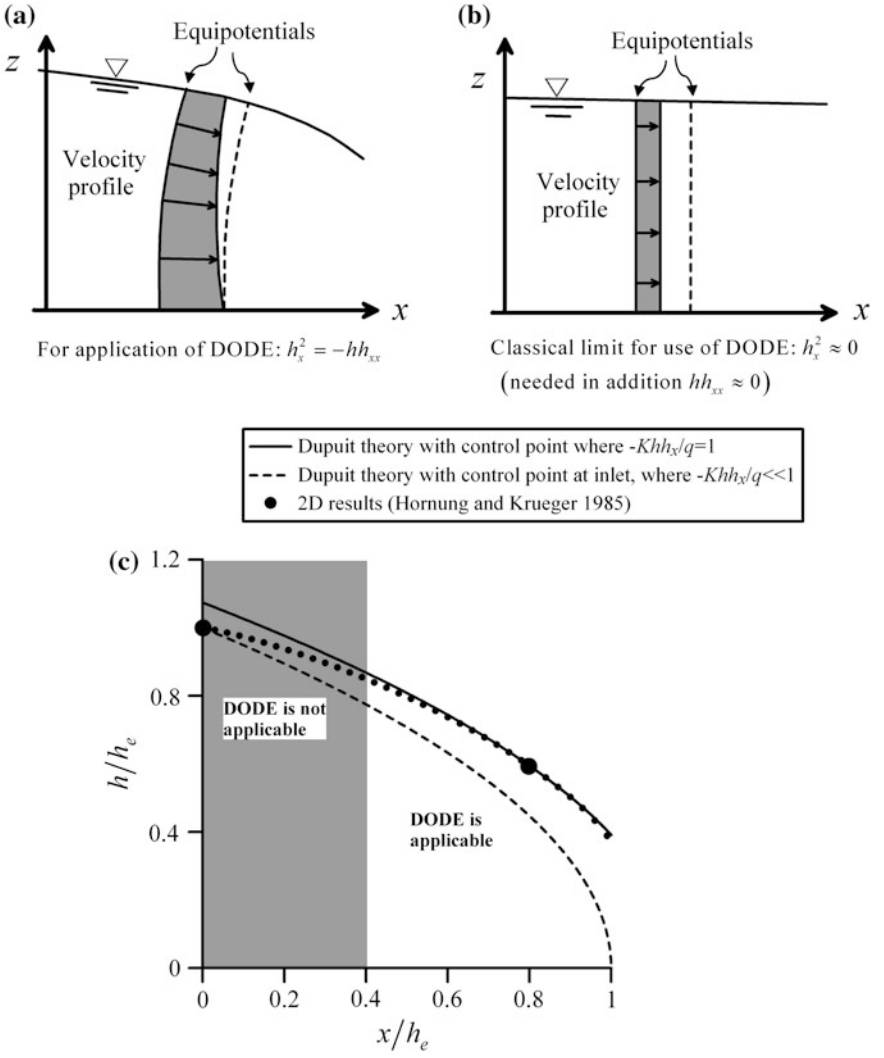

Fig. 4.16 Validity of Dupuit's theory in dam seepage problem for $h_e/L = 1$ and $h_w/h_e = 0$ **a** flow zone with curvilinear flow, **b** near-horizontal and straight phreatic surface, **c** comparison of Eqs. (4.86) and (4.87) (adapted from Castro-Orgaz and Dey 2014)

free surface profile where $h_x^2 \approx -hh_{xx}$. In line with this argument, the control point to integrate the DODE cannot be selected at the origin ($x = 0$), because the differential equation itself is not valid at that section.

This failure reason of Dupuit's parabola (Eq. 4.86) was revealed by Castro-Orgaz and Dey (2014). From the 2D data in Fig. 4.15b, $-Khh_x/q = 1$ occurs at $x/h_e = 0.8375$, resulting from Fig. 4.14a in $h/h_e = 0.5622$. Equation (4.87) is plotted in Fig. 4.16c using this control point ($x/h_e = 0.8375$, $h/h_e = 0.5622$), that

defines a point where the DODE is valid. These results are compared with those obtained by using Eq. (4.86) and the 2D data. The improvement of Eq. (4.87) over Eq. (4.86) is significant, thereby indicating the importance of selecting an appropriate control point to apply the DODE. A traditional statement based on Dupuit's Eq. (4.86) is that the DODE ignores the existence of seepage surfaces. Note, however, that there is nothing assumed regarding the existence of this surface in Eq. (4.23) or its general integrated form, Eq. (4.87). Figure 4.16c and Eq. (4.87) demonstrate that the DODE correctly predicts the existence of seepage surfaces.

The first outcome from Fig. 4.16 is that the u velocity profile is not uniform in the range $0 \leq x/h_e \leq 0.4$, even though $h_x^2 \ll 1$. For steady curvilinear flow over a horizontal bottom, Eq. (4.13) yields [see Eq. (3.63) for a horizontal bottom] for the dam seepage problem

$$u = \frac{q}{h}\left[1 + \left(\frac{hh_{xx}}{2} - h_x^2\right)\left(\frac{3\mu^2 - 1}{3}\right)\right], \quad \mu = \frac{z}{h}. \tag{4.89}$$

Setting the condition $h_x^2 = -hh_{xx}$ in Eq. (4.89) produces (Castro-Orgaz and Dey 2014)

$$u = \frac{q}{h}\left[1 - \frac{h_x^2}{2}\left(3\mu^2 - 1\right)\right]. \tag{4.90}$$

This equation is valid for the flow zone obeying the DODE (Fig. 4.16a). Polubarinova-Kochina (1962) presented a full 2D finite difference solution for a test case of $L/h_e = 2/3$ and $h_w/h_e = 1/6$. Her surface profile is compared in Fig. 4.17 with that derived from Eq. (4.64), demonstrating good agreement. The predicted discharge ratio $-Khh_x/q$ is compared with the values deduced from the 2D solution, by numerical differentiation of the water table profile. Data included in Fig. 4.17 indicate, in agreement with the previous results, that the DODE is not accurate in the upper portion of the flow domain, whereas it serves as a good approximation near the downstream face. The 2D distribution of the potential function $\phi(x, z)$ given by Polubarinova-Kochina was used to numerically compute the vertical profiles of the horizontal velocity, $u/K(\mu)$, using finite differences. The results for three representative locations are shown in Fig. 4.17. These profiles compare well with the results obtained from Eq. (4.89) using Picard's iteration, thereby indicating its accuracy regardless of the 3 selected x values. In addition, computed velocity profiles based on Eq. (4.90) are included. As expected, these profiles are not accurate at $x/h_e = 0.125$, but they follow better the more general Eq. (4.89), and 2D data, with increasing x/h_e. The classical Dupuit theory based on a uniform u profile is included as well, resulting in a poor prediction over the entire flow domain. Muskat (1946) argued that near $x/h_e = 0$, where $h_x = 0$, $u/K(\mu)$ is highly nonuniform, a result in agreement with Eq. (4.90). Furthermore, the significant effect of the curvature term hh_{xx} on the velocity profile, where h_x is almost zero, is also highlighted by Eq. (4.90).

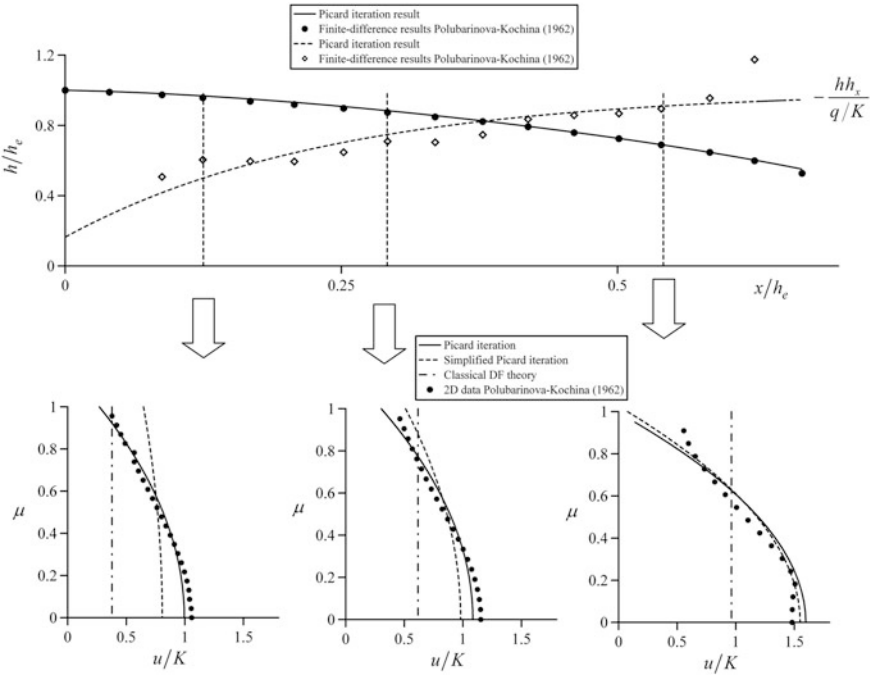

Fig. 4.17 Rectangular dam seepage problem for L/h_e = 2/3 and h_w/h_e = 1/6: comparison of free surface profile $h(x)$, discharge ratio $-Khh_x/q$, and velocity distribution $u/K(\mu)$ at selected locations (x/h_e = 0.125, 0.2915 and 0.541) from Picard's iteration with 2D data (Polubarinova-Kochina 1962) (adapted from Castro-Orgaz and Dey 2014)

4.4.3 Shallow Flow Approximation

The general unsteady flow equations originating from Picard's iteration model, Eqs. (4.18) and (4.19), form a complex system of nonlinear partial differential equations that must be handled numerically. However, they can be reduced to a single equation under shallow flow conditions. For a horizontal aquifer, Eq. (4.18) yields

$$\frac{q}{h}\left(1+\frac{hh_{xx}+h_x^2}{3}-\frac{q_xh_xh}{3q}-\frac{q_{xx}h^2}{3q}\right)+Kh_x=0, \tag{4.91}$$

or

$$\frac{q}{h}\left(1+\frac{hh_{xx}+h_x^2}{3}\right)-\left(\frac{q_xh_x+q_{xx}h}{3}\right)+Kh_x=0. \tag{4.92}$$

Solving Eq. (4.92) for q yields

$$q = -Khh_x \left[\frac{1 - \frac{1}{Khh_x}\left(\frac{q_x h_x h + q_{xx} h^2}{3}\right)}{1 + \frac{hh_{xx} + h_x^2}{3}} \right]. \tag{4.93}$$

The discharge derivative q_x in Eq. (4.92) is given implicitly by Eq. (4.19), rendering the system of equations implicit and difficult to solve. However, Eq. (4.93) contains the Dupuit term $(-Khh_x)$ multiplied by a correction factor, to be approximated by assuming shallow flow. With q given by the Dupuit equation for the water table (Eq. 4.23)

$$q = -Khh_x, \tag{4.94}$$

differentiation of Eq. (4.70) provides estimators of q_x and q_{xx} as

$$\begin{aligned} q_x &= -Khh_{xx} - Kh_x^2, \\ q_{xx} &= -Khh_{xxx} - Kh_x h_{xx} - 2Kh_x h_{xx} = -Khh_{xxx} - 3Kh_x h_{xx}. \end{aligned} \tag{4.95}$$

Inserting Eq. (4.95) into Eq. (4.93) produces

$$\begin{aligned} q &= -Khh_x \left[\frac{1 - \frac{1}{Khh_x}\left(\frac{q_x h_x h + q_{xx} h^2}{3}\right)}{1 + \frac{hh_{xx} + h_x^2}{3}} \right] \\ &\approx -Khh_x \left[\frac{1 - \frac{1}{Khh_x}\left(\frac{\left(-Khh_{xx} - Kh_x^2\right) h_x h + \left(-Khh_{xxx} - 3Kh_x h_{xx}\right) h^2}{3}\right)}{1 + \frac{hh_{xx} + h_x^2}{3}} \right] \\ &= -Khh_x \left[\frac{1 + \frac{1}{Khh_x}\left(\frac{Kh^2 h_x h_{xx} + Khh_x^3 + Kh^3 h_{xxx} + 3Kh^2 h_x h_{xx}}{3}\right)}{1 + \frac{hh_{xx} + h_x^2}{3}} \right] \\ &= -Khh_x \left[\frac{1 + \frac{1}{3}\left(4hh_{xx} + h_x^2 + \frac{h^2 h_{xxx}}{h_x}\right)}{1 + \frac{1}{3}\left(hh_{xx} + h_x^2\right)} \right]. \end{aligned} \tag{4.96}$$

For shallow flows, i.e., weakly curved streamlined flows, the denominator of Eq. (4.96) may be expanded into a Taylor–MacLaurin power series, whose first-order terms are

$$\begin{aligned} q &\approx -Khh_x \left[1 + \frac{1}{3}\left(4hh_{xx} + h_x^2 + \frac{h^2 h_{xxx}}{h_x}\right) \right] \left[1 - \frac{1}{3}\left(hh_{xx} + h_x^2\right) \right] \\ &\approx -Khh_x \left[1 + hh_{xx} + \frac{h^2 h_{xxx}}{3h_x} \right]. \end{aligned} \tag{4.97}$$

Inserting Eq. (4.97) into the depth-integrated mass conservation equation (Eq. 4.19) yields

$$\begin{aligned}\frac{\partial h}{\partial t} &= -\frac{1}{S}\frac{\partial q}{\partial x} + \frac{N}{S} \\ &= \frac{K}{S}\frac{\partial}{\partial x}\left[\underbrace{h\frac{\partial h}{\partial x}}_{\text{Dupuit term}} + \underbrace{h^2\frac{\partial h}{\partial x}\frac{\partial^2 h}{\partial x^2} + \frac{h^3}{3}\frac{\partial^3 h}{\partial x^3}}_{\text{Non-hydrostatic term}}\right] + \frac{N}{S},\end{aligned} \tag{4.98}$$

or

$$\frac{\partial h}{\partial t} = \frac{K}{S}\frac{\partial^2}{\partial x^2}\left[\frac{h^2}{2} + \frac{h^3}{3}\frac{\partial^3 h}{\partial x^3}\right] + \frac{N}{S}. \tag{4.99}$$

Equation (4.98) is a differential equation describing shallow unsteady phreatic flow in a horizontal aquifer. For vanishing accretion ($N = 0$), it simplifies to that of Dagan (Dagan 1967; Nielsen et al. 1997), or that of Liu and Wen (1997) using a power series expansion of the piezometric head. The iteration method used herein provides an alternative theoretical derivation of the second-order theory of shallow groundwater flows. It indicates that the perturbation methods and the Picard iteration converge to the same result under shallow flow conditions. In general, there is no proof that perturbation methods and the Picard iteration converge (van Dyke 1975), and from that view, the convergence of the second-order theory is a relevant mathematical statement. The development further reveals that the second-order theory for shallow flow is a particular case of the more general Picard iteration theory (Castro-Orgaz and Hager 2014).

For steady flow and no accretion rate in the rectangular dam seepage problem, Eq. (4.99) reduces to

$$\frac{\partial^2}{\partial x^2}\left(\frac{h^2}{2} + \frac{h^3}{3}h_{xx}\right) = 0, \tag{4.100}$$

or

$$\frac{\partial^2}{\partial x^2}\left(\frac{h^2}{2} + \frac{h^3}{3}h_{xx}\right) = \frac{\partial}{\partial x}\left[\underbrace{\frac{\partial}{\partial x}\left(\frac{h^2}{2} + \frac{h^3}{3}h_{xx}\right)}_{\text{Eq. (4.97)}}\right] = \frac{\partial}{\partial x}\left[-\frac{q}{K}\right] = 0, \tag{4.101}$$

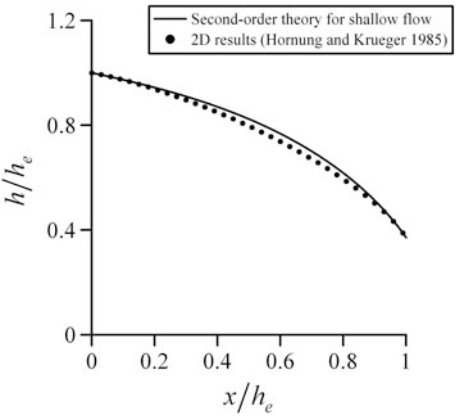

Fig. 4.18 Rectangular dam seepage test case for $h_e/L = 1$ and $h_w/h_e = 0$, comparison of 2D results (Hornung and Kruger 1985) with Eq. (4.103) (adapted from Castro-Orgaz and Dey 2014)

that is, under steady flow, the discharge is a constant. Thus, Eq. (4.101) yields (Fenton 1990)

$$\frac{\partial}{\partial x}\left[\frac{h^2}{2}+\frac{h^3}{3}h_{xx}\right]=-\frac{q}{K}. \tag{4.102}$$

Integration of Eq. (4.102) yields

$$\frac{h^2}{2}+\frac{h^3}{3}h_{xx}=-\frac{q}{K}x+\lambda \tag{4.103}$$

in which λ is a constant of integration. Equation (4.103) is the steady-state second-order shallow flow equation (Fenton 1990; Castro-Orgaz and Dey 2014). It was solved numerically using the standard fourth-order Runge–Kutta method with the boundary conditions: $h = h_e$ and $h_x = h_{xe}$ at $x = 0$, and $h = h_s$ at $x = L$, where h_s is the seepage elevation. There are two unknowns, λ and h_{xe}, so that an iterative strategy is necessary. First, a value of h_{xe} was assumed and then Eq. (4.103) solved numerically, iterating λ until satisfying the boundary condition $h(x = L) = h_s$. The process was repeated by iterating h_{xe} until the best agreement between the computed and the 2D results was found. The final free surface profile is plotted in Fig. 4.18. Even though Eq. (4.103) is less accurate than the more general Eq. (4.22), the result indicates that the second-order shallow flow theory is a good water table predictor.

4.4.4 Validity of Jaeger's Theory

The limitations of Jaeger's (1956) seepage theory, given by Eq. (4.67), are examined as follows. Jaeger (1956) assumed that the velocity distribution V along the equipotential curve 1–2 in Fig. 4.3 is uniform and that the shape of the

equipotential curve is a circular arc. Upon assuming this shape for the normals, but ignoring any assumptions for the distribution of V at this stage, the exact ratio h/N_o is

$$\frac{h}{N_o} = \frac{\sin\theta_s}{\theta_s} = \frac{h_x}{\arctan(h_x)}\left(1+h_x^2\right)^{-1/2}, \tag{4.104}$$

where h is the water depth and N_o the length of the equipotential curve. Setting $r = 0$ in Eq. (4.30), and inserting Eq. (4.104), leads to the equation

$$\begin{aligned} V_s &\approx \frac{q}{N_o}\left(1-\frac{1}{m+2}\frac{N_o}{R_s}\right)^{-1} = \frac{q}{h}\frac{h}{N_o}\left(1-\frac{1}{m+2}\frac{h}{R_s}\frac{N_o}{h}\right)^{-1} \\ &= \frac{q}{h}\frac{\sin\theta_s}{\theta_s}\left(1-\frac{1}{m+2}hh_{xx}\left(1+h_x^2\right)^{-3/2}\frac{\theta_s}{\sin\theta_s}\right)^{-1}, \end{aligned} \tag{4.105}$$

or

$$V_s = \frac{q}{h}\frac{h_x\left(1+h_x^2\right)^{-1/2}}{\arctan(h_x)}\left(1-\frac{hh_{xx}\left(1+h_x^2\right)^{-1}\frac{\arctan(h_x)}{h_x}}{m+2}\right)^{-1}. \tag{4.106}$$

Equating Eq. (4.106) with Eq. (4.39) for $z_b = 0$ produces the equation

$$\begin{aligned} &\frac{q}{h}\frac{h_x\left(1+h_x^2\right)^{-1/2}}{\arctan(h_x)}\left(1-\frac{hh_{xx}\left(1+h_x^2\right)^{-1}\frac{\arctan(h_x)}{h_x}}{m+2}\right)^{-1} = -K\sin\theta_s \\ &= -Kh_x\left(1+h_x^2\right)^{-1/2}, \end{aligned} \tag{4.107}$$

or

$$\frac{q}{Kh}\frac{h_x}{\arctan(h_x)}\left(1-\frac{hh_{xx}\left(1+h_x^2\right)^{-1}\frac{\arctan(h_x)}{h_x}}{m+2}\right)^{-1} + h_x = 0. \tag{4.108}$$

This is a generalized Dupuit–Fawer equation for seepage flow in horizontal aquifers (Castro-Orgaz 2011a, b). If $m \to \infty$, streamline curvature effects are neglected; in this case, Eq. (4.108) reduces to

$$\frac{q}{Kh}\frac{h_x}{\arctan(h_x)} + h_x = 0, \tag{4.109}$$

or

$$\frac{q}{Kh}\frac{1}{\arctan(h_x)}+1=0. \tag{4.110}$$

This is equivalent to Jaeger's (1956) seepage flow Eq. (4.67)

$$\frac{\mathrm{d}h}{\mathrm{d}x}=-\tan\left(\frac{q}{Kh}\right). \tag{4.111}$$

From Eq. (4.29), the velocity distribution along an equipotential line is, for $r = 0$, and $m \to \infty$,

$$V=\lim_{m\to\infty}\left\{V_s\exp\left[\frac{N_o}{R_s}\frac{(v^{m+1}-1)}{m+1}\right]\right\}=V_s=\text{const.}, \tag{4.112}$$

indicating a uniform velocity distribution along the equipotential line. Therefore, the failure of Jaeger's model relies on neglecting streamline curvature effects, which is implicit in the general Eq. (4.108). Retaining the exact Eq. (4.104) and neglecting curvature effects in Eq. (4.108) produces, thus, an inaccurate model.

Equation (4.108) is rewritten as

$$\frac{q}{h}\frac{h_x\left(1+h_x^2\right)^{-1/2}}{\arctan(h_x)}\left(1-\frac{hh_{xx}\left(1+h_x^2\right)^{-3/2}\frac{\arctan(h_x)}{h_x\left(1+h_x^2\right)^{-1/2}}}{m+2}\right)^{-1}+Kh_x\left(1+h_x^2\right)^{-1/2}=0. \tag{4.113}$$

Expanding Eq. (4.104) into a Taylor series yields

$$\begin{aligned}\frac{h}{N_o}=\frac{\sin\theta_s}{\theta_s}&=\frac{h_x}{\arctan(h_x)}\left(1+h_x^2\right)^{-1/2}\approx\frac{h_x}{h_x\left(1-\frac{h_x^2}{3}\right)}\left(1-\frac{h_x^2}{2}\right)\\&\approx\left(1-\frac{h_x^2}{2}\right)\left(1+\frac{h_x^2}{3}\right)\approx1-\frac{h_x^2}{6},\end{aligned} \tag{4.114}$$

and inserting Eq. (4.114) into Eq. (4.113) yields

$$\frac{q}{Kh}\left(1-\frac{h_x^2}{6}\right)\left(1-\frac{hh_{xx}\left(1+h_x^2\right)^{-3/2}\left(1+\frac{h_x^2}{6}\right)}{m+2}\right)^{-1}+h_x\left(1+h_x^2\right)^{-1/2}=0. \tag{4.115}$$

Taking in Eq. (4.115) the first-order terms only finally yields the Dupuit–Fawer Eq. (4.41)

$$\frac{q}{Kh}\left(1+\frac{hh_{xx}\left(1+h_x^2\right)^{-3/2}}{m+2}-\frac{h_x^2}{6}\right)+h_x\left(1+h_x^2\right)^{-1/2}=0. \tag{4.116}$$

4.4.5 Dupuit–Fawer Equations

The integration of Eq. (4.116) with the Runge–Kutta algorithm (Press et al. 2007) for $m = 1$ (Castro-Orgaz 2011a, b), subject to the boundary conditions $h(0) = h_e$ and $h_x(0) = 0$, is plotted in Fig. 4.19a for the test case previously considered in Fig. 4.5. To apply the Runge–Kutta algorithm, Eq. (4.116) was transformed into a pair of ODEs solved simultaneously to produce the solutions for $h(x)$ and $h_x(x)$. The water table height is fairly well predicted, yet its position is overestimated. A second solution of Eq. (4.116) was attempted with m given by [see Eq. (4.46)]

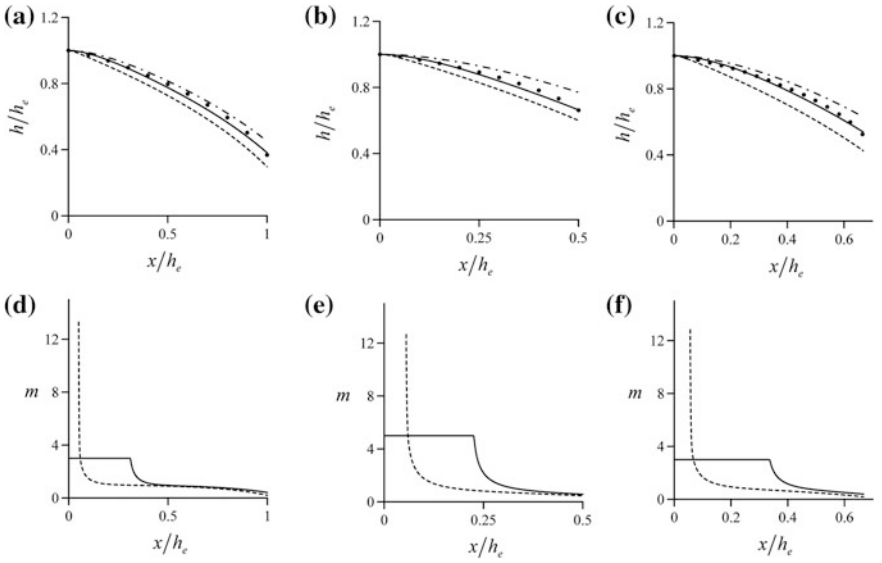

Fig. 4.19 Rectangular dam seepage flow for **a** $L/h_e = 1$ and $h_w/h_e = 0$, (—) Eq. (4.116) with $m_M = 3$, (- -) Eq. (4.116) with $m_M = 25$, (— • —) Eq. (4.116) with $m = 1$, (•) 2D results; **b** $L/h_e = 0.5$ and $h_w/h_e = 0.2$, (—) Eq. (4.116) with $m_M = 5$, (- -) Eq. (4.116) with $m_M = 25$, (— • —) Eq. (4.116) with $m = 1$, (•) 2D results; **c** $L/h_e = 0.665$ and $h_w/h_e = 0.167$, (—) Eq. (4.116) with $m_M = 3$, (- -) Eq. (4.116) with $m_M = 25$, (— • —) Eq. (4.116) with $m = 1$, (•) 2D results; curvature distribution $m(x)$ for **a**, **b,** and **c** given in **d**, **e**, and **f**, respectively (adapted from Castro-Orgaz and Giraldez 2011)

$$m = \left[hh_{xx} \left[1 - \left(1 + h_x^2 \right)^{1/2} \right]^{-1} \right] - 1. \tag{4.117}$$

To keep the numerical scheme as simple as possible, an initial value of $m = 25$ at $x = 0$ was adopted, compatible with almost parallel streamlines, and $m(x)$ at a given section was computed using Eq. (4.117) using the available results for h, h_x, and h_{xx} from the previous computational point. For $x/h_e < 0.1$, the results indicated large m values, implying parallel streamlines. These large m values at the upstream portion of the computational domain produced, in the 1D computation, high free surface slopes. This is the phenomenon observed in a water table profile computed using the DF theory. For example, from Eq. (4.85), the free surface slope predicted by the DF theory at $x = 0$ is

$$\left(\frac{\mathrm{d}h}{\mathrm{d}x} \right)_{x=0} = -\frac{q}{Kh_e}, \tag{4.118}$$

producing a large free surface gradient, highly different from the value $h_x = 0$ used in 2D solutions. Note that upon inserting Eq. (4.118) into Eq. (4.63), non-hydrostatic effects are canceled, resulting in Eq. (4.65). Therefore, a feature of nearly hydrostatic solutions, or computations based on $m \to \infty$, near $x = 0$, is a large free surface slope, as highlighted by the asymptotic value given by Eq. (4.118). Therefore, a computational method to reduce the value of m in the vicinity of $x = 0$ is required.

A maximum value of $m_M = 25$ was set to compute the flow profile. Equation (4.116) was solved numerically using $m = m_M = 25$, and the values produced by Eq. (4.117) were used once $m(x) < m_M$. The resulting flow profile is plotted in Fig. 4.19a as dashed line, and the $m(x)$ distribution is plotted as dashed line in Fig. 4.19d. Note the large initial free surface slope in the water table profile $h(x)$, which is close to the slope of the DF's water table profile. The $m(x)$ results in Fig. 4.19d (dashed line) yield values rapidly reducing to the order of 3 at $x/h_e \approx 0.1$, indicating that the streamlines are almost parallel only along a small portion of the flow profile. Streamline curvature is therefore important along almost the entire water table profile. However, the large m values produced by the computational model in the narrow interval $0 < x/h_e < 0.1$ constrain the accuracy of the 1D computation. For 1D modeling, assuming parallel streamlines at the origin $x = 0$, drastically affects the results. A second set of simulations was conducted using $m_M = 3$. The results for $m(x)$ are plotted in Fig. 4.19d as solid line, whereas the water table profile is included in Fig. 4.19a as solid line. Note the agreement of the new water table profile with the 2D results, so that 1D modeling of the water table needs to relax the hypothesis of parallel streamlines at the origin. This is achieved by the procedure outlined above by constraining the $m(x)$ distribution to an upper limit m_M.

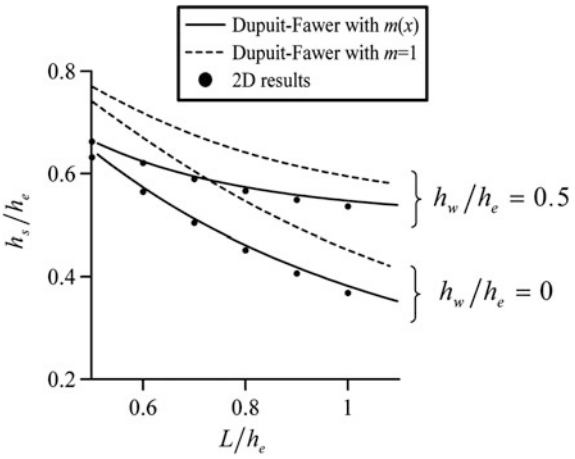

Fig. 4.20 Rectangular dam seepage flow: comparison of 2D seepage face height from 2D results by Hornung and Krueger (1985) with Eq. (4.116) for m variable and $m = 1$ (adapted from Castro-Orgaz and Giraldez 2012)

An additional test case for $L/h_e = 0.5$ and $h_w/h_e = 0.2$ computed by Hornung and Krueger (1985) is plotted in Fig. 4.19b. The computational procedure described above was repeated. The result for $m = 1$ is poor. The streamline curvature distribution was firstly constrained by using $m_M = 25$, and from these results (dashed line in Fig. 4.19e), a new value of $m_M = 5$ was adopted, producing a water table profile (solid line in Fig. 4.19b) in good agreement with the 2D results.

At last, a test case for $L/h_e = 0.665$ and $h_w/h_e = 0.167$ considered by Shaw and Southwell (1941) solving the 2D Laplace equation is plotted in Fig. 4.19c. The results for the computed water table are included in Fig. 4.19c. The streamline curvature distribution was firstly constrained by $m_M = 25$, and from the results, a new value of $m_M = 3$ was adopted. Note that the computation for $m = 1$ is again poor, whereas the computed water table profile using $m_M = 3$ is good. The distribution of $m(x)$ (solid line in Fig. 4.19f) highlights the strong flow curvature.

The reliability of the computed seepage surface height h_s/h_e using this method is highlighted in Fig. 4.20. The computation for $m = 1$ does not provide accurate seepage face positions, yet as shown in Fig. 4.19, the overall position of the water table is good. The computation based on Eqs. (4.116) and (4.117) yields good estimations of h_s/h_e, in addition to good water table profiles. Therefore, computations with $m = 1$ are limited to shallow aquifers ($L/h_e > 1$) (see Fig. 4.8).

4.5 Flow Through Trapezoidal Dam

Dams and levee embankments are trapezoidally shaped, a configuration analyzed below. The flow across an earth dam of upstream slope 1:1 was solved by van Walsum and Koopmans (1984) in the $\phi\psi$-plane (Fig. 4.21) for $q/(Kh_e) = 0.363$. Equation (4.63) was applied subject to the boundary conditions $h(x = 0) = h_e$ and $h_x(x = 0) = -1$. As noted from Fig. 4.21, the agreement between the 1D model with

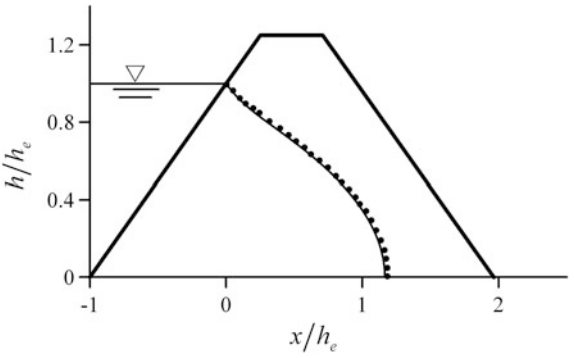

Fig. 4.21 Flow across trapezoidal dam of upstream slope 1:1 from (•) 2D results (van Walsum and Koopmans 1984), (—) Eq. (4.63) (adapted from Castro-Orgaz 2011a)

the 2D results is excellent, with the seepage surface accurately predicted. However, this result should be critically considered, because the Boussinesq-type equations are mathematically valid only for small streamline curvature and slope terms, typically $\left| hh_{xx} \right|$ and $h_x^2 < 0.5$ (Hager and Hutter 1984). Obviously, the boundary condition $h_x(x = 0) = -1$ violates the model constraints. Castro-Orgaz and Hager (2014), however, indicated that the Boussinesq equations may be applied beyond its mathematical range of validity, yet each particular case should be carefully analyzed in this regard. The flatter the upstream dam slope is, the larger will be the free surface slope at the upstream boundary and thus the degree of deviation from the basic assumptions in the mathematical development of Eq. (4.63).

The computational results of Jie et al. (2004) for an earth dam of upstream slope 2.5:1 are considered in Fig. 4.22 for $q/(Kh_e) = 0.174$. Equation (4.63) was applied using the boundary conditions $h(x = 0) = h_e$ and $h_x(x = 0) = -2.5$, with the results included in Fig. 4.22. The agreement is seen to be poor, which, as discussed, is not unexpected, given the large h_x^2 term. Consider the more general Eq. (4.116) for $m = 1$. It was solved numerically using the fourth-order Runge–Kutta method, subject to identical boundary conditions, with the results also shown in Fig. 4.22. A notable improvement is noted, highlighting the importance of nonlinearity where h_x^2 is large. Identical computations using $m = -0.5$ are also included in Fig. 4.22.

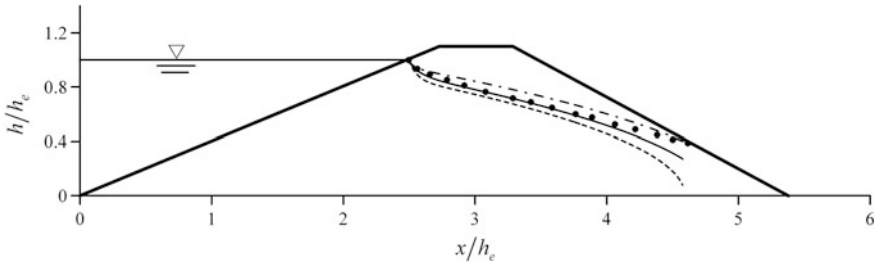

Fig. 4.22 Flow across trapezoidal dam of upstream slope 2.5:1 from (•) 2D results (Jie et al. 2004), (- -) Eq. (4.63), (— • —) Eq. (4.116) for $m = 1$, (—) Eq. (4.116) for $m = -0.5$ (adapted from Castro-Orgaz 2011a)

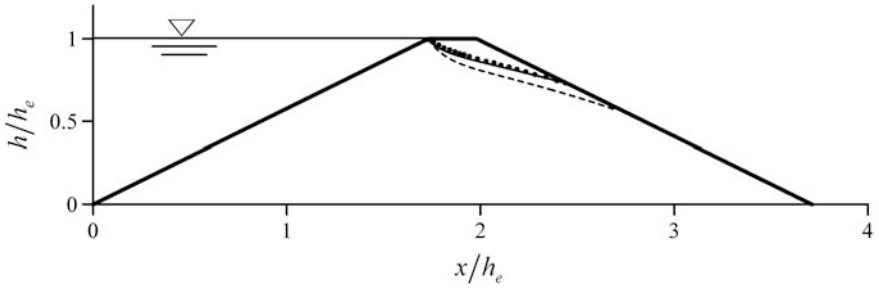

Fig. 4.23 Flow across trapezoidal dam of upstream slope 1.732:1 from (•) 2D results (Muskat 1942), (- -) Eq. (4.63), (—) Eq. (4.116) for $m = 0.6$ (adapted from Castro-Orgaz 2011a)

The agreement of the solution improves over the major part of the seepage line, but the downstream boundary condition is not well predicted, indicating that for this case $m \neq 1$, but its value is not a constant over the entire computational domain.

Data obtained from electric analogy models need also to be considered. The results of Muskat (1942) for a 30° trapezoidal dam are shown in Fig. 4.23. The discharge was estimated from the flow net, resulting in $q/(Kh_e) = 0.23$. Equation (4.63) is in poor agreement with Muskat's data. However, Eq. (4.116) solved numerically with identical boundary conditions as above, using $m = 0.6$ (Fig. 4.23), produces good results.

4.6 Drainage of Recharge

4.6.1 Horizontal Aquifer

Aquifer recharge is one of the relevant current problems in hydrogeology, especially in phreatic aquifers (Jaeger 1956; Bear 1972). The solution of the water flow problem requires the use of the Laplace equation for the potential and stream functions subjected to the different boundary conditions, implying under usual circumstances a numerical solution (Bear 1972; Serrano 1995; Rushton and Youngs 2010). An alternative to this numerical solution is the adoption of DF hypotheses (Dupuit 1863), allowing for a simpler solution. For the particular case of soil water drainage under steady recharge, Rushton and Youngs (2010) demonstrated that the standard first-order ODE arising from the DF theory compares well with water table elevations deduced from a complete 2D numerical integration of the Laplace equation, if the boundary condition is the seepage face height. However, this result must be theoretically discussed and highlighted. Castro-Orgaz (2011b) found that streamline curvature and inclination effects did not affect the water table position for flow to drains. This analysis confirmed that the classical DF equation is a good approach for selected water table studies. The classical DF theory assumes that the

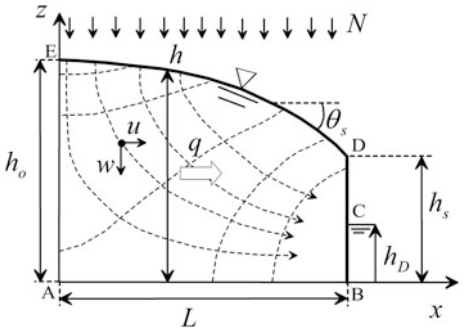

Fig. 4.24 Streamlines and equipotential lines in phreatic aquifer above impervious horizontal layer under uniform and steady recharge of intensity N, with local height of the water table h (adapted from Castro-Orgaz et al. 2012)

water table height at the outflow section of a drainage area is identical to the water level there, equivalent to neglecting the seepage surface (Bear 1972). The DF theory assumes a hydrostatic pressure variation with depth, which is stated to be limited to zones of the water table where its slope is small. Moreover, for drainage problems, this is stated to be incomplete because the water table is not a streamline, and it is also necessary to ensure that the vertical velocity is nearly zero (Bear 1972). The idealized flow condition is therefore an almost horizontal water table where the velocity is nearly horizontal and uniform with depth. The purpose of this section is to critically assess the validity of the DF theory for aquifer recharge based on the Picard iteration method. Two important problems will be addressed: soil drainage with symmetrical downstream boundaries and the toe drain on an impermeable stratum.

For the case considered in Fig. 4.24, the horizontal seepage discharge is $q(x) = Nx$, and the phreatic surface is determined by Eq. (4.21) as

$$\frac{Nx}{h}\left(1+\frac{hh_{xx}+h_x^2}{3}-\frac{h_x h}{3x}\right)+Kh_x=0. \tag{4.119}$$

After mathematical manipulation, this becomes

$$\left[1+\frac{x}{3}\frac{\mathrm{d}}{\mathrm{d}x}\left(\frac{h_x h}{x}\right)\right]+\frac{K}{N}\frac{h_x h}{x}=0. \tag{4.120}$$

Using the change of variable $Y = hh_x/x$, Eq. (4.120) yields

$$x\frac{\mathrm{d}Y}{\mathrm{d}x}=-3\left(1+\frac{K}{N}Y\right). \tag{4.121}$$

Integrating Eq. (4.121) yields

$$\frac{1}{(-3K/N)}\ln\left(-3\frac{K}{N}-3Y\right)=\ln x+\ln c, \tag{4.122}$$

or

$$Y = \frac{c_1}{(-3K/N)} x^{-3K/N} + \frac{N}{K}. \tag{4.123}$$

Using $Y = hh_x/x$, the solution in terms of the constant c_1 is

$$hh_x = \frac{N}{K}\left(-\frac{c_1}{3}x^{1-3K/N} - x\right). \tag{4.124}$$

Separating variables in Eq. (4.124) produces

$$h\mathrm{d}h = \frac{N}{K}\left(-\frac{c_1}{3}x^{1-3K/N} - x\right)\mathrm{d}x, \tag{4.125}$$

which, integrated, yields

$$\frac{1}{2}h^2 = \frac{N}{K}\left[-\frac{c_1}{3\left(2-3\frac{K}{N}\right)}x^{2-3K/N} - \frac{1}{2}x^2\right] + c_2. \tag{4.126}$$

To determine the constants of integration c_1 and c_2, use is first made of the required symmetry condition $h_x = 0$ at $x = 0$ in Eq. (4.124). Note that c_1 depends on the value of K/N. If the exponent of x in Eq. (4.126) is positive, h_x automatically vanishes, regardless the value of c_1. If the exponent is non-positive, i.e., $(2 - 3K/N) \leq 0$ or $N/K \leq 3/2$, then $c_1 = 0$. Hereafter, this condition, $c_1 = 0$, will be adopted, because the numerical calculations to be presented below indicate that the second-order Picard approximations diverge considerably from 2D calculations, and are no longer appropriate, for N/K values larger than approximately 0.6. Moreover, a critical identity that will arise in an estimation of h_o is $(2 - 3K/N) \leq 0$, from which $c_1 = 0$.

The constant c_2 is determined from Eq. (4.126) by imposing the requirement that $h(x = 0) = h_o$, with h_o yet to be determined. Immediately, $c_2 = h_o^2/2$, and Eq. (4.126) becomes the ellipse

$$h^2 = h_o^2 - \frac{N}{K}x^2 \quad \Rightarrow \quad \frac{h^2}{h_o^2} + \frac{x^2}{\left[(K/N)h_o^2\right]} = 1. \tag{4.127}$$

The solution of Eq. (4.119), given by Eq. (4.127), coincides with the result of the DF analysis. This is a fortuitous coincidence, because the u velocity profile associated with Eq. (4.127) is not uniform in the vertical direction, as obtained from Eq. (4.13) for a flat bed ($\eta = z$, $\eta_x = \eta_{xx} = 0$) as

$$u = -\frac{\partial \psi}{\partial z} = U + U_{xx}\left(\frac{h^2}{6} - \frac{z^2}{2}\right) = \frac{q}{h} + \left(\frac{q_{xx}}{h} - \frac{qh_{xx}}{h^2} + 2\frac{qh_x^2}{h^3} - 2\frac{q_x h_x}{h^2}\right)\left(\frac{h^2}{6} - \frac{z^2}{2}\right)$$
$$= \frac{q}{h}\left[1 + \left(\frac{hh_{xx}}{2} - h_x^2 + \frac{q_x h_x h}{q}\right)\left(\frac{3\mu^2 - 1}{3}\right)\right], \quad \mu = \frac{z}{h}. \tag{4.128}$$

Moreover, the w velocity profile, as obtained from Eq. (3.54), does not vanish

$$w = +\frac{\partial \psi}{\partial x} = -U_x z = \frac{q}{h}\left(h_x - \frac{q_x h}{q}\right)\mu. \tag{4.129}$$

Equation (4.127) is a 2D solution for the problem of recharge. Note that Eq. (4.124) with $c_1 = 0$ is rewritten as

$$\frac{K}{N}\frac{hh_x}{x} = -1. \tag{4.130}$$

If Eq. (4.130) is differentiated with respect to x, one finds the peculiar relation

$$\frac{hh_{xx} + h_x^2}{3} - \frac{h_x h}{3x} = 0, \tag{4.131}$$

which, when inserted into Eq. (4.119), produces the simplified form

$$q = Nx = -Khh_x. \tag{4.132}$$

This is the DODE equation for the drainage of recharge. The velocity components from Eqs. (4.128) and (4.129) are, upon using Eqs. (4.131) and (4.132),

$$u = \frac{q}{h}\left[1 + \left(\frac{hh_{xx}}{2} - h_x^2 + \frac{q_x h_x h}{q}\right)\left(\frac{3\mu^2 - 1}{3}\right)\right] = \frac{Nx}{h}\left[1 + \left(\frac{hh_{xx}}{6} - \frac{h_x^2}{3} + \frac{h_x h}{3x}\right)(3\mu^2 - 1)\right]$$
$$= \frac{Nx}{h}\left[1 + \left(\frac{1}{2}\left(\frac{h_x h}{3x} - \frac{h_x^2}{3}\right) - \frac{h_x^2}{3} + \frac{h_x h}{3x}\right)(3\mu^2 - 1)\right]$$
$$= \frac{Nx}{h}\left[1 + \left(\frac{hh_x}{x} - h_x^2\right)\left(\frac{3\mu^2 - 1}{2}\right)\right], \tag{4.133}$$

$$w = \frac{q}{h}\left(h_x - \frac{q_x h}{q}\right)\mu = \frac{Nx}{h}\left(h_x - \frac{h}{x}\right)\mu. \tag{4.134}$$

Equation (4.119) is the exact 2D governing equation to second-order accuracy for the drainage of the recharge problem. It yields the generalized water table profile given by Eq. (4.127). The equation does not suffer from limitations of the classical DF model, implying an almost horizontal water table. It is equally valid for

curvilinear flow with recharge. In addition, the horizontal velocity u is not uniform and the vertical velocity is not zero, as evidenced by Eqs. (4.133) and (4.134). For the limiting case at $x = 0$, Eqs. (4.133) and (4.134) yield $u = 0$ and $w = -N$, implying a vertical flow.

Equation (4.127) requires a boundary value for h_o. This value needs to be accurate to obtain precise water table elevations. Nothing is assumed on the existence of seepage faces. The value of h_o may be taken from the complete 2D solution of the groundwater flow problem. The classical assumptions of the DF theory about the surfaces of seepage are unnecessary and highly limited. The model given by Eq. (4.127) is exact to second order. This result agrees with the findings of Rushton and Youngs (2010), stating good agreement between the DF equation and their 2D solution of Laplace's equation, if the boundary condition for the former is adopted from the seepage face height. The usefulness of a 1D approach as compared with the complete 2D solution was, however, theoretically not justified (Castro-Orgaz et al. 2012). To complete the present model, an estimate of the boundary condition h_o is required.

Green's second identity is used to evaluate h_o using the function $\omega = x$ (Chapman 2003; Castro-Orgaz et al. 2012) [see Eq. (4.52) and Fig. 4.24]

$$\oint \omega \frac{\partial \phi}{\partial n} \mathrm{d}s = \oint \phi \frac{\partial \omega}{\partial n} \mathrm{d}s. \tag{4.135}$$

The arguments to evaluate the integrals in Eq. (4.135) are detailed in Table 4.2. The kinematic boundary condition at the free surface is (Bear 1972; Youngs and Rushton 2009; Rushton and Youngs 2010)

$$N\cos\theta_s = K\frac{\partial \phi}{\partial x}\sin\theta_s + K\frac{\partial \phi}{\partial z}\cos\theta_s = K\frac{\partial \phi}{\partial n}. \tag{4.136}$$

This equation represents mass conservation across the phreatic surface. It is required in Eq. (4.135) for the curvilinear integral along the water table surface. The potential, ϕ, is unknown along the boundaries AB and EA. The contribution of the former is zero, whereas that of the latter needs to be evaluated.

Table 4.2 Evaluation of arguments for Green's second identity, Eq. (4.135)

Line	ω	$K\frac{\partial \phi}{\partial n}$	$K\phi$	$\frac{\partial \omega}{\partial n}$
AB	x	0	Unknown	0
BC	L	$-u$	Kh_D	1
CD	L	$-u$	Kz	1
DE	x	Equation (4.136)	Kz	$-\sin\theta_s$
EA	0	0	Unknown; use Eq. (4.139)	-1

Equation (4.10) gives for the piezometric head in the horizontal aquifer

$$\phi = h - \frac{U_x}{2K}\left(h^2 - z^2\right). \tag{4.137}$$

Using $U_x = q_x/h - qh_x/h^2$, Eq. (4.137) yields

$$\phi = h - \frac{1}{2K}(qh_x - q_x h)\left[\left(\frac{z}{h}\right)^2 - 1\right]. \tag{4.138}$$

At $x = 0$, where $h = h_o$ and $h_x = 0$, Eq. (4.138) simplifies to

$$\phi = h_o - \frac{q_x}{2Kh_o}\left(h_o^2 - z^2\right) = h_o - \frac{N}{2Kh_o}\left(h_o^2 - z^2\right). \tag{4.139}$$

Equation (4.139) is identical to the potential distribution proposed by Chapman (2003), who assumed the streamlines near $x = 0$ as curves xz = const., and the equipotentials $x^2 - z^2$ = const. Therefore, our analysis based on the Picard iteration confirms that Eq. (4.139) is generally valid to this order of accuracy. In addition, the role of the kinematic boundary condition for ϕ is clearly specified with Eq. (4.136). Inserting each term of Table 4.2 into Eq. (4.135), one finds h_o as follows. The left-hand side of the identity in Eq. (4.135), after multiplying it with K, is given by

$$\begin{aligned}
\oint \omega K \frac{\partial \phi}{\partial n} \mathrm{d}s &= \int_{\mathrm{A}}^{\mathrm{B}} x(0)\mathrm{d}x + \int_{\mathrm{B}}^{\mathrm{C}} L(-u)\mathrm{d}z + \int_{\mathrm{C}}^{\mathrm{D}} L(-u)\mathrm{d}z + \int_{\mathrm{D}}^{\mathrm{E}} xN\cos\theta_{\mathrm{s}}(-\mathrm{d}s) \\
&= \int_{\mathrm{B}}^{\mathrm{D}} L(-u)\mathrm{d}z - \int_{\mathrm{D}}^{\mathrm{E}} xN\mathrm{d}x = -L\int_{\mathrm{B}}^{\mathrm{D}} u\mathrm{d}z - \int_{\mathrm{D}}^{\mathrm{E}} xN\mathrm{d}x \\
&= -L(NL) - N\left(\frac{x^2}{2}\right)_L^0 = -\frac{NL^2}{2}.
\end{aligned} \tag{4.140}$$

The right-hand side of the identity in Eq. (4.135) is

$$\begin{aligned}
\oint K\phi \frac{\partial \omega}{\partial n} \mathrm{d}s = &\int_{\mathrm{A}}^{\mathrm{B}} K\phi(0)\mathrm{d}x + \int_{\mathrm{B}}^{\mathrm{C}} Kh_D\mathrm{d}z + \int_{\mathrm{C}}^{\mathrm{D}} Kz\mathrm{d}z \\
&+ \int_{\mathrm{D}}^{\mathrm{E}} (-\sin\theta_s)Kz(-\mathrm{d}s) + \int_{\mathrm{E}}^{\mathrm{A}} K\phi(-1)(-\mathrm{d}z).
\end{aligned} \tag{4.141}$$

Using for the potential function along AE, the parabolic law given by Eqs. (4.139) and (4.141) takes the form

$$\begin{aligned}\oint K\phi\frac{\partial\omega}{\partial n}\mathrm{d}s &= Kh_D^2+\int_{\mathrm{C}}^{\mathrm{E}}Kz\mathrm{d}z+\int_{\mathrm{E}}^{\mathrm{A}}\left[Kh_o-\frac{N}{2h_o}\left(h_o^2-z^2\right)\right]\mathrm{d}z\\ &= Kh_D^2+K\left(\frac{z^2}{2}\right)_{h_D}^{h_o}+\int_{\mathrm{E}}^{\mathrm{A}}Kh_o\mathrm{d}z-\int_{\mathrm{E}}^{\mathrm{A}}\left(h_o^2-z^2\right)\frac{N}{2h_o}\mathrm{d}z\\ &= Kh_D^2+K\left(\frac{z^2}{2}\right)_{h_D}^{h_o}+Kh_o(z)_{h_o}^0-\left(\frac{N}{2h_o}\right)\left[h_o^2z-\frac{z^3}{3}\right]_{h_o}^0\\ &= Kh_D^2+K\left(\frac{h_o^2-h_D^2}{2}\right)-Kh_o^2+N\frac{h_o^2}{3}.\end{aligned}\tag{4.142}$$

Equating Eqs. (4.140) and (4.142) results in

$$-\frac{NL^2}{2}=Kh_D^2+K\left(\frac{h_o^2-h_D^2}{2}\right)-Kh_o^2+N\frac{h_o^2}{3},\tag{4.143}$$

or

$$\frac{Kh_o^2}{2}-N\frac{h_o^2}{3}=K\frac{h_D^2}{2}+\frac{NL^2}{2},\tag{4.144}$$

from which (Chapman 2003; Castro-Orgaz et al. 2012)

$$h_o^2=\frac{h_D^2+\frac{N}{K}L^2}{1-\frac{2}{3}\frac{N}{K}}.\tag{4.145}$$

Its denominator must not be zero, i.e., $3K/N-2\neq 0$; this is also a critical relation required to ensure that $c_1 = 0$ for Eq. (4.124). Equation (4.145) is therefore the generalized second-order result for the upstream boundary condition h_o, originally due to Chapman (2003) by assuming the parabolic distribution of ϕ in Eq. (4.139) and by Castro-Orgaz et al. (2012) using Picard's iteration. These results demonstrate that this function arises from a second-order approximation to the 2D seepage problem.

Equation (4.145) was also obtained by Knight (2005), still employing another approach. Using Eq. (4.145), the generalized result for the water table profile is, from Eq. (4.127),

$$h^2=\left[h_D^2+\frac{N}{K}\left(L^2-x^2\right)+\frac{2}{3}\left(\frac{N}{K}\right)^2x^2\right]\left(1-\frac{2}{3}\frac{N}{K}\right)^{-1}.\tag{4.146}$$

An immediate inference of Eq. (4.146) is the evaluation of h_s, the height of the surface of seepage at $x = L$ (Fig. 4.24),

$$h_s^2 = \left[h_D^2 + \frac{2}{3}\left(\frac{N}{K}\right)^2 L_2\right]\left(1 - \frac{2}{3}\frac{N}{K}\right)^{-1}. \tag{4.147}$$

With the second-order truncation of Picard's iteration and the lack of proof of convergence, it is important to compare the approximate 2D results with detailed 2D solution procedures. Two problems are selected. The first specifies different combinations of the drainage of recharge as investigated by Hornung and Krueger (1985) and Rushton and Youngs (2010). The second problem involves a toe drain on an infinite impermeable layer solved analytically by Engelund (1951).

Equation (4.146) is compared in Fig. 4.25 with the 2D seepage water table results of Rushton and Youngs (2010) based on a finite-difference solution of the Laplace equation

$$\frac{\partial^2 \phi}{\partial x^2} + \frac{\partial^2 \phi}{\partial z^2} = 0 \tag{4.148}$$

subject to the boundary conditions (Fig. 4.24)

$$\begin{array}{ll} \frac{\partial \phi}{\partial z} = 0 & \text{on AB} \\ \phi = h_D & \text{on BC} \\ \phi = z & \text{on CD} \\ \phi = h & \text{on DE} \\ \frac{N}{K}\cos\theta_s = \frac{\partial \phi}{\partial x}\sin\theta_s + \frac{\partial \phi}{\partial z}\cos\theta_s & \text{on DE} \\ \frac{\partial \phi}{\partial x} = 0 & \text{on EA.} \end{array} \tag{4.149}$$

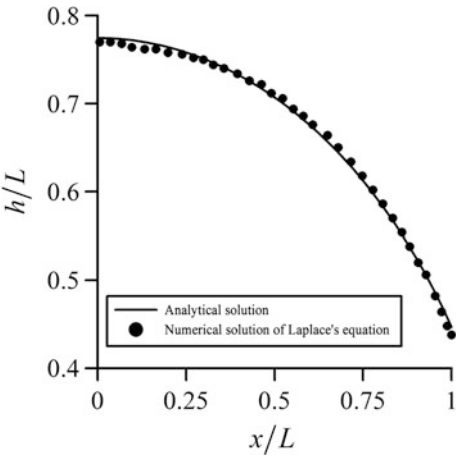

Fig. 4.25 Recharge to symmetrically located downstream boundaries for $N/K = 0.4$ and $h_D/L = 0.2$: comparison of 2D finite-difference results by Rushton and Youngs (2010) with Eq. (4.146) (adapted from Castro-Orgaz et al. 2012)

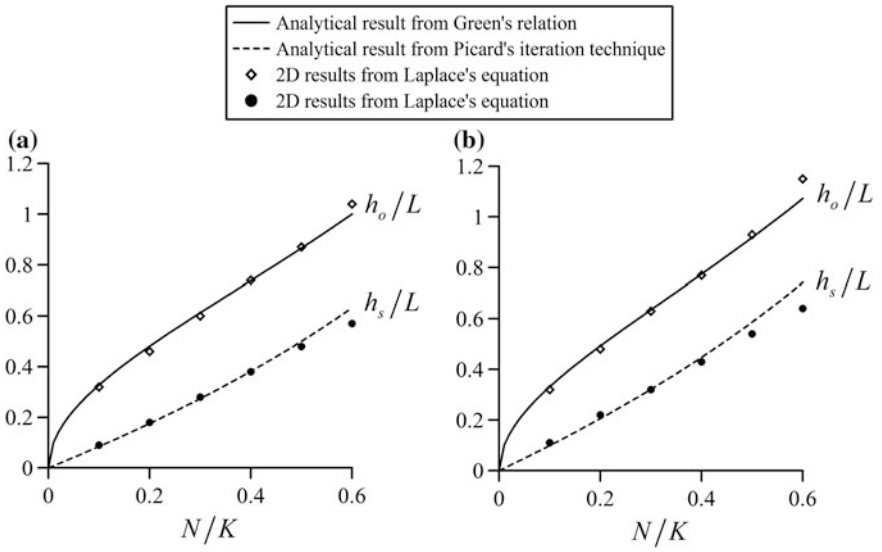

Fig. 4.26 Comparison of ratios h_o/L and h_s/L from the 2D solution of the Laplace equation (Rushton and Youngs 2010) for **a** $h_D/L = 0$, **b** $h_D/L = 0.5N/K$ against Eqs. (4.145) and (4.147) (adapted from Castro-Orgaz et al. 2012)

Figure 4.25 indicates good agreement between the numerical solution of the 2D problem given by Eq. (4.148) subject to conditions stated by Eqs. (4.149), and the 2D Picard solution to second-order accuracy given by Eq. (4.146).

Rushton and Youngs (2010) presented numerical values for h_o/L and h_s/L from Laplacian simulations for two test cases: (a) $h_D/L = 0$ (Fig. 4.26a) and (b) $h_D/L = 0.5N/K$ (Fig. 4.26b). These are compared with estimates given by Eqs. (4.145) and (4.147), respectively. The good agreement of the approximate 2D model based on the Picard iteration is noted. Therefore, the empirical fittings to h_s/L proposed by Rushton and Youngs (2010) to find the free surface profile are replaced by the analytical approach given by Eqs. (4.145), (4.146), and (4.147). The Picard iteration method demonstrates that Eq. (4.127), the so-called DF ellipse of drainage, is not a 1D model. In fact, it is an exact 2D solution of second-order accuracy, justified by the success of its comparison with the 2D numerical results (Castro-Orgaz et al. 2012).

Hornung and Krueger (1985) presented numerical simulations of the water table for $N/K = 0.4$ and 0.1, using $h_D/L = 0$. Their results are compared in Fig. 4.27a with Eq. (4.146), indicating good agreement. Their values of h_o/L and h_s/L are compared against estimates of Eqs. (4.145) and (4.147), respectively, in Fig. 4.27b, resulting in good agreement for $N/K < 0.6$. Youngs' drainage inequality is (Youngs 1965)

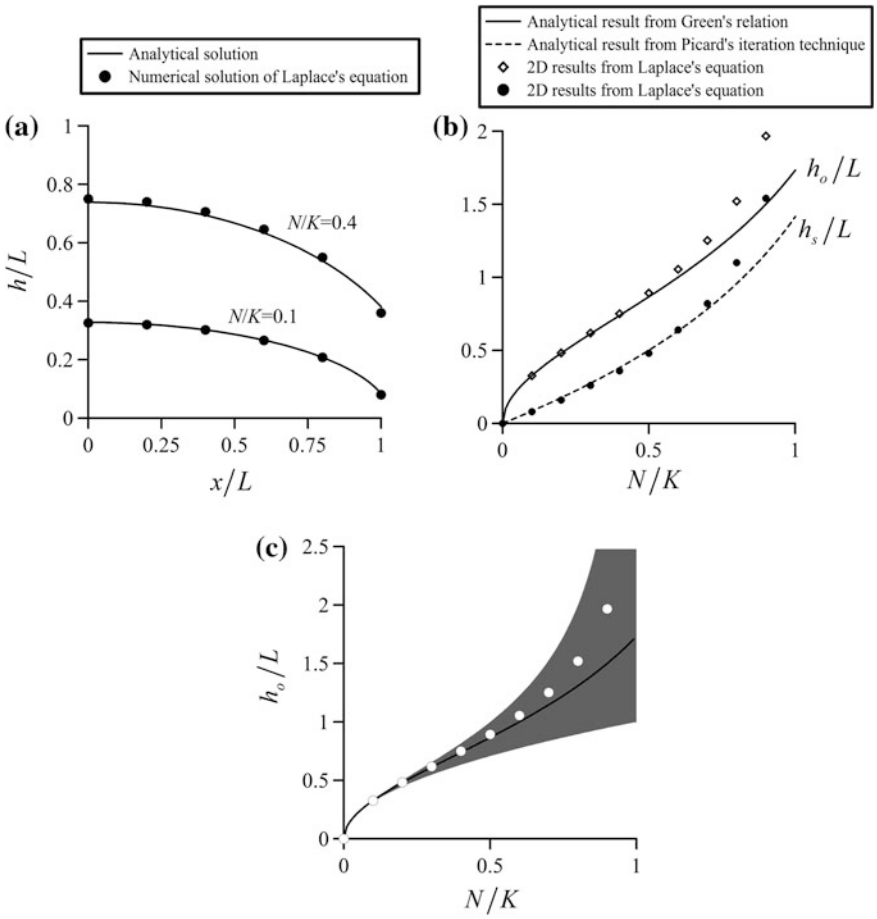

Fig. 4.27 Recharge to symmetrically located downstream boundaries: **a** comparison of 2D seepage water table results by Hornung and Krueger (1985) for $N/K = 0.4$ and 0.1 and $h_D/L = 0$ with Eq. (4.146), **b** comparison of h_o/L and h_s/L from 2D solution of the Laplace equation (Hornung and Krueger 1985) for $h_D/L = 0$ against Eqs. (4.145) and (4.147), **c** Eq. (4.145) for $h_D/L = 0$ and 2D data by Hornung and Krueger (1985) plotted in the drainage inequality diagram of Youngs (1965) (shaded area) (adapted from Castro-Orgaz et al. 2012)

$$\frac{N}{K} \leq h_o^2 \leq \frac{N}{K}\left(1 - \frac{N}{K}\right)^{-1}. \tag{4.150}$$

It is plotted as shadowed domain in Fig. 4.27c, in which the results of Hornung and Krueger (1985) and Eq. (4.145) demonstrate that the latter satisfies Eq. (4.150).

The problem of drainage of recharge with symmetric downstream boundaries is one of the basic and important problems in groundwater hydrology (Kirkham 1967; Rushton and Youngs 2010). This problem may be tackled either by using the

complete 2D solution of the Laplace equation for the hydraulic head, or by using the DF approximation.

The latter 1D theory is presented in papers and books starting with a water table of small inclination, thereby leading to a flow with almost parallel, horizontal streamlines. The limitations of the DF theory are (Bear 1972):

- Almost horizontal water table.
- Almost horizontal flows, so that the vertical velocity needs to be zero, or very small, invalidating the DF theory in the case shown in Fig. 4.24 at $x = 0$, because, there, the vertical velocity is not zero but given by $w = -N$, despite $h_x = 0$.
- Classical DF solution for the case of Fig. 4.24 assumes that the water table reaches the water level h_D, which is equivalent to neglecting the surface of seepage.

The traditional DF approach, as summarized above, was revised by Rushton and Youngs (2010), and the following was outlined in their study:

- DF equation is a 1D model which may be solved subjected to a boundary condition at an undefined position. Rushton and Youngs (2010) indicate that there is no reason why this should not be enforced as a downstream boundary condition.
- Better water table estimations are obtained if the seepage surface is taken as boundary condition.
- For this task, a 2D numerical model was used to solve the problem. Numerical results for the surface of seepage height were fitted to empirical relations to be used in the classical DF differential equation.
- No explanations of reasons are given why this approach is successful for comparisons with the 2D model. Their proposed model also depends on the empirical relations developed for the boundary condition at the seepage surface.

A simple method to obtain higher-order solutions is the Picard iteration method (Matthew 1991). Based on the second-order solution with this technique, the following inferences were found (Castro-Orgaz et al. 2012):

- The DF theory is not limited to flows with $h_x \approx 0$. The local discharge relation $q = -Khh_x$ is generally valid for curvilinear flows with recharge if there is a local equilibrium given by $hh_{xx} + h_x^2 = hh_x/x$, with $N/K < 3/2$. This relation was found to be exact for the drainage of recharge with symmetrically located downstream boundaries (Fig. 4.24). Then, the discharge relation $Nx = -Khh_x$ is the exact differential equation governing the shape of the water table, to second-order accuracy; it is associated with non-uniform horizontal and vertical velocities, given by Eqs. (4.133) and (4.134).
- The differential equation $Nx = -Khh_x$ yields a generalized water table profile function with a water depth boundary condition to be determined. Based on the 2D computation using Green's second identity for harmonic functions, the boundary condition at $x = 0$ was found. The final result is a drainage ellipse,

similar to the classical DF ellipse, but with the correct boundary condition based on the 2D results. It is therefore not necessary to use any empirical relation for the seepage height, h_s, as a boundary condition. Instead, an analytical 2D result for h_D is available.

- Picard's iteration DF ellipse, Eq. (4.146), provides an analytical expression for the height of the seepage surface, Eq. (4.147). It demonstrates that there are no implicit assumptions about the existence of the seepage surfaces in the DF equation. The existence of a seepage surface is demonstrated to be a result of the model itself.
- The result of an improved DF theory, given by Picard's iteration technique, is different from the DF theory of Kirkham (1967). He obtained as a result of his DF "soil" a flow net composed of curvilinear streamlines and vertical equipotentials, invalidating the normal intersection of both families of curves. In contrast, the present second-order result has nothing implicit about these conditions, so that orthogonality of the flow net is preserved.

Engelund (1951) considered the problem of drainage of recharge for a toe drain overlying an impermeable stratum (Fig. 4.28). He applied the hodograph transformation to solve the 2D problem, finding with L as the lateral distance to the point at which $h = 0$ that the water table elevation is given by the ellipse

$$h^2 = \frac{N}{K}\left(L^2 - x^2\right) \quad \Rightarrow \quad \frac{h^2}{\left(\frac{NL^2}{K}\right)} + \frac{x^2}{L^2} = 1. \tag{4.151}$$

Youngs (2012) indicated that Eqs. (4.127) and (4.151) may match under different assumptions. Equation (4.127) was demonstrated to be a 2D solution, of which the boundary condition should be a particular point of the 2D problem. Setting $h(x = L) = 0$ in Eq. (4.127) yields

$$h_o^2 = \frac{N}{K}L^2. \tag{4.152}$$

After inserting Eq. (4.152) into Eq. (4.127), Eq. (4.151) is regained. Therefore, the 2D solution obtained by Picard's iteration to second-order accuracy is identical to the 2D solution obtained by Engelund (1951), if the boundary condition used in Eq. (4.127) is itself a point of the 2D solution. Engelund's solution may be further

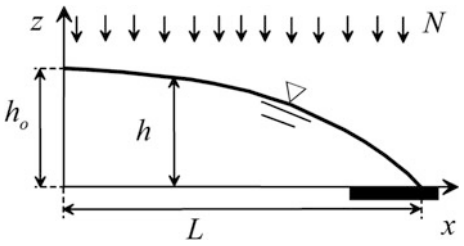

Fig. 4.28 Saturated flow domain of aquifer under uniform recharge rate N with toe drain resting on an impermeable layer (Engelund 1951) (adapted from Castro-Orgaz et al. 2012)

compared with that obtained by Picard iteration in terms of stream and potential functions, from which the full 2D problem is defined. Engelund's full 2D solution is

$$x^2 - z^2 - \left(1 - \frac{N}{K}\right)^2 L^2 = \frac{\psi^2}{NK} - \frac{NK}{\psi^2} x^2 z^2, \tag{4.153}$$

$$x^2 - z^2 - \left(1 - \frac{N}{K}\right)^2 L^2 = -\frac{K\phi^2}{N} + \frac{N}{K\phi^2} x^2 z^2. \tag{4.154}$$

Using the water table differential equation $Khh_x = -Nx$, the velocity profile given by Eq. (4.133) is rewritten from the Picard iteration as

$$\begin{aligned} u = -\frac{\partial \psi}{\partial z} &= \frac{Nx}{h}\left[1 + \left(\frac{hh_x}{x} - h_x^2\right)\left(\frac{3\mu^2 - 1}{2}\right)\right] \\ &= \frac{Nx}{h}\left[1 - \left(\frac{N}{K} + \left(\frac{N}{K}\right)^2 \left(\frac{x}{h}\right)^2\right)\left(\frac{3\mu^2 - 1}{2}\right)\right]. \end{aligned} \tag{4.155}$$

Integrating this equation over the depth yields the stream function ψ as

$$\psi = -Nx\left[\mu - \frac{1}{2}\left(\frac{N}{K}\right)\left(1 + \left(\frac{N}{K}\right)\left(\frac{x}{h}\right)^2\right)(\mu^3 - \mu)\right]. \tag{4.156}$$

On the other hand, Eq. (4.138) yields for the potential function

$$\begin{aligned} \phi &= h - \frac{1}{2K}(qh_x - q_x h)\left[\left(\frac{z}{h}\right)^2 - 1\right] = h - \frac{1}{2K}\left[-\frac{(Nx)^2}{Kh} - Nh\right]\left[\left(\frac{z}{h}\right)^2 - 1\right] \\ &= h\left[1 + \frac{1}{2}\frac{N}{K}\left(1 + \frac{N}{K}\left(\frac{x}{h}\right)^2\right)(\mu^2 - 1)\right]. \end{aligned} \tag{4.157}$$

With the normalized variables $\tilde{\phi} = \phi/h$ and $\tilde{\psi} = \psi/(-Nx)$, and using Eq. (4.151) for h, Eqs. (4.156) and (4.157) are compared in Fig. 4.29 with Eqs. (4.153) and (4.154) for $N/K = 0.2$. Compare $\tilde{\psi}$ between both methods at positions $x/L = 0.2$, 0.4, and 0.6 in Fig. 4.29a–c, and for $\tilde{\phi}$ in Fig. 4.29d–f. Note that the agreement between the full 2D solution and Picard's second-order approximation is excellent for $\tilde{\psi}$ and good for $\tilde{\phi}$. Deviations increase as the boundary condition $h = 0$ is approached, as expected from the mathematical approximation in Eqs. (4.156) and (4.157).

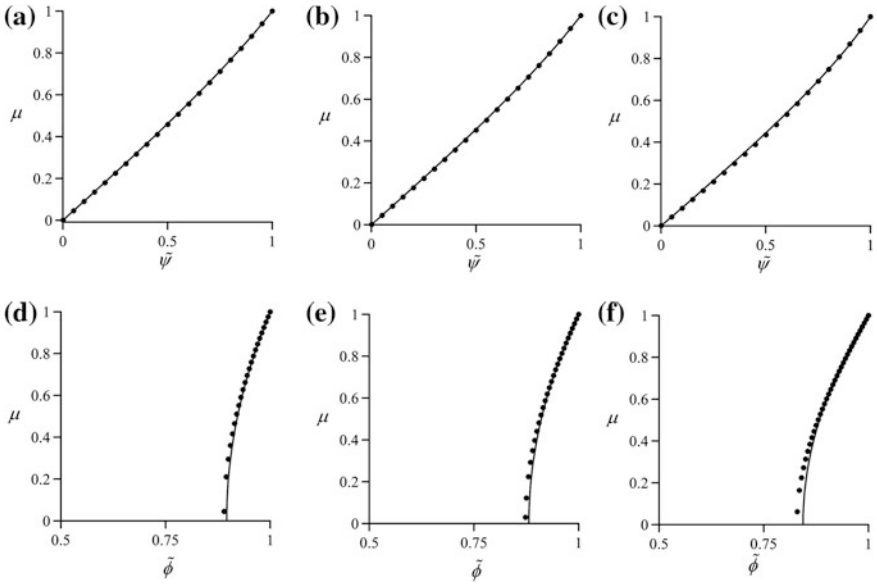

Fig. 4.29 Comparison of results from (•) Eqs. (4.153) and (4.154) with (—) Eqs. (4.156) and (4.157) for $N/K = 0.2$ at positions $x/L =$ **a**, **d** 0.2; **b**, **e** 0.4; **c**, **f** 0.6 (adapted from Castro-Orgaz et al. 2012)

4.6.2 Sloping Aquifer

Consider steady-state groundwater flow with a uniform accretion rate N in a sloping aquifer. This is a case of practical interest in the drainage of soils and railways (Youngs and Rushton 2009). Equation (4.18) then simplifies to

$$\frac{Nx}{h}\left(1 + h_x z_{bx} + z_{bx}^2 + \frac{hh_{xx} + h_x^2}{3} - \frac{h_x h}{3x}\right) + K(h_x + z_{bx}) = 0. \tag{4.158}$$

An inclined aquifer of bottom slope $z_{bx} = -0.4$ is considered in Fig. 4.30a for $N/K = 0.3$. The 2D data of the water table profile determined by Youngs and Rushton (2009) solving numerically the Laplace equation are plotted too. Equation (4.158) was numerically integrated using the fourth-order Runge–Kutta method (Press et al. 2007). The flow depth at the water divide given by the 2D data was used as boundary condition. The comparison indicates that Eq. (4.158) provides an accurate estimation of the water table profile, with small deviations as the seepage face is approached at $x = L$, with L as aquifer length. A step $\Delta x = 0.01L$ was used, because a further reduction in the step produces essentially the same results. A second simulation for $N/K = 0.2$ shown in Fig. 4.30b corroborates the accuracy of Eq. (4.158), indicating a better prediction of the seepage face

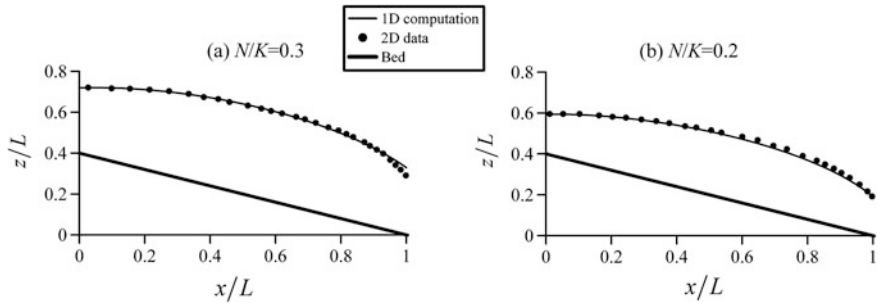

Fig. 4.30 Water table profiles in sloping aquifer for N/K = **a** 0.3, **b** 0.2 (adapted from Castro-Orgaz and Hager 2014)

height at $x = L$. Note that Matthew's theory predicts the existence of the seepage surface, a major drawback of the DF theory (Knight 2005).

4.6.3 Curved Aquifer

A relevant problem of potential flow with bed curvature involves shallow phreatic flow over a curved impermeable bed (Chapman and Dressler 1984; Chapman and Ong 2006). For this case, Eq. (4.18) simplifies to

$$\frac{Nx}{h}\left(1+h_x z_{bx}+z_{bx}^2+\frac{hz_{bxx}}{2}+\frac{hh_{xx}+h_x^2}{3}-\frac{h_x h}{3x}\right)+K(h_x+z_{bx})=0. \tag{4.159}$$

Equation (4.159) is based on $q = Nx$, so that $q_x = N$ and $q_{xx} = 0$. These conditions correspond to a recharge of uniform intensity along the water table (N = const.) in a symmetrical aquifer with respect to a water divide ($q = 0$ at $x = 0$). Chapman and Ong (2006) studied flow over a curved impermeable bed of shape closely approximating many field profiles in hill slope hydrology

$$\frac{z}{L}=A\left[\frac{\left(1-\frac{x}{L}\right)^{\beta}}{\beta}-\frac{\left(1-\frac{x}{L}\right)^{\gamma}}{\gamma}\right]. \tag{4.160}$$

They obtained the 2D solution of the Laplace equation for this wavy bed shape (A = 3.7, β = 2.8, γ = 3.3). The 2D results for N/K = 0.10 and 0.02 are plotted in Fig. 4.31. Equation (4.159) was numerically integrated using the flow depth at the water divide given by the 2D data as boundary condition. The comparisons shown in Fig. 4.31 indicate that Eq. (4.159) is an excellent predictor of shallow flows over

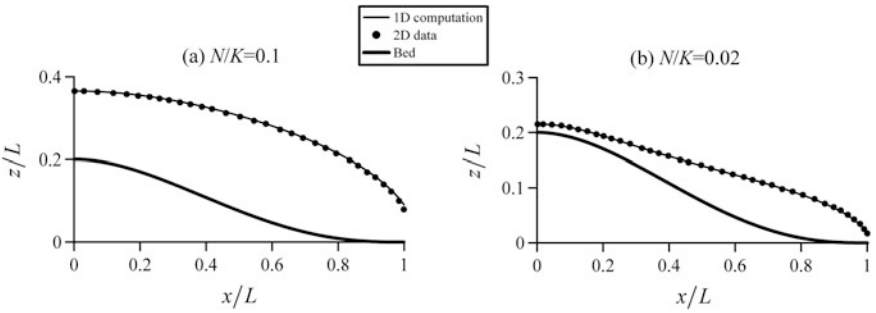

Fig. 4.31 Water table profiles over curved impermeable bed for N/K = **a** 0.10, **b** 0.02 (adapted from Castro-Orgaz and Hager 2014)

curved impermeable beds. These predictions are more accurate than those of Chapman and Ong (2006) using a simplified form of the Chapman and Dressler (1984) equations.

4.7 Flow Over Planar Bedrock with Slope Discontinuity

Groundwater flow in unconfined aquifers is characterized by a free (phreatic) surface and nonlinear boundary conditions there. Common catchment-scale reconnaissance models or regular annual assessment of aquifer resources utilize a hydraulic DF approximation, which in a steady regime requires solution of a boundary-value problem for a second-order ODE. A more general potential theory solves Laplace's equation, provided the aquifer is homogeneous. In arid climate with little recharge from the vadose zone to the water table, the main factor controlling its shape and locus is the subjacent bedrock whose geometry is commonly inferred from geological data. The degree of steepness, position of the water table, and other aquifer characteristics are vital because groundwater is the main resource for agriculture in many countries. In standard DF or potential models, the bedrock boundary of an unconfined aquifer is assumed to be planar. Kacimov et al. (2015) considered an aquifer with an underlying aquifuge whose inclination changes abruptly from the aquifer's upstream slope to the downstream portion. They applied two different techniques: The hodograph method to find the 2D solution and Picard's iteration scheme to produce the corresponding 1D result. Darcian flow was assumed, whereas the capillary fringe, accretion, or evapotranspiration to/from the vadose zone and any sinks–sources (e.g., pumping wells) in the flow domain were ignored.

The bedrock considered is a slope break with an upstream angle α and a reduced inclination angle at the tailwater reach, $\beta < \alpha$. For steady discharge over a planar slope, Eq. (4.18) reduces to

$$\frac{q}{h}\left(1 + h_x z_{bx} + z_{bx}^2 + \frac{h h_{xx} + h_x^2}{3}\right) + K(h_x + z_{bx}) = 0. \tag{4.161}$$

Far up- and downstream of the slopes, the flow is uniform, i.e., $h_x = h_{xx} = 0$. The corresponding (normal) asymptotic depths h_N on each slope are from Eq. (4.161)

$$h_N = -\frac{q}{K}\frac{(1 + z_{bx}^2)}{z_{bx}}. \tag{4.162}$$

Equation (4.161) must be integrated numerically. At a section $x = x_u$ along the upstream slope, a boundary flow depth $h_u = \varepsilon(h_N)_u$ is adopted, with ε as a parameter close to unity, to account for the value of h_N as an asymptotic value not reached at section x_u. At x_u, the value $h_x = 0$ is set in the numerical model. With these boundary conditions at $x = x_u$, Eq. (4.161) was numerically integrated using the fourth-order Runge–Kutta method (Press et al. 2007) until reaching a section $x = x_d$ on the downstream slope. The computed value of the flow depth at this section is h_d. For a physically correct solution, h_d must be close to $(h_N)_d$. Thus, the value h_u was iterated until reaching h_d close to $(h_N)_d$, keeping simultaneously h_u close to $(h_N)_u$. During the numerical computations, continuity of the free surface slope at the slope break section is given by

$$\frac{dz_s}{dx} = (z_{bx} + h_x)_u = (z_{bx} + h_x)_d. \tag{4.163}$$

Figure 4.32 shows the computational results for $\alpha = 0.35\pi$, $\beta = 0.1\pi$, with the scalings used to obtain non-dimensional variables from physical variables as $(X, Y) = (x, z)\pi K/(2q)$, indicating excellent agreement between the 2D and 1D models.

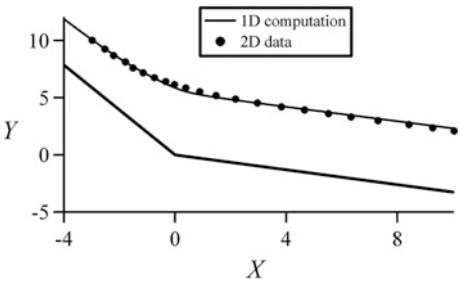

Fig. 4.32 Phreatic surface for $\alpha = 0.35\pi$, $\beta = 0.1\pi$ (adapted from Kacimov et al. 2015)

4.8 Bank Storage Problem

4.8.1 Picard's Iteration for Anisotropic Porous Media

Transient flow in unconfined aquifers is successfully simulated in practical situations using the Dupuit approximation by assuming horizontal flow with a hydrostatic pressure distribution (Bear 1972; Hager 2004). The combination of the depth-averaged mass conservation equation (Eq. 4.19) with the assumption of purely horizontal, uniformly depth-distributed velocity generates the well-known DF theory. From this approach stems the widely used Boussinesq equation for transient flow in phreatic aquifers (Bear 1972; Serrano 2003). The validity of the DF theory is limited to aquifers with a horizontal length much greater than the vertical extent (Bear 1972; Serrano 1995; Liu and Wen 1997; Knight 2005). For modeling unsteady flow in unconfined aquifers, the next level of approximation considers the effects of non-hydrostatic pressure and non-uniform velocity distributions (Dagan 1967; Bear 1972; Liu and Wen 1997; Knight 2005). Dagan (1967) used a perturbation method in which the flow variables are expanded in terms of a small parameter representing the ratio of the aquifer thickness to its length. Dagan (1967) found that the first-order terms reproduce the DF theory, whereas the second-order terms account for the non-hydrostatic pressure distribution. Dagan's solution is applicable to isotropic porous media. Nielsen et al. (1997) and Liu and Wen (1997) also obtained Dagan's second-order equation using alternative approximations. Nielsen et al. (1997) obtained an estimate of the vertical velocity profile using the Dupuit approximation in combination with the 2D continuity equation. Liu and Wen (1997) expanded the piezometric head in a power series of the vertical elevation, a technique widely used to model unsteady water waves (Wei et al. 1995).

Hunt (2005) revealed that the DF theory becomes invalid in very shallow aquifers if the anisotropy of the medium is high. Anisotropy effects are not accounted for in the second-order equations of Dagan (1967) or Liu and Wen (1997), preventing a systematic comparison of their solutions with the Boussinesq equation, or with the full 2D solution to the water table elevation problem. Given that including the anisotropy of the medium is of both practical and theoretical relevance, the derivation of unsteady second-order equations accounting for it will be considered. The accuracy of the resulting generalized second-order model is checked against the full 2D solution in anisotropic porous media, using the bank storage problem as a test case. The 1D non-hydrostatic model is also compared with the Boussinesq equation.[2]

[2]In open-channel hydraulics, a "Boussinesq" equation incorporates the non-hydrostatic pressure distribution. In groundwater hydraulics, the "Boussinesq equation" is used to denote a hydrostatic flow model obtainable by using the depth-averaged mass conservation equation and the DF theory.

For the bank storage case, an analytical solution to the second-order equation is derived and compared with a relevant numerical method, applicable to this specific test case as well as to other transient flow problems. For incompressible, unsteady 2D groundwater flow in anisotropic and homogeneous porous media, the velocity components in the x- and z-directions with t as time, given by $u(x, z, t)$ and $w(x, z, t)$, respectively, are related by the equations (Bear 1972)

$$u = -K_h \frac{\partial \phi}{\partial x} = -\frac{\partial \psi}{\partial z}, \tag{4.164}$$

$$w = -K_v \frac{\partial \phi}{\partial z} = +\frac{\partial \psi}{\partial x}. \tag{4.165}$$

Here, ψ is the stream function, ϕ the potential function or piezometric head, and K_h and K_v are the hydraulic conductivities in the x- and z-directions, respectively. The second of Eqs. (4.164) is

$$u = -\frac{\partial \psi}{\partial z}. \tag{4.166}$$

Integrating it in the vertical direction, using the depth-averaged velocity $U = q/h$ as first approximation to u yields

$$\psi = -Uz, \tag{4.167}$$

which satisfies the condition at the bottom streamline $\psi(z = 0) = 0$. Using the second Eq. (4.165), and Eq. (4.167), produces

$$w = +\frac{\partial \psi}{\partial x} = -U_x z. \tag{4.168}$$

The first Eq. (4.165) states

$$w = -K_v \frac{\partial \phi}{\partial z}, \tag{4.169}$$

delivering ϕ by integration in the vertical direction, with f as an arbitrary function of x and t,

$$-\phi = \frac{1}{K_v}\left[-U_x \frac{z^2}{2} + f(x, t)\right]. \tag{4.170}$$

Using Eq. (4.170) in the first Eq. (4.164) produces the expression

$$u = -K_h \frac{\partial \phi}{\partial x} = -\frac{K_h}{K_v} U_{xx} \frac{z^2}{2} + \frac{K_h}{K_v} f_x. \tag{4.171}$$

Inserting Eq. (4.171) into Eq. (4.166) and integrating the emerging equation with respect to z leads to

$$\psi = \frac{K_h}{K_v} U_{xx} \frac{z^3}{6} - \frac{K_h}{K_v} f_x z. \tag{4.172}$$

Equation (4.172) is used to obtain f_x subject to the boundary condition of the stream function at the free surface

$$\psi[x, z = h(x,t), t] = -q(x,t). \tag{4.173}$$

Using Eq. (4.173) in Eq. (4.172) results in

$$f_x = \frac{K_v}{K_h} U + U_{xx} \frac{h^2}{6}. \tag{4.174}$$

Inserting this into Eq. (4.171) yields

$$u(x,z,t) = U(x,t) + \frac{K_h}{K_v} U_{xx} \left(\frac{h^2}{6} - \frac{z^2}{2} \right). \tag{4.175}$$

The boundary condition for the potential function at the free surface is

$$\phi[x, z = h(x,t), t] = h(x,t). \tag{4.176}$$

Inserted into Eq. (4.170) renders f from the expression

$$-K_v h = -U_x \frac{h^2}{2} + f(x,t). \tag{4.177}$$

Solving Eq. (4.177) for f and then inserting the result into Eq. (4.170) produces

$$-K_v \phi = -K_v h + \frac{U_x}{2} \left(h^2 - z^2 \right). \tag{4.178}$$

Using Eq. (4.178) in the first Eq. (4.164) produces the identity

$$u = -K_h \frac{\partial \phi}{\partial x} = -K_h h_x + \frac{K_h}{K_v} \frac{U_{xx}}{2} \left(h^2 - z^2 \right) + \frac{K_h}{K_v} U_x h h_x. \tag{4.179}$$

Equation (4.175) at the water table ($z = h$) yields

$$u_s = U - \frac{K_h}{K_v} U_{xx} \frac{h^2}{3}, \tag{4.180}$$

whereas from Eq. (4.179), one obtains

$$u_s = -K_h h_x + \frac{K_h}{K_v} U_x h h_x. \tag{4.181}$$

Equating Eqs. (4.180) and (4.181), the differential equation for the water table is obtained as

$$U - \frac{K_h}{K_v}\left(U_x h_x h + U_{xx}\frac{h^2}{3}\right) + K_h h_x = 0. \tag{4.182}$$

Using the relations

$$U_x = \frac{q_x}{h} - \frac{q h_x}{h^2}, \quad U_{xx} = \frac{q_{xx}}{h} - \frac{q h_{xx}}{h^2} + 2\frac{q h_x^2}{h^3} - 2\frac{q_x h_x}{h^2} \tag{4.183}$$

in Eq. (4.182) yields

$$\frac{q}{h} + \frac{K_h}{3K_v}\left(q h_{xx} + \frac{q h_x^2}{h} - q_{xx} h - q_x h_x\right) + K_h h_x = 0. \tag{4.184}$$

Equation (4.184) is an iteratively derived second-order ODE describing unsteady flow in porous media. This equation is different from that presented by Dagan (1967). However, as to be discussed, both equations become similar for shallow flow. For cases with steady flow and a spatially uniform groundwater accretion rate, this equation simplifies to that of Castro-Orgaz et al. (2012) to study steady recharge with symmetrically located boundaries (Eq. 4.119). Furthermore, for steady flow through an earth dam, Eq. (4.184) simplifies to Eq. (4.22). Therefore, Eq. (4.184) generalizes previously obtained results for steady-state problems. The discharge $q(x, t)$ and the free surface elevation $h(x, t)$ result from coupling Eq. (4.184) with the depth-integrated mass conservation equation (Bear 1972)

$$S\frac{\partial h}{\partial t} = N - \frac{\partial q}{\partial x}. \tag{4.185}$$

Here, $N(x, t)$ is the groundwater accretion rate and S is the specific yield. Equation (4.184) is rewritten, with $r = K_h/K_v$ as the anisotropy ratio, as

$$q + \frac{r}{3}\left[q\left(hh_{xx} + h_x^2\right) - q_x h_x h - q_{xx} h^2\right] + K_h h h_x = 0. \tag{4.186}$$

Solving Eq. (4.186) for q yields

$$q = -K_h h h_x \left[\frac{1 - \frac{r}{K_h h h_x}\left(\frac{q_x h_x h + q_{xx} h^2}{3}\right)}{1 + r\left(\frac{hh_{xx} + h_x^2}{3}\right)}\right]. \tag{4.187}$$

The discharge derivative, q_x, in Eq. (4.187) is given implicitly by Eq. (4.185). Equation (4.187) consists of a DF term ($-Khh_x$) (Knight 2005), multiplied by a correction factor; an approximation to the latter by assuming shallow flow conditions follows the steps applied to Eq. (4.93) for isotropic soil. The shallow flow approximation for q is given by the DF differential equation for the water table (Bear 1972)

$$q = -K_h h h_x. \tag{4.188}$$

Differentiation of Eq. (4.188) provides the first derivative of the discharge as

$$q_x = -K_h\left(hh_{xx} + h_x^2\right). \tag{4.189}$$

The second derivative is obtained using Eq. (4.189) as

$$q_{xx} = -K_h(3h_x h_{xx} + hh_{xxx}). \tag{4.190}$$

Inserting Eqs. (4.189) and (4.190) into Eq. (4.187) yields

$$q = -K_h h h_x \left[\frac{1 + \frac{r}{3}\left(4hh_{xx} + h_x^2 + \frac{h^2 h_{xxx}}{h_x}\right)}{1 + \frac{r}{3}\left(hh_{xx} + h_x^2\right)}\right]. \tag{4.191}$$

For shallow flow or weakly curved streamlined flow, the denominator of Eq. (4.191) may be expanded using a Taylor–MacLaurin power series (Hager and Hutter 1984), whose first-order terms are

$$\begin{aligned}\frac{q}{-K_h h h_x} &\approx \left[1 + \frac{r}{3}\left(4hh_{xx} + h_x^2 + \frac{h^2 h_{xxx}}{h_x}\right)\right]\left[1 - \frac{r}{3}\left(hh_{xx} + h_x^2\right)\right] \\ &\approx \left[1 + r\left(hh_{xx} + \frac{h^2 h_{xxx}}{3h_x}\right)\right].\end{aligned} \tag{4.192}$$

If Eq. (4.192) is introduced into the depth-integrated mass conservation equation (Eq. 4.185), then it gives the expression

$$S\frac{\partial h}{\partial t}=\frac{\partial}{\partial x}\left[K_h h h_x\left[1+r\left(hh_{xx}+\frac{h^2h_{xxx}}{3h_x}\right)\right]\right]+N. \tag{4.193}$$

This may also be written as

$$\frac{\partial h}{\partial t}=\frac{K_h}{S}\frac{\partial}{\partial x}\left[h\frac{\partial h}{\partial x}+r\left(h^2\frac{\partial h}{\partial x}\frac{\partial^2 h}{\partial x^2}+\frac{h^3}{3}\frac{\partial^3 h}{\partial x^3}\right)\right]+\frac{N}{S}. \tag{4.194}$$

Equation (4.194) is a partial differential equation describing shallow unsteady unconfined flow in anisotropic porous media. For isotropic media ($r = 1$), Eq. (4.194) simplifies to Eq. (4.98). The limits of validity of the second-order theory applied to shallow unsteady, unconfined flows in anisotropic porous media are now investigated. In particular, the accuracy of the model with variations in r will be analyzed.

For shallow flow, the term $h_x^2 h_{xx}$ is of a lower order compared with the leading terms hh_{xx} and $h^3 h_{xxx}$. Using this simplification, and assuming zero accretion rate, Eq. (4.194) simplifies to

$$\frac{\partial h}{\partial t}=\frac{K_h}{S}\frac{\partial}{\partial x}\left[h\frac{\partial h}{\partial x}+r\frac{h^3}{3}\frac{\partial^3 h}{\partial x^3}\right]. \tag{4.195}$$

It is linearized by assuming small deviations η of the water table thickness around the mean value D [$h = D + \eta$, with $\eta \ll D$ (Fig. 4.33)], simplifying to

$$\frac{\partial \eta}{\partial t}=\frac{K_h}{S}\frac{\partial}{\partial x}\left(D\frac{\partial \eta}{\partial x}+r\frac{D^3}{3}\frac{\partial^3 \eta}{\partial x^3}\right)=\frac{K_h}{S}\left(\underbrace{D\frac{\partial^2 \eta}{\partial x^2}}_{\text{Dupuit term}}+r\underbrace{\frac{D^3}{3}\frac{\partial^4 \eta}{\partial x^4}}_{\text{Non-hydrostatic term}}\right). \tag{4.196}$$

The highest order spatial differentiation in Eq. (4.196) is of fourth order, so that the order of spatial differentiation will be reduced as follows (Liu and Wen 1997).

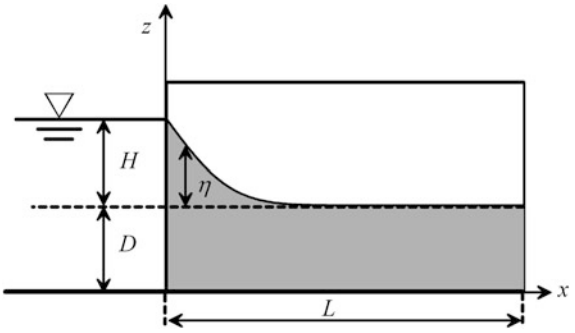

Fig. 4.33 Definition sketch of bank storage problem

Consider the linear Boussinesq equation (Bear 1972; Hunt 2005), obtainable from Eq. (4.196) by neglecting the non-hydrostatic term,

$$\frac{\partial \eta}{\partial t} = \frac{K_h D}{S} \frac{\partial^2 \eta}{\partial x^2}. \tag{4.197}$$

Differentiating Eq. (4.197) twice with respect to x produces

$$\frac{\partial^3 \eta}{\partial t \partial x^2} = \frac{K_h D}{S} \frac{\partial^4 \eta}{\partial x^4}, \tag{4.198}$$

a relation that permits an estimate for η_{xxxx}. Using Eq. (4.198) in Eq. (4.196) yields

$$\frac{\partial \eta}{\partial t} = \frac{K_h}{S} \left[D \frac{\partial^2 \eta}{\partial x^2} + r \frac{SD^2}{3K_h} \frac{\partial^3 \eta}{\partial t \partial x^2} \right]. \tag{4.199}$$

Note that the spatial differentiation is reduced to order two. Manipulation of Eq. (4.199) produces

$$\frac{\partial}{\partial t} \left[\eta - r \frac{D^2}{3} \frac{\partial^2 \eta}{\partial x^2} \right] = \frac{DK_h}{S} \frac{\partial^2 \eta}{\partial x^2}. \tag{4.200}$$

Introducing the auxiliary variable

$$\omega = \eta - r \frac{D^2}{3} \frac{\partial^2 \eta}{\partial x^2}, \tag{4.201}$$

Equation (4.200) is rewritten as

$$\frac{\partial \omega}{\partial t} = \frac{DK_h}{S} \frac{\partial^2 \eta}{\partial x^2}. \tag{4.202}$$

For $\omega = \eta$, Eq. (4.202) reduces to the Boussinesq equation, Eq. (4.197). The effect of the vertical motion is represented by the second term at the right-hand side of Eq. (4.202).

4.8.2 Analytical Solution and Numerical Method

The bank storage problem, illustrated in Fig. 4.33, is of particular interest in hydrology, since it addresses the unsteady flow exchange between channel banks and the surface stream as flood waves travel downward. Anisotropy is the usual field condition because floodplains typically consist of sediment layers with widely varying vertical and horizontal hydraulic conductivities. Hunt (2005) analyzed this

problem by using singular perturbation methods (Van Dyke 1975), obtaining a 2D solution for the water table given by

$$\eta_+(x_+,t_+) = 1 - 2\sum_{n=1}^{\infty} \frac{\sin(\alpha_n x_+)}{\alpha_n} \exp\left[-\frac{\alpha_n t_+}{\delta}\tanh(\alpha_n \delta)\right], \tag{4.203}$$

in which the variable α_n and parameter δ are given by

$$\alpha_n = \left(n - \frac{1}{2}\right)\pi, \quad \text{and} \quad \delta = \frac{D}{L}\left(\frac{K_h}{K_v}\right)^{1/2}. \tag{4.204}$$

Equation (4.203) involves dimensionless variables, denoted by subscript +. The dimensionless vertical displacement, η_+, is η scaled to the level of the river above the initial water level D, denoted by H (Fig. 4.33). The dimensionless x_+ coordinate is x scaled to the aquifer length L, and time t_+ is t scaled to the reference time $SL^2/(K_hD)$. The boundary conditions are $\eta_+(0,\ t_+) = 1$ and $\eta_{+x}(x_+,\ t_+) \to 0$ for $x_+ \to 1$. The initial condition is $\eta_+(x_+,\ 0) = 0$ for $0 < x_+ \leq 1$. Hunt (2005) also determined the analytical solution of the Boussinesq equation (Eq. 4.197) for this problem as

$$\eta_+(x_+,t_+) = 1 - 2\sum_{n=1}^{\infty} \frac{\sin(\alpha_n x_+)}{\alpha_n} \exp\left[-\alpha_n^2 t_+\right]. \tag{4.205}$$

This result arises from the Dupuit assumption for the bank storage problem. Using the above dimensionless variables, the second-order model (Eq. 4.200) is rewritten as

$$\frac{\partial}{\partial t_+}\left[\eta_+ - \frac{\delta^2}{3}\frac{\partial^2 \eta_+}{\partial x_+^2}\right] = \frac{\partial^2 \eta_+}{\partial x_+^2}. \tag{4.206}$$

An analytical solution to Eq. (4.206) is (Castro-Orgaz et al. 2013)

$$\eta_+(x_+,t_+) = 1 - 2\sum_{n=1}^{\infty} \frac{\sin(\alpha_n x_+)}{\alpha_n} \exp\left[-\frac{\alpha_n^2}{1 + \frac{(\delta\alpha_n)^2}{3}} t_+\right]. \tag{4.207}$$

This equation includes the parameter δ, accounting for both the aquifer shallowness D/L and anisotropy $r = K_h/K_v$. These factors are not included in the Dupuit-type Eq. (4.205). As expected, whenever $\delta = 0$, Eq. (4.207) simplifies to the DF solution (Eq. 4.205), which depends neither on D/L nor on r. The 2D solution (Eq. 4.203) depends on δ, as does Eq. (4.207), highlighting an improved feature regained by using non-hydrostatic equations.

Simulations were conducted to compare the performances of Eqs. (4.203), (4.205), and (4.207). Figure 4.34a compares the three equations for $\delta = 0.1$ at times $t_+ = 0.005$, 0.01, and 0.3. The agreement of Eqs. (4.207) and (4.203) is excellent.

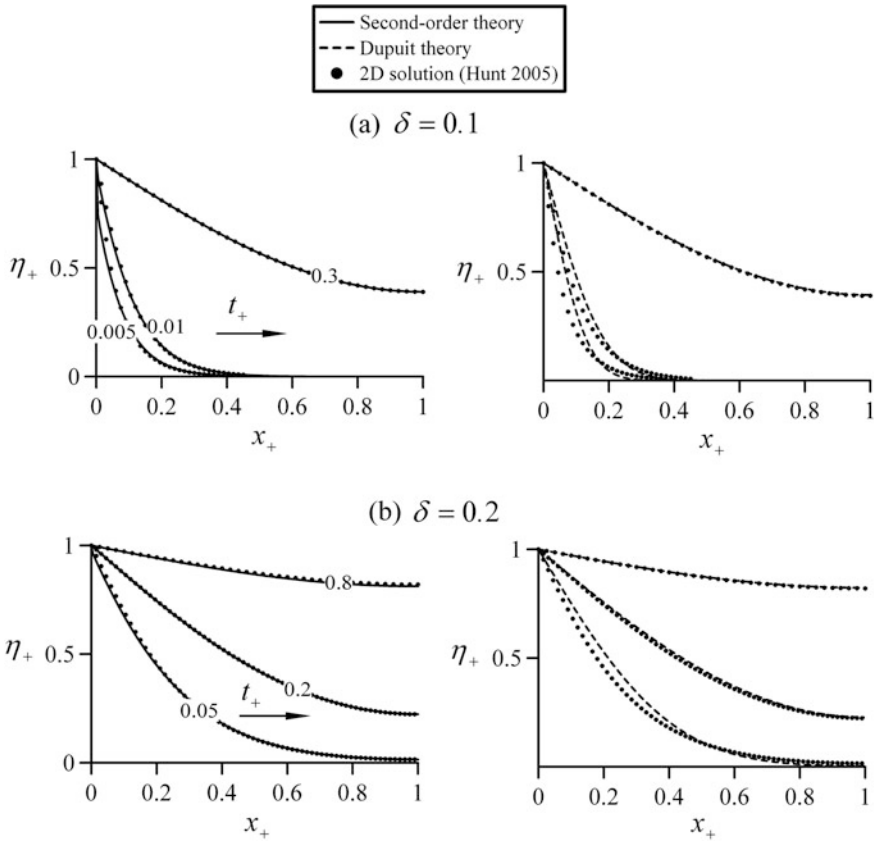

Fig. 4.34 Comparison of water table profiles at indicated times t_+ computed from the 2D solution (Eq. 4.203), the analytical solution of Boussinesq equation (Eq. 4.205), and the analytical solution of second-order shallow flow equation (Eq. 4.207) in anisotropic aquifer for δ = **a** 0.1, **b** 0.2 (adapted from Castro-Orgaz and Dey 2014)

Deviations of Eq. (4.205) from Eq. (4.203) are noticeable during the initial stages of transient flows. The value $\delta = 0.1$ is a threshold of validity for the Dupuit solution. For $0.01 < \delta < 0.1$, the Dupuit solution yields reasonable results only if $t_+ > 0.1$. Simulations for $\delta < 0.01$ (not presented here) reveal that Eq. (4.205) becomes valid regardless of the value of t_+. A second set of simulations for $\delta = 0.2$ (at times $t_+ = 0.05$, 0.2 and 0.8) confirms both the accuracy of Eq. (4.207) and the deviations of Eq. (4.205) from Eq. (4.203) at small transient times (Fig. 4.34b).

To test the limits of applicability of Eq. (4.207), it is necessary to evaluate it under extreme conditions. A main limitation of the second-order model in the bank storage problem arises from the boundary condition at the origin, $x_+ = 0$. Near this section, the boundary condition of water at rest implies a hydrostatic pressure distribution (Hunt 2005). However, in the present second-order model, ϕ is

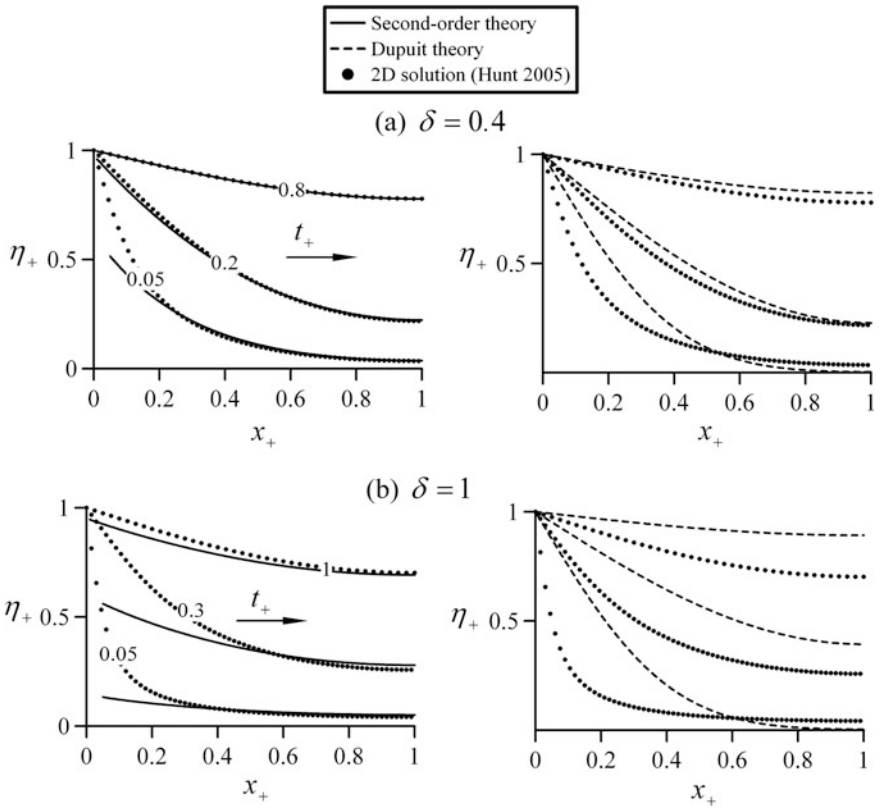

Fig. 4.35 Comparison of water table profiles at indicated times t_+ computed from the 2D solution (Eq. 4.203), the analytical solution of the Boussinesq equation (Eq. 4.205), and the analytical solution of the second-order shallow flow equation (Eq. 4.207) in anisotropic aquifer for δ = **a** 0.4, **b** δ = 1 (adapted from Castro-Orgaz and Dey 2014)

proportional to z^2 at $x = 0$ [see Eq. (4.178)], which is incompatible with a hydrostatic pressure distribution. Therefore, the accuracy of Eq. (4.207) at $x_+ = 0$ cannot be high, especially if δ is large, and during the initial stages of the transient flow. This is in agreement with Dagan's theory (1967), as his outer expansion was demonstrated to be invalid for small x_+. A comparison of the three models for $\delta = 0.4$ reveals in Fig. 4.35a the inadequacy of the Dupuit solution. In contrast, the second-order theory yields excellent predictions for $t_+ > 0.2$. However, the limitations of the simulation at $t_+ = 0.05$ are apparent. In this case, the second-order model yields good estimates only if $x_+ > 0.3$. The test case in Fig. 4.35b is extreme: For $\delta = 1$, the Dupuit solution deviates greatly from the 2D result. Nevertheless, the second-order model still yields reasonable predictions regardless of time, if $x_+ > 0.5$. At time $t_+ = 1$, an acceptable second-order result is obtained along the entire aquifer length.

The analytical solution of the bank storage problem given by Eq. (4.207) is of value to test numerical methods when solving Eq. (4.202). It is rewritten as

$$\frac{\partial \omega}{\partial t} = E. \tag{4.208}$$

Starting with the known values of η_i at time k, ω_i is determined with k as the time counter index and i as the x-coordinate index from

$$\omega_i^k = \eta_i^k - \left(r\frac{D^2}{3}\right)\frac{\partial^2 \eta}{\partial x^2}(i,k). \tag{4.209}$$

The spatial derivatives are discretized using three-point central finite differences as (Press et al. 2007)

$$\frac{\partial^2 \eta}{\partial x^2}(i,k) = \frac{\eta_{i+1}^k - 2\eta_i^k + \eta_{i-1}^k}{(\Delta x)^2}. \tag{4.210}$$

Once a set of ω_i is determined at time k, a high-resolution time-stepping method was selected. A predictor step for ω_i is given by the explicit third-order Adams–Bashforth formula as (Wei et al. 1995)

$$\omega_i^{k+1} = \omega_i^k + \frac{\Delta t}{12}[23E(i,k) - 16E(i,k-1) + 5E(i,k-2)]. \tag{4.211}$$

The function E at each node i at time k is given by

$$E(i,k) = \frac{DK_h}{S}\frac{\partial^2 \eta}{\partial x^2}(i,k). \tag{4.212}$$

Once the predictor step is evaluated, the values of E at each node at time $k + 1$ are computed. A corrector cycle using the fourth-order Adams–Moulton formula is based on

$$\omega_i^{k+1} = \omega_i^k + \frac{\Delta t}{24}[9E(i,k+1) + 19E(i,k) - 5E(i,k-1) + E(i,k-2)]. \tag{4.213}$$

This equation is iteratively applied until the computed values of ω_i converge with a prescribed tolerance. Next, the η_i are computed at this time step. The finite-difference version of Eq. (4.209) yields an equation at nodes $i = 2$ to $N - 1$, where N is the number of nodes in the x-direction, so that

$$\eta_i^{k+1} - \left(r\frac{D^2}{3}\right)\frac{\eta_{i+1}^{k+1} - 2\eta_i^{k+1} + \eta_{i-1}^{k+1}}{(\Delta x)^2} - \omega_i^{k+1} = 0. \tag{4.214}$$

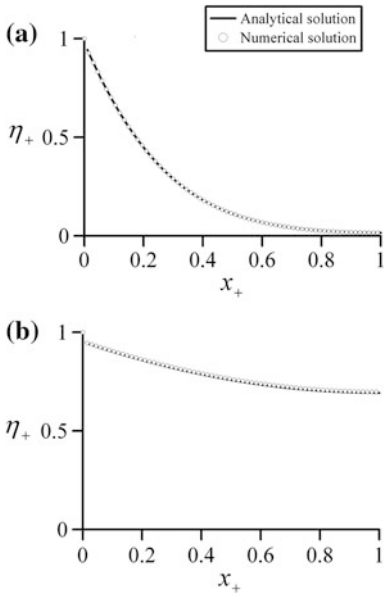

Fig. 4.36 Comparison of water table profiles computed from the analytical solution of second-order shallow flow equation (Eq. 4.207) and the numerical solution of Eq. (4.200) for **a** $\delta = 0.2$ at $t_+ = 0.05$, **b** $\delta = 1$ at $t_+ = 1$

Equation (4.214) produces a tridiagonal system of equations for the $N - 2$ unknown values η_i at the time level $k + 1$. The boundary conditions are introduced at nodes $i = 1$ and $i = N$ for the solution of the system. Equation (4.214) is efficiently solved using the Thomas algorithm (Hirsch 1988). The procedure is repeated to compute the temporal evolution of the water table. Figure 4.36 shows the good agreement between the analytical and numerical solutions.

It is important to remark that the bank storage problem was used to test the accuracy of the second-order theory as compared with the Boussinesq equation. Fortunately, in this particular case, a closed-form analytical solution was obtained. However, to solve other transient problems, it may be necessary to resort to numerical solutions. Therefore, for the sake of generality, the numerical method presented above was checked against the analytical solution.

4.8.3 Validity of Second-Order Solutions

Bear (1972) stated that the DF theory is applicable for shallow flows, setting the limit of applicability to $D/L \leq 0.2$. Taking $K_h/K_v = 1$ and $D/L = 0.2$, one obtains $\delta = 0.2$. The results shown in Fig. 4.34a confirm that the DF theory is not accurate for $\delta = 0.2$ at small t_+. In addition, if $D/L = 0.2$ and $K_h/K_v = 4$ ($\delta = 0.4$), say, the applicability of the DF theory becomes even more limited (Fig. 4.34b). Thus, if anisotropy is important, the DF theory is inaccurate for shallow flows. Further, it is neither accurate for isotropic conditions during the initial stages of transient flow.

The second-order theory overcomes some of the limitations of the DF theory, given that it accounts for D/L, and also for the anisotropy K_h/K_v. However, its limitations need to be determined. Equation (4.206) may be regarded as an identity that is satisfied if the function Ω has a root, i.e.,

$$\Omega(x_+, t_+) = \frac{\partial}{\partial t_+}\left[\eta_+ - \frac{\delta^2}{3}\frac{\partial^2 \eta_+}{\partial x_+^2}\right] - \frac{\partial^2 \eta_+}{\partial x_+^2}. \tag{4.215}$$

Inserting Eq. (4.203) in Eq. (4.215) yields

$$\Omega(x_+, t_+) = 2\sum_{n=1}^{\infty} \sin(\alpha_n x_+) \exp\left[-\frac{\alpha_n t_+}{\delta}\tanh(\alpha_n \delta)\right]\left[\frac{1 + \frac{(\alpha_n \delta)^2}{3}}{\delta}\tanh(\alpha_n \delta) - \alpha_n\right]. \tag{4.216}$$

If $\Omega = 0$ is obtained from Eq. (4.216), this indicates that the 2D solution exactly satisfies the second-order differential equation. Thus, Eq. (4.216) predicts the applicability of the second-order theory for the bank storage problem. Equation (4.216) is plotted in Fig. 4.37a for $\delta = 0.2$ and small times $t_+ = 0.015$, 0.02, and 0.03, using a semilog x_+-scale, to examine the applicability of the second-order theory. Within the domain $0 < x_+ < 0.1$, the second-order equation does not describe the 2D flow solution at $t_+ = 0.015$. At $t_+ = 0.02$, the predictions improve, but the model is still not acceptable. However, at $t_+ > 0.03$, $\Omega \approx 0$, so that the second-order theory is approximately valid. The maxima of the Ω function increase as t_+ reduces. Computations were repeated for $\delta = 1$, $t_+ = 0.14$, 0.2, and 0.25, with the results shown in Fig. 4.37b. In this test, Ω becomes insensitive to time at $x_+ = 0.6$, whereas this occurred at $x_+ = 0.3$ for $\delta = 0.2$ (Fig. 4.37a). For $\delta = 1$, Ω is close to zero within the interval $0 < x_+ < 0.6$ only if $t_+ > 0.25$. From a practical perspective, if $\delta < 0.2$, the second-order theory is an excellent model within the interval $0 < x_+ < 1$ for $t_+ > 0.03$, whereas for $t_+ < 0.03$, it is an excellent

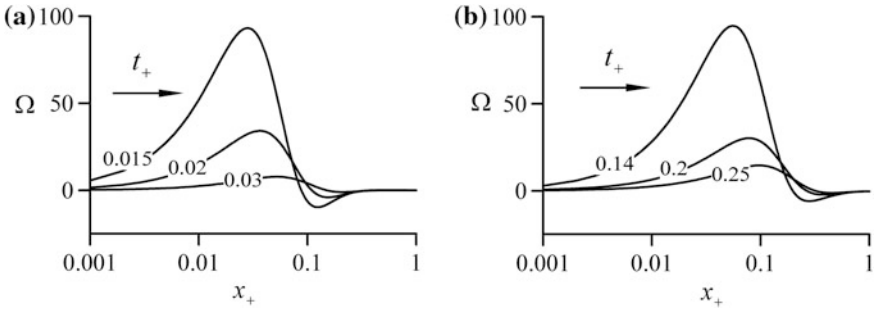

Fig. 4.37 Function Ω from Eq. (4.216) at several times for $\delta =$ **a** 0.2, **b** 1 (adapted from Castro-Orgaz and Dey 2014)

predictor in the interval $0.1 < x_+ < 1$. These spatial and temporal limitations of validity of the second-order theory diminish as δ increases, eventually reaching the extreme conditions depicted in Fig. 4.37b.

References

Bear, J. (1972). *The dynamics of fluids in porous media*. New York: Elsevier.

Billstein, M., Svensson, U., & Johansson, N. (1999). Development and validation of a numerical model of flow through embankment dams: Comparisons with experimental data and analytical solutions. *Transport in Porous Media, 35*(3), 395–406.

Castro-Orgaz, O. (2011a). Steady free-surface flow in porous media: Generalized Dupuit-Fawer equations. *Journal of Hydraulic Research, 49*(1), 55–63.

Castro-Orgaz, O. (2011b). A new model for soil-water drainage problems. *Environmental Fluid Mechanics, 11*(4), 427–435.

Castro-Orgaz, O., & Dey, S. (2014). Second-order shallow flow theory and Dupuit approximation for phreatic aquifers. *Journal of Hydraulic Engineering, 140*(9), paper 04014040.

Castro-Orgaz, O., & Giráldez, J. V. (2012). Steady-state water table height estimations from a pseudo-two-dimensional Dupuit-Forchheimer type improved model. *Journal of Hydrology, 438–439*, 194–202.

Castro-Orgaz, O., Giráldez, J. V., & Mateos, L. (2013). Second-order shallow flow equation for anisotropic aquifers. *Journal of Hydrology, 501*, 183–185.

Castro-Orgaz, O., Giráldez, J. V., & Robinson, N. (2012). Second order two-dimensional solution for the drainage of recharge based on Picard's iteration technique: A generalized Dupuit-Forchheimer equation. *Water Resources Research, 48*, W06516. doi:10.1029/2011WR011751.

Castro-Orgaz, O., & Hager, W. H. (2014). 1D modelling of curvilinear free surface flow: Generalized Matthew theory. *Journal of Hydraulic Research, 52*(1), 14–23.

Chapman, T. G. (1957). Two-dimensional ground-water flow through a bank with vertical faces. *Géotechnique, 7*(1), 35–40; *7*(7), 141–143.

Chapman, T. G. (2003). Steady recharge-induced groundwater flow over a plane bed: Nonlinear and linear solutions. In *MODSIM*, *Proceedings of International Congress on Modelling and Simulation* (Vol. 1, pp. 254–259). D.A. Post, ed. Model. Simul. Soc. Aus., Townsville, Qld.

Chapman, T. G., & Dressler, R. F. (1984). Unsteady shallow groundwater flow over a curved impermeable boundary. *Water Resources Research, 20*(10), 1427–1434.

Chapman, T. G., & Ong, G. (2006). A new equation for shallow groundwater flow over a curved impermeable boundary: Numerical solutions and laboratory tests. *Water Resources Research, 42*, W03427. doi:10.1029/2005WR004437.

Charny, L. A. (1952). A rigorous proof of the Dupuit formula for unconfined seepage with a seepage face. *Doklady Akademii Nauk SSSR, 79*, 937–940. (in Russian).

Courant, R., & Hilbert, D. (1962). *Methods of mathematical physics 2: Partial differential equations*. New York: Interscience Publishers.

Dagan, G. (1967). Second-order theory for shallow free surface flow in porous media. *The Quarterly Journal of Mechanics and Applied Mathematics, 20*(4), 517–526.

Di Nucci, C. (2011). Discussion of Steady free-surface flow in porous media: Generalized Dupuit-Fawer equations. *Journal of Hydraulic Research, 49*(6), 821–823.

Dressler, R. F. (1978). New nonlinear shallow flow equations with curvature. *Journal of Hydraulic Research, 16*(3), 205–222.

Dupuit, J. (1863). *Etudes théoriques et pratiques sur le mouvement des eaux dans les canaux découverts et á travers les terrains perméables* (Theoretical and practical studies on water movement in open channels and across permeable terrains). Paris, Dunod (in French).

Engelund, F. (1951). Mathematical discussion of drainage problems. *Transactions. A.T.S./Danish Academy of Technical Sciences, 3*, 1–64.

Fawer, C. (1937). *Etude de quelques écoulements permanents à filets courbes* (Study of some steady flows with curved streamlines). Thesis, Université de Lausanne. La Concorde, Lausanne, Switzerland (in French).

Fenton, J. D. (1990). Calculating seepage flow with a free surface: Some old methods and some new ones. *Proceedings of New Zealand Geomechanics Society, 16*(1), 31–36.

Hager, W. H. (2004). Jules Dupuit: Eminent hydraulic engineer. *Journal of Hydraulic Engineering, 130*(9), 843–848.

Hager, W. H., & Hutter, K. (1984). Approximate treatment of plane channel flow. *Acta Mechanica, 51*(1), 31–48.

Hirsch, C. (1988). *Numerical computation of internal and external flows 1: Fundamentals of numerical discretization*. New York: Wiley.

Hornung, U., & Krueger, T. (1985). Evaluation of the Polubarinova-Kochina formula for the dam problem. *Water Resources Research, 21*(3), 395–398.

Huard de la Marre, P. (1956). Expressions exactes des débits d'infiltration dans des barrages tridimensionnels à parois verticals (Exact expressions for the infiltration discharges in spatial dams with vertical walls). *Comptes Rendus, Académie des Sciences Paris, 242*(9), 1125–1127 (in French).

Hunt, B. (2005). Bank-storage problem and the Dupuit approximation. *Journal of Hydrologic Engineering, 10*(2), 118–124.

Jaeger, C. (1956). *Engineering fluid mechanics*. Edinburgh: Blackie and Son.

Jie, Y., Jie, G., Mao, Z., & Li, G. (2004). Seepage analysis based on boundary-fitted coordinate transformation method. *Computers and Geotechnics, 31*(4), 279–283.

Kacimov, A., Obnosov, Y., Abdalla, O., & Castro-Orgaz, O. (2015). Groundwater flow in hillslopes: Analytical solutions by the theory of holomorphic functions and hydraulic theory. *Applied Mathematical Modelling, 39*(12), 3380–3397.

Kashef, A. A. (1965). Seepage through earth dams. *Journal of Geophysical Research, 70*(24), 6121–6128.

Kirkham, D. (1967). Explanation of the paradoxes in Dupuit-Forchheimer seepage theory. *Water Resources Research, 3*(2), 609–622.

Knight, J. H. (2005). Improving the Dupuit-Forchheimer groundwater free surface approximation. *Advances in Water Resources, 28*(10), 1048–1056.

Liu, P. L.-F., & Wen, J. (1997). Nonlinear diffusive surface waves in porous media. *Journal of Fluid Mechanics, 37*, 119–139.

Matthew, G. D. (1991). Higher order one-dimensional equations of potential flow in open channels. *Proceedings of ICE, 91*(3), 187–201.

Montes, J. S. (1998). *Hydraulics of open channel flow*. Reston, VA: ASCE Press.

Murray, W. A., & Monkmeyer, P. L. (1973). Validity of the Dupuit-Forchheimer equation. *Journal of the Hydraulics Division ASCE, 99*(HY9), 1573–1583.

Muskat, M. (1942). *Flow of homogeneous fluids through porous media*. New York: McGraw-Hill.

Nielsen, P., Aseervatham, R., Fenton, J. D., & Perrochet, P. (1997). Groundwater waves in aquifers of intermediate depths. *Advances in Water Research, 20*(1), 37–43.

Polubarinova-Kochina, P. Y. (1962). *Theory of groundwater movement*. Princeton: Princeton University Press.

Press, W. H., Teukolsky, S. A., Vetterling, W. T., & Flannery, B. P. (2007). *Numerical recipes: The art of scientific computing* (3rd ed.). Cambridge: Cambridge University Press.

Raudkivi, A. J., & Callander, R. A. (1976). *Analysis of groundwater flow*. London: Arnold.

Rushton, K. R., & Youngs, E. G. (2010). Drainage of recharge to symmetrically located downstream boundaries with special reference to seepage faces. *Journal of Hydrology, 380*, 94–103.

Serrano, S. E. (1995). Analytical solutions of the nonlinear groundwater flow equation in unconfined aquifers and the effect of heterogeneity. *Water Resources Research, 31*(11), 2733–2742.

Serrano, S. E. (2003). Modelling groundwater flow under transient non-linear free surface. *Journal of Hydrologic Engineering, 8*(3), 123–132.

Shaw, F. S., & Southwell, R. V. (1941). Relaxation methods applied to engineering problems 7: Problems relating to percolation of fluids through porous materials. *Philosophical Transactions of the Royal Society of London, Series A, 178*(972), 1–17.

Strack, O. D. L. (1989). *Groundwater mechanics*. Englewood Cliffs, NJ: Prentice Hall.

Strack, O. D. L., Barnes, R. J., & Verrujit, A. (2006). Vertically integrated flows, discharge potential, and the Dupuit-Forchheimer approximation. *Ground Water, 44*(1), 72–75.

Thom, A., & Apelt, C. (1961). *Field computations in engineering and physics*. London: Van Nostrand.

Vallentine, H. R. (1969). *Applied hydrodynamics*. London: Butterworths.

Van Dyke, M. (1975). *Perturbation methods in fluid mechanics*. Stanford, CA: The Parabolic Press.

van Walsum, P. E. V., & Koopmans, R. W. R. (1984). Steady two-dimensional groundwater seepage: Numerical analysis in the $\varphi\psi$-plane. *Journal of Hydrology, 72*(3–4), 331–354.

Wei, G., & Kirby, J. T. (1995). Time-dependent numerical code for extended Boussinesq equations. *Journal of Waterway, Port, Coastal and Ocean Engineering, 121*(5), 251–261.

Youngs, E. G. (1965). Horizontal seepage through unconfined aquifers with hydraulic conductivity varying with depth. *Journal of Hydrology, 3*(3), 283–296.

Youngs, E. G. (1966). Exact analysis of certain problems of ground-water flow with free surface conditions. *Journal of Hydrology, 4*, 277–281.

Youngs, E. G. (1990). An examination of computed steady-state water table heights in unconfined aquifers: Dupuit-Forchheimer estimates and exact analytical results. *Journal of Hydrology, 119* (1–4), 201–214.

Youngs, E. G. (2012). Engelund's two-dimensional drainage equation for a toe drain and the Dupuit-Forchheimer drainage equation for a ditch: A coincidental match. *Journal of Irrigation and Drainage Engineering, 138*(3), 282–284. doi:10.1061/(ASCE)IR.1943-4774.0000388.

Youngs, E. G., & Rushton, K. R. (2009). Dupuit-Forchheimer analyses of steady-state water table heights due to accretion in drained lands overlaying undulating sloping impermeable beds. *Journal of Irrigation and Drainage Engineering, 135*(4), 467–473.

Zaoui, J. (1964). Les écoulements en milieu poreux et l'hypothèse de Dupuit (Flows in porous media and the Dupuit hypothesis). *La Houille Blanche, 19*(3), 385–388 (in French).

Chapter 5
Viscous Channel Flows

Roman Symbols

a	Parameter (–); also gate opening (m)
a_i	Subsection flow area (m^2)
A	Area (m^2); also porosity (–); coefficient in eddy viscosity formula (s^2/m); parameter (–)
A_h	$\partial A/\partial h$ (m)
A_{hh}	$\partial^2 A/\partial h^2$ (–)
b	Coefficient of bottom friction for uniform flow (s^2/m); also parameter (–); channel width (m)
B	Constant of velocity profile (m/s); also coefficient of bottom friction (s^2/m)
c	Celerity of sand wave (m/s); also function (m^2/s)
c_k	Coefficient in k–ε model (–)
C	Coefficient (m/s); also friction coefficient (–); function of s (–); function in integral of vertical velocity (m/s)
C, C_1, C_2, C_3, C_4, C'	Constants (–)
C_μ, $c_{2\varepsilon}$, c_ε, $c_{1\varepsilon}$	Coefficients in k–ε model (–)
C_c	Contraction coefficient (–)
C_d	Discharge coefficient (–)
C_{di}	Discharge coefficient of round-crested weir for ideal fluid flow (–)
C_D	Discharge coefficient of broad-crested weir (–)
C_f	Skin friction coefficient (–)
C_o	Correction coefficient of curvilinear flow (–)
C_σ	Correction coefficient of surface tension (–)
C_v	Correction coefficient of viscosity (–)
D	Dimensionless boundary layer thickness (–); also uniform water depth (m)
e	Energy flux (m^3/s)
E	Specific energy head (m)
$E_{\min}$	Minimum value of specific energy head to avoid scale effects (m)
E_c	Specific energy head of free surface streamline at boundary layer origin (m)

© Springer International Publishing AG 2017

O. Castro-Orgaz and W.H. Hager, *Non-Hydrostatic Free Surface Flows*,
Advances in Geophysical and Environmental Mechanics and Mathematics
DOI 10.1007/978-3-319-47971-2_5

f	Friction factor (–); also factor from perturbation of friction slope (–)
f_o	Friction factor for uniform flow (–)
f_θ	Friction factor from wall-wake boundary layer equation (–)
f_{dump}	Damping factor (–)
F	Froude number (–)
F_o	Froude number of uniform flow (–)
F_α	Compound channel Froude number based on specific energy (–)
F_β	Compound channel Froude number based on specific momentum (–)
F	Specific momentum of flow area A (m^3)
g	Gravity acceleration (m/s^2)
$\mathbf{g}$	Gravity vector (m/s^2)
h	Flow depth (m)
$\hat{h}$	H/D (–)
h_{jump}	Tailwater flow depth of classical hydraulic jump (m)
h_{solitary}	Maximum flow depth of solitary wave (m)
$h_{\text{vena contracta}}$	Depth at vena contracta section of submerged hydraulic jump (m)
h_c	Critical flow depth (m)
h_{cH}	$[q^2/(g\cos\theta)]^{1/3}$ = critical depth for parallel streamline flow in sloping chute (m)
H	Total energy head (m); also H = shape factor (–); uniform flow depth (m)
H_1	Dimensionless first-order perturbation term in flow profile (–)
H_o	Energy head at inlet of broad-crested weir (m); also total energy head of free surface streamline (m)
H_s	Free surface velocity head (m)
i	Bottom slope (–)
i_c	Critical bottom slope (–)
i_o	Limit bottom slope for imaginary roots (–)
$i_{\text{inf, sup}}$	Limit bottom slopes for hydrostatic approximations of roots (–)
I	Moment of inertia of cross section (m^4)
k	Turbulent kinetic energy (m^2/s^2)
k_i	Subsection conveyance (m^3/s)
k_s	Roughness height (m)
K	Total conveyance (m^3/s), also u/u_θ (–)
L	Broad-crested weir length (m); also flow development length (m); scaling length factor in sand solitary wave (m)
m	Pressure coefficient (–)
m_1, m_2, m_3	Roots of characteristic polynomial (m^{-1}); also Boussinesq-type coefficients (–)
M	Momentum flux (m^3/s^2)
n	Exponent of power-law velocity profile (–); also coordinate normal to bottom (m); porosity (–)

n	Manning coefficient ($m^{-1/3}s$); also bed-normal coordinate (m); bed porosity (–)
n_i	Subsection Manning coefficient ($m^{-1/3}s$)
n_1	Main channel Manning coefficient ($m^{-1/3}s$)
n_2	Floodplain Manning coefficient ($m^{-1/3}s$)
N	Exponent of power-law velocity profile (–)
p	Time-averaged pressure (N/m^2)
p^*	Piezometric pressure of inflow/outflow (N/m^2)
p_i	Subsection wetted perimeter (m)
p_s	Free surface pressure (N/m^2)
Δp	Deviation of actual pressure from hydrostatic law (m)
P_h	Production of k due to interaction of turbulent stresses with horizontal velocity gradients (m^2/s^3)
P_{kv}	Production of k due to vertical velocity gradients (m^2/s^3)
$P_{\varepsilon v}$	Production of ε due to vertical velocity gradients (m^2/s^3)
q	Unit discharge (m^2/s)
q^*	Inflow/outflow intensity (m/s)
q_b	Bed load (m^2/s)
q_{bo}	Equilibrium bed load (m^2/s)
Q	Discharge (m^3/s)
r	Dimensionless roughness (–)
r_i	Subsection hydraulic radius (m)
R	Reynolds number (–)
R_s	Reynolds number based on flow development distance (–)
R_θ	Reynolds number based on momentum thickness (–)
R	Radius of bed curvature (m)
R_s	Radius of free surface curvature (m)
s	Curvilinear coordinate measured along bottom profile (m); also submerged jet thickness (m)
s_M	Maximum thickness of separation bubble (m)
s_o	s coordinate of starting point (m)
S	Shape factor (–); also momentum function (m^2)
S_e	Energy line slope (–)
S_f	Friction slope (–)
S_o	Bottom slope (–)
t	Time (s)
t_i	Subsection top width (m)
T	Shear stress (N/m^2); also averaging time (s); total top width (m); time (s)
$\mathbf{T}$	Stress tensor (N/m^2)
u	Horizontal velocity in flow over 3D terrain (m/s); also velocity parallel to bottom (m)
u_i	Subsection flow velocity (m/s)
u_o	Turbulent velocity parallel to bottom near wall (m/s)

u^*	Shear velocity (m/s)
U	Potential flow velocity at boundary layer edge (m/s); also mean velocity q/h (m)
U_c	Critical velocity (m/s)
U_e	Potential bottom velocity (m/s); also velocity at boundary layer edge (m/s)
U_o	Approach flow velocity (m/s)
U_{CL}	Depth-averaged centerline flow velocity (m/s)
v	Lateral velocity in flow over 3D terrain (m/s)
V	Lateral outflow/inflow velocity (m/s)
$\mathbf{V}$	Velocity vector (m/s)
V_s	Free surface velocity (m/s)
w	Vertical velocity in flow over 3D terrain (m/s); also velocity normal to bottom (m/s)
x	Horizontal distance in flow over 3D terrain (m); also distance along bottom (m)
X	x/h_1 (–); also horizontal coordinate in moving axes (m)
$\hat{X}$	X/D (–)
y	Transverse coordinate in flow over 3D terrain (m); also coordinate normal to channel bottom profile (m)
Y	Dimensionless flow depth (–)
Y_p	Dimensionless potential flow depth (–)
z	Vertical elevation (m); also dimensionless potential flow velocity (–)
z_b	Bed elevation (m)
$\hat{z}_b$	Z_b/D (–)
$\bar{z}$	Distance from free surface to total section centroid (m)
Z	Dimensionless boundary layer displacement thickness (–)

Greek Symbols

α	Coefficient of boundary layer profile (–); also Coriolis correction coefficient (–); parameter (–); turbulence parameter (–);
α'	Coefficient in momentum equation (–)
β	Exponent of boundary layer profile (–); also Boussinesq's correction coefficient (–); coefficient of A and B (–); parameter (–); normalized bed load (–)
β'	Coefficient function of A and B (–)
Γ	Buri's shape factor (–); also similarity function (–)
γ	Specific weight (N/m^3); also $[\alpha' i/(gb)] - 1$ (–)
Λ	Coefficient of power-law velocity profile (–); also dimensionless velocity (–)
Λ	Parameter (–)

δ	Boundary layer thickness (m)
δ^*	Boundary layer displacement thickness (m)
ε	Rate of dissipation (m^2s^3); also eddy viscosity (Ns/m^2)
ε_1, ε_2	Boussinesq-type coefficients (–)
ε_p	Perturbation parameter (–)
$1 + \eta$	Momentum flux velocity correction coefficient, or "Boussinesq coefficient" (–)
η	$h - D$ (m); also dimensionless distance perpendicular to channel bottom (–)
η_o	Maximum value of η (m)
θ	Angle of channel bottom with horizontal (rad)
θ_m	Boundary layer momentum thickness (m)
κ	von Kármán constant (–); also bottom curvature (m^{-1})
λ	Approximate ratio of w/U (–); also parameter (–)
λ_1, λ_2, λ_3	Vorticity coefficients (–)
μ	Auxiliary variable (m^{-1}); also dynamic viscosity (Ns/m^2); parameter (–)
$\bar{\mu}$	Mean value of μ in Boussinesq's theory (–)
ν	Kinematic viscosity (m^2/s)
v, v'	Auxiliary functions of m_1 (m^{-1})
ν_t	Eddy viscosity (m^2/s)
Π	Wake parameter (–)
ρ	Water density (N/m^3)
σ	Surface tension coefficient (N/m)
σ_x	Normal Reynolds stress in x-direction (N/m^2)
σ_y	Normal Reynolds stress in y-direction (N/m^2)
σ_1, σ_2, σ_3	Compound channel Froude number terms in energy equation (–)
ς	Parameter (–); also z/h (–); y/h (–), X/L (–)
τ_b	Boundary shear stress (N/m^2)
τ_{ij}	Reynolds stress (N/m^2), with $(i, j) = (x, y, z)$
τ_{yx}	Tangential Reynolds stress (N/m^2)
τ_1, τ_2, τ_3	Compound channel Froude number terms in momentum equation (–)
ϕ	Angle of V vector with x-direction (rad)
χ	Dimensionless streamwise distance (–); also surface velocity coefficient (–); η/D (–)
ψ	Stream function (m^2/s)
Ω	Weir crest parameter (–)
ω	Reduced flow depth around $H = (h/H) - 1$ (–)
(i, j)	Node index in (s, n) directions (–)
(N, M)	Maximum values of (i, j)
(A, B, C)	Auxiliary parameters in boundary layer power-law solution

(ξ, X)	Auxiliary variables in boundary layer power-law differential equation
(A, B)	Auxiliary coefficients in Boussinesq's differential equation
(I, F)	Auxiliary integrals in Boussinesq's theory
(a_1, a_2, a_3, k)	Auxiliary variables for solitary sand wave profile
$(A, B, b_1, b_2, I, \eta)$	Auxiliary variables in dike breach theory

Subscripts

b	Bottom
c	Relative to weir crest
d	Relative to tailwater section
I	Relative to inception point
p	Relative to potential flow
s	Free surface
0	Relative to boundary condition
1	Relative to inflow section
.	Bars indicate time-averaged value in turbulent flow
.	Primes indicate fluctuating component in turbulent flow

5.1 Introduction

The potential flow approximation described in Chap. 3 applies provided that real fluid flow features, namely viscous and surface tension effects, can be discarded. Viscous, incompressible, and isothermal open-channel flows are governed by the mass conservation equation

$$\nabla \cdot \mathbf{V} = 0, \tag{5.1}$$

and the momentum equations (White 1991, 2003)

$$\rho \frac{\mathrm{D}\mathbf{V}}{\mathrm{D}t} = \rho \mathbf{g} - \nabla \cdot p + \mu \nabla^2 \mathbf{V}, \tag{5.2}$$

which together comprise the Navier–Stokes equations. Here, $\mathbf{V}$ is the velocity vector, $\mathbf{g}$ the gravity acceleration, p the fluid pressure, and μ the dynamic viscosity, assumed to be constant. Equations (5.1) and (5.2) define under the stated conditions a rather general 3D flow, and often claimed to remain valid for both laminar and turbulent open-channel flows. If the flow is turbulent, Reynolds' decomposition permits to split the velocity components (u, v, w) into the Cartesian coordinates

(x, y, z), as well as the fluid pressure p, into mean and fluctuating components (denoted by bars and primes, respectively), as follows

$$u = \bar{u} + u', \quad v = \bar{v} + v', \quad w = \bar{w} + w', \quad p = \bar{p} + p'. \tag{5.3}$$

With T as an averaging period that is larger that any time scale associated with the turbulent fluctuations, the mean components are defined, e.g., as

$$\bar{u} = \frac{1}{T}\int_0^T u \mathrm{d}t. \tag{5.4}$$

With this definition, one finds

$$\overline{u'} = \frac{1}{T}\int_0^T (u - \bar{u})\mathrm{d}t = 0. \tag{5.5}$$

However, the mean values of squared fluctuating parts do not vanish, that is,

$$\overline{u'^2} = \frac{1}{T}\int_0^T u'^2 \mathrm{d}t \neq 0. \tag{5.6}$$

If Eq. (5.3) are inserted in Eqs. (5.1), (5.2), and a time average of the emerging PDEs is performed, the continuity equation of the mean flow turns out to be

$$\frac{\partial \bar{u}}{\partial x} + \frac{\partial \bar{v}}{\partial y} + \frac{\partial \bar{w}}{\partial z} = 0. \tag{5.7}$$

However, the time-averaged form of the momentum equations reads, with (g_x, g_y, g_z) as the gravitational acceleration components (White 1991, 2003),

$$\frac{\partial \bar{u}}{\partial t} + \bar{u}\frac{\partial \bar{u}}{\partial x} + \bar{v}\frac{\partial \bar{u}}{\partial y} + \bar{w}\frac{\partial \bar{u}}{\partial z} = -\frac{1}{\rho}\frac{\partial \bar{p}}{\partial x} + g_x + \frac{1}{\rho}\left(\frac{\partial \tau_{xx}}{\partial x} + \frac{\partial \tau_{xy}}{\partial y} + \frac{\partial \tau_{xz}}{\partial z}\right), \tag{5.8}$$

$$\frac{\partial \bar{v}}{\partial t} + \bar{u}\frac{\partial \bar{v}}{\partial x} + \bar{v}\frac{\partial \bar{v}}{\partial y} + \bar{w}\frac{\partial \bar{v}}{\partial z} = -\frac{1}{\rho}\frac{\partial \bar{p}}{\partial y} + g_y + \frac{1}{\rho}\left(\frac{\partial \tau_{yx}}{\partial x} + \frac{\partial \tau_{yy}}{\partial y} + \frac{\partial \tau_{yz}}{\partial z}\right), \tag{5.9}$$

$$\frac{\partial \bar{w}}{\partial t} + \bar{u}\frac{\partial \bar{w}}{\partial x} + \bar{v}\frac{\partial \bar{w}}{\partial y} + \bar{w}\frac{\partial \bar{w}}{\partial z} = -\frac{1}{\rho}\frac{\partial \bar{p}}{\partial z} + g_z + \frac{1}{\rho}\left(\frac{\partial \tau_{zx}}{\partial x} + \frac{\partial \tau_{zy}}{\partial y} + \frac{\partial \tau_{zz}}{\partial z}\right), \tag{5.10}$$

in which the stress tensor is given as

$$\mathbf{T} = \begin{bmatrix} \tau_{xx} = 2\mu\frac{\partial\bar{u}}{\partial x} - \rho\overline{u'^2} & \tau_{xy} = \mu\left(\frac{\partial\bar{u}}{\partial y} + \frac{\partial\bar{v}}{\partial x}\right) - \rho\overline{u'v'} & \tau_{xz} = \mu\left(\frac{\partial\bar{u}}{\partial z} + \frac{\partial\bar{w}}{\partial x}\right) - \rho\overline{u'w'} \\ \tau_{yx} = \mu\left(\frac{\partial\bar{u}}{\partial y} + \frac{\partial\bar{v}}{\partial x}\right) - \rho\overline{u'v'} & \tau_{yy} = 2\mu\frac{\partial\bar{v}}{\partial y} - \rho\overline{v'^2} & \tau_{yz} = \mu\left(\frac{\partial\bar{v}}{\partial z} + \frac{\partial\bar{w}}{\partial y}\right) - \rho\overline{v'w'} \\ \tau_{zx} = \mu\left(\frac{\partial\bar{u}}{\partial z} + \frac{\partial\bar{w}}{\partial x}\right) - \rho\overline{u'w'} & \tau_{zy} = \mu\left(\frac{\partial\bar{v}}{\partial z} + \frac{\partial\bar{w}}{\partial y}\right) - \rho\overline{v'w'} & \tau_{zz} = 2\mu\frac{\partial\bar{w}}{\partial z} - \overline{w'^2} \end{bmatrix} \tag{5.11}$$

The additional terms originating from the time average of the velocity correlations, viz., $\overline{u'^2}$, $\overline{v'^2}$, $\overline{w'^2}$, $\overline{u'v'}$, $\overline{u'w'}$, and $\overline{v'w'}$ are referred to as Reynolds stresses; these are effectively the averages of the convective acceleration terms. Equations (5.7)–(5.11) are the basis to study 3D turbulent open-channel flows (Fig. 5.1) (Liggett 1994; White 1991, 2003). Using the developments of Chap. 2, a general depth-averaged model for turbulent channel flow over 3D terrain follows from Eqs. (5.7)–(5.10) on the basis of Eq. (5.11) for stress tensor closure.

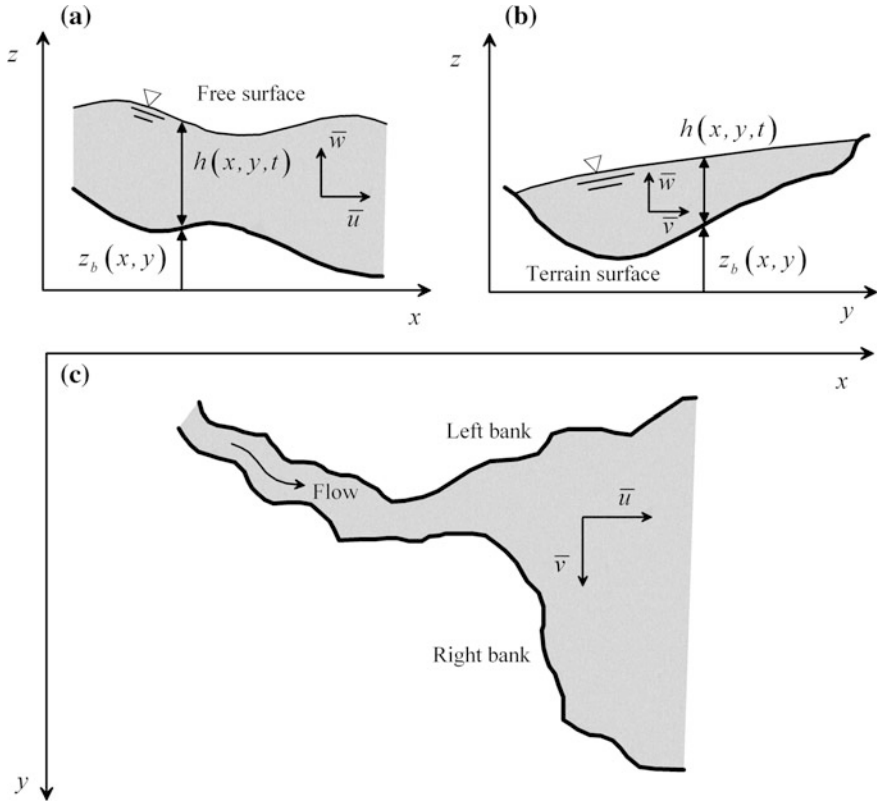

Fig. 5.1 Definition sketch of 3D turbulent open-channel flows **a** profile, **b** section, **c** plan

The developments in this chapter are limited to non-hydrostatic viscous open-channel flows in the vertical plane. Two methods of attack are presented, depending on the nature of the problem, namely the boundary layer theory and the depth-averaged model of the Reynolds-averaged Navier–Stokes equations (RANS). The boundary layer approach assumes that viscous effects are confined to a thin layer close to the solid walls, whereas the main bulk of the (outer) flow behaves essentially as an inviscid fluid under irrotational motion. Therefore, the boundary layer approximation involves essentially a two-layer approach, so that consideration of the outer flow reduces under steady conditions in the vertical plane to the solution of the Laplace equation for the stream function ψ, viz.,

$$\frac{\partial^2\psi}{\partial x^2}+\frac{\partial^2\psi}{\partial z^2}=0. \tag{5.12}$$

Equation (5.12) (or alternative transformations of it) is solved using the techniques presented in Chap. 3. Close to the solid boundary, Eq. (5.12) must be matched with Eqs. (5.1), (5.2) for the boundary layer. For laminar steady flow in the vertical plane, these are given as

$$\frac{\partial u}{\partial x}+\frac{\partial w}{\partial z}=0, \tag{5.13}$$

$$u\frac{\partial u}{\partial x}+w\frac{\partial u}{\partial z}=-\frac{1}{\rho}\frac{\partial p}{\partial x}+g_x+\frac{\mu}{\rho}\left(\frac{\partial^2 u}{\partial x^2}+\frac{\partial^2 u}{\partial z^2}\right), \tag{5.14}$$

$$u\frac{\partial w}{\partial x}+w\frac{\partial w}{\partial z}=-\frac{1}{\rho}\frac{\partial p}{\partial z}+g_z+\frac{\mu}{\rho}\left(\frac{\partial^2 w}{\partial x^2}+\frac{\partial^2 w}{\partial z^2}\right). \tag{5.15}$$

Similar equations emerge for turbulent flows based on Eqs. (5.7)–(5.10). In the boundary layer theory, Eqs. (5.14)–(5.15) are further simplified by quantifying the relative importance of each term of the momentum balances in a thin boundary layer (see White 1991, 2003 for details). Laminar boundary layers are frequently found in hydraulic structures if the dimensions are below a threshold value (Matthew 1961, 1963, 1968; Castro-Orgaz and Hager 2014a).

Other flows involve turbulence within the complete flow depth, as frequently occur in undular hydraulic jumps (Castro-Orgaz et al. 2015). Under these circumstances, the boundary layer approximation is inappropriate because a complete depth-averaged RANS model in the vertical plane is required, based on Eqs. (5.7)–(5.11). Approximate methods for tackling both phenomena under non-hydrostatic, steady 2D flows in a vertical plane are presented in this chapter. Unsteady sediment transport and movable beds are introduced.

5.2 Boundary Layer Approximation

5.2.1 Scale Effects of Round-Crested Weir Flow

Physical modeling in hydraulic engineering suffers from so-called scale effects, distorting a model–prototype relation. Heller (2011) presented a comprehensive review of scale effects in hydraulic engineering. The following section deals specifically with scale effects in the discharge characteristics of the round-crested weir, which is a relevant overflow structure of high dams (Cassidy 1965; Naudascher 1987; Montes 1998), as well as a useful discharge measuring device (Hager 1993; Ramamurthy and Vo 1993a, b). Fuentes-Aguilar and Acuña (1971) and Ramamurthy et al. (1994) reported very thin boundary layers over round-crested weirs and excellent agreement of the ideal fluid flow theory with observations, if the crest curvature radius R is sufficiently large to avoid significant scale effects. The two major sources of scale effects originate from surface tension and viscous effects (Sarginson 1984; Naudascher 1987). Whereas the head loss originating from boundary layers has a small effect on the discharge characteristics of the prototype structures (Naudascher 1987; Montes 1998), laboratory models are of smaller scale so that these may result in significant alterations of the discharge equation (Varshney 1977; Isaacs 1981; Naudascher 1987). Scale effects in control structures were specifically tackled in an IAHR symposium (Kolkman 1984) and further addressed in an IAHR monograph (Kolkman 1994). However, none of these two succeeded in proposing generalized equations for scale effects of round-crested weirs. Experimental works of Lakshmana Rao and Jagannadha Rao (1973), or Varshney (1977) reveal that the boundary layer of round-crested weir flows is laminar at laboratory scale. Maxwell and Weggel (1969) or Sarginson (1972, 1984) specifically observed the importance of viscous effects at low heads. Matthew (1963) found an analytical solution for the laminar boundary layer thickness profile, yet his solution was not verified. Isaacs (1981) computed laminar boundary layers in weir models. He numerically solved the integral boundary layer equations of laminar flow using Thwaites' method, for broad-crested weir flows. A major contradiction to the current engineering approach stems from using the laminar boundary layer equations of the flat plate (Naudascher 1987, 1991), violating basic weir-flow features encompassing accelerating flows and favorable pressure gradients.

In this section, a general round-crested weir-flow equation is presented accounting for the real fluid flow effects originating from viscosity and surface tension, following Castro-Orgaz and Hager (2014a). Their equation accounts for surface tension effects at high heads, given its dependence on streamline curvature. Further, the laminar boundary layer development of round-crested weir flows is modeled by using detailed 2D, and integral 1D, laminar boundary layer solutions. These are employed to present an approximate analytical model used as predictor of viscosity effects in the general weir-flow equation. The prediction of the discharge characteristics is verified with a set of experimental data. The theory is also used to

predict the discharge features of square-edged broad-crested weirs, where a separation bubble triggers the discharge features. A flow analogy between the separation bubble and a round-crested weir is developed, where the shear layer above the bubble and the surface tension at the free surface are both accounted for. The theory is also used to evaluate the minimum overflow head, necessary to avoid significant scale effects in laboratory experimentation.

Consider a partially developed real fluid flow over a weir of arbitrary but smooth bottom profile $z_b(x)$ (Fig. 5.2). The total energy head H of the free surface streamline is (Matthew 1961, 1963, 1968)

$$H = z_b + h + \frac{p_s}{\gamma} + \frac{V_s^2}{2g} = \text{const.} \tag{5.16}$$

Here, V_s is the free surface velocity, p_s the free surface pressure, $\gamma = \rho g$ the specific fluid weight, and h the vertical flow depth. The value of p_s is different from zero due to surface tension, producing with the surface tension coefficient σ and the free surface radius of curvature R_s the boundary condition (Liggett 1994)

$$p_s = -\frac{\sigma}{R_s}. \tag{5.17}$$

To unveil surface tension, the boundary layer displacement thickness δ^* is temporarily overlooked. Therefore, the discharge equation accounting for streamline curvature and surface tension effects is developed as follows. The effects of curvilinearity of free surface flows are basically accounted for by the quotient $V_s/(q/h)$, with q as unit discharge (Wilkinson 1974). These were included in the energy equation by Matthew (1991) using the Picard iteration method [see Sect. 3.3]. Using Eq. (3.70), Eq. (5.16) is rewritten as

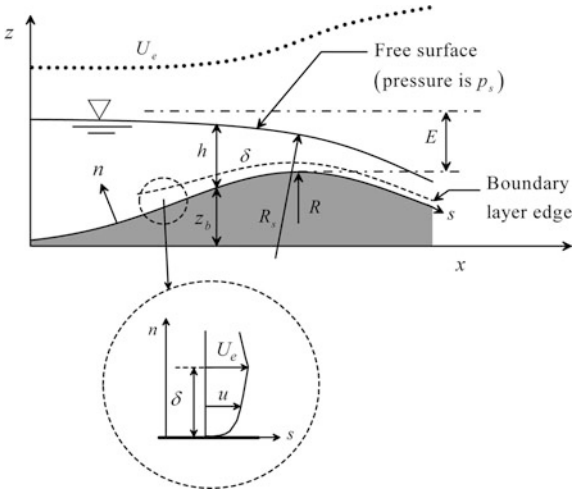

Fig. 5.2 Definition sketch of real fluid flow over round-crested weir (adapted from Castro-Orgaz and Hager 2014a). The boundary layer thickness in the n-direction is δ, and the fluid pressure at the water surface is p_s. At the crest section ($dz_b/dx = 0$), where the specific energy is E, the radii of curvature at the free surface and at the bottom are R_s and R, respectively

$$H = z_b + \frac{p_s}{\gamma} + h + \frac{q^2}{2gh^2}\left(1 + \frac{2hh_{xx} - h_x^2}{3} + hz_{bxx} + z_{bx}^2\right) = \text{const.} \tag{5.18}$$

Inserting Eq. (5.17) into Eq. (5.18) yields

$$H = z_b - \frac{\sigma}{\gamma R_s} + h + \frac{q^2}{2gh^2}\left(1 + \frac{2hh_{xx} - h_x^2}{3} + hz_{bxx} + z_{bx}^2\right) = \text{const.} \tag{5.19}$$

At the weir crest $z_{bx} = 0$, so that Eq. (5.19) simplifies to (additional subscripts are not used to simplify notation)

$$E = H - z_b = -\frac{\sigma}{\gamma R_s} + h + \frac{q^2}{2gh^2}\left(1 + \frac{2hh_{xx} - h_x^2}{3} + hz_{bxx}\right) = \text{const.}, \tag{5.20}$$

where E is the specific energy at the weir crest (Fig. 5.2). Solving Eq. (5.20) for the discharge q yields

$$q = \left(2gh^2\right)^{1/2}\left[E - h + \frac{\sigma}{\gamma R_s}\right]^{1/2}\left(1 + \frac{2hh_{xx} - h_x^2}{3} + hz_{bxx}\right)^{-1/2}. \tag{5.21}$$

The discharge coefficient C_d of the weir is defined via (Montes 1998)

$$q = C_d\left(gE^3\right)^{1/2}. \tag{5.22}$$

Equating Eqs. (5.21) and (5.22), thus, yields

$$C_d = 2^{1/2}\frac{h}{E}\left[1 - \frac{h}{E} + \frac{\sigma}{\gamma R_s}\right]^{1/2}\underbrace{\left(1 + \frac{2hh_{xx} - h_x^2}{3} + hz_{bxx}\right)^{-1/2}}_{C_o}, \tag{5.23}$$

where the coefficient C_o accounts for curvilinear flow of an ideal fluid under irrotational motion. Assuming $h/E = 2/3$, Eq. (5.23) is rewritten with C_σ as a coefficient that accounts for the surface tension effects as

$$C_d = 2^{1/2}\frac{2}{3}\left[1 - \frac{2}{3} + \frac{\sigma}{\gamma R_s}\right]^{1/2}C_o = \left(\frac{2}{3}\right)^{3/2}\underbrace{\left[1 + \frac{3\sigma}{\gamma R_s}\right]^{-1/2}}_{C_\sigma}C_o. \tag{5.24}$$

The weir-flow equation is thus

$$C_d = \left(\frac{2}{3}\right)^{3/2}C_oC_\sigma. \tag{5.25}$$

Here, C_σ is further rewritten as

$$C_\sigma = \left(1 + \frac{3\sigma}{\gamma E R_s}\right)^{1/2} = \left[1 + \frac{3\sigma}{\gamma E}\frac{h_{xx} + z_{bxx}}{\left(1 + h_x^2\right)^{3/2}}\right]^{1/2}. \tag{5.26}$$

Now, surface tension and curvature effects are set aside, and the viscous effects on weir flow are accounted for by using the boundary layer theory. With U_e as the potential velocity of the outer flow, the free surface energy head for a parallel-streamlined flow with a developing boundary layer is, at the crest section (Silberman 1980; Montes 1998)

$$E = h + \frac{U_e^2}{2g}. \tag{5.27}$$

For a flow with no curvature effects, this velocity is for a given section a constant outside the boundary layer. Let δ be the boundary layer thickness at the crest section (additional subscripts are not used to simplify notation); conservation of mass gives

$$\begin{aligned} q &= \int_0^h u\mathrm{d}n = \int_0^\delta u\mathrm{d}n + \int_\delta^h U_e\mathrm{d}n = \int_0^\delta u\mathrm{d}n + U_e(h-\delta) \\ &= \int_0^\delta u\mathrm{d}n - U_e\delta + U_e h, \end{aligned} \tag{5.28}$$

with n as the curvilinear coordinate normal to s (see inset of Fig. 5.2). Using the definition of the boundary layer displacement thickness δ^* in the boundary layer theory yields (Silberman 1980; Castro-Orgaz 2009)

$$\delta^* = \int_0^\delta \left(1 - \frac{u}{U_e}\right)\mathrm{d}n \Rightarrow \delta^* U_e = \int_0^\delta (U_e - u)\mathrm{d}n = U_e\delta - \int_0^\delta u\mathrm{d}n. \tag{5.29}$$

Physically, Eq. $(5.29)_1$ determines the displacement δ^* of a potential flow outward from a solid wall, preserving the mass flux at that section. Combining Eqs. (5.28) and $(5.29)_2$ produces

$$q = \int_0^\delta u\mathrm{d}n - U_e\delta + U_e h = U_e(h - \delta^*) \Rightarrow U_e = \frac{q}{h - \delta^*}. \tag{5.30}$$

Inserting Eq. $(5.30)_2$ in Eq. (5.27) yields for the free surface energy head at the weir crest section

$$E = h + \frac{q^2}{2g(h - \delta^*)^2}. \tag{5.31}$$

To introduce the effects of viscosity in the weir-flow equation, critical flow conditions are set in Eq. (5.31). Considering δ^* as independent of h during the differentiation,[1] the minimum specific energy condition $dE/dh = 0$ in Eq. (5.31) leads to

$$1 - \frac{q^2}{g(h - \delta^*)^3} = 0. \tag{5.32}$$

This approximation produces satisfactory results to model the head–discharge relation of control structures (Ackers et al. 1978; Montes 1998).

Inserting Eq. (5.32) in Eq. (5.31), the critical depth at the weir crest becomes (Ackers et al. 1978; Silberman 1980)

$$h = \frac{2}{3}E + \frac{1}{3}\delta^*. \tag{5.33}$$

Solving Eq. (5.31) for the discharge q produces

$$q = (2g)^{1/2}(h - \delta^*)(E - h)^{1/2}. \tag{5.34}$$

Inserting Eq. (5.33) into Eq. (5.34) results in

$$\begin{aligned} q &= (2g)^{1/2}(h - \delta^*)(E - h)^{1/2} \\ &= (2g)^{1/2}\left(\frac{2}{3}E + \frac{1}{3}\delta^* - \delta^*\right)\left(E - \frac{2}{3}E - \frac{1}{3}\delta^*\right)^{1/2} \\ &= (2g)^{1/2}\left(\frac{2}{3}E - \frac{2}{3}\delta^*\right)\left(\frac{1}{3}E - \frac{1}{3}\delta^*\right)^{1/2} \\ &= g^{1/2}\left(\frac{2}{3}\right)^{3/2}(E - \delta^*)^{3/2}. \end{aligned} \tag{5.35}$$

Equating with Eq. (5.22) yields the discharge coefficient with the effects of viscosity as

[1]The reason underlaying this assumption is that, in the fully developed turbulent-rough regime, δ^* depends mainly on a normalized roughness and weakly on the Reynolds number and, thus, on h.

$$C_d = \left(\frac{2}{3}\right)^{3/2} \underbrace{\left(1 - \frac{\delta^*}{E}\right)^{3/2}}_{C_v}. \tag{5.36}$$

For clarity in the forthcoming computations, subscript c now stands for the boundary layer displacement thickness at the weir crest. The weir discharge q given by Eq. (5.36) is reduced below its value $(2/3)^{3/2}$ for potential, parallel-streamlined flow by the correction coefficient due to viscosity C_v, with δ_c^* as the boundary layer displacement thickness at the weir crest, as

$$C_v = \left(1 - \frac{\delta_c^*}{E}\right)^{3/2}. \tag{5.37}$$

Thus, the general weir-flow equation accounting for scale effects is finally

$$C_d = \left(\frac{2}{3}\right)^{3/2} C_o C_\sigma C_v. \tag{5.38}$$

The coefficient C_o is determined by numerically solving the Laplace equation (Cassidy 1965; Fuentes-Aguilar and Acuña 1971; Montes 1992) or by approximate theories of curvilinear flow (Fawer 1937; Jaeger 1956; Matthew 1963, 1991; Lenau 1967; Montes 1970, 1998; Hager 1985). All these yield results quite close, so that the coefficient from a third-order Boussinesq-type equation is adopted following Matthew (1991),

$$C_o = 1 + \frac{22}{81}\frac{E}{R} - 0.045\left(\frac{E}{R}\right)^2. \tag{5.39}$$

The coefficient C_σ depends on the crest boundary radius of curvature, $z_{bxx} = -1/R$, as well as on the crest derivatives of the flow depth, h_x and h_{xx}. A theoretical equation for C_σ results from the weakly curved relations $h_x^2 = h/(3R)$, $(1 + h_x^2)^{3/2} \approx 1$ and $h_{xx} = (4/9)R$ (Matthew 1961, 1963, 1968; Hager 1985). However, a small weir under high head may have surface tension effects in which nonlinear contributions and higher order terms in h_x and h_{xx} become relevant. Therefore, more accurate predictors of similar mathematical validity to Eq. (5.39) are (Matthew 1991)

$$h_x^2 = \frac{2}{9}\frac{E}{R}\left(1 - \frac{236}{729}\frac{E}{R}\right), \quad h_{xx} = \frac{4}{9R}\left(1 + \frac{4783}{16038}\frac{E}{R}\right). \tag{5.40}$$

By combining Eqs. (5.39) and (5.40) with Eq. (5.26), the discharge characteristics of a weir subjected to scale effects due to surface tension are thus modeled. Computation of C_v requires determining δ_c^* using the boundary layer theory,

as made by Craya and Delleur (1952), Delleur (1955, 1957), Hall (1962), Harrison (1967a, b), and Vierhout (1973) for broad-crested weir flow. For broad-crested weirs, the boundary layer is turbulent so that the initial laminar flow portion is neglected, due to the weak flow acceleration that, in turn, allows for parallel-streamlined flow establishment ($C_o = C_\sigma = 1$). For round-crested weir flow, this is quite different.

Consider accelerating flows over the weir shown in Fig. 5.2. At the upstream weir portion, the free surface is only slightly converging, so that the flow acceleration is weak and the bottom velocity U_e remains essentially constant. An increasing boundary layer thickness profile δ similar to the laminar flat plate is therefore expected. As the flow approaches the weir crest, it accelerates within a short distance from the upstream to the crest velocity, thereby increasing U_e and inhibiting boundary layer development, leading to a decreasing thickness $\delta(x)$. Accordingly, the boundary layer of round-crested weirs, which is laminar upstream, is likely to remain laminar along the crest, as verified experimentally by Lakshmana Rao and Jagannadha Rao (1973). Matthew (1963) assumed laminar flow and produced an approximate expression for the displacement thickness profile $\delta^*(x)$. However, his boundary layer predictions were not verified with 1D or 2D laminar boundary layer flow computations. Whereas Matthew (1963) advocated for the importance of accelerating flow toward a round-crested weir, Naudascher (1987) proposed to use the laminar flat plate equations to account for the boundary layer correction at the weir crest, based on a limited study of two spillway models, in which the effects of surface tension were not accounted for. The two proposals are conflicting and contradictory, given that the flat plate equations fully neglect the existence of flow accelerations. The approach of Naudascher (1987) was also included in an IAHR design monograph (Naudascher 1991), but the use of any of the two theories remains doubtful. The viscous effect in Froude models dominates the scale effects at low weir heads, for which the pressure is essentially hydrostatic (Maxwell and Weggel 1969). In contrast, surface tension is the leading real fluid flow feature at higher heads, for which the flows are curvilinear and the pressures are non-hydrostatic. Sarginson (1972) used an empirical equation to account for viscous effects at low heads. The relevance of viscosity in Froude models was further experimentally verified by Varshney (1977), who found a dependence of C_d on the Reynolds number. He also verified that the boundary layer was laminar. In summary, several works reveal the importance of viscosity in weir-flow models at low heads, and that the boundary layer remains laminar as the flow passes along the crest. A systematic study, producing 1D and 2D laminar boundary layer computations to predict $\delta^*(x)$, was presented by Castro-Orgaz and Hager (2014a).

The flow over a round-crested weir model is treated by using Prandtl's boundary layer approximation (de Oliveira Lemos 1965). The flow is divided into an outer potential flow zone and a thin viscous layer attached to the solid wall (White 1991). The potential flow solution provides the outer flow velocity $U_e(s)$, taken as the potential bottom velocity, given the thin boundary layer, where s is the curvilinear coordinate along the solid wall (Fig. 5.2).

For the potential flow computations, the x–ψ method (Montes 1992, 1994) is used,[2] in which ψ is the stream function. The Laplace equation formulated for the elevation z was derived in Chap. 3 [see Eq. (3.250)] and reads

$$\frac{\partial^2 z}{\partial x^2}\left(\frac{\partial z}{\partial \psi}\right)^2 + \frac{\partial^2 z}{\partial \psi^2}\left[1 + \left(\frac{\partial z}{\partial x}\right)^2\right] - 2\frac{\partial^2 z}{\partial x \partial \psi}\frac{\partial z}{\partial x}\frac{\partial z}{\partial \psi} = 0. \tag{5.41}$$

The solution of Eq. (5.41) for flows over control structures such as weirs or drops is described by Montes (1992, 1994), Dey (2002), and Castro-Orgaz (2013), as detailed in Chap. 3. However, any other method for potential flow computations equally applies, including that of Cassidy (1965), or Fuentes-Aguilar and Acuña (1971).

Viscous flows within the boundary layer are modeled using the system of continuity and momentum equations (White 1991; Schlichting and Gersten 2000)

$$\frac{\partial u}{\partial s} + \frac{\partial w}{\partial n} = 0, \tag{5.42}$$

$$u\frac{\partial u}{\partial s} + w\frac{\partial u}{\partial n} = U_e\frac{\mathrm{d}U_e}{\mathrm{d}s} + \nu\frac{\partial^2 u}{\partial n^2}. \tag{5.43}$$

Here, ν is the kinematic viscosity, and u and w are the velocities in the s- and n-directions, with n as the coordinate normal to the bottom-fitted curvilinear coordinate s. The boundary conditions for no-slip at the wall are $u = 0$ and $w = 0$, whereas $u = U_e$ at the boundary layer edge to match the outer potential flow to the viscous flow close to the wall, where U_e is the potential bottom velocity determined from the solution of Eq. (5.41). The system of Eqs. (5.42), (5.43) implies that the pressure is constant within the boundary layer in the n-direction; therefore, it is prescribed by the outer potential flow. Accordingly, the ratio of the boundary layer thickness δ to the boundary radius of curvature R must be small, as is typical for flows over round-crested weirs (de Oliveira Lemos 1965). To solve Eqs. (5.42), (5.43), a numerical method is required. The full Navier–Stokes equations are elliptic and must be solved simultaneously in the entire computational domain. In contrast, Eqs. (5.42), (5.43) are parabolic and the numerical solution is space-marching, i.e., computations start at a given position s for which the profiles (u, w) along n are prescribed, and computations progress to a new position s, where the velocity profiles are determined. The implicit finite-difference model developed by White (1991) was applied here. The origin of Eqs. (5.42) and (5.43), and the finite-difference technique are described in detail by White (1991; pp. 275–282), so that only the main aspects are discussed here.

[2]The potential flow solution of flow over a round-crested weir is extensively described in Sect. 3.7, so that it is not repeated here.

A rectangular finite-difference mesh with N and M computational nodes in the s- and n-directions is defined. At each computational node, forward and central finite differences are used for $\partial u/\partial s$ and $\partial u/\partial n$, respectively. The term $\partial^2 u/\partial n^2$ is discretized using a 3-point central finite difference at the next position s. Thus, the s-momentum Eq. (5.43) is first written as

$$u\frac{\partial u}{\partial s}+w\frac{\partial u}{\partial n}=\frac{1}{2}\frac{\mathrm{d}U_e^2}{\mathrm{d}s}+v\frac{\partial^2 u}{\partial n^2}, \tag{5.44}$$

and the finite-difference approximation adopted is

$$\begin{aligned}u(i,j)\frac{u(i+1,j)-u(i,j)}{\Delta s}+w(i,j)\frac{u(i,j+1)-u(i,j-1)}{2\Delta n}\\ =\frac{1}{2}\frac{U_e^2(i+1)-U_e^2(i)}{\Delta s}+v\frac{u(i+1,j+1)-2u(i+1,j)+u(i+1,j-1)}{\Delta n^2}.\end{aligned} \tag{5.45}$$

Here, (i, j) are the node indices in the s- and n-directions. Equation (5.45) produces an algebraic system of $(M-2)$ equations for the unknowns $u(i+1, j)$ for each n-node (index j) at the target s-coordinate (index $i+1$) as

$$\begin{aligned}-\alpha u(i+1,j+1)+(1+2\alpha)u(i+1,j)-\alpha u(i+1,j-1)\\ =u(i,j)-\beta[u(i,j+1)-u(i,j-1)]+\frac{U_e^2(i+1)-U_e^2(i)}{2u(i,j)}.\end{aligned} \tag{5.46}$$

Here, $\alpha=(v\Delta x)/[(u(i,j)\Delta n^2]$ and $\beta=[w(i,j)\Delta x]/[2u(i,j)\Delta n]$. The matrix associated with the system generated by Eq. (5.46) is tridiagonal and its inversion is simple using the Thomas algorithm (White 1991). Note that at node $j=M$ the velocity is $u=U_e(s)$, whereas at the wall $u=0$. The values of $w(s, n)$ are obtained at each position using the finite-difference form of the continuity equation, once u is computed. For this task, an average gradient $\partial u/\partial s$ is taken as (White 1991)

$$\left(\frac{\partial u}{\partial s}\right)_{\text{Average}}=\frac{1}{2}\left[\frac{u(i+1,j)-u(i,j)}{\Delta s}+\frac{u(i+1,j-1)-u(i,j-1)}{\Delta s}\right], \tag{5.47}$$

which, inserted into Eq. (5.42), produces the finite-difference approximation

$$\begin{aligned}w(i+1,j)=w(i+1,j-1)\\ -\frac{\Delta n}{2\Delta s}[u(i+1,j)-u(i,j)+u(i+1,j-1)-u(i,j-1)].\end{aligned} \tag{5.48}$$

The starting section is selected upstream of the weir, where streamlines are nearly parallel. The corresponding boundary layer thickness is set to $\delta=0$ so that the velocity profiles are $u(s, n)=U_e(s)$ and $w(s, n)=0$. Once velocity profiles $u(s, n)$ are

available, displacement and momentum thickness profiles are computed by numerical evaluation of the integrals

$$\delta^*(s) = \int_0^{n_{\max}} \left[1 - \frac{u(s,n)}{U_e(s)}\right] \mathrm{d}n, \quad \theta_m(s) = \int_0^{n_{\max}} \frac{u(s,n)}{U_e(s)} \left[1 - \frac{u(s,n)}{U_e(s)}\right] \mathrm{d}n. \tag{5.49}$$

Here, θ_m is the momentum thickness and $n_{\max,}$ the upper limit of the computational grid in the n-direction. To verify that the boundary layer remains indeed laminar along the entire computational domain, the approximate condition with $\mathsf{R}_s = U(s)s/\nu$ was used (White 1991)

$$\frac{U(s)\theta_m(s)}{\nu} < 2.9\mathsf{R}_s^{0.4}. \tag{5.50}$$

Equation (5.50) implies that the local Reynolds number based on the computed θ_m must not reach Michel's transition line for turbulent flow.

The integral solution given by Thwaites' method (White 1991) was used by Isaacs (1981) to estimate the boundary layer development in accelerating flow at the exit drop of a small-scale broad-crested weir. He found that the method produced satisfactory results of boundary layers in accelerating flow. However, the necessity for further verification of his method was stated. Given the good results of Isaacs (1981) using Thwaites' method in a slope break, Castro-Orgaz and Hager (2014a) applied it to round-crested weir flows, testing its accuracy using the 2D solution. The integral form of the boundary layer Eqs. (5.42), (5.43) is given by the von Kármán equation, reduced for a laminar boundary layer by Thwaites to (White 1991; Schlichting and Gersten 2000)

$$\frac{\theta_m^2}{\nu} = \frac{\theta_{mo}^2}{\nu} + aU_e^{-b} \int_{s_o}^{s} U_e^{b-1} \mathrm{d}s'. \tag{5.51}$$

Here, o refers to the upstream section at which computations start, and the empirical parameters are $a = 0.45$ and $b = 6$. Using the outer potential velocity distribution $U_e(s)$, the integral in Eq. (5.51) is evaluated numerically and the profile $\theta_m(s)$ thereby computed. The profile $\delta^*(s)$ is then determined using the shape factor S involving a correlation polynomial developed by White (1991)

$$S = \frac{\delta^*}{\theta_m} = 2 + 4.14k - 83.5k^2 + 854k^3 - 3337k^4 + 4576k^5, \quad k = 0.25 - \frac{\theta_m^2 U_e}{\nu}. \tag{5.52}$$

Matthew (1963) assumed that the potential bottom velocity U_e distribution along the upstream weir portion follows the exponential function

$$U_e = U_c \exp\left[s(2RE)^{-1/2}\right] = U_c \exp[\lambda s]. \tag{5.53}$$

For critical flow with parallel streamlines at the crest ($s = 0$) $h = 2/3E$, and, thus, $U_c = [(2/3)gE]^{1/2}$, where E is the specific energy at the weir crest. Using Eq. (5.53), Matthew (1961, 1963) obtained as solution of the laminar boundary layer displacement thickness

$$\delta^* = 0.7\nu^{1/2}\left(\frac{3R}{g}\right)^{1/4} \exp\left[-\frac{s}{2(2RE)^{1/2}}\right]. \tag{5.54}$$

Equation (5.54) was not tested by Matthew (1963) against numerical solutions of the boundary layer equations, a task attacked below. At the crest section, Eq. (5.54) yields

$$\delta_c^* = 0.7\nu^{1/2}\left(\frac{3R}{g}\right)^{1/4}. \tag{5.55}$$

The usefulness of the analytical Eq. (5.55) is that it can be inserted into Eq. (5.37) to produce an analytical solution for C_v, which is of practical relevance to study model–prototype relations.

Castro-Orgaz and Hager (2014a) noted that Eq. (5.53) allows for an analytical solution of Thwaites' Eq. (5.51). Although the exponential behavior of U_e may be a reasonable approximation close to the weir crest, the parallel-streamlined flow value used for the bottom velocity at the crest U_c is not accurate for high E/R. Thus, the crest bottom velocity is more generally given by the potential flow equations using the weakly curved relation $h_{xx} = (4/9)R$ as (Castro-Orgaz et al. 2008; Castro-Orgaz and Hager 2014a) [see Eq. (3.220)]

$$\begin{aligned} U_c &= V_s \exp\left[-hz_{bxx} - \frac{hh_{xx}}{2}\right] = V_s \exp\left[+\frac{2}{3}\frac{E}{R} - \frac{1}{2}\frac{2}{3}\frac{4}{9}\frac{E}{R}\right] \\ &= V_s \exp\left(\frac{14}{27}\frac{E}{R}\right) \approx \left(\frac{2}{3}gE\right)^{1/2} \exp\left(\frac{14}{27}\frac{E}{R}\right). \end{aligned} \tag{5.56}$$

The free surface velocity V_s is approximated by the critical flow velocity. Inserting Eq. (5.53) into Eq. (5.51) yields the analytical solution for the momentum thickness profile

$$\begin{aligned}\frac{\theta_m^2}{v} &= \frac{\theta_{mo}^2}{v} + aU_c^{-b}\exp(-b\lambda s)\int_{s_o}^{s} U_c^{b-1}\exp[\lambda(b-1)s']\mathrm{d}s' \\ &= \frac{\theta_{mo}^2}{v} + aU_c^{-b}U_c^{b-1}\exp(-b\lambda s)\left[\frac{\exp[\lambda(b-1)s']}{\lambda(b-1)}\right]_{s_o}^{s} \\ &= \frac{\theta_{mo}^2}{v} + \frac{a}{\lambda(b-1)U_c}\exp(-\lambda s)[1-\exp[\lambda(b-1)(s_o-s)]],\end{aligned} \tag{5.57}$$

or

$$\frac{\theta_m^2}{v} = \frac{\theta_{mo}^2}{v} + \frac{a(2RE)^{1/2}}{U_c(b-1)}\exp\left[-(2RE)^{-1/2}s\right]\left[1-\exp\left(\frac{b-1}{(2RE)^{1/2}}(s_o-s)\right)\right]. \tag{5.58}$$

The last term containing the flow development length $(s_o - s)$ is of small magnitude and thus neglected, resulting in

$$\frac{\theta_m^2}{v} = \frac{\theta_{mo}^2}{v} + \frac{a(2RE)^{1/2}}{U_c(b-1)}\exp\left[-(2RE)^{-1/2}s\right]. \tag{5.59}$$

Using the shape factor S, defined by $\delta^* = S\theta_m$, Eq. (5.59) yields for the boundary layer thickness profile

$$\frac{\delta^{*2}}{v} = \frac{S^2\theta_{mo}^2}{v} + \frac{S^2a(2RE)^{1/2}}{U_c(b-1)}\exp\left[-(2RE)^{-1/2}s\right], \tag{5.60}$$

with a crest value of $(s = 0)$

$$\frac{\delta_c^{*2}}{v} = \frac{S^2\theta_{mo}^2}{v} + \frac{S^2a(2RE)^{1/2}}{U_c(b-1)}. \tag{5.61}$$

Equation (5.61) can be rewritten as

$$\delta_c^* = \left(\delta_o^{*2} + \delta_a^{*2}\right)^{1/2}. \tag{5.62}$$

Here, $\delta_o^* = S\theta_{mo}$, and the contribution due to acceleration (subscript a) is

$$\delta_a^{*2} = \frac{vS^2a(2RE)^{1/2}}{(b-1)}\frac{1}{U_c}. \tag{5.63}$$

Inserting Eq. (5.56) into Eq. (5.63) yields

$$\begin{aligned}\delta_a^* &= \left[\frac{S^2 a}{b-1}\right]^{1/2} v^{1/2}(2RE)^{1/4}\left(\frac{2}{3}gE\right)^{-1/4}\exp\left(-\frac{7}{27}\frac{E}{R}\right)\\ &= \left[\frac{S^2 a}{b-1}\right]^{1/2} v^{1/2}\left(\frac{3R}{g}\right)^{1/4}\exp\left(-\frac{7}{27}\frac{E}{R}\right)\\ &= \Lambda v^{1/2}\left(\frac{3R}{g}\right)^{1/4}\exp\left(-\frac{7}{27}\frac{E}{R}\right),\quad \Lambda = \left[\frac{S^2 a}{b-1}\right]^{1/2}.\end{aligned} \tag{5.64}$$

Using $a = 0.45$, $b = 6$, and $S = 2.3$ for laminar flow (White 1991) gives $\Lambda = 0.69$ in Eq. (5.64), i.e., close to 0.7 as in Matthew's equation (5.55).

Potential flow over a round-crested weir of profile $z_b = 20\exp[-0.5(x/24)^2]$ is considered as a test case for operational heads of $E/R = 0.516$ and 0.253, respectively (Fig. 5.3). Free surface and bottom pressure predictions are compared with the experimental data of Sivakumaran et al. (1983), resulting in good agreement. As indicated above, no further details of the potential flow solution are described here, as this is detailed in Chap. 3.

Potential flow simulations were used to obtain the potential bottom velocity U_e, plotted in Fig. 5.4 for comparative purposes with Eq. (5.53) using $U_c = [(2/3)E/g]^{1/2}$ (Matthew 1963), and Eq. (5.56) for improved crest velocity predictions (analytical solution). Note that the exponential function provides excellent bottom velocity predictions close to the crest. Deviations from Matthew's theory are therefore attributed to his use of $U_c = [(2/3)gE]^{1/2}$. Far from the crest, the exponential function deviates from the 2D potential velocity distribution. However, deviations are in a zone of low flow velocity. Given the good match near the crest, good δ^* predictions are expected in this portion of the weir if Eq. (5.53) coupled with Eq. (5.56) is used to predict $U_e(s)$.

The laminar boundary layer displacement thickness profiles from the 2D and 1D models are shown in Fig. 5.5a for a weir of $R = 0.288$ m. The computational mesh used in the 2D model typically included 4500 points in the s-direction and 800

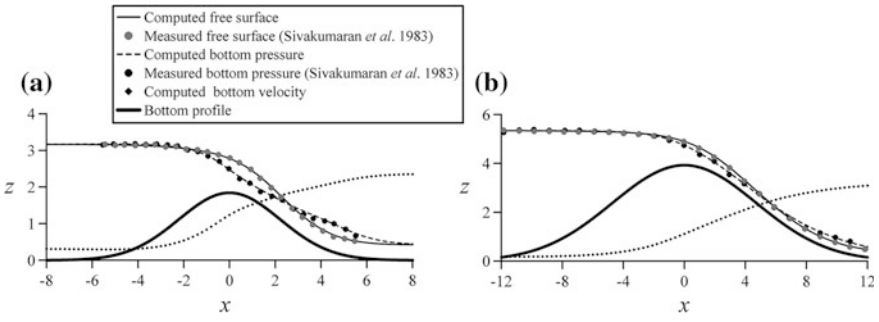

Fig. 5.3 Potential flow solution for round-crested weirs with E/R = **a** 0.516, **b** 0.253. Variables are normalized using critical flow conditions (z/h_c, z_b/h_c, $p_b/(\gamma h_c)$, U_e/U_c, x/h_c), with $h_c = (q^2/g)^{1/3}$ (adapted from Castro-Orgaz and Hager 2014a)

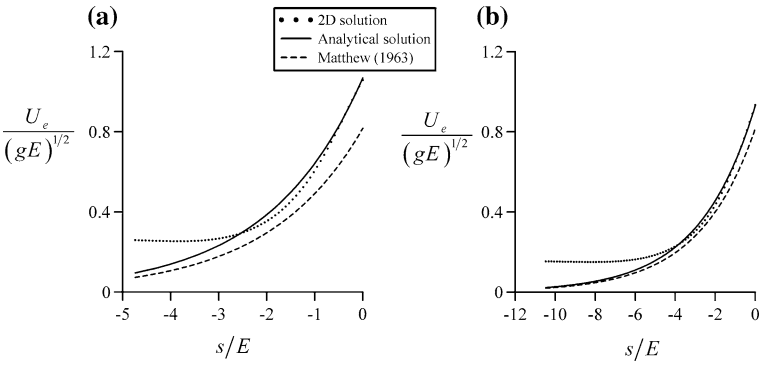

Fig. 5.4 Comparison of relative potential bottom velocity $U_e/(gE)^{1/2}[s/E]$ for E/R = **a** 0.516, **b** 0.253 (adapted from Castro-Orgaz and Hager 2014a)

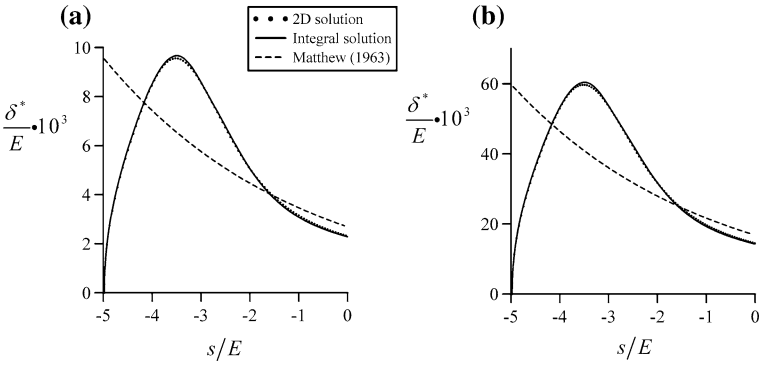

Fig. 5.5 Comparison of boundary layer displacement thickness profiles $(\delta^*/E)\times 10^3[s/E]$ for E/R = 0.516 and R = **a** 0.288 m, **b** 0.025 m (adapted from Castro-Orgaz and Hager 2014a)

points in the n-direction. Computational time was only a few seconds and it was verified that further subdivisions of the mesh did not alter the results. The good agreement of the 1D method of Thwaites with the 2D solution supports its use for computing laminar boundary layers in weir models, thereby generalizing the study of Thwaites' equation applied to the broad-crested weir (Isaacs 1981). The figure includes also Matthew's equation (5.54), which is close neither to 1D nor 2D models, except near the weir crest. Computations for E/R = 0.516 and a weir of R = 0.025 m are shown in Fig. 5.5b, resulting in larger boundary layer thickness, further supporting the accuracy of Thwaites' method.

The results for E/R = 0.253 and weir radii of R = 0.288 m and R = 0.025 m are shown in Fig. 5.6. The boundary layer is thicker under this smaller head for identical R. Results confirm the excellent performance of Thwaites' method along the entire computational domain, although peaks are slightly overpredicted.

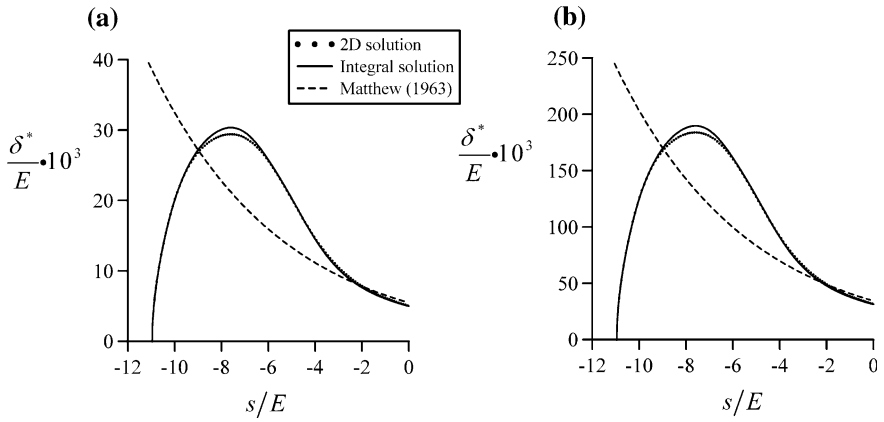

Fig. 5.6 Comparison of boundary layer displacement thickness profiles for $E/R = 0.253$ and R = **a** 0.288 m, **b** 0.025 m (adapted from Castro-Orgaz and Hager 2014a)

Matthew's method is only reliable near the crest. Computations for other heads and weir scales yield the same conclusions.

For discharge prediction, the quantity of main interest is the displacement thickness at the weir crest. The results for δ_c^*/E for heads of $E/R = 0.516$ and 0.253 and different weir scales using the 1D and 2D models are plotted in Fig. 5.7, including the prediction using the analytical solution given by Eq. (5.64). It agrees well with both the 1D and 2D models, thereby confirming its usefulness as predictor. Matthew's equation (5.55) is also compared with 1D and 2D models in Fig. 5.7, yet yielding less precise predictions.

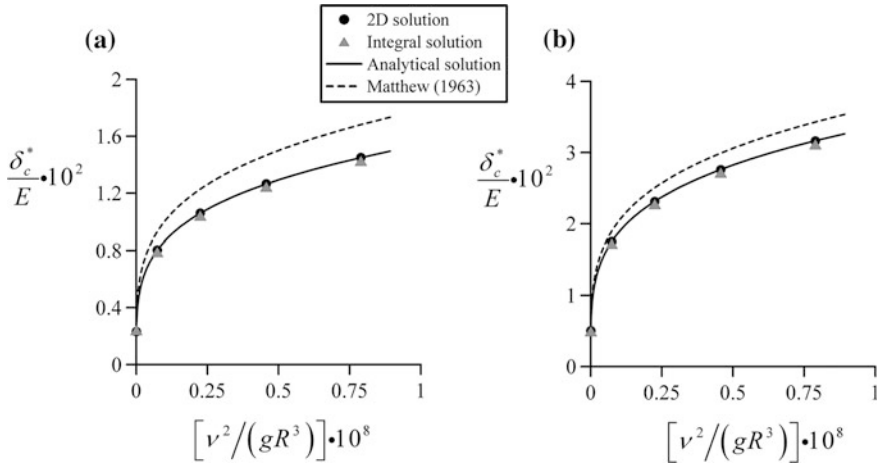

Fig. 5.7 Comparison of crest boundary layer displacement thickness for E/R = **a** 0.516, **b** 0.253 (adapted from Castro-Orgaz and Hager 2014a)

The discharge coefficient C_d from Eq. (5.38) is evaluated by using Eq. (5.39) for C_o, Eq. (5.26) for C_σ, and Eq. (5.37) for C_v along with Eq. (5.62) for δ_c^*/E combined with Eq. (5.64) for δ_d^*/E. Figure 5.8 compares the present approach with data of Matthew (1963) for a circular-crested weir of $R = 0.0254$ m and fluid temperature of 10 °C. Matthew's test setup consisted of a half cylinder mounted with vertical walls (inset of Fig. 5.8), for which the boundary layer displacement thickness at the starting point "a" of the boundary layer was taken zero. Hence, viscous effects on the crest point "b" originate from flow acceleration between "a" and "b." Figure 5.8 indicates that the predictions agree well with the test data. The ideal fluid flow curve is given by $C_d = (2/3)^{3/2} C_o$.

For comparative purposes, Matthew's (1961, 1963) theory is presented as follows. Using the weakly curved approximations at the critical point [see Eqs. (3.203) and (3.205)]

$$h_x^2 = \frac{h}{3R} = \frac{2E}{9R}, \quad hh_{xx} = \frac{4h}{9R} = \frac{8E}{27R}, \quad h = \frac{2}{3}E, \tag{5.65}$$

the coefficient C_o is estimated by [see Eq. (3.207)]

$$\begin{aligned} C_o &= \left(1 + \frac{2hh_{xx} - h_x^2}{3} + hz_{bxx}\right)^{-1/2} \\ &\approx 1 - \frac{hh_{xx}}{3} + \frac{h_x^2}{6} - \frac{hz_{bxx}}{2} \\ &\approx 1 - \frac{8}{81}\frac{E}{R} + \frac{1}{27}\frac{E}{R} + \frac{1}{3}\frac{E}{R} \\ &= 1 + \frac{22}{81}\frac{E}{R}, \end{aligned} \tag{5.66}$$

and the coefficient C_σ follows from Eq. (5.26)

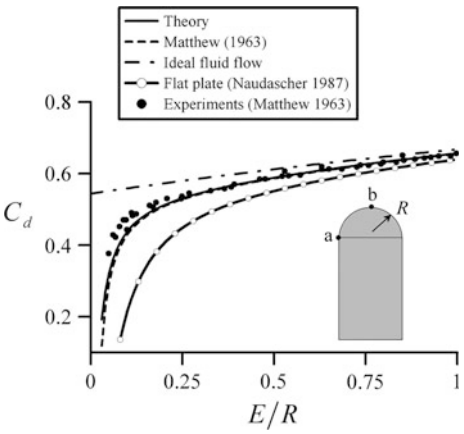

Fig. 5.8 Discharge coefficient $C_d(E/R)$ of a circular weir of $R = 0.0254$ m (adapted from Castro-Orgaz and Hager 2014a)

$$
\begin{aligned}
C_\sigma &= \left[1+\frac{3\sigma}{\gamma E}\frac{h_{xx}+z_{bxx}}{\left(1+h_x^2\right)^{3/2}}\right]^{1/2} \\
&\approx 1+\frac{3\sigma}{2\gamma E}\frac{h_{xx}+z_{bxx}}{\left(1+h_x^2\right)^{3/2}} \\
&\approx 1+\frac{3\sigma}{2\gamma E}\left(h_{xx}+z_{bxx}\right) \\
&\approx 1+\frac{3\sigma}{2\gamma E}\left(\frac{4}{9R}-\frac{1}{R}\right)=1-\frac{5}{6}\frac{\sigma}{\gamma ER}.
\end{aligned}
\tag{5.67}
$$

Using Matthew's boundary layer displacement thickness at the critical section

$$
\delta_c^* = 0.7 v^{1/2}\left(\frac{3R}{g}\right)^{1/4}, \tag{5.68}
$$

the coefficient C_v, stated in Eq. (5.37), takes the form

$$
\begin{aligned}
C_v &= \left(1-\frac{\delta_c^*}{E}\right)^{3/2} \approx 1-\frac{3}{2}\frac{\delta_c^*}{E} \\
&= 1-\frac{3}{2}0.7\frac{v^{1/2}}{E}\left(\frac{3R}{g}\right)^{1/4}=1-1.05\frac{v^{1/2}}{E}\left(\frac{3R}{g}\right)^{1/4}.
\end{aligned}
\tag{5.69}
$$

Inserting Eqs. (5.66)–(5.68) into Eq. (5.38) yields, by taking only first-order terms, Matthew's (1961, 1963) equation as

$$
C_d = \left(\frac{2}{3}\right)^{3/2}\left[1+\frac{22}{81}\frac{E}{R}-1.05\left(\frac{3}{g}\right)^{1/4}v^{1/2}R^{-3/4}\left(\frac{R}{E}\right)-0.833\left(\frac{\sigma}{\gamma R^2}\right)\left(\frac{R}{E}\right)\right]. \tag{5.70}
$$

He later improved the model to allow for larger streamline curvature effects on C_o by using Eq. (5.39) instead of Eq. (5.66); this led to (Matthew 1991)

$$
C_d = \left(\frac{2}{3}\right)^{3/2}\left[1+\frac{22}{81}\frac{E}{R}-0.045\left(\frac{E}{R}\right)^2-1.05\left(\frac{3}{g}\right)^{1/4}v^{1/2}R^{-3/4}\left(\frac{R}{E}\right)-0.833\left(\frac{\sigma}{\gamma R^2}\right)\left(\frac{R}{E}\right)\right]. \tag{5.71}
$$

Note the small deviations in this test from Matthew's Eq. (5.71). This indicates that in this test case Matthew's estimation of δ_c^*/E is adequate for discharge computation. The agreement of predictions confirms that $\delta_o^* = 0$ at point "a," thereby permitting to avoid consideration of the boundary layer development along the vertical weir face.

The present theory predicts the effects of viscosity and surface tension in the model well. Assuming that the prototype operates at $\mathsf{R} \rightarrow \infty$ and then implies that the difference between the ideal curve and the present theory would represent the scale effect. However, since the prototype suffers as well from viscous effects, this corresponds to the largest possible amount of scale effect if viscous effects were negligibly small in the prototype.

The experimental setup was further used to check the flat plate approach for scale effects originating from viscosity (Naudascher 1987, 1991), given by

$$\delta_c^* = 1.73L\left(\frac{U_c L}{\nu}\right)^{-1/2}. \tag{5.72}$$

Here, the flow development length L between points "a" and "b" is $L = \pi R/2$ and $U_c = [(2/3)gE]^{1/2}$. Results using Eq. (5.72) are plotted in Fig. 5.8. They indicate an overestimation of scale effects. Thus, the flat plate equations do not adequately account for the boundary layer behavior of round-crested weir flows.

The present theory is compared in Fig. 5.9a with the 3D numerical simulations by Pfister et al. (2013) for $R = 0.005$ m. The numerical results were obtained by solving the Reynolds equations for turbulent flow using the commercial code Flow 3D. Note that the current analytical theory agrees well with the 3D numerical data. Predictions according to Eq. (5.71) are also included, in which scale effects are overpredicted, as noted by Pfister et al. (2013). The improved predictions of the present theory stem from the improved treatment of surface tension effects at high normalized heads E/R. Predictions of the present theory are also compared with the 3D simulations of Pfister et al. (2013) for $R = 0.010$ m (Fig. 5.9b). Again, the theory agrees well with the numerical data and also improves predictions as compared to Eq. (5.71).

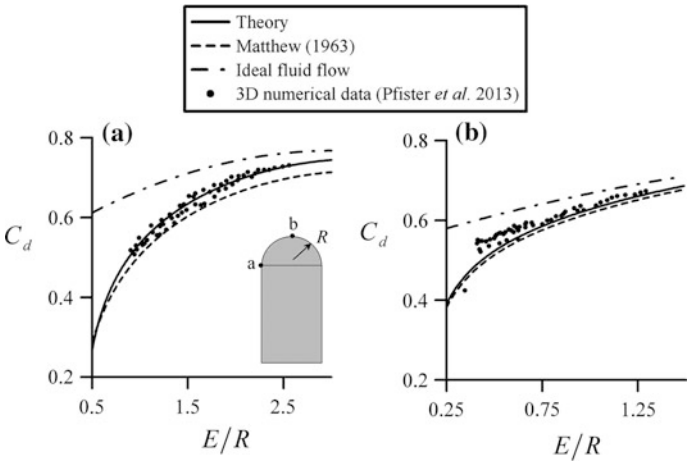

Fig. 5.9 Discharge coefficient $C_d[E/R]$ of a circular weir with $R =$ **a** 0.005 m, **b** 0.010 m (adapted from Castro-Orgaz and Hager 2014a)

Experiments conducted by Montes at the University of Tasmania in 1991 (Chanson and Montes 1997) are considered in Fig. 5.10. The experimental setup consisted of full cylinders mounted on a thin plate (inset of Fig. 5.10a). This is not a practical weir setup for prototypes, but applies for laboratory studies. Only a circular weir of $R = 0.029$ m is considered here, because scale effects were detected. A first data check indicates smaller values of C_d at high normalized heads ($E/R = 2.5$ to 3) than predicted by the ideal fluid flow theory. Comparison of these experimental values for $C_d(E/R)$ with another data set of Montes (1991) using the same R and an upstream ramp indicates the same trend at high E/R. The circular weir with an upstream ramp was also tested by Ramamurthy and Vo (1993a, b). They found that the flow was essentially irrotational, with a very thin boundary layer. Their discharge data were in excellent agreement with ideal fluid flow computations. Montes (1970) states that the crest flow conditions at a circular weir are essentially irrotational under high E/R. For these conditions, a close agreement between the ideal fluid flow theory and experiments of circular weir flows is reported (Fawer 1937; Ramamurthy and Vo 1993a, b; Ramamurthy et al. 1994). The experimental error in discharge was within ±4 % (Chanson and Montes 1997). Corrected data in Fig. 5.10a indicate excellent agreement with the ideal fluid flow theory for high normalized heads. This correction hardly affects the low-head data, for which the kinetic energy head is small. This is the flow zone of interest for the present study, where scale effects are present. Note the appreciable drop in C_d originating from real fluid flow features.

The present theory was then compared with observations in Fig. 5.10a, resulting in a clear underprediction of scale effects at fluid temperature of 20 °C. The reason is at first glance not evident. A re-examination of the experimental setup suggests

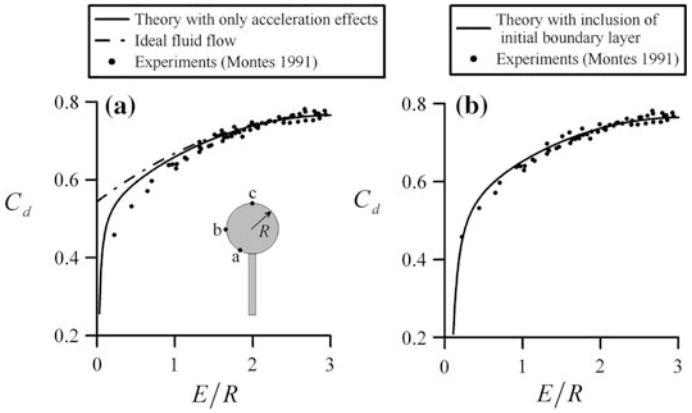

Fig. 5.10 Discharge coefficient $C_d[E/R]$ of a circular weir flow with $R = 0.029$ m for predictions **a** without, **b** with initial boundary layer (adapted from Castro-Orgaz and Hager 2014a)

that the particular design may induce additional scale effects. Along the half cylinder mounted on vertical walls the flow accelerates toward the weir crest, where the boundary layer starts. For a full cylinder mounted on a thin plate, the flow in the half submerged cylinder portion is close to stagnation. However, there may be a boundary layer development from "a" to "b" (inset of Fig. 5.10a), so that at point "b" $\delta_o^* \neq 0$, in contrast to the former setup. Thus, the hypothesis of additionally induced scale effects by this setup was tested by inclusion of the boundary layer development from points "a" to "b." Neglecting acceleration effects between the two points, Thwaites' equation yields for the momentum thickness at point "b"

$$\frac{\theta_{mo}^2}{\nu} = aU_e^{-b}\int_0^{s_o} U_e^{b-1}\mathrm{d}s \approx aU_o^{-1}s_o. \tag{5.73}$$

Inserting Eq. (5.73) into Eq. (5.61), the displacement thickness at point "c" is predicted for prescribed s_o and U_o. The approximations $U_o = U_c\exp[-R(2RE)^{-1/2}]$ and $s_o = 0.5R$ were adopted. Computations were performed with the predictions presented in Fig. 5.10b. The adopted approximations produce an almost perfect prediction of C_d for the smaller heads, also generating reasonable predictions for the remaining portion. Computations thus support the hypothesis that the circular cylinder mounted on a thin plate induces additional scale effects relating to the boundary layer at the starting point "b" of the overflow crest. The present theory accounts for this effect and yields a reasonable prediction of the discharge characteristics accounting for scale effects.

Sarginson (1972, 1984) conducted experiments using full cylinders mounted on thin plates, as in the previous case. His experimental data set was used to further check of the present theory. Predictions are compared with experimental data for $R = 0.0125$, 0.0065, and 0.003 m in Fig. 5.11 at a fluid temperature of 20 °C. The agreement in all cases is good, thereby supporting the approximate theory. Note the large deviations of ideal fluid flow from the present theory for the smallest weir scale of $R = 0.003$ m operating at high head. This case is an extreme deserving more consideration. First, the limits need to be stated for the proposed theory. On inspecting h_x^2 in Eq. $(5.40)_1$, observe that its physical meaning ceases at $E/R \approx 3$, for which $h_x^2 \approx 0$. The C_o coefficient, given by Eq. (5.39), works well up to this limit, so that it is adopted as limit of validity of the current method. The C_d prediction of Eq. (5.71) is included in Fig. 5.11c to highlight its validity limit. First, this relation implicitly contains Eq. (5.39) as the basic effect of potential flow with curvilinear streamlines on the discharge characteristics (Castro-Orgaz 2012). The viscous effect is dominant at low E/R, and its effect is normally small for high E/R, so that the dominating scale effect under high operational head E/R is surface tension, if R is very small (Fig. 5.11c). Surface tension effects accounted for in Eq. (5.71) are based on the weakly curved relations $h_x^2 = h/(3R)$, $(1 + h_x^2)^{3/2} \approx 1$ and $h_{xx} = (4/9)R$ (Hager 1985) [see Eq. (5.65)], from which $C_\sigma = [1 - (5/6)\sigma/(\gamma RE)]$ [see Eq. (5.67)]. The weakly curved relations used to produce C_σ are limited to $E/R < 1$. Surface tension effects fully depend on the curvilinear flow modeling, so that the effects of

surface tension in Eq. (5.71) cannot be expected to be well accounted for beyond the upper bound $E/R = 1$. In short, the inclusion of streamline curvature effects is contradictory in Eq. (5.71); it is large relative to C_o [upper limit $E/R = 3$)], but weak for surface tension effects [upper limit $E/R = 1$)]. Accordingly, Eq. (5.71) is inaccurate for $E/R > 1$, as it is highlighted with the improved performance of the current theory in Fig. 5.11c.

A broad-crested weir is also analyzed using the theory developed for round-crested weirs. Flow in the vicinity of the upstream corner of a broad-crested weir generates a free streamline separating from the bottom. The free streamline provokes a recirculating flow zone. According to Moss (1972), this separation pocket is essentially recirculating, with a shear layer above it. Moss proposed a simplified model, involving a stagnant bubble and an irrotational stream passing above it. The shear layer is approximated by a thin boundary layer, which was

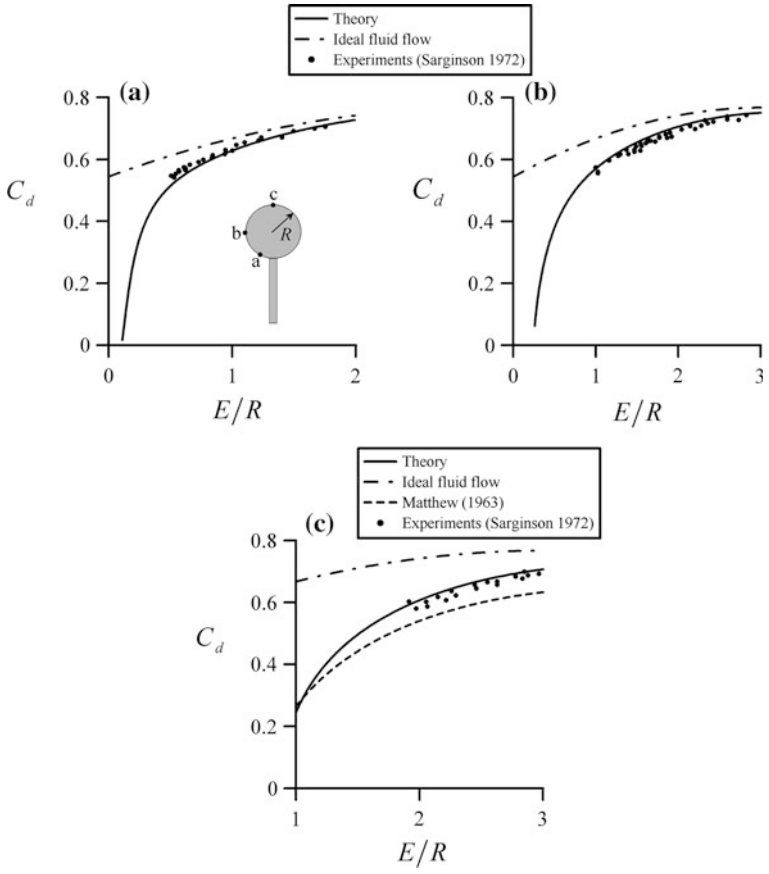

Fig. 5.11 Discharge coefficient $C_d[E/R]$ of a circular weir for $R =$ **a** 0.0125 m, **b** 0.0065 m, **c** 0.003 m (adapted from Castro-Orgaz and Hager 2014a)

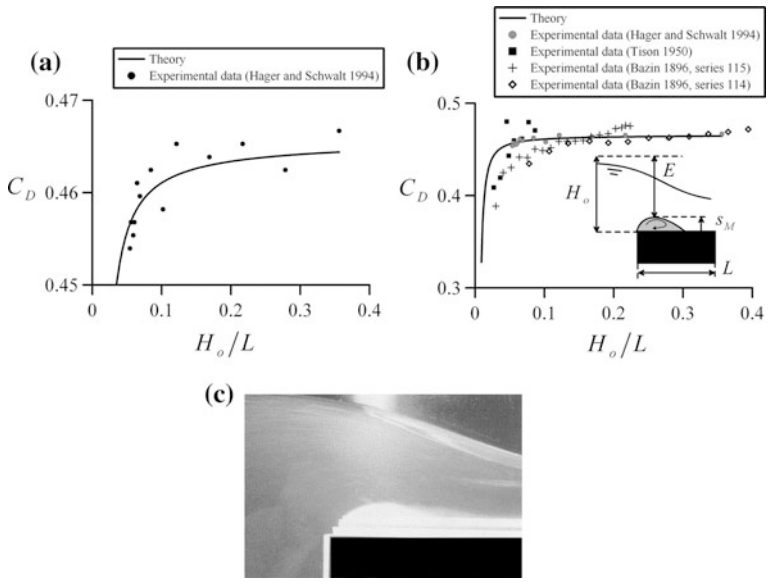

Fig. 5.12 Broad-crested weir flow using the round-crested weir-flow analogy, comparison of theory with **a** data of Hager and Schwalt (1994), **b** several data sets (adapted from Castro-Orgaz and Hager 2014a), **c** photograph of separation bubble (Hager 1999)

overlooked by Moss. His treatment is based on an idea of Hunter Rouse in the 1930s, essentially assuming that a small spillway profile is added to the upstream broad-crested weir corner. The discharge characteristics of the broad-crested weir are then determined using these of round-crested weirs, with s_M as the maximum separation thickness of the corner bubble, and H_o as the upstream head on the broad-crested weir (inset of Fig. 5.12b).

The discharge equation of the broad-crested weir is with C_D as discharge coefficient (Hager and Schwalt 1994)

$$q = C_D\left(gH_o^3\right)^{1/2}; \tag{5.74}$$

for definitions of parameters, see Fig. 5.12. The separation bubble is assumed to be solid, guiding an external irrotational stream (Moss 1972). Using a flow analogy, the specific energy at the virtual round-crested weir is $E = H_o - s_M$. Combining Eqs. (5.74) and (5.22) yields C_D as a function of the discharge coefficient of the round-crested weir C_d as

$$C_D = C_d\left(\frac{H_o - s_M}{H_o}\right)^{3/2}. \tag{5.75}$$

Consider first irrotational flow without surface tension at the water surface and a shear layer above the bubble. Experimental data indicate that $R = 1.2H_o$ (Hager and Schwalt 1994). The value of s_M was determined by Moss (1972) to be $0.15H_o$, whereas Hager and Schwalt's (1994) laboratory data indicate $0.2H_o$. A value $s_M = 0.185H_o$ was considered, so that $E/R = (H_o - s_M)/R = 0.679$, $C_d = (2/3)^{3/2}C_o = 0.633$ [using Eq. (5.39) for C_o], so that $C_D = 0.466$ from Eq. (5.75). This value remarkably agrees with the accepted value of 0.463. Thus, the round-crested weir-flow analogy allows for a realistic prediction of C_D. The broad-crested weir coefficient for ideal fluid flow without a separation bubble originating from Bélanger's critical flow condition is $C_d = (2/3)^{3/2} = 0.544$, so that the reduction of 0.544 to 0.466 is due to flow separation at the upstream corner.

Laboratory data of Hager and Schwalt (1994) are plotted in Fig. 5.12a versus H_o/L. The effects of surface tension and viscosity were then accounted for using Eq. (5.38). This automatically admits the existence of the shear layer above the bubble, a feature so far overlooked. The C_D curve of the present theory using the approximate values of R and s_M varies only with the absolute head H_o. The weir length $L = 0.50$ m was used to scale the results, with the theoretical prediction compared with the data in Fig. 5.12a. Note that the present theory predicts a drop in C_D as H_o/L reduces, in agreement with the experimental data. This reduction is provoked by the inclusion of the effects of viscosity and surface tension, i.e., the scale effects relating to the existence of a shear layer above the separation bubble and surface tension at the water surface. Figure 5.12a shows good theoretical predictions if $0.05 < H_o/L < 0.40$. The data sets of Bazin (1896) and Tison (1950) are also compared with the present theory in Fig. 5.12b, resulting in an overall agreement for the broad-crested weir range. In the long-crested weir domain, $H_o/L < 0.1$, the experimental data indicate a larger reduction in C_D than predicted by the theory. This issue needs further research, yet the present simplified model describes the order of magnitude of C_D in this domain adequately.

Given a round-crested weir model of crest radius R, what is the minimum overflow head $E_{\min}$ to avoid significant scale effects? This basic question is answered by applying the developed theory. For a given R the curve $C_d(E/R)$ is determined from the present theory. Define the ideal (subscript i) fluid flow curve by $C_{di} = (2/3)^{3/2}C_o$. Accepting a drop in C_d due to scale effects of say $C_d/C_{di} = 0.98$, the value of E/R at which this occurs is determined. Multiplying it by R results in $E_{\min}$. This computation was done for $0.006 < R < 0.30$ m. Based on the present theory, Fig. 5.13a indicates that $E_{\min}/R$ is high for small R, which is the domain where Matthew's Eq. (5.71) is inaccurate. For comparative purposes, $E_{\min}$ was determined using Eq. (5.71), with the results in Fig. 5.13b. Note the difference between Matthew's and the present theories for small R (Fig. 5.13c). 3D numerical data of Pfister et al. (2013) are also plotted, confirming values of $E_{\min}$ below those of computations with Eq. (5.71). Given the uncertainty of $E_{\min}$ for $R < 0.01$ m, this is the smallest weir radius recommended for laboratory applications. For practical

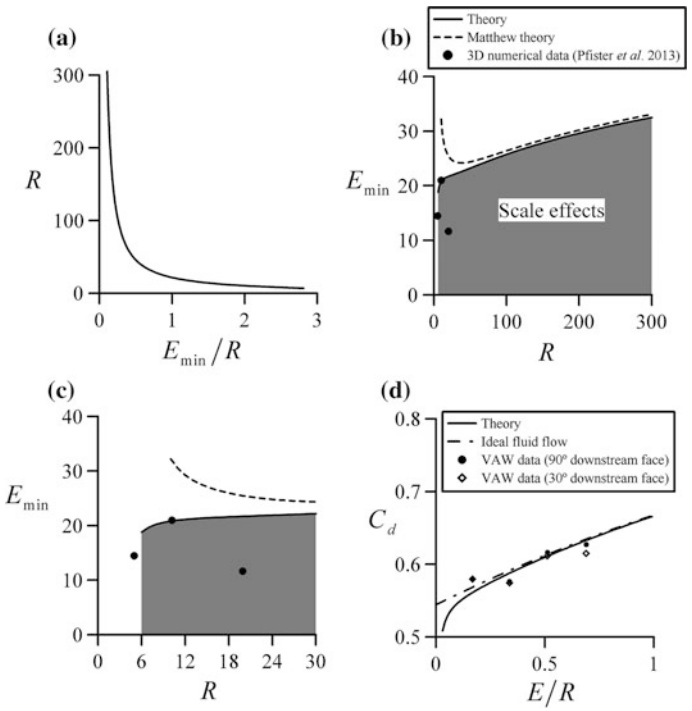

Fig. 5.13 Scale effects of round-crested weir flows **a** Limiting relation $R(E_{min}/R)$ for 2 % reduction in C_d due to scale effects, **b** minimum overflow head E_{min} versus R to avoid significant scale effects (with E_{min} and R in mm), **c** detail of (**b**) for $R < 30$ mm, **d** VAW experiments to avoid significant scale effects (adapted from Castro-Orgaz and Hager 2014a)

applications in the range $0.01 < R < 0.30$ m, the discharge curve is free of significant scale effects if $E_{min} > 0.04$ m. Selected experiments were conducted at VAW, ETH Zurich, to confirm a design free of significant scale effects. A circular weir made with a half-cylindrical crest of $R = 0.30$ m was inserted in a 0.50-m-wide flume. Downstream slopes of 30° and 90° were considered. According to the present theory, $E_{min} = 0.0325$ m for $R = 0.30$ m, corresponding to $E/R = 0.108$. This value was adopted as the minimum overflow head for experimentation. The discharge curve was experimentally determined starting at an overflow head of 0.05 m. The experimental data are plotted in Fig. 5.13d, along with the theoretical C_d and C_{di} curves. Note that the discharge curve is free of significant scale effects, as preferred in the design of experiments.

Note that boundary layer presence does not necessarily result in significant scale effects (e.g., for turbulent flow in both prototype and model). They are likely to result in significant scale effects if the boundary layer is turbulent in the prototype and laminar in the model, or if the boundary layer is laminar in both the prototype and the model. Here, the most frequent case of laminar boundary layer in the model and turbulent boundary layer in the prototype at high R is addressed.

5.2.2 *Developing Flow on Steep Slopes*

As water flows down a chute, a turbulent boundary layer develops (Fig. 5.14). This region is known as *developing zone*, where a turbulent boundary layer coexists with a region of irrotational flow above the boundary layer, up to their intersection. The prediction of the free surface and the turbulent boundary layer profiles is necessary to determine the air inception point at which free surface aeration starts (Falvey 1980) if the turbulent energy at the free surface is sufficiently strong to overcome surface tension effects (Wood 1991). Several methods were proposed in the literature to study the developing zone, including the use of backwater computations based on equations for fully developed flows using the Darcy–Weisbach or Gauckler–Manning–Strickler equations (Falvey 1990; Hager and Blaser 1998), and empirical power-law fits to the boundary layer (Bauer 1954; Campbell et al. 1965). Keller and Rastogi (1975) presented detailed computations of the developing zone by integrating the Reynolds equations with a k–ε model for boundary layer-type flows. However, their model is too complicated for engineering practice so that a set of design charts for the position of the inception point was presented (Keller and Rastogi 1977). Wood et al. (1983) developed a semiempirical fit to their design charts for predicting the characteristics of the inception point of air entrainment (point I in Fig. 5.14).

Castro-Orgaz (2009) presented an analytical approach for the developing zone based on the simultaneous solution of the momentum equation of the boundary layer and the energy equation for the irrotational flow zone. The model applies to flows

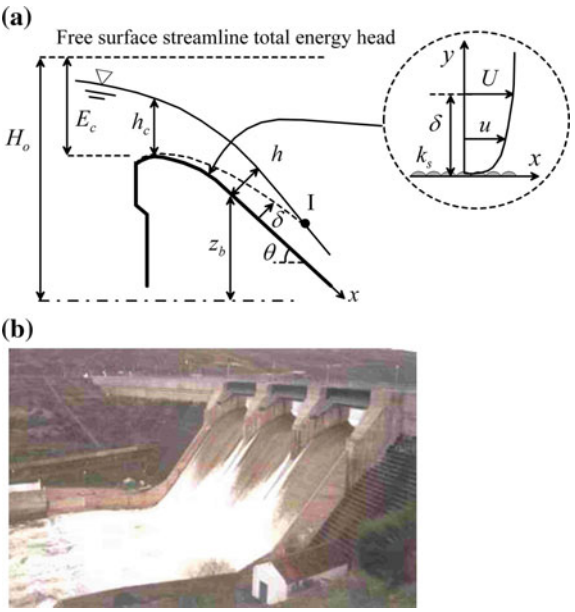

Fig. 5.14 Developing free surface flow over chute spillway **a** definition sketch, **b** Agueda Dam, Spain (adapted from Castro-Orgaz 2009)

over uncontrolled spillways followed by a steep chute of constant slope, typically larger than 0.1, with a developing boundary layer flow in the turbulent-rough regime. Flow on a steep chute is non-hydrostatic (Chap. 2; Appendix H). If the x-coordinate is selected following the chute bottom profile, and the water depth is measured normal to the bottom surface, the pressure head is given by

$$p_b = \rho g h \cos\theta. \tag{5.76}$$

The bottom slope effect is therefore important at steep slopes and must be accounted for in the pressure head (see Appendix H). Consider steady free surface flow over the tailwater portion of an ogee crest (Fig. 5.14). The energy head H_o of the free surface streamline remains constant at (Montes 1998; Castro-Orgaz 2009)

$$H_o = z_b + h\cos\theta + H_s. \tag{5.77}$$

Here, z_b is the chute bottom elevation, h the flow depth measured normal to the bottom curve, θ the channel bottom angle with the horizontal, and H_s the velocity head, given by (Silberman 1980; Montes 1998) [see Eq. (5.30)]

$$H_s = \frac{U^2}{2g} = \frac{q^2}{2g(h-\delta^*)^2}, \tag{5.78}$$

with q as the discharge per unit chute width, U the potential flow velocity, and δ^* the boundary layer displacement thickness. The energy head of the free surface streamline remains constant for potential flow, so that $\mathrm{d}H_o/\mathrm{d}x = 0$, with x as the slope-fitted coordinate along the chute. Inserting Eq. (5.78) into Eq. (5.77) yields

$$H_o = z_b + h\cos\theta + \frac{q^2}{2g(h-\delta^*)^2}. \tag{5.79}$$

Differentiation of Eq. (5.79) with respect to x, noting that $\mathrm{d}H_o/\mathrm{d}x = 0$, produces the generalized drawdown curve for chute flows as (Silberman 1980; Castro-Orgaz 2009)

$$\frac{\mathrm{d}h}{\mathrm{d}x} = \frac{\sin\theta - \dfrac{q^2}{g(h-\delta^*)^3}\dfrac{\mathrm{d}\delta^*}{\mathrm{d}x}}{\cos\theta - \dfrac{q^2}{g(h-\delta^*)^3}}. \tag{5.80}$$

Equation (5.80) describes the free surface profile of chute flows for developing channel flows, contrary to the standard backwater equation (Chanson 2004), which uses friction slope computations based on equations for fully developed flows as those of Darcy–Weisbach or Gauckler–Manning–Strickler. The potential flow version of Eq. (5.80) is given as

$$\frac{\mathrm{d}h}{\mathrm{d}x} = \frac{\sin\theta}{\cos\theta - \frac{q^2}{gh^3}}. \tag{5.81}$$

This statement is mathematically equivalent to the chute flow model previously developed using horizontal–vertical Cartesian coordinates (Appendix H) [see Eq. (3.443)]. However, use of the system of coordinates pursued in the ensuing developments is advantageous, given the inclusion of the boundary layer development in the analysis.

For hypercritical flows with the Froude number $\mathsf{F} = q/(gh^3)^{1/2} > 3$, the drawdown free surface curve is governed by the kinetic energy head variation along the chute (Hager and Blaser 1998; Castro-Orgaz 2009). Then, from Eq. (5.80)

$$\frac{\mathrm{d}h}{\mathrm{d}x} = \frac{\sin\theta - \dfrac{q^2}{g(h-\delta^*)^3}\dfrac{\mathrm{d}\delta^*}{\mathrm{d}x}}{-\dfrac{q^2}{g(h-\delta^*)^3}}. \tag{5.82}$$

With the dimensionless variables $Y = h/h_{cH}$, $Z = \delta^*/h_{cH}$ and $\chi = x/h_{cH}$, Eq. (5.82) yields

$$\frac{\mathrm{d}Y}{\mathrm{d}\chi} = \frac{\tan\theta - \frac{1}{(Y-Z)^3}\frac{\mathrm{d}z}{\mathrm{d}\chi}}{-\frac{1}{(Y-Z)^3}}, \tag{5.83}$$

or

$$\frac{\mathrm{d}}{\mathrm{d}\chi}(Y-Z) = -\tan\theta(Y-Z)^3. \tag{5.84}$$

Here, $h_{cH} = [q^2/(g\cos\theta)]^{1/3}$ is the critical depth of parallel-streamlined potential flows in a sloping channel. Integration of Eq. (5.84) subject to the boundary conditions $Y_0 = Y(\chi = \chi_0)$ and $Z_0 = Z(\chi = \chi_0)$ yields

$$Y = Z + \left[(Y_0 - Z_0)^{-2} + 2\tan\theta(\chi - \chi_0)\right]^{-1/2}. \tag{5.85}$$

Equation (5.85) describes the free surface profile $Y(\chi)$ in chute flow once a closure equation for the dimensionless boundary layer displacement thickness profile $Z(\chi)$ is given. Equation (5.85) is composed of the term Z representing the real fluid flow effects, and a second term accounting for the irrotational flow outside the boundary layer. Thus, the flow depth Y is made up of the potential (subscript p) flow depth Y_p plus the displacement thickness Z of the boundary layer as

$$Y = Y_p + Z. \tag{5.86}$$

The potential flow depth Y_p for the boundary condition involving critical flow ($Y_0 = 1$) at the boundary layer origin ($Z_0 = 0$) is, from Eq. (5.85),

$$Y_p = [1 + 2\chi \tan\theta]^{-1/2}. \tag{5.87}$$

Equation (5.87) is compared in Fig. 5.15 with the exact potential flow solution obtained from Eq. (5.79), which, for critical flow with parallel streamlines at the weir crest, is given by the relation

$$E_c = \frac{3}{2}\left(\frac{q^2}{g}\right)^{1/3} = -x\sin\theta + h\cos\theta + \frac{q^2}{2gh^2}, \tag{5.88}$$

where E_c is the specific energy at the weir crest, or once normalized,

$$\frac{3}{2} = -\chi\tan\theta + Y_p + \frac{1}{2Y_p^2}; \tag{5.89}$$

this can be rewritten as

$$Y_p = \left[3 - 2Y_p + 2\chi\tan\theta\right]^{-1/2}. \tag{5.90}$$

The hypercritical flow approach is seen to give a reasonable estimate of the free surface profile for air inception points away from the weir crest. Only minor discrepancies are expected near the crest, where the hypercritical approach predicts a slight increase in the flow depth. However, this region has no practical relevance so that the hypercritical approach applies for practical purposes.

Conservation of momentum within the boundary layer is given by the von Kármán integral equation as (Bauer 1954; White 1991)

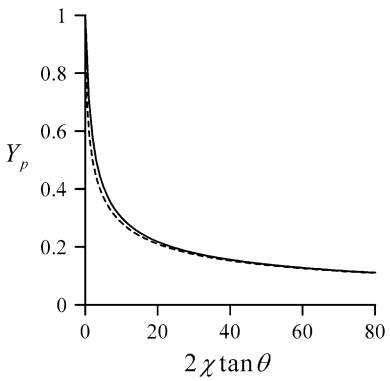

Fig. 5.15 Free surface profile $Y_p(2\chi\tan\theta)$: (—) hypercritical potential flow solution, Eq. (5.87), (- - -) exact potential flow solution, Eq. (5.90) (adapted from Castro-Orgaz 2009)

$$\frac{1}{2}C_f = \frac{\mathrm{d}\theta_m}{\mathrm{d}x} + \left(1 + \frac{1}{2}S\right)\frac{\theta_m}{U^2}\frac{\mathrm{d}U^2}{\mathrm{d}x}. \tag{5.91}$$

Here, $C_f = \tau_b/(\rho U^2/2)$ is the skin friction coefficient, τ_b the boundary shear stress, ρ the water density, θ_m the boundary layer momentum thickness, and S the shape factor of the boundary layer. According to Bauer (1954), the velocity profiles in sloping chutes are better correlated with power-law models than by the classical logarithmic law of the wall, used by Halbronn (1952, 1954). The generalized equation for a power-law velocity profile is (Chen 1991)

$$\frac{u}{u^*} = \Lambda\left(\frac{y}{k_s}\right)^{1/n}, \tag{5.92}$$

where y is the distance normal to the chute face, k_s the equivalent roughness height, u the velocity parallel to the chute face at distance y (Fig. 5.14a), Λ a coefficient, n an exponent, and $u^* = (\tau_b/\rho)^{1/2}$ the shear velocity. Equation (5.92) is rewritten as (Chanson 1997)

$$\frac{u}{U} = \left(\frac{y}{\delta}\right)^{1/n}, \tag{5.93}$$

in which δ is the boundary layer thickness, where $u = U$. The boundary layer displacement thickness δ^* is computed as follows (White 1991)

$$\delta^* = \int_0^\delta \left(1 - \frac{u}{U}\right)\mathrm{d}y = \int_0^\delta \left(1 - \frac{y^{1/n}}{\delta^{1/n}}\right)\mathrm{d}y = \frac{\delta}{1+n}, \tag{5.94}$$

and the momentum thickness θ_m is given by

$$\theta_m = \int_0^\delta \frac{u}{U}\left(1 - \frac{u}{U}\right)\mathrm{d}y = \int_0^\delta \frac{y^{1/n}}{\delta^{1/n}}\left(1 - \frac{y^{1/n}}{\delta^{1/n}}\right)\mathrm{d}y = \frac{\delta n}{(1+n)(2+n)}, \tag{5.95}$$

resulting in the shape factor $S = \delta^*/\theta_m = (n + 2)/n$. Inserting Eqs. (5.94) and (5.95) into Eq. (5.91) yields the expression

$$\frac{1}{2}C_f = \frac{n}{(n+1)(n+2)}\frac{\mathrm{d}\delta}{\mathrm{d}x} + \left(1 + \frac{1}{2}S\right)\frac{n}{(n+1)(n+2)}\frac{\delta}{U^2}\frac{\mathrm{d}U^2}{\mathrm{d}x}. \tag{5.96}$$

Inserting the value of S for the power-law velocity model leads to

$$\frac{1}{2}C_f = \frac{n}{(n+1)(n+2)}\frac{\mathrm{d}\delta}{\mathrm{d}x} + \left(1 + \frac{1}{2}\frac{n+2}{n}\right)\frac{n}{(n+1)(n+2)}\frac{\delta}{U^2}\frac{\mathrm{d}U^2}{\mathrm{d}x}. \tag{5.97}$$

Equation (5.92), evaluated at $y = \delta$, yields

$$\frac{U}{u^*} = \Lambda\left(\frac{\delta}{k_s}\right)^{1/n}, \tag{5.98}$$

and, by definition, τ_b written in the alternative forms

$$\tau_b = \rho C_f \frac{U^2}{2} = \rho u^{*2}, \tag{5.99}$$

leads to

$$\frac{U}{u^*} = \left(\frac{2}{C_f}\right)^{1/2}. \tag{5.100}$$

Equating Eqs. (5.98) and (5.100) yields

$$\left(\frac{2}{C_f}\right)^{1/2} = \Lambda\left(\frac{\delta}{k_s}\right)^{1/n}, \tag{5.101}$$

from which C_f is computed as

$$C_f = 2\Lambda^{-2}\left(\frac{\delta}{k_s}\right)^{-2/n}. \tag{5.102}$$

For hypercritical flows, the kinetic energy is greater than ($h\cos\theta$) in Eq. (5.88). Thus, neglecting ($h\cos\theta$), the following approximation is adopted from the potential flow version of Eq. (5.88)

$$\frac{U^2}{2g} \approx E_c + x\sin\theta, \tag{5.103}$$

where E_c is the specific energy at the weir crest ($x = 0$), resulting in

$$\frac{\mathrm{d}}{\mathrm{d}x}\left(\frac{U^2}{2g}\right) \approx \sin\theta, \tag{5.104}$$

so that

$$\frac{1}{U^2}\frac{\mathrm{d}U^2}{\mathrm{d}x} \approx \frac{\sin\theta}{E_c + x\sin\theta}. \tag{5.105}$$

Inserting Eqs. (5.102) and (5.105) into Eq. (5.97) yields the differential equation for the boundary layer thickness $\delta(x)$ as

$$\Lambda^{-2}\left(\frac{\delta}{k_s}\right)^{-2/n} = \frac{n}{(n+1)(n+2)}\frac{\mathrm{d}\delta}{\mathrm{d}x} + \left(1 + \frac{1}{2}\frac{n+2}{n}\right)\frac{n}{(n+1)(n+2)}\left(\frac{\sin\theta}{E_c + x\sin\theta}\right)\delta. \tag{5.106}$$

This equation is rewritten as

$$\frac{1}{\Lambda^2}k_s^{2/n}\delta^{-2/n} = \frac{n}{(n+1)(n+2)}\frac{\mathrm{d}\delta}{\mathrm{d}x} + \left(\frac{3n+2}{2n}\right)\frac{n}{(n+1)(n+2)}\left(\frac{E_c}{\sin\theta} + x\right)^{-1}\delta, \tag{5.107}$$

or

$$\frac{1}{\Lambda^2}k_s^{2/n} = \frac{n}{(n+1)(n+2)}\delta^{2/n}\frac{\mathrm{d}\delta}{\mathrm{d}x} + \frac{3n+2}{2(n+1)(n+2)}\left(\frac{E_c}{\sin\theta} + x\right)^{-1}\delta^{\frac{2}{n}+1}. \tag{5.108}$$

Noting that

$$\frac{\mathrm{d}}{\mathrm{d}x}\left(\delta^{\frac{2}{n}+1}\right) = \left(\frac{2}{n}+1\right)\delta^{2/n}\frac{\mathrm{d}\delta}{\mathrm{d}x} = \frac{n+2}{n}\frac{\mathrm{d}\delta}{\mathrm{d}x}, \tag{5.109}$$

Equation (5.108) transforms to

$$\frac{1}{\Lambda^2}k_s^{2/n} = \frac{n^2}{(n+1)(n+2)^2}\frac{\mathrm{d}}{\mathrm{d}x}\left(\delta^{\frac{2}{n}+1}\right) + \frac{3n+2}{2(n+1)(n+2)}\left(\frac{E_c}{\sin\theta} + x\right)^{-1}\delta^{\frac{2}{n}+1}, \tag{5.110}$$

or

$$\underbrace{\frac{1}{\Lambda^2}\frac{(n+1)(n+2)^2}{n^2}k_s^{2/n}}_{=A} = \frac{\mathrm{d}}{\mathrm{d}x}\left(\delta^{\frac{2}{n}+1}\right) + \underbrace{\frac{(3n+2)(n+2)}{2n^2}}_{=B}\left(\frac{E_c}{\sin\theta} + x\right)^{-1}\delta^{\frac{2}{n}+1}. \tag{5.111}$$

Using the change of variables

$$\xi = \delta^{\frac{2}{n}+1}, \quad X = \frac{E_c}{\sin\theta} + x, \tag{5.112}$$

Equation (5.111) transforms to the ODE

$$A = \frac{\mathrm{d}\xi}{\mathrm{d}X} + B\frac{\xi}{X}, \tag{5.113}$$

whose solution is

$$\xi = cX, \tag{5.114}$$

with the constant of integration c given by

$$\begin{aligned} c = \frac{A}{1+B} = \frac{\frac{1}{\Lambda^2}\frac{(n+1)(n+2)^2}{n^2}k_s^{2/n}}{1+\frac{(3n+2)(n+2)}{2n^2}} &= \frac{2k_s^{2/n}}{\Lambda^2}\frac{(n+1)(n+2)^2}{[2n^2+(3n+2)(n+2)]} \\ &= \frac{2k_s^{2/n}}{\Lambda^2}\frac{(n+1)(n+2)^2}{(5n^2+8n+4)}. \end{aligned} \tag{5.115}$$

Thus, reverting Eq. (5.114) to the original primitive variables x and δ yields

$$\delta^{(2+n)/n} = \frac{2k_s^{2/n}}{\Lambda^2}\frac{(n+1)(n+2)^2}{(5n^2+8n+4)}\left(\frac{E_c}{\sin\theta}+x\right), \tag{5.116}$$

or, in dimensionless form,

$$\frac{D}{\chi+\Omega} = \left[\frac{2}{\Lambda^2}\frac{(n+1)(n+2)^2}{(5n^2+8n+4)}\right]^{\frac{n}{n+2}}\left(\frac{\chi+\Omega}{r}\right)^{-\frac{2}{n+2}}. \tag{5.117}$$

Here, $D = \delta/h_{cH}$ is the dimensionless boundary layer thickness, $r = k_s/h_{cH}$ the dimensionless roughness, and $\Omega = E_c/(h_{cH}\sin\theta)$ a weir crest parameter. Parameter Ω includes the effects of the spillway crest and the chute slope on the boundary layer growth. For an ungated spillway operating under design head and a chute slope of 45°, $\Omega \approx 1.44$ (Castro-Orgaz et al. 2008). The effect of the crest parameter decreases with the chute slope θ. For a given inflow condition, Ω reduces as the chute slope θ increases. Thus, according to Eq. (5.117), the dimensionless boundary layer thickness D decreases due to the retarding effect of the accelerating flow on the boundary layer growth. This effect, however, is negligible for $\theta > 30°$, so that the boundary layer growth depends mainly on the dimensionless number χ/r. For $\Omega \approx 0$, Eq. (5.117) is in agreement with the classical empirical power-law (Bauer 1954; Campbell et al. 1965; Cain and Wood 1981; Wood et al. 1983; Wood 1991)

$$\frac{\delta}{x} = \alpha \left(\frac{x}{k_s} \right)^{-\beta}, \tag{5.118}$$

with α as a coefficient and β the exponent of the boundary layer profile. From Eq. (5.117), the main parameters of boundary layer growth are (taking $\Omega = 0$)

$$\alpha = \left[\frac{2}{\Lambda^2} \frac{(n+1)(n+2)^2}{(5n^2+8n+4)} \right]^{\frac{n}{n+2}}, \quad \beta = \frac{2}{n+2}. \tag{5.119}$$

To compute α and β, a rational approach is thus required to estimate parameters n and Λ, using Eqs. (5.119). George (2007) proved that there is no universal log-law applicable to channel, pipe, and boundary layer flows. This clearly supports the existence of a wake component in the turbulent velocity profile, which is different for each flow type. George (2007) also noted that developing boundary layers are theoretically better described by power-law velocity profiles than by log-laws, as used by Halbronn (1952). This fact was also observed experimentally by Bauer (1951, 1954), given his finding that the log law was a poor-fit to his test data in most cases. It appears therefore reasonable to simulate velocity profiles of turbulent developing boundary layers with a power-law function, such as Eq. (5.92). However, most of the information available to produce a precise reproduction of the turbulent velocity profile relies on the use of wall-wake models (White 1991). Therefore, taking a wall-wake model as an accurate representation of the turbulent velocity profile, it will be used to define mathematically an equivalent power-law profile. The complete time-averaged velocity profile of a turbulent boundary layer is composed of a logarithmic wall-dominated term plus a wake component (White 1991). In the turbulent-rough regime, this is (Dean 1976; Montes 1998)

$$\frac{u}{u^*} = \frac{1}{\kappa} \ln \left(\frac{y}{k_s} \right) + B + \frac{1}{\kappa} (1 + 6\Pi) \left(\frac{y}{\delta} \right)^2 - \frac{1}{\kappa} (1 + 4\Pi) \left(\frac{y}{\delta} \right)^3. \tag{5.120}$$

Here, $\kappa = 0.41$ is the von Kármán constant, $B = 8.5$ is a constant of integration, and $\Pi \approx 0.2$ is the wake parameter for flows with a weak pressure gradient over rough surfaces (Kironoto and Graf 1994). The value selected for the wake parameter appears reasonable in the present problem, as the free surface profile only slightly converges to the channel bottom, a situation implying a pressure gradient $(\cos\theta \mathrm{d}h/\mathrm{d}x) \approx 0$. Equation (5.120), accounting for a wake component, closely matches experimental data of turbulent velocity profiles (Dean 1976; Montes 1998).

In contrast to the proposal of Chen (1991), Castro-Orgaz (2009) determined n and Λ by imposing a similar behavior between the power-law velocity profile (Eqs. 5.92 and 5.120), in terms of the turbulent boundary layer characteristics, given by C_f and δ^*. The displacement thickness of the boundary layer according to Eq. (5.120) is computed as follows. At the boundary layer edge $y = \delta$, Eq. (5.120) reads

$$\frac{U}{u^*} = \frac{1}{\kappa}\ln\left(\frac{\delta}{k_s}\right) + B + \frac{1}{\kappa}(1+6\Pi) - \frac{1}{\kappa}(1+4\Pi). \tag{5.121}$$

The velocity defect law based on Eqs. (5.120), (5.121) is

$$\frac{U-u}{u^*} = -\frac{1}{\kappa}\ln\eta + \frac{1}{\kappa}(1+6\Pi)\left(1-\eta^2\right) - \frac{1}{\kappa}(1+4\Pi)\left(1-\eta^3\right), \quad \eta = \frac{y}{\delta}, \tag{5.122}$$

or

$$1 - \frac{u}{U} = \underbrace{\frac{u^*}{\kappa U}}_{=z^{-1}}\left[-\ln\eta + (1+6\Pi)\left(1-\eta^2\right) - (1+4\Pi)\left(1-\eta^3\right)\right]. \tag{5.123}$$

The boundary layer displacement thickness is thus computed from

$$\begin{aligned}\delta^* = \delta\int_0^1\left(1-\frac{u}{U}\right)\mathrm{d}\eta &= \frac{\delta}{z}\left[-\eta(\ln\eta - 1) + (1+6\Pi)\left(\eta - \frac{\eta^3}{3}\right) - (1+4\Pi)\left(\eta - \frac{\eta^4}{4}\right)\right]_0^1 \\ &= \frac{\delta}{z}\left[1 + (1+6\Pi)\left(1-\frac{1}{3}\right) - (1+4\Pi)\left(1-\frac{1}{4}\right)\right] \\ &= \frac{\delta}{z}\left(\frac{11}{12} + \Pi\right).\end{aligned} \tag{5.124}$$

For the power-law velocity profile, the displacement thickness is given by Eq. (5.94). Imposing it as displacement thickness by equating Eqs. (5.94) and (5.124) results in

$$n = z\left(\frac{11}{12}+\Pi\right)^{-1} - 1 = \kappa\frac{U}{u^*}\left(\frac{11}{12}+\Pi\right)^{-1} - 1 = \kappa\left(\frac{2}{C_f}\right)^{1/2}\left(\frac{11}{12}+\Pi\right)^{-1} - 1. \tag{5.125}$$

The skin-friction coefficient is given by

$$\tau_b = \frac{1}{2}\rho C_f U^2. \tag{5.126}$$

Therefore, from Eq. (5.102),

$$\Lambda = \left(\frac{2}{C_f}\right)^{1/2}\left(\frac{\delta}{k_s}\right)^{-1/n}. \tag{5.127}$$

Using Eq. (5.121) results in

$$\frac{U}{u^*} = \frac{1}{\kappa}\ln\left(\frac{\delta}{k_s}\right) + 8.5 + \frac{2\Pi}{\kappa} \equiv \left(\frac{2}{C_f}\right)^{1/2}. \tag{5.128}$$

Inserting this into Eqs. (5.125) and (5.127) allows for computation of the power-law velocity profile parameters n and Λ. To avoid iterative computations, the term δ/k_s in Eqs. (5.127) and (5.128) was estimated using $\delta/k_s = 0.08(x/k_s)^{-0.767}$, based on Campbell et al. (1965). Note that the power-law parameters n and Λ vary along the chute, as do α and β, based on the local value of C_f. Equations (5.85) and (5.117) define a system of equations for the free surface profile $Y(\chi)$ and the boundary layer thickness profile $D(\chi)$ for ungated spillways. Using Eqs. (5.125) and (5.127) for the parameters n and Λ gives

$$Y = \frac{D}{1+n} + [1 + 2\chi\tan\theta]^{-1/2}, \tag{5.129}$$

$$D = \left[\frac{2}{\Lambda^2}\frac{(n+1)(n+2)^2}{(5n^2+8n+4)}\right]^{\frac{n}{n+2}} \left(\frac{\chi+\Omega}{r}\right)^{-\frac{2}{n+2}} (\chi+\Omega). \tag{5.130}$$

Results of the model computations are compared in Fig. 5.16 with the data of Bauer (1951, 1954) for a rough sloping chute of $\theta = 20°$, 40°, and 60°. The model results are in excellent agreement with the experimental data, for both the free surface and the boundary layer thickness profiles. Based on these results, an increase of θ moves the inception point upstream toward the spillway crest.

The model computations compare favorably with the test data of Bormann (1968) for a sloping chute of $\theta = 33.5°$ and several values of the relative roughness r. Figure 5.17 reveals the effect of r on the air inception point position for a constant chute slope. An increase of r seemed to increase the thickness D at a given location χ, so that the inception point moves upstream along the chute. This effect is partially counteracted by an increase in the flow depth Y due to the corresponding increase in Z with D.

On inspecting Eq. (5.117), it is found that the empirical Eq. (5.118) is theoretically justified for hypercritical flows using the power-law velocity profile in the integral momentum conservation equation for the boundary layer. Note that α and β were previously considered as empirical constants and determined from curve fitting, regardless of the value selected for n. Based on Eqs. (5.129) and (5.130), it is concluded that the effect of chute slope on the free surface profile is notable, but its effect on the boundary layer thickness development is small, if the chute slope is large. The main effect of chute slope on the position of the inception point thus originates from the free surface profile. Equations (5.129) and (5.130) yield the profiles $Y(\chi)$ and $D(\chi)$ along the chute resulting in the air inception point I at $Y(\chi) = D(\chi)$ (Fig. 5.14a), for given values of r, θ, and Ω. The esthetics of incipient aerated flow is shown in Fig. 5.14b. The computational results for the distance χ_I of

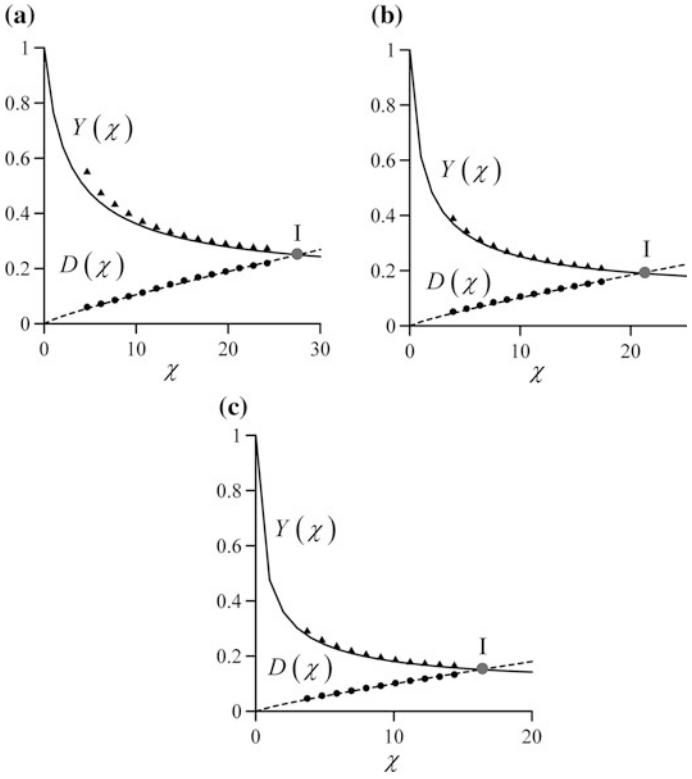

Fig. 5.16 Comparison of boundary layer development according to (▲, ●) Bauer (1951) with (—) $Y(\chi)$ from Eq. (5.129) and (- - -) $D(\chi)$ from Eq. (5.130) for θ = **a** 20°, **b** 40°, **c** 60° (adapted from Castro-Orgaz 2009); I is the inception point

the inception point from the weir crest are compared in Fig. 5.18a with those of Keller and Rastogi (1975, 1977), who used a computer model based on the solution of the Reynolds equations with a k–ε model to simulate flows over WES weir profiles.

As proved in Fig. 5.18a, the present model results agree well with their test data. The dimensionless flow depth at the air inception point is shown in Fig. 5.18b, indicating reasonable agreement with the available Aviemore Dam prototype data.

With $C_d = q/(gE_c^3)^{1/2}$ as spillway discharge coefficient, the model computations account for the crest parameter Ω given by

$$\Omega = \frac{E_c}{h_{cH}\sin\theta} = \frac{E_c}{\sin\theta\left(\frac{q^2}{g\cos\theta}\right)^{1/3}} = \frac{E_c}{\sin\theta\left(\frac{C_d g E_c^3}{g\cos\theta}\right)^{1/3}} = \left(\frac{\cos\theta}{C_d\sin^3\theta}\right)^{1/3}. \qquad (5.131)$$

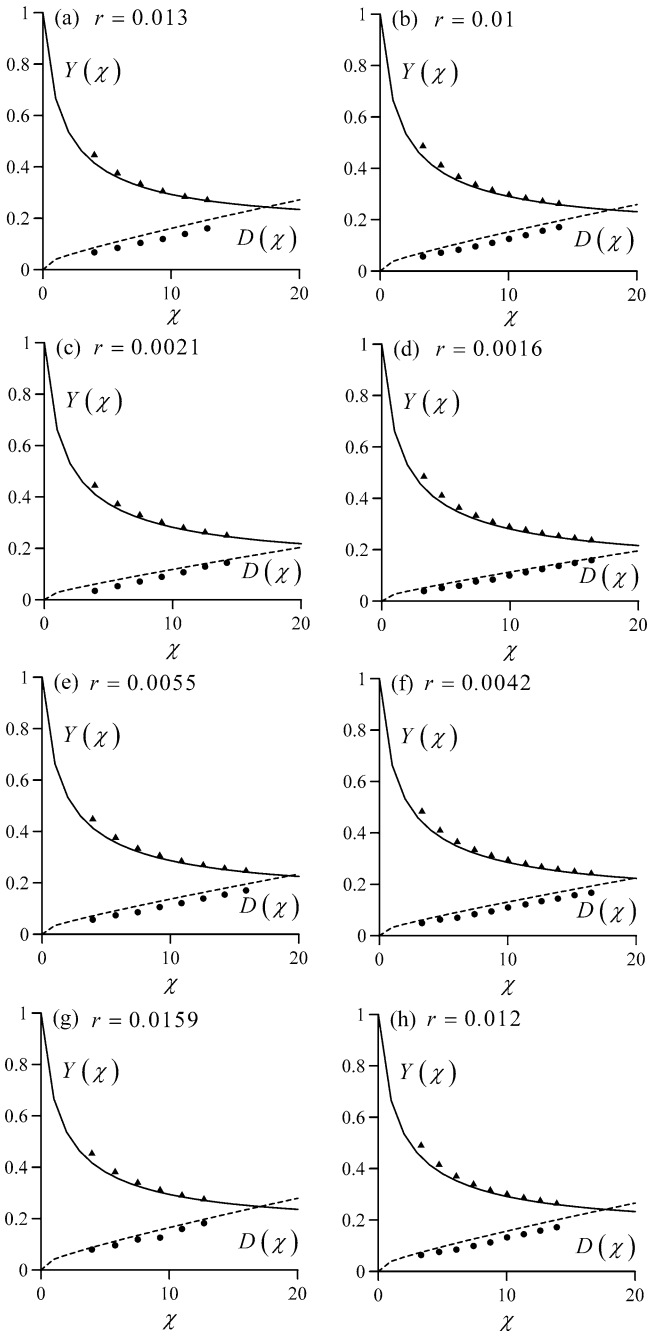

Fig. 5.17 Comparison of boundary layer development between experiments of Bormann (1968) and predictions of (—) $Y(\chi)$ from Eq. (5.129), (- - -) $D(\chi)$ from Eq. (5.130). Bormann data (▲) $Y(\chi)$, and (●) $D(\chi)$ for r = **a** 0.013, **b** 0.010, **c** 0.0021, **d** 0.0016, **e** 0.0055, **f** 0.0042, **g** 0.0159, **h** 0.012 (adapted from Castro-Orgaz 2009)

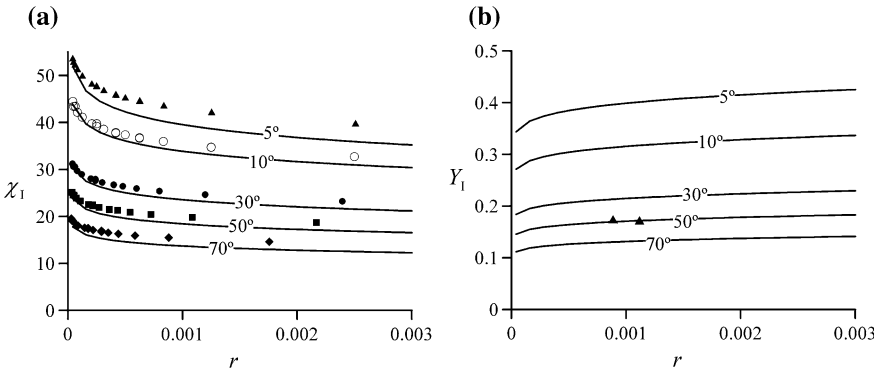

Fig. 5.18 Air inception point on chute **a** relative inception point location $\chi_I(r)$ (—) model results versus data of Keller and Rastogi (1977) for θ = (▲) 5°, (○) 10°, (●) 30°, (■) 50°, (◆) 70°; **b** relative inception point flow depth $Y_I(r)$ with (—) model results, (▲) Aviemore Dam data for θ = 45° (Cain and Wood 1981) (adapted from Castro-Orgaz 2009)

Equation (5.131) was used to reproduce the experimental boundary condition of Keller and Rastogi's (1977) tests, plotted in Fig. 5.18. Based on analytical predictions (Castro-Orgaz et al. 2008), $C_d = 0.70$ was selected, corresponding to the design condition of the spillway crest. The effect of Ω on the boundary layer growth is negligible for $\theta > 30°$, but Ω increases considerably for smaller chute slopes (Castro-Orgaz 2009). Thus, Ω was accounted for in all simulations of the Keller and Rastogi's (1977) data set, particularly for $\theta = 5°$ and 10° (Fig. 5.18) (for $\theta = 5°$, Ω is of the order of 10). For $\theta = 5°$ and $r = 0.0015$, the inception point position is of the order of 40 (Fig. 5.18a), indicating then that Ω is not negligible. The use of the parameter Ω results in a scant increase of the model complexity, supporting its general use for practical purposes. It depends on the spillway discharge coefficient C_d, i.e., the spillway crest shape. Heads different from the spillway design head are accounted for by C_d. Therefore, parameter Ω accounts for effects of streamline curvature in the crest domain.

5.3 Undular Hydraulic Jump

5.3.1 Introduction

The transition from super- to subcritical flow for approach flow Froude numbers F_1 (with subscript 1 referring to the approach flow section) close to but slightly above unity is called *undular hydraulic jump* or *Fawer jump* (Fawer 1937; Castro-Orgaz 2010a). This type of hydraulic jump is characterized by free surface undulations originating from the existence of a vertical velocity component w and thus a non-hydrostatic pressure with a bottom pressure head profile p_b/γ that is different from the water depth h (Fig. 5.19).

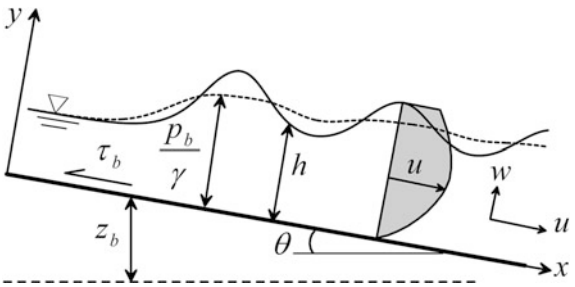

Fig. 5.19 Definition sketch of a 2D undular hydraulic jump in turbulent open-channel flows

The undular hydraulic jump involves a two-dimensional (2D) velocity field with a 1D free surface for $F_1 < 1.2$ (Montes and Chanson 1998) (Fig. 5.19). Under increasing values of F_1, lateral shock waves develop due to flow separation along the sidewalls, resulting in a 3D velocity field and a 2D flow surface (Fig. 5.20) (Chanson and Montes 1995; Reinauer and Hager 1995; Ohtsu et al. 2001, 2003; Gotoh et al. 2005). The undular jump is a complex non-hydrostatic turbulent flow phenomenon, highly dependent on the approach flow conditions at the jump toe, namely the boundary layer development, the aspect ratio, and the Reynolds number, in addition to F_1 and the bottom slope (Ohtsu et al. 2001, 2003; Gotoh et al. 2005). Wave breaking and air entrainment are also induced at higher F_1.

The study of the undular hydraulic jump is important in civil and environmental engineering. For example, a safe design of dam outlet works on earth channels requires the prediction of the bed-shear stress. The processes of erosion and sedimentation are linked to the oscillatory bed-shear stress due to accelerating or

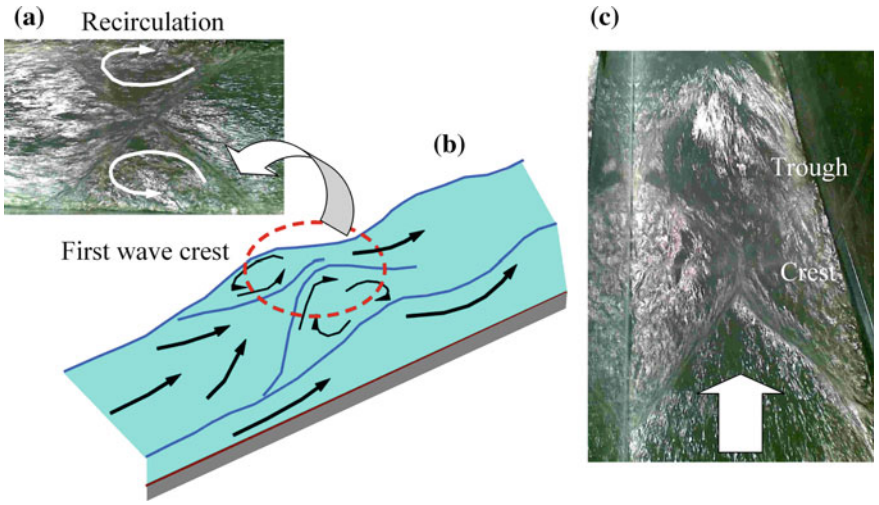

Fig. 5.20 3D non-breaking undular hydraulic jump in turbulent open-channel flow **a** shock waves, **b** 3D sketch, **c** typical view in a physical model (adapted from Castro-Orgaz 2010b)

decelerating near-bed flows. This flow type is not amenable by standard gradually varied flow computations (Chanson 1995; Montes 1998). In environmental flows, undular flow patterns are observed for near-critical flow conditions, as flow over antidunes (Engelund and Hansen 1966; Chanson 1995; Bose and Dey 2009). Engelund and Hansen (1966) developed a Boussinesq-type model for undular flow over erodible beds. They linked the undular free surface and the associated non-uniform bed-shear stress distribution to the bed-form processes in movable-bed flows. Consider an initially straight-bottomed movable-bed channel, where an undular jump is generated. The undular free surface flow leads to shear stress variations via the boundary layer theory (Montes and Chanson 1998), provoking the bed-generation process once erosion is initiated. Therefore, the initial stage of the bed-form process is dominated by bottom friction, in agreement with Engelund and Hansen (1966) and Bose and Dey (2009), who explained the development of dunes by bed shear.

Visualization tests were conducted in a horizontal, smooth-walled channel 0.50 m wide and 0.70 m deep at VAW, ETH Zurich (Castro-Orgaz and Hager 2011a). The discharge was supplied by a jet-box at the channel inlet, and tailwater conditions were set with a gate. Undular hydraulic jumps were generated by fixing the inflow Froude number F_1 at the jet-box and regulating the gate position until a stable undular jump was formed. For $\mathsf{F}_1 > 1.2$, the undular jump is strongly 3D (Figs. 5.21a and 5.22a). Among various flow conditions (Reinauer and Hager 1995), a 3D spatial jump was selected with $\mathsf{F}_1 = U_1/(gh_1)^{1/2} = 1.43$, for a discharge of $Q = 46.1$ l/s and an approach flow depth of $h_1 = 7.5$ cm. Note that for non-breaking undular jumps, the axial free surface profile is wavelike, but there is a

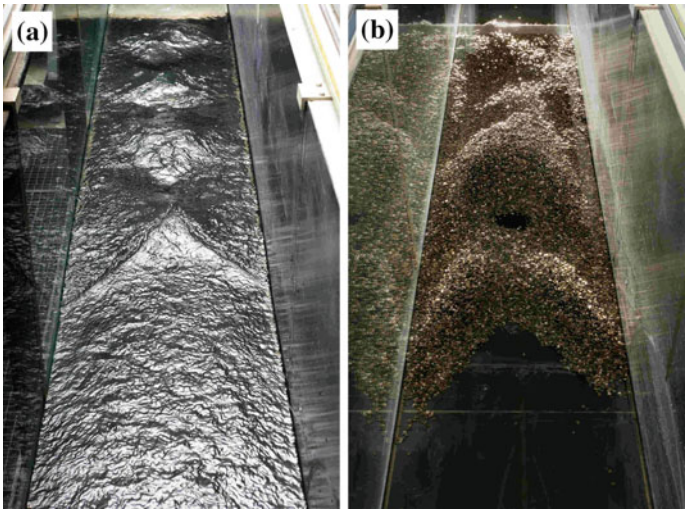

Fig. 5.21 Longitudinal view of 3D undular hydraulic jump with $\mathsf{F}_1 = 1.43$ **a** water surface in rigid bottom test, **b** sediment surface after equivalent test under movable-bed conditions (photographs VAW)

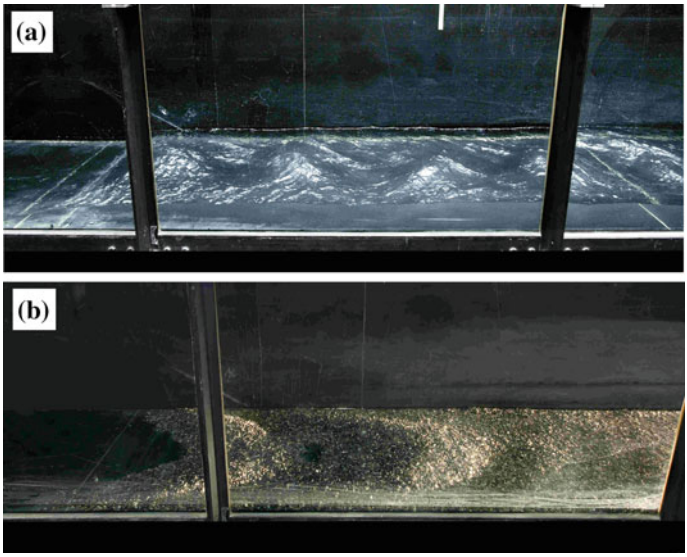

Fig. 5.22 Lateral view of 3D undular hydraulic jump **a** water surface in a rigid bottom test, **b** sediment surface after equivalent test under movable-bed conditions (photographs VAW)

strong transverse variation of the free surface, including shockwave formation. Moreover, wave crests are associated with flow deceleration, whereas at wave troughs the velocity increases. It is expected that at wave crests the shear stress is smaller than at wave troughs.

To compare fixed-bottom with movable-bed data, the same channel was covered over a length of 3 m with a layer of 5.5 mm diameter gravel, to record the bed form below the first wave crest and trough. The channel was filled with water, and the approach flow conditions at the jet-box were set to $F_1 = 1.43$ under submerged conditions to avoid sediment movement using simultaneously metallic plates at the downstream end of the sediment layer. The gate was then slowly lowered until the undular hydraulic jump previously investigated on the fixed-bottom was formed. An unsteady motion was observed, continuously provoking intense sediment motion below the undular jump. A quasi-steady state finally occurred associated with no further sediment movement, so that the visualization test was stopped. The channel was then slowly submerged again to not affect sediment deposition. The discharge was only then stopped and the channel was drained. The resulting bed forms are shown in Figs. 5.21b and 5.22b. From these, a strong correlation is noted between the free surfaces of the undular hydraulic jump in the fixed-bottom channel and the bed forms of the equivalent test in the movable-bed channel. The observed two surfaces are almost in phase, confirming Engelund and Hansen's proposal. Intense erosion is noted along the bed close to the first wave trough (a hole is observed in the bed form), pointing to the strong shear stress. Furthermore, at the zone below the first wave crest there is a V-shaped sediment barrier (Figs. 5.21b and 5.22b) following the shock front (Figs. 5.21a and 5.22a), indicating a reduced

skin-friction drag acting in this region. The results of the movable-bed channel indicate that the bed-form formation is strongly associated with the free surface undulations and the 3D flow pattern of the undular hydraulic jump. Wave crests and troughs are associated with the loci of minimum and maximum shear stresses, thereby constraining the zones of erosion and deposition of the bed.

Other issues in relation to the undular hydraulic jump include energy dissipators in which the excess of hydraulic energy should be adequately dissipated. This important hydraulic structure is typically designed for approach flow Froude numbers F_1 between 3 and 7, say. If $F_1 < 2.5$, say, then the direct hydraulic jump is transformed into an undular hydraulic jump whose energy dissipation efficiency is poor. The results of this feature include tailwater wave generation and erosion of river sides, poor control of tailwater flow including sweep-out of jump from the energy dissipating basin, or excessive length of transitional flow from supercritical approach to subcritical tailwater reaches. In most of the cases, undular hydraulic jumps are undesirable flows so that they should be avoided by adequate approach flow and tailwater conditions. To explore the necessary hydraulic relations, knowledge on these weak jumps is, therefore, needed. Note also the presence of moving undular jumps in environmental hydraulics, which, however, are not considered below.

Given the importance and the beauty of the undular hydraulic jump both in civil and in environmental engineering, this topic attracted a number of investigators to study them over the past 50 years. The modeling strategy of the undular hydraulic jump has progressed since the work of Boussinesq (1877) on curvilinear free surface flows. Fawer (1937) applied the potential flow theory and provided the first systematic experimental investigation by measuring the undular jump profile in the tailwater flow portion. These data compared well with a potential flow simulation, indicating that this wave train is approximated by cnoidal waves. However, the upstream portion of the undular jump profile (first wave crest), where the flow changes from super- to subcritical conditions, was not analyzed. Since the pioneering work of Benjamin and Lighthill (1954), the only stable steady-wave known to emerge from a supercritical flow is the solitary wave, whereas the

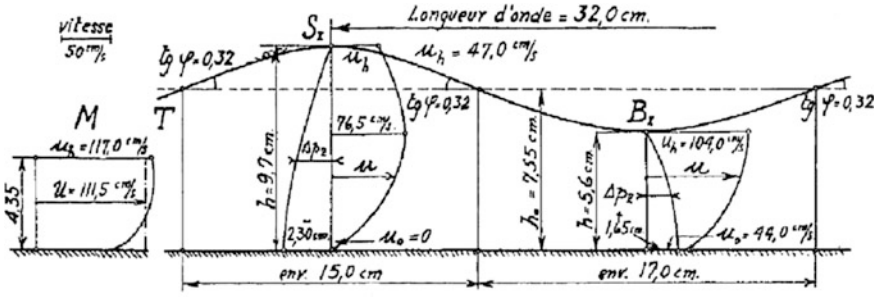

Fig. 21. — Profil observé dans l'axe (*b*).

Fig. 5.23 Original velocity and pressure measurements in an undular hydraulic jump by Fawer (1937)

corresponding steady wave pattern of potential subcritical flow is the cnoidal wave. Therefore, the undular hydraulic jump cannot be modeled with a continuous solution based on the potential flow theory. Consequently, Iwasa (1955), Mandrup-Andersen (1978) and Hager and Hutter (1984a, b) approximated the undular hydraulic jump profile with a composite potential curve matching a solitary wave with a cnoidal wave[3] at an arbitrary point. This discontinuous solution overcomes the impossibility of the potential flow theory of transforming the upstream supercritical flow into a subcritical tailwater flow. Fawer (1937) further measured the velocity profiles along the jump (Fig. 5.23), which differs significantly from those originating from the potential flow theory. This important finding suggests that the undular jump is not a potential flow, indicating the need of a change in modeling strategies.

Yoshiaki Iwasa
was born in 1928 in Kyoto, Japan, and passed away on March 20, 2013, in Kyoto. He graduated as civil engineer from Kyoto Imperial University in 1951 and became research assistant there in 1953, associate professor in 1955, and professor of hydraulic engineering in 1964, staying there until his retirement in 1992. He was the president of the Institute of Earth, Science and Technology, Member of the Engineering Academy of Japan, and president and Honorary Member of the Japan Society of Civil Engineers JSCE. Iwasa was in 1965 a visiting professor to the Massachusetts Institute of Technology MIT, Cambridge, MA; he chaired the JSCE Hydraulic Committee in 1979 and was associated with the International Association of Hydraulic Research IAHR, serving as a vice president from 1986 to 1988 and becoming later Honorary Member.

Iwasa collaborated in the 1950s with a number of illustrious colleagues of the Disaster Prevention Institute, Kyoto, including Tojiro Ishihara (1908–1979). Early in his career, Iwasa was interested in wave hydraulics, with contributions to roll waves as a particular flow instability at sufficiently large Froude numbers, for which the Vedernikov number is in excess of unity as defined by Valentin V. Vedernikov (1904–1980). Iwasa also studied undular hydraulic jumps as occur in open-channel flows at transcritical state, generating complicated spatial surface undulations, referred to also as weak jumps because of their instability to small disturbances. Later he investigated the

[3]Solitary and cnoidal wave solutions of potential water waves are detailed in 3.15.4.

attenuation of solitary waves, the type of waves with the highest energy content. A minimum still water depth was defined for water flow to exclude viscous effects on these waves.

Given the limitations of the potential flow theory, a second modeling strategy considered the specific energy function of an inviscid flow, but included frictional effects in the streamwise energy balance via use of the friction slope and the corresponding flow resistance equations. This mathematical model was proposed by Serre (1953) and further developed by Marchi (1963), and Hager and Hutter (1984a, b). Although some improvements were achieved allowing for the variation of the energy head with friction, other fundamental flow features, such as the turbulent velocity profile, were not explained by this basic pseudo-potential model. The free surface predictions of this model were examined by Castro-Orgaz and Chanson (2011) for undular hydraulic jumps and undular weir flows.

A key point unaddressed in the original work of Serre (1953) is the selection of a suitable turbulent velocity profile for the undular hydraulic jump modeling. Montes (1986) adopted the widely used Prandtl's 1/7-th power-law for the velocity profile of the undular hydraulic jump. This is the first turbulent velocity profile introduced in the system of differential equations used to model the undular jump profile. Following Serre (1953), Montes (1986) included the energy dissipation in the streamwise energy balance using Chézy's equation. However, Montes and Chanson (1998) noted that the computation of friction factors in undular hydraulic jumps using such formulae, adopted for gradually varied flows, was not sufficiently accurate. Therefore, they improved the model of Montes (1986) by computing the bed-shear stress using the boundary layer method of Furuya and Nakamura (1968).

A next step in modeling undular hydraulic jumps started with the Reynolds-averaged Navier–Stokes (RANS) equations. Hosoda and Tada (1994) and Hosoda et al. (1997) introduced the velocity and pressure fields, originating from the potential flow theory, in the streamwise depth-averaged momentum equation for turbulent flows. Turbulence modeling was introduced with a zeroth-order model, using a depth-averaged eddy viscosity with a parametrization proportional to the flow discharge. The resulting model was similar to Serre's (1953), but includes a turbulence term. Bose and Dey (2007, 2009) used the 1/7-th power-law velocity profile and computed the bed-shear stress employing Manning's equation. Under the assumption of gradually varied turbulence, the gradients of the Reynolds stresses in the streamwise direction were neglected, making the analysis free of turbulence modeling. Thus, their model is similar to that of Montes (1986). It is pertinent to remark that Bose and Dey (2007, 2009) introduced a turbulent velocity profile in the momentum balance, neglecting the gradients of the turbulence stresses, whereas Hosoda and Tada (1994) neglected the turbulent velocity profile effects but introduced turbulence modeling considering the normal stress in the streamwise direction. Grillhofer and Schneider (2003) developed a rigorous asymptotic solution of the RANS equations valid for $\mathsf{F} \rightarrow 1$ and $\mathsf{R} \rightarrow \infty$, with R as the Reynolds number.

Each of the introduced models produced specific advances in modeling undular hydraulic jumps by inclusion of aspects of a real turbulent flow. Castro-Orgaz et al. (2015) coupled, in a depth-averaged RANS model, some relevant features for modeling undular hydraulic jumps, namely the turbulent velocity profile for non-hydrostatic flows, turbulence modeling, and friction factor formulae via the boundary layer theory. In this section, the general form of the depth-averaged RANS equations for turbulent non-hydrostatic flows is presented following Castro-Orgaz et al. (2015). For practical application to undular hydraulic jumps, approximate, but physically sound, closures for turbulence stresses, the velocity field, and friction factors are given.

In particular, turbulence is accounted for by using a simplified depth-averaged k–ε model. The time-averaged velocity field is modeled by accounting for vorticity generation near the bed, and the bed-shear stress is computed using a formulation accounting for the skin friction within the framework of the boundary layer theory. The depth-averaged RANS model is compared with the theories of Serre (1953), Montes (1986), Hosoda and Tada (1994), Montes and Chanson (1998) and Grillhofer and Schneider (2003). The inclusion of 3D effects in the 1D modeling of undular jumps is further investigated by introducing a damping factor in the 1D Boussinesq-type equations.

5.3.2 Depth-Averaged RANS Equations

Consider an undular hydraulic jump over a plane sloping channel bottom of inclination θ (Fig. 5.19). The RANS momentum equation in the x-direction is (Paterson and Apelt 1988; Rodi 1993; Steffler and Jin 1993)

$$\frac{\partial u^2}{\partial x} + \frac{\partial}{\partial y}(uw) = -\frac{1}{\rho}\frac{\partial p}{\partial x} + \frac{1}{\rho}\left(\frac{\partial \tau_{yx}}{\partial y} + \frac{\partial \sigma_x}{\partial x}\right) + g\sin\theta. \tag{5.132}$$

Here, the time-averaged velocity field in the (x, y) directions is (u, w). The tangential Reynolds stress is τ_{yx}, the normal turbulent stress in the x-direction is σ_x, and the time-averaged fluid pressure is p. Equation (5.132) is rewritten as

$$\frac{\partial}{\partial x}\left(\frac{u^2}{g} + \frac{p - \sigma_x}{\gamma}\right) = -\frac{1}{g}\frac{\partial}{\partial y}\left(uw - \frac{\tau_{yx}}{\rho}\right) + \sin\theta. \tag{5.133}$$

To integrate it over the time-averaged flow depth $h(x)$, kinematic and dynamic boundary conditions need to be prescribed. At the channel bottom ($y = 0$), the no-slip kinematic boundary conditions are

$$w = u = 0. \tag{5.134}$$

At the time-averaged water surface ($y = h$), the kinematic boundary condition reads (Madsen and Svendsen 1979; Grillhofer and Schneider 2003; Jurisits and Schneider 2012)

$$w = u\frac{\mathrm{d}h}{\mathrm{d}x}. \tag{5.135}$$

This is exact only if the free surface-level fluctuations are negligible as compared to $h(x)$ (Madsen and Svendsen 1979). Under the same limitations, the dynamic boundary condition in the x-direction at a free surface of turbulent flows is (Madsen and Svendsen 1979; Grillhofer and Schneider 2003; Jurisits and Schneider 2012)

$$\tau_{yx} = (\sigma_x - p)\frac{\mathrm{d}h}{\mathrm{d}x}. \tag{5.136}$$

Integrating Eq. (5.133) from $y = 0$ to $y = h$ yields

$$\int_0^h \frac{\partial}{\partial x}\left(\frac{u^2}{g} + \frac{p-\sigma_x}{\gamma}\right)\mathrm{d}y = -\int_0^h \frac{1}{g}\frac{\partial}{\partial y}\left(uw - \frac{\tau_{yx}}{\rho}\right)\mathrm{d}y + h\sin\theta. \tag{5.137}$$

Applying the Leibniz rule yields

$$\begin{aligned}\frac{\partial}{\partial x}\int_0^h \left(\frac{u^2}{g} + \frac{p-\sigma_x}{\gamma}\right)\mathrm{d}y - \left(\frac{u^2}{g} + \frac{p-\sigma_x}{\gamma}\right)_{y=h}\frac{\mathrm{d}h}{\mathrm{d}x} \\ = -\frac{1}{g}\left(uw - \frac{\tau_{yx}}{\rho}\right)_{y=h} + \frac{1}{g}\left(uw - \frac{\tau_{yx}}{\rho}\right)_{y=0} + h\sin\theta,\end{aligned} \tag{5.138}$$

or

$$\begin{aligned}\frac{\partial}{\partial x}\int_0^h \left(\frac{u^2}{g} + \frac{p-\sigma_x}{\gamma}\right)\mathrm{d}y - \left[\frac{u}{g}\left(u\frac{\mathrm{d}h}{\mathrm{d}x} - w\right)\right]_{y=h} + \left(\frac{\sigma_x - p}{\gamma}\frac{\mathrm{d}h}{\mathrm{d}x}\right)_{y=h} \\ = \left(\frac{\tau_{yx}}{\rho g}\right)_{y=h} + \frac{1}{g}\left(uw - \frac{\tau_{yx}}{\rho}\right)_{y=0} + h\sin\theta.\end{aligned} \tag{5.139}$$

Imposing the kinematic and dynamic boundary conditions, namely Eqs. (5.134)–(5.136) into Eq. (5.139) leads, with $\tau_b = \tau_{yx}(y = 0)$ as the bed-shear stress, to the depth-averaged momentum equation as

$$\frac{\mathrm{d}S}{\mathrm{d}x} = h\sin\theta - \frac{\tau_b}{\gamma}. \tag{5.140}$$

The specific momentum S for turbulent flow is

$$S = \int_0^h \left(\frac{u^2}{g} + \frac{p - \sigma_x}{\gamma} \right) \mathrm{d}y. \tag{5.141}$$

To integrate Eq. (5.140), a bottom-drag model and a closed-form S function from Eq. (5.141) are required. For the latter issue, the distributions of velocity u and pressure p must be prescribed, in addition to introducing a turbulent closure for σ_x. The RANS momentum equation in the y-direction is (Paterson and Apelt 1988; Rodi 1993; Steffler and Jin 1993)

$$\frac{\partial}{\partial x}(uw) + \frac{\partial w^2}{\partial y} = -\frac{1}{\rho}\frac{\partial p}{\partial y} + \frac{1}{\rho}\left(\frac{\partial \tau_{yx}}{\partial x} + \frac{\partial \sigma_y}{\partial y} \right) - g\cos\theta. \tag{5.142}$$

The dynamic boundary condition at a turbulent water surface in the y-direction is (Madsen and Svendsen 1979; Grillhofer and Schneider 2003; Jurisits and Schneider 2012)

$$\sigma_y - p = \tau_{yx}\frac{\mathrm{d}h}{\mathrm{d}x}. \tag{5.143}$$

Equation (5.142) is integrated from an arbitrary level y to $y = h$, again by applying the Leibniz rule; this yields

$$\begin{aligned} &\frac{\partial}{\partial x}\int_y^h (uw)\mathrm{d}y' - (uw)_{y=h}\frac{\mathrm{d}h}{\mathrm{d}x} + \int_y^h \frac{\partial w^2}{\partial y'}\mathrm{d}y' \\ &\quad = -\frac{1}{\rho}\int_y^h \frac{\partial p}{\partial y'}\mathrm{d}y' + \frac{1}{\rho}\frac{\partial}{\partial x}\int_y^h \tau_{yx}\mathrm{d}y' - \left(\tau_{yx}\right)_{y=h}\frac{\mathrm{d}h}{\mathrm{d}x} \\ &\qquad + \frac{1}{\rho}\int_y^h \frac{\partial \sigma_y}{\partial y'}\mathrm{d}y' - g\cos\theta(h - y), \end{aligned} \tag{5.144}$$

or

$$\begin{aligned} &\frac{\partial}{\partial x}\int_y^h (uw)\mathrm{d}y' - (uw)_{y=h}\frac{\mathrm{d}h}{\mathrm{d}x} + \left(w^2\right)_{y=h} - w^2 \\ &\quad = -\frac{1}{\rho}\left[p_{y=h} - p\right] + \frac{1}{\rho}\frac{\partial}{\partial x}\int_y^h \tau_{yx}\mathrm{d}y' - \left(\tau_{yx}\right)_{y=h}\frac{\mathrm{d}h}{\mathrm{d}x} \\ &\qquad + \frac{1}{\rho}\left[\left(\sigma_y\right)_{y=h} - \sigma_y\right] - g\cos\theta(h - y). \end{aligned} \tag{5.145}$$

This becomes after grouping,

$$g\cos\theta(h-y)+\frac{\partial}{\partial x}\int_y^h\left(uw-\frac{\tau_{yx}}{\rho}\right)\mathrm{d}y'-w^2+\frac{\sigma_y}{\rho}-\left[w\left\{\left(u\frac{\mathrm{d}h}{\mathrm{d}x}\right)-w\right\}\right]_{y=h}$$
$$=\frac{p}{\rho}+\frac{1}{\rho}\left(\sigma_y-p\right)_{y=h}-\left(\tau_{yx}\right)_{y=h}\frac{\mathrm{d}h}{\mathrm{d}x}. \tag{5.146}$$

Imposing the kinematic and dynamic boundary conditions at the free surface, namely Eqs. (5.135) and (5.143), on Eq. (5.146) leads to the pressure distribution as

$$\frac{p}{\gamma}=(h-y)\cos\theta+\frac{\sigma_y}{\gamma}-\frac{w^2}{g}+\frac{1}{g}\frac{\partial}{\partial x}\int_y^h\left(uw-\frac{\tau_{yx}}{\rho}\right)\mathrm{d}y'. \tag{5.147}$$

If Eq. (5.147) is inserted into Eq. (5.141), the variable pressure is eliminated from the governing equations as

$$S=\int_0^h\left(\frac{u^2}{g}-\frac{\sigma_x}{\gamma}\right)\mathrm{d}y+\int_0^h\underbrace{\left[(h-y)\cos\theta+\frac{\sigma_y}{\gamma}-\frac{w^2}{g}+\frac{1}{g}\frac{\partial}{\partial x}\int_y^h\left(uw-\frac{\tau_{yx}}{\rho}\right)\mathrm{d}y'\right]}_{=p/\gamma}\mathrm{d}y$$
$$=\int_0^h\frac{u^2}{g}\mathrm{d}y-\int_0^h\frac{w^2}{g}\mathrm{d}y+\int_0^h(h-y)\cos\theta\mathrm{d}y$$
$$+\int_0^h\frac{\sigma_y-\sigma_x}{\gamma}\mathrm{d}y+\frac{1}{g}\int_0^h\left[\frac{\partial}{\partial x}\int_y^h\left(uw-\frac{\tau_{yx}}{\rho}\right)\mathrm{d}y'\right]\mathrm{d}y. \tag{5.148}$$

The problem is reduced to find the time-averaged velocity field (u, w) and the turbulence closure for σ_x, σ_y, and τ_{yx}. A widely used approach proposed by Boussinesq (1877) relies on the eddy viscosity concept (denoted by ν_t) (Paterson and Apelt 1988; Rodi 1993, 1995; Molls and Chaudhry 1995). The turbulent stresses are then expressed by the time-averaged velocity field with k as the turbulent kinetic energy as (Paterson and Apelt 1988; Rodi 1993; Raiford and Khan 2013)

$$\sigma_y = 2\rho\nu_t \frac{\partial w}{\partial y} - \frac{2}{3}\rho k, \tag{5.149}$$

$$\sigma_x = 2\rho\nu_t \frac{\partial u}{\partial x} - \frac{2}{3}\rho k, \tag{5.150}$$

$$\tau_{yx} = \rho\nu_t \left(\frac{\partial u}{\partial y} + \frac{\partial w}{\partial x}\right). \tag{5.151}$$

A quantity appearing in the development of the depth-averaged momentum Eq. (5.148) is $\sigma_y - \sigma_x$ (Engelund 1981; Khan and Steffler 1996a). Using the time-averaged continuity equation

$$\frac{\partial u}{\partial x} + \frac{\partial w}{\partial y} = 0, \tag{5.152}$$

one finds by subtracting Eq. (5.150) from Eq. (5.149) the auxiliary relation

$$\sigma_y - \sigma_x = 2\rho\nu_t \frac{\partial w}{\partial y} - 2\rho\nu_t \frac{\partial u}{\partial x} = -4\rho\nu_t \frac{\partial u}{\partial x}. \tag{5.153}$$

Inserting Eqs. (5.151) and (5.153) into Eq. (5.148) yields

$$\begin{aligned} S = {} & \frac{h^2}{2}\cos\theta + \int_0^h \frac{u^2}{g}\mathrm{d}y - \int_0^h \frac{w^2}{g}\mathrm{d}y - \int_0^h 4\frac{\nu_t}{g}\frac{\partial u}{\partial x}\mathrm{d}y \\ & + \frac{1}{g}\int_0^h \left\{ \frac{\partial}{\partial x}\int_y^h \left(uw - \nu_t\left(\frac{\partial u}{\partial y} + \frac{\partial w}{\partial x}\right)\right)\mathrm{d}y' \right\}\mathrm{d}y. \end{aligned} \tag{5.154}$$

Equation (5.154) is the general momentum function for steady, non-hydrostatic, turbulent open-channel flows in the vertical plane. The eddy viscosity appears as a new unknown, so that further equations for turbulence closure are needed. A zeroth-order depth-averaged turbulence closure was proposed by Kim et al. (2009) using a parabolic distribution for the local eddy viscosity. However, a more general closure for the eddy viscosity is given by the k–ε model as (Rodi 1993; Raiford and Khan 2013)

$$\nu_t = C_\mu \frac{k^2}{\varepsilon}. \tag{5.155}$$

Here, ε is the dissipation rate and C_μ an empirical constant. To compute k and ε, and then ν_t using Eq. (5.155), new transport equations are needed. Here, the depth-averaged form of the k–ε model is employed (Rastogi and Rodi 1978; Rodi

1993, 1995; Younus and Chaudhry 1994). Neglecting diffusion as compared to advection, production, and dissipation (Rouse et al. 1959; Madsen and Svendsen 1983; Ohtsu et al. 1990), the depth-averaged k–ε model reads, with $U = q/h$ as the depth-averaged velocity, and k and ε having the meaning of depth-averaged flow variables (Rodi 1995),

$$U\frac{\partial k}{\partial x} = P_h + P_{kv} - \varepsilon, \tag{5.156}$$

$$U\frac{\partial \varepsilon}{\partial x} = c_{1\varepsilon}\frac{\varepsilon}{k}P_h + P_{\varepsilon v} - c_{2\varepsilon}\frac{\varepsilon^2}{k}, \tag{5.157}$$

$$P_{kv} = c_k\frac{u^{*3}}{h}, \quad P_{\varepsilon v} = c_\varepsilon\frac{u^{*4}}{h^2}, \quad P_h = 2\nu_t\left(\frac{\partial U}{\partial x}\right)^2, \tag{5.158}$$

where $u^* = (\tau_b/\rho)^{1/2} = C^{1/2}U$ is the friction velocity, and C the friction coefficient, $c_\varepsilon = 3.6c_{2\varepsilon}C_\mu C^{-3/4}$ and $c_k = 1/C^{1/2}$. In the depth-averaged k–ε model, integral terms originating from the depth-averaging process are absorbed into the production terms P_{kv} and $P_{\varepsilon v}$. Their main contribution stems from the integral of the production term $\nu_t(\partial u/\partial y)^2$ containing vertical velocity gradients (Rastogi and Rodi 1978; Rodi 1993). Paterson and Apelt (1988) presented the full equations of the depth-averaged k–ε model, stating the generalized integrals terms. Here, the simplified 1D model derived from the 2D equations in the horizontal plane is used (Rodi 1993). The coefficients of the standard k–ε model are $C_\mu = 0.09$, $c_{2\varepsilon} = 1.92$, $c_{1\varepsilon} = 1.44$. The depth-averaged k and ε values are used at each position x to compute a depth-averaged eddy viscosity ν_t by using Eq. (5.155).

Given that the turbulence closure used here is based on depth-averaged quantities, the computation of S using Eq. (5.154) is simplified accordingly. Turbulence and velocity measurements of Svendsen et al. (2000) in undular jumps indicated that the contribution to the streamwise momentum balance of the integral containing the term $(\partial u/\partial y + \partial w/\partial x)$, on the right-hand side of Eq. (5.154), is negligible. Using this result, and assuming $\partial u/\partial x \approx \partial U/\partial x = -(q/h^2)\partial h/\partial x$, reduces Eq. (5.154) to

$$S = \frac{h^2}{2}\cos\theta + 4\frac{\nu_t}{g}\frac{q}{h}h_x + \int_0^h \frac{u^2}{g}\mathrm{d}y - \int_0^h \frac{w^2}{g}\mathrm{d}y + \frac{1}{g}\int_0^h \left\{\frac{\partial}{\partial x}\int_y^h uw\mathrm{d}y'\right\}\mathrm{d}y. \tag{5.159}$$

The problem of determining S is now simplified to find a suitable time-averaged velocity field (u, w).

Equation (5.159) is a depth-averaged momentum function for turbulent, non-hydrostatic flows. As a result of the depth-averaging process, S depends on integrals in which the time-averaged velocity profile $u(x, y)$ appears. An important aspect of depth-averaged open-channel flow modeling is the selection of a velocity profile model to its use in the depth-averaged equations (Steffler and Jin 1993; Khan

and Steffler 1996b; Ghamry and Steffler 2002). This is a necessary step to produce a closed model to be solved numerically. Marchi (1963) introduced in the undular jump modeling a second-order potential velocity profile as [see Eq. (3.63) for the horizontal bottom)]

$$u = U\left[1 + \left(\frac{hh_{xx}}{2} - h_x^2\right)\left(\eta^2 - \frac{1}{3}\right)\right], \quad \eta = \frac{y}{h}. \tag{5.160}$$

Another option to model the velocity profile of undular jumps is the turbulent power-law profile, given, with N as the power-law index, by Montes (1986), Bose and Dey (2007)

$$u = U(1+N)\eta^N. \tag{5.161}$$

For hydrostatic depth-averaged RANS modeling, Paterson and Apelt (1988) used the log-law velocity profile instead of Eq. (5.161). However, its use instead of a power-law renders the analytical development of Boussinesq-type equations tedious, if not impossible. Moreover, a standard log-law would neglect the non-hydrostatic flow effects on the turbulent velocity profile, which were found to be significant based on experimental observations (Montes and Chanson 1998). None of Eqs. (5.160), (5.161) appears to accurately describe the experimental velocity profile measured in undular jumps, as shown by Fawer's data (Fig. 5.23). His observations indicate that the velocity profile of undular hydraulic jumps cannot be predicted by using the potential flow theory, a fact in favor of using Eq. (5.161) instead of Eq. (5.160). The velocity profile below a wave crest (Fig. 5.23) indicates that the maximum velocity is not at the free surface. This suggests that streamline curvature is important, and that it may interact with the generation of vorticity near the bottom, accounted for via the exponent N in Eq. (5.161). Thus, a velocity profile model accounting for both effects is required. Kim et al. (2009) proposed a composite velocity profile in which a vorticity term originating from the eddy viscosity approach is added to the velocity profile of potential flows; Jin and Li (1996), in turn, added to a linear potential velocity profile a power-law term. A different velocity profile for non-hydrostatic flows was theoretically obtained by Castro-Orgaz and Hager (2011b) using vorticity conservation along the streamlines of the inviscid flow. Their result is a composite velocity profile accounting for both streamline curvature and vorticity effects [see Eq. (3.562)]. Thus, the velocity field of undular hydraulic jumps is modeled here by coupling Eqs. (5.160) and (5.161) as (Castro-Orgaz et al. 2015)

$$u = U(1+N)\eta^N\left[1 + \left(\frac{hh_{xx}}{2} - h_x^2\right)\left(\eta^2 - \frac{1}{3}\right)\right]. \tag{5.162}$$

The vertical velocity profile is approximated with the aid of the function used by Bose and Dey (2007) as

$$w = Uh_x\eta^{N+1}. \tag{5.163}$$

Using Eqs. (5.162) and (5.163), the following set of computations are conducted, to their use in Eq. (5.159)

$$\begin{aligned} -\int_0^h \frac{w^2}{g}\mathrm{d}y &= -\int_0^h \frac{\left(Uh_x\eta^{N+1}\right)^2}{g}\mathrm{d}y \\ &= -\frac{U^2h_x^2}{gh^{2N+2}}\int_0^h y^{2N+2}\mathrm{d}y \\ &= -\frac{U^2h}{g}\frac{h_x^2}{2N+3} = -\frac{q^2}{gh}\frac{h_x^2}{2N+3}; \end{aligned} \tag{5.164}$$

$$\begin{aligned} \int_0^h \frac{u^2}{g}\mathrm{d}y &= \frac{1}{g}\int_0^h \left\{U(1+N)\eta^N\left[1+\left(\frac{hh_{xx}}{2}-h_x^2\right)\left(\eta^2-\frac{1}{3}\right)\right]\right\}^2\mathrm{d}y \\ &\approx \frac{1}{g}\int_0^h U^2(1+N)^2\eta^{2N}\left[1+2\left(\frac{hh_{xx}}{2}-h_x^2\right)\left(\eta^2-\frac{1}{3}\right)\right]\mathrm{d}y \\ &= \frac{U^2h}{g}\underbrace{\int_0^1 (1+N)^2\eta^{2N}\left[1+2\left(\frac{hh_{xx}}{2}-h_x^2\right)\left(\eta^2-\frac{1}{3}\right)\right]\mathrm{d}\eta}_{=\beta}; \end{aligned} \tag{5.165}$$

$$\begin{aligned} \beta &= (1+N)^2\int_0^1 \left[\eta^{2N}+\frac{2}{3}\left(\frac{hh_{xx}}{2}-h_x^2\right)\left(3\eta^{2N+2}-\eta^{2N}\right)\right]\mathrm{d}\eta \\ &= (1+N)^2\left[\frac{\eta^{2N+1}}{2N+1}+\left(\frac{hh_{xx}}{3}-\frac{2}{3}h_x^2\right)\left(3\frac{\eta^{2N+3}}{2N+3}-\frac{\eta^{2N+1}}{2N+1}\right)\right]_0^1 \\ &= (1+N)^2\left[\frac{1}{2N+1}+\left(\frac{hh_{xx}}{3}-\frac{2}{3}h_x^2\right)\left(\frac{3}{2N+3}-\frac{1}{2N+1}\right)\right] \\ &= \frac{(1+N)^2}{2N+1}\left[1+\left(\frac{hh_{xx}}{3}-\frac{2}{3}h_x^2\right)\left(\frac{4N}{2N+3}\right)\right]; \end{aligned} \tag{5.166}$$

$$\int_0^h \frac{u^2}{g}\mathrm{d}y \approx \frac{q^2}{gh}\frac{(1+N)^2}{2N+1}\left[1+\left(\frac{hh_{xx}}{3}-\frac{2}{3}h_x^2\right)\left(\frac{4N}{2N+3}\right)\right]$$
$$= \frac{q^2}{gh}\frac{(1+N)^2}{2N+1} + \frac{q^2}{gh}\frac{(1+N)^2}{(2N+1)(2N+3)}\frac{4N}{3}hh_{xx} \tag{5.167}$$
$$- \frac{q^2}{gh}\frac{(1+N)^2}{(2N+1)(2N+3)}\frac{8N}{3}h_x^2;$$

$$\int_y^h uw\mathrm{d}y' \approx \int_y^h \frac{U^2}{h^{2N+1}}(1+N)h_x y'^{2N+1}\mathrm{d}y'$$
$$= \frac{U^2}{h^{2N+1}}(1+N)h_x\left(\frac{h^{2N+2}-y^{2N+2}}{2N+2}\right) \tag{5.168}$$
$$= \frac{q^2}{h}\frac{(1+N)}{(2N+2)}h_x\left(1-\eta^{2N+2}\right);$$

$$\frac{\partial}{\partial x}\int_y^h uw\mathrm{d}y' = \frac{\partial}{\partial x}\left[\frac{q^2}{h}\frac{(1+N)}{(2N+2)}h_x\left(1-\eta^{2N+2}\right)\right]$$
$$= q^2\frac{(1+N)}{(2N+2)}\left[\frac{h_{xx}}{h}-\frac{h_x^2}{h^2}\right]\left(1-\eta^{2N+2}\right) + \frac{q^2}{h}\frac{(1+N)}{(2N+2)}h_x\frac{y^{2N+2}}{h^{2N+3}}(2N+2)h_x$$
$$= q^2\frac{(1+N)}{(2N+2)}\left[\frac{h_{xx}}{h}-\frac{h_x^2}{h^2}\right]\left(1-\eta^{2N+2}\right) + \frac{q^2}{h^2}(1+N)h_x^2\eta^{2N+2};$$
(5.169)

$$\frac{1}{g}\int_0^h\left\{\frac{\partial}{\partial x}\int_y^h uw\mathrm{d}y'\right\}\mathrm{d}y = \frac{1}{g}\int_0^h\left\{q^2\frac{(1+N)}{(2N+2)}\left[\frac{h_{xx}}{h}-\frac{h_x^2}{h^2}\right]\left(1-\eta^{2N+2}\right)+\frac{q^2}{h^2}(1+N)h_x^2\eta^{2N+2}\right\}\mathrm{d}y$$
$$= \frac{q^2}{g}h\frac{(1+N)}{(2N+2)}\left[\frac{h_{xx}}{h}-\frac{h_x^2}{h^2}\right]\left(1-\frac{1}{2N+3}\right)+\frac{q^2}{gh}\frac{(1+N)}{(2N+3)}h_x^2$$
$$= \frac{q^2}{gh}\frac{(1+N)}{(2N+3)}\left[hh_{xx}-h_x^2\right]+\frac{q^2}{gh}\frac{(1+N)}{(2N+3)}h_x^2 = \frac{q^2}{gh}\frac{(1+N)}{(2N+3)}hh_{xx}.$$
(5.170)

Inserting Eqs. (5.164), (5.167), and (5.170) into Eq. (5.159) leads to

$$S = \frac{h^2}{2}\cos\theta + 4\frac{v_t}{g}\frac{q}{h}h_x + \frac{q^2}{gh}\left(\lambda_1 + \lambda_2 h h_{xx} - \lambda_3 h_x^2\right). \tag{5.171}$$

Here,

$$\lambda_1 = \frac{(1+N)^2}{2N+1}, \tag{5.172}$$

$$\lambda_2 = \frac{1+N}{2N+3} + \frac{4N(1+N)^2}{3(2N+3)(2N+1)}, \tag{5.173}$$

$$\lambda_3 = \frac{1}{2N+3} + \frac{8N(1+N)^2}{3(2N+3)(2N+1)}. \tag{5.174}$$

Closure for N is now required. Castro-Orgaz and Hager (2011b) found, based on vorticity transport along the streamlines, a theoretical expression for N as follows [see Eq. (3.561)]

$$N = N_1\left(\frac{h}{h_1}\right)^2. \tag{5.175}$$

Here, subscript 1 refers to values at the approach flow section of the jump. This simple equation applies for N closure and avoids the need of additional transport equations to compute it. At section 1, upstream uniform flow conditions are considered, from which N_1 is predicted as function of the friction factor by (Chanson 1995)

$$N_1 = \frac{1}{\kappa}\left(\frac{f_o}{8}\right)^{1/2}. \tag{5.176}$$

Here, κ is the von Kármán constant (=0.41); the friction factor f_o is estimated using Haaland's equation (White 1991), with $\mathsf{R}_1 = q/\nu$ as the approach flow Reynolds number, and ν the coefficient of kinematic viscosity

$$f_o = \left[-1.8\log_{10}\left(\frac{6.9}{4\mathsf{R}_1}\right)\right]^{-2}. \tag{5.177}$$

Note that a power-law velocity profile is used in the depth-averaged model. To simulate the shear stress via friction factors or skin friction coefficients, information is generally not available from power-law models. Therefore, use will be made of existing equations, most of them based on log-wake laws (White 1991).

In non-uniform open-channel flows, the bed-shear stress is modeled as function of the depth-averaged velocity U, with f as the friction factor, by (Montes 1998; Svendsen et al. 2000)

$$\tau_b = \rho \frac{f}{8} U^2. \tag{5.178}$$

The problem reduces to use an adequate value of f. Here, a first initial closure was considered assuming $f = f_o$. However, as discussed below, the bed-shear stress is then overpredicted. A more detailed closure for the bed-shear stress originates from the boundary layer theory, from which follows (White 1991; Schlichting and Gersten 2000)

$$\tau_b = \rho \frac{C_f}{2} U_e^2. \tag{5.179}$$

Here, C_f is the skin friction coefficient, and U_e the velocity at the boundary layer edge. For the undular hydraulic jump, the flow is fully developed and $U_e \approx (1 + N)q/h$ from the power-law model. Using a wall-wake model, White (1991) gives the following correlation function for C_f, with H as the shape factor,

$$C_f = (\log_{10} \mathsf{R}_\theta)^{-1.74-0.31H} \times 0.3 \exp(-1.33H). \tag{5.180}$$

For the power-law model $H = 1 + 2N$. The Reynolds number based on the momentum thickness θ_m is $\mathsf{R}_\theta = U_e \theta_m / \nu$. For fully developed flow in an undular jump, θ_m and h are related as

$$\theta_m = \frac{Nh}{(2N+1)(N+1)}. \tag{5.181}$$

From Eqs. (5.178) and (5.179), the predictor of f based on θ_m is

$$f_\theta = 4C_f (1+N)^2. \tag{5.182}$$

Simulations using $f = f_\theta$ underpredict the shear stress, as discussed below. Thus, the predictor for the friction factor in the depth-averaged model is taken as the average (Castro-Orgaz et al. 2015)

$$f = 0.5(f_o + f_\theta). \tag{5.183}$$

5.3.3 Serre's Theory

François Serre was born at Wiesbaden, Germany, on April 4, 1923, and passed away at age 86 at Courgeout, France, on November 02, 2009. Because his father was shortly after World War I involved in the allied occupation of the Saarland Territory, he had be born there. Serre graduated in 1948 as civil engineer from the *Ecole des Ponts et Chaussées*, Paris, from when he contributed to dam projects in Morocco and Iran. In parallel, he prepared a notable Ph.D. thesis on free surface flows which he submitted in 1952 to the *Faculté des Sciences*, Paris. From 1962 to 1985, Serre was engineer with the *Société Centrale pour l'Equippement du Terroir* SCET, where other than hydraulic questions were solved.

Serre has written the outstanding 1953 paper, covering more than 50 pages and dealing with open-channel flow in rectangular channels. Apart from the topics addressed above, backwater curves under the effect of streamline curvature and general gate flow under steady flow conditions were also considered. Moreover, unsteady flows received interest again under the effect of streamline curvature. A number of practical considerations were also included such as these associated with a moving hydraulic jump. This long work reads still as a modern contribution to free surface hydraulics, and only few more elaborated works have been presented since. Given that he was working in the precomputer times, many solutions are schematic and did not produce numerical results.

Serre's main contributions to practical engineering were not published. Yet, he presented a number of works relating to the settlement of soils with extensions to a French congress. His 1956 paper reconsiders long irrotational waves based on the Boussinesq approach, and in particular investigates the solitary wave and its breaking conditions. His last paper of 1961 deals with exceptional flood waves and analytical means to treat these hydraulically.

Serre's outstanding thesis includes backwater curves under the effect of streamline curvature and friction. This idea was originally proposed by Boussinesq (1877), but his development was obscure and not fully reconsidered until Serre, who was the first proposing a rigorous approach based on a similarity assumption for the turbulent velocity profile. Thus, his approach is different from the potential flow method of Benjamin and Lighthill (1954), published only one year after Serre's Ph.D. thesis. Other approaches dealing with this problem include Mandrup Andersen (1978),

Hager and Hutter (1984a, b), Montes (1986), Montes and Chanson (1998), and Bose and Dey (2007). However, Serre did not publish his research in Anglo-Saxon journals so that his work was largely overlooked, without adequate recognition by the hydraulic community (Castro-Orgaz and Hager 2011c).

The time-averaged turbulent velocity profile u in the x-direction was approximated by using the generalized similarity profile (Serre 1953; Castro-Orgaz and Hager 2011c; Castro-Orgaz and Chanson 2011)

$$\frac{u(x,y)}{U(x)} = \Lambda(\eta), \quad \eta = \frac{y}{h}, \tag{5.184}$$

from which one gets

$$u(x,y) = \frac{q(x)}{h(x)}\Lambda\left(\frac{y}{h}\right), \tag{5.185}$$

which is a predictor for the velocity profile for depth-averaged models. In this section, we follow the original development by Serre (1953). The 2D continuity equation reads

$$\frac{\partial u}{\partial x} + \frac{\partial w}{\partial y} = 0; \tag{5.186}$$

it is automatically satisfied by defining a stream function ψ via

$$u = -\frac{\partial \psi}{\partial y}, \quad w = +\frac{\partial \psi}{\partial x}. \tag{5.187}$$

Inserting Eq. (5.185) into Eq. $(5.187)_1$ yields

$$-\frac{\partial \psi}{\partial y} = \frac{q}{h}\Lambda, \tag{5.188}$$

and after integration,

$$-\psi = q\Gamma(\eta) + c(x), \tag{5.189}$$

where $c = c(x)$ is arbitrary and the new similarity function Γ is defined by the identity

$$\Lambda(\eta) = \frac{\partial \Gamma(\eta)}{\partial \eta}. \tag{5.190}$$

The normalization condition for the stream function at $y = 0$ is $\psi = 0$. Inserting this condition into Eq. (5.188) implies $c = 0$. Thus, the stream function is given by the similarity profile

$$-\psi = q\Gamma(\eta). \tag{5.191}$$

Inserting Eq. (5.191) into Eq. $(5.187)_2$ yields

$$w = +\frac{\partial \psi}{\partial x} = \frac{\partial}{\partial x}[-q\Gamma(\eta)] = -q\frac{\partial \Gamma}{\partial \eta}\frac{\partial \eta}{\partial x} = -q\Lambda\frac{\partial \eta}{\partial x}. \tag{5.192}$$

Next, using the differential relation

$$\frac{\partial \eta}{\partial x} = \frac{\partial}{\partial x}\left(\frac{y}{h}\right) = -\frac{y}{h^2}h_x, \tag{5.193}$$

in Eq. (5.192), produces the linear vertical velocity profile

$$w(x,y) = +q\Lambda\frac{y}{h^2}h_x = U\Lambda\eta h_x = u\eta h_x. \tag{5.194}$$

The pressure distribution is obtained using the y-momentum balance. Taking the inviscid version of Eq. (5.142), written in the following alternative form for convenience,

$$\frac{1}{\rho}\frac{\partial p}{\partial y} = -g\cos\theta - u\frac{\partial w}{\partial x} - w\frac{\partial w}{\partial y}, \tag{5.195}$$

and using Eq. (5.186) in Eq. (5.195) yields

$$\frac{1}{\rho}\frac{\partial p}{\partial y} = -g\cos\theta - u\frac{\partial w}{\partial x} + w\frac{\partial u}{\partial x}. \tag{5.196}$$

Noting that

$$\frac{\partial w}{\partial x} = \frac{\partial}{\partial x}(u\eta h_x) = \frac{\partial u}{\partial x}\eta h_x + u\frac{\partial}{\partial x}(\eta h_x), \tag{5.197}$$

Equation (5.196) can be rewritten as

$$\begin{aligned}\frac{1}{\rho}\frac{\partial p}{\partial y} &= -g\cos\theta - u\left[\frac{\partial u}{\partial x}\eta h_x + u\frac{\partial}{\partial x}(\eta h_x)\right] + w\frac{\partial u}{\partial x} \\ &= -g\cos\theta - \frac{\partial u}{\partial x}\left(\underbrace{u\eta h_x - w}_{=0}\right) - u^2\frac{\partial}{\partial x}(\eta h_x).\end{aligned} \tag{5.198}$$

Inserting Eq. (5.185) yields

$$\frac{1}{\rho}\frac{\partial p}{\partial y} = -g\cos\theta - \frac{q^2}{h^2}\Lambda^2\frac{\partial}{\partial x}(\eta h_x). \tag{5.199}$$

Next, using the differential identity

$$\frac{\partial}{\partial x}\left(\frac{y}{h}h_x\right) = y\left(\frac{h_{xx}}{h} - \frac{h_x^2}{h^2}\right), \tag{5.200}$$

Equation (5.199) is rewritten as

$$\frac{1}{\rho}\frac{\partial p}{\partial y} = -g\cos\theta - \frac{q^2}{h^2}\Lambda^2 y\left(\frac{h_{xx}}{h} - \frac{h_x^2}{h^2}\right), \tag{5.201}$$

or

$$\frac{1}{\rho g}\frac{\partial p}{\partial y} = -\cos\theta - \frac{U^2}{gh}\Lambda^2\eta\left(hh_{xx} - h_x^2\right). \tag{5.202}$$

Equation (5.202) after integration yields the vertical pressure distribution

$$\frac{p}{\gamma} = (h-y)\cos\theta + \frac{U^2}{g}\left(hh_{xx} - h_x^2\right)\int_\eta^1 \eta'\Lambda^2 \mathrm{d}\eta'. \tag{5.203}$$

Inserting Eqs. (5.185) and (5.203) into Eq. (5.141) produces after neglecting σ_x

$$S = \int_0^h \left(\frac{u^2}{g} + \frac{p}{\gamma}\right)\mathrm{d}y = \frac{h^2}{2}\cos\theta + \beta\frac{q^2}{gh} + \frac{q^2}{gh}m\left(hh_{xx} - h_x^2\right), \tag{5.204}$$

where β is the Boussinesq coefficient

$$\beta = \int_0^1 \Lambda^2 \mathrm{d}\eta, \tag{5.205}$$

and m the pressure coefficient

$$m = \int_0^1 \left[\int_\eta^1 \eta'\Lambda^2 \mathrm{d}\eta'\right]\mathrm{d}\eta. \tag{5.206}$$

So far no assumptions on Λ were made aside from its similarity nature. The function is general, and the log-law, the wall-wake law (White 1991), or a power-law velocity profile (Montes 1986; Bose and Dey 2007) may be applied. Serre (1953) considered the simplest case $\Lambda = 1$, from which $\beta = 1$ and, from Eq. (5.206), $m = 1/3$ follow. With these choices, Eq. (5.204) implies

$$S = \frac{h^2}{2}\cos\theta + \frac{q^2}{gh}\left(1 + \frac{hh_{xx} - h_x^2}{3}\right), \tag{5.207}$$

which is, therefore, coupled with Eq. (5.140) for the streamwise variation of S.

Montes (1986) used the power-law model

$$\Lambda = \frac{u}{U} = (1+N)\eta^N, \tag{5.208}$$

from which Eq. (5.205) yields, upon using Eq. (5.208),

$$\beta = \int_0^1 (1+N)^2\eta^{2N}\mathrm{d}\eta = \frac{(1+N)^2}{2N+1}. \tag{5.209}$$

The pressure coefficient m in Eq. (5.206) now takes the form

$$\begin{aligned} m &= \int_0^1 \left[\int_\eta^1 \eta'\Lambda^2\mathrm{d}\eta'\right]\mathrm{d}\eta = (1+N)^2\int_0^1 \left[\int_\eta^1 \eta'^{2N+1}\mathrm{d}\eta'\right]\mathrm{d}\eta \\ &= \frac{(1+N)^2}{2N+2}\int_0^1 \left(1-\eta^{2N+2}\right)\mathrm{d}\eta \\ &= \frac{(1+N)^2}{(2N+2)}\left(1-\frac{1}{2N+3}\right) = \frac{(1+N)^2}{(2N+3)}, \end{aligned} \tag{5.210}$$

so that the pressure distribution in Eq. (5.203) is obtained in the form

$$\begin{aligned} \frac{p}{\gamma} &= (h-y)\cos\theta + \frac{q^2}{gh^2}\left(hh_{xx} - h_x^2\right)\int_\eta^1 \eta'\Lambda^2\mathrm{d}\eta' \\ &= (h-y)\cos\theta + \frac{q^2}{gh^2}\frac{(1+N)^2}{2N+2}\left(hh_{xx} - h_x^2\right)\left(1-\eta^{2N+2}\right) \\ &= (h-y)\cos\theta + \frac{q^2}{2gh^2}(1+N)\left(hh_{xx} - h_x^2\right)\left(1-\eta^{2N+2}\right). \end{aligned} \tag{5.211}$$

The velocity profile w in Eq. (5.194) may be written as

$$w = \frac{q}{h}(1+N)\eta^{N+1}h_x. \tag{5.212}$$

Using Eqs. (5.208), (5.211), and (5.212), the depth-averaged specific energy head in an undular hydraulic jump is computed as follows (Serre 1953; Montes 1986)

$$\begin{aligned}
E &= \frac{1}{h}\int_0^h \left(\frac{u^2}{2g} + \frac{w^2}{2g} + y\cos\theta + \frac{p}{\gamma}\right)\mathrm{d}y \\
&= \frac{1}{h}\int_0^h \left[\frac{U^2(1+N)^2\eta^{2N}}{2g} + \frac{U^2(1+N)^2\eta^{2N+2}h_x^2}{2g} + y\cos\theta\right. \\
&\quad \left. + (h-y)\cos\theta + \frac{U^2}{2g}(1+N)\left(hh_{xx} - h_x^2\right)\left(1-\eta^{2N+2}\right)\right]\mathrm{d}y \\
&= h\cos\theta + \frac{(1+N)^2}{2N+1}\frac{U^2}{2g} + \int_0^1 \frac{U^2(1+N)^2\eta^{2N+2}h_x^2}{2g}\mathrm{d}\eta \\
&\quad + \int_0^1 \frac{U^2}{2g}(1+N)\left(hh_{xx} - h_x^2\right)\left(1-\eta^{2N+2}\right)\mathrm{d}\eta \\
&= h\cos\theta + \frac{(1+N)^2}{2N+1}\frac{U^2}{2g} + \frac{U^2(1+N)^2h_x^2}{2g(2N+3)} + \frac{U^2}{2g}(1+N)\left(hh_{xx} - h_x^2\right)\left(1 - \frac{1}{2N+3}\right) \\
&= h\cos\theta + \frac{(1+N)^2}{2N+1}\frac{U^2}{2g} + \frac{U^2(1+N)^2h_x^2}{2g(2N+3)} + \frac{U^2}{2g}\frac{2(1+N)^2}{(2N+3)}\left(hh_{xx} - h_x^2\right) \\
&= h\cos\theta + \frac{(1+N)^2}{2N+1}\frac{U^2}{2g} + \frac{U^2}{2g}\frac{2(1+N)^2}{(2N+3)}\left(2hh_{xx} - h_x^2\right).
\end{aligned} \tag{5.213}$$

Equation (5.213) was used by Montes (1986) to simulate the undular jump profile. For $N = 0$, it simplifies to

$$E = h\cos\theta + \frac{q^2}{2gh^2}\left(1 + \frac{2hh_{xx} - h_x^2}{3}\right). \tag{5.214}$$

Coupled with

$$\frac{\mathrm{d}E}{\mathrm{d}x} = \sin\theta - S_f, \tag{5.215}$$

this is equivalent to the system given by Eqs. (5.140) and (5.207), where S_f is the friction slope.

5.3.4 Boundary Layer Model

Montes and Chanson (1998) modified the potential velocity distribution along an equipotential line, with V_s as the free surface (subscript s) velocity [Appendix G, Eq. (G.14)],

$$V = V_s \exp\left[-hh_{xx}\left(1+h_x^2\right)^{-1}\frac{1-\eta^2}{2}\right]. \tag{5.216}$$

If we set a power-law vorticity factor to account for boundary shear and use N as a Prandtl-type velocity distribution exponent, then

$$V = V_s\eta^N \exp\left[-hh_{xx}\left(1+h_x^2\right)^{-1}\frac{1-\eta^2}{2}\right]. \tag{5.217}$$

Using Eq. (5.217), and its associated pressure distribution, the extended Boussinesq-type energy equation takes the form (Montes and Chanson 1998; Castro-Orgaz 2010b) [Appendix G, Eq. (G.39)]

$$E = h\cos\theta + \beta\frac{q^2}{2gh^2}\left[1+m_1hh_{xx}\left(1+h_x^2\right)^{-1} - m_2h_x^2\left(1+h_x^2\right)^{-1}\right], \tag{5.218}$$

where the boundary shear coefficients are given as

$$m_1 = \frac{2}{2N+3}\left(\frac{2N+1}{2} - \frac{(N+1)(2N+3)}{2(N+3)} + 2N + 1\right), \tag{5.219}$$

$$m_2 = \frac{(N+1)}{(N+3)}. \tag{5.220}$$

A linear variation of streamline curvature was prescribed in Eq. (5.219). The Boussinesq momentum coefficient is

$$\beta = \frac{(1+N)^2}{2N+1}. \tag{5.221}$$

Neglecting bottom shear effects on the velocity and pressure distributions, i.e., $N \to 0$, yields $m_1 \to 2/3$, $m_2 \to 1/3$ and $\beta \to 1$. The streamwise variation of the specific energy $E = E(x)$ along the undular jump is given by Eq. (5.215). A first point deserving consideration is that bottom shear is present in the extended Boussinesq-type system of equations by two different effects: (1) frictional velocity exponent N results in values for β, m_1, and m_2 that differ from those of the classical potential flow approach, thereby influencing the integration of Eq. (5.218); (2) the

friction factor f to be used in Eq. (5.215) depends on C_f, the skin friction coefficient, which is linked to N by the turbulent boundary layer characteristics.

Closure of the system of Eqs. (5.215) and (5.218) is needed in terms of bottom shear effects. Montes and Chanson (1998) proposed the boundary layer method of Furuya and Nakamura (1968) to estimate f and N. This method is valid for adverse pressure gradient boundary layer flows, like those occurring in undular hydraulic jumps. To produce closure differential equations, the 2D x-momentum equation is first integrated across the boundary layer thickness producing the well-known von Kármán equation (White 1991; Montes and Chanson 1998)

$$\frac{\mathrm{d}\theta_m}{\mathrm{d}x} = -\frac{\theta_m}{U_e}\frac{\mathrm{d}U_e}{\mathrm{d}x}(H+2) + \frac{C_f}{2}. \tag{5.222}$$

Here, θ_m is the boundary layer momentum thickness, U_e the maximum velocity at the boundary layer edge $\approx (1 + N)(q/h)$, H the shape factor $= \delta^*/\theta_m$, $\delta^* = [N/(1 + N)]h$ the boundary layer displacement thickness for fully developed boundary layer flows ($\delta = h$), $C_f = \tau_b/(\rho U_e^2/2)$ the skin-friction coefficient, and τ_b the boundary shear stress. A second closure equation is produced by integrating the 2D x-momentum equation from $y = 0$ to $y = \theta_m$ as (Furuya and Nakamura 1968; Montes and Chanson 1998)

$$\frac{\mathrm{d}K}{\mathrm{d}x} = 1.46\frac{1-K^2}{(A+K)\theta_m \mathsf{R}_\theta^{1/4}}[\Gamma + 0.118(0.67-K)], \tag{5.223}$$

with $\Gamma = (\theta_m/U_e)(\mathrm{d}U_e/\mathrm{d}x)\mathsf{R}_\theta^{1/4}$ as Buri's shape factor, u_θ as the velocity at $y = \theta_m$, A a stability factor, and $K = u_\theta/U_e$. Montes and Chanson (1998) used $A = 1.5$. The skin-friction coefficient C_f was correlated by Ludwieg and Tillman as (White 1991)

$$C_f = 0.246\mathsf{R}_\theta^{-0.268} \times 10^{-0.678H}, \tag{5.224}$$

with $\mathsf{R}_\theta = (U_e\theta_m)/\nu = [\mathsf{R}_1(1 + N)\theta_m)]/h$, where the shape factor H is correlated with K by (Furuya and Nakamura 1968; Montes and Chanson 1998)

$$H = \left[1.3 + 1.3(0.7-K) + 3(0.7-K)^2\right]^{2/3}. \tag{5.225}$$

Once H is known, the velocity exponent follows from $N = (H - 1)/2$. The system of differential Eqs. (5.215), (5.218), (5.222) and (5.223) may be solved for the unknowns $h(x)$, $E(x)$, $\theta_m(x)$, and $K(x)$ with a fourth-order Runge–Kutta method. The streamwise evolutions of $f(x)$, $C_f(x)$, $H(x)$, $N(x)$ are produced as part of the solution. The boundary conditions at the toe of the undular jump are $h_1 = h_c\mathsf{F}_1^{-2/3}$, $h_{x1} = 0$, $h_{xx1} = 0$ and $N = N_1$. The value E_1 is deduced from Eq. (5.218) by assuming $h_{x1} = h_{xx1} = 0$. Using the known value of N_1, and the condition for a fully developed approach flow, namely $h = \delta$, results in $\theta_{m1} = (N_1h_1)/[(2N_1 + 1)(N_1 + 1)]$. The shape factor is $H_1 = 2N_1 + 1$, whereas K_1 is deduced from Eq. (5.225) using

the value of H_1. These boundary conditions are equivalent to an approach flow with a hydrostatic pressure distribution and a fully developed turbulent velocity profile following a power-law with exponent N_1.

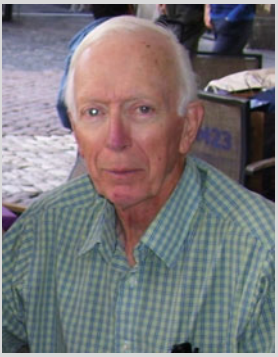

José Sergio Montes-Videla
was born in Santiago, Chile, on January 15, 1937. He graduated as a civil engineer from the University of Chile in 1961, moving then to Wallingford Hydraulics Laboratory in Great Britain, returning to Chile in 1963 as a director of the Laboratory of Hydraulics. He directed the laboratory until 1968, a period during which Montes shared the teaching of hydraulics with his mentor, Prof. Francisco Javier Dominguez Solar (1890–1988). In 1969, Montes moved to the Massachusetts Institute of Technology MIT, pursuing studies toward a Ph.D. in civil engineering under Prof. Arthur Thomas Ippen (1907–1974), submitting a Ph.D. thesis on the interaction of suspended sediment particles with turbulent flows in 1973. Sergio Montes was Ippen's last Ph.D. student; unfortunately, this work remained almost unnoticed given that the unexpected death of Ippen suddenly stopped preparation of results for publication in any leading journal. Montes then emigrated to Australia, where he taught hydraulics and fluid mechanics at the University of Hobart, Tasmania, retiring in 1998. Montes lives in Hobart with his wife and sons, where he enjoys his hobbies, among which is aeromodeling.

Montes demonstrated in his Ph.D. thesis that the von Kármán constant is variable in sediment-laden flows, a topic of great controversy in the past decades, despite this fact was mostly elucidated by Montes and Ippen. The major contributions of Montes were in the field of non-hydrostatic open-channel flows. He developed the x–ψ method for the computation of irrotational flow over weirs, drops, and gates, comparing well with observations at the time that computational efforts kept reduced. He also generalized Jaeger's theory for weir flows and added to the definition of the spillway crest for high dams. Montes further contributed to the study of the fascinating problem of the undular hydraulic jump, initiated by Carlos Fawer (1910–1996). Given the failure of potential flow theory to model these complex turbulent flows, he developed a viscous flow model of boundary layer type that successfully captured the main real flow features. Montes is the author of a well-recognized open-channel flow book published in 1998, just after his retirement, which is considered his legacy to the science of hydraulics.

5.3.5 *Simulations: Plane Undular Jump*

The measured free surface profile of an undular hydraulic jump for $\mathsf{F}_1 = q/(gh_1^3)^{1/2} = 1.11$ in a channel of bottom slope 1/282 is plotted in Fig. 5.24 (Gotoh et al. 2005). This is an adequate case to test the depth-averaged undular jump model, given the absence of cross-waves, leading to a perfect 2D structure of the undular jump; the numerical simulations of Schneider et al. (2010) are also included. These authors solved the 2D RANS equations numerically using the k–ε turbulence model. Here, the depth-averaged RANS model with the simplified k–ε turbulence model was numerically solved, namely Eqs. (5.140), (5.156), (5.157), and (5.171) for the unknowns $S(x)$, $k(x)$, $\varepsilon(x)$, $h_x(x)$, and $h(x)$. The fourth-order Runge–Kutta method was used to solve the system of ordinary differential equations, taking the approach flow section as starting point. At point 1, the flow depth is experimentally given by $h_1 = 0.0953$ m and the free surface slope is set equal to $h_x = 0$. The power-law exponent N_1 is computed from Eq. (5.176) using Eq. (5.177) for f_o. With that information, coefficients λ_1, λ_2, and λ_3 are computed from Eqs. (5.172)–(5.174). The value of ε for uniform open-channel flow ($\partial k/\partial x = \partial\varepsilon/\partial x = 0$) is, from Eq. (5.156), $\varepsilon_1 = P_{kv} = (f_o/8)q^3h_1^{-4}$, and, from Eq. (5.157), $k_1 = h_1^2(f_o/8)^{-2}(q/h_1)^{-4}\varepsilon_1^2 c_{2\varepsilon}c_\varepsilon^{-1}$. Thus, v_{t1} is given by Eq. (5.155) and S_1 is computed from Eq. (5.171). The normalized free surface profile $h/h_c[x/h_c]$ predicted from the depth-averaged model is plotted in Fig. 5.24, with $h_c = (q^2/g)^{1/3}$. The results of the depth-averaged RANS model are in excellent agreement with the 2D results (Schneider et al. 2010) and with the experimental data (Gotoh et al. 2005). The 1D depth-averaged model is a simplification of the 2D RANS model. In the latter, the free surface profile needs iterative computation, in which the full 2D computation of velocity, pressure, and turbulence variables is performed in each iteration cycle (Bradford and Katopodes 1998; Schneider et al. 2010). In contrast, the 1D depth-averaged model yields the free surface profile with a direct computation due to the simplifications previously introduced. A specific aspect deserving consideration is that the depth-averaged model follows the 2D RANS undulating pattern, keeping a similar wave length and amplitude, which is an improvement over previous 1D models.

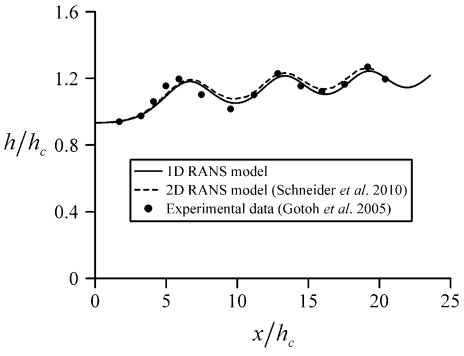

Fig. 5.24 Free surface profile $h/h_c[x/h_c]$ of an undular hydraulic jump for $\mathsf{F}_1 = 1.11$ (adapted from Castro-Orgaz et al. 2015)

The RANS depth-averaged model is now compared with other modeling approximations available in the literature. The Serre (1953) model uses the depth-averaged specific momentum S of a potential flow, and the streamwise momentum balance including bottom friction and the standard friction factor formulae as [see Eq. (5.207)]

$$S = \frac{h^2}{2}\cos\theta + \frac{q^2}{gh}\left(1 + \frac{hh_{xx} - h_x^2}{3}\right), \quad \frac{\mathrm{d}S}{\mathrm{d}x} = h\sin\theta - \frac{f_o}{8g}\frac{q^2}{h^2}. \tag{5.226}$$

A simulation corresponding to Eq. (5.226) is plotted in Fig. 5.25a for comparative purposes with the depth-integrated RANS model. Note that Serre's model produces a first wave crest close to the 2D RANS model, which is overpredicted, however. Along the entire wave train, the solution given by Serre's model produces over- and underpredictions of wave crests and troughs, respectively. The depth-averaged model produces underpredictions of both wave crests and troughs, but the results are much closer to 2D data. Additionally, Serre's model diverges from the 2D RANS model in wave phase, contrary to the depth-integrated RANS model, which produces a wave train almost in phase with the full 2D RANS solution.

Hosoda and Tada (1994) developed an undular flow model in which the turbulence contribution in the streamwise momentum equation was accounted for. Using Serre's (1953) potential velocity and pressure distributions, and σ_x as given by Eq. (5.150) neglecting k, yields for the momentum model of Hosoda and Tada (1994)

$$S = \int_0^h \left(\frac{u^2}{g} + \frac{p - \sigma_x}{\gamma}\right)\mathrm{d}y = \underbrace{\int_0^h \left(\frac{u^2}{g} + \frac{p}{\gamma}\right)\mathrm{d}y}_{\substack{\text{Serre theory} \\ \text{with } \Lambda=1}} - \underbrace{\int_0^h \frac{\sigma_x}{\gamma}\mathrm{d}y}_{\substack{\text{Closure with} \\ \text{eddy viscosity}}}, \tag{5.227}$$

where

$$\sigma_x \approx 2\rho\nu_t\frac{\partial U}{\partial x} = -2\rho\nu_t\frac{q}{h^2}\frac{\partial h}{\partial x}. \tag{5.228}$$

Inserting this expression into Eq. (5.227) and using Eq. (5.207) as the result of Serre's (1953) theory with $\Lambda = 1$ yield

$$S = \frac{h^2}{2}\cos\theta + \frac{q^2}{gh}\left(1 + \frac{hh_{xx} - h_x^2}{3}\right) - \frac{\sigma_x}{\rho g}h, \tag{5.229}$$

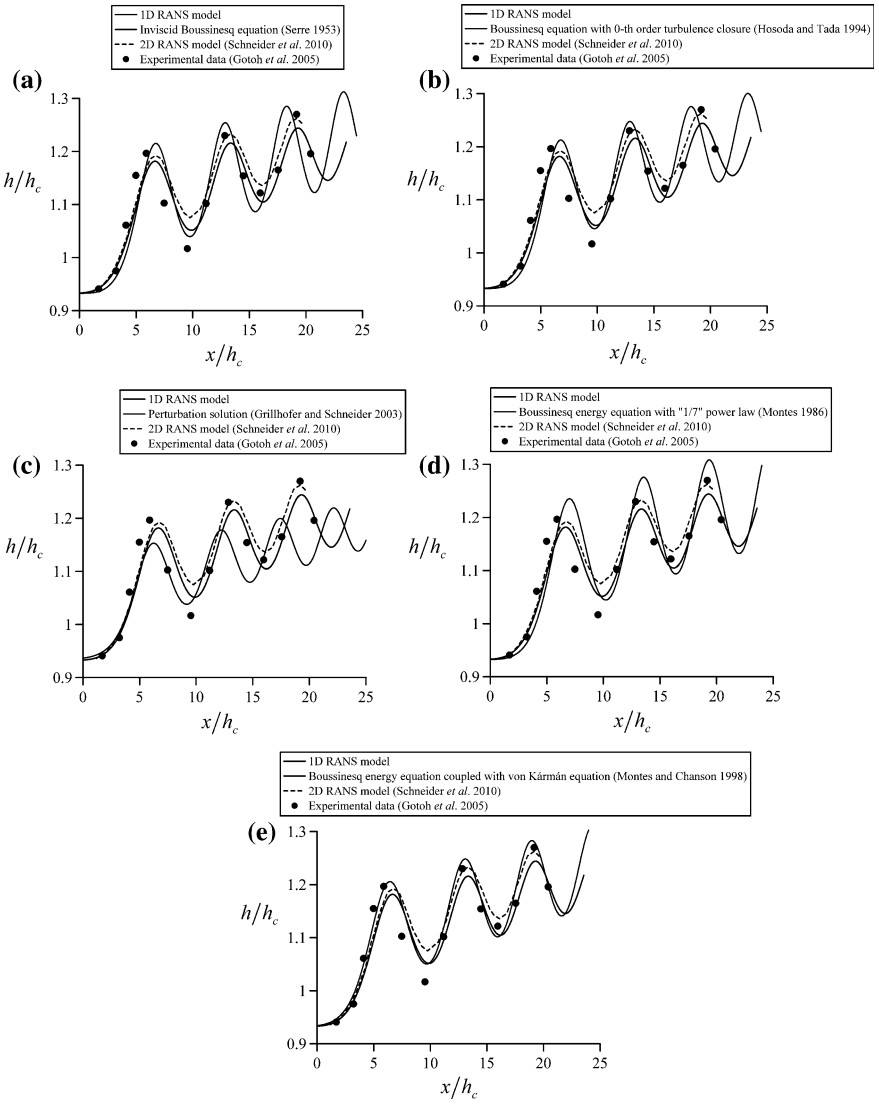

Fig. 5.25 Comparison of free surface profiles $h/h_c[x/h_c]$ with previous solutions for $\mathsf{F}_1 = 1.11$. For details, see main text (adapted from Castro-Orgaz et al. 2015)

or

$$S = \frac{h^2}{2}\cos\theta + \frac{q^2}{gh}\left(1 + \frac{hh_{xx} - h_x^2}{3}\right) + 2\frac{\nu_t}{g}\frac{q}{h}h_x, \quad \frac{\mathrm{d}S}{\mathrm{d}x} = h\sin\theta - \frac{f_o}{8g}\frac{q^2}{h^2}. \quad (5.230)$$

The depth-averaged eddy viscosity is estimated here as $\nu_t = (\kappa/6)u^* h$ (Li and Jin 1996; Kim et al. 2009; Ghamry and Steffler 2002). Simulations using Eq. (5.230)

were conducted using identical boundary conditions, with the results plotted in Fig. 5.25b. The solution is close to the simulations using Eq. (5.226).

Grillhofer and Schneider (2003) developed a perturbation solution of the RANS equations near the critical depth, $\mathsf{F}(x) \to 1$, for large Reynolds numbers, $\mathsf{R}(x) \to \infty$. They obtained the following third-order differential equation describing the free surface profile

$$\frac{\mathrm{d}^3 H_1}{\mathrm{d}X^3} = (1 - H_1)\frac{\mathrm{d}H_1}{\mathrm{d}X} + \mu H_1. \tag{5.231}$$

Here, $X = x/h_1$, $H_1 = (h - h_1)/(\varepsilon_p h_1)$, $\varepsilon_p = (2/3)(\mathsf{F}_1 - 1)$ and $\mu = (1/3)(\theta\varepsilon_p)^{-3/2}$. Equation (5.231) was numerically solved using the fourth-order Runge–Kutta method, with the results plotted in Fig. 5.25c. The first wave crest is underpredicted by the perturbation solution, resulting in successive underprediction of wave crests and troughs along the entire wave train. Beyond the first wave crest, the perturbation solution produces a wave train with a phase shift as compared to the 2D RANS simulations.

Montes (1986) introduced the effect of the turbulent velocity profile in the Serre (1953) model employing the 1/7-th power-law. After depth averaging of the local energy head, the system of differential equations for the undular jump profile reads, with E as the specific energy and $N = 1/7$ [see Eq. (5.213)],

$$E = h\cos\theta + \frac{q^2}{2gh^2}\left[\frac{(1+N)^2}{2N+1} + \frac{(1+N)^2}{(3+2N)}\left(2hh_{xx} - h_x^2\right)\right], \quad \frac{\mathrm{d}E}{\mathrm{d}x} = \sin\theta - \frac{f_o}{8g}\frac{q^2}{h^3}. \tag{5.232}$$

The functions for E and $\mathrm{d}E/\mathrm{d}x$ given by Eqs. (5.232) were solved numerically. The results are plotted in Fig. 5.25d. Note that the effect of the exponent 1/7 is significant, but the solution deteriorates when compared with that of Serre's (1953) model, that is regained from Eq. (5.232) by setting $N = 0$.

Montes and Chanson (1998) produced an improved boundary layer-type Boussinesq-type model accounting for friction effects, given by the system of the differential Eqs. (5.215), (5.218), (5.222), and (5.223). These were solved as previously described and the unknowns $h(x)$, $E(x)$, $\theta_m(x)$, $K(x)$ were computed with a fourth-order Runge–Kutta method. The results are plotted in Fig. 5.25e, showing excellent agreement with test data, 2D RANS simulations, and the depth-averaged RANS model. It supports the relevance of this boundary layer-type approximation.

An additional flow feature of importance in undular hydraulic jumps is the bed-shear stress. Consider the accuracy of its prediction if the bed-shear stress closure $f = f_o$ is used in the depth-averaged model, with the numerical predictions shown in Fig. 5.26a. Note that the use of a standard friction factor overpredicts the bed-shear stress along the entire wave train because Eq. (5.177) is independent of local conditions on the wave train and is fully determined by the upstream value of R_1. The depth-averaged model was run using the closure $f = f_\theta$, of which the results

are also shown in Fig. 5.26a. In this case, the f-prediction using the boundary layer theory produces underpredictions of the bed-shear stress. The only work available in the literature, in which the bed-shear stress of undular hydraulic jumps was analyzed in the context of the boundary layer theory, is that of Dunbabin (1996), whose results are summarized by Montes and Chanson (1998). However, Dunbabin's work relates only the approach flow to the first wave crest with positive values of h_x. Figure 5.26a suggests that a bed-shear stress closure using f as given by Eq. (5.183) produces an acceptable τ_b predictor for depth-averaged modeling along the entire jump profile. This is explored in Fig. 5.26b, in which the bed-shear stress is close to the 2D RANS data, except for the first wave trough, where the depth-averaged model overpredicts τ_b. The free surface profile remains almost unaffected by the bed-shear stress closure. The possible physical explanation for the results of Fig. 5.26 relies on the dependence of each friction factor formulae on a different Reynolds number. The closure $f = f_o$ implies that R_1 fully determines the friction factor along the entire undular flow, i.e., remains constant [see Eq. (5.177)]. This is, obviously, physically unrealistic, as the friction factor should depend on both R and free surface flow effects, which ideally depends on a type of Froude number F (Yen 2002). The closure $f = f_\theta$ implies, in contrast, that the friction factor along the undular jump is a variable, which is a more physically based approach. The computation of the friction factor then depends on the Reynolds number $\mathsf{R}_\theta = U_e\theta_m/\nu$. Both U_e and θ_m are directly related to the local value of the flow depth $h(x)$ that, in turn, is related to the local Froude number $\mathsf{F}(x)$. Thus, friction factors with this closure are spatially varied in response to the free surface configuration. Given the number of empirical constants in the wall-wake model, and the simplifications adopted in the computation of N and U_e, a precise description of the bed-shear stress appears not feasible. More experimental data on the friction law of undular flows are required, but in the absence of definite experimental facts in this regard, the simplest mean closure described above was adopted.

The measured centerline free surface profile of an undular hydraulic jump of $\mathsf{F}_1 = 1.31$ in a channel of bottom slope 0.0067 is plotted in Fig. 5.27 (Chanson

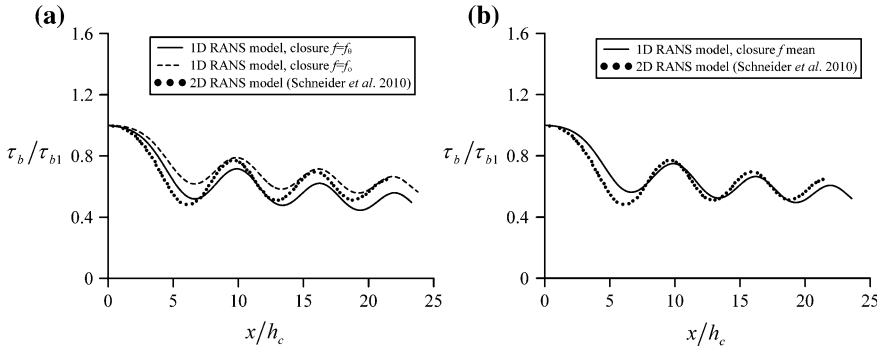

Fig. 5.26 Comparison of bed-shear stress $\tau_b/\tau_{b1}[x/h_c]$ **a** standard closure, **b** closure using mean f from Eq. (5.183) (adapted from Castro-Orgaz et al. 2015)

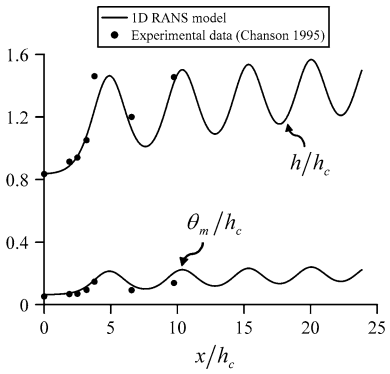

Fig. 5.27 Free surface and momentum thickness profiles of undular hydraulic jump for $F_1 = 1.31$ (adapted from Castro-Orgaz et al. 2015)

1995). This is a 3D test case beyond the theoretical validity of the depth-averaged undular jump model, and thus relevant to highlight the limitations of the 2D approach. Note that the model produces a 1D free surface profile $h(x)$, and therefore is unable to reproduce the effects of shock waves. The depth-averaged simulation results for the free surface profile are plotted in Fig. 5.27 for this limit test, for which the agreement is only satisfactory due to 3D effects. The momentum thickness was computed from the measured velocity profiles by Chanson (1995), and these data are included as well, together with the depth-averaged results for θ_m/h_c. Even with the 3D effects, the depth-averaged model produces results in reasonable agreement with observations.

The experimental velocity profile at the first wave crest of this test is plotted in Fig. 5.28a to depict the physical interaction of streamline curvature and vorticity. Note from the experimental data that the occurrence of maximum velocity is below the free surface. The potential velocity profile (Eq. 5.160) is also plotted, resulting in large deviations from the experiments. The potential velocity profile predicts a minimum velocity at the free surface, with an increasing profile as the bottom is approached, resulting in a slip velocity. The simple power-law Eq. (5.161) that neglects streamline curvature predicts the maximum velocity at the free surface, with decreasing velocities as the bottom is approached. The computed $N = 0.3107$ below the first wave crest (which is highly different from the standard $1/7 = 0.1429$) was used to plot this velocity profile, resulting again in systematic deviations, with underpredicted velocity. The composite power-law velocity profile used in the depth-averaged RANS model, Eq. (5.162), is plotted in Fig. 5.28a, showing qualitative agreement with the physical trend of the experimental data. It highlights the importance of the interaction between vorticity and streamline curvature in the velocity profile of undular hydraulic jumps.

The same comparison is shown in Fig. 5.28b for the first wave trough using the computed value $N = 0.148$ (i.e., close to 1/7). In this case, potential flow results are still poor, whereas differences between Eqs. (5.161) and (5.162) are smaller, indicating that the simple power-law is a good model at this section.

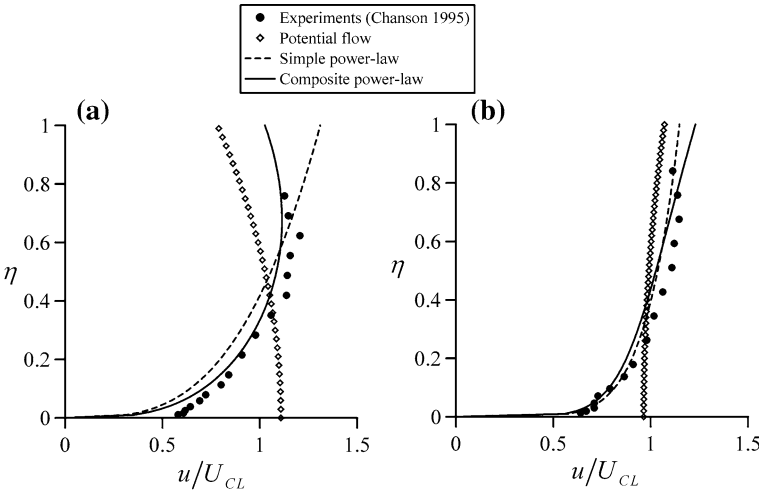

Fig. 5.28 Velocity profile $u/U_{CL}[\eta]$ below first wave **a** crest, **b** trough of an undular hydraulic jump for $F_1 = 1.31$, with U_{CL} as depth-averaged velocity at channel centerline (adapted from Castro-Orgaz et al. 2015)

The vertical stress σ_y from Eq. (5.149) is obtained as follows

$$\begin{aligned}\sigma_y &= 2\rho\nu_t\frac{\partial w}{\partial y} - \frac{2}{3}\rho k \\ &= 2\rho\nu_t\frac{\partial}{\partial y}\underbrace{\left(Uh_x\eta^{N+1}\right)}_{\text{Eq. (5.163)}} - \frac{2}{3}\rho k \\ &= 2\rho\nu_t\frac{Uh_x}{h}(N+1)\eta^N - \frac{2}{3}\rho k.\end{aligned} \tag{5.233}$$

If in the pressure distribution of Eq. (5.147), the shear stress is neglected, $\tau_{yx} = 0$, as previously done, and Eq. (5.233) is employed, one obtains

$$\begin{aligned}\frac{p}{\gamma} &= (h-y)\cos\theta + \underbrace{\frac{\sigma_y}{\gamma}}_{\text{Eq. (5.233)}} - \underbrace{\frac{w^2}{g}}_{\text{Eq. (5.163)}} + \underbrace{\frac{1}{g}\frac{\partial}{\partial x}\int_y^h\left(uw - \frac{\tau_{yx}}{\rho}\right)\mathrm{d}y'}_{\text{Eq. (5.169)}} \\ &= (h-y)\cos\theta + 2\frac{\nu_t}{g}\frac{Uh_x}{h}(N+1)\eta^N - \frac{2}{3}\frac{k}{g} - \frac{U^2h_x^2\eta^{2N+2}}{g} \\ &\quad + \frac{q^2}{g}\frac{(1+N)}{(2N+2)}\left[\frac{h_{xx}}{h} - \frac{h_x^2}{h^2}\right]\left(1-\eta^{2N+2}\right) + \frac{q^2}{gh^2}(1+N)h_x^2\eta^{2N+2}.\end{aligned} \tag{5.234}$$

At the flow depth extrema ($h_x = 0$), this yields, upon neglecting k,

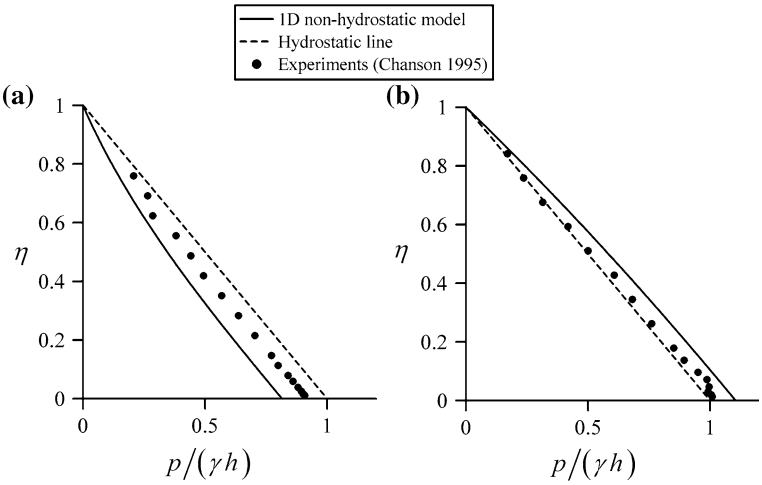

Fig. 5.29 Pressure distribution $p/(\gamma h)[\eta]$ below the first wave **a** crest, **b** trough of an undular hydraulic jump for $F_1 = 1.31$ (adapted from Castro-Orgaz et al. 2015)

$$\frac{p}{\gamma h} = (1-\eta)\cos\theta + \frac{F^2}{2} h h_{xx}\left(1-\eta^{2N+2}\right). \tag{5.235}$$

Pressure profiles obtained with Eq. (5.235) are compared in Fig. 5.29 with the data for the same test case of Fig. 5.28. Predictions are in fair agreement with observations. Deviations are again attributed to 3D flow effects.

5.3.6 *Simulations: Spatial Undular Jump*

Shock waves (Fig. 5.20) and wave breaking induce 3D spatial features for $F_1 > 1.2$ in the undular hydraulic jump. Wave breaking of the first crest of undular hydraulic jumps appears, roughly, if $F_1 > 1.36$ for horizontal channels (Reinauer and Hager 1995), but this limit may vary for sloping channels (Gotoh et al. 2005). A small roller appears at the first wave crest, which modifies the streamwise momentum balance. When $F_1 > 1.36$, the roller grows and its contribution to the momentum balance increases accordingly. Therefore, the non-breaking undular jump (Fig. 5.30a) tends to a classical hydraulic jump (Fig. 5.30b). Boussinesq equations are not able to simulate wave breaking or shockwave processes unless a special treatment is introduced. Based on model observations, the height of the first wave of the plane undular hydraulic jump is well approached by the solitary wave maximum (Iwasa 1955; Reinauer and Hager 1995)

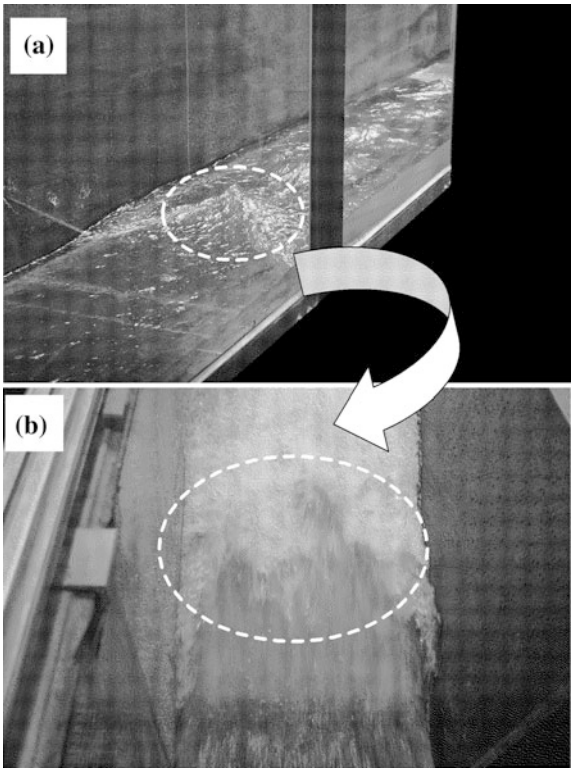

Fig. 5.30 **a** Non-breaking undular jump, **b** classical hydraulic jump (photographs VAW)

$$h_{\text{solitary}} = h_1 \mathsf{F}_1^2. \tag{5.236}$$

Once shock waves and wave breaking occur, the first wave crest flow depth h_m is less than predicted by Eq. (5.236), but higher than the tailwater flow depth of a classical hydraulic jump with a surface roller

$$h_{\text{jump}} = \frac{h_1}{2}\left[\left(1 + 8\mathsf{F}_1^2\right)^{1/2} - 1\right]. \tag{5.237}$$

Equation (5.236) is a result of vertical accelerations, whereas Eq. (5.237) is the follow-up to the existence of a surface roller. Note that, while the surface roller of the classical hydraulic jump develops, the shock waves become progressively trapped and hidden below it, thereby becoming a part of this complex spatial flow. Therefore, shock waves and wave breaking tend to evolve the relevant equation describing the first wave crest from Eq. (5.236) to Eq. (5.237). This observation suggests that, as shock waves and wave breaking progress, the effect of vertical acceleration is less important, thereby leading to quasi-hydrostatic flow conditions. Based on this physical reasoning, a means to produce Boussineq-type equations

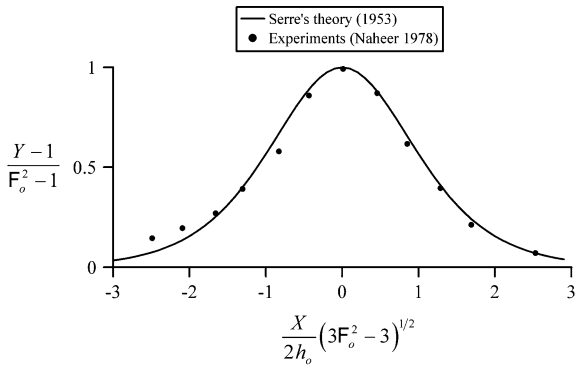

Fig. 5.31 Solitary wave profile for $F_o = 1.265$

with 3D effects is to include a damping factor to reduce the contribution of the non-hydrostatic pressure terms to the streamwise momentum balance.

Hosoda and Tada (1994) proposed a damping-factor model based on a study of the solitary wave profile. With $Y = h/h_{\text{solitary}}$, X the streamwise coordinate in moving axes, and F_o as the uniform flow Froude number, the solitary wave profile is (Serre 1953) [see Eq. (3.652)]

$$\frac{Y-1}{\left(F_o^2-1\right)} = \text{sech}^2\left[\frac{\left(3F_o^2-3\right)^{1/2}}{F_o}\frac{X}{2h_o}\right], \tag{5.238}$$

Results from Eq. (5.238) are compared with experimental data in Fig. 5.31 for $F_o^2 = 1.6$ (Naheer 1978), resulting in good agreement.

Consider that the ascending branch of the solitary wave profile describes the first wave crest of the undular jump (Iwasa 1955; Reinauer and Hager 1995). Hosoda and Tada (1994) adopted as limiting F_1 for wave breaking of the first crest the value $F_1 = 1.25$, based on undular bore data. Thus, the maximum water surface slope on the upstream part of the solitary wave profile is located at the inflection point, with a value

$$\left|\frac{dh}{dx}\right|_{br} = 0.225. \tag{5.239}$$

This value is therefore considered a threshold value above which wave breaking occurs. Hosoda and Tada (1994) proposed a damping factor f_{dump} given by

$$f_{\text{dump}} = \begin{cases} \exp\left[-\varsigma\left(\left|\frac{dh}{dx}\right| - \left|\frac{dh}{dx}\right|_{br}\right)\right], & \text{if } \left|\frac{dh}{dx}\right| > \left|\frac{dh}{dx}\right|_{br} \\ 1, & \text{else} \end{cases}. \tag{5.240}$$

Comparison with laboratory data indicates a calibration parameter $\varsigma = 2$ (Hosoda and Tada 1994). The specific momentum of Serre's theory, given by Eq. (5.207), is then modified to

$$S = \frac{h^2}{2}\cos\theta + \frac{q^2}{gh}\left[1 + f_{\text{dump}}\left(\frac{hh_{xx} - h_x^2}{3}\right)\right]. \tag{5.241}$$

If $f_{\text{dump}} = 1$, Eq. (5.241) reduces to Serre's theory. The bottom pressure profile of Serre's theory is, from Eq. (5.203), using $\Lambda = 1$,

$$\frac{p_b}{\gamma} = h\cos\theta + \frac{q^2}{2gh^2}\left(hh_{xx} - h_x^2\right). \tag{5.242}$$

It is modified to allow for wave breaking and shockwave effects as

$$\frac{p_b}{\gamma} = h\cos\theta + \frac{q^2}{2gh^2} f_{\text{dump}}\left(hh_{xx} - h_x^2\right). \tag{5.243}$$

Note that the damping factor accounts for the simultaneous effect of wave breaking and shock waves, i.e., 3D flow effects on the centerline free surface and bottom pressure head profiles. An experiment for an undular jump of $\mathsf{F}_1 = q/(gh_1^3)^{1/2} = 1.47$ in a channel of bottom slope 1/163 is plotted in Fig. 5.32, where centerline water depth and bottom pressure head profiles are shown (Gotoh et al. 2005). In this experiment, wave breaking is absent, given its dependence on the channel slope (Gotoh et al. 2005). Therefore, 3D effects are given exclusively by shockwave development. The solution of Eqs. (5.140) and (5.241), assuming $f_{\text{dump}} = 1$ (Serre's theory) and using the fourth-order Runge–Kutta method, is plotted in Fig. 5.32a. Note that Serre's model over- and underpredicts wave crest and trough water depths, respectively. The bottom pressure head prediction by Eq. (5.242) also differs from experiments, with an excessive drop at wave troughs. Another simulation was conducted accounting for f_{dump} as given by Eq. (5.240). The results are plotted in Fig. 5.32b, showing a reduced wave crest height, in better agreement with experiments, as expected. However, there is an appreciable phase lag in the water depth wave train, and minimum water depths are still underpredicted above the first wave.

Hosoda and Tada (1994) accounted for the streamwise turbulence contribution by writing [see Eq. $(5.230)_1$]

$$\begin{aligned} S &= \frac{h^2}{2}\cos\theta + \frac{q^2}{gh}\left(1 + \frac{hh_{xx} - h_x^2}{3}\right) + 2\frac{\nu_t}{g}\frac{q}{h}h_x \\ &= \frac{h^2}{2}\cos\theta + \frac{q^2}{gh}\left(1 + 2\frac{\nu_t}{q}h_x + \frac{hh_{xx} - h_x^2}{3}\right). \end{aligned} \tag{5.244}$$

They assumed that the eddy viscosity is proportional to the discharge, e.g.,

$$\alpha = \frac{2\nu_t}{q}, \tag{5.245}$$

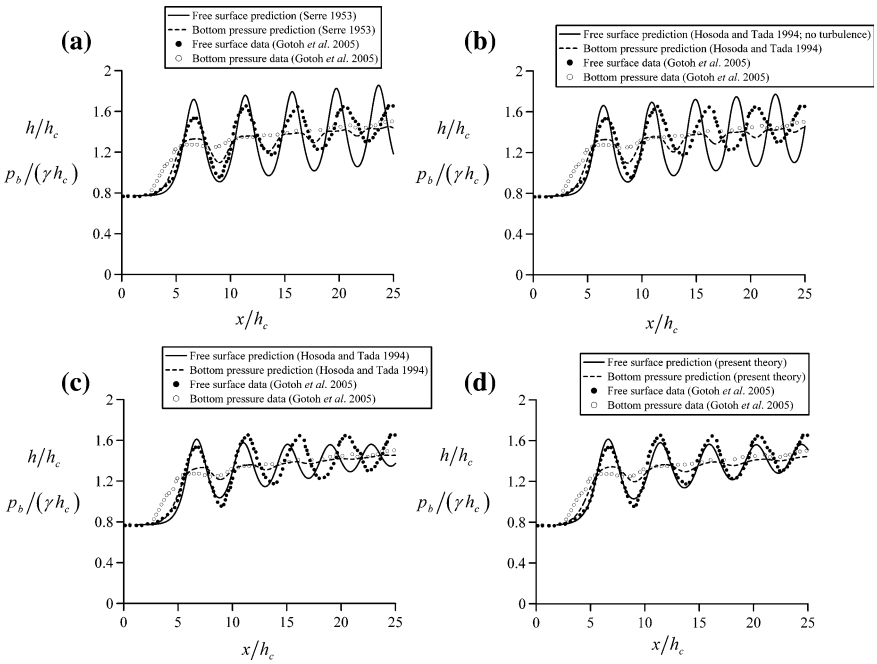

Fig. 5.32 Comparison of free surface profiles $h/h_c(x/h_c)$ and bottom pressure profiles $p_b/(\gamma h_c)(x/h_c)$ with different modeling solutions for undular jump of $F_1 = 1.47$

so that from Eq. (5.244)

$$S = \frac{h^2}{2}\cos\theta + \frac{q^2}{gh}\left[1 + \alpha h_x + f_{\text{dump}}\left(\frac{hh_{xx} - h_x^2}{3}\right)\right]. \tag{5.246}$$

They proposed a mean value $\alpha = 0.05$. The simulation based on Eq. (5.246) is plotted in Fig. 5.32c, with success in predicting the crest and trough water depths. The bottom pressure head prediction as given by Eq. (5.243) agrees now well with observations. However, a phase lag still persists which is attributed to the use of the depth-averaged velocity U for the velocity profile u in the momentum balance.

Montes (1986) proposed a power-law profile for the undular jump as [see Eq. (5.208)]

$$\frac{u(x,y)}{U(x)} = \Lambda = (1+N)\eta^N, \tag{5.247}$$

from which the pressure distribution is obtained in the form [see Eq. (5.211)]

$$\begin{aligned}\frac{p}{\gamma} &= (h-y)\cos\theta + \frac{U^2}{g}\left(hh_{xx} - h_x^2\right)\int_{\eta}^{1} \eta\Lambda^2 \mathrm{d}\eta' \\ &= (h-y)\cos\theta + (1+N)\frac{U^2}{2g}\left(hh_{xx} - h_x^2\right)\left(1-\eta^{2N+2}\right).\end{aligned} \tag{5.248}$$

From Eq. (5.248), the bottom pressure head is then given by

$$\frac{p_b}{\gamma} = h\cos\theta + (1+N)\frac{q^2}{2gh^2}\left(hh_{xx} - h_x^2\right). \tag{5.249}$$

Using Eqs. (5.247) and (5.248), the momentum function S becomes [see Eqs. (5.204), (5.209) and (5.210)]

$$S = \frac{h^2}{2}\cos\theta + \frac{q^2}{gh}\left[\beta + m\left(hh_{xx} - h_x^2\right)\right], \tag{5.250}$$

with

$$\beta = \frac{(1+N)^2}{2N+1}, \tag{5.251}$$

$$m = \frac{(1+N)^2}{(3+2N)}. \tag{5.252}$$

Based on Eqs. (5.246) and (5.250), a generalized approach is proposed for S as

$$S = \frac{h^2}{2}\cos\theta + \frac{q^2}{gh}\left[\beta + \alpha h_x + f_{\mathrm{dump}} m\left(hh_{xx} - h_x^2\right)\right], \tag{5.253}$$

and the germane result for p_b is, based on Eqs. (5.243) and (5.249),

$$\frac{p_b}{\gamma} = h\cos\theta + \frac{q^2}{2gh^2}(1+N) f_{\mathrm{dump}}\left(hh_{xx} - h_x^2\right), \tag{5.254}$$

thereby accounting for the combined effects of streamwise turbulence, shock waves, wave breaking, and the velocity profile on the undular jump. Simulations based on Eqs. (5.253), (5.254) are plotted in Fig. 5.32d and compared with observations, resulting in excellent agreement. The friction factor was computed based on the N index from Chanson (1996) [see Eq. (5.176)]

$$f = 8\kappa^2 N^2, \tag{5.255}$$

where $\kappa = 0.41$, and $N = 1/7$ for this experimental test (Gotoh et al. 2005). Figure 5.32d demonstrates that the phase lag is resolved if the turbulent velocity profile is properly accounted for, and that the proposed model gives a fair estimation of centerline water depth and bottom pressure head.

5.4 Undular Weir Flow

Undular weir flows involve the transition from subcritical ($\mathsf{F} < 1$) to supercritical ($\mathsf{F} > 1$) flow states in the form of steady waves, typically if $H_o/L < 0.1$ (Chanson 1996; Montes 1998; Hager 1999), with H_o as the upstream energy head above the weir crest and L as the crest length. Flows over the broad-crested weir for $H_o/L < 0.5$ are usually modeled by the parallel-streamlined flow approach, with free surface undulations appearing on the weir crest for $H_o/L < 0.1$ invalidating this approach (Fig. 5.33). Contrary to the undular hydraulic jump, this flow type is fully 2D and Serre's theory is expected to apply under any operational head.

The undular flow over a horizontal, rough broad-crested weir is considered in Fig. 5.34 (Serre 1953; Montes 1986; Castro-Orgaz and Chanson 2011). Serre's Eqs. (5.214) and (5.215) were integrated numerically using the fourth-order Runge–Kutta method for a test case of Tison (1950) corresponding to $H_o/h_c = 1.626$. The boundary conditions used were the test data at the first wave trough, i.e., $h/h_c = 1.196$ and $h_x = 0$. The friction slope $\mathrm{d}E/\mathrm{d}x$ was determined using a Bazin roughness

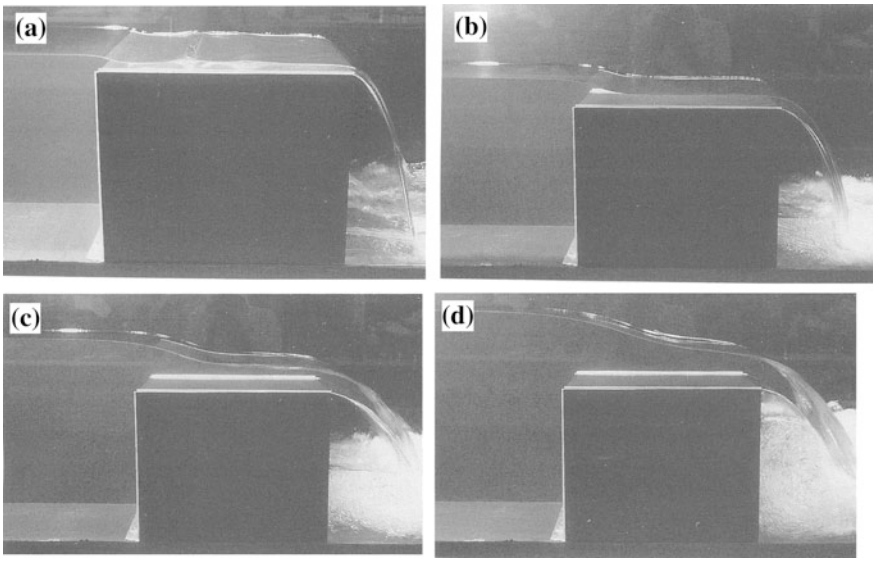

Fig. 5.33 Flow patterns in broad-crested weir flow for $H_o/L =$ **a** 0.06, **b** 0.13, **c** 0.27, **d** 0.39 (Hager 1999)

coefficient of 0.41 (Serre 1953). The results for $h = h(x)$ are compared with test data in Fig. 5.34b, resulting in excellent agreement both for the wave crests and troughs. Whereas the ideal fluid flow theory gives cnoidal waves and no transition from sub- ($\mathsf{F} < 1$) to supercritical ($\mathsf{F} > 1$) flow, the inclusion of the friction term allows for the establishment of transitional flow at the vicinity of the brink section. Moreover, the theoretical result correctly predicts the downstream boundary condition, corresponding to a free overfall.

Model test data for a horizontal broad-crested weir with a rounded upstream nose (Fig. 5.35a) of 0.10 m radius (Viherout 1973) are plotted in Fig. 5.35 for three different dimensionless upstream heads H_o/L. The comparison between Serre's theory and these data was conducted by solving the system of differential Eqs. (5.214) and (5.215) for the unknowns $h(x)$ and $E(x)$ with the fourth-order Runge–Kutta method. The boundary conditions were taken at the first experimental point of the free surface profile. The computational results are also included in Fig. 5.35, showing excellent agreement with observations. The first point that deserves consideration is that the free surface profile $h = h(x)$ of the broad-crested weir shows a considerable slope h_x and curvature h_{xx} for a wide range of operational heads. The free surface profile of broad-crested weir flows involves a cnoidal wave-type profile for $H_o/L < 0.1$ (Fig. 5.34). For $0.1 < H_o/L < 0.33$, the free surface corresponds to an incomplete cnoidal wave profile, as shown in Fig. 5.35, with only one inflexion point but no full waves being present. As $H_o/L \approx 0.5$, the free surface

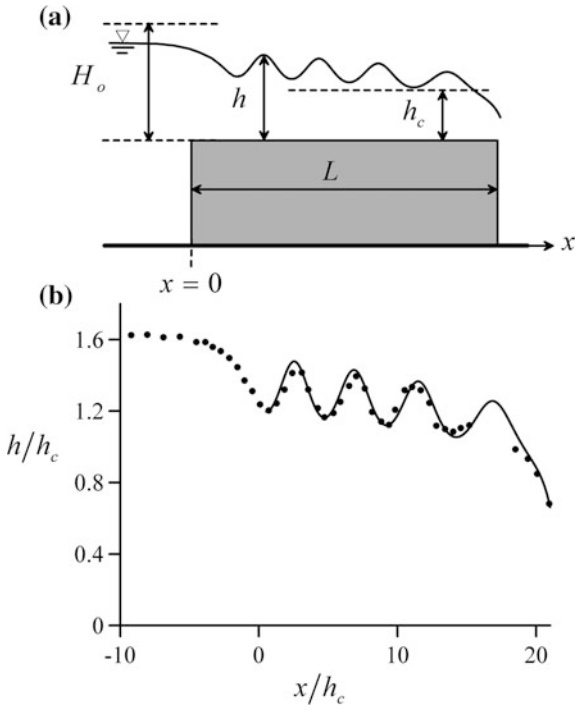

Fig. 5.34 Transition from $\mathsf{F} < 1$ to $\mathsf{F} > 1$: **a** Definition sketch, **b** undular weir-flow profile $h/h_c(x/h_c)$ for $H_o/L = 0.078$ from (—) Serre's theory, (●) experimental data (Serre 1953) (adapted from Castro-Orgaz and Chanson 2011) (the coordinate origin $x = 0$ is at the upstream weir edge)

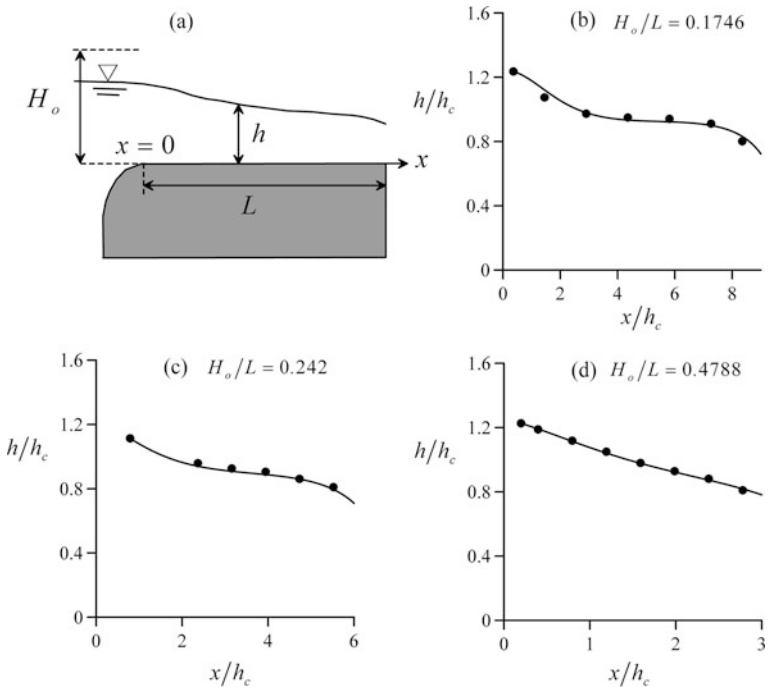

Fig. 5.35 Transition from F < 1 to F > 1: **a** Round-nosed broad-crested weir sketch, **b–d** $h/h_c(x/h_c)$ from (—) Serre's theory, (●) experimental data (Vierhout 1973) (adapted from Castro-Orgaz and Chanson 2011) (the coordinate origin $x = 0$ is at the upstream weir edge)

profile is almost a straight line sloping downward from the approach flow depth to the free overfall brink depth (Fig. 5.35d). Thus, broad-crested weir flows for $H_o/L < 0.1$ are governed by the cnoidal wave theory, associated with non-hydrostatic conditions and a marked wave-type free surface. For $H_o/L > 0.5$, the flow surface is almost a straight drawdown curve, associated also with non-hydrostatic flow conditions. In the interval of operational heads $0.1 < H_o/L < 0.33$, however, a short region of the crest length L is governed by quasi-parallel streamlined flow along which Bélanger's classical hydrostatic pressure assumption applies (Fig. 5.35b, c).

5.5 Hydraulic Jump

5.5.1 Submerged Hydraulic Jump

As the tailwater level increases downstream of a sluice gate, the free jet described in Chap. 3 may become submerged, resulting in the so-called submerged hydraulic jump (Henry 1950; Henderson 1966; Montes 1998) (Fig. 5.36). The submergence

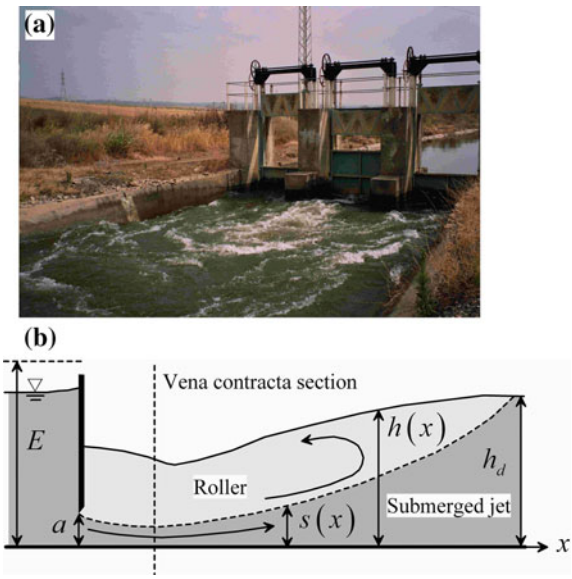

Fig. 5.36 Submerged hydraulic jump, **a** irrigation canal in Southern Spain (Image O. Castro-Orgaz), **b** definition sketch

effect on the drowned jet, emerging below the gate, is investigated by applying the Boussinesq-type equations for submerged flows developed in Chap. 3 (see Sect. 3.13.4). With h_d as the tailwater depth, the momentum is conserved along a submerged hydraulic jump (Castro-Orgaz and Hager 2014b). Assuming a linear distribution of streamline curvature, the submerged jet momentum equation is

$$S = \frac{h^2}{2} + \frac{q^2}{gs}\left(1 + \frac{ss_{xx} - s_x^2}{3}\right) = \frac{h_d^2}{2} + \frac{q^2}{gh_d}, \tag{5.256}$$

in which h is the flow depth and s the submerged jet thickness (Castro-Orgaz and Hager 2014b). Equation (5.256) is a generalization of Serre's theory for submerged flows.

To compute the submerged jet profile $s(x)$, the free surface profile $h(x)$ must be prescribed. The discharge q is estimated based on the conservation of the energy head between the upstream section and the vena contracta using $C_c = 0.61$ as

$$E = h_{\text{vena contracta}} + \frac{q^2}{2ga^2C_c^2}. \tag{5.257}$$

Integrating Eq. (5.256) using the fourth-order Runge–Kutta method with $s(0) = a$ for $E/a = 13$ and $h_d/a = 7.9$ results in Fig. 5.37a. The free surface profile was assumed to vary linearly, starting at the gate section with $h/a = 7.14$. The jet interface slope at $x = 0$ was found by iteration until the best agreement resulted for the jet profile. The theoretical jet profile agrees well with the measurements of Henry (1950), with small deviations only near the jump end. The theoretical

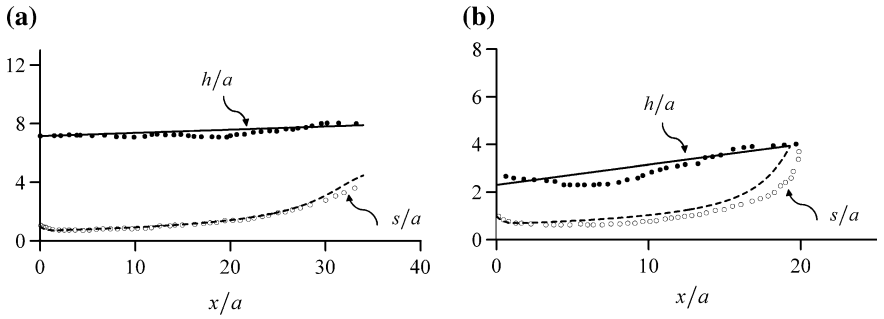

Fig. 5.37 Submerged hydraulic jump in the tailwater gate portion for the experimental conditions (E/a; h_d/a) **a** (13; 7.9), **b** (7.95; 4.0), with (—) assumed free surface profile $h/a(x/a)$, (- - -) computed submerged jet profile $s/a(x/a)$, (●) measured free surface profile (Henry 1950), (○) measured jet profile (Henry 1950) (adapted from Castro-Orgaz and Hager 2014b)

Eq. (5.256) predicts the rapid jet contraction near the gate at $x/a \approx 1$ followed by a long expanding portion toward the roller end. A less submerged hydraulic jump of $E/a = 7.95$ and $h_d/a = 4$ is considered in Fig. 5.37b. The theoretical jet prediction is in fair agreement with observations, with deviations due to the assumed free surface profile; again, the computation predicts the contraction–expansion features of the submerged flow well.

It is relevant to investigate the portion of the submerged free jet where streamline curvature effects are significant. The bottom pressure head of the submerged jet is given by (Castro-Orgaz and Hager 2014b) (see Sect. 3.13.4)

$$\frac{p_b}{\gamma} = h + \frac{q^2}{2gs^2}\left(ss_{xx} - s_x^2\right), \tag{5.258}$$

where s is the jet thickness. The ratio $p_b/(\gamma h)$ is plotted for the former submerged jumps in Fig. 5.38a, c, respectively, showing the non-hydrostatic pressure distribution along the contracted jet zone just past the gate, up to the vicinity of the vena contracta section. Shortly downstream from it, the flow is hydrostatic, with a weak departure near the toe of the jump.

The hydrostatic version of Eq. (5.256) used to compute $s(x)$ in classical hydraulic jumps is (Castro-Orgaz and Hager 2009)

$$S = \frac{h^2}{2} + \frac{q^2}{gs} = \frac{h_d^2}{2} + \frac{q^2}{gh_d}. \tag{5.259}$$

The results obtained using Eq. (3.259) are compared in Fig. 5.38b, c with the numerical solution of Eq. (5.256), showing deviations along the contracted reach and the expansion toe. In the central portion of the submerged jump, the flow is hydrostatic from a 1D view point. However, a full solution of the submerged jet requires resort to Eq. (5.256), given that boundary conditions are known at the gate

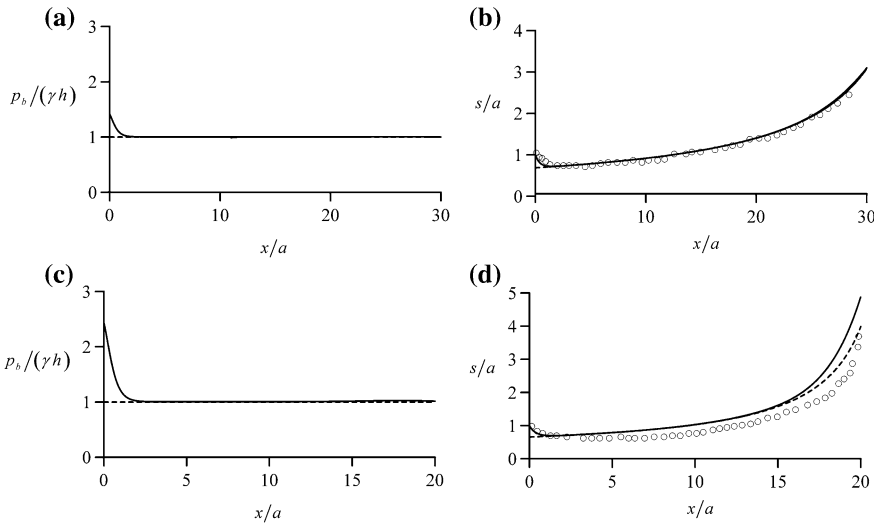

Fig. 5.38 Submerged hydraulic jump in the tailwater portion of a gate for (E/a; h_d/a) **a** (13; 7.9) with (—) ratio $p_b/(\gamma h)(x/a)$, **b** (13; 7.9) using the (—) non-hydrostatic and (- - -) hydrostatic approach for $s/(a)(x/a)$, **c** (7.95; 4.0) with (—) ratio $p_b/(\gamma h)(x/a)$, **d** (7.95; 4.0) using the (—) non-hydrostatic and (- - -) hydrostatic approach for $s/(a)(x/a)$; (○) measured jet profile (Henry 1950)

section, where the flow is non-hydrostatic, and at the jump toe, where the flow is weakly hydrostatic. These computations further support the physical relevance of the Boussinesq equations for submerged jets.

5.5.2 *Classical Hydraulic Jump*

Castro-Orgaz and Hager (2009) applied Eq. (5.259) to the classical hydraulic jump (Fig. 5.39), concluding that it is accurate and that consideration of Eq. (5.256) is not necessary. Thus, despite the classical hydraulic jump is a rapidly varied flow, it is essentially a hydrostatic flow from a 1D point of view. Note that the time-averaged pressure is quasi-hydrostatic, but the turbulent fluctuations are extremely large, so that they must be accounted for in designing energy dissipators. However, for computation of 1D flows, consideration of hydrostatic pressure conditions is sufficient. The rapidly varied phenomenon of the classical hydraulic

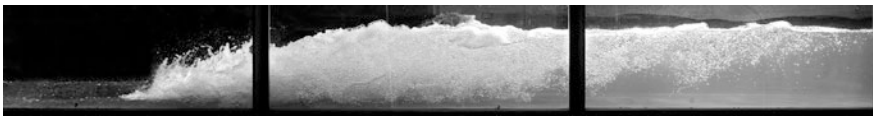

Fig. 5.39 Classical hydraulic jump (photograph VAW, ETH Zurich)

jump can be mainly explained in terms of the highly non-uniform turbulent velocity profile originating from roller flow above the submerged jet. Based on laboratory data, the Boussinesq velocity correction coefficient was found to compare well with the theoretical predictor implicit in Eq. (5.259)

$$\beta = \frac{h}{s}. \tag{5.260}$$

The coefficient β in classical hydraulic jumps can easily reach values of 2.5, given the highly non-uniform velocity profile. A detailed investigation into the non-uniform velocity profile features is given by Castro-Orgaz and Hager (2009). The effects of air entrainment and air detrainment, along with the non-hydrostatic pressure distribution due to air presence, are therein excluded, despite its obvious presence, as is also noted in Fig. 5.39.

5.6 Boussinesq's Original Theory for Non-hydrostatic Turbulent Open-Channel Flows

5.6.1 Introduction

Joseph Boussinesq's original book (Boussinesq 1877) is difficult to understand, given the hard mathematical developments, sometimes overlooking basic explanations, let alone his complicated descriptions. However, it is a masterpiece of hydraulics. The aim of this section is to present the original theory of Boussinesq for non-hydrostatic steady turbulent flows in the vertical plane. Original notation was followed as far as possible (Castro-Orgaz and Hager 2011d) to render the current portion of the text as a useful guide if the reader wishes to refer to Boussinesq's original treatise.[4]

5.6.2 Equations of Motion

Boussinesq (1877) started his analysis of steady turbulent flows in the vertical plane formulating the conservation equations for mass and momentum in the x- and z-directions of a Cartesian coordinate system inclined at angle i with the horizontal line as [see Eqs. (5.132) and (5.133)] (Fig. 5.40)

[4]The book of Joseph Boussinesq (1877). Essai sur la théorie des eaux courantes. *Mémoires* présentés par Divers Savants á l'Académie des Sciences, Paris 23(1), 1–608, can be downloaded from http://gallica.bnf.fr/ark:/12148/bpt6k56673076#. We strongly encourage the book readers to download it. It is a formidable source of mathematical developments and the origin of the ideas developed in this book.

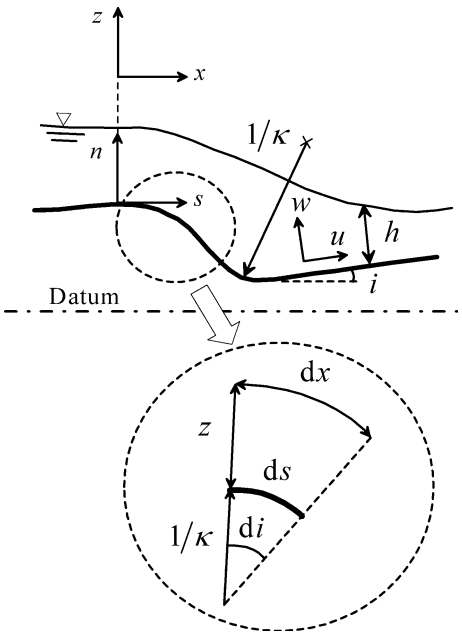

Fig. 5.40 Definition sketch of turbulent flows over curved bed following Boussinesq's original theory (The equations of motion are formulated in the (x, z) Cartesian coordinates, with z as the bed-normal coordinate and x the orthogonal coordinate to z. The (x, z) system is rotated at angle i with respect to the gravity direction, where i is the inclination of the bed curve with the horizontal line. Obviously, at each curvilinear coordinate s measured along the curved bed, there is a different system of reference, rotated at different angles i, with z as the local bed-normal direction. Boussinesq made an ingenious transformation of the x- to the s-curvilinear coordinate by assuming that the flow is shallow and therefore dx and ds are concentric arcs.)

$$\frac{\partial u}{\partial x} + \frac{\partial w}{\partial z} = 0, \tag{5.261}$$

$$u\frac{\partial u}{\partial x} + w\frac{\partial u}{\partial z} = g\sin i - \frac{1}{\rho}\frac{\partial p}{\partial x} + \frac{1}{\rho}\left(\frac{\partial \tau_{zx}}{\partial z} + \frac{\partial \sigma_x}{\partial x}\right), \tag{5.262}$$

$$u\frac{\partial w}{\partial x} + w\frac{\partial w}{\partial z} = -g\cos i - \frac{1}{\rho}\frac{\partial p}{\partial z} + \frac{1}{\rho}\left(\frac{\partial \tau_{zx}}{\partial x} + \frac{\partial \sigma_z}{\partial z}\right), \tag{5.263}$$

with p as the pressure, and (u, w) the velocity components in the (x, z)-directions. Boussinesq's original turbulent closure is given by the equations

$$\sigma_z = 2\varepsilon\frac{\partial w}{\partial z}, \tag{5.264}$$

$$\sigma_x = 2\varepsilon \frac{\partial u}{\partial x}, \tag{5.265}$$

$$\tau_{zx} = \varepsilon \left(\frac{\partial u}{\partial z} + \frac{\partial w}{\partial x} \right), \tag{5.266}$$

where $\varepsilon = \rho v_t$, with v_t as the eddy viscosity (Hager and Raemy 1997); and σ and τ denote normal and tangential turbulent stresses, as usual. Boussinesq adopted a depth-averaged value of $\varepsilon = \rho g A h u_o$, where ρ is the water density, g gravity acceleration, A a constant, h the flow depth, and u_o the near-bed velocity.

Comparing Eqs. (5.264)–(5.266) with Eqs. (5.149)–(5.151), it is noted that the turbulent kinetic energy k was not included in the original eddy viscosity turbulence closure; it is rather a modern addition (Rodi 1993; Hutter and Wang 2016).

Inserting Eqs. (5.265) and (5.266) into Eq. (5.262) yields

$$u \frac{\partial u}{\partial x} + w \frac{\partial u}{\partial z} = g \sin i - \frac{1}{\rho} \frac{\partial p}{\partial x} + \frac{1}{\rho} \left[\varepsilon \frac{\partial}{\partial z} \left(\frac{\partial u}{\partial z} + \frac{\partial w}{\partial x} \right) + 2\varepsilon \frac{\partial}{\partial x} \left(\frac{\partial u}{\partial x} \right) \right]. \tag{5.267}$$

Using the continuity Eq. (5.261)

$$u \frac{\partial u}{\partial x} + w \frac{\partial u}{\partial z} = g \sin i - \frac{1}{\rho} \frac{\partial p}{\partial x} + \frac{1}{\rho} \left[\varepsilon \frac{\partial^2 u}{\partial z^2} + \varepsilon \frac{\partial}{\partial z} \left(\frac{\partial w}{\partial x} \right) + 2\varepsilon \frac{\partial}{\partial x} \left(- \frac{\partial w}{\partial z} \right) \right], \tag{5.268}$$

or

$$u \frac{\partial u}{\partial x} + w \frac{\partial u}{\partial z} = g \sin i - \frac{1}{\rho} \frac{\partial p}{\partial x} + \frac{1}{\rho} \left[\varepsilon \frac{\partial^2 u}{\partial z^2} - \varepsilon \frac{\partial}{\partial x} \left(\frac{\partial w}{\partial z} \right) \right], \tag{5.269}$$

and using again the continuity equation, Eq. (5.269) takes the form

$$u \frac{\partial u}{\partial x} + w \frac{\partial u}{\partial z} = g \sin i - \frac{1}{\rho} \frac{\partial p}{\partial x} + \frac{\varepsilon}{\rho} \left(\frac{\partial^2 u}{\partial z^2} + \frac{\partial^2 u}{\partial x^2} \right). \tag{5.270}$$

The convective acceleration in Eq. (5.270) is transformed using the continuity equation as follows

$$u \frac{\partial u}{\partial x} + w \frac{\partial u}{\partial z} = -u \frac{\partial w}{\partial z} + w \frac{\partial u}{\partial z} = -u^2 \frac{w \frac{\partial u}{\partial z} - u \frac{\partial w}{\partial z}}{u^2} = -u^2 \frac{\partial}{\partial z} \left(\frac{w}{u} \right). \tag{5.271}$$

Inserting Eq. (5.271) into Eq. (5.270) produces

$$-u^2\frac{\partial}{\partial z}\left(\frac{w}{u}\right)=g\sin i-\frac{1}{\rho}\frac{\partial p}{\partial x}+\frac{\varepsilon}{\rho}\left(\frac{\partial^2 u}{\partial z^2}+\frac{\partial^2 u}{\partial x^2}\right). \tag{5.272}$$

Assuming that the variation of u with x is small as compared to its variation with z, Eq. (5.272) simplifies to

$$\frac{\varepsilon}{\rho}\frac{\partial^2 u}{\partial z^2}+g\sin i-\frac{1}{\rho}\frac{\partial p}{\partial x}=-u^2\frac{\partial}{\partial z}\left(\frac{w}{u}\right)-\underbrace{\mathrm{O}\left(\frac{\varepsilon}{\rho}\frac{\partial^2 u}{\partial x^2}\right)}_{\text{negligible}}. \tag{5.273}$$

A similar derivation is performed using the z-momentum equation as follows. Inserting Eqs. (2.264) and (2.266) into Eq. (5.263) gives

$$u\frac{\partial w}{\partial x}+w\frac{\partial w}{\partial z}=-g\cos i-\frac{1}{\rho}\frac{\partial p}{\partial z}+\frac{1}{\rho}\left[\varepsilon\frac{\partial}{\partial x}\left(\frac{\partial u}{\partial z}+\frac{\partial w}{\partial x}\right)+2\varepsilon\frac{\partial}{\partial z}\left(\frac{\partial w}{\partial z}\right)\right]. \tag{5.274}$$

Using the continuity Eq. (5.261)

$$u\frac{\partial w}{\partial x}+w\frac{\partial w}{\partial z}=-g\cos i-\frac{1}{\rho}\frac{\partial p}{\partial z}+\frac{1}{\rho}\left[\varepsilon\frac{\partial}{\partial x}\left(\frac{\partial u}{\partial z}\right)+\varepsilon\frac{\partial^2 w}{\partial x^2}+2\varepsilon\frac{\partial}{\partial z}\left(-\frac{\partial u}{\partial x}\right)\right], \tag{5.275}$$

or

$$u\frac{\partial w}{\partial x}+w\frac{\partial w}{\partial z}=-g\cos i-\frac{1}{\rho}\frac{\partial p}{\partial z}+\frac{1}{\rho}\left[\varepsilon\frac{\partial}{\partial z}\left(-\frac{\partial u}{\partial x}\right)+\varepsilon\frac{\partial^2 w}{\partial x^2}\right], \tag{5.276}$$

and using again the continuity equation gives

$$u\frac{\partial w}{\partial x}+w\frac{\partial w}{\partial z}=-g\cos i-\frac{1}{\rho}\frac{\partial p}{\partial z}+\frac{\varepsilon}{\rho}\left(\frac{\partial^2 w}{\partial z^2}+\frac{\partial^2 w}{\partial x^2}\right). \tag{5.277}$$

The convective acceleration term is transformed as follows

$$u\frac{\partial w}{\partial x}+w\frac{\partial w}{\partial z}=u\frac{\partial w}{\partial x}-w\frac{\partial u}{\partial x}=u^2\frac{u\frac{\partial w}{\partial x}-w\frac{\partial u}{\partial x}}{u^2}=u^2\frac{\partial}{\partial x}\left(\frac{w}{u}\right). \tag{5.278}$$

Using this identity in Eq. (5.277) produces

$$u^2\frac{\partial}{\partial x}\left(\frac{w}{u}\right)=-g\cos i-\frac{1}{\rho}\frac{\partial p}{\partial z}+\frac{\varepsilon}{\rho}\left(\frac{\partial^2 w}{\partial z^2}+\frac{\partial^2 w}{\partial x^2}\right). \tag{5.279}$$

Neglecting the Laplacian $\nabla^2 w$, following Boussinesq, further simplifies Eq. (5.279) to

$$u^2 \frac{\partial}{\partial x}\left(\frac{w}{u}\right) = -g\cos i - \frac{1}{\rho}\frac{\partial p}{\partial z} + \underbrace{O\left(\frac{\varepsilon}{\rho}\nabla^2 w\right)}_{\text{negligible}}. \tag{5.280}$$

Using the depth-averaged value for ε, the fluid flow equations used by Boussinesq are

$$(5.261) \rightarrow \quad \frac{\partial u}{\partial x} + \frac{\partial w}{\partial z} = 0, \tag{5.281}$$

$$(5.273) \rightarrow \quad A h u_o \frac{\partial^2 u}{\partial z^2} + \sin i - \frac{1}{\rho g}\frac{\partial p}{\partial x} = -\frac{u^2}{g}\frac{\partial}{\partial z}\left(\frac{w}{u}\right), \tag{5.282}$$

$$(5.279) \rightarrow \quad \frac{1}{\rho g}\frac{\partial p}{\partial z} = -\cos i - \frac{u^2}{g}\frac{\partial}{\partial x}\left(\frac{w}{u}\right). \tag{5.283}$$

Equations (5.282) and (5.283) therefore depend on the local streamline inclination w/u. These equations are based on a Cartesian coordinate system (x, z) inclined at angle i, differing for each curvilinear coordinate s measured along a wavy bottom profile (Fig. 5.40).

A rigorous procedure to express the governing equations in curvilinear coordinates involves the Jacobian matrix for the coordinate transformations (Dressler 1978). However, Boussinesq adopted a simplified but ingenious approximation. He assumed that between the sections s and $s + \mathrm{d}s$, involving a variation of the bottom profile inclination $\mathrm{d}i$, $\mathrm{d}x$ at distance z from the bed is a portion of a concentric arc (see inset of Fig. 5.40), so that from basic geometry

$$\mathrm{d}x = \left(\frac{1}{\kappa} + z\right)\mathrm{d}i = \mathrm{d}s + z\mathrm{d}i = \mathrm{d}s\left(1 + z\frac{\mathrm{d}i}{\mathrm{d}s}\right). \tag{5.284}$$

Here, $\kappa = \mathrm{d}i/\mathrm{d}s$ is the bottom curvature of the arc formed between sections s and $s + \mathrm{d}s$. Therefore, based on Eq. (5.284), the coordinate transformation from Cartesian to curvilinear coordinates is symbolically expressed as

$$\frac{\partial}{\partial x}(\cdot) = \left(1 + \frac{\mathrm{d}i}{\mathrm{d}s}z\right)^{-1}\frac{\partial}{\partial s}(\cdot) \approx \left(1 - \frac{\mathrm{d}i}{\mathrm{d}s}z\right)\frac{\partial}{\partial s}(\cdot), \tag{5.285}$$

which assumes that $|\mathrm{d}i/\mathrm{d}s|z \ll 1$. Using the symbolic operator given by Eq. (5.285) in Eq. (5.281) produces

$$\left(1 - \frac{\mathrm{d}i}{\mathrm{d}s}z\right)\frac{\partial u}{\partial s} + \frac{\partial w}{\partial z} = 0. \tag{5.286}$$

Boussinesq consequently assumed that the flow is shallow,

$$\left(1 - \frac{\mathrm{d}i}{\mathrm{d}s}z\right) \approx 1, \tag{5.287}$$

implying that the curvature of the bottom profile must be small. Using this approximation, the operator in Eq. (5.285) reduces to

$$\frac{\partial}{\partial x}(\cdot) \approx \frac{\partial}{\partial s}(\cdot). \tag{5.288}$$

Boussinesq thus simplified Eqs. (5.281)–(5.283) to

$$\frac{\partial u}{\partial s} + \frac{\partial w}{\partial z} = 0, \tag{5.289}$$

$$Ahu_o\frac{\partial^2 u}{\partial z^2} + \sin i - \frac{1}{\rho g}\frac{\partial p}{\partial s} = -\frac{u^2}{g}\frac{\partial}{\partial z}\left(\frac{w}{u}\right), \tag{5.290}$$

$$\frac{1}{\rho g}\frac{\partial p}{\partial z} = -\cos i - \frac{u^2}{g}\frac{\partial}{\partial s}\left(\frac{w}{u}\right). \tag{5.291}$$

5.6.3 Turbulent Velocity Profile

To solve the free surface flow problem by successive approximations, Boussinesq first determined the streamline inclination $\lambda = w/u$. He expressed Eq. (5.289) as

$$\frac{\partial u}{\partial s} + \frac{\partial}{\partial z}(\lambda u) = 0, \tag{5.292}$$

and adopted as first approximation $u(s, z) = U(s) = q/h(s)$, where q is the unit discharge. Inserting this result into Eq. (5.292), he found

$$\frac{\partial U}{\partial s} + U\frac{\partial \lambda}{\partial z} = 0. \tag{5.293}$$

Boussinesq then produced an approximate integration of Eq. (5.293) as follows

$$\lambda = -\frac{1}{U}\int_0^z \frac{\partial U}{\partial s}\mathrm{d}z' = -\frac{1}{U}\frac{\partial U}{\partial s}z = \frac{z}{h}\frac{\mathrm{d}h}{\mathrm{d}s}. \tag{5.294}$$

Obviously, Eq. (5.294) is a valid approximation for a flat bottom, but, irrealistic if it is wavy, given that w/u experiences variations in response to the variable inclination $i = i(s)$. Thus, Boussinesq proposed as spatial gradient of w/u the relation

$$\frac{\partial}{\partial s}\left(\frac{w}{u}\right) = \frac{\partial \lambda}{\partial s} - \frac{\mathrm{d}i}{\mathrm{d}s}. \tag{5.295}$$

Equation (5.295) is better understood by considering the more general integral to Eq. (5.293)

$$\frac{w}{u} = -\frac{1}{U}\frac{\partial U}{\partial s}z + C(s), \tag{5.296}$$

where $C(s)$ is an arbitrary function of s. Differentiation of Eq. (5.296) with respect to s yields

$$\frac{\partial}{\partial s}\left(\frac{w}{u}\right) = -\frac{\partial}{\partial s}\left(\frac{1}{U}\frac{\partial U}{\partial s}\right)z + \frac{\partial C}{\partial s}. \tag{5.297}$$

Noting that at the bottom, $z = 0$, the streamline curvature $\partial(w/u)/\partial s$ equals the bottom curvature $-\mathrm{d}i/\mathrm{d}s$, Eq. (5.297) transforms into Eq. (5.295). Using Eq. (5.295) in Eq. (5.291), the pressure distribution obtained by Boussinesq in the z-direction is

$$\frac{p}{\rho g} = (h - z)\cos i + \int_z^h \frac{u^2}{g}\left(\frac{\partial \lambda}{\partial s} - \frac{\mathrm{d}i}{\mathrm{d}s}\right)\mathrm{d}z'. \tag{5.298}$$

Based on Eq. (5.290), Boussinesq sought the turbulent velocity profile, but the gradient $\partial p/\partial s$ had first to be quantified. To this end, Boussinesq differentiated Eq. (5.298) with respect to s and found

$$\frac{1}{\rho g}\frac{\partial p}{\partial s} = \frac{\mathrm{d}h}{\mathrm{d}s}\cos i - (h - z)\sin i\frac{\mathrm{d}i}{\mathrm{d}s} + \frac{\mathrm{d}}{\mathrm{d}s}\int_z^h \frac{u^2}{g}\left(\frac{\partial \lambda}{\partial s} - \frac{\mathrm{d}i}{\mathrm{d}s}\right)\mathrm{d}z'. \tag{5.299}$$

Inserting Eq. (5.299) into Eq. (5.290) produces

$$Ahu_o\frac{\partial^2 u}{\partial z^2}+\sin i=\frac{\mathrm{d}h}{\mathrm{d}s}\cos i-(h-z)\sin i\frac{\mathrm{d}i}{\mathrm{d}s}+\frac{\mathrm{d}}{\mathrm{d}s}\int_z^h\frac{u^2}{g}\left(\frac{\partial\lambda}{\partial s}-\frac{\mathrm{d}i}{\mathrm{d}s}\right)\mathrm{d}z'-\frac{u^2}{g}\frac{\partial\lambda}{\partial z},\tag{5.300}$$

or

$$Ahu_o\frac{\partial^2 u}{\partial z^2}+\sin i-\cos i\frac{\mathrm{d}h}{\mathrm{d}s}=-(h-z)\frac{\mathrm{d}i}{\mathrm{d}s}\sin i-\frac{u_o^2}{gh}\mu,\tag{5.301}$$

with the auxiliary variable μ defined by Boussinesq as

$$\mu=h\frac{\partial\lambda}{\partial z}\left(\frac{u}{u_o}\right)^2-\frac{h}{u_o^2}\frac{\mathrm{d}}{\mathrm{d}s}\left[\int_z^h u_o^2\frac{u^2}{u_o^2}\left(\frac{\partial\lambda}{\partial s}-\frac{\mathrm{d}i}{\mathrm{d}s}\right)\mathrm{d}z'\right].\tag{5.302}$$

Algebraic manipulation of Eq. (5.301) permits to write it in the alternative form

$$\begin{aligned}&Ahu_o\frac{\partial^2 u}{\partial z^2}+\sin i-\cos i\frac{\mathrm{d}h}{\mathrm{d}s}+\frac{h}{2}\frac{\mathrm{d}i}{\mathrm{d}s}\sin i+\frac{u_o^2}{gh}\int_0^h\mu\frac{\mathrm{d}z}{h}\\&=-\left(\frac{h}{2}-z\right)\frac{\mathrm{d}i}{\mathrm{d}s}\sin i-\frac{u_o^2}{gh}\left(\mu-\int_0^h\mu\frac{\mathrm{d}z}{h}\right).\end{aligned}\tag{5.303}$$

Integrating Eq. (5.303) from an arbitrary elevation z to $z = h$, assuming that $\partial u/\partial z = 0$ at the free surface ($z = h$) results in

$$\begin{aligned}&Ahu_o\frac{\partial u}{\partial z}-\left(\sin i-\cos i\frac{\mathrm{d}h}{\mathrm{d}s}+\frac{h}{2}\frac{\mathrm{d}i}{\mathrm{d}s}\sin i+\frac{u_o^2}{gh}\int_0^h\mu\frac{\mathrm{d}z}{h}\right)(h-z)\\&=-\frac{1}{2}\left(hz-z^2\right)\frac{\mathrm{d}i}{\mathrm{d}s}\sin i+\frac{u_o^2}{gh}\int_z^h\left(\mu-\int_0^h\mu\frac{\mathrm{d}z}{h}\right)\mathrm{d}z'.\end{aligned}\tag{5.304}$$

Note that for $z = 0$, Boussinesq defined a bed-shear stress coefficient B, expressed in terms of the near-bottom velocity u_o, based on the identity

$$\left(Ahu_o\frac{\partial u}{\partial z}\right)_{z=0}=Bu_o^2.\tag{5.305}$$

Therefore, evaluating Eq. (5.304) at $z = 0$ yields

$$Bu_o^2 = \left(\sin i - \cos i \frac{\mathrm{d}h}{\mathrm{d}s} + \frac{h}{2} \frac{\mathrm{d}i}{\mathrm{d}s} \sin i + \frac{u_o^2}{gh} \int_0^h \mu \frac{\mathrm{d}z}{h} \right) h. \tag{5.306}$$

Note that the last integral in Eq. (5.304) is exactly zero if the lower limit is taken as $z = 0$. Inserting Eq. (5.306) into Eq. (5.304) produces,

$$Ahu_o \frac{\mathrm{d}u}{\mathrm{d}z} - \frac{1}{h} Bu_o^2 (h - z) = -\frac{1}{2} \left(hz - z^2 \right) \frac{\mathrm{d}i}{\mathrm{d}s} \sin i + \frac{u_o^2}{gh} \int_z^h \left(\mu - \int_0^h \mu \frac{\mathrm{d}z}{h} \right) \mathrm{d}z'. \tag{5.307}$$

Dividing by Ahu_o^2, the differential equation describing the turbulent velocity profile is

$$\frac{1}{u_o} \frac{\mathrm{d}u}{\mathrm{d}z} - \frac{B}{Ah^2} (h - z) = -\frac{1}{2Ahu_o^2} \left(hz - z^2 \right) \frac{\mathrm{d}i}{\mathrm{d}s} \sin i + \frac{1}{gAh^2} \int_z^h \left(\mu - \int_0^h \mu \frac{\mathrm{d}z}{h} \right) \mathrm{d}z', \tag{5.308}$$

or

$$\frac{1}{u_o} \frac{\mathrm{d}u}{\mathrm{d}z} = \frac{B}{A} \left(\frac{1}{h} - \frac{z}{h^2} \right) - \frac{h}{2Au_o^2} \left(\frac{z}{h} - \frac{z^2}{h^2} \right) \frac{\mathrm{d}i}{\mathrm{d}s} \sin i + \frac{1}{gAh} \int_z^h \left(\mu - \int_0^h \mu \frac{\mathrm{d}z}{h} \right) \frac{\mathrm{d}z'}{h}. \tag{5.309}$$

Integrating from $z = 0$ to $z = h$, noting that at $z = 0$ the slip velocity is $u = u_o$, the turbulent velocity profile is given by Boussinesq as

$$\frac{u}{u_o} = 1 + \frac{B}{A} \left(\frac{z}{h} - \frac{1}{2} \frac{z^2}{h^2} \right) - \frac{h^2}{4Au_o^2} \left(\frac{z^2}{h^2} - \frac{2}{3} \frac{z^3}{h^3} \right) \frac{\mathrm{d}i}{\mathrm{d}s} \sin i + \frac{1}{Ag} \int_0^z \frac{\mathrm{d}z'}{h} \int_z^h \left(\mu - \int_0^h \mu \frac{\mathrm{d}z}{h} \right) \frac{\mathrm{d}z'}{h}. \tag{5.310}$$

For uniform open-channel flows, for which $\mathrm{d}i/\mathrm{d}s = 0$ and $\mu = 0$, Eq. (5.310) is simplified to (Hager and Raemy 1997)

$$\frac{u}{u_o} = 1 + \frac{B}{A}\left(\frac{z}{h} - \frac{1}{2}\frac{z^2}{h^2}\right). \tag{5.311}$$

Boussinesq (1877) produced an approximate solution of Eq. (5.310) as follows: From Eq. (5.294) follow the identities

$$\frac{\partial \lambda}{\partial z} = \frac{1}{h}\frac{\mathrm{d}h}{\mathrm{d}s}, \tag{5.312}$$

and

$$\frac{\partial \lambda}{\partial s} = z\frac{\partial}{\partial s}\left(\frac{1}{h}\frac{\mathrm{d}h}{\mathrm{d}s}\right) = z\left[\frac{1}{h}\frac{\mathrm{d}^2 h}{\mathrm{d}s^2} - \frac{1}{h^2}\left(\frac{\mathrm{d}h}{\mathrm{d}s}\right)^2\right] \approx \frac{z}{h}\frac{\mathrm{d}^2 h}{\mathrm{d}s^2}. \tag{5.313}$$

To evaluate μ using Eq. (5.302), one deduces

$$\mu = \underbrace{h\frac{\partial \lambda}{\partial z}\left(\frac{u}{u_o}\right)^2}_{\text{term I}} \underbrace{- \frac{h}{u_o^2}\frac{\mathrm{d}}{\mathrm{d}s}\left[\int_z^h u_o^2 \frac{u^2}{u_o^2}\left(\frac{\partial \lambda}{\partial s} - \frac{\mathrm{d}i}{\mathrm{d}s}\right)\mathrm{d}z'\right]}_{\text{term II}}. \tag{5.314}$$

Term I is computed by using Eq. (5.311) to estimate u/u_o, resulting in

$$\begin{aligned} h \underbrace{\frac{\partial \lambda}{\partial z}}_{\text{Eq. (5.312)}} \underbrace{\left(\frac{u}{u_o}\right)^2}_{\text{Eq. (5.311)}} &= \frac{\mathrm{d}h}{\mathrm{d}s}\left[1 + \frac{B}{A}\left(\frac{z}{h} - \frac{1}{2}\frac{z^2}{h^2}\right)\right]^2 \\ &= \frac{\mathrm{d}h}{\mathrm{d}s}\left[1 + \frac{2B}{A}\left(\frac{z}{h} - \frac{1}{2}\frac{z^2}{h^2}\right) + \frac{B^2}{A^2}\left(\frac{z^2}{h^2} + \frac{1}{4}\frac{z^4}{h^4} - \frac{z^3}{h^3}\right)\right]. \end{aligned} \tag{5.315}$$

Term II is computed using Eq. (5.313), and approximating u by U inside the integral, resulting in

$$\begin{aligned} -\frac{h}{u_o^2}\frac{\mathrm{d}}{\mathrm{d}s}\left[\int_z^h u^2\left(\frac{\partial \lambda}{\partial s} - \frac{\mathrm{d}i}{\mathrm{d}s}\right)\mathrm{d}z'\right] &\approx -\frac{h}{u_o^2}\frac{\mathrm{d}}{\mathrm{d}s}\left[\int_z^h U^2\left(\frac{z}{h}\frac{\mathrm{d}^2 h}{\mathrm{d}s^2} - \frac{\mathrm{d}i}{\mathrm{d}s}\right)\mathrm{d}z'\right] \\ &= -\frac{h}{u_o^2}\frac{\mathrm{d}}{\mathrm{d}s}\left[U^2\left\{\frac{1}{h}\frac{\mathrm{d}^2 h}{\mathrm{d}s^2}\left(\frac{h^2 - z^2}{2}\right) - \frac{\mathrm{d}i}{\mathrm{d}s}(h - z)\right\}\right] \\ &= -\frac{h}{u_o^2}\frac{\mathrm{d}}{\mathrm{d}s}\left[U^2\left\{\frac{h}{2}\frac{\mathrm{d}^2 h}{\mathrm{d}s^2}\left(1 - \frac{z^2}{h^2}\right) - h\frac{\mathrm{d}i}{\mathrm{d}s}\left(1 - \frac{z}{h}\right)\right\}\right]. \end{aligned} \tag{5.316}$$

An additional approximation introduced by Boussinesq involved the computation of the derivative d()/ds in Eq. (5.316). He assumed that the main contributions originate from the spatial variations of $\mathrm{d}^2h/\mathrm{d}s^2$ and $\mathrm{d}^2i/\mathrm{d}s^2$. Thus, Eq. (5.316) is simplified to

$$-\frac{h}{u_o^2}\frac{\mathrm{d}}{\mathrm{d}s}\left[\int_z^h u^2\left(\frac{\partial\lambda}{\partial s}-\frac{\mathrm{d}i}{\mathrm{d}s}\right)\mathrm{d}z'\right]\approx-\frac{h^2U^2}{u_o^2}\left[\frac{1}{2}\frac{\mathrm{d}^3h}{\mathrm{d}s^3}\left(1-\frac{z^2}{h^2}\right)-\frac{\mathrm{d}^2i}{\mathrm{d}s^2}\left(1-\frac{z}{h}\right)\right]. \tag{5.317}$$

By coupling Eqs. (5.315) and (5.317), μ is estimated as

$$\begin{aligned}\mu=&\frac{\mathrm{d}h}{\mathrm{d}s}\left[1+\frac{2B}{A}\left(\frac{z}{h}-\frac{1}{2}\frac{z^2}{h^2}\right)+\frac{B^2}{A^2}\left(\frac{z^2}{h^2}+\frac{1}{4}\frac{z^4}{h^4}-\frac{z^3}{h^3}\right)\right]\\&-\frac{h^2U^2}{u_o^2}\left[\frac{1}{2}\frac{\mathrm{d}^3h}{\mathrm{d}s^3}\left(1-\frac{z^2}{h^2}\right)-\frac{\mathrm{d}^2i}{\mathrm{d}s^2}\left(1-\frac{z}{h}\right)\right].\end{aligned} \tag{5.318}$$

Next, by integrating Eq. (5.318) across the flow depth h, the average value of μ is obtained as

$$\begin{aligned}\bar{\mu}=\int_0^h\mu\frac{\mathrm{d}z}{h}=&\frac{\mathrm{d}h}{\mathrm{d}s}\left[1+\frac{2B}{A}\left(\frac{1}{2}-\frac{1}{6}\right)+\frac{B^2}{A^2}\left(\frac{1}{3}+\frac{1}{20}-\frac{1}{4}\right)\right]\\&-\frac{h^2U^2}{u_o^2}\left[\frac{1}{2}\frac{\mathrm{d}^3h}{\mathrm{d}s^3}\left(1-\frac{1}{3}\right)-\frac{\mathrm{d}^2i}{\mathrm{d}s^2}\left(1-\frac{1}{2}\right)\right]\\=&\frac{\mathrm{d}h}{\mathrm{d}s}\left(1+\frac{2B}{3A}+\frac{2B^2}{15A^2}\right)-\frac{h^2U^2}{u_o^2}\left[\frac{1}{3}\frac{\mathrm{d}^3h}{\mathrm{d}s^3}-\frac{1}{2}\frac{\mathrm{d}^2i}{\mathrm{d}s^2}\right].\end{aligned} \tag{5.319}$$

The deviation of μ from its depth-averaged value, is, thus, subtracting Eq. (5.319) from Eq. (5.318),

$$\begin{aligned}\mu-\bar{\mu}=&\frac{\mathrm{d}h}{\mathrm{d}s}\left[\frac{2B}{A}\left(\frac{z}{h}-\frac{1}{2}\frac{z^2}{h^2}-\frac{1}{3}\right)+\frac{B^2}{A^2}\left(\frac{z^2}{h^2}+\frac{1}{4}\frac{z^4}{h^4}-\frac{z^3}{h^3}-\frac{2}{15}\right)\right]\\&-\frac{h^2U^2}{u_o^2}\left[\frac{1}{2}\frac{\mathrm{d}^3h}{\mathrm{d}s^3}\left(1-\frac{z^2}{h^2}-\frac{2}{3}\right)-\frac{\mathrm{d}^2i}{\mathrm{d}s^2}\left(1-\frac{z}{h}-\frac{1}{2}\right)\right].\end{aligned} \tag{5.320}$$

The following integral is computed using Eq. (5.320)

$$I=\int_{\varsigma}^{1}(\mu-\bar{\mu})\mathrm{d}\varsigma'=\frac{\mathrm{d}h}{\mathrm{d}s}\left[\frac{2B}{A}\left(\frac{1-\varsigma^2}{2}-\frac{1-\varsigma^3}{6}-\frac{1-\varsigma}{3}\right)\right.$$
$$\left.+\frac{B^2}{A^2}\left(\frac{1-\varsigma^3}{3}+\frac{1-\varsigma^5}{20}-\frac{1-\varsigma^4}{4}-2\frac{1-\varsigma}{15}\right)\right]$$
$$-\frac{h^2U^2}{u_o^2}\left[\frac{1}{2}\frac{\mathrm{d}^3h}{\mathrm{d}s^3}\left(1-\varsigma-\frac{1-\varsigma^3}{3}-2\frac{1-\varsigma}{3}\right)\right.$$
$$\left.-\frac{\mathrm{d}^2i}{\mathrm{d}s^2}\left(1-\varsigma-\frac{1-\varsigma^2}{2}-\frac{1-\varsigma}{2}\right)\right],\quad \varsigma=\frac{z}{h}, \tag{5.321}$$

and the integral of Eq. (5.321) is computed as

$$F=\int_{0}^{\varsigma}I\mathrm{d}\varsigma'=\frac{\mathrm{d}h}{\mathrm{d}s}\left[\frac{2B}{A}\left(\frac{\varsigma}{2}-\frac{\varsigma^3}{6}-\frac{\varsigma}{6}+\frac{\varsigma^4}{24}-\frac{\varsigma}{3}+\frac{\varsigma^2}{6}\right)\right.$$
$$\left.+\frac{B^2}{A^2}\left(\frac{\varsigma}{3}-\frac{\varsigma^4}{12}+\frac{\varsigma}{20}-\frac{\varsigma^6}{120}-\frac{\varsigma}{4}+\frac{\varsigma^5}{20}-\frac{2\varsigma}{15}+\frac{\varsigma^2}{15}\right)\right]$$
$$-\frac{h^2U^2}{u_o^2}\left[\frac{1}{2}\frac{\mathrm{d}^3h}{\mathrm{d}s^3}\left(\varsigma-\frac{\varsigma^2}{2}-\frac{\varsigma}{3}+\frac{\varsigma^4}{12}-\frac{2\varsigma}{3}+\frac{\varsigma^2}{3}\right)\right.$$
$$\left.-\frac{\mathrm{d}^2i}{\mathrm{d}s^2}\left(\varsigma-\frac{\varsigma^2}{2}-\frac{\varsigma}{2}+\frac{\varsigma^3}{6}-\frac{\varsigma}{2}+\frac{\varsigma^2}{4}\right)\right]. \tag{5.322}$$

After collecting terms, Eq. (5.322) is written in the simplified form

$$F=\frac{\mathrm{d}h}{\mathrm{d}s}\frac{B}{3A}\left[\left(1+\frac{1}{5}\frac{B}{A}\right)\varsigma^2-\varsigma^3+\frac{1}{4}\left(1-\frac{B}{A}\right)\varsigma^4+\frac{3}{20}\frac{B}{A}\left(\varsigma^5-\frac{\varsigma^6}{6}\right)\right]$$
$$+\frac{h^2U^2}{4u_o^2}\left[\frac{1}{3}\frac{\mathrm{d}^3h}{\mathrm{d}s^3}\left(\varsigma^2-\frac{\varsigma^4}{2}\right)-\frac{\mathrm{d}^2i}{\mathrm{d}s^2}\left(\varsigma^2-\frac{2}{3}\varsigma^3\right)\right], \tag{5.323}$$

originally due to Boussinesq. Inserting Eq. (5.323) into Eq. (5.310), the turbulent velocity profile is obtained as

$$\frac{u}{u_o}=1+\frac{B}{A}\left(\frac{z}{h}-\frac{1}{2}\frac{z^2}{h^2}\right)$$
$$+\frac{1}{Ag}\frac{\mathrm{d}h}{\mathrm{d}s}\frac{B}{3A}\left[\left(1+\frac{B}{5A}\right)\frac{z^2}{h^2}-\frac{z^3}{h^3}+\frac{1}{4}\left(1-\frac{B}{A}\right)\frac{z^4}{h^4}+\frac{3}{20}\frac{B}{A}\left(\frac{z^5}{h^5}-\frac{1}{6}\frac{z^6}{h^6}\right)\right]$$
$$-\frac{h^2}{4Au_o^2}\left(\frac{z^2}{h^2}-\frac{2}{3}\frac{z^3}{h^3}\right)\frac{\mathrm{d}i}{\mathrm{d}s}\sin i$$
$$+\frac{U^2h^2}{4Agu_o^2}\left[\frac{1}{3}\frac{\mathrm{d}^3h}{\mathrm{d}s^3}\left(\frac{z^2}{h^2}-\frac{1}{2}\frac{z^4}{h^4}\right)-\frac{\mathrm{d}^2i}{\mathrm{d}s^2}\left(\frac{z^2}{h^2}-\frac{2}{3}\frac{z^3}{h^3}\right)\right]. \tag{5.324}$$

This is an approximation for the turbulent velocity profile by accounting for bottom friction B, the depth-averaged shear stress coefficient A, and for the non-hydrostatic pressure. Furthermore, for $z = 0$, one has $u = u_o$ as slip velocity. Boussinesq denoted u_o as the "near-bed velocity," recognizing that at the wall one should have exactly $u = 0$. However, a certain degree of slip is accepted for depth-averaged flow modeling of open-channel flows (Steffler and Jin 1993), so that Eq. (5.324) deserves recognition not only for its historical value, but also for the practical relevance of Boussinesq's ideas.

5.6.4 Differential Equation Describing Water Surface Profiles

The streamwise momentum equation is given by Eq. (5.306). To obtain a closed-form differential equation to solve for $h = h(s)$, the unknown term Bu_o^2 needs to be estimated. Integrating Eq. (5.324) across the flow depth, Boussinesq obtained as the mean flow velocity U

$$\begin{aligned}\frac{U}{u_o} &= \int_0^1 \frac{u}{u_o}\mathrm{d}\varsigma = 1 + \frac{B}{A}\left(\frac{1}{2} - \frac{1}{6}\right) \\ &+ \frac{1}{Ag}\frac{\mathrm{d}h}{\mathrm{d}s}\frac{B}{3A}\left[\left(1 + \frac{B}{5A}\right)\frac{1}{3} - \frac{1}{4} + \frac{1}{20}\left(1 - \frac{B}{A}\right) + \frac{3}{20}\frac{B}{A}\left(\frac{1}{6} - \frac{1}{6}\frac{1}{7}\right)\right] \\ &- \frac{h^2}{4Au_o^2}\left(\frac{1}{3} - \frac{2}{12}\right)\frac{\mathrm{d}i}{\mathrm{d}s}\sin i + \frac{U^2h^2}{4Agu_o^2}\left[\frac{1}{3}\frac{\mathrm{d}^3h}{\mathrm{d}s^3}\left(\frac{1}{3} - \frac{1}{10}\right) - \frac{\mathrm{d}^2i}{\mathrm{d}s^2}\left(\frac{1}{3} - \frac{2}{12}\right)\right] \\ &= 1 + \frac{B}{3A} + \frac{1}{Ag}\frac{\mathrm{d}h}{\mathrm{d}s}\frac{2B}{45A}\left(1 + \frac{2B}{7A}\right) - \frac{h^2}{24Au_o^2}\frac{\mathrm{d}i}{\mathrm{d}s}\sin i + \frac{U^2h^2}{24Agu_o^2}\left(\frac{7}{15}\frac{\mathrm{d}^3h}{\mathrm{d}s^3} - \frac{\mathrm{d}^2i}{\mathrm{d}s^2}\right).\end{aligned} \tag{5.325}$$

Equation (5.325) is rewritten as

$$\begin{aligned}\frac{U}{u_o} &= 1 + \frac{B}{3A} + \frac{1}{Ag}\frac{\mathrm{d}h}{\mathrm{d}s}\frac{2B}{45A}\left(1 + \frac{2B}{7A}\right) \\ &- \frac{h^2}{24Au_o^2}\frac{\mathrm{d}i}{\mathrm{d}s}\sin i + \frac{U^2h^2}{24Agu_o^2}\left(\frac{7}{15}\frac{\mathrm{d}^3h}{\mathrm{d}s^3} - \frac{\mathrm{d}^2i}{\mathrm{d}s^2}\right) \\ &= \left(1 + \frac{B}{3A}\right)\left[1 + \frac{1}{Ag}\frac{\mathrm{d}h}{\mathrm{d}s}\frac{2B}{45A}\frac{\left(1 + \frac{2B}{7A}\right)}{\left(1 + \frac{B}{3A}\right)} - \frac{h^2}{24Au_o^2\left(1 + \frac{B}{3A}\right)}\frac{\mathrm{d}i}{\mathrm{d}s}\sin i\right. \\ &\left. + \frac{U^2h^2}{24Agu_o^2\left(1 + \frac{B}{3A}\right)}\left(\frac{7}{15}\frac{\mathrm{d}^3h}{\mathrm{d}s^3} - \frac{\mathrm{d}^2i}{\mathrm{d}s^2}\right)\right],\end{aligned} \tag{5.326}$$

Using the approximate relation

$$\frac{U}{u_o} = 1 + 3\frac{B}{A}, \tag{5.327}$$

to eliminate u_o in Eq. (5.326) yields

$$\begin{aligned}\frac{U}{u_o} = \left(1+\frac{B}{3A}\right)\Bigg[1 + \frac{2}{45}\frac{B}{gA^2}\frac{\left(1+\frac{2B}{7A}\right)}{\left(1+\frac{B}{3A}\right)}\frac{\mathrm{d}h}{\mathrm{d}s} - \frac{h^2\left(1+\frac{B}{3A}\right)^2}{24AU^2\left(1+\frac{B}{3A}\right)}\frac{\mathrm{d}i}{\mathrm{d}s}\sin i \\ + \frac{h^2\left(1+\frac{B}{3A}\right)}{24Ag}\left(\frac{7}{15}\frac{\mathrm{d}^3h}{\mathrm{d}s^3} - \frac{\mathrm{d}^2i}{\mathrm{d}s^2}\right)\Bigg],\end{aligned} \tag{5.328}$$

or

$$\begin{aligned}\frac{U}{u_o} = \left(1+\frac{B}{3A}\right)\Bigg[1 + \beta\frac{\left(1+\frac{B}{3A}\right)^2}{2Bg}\frac{\mathrm{d}h}{\mathrm{d}s} - \beta'\frac{h^2\left(1+\frac{B}{3A}\right)^2}{2BU^2}\frac{\mathrm{d}i}{\mathrm{d}s}\sin i \\ + \beta'\frac{h^2\left(1+\frac{B}{3A}\right)^2}{2Bg}\left(\frac{7}{15}\frac{\mathrm{d}^3h}{\mathrm{d}s^3} - \frac{\mathrm{d}^2i}{\mathrm{d}s^2}\right)\Bigg],\end{aligned} \tag{5.329}$$

with the parameters

$$\beta = \frac{\frac{4B^2}{45A^2}\left(1+\frac{2B}{7A}\right)}{\left(1+\frac{B}{3A}\right)^3}, \quad \text{and} \quad \beta' = \frac{\frac{B}{12A}}{1+\frac{B}{3A}}. \tag{5.330}$$

From Eq. (5.329), the term Bu_o^2 is

$$\begin{aligned}Bu_o^2 = \frac{BU^2}{\left(1+\frac{B}{3A}\right)^2}\Bigg[1 + \beta\frac{\left(1+\frac{B}{3A}\right)^2}{2Bg}\frac{\mathrm{d}h}{\mathrm{d}s} - \beta'\frac{h^2\left(1+\frac{B}{3A}\right)^2}{2BU^2}\frac{\mathrm{d}i}{\mathrm{d}s}\sin i \\ + \beta'\frac{h^2\left(1+\frac{B}{3A}\right)^2}{2Bg}\left(\frac{7}{15}\frac{\mathrm{d}^3h}{\mathrm{d}s^3} - \frac{\mathrm{d}^2i}{\mathrm{d}s^2}\right)\Bigg]^{-2},\end{aligned} \tag{5.331}$$

or, taking only first-order terms,

$$\begin{aligned}Bu_o^2 &\approx \frac{BU^2}{\left(1+\frac{B}{3A}\right)^2}\Bigg[1 - \beta\frac{\left(1+\frac{B}{3A}\right)^2}{Bg}\frac{\mathrm{d}h}{\mathrm{d}s} + \beta'\frac{h^2\left(1+\frac{B}{3A}\right)^2}{BU^2}\frac{\mathrm{d}i}{\mathrm{d}s}\sin i \\ &\qquad - \beta'\frac{h^2\left(1+\frac{B}{3A}\right)^2}{Bg}\left(\frac{7}{15}\frac{\mathrm{d}^3h}{\mathrm{d}s^3} - \frac{\mathrm{d}^2i}{\mathrm{d}s^2}\right)\Bigg] \\ &= \underbrace{B\left(1+\frac{B}{3A}\right)^{-2}}_{=b}U^2 - \beta\frac{U^2}{g}\frac{\mathrm{d}h}{\mathrm{d}s} + \beta' h^2\frac{\mathrm{d}i}{\mathrm{d}s}\sin i - \beta'\frac{h^2U^2}{g}\left(\frac{7}{15}\frac{\mathrm{d}^3h}{\mathrm{d}s^3} - \frac{\mathrm{d}^2i}{\mathrm{d}s^2}\right).\end{aligned} \tag{5.332}$$

The resistance coefficient $b = b(h)$ is, according to Boussinesq, a function of the local water depth h. Furthermore, the following transformation is adopted

$$\frac{u_o^2}{g}\int_0^h h\frac{\partial\lambda}{\partial z}\left(\frac{u}{u_o}\right)^2\frac{\mathrm{d}z}{h} = \frac{h}{g}\int_0^h \underbrace{\frac{\partial\lambda}{\partial z}}_{\text{Eq. (5.312)}} u^2\frac{\mathrm{d}z}{h} = \frac{1}{g}\int_0^1 \frac{\mathrm{d}h}{\mathrm{d}s}u^2\mathrm{d}\varsigma, \tag{5.333}$$

or

$$\frac{u_o^2}{g}\int_0^h h\frac{\partial\lambda}{\partial z}\left(\frac{u}{u_o}\right)^2\frac{\mathrm{d}z}{h} = \frac{\mathrm{d}h}{\mathrm{d}s}\frac{U^2}{g}\int_0^1\left(\frac{u}{U}\right)^2\mathrm{d}\varsigma. \tag{5.334}$$

Equation (5.334) is obtained by performing the integral of the first term of μ [given by Eq. (5.302)], and then multiplying by $u_o^2/(gh)$. Using Eq. (5.334), and the second term of Eq. (5.319), Boussinesq used the identity

$$\frac{u_o^2}{gh}\int_0^h \mu\frac{\mathrm{d}z}{h} = \frac{U^2}{gh}\frac{\mathrm{d}h}{\mathrm{d}s}(1+\eta) - \frac{U^2h}{g}\left(\frac{1}{3}\frac{\mathrm{d}^3h}{\mathrm{d}s^3} - \frac{1}{2}\frac{\mathrm{d}^2i}{\mathrm{d}s^2}\right), \tag{5.335}$$

in which the widely used Boussinesq velocity coefficient originally defined by

$$1+\eta = \int_0^1\left(\frac{u}{U}\right)^2\mathrm{d}\varsigma \tag{5.336}$$

was employed. Substituting Eqs. (5.332) and (5.335) into Eq. (5.306) yields the generalized Boussinesq momentum equation in one-dimensional form,

$$\begin{aligned}\frac{U^2h^2}{g}\left[\left(\frac{1}{3}-\frac{7}{15}\beta'\right)\frac{\mathrm{d}^3h}{\mathrm{d}s^3} - \left(\frac{1}{2}-\beta'\right)\frac{\mathrm{d}^2i}{\mathrm{d}s^2}\right] + \left[h\cos i - \underbrace{(1+\eta+\beta)}_{=\alpha'}\frac{U^2}{g}\right]\frac{\mathrm{d}h}{\mathrm{d}s}\\ = h\sin i - bU^2 + \left(\frac{1}{2}-\beta'\right)h^2\frac{\mathrm{d}i}{\mathrm{d}s}\sin i.\end{aligned} \tag{5.337}$$

Upon simplification, Boussinesq reduced Eq. (5.337) to

$$\frac{U^2h^2}{g}\left(\frac{1}{3}\frac{\mathrm{d}^3h}{\mathrm{d}s^3} - \frac{1}{2}\frac{\mathrm{d}^2i}{\mathrm{d}s^2}\right) + \left(h - \frac{\alpha'}{g}U^2\right)\frac{\mathrm{d}h}{\mathrm{d}s} = hi - bU^2. \tag{5.338}$$

This is an approximate turbulent flow equation expressed in bottom-fitted curvilinear coordinates, like that of Dressler (1978). The terms containing β' were demonstrated by Boussinesq to be of second order and therefore dropped. Furthermore, the last term in Eq. (5.337) involving $(\mathrm{d}i/\mathrm{d}s)(\sin i)$ was neglected, so that $\sin i \to i$ and $\cos i \to 1$. The term $\alpha' = 1 + \eta + \beta$ in Eq. (5.338) is not, therefore, the famous "*Boussinesq velocity correction coefficient,*" as it includes the term β resulting from the variation of boundary resistance. This misleading interpretation of the Boussinesq non-hydrostatic channel flow equation persisted over time. Likewise, the belief that Boussinesq assumed a "uniform" velocity profile is false. The fact is that Eq. (5.338) originated from a detailed solution of the turbulent velocity profile with a non-hydrostatic pressure field. Boussinesq considered mean values for A and B and argued that for a wide rectangular channel $\alpha' = 1.112$, i.e., close to the Coriolis velocity correction coefficient based on the energy equation. Note that α' in Eq. (5.338) is not an "energy coefficient" but a combined coefficient made up of both a momentum and a boundary resistance effect. Boussinesq attributed the success of the erroneous use of the momentum equation by others introducing the Coriolis coefficient to this causality. Surprisingly, his comment is closely related to the critique of Vauthier to the Coriolis velocity correction coefficient (Rouse and Ince 1957), who deduced the backwater equation using the momentum approach.

For a straight bottom, Eq. (5.338) simplifies to

$$\frac{q^2}{3g}\frac{\mathrm{d}^3 h}{\mathrm{d}s^3} + \left(h - \frac{\alpha'}{g}\frac{q^2}{h^2}\right)\frac{\mathrm{d}h}{\mathrm{d}s} = h\left(i - b\frac{q^2}{h^3}\right), \tag{5.339}$$

which is the equation usually referred to as the "*Boussinesq equation*" in open-channel flow books (Jaeger 1956; Montes 1998).

5.6.5 *Linearized Equation Valid for Water Depths Close to the Normal Depth*

Equation (5.339) was linearized by Boussinesq around the uniform flow depth H. The normal depth is found by setting $\mathrm{d}^3 h/\mathrm{d}s^3 = \mathrm{d}h/\mathrm{d}s = 0$ in Eq. (5.339), corresponding to the identity

$$H^3 i = q^2 b(H). \tag{5.340}$$

Note that in general the resistance coefficient b is a function of the water depth, e.g., $b = b(H)$, as noted by Boussinesq. Equation (5.339) is rewritten using Eq. (5.340) as

$$\frac{H^3 i}{3gb(H)}\frac{\mathrm{d}^3 h}{\mathrm{d}s^3}+\left[h-\frac{\alpha'}{g}\frac{H^3 i}{h^2 b(H)}\right]\frac{\mathrm{d}h}{\mathrm{d}s}=hi\left[1-\frac{b(h)}{b(H)}\frac{H^3}{h^3}\right]. \tag{5.341}$$

Let two auxiliary functions be defined as $\omega = (h/H) - 1$ and $\gamma = [\alpha' i/(gb)] - 1$, where ω is a normalized measure of the deviation of the local water depth from the uniform flow depth; using the change of variable $h = H(1 + \omega)$, Eq. (5.341) transforms to

$$\begin{aligned}&\frac{H^4 i}{3gb(H)}\frac{\mathrm{d}^3\omega}{\mathrm{d}s^3}+H\left[H(1+\omega)-\frac{\alpha'}{g}\frac{H^3 i}{H^2(1+\omega)^2 b(H)}\right]\frac{\mathrm{d}\omega}{\mathrm{d}s}\\&\quad=H(1+\omega)i\left[1-\frac{b(h)}{b(H)}\frac{1}{(1+\omega)^3}\right],\end{aligned} \tag{5.342}$$

or

$$\begin{aligned}&\frac{H^3 i}{3gb(H)}\frac{\mathrm{d}^3\omega}{\mathrm{d}s^3}+\frac{H}{(1+\omega)^2}\left[(1+\omega)^3-\frac{\alpha' i}{gb(H)}\right]\frac{\mathrm{d}\omega}{\mathrm{d}s}\\&\quad=\frac{i}{(1+\omega)^2}\left[(1+\omega)^3-\frac{b(H+H\omega)}{b(H)}\right].\end{aligned} \tag{5.343}$$

Moreover, using the definition of γ gives

$$\begin{aligned}&\frac{H^3 i}{3gb(H)}\frac{\mathrm{d}^3\omega}{\mathrm{d}s^3}+\frac{H}{(1+\omega)^2}\left[(1+\omega)^3-(1+\gamma)\right]\frac{\mathrm{d}\omega}{\mathrm{d}s}\\&\quad=\frac{i}{(1+\omega)^2}\left[(1+\omega)^3-\frac{b(H+H\omega)}{b(H)}\right].\end{aligned} \tag{5.344}$$

The following Taylor series expansions are adopted on the basis that ω is considered small

$$\begin{aligned}\frac{H}{(1+\omega)^2}\left[(1+\omega)^3-(1+\gamma)\right]&\approx H(1-2\omega)[(1+3\omega)-(1+\gamma)]\\&=H(1-2\omega)(3\omega-\gamma)\\&\approx H(3\omega-\gamma)\\&\approx -\gamma H.\end{aligned} \tag{5.345}$$

Hence,

$$\begin{aligned}\frac{i}{(1+\omega)^2}\left[(1+\omega)^3-\frac{b(H+H\omega)}{b(H)}\right] &\approx (1-2\omega)i\left[(1+3\omega)-\frac{b(H+H\omega)}{b(H)}\right]\\ &\approx (1-2\omega)i\left[(1+3\omega)-\frac{b(H)+b'H\omega}{b(H)}\right]\\ &\approx 3\omega i\underbrace{\left(1-\frac{b'H}{3b(H)}\right)}_{=f},\end{aligned} \tag{5.346}$$

where $b' = (\mathrm{d}b/\mathrm{d}h)_{h=H}$. Inserting Eqs. (5.345) and (5.346) into Eq. (5.344) yields

$$\frac{H^3 i}{3gb(H)}\frac{\mathrm{d}^3\omega}{\mathrm{d}s^3} = \gamma H\frac{\mathrm{d}\omega}{\mathrm{d}s} + 3\omega i f, \tag{5.347}$$

or

$$\frac{H^3 i}{3gb(H)}\frac{\mathrm{d}^3\omega}{\mathrm{d}s^3} = \left(\frac{\alpha' i}{gb(H)} - 1\right)H\frac{\mathrm{d}\omega}{\mathrm{d}s} + 3\omega i f. \tag{5.348}$$

The final form adopted by Boussinesq was

$$\frac{\mathrm{d}^3\omega}{\mathrm{d}s^3} - \frac{3\alpha'}{H^2}\left(1-\frac{gb(H)}{\alpha' i}\right)\frac{\mathrm{d}\omega}{\mathrm{d}s} - \frac{9fgb(H)}{H^3}\omega = 0. \tag{5.349}$$

Equation (5.349) is valid near the uniform flow depth $H = (q^2 gb/i)^{1/3}$, say, if $|\omega| < 0.2$ as suggested by Boussinesq, because $3\omega \ll \gamma$ was assumed while resorting to Eq. (5.345). Furthermore, for the critical slope[5] $\gamma = 0$, so that 3ω may not be neglected in Eq. (5.344). In this case, a solution can be found by resorting to the numerical integration of Eq. (5.344). Boussinesq then systematically solved for the possible free surface profiles $h = h(s)$ emerging from Eq. (5.349), either asymptotically converging to H (referred to as "*creation of uniform flow*") or deviating from H (referred to as "*destruction of uniform flow*").

The general solution of Eq. (5.349) is

$$\omega = C_1\exp(m_1 s) + C_2\exp(m_2 s) + C_3\exp(m_3 s), \tag{5.350}$$

where C_1, C_2, and C_3 are constants to be determined from suitable boundary conditions. Equation (5.349) can be rewritten as

[5]The slope at which the flow is simultaneously uniform and critical is denoted as "*critical slope*" i_c. For critical flow $\alpha' q^2/gH^3 = 1$; coupling this result with Eq. (5.340) yields $i_c = gb(H)/\alpha'$, or $\gamma = 0$.

$$\frac{\mathrm{d}^3\omega}{\mathrm{d}s^3} - A\frac{\mathrm{d}\omega}{\mathrm{d}s} - B\omega = 0, \tag{5.351}$$

where

$$A = \frac{3\alpha'}{H^2}\left(1 - \frac{gb(H)}{\alpha' i}\right), \quad B = \frac{9fgb(H)}{H^3}. \tag{5.352}$$

The successive derivatives of Eq. (5.350) are

$$\begin{aligned}
\frac{\mathrm{d}\omega}{\mathrm{d}s} &= C_1 m_1 \exp(m_1 s) + C_2 m_2 \exp(m_2 s) + C_3 m_3 \exp(m_3 s),\\
\frac{\mathrm{d}^2\omega}{\mathrm{d}s^2} &= C_1 m_1^2 \exp(m_1 s) + C_2 m_2^2 \exp(m_2 s) + C_3 m_3^2 \exp(m_3 s),\\
\frac{\mathrm{d}^3\omega}{\mathrm{d}s^3} &= C_1 m_1^3 \exp(m_1 s) + C_2 m_2^3 \exp(m_2 s) + C_3 m_3^3 \exp(m_3 s).
\end{aligned} \tag{5.353}$$

Inserting Eqs. (5.350) and $(5.353)_{1,3}$ into Eq. (5.351), the following identity is formed

$$\begin{aligned}
&C_1 m_1^3 \exp(m_1 s) + C_2 m_2^3 \exp(m_2 s) + C_3 m_3^3 \exp(m_3 s)\\
&\quad = A[C_1 m_1 \exp(m_1 s) + C_2 m_2 \exp(m_2 s) + C_3 m_3 \exp(m_3 s)]\\
&\qquad + B[C_1 \exp(m_1 s) + C_2 \exp(m_2 s) + C_3 \exp(m_3 s)].
\end{aligned} \tag{5.354}$$

Collecting terms in Eq. (5.354), and accounting for the definitions of A and B given by Eqs. (5.352), the 3 m-coefficients, m_1 (the largest and positive root), m_2, and m_3, must satisfy the identity, usually denoted as the characteristic polynomial of Eq. (5.351),

$$m^3 - \frac{3\alpha'}{H^2}\left[1 - \frac{gb(H)}{\alpha' i}\right]m - \frac{9fgb(H)}{H^3} = 0. \tag{5.355}$$

Once m_1 is determined, the other two roots are given by

$$m_2 = -0.5m_1 - \left(\frac{m_1^2}{4} - \frac{9fgb}{H^3 m_1}\right)^{1/2}, \quad m_3 = -0.5m_1 + \left(\frac{m_1^2}{4} - \frac{9fgb}{H^3 m_1}\right)^{1/2}. \tag{5.356}$$

Using Eqs. (5.356), Eq. (5.350) is rewritten as

$$\omega = C_1 \exp(m_1 s) + \exp(-0.5 m_1 s)\left[C_2 \exp\left\{-\left(\frac{m_1^2}{4} - \frac{9fgb}{H^3 m_1}\right)^{1/2} s\right\} + C_3 \exp\left\{\left(\frac{m_1^2}{4} - \frac{9fgb}{H^3 m_1}\right)^{1/2} s\right\}\right]. \tag{5.357}$$

Two separate cases arise, depending on the existence of imaginary roots. Upon setting the square root in Eqs. (5.356) equal to zero results in

$$m_1 = \left(\frac{36fgb}{H^3}\right)^{1/3}. \tag{5.358}$$

Inserting this equation into Eq. (5.355) produces an expression for the limiting channel slope for the existence of complex roots i_o as

$$i_o = \frac{gb}{\alpha'}\left[1 + \frac{1}{4\alpha'}(36fgb)^{2/3}\right]. \tag{5.359}$$

Note that $i_o > i_c = gb/\alpha'$. There are two possible cases[6]:
Case 1 (mild slope channels): $i \leq i_c \leq i_o$ The roots (m_2, m_3) are here complex. Thus, the two last exponential terms in Eq. (5.357) transform to a cosine function taking the real parts using standard methods; Boussinesq then proposed as general primitive of Eq. (5.351)

$$\omega = C_1 \exp(m_1 s) + C\exp(-0.5 m_1 s)\cos[v(s - C')], \tag{5.360}$$

where C and C' are alternative constants introduced by Boussinesq for convenience, and v is defined as

$$v = \left(\frac{9fgb}{H^3 m_1} - \frac{m_1^2}{4}\right)^{1/2}. \tag{5.361}$$

Boussinesq first considered the case in which a non-uniform free surface gradually approaches the uniform flow depth. In this case, $\omega \to 0$ for $s \to +\infty$, which is the "*creation of uniform flow,*" in the words of Boussinesq.[7] Therefore, $C_1 = 0$ from Eq. (5.360), resulting in

$$\omega = C\exp(-0.5 m_1 s)\cos[v(s - C')]. \tag{5.362}$$

[6]Solutions near the critical slope are excluded. It was already demonstrated that $i = i_c$ yields $\gamma = 0$ and therefore, Eq. (5.351) is not a good model.

[7]Boussinesq was thinking on how the free surface changes the direction of the flow. The flow moves for Boussinesq from $-\infty$ to $+\infty$.

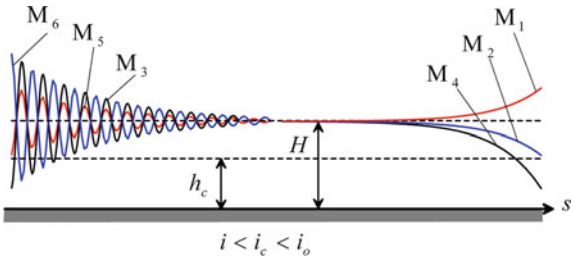

Fig. 5.41 Boussinesq's backwater curves of mildly sloping channels (adapted from Castro-Orgaz and Hager 2011e)

The constants C and C' are determined from Eq. (5.362) using known values of ω and $d\omega/ds$ at a section. The resulting surface profiles are undular, asymptotically converging to H (Fig. 5.41). Depending on the relative value of the known flow depth h at the section where computations start, with respect to H and the critical depth $h_c = (\alpha' q^2/g)^{1/3}$, curves labeled M3, M5, and M6 are obtained, the first corresponding to an undular hydraulic jump, and the others to subcritical undular flows. The curve M6, for example, is typical for undular flows over round-nosed broad-crested weir flows, which cannot be predicted by the standard gradually varied flow theory.

Boussinesq then considered the case in which the flow is uniform (at $-\infty$) and gradually becomes non-uniform in the flow direction. In this case, $\omega \to 0$ for $s \to -\infty$, which is the "*destruction of uniform flow,*" in the words of Boussinesq. Thus, this condition requires to set $C = 0$ in Eq. (5.360), resulting in

$$\omega = C_1 \exp(m_1 s), \tag{5.363}$$

with C_1 determined by using a boundary condition for ω. The possible curves are labeled M1, M2, and M4 in Fig. 5.41, with M1 as a backwater curve from a fixed tailwater depth (restricted to the condition that $h \cong H$). M2 is a profile dropping into subcritical flow toward a level $h < H$, whereas M4 passes across the critical depth, so that it is the free overfall profile under subcritical approach flow.

Figure 5.42 shows the flow from a reservoir toward a chute with $i < i_c$, adapted from Chow (1959). The curve at the inlet is clearly undular, referred here to as M6. At the downstream chute end, there is a free overfall, and the profile type is M4. None of them were explained by Chow (1959), because Boussinesq's general analysis was not adopted by him.

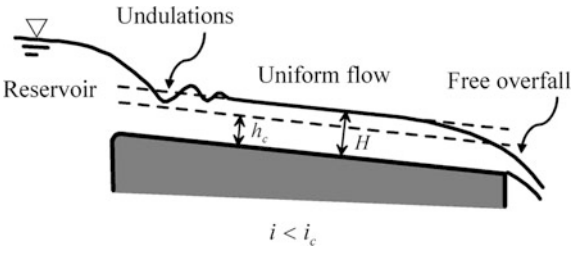

Fig. 5.42 Free surface profile in a chute of a reservoir, for $i < i_c$ (adapted from Castro-Orgaz and Hager 2011e)

To finish the relevant computations, Boussinesq proposed an approximate method to find the root m_1, whose knowledge is needed in the preceding developments. He considered the case where m_1 follows by dropping the term m^3 in Eq. (5.355) originating from the existence of the flow derivative $\mathrm{d}^3h/\mathrm{d}s^3$, so that Eq. (5.355) simplifies to

$$m_1 = \frac{1}{H}\frac{\frac{3fgb}{\alpha'}}{\left(\frac{gb}{\alpha' i}-1\right)+\frac{H^2m_1^2}{3\alpha'}} \approx \frac{1}{H}\frac{\frac{3fgb}{\alpha'}}{\frac{gb}{\alpha' i}-1}. \tag{5.364}$$

Therefore, m_1 is estimated based on the hydrostatic version of the linearized Eq. (5.351). Boussinesq analyzed the error associated with this approximation as follows. In order to have a good approximation of m_1, and with n as an integer, it is necessary that

$$\frac{H^2m_1^2}{3\alpha'} \ll \frac{1}{n}\left(\frac{gb}{\alpha' i}-1\right). \tag{5.365}$$

Boussinesq adopted $n = 9$ and solved Eq. (5.365), resulting in

$$i < i_{\mathrm{inf}} = \frac{gb}{\alpha'}\left[1+\frac{3}{\alpha'}(fgb)^{2/3}\right]^{-1} \approx \frac{gb}{\alpha'}\left[1-\frac{3}{\alpha'}(fgb)^{2/3}\right], \tag{5.366}$$

where the limiting slope i_{inf} cannot be exceeded to secure a good estimate of m_1 from Eq. (5.364). Accordingly, Eq. (5.366) yields slopes for which the hydrostatic approach applies to estimate m_1. This does not mean that the actual free surface profile is governed by a hydrostatic pressure; it simply implies a surface profile that may be undular, where a hydrostatic approximation produces a good estimate of the root m_1.

Case 2 (steep slope channels): $i \geq i_o \geq i_c$ In this case, all roots are real. Let

$$v' = \left(\frac{m_1^2}{4}-\frac{9fgb}{H^3m_1}\right)^{1/2}, \tag{5.367}$$

then Eq. (5.357) is rewritten as

$$\omega = C_1\exp(m_1 s) + \exp(-0.5m_1 s)[C_2\exp(-v's)+C_3\exp(v's)]. \tag{5.368}$$

Boussinesq considered first flow profiles with $\omega \to 0$ for $s \to +\infty$, implying $C_1 = 0$ in Eq. (5.368), which transforms to

$$\omega = \exp(-0.5m_1 s)[C_2\exp(-v's)+C_3\exp(v's)]. \tag{5.369}$$

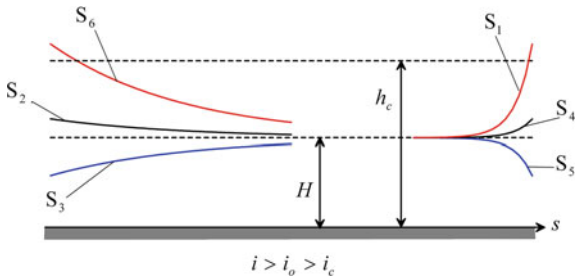

Fig. 5.43 Boussinesq's backwater curves in steeply sloping channels (adapted from Castro-Orgaz and Hager 2011e)

Boussinesq also indicated that the term containing $C_2\exp(-v's)$ is negligible for large s, given the large magnitude of v'. Therefore, Eq. (5.369) simplifies to

$$\omega = C_3 \exp(-0.5m_1 s + v's) = C_3 \exp(m_3 s). \tag{5.370}$$

Three types of profiles are possible, namely S2, S3, and S6 (Fig. 5.43). Note that these are drawdown curves in steep channels, depending on the relative position of the control point used to determine C_3, compared to H and h_c.

Boussinesq considered $\omega \to 0$ for $s \to -\infty$, from which $C_2 = C_3 = 0$ follows, with Eq. (5.368) reducing to

$$\omega = C_1 \exp(m_1 s). \tag{5.371}$$

This equation indicates that the free surface slope is large, given the magnitude of m_1. Three theoretical curves S1, S4, and S5 are possible, depending on the downstream control point (Fig. 5.43). Curve S1 is only realistic if $h < h_c$, given the formation of a hydraulic jump to cross the critical depth, as noted by Boussinesq. Curve S4 describes a backwater curve forced by high supercritical tailwater, whereas S5 corresponds to a free overfall profile for supercritical approach flow. Once the analytical solution of the free surface profile is available, e.g., by Eq. (5.368), then the boundary conditions may be selected at the up- or downstream sections, so that the standard rules of backwater computations do not necessarily apply, based on Boussinesq's generalized approach.

For $i > i_o$, it follows that m_1 is larger than for the former case where $i < i_o$, as argued by Boussinesq. Therefore, he wrote Eq. (5.355) as

$$Hm_1 = \left[3\alpha'\left(1 - \frac{gb}{\alpha' i} + \frac{3fgb}{\alpha' m_1 H}\right)\right]^{1/2}, \tag{5.372}$$

and adopted as first approximation for m_1

$$m_1 = \frac{1}{H}\left[3\alpha'\left(1 - \frac{gb}{\alpha' i}\right)\right]^{1/2}. \tag{5.373}$$

Comparison with Eq. (5.372) reveals that the accuracy of Eq. (5.373) increases for large m_1. Boussinesq limited the error by forcing the neglected term to be small, e.g.,

$$\frac{3fgb}{\alpha' m_1 H} \ll \frac{1}{\sqrt{n}}\left(1 - \frac{gb}{\alpha' i}\right), \tag{5.374}$$

with n as an integer. Using Eq. (5.373) to estimate m_1 in Eq. (5.374), and solving for i, produces for $n = 9$ as adopted by Boussinesq

$$i > i_{\text{sup}} = \frac{\frac{gb}{\alpha'}}{1 - \frac{(3n)^{1/3}}{\alpha'}(fgb)^{2/3}} = \frac{\frac{gb}{\alpha'}}{1 - \frac{3}{\alpha'}(fgb)^{2/3}} \approx \frac{gb}{\alpha'}\left[1 + \frac{3}{\alpha'}(fgb)^{2/3}\right]. \tag{5.375}$$

This is simply the condition to ensure that m_1 is accurately estimated using Eq. (5.373).

Root m_3 is smallest if $i > i_o$; from Eq. (5.355), its computation can be approximated as

$$-m_3 = \frac{1}{H}\frac{\frac{3fgb}{\alpha'}}{\left(1 - \frac{gb}{\alpha' i}\right) - \frac{H^2 m_3^2}{3\alpha'}} \approx \frac{1}{H}\frac{\frac{3fgb}{\alpha'}}{\left(1 - \frac{gb}{\alpha' i}\right)}. \tag{5.376}$$

Equation (5.376) is accurate if streamline curvature effects are small for computing m_3, i.e.,

$$\frac{H^2 m_3^2}{3\alpha'} \ll \left(\frac{gb}{\alpha' i} - 1\right). \tag{5.377}$$

5.6.6 *Classification of Free Surface Profiles*

Based on the set of the above results, Boussinesq proposed three types of free surface profiles:

(i) $i < i_{\text{inf}}$: Free surface profiles are governed by streamline curvature if $\omega(+\infty) \to 0$, e.g., if near the uniform flow depth undular flow is formed. Streamline curvature may be neglected as $\omega(-\infty) \to 0$, e.g., backwater curves due to a dam. An exception not noted by Boussinesq is the free overfall profile, for which streamline curvature becomes important.

(ii) $i_{\text{inf}} < i < i_{\text{sup}}$: Streamline curvature is always important. The bottom slope is near the critical slope, so that a full numerical analysis of Eq. (5.339) is required, e.g., for the undular hydraulic jump or the free overfall profiles in the critical slope reach.

(iii) $i > i_{sup}$: Streamline curvature may be neglected if $\omega(+\infty) \rightarrow 0$, e.g., drawdown curves for chute flow, but the free surface slope is large if $\omega(-\infty) \rightarrow 0$, and streamline curvature needs to be considered, e.g., for a free overfall at supercritical approach flow. This flow type may be analyzed based on the linearized approach, provided that $\gamma \gg 3\omega$.

Types (i) and (iii) may be curvilinear or parallel-streamlined flows, depending on the boundary conditions. These flow types are treated by Boussinesq's linear solution. The roots m_1 and m_3 can in some cases be computed based on a hydrostatic pressure approximation. However, despite m_1 or m_3 are approximated by a hydrostatic computation, the surface profile may be curvilinear, depending on the boundary conditions. Therefore, streamline curvature effects persist away from the critical point, $\mathsf{F} = 1$, depending on the boundary conditions.

Equations (5.364) and (5.373) are in excellent agreement with Eq. (5.355) for $m_1(i)$, despite the singularity for near-critical slopes (Fig. 5.44a), for the test case

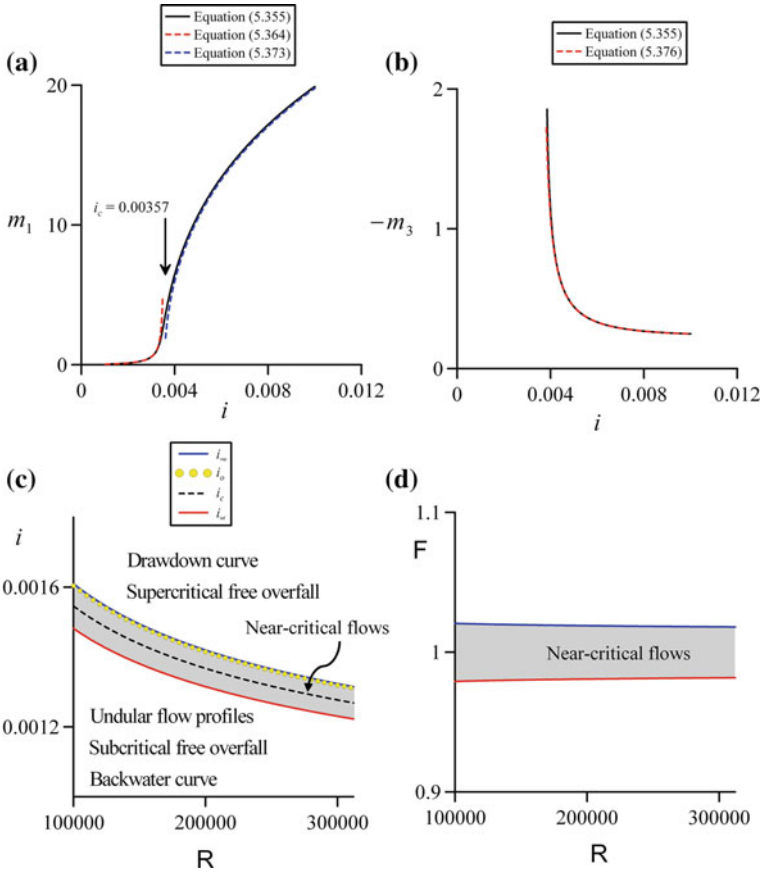

Fig. 5.44 Boussinesq's original theory **a** root $m_1(i)$, **b** root $-m_3(i)$, **c** free surface profile types, **d** free surface profiles in the plane F–R (adapted from Castro-Orgaz and Hager 2011e)

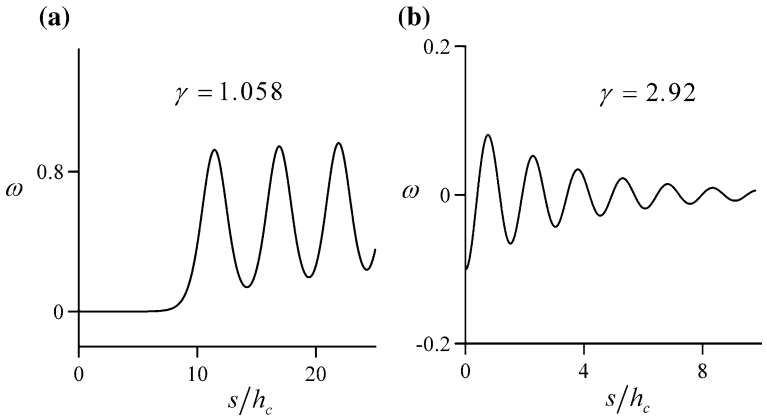

Fig. 5.45 Undular hydraulic jump profiles, after Marchi (1963), for **a** $i > i_c$, **b** $i < i_c$ (adapted from Castro-Orgaz and Hager 2011e)

$gb = 0.003924$, $\alpha' = 1.1$, $f = 1.1$, $q = 0.1$ m^2/s. Moreover, Eq. (5.376) yields almost identical results as Eq. (5.355) for $-m_3(i)$ (Fig. 5.44b). The values $gb = 0.003924$, $\alpha' = 1.1$, and $f = 1.1$ correspond to Boussinesq's test case to classify the flow profiles. Boussinesq limited the different flow types by the slopes of 0.0033 and 0.0039 for i_{inf} and i_{sup}. These were obtained by Boussinesq (1877) using $bg = 0.003924$, and it is equivalent to a quite large value of the friction factor $8bg = 0.0314$. Thus, Haaland's equation (White 1991) was used to obtain more realistic slopes as a function of R. The classification of Boussinesq's flow profiles is plotted (Fig. 5.44c) using Haaland's friction factor $8gb = [-1.8\log_{10}(6.9/\mathsf{R})]^2$ to express the results versus R. Note that $i_{inf} < i_c < i_o \approx i_{sup}$, as indicated in Fig. 5.44c. Therefore, inside the shaded domain, the full equation needs to be considered. The curves are also plotted in the plane F–R, with $\mathsf{F} = [\alpha' q^2/(gh^3)]^{1/2} = [i/(gb)]^{1/2}$, indicating a small effect of R (Fig. 5.44d). Flow type (ii) prevails only if $0.98 < \mathsf{F} < 1.02$.

Undular hydraulic jumps on a steep slope with upstream uniform supercritical flow do not satisfy the constraint $\gamma \gg 3\omega$, and the numerical integration of Eq. (5.339) is therefore necessary. Figure 5.45 compares a test case for the latter conditions with the undular hydraulic jump of flow type (i), indicating its different nature, as discussed by Marchi (1963). Therefore, a careful consideration of the ratio $\gamma/(3\omega)$ is required prior to using the linear, analytical approach instead of the numerical integration of the full equation.

5.6.7 *Boussinesq and the Solitary Wave*

When Boussinesq (1872) first elucidated the theory of the solitary wave, the world of hydraulics was astonished: A young researcher was able to explain a

phenomenon that was first described by Russell (1837, 1845), 35 years earlier, and nobody had been able to clarify this fundamental issue. Boussinesq had realized that the common hydraulic approach, i.e., the theory assuming hydrostatic pressure and thus uniform velocity distributions was limited to a class of hydraulic problems in which streamline curvature effects were small. By combining mathematical knowledge with genius in simplification of physical processes, Boussinesq arrived at the complete description of open-channel flows governed by small curvature effects, as discussed in the former section. His monumental work (Boussinesq 1877) adds to the original approach by expanding the topic to other basic flow problems.

It is pertinent to remember that the year 1871 (during which the French Army was defeated by the Prussians) marks the introduction of two important additions to hydraulics, namely the shallow water equations of Saint-Venant based on hydrostatic pressure distribution, and a short review of Boussinesq (1871a, b) on the solitary wave. As noted by Hager and Castro-Orgaz (2017), Saint-Venant should be credited for the current Froude number, because he was the first stating the difference between sub- ($F < 1$) and supercritical ($F > 1$) flows. He in addition outlined the important implications of his finding on open-channel wave propagation depending only on the Froude number. Boussinesq added in the same year the expansion to pseudo-2D flows with his approach previously mentioned, thereby allowing for a much larger class of open-channel flows. It is also notable that Boussinesq took over the seat of Saint-Venant in the *Académie des Sciences*, Paris, once his mentor had passed away in 1886. Boussinesq further prepared the "official" obituary of Saint-Venant together with his colleague Alfred A. Flamant (1839–1915). Therefore, both Saint-Venant and Boussinesq have fundamentally added to the modern science of hydraulics, allowing for the mathematical description of basic flow features thereby opening the way to the twentieth-century hydrodynamics.

The experimental discovery of the propagation of solitary waves by Russell (1837, 1845) attracted the mathematical interest of Boussinesq, who was able to develop a theory to explain it (Boussinesq 1872, 1877). At this time, water waves were a topic of great interest for water engineers, given their importance for naval hydrodynamics. Therefore, the solitary wave is a basic wave motion from which the subdiscipline of hydrodynamics named "water waves" was founded. Even today, the solitary wave is an excellent analytical solution for wave motion used to check advanced numerical schemes for the solution of Boussinesq-type models (Kim et al. 2009). The famous Lord Rayleigh (1876) wrote the excellent paper *On waves*: "*noting at the proof stage 'I have lately seen a memoir by M. Boussinesq (1871 Comptes Rendus), in which is contained a theory of the solitary wave very similar to that of this paper. So far as our results are common, the credit of priority belongs of course to M. Boussinesq.*" It should also be noted that the eminent hydrodynamicist George G. Stokes (1819–1903) wrote a paper on the topic, attempting to physically clarify the features of the solitary wave, among other waves, but was unable to forward an explanation (Stokes 1847).

As to the experimental verification of the solitary wave theory, the first real scientific team attacked this task, namely Boussinesq with the possibly best experimentor of the nineteenth century, Henry Bazin (1829–1917). During his younger years, Bazin had collaborated with Henry Darcy (1803–1858), finalizing after the latter's death the open-channel uniform flow research at *Canal de Bourgogne* in Dijon, France. As a by-product, this research also contains a chapter on the solitary wave (Darcy and Bazin 1865; Hager and Gisonni 2003), which was of course used by Boussinesq to test his predictions. After having been charged with work as Departmental Engineer, Bazin continued with research projects mainly on weir flow. In between, he studied the wave propagation under super-critical flow conditions, confirming the results of Boussinesq (Bazin 1885). During the same year, Saint-Venant (1885) also published a paper on the solitary wave in which its internal flow structure was determined. Flamant (1889) further added to the understanding of solitary waves using a simplified approach.

McCowan (1891, 1894) studied the propagation of solitary waves observing that this wave hardly changes its shape, except due to effects of viscosity. The second paper explores its maximum wave height before wave breaking is reached, resulting in 78 % of the still water depth. An addition to these results was formulated by Korteweg and de Vries (1895) as the founders of the so-called KdV wave theory. It is stated that the solitary wave is a limiting case of the so-called cnoidal (in analogy to the sinusoidal waves governed by the cn-function) waves. These waves are shown to exist absolutely steady in frictionless fluid; this research thus deals with the behavior of standing cnoidal waves. It is concluded that a solitary wave is steeper than the cnoidal wave but has identical wave height, becoming less steep in front and steeper at its rear.

These wave theories have been summarized in excellent books, which provide often a better overview than the individual papers. The authors of these summaries include Flamant (1990), Boulanger (1909) as a former student of Boussinesq, and Forchheimer (1914). A historical note on the solitary wave was presented by Sander and Hutter (1991). Note further that the writing style of Boussinesq was extremely difficult sometimes including sentences longer than a page and using no explaining figures. The only definition sketch figure in his 1877 book is a plot of the solitary wave (Fig. 5.46a). Therefore, the books mentioned are a precious addition to his personal papers by which their essence can at least be caught. Note further the excellent book of Miller and Yevjevich (1975) on unsteady open-channel flows, in which both writings on the hydrostatic and the non-hydrostatic approaches are cited along with summaries of their contents. A total of almost 1900 papers are included. The solitary wave is classically considered a potential flow problem (Chap. 3). Despite the propagation of solitary waves was first investigated by Russell (1837, 1845), this is still currently a topic of intense research to account for real fluid flow effects, including wave breaking under scale effects during wave run-up processes (Fig. 5.46b) and analytical solutions for the turbulent solitary wave (Schneider 2013). The solitary wave problem will therefore keep forever a priority place in water wave books (e.g., Whitham 1974), as a fundamental solution of the irrotational wave motion of an inviscid and incompressible fluid.

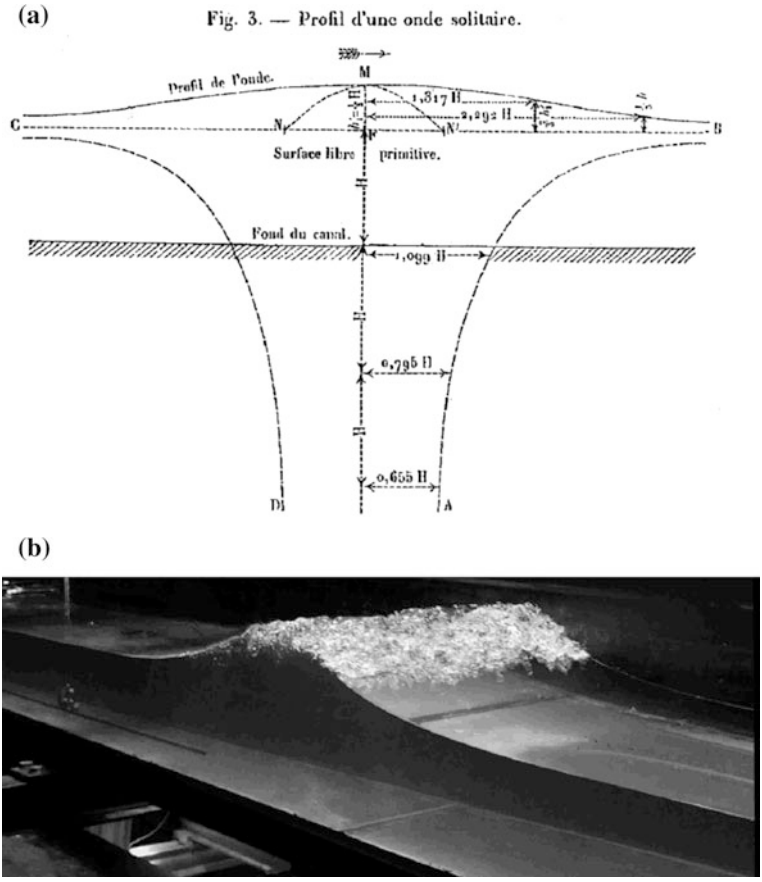

Fig. 5.46 Solitary wave **a** original drawing after Boussinesq (1877), **b** wave breaking (Photograph VAW)

5.7 Spatially Varied Flows

5.7.1 Hydrodynamic Equations

Spatially varied open channel flows are frequent in hydraulic engineering, including distribution channels, bottom outlets or side-channel spillways. The existence of a spatially varied discharge in the streamwise direction invalidates the standard energy and momentum equations used in steady flow problems of constant discharge. Favre (1933) presented the first rigorous hydraulic derivation of both the energy and momentum equations for these flows by assuming uniform velocity and hydrostatic pressure distributions. However, streamline curvature effects are important in spatially varied flows, so that higher order approximations are

necessary (Hager 1981; Castro-Orgaz and Hager 2011e). Yen and Wenzel (1970) derived the general energy and momentum equations for arbitrary velocity and pressure distributions. These equations contain undetermined velocity and pressure correction coefficients which render the system of equations not directly applicable, unless information on the pressure and velocity fields is incorporated (Yen 1971, 1973, 1975). These correction coefficients were earlier dealt with by Jaeger (1956), although Yen and Wenzel (1970) made no reference to this work. Experiments conducted by Nasser et al. (1980a, b) indicate strong deviations of Yen and Wenzel's correction coefficients from the basic values used in hydraulic computations, thereby indicating their importance in spatially varied flows. Field et al. (1998) retained a variable velocity correction factor in Yen and Wenzel's equations and applied the results to compound channel flows, whereas Venkatamaran et al. (1982) provided a review of possible water surface profiles derived from Yen and Wenzel's equations, assuming hydrostatic pressure and uniform velocity. Balmforth and Sarginson (1983) developed a linear Boussinesq-type equation for side-weir flow, but both the model and its solution were questionable (Hager 1984). Hager and Hager (1985) and Hager et al. (1988) applied Boussinesq-type equations (Hager and Hutter 1984a) to distribution channels and side channels, respectively. Variable velocity and pressure fields were incorporated in the energy and momentum equations by Castro-Orgaz and Hager (2011e) following Boussinesq's (1877) approximation. In this section, Yen and Wenzel's (1970) equations are reconsidered using Serre's theory for turbulent channel flow, resulting in generalized energy and momentum equations for spatially varied flow with streamline curvature.

Let q^* be the inflow/outflow discharge, x the streamwise coordinate and q the unit discharge. The depth-averaged mass conservation equation in two-dimensional (2D) steady, spatially varied flows is (Yen and Wenzel 1970; Hager 1981; Montes 1998)

$$q^* = \frac{\mathrm{d}q}{\mathrm{d}x}. \tag{5.378}$$

Depth integration of the Reynolds-averaged Navier–Stokes (RANS) momentum equation in the x-direction gives for small bottom slopes the equation (Yen and Wenzel 1970; Hager 1981; Montes 1998)

$$\frac{\mathrm{d}}{\mathrm{d}x}\int_0^h \left(\frac{u^2}{g}\mathrm{d}y\right) - \frac{\mathrm{d}q}{\mathrm{d}x}\frac{V\cos\phi}{g} = hS_o - \frac{\tau_b}{\gamma} - \frac{\mathrm{d}}{\mathrm{d}x}\int_0^h \frac{p}{\gamma}\mathrm{d}y. \tag{5.379}$$

Here, u is the velocity in the x-direction, V the lateral outflow/inflow velocity, g the gravity acceleration, S_o the bottom slope, h the flow depth, p the pressure, γ the specific weight of water, τ_b the bottom shear stress, y the coordinate normal to x, measured positively upwards from the channel bottom, and ϕ the angle between the V vector and the x-direction (Fig. 5.47). Secondary terms relating to normal

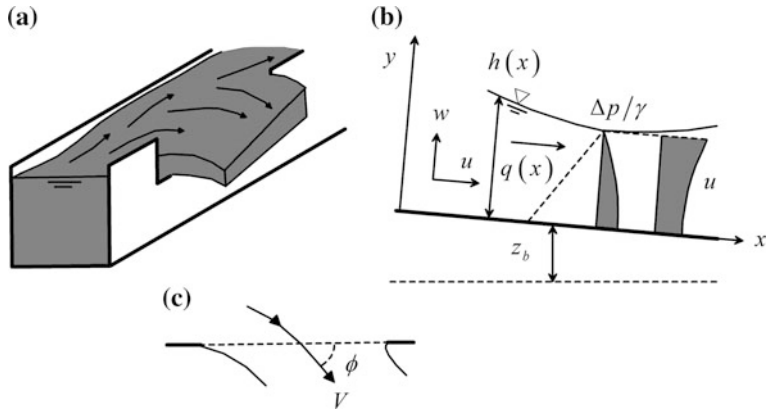

Fig. 5.47 Side-weir flow **a** 3D view, **b** axial flow profile $h(x)$ with horizontal velocity $u(y)$ and pressure deviation $\Delta p(y)$ from hydrostatic line at the section with flow depth h, **c** detail of lateral outflow (adapted from Castro-Orgaz and Hager 2011e)

Reynolds stresses were neglected in Eq. (5.379) (Yen 1971, 1973, 1975). For rectangular channels, it can be rewritten as the system

$$\frac{\mathrm{d}S}{\mathrm{d}x} = h\left(S_o - S_f\right) + \frac{\mathrm{d}q}{\mathrm{d}x}\frac{V\cos\phi}{g}, \tag{5.380}$$

$$S = \int_0^h \left(\frac{u^2}{g} + \frac{p}{\gamma}\mathrm{d}y\right) = \beta\frac{q^2}{gh} + \frac{h^2}{2} + \int_0^h \frac{\Delta p}{\gamma}\mathrm{d}y. \tag{5.381}$$

Here, S is the specific momentum, S_f the friction slope, $\Delta p = p - \rho g(h - y)$ the pressure deviation from the hydrostatic distribution, and β the Boussinesq momentum velocity correction factor, given with $U = q/h$ as the mean flow velocity by

$$\beta = \int_0^h \frac{u^2}{U^2 h}\mathrm{d}y. \tag{5.382}$$

The depth-integrated work–energy equation, deduced from the RANS equations, is for spatially varied flows (Yen and Wenzel 1970; Hager 1981; Montes 1998)

$$\underbrace{\frac{\mathrm{d}}{\mathrm{d}x}\left[\int_0^h \left(\frac{u^2+w^2}{2g} + y + \frac{p}{\gamma}\right)u\mathrm{d}y\right]}_{=Eq} = qS_o + \frac{\mathrm{d}e}{\mathrm{d}x} + \frac{\mathrm{d}q}{\mathrm{d}x}\left(\frac{p^*}{\gamma} + \frac{V^2}{2g}\right). \tag{5.383}$$

Here, E is the specific energy, e is the energy flux, w the velocity in the y-direction, and p^* the piezometric pressure of lateral inflow/outflow. In Eq. (5.383), secondary terms related to the work done by viscous and Reynolds stresses on normal sections as well as along the free surface are neglected (Yen 1971). Noting that $\mathrm{d}(Eq)/\mathrm{d}x = q\mathrm{d}E/\mathrm{d}x + E\mathrm{d}q/\mathrm{d}x$, Eq. (5.383) is rewritten as the system of equations

$$\frac{\mathrm{d}E}{\mathrm{d}x} = S_o - S_e - \frac{1}{q}\frac{\mathrm{d}q}{\mathrm{d}x}\left[E - \left(\frac{p^*}{\gamma} + \frac{V^2}{2g}\right)\right], \tag{5.384}$$

$$E = \frac{1}{q}\int_0^h \left(\frac{u^2+w^2}{2g} + y + \frac{p}{\gamma}\right)u\mathrm{d}y = h + \alpha\frac{q^2}{2gh^2} + \frac{1}{q}\int_0^h \frac{\Delta p}{\gamma}u\mathrm{d}y + \frac{1}{q}\int_0^h \frac{w^2}{2g}u\mathrm{d}y. \tag{5.385}$$

Here, S_e is the energy line slope $= -(1/q)\mathrm{d}e/\mathrm{d}x$ and α the Coriolis velocity correction factor (in open-channel hydraulics, Coriolis name is used in reference to this coefficient), given by

$$\alpha = \int_0^h \frac{u^3}{U^3 h}\mathrm{d}y. \tag{5.386}$$

The systems of Eqs. (5.380), (5.381) for momentum, and (5.384), (5.385) for energy, include the velocity and pressure fields of turbulent, spatially varied flows. No general information on these distributions is available to obtain exact closed-form solutions. Hager and Hager (1985), and Hager et al. (1988) applied to spatially varied flows the extended momentum and energy equations (Hager and Hutter 1984a)

$$S = \frac{h^2}{2} + \frac{q^2}{gh}\left(1 + \frac{hh_{xx} - h_x^2}{3}\right), \tag{5.387}$$

$$E = h + \frac{q^2}{2gh^2}\left(1 + \frac{2hh_{xx} - h_x^2}{3}\right), \tag{5.388}$$

where the subscript denotes ordinary differentiation with respect to x. However, Eqs. (5.387) and (5.388) are limited to potential flows of constant discharge. Therefore, a generalized system of Boussinesq-type equations for turbulent channel flows with variable discharge $q = q(x)$ is presented based on Serre's theory (Serre 1953; Castro-Orgaz and Hager 2011e), as highlighted below.

5.7.2 Side-Weir Flow

Consider side-weir flow, as depicted in Fig. 5.47. The horizontal velocity u in a vertical section is approximated by (Serre 1953; Castro-Orgaz and Hager 2011e)

$$u \approx U(x) = \frac{q(x)}{h(x)}. \tag{5.389}$$

The 2D continuity equation,

$$\frac{\partial u}{\partial x} + \frac{\partial w}{\partial y} = 0, \tag{5.390}$$

permits to find the solution

$$w = -\frac{\partial U}{\partial x} y, \tag{5.391}$$

where the bottom boundary condition $w = 0$ was used (the bottom is a streamline, whereas the free surface is not). Using the definition of U in Eq. (5.391) yields

$$w = -y \frac{\partial}{\partial x}\left(\frac{q}{h}\right) = -q_x \frac{y}{h} + q \frac{y}{h^2} h_x. \tag{5.392}$$

Note that the term involving q_x is not included in standard Boussinesq equations (e.g., Serre 1953; or Matthew 1963). For this reason, Eqs. (5.387) and (5.388), as well as those of Balmforth and Sarginson (1983), are mathematically not rigorous for spatially varied flows. At the free surface, Eq. (5.392) reduces to

$$w = -q_x + \frac{q}{h} h_x, \tag{5.393}$$

highlighting that the free surface is not a streamline, given the contribution of q_x. The term Δp follows from the momentum equation in the vertical direction as (Montes 1998; Bose and Dey 2007) [see Eq. (5.283)]

$$\frac{\Delta p}{\gamma} = \int_y^h \frac{u^2}{g} \frac{\partial}{\partial x}\left(\frac{w}{u}\right) \mathrm{d}y'. \tag{5.394}$$

From Eq. (5.392), one gets

$$\frac{w}{u} \approx \frac{1}{U}\left(-q_x \frac{y}{h} + q \frac{y}{h^2} h_x\right) = -\frac{q_x}{q} y + \frac{y}{h} h_x. \tag{5.395}$$

Differentiation of Eq. (5.395) permits to write

$$\begin{aligned}\frac{\partial}{\partial x}\left(\frac{w}{u}\right) &= -\frac{q_{xx}}{q}y+\frac{q_x^2}{q^2}y+h_{xx}\frac{y}{h}-\frac{h_x^2}{h^2}y\\ &= \left(h_{xx}-\frac{h_x^2}{h}+h\frac{q_x^2}{q^2}-h\frac{q_{xx}}{q}\right)\frac{y}{h}.\end{aligned} \tag{5.396}$$

Inserting Eq. (5.396) into Eq. (5.394) yields after integration, assuming $u = U$,

$$\begin{aligned}\frac{\Delta p}{\gamma} &= \int_y^h \frac{u^2}{g}\frac{\partial}{\partial x}\left(\frac{w}{u}\right)\mathrm{d}y' \approx \int_y^h \frac{U^2}{g}\left(h_{xx}-\frac{h_x^2}{h}+h\frac{q_x^2}{q^2}-h\frac{q_{xx}}{q}\right)\frac{y'}{h}\mathrm{d}y'\\ &= \frac{U^2}{2g}\left[hh_{xx}-h_x^2+\left(\frac{q_x h}{q}\right)^2-\frac{q_{xx}h^2}{q}\right]\left(1-\frac{y^2}{h^2}\right).\end{aligned} \tag{5.397}$$

The integral of Eq. (5.397) over the depth is

$$\begin{aligned}\int_0^h \frac{\Delta p}{\gamma}\mathrm{d}y &= \int_0^h \frac{U^2}{2g}\left[hh_{xx}-h_x^2+\left(\frac{q_x h}{q}\right)^2-\frac{q_{xx}h^2}{q}\right]\left(1-\frac{y^2}{h^2}\right)\mathrm{d}y\\ &= \frac{U^2}{2g}\left[hh_{xx}-h_x^2+\left(\frac{q_x h}{q}\right)^2-\frac{q_{xx}h^2}{q}\right]\left(h-\frac{h^3}{3h^2}\right)\\ &= \frac{U^2 h}{3g}\left[hh_{xx}-h_x^2+\left(\frac{q_x h}{q}\right)^2-\frac{q_{xx}h^2}{q}\right].\end{aligned} \tag{5.398}$$

Inserting Eq. (5.398) into Eq. (5.381) yields for specific momentum

$$S = \frac{h^2}{2}+\frac{q^2}{gh}\left[\beta+\frac{hh_{xx}-h_x^2+(q_x h/q)^2-\left(q_{xx}h^2/q\right)}{3}\right]. \tag{5.399}$$

The specific energy is from Eq. (5.385) with $u \approx U = q/h$,

$$\begin{aligned}E &= h+\alpha\frac{q^2}{2gh^2}+\frac{1}{q}\int_0^h \frac{\Delta p}{\gamma}u\mathrm{d}y+\frac{1}{q}\int_0^h \frac{w^2}{2g}u\mathrm{d}y\\ &\approx h+\alpha\frac{q^2}{2gh^2}+\frac{1}{h}\int_0^h \frac{\Delta p}{\gamma}\mathrm{d}y+\frac{1}{h}\int_0^h \frac{w^2}{2g}\mathrm{d}y.\end{aligned} \tag{5.400}$$

The kinetic energy of the vertical velocity is from Eq. (5.392)

$$\frac{w^2}{2g} = \frac{1}{2g}\left(\frac{q}{h}h_x - q_x\right)^2\left(\frac{y}{h}\right)^2, \tag{5.401}$$

with a depth-averaged value given by

$$\begin{aligned}\frac{1}{h}\int_0^h \frac{w^2}{2g}\mathrm{d}y &= \frac{1}{h}\int_0^h \frac{1}{2g}\left(\frac{q}{h}h_x - q_x\right)^2\left(\frac{y}{h}\right)^2\mathrm{d}y \\ &= \frac{1}{6g}\left(\frac{q}{h}h_x - q_x\right)^2 = \frac{U^2}{6g}\left(h_x - \frac{q_x h}{q}\right)^2 \\ &= \frac{U^2}{6g}\left[h_x^2 + \left(\frac{q_x h}{q}\right)^2 - 2\frac{q_x h_x h}{q}\right].\end{aligned} \tag{5.402}$$

Inserting Eqs. (5.398) and (5.402) into Eq. (5.400) yields for the specific energy head

$$\begin{aligned}E &= h + \alpha\frac{q^2}{2gh^2} + \frac{U^2}{3g}\left[hh_{xx} - h_x^2 + \left(\frac{q_x h}{q}\right)^2 - \frac{q_{xx}h^2}{q}\right] \\ &\quad + \frac{U^2}{6g}\left[h_x^2 + \left(\frac{q_x h}{q}\right)^2 - 2\frac{q_x h_x h}{q}\right] \\ &= h + \alpha\frac{q^2}{2gh^2} + \frac{U^2}{2g}\left[\frac{2hh_{xx} - 2h_x^2}{3} + \frac{2}{3}\left(\frac{q_x h}{q}\right)^2 - \frac{2}{3}\frac{q_{xx}h^2}{q}\right] \\ &\quad + \frac{U^2}{2g}\left[\frac{h_x^2}{3} + \frac{1}{3}\left(\frac{q_x h}{q}\right)^2 - \frac{2}{3}\frac{q_x h_x h}{q}\right] \\ &= h + \frac{q^2}{2gh^2}\left(\alpha + \frac{2hh_{xx} - h_x^2}{3} + \left(\frac{q_x h}{q}\right)^2 - \frac{2}{3}\frac{q_x h h_x}{q} - \frac{2}{3}\frac{q_{xx}h^2}{q}\right).\end{aligned} \tag{5.403}$$

Equations (5.399) and (5.403) contain the higher order terms hh_{xx} and h_x^2 accounting for streamline curvature effects on the free surface profile $h = h(x)$. These are relevant near the critical point $\mathsf{F} \approx 1$. Further, these equations include the spatially varied discharge terms $q_x h/q$, $q_{xx}h^2/q$ and $q_x h h_x/q$. These originate from the readjustment of the vertical velocity profile to the discharge $q = q(x)$. The term $q_x h/q$ is high for large q_x, e.g., for large flow depths $h(x)$ in side weir flow, or for small $q(x)/h(x)$, e.g., under decelerating flows. Both conditions indicate that the spatially varied terms are important not only at the critical point, but also for small F.

Equations (5.399) and (5.403) correspond to generalized Boussinesq equations for spatially varied flows with increasing/decreasing discharge. For spatially

decreasing discharge due to side weir flow, the equations are only approximate given the assumed 2D flow field, whereas the actual flow pattern is 3D (Hager 1981). Using the basic weir-flow relation [see Eq. (3.195)] for lateral discharge as

$$q^* = \frac{\mathrm{d}q}{\mathrm{d}x} = -\frac{C_d}{b}\left(gh^3\right)^{1/2}, \tag{5.404}$$

where C_d is the discharge coefficient and b the channel width, leads to the identity

$$\begin{aligned} q_{xx} &= \frac{\mathrm{d}}{\mathrm{d}x}\left[-\frac{C_d}{b}\left(gh^3\right)^{1/2}\right] = -\frac{3}{2}\frac{C_d}{b}(g)^{1/2}h^{1/2}\frac{\mathrm{d}h}{\mathrm{d}x} \\ &= -\frac{3}{2}\frac{C_d}{b}\left(gh^3\right)^{1/2}\frac{1}{h}\frac{\mathrm{d}h}{\mathrm{d}x} = \frac{3}{2}\frac{q_x h_x}{h}. \end{aligned} \tag{5.405}$$

Using Eq. (5.405), Eqs. (5.399) and (5.403) transform into

$$S = \frac{h^2}{2} + \frac{q^2}{gh}\left(\beta + \frac{hh_{xx} - h_x^2 + (q_x h/q)^2}{3} - \frac{1}{2}\frac{q_x h_x h}{q}\right), \tag{5.406}$$

$$E = h + \frac{q^2}{2gh^2}\left(\alpha + \frac{2hh_{xx} - h_x^2}{3} + \left(\frac{q_x h}{q}\right)^2 - \frac{5}{3}\frac{q_x h h_x}{q}\right). \tag{5.407}$$

5.7.3 Bottom Outlet Flow

Consider a bottom outlet corresponding to a channel whose bottom has an opening to discharge water (Fig. 5.48). The free surface boundary condition is

$$w(h) = \frac{q}{h}h_x, \tag{5.408}$$

given that the free surface is a streamline, whereas the bottom is not. Integration of Eq. (5.390) yields, assuming $u \approx U$,

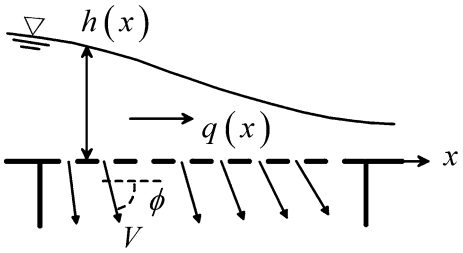

Fig. 5.48 Spatially varied flow along a bottom outlet (adapted from Castro-Orgaz and Hager 2011e)

$$w(y) - w(0) = -y\frac{\partial}{\partial x}\left(\frac{q}{h}\right) = -q_x\frac{y}{h} + q\frac{y}{h^2}h_x. \tag{5.409}$$

Using Eq. (5.408) in Eq. (5.409), the vertical velocity at the bottom is

$$w(0) = q_x - \frac{q}{h}h_x + w(h) = q_x - \frac{q}{h}h_x + \frac{q}{h}h_x = q_x. \tag{5.410}$$

Inserting Eq. (5.410) into Eq. (5.409), the vertical velocity distribution is thus

$$w = q_x\left(1 - \frac{y}{h}\right) + U\frac{y}{h}h_x. \tag{5.411}$$

Mostkow (1957) indicated a strong deviation of the pressure field from the hydrostatic distribution in bottom outlet flows, but incorrectly proposed the vertical velocity profile $w = Uyh_x/h$ as deduced from the standard Boussinesq theory. However, the correct vertical velocity profile is given by Eq. (5.411).

Using Eq. (5.411), the streamline inclination is written as

$$\frac{w}{u} = \frac{q_x}{q}h\left(1 - \frac{y}{h}\right) + \frac{y}{h}h_x \tag{5.412}$$

provided that u is approximated by U. Differentiation of Eq. (5.412) produces

$$\frac{\partial}{\partial x}\left(\frac{w}{u}\right) = \frac{q_{xx}}{q}(h-y) - \frac{q_x^2}{q^2}(h-y) + \frac{q_x h_x}{q} + h_{xx}\frac{y}{h} - \frac{h_x^2}{h^2}y. \tag{5.413}$$

Using the basic orifice equation for the bottom outlet,

$$\frac{\mathrm{d}q}{\mathrm{d}x} = -C_d A(2gh)^{1/2}, \tag{5.414}$$

in which A is the porosity of the bottom grid, yields

$$q_{xx} = \frac{\mathrm{d}}{\mathrm{d}x}\left[-C_d A(2gh)^{1/2}\right] = -\frac{1}{2}C_d A(2g)^{1/2}h^{-1/2}\frac{\mathrm{d}h}{\mathrm{d}x} = \frac{1}{2}\frac{q_x h_x}{h}. \tag{5.415}$$

Inserting Eq. (5.415) into Eq. (5.413) leads to the simplified expression

$$\frac{\partial}{\partial x}\left(\frac{w}{u}\right) = \left(h_{xx} - \frac{h_x^2}{h}\right)\frac{y}{h} - \frac{q_x^2 h}{q^2}\left(1 - \frac{y}{h}\right) + \frac{q_x h_x}{q}\left[1 + \frac{1}{2}\left(1 - \frac{y}{h}\right)\right]. \tag{5.416}$$

The deviation of the pressure from the hydrostatic distribution follows from Eq. (5.394), using Eq. (5.416), and by assuming $u \approx U$,

$$\begin{aligned}
\frac{\Delta p}{\gamma} &= \int_y^h \frac{u^2}{g}\frac{\partial}{\partial x}\left(\frac{w}{u}\right)\mathrm{d}y' \\
&\approx \int_y^h \frac{U^2}{g}\left\{\left(h_{xx}-\frac{h_x^2}{h}\right)\frac{y'}{h}-\frac{q_x^2 h}{q^2}\left(1-\frac{y'}{h}\right)+\frac{q_x h_x}{q}\left[1+\frac{1}{2}\left(1-\frac{y'}{h}\right)\right]\right\}\mathrm{d}y' \\
&= \frac{U^2 h}{g}\int_\varsigma^1 \left\{\left(h_{xx}-\frac{h_x^2}{h}\right)\varsigma'-\frac{q_x^2 h}{q^2}(1-\varsigma')+\frac{q_x h_x}{q}\left[1+\frac{1}{2}(1-\varsigma')\right]\right\}\mathrm{d}\varsigma' \\
&= \frac{U^2 h}{g}\left\{\left(h_{xx}-\frac{h_x^2}{h}\right)\right\}\left(\frac{1-\varsigma^2}{2}\right)-\frac{q_x^2 h}{q^2}(1-\varsigma) \\
&\quad +\frac{q_x^2 h}{q^2}\left(\frac{1-\varsigma^2}{2}\right)+\frac{3}{2}\frac{q_x h_x}{q}(1-\varsigma)-\frac{q_x h_x}{2q}\left(\frac{1-\varsigma^2}{2}\right) \\
&= \frac{U^2}{2g}\left(hh_{xx}-h_x^2\right)\left(1-\frac{y^2}{h^2}\right)+\frac{U^2}{g}\left[-\left(\frac{q_x h}{q}\right)^2\left(\frac{1}{2}-\frac{y}{h}+\frac{y^2}{2h^2}\right)\right] \\
&\quad +\frac{U^2}{g}\left[\frac{q_x h h_x}{q}\left(\frac{5}{4}-\frac{3y}{2h}+\frac{y^2}{4h^2}\right)\right],
\end{aligned} \tag{5.417}$$

where $\varsigma = y/h$ was used. Integration of Eq. (5.417) across the flow depth results in

$$\begin{aligned}
\int_0^h \frac{\Delta p}{\gamma}\mathrm{d}y &= \int_0^h \left\{\frac{U^2}{2g}\left(hh_{xx}-h_x^2\right)\left(1-\frac{y^2}{h^2}\right)+\frac{U^2}{g}\left[-\left(\frac{q_x h}{q}\right)^2\left(\frac{1}{2}-\frac{y}{h}+\frac{y^2}{2h^2}\right)\right]\right. \\
&\quad \left.+\frac{U^2}{g}\left[\frac{q_x h h_x}{q}\left(\frac{5}{4}-\frac{3y}{2h}+\frac{y^2}{4h^2}\right)\right]\mathrm{d}y\right\} \\
&= \frac{U^2}{2g}\left(hh_{xx}-h_x^2\right)\left(h-\frac{h^3}{3h^2}\right)+\frac{U^2}{g}\left[-\left(\frac{q_x h}{q}\right)^2\left(\frac{h}{2}-\frac{h^2}{2h}+\frac{h^3}{6h^2}\right)\right] \\
&\quad +\frac{U^2}{g}\left[\frac{q_x h h_x}{q}\left(\frac{5}{4}h-\frac{3h^2}{4h}+\frac{h^3}{12h^2}\right)\right] \\
&= \frac{U^2 h}{3g}\left(hh_{xx}-h_x^2\right)-\frac{U^2 h}{6g}\left(\frac{q_x h}{q}\right)^2+\frac{7}{12}\frac{U^2 h}{g}\left(\frac{q_x h h_x}{q}\right).
\end{aligned} \tag{5.418}$$

Inserting Eq. (5.418) into Eq. (5.381), the specific momentum S takes the form

$$S = \frac{h^2}{2} + \frac{q^2}{gh}\left(\beta + \frac{hh_{xx} - h_x^2}{3} - \frac{(q_x h/q)^2}{6} + \frac{7}{12}\frac{q_x h h_x}{q}\right). \tag{5.419}$$

The kinetic energy of the vertical velocity for a bottom outlet flow is, from Eq. (5.411),

$$\begin{aligned}\frac{w^2}{2g} &= \frac{1}{2g}\left[q_x\left(1 - \frac{y}{h}\right) + q\frac{y}{h^2}h_x\right]^2 \\ &= \frac{1}{2g}\left[q_x^2\left(1 - \frac{y}{h}\right)^2 + q^2\frac{y^2}{h^4}h_x^2 + 2q_x q\frac{y}{h^2}h_x\left(1 - \frac{y}{h}\right)\right] \\ &= \frac{1}{2g}\left[q_x^2\left(1 + \frac{y^2}{h^2} - 2\frac{y}{h}\right) + q^2\frac{h_x^2}{h^4}y^2 + 2q_x q\frac{h_x}{h^2}\left(y - \frac{y^2}{h}\right)\right].\end{aligned} \tag{5.420}$$

Its depth-averaged value is determined by

$$\begin{aligned}\frac{1}{h}\int_0^h \frac{w^2}{2g}\mathrm{d}y &= \frac{1}{h}\int_0^h \frac{1}{2g}\left[q_x^2\left(1 + \frac{y^2}{h^2} - 2\frac{y}{h}\right) + q^2\frac{h_x^2}{h^4}y^2 + 2q_x q\frac{h_x}{h^2}\left(y - \frac{y^2}{h}\right)\right]\mathrm{d}y \\ &= \frac{1}{h}\frac{1}{2g}\left[q_x^2\left(h + \frac{h^3}{3h^2} - 2\frac{h^2}{2h}\right) + q^2\frac{h_x^2}{h^4}\frac{h^3}{3} + 2q_x q\frac{h_x}{h^2}\left(\frac{h^2}{2} - \frac{h^3}{3h}\right)\right] \\ &= \frac{1}{2g}\left(\frac{q_x^2}{3} + \frac{q^2 h_x^2}{3h^2} + q_x q\frac{h_x}{3h}\right) = \frac{U^2}{2g}\left(\frac{q_x^2 h^2}{3q^2} + \frac{h_x^2}{3} + \frac{q_x h_x h}{3q}\right).\end{aligned} \tag{5.421}$$

Inserting Eqs. (5.418) and (5.421) into Eq. (5.385) yields the specific energy E as

$$\begin{aligned}E &= h + \alpha\frac{q^2}{2gh^2} + \frac{U^2}{3g}\left(hh_{xx} - h_x^2\right) - \frac{U^2}{6g}\left(\frac{q_x h}{q}\right)^2 \\ &\quad + \frac{7}{12}\frac{U^2}{g}\left(\frac{q_x h h_x}{q}\right) + \frac{U^2}{2g}\left(\frac{q_x^2 h^2}{3q^2} + \frac{h_x^2}{3} + \frac{q_x h_x h}{3q}\right) \\ &= h + \frac{q^2}{2gh^2}\left[\alpha + \frac{2hh_{xx} - h_x^2}{3} + \frac{3}{2}\left(\frac{q_x h h_x}{q}\right)\right].\end{aligned} \tag{5.422}$$

Equations (5.419) and (5.422) are again generalized Boussinesq equations for spatially varied flows with decreasing discharge along a bottom outlet. Note again the spatially varied discharge terms which are not so obtained for the classical Boussinesq solutions and invalidate the latter (Fawer 1937; Serre 1953; Matthew 1963, 1991; Hager and Hutter 1984a).

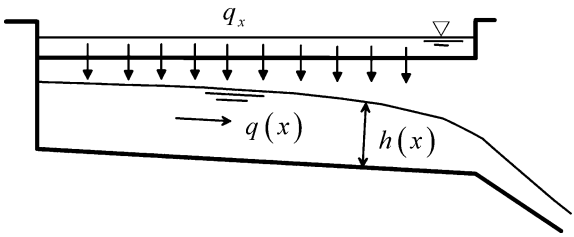

Fig. 5.49 Spatially varied flow in side channel (adapted from Castro-Orgaz and Hager 2011e)

5.7.4 *Side-Channel Flows*

This flow type is shown in Fig. 5.49, where the inflow discharge is $q^* = \mathrm{d}q/\mathrm{d}x = \text{const}$. This problem can be treated as a particular case of Eqs. (5.399) and (5.403) for which $q_{xx} = 0$, resulting in

$$S = \frac{h^2}{2} + \frac{q^2}{gh}\left(\beta + \frac{hh_{xx} - h_x^2 + (q_x h/q)^2}{3}\right), \tag{5.423}$$

$$E = h + \frac{q^2}{2gh^2}\left(\alpha + \frac{2hh_{xx} - h_x^2}{3} + \left(\frac{q_x h}{q}\right)^2 - \frac{2}{3}\frac{q_x h h_x}{q}\right). \tag{5.424}$$

Note that Eq. (5.423) again differs from Eq. (5.387) used by Hager et al. (1988) to produce an approximate non-hydrostatic model for side-channel flow. Equations (5.423) and (5.424) constitute, therefore, the generalized Boussinesq equations for spatially varied flows with increasing discharge. The higher order 2D spatially varied flow equations are more appropriate for dividing than for combining flows as in side channels. This is due to the large vertical velocities in the falling flow portion, generating excessive turbulence and a large energy loss in the ensuing 3D flow.

5.7.5 *Test Case:* Flow Over Bottom Rack

Consider spatially varied flows in a horizontal, rectangular bottom outlet (Fig. 5.48). Neglecting friction ($S_e = 0$), assuming $\alpha = 1$ and $E \approx [(p^*/\gamma) + V^2/(2g)]$, Eqs. (5.384) and (5.422) for a bottom outlet simplify, with E_o as the specific energy head at the bottom inlet section ($x = 0$), to

$$\frac{\mathrm{d}E}{\mathrm{d}x} = 0 \Rightarrow E = E_o, \tag{5.425}$$

$$E = h + \frac{q^2}{2gh^2}\left(1 + \frac{2hh_{xx} - h_x^2}{3} + \frac{3}{2}\frac{q_x h h_x}{q}\right). \tag{5.426}$$

A data analysis of Mostkow (1957) indicates that E remains nearly constant, and that the velocity profiles are almost uniform, thereby supporting the proposed Eqs. (5.425) and (5.426). The discharge for a bottom outlet is given by

$$\frac{dq}{dx} = -C_d A(2gh)^{1/2}. \tag{5.427}$$

Equations (5.426) and (5.427) were numerically solved using the fourth-order Runge–Kutta algorithm for a test case of Noseda (1956) with $S_o = 0$. The bottom outlet was 0.90 m long, with $A = 0.16$. For this small porosity, $C_d = 0.90$ was assumed. The channel width was 0.50 m and the spacing between the T-shaped bars of the bottom outlet was 5.7 mm. The system of equations is equivalent to the solution of three ordinary differential equations for $h(x)$, $q(x)$, and $dh/dx(x)$. Therefore, at the inflow section, three boundary conditions for h, q, and h_x were prescribed. The approach flow unit discharge was $q_o = 0.1983$ m^2/s, and E_o was estimated as the critical energy head (= 0.2382 m). The approach flow depth is 0.1302 m. The numerical computation assumed the value for h_x at the starting point. It was iteratively improved until a stable free surface profile emerged. The numerical results for $h = h(x)$ are successfully compared with the test data in Fig. 5.50a. For this problem, the energy equation was adopted because of negligible energy dissipation. The variation of S along the bottom outlet cannot be computed unless a relation for $\phi(x)$ is prescribed. Therefore, the energy equation is simpler to apply than the momentum approach.

Figure 5.50b shows the discharge distribution $q = q(x)$, resulting again in reasonable agreement with the test data. Note that the Boussinesq model correctly reproduces the free surface profile along the entire computational domain, despite slight local deviations in the test data. Note further the regions of negative free surface curvature at the bottom outlet start ($x < 0.2$ m), implying large streamline

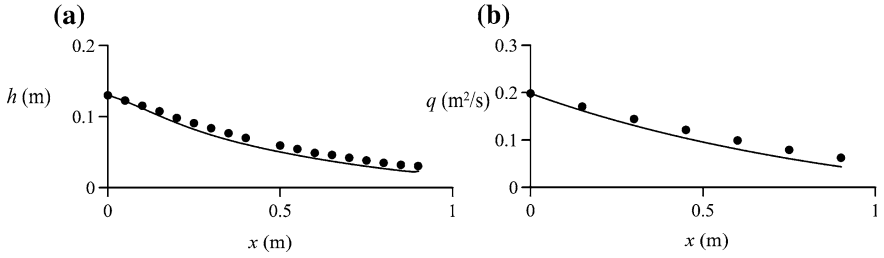

Fig. 5.50 Free surface and discharge profiles for bottom outlet flow with $S_o = 0$: Comparison of simulations using (—) Eqs. (5.426) and (5.427) with (•) test data of Noseda (1956) for **a** free surface profile $h = h(x)$, **b** discharge distribution $q = q(x)$ (adapted from Castro-Orgaz and Hager 2011e)

curvature and slope (Mostkow 1957; Montes 1998), whereas the remainder of the profile has positive curvature. Castro-Orgaz and Hager (2011e) presented the first computation of the entire free surface profile of a bottom outlet using the Boussinesq equations. The standard drawdown curve derived from the gradually varied flow theory delivers a positive curvature throughout, and thus fails near the bottom outlet start, where streamlines are considerably curved and sloped, resulting in a notable spatially varied discharge contribution.

The gradually varied flow equation derived from Eq. (5.426) assuming hydrostatic pressure is (Montes 1998)

$$\frac{\mathrm{d}h}{\mathrm{d}x} = \frac{-\dfrac{q}{gh^2}\dfrac{\mathrm{d}q}{\mathrm{d}x}}{1 - \dfrac{q^2}{gh^3}} \tag{5.428}$$

Equations (5.427) and (5.428) were solved numerically subject to identical boundary conditions for q and h. Figure 5.51 shows the inaccuracies of the hydrostatic pressure approach in the starting zone, given the large pressure deviation from the hydrostatic distribution. The standard drawdown curve is unable to reproduce negative profile curvature. To highlight the effects of the spatial discharge terms in Eq. (5.426), this was solved subject to identical boundary conditions except for setting $q_x = 0$, corresponding to Hager and Hutter's (1984a) equation, which was then coupled with Eq. (5.427). The results are also compared with other approaches in Fig. 5.51. Note that the standard Boussinesq equation reproduces the free surface profile adequately, yet it is located below the spatially varied Boussinesq model. Thus, given the scant increase in computational complexities, and the better agreement found against test data, the general Boussinesq equation, Eq. (5.426), is recommended. Local deviations between the test data and the Boussinesq equations reflect the approximate C_d value adopted. A more rigorous computation may be considered by coupling the spatially varied Boussinesq equations with refined outflow equations developed by Hager (1981). For this test case, the flow is reasonably 2D with minimum frictional effects and low turbulence. Note that turbulence due to a slot is swept below the outlet. Moreover, an adverse

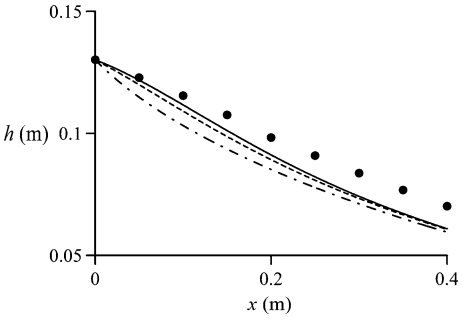

Fig. 5.51 Comparison of the free surface profile for the (—) general Boussinesq equation, (- - -) standard Boussinesq equation, (- • -) gradually varied flow equation, (•) test data of Noseda (1956) (adapted from Castro-Orgaz and Hager 2011e)

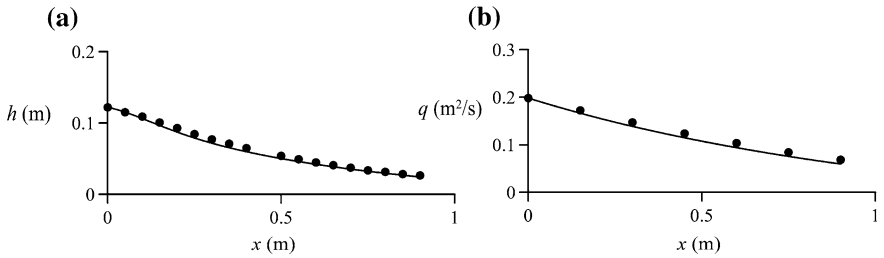

Fig. 5.52 Free surface and discharge profiles for bottom outlet flow with $S_o = 0.1$: Comparison of simulations using (—) Eqs. (5.426), (5.427), and (5.429) with (•) test data of Noseda (1956) for **a** free surface profile $h = h(x)$, **b** discharge distribution $q = q(x)$ (adapted from Castro-Orgaz and Hager 2011e)

pressure gradient is absent, given that the depth reduces although the discharge decreases along the axial direction. These particular flow conditions render the model equations therefore accurate.

Data from Noseda (1956) for the same bottom outlet but inclined by $S_o = 0.1$ are considered in Fig. 5.52. For inclined bottom outlets, Eq. (5.384) yields under the above-stated simplifications

$$\frac{\mathrm{d}E}{\mathrm{d}x} = S_o \Rightarrow E = E_o + S_o x. \tag{5.429}$$

The approach flow unit discharge is $q_o = 0.1983$ m^2/s and $h_o = 0.122$ m. The theoretical simulations for $h(x)$ and $q(x)$ using Eqs. (5.426), (5.427), and (5.429) are included in Fig. 5.52, showing good agreement with the experimental data.

Lastly, test data of Noseda (1956) for the same bottom outlet but $S_o = 0.2$ are plotted in Fig. 5.53, involving $q_o = 0.1983$ m^2/s and $h_o = 0.1175$ m. Computational results indicate good a agreement with experiments, regardless the bottom slope.

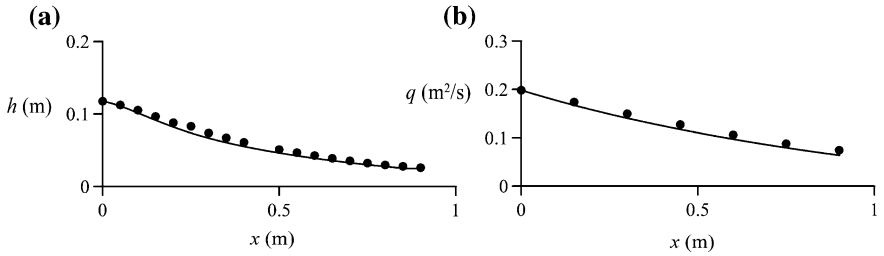

Fig. 5.53 Free surface and discharge profiles for bottom outlet flow with $S_o = 0.2$: Comparison of simulations using (—) Eqs. (5.426), (5.427), and (5.429) with (•) test data of Noseda (1956) for **a** free surface profile $h = h(x)$, **b** discharge distribution $q = q(x)$ (adapted from Castro-Orgaz and Hager 2011e)

5.8 Compound Channel Flows

5.8.1 *Introduction to Gradually Varied Flow*

The roughness variation from the main channel to the flood plains in a compound channel section (Fig. 5.54a) provokes a non-uniform lateral velocity distribution (Montes 1998). The specific energy E of gradually varied flows in a channel of arbitrary cross section is (Montes 1998; Sturm 2001; Chaudhry 2008; Dey 2014)

$$E = h + \alpha \frac{Q^2}{2gA^2}. \tag{5.430}$$

Here, h is the maximum flow depth in the main channel, Q the discharge, A the flow area, and g the gravity acceleration. Dividing the flow area A in i-subsections a_i, where the roughness is a constant, the kinetic energy correction coefficient (or Coriolis coefficient) α is given by (Blalock and Sturm 1981; Field et al. 1998)

$$\alpha = \frac{\int_A u^3 \mathrm{d}A}{U^3 A} = \frac{\sum_i \left(u_i^3 a_i\right)}{U^3 A}, \tag{5.431}$$

where u_i is the velocity in a subsection, a_i the area of a subsection, and $U = Q/A$ is the mean flow velocity. In Eq. (5.430), the channel bottom slope is assumed to be small, as usual for typical river flows. For a sloping channel, the gravity term h in Eq. (5.430) can be simply replaced by the pressure head $h\cos\theta$, where θ is the angle of the channel bottom with the horizontal plane (Chow 1959). The 1D energy balance for steady flow is (Montes 1998; Sturm 2001)

$$\frac{\mathrm{d}E}{\mathrm{d}x} = S_o - S_e, \tag{5.432}$$

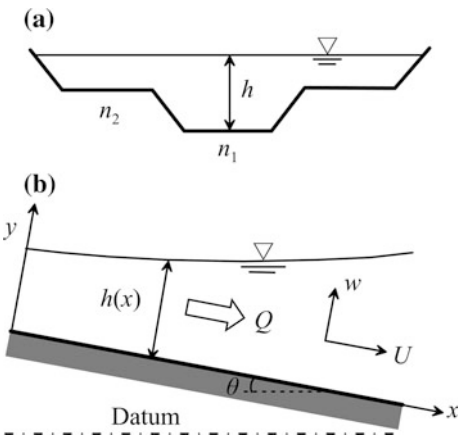

Fig. 5.54 Compound channel flow **a** cross section, **b** axial flow profile (adapted from Cantero et al. 2015)

where x is the streamwise distance, $S_o = \tan\theta$ the channel bottom slope and S_e the gradient of the dissipated energy. Inserting Eq. (5.430) into Eq. (5.432) produces, with T as the free surface width and F_α as the compound channel Froude number based on the energy principle (Blalock and Sturm 1981; Sturm and Sadiq 1996),

$$\frac{\mathrm{d}h}{\mathrm{d}x} = \frac{S_o - S_e}{1 - \left(\dfrac{\alpha Q^2 T}{gA^3} - \dfrac{Q^2}{2gA^2}\dfrac{\mathrm{d}\alpha}{\mathrm{d}h}\right)} = \frac{S_o - S_e}{1 - \mathsf{F}_\alpha^2}. \tag{5.433}$$

The latter was approximated by Blalock and Sturm (1981) as[8]

$$\mathsf{F}_\alpha = \left(\frac{\alpha Q^2 T}{gA^3} - \frac{Q^2}{2gA^2}\frac{\mathrm{d}\alpha}{\mathrm{d}h}\right)^{1/2} = \left[\frac{Q^2}{2gK^3}\left(\frac{\sigma_2\sigma_3}{K} - \sigma_1\right)\right]^{1/2}, \tag{5.434}$$

where

$$\sigma_1 = \sum_i \left[\left(\frac{k_i}{a_i}\right)^3 \left(3t_i - 2r_i\frac{\mathrm{d}p_i}{\mathrm{d}h}\right)\right], \tag{5.435}$$

$$\sigma_2 = \sum_i \left(\frac{k_i^3}{a_i^2}\right), \tag{5.436}$$

$$\sigma_3 = \sum_i \left[\left(\frac{k_i}{a_i}\right)\left(5t_i - 2r_i\frac{\mathrm{d}p_i}{\mathrm{d}h}\right)\right]. \tag{5.437}$$

In these equations, t_i is the subsection top width, p_i the subsection wetted perimeter, r_i the subsection hydraulic radius, k_i the subsection conveyance [$= (1/n_i)a_i r_i^{2/3}$], K the total conveyance of the flow section and n_i the subsection Manning's n.

The specific momentum[9] F of the gradually varied open-channel flow is, with $\bar{z}$ as the distance from the free surface to the centroid of the section (Montes 1998; Sturm 2001; Chaudhry 2008; Dey 2014)

$$F = \bar{z}A + \beta\frac{Q^2}{gA}. \tag{5.438}$$

The momentum correction coefficient (or Boussinesq coefficient) β is (Chaudhry and Bhallamudi 1988; Field et al. 1998)

[8]The development used to define the compound channel flow Froude number based on Manning's equation is routinely presented in channel flow books. For details of these derivations, see Blalock and Sturm (1981) or Montes (1998).

[9]Here, F is the specific momentum of the area A. While using vertically integrated equations, the specific momentum per unit width S appears in the developments.

$$\beta = \frac{\int_A u^2 \mathrm{d}A}{U^2 A} = \frac{\sum_i \left(u_i^2 a_i\right)}{U^2 A}. \tag{5.439}$$

The streamwise momentum balance is given by (Field et al. 1998)

$$\frac{\mathrm{d}F}{\mathrm{d}x} = A\left(S_o - S_f\right), \tag{5.440}$$

where S_f is the friction slope. Inserting Eq. (5.438) into Eq. (5.440) yields

$$\frac{\mathrm{d}h}{\mathrm{d}x} = \frac{S_o - S_f}{1 - \left(\dfrac{\beta Q^2 T}{gA^3} - \dfrac{Q^2}{gA^2}\dfrac{\mathrm{d}\beta}{\mathrm{d}h}\right)} = \frac{S_o - S_f}{1 - \mathsf{F}_\beta^2}, \tag{5.441}$$

where F_β is the compound channel Froude number based on the momentum principle, given by (Chaudhry and Bhallamudi 1988; Field et al. 1998)

$$\mathsf{F}_\beta = \left(\frac{\beta Q^2 T}{gA^3} - \frac{Q^2}{gA^2}\frac{\mathrm{d}\beta}{\mathrm{d}h}\right)^{1/2}. \tag{5.442}$$

Using the same development pursued by Blalock and Sturm (1981), F_β is estimated by (Field et al. 1998; Cantero et al. 2015)

$$\mathsf{F}_\beta^2 = \frac{2Q^2}{3gAK^2}\left(\frac{\tau_2 \tau_3}{K} - \tau_1\right), \tag{5.443}$$

where

$$\tau_1 = \sum_i \left[\left(\frac{k_i}{a_i}\right)^2 \left(4t_i - 2r_i \frac{\mathrm{d}p_i}{\mathrm{d}h}\right)\right], \tag{5.444}$$

$$\tau_2 = \sum_i \left(\frac{k_i^2}{a_i}\right), \tag{5.445}$$

$$\tau_3 = \sum_i \left[\left(\frac{k_i}{a_i}\right)\left(5t_i - 2r_i \frac{\mathrm{d}p_i}{\mathrm{d}h}\right)\right]. \tag{5.446}$$

Gradually varied flow computations using Eqs. (5.433) and (5.434) for the energy principle, and Eqs. (5.441) and (5.443) for the momentum principle, are limited to portions of the compound channel flow where the vertical acceleration can be neglected (Sturm 2001; Chaudhry 2008). This is not fulfilled at the drawdown curve of free overfalls or along undular wave trains around the normal depth, like those measured by Sturm and Sadiq (1996). Higher order free surface computations require resort to Boussinesq-type equations; see Serre (1953) and Cantero et al. (2015). The Serre (1953) equations for channels of arbitrary cross sections were developed and applied to compound channel flows by Cantero et al. (2015). These are presented in the next section.

5.8.2 Extended Serre Theory

Consider steady flow in a compound channel cross section, where the origin of y is taken at its lowest point (Fig. 5.54b). The pressure distribution is with $U_x = \partial U/\partial x$ and $U_{xx} = \partial^2 U/\partial x^2$ (Serre 1953) [see Eq. (3.592) for steady flow]

$$\frac{p}{\gamma} = (h-y)\cos\theta + \left(U_x^2 - UU_{xx}\right)\left(\frac{h^2-y^2}{2g}\right). \tag{5.447}$$

This pressure distribution represents the basis to produce higher order energy and momentum equations for flows in compound channels. Non-hydrostatic contributions are given by the terms U_x and U_{xx}; for significant velocity variations, the hydrostatic pressure approach becomes invalid. The specific momentum F in a flow of cross-sectional area A is given by (Montes 1998)

$$F = \int_A \left(\frac{u^2}{g} + \frac{p}{\gamma}\right) \mathrm{d}A. \tag{5.448}$$

The integral of the velocity term in Eq. (5.448) is expressed by

$$\int_A \frac{u^2}{g}\,\mathrm{d}A = \beta\frac{U^2}{g}A, \tag{5.449}$$

and the pressure force acting on the cross section is then

$$\begin{aligned}
\int_A \frac{p}{\gamma}\mathrm{d}A &= \int_A \left[(h-y)\cos\theta + \left(U_x^2 - UU_{xx}\right)\left(\frac{h^2-y^2}{2g}\right)\right]\mathrm{d}A \\
&= \underbrace{\int_A (h-y)\cos\theta\mathrm{d}A}_{\substack{\text{Static term with slope} \\ \text{correction}}} + \underbrace{\int_A \left(U_x^2 - UU_{xx}\right)\left(\frac{h^2-y^2}{2g}\right)\mathrm{d}A}_{\text{Dynamic term}} \\
&= \left(hA - \int_A y\mathrm{d}A\right)\cos\theta + \frac{\left(U_x^2 - UU_{xx}\right)}{2g}\left(h^2A - \int_A y^2\mathrm{d}A\right) \\
&= \bar{z}A\cos\theta + \frac{\left(U_x^2 - UU_{xx}\right)}{2g}(h^2A - I),
\end{aligned} \tag{5.450}$$

where $\bar{z}$ is the vertical distance from the free surface to the centroid of the section, and I the moment of inertia of the cross-sectional area A. Inserting Eqs. (5.449) and (5.450) into Eq. (5.448) yields (Cantero et al. 2015)

$$F = \beta \frac{Q^2}{gA} + \bar{z}A\cos\theta + \frac{U_x^2 - UU_{xx}}{2g}\left(h^2 A - I\right). \tag{5.451}$$

With $h_x = \mathrm{d}h/\mathrm{d}x$, $h_{xx} = \mathrm{d}^2h/\mathrm{d}x^2$, $A_h = \partial A/\partial h$, and $A_{hh} = \partial^2 A/\partial h^2$, noting that $\partial(\bullet)/\partial x = [\partial(\bullet)/\partial h](\mathrm{d}h/\mathrm{d}x)$, the derivatives of $U = Q/A$ are given by

$$\begin{aligned} U_x &= -\frac{Q}{A^2}\frac{\partial A}{\partial x} = -\frac{Q}{A^2}A_h h_x, \\ U_{xx} &= \frac{\partial}{\partial x}\left(-\frac{Q}{A^2}A_h h_x\right) = \frac{2Q}{A^3}A_h h_x \frac{\partial A}{\partial x} - \frac{Q}{A^2}\frac{\partial}{\partial x}\left(A_h h_x\right) \\ &= \frac{2Q}{A^3}A_h h_x \frac{\partial A}{\partial x} - \frac{Q}{A^2}\left(\frac{\partial A_h}{\partial x}h_x + A_h h_{xx}\right) \\ &= \frac{2Q}{A^3}A_h^2 h_x^2 - \frac{Q}{A^2}\left(A_h h_{xx} + A_{hh}h_x^2\right). \end{aligned} \tag{5.452}$$

Using Eqs. (5.452), the following identity is formed

$$\begin{aligned} U_x^2 - UU_{xx} &= \frac{Q^2}{A^4}A_h^2 h_x^2 - \frac{2Q^2}{A^4}A_h^2 h_x^2 + \frac{Q^2}{A^3}\left(A_h h_{xx} + A_{hh}h_x^2\right) \\ &= \frac{Q^2}{A^4}\left[\left(AA_{hh} - A_h^2\right)h_x^2 + AA_h h_{xx}\right]. \end{aligned} \tag{5.453}$$

Inserting Eq. (5.453) into Eq. (5.451) leads to (Cantero et al. 2015)

$$F = \bar{z}A\cos\theta + \frac{Q^2}{gA}\left(\beta + \frac{(h^2A - I)}{2A^3}\left(AA_h h_{xx} + \left(AA_{hh} - A_h^2\right)h_x^2\right)\right). \tag{5.454}$$

In Eq. (5.454), the significant lateral velocity variation of compound channel flows is accounted for by the coefficient β, whereas non-hydrostatic pressures are approximately accounted for on the basis of Eq. (5.447). The specific energy E in open-channel flows is given by the general equation (Montes 1998)

$$E = \frac{1}{Q}\int_A \left(\frac{u^2 + w^2}{2g} + y\cos\theta + \frac{p}{\gamma}\right)u\mathrm{d}A, \tag{5.455}$$

or

$$E = \frac{1}{Q}\int_A \left[\frac{u^2}{2g} + y\cos\theta + (h - y)\cos\theta\right]u\mathrm{d}A + \frac{1}{Q}\int_A \left(\frac{w^2}{2g} + \frac{\Delta p}{\gamma}\right)u\mathrm{d}A. \tag{5.456}$$

Equation (5.456) can be written in the alternative form

$$E = h\cos\theta + \alpha\frac{U^2}{2g} + \frac{1}{Q}\int_A \left(\frac{w^2}{2g} + \frac{\Delta p}{\gamma}\right)u\mathrm{d}A, \tag{5.457}$$

where α is the Coriolis coefficient, given by Eq. (5.431), and on the basis of Eq. (5.447), Δp is the dynamic pressure term, given by

$$\frac{\Delta p}{\gamma} = \left(U_x^2 - UU_{xx}\right)\left(\frac{h^2 - y^2}{2g}\right). \tag{5.458}$$

The average dynamic pressure term of the specific energy is then given by

$$\frac{1}{Q}\int_A \frac{\Delta p}{\gamma}u\mathrm{d}A \approx \frac{1}{A}\int_A \frac{\Delta p}{\gamma}\mathrm{d}A = \frac{\left(U_x^2 - UU_{xx}\right)}{2gA}\left(h^2A - I\right), \tag{5.459}$$

where use was made of the results presented in Eq. (5.450). Using the 2D continuity equation in the x–y plane,

$$\frac{\partial u}{\partial x} + \frac{\partial w}{\partial y} = 0, \tag{5.460}$$

and approximating u by the average flow velocity U, the velocity component w is given by the relation

$$w = -\frac{\partial U}{\partial x}y, \tag{5.461}$$

satisfying the bottom boundary condition $w = 0$. Using Eq. (5.461), the average kinetic energy of the vertical component of the flow velocity is

$$\frac{1}{Q}\int_A \frac{w^2}{2g}u\mathrm{d}A \approx \frac{1}{A}\int_A \frac{w^2}{2g}\mathrm{d}A = \frac{U_x^2}{2gA}\int_A y^2\mathrm{d}A = \frac{U_x^2}{2gA}I. \tag{5.462}$$

Inserting Eqs. (5.459) and (5.462) into Eq. (5.457) produces

$$E = h\cos\theta + \alpha\frac{Q^2}{2gA^2} + \frac{U_x^2 - UU_{xx}}{2g}\frac{\left(h^2A - I\right)}{A} + \frac{U_x^2}{2gA}I. \tag{5.463}$$

Inserting Eq. (5.452) into Eq. (5.463), the higher order specific energy for flow in compound channels is (Cantero et al. 2015)

$$E = h\cos\theta + \frac{Q^2}{2gA^2}\left\{\alpha + \frac{\left(h^2A - I\right)}{A^3}\left[AA_hh_{xx} + \left(AA_{hh} - A_h^2\right)h_x^2\right] + \frac{A_h^2}{A^3}Ih_x^2\right\}. \tag{5.464}$$

Equations (5.454) and (5.464) are the higher order expressions for E and F in compound channel flows, thereby generalizing the Serre (1953) theory. Coupling these equations with Eqs. (5.432) and (5.440), respectively, higher order energy and momentum models for flows in compound channels are obtained. These apply to 1D flows with non-hydrostatic pressure, i.e., without lateral variations of the free surface.

If the free surface level in the main channel falls beyond a certain limit, a lateral free surface gradient appears, and the flows in the main channel and flood plain become a 2D flow in the cross-sectional plane. In this case, the flow cannot be tackled with the 1D approach. For a rectangular channel of width b, one obtains the following relations

$$\begin{aligned} A &= bh, \quad A_h = b, \quad A_{hh} = 0, \\ \bar{z} &= \frac{h}{2}, \quad I = b\frac{h^3}{3}. \end{aligned} \tag{5.465}$$

Inserting these expressions into Eqs. (5.454) and (5.464) yields, by assuming a uniform velocity distribution,

$$F = b\frac{h^2}{2} + \frac{Q^2}{gbh}\left(1 + \frac{hh_{xx} - h_x^2}{3}\right), \tag{5.466}$$

$$E = h + \frac{Q^2}{2gb^2h^2}\left(1 + \frac{2hh_{xx} - h_x^2}{3}\right). \tag{5.467}$$

These are the higher order E and F equations developed by Serre (1953).

An experimental free surface profile for a free overfall for $Q = 0.113$ m^3/s, measured by Sturm and Sadiq (1996), is presented in Fig. 5.55. The discharge is outside the range of multiple critical depths, and the flow profile is therefore 1D. It is well known that the gradually varied flow computations cannot tackle this flow profile (Serre 1953), where streamlines at the brink section are highly curvilinear. In addition, upstream of the free overfall, a wave train around the normal depth is revealed from the experiments. This wavy free surface cannot be explained by the gradually varied flow theory. Simulations were therefore performed using the higher order specific energy equation given by Eq. (5.464).

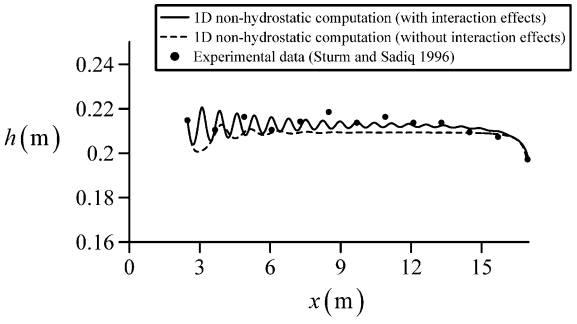

Fig. 5.55 Flow profile $h(x)$ near a free overfall in compound channel (adapted from Cantero et al. 2015)

The variation of E along the x-direction is given by the dynamic Eq. (5.432), using Manning's equation for the computation of S_e. Both equations were expressed as a system of three first-order ODEs for the unknowns $h(x)$, $h_x(x)$, and $E(x)$, and solved using the fourth-order Runge–Kutta method (Cantero et al. 2015). Three boundary conditions are needed to solve the resulting system of differential equations. The flow depth at the first experimental point (x = 2.47 m) was used as a boundary condition. The flow depth at the brink section of the free overfall (x = 17.1 m) served as the second boundary condition. The specific energy at the boundary section upstream was estimated from Eq. (5.464), neglecting the flow curvature. At this section, however, h_x is unknown. The system of equations was then solved using a shooting approach. A value of h_x was assumed at the upstream flow section, and the system of equations was then integrated up to the brink section. The flow depth computed there was compared with the measured value; if the results did not match, then the process was repeated with a new value of h_x. The process continued until a convergence within a prescribed tolerance was reached. Computations were done using the vertical division method (Montes 1998), i.e., without any interaction between the main channel and flood plains. Computations were repeated modeling the interaction effects for the main channel with Manning's n adjusted to $1.19n_1$ (Sturm and Sadiq 1996). Computational results are displayed in Fig. 5.55.

The first notable aspect is that the higher order energy model with interaction effects is capable to produce a realistic flow profile when taking the upstream and brink depths as boundary conditions. Upstream of the brink, a wave train appears with oscillations around the uniform depth, with a wave-amplitude dissipating as the flow approaches the brink section. Experimental data indicate also an upstream wave train that is attenuated as the flow approaches the brink. The agreement between the measured and the simulated profiles is considered fair, but the main flow features, namely the wave train and the drawdown curve at the overfall are correctly simulated by the higher order theory. The predicted wave-amplitude is also quite close to the experimental data. The flow profile without interaction effects is unrealistic, indicating the important effect of the lateral momentum transfer and the streamwise energy balance when accounting for the vertical velocity. The non-hydrostatic solution with interaction effects is the better one when compared with the experimental data.

5.9 Sand Solitary Wave

5.9.1 Existence of Sand Solitary Waves

The bed-form development and migration in erodible beds are processes associated with turbulent shear flows involving significant streamline curvature, so that they are subjected to a non-hydrostatic pressure (Iwasa and Kennedy 1968; Engelund

and Hansen 1966; Hosoda et al. 1997) (Chap. 2, Sect. 2.5). The purpose of this section is to illustrate the kind of solutions that may be obtained using depth-averaged models enhanced with non-hydrostatic pressure. A simple but illustrative case is the so-called sand solitary wave (Engelund 1971). Brooks (1958) observed in his classical sediment transport experiments a single flat wave traveling in his flume, without changing its shape and size. Above this bed formation, the water flowed with reduced depth, increased velocity, and bed load. Engelund (1971) presented a simplified analytical solution using an enhanced model involving non-hydrostatic pressure. In this section, a more general solution is numerically determined, to be compared with Engelund's analytical solution.

5.9.2 Governing Equations

Consider sediment and water translation waves in the x-direction at constant propagation speed c (Fig. 5.56). Using the change of variables $X = x - ct$ and $T = t$ (Galilei transformation), these waves appear steady in a moving system of reference, given that the constant celerity c implies a wave profile that is not deformed (Serre 1953; Liggett 1994). With n as bed porosity, z_b as bed elevation, t as time, and x as longitudinal coordinate, the Exner sediment mass conservation equation reads (Engelund 1971; Chaudhry 2008)

$$(1-n)\frac{\partial z_b}{\partial t} = -\frac{\partial q_b}{\partial x}, \tag{5.468}$$

where q_b is the bed-load flux of sediments per unit channel width. Thus, for a translation wave, the governing equation reduces to

$$(1-n)\frac{\partial z_b}{\partial X}(-c) = -\frac{\partial q_b}{\partial X}. \tag{5.469}$$

Equation (5.469) implies

$$\frac{\partial}{\partial X}[q_b - c(1-n)z_b] = 0. \tag{5.470}$$

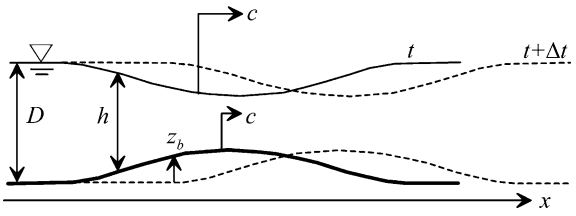

Fig. 5.56 Sketch of a sand solitary wave

Its general integral is,

$$q_b = q_{bo} + c(1-n)z_b, \tag{5.471}$$

with q_{bo} as the bed-load sediment flux in the uniform flow region of flow depth D, where the bed is flat ($z_b = 0$) (Engelund and Hansen 1966). This result implies that for translation sand waves the bed load is linearly proportional to the bed-form elevation.

A second equation is found assuming negligible energy losses across the solitary sand wave domain. Thus, the energy conservation equation in the moving system of reference, where the flow becomes steady, is (Engelund 1971) [see Eq. (3.70)][10]

$$H = z_b + h + \frac{q^2}{2gh^2}\left(1 + \frac{2hh_{XX} - h_X^2}{3} + hz_{bXX} + z_{bX}^2\right). \tag{5.472}$$

Here, H is the total energy head (a constant in this problem), h the flow depth, q the water discharge per unit width, and subscripts X indicate differentiation. Equation (5.472), with $\mathsf{F} = q/(gD^3)^{1/2}$ as the Froude number, gives for the conservation of energy between the uniform flow region and an arbitrary section on the sand wave,

$$D + \frac{\mathsf{F}^2}{2}D = z_b + h + D^3\frac{\mathsf{F}^2}{2h^2}\left(1 + \frac{2hh_{XX} - h_X^2}{3} + hz_{bXX} + z_{bX}^2\right), \tag{5.473}$$

in which $H = D + q^2/(2gD^2)$ at the initial section. To compute the bed form $z_b(X)$ and water depth $h(X)$ profiles for given F and D values, an additional empirical equation linking q_b to h is needed for model closure. Following Engelund's approximation (Engelund 1971), it is assumed that the bed load obeys the law

$$q_b = q_{bo}\left(\frac{D}{h}\right)^4, \tag{5.474}$$

which transforms Eq. (5.471) into

$$z_b = \frac{q_b - q_{bo}}{c(1-n)}, \tag{5.475}$$

[10]Engelund used a steady Boussinesq-type energy equation for a translation wave, given that in the moving frame the flow becomes steady. However, for a general solution of unsteady, non-hydrostatic sediment transport processes, resort to the numerical integration of depth-averaged mass and momentum equations for a mixture of fluid and sediments, coupled with a non-equilibrium sediment transport model, is necessary. These general equations are detailed in Appendix I.

and, when inserting Eq. (5.474), produces

$$z_b = \frac{q_{bo}}{c(1-n)}\left[\left(\frac{D}{h}\right)^4 - 1\right]. \tag{5.476}$$

To apply Eq. (5.473), it is necessary to compute $z_{bX} = \mathrm{d}z_b/\mathrm{d}X$ and $z_{bXX} = \mathrm{d}^2 z_b/\mathrm{d}X^2$, using Eq. (5.476). These derivatives take the forms

$$\begin{aligned}
\frac{\mathrm{d}z_b}{\mathrm{d}X} &= \frac{q_{bo}}{c(1-n)}\left[-4\left(\frac{D}{h}\right)^3 \frac{D}{h^2} h_X\right] = \frac{q_{bo}}{c(1-n)}\left[-4\frac{D^4}{h^5} h_X\right], \\
\frac{\mathrm{d}^2 z_b}{\mathrm{d}X^2} &= \frac{q_{bo}}{c(1-n)}\left[-12\left(\frac{D}{h}\right)^2\left(-\frac{D}{h^2}h_X\right)\left(\frac{D}{h^2}h_X\right) - 4\left(\frac{D}{h}\right)^3 D\left(\frac{h_{XX}}{h^2} - 2\frac{h_X^2}{h^3}\right)\right] \\
&= \frac{q_{bo}}{c(1-n)}\left[12\frac{D^4}{h^6}h_X^2 - 4\frac{D^4}{h^5}h_{XX} + 8\frac{D^4}{h^6}h_X^2\right] = \frac{q_{bo}}{c(1-n)}\left[20\frac{D^4}{h^6}h_X^2 - 4\frac{D^4}{h^5}h_{XX}\right].
\end{aligned} \tag{5.477}$$

The governing equations are also normalized using the dimensionless variables $\hat{h} = h/D$, $\hat{X} = X/D$, and $\hat{z}_b = z_b/D$. Equation (5.473) transforms then into

$$1 + \frac{\mathsf{F}^2}{2} = \hat{z}_b + \hat{h} + \frac{\mathsf{F}^2}{2\hat{h}^2}\left(1 + \frac{2\hat{h}\hat{h}_{\hat{X}\hat{X}} - \hat{h}_{\hat{X}}^2}{3} + \hat{h}\hat{z}_{b\hat{X}\hat{X}} + \hat{z}_{b\hat{X}}^2\right). \tag{5.478}$$

The bed profile and its derivatives are similarly normalized and obtain the forms

$$\begin{aligned}
\hat{z}_b &= \underbrace{\frac{q_{bo}}{c(1-n)D}}_{=\beta}\left[\left(\frac{1}{\hat{h}}\right)^4 - 1\right] = \beta\left(\hat{h}^{-4} - 1\right), \\
\frac{\mathrm{d}\hat{z}_b}{\mathrm{d}\hat{X}} &= \frac{q_{bo}}{c(1-n)D}\left(-4\frac{D^5}{h^5}h_X\right) = -4\beta\hat{h}^{-5}\hat{h}_{\hat{X}}, \\
\frac{\mathrm{d}^2\hat{z}_b}{\mathrm{d}\hat{X}^2} &= \frac{q_{bo}}{c(1-n)D}D^2\left(20\frac{D^4}{h^6}h_X^2 - 4\frac{D^4}{h^5}h_{XX}\right) \\
&= \beta\left(20\hat{h}^{-6}\hat{h}_{\hat{X}}^2 - 4\hat{h}^{-6}\hat{h}\hat{h}_{\hat{X}\hat{X}}\right).
\end{aligned} \tag{5.479}$$

Inserting Eqs. (5.479) into Eq. (5.478) produces the result

$$\begin{aligned}
1 + \frac{\mathsf{F}^2}{2} &= \hat{z}_b + \hat{h} \\
&\quad + \frac{\mathsf{F}^2}{2\hat{h}^2}\left[1 + \frac{2\hat{h}\hat{h}_{\hat{X}\hat{X}} - \hat{h}_{\hat{X}}^2}{3} + \beta\left(20\hat{h}^{-5}\hat{h}_{\hat{X}}^2 - 4\hat{h}^{-5}\hat{h}\hat{h}_{\hat{X}\hat{X}}\right) + \left(-4\beta\hat{h}^{-5}\hat{h}_{\hat{X}}\right)^2\right]
\end{aligned} \tag{5.480}$$

or

$$1+\frac{\mathsf{F}^2}{2}=\beta\left(\hat{h}^{-4}-1\right)+\hat{h}+\frac{\mathsf{F}^2}{2\hat{h}^2}\left[1+\frac{2\hat{h}\hat{h}_{\hat{X}\hat{X}}-\hat{h}_{\hat{X}}^2}{3}+20\beta\hat{h}^{-5}\hat{h}_{\hat{X}}^2-4\beta\hat{h}^{-5}\hat{h}\hat{h}_{\hat{X}\hat{X}}+16\beta^2\hat{h}^{-10}\hat{h}_{\hat{X}}^2\right]. \tag{5.481}$$

Collecting terms, one obtains

$$1+\frac{\mathsf{F}^2}{2}=\beta\left(\hat{h}^{-4}-1\right)+\hat{h}+\frac{\mathsf{F}^2}{2\hat{h}^2}\left(1+m_1\hat{h}\hat{h}_{\hat{X}\hat{X}}+m_2\hat{h}_{\hat{X}}^2\right), \tag{5.482}$$

where

$$m_1=\frac{2}{3}-4\beta\hat{h}^{-5},\quad m_2=20\beta\hat{h}^{-5}+16\beta^2\hat{h}^{-10}-\frac{1}{3},\quad \beta=\frac{q_{bo}}{cD(1-n)}. \tag{5.483}$$

Equation (5.483) can be numerically solved for given values of F and β to obtain the profile $\hat{h}\left(\hat{X}\right)$. The bed-form profile $\hat{z}_b\left(\hat{X}\right) = z_b/D$ is then obtained from Eq. (5.476).

5.9.3 Analytical Solution

Engelund (1971) presented a simplified analytical solution for the sand solitary wave to be described now. He adopted a simplified version of Eq. (5.473), obtained by neglecting slope effects as

$$D+\frac{\mathsf{F}^2}{2}D=z_b+h+D^3\frac{\mathsf{F}^2}{2h^2}\left(1+\frac{2hh_{XX}}{3}+hz_{bXX}\right). \tag{5.484}$$

Engelund then introduced the change of variable $h = D + \eta$, where η is assumed to be small as compared to D. Equation (5.484) is then rewritten as

$$\frac{\mathsf{F}^2}{2}D=z_b+\eta+D^3\frac{\mathsf{F}^2}{2(D+\eta)^2}\left[1+\frac{2(D+\eta)\eta_{XX}}{3}+(D+\eta)z_{bXX}\right], \tag{5.485}$$

or

$$\frac{D\mathsf{F}^2}{2} = z_b + \eta + \frac{D\mathsf{F}^2}{2\left(1+\frac{\eta}{D}\right)^2} + \frac{D^2\mathsf{F}^2}{6\left(1+\frac{\eta}{D}\right)^2}\left[2\left(1+\frac{\eta}{D}\right)\eta_{XX} + 3\left(1+\frac{\eta}{D}\right)z_{bXX}\right]. \tag{5.486}$$

On the basis that $\chi = \eta/D$ is small, consider the following Taylor series expansion

$$\begin{aligned}(1+\chi)^{-2} &\approx \left\{(1+\chi)^{-2}\right\}_{\chi=0} + \left[\frac{\mathrm{d}}{\mathrm{d}\chi}\left\{(1+\chi)^{-2}\right\}\right]_{\chi=0}\chi + \left[\frac{\mathrm{d}^2}{\mathrm{d}\chi^2}\left\{(1+\chi)^{-2}\right\}\right]_{\chi=0}\frac{1}{2}\chi^2 \\ &= 1 - 2\chi + 3\chi^2.\end{aligned} \tag{5.487}$$

Using it on the right-hand side of Eq. (5.486) indicates that the latter can be approximated as

$$0 = z_b + \eta + \frac{D\mathsf{F}^2}{2}\left[-2\frac{\eta}{D} + 3\left(\frac{\eta}{D}\right)^2\right] + \frac{D^2\mathsf{F}^2}{6}(2\eta_{XX} + 3z_{bXX}), \tag{5.488}$$

or

$$z_b + \eta - \mathsf{F}^2\left(\eta - \frac{3}{2}\frac{\eta^2}{D}\right) + \frac{D^2\mathsf{F}^2}{6}(2\eta_{XX} + 3z_{bXX}) = 0. \tag{5.489}$$

The bed profile Eq. (5.476) is now written as

$$\begin{aligned}z_b &= \frac{q_{bo}}{c(1-n)}\left[\left(\frac{D}{h}\right)^4 - 1\right] \\ &= \frac{q_{bo}}{c(1-n)}\left[\left(\frac{D}{\eta+D}\right)^4 - 1\right] = \frac{q_{bo}}{c(1-n)}\left[(1+\chi)^{-4} - 1\right].\end{aligned} \tag{5.490}$$

Consider the Taylor series expansion as

$$\begin{aligned}(1+\chi)^{-4} &\approx \left\{(1+\chi)^{-4}\right\}_{\chi=0} + \left[\frac{\mathrm{d}}{\mathrm{d}\chi}\left\{(1+\chi)^{-4}\right\}\right]_{\chi=0}\chi \\ &\quad + \left[\frac{\mathrm{d}^2}{\mathrm{d}\chi^2}\left\{(1+\chi)^{-4}\right\}\right]_{\chi=0}\frac{1}{2}\chi^2 \\ &= 1 - 4\chi + 10\chi^2.\end{aligned} \tag{5.491}$$

Substituting this into Eq. (5.490) generates Engelund's result

$$z_b \approx \frac{q_{bo}}{c(1-n)}\left(-4\frac{\eta}{D}+10\frac{\eta^2}{D^2}\right)=\beta\left(-4\eta+10\frac{\eta^2}{D}\right), \tag{5.492}$$

and approximates the curvature of the sand wave as

$$\begin{aligned}\frac{\mathrm{d}^2 z_b}{\mathrm{d}X^2} &= \frac{q_{bo}}{c(1-n)}\left(20\frac{D^4}{h^6}h_X^2-4\frac{D^4}{h^5}h_{XX}\right)\\ &\approx \frac{q_{bo}}{c(1-n)}\left(\frac{20}{D^2}\eta_X^2-\frac{4}{D}\eta_{XX}\right)\\ &= -4\beta\eta_{XX}+20\frac{\beta}{D}\eta_X^2.\end{aligned} \tag{5.493}$$

Inserting Eqs. (5.492) and (5.493) into Eq. (5.489) generates the ODE for η

$$\begin{aligned}&\beta\left(-4\eta+10\frac{\eta^2}{D}\right)+\eta-\mathsf{F}^2\left(\eta-\frac{3}{2}\frac{\eta^2}{D}\right)\\ &\quad+\frac{D^2\mathsf{F}^2}{6}\left[2\eta_{XX}+3\left(-4\beta\eta_{XX}+20\frac{\beta}{D}\eta_X^2\right)\right]=0,\end{aligned} \tag{5.494}$$

or, after collecting terms,

$$\begin{aligned}&\eta\left(1-4\beta-\mathsf{F}^2\right)+\eta^2\left(\frac{3}{2}\frac{\mathsf{F}^2}{D}+\frac{10\beta}{D}\right)\\ &\quad+\eta_{XX}\frac{1}{3}\mathsf{F}^2D^2(1-6\beta)+10\beta\mathsf{F}^2D\eta_X^2=0,\end{aligned} \tag{5.495}$$

which upon using of the differential identity

$$\eta_{XX}=\frac{1}{2}\frac{\mathrm{d}}{\mathrm{d}\eta}\left(\eta_X^2\right), \tag{5.496}$$

can be rewritten as

$$\begin{aligned}&\frac{\mathsf{F}^2D^2}{6}(1-6\beta)\frac{\mathrm{d}}{\mathrm{d}\eta}\left(\eta_X^2\right)+10\beta\mathsf{F}^2D\eta_X^2\\ &\quad=\eta\left(\mathsf{F}^2-1+4\beta\right)-\eta^2\left(\frac{3}{2}\frac{\mathsf{F}^2}{D}+\frac{10\beta}{D}\right).\end{aligned} \tag{5.497}$$

This second-order nonlinear ODE has the form

$$\frac{\mathrm{d}}{\mathrm{d}\eta}\left(\eta_X^2\right) = a_1\eta_X^2 + a_2\eta + a_3\eta^2, \tag{5.498}$$

where

$$a_1 = \frac{60\beta}{(6\beta-1)D}, \quad a_2 = \frac{6\left(1-4\beta-\mathsf{F}^2\right)}{\mathsf{F}^2D^2(6\beta-1)}, \quad a_3 = \frac{9\mathsf{F}^2+60\beta}{\mathsf{F}^2D^3(6\beta-1)}. \tag{5.499}$$

A first integral of Eq. (5.498), satisfying the boundary condition $\eta_X = 0$ for $\eta = 0$, has been constructed by Engelund (1971) and is given as

$$\eta_X^2 = \left(\frac{a_2}{a_1^2} + \frac{2a_3}{a_1^3}\right)[\exp(a_1\eta) - 1 - a_1\eta] - \frac{a_3}{a_1}\eta^2. \tag{5.500}$$

The reader may verify this by simple back substitution. A primitive of Eq. (5.500), however, is not known. Thus, Engelund transformed Eq. (5.500) into an ODE which allows for the computation of a primitive, by using an approximate method. If η_o is the maximum value of η such that $\eta = -\eta_o$ for $h_X = 0$, Eq. (5.500) provides the identity

$$\exp(-a_1\eta_o) = 1 - a_1\eta_o + \frac{a_3a_1}{a_2 + (2a_3/a_1)}\eta_o^2, \tag{5.501}$$

from which η_o is determined numerically. Engelund stated the approximation

$$\exp(a_1\eta) - 1 - a_1\eta = \frac{a_1^2}{2}\eta^2 + k\eta^3. \tag{5.502}$$

Using it in Eq. (5.500) yields the new ODE

$$\begin{aligned}\eta_X^2 &= \left(\frac{a_2}{a_1^2} + \frac{2a_3}{a_1^3}\right)\left(\frac{a_1^2}{2}\eta^2 + k\eta^3\right) - \frac{a_3}{a_1}\eta^2 \\ &= \frac{a_2}{2}\eta^2 + \left(\frac{a_2}{a_1^2} + \frac{2a_3}{a_1^3}\right)k\eta^3,\end{aligned} \tag{5.503}$$

which is a function of the unknown value k. Engelund selected for k the value that satisfies Eq. (5.502) for $\eta = -\eta_o$,

$$k = \frac{\frac{a_1^2}{2\eta_o}a_2}{a_2 + (2a_3/a_1)}. \tag{5.504}$$

Then, inserting Eq. (5.504) into Eq. (5.503), the latter equation is simplified to the form

$$\eta_X^2 = \frac{a_2}{2}\eta^2 + \left(\frac{a_2}{a_1^2} + \frac{2a_3}{a_1^3}\right)k\eta^3 = \frac{a_2}{2}\eta^2 + \left(\frac{a_2}{a_1^2} + \frac{2a_3}{a_1^3}\right)\frac{\frac{a_1^2}{2\eta_o}a_2}{[a_2 + (2a_3/a_1)]}\eta^3$$
$$= \frac{a_2}{2}\eta^2 + \frac{a_2}{2\eta_o}\left(a_2 + \frac{2a_3}{a_1}\right)\frac{\eta^3}{[a_2 + (2a_3/a_1)]} = \frac{a_2}{2}\eta^2\left(1 + \frac{\eta}{\eta_o}\right). \tag{5.505}$$

Using the value of a_2 defined in Eq. $(5.499)_2$, it can also be written as

$$\eta_X^2 = \frac{1}{2}\frac{6(1 - 4\beta - \mathsf{F}^2)}{\mathsf{F}^2 D^2(6\beta - 1)}\eta^2\left(1 + \frac{\eta}{\eta_o}\right) = \frac{3(1 - 4\beta - \mathsf{F}^2)}{\mathsf{F}^2 D^2(6\beta - 1)\eta_o}\eta^2(\eta + \eta_o), \tag{5.506}$$

or

$$\frac{\mathrm{d}\eta}{\mathrm{d}X} = \pm\left[\frac{3(1 - 4\beta - \mathsf{F}^2)}{\mathsf{F}^2 D^2 \eta_o(6\beta - 1)}\right]^{1/2}\eta(\eta_o + \eta)^{1/2}. \tag{5.507}$$

Defining a scaling length L as

$$L = D\left[\frac{4\mathsf{F}^2(6\beta - 1)}{3(1 - 4\beta - \mathsf{F}^2)}\right]^{1/2}, \tag{5.508}$$

and the dimensionless variables

$$Y = \frac{\eta}{\eta_o}, \quad \zeta = \frac{X}{L}, \tag{5.509}$$

Equation (5.507) can be rewritten as

$$\frac{\mathrm{d}Y}{\mathrm{d}\zeta} = \pm 2Y(1 + Y)^{1/2}. \tag{5.510}$$

It can be easily verified that the general integral of Eq. (5.510) is

$$-Y = (\cosh\varsigma)^{-2}, \tag{5.511}$$

or reverting to the original variables

$$\frac{\eta}{\eta_o} = -\left[\cosh\left(\frac{X}{L}\right)\right]^{-2}, \tag{5.512}$$

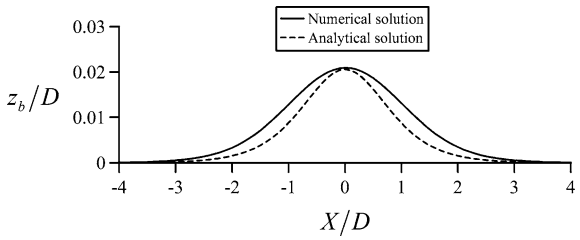

Fig. 5.57 Computed sand solitary wave $z_b/D(X/D)$ for $\mathsf{F} = 0.4$ and $\beta = 0.2$

due to Engelund (1971). Thus, solitary sand waves are "bell-shaped." Based on Eq. (5.508), it is observed that if $\beta = 1/6$ then $L = 0$. If β is set equal to 1/4, complex roots are obtained. Therefore, physical solutions are only possible if $1/6 < \beta < 1/4$. Further, if $\beta = 1/6$, the limiting value of F to avoid imaginary roots is $\mathsf{F}^2 = 1 - (4/6) = 1/3$. Therefore, F must be less than $(1/3)^{1/2} \approx 0.58$ for solitary sand waves to occur.

A sand solitary wave for $\mathsf{F} = 0.4$ and $\beta = 0.2$ was selected as illustrative test case. The analytical solution given by Eq. (5.512) is plotted in Fig. 5.57, showing a Gaussian-like profile. The more general ODE given by Eq. (5.482) was numerically solved using the fourth-order Runge–Kutta method transforming it into a system of two first-order ODEs. At the inflow section $h = D$, and h_X was set to the arbitrary value −0.00001 to deviate the flow from uniform flow conditions. The bed-form profile obtained is also plotted in Fig. 5.57, where the X origin was shifted to locate the maxima of the two computed bed profiles to the same section. It is observed that Engelund's theory is accurate in predicting the maximum sand solitary wave elevation and the horizontal extension of the bed form. The computed elevations are, however, lower when compared with the full numerical solution.

A main fact derived from the present computations is the S-shaped profile predicted by the Boussinesq theory for each branch of the solitary sand wave profile. It is well known that dunes involve separation at their downstream face, so that this type of solution is obviously unrealistic there. However, the upstream face profile of a dune is also S-shaped (Engelund and Hansen 1966; Hosoda et al. 1997; Tjerry and Fredsøe 2005), similar to the profiles computed here. Therefore, depth-averaged models enhanced with non-hydrostatic pressure are physically relevant for this portion of the dune profile.

5.10 Dike Breaches

5.10.1 Extended Serre Theory

Erosion of trapezoidal dikes is a class of unsteady channel flows over an erodible bed. Progressive bed erosion transforms a trapezoidal-shaped dike into a wavy remnant of noticeable bed curvature and slope (Schmocker and Hager 2009) (Fig. 5.58a). The

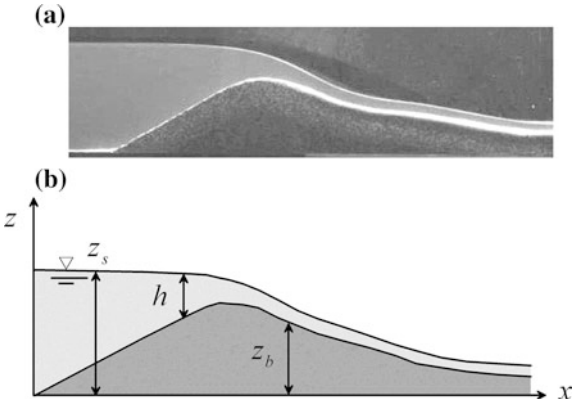

Fig. 5.58 Dike breach **a** typical wavy bed observed during model test (Photograph VAW, ETH Zurich), **b** notation

simulation of this type of flow was investigated using an erosion model based on the Saint-Venant Shallow Water Equations (SWE) (Pontillo et al. 2010). Its x-momentum equation for the water transport is, with q as the unit discharge, h as flow depth, S_o as bed slope, S_f as friction slope, and x as streamwise coordinate,

$$\frac{1}{g}\frac{\partial q}{\partial t} + \frac{\partial}{\partial x}\left(\frac{q^2}{gh} + \frac{h^2}{2}\right) = h(S_o - S_f). \tag{5.513}$$

The numerical simulations for dike erosion of Pontillo et al. (2010) resulted in improved predictions as compared to the classical morpho-dynamic model based on Exner's equation. However, water-level predictions along the curved dike bed were in disagreement with observations of Pontillo et al. (2010). This indicates that the water-phase component of the model, given by Eq. (5.513), requires a higher order closure for momentum balance (Castro-Orgaz and Hager 2013). Modeling dike breaches by overtopping requires an adequate representation of both the hydrodynamic and sediment transport processes. An improved treatment of the former is considered by using Boussinesq-type equations as a higher order closure model.

The flow over a curved bed results in streamline inclination and curvature effects to be accounted for in the momentum equation (Boussinesq 1877; Hager and Hutter 1984a; Basco 1987). Therefore, an improvement of dike breach erosion models relies on the inclusion of the vertical acceleration effects in the momentum equations. Dressler (1978) and Sivakumaran et al. (1983) proposed an approximate model for curved bed flow accounting only for bottom curvature. Steffler and Jin (1993) and Khan and Steffler (1996b) made significant advances in modeling 1D unsteady open-channel flows over rigid curved beds, proposing a more general set of equations. The Boussinesq equations proposed by Khan and Steffler (1996b) are advanced SWEs in which the velocity and pressure distributions functions are a priori assumed. For example, the pressure distribution is assumed to vary linearly and the unspecified deviation of the bottom pressure from water depth is computed

using the vertical momentum equation (see Chap. 2). Their equations do not include a specific treatment of a movable bed. Basco (1987) investigated unsteady Boussinesq-type equations for rigid bottoms originating from the Euler equations for inviscid flows. Engelund and Hansen (1966) studied the formation of sand dunes in alluvial streams using the steady Boussinesq approach. Castro-Orgaz and Hager (2013) developed unsteady Boussinesq-type flow equations for an erodible curved bed (see Chap. 2, Sect. 2.5), a modeling approach suitable for dike breaches due to overtopping.

Consider a curved bed profile $z = z_b(x, t)$ during overtopping (Fig. 5.58b), in which z is the vertical coordinate and t is time. The water surface is described by $z = z_s(x, t)$ (Rouse 1938; Liggett 1994; Chaudhry 2008). The kinematic boundary condition at the material free surface is (Liggett 1994; Chaudhry 2008)

$$w_s(x,t) = \frac{\partial z_s}{\partial t} + u_s\left(\frac{\partial z_b}{\partial x} + \frac{\partial h}{\partial x}\right), \tag{5.514}$$

whereas at the bed, it is assumed that the sediment surface is also a material surface[11]

$$w_b(x,t) = \frac{\partial z_b}{\partial t} + u_b\frac{\partial z_b}{\partial x}. \tag{5.515}$$

Conservation of momentum in the x-direction is then given by (Castro-Orgaz and Hager 2013) (see Chap. 2)

$$\frac{1}{g}\frac{\partial q}{\partial t} + \frac{\partial S}{\partial x} = \frac{p_b}{\gamma}S_o - hS_f, \tag{5.516}$$

where p_b is the bed pressure and the specific momentum S is

$$S = \int_{z_b}^{z_s}\left(\frac{u^2}{g} + \frac{p}{\gamma}\right)\mathrm{d}z. \tag{5.517}$$

Equation (5.516) is a generalization of the standard SWE for unsteady open-channel flow (Chap. 2) because, as compared to Eq. (5.513): (i) momentum S contributes to the conservation equation with a pressure integral that in general differs from $h^2/2$;

[11]The bed profile $z_b(x, t)$ is defined here as the upper interface of the bed-load layer with the fluid flow above it, and it is assumed that there is not a mass exchange across it. That is, the suspended-load is neglected, and there is a clear-water flow above the dike sediment surface. This simplification was observed while conducting experimental tests on dike breaching. Vertical velocities are positive upwards. For a more general non-hydrostatic model accounting for suspended and bed-load sediment transport, see Appendix I.

(ii) bottom pressure p_b is coupled with the slope term S_o, rather than flow depth h. For unsteady flows over curved beds, S differs, therefore, from $[q^2/(gh) + h^2/2]$ as p_b differs from h, both affecting the streamwise momentum balance. Assume that, with $h = z_s - z_b$ as the flow depth, the velocity u is replaced by its depth-averaged value U (Boussinesq 1877; Serre 1953; Chaudhry 2008), which is in general a function of both x and t given by

$$u = U(x,t) = \frac{q(x,t)}{h(x,t)}. \tag{5.518}$$

Integration of the 2D continuity equation

$$\frac{\partial u}{\partial x} + \frac{\partial w}{\partial z} = 0, \tag{5.519}$$

using Eq. (5.518) produces

$$w(x,z,t) = -\frac{\partial U(x,t)}{\partial x} z + C(x,t). \tag{5.520}$$

Here, C depends on (x, t), but not on z. In the classical theory of Serre (1953), this function is set to zero, $C = 0$, excluding bed deformation in time and space due to erosion, as discussed below. The vertically integrated continuity equation is

$$\frac{\partial h}{\partial t} + \frac{\partial q}{\partial x} = 0, \tag{5.521}$$

or

$$\frac{\partial h}{\partial t} + h\frac{\partial U}{\partial x} + U\frac{\partial h}{\partial x} = 0. \tag{5.522}$$

Inserting $\partial U/\partial x$ from Eq. (5.522) into Eq. (5.520) yields

$$w(x,z,t) = \frac{1}{h}\left(\frac{\partial h}{\partial t} + U\frac{\partial h}{\partial x}\right) z + C(x,t). \tag{5.523}$$

Imposing the kinematic boundary condition at the bed yields

$$\frac{\partial z_b}{\partial t} + U\frac{\partial z_b}{\partial x} = \frac{1}{h}\left(\frac{\partial h}{\partial t} + U\frac{\partial h}{\partial x}\right) z_b + C(x,t), \tag{5.524}$$

from which the value of function C is obtained as

$$C(x,t) = \frac{\partial z_b}{\partial t} - \frac{\partial h}{\partial t}\frac{z_b}{h} + U\left(\frac{\partial z_b}{\partial x} - \frac{\partial h}{\partial x}\frac{z_b}{h}\right). \tag{5.525}$$

By inserting Eq. (5.525) into Eq. (5.523), the vertical velocity profile is obtained in the form

$$w(x,z,t) = \frac{\partial z_b}{\partial t} + \frac{\partial h}{\partial t}\frac{z-z_b}{h} + U\left(\frac{\partial z_b}{\partial x} + \frac{\partial h}{\partial x}\frac{z-z_b}{h}\right). \tag{5.526}$$

Note that Eq. (5.526) satisfies as well the kinematic boundary condition at the free surface, that is,

$$w_s = \frac{\partial z_b}{\partial t} + \frac{\partial h}{\partial t} + U\left(\frac{\partial z_b}{\partial x} + \frac{\partial h}{\partial x}\right). \tag{5.527}$$

Equation (5.525) states that C is essentially a term accounting for the variable bed profile in space and deforming in time. Note that for steady flows over a rigid bed $C \neq 0$. The momentum equation in the vertical direction is, neglecting the turbulent stresses (Rouse 1938; Yen 1973; Steffler and Jin 1993; Liggett 1994; Chaudhry 2008)

$$\frac{\partial w}{\partial t} + u\frac{\partial w}{\partial x} + w\frac{\partial w}{\partial z} = -\frac{1}{\rho}\frac{\partial p}{\partial z} - g. \tag{5.528}$$

Integrating this by using Eqs. (5.518) and (5.519) yields the vertical pressure distribution as

$$\frac{p}{\gamma} = z_s - z + \frac{1}{g}\int_z^{z_s}\left(\frac{\partial w}{\partial t} + U\frac{\partial w}{\partial x} - w\frac{\partial U}{\partial x}\right)\mathrm{d}z'. \tag{5.529}$$

Now, Eq. (5.526), rewritten as

$$w = A + B\eta, \quad A = \frac{\partial z_b}{\partial t} + U\frac{\partial z_b}{\partial x}, \quad B = \frac{\partial h}{\partial t} + U\frac{\partial h}{\partial x}, \quad \eta = \frac{z-z_b}{h}, \tag{5.530}$$

will be used to evaluate the derivatives inside the integral in Eq. (5.529). The following derivatives are computed to their use in the ensuing developments,

$$\begin{aligned}
\frac{\partial A}{\partial x} &= \frac{\partial^2 z_b}{\partial t \partial x} + \frac{\partial U}{\partial x}\frac{\partial z_b}{\partial x} + U\frac{\partial^2 z_b}{\partial x^2},\\
\frac{\partial A}{\partial t} &= \frac{\partial^2 z_b}{\partial t^2} + \frac{\partial U}{\partial t}\frac{\partial z_b}{\partial x} + U\frac{\partial^2 z_b}{\partial t \partial x},\\
\frac{\partial B}{\partial x} &= \frac{\partial^2 h}{\partial t \partial x} + \frac{\partial U}{\partial x}\frac{\partial h}{\partial x} + U\frac{\partial^2 h}{\partial x^2},\\
\frac{\partial B}{\partial t} &= \frac{\partial^2 h}{\partial t^2} + \frac{\partial U}{\partial t}\frac{\partial h}{\partial x} + U\frac{\partial^2 h}{\partial t \partial x},\\
\frac{\partial \eta}{\partial x} &= -\frac{1}{h}\frac{\partial z_b}{\partial x} - \frac{1}{h}\frac{\partial h}{\partial x}\eta,\\
\frac{\partial \eta}{\partial t} &= -\frac{1}{h}\frac{\partial z_b}{\partial t} - \frac{1}{h}\frac{\partial h}{\partial t}\eta.
\end{aligned} \tag{5.531}$$

The derivatives of w are

$$\begin{aligned}
\frac{\partial w}{\partial t} &= \frac{\partial A}{\partial t} + \frac{\partial B}{\partial t}\eta + B\frac{\partial \eta}{\partial t},\\
\frac{\partial w}{\partial x} &= \frac{\partial A}{\partial x} + \frac{\partial B}{\partial x}\eta + B\frac{\partial \eta}{\partial x}.
\end{aligned} \tag{5.532}$$

Based on Eqs. (5.532), the function I to be integrated in Eq. (5.529) is, thus, expressible as

$$\begin{aligned}
I &= \frac{\partial w}{\partial t} + U\frac{\partial w}{\partial x} - w\frac{\partial U}{\partial x}\\
&= \frac{\partial A}{\partial t} + \frac{\partial B}{\partial t}\eta + B\frac{\partial \eta}{\partial t}\\
&\quad + U\left(\frac{\partial A}{\partial x} + \frac{\partial B}{\partial x}\eta + B\frac{\partial \eta}{\partial x}\right) - (A + B\eta)\frac{\partial U}{\partial x},
\end{aligned} \tag{5.533}$$

or, using the definitions,

$$\begin{aligned}
&\frac{\mathrm{D}A}{\mathrm{D}t} = \frac{\partial A}{\partial t} + U\frac{\partial A}{\partial x}, \quad \frac{\mathrm{D}B}{\mathrm{D}t} = \frac{\partial B}{\partial t} + U\frac{\partial B}{\partial x},\\
&b_1 = -\frac{1}{h}\frac{\partial z_b}{\partial t} - \frac{U}{h}\frac{\partial z_b}{\partial x}, \quad b_2 = -\frac{1}{h}\frac{\partial h}{\partial t} - \frac{U}{h}\frac{\partial h}{\partial x},
\end{aligned} \tag{5.534}$$

as,

$$I = \underbrace{\left(\frac{\mathrm{D}A}{\mathrm{D}t} + Bb_1 - A\frac{\partial U}{\partial x}\right)}_{=a_1} + \underbrace{\left(\frac{\mathrm{D}B}{\mathrm{D}t} + Bb_2 - B\frac{\partial U}{\partial x}\right)}_{=a_2}\eta, \tag{5.535}$$

where, after using Eqs. (5.531) and (5.534), the coefficients a_1 and a_2 are given by the expressions

$$\begin{aligned}
a_1 &= \left(\frac{\partial^2 z_b}{\partial t^2} + \frac{\partial U}{\partial t}\frac{\partial z_b}{\partial x} + U\frac{\partial^2 z_b}{\partial t \partial x}\right) + U\left(\frac{\partial^2 z_b}{\partial t \partial x} + \frac{\partial U}{\partial x}\frac{\partial z_b}{\partial x} + U\frac{\partial^2 z_b}{\partial x^2}\right) \\
&\quad + \left(\frac{\partial h}{\partial t} + U\frac{\partial h}{\partial x}\right)\left(-\frac{1}{h}\frac{\partial z_b}{\partial t} - \frac{U}{h}\frac{\partial z_b}{\partial x}\right) \\
&\quad - \left(\frac{\partial z_b}{\partial t} + U\frac{\partial z_b}{\partial x}\right)\frac{\partial U}{\partial x}, \\
a_2 &= \left(\frac{\partial^2 h}{\partial t^2} + \frac{\partial U}{\partial t}\frac{\partial h}{\partial x} + U\frac{\partial^2 h}{\partial t \partial x}\right) + U\left(\frac{\partial^2 h}{\partial t \partial x} + \frac{\partial U}{\partial x}\frac{\partial h}{\partial x} + U\frac{\partial^2 h}{\partial x^2}\right) \\
&\quad + \left(\frac{\partial h}{\partial t} + U\frac{\partial h}{\partial x}\right)\left(-\frac{1}{h}\frac{\partial h}{\partial t} - \frac{U}{h}\frac{\partial h}{\partial x}\right) \\
&\quad - \left(\frac{\partial h}{\partial t} + U\frac{\partial h}{\partial x}\right)\frac{\partial U}{\partial x}.
\end{aligned} \tag{5.536}$$

Using Eq. (5.535) in Eq. (5.529), the pressure distribution is given by

$$\begin{aligned}
\frac{p}{\gamma} &= z_s - z + \frac{1}{g}\int_z^{z_s}\left(\frac{\partial w}{\partial t} + U\frac{\partial w}{\partial x} - w\frac{\partial U}{\partial x}\right)\mathrm{d}z' \\
&= z_s - z + \frac{h}{g}\int_\eta^1 (a_1 + a_2\eta')\mathrm{d}\eta' \\
&= z_s - z + \frac{h}{g}\left[a_1(1-\eta) + a_2\left(\frac{1-\eta^2}{2}\right)\right] \\
&= h(1-\eta) + \frac{U^2}{2g}\left[\frac{2h}{U^2}\left\{a_1(1-\eta) + a_2\left(\frac{1-\eta^2}{2}\right)\right\}\right] \\
&= h(1-\eta) + \frac{U^2}{2g}\left[2\varepsilon_1(1-\eta) + \varepsilon_2\left(1-\eta^2\right)\right].
\end{aligned} \tag{5.537}$$

Using Eqs. (5.536), the coefficients ε_1 and ε_2 are, after collecting terms,

$$\begin{aligned}
\varepsilon_1 = \frac{h}{U^2}a_1 &= \frac{h}{U^2}\frac{\partial^2 z_b}{\partial t^2} - \frac{1}{U^2}\frac{\partial h}{\partial t}\frac{\partial z_b}{\partial t} + \frac{h}{U^2}\frac{\partial U}{\partial t}\frac{\partial z_b}{\partial x} + \frac{h}{U}\left(2\frac{\partial^2 z_b}{\partial x \partial t} - \frac{1}{h}\frac{\partial h}{\partial x}\frac{\partial z_b}{\partial t}\right) \\
&\quad - \frac{h}{U}\frac{1}{h}\frac{\partial h}{\partial t}\frac{\partial z_b}{\partial x} + h\left(\frac{\partial^2 z_b}{\partial x^2} - \frac{1}{h}\frac{\partial h}{\partial x}\frac{\partial z_b}{\partial x}\right) - \frac{h}{U^2}\frac{\partial z_b}{\partial t}\frac{\partial U}{\partial x}, \\
\varepsilon_2 = \frac{h}{U^2}a_2 &= \frac{h}{U^2}\frac{\partial^2 h}{\partial t^2} - \frac{1}{U^2}\left(\frac{\partial h}{\partial t}\right)^2 + \frac{h}{U^2}\frac{\partial U}{\partial t}\frac{\partial h}{\partial x} + \frac{h}{U}\left(2\frac{\partial^2 h}{\partial x \partial t} - \frac{1}{h}\frac{\partial h}{\partial x}\frac{\partial h}{\partial t}\right) \\
&\quad - \frac{1}{U}\frac{\partial h}{\partial t}\frac{\partial h}{\partial x} + h\left(\frac{\partial^2 h}{\partial x^2} - \frac{1}{h}\left(\frac{\partial h}{\partial x}\right)^2\right) - \frac{h}{U^2}\frac{\partial h}{\partial t}\frac{\partial U}{\partial x}.
\end{aligned} \tag{5.538}$$

Note that the assumption $u = U$ determines the vertical velocity profile by Eq. (5.526), allowing for the computation of the vertical pressure distribution and, therefore, evaluation of S. Generally, the Boussinesq coefficients ε_1 and $\varepsilon_2 \neq 0$ depend on $h(x, t)$, $U(x, t)$, $z_b(x, t)$, and their temporal and spatial derivatives. This generalization of the equation of Serre (1953) allows for the inclusion of a variable bed profile $z = z_b(x, t)$ in the computations. The bed pressure profile p_b/γ follows from Eq. (5.537) by setting $\eta = 0$ as

$$\frac{p_b}{\gamma} = h + \frac{U^2}{2g}[2\varepsilon_1 + \varepsilon_2]. \tag{5.539}$$

Note that if the water surface and the bed profile derivatives in space and time are large, then ε_1 and ε_2 are significantly different from zero. The vertical velocity profile thus provokes a bed pressure $p_b/\gamma \neq h$, thereby affecting the streamwise momentum balance Eq. (5.516) as a source term. Using Eq. (5.537), the momentum function is, after evaluation of the pressure integral,

$$\begin{aligned} S = \frac{U^2 h}{g} + \int_{z_b}^{z_s} \frac{p}{\gamma} \mathrm{d}z &= \frac{U^2 h}{g} + h \int_0^1 \left\{ h(1-\eta) + \frac{U^2}{2g}\left[2\varepsilon_1(1-\eta) + \varepsilon_2\left(1-\eta^2\right)\right] \mathrm{d}\eta \right\} \\ &= \frac{h^2}{2} + \frac{q^2}{gh}\left(1 + \frac{\varepsilon_1}{2} + \frac{\varepsilon_2}{3}\right). \end{aligned} \tag{5.540}$$

5.10.2 Experimental Investigation

Pontillo et al. (2010) conducted simulations of dike breaches due to overtopping using the SWE. Their simulations gave water levels considerably above the experimental data (Schmocker 2011) in the upstream subcritical reach and the crest domain. If the SWE were applicable, one would expect that $\varepsilon_1 = \varepsilon_2 \approx 0$. In contrast, if they were not, then ε_1 and ε_2 differ from zero and must be accounted for. Therefore, an experimental evaluation of ε_1 and ε_2 was conducted to assess their orders of magnitude.

Test 51 of Schmocker (2011) is considered in Fig. 5.59. Schmocker's camera images contained the experimental data for $z_s(x, t)$ and $z_b(x, t)$. The unit discharge $q(x, t)$ was estimated solving the depth-averaged continuity equation in finite-difference form, and the depth-averaged velocity was determined as $U(x, t) = q(x, t)/[z_s(x, t) - z_b(x, t)]$. The derivatives necessary to evaluate ε_1 and ε_2 were estimated using 3-point central finite differences. The results for times $t = 4$, 8 and 25 s after test inception are plotted in Fig. 5.59a, c, e, respectively. The experimental profiles for $z_s(x, t)$ and $z_b(x, t)$ are also presented to highlight their variations with time along the dike. Note that generally $|\varepsilon_1(x,t)| > |\varepsilon_2(x,t)|$, indicating the

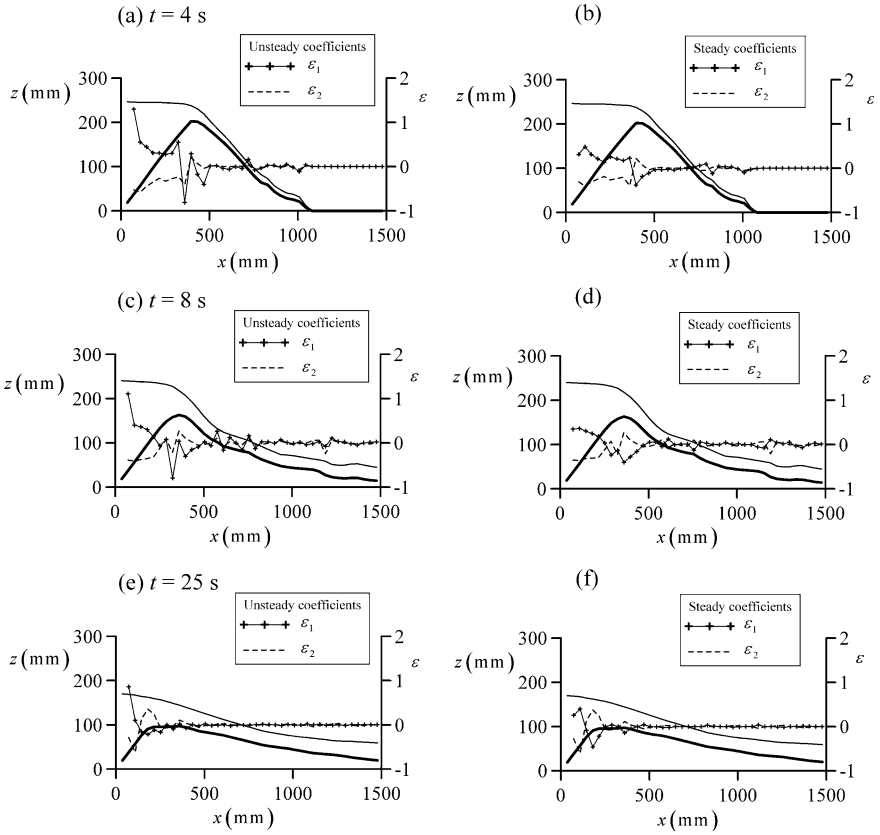

Fig. 5.59 Dike breach Test 51 (Schmocker 2011): height = 0.2 m, crest length = 0.1 m, slope 1:2, sediment diameter = 2 mm, discharge = 6 l/s, channel width = 0.2 m **a**, **c**, **e** Unsteady flow coefficients ε_1 and ε_2 at times t = 4, 8, and 25 s after test start, **b**, **d**, **f** idem but for steady flow coefficients ε_1 and ε_2 (adapted from Castro-Orgaz and Hager 2013)

important contribution of the bed profile, an effect accounted for by $\varepsilon_1(x, t)$. Further, in general, $\varepsilon_1 \neq 0$ and $\varepsilon_2 \neq 0$. Note that only in the tailwater reach, where the flow is definitely supercritical, $\varepsilon_1 = \varepsilon_2 = 0$. In contrast, at the upstream reach and near the crest vicinity, $\varepsilon_1 \neq 0$ and $\varepsilon_2 \neq 0$, and, thus, the SWEs are inappropriate. It explains the discrepancies between the simulated and measured water levels upstream and in the vicinity of the dike crest found by Pontillo et al. (2010). In flows over a curved bed of convex shape, i.e., in the vicinity of the dike crest, the SWE model predicts water levels higher than the experimental data (Sivakumaran et al. 1983). This effect is attributed to the hydrostatic pressure assumption, i.e., the actual dynamic pressure distribution is less than hydrostatic. Boussinesq-type flow equations, in contrast, are able to reproduce a more realistic pressure distribution and water levels for wavy beds (Hager and Hutter 1984a).

The steady flow versions of ε_1 and ε_2, that is,

$$\varepsilon_1 = h\frac{\partial^2 z_b}{\partial x^2} - \frac{\partial h}{\partial x}\frac{\partial z_b}{\partial x}, \quad \varepsilon_2 = h\frac{\partial^2 h}{\partial x^2} - \left(\frac{\partial h}{\partial x}\right)^2, \tag{5.541}$$

were applied to the test data for comparative purposes. The results for the same three instants of time are plotted in Fig. 5.59b, d, f, respectively. Note that the steady approximation to ε_2 does not essentially differ from its unsteady version. However, this is not the case for ε_1, which is clearly above the steady-state version during the initial part of the test. For large time, the unsteady flow coefficients tend to the steady flow versions, as expected. Moreover, note the reduced values of both coefficients as the dike is flattened. In general, $\varepsilon_1 \neq 0$ and $\varepsilon_2 \neq 0$ upstream from the crest zone, with a larger magnitude due to unsteady flow effects during overtopping initiation.

References

Ackers, P., White, W. R., Perkins, J. A., & Harrison, A. J. M. (1978). *Weirs and flumes for flow measurement*. New York: Wiley.

Balmforth, D. J., & Sarginson, E. J. (1983). The effects of curvature in supercritical side weir flow. *Journal of Hydraulic Research, 21*(5), 333–343; *22*(4), 291–298.

Basco, D. R. (1987). Computation of rapidly varied, unsteady free surface flow. In *Water Resources Investigation Report 83-4284*. Reston VA: US Geological Survey.

Bauer, W. J. (1951). The development of the turbulent boundary layer on steep slopes (*Ph.D. thesis*). University of Iowa, Iowa IA.

Bauer, W. J. (1954). Turbulent boundary layer on steep slopes. *Transactions ASCE, 119*, 1212–1233.

Bazin, H. (1885). Expériences sur la propagation des ondes le long d'un cours d'eau torrentueux, et confirmation par ces expériences des formules données par Boussinesq, dans sa théorie du mouvement graduellement varié des fluides (Experiments on wave propagation in torrential flow and confirmation of Boussinesq's equations for gradually-varied fluid flow). *Comptes Rendus, Académie des Sciences, Paris 100*, 1492–1494 (in French).

Bazin, H. (1896). Expériences nouvelles sur l'écoulement par déversoir (Recent experiments on water flow of over weirs). *Annales des Ponts et Chaussées, Série 7, 12*, 645–731 with Plates (in French).

Benjamin, T. B., & Lighthill, M. J. (1954). On cnoidal waves and bores. *Proceedings of the Royal Society London A, 224*, 448–460.

Blalock, M. E., & Sturm, T. W. (1981). Minimum specific energy in compound open channel. *Journal of the Hydraulics Division, ASCE, 107*(6), 699–717.

Bormann, K. (1968). Der Abfluss in Schussrinnen unter Berücksichtigung der Luftaufnahme (Chute flow under consideration of air entrainment). *Bericht 13*, Versuchsanstalt für Wasserbau, Oskar von Miller Institut. Technische Hochschule, München (in German).

Bose, S. K., & Dey, S. (2007). Curvilinear flow profiles based on Reynolds averaging. *Journal of Hydraulic Engineering, 133*(9), 1074–1079.

Bose, S. K., & Dey, S. (2009). Reynolds averaged theory of turbulent shear flows over undulating beds and formation of sand waves. *Physical Review E, 80*(3), 036304–1/036304-9.

Boulanger, A. (1909). *Hydraulique générale (General hydraulics)*. Paris: Octave Doin (in French).

Boussinesq, J. (1871a). Théorie de l'intumescence liquide appelée onde solitaire ou de translation, se propageant dans un canal rectangulaire (Theory of liquid wave referred to as solitary wave or translation wave in a rectangular canal). *Comptes Rendus, Académie des Sciences, Paris, 72*, 755–759; *73*, 256–260; *73*, 1210–1212 (in French).

Boussinesq, J. (1871b). Sur le mouvement permanent varié de l'eau dans les tuyaux de conduite et dans les canaux découverts (On steady, varied flow in conduits and open channels). *Comptes Rendus, Académie des Sciences, Paris, 73*, 34–38; *73*, 101–105 (in French).

Boussinesq, J. (1872). Théorie des ondes et des remous qui se propagent le long d'un canal rectangulaire horizontal, en communiquant au liquide contenu dans ce canal des vitesses sensiblement pareilles de la surface au fond (Theory of waves and backwater propagating in rectangular horizontal canals, generating in the fluid velocities almost identical from the surface to the bottom). *J. Mathématiques Pures et Appliquées Série 2, 17*, 55–108; *Série 2, 18*, 47–52 (in French).

Boussinesq, J. (1877). Essai sur la théorie des eaux courantes (Essay on the theory of flowing water). *Mémoires présentés par Divers Savants á l'Académie des Sciences, Paris, 23*(1), 1–608 (in French).

Bradford, S. F., & Katopodes, N. (1998). Non-hydrostatic model for surface irrigation. *Journal of Irrigation and Drainage Engineering, 124*(4), 200–212.

Brooks, N. (1958). Mechanics of streams with movable beds of fine sand. *Transactions ASCE, 123*, 526–549.

Cain, P., & Wood, I. R. (1981). Measurements of self-aerated flow on a spillway. *Journal of the Hydraulics Division ASCE, 107*(HY11), 1425–1444.

Campbell, F. B., Cox, R. G., & Boyd, M. B. (1965). Boundary layer development and spillway energy losses. *Journal of the Hydraulics Division ASCE, 91*(HY3), 149–163; *91*(HY6), 238–245; *92*(HY1), 107–108; *92*(HY2), 370–378; *92*(HY6), 201–203.

Cantero, F., Castro-Orgaz, O., Garcia, A., Ayuso, J. L., & Dey, S. (2015). Free surface profile of river flows: Can standard energy-based gradually-varied flow computations be pursued? *Journal of Hydrology, 529*(Part3), 1644–1656.

Cassidy, J. J. (1965). Irrotational flow over spillways of finite height. *Journal of the Engineering Mechanics Division ASCE, 91*(EM6), 155–173.

Castro-Orgaz, O. (2009). Hydraulics of developing chute flow. *Journal of Hydraulic Research, 47*(2), 185–194.

Castro-Orgaz, O. (2010a). Steady open channel flows with curved streamlines: The Fawer approach revised. *Environmental Fluid Mechanics, 10*(3), 297–310.

Castro-Orgaz, O. (2010b). Weakly undular hydraulic jump: Effects of friction. *Journal of Hydraulic Research, 48*(4), 453–465.

Castro-Orgaz, O. (2012). Discussion of Overflow characteristics of circular-crested weirs. *Journal of Hydraulic Research, 50*(2), 241–243.

Castro-Orgaz, O. (2013). Potential flow solution for open channel flows and weir-crest overflow. *Journal of Irrigation and Drainage Engineering, 139*(7), 551–559.

Castro-Orgaz, O., & Chanson, H. (2011). Near-critical free-surface flows: Real fluid flow analysis. *Environmental Fluid Mechanics, 11*(5), 499–516.

Castro-Orgaz, O., Giraldez, J. V., & Ayuso, J. L. (2008). Higher order critical flow condition in curved streamline flow. *Journal of Hydraulic Research, 46*(6), 849–853.

Castro-Orgaz, O., & Hager, W. H. (2009). Classical hydraulic jump: Basic flow features. *Journal of Hydraulic Research, 47*(6), 744–754.

Castro-Orgaz, O., & Hager, W. H. (2011a). Observations on undular jump in movable bed. *Journal of Hydraulic Research, 49*(5), 689–692.

Castro-Orgaz, O., & Hager, W. H. (2011b). Vorticity equation for the streamline and the velocity profile. *Journal of Hydraulic Research, 49*(6), 775–783.

Castro-Orgaz, O., & Hager, W. H. (2011c). Turbulent near-critical open channel flow: Serre's similarity theory. *Journal of Hydraulic Engineering, 137*(5), 497–503.

Castro-Orgaz, O., & Hager, W. H. (2011d). Joseph Boussinesq and his theory of water flow in open channels. *Journal of Hydraulic Research, 49*(5), 569–577.

Castro-Orgaz, O., & Hager, W. H. (2011e). Spatially-varied open channel flow equations with vertical inertia. *Journal of Hydraulic Research, 49*(5), 667–675.

Castro-Orgaz, O., & Hager, W. H. (2013). Unsteady Boussinesq-type flow equations for gradually-eroded beds: Application to dike breaches. *Journal of Hydraulic Research, 51*(2), 203–208.

Castro-Orgaz, O., & Hager, W. H. (2014a). Scale effects of round-crested weir flow. *Journal of Hydraulic Research, 52*(5), 653–665.

Castro-Orgaz, O., & Hager, W. H. (2014b). Transitional flow at standard sluice gate. *Journal of Hydraulic Research, 52*(2), 264–273.

Castro-Orgaz, O., Hager, W. H., & Dey, S. (2015). Depth-averaged model for the undular hydraulic jump. *Journal of Hydraulic Research, 53*(3), 351–363.

Chanson, H. (1995). Flow characteristics of undular hydraulic jumps: Comparison with near-critical flows. *Research Report* CH45/95. Brisbane, Australia: Department of Civil Engineering, University of Queensland.

Chanson, H. (1996). Free surface flows with near critical flow conditions. *The Canadian Journal of Civil Engineering, 23*(6), 1272–1284.

Chanson, H. (1997). *Air bubble entrainment in free-surface turbulent shear flows*. London: Academic Press.

Chanson, H. (2004). *The hydraulics of open channel flows: An introduction*. Oxford, UK: Butterworth-Heinemann.

Chanson, H., & Montes, J. S. (1995). Characteristics of undular hydraulic jumps: Experimental apparatus and flow patterns. *Journal of Hydraulic Engineering, 121*(2), 129–144; *123*(2), 161–164.

Chanson, H., & Montes, J. S. (1997). Overflow characteristics of cylindrical weirs. *Research Report CE 154*. Brisbane: Department of Civil Engineering, University of Queensland.

Chaudhry, M. H. (2008). *Open-channel flow* (2nd ed.). New York: Springer.

Chaudhry, M. H., & Bhallamudi, S. (1988). Computation of critical depth in symmetrical compound channels. *Journal of Hydraulic Research, 26*(4), 377–396.

Chen, C. L. (1991). Unified theory on power laws for resistance. *Journal of Hydraulic Engineering, 117*(3), 371–389.

Chow, V. T. (1959). *Open channel hydraulics*. New York, NY: McGraw-Hill.

Craya, A. E., & Delleur, J. W. (1952). An analysis of boundary layer growth in open conduits near critical regime. *Technical Report 1*. New York: Department of Civil Engineering, Columbia University.

Darcy, H., & Bazin, H. (1865). *Recherches hydrauliques (Hydraulic researches)*. Paris: Imprimerie Impériale (in French).

de Oliveira Lemos, F. (1965). A instabilidade da camada limite: Sua influencia na concepcao dos descarregadores das barragens (Instability of boundary layer: Influence on design of dam spillways). *Thesis*, Laboratorio Nacional de Engenharia Civil LNEC, Lisboa (in Portuguese).

Dean, R. B. (1976). A single formula for the complete velocity profile in a turbulent boundary layer. *The Journal of Fluids Engineering, 98*(12), 723–726.

Delleur, J. W. (1955). The boundary layer development on a broad crested weir. In *Proceedings of 4th Midwestern Conference on Fluid Mechanics* (pp. 183–193). Purdue University.

Delleur, J. W. (1957). The boundary layer development in open channels. *Journal of the Engineering Mechanics Division ASCE, 83*(1), 1–24.

Dey, S. (2002). Free overfall in open channels: State-of-the-art review. *Flow Measurement and Instrumentation, 13*(5–6), 247–264.

Dey, S. (2014). *Fluvial hydrodynamics: Hydrodynamic and sediment transport phenomena*. Berlin: Springer.

Dressler, R. F. (1978). New nonlinear shallow flow equations with curvature. *Journal of Hydraulic Research, 16*(3), 205–220.

Dunbabin, R. (1996). Velocity distributions within an undular hydraulic jump. *Bachelor Thesis*. Department of Civil and Mechanic Engineering, University of Tasmania, Hobart, Australia.

Engelund, F. (1971). The solitary sand wave. *Progress Report 24* (pp. 51–54). Copenhagen: Institute of Hydrodynamics and Hydraulic Engineering, Technical University of Denmark.

Engelund, F. (1981). Energy and momentum equation for non-uniform flow. *Series Paper 29.* Copenhagen: Institute of Hydrodynamics and Hydraulic Engineering, Technical University of Denmark.

Engelund, F., & Hansen, E. (1966). Investigations of flow in alluvial streams. *Bulletin 9*, Hydraulic Laboratory, Technical University of Demark, Copenhagen.

Falvey, H. T. (1980). Air water flow in hydraulic structures. *Engineering monograph 41*. Water Resources Technical Publication. U.S. Department of the Interior, U.S. Printing Office, Denver CO.

Falvey, H. T. (1990). Cavitation in chutes and spillways. *Engineering monograph 42*, Water Resources Technical Publication. U.S. Department of Interior, U.S. Printing Office, Denver CO.

Favre, H. (1933). *Contribution à l'étude des courants liquides* (Contribution to the study of liquid flows). Zurich: Rascher (in French).

Fawer, C. (1937). Étude de quelques écoulements permanents à filets courbes (Study of some steady flows with curved streamlines). *Thesis*, La Concorde. Université de Lausanne, Lausanne (in French).

Field, W. G., Lambert, M. F., & Williams, B. J. (1998). Energy and momentum in one-dimensional open channel flow. *Journal of Hydraulic Research, 36*(1), 29–42.

Flamant, A. (1889). Des ondes liquides non périodiques et, en particulier, de l'onde solitaire (On liquid non-periodic waves and particularly, on the solitary wave). *Annales des Ponts et Chaussées, 59*(2), 5–48 (in French).

Flamant, A. (1990). *Hydraulique (Hydraulics)*. Béranger: Paris (in French).

Forchheimer, P. (1914). *Hydraulik (Hydraulics)*. Leipzig: Teubner (in German).

Fuentes-Aguilar, R., & Acuña, E. (1971). Estudio de algunas características del escurrimiento sobre vertederos de arista redondeada mediante la solución numérica de la ecuación de Laplace (Study of some flow features of round-crested weir flow using a numerical solution of the Laplace equation). Publicación SH5. Departamento de Obras Civiles, Facultad de Ciencias Físicas y Matemáticas, Universidad de Chile (in Spanish).

Furuya, Y., & Nakamura, L. (1968). A semi-integrated momentum method for the auxiliary equation. In *Proceedings of Computation of Turbulent Boundary Layers—1968, AFOSR-IFP-STANFORD Conference* (Vol. 1, pp. 235–246).

George, W. K. (2007). Is there a universal log-law for turbulent wall-bounded flows? *Philosophical Transactions of the Royal Society A, 365*, 789–806.

Ghamry, H. K., & Steffler, P. M. (2002). Effects of applying different distribution shapes of velocity and pressure on simulation of curved open channels. *Journal of Hydraulic Engineering, 128*(11), 969–982.

Gotoh, H., Yasuda, Y., & Ohtsu, I. (2005). Effect of channel slope on flow characteristics of undular hydraulic jumps. *Transactions on Ecology and the Environment, 83*(1), 33–42.

Grillhofer, W., & Schneider, W. (2003). The undular hydraulic jump in turbulent open channel flow at large Reynolds numbers. *Physics of Fluids, 15*(3), 730–735.

Hager, W. H. (1981). *Die Hydraulic von Verteilkanälen 1: Theorie der Verteilkanäle* (Hydraulics of distribution channels 1: Theory). (Ph.D. Dissertation. ETH Zurich, Zürich) (in German).

Hager, W. H. (1984). Discussion of The effects of curvature in supercritical side weir flow. *Journal of Hydraulic Research, 22*(4), 291–298.

Hager, W. H. (1985). Critical flow condition in open channel hydraulics. *Acta Mechanica, 54*(3/4), 157–179.

Hager, W. H. (1993). Abfluss über Zylinderwehr (Flow over cylindrical weir). *Wasser und Boden, 44*(1), 9–14 (in German).

Hager, W. H. (1999). *Wastewater hydraulics: Theory and practice*. Berlin: Springer.

Hager, W. H., & Blaser, F. (1998). Drawdown curve and incipient aeration for chute flow. *Canadian Journal of Civil Engineering, 25*(3), 467–473.

Hager, W. H., & Castro-Orgaz, O. (2017). William Froude and the Froude number. *Journal of Hydraulic Engineering* (in press).

Hager, W. H., Edder, O., & Rappaz, J. (1988). Streamline curvature effects in side-channel spillway flow. *Acta Mechanica, 72*(1–2), 95–110.

Hager, W. H., & Gisonni, C. (2003). Henry Bazin: Hydraulician. In G. O. Brown, J. D. Garbrecht, & W. H. Hager (Eds.), *Henry P. G. Darcy and other pioneers in hydraulics*, Philadelphia (pp. 90–115), New York: ASCE.

Hager, W. H., & Hager, K. (1985). Streamline curvature effects in distribution channels. *Proceedings of the IME, 199*(3), 165–172.

Hager, W. H., & Hutter, K. (1984a). Approximate treatment of plane channel flow. *Acta Mechanica, 51*(3–4), 31–48.

Hager, W. H., & Hutter, K. (1984b). On pseudo-uniform flow in open channel hydraulics. *Acta Mechanica, 53*(3–4), 183–200.

Hager, W. H., & Raemy, F. (1997). Joseph Boussinesq (1842–1929), un hydraulicien mathématicien (Joseph Boussinesq, a mathematical hydraulician). *La Houille Blanche, 53* (6), 89–93 (in French).

Hager, W. H., & Schwalt, M. (1994). Broad crested weir. *Journal of Irrigation and Drainage Engineering, 120*(1), 13–26.

Halbronn, G. (1952). Étude de la mise en régime des écoulements sur les ouvrages à forte pente: Application au problème de l'entrainement d'air (Study of flows in steep chutes: Application to the problem of air entrainment). *La Houille Blanche, 7*(1), 21–40; *7*(3), 347–371; *7*(5), 702–722 (in French).

Halbronn, G. (1954). Discussion of Turbulent boundary layer on steep slopes. *Transactions ASCE, 119*, 1234–1240.

Hall, G. W. (1962). Analytical determination of the discharge characteristics of broad-crested weirs using boundary layer theory. *Proceedings of ICE, 22*(2), 177–190.

Harrison, A. J. M. (1967a). Boundary layer displacement thickness on flat plates. *Journal of the Hydraulics Division ASCE, 93*(HY4), 79–91.

Harrison, A. J. M. (1967b). The streamlined broad crested weir. *Proceedings of ICE, 38*(4), 657–678.

Heller, V. (2011). Scale effects in physical hydraulic engineering models. *Journal of Hydraulic Research, 49*(3), 293–306; *50*(2), 246–250.

Henderson, F. M. (1966). *Open channel flow*. New York: MacMillan.

Henry, H. R. (1950). A study of flow from a submerged sluice gate. *M. S. Thesis*. Department of Mechanics and Hydraulics, Iowa City IA: State University of Iowa.

Hosoda, T., Muramoto, Y., & Miyamoto, M. (1997). Bottom shear stress of flows over a wavy bed by using depth averaged flow equations. *Annual Journal of Hydraulics Engineering JSCE, 558* (II-38), 81–89 (in Japanese).

Hosoda, T., & Tada, A. (1994). Free surface profile analysis on open channel flow by means of 1-D basic equations with effect of vertical acceleration. *Annual Journal of Hydraulics Engineering JSCE, 38*, 457–462. (in Japanese).

Hutter, K., & Wang, Y. (2016). *Fluid and thermodynamics 1: Basic fluid mechanics. Series Advances in Geophysical and Environmental Mechanics and Mathematics*. Berlin: Springer.

Isaacs, L. T. (1981). *Effects of laminar boundary layer on a model broad-crested weir* (Research Report CE28). Department of Civil Engineering, Brisbane, University of Queensland.

Iwasa, Y. (1955). Undular jump and its limiting conditions for existence. In *Proceedings of 5th Japan National Congress Applied Mechanics* (Vol. II, No. 14, pp. 315–319).

Iwasa, J., & Kennedy, J. (1968). Free surface shear flow over a wavy bed. *Journal of the Hydraulics Division ASCE, 94*(HY3), 431–454.

Jaeger, C. (1956). *Engineering fluid mechanics*. Glasgow: Blackie & Son.

Jin, Y. C., & Li, B. (1996). The use of a one-dimensional depth-averaged moment of momentum equation for the nonhydrostatic pressure condition. *Canadian Journal of Civil Engineering, 23* (1), 150–156.

Jurisits, R., & Schneider, W. (2012). Undular hydraulic jumps arising in non-developed turbulent flows. *Acta Mechanica, 223*(8), 1723–1738.

Keller, R. J., & Rastogi, A. K. (1975). Prediction of flow development on spillways. *Journal of the Hydraulics Division ASCE, 101*(9), 1171–1184.

Keller, R. J., & Rastogi, A. K. (1977). Design chart for prediction critical point on spillways. *Journal of the Hydraulics Division ASCE 103*(HY12), 1417–1429; *104*(HY9), 1401; *105*(HY6), 664.

Khan, A. A., & Steffler, P. (1996a). Physically-based hydraulic jump model for depth-averaged computations. *Journal of Hydraulic Engineering, 122*(10), 540–548.

Khan, A. A., & Steffler, P. M. (1996b). Vertically averaged and moment equations model for flow over curved beds. *Journal of Hydraulic Engineering, 122*(1), 3–9.

Kim, D.-H., Lynett, P. J., & Socolofsky, S. (2009). A depth-integrated model for weakly dispersive, turbulent, and rotational fluid flows. *Ocean Modelling, 27*(3), 198–214.

Kironoto, B. A., & Graf, W. H. (1994). Turbulence characteristics in rough uniform open channel flow. *Water, Maritime and Energy ICE, 106*(4), 333–344.

Kolkman, P. A. (1984). Considerations about the accuracy of discharge relations of hydraulic structures and the use of scale models for their calibration. In H. Kobus (Ed.), *Symposium on scale effects in modelling hydraulic structures*, *Esslingen, Germany 2.1* (pp. 1–12), Esslingen: Akademie.

Kolkman, P. A. (1994). Discharge relationships and component head losses for hydraulic structures. *Discharge characteristics, IAHR Hydraulic Structures Design Manual, 8*(3), 55–151 (A.A. Balkema, Rotterdam).

Korteweg, D. J., & de Vries, G. (1895). On the change of form of long waves advancing in a rectangular canal, and on a new type of long stationary waves. *Philosophical Magazine Series, 5*(39), 422–443.

Lakshmana Rao, N. S., & Jagannadha Rao, M. V. (1973). Characteristics of hydrofoil weirs. *Journal of the Hydraulics Division ASCE, 99*(HY2), 259–283; *100*(HY7), 1076–1079; *100* (HY12), 1836–1837.

Lenau, C. W. (1967). Potential flow over spillways at low heads. *Journal of the Engineering Mechanics Division ASCE, 93*(EM3), 95–107.

Liggett, J. A. (1994). *Fluid mechanics*. New York: McGraw-Hill.

Madsen, P. A., & Svendsen, I. A. (1979). *On the form of the integrated conservation equations for waves in the surf zone* (*Progress Report 48,* pp. 31–39). TU Denmark: Institute of Hydrodynamics and Hydraulic Engineering.

Madsen, P. A., & Svendsen, I. A. (1983). Turbulent bores and hydraulic jumps. *Journal of Fluid Mechanics, 129*, 1–25.

Mandrup-Andersen, V. (1978). Undular hydraulic jump. *Journal of Hydraulics Division, ASCE, 104*(HY8), 1185–1188; *105*(HY9), 1208–1211.

Marchi, E. (1963). Contributo allo studio del risalto ondulato (Contribution to the study of undular jumps). *Giornale del Genio Civile, 101*(9), 466–476 (in Italian).

Matthew, G. D. (1961). The influence of curvature, surface tension and viscosity on flow over round-crested weirs. *Ph.D. Thesis*. University of Aberdeen, Aberdeen UK.

Matthew, G. D. (1963). On the influence of curvature, surface tension and viscosity on flow over round-crested weirs. *Proceedings of ICE, 25*(4), 511–524; *28*(4), 557–569.

Matthew, G. D. (1968). Discussion of Potential flow over spillways at low heads. *Journal of the Engineering Mechanics Division, 94*(1), 354–359.

Matthew, G. D. (1991). Higher order one-dimensional equations of potential flow in open channels. *Proceedings of ICE, 91*(3), 187–201.

Maxwell, W. H., & Weggel, R. (1969). Surface tension in Froude models. *Journal of the Hydraulics Division ASCE, 95*(HY2), 677–701.

McCowan, J. (1891). On the solitary wave. *Philosophical Magazine*, *Series 5*(32), 45–58.

McCowan, J. (1894). On the highest wave of permanent type. *Philosophical Magazine*, *Series 5*(38), 351–358.

Miller, W. A., & Yevjevich, V. (1975). *Unsteady flow in open channels 3*: *Bibliography*. Water Resources Publications, Fort Collins CO.

Molls, T., & Chaudhry, M. H. (1995). Depth averaged open channel flow model. *Journal of Hydrologic Engineering, 121*(6), 453–465.

Montes, J. S. (1970). Flow over round-crested weirs. *L'Energia Elettrica, 47*(3), 155–164.

Montes, J. S. (1986). A study of the undular jump profile. In *9th Australasian Fluid Mechanics Conference* (pp. 148–151). Auckland.

Montes, J. S. (1992). Potential flow analysis of flow over a curved broad crested weir. In *11th Australasian Fluid Mechanics Conference* (pp. 1293–1296). Auckland.

Montes, J. S. (1994). Potential flow solution to the 2D transition form mild to steep slope. *Journal of Hydrologic Engineering, 120*(5), 601–621; *121*(9), 681–682.

Montes, J. S. (1998). *Hydraulics of open channel flow*. Reston VA: ASCE Press.

Montes, J. S., & Chanson, H. (1998). Characteristics of undular hydraulic jumps: Results and calculations. *Journal of Hydrologic Engineering, 124*(2), 192–205.

Moss, W. D. (1972). Flow separation at the upstream edge of a square-edged broad-crested weir. *Journal of Fluid Mechanics, 52*, 307–320.

Mostkow, M. A. (1957). Sur le calcul des grilles de prise d'eau (On the computation of bottom outlets). *La Houille Blanche,12*(4), 570–580 (in French).

Naheer, E. (1978). Laboratory experiments with solitary wave. *Journal of Waterway, Port, Coastal, and Ocean Engineering, 104*(4), 421–436.

Nasser, M. S., Venkatamaran, P., & Ramamurthy, A. S. (1980a). Curvature corrections in open channel flow. *The Canadian Journal of Civil Engineering, 7*(3), 421–431.

Nasser, M. S., Venkatamaran, P., & Ramamurthy, A. S. (1980b). Flow in a channel with a slot in the bed. *Journal of Hydraulic Research, 18*(4), 359–367.

Naudascher, E. (1987). *Hydraulik der Gerinne und Gerinnebauwerke* (Hydraulics of channels and canal structures). Springer, Wien (in German).

Naudascher, E. (1991). Hydrodynamic forces. *IAHR Hydraulic Structures Design Manual 3*. Rotterdam: A.A. Balkema.

Noseda, G. (1956). Correnti permanenti con portata progressivamente decrescente, defluenti su griglie di fondo (Steady flows with spatially-decreasing discharge deflected by bottom outlets). *L' Energia Elettrica, 33*(6), 565–581 (in Italian).

Ohtsu, I., Yasuda, Y, & Awazu, S. (1990). *Free and submerged hydraulic jumps in rectangular channels* (Report 35, pp. 1–50). Tokyo, Japan: Research Institute of Science and Technology, Nihon University.

Ohtsu, I., Yasuda, Y., & Gotoh, H. (2001). Hydraulic condition for undular jump formations. *Journal of Hydraulic Research, 39*(2), 203–209; *40*(3), 379–384.

Ohtsu, I., Yasuda, Y., & Gotoh, H. (2003). Flow conditions of undular hydraulic jumps in horizontal rectangular channels. *Journal of Hydraulic Engineering, 129*(12), 948–955.

Paterson, D. A., & Apelt, C. (1988). *Depth-averaged equations for turbulent free surface flows* (Resolution Report 100). Brisbane, Australia: Department of Civil Engineering, University of Queensland.

Pfister, M., Battisacco, E., De Cesare, G., & Schleiss, A. J. (2013). Scale effects related to the rating curve of cylindrically crested piano key weirs. In *2nd International Workshop on Labyrinth and Piano Key Weirs Paris, France* (pp. 73–82).

Pontillo, M., Schmocker, L., Greco, M., & Hager, W. H. (2010). 1D numerical evaluation of dike erosion due to overtopping. *Journal of Hydraulic Research, 48*(5), 573–582.

Raiford, J. P., & Khan, A. A. (2013). Turbulence schemes for modelling a submerged hydraulic jump. Engineering and Computational Mechanics, *Proceeding of ICE, 166*(EM1), 40–51.

Ramamurthy, A. S., & Vo, N. D. (1993a). Application of Dressler theory to weir flow. *Journal of Applied Mechanics, 60*(1), 163–166.

Ramamurthy, A. S., & Vo, N. D. (1993b). Characteristics of circular-crested weirs. *Journal of Hydraulic Engineering, 119*(9), 1055–1062.

Ramamurthy, A. S., Vo, N. D., & Balachandar, R. (1994). A note on irrotational curvilinear flow past a weir. *The Journal of Fluids Engineering, 116*(2), 378–381.

Rastogi, A. K., & Rodi, W. (1978). Predictions of heat and mass transfer in open channels. *Journal of the Hydraulics Division, ASCE, 104*(HY3), 397–420.

Rayleigh, L. (1876). On waves. *Philosophical Magazine and Journal of Science Series 5, 1*, 257–279.

Reinauer, R., & Hager, W. H. (1995). Non-breaking undular hydraulic jump. *Journal of Hydraulic Research, 33*(5), 1–16; *34*(2), 279–287; *34*(4), 567–573.

Rodi, W. (1993). *Turbulence models and their application in hydraulics* (3rd ed.). Balkema, Rotterdam: IAHR Monograph.

Rodi, W. (1995). Impact of Reynolds-average modelling in hydraulics. *Proceedings of the Royal Society of London A, 451*, 141–164.

Rouse, H. (1938). *Fluid mechanics for hydraulic engineers*. New York: McGraw-Hill.

Rouse, H., & Ince, S. (1957). *History of hydraulics*. New York: Dover.

Rouse, H., Siao, T. T., & Nagaratnam, S. (1959). Turbulence characteristics of the hydraulic jump. *Transaction ASCE, 124*, 926–966.

Russell, J. S. (1837). Report of the Committee on waves. *Report British Association for the Advancement of Science 7*, 417–439; *7*, 463–496 (with Plates).

Russell, J. S. (1845). Report on waves. *Report British Association for the Advancement of Science 14*, 311–390 (with Plates).

Saint-Venant, A. B. de (1885). Mouvement des molécules de l'onde dite solitaire, propagée à la surface de l'eau d'un canal (The movement of molecules of the wave referred to as solitary, propagating on the water surface of a canal). *Comptes Rendus, Académie des Sciences, Paris 101*, 1101–1105; *101*, 1215–1218; *101*, 1445–1447 (in French).

Sander, J., & Hutter, K. (1991). On the development of the theory of the solitary wave: A historical essay. *Acta Mechanica, 86*, 111–152.

Sarginson, E. J. (1972). The influence of surface tension on weir flow. *Journal of Hydraulic Research, 10*(4), 431–445.

Sarginson, E. J. (1984). Scale effects in model tests on weir. In H. Kobus (Ed.), *Symposium on Scale Effects in Modelling Hydraulic Structures, Esslingen, Germany* (Part 3, No. 3, pp. 1–4). Esslingen: Techn. Akademie.

Schlichting, H., & Gersten, K. (2000). *Boundary layer theory*. Berlin, Germany: Springer.

Schmocker, L. (2011). Hydraulics of dike breaching. *Dissertation ETH 19983*. Zürich, Switzerland: ETH Zurich.

Schmocker, L., & Hager, W. H. (2009). Modelling dike breaching due to overtopping. *Journal of Hydraulic Research, 47*(5), 585–597.

Schneider, W. (2013). The solitary wave in turbulent open-channel flow. *Journal of Fluid Mechanics, 726*, 137–159.

Schneider, W., Jurisits, R., & Bae, Y. S. (2010). An asymptotic iteration method for the numerical analysis of near-critical free-surface flows. *Journal of Heat and Fluid Flow, 31*(6), 1119–1124.

Serre, F. (1953). Contribution à l'étude des écoulements permanents et variables dans les canaux (Contribution to the study of steady and unsteady channel flows). *La Houille Blanche, 8*(6–7), 374–388; *8*(12), 830–887 (in French).

Silberman, E. (1980). Boundary layers in developing open channel flow. *Journal of the Hydraulics Division, ASCE*, *106*(7), 1237–1241.

Sivakumaran, N. S., Tingsanchali, T., & Hosking, R. J. (1983). Steady shallow flow over curved beds. *Journal of Fluid Mechanics, 128*, 469–487.

Steffler, P. M., & Jin, Y. C. (1993). Depth averaged and moment equations for moderately shallow free surface flow. *Journal of Hydraulic Research, 31*(1), 5–17.

Stokes, G. G. (1847). Report on recent researches in hydrodynbamics. *Report, British Association for the Advancement of Science, 16*, 1–20.

Sturm, T. W. (2001). *Open channel hydraulics*. New York: McGraw-Hill.

Sturm, T. W., & Sadiq, A. (1996). Water surface profiles in compound channel with multiple critical depths. *Journal of Hydraulic Engineering, 122*(12), 703–709.

Svedsen, I. A., Veeramony, J., Bakunin, J., & Kirby, J. T. (2000). The flow in weak turbulent hydraulic jumps. *Journal of Fluid Mechanics, 418*, 25–57.

Tison, L. J. (1950). Le déversoir épais (Broad-crested weir). *La Houille Blanche, 5*(4), 426–439 (in French).

Tjerry, S., & Fredsøe, J. (2005). Calculation of dune morphology. *Journal of Geophysical Research, 110*, F04013 (13 pages).

Varshney, D. V. (1977). Model scale and the discharge coefficient. *Water Power and Dam Construction, 29*(4), 48–52.

Venkatamaran, P., Nasser, M. S., & Ramamurthy, A. S. (1982). Dynamic equations for steady spatially-varied open channel flow: A critical review. *Advanced Water Resources, 5*(2), 66–72.

Vierhout, M. M. (1973). On the boundary layer development in rounded broad-crested weirs with a rectangular control section. *Resolution Report 3*. Laboratory of Hydraulics and Catchment Hydrology, Agricultural University, Wageningen NL.

White, F.M. (1991). *Viscous fluid flow*. New York, NY: McGraw-Hill.

White, F. M. (2003). *Fluid mechanics*. New York, NY: McGraw-Hill.

Whitham, G. B. (1974). *Linear and non-linear waves*. New York, NY: Wiley.

Wilkinson, D. L. (1974). Free surface slopes at controls in channel flow. *Journal of the Hydraulics Division, ASCE, 100*(HY8), 1107–1117.

Wood, I. R. (1991). Air entrainment in free-surface flows. *IAHR Hydraulic Structures Design Manual 4*. IAHR, Delft NL.

Wood, I. R., Ackers, P., & Loveless, J. (1983). General method for critical point on spillways. *Journal of Hydraulic Engineering, 109*(2), 308–312.

Yen, B. C. (1971). Spatially varied open-channel flow equations. *WRC Research Report 51*. University of Illinois, Champaign IL.

Yen, B. C. (1973). Open-channel flow equations revisited. *Journal of the Hydraulics Division, ASCE, 99*(5), 979–1009; *100*(HY5), 1055–1060; *101*(HY4), 485–488.

Yen, B. C. (1975). Further study on open-channel flow equations. *Sonderforschungsbereich SFB* 80/T/49. Universität Karlsruhe, Karlsruhe.

Yen, B. C. (2002). Open channel flow resistance. *Journal of Hydraulic Engineering, 128*(1), 20–39.

Yen, B. C., & Wenzel, H. G. (1970). Dynamic equation for steady spatially-varied flow. *Journal of the Hydraulics Division, ASCE, 96*(3), 801–814.

Younus, M., & Chaudhry, M. H. (1994). A depth-averaged k-ε turbulence model for the computation of free-surface flow. *Journal of Hydraulic Research, 32*(3), 415–444.

Chapter 6
Granular Flows

Roman Symbols

c	Celerity (m/s)
C	Constant of integration (m)
$\mathbf{F}$	Vector of fluxes in the x-direction (m^2/s, m^3/s^2)
F_o	Froude number of undisturbed flow (–)
$\mathbf{g}$	Gravity vector (m/s^2)
g	Gravity acceleration (m/s^2)
g'	Enhanced gravity acceleration (m/s^2)
h	Flow depth normal to channel bed (m)
h_c	Critical flow depth (m)
h_o	Undisturbed flow depth (m)
K	Earth yield coefficient (–)
K_{ac}	Active earth yield coefficient (–)
K_{pas}	Passive earth yield coefficient (–)
M	Momentum function (m^2)
M_o	Momentum function in moving axes (m^2)
N	Number of constituents in a mixture (–)
q	Unit discharge (m^2/s)
$\mathbf{S}$	Vector of source terms (m/s, m^2/s^2)
t	Time (s)
$\mathbf{T}$	Stress tensor (N/m^2)
u	Velocity in the x-direction (m/s)
U	Depth-averaged flow velocity in the x-direction (m/s)
$\mathbf{U}$	Vector of conserved variables (m, m^2/s)
$\mathbf{V}_\beta$	Constituent velocity (m/s)
$\mathbf{V}_{\text{bar}}$	Density weighted or barycentric velocity (m/s)
w	Velocity in the z-direction (m/s)
$\overline{w}$	Depth-averaged velocity in the vertical direction (m/s)
x	Coordinate along the channel bed (m)
x_o	Characteristic x-coordinate in solitary wave problem (m)
X	Coordinate along the channel bed in moving system of reference (m)
y	Dimensionless flow depth (–)
$y_{\max}$	Maximum value of y (–)

© Springer International Publishing AG 2017

O. Castro-Orgaz and W.H. Hager, *Non-Hydrostatic Free Surface Flows*,
Advances in Geophysical and Environmental Mechanics and Mathematics
DOI 10.1007/978-3-319-47971-2_6

Y Relative variation of y (–)
z Coordinate normal to channel bed (m)
z_b Bed vertical elevation (m)

Greek Symbols

α Coefficient of dispersion term (–)
β Identifier of the constituent (–)
ζ Dimensionless x-coordinate using h_c (–)
θ Angle of bottom with horizontal (rad)
λ Parameter (–)
ρ Mixture density (kg/m^3)
ρ_β Constituent density (N/m^3)
$\widetilde{\rho_\beta}$ Mass density of the pure constituent β (N/m^3)
$\widehat{\rho}_\beta$ Mass production rate of constituent β (kg/s/m^3)
τ_{ij} Stress in continuum medium, with $(i, j) = (x, z)$ (N/m^2)
ϕ_{int} Internal friction angle (rad)
ϕ_{bed} Bed friction angle (rad)
χ Dimensionless x-coordinate using x_o (–)

Subindex

b With reference to conditions at the basal plane

6.1 Introduction

Many natural or man-made disasters are caused by mass movement all over the earth's surface. Mass movement types range from rock avalanches, for which the fluid pore pressure is negligible, to saturated debris flow, where the fluid enhances mass displacement (Iverson 1997; Iverson and Denlinger 2001). Physical mathematical models for mass movement provide a solid foundation to investigate the behavior of geophysical flows (Iverson 2014). These models are based on mass and momentum conservation equations using the continuum mechanics approach. Mass and momentum conservation equations have been in use to model water flows for more than a century, since Saint-Venant presented his classic depth-averaged water flow equations. This mathematical tool is relatively new in debris flow modeling, however. The simplest model for rapid flow of debris masses was introduced by Savage and Hutter (1989, 1991), who developed depth-averaged mass and momentum conservation equations for the one-phase grain case. Their theory [now called the Savage–Hutter (SH) equations] set up a new perspective into the

dynamics of granular materials.[1] Fluidized granular masses, common in nature, are often influenced by the fluid pore pressure (Iverson 1997, 2005, 2014; Savage and Iverson 2003; Pudasaini et al. 2005b). Iverson (1997) presented the mixture mass and momentum equations for binary solid–fluid mixtures, but simplified this concept later by identifying the constituent material velocities and reducing the momentum balances to a single balance of momentum for the mixture as a whole; this led to an explicit account of the pore pressure as a significant dynamic agent, but ignored the solid–fluid interaction force (Iverson and Denlinger 2001). The analogous approach was also taken by Pudasaini et al. (2005b) within a curvilinear coordinate setting. An early mixture concept for rapid debris flows was suggested by Iverson (1997). It was, however, employed in a rapid shear flow context with higher generality, i.e., without imposing the assumption of vanishing relative slip of the constituents as done by Iverson and Denlinger (2001). These more general mixture settings have been described, among others, e.g., by Pelanti et al. (2008), Pitman and Lee (2005), Pailha and Pouliquen (2009), Pudasaini (2011), and Luca et al. (2009b). Applications of two-layer mixture formulations are proposed by Luca et al. (2009c, 2012), and by Hutter and Luca (2012).

These formulations demonstrate the considerable advantage of the mixture formulation over the single constituent concept, as only they allow for proper parameterizations of erosion and deposition processes and mass flow of the solid and fluid constituents across interior interfaces. Moreover, it is only in the context of mixture formulations that the constituent interaction forces are accounted for. Current mixture flow models for flow over three-dimensional (3D) terrain are based on depth-averaged mass and momentum conservation equations to gain computational efficiency. Their stress tensor is defined using a Coulomb-like proportionality between shear and normal stresses (Bagnold 1954; Hungr and Morgenstern 1984; Savage and Hutter 1989; Iverson and Denlinger 2001; Hunt et al. 2002). Denlinger and Iverson (2001) developed a depth-averaged model on a curvilinear reference system following basal topography, as introduced by Hutter and Savage (1988) and Savage and Hutter (1989, 1991) and adopted to complex surfaces by Gray et al. (1999) and Wieland et al. (1999). The model was a generalization to 3D terrain and fluidized masses of the SH model (1989, 1991). The basal curvilinear reference system corresponds to that introduced by Dressler (1978) to analyze water waves.

[1]It was elaborated on and generalized by Hutter and Koch (1991), Hutter et al. (1993), Iverson et al. (1997), Gray et al. (1999), Denlinger and Iverson (2001), Iverson and Denlinger (2001), Iverson and Vallance (2001), Pudasaini and Hutter (2003), Pudasaini et al. (2003, 2005a, b, 2008), Wang et al. (2004), Chiou et al. (2005), Hutter (2005), Hutter et al. (2005), Luca et al. (2009a, b, c, 2012), Hutter and Luca (2012), and Wieland et al. (1999). Hutter (1996) and Pudasaini and Hutter (2007) summarized the state-of-the-art and further scrutinized and interpreted alternative formulations, e.g., by McDougall and Hungr (2003, 2004, 2005). Formulations for a gravity-driven viscous fluid model in curvilinear coordinates following the basal topography were introduced by Bouchut and Westdickenberg (2004) with follow-up publications on SH-type formulations by Luca et al. (2009a, b), and Kuo et al. (2009).

The transformation of the mass and momentum equations to basal-fitted coordinates enhances the latter equations by including the centripetal acceleration, which implies a non-hydrostatic pressure normal to the terrain surface. Hutter and Savage (1988), Gray et al. (1999), Iverson and Denlinger (2001), Mangeney-Castelnau et al. (2003), and Hutter et al. (2005) presented solutions similar to those of Saint-Venant in this reference system, some neglecting centripetal accelerations and assuming isotropic normal stresses. The basal curvilinear coordinates for the deduction of depth-averaged conservation equations of mass and momentum involve the determination of curvatures over highly irregular and rapidly changing terrain, a challenging task.

A crucial aspect of flow over natural terrain is that the vertical velocity component is nonzero and of magnitude comparable to the hydrostatic pressure (Iverson 2005, 2014; Andreotti et al. 2013). Consideration of such flows in a Cartesian framework was done by Denlinger and Iverson (2004), Castro-Orgaz et al. (2015), and Hutter and Castro-Orgaz (2016) for describing dry avalanches of granular materials, whereas Iverson and Ouyang (2015) reformulated depth-integrated models for erosive flows introducing jump conditions across the interface between a static bed and the dynamic flow layer subtracting/depositing sediments above it. Denlinger and Iverson (2004) presented an approximate method by introducing a mean value of the vertical acceleration in the momentum equations, estimated from a mean vertical velocity derived from kinematic boundary conditions at the free and basal surfaces. This acceleration was then coupled with the gravity acceleration to enhance the system of equations, assuming a linear distribution for the stresses in the vertical direction. Iverson (2014) stated that simplifying vertical velocity components causes a loss of accuracy in the momentum estimation of the mass flow. He stressed that efforts to correct the effect of the neglected or approximated momentum are only at the start in debris flow modeling, despite the long-time tradition in water flow modeling. Additionally, Andreotti et al. (2013) have indicated that depth-averaged models need to include vertical acceleration effects, given their fundamental role in mass flow over natural terrain. Castro-Orgaz et al. (2015) explored the inclusion of vertical acceleration effects in the momentum equations. The general conservation laws were, therefore, presented in Chap. 2 as general evolution equations of the velocity field and stress tensor; they are of use here.

In this chapter, 1D flows of dry granular avalanches are considered. Non-hydrostatic effects are evaluated using simplified analytical solutions obtained from the 1D depth-averaged equations. While exact analytical solutions of simplified forms of the governing equations do not necessarily represent real cases, they provide insights into specific model aspects, as the treatment of dispersive effects. For this purpose, the analytical solutions of the solitary wave and the free fall of dry granular mass flows are developed.

6.2 Mixture Flow Equations

For a mixture, say a solid–fluid debris flow, the balance of mass for the mixture velocity is often defined as solenoidal, and this custom will be followed here as well, but explain its restrictions. Consider a mixture of a number N of constituents, for which the constituent mass balance law has the form (Hutter et al. 2014)

$$\frac{\partial \rho_\beta}{\partial t} + \operatorname{div}\left(\rho_\beta \mathbf{V}_\beta\right) = \hat{\rho}_\beta, \quad \beta = 1, 2, \ldots, N. \tag{6.1}$$

The corresponding mass balance for the mixture is given by

$$\frac{\partial \rho}{\partial t} + \rho \operatorname{div}(\mathbf{V}_{\text{bar}}) = 0, \quad \rho = \sum_\beta \rho_\beta, \quad \rho \mathbf{V}_{\text{bar}} = \sum_\beta \rho_\beta \mathbf{V}_\beta. \tag{6.2}$$

Here, β is the identifier of the constituent and $(\rho_\beta, \mathbf{V}_\beta)$ are the constituent density, referred to as *partial density*, and the velocity. The mixture density and velocity are $(\rho, \mathbf{V}_{\text{bar}})$, respectively, with $\mathbf{V}_{\text{bar}}$ as the density weighted or *barycentric velocity*. The quantity $\hat{\rho}_\beta$ is the mass production rate of constituent β.

In solid–fluid mixtures (e.g., of immiscible components), the volume fraction v_β is that part of the volume of a representative volume element which is filled by constituent β. If $\widetilde{\rho_\beta}$ is the true density, i.e., the mass density of the pure constituent β, then $\rho_\beta = v_\beta \widetilde{\rho_\beta}$. Consider a mixture satisfying the following conditions:

(i) All components are density-preserving, $\widetilde{\rho_\beta} = \text{const.}$, for all β.
(ii) Mixture is saturated: $\sum_\beta v_\beta = 1$, i.e., the constituents fill the entire space.
(iii) All mass production rates are zero, $\hat{\rho}_\beta = 0$.

We note and stress this fact that for a mixture, of which all constituents are density-preserving, the mixture must not be volume preserving. For a mixture satisfying these constraints, the mass balance (6.1) can be divided by $\widetilde{\rho_\beta}$ to yield

$$\frac{\partial v_\beta}{\partial t} + \operatorname{div}\left(v_\beta \mathbf{V}_\beta\right) = 0. \tag{6.3}$$

After summation over all β, because of saturation,[2] $\sum_\beta v_\beta = 1$,

$$\operatorname{div}\left(\sum_\beta v_\beta \mathbf{V}_\beta\right) = 0. \tag{6.4}$$

[2]Non-saturated or partly-saturated mixtures possess pores which are not filled with matter. They are simply empty space. For these $\sum_\beta v_\beta < 1$, where β is summed over all constituents having mass.

In analogy to the barycentric velocity Eq. (6.2), one may now also define the *volume-weighted* mixture velocity as

$$\mathbf{V}_{\text{vol}} = \sum_{\beta} v_{\beta} \mathbf{V}_{\beta}. \tag{6.5}$$

For mixtures satisfying constraints (i)–(iii), the volume-weighted mixture velocity is solenoidal, therefore. This is a convenient property and is the likely reason why some modelers in geophysical mass flows use it as the mixture velocity (e.g., Iverson 1997, 2005, or Andreotti et al. 2013).

With $\mathbf{T}$ as the stress tensor and $\mathbf{g}$ as the gravity acceleration vector, the momentum equations read

$$\rho \frac{\mathrm{d}\mathbf{V}_{\text{bar}}}{\mathrm{d}t} = -\text{div}\mathbf{T} + \rho\mathbf{g}. \tag{6.6}$$

This form applies if the mixture velocity is defined as barycentric velocity, whose field is not solenoidal (the pore space can still vary with space and time). Pore space variations, however, are ignored in ensuing developments.

6.3 Depth-averaged Equations for Dry Granular Flows

6.3.1 1D Savage–Hutter Theory Down an Inclined Plane

Consider the idealized case[3] of flow of a continuum dry granular material of constant density ρ moving across an inclined plane terrain (Fig. 6.1), without erosion/deposition of solid material at the basal plane. The 2D solenoidal mass momentum conservation in the terrain-fitted coordinates (x, z) of Fig. 6.1 is, with (u, w) as the velocity components in the (x, z) directions (Savage and Hutter 1989; Iverson 1997; Andreotti et al. 2013; Hutter et al. 2014),

$$\frac{\partial u}{\partial x} + \frac{\partial w}{\partial z} = 0. \tag{6.7}$$

[3]While this case is in fact too idealistic to be in conformity with many real geophysical flows, it is considered illustrative for the educational objective pursued here, namely to highlight the role of non-hydrostaticity in the depth-averaged equations. To help modelers to produce advanced systems of vertically integrated conservation laws, the general layer-integrated equations for the flow of a mixture of fluid and sediments with arbitrary mass transfers across the interfaces bounding the layer are presented in Appendix J, as evolution equations of the stress tensor and the velocity field, following Hutter et al. (2014), Castro-Orgaz et al. (2015), and Iverson and Ouyang (2015). These form the basis to produce multilayer models of two-phase flows over arbitrary 3D terrain.

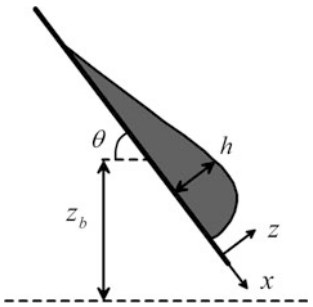

Fig. 6.1 Definition sketch of granular mass flow down an inclined plane

The corresponding momentum equations in the x- and z-directions are from Eq. (6.6), after using Eq. (6.7) (see Chap. 2)

$$\frac{\partial u}{\partial t}+\frac{\partial u^2}{\partial x}+\frac{\partial}{\partial z}(uw)=g\sin\theta-\frac{1}{\rho}\left(\frac{\partial \tau_{xx}}{\partial x}+\frac{\partial \tau_{xz}}{\partial z}\right), \tag{6.8}$$

$$\frac{\partial w}{\partial t}+\frac{\partial}{\partial x}(uw)+\frac{\partial w^2}{\partial z}=-g\cos\theta-\frac{1}{\rho}\left(\frac{\partial \tau_{zx}}{\partial x}+\frac{\partial \tau_{zz}}{\partial z}\right). \tag{6.9}$$

Here, θ is the inclination angle of the slope (Fig. 6.1), and τ denotes the stress components in the x–z plane, with the usual meaning for each subindex (see Chap. 2). Using the depth-averaging technique extensively described in Chap. 2,[4] and assuming zero stresses at the material free surface and that mixture velocity in the x-direction is correctly described by the depth-averaged flow velocity U, Eqs. (6.7)–(6.9) produce the depth-averaged system [see development of Eqs. (2.9), (2.14) and (2.19)]

$$\frac{\partial h}{\partial t}+\frac{\partial (Uh)}{\partial x}=0, \tag{6.10}$$

$$\frac{\partial}{\partial t}(Uh)+\frac{\partial}{\partial x}\left(U^2h\right)=gh\sin\theta-\frac{1}{\rho}\left[\frac{\partial}{\partial x}\int_0^h \tau_{xx}\mathrm{d}z-(\tau_{xz})_b\right], \tag{6.11}$$

$$\tau_{zz}=\rho g(h-z)\cos\theta-\rho w^2+\rho\frac{\partial}{\partial t}\int_z^h w\mathrm{d}z'+\rho\frac{\partial}{\partial x}\left[U\int_z^h w\mathrm{d}z'\right]+\int_z^h\frac{\partial \tau_{zx}}{\partial x}\mathrm{d}z'. \tag{6.12}$$

From Eq. (6.7), the bed-normal velocity profile is after integration [see development of Eq. (2.37)]

[4]Depth-averaging methods are also explained in detail in Appendix J.

$$w = -\frac{\partial U}{\partial x} z. \tag{6.13}$$

The streamwise momentum Eq. (6.11) can be rewritten as

$$\frac{\partial}{\partial t}(Uh) + \frac{\partial}{\partial x}\left(U^2 h + \int_0^h \frac{\tau_{xx}}{\rho} \mathrm{d}z\right) = gh\sin\theta + \frac{(\tau_{xz})_b}{\rho}. \tag{6.14}$$

For a Mohr–Coulomb yield criterion of the granular mass with an angle of internal friction ϕ_{int}, horizontal and vertical stresses are related by

$$\tau_{xx} = K\tau_{zz}. \tag{6.15}$$

Here, the earth coefficient K is given by the active pressure coefficient if the mass is under expansion and by the passive pressure coefficient if the mass is under compression,

$$K = K_{\text{act}}, \quad \text{if } \partial U/\partial x > 0, \quad K = K_{\text{pas}}, \quad \text{if } \partial U/\partial x < 0, \tag{6.16}$$

with

$$K_{\text{pas/act}} = 2\sec^2\phi_{\text{int}}\left\{1 \pm \left(1 - \cos^2\phi_{\text{int}}\sec^2\phi_{\text{bed}}\right)^{1/2}\right\} - 1. \tag{6.17}$$

The sign "+" in Eq. (6.17) is used for K_{pas} and the sign "−" for K_{act}.

Using Eq. (6.15), the momentum function in the x-direction down the plane is

$$M = U^2 h + \frac{1}{\rho} K \int_0^h \tau_{zz} \mathrm{d}z. \tag{6.18}$$

If the effects of the bed-normal velocity w and the stress integral are neglected in Eq. (6.12), stresses are still non-hydrostatic, given the bottom slope angle effect (Appendix H). The simplified form is written thus as (Savage and Hutter 1989; Andreotti et al. 2013)

$$\tau_{zz} = \rho g(h - z)\cos\theta. \tag{6.19}$$

Inserting Eq. (6.19) into Eq. (6.14) gives

$$\frac{\partial}{\partial t}(Uh) + \frac{\partial}{\partial x}\left(U^2 h + gK\cos\theta\frac{h^2}{2}\right) = gh\sin\theta + \frac{(\tau_{zx})_b}{\rho}. \tag{6.20}$$

For a Coulomb sliding law with a basal friction angle ϕ_{bed} (Pudasaini and Hutter 2007, pp. 117–121), one may state

$$(\tau_{zx})_b = -\rho g \mathrm{sgn}(U) h \tan\phi_{\mathrm{bed}}. \tag{6.21}$$

It follows that the dynamical system of Eqs. (6.10) and (6.11) takes here the form, with K given by Eq. (6.17),

$$\frac{\partial \mathbf{U}}{\partial t} + \frac{\partial \mathbf{F}}{\partial x} = \mathbf{S}, \tag{6.22}$$

where

$$\mathbf{U} = \begin{pmatrix} h \\ Uh \end{pmatrix}, \quad \mathbf{F} = \begin{pmatrix} Uh \\ U^2 h + gK\cos\theta \frac{h^2}{2} \end{pmatrix}, \quad \mathbf{S} = \begin{pmatrix} 0 \\ gh\sin\theta - g\mathrm{sgn}(U) h \tan\phi_{\mathrm{bed}} \end{pmatrix}. \tag{6.23}$$

Equations (6.22) and (6.23) are the so-called Savage–Hutter equations for the description of dry granular flows. Note that the approximate stress law given by Eq. (6.19) is often erroneously called in the literature "hydrostatic law." It is not hydrostatic, given the important reduction provoked by $\cos\theta$ on steep slopes [Chap. 2, Eq. (2.59)]. It is rather an approximation where bed-normal velocity effects are ignored.

6.3.2 *Effect of Bed-Normal Velocity*

Denlinger and Iverson (2004) found that the stresses generated by granular avalanches over irregular terrain are non-hydrostatic and that the magnitude of $\mathrm{D}\overline{w}/\mathrm{D}t$ was high in granular avalanche flows, with $(\mathrm{D}\overline{w}/\mathrm{D}t)/g$ ranging from −0.9 to +0.6, where $\overline{w}$ is the depth-averaged vertical velocity. This suggests that the vertical acceleration is of the same order as the gravity term, implying its relevance in avalanche dynamics (Andreotti et al. 2013).

To gain physical insight, consider 1D *steady* dry granular flows over a horizontal plane. The momentum function in the x-direction is given by Eq. (6.18). Consider a linear distribution of vertical stresses as used by Denlinger and Iverson (2004) and Denlinger and O'Connel (2008) [Chap. 2, Eq. (2.69)], for which Eq. (6.18) yields

$$M = U^2 h + Kg' \frac{h^2}{2}. \tag{6.24}$$

The enhanced gravity acceleration g' reduces then to [Chap. 2, Eq. (2.71)]

$$g' = g + \frac{U}{2}\frac{\partial}{\partial x}\left(U\frac{\partial h}{\partial x}\right). \tag{6.25}$$

Consequently, since the discharge is $q = Uh$ = constant in steady state, U can be replaced by q/h, so that

$$M = U^2h + K\left\{g + \frac{U}{2}(Uh_x)_x\right\}\frac{h^2}{2} = U^2h + K\left\{g + \frac{U}{2}(U_xh_x + Uh_{xx})\right\}\frac{h^2}{2}. \tag{6.26}$$

Because $\partial U/\partial x = U_x = \partial(q/h)/\partial x = -(q/h^2)h_x$, this turns into

$$\begin{aligned} M &= U^2h + K\left\{g + \frac{U}{2}\left(-\frac{q}{h^2}h_x^2 + \frac{q}{h}h_{xx}\right)\right\}\frac{h^2}{2} \\ &= U^2h + K\left\{g + \frac{U^2}{2}\left(-\frac{h_x^2}{h} + h_{xx}\right)\right\}\frac{h^2}{2}, \end{aligned} \tag{6.27}$$

which yields

$$M = Kg\frac{h^2}{2} + \frac{q^2}{h}\left(1 + K\frac{hh_{xx} - h_x^2}{4}\right). \tag{6.28}$$

As above, subscript x denotes differentiation with respect to the variable x.

For comparative purposes, Eq. (6.12) yields, for a dry granular 1D steady flow [see development of Eq. (2.47)]

$$\frac{\tau_{zz}}{\rho} = g(h - z) + \left(U_x^2 - UU_{xx}\right)\frac{(h^2 - z^2)}{2}. \tag{6.29}$$

Inserting this distribution into Eq. (6.18), performing the corresponding integral, and using $U = q/h$, $U_x = -(q/h^2)h_x$, and $U_{xx} = -(q/h^2)h_{xx} + 2(q/h^3)h_x^2$, results in

$$\begin{aligned} M &= U^2h + \frac{1}{\rho}K\int_0^h \tau_{zz}\mathrm{d}z = U^2h + K\int_0^h \left[g(h - z) + \left(U_x^2 - UU_{xx}\right)\frac{(h^2 - z^2)}{2}\right]\mathrm{d}z \\ &= U^2h + K\left[g\frac{h^2}{2} + \left(U_x^2 - UU_{xx}\right)\frac{h^3}{3}\right] \\ &= \frac{q^2}{h} + K\left[g\frac{h^2}{2} + \left\{\frac{q^2}{h^4}h_x^2 - \frac{q}{h}\left(-\frac{q}{h^2}h_{xx} + 2\frac{q}{h^3}h_x^2\right)\right\}\frac{h^3}{3}\right] \\ &= Kg\frac{h^2}{2} + \frac{q^2}{h}\left(1 + K\frac{hh_{xx} - h_x^2}{3}\right). \end{aligned} \tag{6.30}$$

This is a generalization for dry granular material of the water wave equation developed by Serre (1953), Benjamin and Lighthill (1954), or Iwasa (1956), to study cnoidal waves and bores. Note that the water wave formulation is regained from

Eq. (6.30) simply by setting $K = 1$, as deduced by Hager and Hutter (1984a, b) using streamline coordinates. Comparison between Eqs. (6.28) and (6.30) reveals that Denlinger and Iverson's approach introduces a factor (1/4) into the non-hydrostatic terms as compared with the exact factor (1/3) originating from the full analytical model. This effect must be investigated considering the family of equations given by

$$M = Kg\frac{h^2}{2} + \frac{q^2}{h}\left(1 + K\frac{hh_{xx} - h_x^2}{\alpha}\right). \tag{6.31}$$

An important result is that the enhanced gravity approach has embedded wavelike solutions as cnoidal waves and bores. This result allows for the use of the analytical methods of water wave theories to investigate the behavior of basic, simplified solutions for the flow of granular materials. Evidently, Denlinger and Iverson (2004) proposed the first Boussinesq-type model for granular media yet without exploiting it any further.

6.4 Simplified Solutions

6.4.1 Pseudo-uniform Flow Conditions

In this section, analytical results of the water wave theory will be applied to the motion of dry granular materials. The existence of simplified analytical solutions embedded into the general unsteady flow equations of dry granular material over a 3D terrain has important implications. First, the simplified analytical solutions allow for an inspection of a specific model component, i.e., the non-hydrostatic contribution. These particular solutions may not be directly found in nature, but they are particular solutions of a general model to understand the behavior of its physical issues. Second, simplified analytical solutions apply as test cases for numerical solutions of the full system of equations. It is difficult to evaluate the accuracy of a numerical code in unsteady flow over 3D terrain, if analytical solutions are not available. However, under simplified and controlled flow conditions, it is possible to investigate how a numerical solver behaves, before expanding it to simulations in nature. This has been a traditional practice in hydraulic research, where, e.g., the analytical solitary wave solution (Hager and Hutter 1984a, b; Sander and Hutter 1991; Sander and Hager 1991) was used as test case for comparison of solitary wave predictions using numerical solvers of the full system of equations (Sander and Hutter 1992; Antunes do Carmo et al. 1993; Kim et al. 2009).

In this section, the ideal case of wavelike mass motion, denominated "*pseudo-uniform flow*" (Hager and Hutter 1984b), is considered. In multidimensional flows, this ideal case implies that the source term vector of the depth-averaged model vanishes, $\mathbf{S} = \mathbf{0}$. It does not mean horizontal topography; it rather implies the

idealistic situation in which the basal slope driving components are exactly balanced by resistive forces, leading for 1D depth-averaged flows to the system

$$\frac{\partial \mathbf{U}}{\partial t}+\frac{\partial \mathbf{F}}{\partial x}=\mathbf{0},\quad \mathbf{U}=\begin{pmatrix} h \\ Uh \end{pmatrix},\quad \mathbf{F}=\begin{pmatrix} Uh \\ M \end{pmatrix}. \tag{6.32}$$

6.4.2 Granular Solitary Wave

Consider a translation wave in the x-direction with constant propagation speed c. Using the change of variables $X = x - ct$, $T = t$ (Galilean transformation), these waves appear as steady in a moving system of reference, given that the constant celerity c implies a wave profile that is not deformed (Serre 1953; Iwasa 1956; Liggett 1994). Thus, under this pseudo-uniform flow condition, the governing equations reduce to

$$\frac{\partial}{\partial X}(\mathbf{F}-c\mathbf{U})=0, \tag{6.33}$$

implying that the momentum in the moving reference system is conserved,

$$U^2h-cUh+\frac{1}{\rho}K\int_{z_b}^{z_s}\tau_{zz}\mathrm{d}z=\text{const.} \tag{6.34}$$

The mass (volume) balance equation yields the constant progressive discharge $q = (U - c)h$. Using for τ_{zz}, [see development of Eq. (2.47)]

$$\begin{aligned}\frac{\tau_{zz}}{\rho}&=g(h-z)\cos\theta+\left(U_x^2-U_{xt}-UU_{xx}\right)\frac{(h^2-z^2)}{2}\\&=g(h-z)\cos\theta+\left(U_X^2+cU_{XX}-UU_{XX}\right)\frac{(h^2-z^2)}{2},\end{aligned} \tag{6.35}$$

and inserting it into Eq. (6.34), neglecting the slope effect ($\cos\theta \to 1$), and using the definition of the progressive discharge give,

$$Kg\frac{h^2}{2}+\frac{q^2}{h}\left(1+K\frac{hh_{XX}-h_X^2}{3}\right)=\text{const.}, \tag{6.36}$$

which is, as expected, of the same form as Eq. (6.30). Thus, with M_o as the invariant momentum along the moving axis, wave solutions are generally given by the integrals of

$$Kg\frac{h^2}{2}+\frac{q^2}{h}\left(1+K\frac{hh_{XX}-h_X^2}{\alpha}\right)=\text{const.}=M_o. \tag{6.37}$$

Here, $\alpha = 3$ for the general depth-averaged theory (Serre 1953; Benjamin and Lighthill 1954; Iwasa 1956; Hager and Hutter 1984b) and $\alpha = 4$ for the enhanced gravity approach (Denlinger and Iverson 2004). Let $\sigma = h_X^2$ be an auxiliary variable; with it, Eq. (6.37) is rewritten with $\lambda = 3K/\alpha$ as

$$\lambda\frac{q^2}{6g}h^2\frac{\mathrm{d}}{\mathrm{d}h}\left(\frac{\sigma}{h^2}\right)=\frac{M_o}{g}-K\frac{h^2}{2}-\frac{q^2}{gh}. \tag{6.38}$$

Equation (6.38) is integrated with respect to h to yield

$$\lambda\frac{q^2}{6g}h_X^2=-\frac{M_o}{g}h-K\frac{h^3}{2}+\frac{q^2}{2g}+Ch^2. \tag{6.39}$$

Here, C is a constant of integration, determined by imposing the solitary wave [5] boundary conditions at $x \to \pm\infty$, namely $h_X \to 0$ for $h \to h_o$, with h_o as the uniform flow depth. Note that $M_o = gKh_o^2/2 + q^2/h_o$. Using this in Eq. (6.39), the constant is $C = Kh_o + q^2/\left(2gh_o^2\right)$. Equation (6.39) is, therefore, rewritten with $y = h/h_o$, and $\mathsf{F}_o = q\left(gh_o^3\right)^{-1/2}$ as undisturbed Froude number as

$$h_X^2=\frac{3}{\lambda\mathsf{F}_o^2}\left[-Ky^3+\left(2K+\mathsf{F}_o^2\right)y^2-\left(K+2\mathsf{F}_o^2\right)y+\mathsf{F}_o^2\right]=\frac{3}{\lambda\mathsf{F}_o^2}\left[(y-1)^2\left(\mathsf{F}_o^2-Ky\right)\right]. \tag{6.40}$$

If the left-hand side is also written in dimensionless variables, it takes the form

$$\left(\frac{\mathrm{d}y}{\mathrm{d}\chi}\right)^2=\frac{4}{\lambda\left(\mathsf{F}_o^2-1\right)}(y-1)^2\left(\mathsf{F}_o^2-Ky\right), \tag{6.41}$$

with $\chi = x/x_o$ and $x_o = 2\mathsf{F}_o h_o[3(\mathsf{F}_o^2-1)]^{-1/2}$. Note that consideration of the slope effects amounts to replacing K by $K\cos\theta$ in the gravity load $(Kh^2/2)$ component of Eq. (6.38). Consider as a first case a dry granular solitary wave with isotropic stresses, with $K = \tau_{xx}/\tau_{zz} = 1$, which is identical to the clear-water flow. Solitary wave solutions of Eq. (6.41) are given by the following analytical family of solutions (Serre 1953)

$$Y=\frac{y-1}{\left(\mathsf{F}_o^2-1\right)}=\operatorname{sech}^2\left[(\alpha/3)^{1/2}\chi\right], \tag{6.42}$$

[5] Solitary wave solutions are extensively described in Sect. 3.15.4.

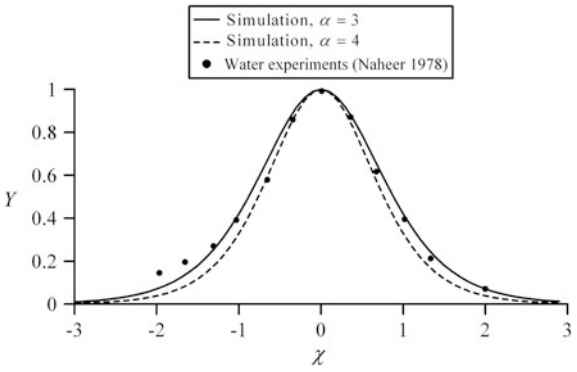

Fig. 6.2 Solitary waves for isotropic stresses (adapted from Castro-Orgaz et al. 2015)

in which $\lambda = 3/\alpha$ and $Y = (y - 1)/(y_{max} - 1)$ are used. Parameter α determines the solitary wave profile. Equation (6.42) is plotted in Fig. 6.2 for $\alpha = 3$ and 4 and compared with solitary water wave laboratory data (Naheer 1978). Figure 6.2 indicates that the solution for $\alpha = 3$ is generally closer to the experimental data than that for $\alpha = 4$.

The earth pressure coefficient K generally does not imply isotropic stresses. From the Mohr–Coulomb criterion, it is given by Eq. (6.17). For a derivation, see Pudasaini and Hutter (2007), or Savage and Hutter (1989); there are also other formulae available, which then imply differently used stress anisotropies. Coefficient K equals the passive earth coefficient [plus sign in Eq. (6.17)] for a granular medium in compression, whereas it is taken as the active earth pressure coefficient for a dilated mass. However, the solitary wave solution requires a unique constant value for K. To model the solitary wave with anisotropic stresses, the ideal situation of maximum bed roughness ($\phi_{bed} = \phi_{int}$) applies so that K has a unique value from Eq. (6.17) given by

$$K_{act/pas} = \frac{1 + \sin^2\phi_{int}}{1 - \sin^2\phi_{int}}. \tag{6.43}$$

Equation (6.41) was solved numerically using the fourth-order Runge–Kutta method (Press et al. 2007) for $\alpha = 3$ and 4 (Fig. 6.3), using $\phi_{bed} = \phi_{int} = 30°$, so that $K = 1.667$ from Eq. (6.43). The results confirm that the solutions are notably different, depending on the α-value. In addition, the sensitivity of the wave profile on K is highlighted, given the significant variations as compared with the former isotropic computations. The maximum solitary wave height is $y_{max} = \mathsf{F}_o^2/K$ from Eq. (6.41).

The above procedure gives rise to construct from Eq. (6.41) an entire series of granular solitary wave solutions, in which the real axis $x \in \mathrm{R}$ is divided into regimes, with dilatational ($x\partial U/x\partial x > 0$) and compressive ($x\partial U/x\partial x < 0$) flows, respectively. For instance, the dilative solution of Eq. (6.41) with $K = K_{act}$ in x $(-\infty, x_{sep})$ is connected discontinuously with a solution involving $K = K_{pas}$ for

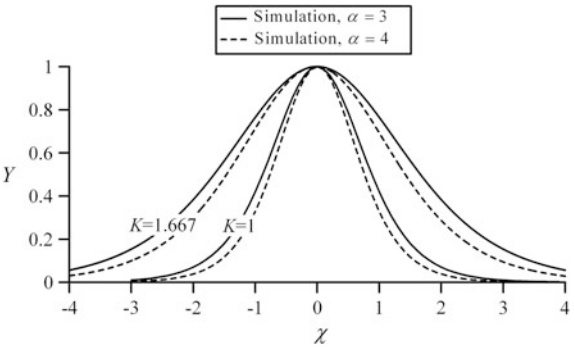

Fig. 6.3 Granular solitary waves for anisotropic stresses (adapted from Castro-Orgaz et al. 2015)

$x \in (x_{sep}, +\infty)$. The transition conditions at x_{sep} must thereby satisfy the Rankine–Hugoniot (= mass and momentum jump) conditions of the granular material. These solutions describe granular shocks and may be generated for a dry granular layer flowing on a bed with a small hump. However, the equations in this section do not apply since $z_b = 0$ is assumed.

6.4.3 Granular Free Overfall

Consider a steady-state case under pseudo-uniform flow conditions, namely the free overfall (Hager 1983; Marchi 1992, 1993). It occurs in a straight-bottomed flume abruptly ending in a free fall, where the upstream mass flow separates, continuing as a free jet. It is well known from open-channel hydraulics that changes in non-hydrostatic pressure are intensified under rapid variations of the bed geometry (Hager and Hutter 1984a; Matthew 1991; Montes 1998). This test case highlights how the granular flow behaves in response to vertical accelerations if abrupt topographical changes play a significant role. The flow in the upstream free overfall portion has attracted a number of studies to analyze the effects of vertical acceleration. A typical case is the free overfall with critical approach flow conditions $\mathsf{F}_o = 1$ (Hager 1983). Equation (6.41) is singular in this case, so that it must be rescaled with

$$y = \frac{h}{h_c}, \quad \varsigma = \frac{x}{h_c}, \quad h_c = \left(\frac{q^2}{g}\right)^{1/3}. \tag{6.44}$$

With these scales, the singularity is removed; the equation analogous to Eq. (6.41) states

$$\left(\frac{dy}{d\varsigma}\right)^2 = \frac{3}{\lambda}(y-1)^2(1-Ky). \tag{6.45}$$

Consider a dry granular free overfall with isotropic stresses $K = 1$. Note the full analogy with clear-water flow, for which Eq. (6.45) integrates to

$$\varsigma = 2\left(\frac{\lambda}{3}\right)^{1/2}(1-y)^{-1/2} + C. \tag{6.46}$$

For $\lambda = 1$ ($\alpha = 3$), this equation was obtained by Hager (1983) for clear-water flow. Equation (6.46) is plotted in Fig. 6.4 for $\alpha = 3$ using as boundary condition to compute C the point $y(-3.5) = 0.958$. The computed free surface profile excellently compares with the data of Marchi (1993). The solution for $\alpha = 4$ and the same boundary condition is also plotted to highlight the effect of α. Significant variations result in this case, indicating the sensitivity to this factor near extreme changes of the basal geometry.

If $K \neq 1$, the general solution of Eq. (6.45) reads (Bronshtein and Semendiaev 1971, Chap. III, pp. 385–404)

$$\left(\frac{3}{\lambda}\right)^{1/2}\varsigma + C = (1-K)^{-1/2}\ln\left[\frac{(1-Ky)^{1/2} - (1-K)^{1/2}}{(1-Ky)^{1/2} + (1-K)^{1/2}}\right]. \tag{6.47}$$

For flows approaching a free fall, the grain particles are under an active tension state, so that K is given by the active earth coefficient ($K < 1$). A value of $K = 0.6$ was considered with Eq. (6.47) plotted in Fig. 6.5 for $\alpha = 3$ and 4 using the point $y(-3.5) = 0.998$ as boundary condition to compute C. Results indicate that the solutions for $\alpha = 3$ and $\alpha = 4$ significantly deviate as the fall portion is approached. The same case was also solved using $K = 0.75$, with the results also included in Fig. 6.5. Note that moderate variations in K induce significant variations of the computed $y(0)$ for identical boundary conditions. Boussinesq-type wave solutions for flows over varying topography are thus sensitive to both the anisotropy of stresses and the dispersion coefficient of the non-hydrostatic part of the model.

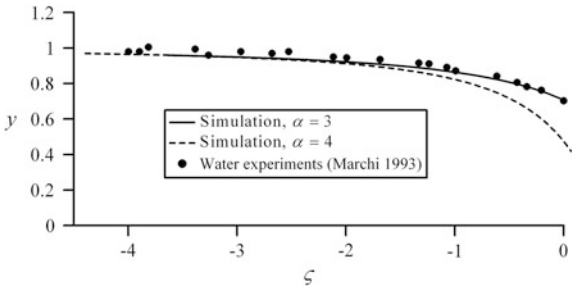

Fig. 6.4 Granular free overfalls for isotropic stresses (adapted from Castro-Orgaz et al. 2015)

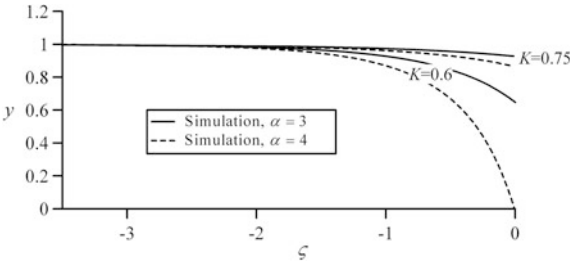

Fig. 6.5 Granular free overfalls for anisotropic stresses (adapted from Castro-Orgaz et al. 2015)

6.5 1D Hutter–Serre Enhanced Equations Down an Inclined Plane

Consider again the flow of a continuum dry granular material of constant density ρ moving across an inclined plane terrain (Fig. 6.1). It will now be shown how to enhance the Savage–Hutter theory for granular flows down an inclined plane using the Serre (1953) theory to account for the bed-normal velocity component. The streamwise momentum equation is, from Eqs. (6.14) and (6.15),

$$\frac{\partial}{\partial t}(Uh)+\frac{\partial}{\partial x}\left(U^2h+K\int_0^h\frac{\tau_{zz}}{\rho}\mathrm{d}z\right)=gh\sin\theta+\frac{(\tau_{xz})_b}{\rho}. \tag{6.48}$$

The momentum function in the x-direction down the plane is

$$M=U^2h+\frac{1}{\rho}K\int_0^h\tau_{zz}\mathrm{d}z. \tag{6.49}$$

The vertical stress τ_{zz} is from Eq. (6.12), using Eq. (6.13) to approximate the bed-normal velocity component w and neglecting the tangential stress integral [see development of Eq. (2.47)]

$$\frac{\tau_{zz}}{\rho}=g(h-z)\cos\theta+\left(U_x^2-U_{xt}-UU_{xx}\right)\frac{(h^2-z^2)}{2}. \tag{6.50}$$

Inserting it into Eq. (6.49) gives after integration [see development of Eq. (6.30)]

$$M=U^2h+gK\cos\theta\frac{h^2}{2}+\left(U_x^2-U_{xt}-UU_{xx}\right)K\frac{h^3}{3}. \tag{6.51}$$

The dynamical system takes the form

$$\frac{\partial \mathbf{U}}{\partial t} + \frac{\partial \mathbf{F}}{\partial x} = \mathbf{S}, \tag{6.52}$$

with

$$\mathbf{U} = \begin{pmatrix} h \\ Uh \end{pmatrix}, \quad \mathbf{F} = \begin{pmatrix} Uh \\ M \end{pmatrix}, \quad \mathbf{S} = \begin{pmatrix} 0 \\ gh\sin\theta - g\,\mathrm{sgn}(U)h\tan\phi_{\mathrm{bed}} \end{pmatrix}. \tag{6.53}$$

Equations (6.52) and (6.53) are named the *Hutter–Serre* equations for the description of dry granular flows. The system accounts for the non-hydrostatic slope effect given by $\cos\theta$ and for the local and convective accelerations originating from the bed-normal velocity component, which is the key ingredient of Serre's (1953) theory.

References

Andreotti, B., Forterre, Y., & Pouliquen, O. (2013). *Granular media: Between fluid and solid*. Cambridge: Cambridge University Press.

Antunes do Carmo, J. S., Santos, F. J., & Almeida, A. B. (1993). Numerical solution of the generalized Serre equations with the MacCormack finite difference scheme. *International Journal for Numerical Methods in Fluids, 16*(8), 725–738.

Bagnold, R. A. (1954). Experiments on gravity-free dispersion of large solid spheres in a Newtonian fluid under shear. *Proceedings of the Royal Society of London Series A*, *225*, 49–63.

Benjamin, T. B., & Lighthill, M. J. (1954). On cnoidal waves and bores. *Proceedings of the Royal Society of London A, 224*, 448–460.

Bouchut, F., & Westdickenberg, M. (2004). Gravity driven shallow water models for arbitrary topography. *Communications in Mathematical Sciences, 2*, 359–389.

Bronshtein, I., & Semendiaev, K. (1971). *Mathematical handbook for engineers and students*. Ed. Mir, Moscow (translated into Spanish, 1977).

Castro-Orgaz, O., Hutter, K., Giráldez, J. V., & Hager, W. H. (2015). Non-hydrostatic granular flow over 3D terrain New Boussinesq-type gravity waves. *Journal of Geophysical Research: Earth Surface, 120*(1), 1–28.

Chiou, M.-C., Wang, Y., & Hutter, K. (2005). Influence of obstacles on rapid granular flows. *Acta Mechanica, 175*, 105–122.

Denlinger, R. P., & Iverson, R. M. (2001). Flow of variably fluidized granular masses across three-dimensional terrain 2: Numerical predictions and experimental tests. *Journal Geophysical Research, 106*(B1), 553–566.

Denlinger, R. P., & Iverson, R. M. (2004). Granular avalanches across irregular three-dimensional terrain 1: Theory and computation. *Journal Geophysical Research*, *109*, F01014. doi:10.1029/2003JF000085

Denlinger, R. P., & O'Connell, D. R. H. (2008). Computing nonhydrostatic shallow-water flow over steep terrain. *Journal of Hydraulic Engineering, 134*(11), 1590–1602.

Dressler, R. F. (1978). New nonlinear shallow flow equations with curvature. *Journal of Hydraulic Research, 16*(3), 205–222.

Gray, J. M. N. T., Wieland, M., & Hutter, K. (1999). Gravity driven free surface flow of granular avalanches over complex basal topography. *Proceedings of the Royal Society of London Series A, 455*, 1841–1874.

Hager, W. H. (1983). Hydraulics of the plane free overfall. *Journal of Hydraulic Engineering, 109*(12), 1683–1697.

Hager, W. H., & Hutter, K. (1984a). Approximate treatment of plane channel flow. *Acta Mechanica, 51*(3–4), 31–48.

Hager, W. H., & Hutter, K. (1984b). On pseudo-uniform flow in open channel hydraulics. *Acta Mechanica, 53*(3–4), 183–200.

Hungr, O., & Morgenstern, N. R. (1984). Experiments on the flow behavior of granular materials at high velocity in an open channel. *Geotechnique, 34*(3), 405–413.

Hunt, M. L., Zenit, R., Campbell, C. S., & Brennen, C. E. (2002). Revisiting the 1954 suspension experiments of R.A. Bagnold. *Journal of Fluid Mechanics, 452*, 1–24.

Hutter, K. (1996). Avalanche dynamics: A review. In V. P. Singh (Ed.), *Hydrology of disasters* (pp. 313–390). Amsterdam: Kluwer Academic.

Hutter, K. (2005). Geophysical granular and particle-laden flows: Review of the field. *Philosophical Transactions of the Royal Society of London, 363*, 1497–1505.

Hutter, K., & Savage, S. B. (1988). Avalanche dynamics: The motion of a finite mass of gravel down a mountain side. In *5th International Symposium* on *Landslides*, Lausanne (pp. 691–697).

Hutter, K., & Koch, T. (1991). Motion of a granular avalanche in an exponentially curved chute: Experiments and theoretical results. *Philosophical Transactions of the Royal Society of London Series A, 334*, 93–138.

Hutter, K., Siegel, M., Savage, S. B., & Nohguchi, Y. (1993). Two-dimensional spreading of a granular avalanche down an inclined plane 1: Theory. *Acta Mechanica, 100*, 37–68.

Hutter, K., Wang, Y., & Pudasaini, S. P. (2005). The Savage-Hutter avalanche model, how far can it be pushed. *Philosophical Transactions of the Royal Society of London, 363*, 1507–1528.

Hutter, K., & Luca, I. (2012). Two-layer debris mixture flows on arbitrary terrain with mass exchange at the base and the interface. *Continuum Mechanics and Thermodynamics, 24*(4–6), 525–558.

Hutter, K., Wang, Y., & Chubarenko, I. P. (2014). Sediment transport in alluvial systems, Chap. 32. In *Physics of lakes: Vol. 3. Methods of Understanding Lakes as Components of the Geophysical Environment* (pp. 487–579). Book series *Advances in Geophysical and Environmental Mechanics and Mathematics*, AGEM^2. Heidelberg: Springer.

Hutter, K., & Castro-Orgaz, O. (2016). Non-hydrostatic free surface flows: Saint Venant versus Boussinesq depth integrated dynamic equations for river and granular flows, Chap. 17. In *Continuous media with microstructure* (Vol. 2, pp. 245–265), Berlin: Springer.

Iverson, R. M. (1997). The physics of debris flows. *Reviews of Geophysics, 35*(3), 245–296.

Iverson, R. M. (2005). Debris-flow mechanics. In M. Jakob & O. Hungr (Eds.), *Debris flow hazards and related phenomena* (pp. 105–134). Heidelberg: Springer-Praxis.

Iverson, R. M. (2014). Debris flows: Behaviour and hazard assessment. *Geology Today, 30*(1), 15–20.

Iverson, R. M., & Denlinger, R. P. (2001). Flow of variably fluidized granular masses across three-dimensional terrain: 1. Coulomb mixture theory. *Journal of Geophysical Research, 106*(B1), 537–552.

Iverson, R. M., & Vallance, J. W. (2001). New views of granular mass flows. *Geology, 29*(2), 115–118.

Iverson, R. M., Reid, M. E., & LaHusen, R. G. (1997). Debris flow mobilization from landslides. *Annual Review of Earth and Planetary Sciences, 25*, 85–138.

Iverson, R. M., & Ouyang, C. (2015). Entrainment of bed material by Earth-surface mass flows: Review and reformulation of depth-integrated theory. *Reviews of Geophysics*, *53*. doi:10.1002/2013RG000447

Iwasa, Y. (1956). Analytical considerations on cnoidal and solitary waves. *Transactions, Japan Society of Civil Engineers, 32*, 43–49.

Kim, D.-H., Lynett, P. J., & Socolofsky, S. (2009). A depth-integrated model for weakly dispersive, turbulent, and rotational fluid flows. *Ocean Modelling, 27*(3–4), 198–214.

Kuo, C. Y., Tai, Y. C., Bouchut, F., Mangeney, A., Pelanti, M., Chen, R. F., et al. (2009). Simulation of Tsaoling landslide, Taiwan, based on Saint Venant equations over general topography. *Engineering Geology, 104*(3–4), 181–189.

Liggett, J. A. (1994). *Fluid mechanics*. New York: McGraw-Hill.

Luca, I., Hutter, K., Tai, Y. C., & Kuo, C. Y. (2009a). A hierarchy of avalanche models on arbitrary topography. *Acta Mechanica, 205*, 121–149.

Luca, I., Tai, Y. C., & Kuo, C. Y. (2009b). Non-cartesian topography based avalanche equations and approximations of gravity driven flows of ideal and viscous fluids. *Mathematical Models and Methods in Applied Sciences, 19*(1), 127–171.

Luca, I., Hutter, K., Kuo, C. Y., & Tai, Y. C. (2009c). Two layer models for shallow avalanche flows over arbitrary variable topography. *International Journal of Advances in Engineering Sciences and Applied Mathematics, 1*(2–3), 99–121.

Luca, I., Kuo, C. Y., Hutter, K., & Tai, Y. C. (2012). Modeling shallow over-saturated mixtures on arbitrary rigid topography. *Journal of Mechanics, 28*(3), 523–541.

Mangeney-Castelnau, A., Vilotte, J.-P., Bristeau, M. O., Perthame, B., Bouchut, F., Simeoni, C., & Yerneni, S. (2003). Numerical modeling of avalanches based on Saint Venant equations using a kinetic scheme. *Journal of Geophysical Research*, *108*. doi:10.1029/2002JB002024

Marchi, E. (1992). The nappe profile of a free overfall. *Rendiconti dei Lincei, Matematica e Applicazioni, Serie 9*, *3*(2), 131–140.

Marchi, E. (1993). On the free overfall. *Journal of Hydraulic Research*, *31*(6), 777–790; *32*(5), 794–796.

Matthew, G. D. (1991). Higher order one-dimensional equations of potential flow in open channels. *Proceedings of the ICE, 91*(3), 187–201.

McDougall, S., & Hungr, O. (2003). Objectives for the development of an integrated three dimensional continuum model for the analysis of landslide runout. In D. Rickenmann & C. L. Chen (Eds.), *Proceedings of the Third International Conference on Debris Hazards Mitigation*: *Mechanics, Prediction And Assessment* (pp. 481–490). Rotterdam: Mill Press.

McDougall, S., & Hungr, O. (2004). A model for the analysis of rapid landslide motion across three-dimensional terrain. *Canadian Geotechnical Journal, 41*(6), 1084–1097.

McDougall, S., & Hungr, O. (2005). Dynamic modelling of entrainment in rapid landslides. *Canadian Geotechnical Journal, 41*(6), 1437–1448.

Montes, J. S. (1998). *Hydraulics of open channel flow*. Reston, VA: ASCE Press.

Naheer, E. (1978). Laboratory experiments with solitary wave. *Journal of the Waterway Port Coastal and Ocean Division, ASCE 104*(4), 421–436.

Pailha, M., & Pouliquen, O. (2009). A two-phase flow description of the initiation of underwater granular avalanches. *Journal of Fluid Mechanics, 636*, 295–319.

Pelanti, M., Bouchut, F., & Mangeney, A. (2008). A Roe-type scheme for two-phase shallow granular flows over variable topography. *Mathematical Modelling and Numerical Analysis, 42*(5), 851–885.

Pitman, E. B., & Le, L. (2005). A two-fluid model for avalanche and debris flows. *Philosophical Transactions of the Royal Society of London, A363*, 1573–1602.

Press, W. H., Teukolsky, S. A., Vetterling, W. T., & Flannery, B. P. (2007). *Numerical recipes*: *The art of scientific computing* (3rd ed.). Cambridge, UK: Cambridge University Press.

Pudasaini, S. P. (2011). A general two-phase debris flow model. *Journal Geophysical Research, 117*(F3), F03010. doi:10.1029/2011JF002186.

Pudasaini, S. P., & Hutter, K. (2003). Rapid shear flows of dry granular masses down curved and twisted channels. *Journal of Fluid Mechanics, 495*, 193–208.

Pudasaini, S. P., & Hutter, K. (2007). *Avalanche dynamics*. Berlin: Springer.

Pudasaini, S. P., Hutter, K., & Eckart, W. (2003). Gravity-driven rapid shear flows of dry granular masses in topographies with orthogonal and non-orthogonal metrics. In K. Hutter & N. Kirchner (Eds.), *Dynamic response of granular and porous materials under large and*

catastrophic deformation. *Lecture Notes in Applied and Computational Mechanics* (Vol. 11, pp. 43–82). Berlin: Springer.

Pudasaini, S. P., Wang, Y., & Hutter, K. (2005a). Dynamics of avalanches along general mountain slopes. *Annals Glaciology, 38*(1), 257–262.

Pudasaini, S. P., Wang, Y., & Hutter, K. (2005b). Modelling two-phase debris flows down general channels and their numerical simulation. *Natural Hazards and Earth System Sciences, 5*, 799–819.

Pudasaini, S. P., Wang, Y., Sheng, L.-T., Hsiau, S.-S., Hutter, K., & Katzenbach, R. (2008). Avalanching granular flows down curved and twisted channels: Theoretical and experimental results. *Physics of Fluids, 20*(7), 073302-1-11.

Sander, J., & Hutter, K. (1991). On the development of the theory of the solitary wave: A historical essay. *Acta Mechanica, 86*(1–4), 111–152.

Sander, J., & Hager, W. H. (1991). Solitäre Wellen (Solitary waves). *Österreichische Wasserwirtschaft, 43*(7/8), 185–190 (in German).

Sander, J., & Hutter, K. (1992). Evolution of weakly non-linear shallow water waves generated by a moving boundary. *Acta Mechanica, 91*(3–4), 119–155.

Savage, S. B., & Hutter, K. (1989). The motion of a finite mass of granular material down a rough incline. *Journal of Fluid Mechanics, 199*, 177–215.

Savage, S. B., & Hutter, K. (1991). The dynamics of avalanches of granular materials from initiation to runout, Part I. Analysis. *Acta Mechanica, 86*(1–4), 201–223.

Savage, S. B., & Iverson, R. M. (2003). Surge dynamics coupled to pore pressure evolution in debris flows. In *3rd International Conference on Debris-Flow Hazards Mitigation,* Davos, Switzerland (pp. 503–514).

Serre, F. (1953). Contribution à l'étude des écoulements permanents et variables dans les canaux (Contribution to the study of steady and unsteady channel flows). *La Houille Blanche, 8*(6-7), 374–388; *8*(12), 830–887 (in French).

Wang, Y., Hutter, K., & Pudasaini, S. P. (2004). The Savage-Hutter theory: A system of partial differential equations for avalanche flows of snow, debris and mud. *ZAMM, 84*(8), 507–527.

Wieland, M., Gray, J. M. N. T., & Hutter, K. (1999). Channelised free surface flow of cohesionless granular avalanche in a chute with shallow lateral curvature. *Journal of Fluid Mechanics, 392*, 73–100.

Chapter 7
Concluding Remarks

The theory of depth-averaged non-hydrostatic free surface flows is presented in this book, including open channel, groundwater, and avalanche flows. Boussinesq's theory and its extension to several problems investigated in the past 140 years are presented, resulting in a general agreement with the experimental observations. His theory is an attractive alternative to more complex 3D or 2D computations, given that it is conceptually considered a generalization of the routinely used Saint-Venant theory, rendering computationally simpler solutions than those originating from a fully 3D or 2D numerical solution. The main conclusions and recommendations are as follows.

In Chap. 1, a general introduction to non-hydrostatic flows is given with a historical note on the key developments since Boussinesq (1877). The role of non-hydrostatic pressure distribution in civil, environmental, and coastal engineering is discussed and is used to demonstrate that its inclusion is important in many real-life problems.

In Chap. 2, the general mass and momentum vertically integrated equations for unsteady non-hydrostatic flows over 3D terrain are presented, following Castro-Orgaz et al. (2015). Using Serre's (1953) approximation of depth-independent velocity components in the horizontal plane, general equations for the vertical velocity and non-hydrostatic vertical stress are then given. The conservation equations are specified in a compact conservative form, suitable for constructing numerical schemes using modern shock-capturing methods as the finite volume method (Toro 2001) or the discontinuous method of Galerkin (Khan and Lai 2014). Examples of suitable numerical schemes to solve the generalized Serre equations are available from Denlinger and O'Connel (2008) or Kim et al. (2009).

In Chap. 3, the computation of non-hydrostatic inviscid flows is considered. Most of the applications presented refer to 1D steady potential flows. For these, the energy head remains a constant within the entire computational domain, rendering the extended energy equation a useful tool. Despite these flows can also be solved using the generalized Serre theory presented in Chap. 2, applications mostly focus

© Springer International Publishing AG 2017

O. Castro-Orgaz and W.H. Hager, *Non-Hydrostatic Free Surface Flows*,
Advances in Geophysical and Environmental Mechanics and Mathematics
DOI 10.1007/978-3-319-47971-2_7

on energy conservation, given its simplicity and conceptual interest. Extended energy equations are derived using Picard's iteration theory (Matthew 1991), Dressler's (1978) theory in bottom-fitted coordinates, and Hager and Hutter's (1984) approximate treatment of the flow net. All these model equations give similar results. Thus, Matthew's Picard iteration theory is recommended for 1D steady potential flow (Castro-Orgaz and Hager 2009), given its simplicity and mathematical elegance.

In Chap. 4, non-hydrostatic groundwater flows with a phreatic surface are considered. General differential equations describing the seepage position are derived using Picard's iteration technique (Castro-Orgaz et al. 2012) and Fawer's theory. Given that the Picard iteration method allows for the systematic inclusion of relevant hydrological phenomena as recharge and anisotropy on the seepage surface prediction, it is recommended. Picard's iteration was employed to investigate the reliability of the Dupuit-Forchheimer theory. In general, Picard's iteration theory produces better solutions, given that it works well in the cases where the Dupuit–Forchheimer theory is accurate, and also where the latter theory fails because hydrostatic pressure distribution is assumed.

In Chap. 5, the non-hydrostatic modeling of viscous steady flows in the vertical plane is considered. Boundary layer-type computations are presented for developing flows on steep slopes and flows over round-crested weirs, involving an outer potential flow zone. For turbulent flows, the depth-averaged form of the RANS equations is presented. Several degrees of approximation to the RANS depth-averaged model are discussed, with Serre's (1953) theory as a particular case. Undular flows are then considered, stating that the overall performance of Serre's theory is good. This theory is further expanded to gate flows, submerged jets, spatially varied flows, sediment bed erosion during dike breaches, solitary sand waves, and to compound channel flows.

In Chap. 6, the fast motion of granular material is considered. The Savage–Hutter theory (1989) for dry granular flows down an inclined plane is used to demonstrate the non-hydrostatic bed-slope effect. Then, the bed-normal velocity effect is revealed using simplified solutions, namely the granular solitary wave and the granular-free overfall. Finally, the Savage–Hutter theory is enhanced using Serre's theory, thereby producing a model for dry granular flows down an inclined plane, where both bed slope and bed-normal velocity effects are accounted for.

As a main conclusion and recommendation, it is highlighted throughout the book that consideration of non-hydrostatic pressure in depth-averaged models results in a small increase of mathematical complexities at the current state of knowledge, whereas the gain in physical accuracy is high as compared with the Saint-Venant hydrostatic theory. This effect becomes particularly evident when looking at the bottom pressures, which in most cases are poorly estimated by Saint-Venant's theory from which it is equal to the water depth. In general, an unsteady non-hydrostatic flow model follows Serre's (1953) theory and its generalizations (Castro-Orgaz et al. 2015). The 2D or even 1D computation of non-hydrostatic

flows using depth-averaged models gives in most cases enough information for engineering purposes, resulting in a viable and simplified alternative to more complex 3D models.

References

Boussinesq, J. (1877). *Essai sur la théorie des eaux courantes* (Essay on the theory of water flow). In *Mémoires* présentés par divers savants à l'Académie des Sciences (Vol. 23, pp. 1–680). Paris (in French).

Castro-Orgaz, O., Giráldez, J. V., & Robinson, N. (2012). Second order two-dimensional solution for the drainage of recharge based on Picard's iteration technique: A generalized Dupuit-Forchheimer equation. *Water Resources Research, 48*, W06516. doi:10.1029/2011WR011751

Castro-Orgaz, O., & Hager, W. H. (2009). Curved streamline transitional flow from mild to steep slopes. *Journal of Hydraulic Research, 47*(5), 574–584.

Castro-Orgaz, O., Hutter, K., Giráldez, J. V., & Hager, W. H. (2015). Non-hydrostatic granular flow over 3D terrain: New Boussinesq-type gravity waves? *Journal of Geophysical Research: Earth Surface, 120*(1), 1–28.

Denlinger, R. P., & O'Connell, D. R. H. (2008). Computing nonhydrostatic shallow-water flow over steep terrain. *Journal of Hydraulic Engineering, 134*(11), 1590–1602.

Dressler, R. F. (1978). New nonlinear shallow flow equations with curvature. *Journal of Hydraulic Research, 16*(3), 205–222.

Hager, W. H., & Hutter, K. (1984). Approximate treatment of plane channel flow. *Acta Mechanica, 51*(3–4), 31–48.

Khan, A. A., & Lai, W. (2014). *Modelling shallow water flows using the discontinuous Galerkin method*. London: CRC Press, Taylor and Francis.

Kim, D.-H., Lynett, P. J., & Socolofsky, S. (2009). A depth-integrated model for weakly dispersive, turbulent, and rotational fluid flows. *Ocean Modelling, 27*(3–4), 198–214.

Matthew, G. D. (1991). Higher order one-dimensional equations of potential flow in open channels. *Proceedings of the ICE, 91*(3), 187–201.

Savage, S. B., & Hutter, K. (1989). The motion of a finite mass of granular material down a rough incline. *Journal of Fluid Mechanics, 199*, 177–215.

Serre, F. (1953). Contribution à l'étude des écoulements permanents et variables dans les canaux (Contribution to the study of steady and unsteady channel flows). *La Houille Blanche 8*(6–7), 374–388; *8*(12), 830–887 (in French).

Toro, E. F. (2001). *Shock-capturing methods for free-surface shallow flows*. New York: Wiley.

Appendix A
Pressure Distribution in Flows Over Curved Bed

This appendix starts with Eqs. (2.64) and (2.66), repeated here for convenience,

$$w = U\left[\frac{\partial z_b}{\partial x} + \frac{\partial h}{\partial x}\frac{\eta}{h}\right], \quad \eta(x,z) = z - z_b(x), \tag{A.1}$$

$$p(z) = \rho g(h-\eta) - \rho w^2 + \rho\frac{\partial}{\partial x}\left(U\int_{\eta}^{h} w\mathrm{d}\eta'\right). \tag{A.2}$$

Of significance are expressions for w^2 and the integral arising in Eq. (A.2)

$$-w^2 = -U^2\left[z_{bx}^2 + h_x^2\frac{\eta^2}{h^2} + 2z_{bx}h_x\frac{\eta}{h}\right], \tag{A.3}$$

$$U\int_{\eta}^{h} w\mathrm{d}\eta' = U^2\left[z_{bx}(h-\eta) + \frac{h_x}{h}\frac{h^2-\eta^2}{2}\right]. \tag{A.4}$$

Subscripts represent differentiations with respect to x. Since $\eta = z - z_b(x)$ and $q = Uh$ = const.,

$$\eta_x = -z_{bx}, \quad \text{and} \quad U_x = -\frac{U}{h}h_x. \tag{A.5}$$

© Springer International Publishing AG 2017

O. Castro-Orgaz and W.H. Hager, *Non-Hydrostatic Free Surface Flows*,
Advances in Geophysical and Environmental Mechanics and Mathematics
DOI 10.1007/978-3-319-47971-2

Equation (A.4) implies straightforwardly

$$\frac{\partial}{\partial x}\left(U\int_{\eta}^{h} w\mathrm{d}\eta'\right) = 2U\frac{\partial U}{\partial x}\left[z_{bx}(h-\eta)+\frac{h_x}{h}\frac{h^2-\eta^2}{2}\right] + U^2\left[z_{bxx}(h-\eta)+z_{bx}(h_x-\eta_x)+\left(\frac{h_{xx}}{h}-\frac{h_x^2}{h^2}\right)\frac{h^2-\eta^2}{2}+\frac{h_x}{h}\left(\frac{2hh_x-2\eta\eta_x}{2}\right)\right]. \tag{A.6}$$

Using Eq. (A.5), this is also expressible as

$$\frac{\partial}{\partial x}\left(U\int_{\eta}^{h} w\mathrm{d}\eta'\right) = -2U^2\frac{h_x}{h}\left[z_{bx}(h-\eta)+\frac{h_x}{h}\frac{h^2-\eta^2}{2}\right] + U^2\left[z_{bxx}(h-\eta)+z_{bx}(h_x+z_{bx})+\left(\frac{h_{xx}}{h}-\frac{h_x^2}{h^2}\right)\frac{h^2-\eta^2}{2}+\frac{h_x}{h}(hh_x+\eta z_{bx})\right]. \tag{A.7}$$

From Eqs. (A.3) and (A.7), the pressure distribution is

$$\begin{aligned}\frac{p(z)}{\rho g} &= (h-\eta)-\frac{U^2}{g}\left[z_{bx}^2+h_x^2\frac{\eta^2}{h^2}+2z_{bx}h_x\frac{\eta}{h}\right]\\ &\quad -2\frac{U^2}{g}\frac{h_x}{h}\left[z_{bx}(h-\eta)+\frac{h_x}{h}\frac{h^2-\eta^2}{2}\right]\\ &\quad +\frac{U^2}{g}\left[z_{bxx}(h-\eta)+z_{bx}(h_x+z_{bx})\right.\\ &\quad \left.+\left(\frac{h_{xx}}{h}-\frac{h_x^2}{h^2}\right)\frac{h^2-\eta^2}{2}+\frac{h_x}{h}(hh_x+\eta z_{bx})\right].\end{aligned} \tag{A.8}$$

This expression is in the next steps subjected to a number of operations to simplify it. First, Eq. (A.8) may be put into the form

$$\begin{aligned}\frac{p(z)}{\rho g} &= (h-\eta)-\frac{U^2}{g}h_x^2\frac{\eta^2}{h^2}-\frac{U^2}{g}2z_{bx}h_x\frac{\eta}{h}-2\frac{U^2}{g}\frac{h_x}{h}z_{bx}(h-\eta)\\ &\quad -2\frac{U^2}{g}\frac{h_x^2}{h^2}\frac{h^2-\eta^2}{2}+\frac{U^2}{g}z_{bxx}(h-\eta)+\frac{U^2}{g}z_{bx}h_x\\ &\quad +\frac{U^2}{g}\left(\frac{h_{xx}}{h}-\frac{h_x^2}{h^2}\right)\frac{h^2-\eta^2}{2}+\frac{U^2}{g}h_x^2+\frac{U^2}{g}\frac{h_x}{h}\eta z_{bx},\end{aligned} \tag{A.9}$$

to be regrouped as

$$\frac{p(z)}{\rho g} = (h-\eta) + \frac{U^2}{g} z_{bxx}(h-\eta) + \frac{U^2}{g}\left(\frac{h_{xx}}{h} - \frac{h_x^2}{h^2}\right)\frac{h^2-\eta^2}{2} + \frac{U^2}{g}\frac{h_x}{h}\eta z_{bx} \underbrace{+2\frac{U^2}{g}\frac{h_x^2}{h^2}\frac{h^2}{2} - 2\frac{U^2}{g}h_x^2\frac{\eta^2}{2h^2} - 2\frac{U^2}{g}\frac{h_x^2}{h^2}\frac{h^2-\eta^2}{2}}_{=0} \underbrace{-2\frac{U^2}{g}\frac{h_x}{h}z_{bx}(h-\eta) + \frac{U^2}{g}z_{bx}h_x - \frac{U^2}{g}2z_{bx}h_x\frac{\eta}{h}}_{=-(U^2/g)h_x z_{bx}}. \tag{A.10}$$

Its final form reduces to

$$\frac{p(z)}{\rho g} = h - \eta + \frac{U^2}{g}\left[z_{bxx}(h-\eta) + \left(\frac{h_{xx}}{h} - \frac{h_x^2}{h^2}\right)\frac{h^2-\eta^2}{2} + \frac{h_x}{h}\eta z_{bx} - z_{bx}h_x\right], \tag{A.11}$$

or

$$\frac{p(z)}{\rho g} = h - \eta + \frac{U^2}{2g}\left[2hz_{bxx}\left(1-\frac{\eta}{h}\right) + \left(hh_{xx} - h_x^2\right)\left(1-\frac{\eta^2}{h^2}\right) - 2h_x z_{bx}\left(1-\frac{\eta}{h}\right)\right]. \tag{A.12}$$

This agrees with Eq. (2.67). As evident from Eq. (A.12), the depth dependence of the pressure is parabolic,

$$\begin{aligned} &\frac{p(z)}{\rho g} = a\left(1-\frac{\eta}{h}\right) + b\left(1-\frac{\eta^2}{h^2}\right), \\ &a = h + \frac{U^2}{2g}(2hz_{bxx} - 2h_x z_{bx}), \quad b = \frac{U^2}{2g}(hh_{xx} - h_x^2). \end{aligned} \tag{A.13}$$

Therefore, when integrated over depth, Eq. (A.12) yields

$$\int_0^h \frac{p}{\rho g}\mathrm{d}\eta = h\int_0^1 \frac{p}{\rho g}\mathrm{d}\xi = h\int_0^1 \left(a\xi + b(1-\xi^2)\right) = h\left(\frac{a}{2} + \frac{2b}{3}\right). \tag{A.14}$$

The momentum function S now becomes

$$S = \frac{U^2 h}{g} + \int_0^h \frac{p}{\rho g}\mathrm{d}\eta = \frac{q^2}{gh} + h\left(\frac{a}{2} + \frac{2b}{3}\right). \tag{A.15}$$

With a and b as in Eq. (A.13)

$$S = \frac{h^2}{2} + \frac{q^2}{gh}\left(1 + \frac{hh_{xx} - h_x^2}{3} + \frac{hz_{bxx}}{2} - \frac{h_x z_{bx}}{2}\right), \tag{A.16}$$

or as in Eq. (2.68),

$$M = g\frac{h^2}{2} + hU^2\left(1 + \frac{hh_{xx} - h_x^2}{3} + \frac{hz_{bxx}}{2} - \frac{h_x z_{bx}}{2}\right). \tag{A.17}$$

Appendix B
Second Picard Iteration Cycle in Cartesian Coordinates

The ensuing mathematical procedure involves Eqs. (3.52)–(3.55) and the Cauchy–Riemann Eq. (3.9),

$$u = -\frac{\partial \phi}{\partial x} = -\frac{\partial \psi}{\partial z}, \quad w = -\frac{\partial \phi}{\partial z} = +\frac{\partial \psi}{\partial x}, \tag{B.1}$$

where ϕ and ψ are the potential and stream functions, respectively, and (u, w) the velocity components in the (x, z) directions. The cycle is now commencing with the second-order u-velocity approximation, Eq. (3.63),

$$u = \frac{q}{h}\left[1 + \left(z_{bxx} - \frac{2h_x z_{bx}}{h}\right)\left(\frac{2\eta - h}{2}\right) + \left(\frac{h_{xx}}{2h} - \frac{h_x^2}{h^2}\right)\left(\frac{3\eta^2 - h^2}{3}\right)\right], \tag{B.2}$$

where $\eta(x, z) = z - z_b(x)$ is the vertical elevation above the channel bottom profile $z_b(x)$, and subindex x indicates the differentiation $\partial()/\partial x$. According to Eq. (B.1),

$$u = -\frac{\partial \psi}{\partial z} = -\frac{\partial \psi}{\partial \eta}. \tag{B.3}$$

Substitution of Eq. (B.2) into Eq. (B.3), and performing the integration in η (noting that $\mathrm{d}\eta = \mathrm{d}z$), leads to

$$\psi = -\frac{q\eta}{h}\left[1 + \left(z_{bxx} - \frac{2h_x z_{bx}}{h}\right)\left(\frac{\eta - h}{2}\right) + \left(\frac{h_{xx}}{2h} - \frac{h_x^2}{h^2}\right)\left(\frac{\eta^2 - h^2}{3}\right)\right]. \tag{B.4}$$

Alternatively, (B.4) can be written as

$$\begin{aligned} -\frac{\psi}{q} &= \frac{\eta}{h}\left[1 + a_1(\eta - h) + a_2(\eta^2 - h^2)\right], \\ a_1 &= \frac{1}{2}\left(z_{bxx} - \frac{2h_x z_{bx}}{h}\right), \quad a_2 = \frac{1}{3}\left(\frac{h_{xx}}{2h} - \frac{h_x^2}{h^2}\right). \end{aligned} \tag{B.5}$$

© Springer International Publishing AG 2017

O. Castro-Orgaz and W.H. Hager, *Non-Hydrostatic Free Surface Flows*,
Advances in Geophysical and Environmental Mechanics and Mathematics
DOI 10.1007/978-3-319-47971-2

or,

$$
\begin{aligned}
-\frac{\psi}{q} &= b_1\eta + b_2\eta^2 + b_3\eta^3,\\
b_1 &= \frac{1}{h} - a_1 - a_2 h = \frac{1}{h} - \frac{1}{2}\left(z_{bxx} - \frac{2h_x z_{bx}}{h}\right) - \frac{1}{3}\left(\frac{h_{xx}}{2} - \frac{h_x^2}{h}\right),\\
b_2 &= \frac{a_1}{h} = \frac{1}{2}\left(\frac{z_{bxx}}{h} - \frac{2h_x z_{bx}}{h^2}\right),\\
b_3 &= \frac{a_2}{h} = \frac{1}{3}\left(\frac{h_{xx}}{2h^2} - \frac{h_x^2}{h^3}\right).
\end{aligned}
\tag{B.6}
$$

Next, based on the stream function property,

$$
w = +\frac{\partial\psi}{\partial x},
\tag{B.7}
$$

the vertical velocity follows by differentiating the first of equations (B.6) with respect to x; this yields, noting that $\eta_x = \partial\eta/\partial x = -\partial z_b/\partial x$,

$$
w = +\frac{\partial\psi}{\partial x} = -q\left[\underbrace{b_1\eta_x}_{c_1} + \left(\underbrace{b_{1x} + 2b_2\eta_x}_{c_2}\right)\eta + \left(\underbrace{b_{2x} + 3b_3\eta_x}_{c_3}\right)\eta^2 + \underbrace{b_{3x}}_{c_4}\eta^3\right],
\tag{B.8}
$$

with

$$
\begin{aligned}
c_1 &= -\frac{z_{bx}}{h} + \frac{1}{2}\left(z_{bxx}z_{bx} - \frac{2h_x z_{bx}^2}{h}\right) + \frac{z_{bx}h_{xx}}{6} - \frac{z_{bx}h_x^2}{3h},\\
c_2 &= -\frac{h_x}{h^2} - \frac{z_{bxxx}}{2} - \frac{z_{bx}h_x^2}{h^2} + \frac{h_{xx}z_{bx}}{h} + \frac{h_x z_{bxx}}{h} - \frac{h_{xxx}}{6}\\
&\quad + \frac{2h_x h_{xx}}{3h} - \frac{h_x^3}{3h^2} - \frac{z_{bxx}z_{bx}}{h} + \frac{2h_x z_{bx}^2}{h^2},\\
c_3 &= \frac{z_{bxxx}}{2h} - \frac{3}{2}\frac{z_{bxx}h_x}{h^2} + 3\frac{z_{bx}h_x^2}{h^3} - \frac{3}{2}\frac{z_{bx}h_{xx}}{h^2},\\
c_4 &= \frac{h_{xxx}}{6h^2} - \frac{h_x h_{xx}}{h^3} + \frac{h_x^3}{h^4}.
\end{aligned}
\tag{B.9}
$$

The coefficients b and c have been straightforwardly evaluated from earlier coefficients a by successive substitution. It is convenient to define the coefficients

$$
\begin{aligned}
\alpha_1 &= -c_1 h = z_{bx} - \frac{1}{2}\left(z_{bxx} z_{bx} h - 2h_x z_{bx}^2\right) - \frac{z_{bx} h_{xx} h}{6} + \frac{z_{bx} h_x^2}{3}, \\
\alpha_2 &= -c_2 h = \frac{h_x}{h} + \frac{h z_{bxxx}}{2} + \frac{z_{bx} h_x^2}{h} - h_{xx} z_{bx} - h_x z_{bxx} + \frac{h h_{xxx}}{6} \\
&\quad - \frac{2h_x h_{xxx}}{3} + \frac{h_x^3}{3h} + z_{bxx} z_{bx} - \frac{2h_x z_{bx}^2}{h}, \\
\alpha_3 &= -c_3 h = -\frac{z_{bxxx}}{2} + \frac{3}{2}\frac{z_{bxx} h_x}{6h} - \frac{3 z_{bx} h_x}{h^2} + \frac{3}{2}\frac{z_{bx} h_{xx}}{h}, \\
\alpha_4 &= -c_4 h = -\frac{h_{xxx}}{6h} + \frac{h_x h_{xx}}{h^2} - \frac{h_x^3}{h^3}.
\end{aligned}
\tag{B.10}
$$

These results agree with Eq. (3.77). The result of the second iteration for w becomes now, using Eq. (B.10) into Eq. (B.8),

$$
w = \frac{q}{h}\left(\alpha_1 + \alpha_2 \eta + \alpha_3 \eta^2 + \alpha_4 \eta^3\right) = \varepsilon_1 + \varepsilon_2 \eta + \varepsilon_3 \eta^2 + \varepsilon_4 \eta^3. \tag{B.11}
$$

Now, from Eq. (B.1),

$$
w = -\frac{\partial \phi}{\partial z} = -\frac{\partial \phi}{\partial \eta}. \tag{B.12}
$$

This leads upon integration to

$$
-\phi = \varepsilon_1 \eta + \varepsilon_2 \frac{\eta^2}{2} + \varepsilon_3 \frac{\eta^3}{3} + \varepsilon_4 \frac{\eta^4}{4} + f(x), \tag{B.13}
$$

where $f(x)$ is an arbitrary function. Now, based again on Eq. (B.1),

$$
u = -\frac{\partial \phi}{\partial x}, \tag{B.14}
$$

and inserting in it Eq. (B.13) produces

$$
\begin{aligned}
u = -\frac{\partial \phi}{\partial x} &= \frac{\partial}{\partial x}\left(\varepsilon_1 \eta + \varepsilon_2 \frac{\eta^2}{2} + \varepsilon_3 \frac{\eta^3}{3} + \varepsilon_4 \frac{\eta^4}{4}\right) + f_x(x) \\
&= (\varepsilon_{1x} \eta + \varepsilon_1 \eta_x) + \left(\varepsilon_{2x} \frac{\eta^2}{2} + \varepsilon_2 \eta \eta_x\right) + \left(\varepsilon_{3x} \frac{\eta^3}{3} + \varepsilon_3 \eta^2 \eta_x\right) \\
&\quad + \left(\varepsilon_{4x} \frac{\eta^4}{4} + \varepsilon_4 \eta^3 \eta_x\right) + f_x(x).
\end{aligned}
\tag{B.15}
$$

This is the third-order approximation to the horizontal velocity component u.

Next, use is made of the Cauchy–Riemann equation

$$u = -\frac{\partial \psi}{\partial z} = -\frac{\partial \psi}{\partial \eta}, \tag{B.16}$$

where the above approximation to u is inserted. Integration of the emerging equation in the vertical direction yields

$$\begin{aligned} -\psi = &\left(\varepsilon_{1x}\frac{\eta^2}{2} + \varepsilon_1\eta_x\eta\right) + \left(\varepsilon_{2x}\frac{\eta^3}{6} + \varepsilon_2\eta_x\frac{\eta^2}{2}\right) + \left(\varepsilon_{3x}\frac{\eta^4}{12} + \varepsilon_3\eta_x\frac{\eta^3}{3}\right) \\ &+ \left(\varepsilon_{4x}\frac{\eta^5}{20} + \varepsilon_4\eta_x\frac{\eta^4}{4}\right) + f_x(x)\eta - g(x), \end{aligned} \tag{B.17}$$

in which $g(x)$ is yet another unspecified differentiable function. The boundary conditions imply

(i) at $\eta = 0, \psi$ (by choice) : $\quad\rightarrow\quad g(x) \equiv 0,$
(ii) at $\eta = h, \psi = -q$:

$$\begin{aligned} q = &\left(\varepsilon_{1x}\frac{h^2}{2} + \varepsilon_1\eta_x h\right) + \left(\varepsilon_{2x}\frac{h^3}{6} + \varepsilon_2\eta_x\frac{h^2}{2}\right) + \left(\varepsilon_{3x}\frac{h^4}{12} + \varepsilon_3\eta_x\frac{h^3}{3}\right) \\ &+ \left(\varepsilon_{4x}\frac{h^5}{20} + \varepsilon_4\eta_x\frac{h^4}{4}\right) + f_x(x)h, \end{aligned} \tag{B.18}$$

from which f_x is finally given by

$$\begin{aligned} f_x = &\frac{q}{h} - \left(\varepsilon_{1x}\frac{h}{2} + \varepsilon_1\eta_x\right) - \left(\varepsilon_{2x}\frac{h^2}{6} + \varepsilon_2\eta_x\frac{h}{2}\right) - \left(\varepsilon_{3x}\frac{h^3}{12} + \varepsilon_3\eta_x\frac{h^2}{3}\right) \\ &- \left(\varepsilon_{4x}\frac{h^4}{20} + \varepsilon_4\eta_x\frac{h^3}{4}\right). \end{aligned} \tag{B.19}$$

Back-substitution of this value of f_x into (B.15) delivers the third iteration of u,

$$\begin{aligned} u = &\frac{q}{h} + \varepsilon_{1x}\left(\eta - \frac{h}{2}\right) + \varepsilon_{2x}\left(\frac{\eta^2}{2} - \frac{h^2}{6}\right) + \varepsilon_2\eta_x\left(\eta - \frac{h}{2}\right) \\ &+ \varepsilon_{3x}\left(\frac{\eta^3}{3} - \frac{h^3}{12}\right) + \varepsilon_3\eta_x\left(\eta^2 - \frac{h^2}{3}\right) \\ &+ \varepsilon_{4x}\left(\frac{\eta^4}{4} - \frac{h^4}{20}\right) + \varepsilon_4\eta_x\left(\eta^3 - \frac{h^3}{4}\right), \end{aligned} \tag{B.20}$$

or,

$$
\begin{aligned}
u &= \frac{q}{h} + \underbrace{(\varepsilon_{1x} + \varepsilon_2 \eta_x)}_{\gamma_1}\left(\eta - \frac{h}{2}\right) + \underbrace{\left(\frac{\varepsilon_{2x}}{2} + \varepsilon_3 \eta_x\right)}_{\gamma_2}\left(\eta^2 - \frac{h^2}{3}\right) \\
&\quad + \underbrace{\left(\frac{\varepsilon_{3x}}{3} + \varepsilon_4 \eta_x\right)}_{\gamma_3}\left(\eta^3 - \frac{h^3}{4}\right) + \underbrace{\left(\frac{\varepsilon_{4x}}{4}\right)}_{\gamma_4}\left(\eta^4 - \frac{h^4}{5}\right) \\
&= \frac{q}{h}\left[1 + \beta_1\left(\eta - \frac{h}{2}\right) + \beta_2\left(\eta^2 - \frac{h^2}{3}\right)\right. \\
&\quad \left. + \beta_3\left(\eta^3 - \frac{h^3}{4}\right) + \beta_4\left(\eta^4 - \frac{h^4}{5}\right)\right].
\end{aligned}
\tag{B.21}
$$

Determination of the γ-coefficients is conducted by differentiation with respect to x of the ε-coefficients that are simply the α-coefficients (Eq. B.10) multiplied by (q/h). The process is long and tedious, but there is nothing special on it. After carefully conducting these operations, the result is

$$
\begin{aligned}
\beta_1 &= z_{bxx} - \frac{2h_x z_{bx}}{h} - z_{bx} z_{bxxx} h - \frac{2h_x^2 z_{bx}^2}{h} - \frac{h z_{bxx}^2}{2} + 2h_{xx} z_{bx}^2 + 3h_x z_{bx} z_{bxx} \\
&\quad - \frac{z_{bx} h_{xxx} h}{3} - \frac{2h_x^3 z_{bx}}{3h} - z_{bx}^2 z_{bxx} + \frac{2h_x z_{bx}^3}{h} + \frac{4h_x z_{bx} h_{xx}}{3} + \frac{h_x^2 z_{bxx}}{3} - \frac{h_{xx} z_{bxx} h}{6}, \\
\beta_2 &= \frac{h_{xx}}{2h} - \frac{h_x^2}{h^2} + \frac{h z_{bxxx}}{4} - \frac{z_{bx} h_x^3}{h^2} + \frac{z_{bxx} h_x^2}{h} + \frac{3 z_{bx} h_x h_{xx}}{2h} - \frac{h_{xxx} z_{bx}}{2} \\
&\quad - h_{xx} z_{bxx} - \frac{h_x z_{bxx}}{2} + \frac{h h_{xxx}}{12} + \frac{5h_x^2 h_{xx}}{6h} - \frac{h_{xx}^2}{3} - \frac{h_x h_{xxx}}{3} - \frac{h_x^4}{3h^2} - \frac{4h_x z_{bx} z_{bxx}}{h} \\
&\quad + \frac{z_{bxx}^2}{2} + z_{bx} z_{bxxx} + \frac{5h_x^2 z_{bx}^2}{h^2} - \frac{5h_{xx} z_{bx}^2}{2h}, \\
\beta_3 &= -\frac{z_{bxxx}}{6} + \frac{2z_{bxx} h_x}{3h} - \frac{2h_x^2 z_{bxx}}{h^2} + \frac{4h_x^3 z_{bx}}{h^3} + \frac{z_{bxx} h_{xx}}{h} - \frac{4 z_{bx} h_x h_{xx}}{h^2} + \frac{2 z_{bx} h_{xxx}}{3h}, \\
\beta_4 &= -\frac{h_{xxxx}}{24h} + \frac{h_x^4}{h^4} + \frac{h_{xx}^2}{4h^2} - \frac{3h_x^2 h_{xx}}{h^3} + \frac{h_x h_{xxx}}{3h^2}.
\end{aligned}
\tag{B.22}
$$

These results correspond to the coefficients stated in the main text as Eq. (3.79).

Appendix C
Picard Iteration in Curvilinear Coordinates

The continuity equation in a curvilinear system of coordinates, with ξ as the bottom-fitted coordinate and ζ as the orthogonal coordinate to the bottom, is (Dressler 1978)

$$\frac{\partial u_\xi}{\partial \xi} + \frac{\partial}{\partial \varsigma}[(1 - \kappa_b \varsigma) w_\varsigma] = 0. \tag{C.1}$$

Here u_ξ is the velocity component in the ξ-direction, $\kappa_b = \kappa_b(\xi)$ the curvature of the bottom profile, and w_ζ the velocity component in the ζ-direction[1]. The irrotational flow condition is given by (Dressler 1978)

$$\frac{\partial w_\varsigma}{\partial \xi} - \frac{\partial}{\partial \varsigma}[(1 - \kappa_b \varsigma) u_\xi] = 0. \tag{C.2}$$

To find the velocity components, a stream function ψ is defined by the equations

$$u_\xi = -\frac{\partial \psi}{\partial \varsigma}, \quad w_\varsigma = +\frac{1}{(1 - \kappa_b \varsigma)} \frac{\partial \psi}{\partial \xi}. \tag{C.3}$$

Inserting Eq. (C.3) into Eq. (C.1) yields

$$-\frac{\partial^2 \psi}{\partial \xi \partial \varsigma} + \frac{\partial}{\partial \varsigma}\left[\underbrace{\frac{(1 - \kappa_b \varsigma)}{(1 - \kappa_b \varsigma)}}_{=1} \frac{\partial \psi}{\partial \xi}\right] = 0. \tag{C.4}$$

This proves that the definition of ψ by Eq. (C.3) satisfies the mass conservation balance. Inserting Eq. (C.3) into Eq. (C.2) yields the field equation for ψ as

[1]For a physical solution, the Jacobian of the transformation $(x, z) \rightarrow (\xi, \zeta)$, $J = 1 - \kappa_b N$ must be positive. Therefore, for $\kappa_b > 0$, i.e., the flow over a spillway flip bucket, the constraint $\kappa_b N < 1$ is needed to preserve physically correct solutions.

© Springer International Publishing AG 2017

O. Castro-Orgaz and W.H. Hager, *Non-Hydrostatic Free Surface Flows*,
Advances in Geophysical and Environmental Mechanics and Mathematics
DOI 10.1007/978-3-319-47971-2

$$\frac{\partial}{\partial\xi}\left(\frac{1}{(1-\kappa_b\varsigma)}\frac{\partial\psi}{\partial\xi}\right)+\frac{\partial}{\partial\varsigma}\left[(1-\kappa_b\varsigma)\frac{\partial\psi}{\partial\varsigma}\right]=0. \tag{C.5}$$

Obviously, for straight-bottomed channels, $\kappa_b = 0$ so that Eq. (C.5) reduces to the standard Laplacian of the stream function

$$\frac{\partial^2\psi}{\partial\xi^2}+\frac{\partial^2\psi}{\partial\varsigma^2}=0. \tag{C.6}$$

Further, let a potential function ϕ be defined by

$$u_\xi=-\frac{1}{(1-\kappa_b\varsigma)}\frac{\partial\phi}{\partial\xi},\quad w_\varsigma=-\frac{\partial\phi}{\partial\varsigma}. \tag{C.7}$$

Inserting Eq. (C.7) into Eq. (C.2) yields

$$-\frac{\partial^2\phi}{\partial\xi\partial\varsigma}+\frac{\partial}{\partial\varsigma}\left[\underbrace{\frac{(1-\kappa_b\varsigma)}{(1-\kappa_b\varsigma)}}_{=1}\frac{\partial\phi}{\partial\xi}\right]=0. \tag{C.8}$$

This proves that the definition of ϕ by Eq. (C.7) satisfies the zero vorticity requirement. Inserting Eq. (C.7) into Eq. (C.1) yields a field equation for ϕ as

$$-\frac{\partial}{\partial\xi}\left(\frac{1}{(1-\kappa_b\varsigma)}\frac{\partial\phi}{\partial\xi}\right)-\frac{\partial}{\partial\varsigma}\left[(1-\kappa_b\varsigma)\frac{\partial\phi}{\partial\varsigma}\right]=0. \tag{C.9}$$

For $\kappa_b = 0$, Eq. (C.9) reduces to the usual Laplacian of the potential function

$$\frac{\partial^2\phi}{\partial\xi^2}+\frac{\partial^2\phi}{\partial\varsigma^2}=0. \tag{C.10}$$

Equating velocity components in Eqs. (C.3) and (C.7), one finds the Cauchy–Riemann equations in curvilinear coordinates as

$$u_\xi=-\frac{1}{(1-\kappa_b\varsigma)}\frac{\partial\phi}{\partial\xi}=-\frac{\partial\psi}{\partial\varsigma},\quad w_\varsigma=-\frac{\partial\phi}{\partial\varsigma}=+\frac{1}{(1-\kappa_b\varsigma)}\frac{\partial\psi}{\partial\xi}. \tag{C.11}$$

The solution to the potential flow problem is either conducted by solving the field equations for ϕ and ψ, or, alternatively, by a Picard iteration of the Cauchy–Riemann equations. This last method is explained below.

The first cycle starts with a zero bottom-normal velocity $w_\varsigma^{(0)} = 0$, with the superindex indicating the order of iteration cycle. With g as an arbitrary function of ξ, the initial approximation to the potential function is from the second of Eq. (C.7)

$$\phi^{(0)} = -\int w_\varsigma^{(0)} \mathrm{d}\varsigma - g(\xi) = -g(\xi). \tag{C.12}$$

The first approximation to the bottom-parallel velocity component is from the first of Eq. (C.7), with $g' = \partial g/\partial\xi$,

$$u_\xi^{(1)} = -\frac{1}{(1-\kappa_b\varsigma)}\frac{\partial\phi^{(0)}}{\partial\xi} = \frac{g'}{(1-\kappa_b\varsigma)}. \tag{C.13}$$

Let f be an arbitrary function of the ξ-coordinate, then the first approximation of the stream function follows using the first of Eq. (C.3) after inserting Eq. (C.13) as

$$\psi^{(1)} = -\int u_\xi^{(1)} \mathrm{d}\varsigma + f(\xi) = +\frac{g'}{\kappa_b}\ln(1-\kappa_b\varsigma) + f(\xi). \tag{C.14}$$

The boundary condition at the bottom level is $\psi^{(1)}(\varsigma = 0) = 0$ and yields

$$\psi^{(1)}(\varsigma = 0) = 0 \quad \Rightarrow \quad f = 0. \tag{C.15}$$

The free surface boundary condition at $\varsigma = N$ is used to find g' from Eq. (C.14) as

$$\psi^{(1)}(\varsigma = N) = -q \quad \Rightarrow \quad g' = \frac{-q\kappa_b}{\ln(1-\kappa_b N)}. \tag{C.16}$$

Inserting Eq. (C.16) into Eq. (C.13), the velocity profile of the first iteration cycle is given by the free vortex law as

$$u_\xi^{(1)} = \frac{C^{(1)}}{(1-\kappa_b\varsigma)}. \tag{C.17}$$

Here, $C^{(1)} = g'$ is the first approximation to the tangential bottom velocity, and the stream function associated to this law is from Eq. (C.14)

$$\psi^{(1)} = \frac{C^{(1)}}{\kappa_b}\ln(1-\kappa_b\varsigma). \tag{C.18}$$

The second iterative cycle starts by computing the first approximation to the bottom-normal velocity component $w_\varsigma^{(1)}$, which is from the second of Eq. (C.3)

$$w_\varsigma^{(1)} = +\frac{1}{(1-\kappa_b\varsigma)}\frac{\partial\psi^{(1)}}{\partial\xi}. \tag{C.19}$$

Inserting Eq. (C.18) into Eq. (C.19) gives after differentiation

$$w_{\xi}^{(1)} = \frac{\ln(1-\kappa_b\varsigma)}{\kappa_b(1-\kappa_b\varsigma)}\frac{\partial C^{(1)}}{\partial \xi} - \frac{1}{\kappa^2}\frac{\partial \kappa_b}{\partial \xi}\left[\frac{\ln(1-\kappa_b\varsigma)}{(1-\kappa_b\varsigma)} + \frac{\kappa_b\varsigma}{(1-\kappa_b\varsigma)^2}\right]C^{(1)}. \tag{C.20}$$

Equation (C.20) is identical to that of Dressler (1978) using asymptotic expansions.

With h as an arbitrary function of ξ, the first approximation to the potential function is, from the second of Eq. (C.7),

$$\phi^{(1)} = -\int w_{\varsigma}^{(1)} \mathrm{d}\varsigma - h(\xi). \tag{C.21}$$

Inserting Eq. (C.20) into Eq. (C.21) gives, after integration,

$$\begin{aligned}\phi^{(1)} = {} & \frac{1}{2\kappa_b^2}[\ln(1-\kappa_b\varsigma)]^2\frac{\partial C^{(1)}}{\partial \xi} \\ & + \frac{1}{\kappa_b^2}\frac{\partial \kappa_b}{\partial \xi}\left[-\frac{[\ln(1-\kappa_b\varsigma)]^2}{2\kappa_b} + \frac{1}{\kappa_b(1-\kappa_b\varsigma)} + \frac{\ln(1-\kappa_b\varsigma)}{\kappa_b}\right]C^{(1)} - h\,.\end{aligned} \tag{C.22}$$

In the integration of Eq. (C.21), use was made of the primitive functions

$$\begin{aligned}\int \frac{\ln(1-\kappa_b\varsigma)}{(1-\kappa_b\varsigma)}\mathrm{d}\varsigma &= -\frac{1}{2\kappa_b}[\ln(1-\kappa_b\varsigma)]^2, \\ \int \frac{\kappa_b\varsigma}{(1-\kappa_b\varsigma)^2}\mathrm{d}\varsigma &= \frac{1}{\kappa_b}\left[\frac{1}{(1-\kappa_b\varsigma)} + \ln(1-\kappa_b\varsigma)\right].\end{aligned} \tag{C.23}$$

Next, for simplicity, assume a constant curvature surface; then, Eq. (C.22) reduces to

$$\phi^{(1)} = \frac{1}{2\kappa_b^2}[\ln(1-\kappa_b\varsigma)]^2\frac{\partial C^{(1)}}{\partial \xi} - h. \tag{C.24}$$

The second approximation to the bottom-parallel velocity component is obtained from the first of Eq. (C.7) as

$$u_{\xi}^{(2)} = -\frac{1}{(1-\kappa_b\varsigma)}\frac{\partial \phi^{(1)}}{\partial \xi}. \tag{C.25}$$

Inserting Eq. (C.24) into Eq. (C.25) gives after differentiation

$$u_{\xi}^{(2)} = \frac{h'}{(1-\kappa_b\varsigma)} - \frac{1}{2\kappa_b^2}\frac{[\ln(1-\kappa_b\varsigma)]^2}{(1-\kappa_b\varsigma)}\frac{\partial^2 C^{(1)}}{\partial \xi^2}. \tag{C.26}$$

Equation (C.26) is the second approximation for the velocity parallel to the bottom. To find a closed-form model, i.e., a differential equation to compute $N = N(\xi)$, $h' = \partial h/\partial\xi$ must be determined using the boundary conditions for the stream function, and the second derivative of $C^{(1)}$ expressed versus the derivatives of N with respect to ξ.

The first derivative of $C^{(1)}$ is deduced from Eq. (C.16)

$$\begin{aligned}\frac{\partial C^{(1)}}{\partial\xi} &= \frac{\partial}{\partial\xi}\left(\frac{-q\kappa_b}{\ln(1-\kappa_b N)}\right) = \frac{-q\kappa_b^2}{[\ln(1-\kappa_b N)]^2}\frac{1}{(1-\kappa_b N)}\frac{\partial N}{\partial\xi}\\ &= \frac{\kappa_b C^{(1)}}{(1-\kappa_b N)\ln(1-\kappa_b N)}\frac{\partial N}{\partial\xi}.\end{aligned} \tag{C.27}$$

The second derivative of $C^{(1)}$ follows by differentiating Eq. (C.27); the result is

$$\begin{aligned}\frac{\partial^2 C^{(1)}}{\partial\xi^2} &= \frac{\kappa_b C^{(1)}}{(1-\kappa_b N)\ln(1-\kappa_b N)}\frac{\partial^2 N}{\partial\xi^2}\\ &+ \frac{\kappa_b^2 C^{(1)}}{(1-\kappa_b N)^2\ln(1-\kappa_b N)}\left(\frac{\partial N}{\partial\xi}\right)^2\left[1+\frac{2}{\ln(1-\kappa_b N)}\right].\end{aligned} \tag{C.28}$$

Inserting Eq. (C.28) into Eq. (C.26) yields after some manipulation

$$u_\xi^{(2)} = \frac{h'}{(1-\kappa_b\varsigma)} + \frac{C^{(1)}}{(1-\kappa_b\varsigma)}\frac{\Omega}{2}\frac{[\ln(1-\kappa_b\varsigma)]^2}{[\ln(1-\kappa_b N)]^2}, \tag{C.29}$$

or with Eq. (C.17)

$$u_\xi^{(2)} = \frac{h'}{(1-\kappa_b\varsigma)} + u_\xi^{(1)}\frac{\Omega}{2}\frac{[\ln(1-\kappa_b\varsigma)]^2}{[\ln(1-\kappa_b N)]^2}. \tag{C.30}$$

With $N_\xi = \partial N/\partial\xi$ and $N_{\xi\xi} = \partial^2 N/\partial\xi^2$, Ω is

$$\Omega = -\frac{N_{\xi\xi}}{\kappa_b}\frac{\ln(1-\kappa_b N)}{(1-\kappa_b N)} - \frac{N_\xi^2[2+\ln(1-\kappa_b N)]}{(1-\kappa_b N)^2}. \tag{C.31}$$

Using the first of Eq. (C.3), the second approximation of the stream function is

$$\psi^{(2)} = -\int u_\xi^{(2)}\mathrm{d}\varsigma + b(\xi). \tag{C.32}$$

The boundary condition at the bottom level $\varsigma = 0$ then yields

$$\psi^{(2)}(\varsigma = 0) = 0 \quad \Rightarrow \quad b = 0. \tag{C.33}$$

Inserting Eq. (C.30) into Eq. (C.32) produces

$$-\psi(\varsigma) = h' \int \frac{\mathrm{d}\varsigma}{(1-\kappa_b\varsigma)} + \frac{C^{(1)}\Omega}{2[\ln(1-\kappa_b N)]^2} \int \frac{[\ln(1-\kappa_b\varsigma)]^2}{(1-\kappa_b\varsigma)} \mathrm{d}\varsigma. \tag{C.34}$$

Using the primitive functions

$$\begin{aligned} \int \frac{[\ln(1-\kappa_b\varsigma)]^2}{(1-\kappa_b\varsigma)} \mathrm{d}\varsigma &= -\frac{1}{3\kappa_b}[\ln(1-\kappa_b\varsigma)]^3, \\ \int \frac{\mathrm{d}\varsigma}{(1-\kappa_b\varsigma)} &= -\frac{1}{\kappa_b}\ln(1-\kappa_b\varsigma), \end{aligned} \tag{C.35}$$

Equation (C.34) is transformed to

$$-\psi(\varsigma) = -\frac{h'}{\kappa_b}\ln(1-\kappa_b\varsigma) - \frac{C^{(1)}\Omega}{6\kappa_b[\ln(1-\kappa_b N)]^2}[\ln(1-\kappa_b\varsigma)]^3, \tag{C.36}$$

which satisfies the boundary condition $\psi(\varsigma = 0) = 0$.

Evaluating Eq. (C.36) at the free surface $\varsigma = N$ produces the following identity by invoking the stream function boundary condition $\psi = -q$ there, namely

$$q = -\frac{h'}{\kappa_b}\ln(1-\kappa_b N) - \frac{C^{(1)}\Omega}{6\kappa_b}[\ln(1-\kappa_b N)]. \tag{C.37}$$

From Eq. (C.37), h' is given by

$$h' = -\frac{q\kappa_b}{\ln(1-\kappa_b N)} - \frac{C^{(1)}\Omega}{6}. \tag{C.38}$$

Substituting Eq. (C.38) into Eq. (29) gives

$$u_\xi^{(2)} = -\frac{q\kappa_b}{\ln(1-\kappa_b N)(1-\kappa_b\varsigma)} - \frac{C^{(1)}\Omega}{6(1-\kappa_b\varsigma)} + \frac{C^{(1)}}{(1-\kappa_b\varsigma)}\frac{\Omega}{2}\frac{[\ln(1-\kappa_b\varsigma)]^2}{[\ln(1-\kappa_b N)]^2}, \tag{C.39}$$

or after some manipulation,

$$u_\xi^{(2)} = \frac{C^{(1)}}{(1-\kappa_b\varsigma)}\left[1 - \frac{\Omega}{2}\left\{\frac{1}{3} - \frac{[\ln(1-\kappa_b\varsigma)]^2}{[\ln(1-\kappa_b N)]^2}\right\}\right]. \tag{C.40}$$

Eliminating $C^{(1)}$ with the aid of Eq. (C.17) finally yields

$$u_{\xi}^{(2)} = u_{\xi}^{(1)} \left[1 - \frac{\Omega}{2} \left\{ \frac{1}{3} - \frac{[\ln(1 - \kappa_b \varsigma)]^2}{[\ln(1 - \kappa_b N)]^2} \right\} \right]. \tag{C.41}$$

Reference

Dressler, R. F. (1978). New nonlinear shallow flow equations with curvature. *Journal of Hydraulic Research, 16*(3), 205–222.

Appendix D
Derivation of the Laplace Equation for the x-ψ Transformation

The purpose of this section is to derive Eq. (3.250) for the Laplace operator in the x-ψ transformation. Details are given by Montes (1994), but clarity in some derivations is regained by following Thom and Apelt (1961). In this Appendix, the vertical coordinate is denoted by y and not by z as used in Eq. (3.250) due to the use of complex variables, with $z = x + iy$. First, the inverse transformation is defined, with the physical coordinates (x, y) given as functions of the stream, ψ, and potential, ϕ, functions as

$$x = x(\phi, \psi),\ y = y(\phi, \psi). \tag{D.1}$$

Let $W = \phi + i\psi$ be the complex potential and $z = f(W)$; standard rules of calculus furnish then the identities

$$\frac{\partial z}{\partial \phi} = \frac{\partial x}{\partial \phi} + i\frac{\partial y}{\partial \phi} = \frac{\mathrm{d}f}{\mathrm{d}W}\frac{\partial W}{\partial \phi}, \tag{D.2}$$

$$\frac{\partial z}{\partial \psi} = \frac{\partial x}{\partial \psi} + i\frac{\partial y}{\partial \psi} = \frac{\mathrm{d}f}{\mathrm{d}W}\frac{\partial W}{\partial \psi}. \tag{D.3}$$

Note that

$$\frac{\partial W}{\partial \psi} = i, \quad \frac{\partial W}{\partial \phi} = 1. \tag{D.4}$$

Inserting Eq. (D.4) into Eqs. (D.2) and (D.3) yields

$$\frac{\partial x}{\partial \phi} + i\frac{\partial y}{\partial \phi} = \frac{\mathrm{d}z}{\mathrm{d}W}, \tag{D.5}$$

$$\frac{\partial x}{\partial \psi} + i\frac{\partial y}{\partial \psi} = i\frac{\mathrm{d}z}{\mathrm{d}W}. \tag{D.6}$$

© Springer International Publishing AG 2017

O. Castro-Orgaz and W.H. Hager, *Non-Hydrostatic Free Surface Flows*,
Advances in Geophysical and Environmental Mechanics and Mathematics
DOI 10.1007/978-3-319-47971-2

Moreover, if Eq. (D.6) is multiplied by $-i$, thereby observing that $i^2 = -1$, then

$$\frac{\partial y}{\partial \psi} - i\frac{\partial x}{\partial \psi} = \frac{\mathrm{d}z}{\mathrm{d}W}. \tag{D.7}$$

Identifying real and imaginary parts in Eqs. (D.5) and (D.7) results in

$$\frac{\partial x}{\partial \phi} = \frac{\partial y}{\partial \psi}, \tag{D.8}$$

$$\frac{\partial y}{\partial \phi} = -\frac{\partial x}{\partial \psi}. \tag{D.9}$$

These are the Cauchy–Riemann equations for the inverse transformation given by Eq. (D.1). The Laplacians emerge by further differentiations of Eqs. (D.5)–(D.7). For Eq. (D.5), this gives

$$\frac{\partial^2 x}{\partial \phi^2} + i\frac{\partial^2 y}{\partial \phi^2} = \frac{\partial}{\partial \phi}\left(\frac{\mathrm{d}z}{\mathrm{d}W}\right) = \frac{\mathrm{d}^2 z}{\mathrm{d}W^2}\frac{\partial W}{\partial \phi} = \frac{\mathrm{d}^2 z}{\mathrm{d}W^2}. \tag{D.10}$$

Similarly, differentiation of Eq. (D.7) gives

$$\frac{\partial^2 y}{\partial \psi^2} - i\frac{\partial^2 x}{\partial \psi^2} = \frac{\partial}{\partial \psi}\left(\frac{\mathrm{d}z}{\mathrm{d}W}\right) = \frac{\mathrm{d}^2 z}{\mathrm{d}W^2}\frac{\partial W}{\partial \psi} = i\frac{\mathrm{d}^2 z}{\mathrm{d}W^2}, \tag{D.11}$$

or

$$\frac{\partial^2 x}{\partial \psi^2} + i\frac{\partial^2 y}{\partial \psi^2} = -\frac{\mathrm{d}^2 z}{\mathrm{d}W^2}. \tag{D.12}$$

Summing Eqs. (D.10) and (D.12) and equating real and imaginary parts yield, respectively, the Laplace operators for the inverse transformation as

$$\nabla^2 x = \frac{\partial^2 x}{\partial \psi^2} + \frac{\partial^2 x}{\partial \phi^2} = 0, \tag{D.13}$$

$$\nabla^2 y = \frac{\partial^2 y}{\partial \psi^2} + \frac{\partial^2 y}{\partial \phi^2} = 0. \tag{D.14}$$

Consider a transformation where one seeks $y = y(x, Q)$, with Q as an auxiliary function of (ψ, ϕ). Further, $x = x(\psi, \phi)$ as previously stated in Eq. (D.1). Use of Eq. (D.14) requires, therefore, determination of the derivatives of y with respect to (ψ, ϕ). Again, basic rules of differentiation yield

$$\frac{\partial y}{\partial \phi} = \frac{\partial y}{\partial x}\frac{\partial x}{\partial \phi} + \frac{\partial y}{\partial Q}\frac{\partial Q}{\partial \phi}, \tag{D.15}$$

$$\frac{\partial y}{\partial \psi} = \frac{\partial y}{\partial x}\frac{\partial x}{\partial \psi} + \frac{\partial y}{\partial Q}\frac{\partial Q}{\partial \psi}. \tag{D.16}$$

A second differential of Eq. (D.15) gives

$$\frac{\partial^2 y}{\partial \phi^2} = \frac{\partial^2 y}{\partial x \partial \phi}\frac{\partial x}{\partial \phi} + \frac{\partial y}{\partial x}\frac{\partial^2 x}{\partial \phi^2} + \frac{\partial^2 y}{\partial Q \partial \phi}\frac{\partial Q}{\partial \phi} + \frac{\partial y}{\partial Q}\frac{\partial^2 Q}{\partial \phi^2}. \tag{D.17}$$

Noting the differential identity

$$\frac{\partial (\cdot)}{\partial \phi} = \frac{\partial (\cdot)}{\partial x}\frac{\partial x}{\partial \phi} + \frac{\partial (\cdot)}{\partial Q}\frac{\partial Q}{\partial \phi}, \tag{D.18}$$

one easily finds

$$\frac{\partial^2 y}{\partial x \partial \phi} = \frac{\partial^2 y}{\partial x^2}\frac{\partial x}{\partial \phi} + \frac{\partial^2 y}{\partial x \partial Q}\frac{\partial Q}{\partial \phi}, \tag{D.19}$$

$$\frac{\partial^2 y}{\partial \phi \partial Q} = \frac{\partial^2 y}{\partial x \partial Q}\frac{\partial x}{\partial \phi} + \frac{\partial^2 y}{\partial Q^2}\frac{\partial Q}{\partial \phi}. \tag{D.20}$$

Inserting Eqs. (D.19)–(D.20) into Eq. (D.17) yields

$$\frac{\partial^2 y}{\partial \phi^2} = \frac{\partial^2 y}{\partial x^2}\left(\frac{\partial x}{\partial \phi}\right)^2 + 2\frac{\partial^2 y}{\partial x \partial Q}\frac{\partial Q}{\partial \phi}\frac{\partial x}{\partial \phi} + \frac{\partial^2 y}{\partial Q^2}\left(\frac{\partial Q}{\partial \phi}\right)^2 + \frac{\partial y}{\partial x}\frac{\partial^2 x}{\partial \phi^2} + \frac{\partial y}{\partial Q}\frac{\partial^2 Q}{\partial \phi^2}. \tag{D.21}$$

Similarly, a further differentiation of Eq. (D.16) gives

$$\frac{\partial^2 y}{\partial \psi^2} = \frac{\partial^2 y}{\partial x^2}\left(\frac{\partial x}{\partial \psi}\right)^2 + 2\frac{\partial^2 y}{\partial x \partial Q}\frac{\partial Q}{\partial \psi}\frac{\partial x}{\partial \psi} + \frac{\partial^2 y}{\partial Q^2}\left(\frac{\partial Q}{\partial \psi}\right)^2 + \frac{\partial y}{\partial x}\frac{\partial^2 x}{\partial \psi^2} + \frac{\partial y}{\partial Q}\frac{\partial^2 Q}{\partial \psi^2}. \tag{D.22}$$

Inserting Eqs. (D.21) and (D.22) into Eq. (D.14), the following equation is generated

$$\begin{aligned}&\frac{\partial^2 y}{\partial x^2}\left[\left(\frac{\partial x}{\partial \phi}\right)^2 + \left(\frac{\partial x}{\partial \psi}\right)^2\right] + 2\frac{\partial^2 y}{\partial x \partial Q}\left(\frac{\partial Q}{\partial \phi}\frac{\partial x}{\partial \phi} + \frac{\partial Q}{\partial \psi}\frac{\partial x}{\partial \psi}\right)\\ &+ \frac{\partial^2 y}{\partial Q^2}\left[\left(\frac{\partial Q}{\partial \phi}\right)^2 + \left(\frac{\partial Q}{\partial \psi}\right)^2\right] + \frac{\partial y}{\partial x}\left(\frac{\partial^2 x}{\partial \phi^2} + \frac{\partial^2 x}{\partial \psi^2}\right) + \frac{\partial y}{\partial Q}\left(\frac{\partial^2 Q}{\partial \phi^2} + \frac{\partial^2 Q}{\partial \psi^2}\right) = 0.\end{aligned} \tag{D.23}$$

Consider next the function $Q = \psi$. The independent variables are x and ψ in this case, implying that $\partial x/\partial\psi = 0$. Imposing these conditions in Eq. (D.23) gives

$$\frac{\partial^2 y}{\partial x^2}\left(\frac{\partial x}{\partial \phi}\right)^2 + 2\frac{\partial^2 y}{\partial x \partial \psi}\frac{\partial \psi}{\partial \phi}\frac{\partial x}{\partial \phi} + \frac{\partial^2 y}{\partial \psi^2}\left[\left(\frac{\partial \psi}{\partial \phi}\right)^2 + 1\right] + \frac{\partial y}{\partial x}\left(\frac{\partial^2 x}{\partial \phi^2} + \frac{\partial^2 x}{\partial \psi^2}\right) + \frac{\partial y}{\partial \psi}\left(\frac{\partial^2 \psi}{\partial \phi^2} + \frac{\partial^2 \psi}{\partial \psi^2}\right) = 0. \tag{D.24}$$

Using Eq. (D.13), and noting that the last term in Eq. (D.24) is zero, one obtains

$$\frac{\partial^2 y}{\partial x^2}\left(\frac{\partial x}{\partial \phi}\right)^2 + 2\frac{\partial^2 y}{\partial x \partial \psi}\frac{\partial \psi}{\partial \phi}\frac{\partial x}{\partial \phi} + \frac{\partial^2 y}{\partial \psi^2}\left[\left(\frac{\partial \psi}{\partial \phi}\right)^2 + 1\right] = 0. \tag{D.25}$$

By resort to Eq. (D.8)

$$\frac{\partial^2 y}{\partial x^2}\left(\frac{\partial y}{\partial \psi}\right)^2 + 2\frac{\partial^2 y}{\partial x \partial \psi}\frac{\partial y}{\partial \psi}\frac{\partial \psi}{\partial \phi} + \frac{\partial^2 y}{\partial \psi^2}\left[\left(\frac{\partial \psi}{\partial \phi}\right)^2 + 1\right] = 0, \tag{D.26}$$

from where it remains to compute $\partial\psi/\partial\phi$. From Eqs. (D.2)–(D.3), one deduces

$$\frac{\partial z}{\partial \phi} = \frac{\partial x}{\partial \phi} + i\frac{\partial y}{\partial \phi} = \frac{\partial x}{\partial \phi} + i\left(\frac{\partial y}{\partial x}\frac{\partial x}{\partial \phi} + \frac{\partial y}{\partial Q}\frac{\partial Q}{\partial \phi}\right) = \frac{\mathrm{d}z}{\mathrm{d}W}, \tag{D.27}$$

$$\frac{\partial z}{\partial \psi} = \frac{\partial x}{\partial \psi} + i\frac{\partial y}{\partial \psi} = \frac{\partial x}{\partial \psi} + i\left(\frac{\partial y}{\partial x}\frac{\partial x}{\partial \psi} + \frac{\partial y}{\partial Q}\frac{\partial Q}{\partial \psi}\right) = i\frac{\mathrm{d}z}{\mathrm{d}W}. \tag{D.28}$$

Equating the imaginary parts reveals the identity

$$\frac{\partial y}{\partial x}\frac{\partial x}{\partial \phi} + \frac{\partial y}{\partial Q}\frac{\partial Q}{\partial \phi} = -\frac{\partial x}{\partial \psi}. \tag{D.29}$$

Setting again $Q = \psi$ and $\partial x/\partial\psi = 0$ yields

$$\frac{\partial y}{\partial x}\frac{\partial x}{\partial \phi} + \frac{\partial y}{\partial \psi}\frac{\partial \psi}{\partial \phi} = 0. \tag{D.30}$$

After inserting Eq. (D.8),

$$\frac{\partial \psi}{\partial \phi} = -\frac{\partial y}{\partial x}. \tag{D.31}$$

Inserting Eq. (D.31) into Eq. (D.26) produces, finally, Eq. (3.250) as

$$\frac{\partial^2 y}{\partial x^2}\left(\frac{\partial y}{\partial \psi}\right)^2 - 2\frac{\partial^2 y}{\partial x \partial \psi}\frac{\partial y}{\partial \psi}\frac{\partial y}{\partial x} + \frac{\partial^2 y}{\partial \psi^2}\left[1 + \left(\frac{\partial y}{\partial x}\right)^2\right] = 0. \tag{D.32}$$

References

Montes, J. S. (1994). Potential flow solution to the 2D transition form mild to steep slope. *Journal of Hydraulic Engineering*, *120*(5), 601–621.

Thom, A., & Apelt, C. (1961). *Field computations in engineering and physics*. London: Van Nostrand.

Appendix E
Plane Open-Channel Flow Using Flow Net-Based Coordinates

Consider potential curvilinear flow over a curved bed (Fig. E.1a). The bed and free surface streamlines, determined by respective values of the stream function $\psi = 0$ and $\psi = -q$, are given by the coordinates (x_b, z_b) and (x_s, z_s), respectively. Both curves $z_s = z_s(x_s)$ and $z_b = z_b(x_b)$ are connected by equipotential lines $\phi = \text{const}$. The connecting points b and s are shifted by the distances $\varepsilon(x_s)$ and $t(x_s)$ in the horizontal and vertical directions, given by,

$$t = \int_0^{N_o} \cos\theta \mathrm{d}n, \quad \varepsilon = \int_0^{N_o} \sin\theta \mathrm{d}n. \tag{E.1}$$

Here, θ is the streamline inclination angle with the horizontal, at distance n measured along the line $\phi = \text{const.}$, and N_o is its length. For each equipotential line, ε is different. In this section, the limitations in the approximate treatment of plane open-channel flows by Matthew (1963) and Hager and Hutter (1984) based on stream and equipotential lines-based coordinates are discussed, and then, this theory is related to the Picard iteration method by Matthew (1991) using Cartesian coordinates.

The velocity distribution along the equipotential line b–s in Fig. E.1a is

$$V = V_s \exp\left(- \int_n^{N_o} \frac{\mathrm{d}n'}{R} \right), \tag{E.2}$$

where V_s is the modulus of the velocity vector at the free surface and R the radius of the streamline curvature at the coordinate n. Matthew (1963) and Hager and Hutter (1984) approximated the function $1/R$, with $v = n/N_o$, by

$$\frac{1}{R} = \frac{1}{R_b} + \left(\frac{1}{R_s} - \frac{1}{R_b} \right) v. \tag{E.3}$$

© Springer International Publishing AG 2017

O. Castro-Orgaz and W.H. Hager, *Non-Hydrostatic Free Surface Flows*,
Advances in Geophysical and Environmental Mechanics and Mathematics
DOI 10.1007/978-3-319-47971-2

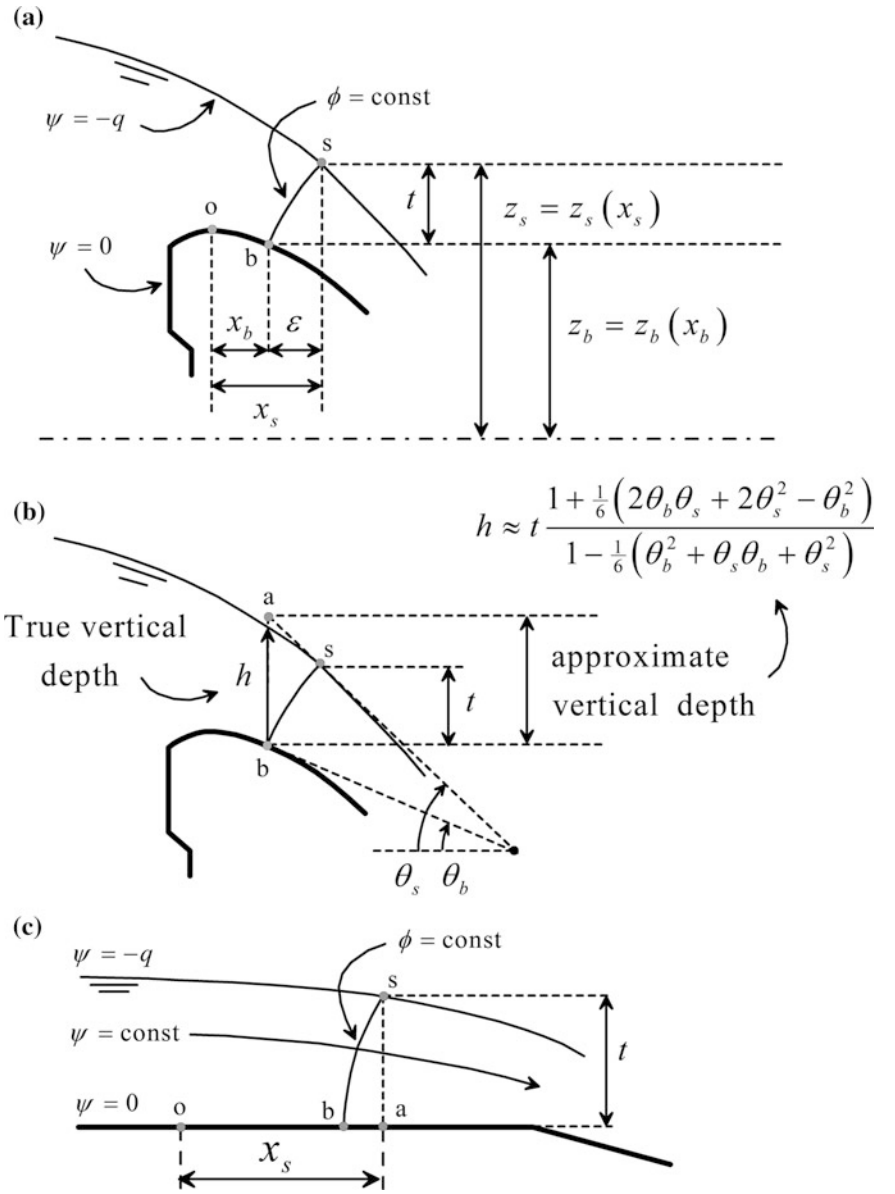

Figure E.1 **a** Curvilinear potential flow over curved bed, **b** vertical and projected flow depths, and **c** flow over straight-bottomed channel

Thus, $1/R_s$ and $1/R_b$ need to be quantified. For weakly curved and sloped streamlines, these functions can be approximated by

$$\frac{1}{R_s} \approx \frac{\mathrm{d}^2 z_s}{\mathrm{d}x_s^2}, \quad \frac{1}{R_b} \approx \frac{\mathrm{d}^2 z_b}{\mathrm{d}x_b^2}. \tag{E.4}$$

For an arbitrary equipotential line, the horizontal coordinates of the points connecting it to the free surface and bed streamlines are related by

$$x_b = x_s - \varepsilon. \tag{E.5}$$

Succesive differentiation of Eq. (E.5) yields

$$\frac{\mathrm{d}x_b}{\mathrm{d}x_s} = 1 - \frac{\mathrm{d}\varepsilon}{\mathrm{d}x_s}, \quad \frac{\mathrm{d}^2 x_b}{\mathrm{d}x_s^2} = -\frac{\mathrm{d}^2 \varepsilon}{\mathrm{d}x_s^2}. \tag{E.6}$$

A simple rule of calculus permits to write

$$\frac{\mathrm{d}(\cdot)}{\mathrm{d}x_s} = \frac{\mathrm{d}(\cdot)}{\mathrm{d}x_b}\frac{\mathrm{d}x_b}{\mathrm{d}x_s}. \tag{E.7}$$

Therefore, using Eqs. (E.6) and (E.7), the free surface curvature is determined from

$$\begin{aligned} \frac{1}{R_s} \approx \frac{\mathrm{d}^2 z_s}{\mathrm{d}x_s^2} &= \frac{\mathrm{d}}{\mathrm{d}x_s}\left(\frac{\mathrm{d}z_s}{\mathrm{d}x_b}\frac{\mathrm{d}x_b}{\mathrm{d}x_s}\right) = \frac{\mathrm{d}x_b}{\mathrm{d}x_s}\frac{\mathrm{d}}{\mathrm{d}x_s}\left(\frac{\mathrm{d}z_s}{\mathrm{d}x_b}\right) + \frac{\mathrm{d}z_s}{\mathrm{d}x_b}\frac{\mathrm{d}^2 x_b}{\mathrm{d}x_s^2} \\ &= \left(\frac{\mathrm{d}x_b}{\mathrm{d}x_s}\right)^2 \frac{\mathrm{d}^2 z_s}{\mathrm{d}x_b^2} + \frac{\mathrm{d}z_s}{\mathrm{d}x_b}\frac{\mathrm{d}^2 x_b}{\mathrm{d}x_s^2} = \left(1 - \frac{\mathrm{d}\varepsilon}{\mathrm{d}x_s}\right)^2 \frac{\mathrm{d}^2 z_s}{\mathrm{d}x_b^2} - \frac{\mathrm{d}^2 \varepsilon}{\mathrm{d}x_s^2}\frac{\mathrm{d}z_s}{\mathrm{d}x_b}, \end{aligned} \tag{E.8}$$

from which the following approximate relation emerges

$$\frac{1}{R_s} - \frac{1}{R_b} = \left(1 - \frac{\mathrm{d}\varepsilon}{\mathrm{d}x_s}\right)^2 \frac{\mathrm{d}^2 z_s}{\mathrm{d}x_b^2} - \frac{\mathrm{d}^2 \varepsilon}{\mathrm{d}x_s^2}\frac{\mathrm{d}z_s}{\mathrm{d}x_b} - \frac{\mathrm{d}^2 z_b}{\mathrm{d}x_b^2}. \tag{E.9}$$

The vertical coordinates of the points connecting an equipotential line to the free surface and bed streamlines are related by

$$z_s = t + z_b. \tag{E.10}$$

Inserting Eq. (E.10) into Eq. (E.9) produces

$$\frac{1}{R_s} - \frac{1}{R_b} = \left(1 - \frac{\mathrm{d}\varepsilon}{\mathrm{d}x_s}\right)^2 \frac{\mathrm{d}^2 t}{\mathrm{d}x_b^2} - \frac{\mathrm{d}^2 \varepsilon}{\mathrm{d}x_s^2}\frac{\mathrm{d}}{\mathrm{d}x_b}(t + z_b) + \left[\left(1 - \frac{\mathrm{d}\varepsilon}{\mathrm{d}x_s}\right)^2 - 1\right]\frac{\mathrm{d}^2 z_b}{\mathrm{d}x_b^2}. \tag{E.11}$$

If ε = const., then

$$\frac{\mathrm{d}\varepsilon}{\mathrm{d}x_s} \approx \frac{\mathrm{d}^2\varepsilon}{\mathrm{d}x_s^2} \approx 0, \tag{E.12}$$

and from Eq. (E.11)

$$\frac{1}{R_s} - \frac{1}{R_b} \approx \frac{\mathrm{d}^2 t}{\mathrm{d}x_b^2}. \tag{E.13}$$

Equation (E.13) is a basic relation used by Matthew (1963), and Hager and Hutter (1984), which holds only if $\varepsilon \approx$ constant, i.e., if the shift in the horizontal direction between points b and s is nearly identical for all equipotential lines. This is tantamount to the assumption that spatial differentiation is conducted only with respect to the coordinate x_b at the intersection of an equipotential line with the bed-free streamline, that is

$$\frac{1}{R_s} \approx \frac{\mathrm{d}^2 z_s}{\mathrm{d}x_b^2} = \frac{\mathrm{d}^2}{\mathrm{d}x_b^2}(t + z_b), \quad \frac{1}{R_b} \approx \frac{\mathrm{d}^2 z_b}{\mathrm{d}x_b^2}. \tag{E.14}$$

Thus, in the approach of Matthew (1963), and Hager and Hutter (1984), the extended energy equation

$$H = z_b + t + \frac{q^2}{2gt^2}\left(1 + \frac{2tt_{xx} - t_x^2}{3} + tz_{bxx} - z_{bx}t_x - z_{bx}^2\right) \tag{E.15}$$

implies

$$t_x \approx \frac{\mathrm{d}t}{\mathrm{d}x_b} = \frac{\mathrm{d}t}{\mathrm{d}x}, \quad t_{xx} \approx \frac{\mathrm{d}^2 t}{\mathrm{d}x_b^2} = \frac{\mathrm{d}^2 t}{\mathrm{d}x^2}, \quad z_{bx} \approx \frac{\mathrm{d}z_b}{\mathrm{d}x_b} = \frac{\mathrm{d}z_b}{\mathrm{d}x}, \quad z_{bxx} \approx \frac{\mathrm{d}^2 z_b}{\mathrm{d}x_b^2} = \frac{\mathrm{d}^2 z_b}{\mathrm{d}x^2}. \tag{E.16}$$

It is clear, thus, that in Eq. (E.15), x means the horizontal coordinate of point "b". The model is therefore approximate, given that a constant ε-value was assumed. At this point "b" of the coordinate x, the solution of the differential Eq. (E.15) gives the projected depth t. However, it is desirable to compute the vertical flow depth h. By simple geometry, the vertical distance between point b and point a, lying on the tangent to the free surface at s (Fig. E.1b), is (Hager and Hutter 1984) [Eq. 3.110]

$$h \approx \overline{\mathrm{ab}} = t\frac{1 + \frac{1}{6}\left(2\theta_b\theta_s + 2\theta_s^2 - \theta_b^2\right)}{1 - \frac{1}{6}\left(\theta_b^2 + \theta_s\theta_b + \theta_s^2\right)}, \tag{E.17}$$

which is an approximation (not an exact computation) of the true vertical depth h (Fig. E.1b). Therefore, the approximate treatment of plane channel flows by Hager and Hutter (1984) allows for the computation of an approximation of the vertical flow depth t at the coordinate x of point b, at the base of an equipotential line. In general, it is consequently not possible to have full equivalence with Matthew's (1991) Picard iteration equations, given the above approximations.

Consider now flows over a straight-bottomed channel (Fig. E.1c). The free surface curvature at point s is then approximately given by

$$\frac{1}{R_s} \approx \frac{\mathrm{d}^2 z_s}{\mathrm{d}x_s^2} = \frac{\mathrm{d}^2}{\mathrm{d}x_s^2}(t + z_b). \tag{E.18}$$

With the aid of Eq. (E.2) using Eq. (E.3)[2], the velocity components (u, w) along the curve b-s are then expressible as, with μ as the dimensionless vertical coordinate,

$$u = \left(\frac{q}{t}\right)\left[1 + \frac{tt_{xx}}{6}\left(3\mu^2 - 1\right) - \frac{t_x^2}{6}\left(1 + 3\mu^2\right)\right], \tag{E.19}$$

$$w = \left(\frac{q}{t}\right)(t_x \mu). \tag{E.20}$$

Here, x means generally the horizontal coordinate of point s at the free surface, that is

$$t_x \approx \frac{\mathrm{d}t}{\mathrm{d}x_s} = \frac{\mathrm{d}t}{\mathrm{d}x}, \quad t_{xx} \approx \frac{\mathrm{d}^2 t}{\mathrm{d}x_s^2} = \frac{\mathrm{d}^2 t}{\mathrm{d}x^2}. \tag{E.21}$$

The absolute velocity V is, from Eqs. (E.19)–(E.20),

$$V = \left(u^2 + w^2\right)^{1/2} \approx \frac{q}{t}\left[1 + \frac{tt_{xx}}{6}\left(3\mu^2 - 1\right) - \frac{t_x^2}{6}\left(1 + 3\mu^2\right) + \frac{t_x^2 \mu^2}{2}\right], \tag{E.22}$$

with a free surface value at $\mu = 1$ of

$$V_s = \frac{q}{t}\left[1 + \frac{tt_{xx}}{3} - \frac{t_x^2}{6}\right]. \tag{E.23}$$

[2]The details on this integration process are extensively described in Sect. 3.4 and are not repeated here.

The extended energy equation corresponding to Eq. (E.23) is then

$$H = t + \frac{V_s^2}{2g} = t + \frac{q^2}{2gt^2}\left(1 + \frac{2tt_{xx} - t_x^2}{3}\right). \tag{E.24}$$

Thus, Eq. (E.24) is "exact" with regard to coordinate differentiation, given that no assumptions on ε are needed. Note the different meaning of x in Eqs. (E.15) and (E.24). Equation (E.24) is based on tracking the free surface coordinates of "type s" points, whereas Eq. (15) tracks "type b" points. Thus, based on this rigorous interpretation of Eq. (E.24), there is no need to approximate the vertical flow depth, which is exactly given by t at the coordinate $x = x_s$.

Consider now the Picard iteration for a vertical section like s–a in Fig. E.1c. The extended energy equation reads[3]

$$H = h + \frac{q^2}{2gh^2}\left(1 + \frac{2hh_{xx} - h_x^2}{3}\right), \tag{E.25}$$

where

$$h_x \approx \frac{\mathrm{d}h}{\mathrm{d}x_s} = \frac{\mathrm{d}h}{\mathrm{d}x}, \quad h_{xx} \approx \frac{\mathrm{d}^2h}{\mathrm{d}x_s^2} = \frac{\mathrm{d}^2h}{\mathrm{d}x^2}. \tag{E.26}$$

Obviously, for the vertical section s-a, the flow depth $t \equiv h$; that is, the vertical flow depth h corresponding to the Picard iteration in a vertical section s-a is identical to the projected depth t of the equipotential curve b-s. Convergence of the corresponding results is further demonstrated as follows. The velocity V at any point of the vertical line s-a is, from the Picard iteration Eq. (3.68),

$$V = \left(u^2 + w^2\right)^{1/2} \approx \frac{q}{h}\left[1 + \left(\frac{h_{xx}}{2h} - \frac{h_x^2}{h^2}\right)\left(\frac{6\eta^2 - 2h^2}{6}\right) + \frac{\eta^2}{2h^2}h_x^2\right], \tag{E.27}$$

with a free surface value at $\eta = h$

$$V_s = \frac{q}{h}\left[1 + \frac{hh_{xx}}{3} - \frac{h_x^2}{6}\right]. \tag{E.28}$$

Given that $h = t$, this result states that Eqs. (E.23) and (E.28) are identical. Both methods yield the same free surface velocity and agree to the same order of accuracy. The second-order solution of the potential flow equations based on

[3]The details on this integration process are extensively described in Sect. 3.3, and are not repeated here.

Picard's iteration is, therefore, mathematically consistent with the assumption of circular-shaped equipotentials. The resulting extended Boussinesq equations are, thus, identical for flat-bed channels.

Finally, bottom pressures are examined as follows. The extended energy equation at point s of Fig. E.1c is given by either Eq. (E.24) or Eq. (E.25). As demonstrated above, it implies identical velocities at the free surface computed either from Picard's iteration in the vertical section s-a and or by integration of Eq. (E.2) along b-s.

The bottom pressure head at point a is from Picard's iteration, based on Eq. (E.28), and Eq. (E.27) at $\eta = 0$,

$$\frac{p_a}{\gamma} = h + \frac{q^2}{2gh^2}\left(hh_{xx} - h_x^2\right). \tag{E.29}$$

Thus, the pressure head below the free surface in a vertical line depends on both the free surface and its curvature. Consider the equipotential line b-s. The velocity at point b is from Eq. (E.22) for $\mu = 0$

$$V_b = \frac{q}{t}\left[1 - \frac{tt_{xx}}{6} - \frac{t_x^2}{6}\right]. \tag{E.30}$$

The pressure head at point b is computed using Eqs. (E.24) and (E.30), the result being

$$\frac{p_b}{\gamma} = H - \frac{V_b^2}{2g} \approx t + \frac{q^2}{2gt^2}tt_{xx} = h + \frac{q^2}{2gh^2}hh_{xx}. \tag{E.31}$$

Thus, the pressure head at the base of an equipotential curve depends only on the free surface curvature. This result is not trivial, given that after using Eqs. (E.24) or (E.25) to compute $t = t(x)$, with $x = x_s$, the bottom pressure head as given by Eq. (E.31) is not at coordinate x_s, but rather at coordinate x_b. This should be borne in mind to avoid misleading results.

References

Hager, W. H., & Hutter, K. (1984). Approximate treatment of plane channel flow. *Acta Mechanica*, *51*(3–4), 31–48.

Matthew, G. D. (1963). On the influence of curvature, surface tension and viscosity on flow over round-crested weirs. *Proceedings of ICE, 25*, 511–524; *28*, 557–569.

Matthew, G. D. (1991). Higher order one-dimensional equations of potential flow in open channels. *Proceedings of ICE, 91*(3), 187–201.

Appendix F
Specific Energy for Flow Over Curved Bottoms

Jaeger (1939, 1956) developed a curvilinear flow theory involving the differential equation describing the velocity profile V along an equipotential curve as

$$\frac{\partial V}{\partial n} = \kappa V. \tag{F.1}$$

Here, κ is the streamline curvature at coordinate n along the equipotential line. Equation (F.1) was integrated using a Taylor series development of the radius of streamline curvature as[4]

$$R(n) = R_b + \left(\frac{\partial R}{\partial n}\right)_b n + \left(\frac{\partial^2 R}{\partial n^2}\right)_b \frac{n^2}{2} + \cdots = -\frac{1}{\kappa(n)}. \tag{F.2}$$

The resulting model equations were extensively verified for critical flow at the round-crested weir (Jaeger 1939, Montes 1970). This development is known as Jaeger's theory of round-crested weir flows (Jaeger 1956; Montes 1998). Therein, the 1D potential flow equations were derived by integrating Eq. (F.1) in the vertical direction, thereby assuming vertical equipotential curves. The good performance of the theory for critical flow over the round-crested weir indicates that the error introduced by this assumption is small. However, Jaeger did not apply his theory to compute the entire free surface profile along the weir structures. The purpose of this Appendix is thus to expand Jaeger's theory for general water surface profile computations over curved bottoms.

For flows over a curved and sloping bottom, e.g., along a spillway structure (Fig. F1), the equipotential lines are better approximated as sections normal to the channel bottom, than by vertical lines. Therefore, the n-coordinate in Eq. (F.1) is approximated here by the coordinate normal to the bottom profile $z_b(x)$ (Fig. F1).

[4]The negative sign in Eq. (F.2) accounts for the absolute value of R, given that the streamline curvature κ is negative in weir flow (convex bottom profile).

© Springer International Publishing AG 2017

O. Castro-Orgaz and W.H. Hager, *Non-Hydrostatic Free Surface Flows*,
Advances in Geophysical and Environmental Mechanics and Mathematics
DOI 10.1007/978-3-319-47971-2

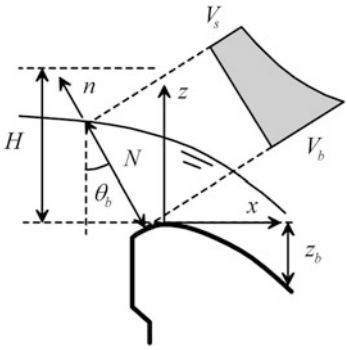

Figure F1 Potential flow over curved bottom

Truncation of the series in Eq. (F.2) after the first term gives with $K = (\partial R/\partial n)_b$ as a quantity to be determined

$$R(n) \approx R_b + \left(\frac{\partial R}{\partial n}\right)_b n = R_b + Kn. \tag{F.3}$$

Inserting Eq. (F.3) into Eq. (F.1) gives

$$\frac{\partial V}{\partial n} = -\frac{V}{R_b + Kn}. \tag{F.4}$$

Integrating Eq. (F.4) between an arbitrary point and the free surface, one finds with V_s as the free surface velocity

$$\frac{V}{V_s} = \left[\frac{R_b + KN}{R_b + Kn}\right]^{1/K}. \tag{F.5}$$

Here, N is the flow depth in the direction normal to the bottom profile, such that Eq. (F.5) differs from Jaeger's (1939) development. Both theories are however identical at the weir crest, where N coincides with the vertical flow depth. For $K = 1$, Eq. (F.5) gives the potential vortex velocity distribution (Sivakumaran et al. 1981)

$$\frac{V}{V_s} = \frac{R_b + N}{R_b + n}. \tag{F.6}$$

This is the fundamental velocity profile originating from Dressler's (1978) perturbation theory. The unit discharge q is obtained by integrating Eq. (F.5) across the flow depth N as (Jaeger 1956)

$$q = \int_0^N V \mathrm{d}n = \frac{V_s R_b}{K-1}\left[\left(1 + \frac{KN}{R_b}\right) - \left(1 + \frac{KN}{R_b}\right)^{\frac{1}{K}}\right], \quad \text{for } K \neq 1. \tag{F.7}$$

For the free vortex case ($K = 1$), the unit discharge q is obtained by integrating Eq. (F.6) as (Jaeger 1956)

$$q = \int_0^N V \mathrm{d}n = V_s R_b \left(1 + \frac{N}{R_b}\right) \ln\left(1 + \frac{N}{R_b}\right), \quad \text{for } K = 1. \tag{F.8}$$

With E as specific energy, the total energy head H of a potential flow is (Montes 1998)

$$H = z_b + N\cos\theta_b + \frac{V_s^2}{2g} = E + z_b = \text{const.} \tag{F.9}$$

Inserting Eq. (F.7) into Eq. (F.9) gives as total energy head for flows over a curved bottom

$$H = z_b + N\cos\theta_b + \frac{q^2}{2gN^2}\left[\frac{N/R_b(K-1)}{\{1 + (KN/R_b)\} - \{1 + (KN/R_b)\}^{1/K}}\right]^2 = \text{const.} \tag{F.10}$$

Inserting Eq. (F.8) into Eq. (F.9) gives the total energy head equation of Sivakumaran et al. (1981) as

$$H = z_b + N\cos\theta_b + \frac{q^2}{2gN^2}\left[\frac{N/R_b}{\{1 + (N/R_b)\}\ln\{1 + (N/R_b)\}}\right]^2 = \text{const.} \tag{F.11}$$

For shallow free-surface flows approaching the limit $N/R_b \to 0$, the hydrostatic pressure distribution prevails, resulting from either Eq. (F.10) or (F.11) in

$$H = z_b + N\cos\theta_b + \frac{q^2}{2gN^2}. \tag{F.12}$$

This is an equation routinely used in the hydraulics literature (Montes 1998).

To illustrate the relevance of Eq. (F.10), an application to model the flow over a spillway profile is presented. Using the design head of the spillway profile H_D as the scaling variable, Eq. (F.10) is rewritten as

$$\frac{H}{H_D} = \frac{z_b}{H_D} + \frac{N\cos\theta_b}{H_D} + \frac{q^2}{2gN^2H_D}\lambda, \tag{F.13}$$

where

$$\lambda = \left[\frac{N/R_b(K-1)}{\{1+(KN/R_b)\}-\{1+(KN/R_b)\}^{1/K}}\right]^2. \tag{F.14}$$

With the discharge coefficient C_d of spillway flow defined by

$$q = C_d\left(g\,H^3\right)^{1/2}, \tag{F.15}$$

the specific energy is, from Eq. (F.13),

$$\frac{E}{H_D} = \frac{H}{H_D} - \frac{z_b}{H_D} = \frac{N}{H_D}\cos\theta_b + \frac{\lambda C_d^2}{2}\frac{(H/H_D)^3}{(N/H_D)^2}. \tag{F.16}$$

Equation (F.16) depends on C_d, which is a function of the normalized operating head $\chi = H/H_D$, as well as on χ, $\cos\theta_b$, and λ. Therefore, Eq. (F.16) is rewritten as

$$\frac{E}{H_D}(x/H_D) = \frac{N}{H_D}\cos\theta_b + \lambda(N/H_D, H_D/R_b)C_d^2(\chi)\frac{\chi^3}{2}\left(\frac{N}{H_D}\right)^{-2}. \tag{F.17}$$

Equation (F.17) is the generalized specific energy equation for flow over a curved and sloping bottom. To produce the curvilinear specific energy diagram (E/H_D versus N/H_D), a bottom geometry function is required to compute H_D/R_b and $\cos\theta_b$ at an arbitrary section located at coordinate x/H_D. For the hydrostatic pressure distribution, $C_d = (2/3)^{3/2}$ and $\lambda = 1$, so that from Eq. (F.17)

$$\frac{E}{H_D} = \frac{N}{H_D}\cos\theta_b + \frac{(2/3)^3}{2}\chi^3\left(\frac{N}{H_D}\right)^{-2}. \tag{F.18}$$

Hager (1987, 1991) proposed a continuous profile for the standard spillway, defined by the mathematical curve

$$\overline{Z} = -\overline{X}\cdot\ln\overline{X}, \tag{F.19}$$

where

$$\begin{aligned}\overline{Z} &= 2.705(Z+0.136) \text{ with } Z = z_b/H_D,\\ \overline{X} &= 1.3055(X+0.2818) \text{ with } X = x/H_D.\end{aligned} \tag{F.20}$$

Differentiation of Eq. (F.19) yields

$$\frac{dZ}{dX} = -\frac{1.3055}{2.705}\left(\ln\overline{X} + 1\right), \tag{F.21}$$

$$\frac{d^2Z}{dX^2} = -\frac{1.3055^2}{2.705}\frac{1}{\overline{X}}. \tag{F.22}$$

Therefore, the bottom-dependent variables for spillway computations are obtained from

$$\frac{H_D}{R_b} = -\frac{d^2Z}{dX^2}\left[1 + \left(\frac{dZ}{dX}\right)^2\right]^{-3/2}, \tag{F.23}$$

$$\cos\theta_b = \left[1 + \left(\frac{dZ}{dX}\right)^2\right]^{-1/2}, \tag{F.24}$$

$$\sin\theta_b = \left(\frac{dZ}{dX}\right)\cos\theta_b. \tag{F.25}$$

To highlight the physical effects of the bottom curvature on the specific energy E, Eq. (F.17) is plotted at the spillway crest ($x/H_D = 0$) for $\chi = 1$ using $K = 2$. The value of C_d is determined from the semiempirical equation (Hager 1991)[5]

$$C_d = \left(\frac{2}{3}\right)^{3/2}\left(1 + \frac{4\chi}{9 + 5\chi}\right), \tag{F.26}$$

which approximates the discharge characteristics of ungated spillway flows with transitional flow from subcritical to supercritical conditions. From Eqs. (F.23)–(F.24), the spillway crest yields $H_D/R_b \approx 1.71$ and $\cos\theta_b = 1$. For comparative purposes, the hydrostatic specific energy function given by Eq. (F.18) is plotted in the same figure, showing large deviations. It is of particular interest to note that the points of minimum specific energy of the two curves are clearly different. In particular, the minimum value of E/H_D for the hydrostatic curve is unity ($H = H_D$). In contrast, for the non-hydrostatic curve, the minimum value of E/H_D is less than unity. It implies that

[5]Matthew's (1963) discharge equation for flows over a round crested weir is $C_d = (2/3)^{3/2}(1+22/81\ H/R_b)$, valid for low heads, e.g., for $H/R_b < 0.5$. For spillway flow, Eq. (F.19) gives the crest scaling $H_D/R_b \approx 1.71$. Inserting it into Matthew's equation results, approximately, in $C_d = (2/3)^{3/2}[1 + (2 \cdot 11)/(9 \cdot 9)\cdot 1.71\cdot H/H_D)] \approx (2/3)^{3/2}[1 + (2/9)\cdot 2 \cdot H/H_D)] = (2/3)^{3/2}(1 + 4\chi/9)$. This equation is valid, therefore, up to $\chi \approx 0.5/1.71 \approx 0.29$. To expand its validity range, Hager (1991) proposed an empirical correction, resulting in Eq. (F.26), allowing for an accurate computation of C_d for high heads, e.g., typically for $\chi < 3$.

for a spillway operating at design head ($H = H_D$), the actual flow conditions at the crest cannot correspond to critical flow. Note further that the minimum value of $N/H_D = 2/3$ for hydrostatic flow, whereas for the non-hydrostatic flow, this value is close to 0.7, in agreement with experimental observations (Hager 1991).

To test Jaeger's theory for the computation of the free surface profile $N/H_D(x/H_D)$ of spillway flow, Eq. (F.17) is rewritten as

$$\frac{E}{H_D} - \frac{N}{H_D}\cos\theta_b - \frac{\lambda C_d^2}{2}\chi^3\left(\frac{N}{H_D}\right)^{-2} = 0. \tag{F.27}$$

The roots of Eq. (F.27) are to be determined numerically. At each position $X = x/H_D$, the specific energy is computed as

$$\frac{E}{H_D} = \chi - Z(X). \tag{F.28}$$

The values of Z, H_D/R_b, and $\cos\theta_b$ at X are then determined from Eqs. (F.19)–(F.24). For given values of E, χ and C_d, Eq. (F.27) has two roots for N/H_D (see Fig. F.2), one corresponding to subcritical (curvilinear) flow and the other to supercritical (curvilinear) flow. Once the flow depth N/H_D is determined, the coordinates of the free surface points (X_s, Z_s) are given by

$$Z_s = Z + \cos\theta_b \frac{N}{H_D}, \quad X_s = X - \sin\theta_b \frac{N}{H_D}. \tag{F.29}$$

Sub- and supercritical flow profiles along the spillway structure were determined numerically by computing the two roots of Eq. (F.27) at each position X, using $K = 2$, which is the value previously determined for critical flow computations at a weir crest (Jaeger 1939; Montes 1970). Results for $\chi = 1$ and values of $C_d = 0.62$ and 0.68 are shown in Fig. F.3.

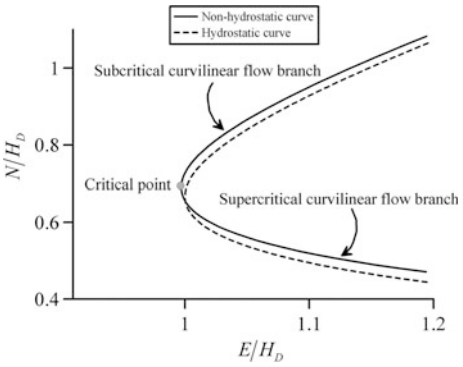

Figure F.2 Specific energy diagram at the spillway crest for $\chi = 1$

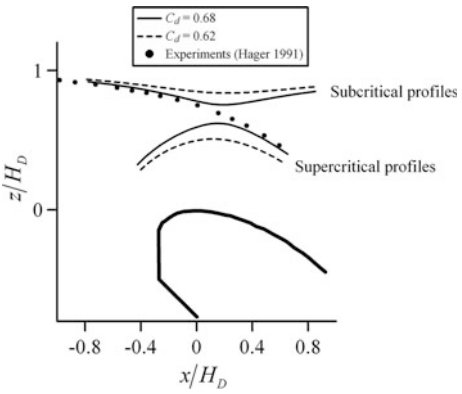

Figure F.3 Sub- and supercritical flow profiles $z/H_D(x/H_D)$ at the spillway crest zone for $\chi = 1$

Note that, as the value of C_d is increased for χ fixed, the sub- and supercritical profiles tend to merge, ultimately touching at a common point, for a particular value of C_d to be determined by trial and error. Simultaneously, the far up- and downstream branches of the sub- and supercritical profiles, respectively, progressively converge to the experimental data of Hager (1991), corresponding to the transition from sub- to supercritical flow. Accordingly, while C_d increases, the critical flow condition is approached at an undetermined spillway section. This flow section is located where the actual specific energy $E(X)$ coincides with the minimum of the specific energy curve. Thus, for this particular value of C_d, the flow changes from sub- to supercritical conditions, and the actual free surface profile is composed of upstream subcritical and downstream supercritical branches, linked at the critical point (Hager and Castro-Orgaz 2016). For $C_d = 0.691$, the transcritical flow profile shown in Fig. F.4 was obtained, corresponding to the merging of the up- and downstream sub- and supercritical profiles, respectively. This iteratively computed value of C_d is close to that of the empirical Eq. (F.26) ($C_d = 0.7$; 1.26 % deviation from numerical computation). An attempt to compute the free surface profile of

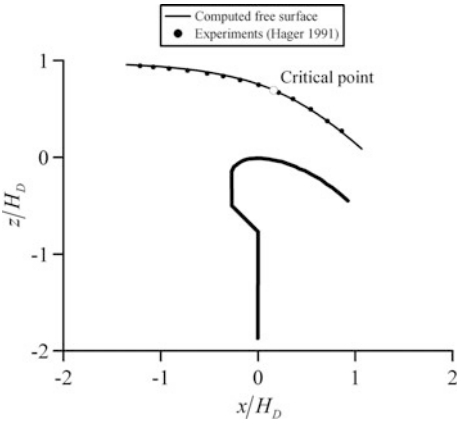

Figure F.4 Transcritical flow profile $z/H_D(x/H_D)$ at spillway for $\chi = 1$

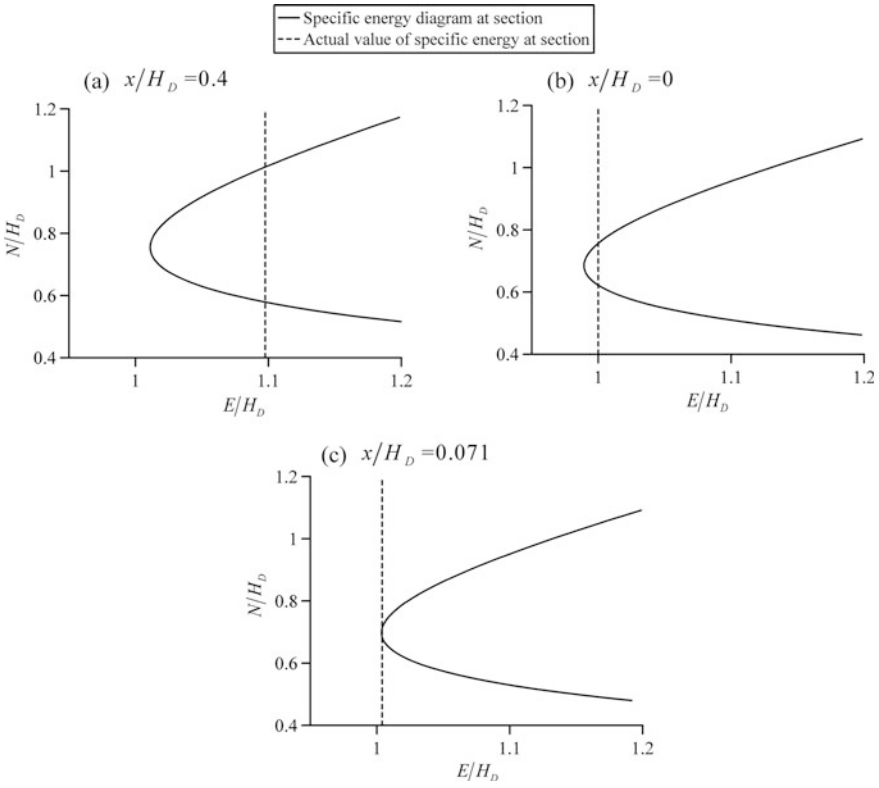

Figure F.5 Specific energy diagrams at several sections along the spillway profile

spillway flow for $K = 1$, and using the corresponding free vortex relations, failed. Computed flow depths at the subcritical flow portion were inaccurate (not shown here). In turn, good computational results resulted along the supercritical portion. The failure of the free vortex theory is associated with the non-concentrical streamlines in the upstream subcritical flow portion, where the spillway profile is significantly sloping, and the free surface is only slightly inclined. In contrast, along the supercritical portion, the flow is shallow, and the free surface is nearly parallel to the bottom profile, so that the streamlines are approximately concentrical.

The actual specific energy E and the specific energy diagram at several sections along the spillway profile are plotted in Fig. F.5. It highlights that the actual E value is not a minimum at the spillway crest ($x/H_D = 0$), but rather occurs at $x/H_D \approx 0.071$. This displacement of the critical flow section from the weir crest to the downstream reach is provoked by the strong variation of the bottom curvature. Previous applications of Jaeger's theory at a weir crest rely on a constant value of the bottom curvature and critical flow (Jaeger 1939), thereby ignoring the actual displacement of the control section to the downstream portion of the spillway profile. Figure F.6 shows the operation point for supercritical conditions at section

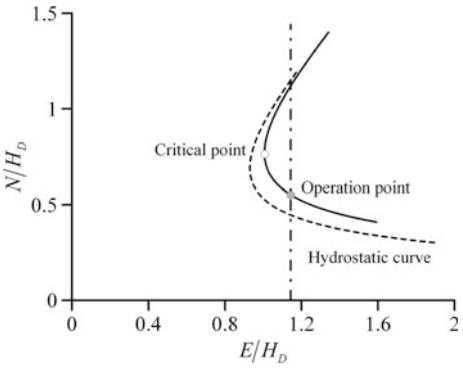

Figure F.6 Operation conditions at section $x/H_D = 0.5$

$x/H_D = 0.5$, which implies a flow depth larger than that obtained on the basis of hydrostatic flow computations. This highlights the inaccuracy of hydrostatic computations in spillway flow.

References

Dressler, R. F. (1978). New nonlinear shallow flow equations with curvature. *Journal of Hydraulic Research, 16*(3), 205–222.

Hager, W. H. (1987). Continuous crest profile for standard spillway. *Journal of Hydraulic Engineering*, *113*(11), 1453–1457.

Hager, W. H. (1991). Experiments on standard spillway flow. *Proceeding of ICE, 91*(2), 399–416.

Hager, W. H., & Castro-Orgaz O. (2016). Transcritical flow in open channel hydraulics: From Böss to De Marchi. *Journal of Hydraulic Engineering*, *142*(1), 1–9.

Jaeger, C. (1939). Remarques sur quelques écoulements le long des lits à pente variant graduellement (Remarks on some flows along bottoms of gradually varied slope). *Schweizerische Bauzeitung, 114*(20), 231–234 (in French).

Jaeger, C. (1956). *Engineering fluid mechanics*. Edinburgh: Blackie and Son.

Matthew, G. D. (1963). On the influence of curvature, surface tension and viscosity on flow over round-crested weirs. *Proceedings of ICE, 25*, 511–524; *28*, 557–569.

Montes, J. S. (1970). Flow over round crested weirs. *L´Energia Elettrica, 47*(3), 155–164.

Montes, J. S. (1998). *Hydraulics of open channel flow*. Reston, VA: ASCE Press.

Sivakumaran, N. S., Hosking, R. J., & Tingsanchali, T. (1981). Steady shallow flow over a spillway. *Journal of Fluid Mechanics*, *111*, 411–420.

Appendix G
Viscous Boussinesq-type equations

In this Appendix, the viscous Boussinesq-type equations presented by Montes and Chanson (1998) are derived on the basis of the velocity profile given by Eq. (3.550). The development is presented in two steps. First, the inviscid velocity distribution is derived. Second, viscous effects are introduced and the resulting velocity and pressure distributions are used to produce the extended Boussinesq-type equations for the specific momentum S and the specific energy E. To simplify the analysis, the channel bottom is assumed to be horizontal. Consider steady inviscid and irrotational (potential) flow with a wavy free surface (Fig. G1). The equipotential (ϕ = const) and streamline (ψ = const) plotted in Fig. G.1 intersect at point P, where the radius of the streamline curvature is R and the angle formed by the tangent to the streamline with the x-axis is θ.

The potential velocity profile along the equipotential line is

$$V = V_s \exp\left(-\int_z^h \frac{\mathrm{d}z'}{R\cos\theta}\right), \tag{G.1}$$

where z is the vertical coordinate above the channel bottom, h the flow depth, and V_s the velocity at the free surface. The interpolation function

$$\frac{1}{R\cos\theta} = \frac{1}{R_s\cos\theta_s}\left(\frac{z}{h}\right)^K \tag{G.2}$$

is used to prescribe the variation of R and θ along the equipotential line s–b, with K as an empirical coefficient. The shape of the equipotential curve s–b is assumed to be a circular arc. Therefore, the following geometric relation emerges

$$\frac{\sin\theta}{z} = \frac{\sin\theta_s}{h}. \tag{G.3}$$

© Springer International Publishing AG 2017

O. Castro-Orgaz and W.H. Hager, *Non-Hydrostatic Free Surface Flows*,
Advances in Geophysical and Environmental Mechanics and Mathematics
DOI 10.1007/978-3-319-47971-2

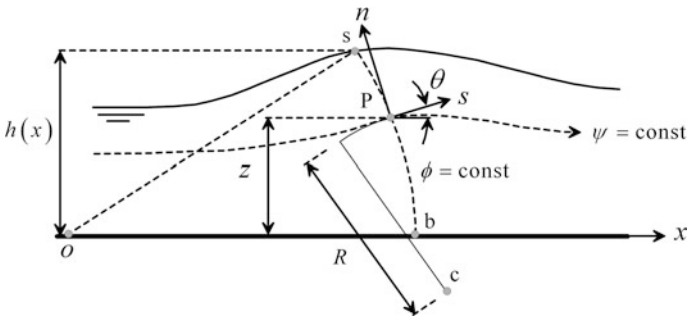

Figure G.1 Potential flow with wavy free surface

At the free surface, the following trigonometric relation is formed

$$\sin^2\theta_s + \cos^2\theta_s = 1, \tag{G.4}$$

from which

$$\sin^2\theta_s = \frac{\tan^2\theta_s}{1+\tan^2\theta_s}. \tag{G.5}$$

Noting that

$$h_x = \tan\theta_s \tag{G.6}$$

results in

$$\sin\theta_s = \left(\frac{h_x^2}{1+h_x^2}\right)^{1/2} = \varepsilon_1^{1/2}, \tag{G.7}$$

with ε_1 as the Boussinesq-type slope coefficient. Inserting Eq. (G.7) into Eq. (G.3) yields

$$\sin\theta = \varepsilon_1^{1/2}\frac{z}{h}. \tag{G.8}$$

Using Eq. (G.8) in

$$\sin^2\theta + \cos^2\theta = 1 \tag{G.9}$$

produces

$$\cos\theta = \left[1 - \varepsilon_1 \left(\frac{z}{h}\right)^2\right]^{1/2}. \tag{G.10}$$

Equations (G.2), (G.8), and (G.10) yield closure for the flow geometry. Using the definition of R_s

$$\frac{1}{R_s} = \frac{h_{xx}}{\left(1 + h_x^2\right)^{3/2}}, \tag{G.11}$$

and Eq. (G.10) evaluated at the free surface ($z = h$),

$$\frac{1}{\cos\theta_s} = \left(1 + h_x^2\right)^{1/2}, \tag{G.12}$$

Eq. (G.2) reduces to

$$\frac{1}{R\cos\theta} = \frac{h_{xx}}{1 + h_x^2} \left(\frac{z}{h}\right)^K. \tag{G.13}$$

Inserting Eq. (G.13) into Eq. (G.1) yields, after integration, with $\mu = z/h$, the potential velocity distribution

$$V = V_s \exp\left(-\frac{h h_{xx}}{1 + h_x^2} \frac{1 - \mu^{K+1}}{K + 1}\right) = V_s \exp\left(-\varepsilon_o \frac{1 - \mu^{K+1}}{K + 1}\right), \tag{G.14}$$

where ε_o is the Boussinesq-type curvature coefficient. Using Eq. (G.14), the viscous velocity distribution is, based on Eq. (3.560),

$$V = V_s \mu^N \exp\left(-\varepsilon_o \frac{1 - \mu^{K+1}}{K + 1}\right). \tag{G.15}$$

For small arguments of the exponential function, Eq. (G.15) is approximated by

$$V = V_s \mu^N \exp\left(-\varepsilon_o \frac{1 - \mu^{K+1}}{K + 1}\right) \approx V_s \mu^N \left(1 - \varepsilon_o \frac{1 - \mu^{K+1}}{K + 1}\right), \tag{G.16}$$

and from Eq. (G.10)[6]

$$\cos\theta^{-1} = \left[1 - \varepsilon_1 \left(\frac{z}{h}\right)^2\right]^{-1/2} \approx 1 + \frac{\varepsilon_1}{2} \mu^2. \tag{G.17}$$

[6]We shall employ analogous approximations for small ε_o and ε_1 without further mentioning.

Thus, the function

$$\begin{aligned} V\cos\theta^{-1} &\approx V_s\mu^N\left(1-\varepsilon_o\frac{1-\mu^{K+1}}{K+1}\right)\left(1+\frac{\varepsilon_1}{2}\mu^2\right) \\ &\approx V_s\left(\mu^N-\varepsilon_o\frac{\mu^N-\mu^{K+1+N}}{K+1}+\frac{\varepsilon_1}{2}\mu^{2+N}\right), \end{aligned} \tag{G.18}$$

is used to compute the unit discharge q across the equipotential line as

$$q=\int_0^h\frac{V}{\cos\theta}dz\approx V_sh\left(\frac{1}{1+N}-\frac{\varepsilon_o}{K+1}\left(\frac{1}{1+N}-\frac{1}{K+2+N}\right)+\frac{\varepsilon_1}{2(N+3)}\right). \tag{G.19}$$

Inverting Eq. (G.19) produces

$$V_s\approx(1+N)\frac{q}{h}\left(1+\frac{\varepsilon_o}{K+1}\left(1-\frac{1+N}{K+2+N}\right)-\frac{\varepsilon_1(N+1)}{2(N+3)}\right). \tag{G.20}$$

Using Eqs. (G.16) and (G.10), the velocity component u in the x-direction is

$$\begin{aligned} u=V\cos\theta &= V_s\mu^N\exp\left(-\varepsilon_o\frac{1-\mu^{K+1}}{K+1}\right)\left[1-\varepsilon_1\mu^2\right]^{1/2} \\ &\approx V_s\mu^N\left(1-\varepsilon_o\frac{1-\mu^{K+1}}{K+1}\right)\left(1-\frac{\varepsilon_1}{2}\mu^2\right). \end{aligned} \tag{G.21}$$

Inserting Eq. (G.20) into Eq. (G.21) yields

$$\begin{aligned} u &\approx (1+N)\frac{q}{h}\mu^N\left(1+\frac{\varepsilon_o}{K+1}\left(1-\frac{1+N}{K+2+N}\right)-\frac{\varepsilon_1(N+1)}{2(N+3)}\right)\left(1-\varepsilon_o\frac{1-\mu^{K+1}}{K+1}\right)\left(1-\frac{\varepsilon_1}{2}\mu^2\right) \\ &\approx (1+N)\frac{q}{h}\mu^N\left(1-\frac{\varepsilon_o}{K+1}\left(\frac{1+N}{K+2+N}-\mu^{K+1}\right)-\frac{\varepsilon_1}{2}\left(\frac{N+1}{N+3}+\mu^2\right)\right). \end{aligned} \tag{G.22}$$

Likewise, the velocity component w in the z-direction is, using Eqs. (G.8) and (G.16),

$$\begin{aligned} w=V\sin\theta &= V_s\mu^N\exp\left(-\varepsilon_o\frac{1-\mu^{K+1}}{K+1}\right)\varepsilon_1^{1/2}\mu \\ &\approx V_s\mu^N\left(1-\varepsilon_o\frac{1-\mu^{K+1}}{K+1}\right)\varepsilon_1^{1/2}\mu. \end{aligned} \tag{G.23}$$

Inserting Eq. (G.20) into Eq. (G.23) yields

$$w \approx (1+N)\frac{q}{h}\mu^N\left(1+\frac{\varepsilon_o}{K+1}\left(1-\frac{1+N}{K+2+N}\right)-\frac{\varepsilon_1(N+1)}{2(N+3)}\right)\left(1-\varepsilon_o\frac{1-\mu^{K+1}}{K+1}\right)\varepsilon_1^{1/2}\mu$$
$$\approx (1+N)\frac{q}{h}\mu^{N+1}\varepsilon_1^{1/2}\left(1-\frac{\varepsilon_o}{K+1}\left(\frac{1+N}{K+2+N}-\mu^{K+1}\right)-\frac{\varepsilon_1}{2}\frac{N+1}{N+3}\right). \tag{G.24}$$

Using the intrinsic coordinates (s, n) based on equipotential and streamlines (Fig. G.1), the Euler equation in the n-direction is (Eq. 3.46)

$$\frac{V^2}{R} = -\frac{1}{\rho}\frac{\partial p}{\partial n} - g\frac{\partial z}{\partial n}, \tag{G.25}$$

from which the pressure distribution becomes, noting that $\mathrm{d}n = \mathrm{d}z/\cos\theta$,

$$p = \rho g(h-z) + \rho\int_z^h \frac{V^2}{R\cos\theta}\mathrm{d}z'. \tag{G.26}$$

From Eq. (G.13), multiplied with h,

$$\frac{h}{R\cos\theta} = \varepsilon_o\mu^K, \tag{G.27}$$

and from Eqs. (G.16) and (G.20)

$$V \approx V_s\mu^N\left(1-\varepsilon_o\frac{1-\mu^{K+1}}{K+1}\right)$$
$$\approx \mu^N\left(1-\varepsilon_o\frac{1-\mu^{K+1}}{K+1}\right)(1+N)\frac{q}{h}\left(1+\frac{\varepsilon_o}{K+1}\left(1-\frac{1+N}{K+2+N}\right)-\frac{\varepsilon_1(N+1)}{2(N+3)}\right)$$
$$\approx (1+N)\frac{q}{h}\mu^N\left(1-\frac{\varepsilon_o}{K+1}\left(\frac{1+N}{K+2+N}-\mu^{K+1}\right)-\frac{\varepsilon_1}{2}\frac{N+1}{N+3}\right). \tag{G.28}$$

From Eqs. (G.27) and (G.28), one obtains to order ε_o, ε_1,

$$\frac{hV^2}{R\cos\theta} \approx (1+N)^2\frac{q^2}{h^2}\varepsilon_o\mu^{K+2N}. \tag{G.29}$$

Using Eq. (G.29), Eq. (G.26) yields the pressure distribution

$$\frac{p}{\rho gh} = 1 - \mu + \frac{1}{gh}\int_{\mu}^{1} \frac{hV^2}{R\cos\theta}\mathrm{d}\mu' \approx 1 - \mu + \frac{\varepsilon_o(1+N)^2}{K+2N+1}\frac{q^2}{gh^3}\left(1-\mu^{1+2N+K}\right). \tag{G.30}$$

The specific momentum S is given by [Eq. (3.18)]

$$S = \int_0^N \left(\frac{uV}{g} + \frac{p\,\cos\theta}{\rho g}\right)\mathrm{d}n = \int_0^h \left(\frac{V^2}{g} + \frac{p}{\rho g}\right)\mathrm{d}z, \tag{G.31}$$

where N is the length of the equipotential curve b–s (Fig. G.1). From Eq. (G.28)

$$V^2 \approx (1+N)^2\frac{q^2}{h^2}\mu^{2N}\left(1 - \frac{2\varepsilon_o}{K+1}\left(\frac{1+N}{K+2+N} - \mu^{K+1}\right) - \varepsilon_1\frac{N+1}{N+3}\right). \tag{G.32}$$

Integration of Eq. (G.32) yields

$$\int_0^h \frac{V^2}{g}\mathrm{d}z = (1+N)^2\frac{q^2}{gh}\left(\frac{1}{2N+1} - \frac{2\varepsilon_o}{K+1}\left(\frac{1+N}{K+2+N}\frac{1}{2N+1} - \frac{1}{K+2N+2}\right) - \varepsilon_1\frac{N+1}{N+3}\frac{1}{2N+1}\right). \tag{G.33}$$

After algebraic manipulation, Eq. (G.33) is rewritten as

$$\int_0^h \frac{V^2}{g}\mathrm{d}z = \beta\frac{q^2}{gh}\left(1 - \frac{2\varepsilon_o}{K+1}\left(\frac{1+N}{K+2+N} - \frac{2N+1}{K+2N+2}\right) - \varepsilon_1\frac{N+1}{N+3}\right). \tag{G.34}$$

Here, β is the Boussinesq momentum velocity correction coefficient for the power-law velocity profile,

$$\beta = \frac{(1+N)^2}{2N+1}. \tag{G.35}$$

Using Eq. (G.30), the pressure integral is

$$\int_0^h \frac{p}{\rho g}\mathrm{d}z = \frac{h^2}{2} + \frac{\varepsilon_o(1+N)^2}{K+2N+1}\frac{q^2}{gh}\left(1 - \frac{1}{2+2N+K}\right) = \frac{h^2}{2} + \beta\varepsilon_o\frac{2N+1}{K+2N+2}\frac{q^2}{gh}. \tag{G.36}$$

Inserting Eqs. (G.34) and (G.36) in Eq. (G.31) yields

$$S = \beta\frac{q^2}{gh}\left(1 - \frac{2\varepsilon_o}{K+1}\left(\frac{1+N}{K+2+N} - \frac{2N+1}{K+2N+2}\right) - \varepsilon_1\frac{N+1}{N+3}\right) + \frac{h^2}{2} + \beta\varepsilon_o\frac{2N+1}{K+2N+2}\frac{q^2}{gh}$$
$$= \frac{h^2}{2} + \beta\frac{q^2}{gh}\left(1 + \varepsilon_o\left(\frac{2N+1}{K+2N+2} - \frac{2(N+1)}{(K+1)(2+N+K)} + \frac{2(1+2N)}{(K+1)(2N+K+2)}\right) - \varepsilon_1\frac{N+1}{N+3}\right). \tag{G.37}$$

The depth-averaged specific energy head E is

$$E = \frac{1}{h}\int_0^h \left(\frac{V^2}{2g} + \frac{p}{\rho g} + z\right)\mathrm{d}z. \tag{G.38}$$

Using the computed velocity and pressure integrals, Eqs. (G.34) and (G.36), respectively, evaluation of Eq. (G.38) yields

$$E = h + \beta\frac{q^2}{2gh^2}\left(1 - \frac{2\varepsilon_o}{K+1}\left(\frac{1+N}{K+2+N} - \frac{2N+1}{K+2N+2}\right) + 2\varepsilon_o\frac{2N+1}{K+2N+2} - \varepsilon_1\frac{N+1}{N+3}\right)$$
$$= h + \beta\frac{q^2}{2gh^2}\left(1 + \frac{2\varepsilon_o}{K+2N+2}\left(\frac{2N+1}{K+1} - \frac{(N+1)(K+2N+2)}{(K+N+2)(K+1)} + 2N+1\right) - \varepsilon_1\frac{N+1}{N+3}\right). \tag{G.39}$$

Equations (G.37) and (G.39) are the extended viscous Boussinesq-type equations. For $N = 0$ (inviscid flow), $K = 1$ (weakly curved flow) and reducing the curvature and slope parameters to

$$\varepsilon_o = \frac{hh_{xx}}{1+h_x^2} \approx hh_{xx}, \quad \varepsilon_1 = \frac{h_x^2}{1+h_x^2} \approx h_x^2, \tag{G.40}$$

the original equations of Benjamin and Lighthill (1954) are obtained, namely

$$S = \frac{h^2}{2} + \frac{q^2}{gh}\left(1 + \frac{hh_{xx} - h_x^2}{3}\right), \tag{G.41}$$

$$E = h + \frac{q^2}{2gh^2}\left(1 + \frac{2hh_{xx} - h_x^2}{3}\right). \tag{G.42}$$

For inviscid flow, neglecting the slope term h_x^2, Eq. (G.39) reduces to the relation originally developed by Fawer (1937) as

$$E = h + \frac{q^2}{2gh^2}\left(1 + \frac{2hh_{xx}}{K+2}\right). \tag{G.43}$$

A first integral of Eq. (G.43), with the boundary conditions $h = h_o$ and $h_x = h_{xo}$, is by simple separation of variables,

$$y_x^2 - y_{xo}^2 = (K+2)\left[E\left(y^2 - y_o^2\right) - \frac{2}{3}\left(y^3 - y_o^3\right) - \ln\left(\frac{y}{y_o}\right)\right], \tag{G.44}$$

where $y = h/h_c$ and $h_c = (q^2/g)^{1/3}$ the critical depth. For turbulent flow in hydraulic jumps, the characteristics of the undular wave train beyond the first wave (namely wave length and amplitude) are approximately determined when assuming E or S constant (Montes and Chanson 1998). As to undular hydraulic jumps, it was found from numerical simulations that ε_1 is an order of magnitude below ε_o. Therefore, Eq. (G.39) may be reduced to

$$\begin{aligned} E &\approx h + \frac{q^2}{2gh^2}\left(1 + \frac{2hh_{xx}}{K+2N+2}\left(\frac{2N+1}{K+1} - \frac{(N+1)(K+2N+2)}{(K+N+2)(K+1)} + 2N + 1\right)\right) \\ &= h + \frac{q^2}{2gh^2}\left(1 + \frac{2hh_{xx}}{\lambda}\right). \end{aligned} \tag{G.45}$$

Therefore, if N is assumed constant, an approximate analytical solution for the tailwater wave train of the undular hydraulic jump is given by the ordinary differential equation

$$y_x^2 - y_{xo}^2 = (\lambda+2)\left[E\left(y^2 - y_o^2\right) - \frac{2}{3}\left(y^3 - y_o^3\right) - \ln\left(\frac{y}{y_o}\right)\right]. \tag{G.46}$$

References

Benjamin, T. B., & Lighthill, M. J. (1954). On cnoidal waves and bores. *Proceedings of Royal Society London A*, 224, 448–460.

Fawer, C. (1937). Etude de quelques écoulements permanents à filets courbes (Study of some steady flows with curved streamlines). *Thesis*. Université de Lausanne. La Concorde, Lausanne, Switzerland (in French).

Montes, J. S., & Chanson, H. (1998). Characteristics of undular hydraulic jumps: Experiments and analysis. *Journal of Hydraulic Engineering*, *124*(2), 192–205.

Appendix H
Non-hydrostatic Gradually Varied Flow on Steep Slopes

In the open-channel hydraulics literature, the expression "*rapidly varied flows*" describes surface profiles involving a large variation of the flow depth with distance (Jain 2001; Chaudhry 2008), and it is frequently used as synonymous of non-hydrostatic flow. The expression "*gradually varied flows*," in turn, is used as synonymous of hydrostatic flows, pointing at surface profiles with a small variation of depth with distance. However, the classical hydraulic jump, involving an abrupt variation of depth over a short distance, is essentially a hydrostatic flow (Khan and Steffler 1996a; Castro-Orgaz and Hager 2009a), whereas a gradually varied flow can also be non-hydrostatic. Flows on a steep slope, as on dam chutes, are examples. In this Appendix, the equations of non-hydrostatic, gradually varied flows on a steep slope are derived using the Boussinesq-type equations of Khan and Steffler (1996b). For clarity, steps already detailed in Chap. 2 are repeated.

The x-momentum equation for 1D unsteady flow over an arbitrary bottom profile is [see Eq. (2.86)]

$$\frac{\partial}{\partial t}(Uh)+\frac{\partial}{\partial x}\left(U^2h+\frac{h}{2}\frac{p_b}{\rho}\right)=-\frac{p_b}{\rho}\frac{\partial z_b}{\partial x}-\frac{\tau_b}{\rho}, \tag{H.1}$$

whereas the z-momentum balance is given by (see Eq. 2.85)

$$p_b=\rho gh+\rho\frac{\partial}{\partial t}(\bar{w}h)+\rho\frac{\partial}{\partial x}(\bar{w}Uh)+\tau_b\frac{\partial z_b}{\partial x}. \tag{H.2}$$

Here, h is the flow depth, U the depth-averaged horizontal velocity, p_b the bottom pressure, and ρ the water density. Moreover, t is time, τ_b the bed-shear stress locally tangent to the terrain, and $z_b(x)$ the bottom profile. The depth-averaged vertical velocity $\bar{w}$ is

$$\bar{w}=\frac{w_s+w_b}{2}, \tag{H.3}$$

© Springer International Publishing AG 2017

O. Castro-Orgaz and W.H. Hager, *Non-Hydrostatic Free Surface Flows*,
Advances in Geophysical and Environmental Mechanics and Mathematics
DOI 10.1007/978-3-319-47971-2

with the free surface and bottom kinematic boundary conditions given by

$$w_s = \frac{\partial}{\partial t}(h + z_b) + U\frac{\partial}{\partial x}(h + z_b), \tag{H.4}$$

$$w_b = \frac{\partial z_b}{\partial t} + U\frac{\partial z_b}{\partial x}, \tag{H.5}$$

respectively. Equations (H.1)–(H.2) are obtained assuming that the velocity component in the x-direction is uniform and equal to its depth-averaged value U; the pressure distribution is linear and non-hydrostatic; the vertical velocity distribution is linear; and the bottom stress state is pure shearing (Steffler and Jin 1993; Khan and Steffler 1996b; Denlinger and Iverson 2004; Castro-Orgaz et al. 2015) [see Eqs. (2.194)–(2.196)]. This is essentially a Boussinesq-type system of equations for clear-water flow. Equation (H.2) is rearranged as follows

$$\begin{aligned} p_b &= \rho g h + \rho\frac{\partial}{\partial t}(\bar{w}h) + \rho\frac{\partial}{\partial x}(\bar{w}Uh) + \tau_b\frac{\partial z_b}{\partial x} \\ &= \rho g h + \rho h\frac{\partial \bar{w}}{\partial t} + \rho\bar{w}\frac{\partial h}{\partial t} + \rho U h\frac{\partial \bar{w}}{\partial x} + \rho\bar{w}\frac{\partial (Uh)}{\partial x} + \tau_b\frac{\partial z_b}{\partial x} \\ &= \rho g h + \rho h\underbrace{\left(\frac{\partial \bar{w}}{\partial t} + U\frac{\partial \bar{w}}{\partial x}\right)}_{=\mathrm{D}\bar{w}/\mathrm{D}t} + \rho\bar{w}\underbrace{\left(\frac{\partial h}{\partial t} + \frac{\partial (Uh)}{\partial x}\right)}_{=0} + \tau_b\frac{\partial z_b}{\partial x} \\ &= \rho g h + \rho h\frac{\mathrm{D}\bar{w}}{\mathrm{D}t} + \tau_b\frac{\partial z_b}{\partial x}, \end{aligned} \tag{H.6}$$

where the mean vertical acceleration is given by

$$\frac{\mathrm{D}\bar{w}}{\mathrm{D}t} = \frac{\partial \bar{w}}{\partial t} + U\frac{\partial \bar{w}}{\partial x}. \tag{H.7}$$

Equation (H.1) is rewritten using Eq. (H.6) as

$$\frac{\partial}{\partial t}(Uh) + \frac{\partial}{\partial x}\underbrace{\left(U^2 h + g\frac{h^2}{2} + \frac{\mathrm{D}\bar{w}}{\mathrm{D}t}\frac{h^2}{2} + \frac{h\tau_b}{2\rho}\frac{\partial z_b}{\partial x}\right)}_{=M} = -\frac{p_b}{\rho}\frac{\partial z_b}{\partial x} - \frac{\tau_b}{\rho}, \tag{H.8}$$

from which the momentum function M is

$$M = U^2 h + g\frac{h^2}{2} + \frac{\mathrm{D}\bar{w}}{\mathrm{D}t}\frac{h^2}{2} + \frac{h\tau_b}{2\rho}\frac{\partial z_b}{\partial x}. \tag{H.9}$$

The kinematic boundary conditions, Eqs. (H.4) and (H.5), are inserted into Eq. (H.3), producing

$$\bar{w} = \frac{1}{2}\left(\frac{\partial h}{\partial t} + U\frac{\partial h}{\partial x}\right) + \frac{\partial z_b}{\partial t} + U\frac{\partial z_b}{\partial x}. \tag{H.10}$$

Using the depth-averaged continuity equation as, viz.

$$\frac{\partial h}{\partial t} + \frac{\partial}{\partial x}(Uh) = 0 \;\Rightarrow\; \frac{\partial h}{\partial t} = -U\frac{\partial h}{\partial x} - h\frac{\partial U}{\partial x}, \tag{H.11}$$

the alternative form of Eq. (H.10) is

$$\bar{w} = -\frac{h}{2}\frac{\partial U}{\partial x} + w_b, \quad w_b = \frac{\partial z_b}{\partial t} + U\frac{\partial z_b}{\partial x}. \tag{H.12}$$

Using Eq. (H.12), the following identities are generated

$$\begin{aligned}
\frac{\partial \bar{w}}{\partial x} &= -\frac{h}{2}\frac{\partial^2 U}{\partial x^2} - \frac{1}{2}\frac{\partial h}{\partial x}\frac{\partial U}{\partial x} + \frac{\partial w_b}{\partial x},\\
\frac{\partial \bar{w}}{\partial t} &= -\frac{h}{2}\frac{\partial^2 U}{\partial x \partial t} - \frac{1}{2}\frac{\partial h}{\partial t}\frac{\partial U}{\partial x} + \frac{\partial w_b}{\partial t}.
\end{aligned} \tag{H.13}$$

Inserting Eq. (H.13) into Eq. (H.7) provides the following transformation

$$\begin{aligned}
\frac{\mathrm{D}\bar{w}}{\mathrm{D}t} &= \frac{\partial \bar{w}}{\partial t} + U\frac{\partial \bar{w}}{\partial x} = \left(-\frac{h}{2}\frac{\partial^2 U}{\partial x \partial t} - \frac{1}{2}\frac{\partial h}{\partial t}\frac{\partial U}{\partial x} + \frac{\partial w_b}{\partial t}\right) + U\left(-\frac{h}{2}\frac{\partial^2 U}{\partial x^2} - \frac{1}{2}\frac{\partial h}{\partial x}\frac{\partial U}{\partial x} + \frac{\partial w_b}{\partial x}\right)\\
&= \left(-\frac{\partial^2 U}{\partial x \partial t} - U\frac{\partial^2 U}{\partial x^2}\right)\frac{h}{2} - \frac{1}{2}\frac{\partial h}{\partial t}\frac{\partial U}{\partial x} - \frac{1}{2}U\frac{\partial h}{\partial x}\frac{\partial U}{\partial x} + \left(\frac{\partial w_b}{\partial t} + U\frac{\partial w_b}{\partial x}\right)\\
&= \left(-\frac{\partial^2 U}{\partial x \partial t} - U\frac{\partial^2 U}{\partial x^2}\right)\frac{h}{2} - \frac{1}{2}\underbrace{\left(-U\frac{\partial h}{\partial x} - h\frac{\partial U}{\partial x}\right)}_{=\frac{\partial h}{\partial t}}\frac{\partial U}{\partial x} - \frac{1}{2}U\frac{\partial h}{\partial x}\frac{\partial U}{\partial x} + \underbrace{\left(\frac{\partial w_b}{\partial t} + U\frac{\partial w_b}{\partial x}\right)}_{=\frac{\mathrm{D}w_b}{\mathrm{D}t}}\\
&= \left(U_x^2 - U_{xt} - UU_{xx}\right)\frac{h}{2} + \frac{\mathrm{D}w_b}{\mathrm{D}t}.
\end{aligned} \tag{H.14}$$

Inserting Eq. (H.14) into Eqs. (H.2) and (H.9) produces the non-hydrostatic Boussinesq-type functions (M, p_b) for turbulent flow over arbitrary terrain, based on Khan and Steffler (1996b), as

$$M = U^2 h + g\frac{h^2}{2} + \left(U_x^2 - U_{xt} - UU_{xx}\right)\frac{h^3}{4} + \frac{h^2}{2}\frac{\mathrm{D}w_b}{\mathrm{D}t} + \frac{h\tau_b}{2\rho}\frac{\partial z_b}{\partial x}, \tag{H.15}$$

$$p_b = \rho g h + \rho\left(U_x^2 - U_{xt} - UU_{xx}\right)\frac{h^2}{2} + \rho h\frac{\mathrm{D}w_b}{\mathrm{D}t} + \tau_b\frac{\partial z_b}{\partial x}. \tag{H.16}$$

The total time derivative Dw_b/Dt is

$$\frac{Dw_b}{Dt} = \frac{\partial w_b}{\partial t} + U\frac{\partial w_b}{\partial x}, \tag{H.17}$$

where

$$\frac{\partial w_b}{\partial t} = \frac{\partial}{\partial t}\left(\frac{\partial z_b}{\partial t} + U\frac{\partial z_b}{\partial x}\right) = \frac{\partial^2 z_b}{\partial t^2} + \frac{\partial U}{\partial t}\frac{\partial z_b}{\partial x} + U\frac{\partial^2 z_b}{\partial x \partial t}, \tag{H.18}$$

$$\frac{\partial w_b}{\partial x} = \frac{\partial}{\partial x}\left(\frac{\partial z_b}{\partial t} + U\frac{\partial z_b}{\partial x}\right) = \frac{\partial^2 z_b}{\partial x \partial t} + \frac{\partial U}{\partial x}\frac{\partial z_b}{\partial x} + U\frac{\partial^2 z_b}{\partial x^2}. \tag{H.19}$$

For steady flow, Eqs. (H.15)–(H.16) reduce to

$$M = U^2 h + g\frac{h^2}{2} + \left(U_x^2 - UU_{xx}\right)\frac{h^3}{4} + \frac{h^2}{2}U\left(\frac{\partial U}{\partial x}\frac{\partial z_b}{\partial x} + U\frac{\partial^2 z_b}{\partial x^2}\right) + \frac{h}{2}\frac{\tau_b}{\rho}\frac{\partial z_b}{\partial x}, \tag{H.20}$$

$$p_b = \rho g h + \rho\left(U_x^2 - UU_{xx}\right)\frac{h^2}{2} + \rho h U\left(\frac{\partial U}{\partial x}\frac{\partial z_b}{\partial x} + U\frac{\partial^2 z_b}{\partial x^2}\right) + \tau_b\frac{\partial z_b}{\partial x}. \tag{H.21}$$

For constant unit discharge q and $U = q/h$, one has

$$U_x = -\frac{qh_x}{h^2}, \quad U_{xx} = -\frac{qh_{xx}}{h^2} + 2\frac{qh_x^2}{h^3}. \tag{H.22}$$

Inserting these into Eqs. (H.20)–(H.21) yields, after rearrangement,

$$M = g\frac{h^2}{2} + \frac{q^2}{h}\left(1 + \frac{1}{4}h\frac{\partial^2 h}{\partial x^2} - \frac{1}{4}\left(\frac{\partial h}{\partial x}\right)^2 + \frac{h}{2}\frac{\partial^2 z_b}{\partial x^2} - \frac{1}{2}\frac{\partial h}{\partial x}\frac{\partial z_b}{\partial x}\right) + \frac{h}{2}\frac{\tau_b}{\rho}\frac{\partial z_b}{\partial x}, \tag{H.23}$$

$$p_b = \rho g h + \rho\frac{q^2}{2h^2}\left(h\frac{\partial^2 h}{\partial x^2} - \left(\frac{\partial h}{\partial x}\right)^2 - 2\frac{\partial h}{\partial x}\frac{\partial z_b}{\partial x} + 2h\frac{\partial^2 z_b}{\partial x^2}\right) + \tau_b\frac{\partial z_b}{\partial x}. \tag{H.24}$$

Inserting Eqs. (H.23)–(H.24) into the steady-state version of Eq. (H.8), namely

$$\frac{dM}{dx} = -\frac{p_b}{\rho}\frac{\partial z_b}{\partial x} - \frac{\tau_b}{\rho}, \tag{H.25}$$

results in a third-order differential equation for the surface profile $h = h(x)$. This model is valid for turbulent flows with arbitrarily sloped and curved free surface and bottom profiles.

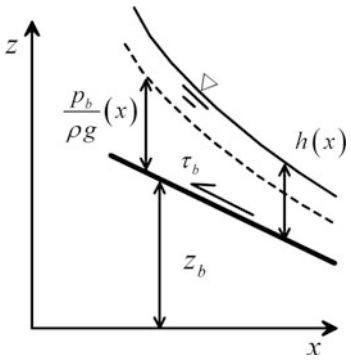

Figure H.1 Gradually varied flow on a steep slope

It is pertinent to remark that some of the non-hydrostatic effects accounted for in Eqs. (H.23)–(H.24) originate from the curvature terms $\partial^2 h/\partial x^2$ and $\partial^2 z_b/\partial x^2$, but non-negligible contributions are introduced by the slope terms $\partial h/\partial x$ and $\partial z_b/\partial x$. In general, the assumption that *in gradually varied flows, the pressure is hydrostatic, given the small variation of depth with distance and therefore the small streamline curvatures,* is wrong. Indeed, consider gradually varied flows on a steep slope (Fig. H.1), for which the variation of h with x is small. For these flows, it can be assumed that $h_x^2 \approx h_{xx} \approx 0$. Furthermore, on a plane slope, the bottom is flat, resulting in $\partial^2 z_b/\partial x^2 = 0$. On a steep slope, however, the term $\partial z_b/\partial x$ is finite. Therefore, despite small h_x^2, the product $(\partial h/\partial x \cdot \partial z_b/\partial x)$ remains finite. Using these simplifications, Eqs. (H.23)–(H.24) reduce to

$$M = g\frac{h^2}{2} + \frac{q^2}{h}\left(1 - \frac{1}{2}\frac{\partial h}{\partial x}\frac{\partial z_b}{\partial x}\right) + \frac{h}{2}\frac{\tau_b}{\rho}\frac{\partial z_b}{\partial x}, \tag{H.26}$$

$$p_b = \rho g h - \rho\frac{q^2}{h^2}\frac{\partial h}{\partial x}\frac{\partial z_b}{\partial x} + \tau_b\frac{\partial z_b}{\partial x}. \tag{H.27}$$

The bottom pressure contribution in the x-momentum balance is, from Eq. (H.27),

$$p_b\frac{\partial z_b}{\partial x} = \rho g h\frac{\partial z_b}{\partial x} - \rho\frac{q^2}{h^2}\frac{\partial h}{\partial x}\left(\frac{\partial z_b}{\partial x}\right)^2 + \tau_b\left(\frac{\partial z_b}{\partial x}\right)^2, \tag{H.28}$$

so that the source term in Eq. (H.25) takes the form

$$-\frac{p_b}{\rho}\frac{\partial z_b}{\partial x} - \frac{\tau_b}{\rho} = -gh\frac{\partial z_b}{\partial x} + \frac{q^2}{h^2}\frac{\partial h}{\partial x}\left(\frac{\partial z_b}{\partial x}\right)^2 - \frac{\tau_b}{\rho}\left(\frac{\partial z_b}{\partial x}\right)^2 - \frac{\tau_b}{\rho}. \tag{H.29}$$

The variation of M with x is, from Eq. (H.26),

$$\frac{\mathrm{d}M}{\mathrm{d}x} = \frac{\mathrm{d}}{\mathrm{d}x}\left[g\frac{h^2}{2} + \frac{q^2}{h}\left(1 - \frac{1}{2}\frac{\partial h}{\partial x}\frac{\partial z_b}{\partial x}\right) + \frac{h}{2}\frac{\tau_b}{\rho}\frac{\partial z_b}{\partial x}\right] \approx gh\frac{\partial h}{\partial x} - \frac{q^2}{h^2}\frac{\partial h}{\partial x} + \frac{\tau_b}{2\rho}\frac{\partial h}{\partial x}\frac{\partial z_b}{\partial x}. \tag{H.30}$$

Equating Eqs. (H.29) and (H.30) yields

$$gh\frac{\partial h}{\partial x} - \frac{q^2}{h^2}\frac{\partial h}{\partial x} + \frac{\tau_b}{2\rho}\frac{\partial h}{\partial x}\frac{\partial z_b}{\partial x} \equiv -gh\frac{\partial z_b}{\partial x} + \frac{q^2}{h^2}\frac{\partial h}{\partial x}\left(\frac{\partial z_b}{\partial x}\right)^2 - \frac{\tau_b}{\rho}\left(\frac{\partial z_b}{\partial x}\right)^2 - \frac{\tau_b}{\rho}, \tag{H.31}$$

or

$$\frac{\partial h}{\partial x}\left[1 - \frac{q^2}{gh^3}\left(1 + \left(\frac{\partial z_b}{\partial x}\right)^2\right) + \frac{\tau_b}{2\rho gh}\frac{\partial z_b}{\partial x}\right] = -\frac{\partial z_b}{\partial x} - \frac{\tau_b}{\rho gh}\left[1 + \left(\frac{\partial z_b}{\partial x}\right)^2\right]. \tag{H.32}$$

With $\mathsf{F} = q/(gh^3)^{1/2}$ as the Froude number and $S_f = \tau_b/(\rho gh)$ as friction slope, Eq. (H.32) can be rewritten as

$$\frac{\mathrm{d}h}{\mathrm{d}x}\left[1 - \mathsf{F}^2\left(1 + \left(\frac{\mathrm{d}z_b}{\mathrm{d}x}\right)^2\right) + \frac{S_f}{2}\frac{\mathrm{d}z_b}{\mathrm{d}x}\right] = -\frac{\mathrm{d}z_b}{\mathrm{d}x} - S_f\left[1 + \left(\frac{\mathrm{d}z_b}{\mathrm{d}x}\right)^2\right]. \tag{H.33}$$

Likewise, Eq. (H.27) is rearranged as

$$\frac{p_b}{\rho gh} = 1 + S_f\frac{\mathrm{d}z_b}{\mathrm{d}x} - \mathsf{F}^2\frac{\mathrm{d}h}{\mathrm{d}x}\frac{\mathrm{d}z_b}{\mathrm{d}x}. \tag{H.34}$$

Equations (H.33)–(H.34) are the general gradually varied flow equations for the profiles $h(x)$ and $p_b(x)$ on a steep slope. Note from Eq. (H.34) that the bottom pressure head is non-hydrostatic, even though the variation of h with x is small (gradually varied flow).

For uniform flow, $\mathrm{d}h/\mathrm{d}x = 0$, and, thus, $h = h_o = \text{const}$. Therefore, Eq. (H.33) reduces to

$$0 = -\frac{\mathrm{d}z_b}{\mathrm{d}x} - S_f\left[1 + \left(\frac{\mathrm{d}z_b}{\mathrm{d}x}\right)^2\right], \tag{H.35}$$

or,

$$S_f = -\frac{\dfrac{\mathrm{d}z_b}{\mathrm{d}x}}{1+\left(\dfrac{\mathrm{d}z_b}{\mathrm{d}x}\right)^2}. \tag{H.36}$$

Equation (H.34) yields for uniform flow, after inserting in it Eq. (H.36),

$$\frac{p_b}{\rho g h_o} = 1 + S_f \frac{\mathrm{d}z_b}{\mathrm{d}x} = 1 - \frac{\left(\dfrac{\mathrm{d}z_b}{\mathrm{d}x}\right)^2}{1+\left(\dfrac{\mathrm{d}z_b}{\mathrm{d}x}\right)^2} = \frac{1}{1+\left(\dfrac{\mathrm{d}z_b}{\mathrm{d}x}\right)^2}. \tag{H.37}$$

This equation was derived by Castro-Orgaz et al. (2015) [see Eq. (2.59)].

For potential flow, $S_f = 0$, so that Eq. (H.33) reduces to

$$\frac{\mathrm{d}h}{\mathrm{d}x} = \frac{-\dfrac{\mathrm{d}z_b}{\mathrm{d}x}}{1-\mathsf{F}^2\left[1+\left(\dfrac{\mathrm{d}z_b}{\mathrm{d}x}\right)^2\right]}. \tag{H.38}$$

This equation was alternatively derived by Castro-Orgaz and Hager (2009b) using the energy principle [see Eq. (3.443)]. Flow on a steep slope, as in a chute, is typically hypercritical with $\mathsf{F}^2 \gg 1$, for which Eq. (H.38) simplifies to (Hager and Blaser 1998, Castro-Orgaz 2009, Castro-Orgaz and Hager 2009b)

$$\frac{\mathrm{d}h}{\mathrm{d}x} = \frac{-\dfrac{\mathrm{d}z_b}{\mathrm{d}x}}{1-\mathsf{F}^2\left[1+\left(\dfrac{\mathrm{d}z_b}{\mathrm{d}x}\right)^2\right]} \approx \frac{\dfrac{\mathrm{d}z_b}{\mathrm{d}x}}{\mathsf{F}^2\left[1+\left(\dfrac{\mathrm{d}z_b}{\mathrm{d}x}\right)^2\right]}. \tag{H.39}$$

Inserting Eq. (H.39) into Eq. (H.34) produces, with $S_f = 0$,

$$\begin{aligned}\frac{p_b}{\rho g h} = 1 - \mathsf{F}^2 \frac{\mathrm{d}h}{\mathrm{d}x}\frac{\mathrm{d}z_b}{\mathrm{d}x} &\approx 1 - \mathsf{F}^2 \left\{\frac{\dfrac{\mathrm{d}z_b}{\mathrm{d}x}}{\mathsf{F}^2\left[1+\left(\dfrac{\mathrm{d}z_b}{\mathrm{d}x}\right)^2\right]}\right\}\frac{\mathrm{d}z_b}{\mathrm{d}x} \\ &= 1 - \frac{\left(\dfrac{\mathrm{d}z_b}{\mathrm{d}x}\right)^2}{1+\left(\dfrac{\mathrm{d}z_b}{\mathrm{d}x}\right)^2} = \frac{1}{1+\left(\dfrac{\mathrm{d}z_b}{\mathrm{d}x}\right)^2}.\end{aligned} \tag{H.40}$$

This is the bottom pressure equation for potential flows obtained here by using the momentum equations. It can also be derived based on the energy principle and Boussinesq-type equations (Castro-Orgaz and Hager 2009b).

For turbulent gradually varied flow, the general ODE, from Eq. (H.33), can be written as

$$\frac{\mathrm{d}h}{\mathrm{d}x} = \frac{-\frac{\mathrm{d}z_b}{\mathrm{d}x} - S_f\left[1+\left(\frac{\mathrm{d}z_b}{\mathrm{d}x}\right)^2\right]}{1-\mathsf{F}^2\left[1+\left(\frac{\mathrm{d}z_b}{\mathrm{d}x}\right)^2\right]+\frac{S_f}{2}\frac{\mathrm{d}z_b}{\mathrm{d}x}}. \tag{H.41}$$

In the definition of S_f, the stress τ_b acts tangentially to the sloping plane (Steffler and Jin 1993) (Fig. H.1). Therefore, it is computed by using the equation (Khan and Steffler 1996b)

$$\tau_b = \rho C_f U_o^2, \tag{H.42}$$

with C_f as the skin friction coefficient and U_o the velocity component parallel to the sloping plane. The velocity components of the Boussinesq-type model in the (x, z) directions are $(U, \bar{w})$. The modulus of the velocity V and its angle α with respect to the x-axis are, therefore,

$$V = \left(U^2+\bar{w}^2\right)^{1/2}, \quad \tan\alpha = \frac{\bar{w}}{U}. \tag{H.43}$$

The velocity component parallel to the slope is, with θ as the bottom angle with the x-axis,

$$U_o = V\cos(\alpha-\theta) = \left(U^2+\bar{w}^2\right)^{1/2}\cos(\alpha-\theta). \tag{H.44}$$

Khan and Steffler (1996b) suggested Eq. (H.44) with $\cos(\alpha-\theta) \approx 1$, assuming that the flow velocity V is parallel to the bottom. For uniform flow on a steep slope, Eqs. (H.43) yield exactly (or approximately, for gradually varied flow, e.g., $h_x \approx 0$) (Castro-Orgaz et al. 2015)

$$V = \left[U^2+U^2\left(\frac{\mathrm{d}z_b}{\mathrm{d}x}\right)^2\right]^{1/2} = U\left[1+\left(\frac{\mathrm{d}z_b}{\mathrm{d}x}\right)^2\right]^{1/2}, \quad \tan\alpha = \frac{U\frac{\mathrm{d}z_b}{\mathrm{d}x}}{U} \equiv \frac{\mathrm{d}z_b}{\mathrm{d}x}. \tag{H.45}$$

Thus, combining Eqs. (H.42), (H.44), and (H.45) generates the bottom shear stress as

$$\tau_b = \rho C_f U^2\left[1+\left(\frac{\mathrm{d}z_b}{\mathrm{d}x}\right)^2\right], \tag{H.46}$$

from which the friction slope can be deduced as

$$S_f = \frac{\tau_b}{\rho g h} = C_f \mathsf{F}^2 \left[1 + \left(\frac{\mathrm{d}z_b}{\mathrm{d}x}\right)^2\right]. \tag{H.47}$$

Inserting Eq. (H.47) into Eq. (H.41) then produces

$$\frac{\mathrm{d}h}{\mathrm{d}x} = \frac{-\frac{\mathrm{d}z_b}{\mathrm{d}x} - C_f \mathsf{F}^2 \left[1 + \left(\frac{\mathrm{d}z_b}{\mathrm{d}x}\right)^2\right]^2}{1 - \mathsf{F}^2 \left[1 + \left(\frac{\mathrm{d}z_b}{\mathrm{d}x}\right)^2\right] + \frac{1}{2}\frac{\mathrm{d}z_b}{\mathrm{d}x} C_f \mathsf{F}^2 \left[1 + \left(\frac{\mathrm{d}z_b}{\mathrm{d}x}\right)^2\right]}. \tag{H.48}$$

For hypercritical flow, with $\mathsf{F}^2 \gg 1$, Eq. (H.48) simplifies to

$$\begin{aligned}
\frac{\mathrm{d}h}{\mathrm{d}x} &= \frac{-\frac{\mathrm{d}z_b}{\mathrm{d}x} - C_f \mathsf{F}^2 \left[1 + \left(\frac{\mathrm{d}z_b}{\mathrm{d}x}\right)^2\right]^2}{\mathsf{F}^2 \left\{\frac{1}{\mathsf{F}^2} - \left[1 + \left(\frac{\mathrm{d}z_b}{\mathrm{d}x}\right)^2\right] + \frac{1}{2}\frac{\mathrm{d}z_b}{\mathrm{d}x} C_f \left[1 + \left(\frac{\mathrm{d}z_b}{\mathrm{d}x}\right)^2\right]\right\}} \\
&\approx \frac{-\frac{\mathrm{d}z_b}{\mathrm{d}x} - C_f \mathsf{F}^2 \left[1 + \left(\frac{\mathrm{d}z_b}{\mathrm{d}x}\right)^2\right]^2}{\mathsf{F}^2 \left\{-\left[1 + \left(\frac{\mathrm{d}z_b}{\mathrm{d}x}\right)^2\right] + \frac{1}{2}\frac{\mathrm{d}z_b}{\mathrm{d}x} C_f \left[1 + \left(\frac{\mathrm{d}z_b}{\mathrm{d}x}\right)^2\right]\right\}} \\
&= \frac{\frac{\mathrm{d}z_b}{\mathrm{d}x}}{\mathsf{F}^2 \left(1 - \frac{1}{2}\frac{\mathrm{d}z_b}{\mathrm{d}x} C_f\right) \left[1 + \left(\frac{\mathrm{d}z_b}{\mathrm{d}x}\right)^2\right]} + \frac{C_f \left[1 + \left(\frac{\mathrm{d}z_b}{\mathrm{d}x}\right)^2\right]}{\left(1 - \frac{1}{2}\frac{\mathrm{d}z_b}{\mathrm{d}x} C_f\right)}.
\end{aligned} \tag{H.49}$$

For usual values of $C_f \approx 0.001$ in open-channel flows, the quantity $C_f \cdot \mathrm{d}z_b/\mathrm{d}x$ is much smaller than unity and can, thus, be neglected. The free surface profile equation for hypercritical flow on steep slopes, obtained from Boussinesq-type equations (Khan and Steffler 1996b), is, thus, from Eq. (H.49), approximately given by

$$\frac{\mathrm{d}h}{\mathrm{d}x} = \frac{\frac{\mathrm{d}z_b}{\mathrm{d}x}}{\mathsf{F}^2 \left[1 + \left(\frac{\mathrm{d}z_b}{\mathrm{d}x}\right)^2\right]} + C_f \left[1 + \left(\frac{\mathrm{d}z_b}{\mathrm{d}x}\right)^2\right]. \tag{H.50}$$

Inserting Eq. (H.50) into Eq. (H.34) then produces

$$\frac{p_b}{\rho g h} = 1 + S_f \frac{\mathrm{d}z_b}{\mathrm{d}x} - \mathsf{F}^2 \frac{\mathrm{d}h}{\mathrm{d}x}\frac{\mathrm{d}z_b}{\mathrm{d}x} \approx 1 + S_f \frac{\mathrm{d}z_b}{\mathrm{d}x} - \mathsf{F}^2 \left\{ \frac{\dfrac{\mathrm{d}z_b}{\mathrm{d}x}}{\mathsf{F}^2\left[1 + \left(\dfrac{\mathrm{d}z_b}{\mathrm{d}x}\right)^2\right]} + C_f\left[1 + \left(\frac{\mathrm{d}z_b}{\mathrm{d}x}\right)^2\right] \right\} \frac{\mathrm{d}z_b}{\mathrm{d}x}$$

$$= 1 + S_f \frac{\mathrm{d}z_b}{\mathrm{d}x} - \frac{\left(\dfrac{\mathrm{d}z_b}{\mathrm{d}x}\right)^2}{1 + \left(\dfrac{\mathrm{d}z_b}{\mathrm{d}x}\right)^2} - C_f \mathsf{F}^2 \left[1 + \left(\frac{\mathrm{d}z_b}{\mathrm{d}x}\right)^2\right] \frac{\mathrm{d}z_b}{\mathrm{d}x}$$

$$= 1 + C_f \mathsf{F}^2 \left[1 + \left(\frac{\mathrm{d}z_b}{\mathrm{d}x}\right)^2\right] \frac{\mathrm{d}z_b}{\mathrm{d}x} - \frac{\left(\dfrac{\mathrm{d}z_b}{\mathrm{d}x}\right)^2}{1 + \left(\dfrac{\mathrm{d}z_b}{\mathrm{d}x}\right)^2} - C_f \mathsf{F}^2 \left[1 + \left(\frac{\mathrm{d}z_b}{\mathrm{d}x}\right)^2\right] \frac{\mathrm{d}z_b}{\mathrm{d}x}$$

$$= \frac{1}{1 + \left(\dfrac{\mathrm{d}z_b}{\mathrm{d}x}\right)^2}. \tag{H.51}$$

This equation is identical to that obtained for potential flows (Eq. H.40) and to the exact result for turbulent uniform flow (Eq. H.37). Therefore, Eq. (H.51) is the bottom pressure head function for gradually varied flows on steep slopes, regardless whether the flows are potential or turbulent, provided that they are hypercritical.

Equation (H.50) applies to compute the drawdown curve in a chute and thus to locate the point of incipient air entrainment; once $h = h(x)$ is available, Eq. (H.51) produces the bottom pressure head $p_b(x)$ so that the cavitation risk can be analyzed. An alternative approach is due to Hager and Blaser (1998), whereas Castro-Orgaz (2009) obtained approximate analytical solutions for the free surface and turbulent boundary layer profiles.

Hager and Blaser (1998) and Castro-Orgaz (2009) obtained approximate analytical solutions for chute flows assuming hypercritical flow, but defining the equations based on the flow depth N measured normal to the channel bottom and the slope-fitted coordinate s (Fig. H.2). Use of these variables is especially advantageous if boundary layers are introduced in the computations, given that the velocity profile is defined in the direction normal to the bottom curve. It will be demonstrated that this formulation is fully equivalent to that pursued using Cartesian coordinates (x, z). Developments are conducted by assuming potential flows, and resort is made to the energy equation, given its use in boundary layer methods (Castro-Orgaz 2009).

Based on the energy principle, Castro-Orgaz and Hager (2009b) derived the gradually varied flow equation for potential flows on a steep slope as (see Eq. 3.443)

$$\frac{\mathrm{d}h}{\mathrm{d}x} = \frac{\tan\theta}{1 - \dfrac{q^2}{g h^3 \cos^2\theta}}. \tag{H.52}$$

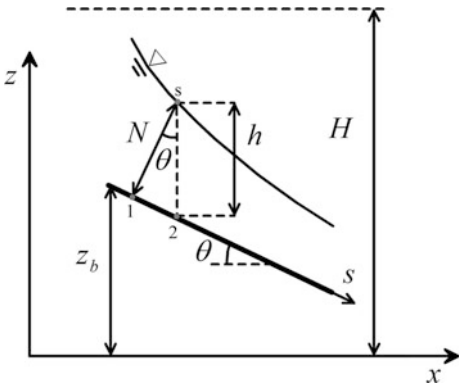

Figure H.2 Alternative definitions for chute flows, assuming potential flows

However, Hager and Blaser (1998) and Castro-Orgaz (2009) pursued chute flow models based on the potential flow equation[7]

$$\frac{\mathrm{d}N}{\mathrm{d}s} = \frac{\sin\theta}{\cos\theta - \dfrac{q^2}{gN^3}}. \tag{H.53}$$

Here, N is the flow depth measured normal to the channel bottom, and s the slope-fitted coordinate (Fig. H.2).

To mathematically transform Eq. (H.52) to Eq. (H.53), the former is rewritten as

$$\frac{\mathrm{d}h}{\mathrm{d}x} = \frac{\tan\theta}{1 - \dfrac{q^2}{gh^3\cos^2\theta}} = \frac{-\dfrac{\mathrm{d}z_{b2}}{\mathrm{d}x}}{1 - \dfrac{q^2}{gh^3\cos^2\theta}}. \tag{H.54}$$

Basic trigonometry gives the following identities (see triangle 1-s-2 in Fig. H.2)

$$N = h\cos\theta, \tag{H.55}$$

$$\mathrm{d}x = \cos\theta\mathrm{d}s, \tag{H.56}$$

$$z_{b1} - z_{b2} = \tan\theta(N\ \sin\theta) = N\frac{\sin^2\theta}{\cos\theta}. \tag{H.57}$$

Based on Eqs. (H.55) and (H.56), the following identity prevails

$$\frac{\mathrm{d}N}{\mathrm{d}s} = \left(\frac{\mathrm{d}h}{\mathrm{d}x}\frac{\mathrm{d}x}{\mathrm{d}s}\right)\frac{\mathrm{d}N}{\mathrm{d}h} = \frac{\mathrm{d}h}{\mathrm{d}x}\cos^2\theta. \tag{H.58}$$

[7]Hager and Blaser (1998) and Castro-Orgaz (2009) included the friction effects in Eq. (H.53) using different methods.

Differentiation of Eq. (H.57) produces

$$\frac{\mathrm{d}z_{b2}}{\mathrm{d}s} = \frac{\mathrm{d}z_{b1}}{\mathrm{d}s} - \frac{\mathrm{d}N}{\mathrm{d}s}\frac{\sin^2\theta}{\cos\theta}. \tag{H.59}$$

This relation implies that given a variation in z_{b1}, the variation of z_{b2} is influenced by the actual shape of the free surface curve $N(s)$. This is a key issue to perform a correct mathematical transformation from the gradually varied flow equation using the Cartesian coordinate x with $h(x)$ measured vertically, to the equivalent equation using the bottom-normal flow depth $N(s)$ based on a bottom-fitted coordinate s. Inserting Eqs. (H.58) and (H.59) into Eq. (H.54) generates the equation

$$\frac{1}{\cos^2\theta}\frac{\mathrm{d}N}{\mathrm{d}s}\left(1 - \frac{q^2}{gh^3\cos^2\theta}\right) + \frac{\mathrm{d}s}{\mathrm{d}x}\left(\frac{\mathrm{d}z_{b1}}{\mathrm{d}s} - \frac{\mathrm{d}N}{\mathrm{d}s}\frac{\sin^2\theta}{\cos\theta}\right) = 0. \tag{H.60}$$

Using Eqs. (H.55)–(H.56) in Eq. (H.60) yields

$$\frac{1}{\cos^2\theta}\frac{\mathrm{d}N}{\mathrm{d}s}\left(1 - \frac{q^2\cos\theta}{gN^3}\right) + \frac{1}{\cos\theta}\left(\frac{\mathrm{d}z_{b1}}{\mathrm{d}s} - \frac{\mathrm{d}N}{\mathrm{d}s}\frac{\sin^2\theta}{\cos\theta}\right) = 0, \tag{H.61}$$

or

$$\frac{\mathrm{d}N}{\mathrm{d}s}\underbrace{\left(\frac{1}{\cos^2\theta} - \frac{\sin^2\theta}{\cos^2\theta}\right)}_{=1} - \frac{\mathrm{d}N}{\mathrm{d}s}\frac{q^2}{gN^3\cos\theta} + \frac{1}{\cos\theta}\frac{\mathrm{d}z_{b1}}{\mathrm{d}s} = 0, \tag{H.62}$$

so that finally,

$$\frac{\mathrm{d}N}{\mathrm{d}s} = \frac{-\dfrac{\mathrm{d}z_{b1}}{\mathrm{d}s}}{\cos\theta - \dfrac{q^2}{gN^3}} = \frac{\sin\theta}{\cos\theta - \dfrac{q^2}{gN^3}}. \tag{H.63}$$

Therefore, Eqs. (H.52) and (H.53) are fully equivalent for chute flows. The selection of the type of formulation is a crucial aspect for a modeler. Generally, the use of horizontal–vertical Cartesian coordinates and Eq. (H.52) is immediate to compare simulations with laboratory observations, given that h is usually the measured variable. However, if friction effects in chute flows are accounted for via the boundary layer theory, resort to bottom-fitted coordinates and Eq. (H.53) is advantageous.

References

Castro-Orgaz, O. (2009). Hydraulics of developing chute flow. *Journal of Hydraulic Research, 47*(2), 185–194.

Castro-Orgaz, O., & Hager, W. H. (2009a). Classical hydraulic jump: Basic flow features. *Journal of Hydraulic Research, 47*(6), 744–754.

Castro-Orgaz, O., & Hager, W. H. (2009b). Curved streamline transitional flow from mild to steep slopes. *Journal of Hydraulic Research, 47*(5), 574–584.

Castro-Orgaz, O., Hutter, K., Giráldez, J. V., & Hager, W. H. (2015). Non-hydrostatic granular flow over 3D terrain: New Boussinesq-type gravity waves? *Journal of Geophysical Research: Earth Surface,* 120(1), 1–28.

Chaudhry, M. H. (2008). *Open-channel flow*, 2nd ed. Berlin: Springer.

Denlinger, R. P., & Iverson, R. M. (2004). Granular avalanches across irregular three-dimensional terrain: 1. Theory and Computation. *Journal of Geophysical Research, 109*(F1), F01014, doi:10.1029/2003JF000085.

Hager, W. H., & Blaser, F. (1998). Drawdown curve and incipient aeration for chute flow. *Canadian Journal of Civil Engineering*, *25*(3), 467–473.

Jain, S. C. (2001). *Open channel flow*. New York: Wiley.

Khan, A. A., & Steffler, P. M. (1996a). Physically based hydraulic jump model for depth-averaged computations. *Journal of Hydraulic Engineering*, *122*(10), 540–548.

Khan, A. A., & Steffler, P. M. (1996b). Vertically averaged and moment equations model for flow over curved beds. *Journal of Hydraulic Engineering*, *122*(1), 3–9.

Steffler, P. M., & Jin, Y. C. (1993). Depth-averaged and moment equations for moderately shallow free surface flow. *Journal of Hydraulic Research, 31*(1), 5–17.

Appendix I
Derivation of Vertically Integrated Equations for Non-hydrostatic Mixture Flows

The computation of geomorphic free surface flows, like those developed when a dam collapses on a granular bed, has been typically treated with models based on a hydrostatic pressure assumption (e.g., Capart and Young 1998; Wu and Wang 2007; Wu 2008; among others). Based on the work of Peregrine (1966) for the undular bore, Capart and Young (1998) concluded that the deviations from experimental observations of the free surface predictions based on such a family of models, when solved using high-accurate numerical schemes, can be explained on the basis of the neglected non-hydrostatic dynamic stress components. Following this critical outlook, Cantero-Chinchilla et al. (2016) developed an unsteady, non-hydrostatic, and non-equilibrium mixture flow model for geomorphic flows, which is described here. The flow is composed of three layers, depicted in Fig. I.1: A suspended-load layer, where sediment particles are transported in suspension by fluid turbulence, while they simultaneously deposit and reenter into suspension across its common interface with the bed-load layer, where the fluidized bed of moving particles, rolling, sliding, and saltating, determine the upper bathymetry of the river bed, that changes in time and space. Below the bed-load layer, particles are eroded and deposited into a static bed of alluvial material.

The RANS mass and momentum conservation equations in the x- and z-directions for a sediment–water mixture flowing over an erodible bed are (Wu 2008, pp. 42–43; Hutter et al. 2014, pp. 502)

$$\frac{\partial \rho}{\partial t} + \frac{\partial (\rho u)}{\partial x} + \frac{\partial (\rho w)}{\partial z} = 0, \tag{I.1}$$

$$\frac{\partial (\rho u)}{\partial t} + \frac{\partial}{\partial x}\left(\rho u^2 + p - \sigma_x\right) + \frac{\partial (\rho u w)}{\partial z} = \frac{\partial \tau_{xz}}{\partial z}, \tag{I.2}$$

$$\frac{\partial (\rho w)}{\partial t} + \frac{\partial (\rho u w)}{\partial x} + \frac{\partial}{\partial z}\left(\rho w^2 + p - \sigma_z\right) = \frac{\partial \tau_{zx}}{\partial x} - \rho g. \tag{I.3}$$

Here, (u, w) are the mixture velocity components in the (x, z) directions, ρ is the density of the mixture of water and solids, p is the pressure, τ and σ are the tangential and normal turbulent stresses, and g is the gravity acceleration.

© Springer International Publishing AG 2017

O. Castro-Orgaz and W.H. Hager, *Non-Hydrostatic Free Surface Flows*,
Advances in Geophysical and Environmental Mechanics and Mathematics
DOI 10.1007/978-3-319-47971-2

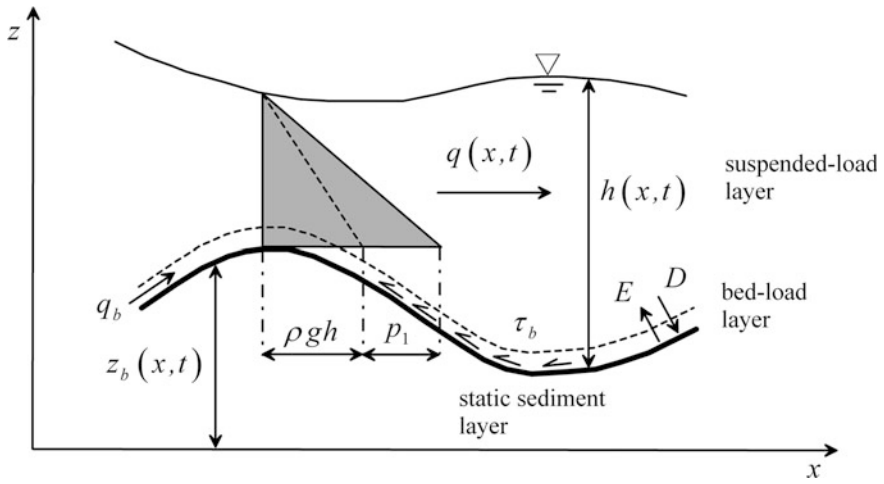

Figure I.1 Non-hydrostatic unsteady flow over an erodible bed

To obtain a 1D system of equations, the conservation laws for a 2D flow in the vertical plane are first vertically integrated, then Leibnitz's rule is used, and finally, the kinematic boundary conditions are applied (Steffler and Jin 1993; Castro-Orgaz et al. 2015). The terms of the mass conservation Eq. (I.1) then produce

$$\int_{z_b}^{z_s} \frac{\partial \rho}{\partial t} \mathrm{d}z = \frac{\partial}{\partial t} \int_{z_b}^{z_s} \rho \mathrm{d}z - \rho_s \frac{\partial z_s}{\partial t} + \rho_b \frac{\partial z_b}{\partial t}, \tag{I.4}$$

$$\int_{z_b}^{z_s} \frac{\partial (\rho u)}{\partial x} \mathrm{d}z = \frac{\partial}{\partial x} \int_{z_b}^{z_s} \rho u \mathrm{d}z - \rho_s u_s \frac{\partial z_s}{\partial x} + \rho_b u_b \frac{\partial z_b}{\partial x}, \tag{I.5}$$

$$\int_{z_b}^{z_s} \frac{\partial (\rho w)}{\partial z} \mathrm{d}z = \rho_s w_s - \rho_b w_b, \tag{I.6}$$

where the free surface level is $z_s = h + z_b$. Summing Eqs. (I.4)–(I.6) produces the depth-averaged continuity equation

$$\frac{\partial}{\partial t} \int_{z_b}^{z_s} \rho \mathrm{d}z + \frac{\partial}{\partial x} \int_{z_b}^{z_s} \rho u \mathrm{d}z - \rho_s \left(\frac{\partial z_s}{\partial t} + u_s \frac{\partial z_s}{\partial x} - w_s \right) + \rho_b \left(\frac{\partial z_b}{\partial t} + u_b \frac{\partial z_b}{\partial x} - w_b \right) = 0. \tag{I.7}$$

The free surface kinematic boundary condition is, for a material free surface (Wu 2008; Hutter et al. 2014),

$$\frac{\partial z_s}{\partial t} + u_s \frac{\partial z_s}{\partial x} - w_s = 0, \tag{I.8}$$

and, at the static sediment bed, the no-slip conditions are (Wu 2008)

$$u_b = w_b = 0. \tag{I.9}$$

Inserting Eqs. (I.8)–(I.9) into Eq.(I.7) yields

$$\frac{\partial}{\partial t}\int_{z_b}^{z_s} \rho \mathrm{d}z + \frac{\partial}{\partial x}\int_{z_b}^{z_s} \rho u \mathrm{d}z + \rho_b \frac{\partial z_b}{\partial t} = 0. \tag{I.10}$$

Considering depth-averaged values of the density ρ and velocity U permits to express the depth-averaged mass conservation equation in the form

$$\frac{\partial(\rho h)}{\partial t} + \frac{\partial(\rho U h)}{\partial x} + \rho_b \frac{\partial z_b}{\partial t} = 0, \tag{I.11}$$

in which $h = z_s - z_b$ is the water depth. Vertical integration of each term of the x-momentum in Eq. (I.2) yields, upon use of the Leibniz rule, the following identities:

$$\int_{z_b}^{z_s} \frac{\partial(\rho u)}{\partial t}\mathrm{d}z = \frac{\partial}{\partial t}\int_{z_b}^{z_s} \rho u \mathrm{d}z - \rho_s u_s \frac{\partial z_s}{\partial t} + \rho_b u_b \frac{\partial z_b}{\partial t}, \tag{I.12}$$

$$\int_{z_b}^{z_s} \frac{\partial(\rho u^2)}{\partial x}\mathrm{d}z = \frac{\partial}{\partial x}\int_{z_b}^{z_s} \rho u^2 \mathrm{d}z - \rho_s u_s^2 \frac{\partial z_s}{\partial x} + \rho_b u_b^2 \frac{\partial z_b}{\partial x}, \tag{I.13}$$

$$\int_{z_b}^{z_s} \frac{\partial p}{\partial x}\mathrm{d}z = \frac{\partial}{\partial x}\int_{z_b}^{z_s} p \mathrm{d}z - p_s \frac{\partial z_s}{\partial x} + p_b \frac{\partial z_b}{\partial x}, \tag{I.14}$$

$$\int_{z_b}^{z_s} \frac{\partial \sigma_x}{\partial x}\mathrm{d}z = \frac{\partial}{\partial x}\int_{z_b}^{z_s} \sigma_x dz - (\sigma_x)_s \frac{\partial z_s}{\partial x} + (\sigma_x)_b \frac{\partial z_b}{\partial x}, \tag{I.15}$$

$$\int_{z_b}^{z_s} \frac{\partial(\rho u w)}{\partial z}\mathrm{d}z = \rho_s u_s w_s - \rho_b u_b w_b, \tag{I.16}$$

$$\int_{z_b}^{z_s} \frac{\partial \tau_{xz}}{\partial z} \mathrm{d}z = (\tau_{xz})_s - (\tau_{xz})_b. \tag{I.17}$$

Collecting Eqs. (I.12)–(I.17), the depth-averaged x-momentum equation reads

$$\frac{\partial}{\partial t}\int_{z_b}^{z_s} \rho u \mathrm{d}z + \frac{\partial}{\partial x}\left(\int_{z_b}^{z_s} \rho u^2 \mathrm{d}z + \int_{z_b}^{z_s} p \mathrm{d}z - \int_{z_b}^{z_s} \sigma_x \mathrm{d}z\right) - \rho_s u_s \frac{\partial z_s}{\partial t} + \rho_b u_b \frac{\partial z_b}{\partial t} - \rho_s u_s^2 \frac{\partial z_s}{\partial x}$$
$$+ \rho_b u_b^2 \frac{\partial z_b}{\partial x} - p_s \frac{\partial z_s}{\partial x} + p_b \frac{\partial z_b}{\partial x} + (\sigma_x)_s \frac{\partial z_s}{\partial x} - (\sigma_x)_b \frac{\partial z_b}{\partial x} + \rho_s u_s w_s - \rho_b u_b w_b = (\tau_{xz})_s - (\tau_{xz})_b. \tag{I.18}$$

Grouping terms yields

$$\begin{aligned} &\frac{\partial}{\partial t}\int_{z_b}^{z_s} \rho u \mathrm{d}z + \frac{\partial}{\partial x}\left(\int_{z_b}^{z_s} \rho u^2 \mathrm{d}z + \int_{z_b}^{z_s} p \mathrm{d}z - \int_{z_b}^{z_s} \sigma_x \mathrm{d}z\right) \\ &- \rho_s u_s \left(\frac{\partial z_s}{\partial t} + u_s \frac{\partial z_s}{\partial x} - w_s\right) + \rho_b u_b \left(\frac{\partial z_b}{\partial t} + u_b \frac{\partial z_b}{\partial x} - w_b\right) \\ &+ \left[p_b - (\sigma_x)_b\right] \frac{\partial z_b}{\partial x} - \left[p_s - (\sigma_x)_s\right] \frac{\partial z_s}{\partial x} = (\tau_{xz})_s - (\tau_{xz})_b. \end{aligned} \tag{I.19}$$

Inserting Eqs. (I.8)–(I.9) into Eq. (I.19), and considering zero pressure and stresses at the free surface, yields

$$\frac{\partial}{\partial t}\int_{z_b}^{z_s} \rho u \mathrm{d}z + \frac{\partial}{\partial x}\left(\int_{z_b}^{z_s} \rho u^2 \mathrm{d}z + \int_{z_b}^{z_s} p \mathrm{d}z - \int_{z_b}^{z_s} \sigma_x \mathrm{d}z\right) + \left[p_b - (\sigma_x)_b\right] \frac{\partial z_b}{\partial x} = -(\tau_{xz})_b. \tag{I.20}$$

Neglecting the integral of the stress σ_x, and taking depth-averaged values of density ρ and velocity U, Eq. (I.20) reduces to

$$\frac{\partial}{\partial t}(\rho h U) + \frac{\partial}{\partial x}\left(\rho h U^2\right) + \frac{\partial}{\partial x}\int_{z_b}^{z_s} p \mathrm{d}z + \left[p_b - (\sigma_x)_b\right] \frac{\partial z_b}{\partial x} = -(\tau_{xz})_b. \tag{I.21}$$

The pressure distribution is assumed to be non-hydrostatic and linearly distributed with depth (Steffler and Jin 1993; Khan and Steffler 1996; Denlinger and

Iverson 2004; Denlinger and O'Connell 2008; Castro-Orgaz et al. 2015; Cantero-Chinchilla et al. 2016),

$$p = p_b\left(1 - \frac{z - z_b}{h}\right), \tag{I.22}$$

where the bottom pressure p_b can be rewritten as

$$p_b = \rho g h + p_1, \tag{I.23}$$

in which p_1 is the deviation of the bed pressure from its hydrostatic counterpart (Fig. I.1). Inserting Eq. (I.22) into Eq. (I.21), performing the pressure integral, and using Eq. (I.23), produces the relation

$$\frac{\partial}{\partial t}(\rho h U) + \frac{\partial}{\partial x}\left(\rho h U^2\right) + \frac{\partial}{\partial x}\left(\frac{1}{2}\rho g h^2 + \frac{h p_1}{2}\right) + \left[\rho g h + p_1 - (\sigma_x)_b\right]\frac{\partial z_b}{\partial x} = -(\tau_{xz})_b. \tag{I.24}$$

Assuming that the state of stress at the bed is of pure shearing, rotation of the stress tensor an angle equal to the bed slope angle θ permits to express Cartesian stresses as functions of the shear stress τ_b locally tangential to the bed[8] as

$$\begin{aligned}(\sigma_z)_b &= 2\tau_b \cos\theta\, \sin\theta,\\ (\sigma_x)_b &= -2\tau_b \cos\theta\, \sin\theta,\\ (\tau_{xz})_b &= \tau_b\left(\cos^2\theta - \sin^2\theta\right).\end{aligned} \tag{I.25}$$

The Reynolds stresses in the x-momentum equation are then transformed to (Khan and Steffler 1996)

$$\begin{aligned}-(\sigma_x)_b\frac{\partial z_b}{\partial x} + (\tau_{xz})_b &= 2\tau_b \cos\theta\, \sin\theta\left(\frac{\sin\theta}{\cos\theta}\right) + \tau_b\left(\cos^2\theta - \sin^2\theta\right)\\ &= \tau_b\left(\cos^2\theta + \sin^2\theta\right) = \tau_b.\end{aligned} \tag{I.26}$$

The x-momentum equation (I.24) can now be written as

$$\frac{\partial}{\partial t}(\rho h U) + \frac{\partial}{\partial x}\left(\rho h U^2\right) + \frac{\partial}{\partial x}\left(\frac{1}{2}\rho g h^2 + \frac{h p_1}{2}\right) + (\rho g h + p_1)\frac{\partial z_b}{\partial x} = -\tau_b, \tag{I.27}$$

[8]This development is extensively described in Chap. 2, see Eqs. (2.55)–(2.56), and it is not repeated here.

or,

$$\frac{\partial}{\partial t}(\rho hU)+\frac{\partial}{\partial x}\left(\rho hU^2+\frac{1}{2}\rho gh^2\right)=-(\rho gh+p_1)\frac{\partial z_b}{\partial x}-\tau_b-\frac{\partial}{\partial x}\left(\frac{hp_1}{2}\right). \quad \text{(I.28)}$$

Similarly, vertical integration of each term of the z-momentum Eq. (I.3) yields

$$\int_{z_b}^{z_s}\frac{\partial(\rho w)}{\partial t}\mathrm{d}z=\frac{\partial}{\partial t}\int_{z_b}^{z_s}\rho w\mathrm{d}z-\rho_s w_s\frac{\partial z_s}{\partial t}+\rho_b w_b\frac{\partial z_b}{\partial t}, \quad \text{(I.29)}$$

$$\int_{z_b}^{z_s}\frac{\partial(\rho uw)}{\partial x}\mathrm{d}z=\frac{\partial}{\partial x}\int_{z_b}^{z_s}\rho uw\mathrm{d}z-\rho_s u_s w_s\frac{\partial z_s}{\partial x}+\rho_b u_b w_b\frac{\partial z_b}{\partial x}, \quad \text{(I.30)}$$

$$\int_{z_b}^{z_s}\frac{\partial}{\partial z}\left(\rho w^2+p-\sigma_z\right)\mathrm{d}z=\rho_s w_s^2+p_s-(\sigma_z)_s-\rho_b w_b^2-p_b+(\sigma_z)_b, \quad \text{(I.31)}$$

$$\int_{z_b}^{z_s}\frac{\partial\tau_{zx}}{\partial x}\mathrm{d}z=\frac{\partial}{\partial x}\int_{z_b}^{z_s}\tau_{zx}\mathrm{d}z-(\tau_{zx})_s\frac{\partial z_s}{\partial x}+(\tau_{zx})_b\frac{\partial z_b}{\partial x}, \quad \text{(I.32)}$$

$$\int_{z_b}^{z_s}-\rho g\mathrm{d}z=-g\int_{z_b}^{z_s}\rho\mathrm{d}z. \quad \text{(I.33)}$$

Therefore, collecting Eqs. (I.29)–(I.33) yields

$$\begin{aligned}&\frac{\partial}{\partial t}\int_{z_b}^{z_s}\rho w\mathrm{d}z+\frac{\partial}{\partial x}\left(\int_{z_b}^{z_s}\rho uw\mathrm{d}z-\int_{z_b}^{z_s}\tau_{zx}\mathrm{d}z\right)\\&\quad-\rho_s w_s\frac{\partial z_s}{\partial t}+\rho_b w_b\frac{\partial z_b}{\partial t}-\rho_s u_s w_s\frac{\partial z_s}{\partial x}+\rho_b u_b w_b\frac{\partial z_b}{\partial x}\\&\quad+\rho_s w_s^2+p_s-(\sigma_z)_s-\rho_b w_b^2-p_b+(\sigma_z)_b\\&=-(\tau_{zx})_s\frac{\partial z_s}{\partial x}+(\tau_{zx})_b\frac{\partial z_b}{\partial x}-g\int_{z_b}^{z_s}\rho\mathrm{d}z.\end{aligned} \quad \text{(I.34)}$$

Neglecting the integral of the stress τ_{zx}, assuming zero pressure and stresses at the free surface, applying Eqs. (I.8)–(I.9), and considering depth-averaged values of the density ρ and velocity U reduce Eq. (I.34) to

$$p_b = \rho g h + (\sigma_z)_b - (\tau_{zx})_b \frac{\partial z_b}{\partial x} + \frac{\partial}{\partial t}\left(\rho \int_{z_b}^{z_s} w \mathrm{d}z\right) + \frac{\partial}{\partial x}\left(\rho U \int_{z_b}^{z_s} w \mathrm{d}z\right). \tag{I.35}$$

The stresses at the bed generate the following contribution, based on Eq. (I.25),

$$\begin{aligned}
&(\sigma_z)_b - (\tau_{zx})_b \frac{\partial z_b}{\partial x} = 2\tau_b \cos\theta \sin\theta - \tau_b\left(\cos^2\theta - \sin^2\theta\right)\left(\frac{\sin\theta}{\cos\theta}\right) \\
&= 2\tau_b \cos\theta \sin\theta - \tau_b\left(\cos\theta \sin\theta - \sin^2\theta \frac{\sin\theta}{\cos\theta}\right) \\
&= \tau_b \cos\theta \sin\theta + \tau_b\left(\sin^2\theta \frac{\sin\theta}{\cos\theta}\right) = \tau_b \sin\theta\left[\cos\theta + \left(\frac{\sin^2\theta}{\cos\theta}\right)\right] \\
&= \tau_b \sin\theta\left[\frac{\sin^2\theta + \cos^2\theta}{\cos\theta}\right] = \tau_b \frac{\sin\theta}{\cos\theta} = \tau_b \frac{\partial z_b}{\partial x}.
\end{aligned} \tag{I.36}$$

Defining the depth-averaged vertical velocity W by

$$W = \frac{1}{h}\int_{z_b}^{z_s} w \mathrm{d}z, \tag{I.37}$$

Eq. (I.35) is rewritten as, using Eq. (I.36),

$$p_b = \rho g h + \tau_b \frac{\partial z_b}{\partial x} + \frac{\partial(\rho h W)}{\partial t} + \frac{\partial(\rho h U W)}{\partial x}, \tag{I.38}$$

or

$$\frac{\partial(\rho h W)}{\partial t} + \frac{\partial(\rho h U W)}{\partial x} = p_1 - \tau_b \frac{\partial z_b}{\partial x}. \tag{I.39}$$

The non-hydrostatic vertically averaged equations for a mixture of fluid and sediments are,

$$\frac{\partial(\rho h)}{\partial t} + \frac{\partial(\rho U h)}{\partial x} + \rho_b \frac{\partial z_b}{\partial t} = 0, \tag{I.40}$$

$$\frac{\partial}{\partial t}(\rho h U) + \frac{\partial}{\partial x}\left(\rho h U^2 + \frac{1}{2}\rho g h^2\right) = -(\rho g h + p_1)\frac{\partial z_b}{\partial x} - \tau_b - \frac{\partial}{\partial x}\left(\frac{h p_1}{2}\right). \tag{I.41}$$

$$\frac{\partial(\rho h W)}{\partial t} + \frac{\partial(\rho h U W)}{\partial x} = p_1 - \tau_b \frac{\partial z_b}{\partial x}. \tag{I.42}$$

Now, the effects of density ρ will be collected into a source term to obtain a useable form of the depth-averaged equations for implementing numerical solutions based on the finite-volume method and Riemann solvers (Cantero-Chinchilla et al. 2016). The depth-averaged conservation of mass Eq. (I.40) is rewritten as

$$\frac{\partial(\rho h)}{\partial t} + \frac{\partial(\rho h U)}{\partial x} + \frac{\partial(\rho_b z_b)}{\partial t} = 0. \tag{I.43}$$

With the definitions $\rho = \rho_w(1 - C_t) + \rho_s C_t$ and $\rho_b = \rho_w p_m + \rho_s(1 - p_m)$, where $\rho(x, t)$ is the density of the water–sediment mixture, ρ_w the clear-water density, $C_t(x, t)$ the depth-averaged total sediment concentration in the fluid layer of thickness h (suspended plus bed-load layers; see Fig. I.1), ρ_b the density of the static sediment layer, p_m the porosity of the static sediment layer, and ρ_s the density of the solids in the static layer (Wu 2008), Eq. (I.43) is transformed to

$$\begin{aligned}&\rho_w \frac{\partial h}{\partial t} - \rho_w \frac{\partial(hC_t)}{\partial t} + \rho_s \frac{\partial(hC_t)}{\partial t} + \rho_w \frac{\partial(hU)}{\partial x} - \rho_w \frac{\partial(hUC_t)}{\partial x} + \rho_s \frac{\partial(hUC_t)}{\partial x} \\ &\quad + \rho_w p_m \frac{\partial z_b}{\partial t} + \rho_s(1 - p_m)\frac{\partial z_b}{\partial t} = 0,\end{aligned} \tag{I.44}$$

or,

$$\begin{aligned}&\rho_w \left[\frac{\partial h}{\partial t} + \frac{\partial(hU)}{\partial x}\right] - \rho_w \left[\frac{\partial(hC_t)}{\partial t} + \frac{\partial(hUC_t)}{\partial x}\right] + \rho_s \left[\frac{\partial(hC_t)}{\partial t} + \frac{\partial(hUC_t)}{\partial x}\right] \\ &\quad + \rho_w p_m \frac{\partial z_b}{\partial t} + \rho_s(1 - p_m)\frac{\partial z_b}{\partial t} = 0.\end{aligned} \tag{I.45}$$

Let q_b be the bed-load flux per unit width, and C the depth-averaged suspended-load concentration. The total sediment concentration is defined by $C_t = C + q_b/(hU)$. Using this definition, Eq. (I.45) is further written as

$$\begin{aligned}&\rho_w \left[\frac{\partial h}{\partial t} + \frac{\partial(hU)}{\partial x}\right] - \rho_w \left[\frac{\partial(hC)}{\partial t} + \frac{\partial}{\partial t}\left(\frac{q_b}{U}\right) + \frac{\partial(hUC)}{\partial x} + \frac{\partial q_b}{\partial x}\right] \\ &\quad + \rho_s \left[\frac{\partial(hC)}{\partial t} + \frac{\partial}{\partial t}\left(\frac{q_b}{U}\right) + \frac{\partial(hUC)}{\partial x} + \frac{\partial q_b}{\partial x}\right] + \rho_w p_m \frac{\partial z_b}{\partial t} + \rho_s(1 - p_m)\frac{\partial z_b}{\partial t} = 0.\end{aligned} \tag{I.46}$$

The mass balance equation in the bed-load layer can be written as the non-equilibrium equation (Wu and Wang 2007; Wu 2008)

$$\frac{\partial}{\partial t}\left(\frac{q_b}{U}\right) + \frac{\partial q_b}{\partial x} = \frac{q_b^* - q_b}{L}, \tag{I.47}$$

where the velocity of the bed-load particles is assumed to equal U; here, q_b^* is the equilibrium bed-load flux, and L is an adaptation length for the bed-load sediment transport (Wu 2008). The suspended sediment mass conservation equation is (Wu 2008)

$$\frac{\partial(hC)}{\partial t} + \frac{\partial(hUC)}{\partial x} = E - D, \tag{I.48}$$

where E and D are the fluxes of sediment particles (erosion/deposition, respectively) entering and leaving the suspended-load layer across its interface with the bed-load layer. Summing up Eqs. (I.47) and (I.48) yields the conservation equation for the total mass of sediments as

$$\frac{\partial(hC)}{\partial t} + \frac{\partial}{\partial t}\left(\frac{q_b}{U}\right) + \frac{\partial(hUC)}{\partial x} + \frac{\partial q_b}{\partial x} = E - D + \frac{q_b^* - q_b}{L}. \tag{I.49}$$

Inserting this equation into Eq. (I.46) yields

$$\begin{aligned}\rho_w\left[\frac{\partial h}{\partial t} + \frac{\partial(hU)}{\partial x}\right] - \rho_w \underbrace{\left[E - D + \frac{q_b^* - q_b}{L}\right]}_{\text{Eq. (I.49)}} + \rho_s \underbrace{\left[E - D + \frac{q_b^* - q_b}{L}\right]}_{\text{Eq. (I.49)}} \\ + \rho_w p_m \frac{\partial z_b}{\partial t} + \rho_s(1 - p_m)\frac{\partial z_b}{\partial t} = 0.\end{aligned} \tag{I.50}$$

The evolution of the static sediment bed level is given by the mass balance of the sediments (Wu and Wang 2007; Wu 2008)

$$(1 - p_m)\frac{\partial z_b}{\partial t} = D - E + \frac{q_b - q_b^*}{L}, \tag{I.51}$$

and using this equation into Eq. (I.50) produces

$$\begin{aligned}\rho_w\left[\frac{\partial h}{\partial t} + \frac{\partial(hU)}{\partial x}\right] + (\rho_s - \rho_w)\left(E - D + \frac{q_b^* - q_b}{L}\right) \\ + \frac{\rho_w p_m}{1 - p_m}\left(D - E + \frac{q_b - q_b^*}{L}\right) + \rho_s\left(D - E + \frac{q_b - q_b^*}{L}\right) = 0,\end{aligned} \tag{I.52}$$

or

$$\frac{\partial h}{\partial t} + \frac{\partial(hU)}{\partial x} = \frac{1}{1 - p_m}\left(E - D + \frac{q_b^* - q_b}{L}\right). \tag{I.53}$$

Defining $\rho = \rho_w(1 - C_t) + \rho_s C_t$, Eq. (I.41) for the x-momentum balance reads

$$\rho_w\left[\frac{\partial(hU)}{\partial t} - \frac{\partial(hUC_t)}{\partial t}\right] + \rho_s\frac{\partial(hUC_t)}{\partial t} + \rho_w\left[\frac{\partial}{\partial x}\left(hU^2 + \frac{1}{2}gh^2\right) - \frac{\partial}{\partial x}\left(C_t hU^2 + \frac{1}{2}C_t gh^2\right)\right] + \rho_s\frac{\partial}{\partial x}\left(C_t hU^2 + \frac{1}{2}C_t gh^2\right) = -\rho gh\frac{\partial z_b}{\partial x} - \tau_b - p_1\frac{\partial z_b}{\partial x} - \frac{\partial}{\partial x}\left(\frac{hp_1}{2}\right). \tag{I.54}$$

The left-hand side (LHS) of Eq. (I.54) is

$$\rho_w\left[\frac{\partial(hU)}{\partial t} + \frac{\partial}{\partial x}\left(hU^2 + \frac{1}{2}gh^2\right)\right] + (\rho_s - \rho_w)\underbrace{\left[\frac{\partial(hUC_t)}{\partial t} + \frac{\partial}{\partial x}\left(hU^2C_t + \frac{1}{2}gh^2C_t\right)\right]}_{\text{Term I}}, \tag{I.55}$$

where Term I can be expressed as

$$\underbrace{\frac{\partial(hUC_t)}{\partial t} + \frac{\partial}{\partial x}\left(hU^2C_t + \frac{1}{2}gh^2C_t\right)}_{\text{Term I}} = C_t\frac{\partial(hU)}{\partial t} + hU\frac{\partial C_t}{\partial t} + C_t\frac{\partial}{\partial x}\left(hU^2 + \frac{1}{2}gh^2\right) + \left(hU^2 + \frac{1}{2}gh^2\right)\frac{\partial C_t}{\partial x} = C_t\left[\frac{\partial(hU)}{\partial t} + \frac{\partial}{\partial x}\left(hU^2 + \frac{1}{2}gh^2\right)\right] + \frac{1}{2}gh^2\frac{\partial C_t}{\partial x} + \underbrace{hU\frac{\partial C_t}{\partial t} + hU^2\frac{\partial C_t}{\partial x}}_{\text{Term II}}. \tag{I.56}$$

Now, Eq. (I.49) is written as

$$\frac{\partial}{\partial t}\left(hC + \frac{q_b}{U}\right) + \frac{\partial}{\partial x}(hUC + q_b) = E - D + \frac{q_b^* - q_b}{L}, \tag{I.57}$$

or, as a function of the total load, using $C_t = C + q_b/(hU)$,

$$\frac{\partial(hC_t)}{\partial t} + \frac{\partial(hUC_t)}{\partial x} = E - D + \frac{q_b^* - q_b}{L}. \tag{I.58}$$

Equation (I.58) can also be written as the differential identity

$$h\left[\frac{\partial C_t}{\partial t} + U\frac{\partial C_t}{\partial x}\right] = E - D + \frac{q_b^* - q_b}{L} - C_t\left[\frac{\partial h}{\partial t} + \frac{\partial(hU)}{\partial x}\right]. \tag{I.59}$$

If this expression is inserted into Term II of Eq. (I.56), one obtains

$$\frac{\partial(hUC_t)}{\partial t}+\frac{\partial}{\partial x}\left(hU^2C_t+\frac{1}{2}gh^2C_t\right)=U\left(E-D+\frac{q_b^*-q_b}{L}\right)+C_t\left[\frac{\partial(hU)}{\partial t}+\frac{\partial}{\partial x}\left(hU^2+\frac{1}{2}gh^2\right)\right]-C_tU\underbrace{\left[\frac{\partial h}{\partial t}+\frac{\partial(hU)}{\partial x}\right]}_{\text{Term III}}+\frac{1}{2}gh^2\frac{\partial C_t}{\partial x},\tag{I.60}$$

and using the continuity Eq. (I.53) in Term III in Eq. (I.60) yields

$$\frac{\partial(hUC_t)}{\partial t}+\frac{\partial}{\partial x}\left(hU^2C_t+\frac{1}{2}gh^2C_t\right)=U\left(1-\frac{C_t}{1-p_m}\right)\left(E-D+\frac{q_b^*-q_b}{L}\right)+C_t\left[\frac{\partial(hU)}{\partial t}+\frac{\partial}{\partial x}\left(hU^2+\frac{1}{2}gh^2\right)\right]+\frac{1}{2}gh^2\frac{\partial C_t}{\partial x}.\tag{I.61}$$

The RHS of Eq. (I.61) is an alternative expression for Term I in Eq. (I.55); using this expression in Eq. (I.55), and noting that the ensuing relation is the LHS on the x-momentum balance expressed by Eq. (I.54), this latter equation takes the form

$$\begin{aligned}&\rho w\left[\frac{\partial(hU)}{\partial t}+\frac{\partial}{\partial x}\left(hU^2+\frac{1}{2}gh^2\right)\right]\\&\quad+(\rho_s-\rho_w)\left\{U\left(1-\frac{C_t}{1-p_m}\right)\left(E-D+\frac{q_b^*-q_b}{L}\right)\right.\\&\quad\left.+C_t\left[\frac{\partial(hU)}{\partial t}+\frac{\partial}{\partial x}\left(hU^2\frac{1}{2}gh^2\right)\right]+\frac{1}{2}gh^2\frac{\partial C_t}{\partial x}\right\}\\&=-\rho gh\frac{\partial z_b}{\partial x}-\tau_b-p_1\frac{\partial z_b}{\partial x}-\frac{\partial}{\partial x}\left(\frac{hp_1}{2}\right).\end{aligned}\tag{I.62}$$

Using the definition $\rho=\rho_w(1-C_t)+\rho_sC_t$, this relation is written in the alternative form

$$\rho\left[\frac{\partial(hU)}{\partial t}+\frac{\partial}{\partial x}\left(hU^2+\frac{1}{2}gh^2\right)\right]+(\rho_s-\rho_w)\left[U\left(1-\frac{C_t}{1-p_m}\right)\left(E-D+\frac{q_b^*-q_b}{L}\right)\right]+\underline{(\rho_s-\rho_w)\frac{1}{2}gh^2\frac{\partial C_t}{\partial x}}=-\rho gh\frac{\partial z_b}{\partial x}-\tau_b-p_1\frac{\partial z_b}{\partial x}-\frac{\partial}{\partial x}\left(\frac{hp_1}{2}\right).\tag{I.63}$$

In this expression, the underlined term can be rewritten by use of

$$\frac{\partial \rho}{\partial x} = (\rho_s - \rho_w)\frac{\partial C_t}{\partial x}, \tag{I.64}$$

obtained from $\rho = \rho_w(1 - C_t) + \rho_s C_t$. Equation (I.63) then takes the alternative form

$$\begin{aligned}\frac{\partial (hU)}{\partial t} + \frac{\partial}{\partial x}\left(hU^2 + \frac{1}{2}gh^2\right) &= -gh\frac{\partial z_b}{\partial x} - \frac{\tau_b}{\rho} - \frac{p_1}{\rho}\frac{\partial z_b}{\partial x} - \frac{1}{\rho}\frac{\partial}{\partial x}\left(\frac{hp_1}{2}\right) \\ &\quad - \frac{1}{2}g\frac{h^2}{\rho}\frac{\partial \rho}{\partial x} - \frac{\rho_s - \rho_w}{\rho}U\left(1 - \frac{C_t}{1 - p_m}\right)\left(E - D + \frac{q_b^* - q_b}{L}\right).\end{aligned} \tag{I.65}$$

Likewise, with the definition $\rho = \rho_w(1 - C_t) + \rho_s C_t$, Eq. (I.42) for the z-momentum balance can be written as

$$\rho_w\left[\frac{\partial (hW)}{\partial t} + \frac{\partial (hUW)}{\partial x}\right] + (\rho_s - \rho_w)\underbrace{\left[\frac{\partial (hWC_t)}{\partial t} + \frac{\partial (hUWC_t)}{\partial x}\right]}_{\text{Term IV}} = p_1 - \tau_b\frac{\partial z_b}{\partial x}, \tag{I.66}$$

in which Term IV can be expressed as

$$\begin{aligned}\frac{\partial (hWC_t)}{\partial t} + \frac{\partial (hUWC_t)}{\partial x} &= W\frac{\partial (hC_t)}{\partial t} + hC_t\frac{\partial W}{\partial t} + W\frac{\partial (hUC_t)}{\partial x} + hUC_t\frac{\partial W}{\partial x} \\ &= W\left[\frac{\partial (hC_t)}{\partial t} + \frac{\partial (hUC_t)}{\partial x}\right] + hC_t\left(\frac{\partial W}{\partial t} + U\frac{\partial W}{\partial x}\right).\end{aligned} \tag{I.67}$$

Using Eq. (I.58) for the total sediment balance in Eq. (I.67) yields

$$\frac{\partial (hWC_t)}{\partial t} + \frac{\partial (hUWC_t)}{\partial x} = W\left(E - D + \frac{q_b^* - q_b}{L}\right) + \underbrace{hC_t\left(\frac{\partial W}{\partial t} + U\frac{\partial W}{\partial x}\right)}_{\text{Term V}}. \tag{I.68}$$

Term V in Eq. (I.68) can be written as

$$hC_t\left(\frac{\partial W}{\partial t} + U\frac{\partial W}{\partial x}\right) = C_t\left[\frac{\partial (hW)}{\partial t} + \frac{\partial (hUW)}{\partial x}\right] - WC_t\left[\frac{\partial h}{\partial t} + \frac{\partial (hU)}{\partial x}\right]. \tag{I.69}$$

Inserting the continuity Eq. (I.53) into Eq. (I.69), one obtains

$$hC_t\left(\frac{\partial W}{\partial t}+U\frac{\partial W}{\partial x}\right)=C_t\left[\frac{\partial(hW)}{\partial t}+\frac{\partial(hUW)}{\partial x}\right]-\frac{WC_t}{1-p_m}\left(E-D+\frac{q_b^*-q_b}{L}\right). \tag{I.70}$$

Inserting this expression into Term V of Eq. (I.68) yields

$$\frac{\partial(hWC_t)}{\partial t}+\frac{\partial(hUWC_t)}{\partial x}=W\left(1-\frac{C_t}{1-p_m}\right)\left(E-D+\frac{q_b^*-q_b}{L}\right)+C_t\left[\frac{\partial(hW)}{\partial t}+\frac{\partial(hUW)}{\partial x}\right], \tag{I.71}$$

and using this result in Eq. (I.66) yields for the z-momentum balance

$$\begin{aligned}&\rho_w\left[\frac{\partial(hW)}{\partial t}+\frac{\partial(hUW)}{\partial x}\right]+(\rho_s-\rho_w)W\left(1-\frac{C_t}{1-p_m}\right)\left(E-D+\frac{q_b^*-q_b}{L}\right)\\&\quad+(\rho_s-\rho_w)C_t\left[\frac{\partial(hW)}{\partial t}+\frac{\partial(hUW)}{\partial x}\right]=p_1-\tau_b\frac{\partial z_b}{\partial x}.\end{aligned} \tag{I.72}$$

Rearranging Eq. (I.72), thereby using the definition $\rho = \rho_w(1 - C_t) + \rho_s C_t$, finally produces

$$\begin{aligned}&\rho\left[\frac{\partial(hW)}{\partial t}+\frac{\partial(hUW)}{\partial x}\right]+(\rho_s-\rho_w)W\left(1-\frac{C_t}{1-p_m}\right)\left(E-D+\frac{q_b^*-q_b}{L}\right)\\&\quad=p_1-\tau_b\frac{\partial z_b}{\partial x},\end{aligned} \tag{I.73}$$

or,

$$\begin{aligned}\frac{\partial(hW)}{\partial t}+\frac{\partial(hUW)}{\partial x}=&\frac{p_1}{\rho}-\frac{\tau_b}{\rho}\frac{\partial z_b}{\partial x}\\&-\frac{(\rho_s-\rho_w)}{\rho}W\left(1-\frac{C_t}{1-p_m}\right)\left(E-D+\frac{q_b^*-q_b}{L}\right).\end{aligned} \tag{I.74}$$

The governing equations for non-hydrostatic unsteady open-channel flows over an erodible bed are given by Eqs. (I.47), (I.48) (I.51), (I.53), (I.65), and (I.74) (mass balances of sediment in bed-load layer, of sediment in suspended-load layer, sediment in static alluvial bed, and of the mixture in suspended + bed-load layers and conservation of z-momentum for the mixture in suspended + bed-load layers, and of z-momentum for the mixture in suspended + bed-load layers, respectively).

They can be written in conservative form with **U**, **F,** and **S** as the vector of unknowns, fluxes, and source terms, respectively, in the form

$$\frac{\partial \mathbf{U}}{\partial t} + \frac{\partial \mathbf{F}}{\partial x} = \mathbf{S}, \tag{I.75}$$

where

$$\mathbf{U} = \begin{bmatrix} h \\ hU \\ hW \\ hC \\ q_b/U \\ z_b \end{bmatrix}, \quad \mathbf{F} = \begin{bmatrix} hU \\ hU^2 + \frac{1}{2}gh^2 \\ hUW \\ hUC \\ q_b \\ 0 \end{bmatrix}, \tag{I.76}$$

$$\mathbf{S} = \begin{bmatrix} \frac{1}{1-p_m}\left(E - D + \frac{q_b^* - q_b}{L}\right) \\ \left\{ \begin{array}{c} -gh\dfrac{\partial z_b}{\partial x} - \dfrac{\tau_b}{\rho} - \dfrac{p_1}{\rho}\dfrac{\partial z_b}{\partial x} - \dfrac{1}{\rho}\dfrac{\partial}{\partial x}\left(\dfrac{hp_1}{2}\right) - \dfrac{1}{2}g\dfrac{h^2}{\rho}\dfrac{\partial \rho}{\partial x} \\ -\dfrac{(\rho_s - \rho_w)}{\rho}U\left(1 - \dfrac{C_t}{1-p_m}\right)\left(E - D + \dfrac{q_b^* - q_b}{L}\right) \end{array} \right\} \\ \dfrac{p_1}{\rho} - \dfrac{\tau_b}{\rho}\dfrac{\partial z_b}{\partial x} - \dfrac{(\rho_s - \rho_w)}{\rho}W\left(1 - \dfrac{C_t}{1-p_m}\right)\left(E - D + \dfrac{q_b^* - q_b}{L}\right) \\ E - D \\ \dfrac{q_b^* - q_b}{L} \\ \frac{1}{1-p_m}\left(D - E + \dfrac{q_b - q_b^*}{L}\right) \end{bmatrix}. \tag{I.77}$$

Equations (I.75) were solved by Cantero-Chinchilla et al. (2016) using a high-resolution finite-volume scheme to compute geomorphic dam break waves, resulting in a significant improvement of predictions as compared to hydrostatic models.

References

Cantero-Chinchilla, F., Castro-Orgaz, O., Dey, S., & Ayuso, J. L. (2016). Nonhydrostatic dam break flows II: One-dimensional depth-averaged modeling for movable bed flows. *Journal of Hydraulic Engineering, 142*(12), 04016069.

Capart, H., & Young, D. L. (1998). Formation of a jump by the dam-break wave over a granular bed. *Journal of Fluid Mechanics*, *372*, 165–187.

Castro-Orgaz, O., Hutter, K., Giráldez, J.V., & Hager, W. H. (2015). Non-hydrostatic granular flow over 3D terrain: New Boussinesq-type gravity waves? *Journal of Geophysical Research: Earth Surface*, *120*(1), 1–28.

Denlinger, R. P., & Iverson, R. M. (2004). Granular avalanches across irregular three-dimensional terrain: 1. Theory and computation. *Journal of Geophysical Research: Earth Surface, 109*(F1), F01014. doi:10.1029/2003JF000085.

Denlinger, R. P., & O'Connell, D. R. H. (2008). Computing nonhydrostatic shallow-water flow over steep terrain. *Journal of Hydraulic Engineering, 134*(11), 1590–1602.

Hutter, K., Wang, Y., & Chubarenko, I. P. (2014). Sediment transport in alluvial systems (Chap. 32). In *Physics of lakes*: *Methods of understanding lakes as components of the geophysical environment. Advances in geophysical and environmental mechanics and mathematics* (Vol. 3, pp. 487–579). Heidelberg: AGEM^2, Springer.

Khan, A. A., & Steffler, P. M. (1996). Vertically averaged and moment equations model for flow over curved beds. *Journal of Hydraulic Engineering, 122*(1), 3–9.

Peregrine, D. H. (1966). Calculations of the development of an undular bore. *Journal of Fluid Mechanics, 25*(2), 321–330.

Steffler, P. M., & Jin, Y. C. (1993). Depth-averaged and moment equations for moderately shallow free surface flow. *Journal of Hydraulic Research, 31*(1), 5–17.

Wu, W. (2008). *Computational river dynamics*. London, U.K: Taylor and Francis.

Wu, W., Wang, & S. S. Y. (2007). One-dimensional modeling of dam-break flow over movable beds. *Journal of Hydraulic Engineering, 133*(1), 48–58.

Appendix J
Layer-Integrated Equations for Mixture Flows

The purpose of this Appendix is the development of the general vertically integrated layer equations for a mixture of fluid and sediments, bounded by arbitrary non-material interfaces. Consider the flow of a continuum mixture of a fluid and solid with density $\rho(x, y, z, t)$ bounded by two general interface surfaces "s" and "b", given by the mathematical statements $z = z_s(x, y, t)$ and $z = z_b(x, y, t)$, respectively (Fig. J.1). The mass conservation equation for the mixture is, defining the velocity of the mixture $\mathbf{V} = (u, w, v)$ as the barycentric velocity (Hutter et al. 2014),

$$\frac{\partial \rho}{\partial t} + \frac{\partial(\rho u)}{\partial x} + \frac{\partial(\rho v)}{\partial y} + \frac{\partial(\rho w)}{\partial z} = 0. \tag{J.1}$$

Likewise, in the horizontal-vertical Cartesian system of coordinates represented in Fig. J.1, Newton's second law gives for the mixture the momentum equations (Hutter et al. 2014)

$$\frac{\partial}{\partial t}(\rho u) + \frac{\partial}{\partial x}\left(\rho u^2\right) + \frac{\partial}{\partial y}(\rho uv) + \frac{\partial}{\partial z}(\rho uw) = -\left(\frac{\partial \tau_{xx}}{\partial x} + \frac{\partial \tau_{xy}}{\partial y} + \frac{\partial \tau_{xz}}{\partial z}\right), \tag{J.2}$$

$$\frac{\partial}{\partial t}(\rho v) + \frac{\partial}{\partial x}(\rho uv) + \frac{\partial}{\partial y}\left(\rho v^2\right) + \frac{\partial}{\partial z}(\rho vw) = -\left(\frac{\partial \tau_{yx}}{\partial x} + \frac{\partial \tau_{yy}}{\partial y} + \frac{\partial \tau_{yz}}{\partial z}\right), \tag{J.3}$$

$$\frac{\partial}{\partial t}(\rho w) + \frac{\partial}{\partial x}(\rho uw) + \frac{\partial}{\partial y}(\rho vw) + \frac{\partial}{\partial z}\left(\rho w^2\right) = -\rho g - \left(\frac{\partial \tau_{zx}}{\partial x} + \frac{\partial \tau_{zy}}{\partial y} + \frac{\partial \tau_{zz}}{\partial z}\right). \tag{J.4}$$

Here τ_{ij} is the stress tensor, with $(i, j) = (x, y, z)$.

Prior to integrating Eqs. (J.1)–(J.4) in the z-direction across the layer, the general kinematic boundary condition at an interface is derived following Hutter et al. (2014)

© Springer International Publishing AG 2017

O. Castro-Orgaz and W.H. Hager, *Non-Hydrostatic Free Surface Flows*,
Advances in Geophysical and Environmental Mechanics and Mathematics
DOI 10.1007/978-3-319-47971-2

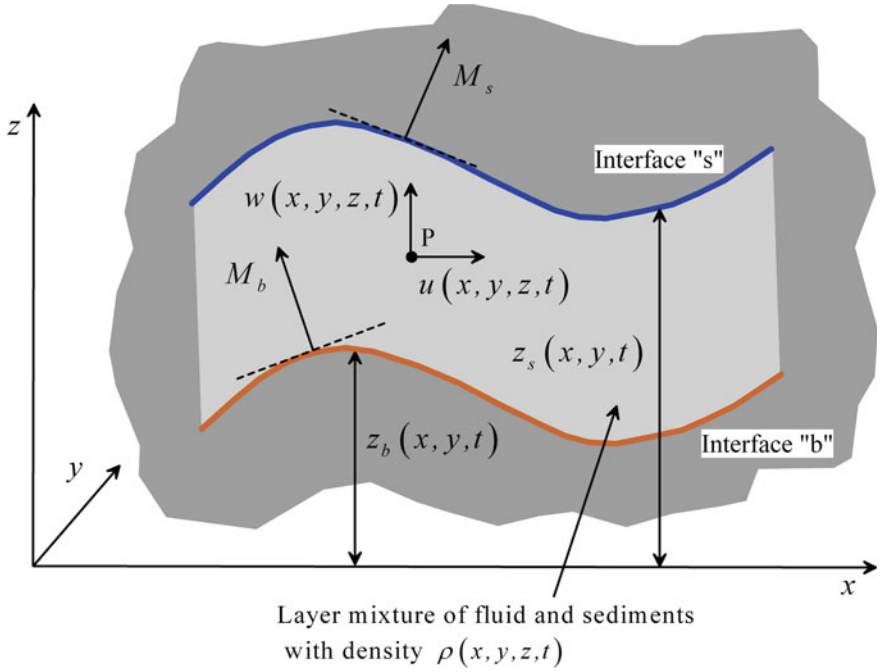

Figure J.1 Layer of mixture of fluid and sediments bounded by non-material interfaces "s" and "b" (view projected in the *xz* plane). At point P on the *xz* plane, the velocity components are (*u*, *w*)

and Iverson and Ouyang (2015). Consider for illustrative purposes the interface b, whose mathematical equation is, with generality, written as

$$F(x,y,z,t) = z - z_b(x,y,t) = 0. \tag{J.5}$$

The material derivative of F following its motion is, therefore, given by

$$\frac{\mathrm{D}F}{\mathrm{D}t} = \frac{\partial F}{\partial t} + \mathbf{U} \cdot \nabla F = 0, \tag{J.6}$$

where $\mathbf{U}$ is the interface velocity vector. It should be noted that the velocity of displacement of an interface is not necessarily equal to that of the particles that are momentarily lying upon it. In general, the velocity of the displacement of the surface is given by the kinematic statement

$$\mathbf{U} = \mathbf{V}_b - M_b \mathbf{n}, \tag{J.7}$$

where $\mathbf{V}_b$ is the mixture velocity on the surface, M_b the net volume of mixture crossing normal to the interface "b" per unit area and time, and $\mathbf{n}$ is the unit vector normal to the interface.[9] Inserting Eq. (J.7) into Eq. (J.6) yields

$$\begin{aligned}\frac{\mathrm{D}F}{\mathrm{D}t} &= \frac{\partial F}{\partial t} + (\mathbf{V}_b - M_b\mathbf{n})\cdot\nabla F = \frac{\partial F}{\partial t} + \mathbf{V}_b\cdot\nabla F - M_b|\nabla F| \\ &= \frac{\partial F}{\partial t} + \frac{\partial F}{\partial x}u_b + \frac{\partial F}{\partial y}v_b + \frac{\partial F}{\partial z}w_b - M_b|\nabla F| = 0.\end{aligned} \tag{J.8}$$

The derivatives of F are

$$\frac{\partial F}{\partial t} = -\frac{\partial z_b}{\partial t}, \quad \frac{\partial F}{\partial x} = -\frac{\partial z_b}{\partial x}, \quad \frac{\partial F}{\partial y} = -\frac{\partial z_b}{\partial y}, \quad \frac{\partial F}{\partial z} = 1. \tag{J.9}$$

Inserting Eq. (J.9) into Eq. (J.8), one finds

$$\frac{\mathrm{D}F}{\mathrm{D}t} = -\frac{\partial z_b}{\partial t} - \frac{\partial z_b}{\partial x}u_b - \frac{\partial z_b}{\partial y}v_b + w_b - M_b|\nabla F| = 0, \tag{J.10}$$

and noting that the modulus of F is given by

$$|\nabla F| = \left[\left(\frac{\partial F}{\partial x}\right)^2 + \left(\frac{\partial F}{\partial y}\right)^2 + \left(\frac{\partial F}{\partial z}\right)^2\right]^{1/2} = \left[\left(\frac{\partial z_b}{\partial x}\right)^2 + \left(\frac{\partial z_b}{\partial y}\right)^2 + 1\right]^{1/2}, \tag{J.11}$$

Eq. (J.10) gives after rearrangement

$$\frac{\partial z_b}{\partial t} + \frac{\partial z_b}{\partial x}u_b + \frac{\partial z_b}{\partial y}v_b - w_b = -M_b\left[\left(\frac{\partial z_b}{\partial x}\right)^2 + \left(\frac{\partial z_b}{\partial y}\right)^2 + 1\right]^{1/2}, \tag{J.12}$$

or

$$\frac{\partial z_b}{\partial t} + \frac{\partial z_b}{\partial x}u_b + \frac{\partial z_b}{\partial y}v_b - w_b = -M_b\xi_b, \tag{J.13}$$

where

$$\xi_b = \left[\left(\frac{\partial z_b}{\partial x}\right)^2 + \left(\frac{\partial z_b}{\partial y}\right)^2 + 1\right]^{1/2}. \tag{J.14}$$

[9]The interfaces are orientable surfaces, i.e., they have a positive and negative side and the vector $\mathbf{n}$ is strictly assumed to point into that side, which has a priori been assumed to be the positive side.

Equation (J.13) is the kinematic boundary condition at a generic interface. Vertical integration of Eq. (J.1) yields

$$\int_{z_b}^{z_s}\left[\frac{\partial\rho}{\partial t}+\frac{\partial(\rho u)}{\partial x}+\frac{\partial(\rho v)}{\partial y}+\frac{\partial(\rho w)}{\partial z}\right]\mathrm{d}z=0. \tag{J.15}$$

It is now transformed computing the following identities (Leibniz's rule)

$$\int_{z_b}^{z_s}\frac{\partial\rho}{\partial t}\mathrm{d}z=\frac{\partial}{\partial t}\int_{z_b}^{z_s}\rho\mathrm{d}z-\rho_s\frac{\partial z_s}{\partial t}+\rho_b\frac{\partial z_b}{\partial t}, \tag{J.16}$$

$$\int_{z_b}^{z_s}\frac{\partial(\rho u)}{\partial x}\mathrm{d}z=\frac{\partial}{\partial x}\int_{z_b}^{z_s}\rho u\mathrm{d}z-\rho_s u_s\frac{\partial z_s}{\partial x}+\rho_b u_b\frac{\partial z_b}{\partial x}, \tag{J.17}$$

$$\int_{z_b}^{z_s}\frac{\partial(\rho v)}{\partial y}\mathrm{d}z=\frac{\partial}{\partial y}\int_{z_b}^{z_s}\rho v\mathrm{d}z-\rho_s v_s\frac{\partial z_s}{\partial y}+\rho_b v_b\frac{\partial z_b}{\partial y}, \tag{J.18}$$

$$\int_{z_b}^{z_s}\frac{\partial(\rho w)}{\partial z}\mathrm{d}z=\rho_s w_s-\rho_b w_b. \tag{J.19}$$

Summing Eqs. (J.16)–(J.19) produces

$$\begin{aligned}&\frac{\partial}{\partial t}\int_{z_b}^{z_s}\rho\mathrm{d}z+\frac{\partial}{\partial x}\int_{z_b}^{z_s}\rho u\mathrm{d}z+\frac{\partial}{\partial y}\int_{z_b}^{z_s}\rho v\mathrm{d}z-\rho_s\frac{\partial z_s}{\partial t}+\rho_b\frac{\partial z_b}{\partial t}-\rho_s u_s\frac{\partial z_s}{\partial x}\\&\quad+\rho_b u_b\frac{\partial z_b}{\partial x}-\rho_s v_s\frac{\partial z_s}{\partial y}+\rho_b v_b\frac{\partial z_b}{\partial y}+\rho_s w_s-\rho_b w_b=0,\end{aligned} \tag{J.20}$$

or,

$$\begin{aligned}&\frac{\partial}{\partial t}\int_{z_b}^{z_s}\rho\mathrm{d}z+\frac{\partial}{\partial x}\int_{z_b}^{z_s}\rho u\mathrm{d}z+\frac{\partial}{\partial y}\int_{z_b}^{z_s}\rho v\mathrm{d}z\\&\quad-\rho_s\left(\frac{\partial z_s}{\partial t}+u_s\frac{\partial z_s}{\partial x}+v_s\frac{\partial z_s}{\partial y}-w_s\right)+\rho_b\left(\frac{\partial z_b}{\partial t}+u_b\frac{\partial z_b}{\partial x}+v_b\frac{\partial z_b}{\partial y}-w_b\right)=0.\end{aligned} \tag{J.21}$$

Using the general kinematic boundary condition at an interface, given by Eq. (J.13), and inserting it into Eq. (J.21) yields

$$\frac{\partial}{\partial t}\int_{z_b}^{z_s}\rho \mathrm{d}z+\frac{\partial}{\partial x}\int_{z_b}^{z_s}\rho u\mathrm{d}z+\frac{\partial}{\partial y}\int_{z_b}^{z_s}\rho v\mathrm{d}z+\rho_s M_s\xi_s-\rho_b M_b\xi_b=0, \tag{J.22}$$

which is the general layer-integrated continuity equation for the mixture flow.

Next, the x-momentum Eq. (J.2) is vertically integrated

$$\int_{z_b}^{z_s}\left[\frac{\partial}{\partial t}(\rho u)+\frac{\partial}{\partial x}\left(\rho u^2\right)+\frac{\partial}{\partial y}(\rho uv)+\frac{\partial}{\partial z}(\rho uw)\right]\mathrm{d}z$$
$$=\int_{z_b}^{z_s}-\left(\frac{\partial \tau_{xx}}{\partial x}+\frac{\partial \tau_{xy}}{\partial y}+\frac{\partial \tau_{xz}}{\partial z}\right)\mathrm{d}z. \tag{J.23}$$

Employing the transformations produces (following again Leibniz's rule)

$$\int_{z_b}^{z_s}\frac{\partial}{\partial t}(\rho u)\mathrm{d}z=\frac{\partial}{\partial t}\int_{z_b}^{z_s}\rho u\mathrm{d}z-\rho_s u_s\frac{\partial z_s}{\partial t}+\rho_b u_b\frac{\partial z_b}{\partial t}, \tag{J.24}$$

$$\int_{z_b}^{z_s}\frac{\partial}{\partial x}\left(\rho u^2\right)\mathrm{d}z=\frac{\partial}{\partial x}\int_{z_b}^{z_s}\rho u^2\mathrm{d}z-\rho_s u_s^2\frac{\partial z_s}{\partial x}+\rho_b u_b^2\frac{\partial z_b}{\partial x}, \tag{J.25}$$

$$\int_{z_b}^{z_s}\frac{\partial}{\partial y}(\rho uv)\mathrm{d}z=\frac{\partial}{\partial y}\int_{z_b}^{z_s}\rho uv\mathrm{d}z-\rho_s u_s v_s\frac{\partial z_s}{\partial y}+\rho_b u_b v_b\frac{\partial z_b}{\partial y}, \tag{J.26}$$

$$\int_{z_b}^{z_s}\frac{\partial}{\partial z}(\rho uw)\mathrm{d}z=\rho_s u_s w_s-\rho_b u_b w_b, \tag{J.27}$$

$$\int_{z_b}^{z_s}\frac{\partial \tau_{xx}}{\partial x}\mathrm{d}z=\frac{\partial}{\partial x}\int_{z_b}^{z_s}\tau_{xx}\mathrm{d}z-(\tau_{xx})_s\frac{\partial z_s}{\partial x}+(\tau_{xx})_b\frac{\partial z_b}{\partial x}, \tag{J.28}$$

$$\int_{z_b}^{z_s}\frac{\partial \tau_{xy}}{\partial y}\mathrm{d}z=\frac{\partial}{\partial y}\int_{z_b}^{z_s}\tau_{xy}\mathrm{d}z-\left(\tau_{xy}\right)_s\frac{\partial z_s}{\partial y}+\left(\tau_{xy}\right)_b\frac{\partial z_b}{\partial y}, \tag{J.29}$$

$$\int_{z_b}^{z_s} \frac{\partial \tau_{xz}}{\partial z} \mathrm{d}z = (\tau_{xz})_s - (\tau_{xz})_b. \tag{J.30}$$

Equations (J.24)–(J.30) form a set of identities that are substituted into Eq. (J.23), transforming it into

$$\begin{aligned}
&\frac{\partial}{\partial t}\int_{z_b}^{z_s} \rho u \mathrm{d}z - \rho_s u_s \frac{\partial z_s}{\partial t} + \rho_b u_b \frac{\partial z_b}{\partial t} + \frac{\partial}{\partial x}\int_{z_b}^{z_s} \rho u^2 \mathrm{d}z - \rho_s u_s^2 \frac{\partial z_s}{\partial x} + \rho_b u_b^2 \frac{\partial z_b}{\partial x} + \frac{\partial}{\partial y}\int_{z_b}^{z_s} \rho uv \mathrm{d}z \\
&- \rho_s u_s v_s \frac{\partial z_s}{\partial y} + \rho_b u_b v_b \frac{\partial z_b}{\partial y} + \rho_s u_s w_s - \rho_b u_b w_b = -\left[\frac{\partial}{\partial x}\int_{z_b}^{z_s} \tau_{xx} \mathrm{d}z - (\tau_{xx})_s \frac{\partial z_s}{\partial x} + (\tau_{xx})_b \frac{\partial z_b}{\partial x}\right. \\
&\left. + \frac{\partial}{\partial y}\int_{z_b}^{z_s} \tau_{xy} \mathrm{d}z - (\tau_{xy})_s \frac{\partial z_s}{\partial y} + (\tau_{xy})_b \frac{\partial z_b}{\partial y} + (\tau_{xz})_s - (\tau_{xz})_b\right].
\end{aligned} \tag{J.31}$$

Collecting terms, one finds

$$\begin{aligned}
&\frac{\partial}{\partial t}\int_{z_b}^{z_s} \rho u \mathrm{d}z + \frac{\partial}{\partial x}\int_{z_b}^{z_s} \rho u^2 \mathrm{d}z + \frac{\partial}{\partial y}\int_{z_b}^{z_s} \rho uv \mathrm{d}z - \rho_s u_s \left(\frac{\partial z_s}{\partial t} + u_s \frac{\partial z_s}{\partial x} + v_s \frac{\partial z_s}{\partial y} - w_s\right) \\
&+ \rho_b u_b \left(\frac{\partial z_b}{\partial t} + u_b \frac{\partial z_b}{\partial x} + v_b \frac{\partial z_b}{\partial y} - w_b\right) + \left\{\frac{\partial}{\partial x}\int_{z_b}^{z_s} \tau_{xx} \mathrm{d}z + \frac{\partial}{\partial y}\int_{z_b}^{z_s} \tau_{xy} \mathrm{d}z\right. \\
&\left. - \left[(\tau_{xx})_s \frac{\partial z_s}{\partial x} + (\tau_{xy})_s \frac{\partial z_s}{\partial y} - (\tau_{xz})_s\right] + \left[(\tau_{xx})_b \frac{\partial z_b}{\partial x} + (\tau_{xy})_b \frac{\partial z_b}{\partial y} - (\tau_{xz})_b\right]\right\} = 0,
\end{aligned} \tag{J.32}$$

and, using Eq. (J.13), implies

$$\begin{aligned}
&\frac{\partial}{\partial t}\int_{z_b}^{z_s} \rho u \mathrm{d}z + \frac{\partial}{\partial x}\int_{z_b}^{z_s} \rho u^2 \mathrm{d}z + \frac{\partial}{\partial y}\int_{z_b}^{z_s} \rho uv \mathrm{d}z + \rho_s u_s M_s \xi_s - \rho_b u_b M_b \xi_b + \frac{\partial}{\partial x}\int_{z_b}^{z_s} \tau_{xx} \mathrm{d}z \\
&+ \frac{\partial}{\partial y}\int_{z_b}^{z_s} \tau_{xy} \mathrm{d}z - \left[(\tau_{xx})_s \frac{\partial z_s}{\partial x} + (\tau_{xy})_s \frac{\partial z_s}{\partial y} - (\tau_{xz})_s\right] + \left[(\tau_{xx})_b \frac{\partial z_b}{\partial x} + (\tau_{xy})_b \frac{\partial z_b}{\partial y} - (\tau_{xz})_b\right] = 0.
\end{aligned} \tag{J.33}$$

Equation (J.33) is the general x-momentum layer-integrated equation for non-hydrostatic mixture flows. Integration of Eq. (J.3) follows the same steps, and

no additional insights are regained. Analogously, the same procedure for the layer-integrated y-momentum equation leads to

$$\frac{\partial}{\partial t}\int_{z_b}^{z_s}\rho v\mathrm{d}z+\frac{\partial}{\partial y}\int_{z_b}^{z_s}\rho v^2\mathrm{d}z+\frac{\partial}{\partial x}\int_{z_b}^{z_s}\rho uv\mathrm{d}z+\rho_s v_s M_s\xi_s-\rho_b v_b M_b\xi_b+\frac{\partial}{\partial y}\int_{z_b}^{z_s}\tau_{yy}\mathrm{d}z$$
$$+\frac{\partial}{\partial x}\int_{z_b}^{z_s}\tau_{yx}\mathrm{d}z-\left[\left(\tau_{yy}\right)_s\frac{\partial z_s}{\partial y}+\left(\tau_{yx}\right)_s\frac{\partial z_s}{\partial x}-\left(\tau_{yz}\right)_s\right]+\left[\left(\tau_{yy}\right)_b\frac{\partial z_b}{\partial y}+\left(\tau_{yx}\right)_b\frac{\partial z_b}{\partial x}-\left(\tau_{yz}\right)_b\right]=0. \tag{J.34}$$

The z-momentum Eq. (J.4) is vertically integrated, viz,

$$\int_{z_b}^{z_s}\left[\frac{\partial}{\partial t}(\rho w)+\frac{\partial}{\partial x}(\rho uw)+\frac{\partial}{\partial y}(\rho vw)+\frac{\partial}{\partial z}\left(\rho w^2\right)\right]\mathrm{d}z$$
$$=-g\int_{z_b}^{z_s}\rho\mathrm{d}z-\int_{z_b}^{z_s}\left(\frac{\partial\tau_{zx}}{\partial x}+\frac{\partial\tau_{zy}}{\partial y}+\frac{\partial\tau_{zz}}{\partial z}\right)\mathrm{d}z. \tag{J.35}$$

Employing the transformations

$$\int_{z_b}^{z_s}\frac{\partial}{\partial t}(\rho w)\mathrm{d}z=\frac{\partial}{\partial t}\int_{z_b}^{z_s}\rho w\mathrm{d}z-\rho_s w_s\frac{\partial z_s}{\partial t}+\rho_b w_b\frac{\partial z_b}{\partial t}, \tag{J.36}$$

$$\int_{z_b}^{z_s}\frac{\partial}{\partial x}(\rho uw)\mathrm{d}z=\frac{\partial}{\partial x}\int_{z_b}^{z_s}\rho uw\mathrm{d}z-\rho_s u_s w_s\frac{\partial z_s}{\partial x}+\rho_b u_b w_b\frac{\partial z_b}{\partial x}, \tag{J.37}$$

$$\int_{z_b}^{z_s}\frac{\partial}{\partial y}(\rho vw)\mathrm{d}z=\frac{\partial}{\partial y}\int_{z_b}^{z_s}\rho vw\mathrm{d}z-\rho_s v_s w_s\frac{\partial z_s}{\partial y}+\rho_b v_b w_b\frac{\partial z_b}{\partial y}, \tag{J.38}$$

$$\int_{z_b}^{z_s}\frac{\partial}{\partial z}\left(\rho w^2\right)\mathrm{d}z=\rho_s w_s^2-\rho_b w_b^2, \tag{J.39}$$

$$\int_{z_b}^{z_s}\frac{\partial\tau_{zx}}{\partial x}\mathrm{d}z=\frac{\partial}{\partial x}\int_{z_b}^{z_s}\tau_{zx}\mathrm{d}z-\left(\tau_{zx}\right)_s\frac{\partial z_s}{\partial x}+\left(\tau_{zx}\right)_b\frac{\partial z_b}{\partial x}, \tag{J.40}$$

$$\int_{z_b}^{z_s} \frac{\partial \tau_{zy}}{\partial y} \mathrm{d}z = \frac{\partial}{\partial y} \int_{z_b}^{z_s} \tau_{zy} \mathrm{d}z - (\tau_{zy})_s \frac{\partial z_s}{\partial y} + (\tau_{zy})_b \frac{\partial z_b}{\partial y}, \tag{J.41}$$

$$\int_{z_b}^{z_s} \frac{\partial \tau_{zz}}{\partial z} \mathrm{d}z = (\tau_{zz})_s - (\tau_{zz})_b, \tag{J.42}$$

applied to Eq. (J.35), and subsequently grouping terms, leads to

$$\begin{aligned} &\frac{\partial}{\partial t} \int_{z_b}^{z_s} \rho w \mathrm{d}z + \frac{\partial}{\partial x} \int_{z_b}^{z_s} \rho u w \mathrm{d}z + \frac{\partial}{\partial y} \int_{z_b}^{z_s} \rho v w \mathrm{d}z - \rho_s w_s \left(\frac{\partial z_s}{\partial t} + u_s \frac{\partial z_s}{\partial x} + v_s \frac{\partial z_s}{\partial y} - w_s \right) \\ &+ \rho_b w_b \left(\frac{\partial z_b}{\partial t} + u_b \frac{\partial z_b}{\partial x} + v_b \frac{\partial z_b}{\partial y} - w_b \right) + g \int_{z_b}^{z_s} \rho \mathrm{d}z + \left\{ \frac{\partial}{\partial x} \int_{z_b}^{z_s} \tau_{zx} \mathrm{d}z + \frac{\partial}{\partial y} \int_{z_b}^{z_s} \tau_{zy} \mathrm{d}z \right. \\ &\left. - \left[(\tau_{zx})_s \frac{\partial z_s}{\partial x} + (\tau_{zy})_s \frac{\partial z_s}{\partial y} - (\tau_{zz})_s \right] + \left[(\tau_{zx})_b \frac{\partial z_b}{\partial x} + (\tau_{zy})_b \frac{\partial z_b}{\partial y} - (\tau_{zz})_b \right] \right\} = 0, \end{aligned} \tag{J.43}$$

or, using the kinematic boundary conditions at each interface,

$$\begin{aligned} &\frac{\partial}{\partial t} \int_{z_b}^{z_s} \rho w \mathrm{d}z + \frac{\partial}{\partial x} \int_{z_b}^{z_s} \rho u w \mathrm{d}z + \frac{\partial}{\partial y} \int_{z_b}^{z_s} \rho v w \mathrm{d}z + \rho_s w_s M_s \xi_s - \rho_b w_b M_b \xi_b + g \int_{z_b}^{z_s} \rho \mathrm{d}z \\ &+ \frac{\partial}{\partial x} \int_{z_b}^{z_s} \tau_{zx} \mathrm{d}z + \frac{\partial}{\partial y} \int_{z_b}^{z_s} \tau_{zy} \mathrm{d}z - \left[(\tau_{zx})_s \frac{\partial z_s}{\partial x} + (\tau_{zy})_s \frac{\partial z_s}{\partial y} - (\tau_{zz})_s \right] + \left[(\tau_{zx})_b \frac{\partial z_b}{\partial x} + (\tau_{zy})_b \frac{\partial z_b}{\partial y} - (\tau_{zz})_b \right] = 0. \end{aligned} \tag{J.44}$$

Equations (J.22), (J.33), (J.34), and (J.44) are the general non-hydrostatic layer-integrated mass and momentum conservation equations for mixture flows. These are a generalization of the single-layer flow equations with material interfaces presented by Castro-Orgaz et al. (2015) and are similar to those recently presented by Iverson and Ouyang (2015).

As an *application example*, to show how to use the equations to construct models, a geomorphic model for the bed-load transport of sediments in an alluvial river is produced. Consider the simplified configuration of flow over an alluvial bed depicted in Fig. J.2, where the bed-load layer thickness of sediments moving with the flow is h_1, its mixture velocity is u_1, and mixture density is ρ_1. Sediments are eroded from (or deposited in) a static bed of alluvial material of mixture density ρ_2 and thickness with reference to an arbitrary datum z_b. The flow above the river is assumed to be of clear water (no suspended sediments are considered). It will be shown how to obtain the morphodynamic model of Capart and Young (1998) from the general equations

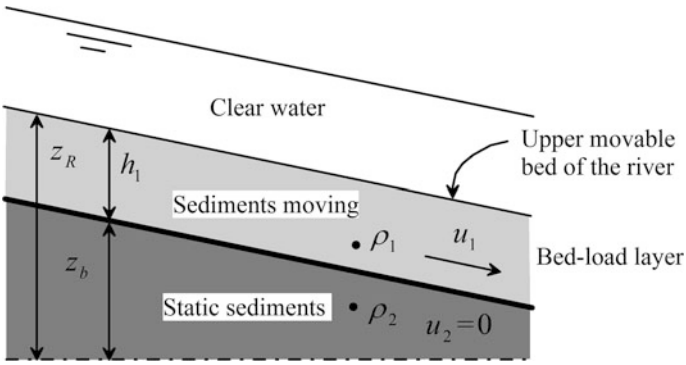

Figure J.2 Simplified layer structure for a morphodynamic model of alluvial river

presented here and use it to derive the Exner equation, widely applied and coupled with non-hydrostatic Boussinesq-type equations for the clear-water layer (Engelund and Hansen 1966; Engelund 1971; Bose and Dey 2009).

The conservation of the mixture mass within the bed-load layer is from Eq. (J.22)

$$\frac{\partial}{\partial t}(\rho_1 h_1) + \frac{\partial}{\partial x}[\rho_1 h_1 u_1] = \rho_1 M_1 \xi_b, \tag{J.45}$$

where M_1 is the volume of mixture per unit time and unit area crossing normal to the bed-load layer interface with the static sediment bed, and the slope correction factor is

$$\xi_b = \left[1 + \left(\frac{\partial z_b}{\partial x}\right)^2\right]^{1/2}. \tag{J.46}$$

The same equation applied to the static alluvial bed is

$$\frac{\partial}{\partial t}(\rho_2 z_b) + \frac{\partial}{\partial x}[\rho_2 z_b u_2] = -\rho_2 M_2 \xi_b, \tag{J.47}$$

and, setting $u_2 = 0$,

$$\frac{\partial}{\partial t}(\rho_2 z_b) = -\rho_2 M_2 \xi_b, \tag{J.48}$$

where the slope factor ξ_b is identical to that of Eq. (J.45) (the interface is common), but the volumetric transfer per unit area and time is different, given the density jump across the interface. Jump conditions across an interface are detailed by Hutter et al. (2014) and Iverson and Ouyang (2015); here, the jump condition states that the

source terms of Eqs. (J.45) and (J.48) must cancel to have overall conservation of the mixture mass in the layer $z_R = h_1 + z_b$. Thus, one can write the identity

$$\rho_1 M_1 = \rho_2 M_2. \tag{J.49}$$

It is illuminating to write now the kinematic boundary condition at the interface, which is affected by the jump of velocities, namely

$$\frac{\partial z_b}{\partial t} + \frac{\partial z_b}{\partial x} u_1 - w_1 = -M_1 \xi_b, \tag{J.50}$$

or

$$\frac{\partial z_b}{\partial t} = -M_2 \xi_b. \tag{J.51}$$

It is pertinent to remark that Eq. (J.51), which is a pure kinematic statement, reduces to Eq. (J.48), which is a mass conservation balance, only if ρ_2 is a constant, that is, if pore variations on the alluvial bed are ignored. It implies that the granular skeleton of the static bed must not deform in time due to the stresses acting on it.

Let us consider the solid-phase mass balances from Eqs. (J.45) and (J.48)

$$\frac{\partial}{\partial t}(\rho_s c_1 h_1) + \frac{\partial}{\partial x}[\rho_s c_1 h_1 u_1] = \rho_s c_1 M_1 \xi_b, \tag{J.52}$$

$$\frac{\partial}{\partial t}(\rho_s c_2 z_b) = -\rho_s c_2 M_2 \xi_b, \tag{J.53}$$

where ρ_s is the density of solids and c is the volumetric concentration of solids in the mixture. Equations (J.52) and (J.53) can also be written as

$$\frac{\partial}{\partial t}(c_1 h_1) + \frac{\partial}{\partial x}[c_1 h_1 u_1] = c_1 M_1 \xi_b, \tag{J.54}$$

$$\frac{\partial}{\partial t}(c_2 z_b) = -c_2 M_2 \xi_b. \tag{J.55}$$

Assuming that c_2 is a constant, Eq. (J.55) simplifies to

$$c_2 \frac{\partial z_b}{\partial t} = -c_2 M_2 \xi_b, \tag{J.56}$$

and the jump condition from Eqs. (J.54) and (J.56) is

$$c_1 M_1 = c_2 M_2 = N_b. \tag{J.57}$$

Using it, the morphodynamic model is finally written as

$$\frac{\partial}{\partial t}(c_1 h_1) + \frac{\partial}{\partial x}[c_1 h_1 u_1] = N_b \xi_b, \tag{J.58}$$

$$c_2 \frac{\partial z_b}{\partial t} = -N_b \xi_b, \tag{J.59}$$

which is equivalent to the system proposed by Capart and Young (1998). Assuming a non-equilibrium predictor for the source term in the mass balance equation for the bed-load layer (Wu 2008),

$$N_b \xi_b \approx \frac{q_b^* - q_b}{L}, \tag{J.60}$$

where $q_b = c_1 h_1 u_1$ is the actual bed-load flux in non-uniform unsteady flow, q_b^* its equilibrium value in steady uniform flow, and L an adaptation length, Eqs. (J.58)–(J.59) are rewritten as

$$\frac{\partial}{\partial t}\left(\frac{q_b}{u_1}\right) + \frac{\partial q_b}{\partial x} = \frac{q_b^* - q_b}{L}, \tag{J.61}$$

$$\frac{\partial z_b}{\partial t} = -\frac{1}{c_2}\left(\frac{q_b^* - q_b}{L}\right), \tag{J.62}$$

which is the bed-load layer morphodynamic model used by Wu (2008) [if the suspended-load is neglected]. Finally, summing Eqs. (J.54) and (J.55), and using the jump condition Eq. (J.57), produces the global mass conservation equation

$$\frac{\partial}{\partial t}(c_1 h_1 + c_2 z_b) + \frac{\partial q_b}{\partial x} = 0. \tag{J.63}$$

If it is assumed that the porosity of the alluvial bed is identical to that of the bed-load layer and that it is a constant, e.g., $c_1 = c_2 = c = \text{const.}$, then Eq. (J.63) reduces to

$$c \frac{\partial z_R}{\partial t} + \frac{\partial q_b}{\partial x} = 0, \tag{J.64}$$

which is the Exner mass conservation equation (Engelund and Hansen 1966). It gives the evolution of the upper movable bed of the river z_R, that is, the interface of the bed-load layer with the clear-water flow (Fig. J.2). This equation is frequently

used in river flows to predict the formation of sand waves, e.g., dunes and antidunes (Engelund and Hansen 1966; Bose and Dey 2009), or the solitary sand wave (Engelund 1971), coupled with Boussinesq-type equations for the clear-water non-hydrostatic flow above the erodible bed. The hypothesis of constant c is not likely to apply to geomorphic flows with intense bed-load motion, like those occurring in dam break flows over granular beds (Capart and Young 1998). In those flows, a non-equilibrium sediment transport model based on Eqs. (J.58)–(J.59) is advisable to its coupling with non-hydrostatic equations for the fluid flow above the bed (Cantero-Chinchilla et al. 2016; see Appendix I).

References

Cantero-Chinchilla, F., Castro-Orgaz, O., Dey, S., & Ayuso, J. L. (2016). Nonhydrostatic dam break flows II: One-dimensional depth-averaged modelling for movable bed flows. *Journal of Hydraulic Engineering, 142*(12), 04016069.

Capart, H., & Young, D. L. (1998). Formation of a jump by the dam-break wave over a granular bed. *Journal of Fluid Mechanics*, *372*, 165–187.

Castro-Orgaz, O., Hutter, K., Giráldez, J. V., & Hager, W. H. (2015). Non-hydrostatic granular flow over 3D terrain: New Boussinesq-type gravity waves? *Journal of Geophysical Research: Earth Surface*, *120*(1), 1–28.

Engelund, F., & Hansen, E. (1966). Investigations of flow in alluvial streams. *Bulletin* 9, Hydraulic Laboratory, Technical University of Denmark, Copenhagen.

Engelund, F. (1971). The solitary sand wave. In *Progress Report* (Vol. 24, pp. 51–54). Copenhagen: Institute of Hydrodynamics and Hydraulic Engineering, Technical University of Denmark.

Bose, S. K., & Dey, S. (2009). Reynolds averaged theory of turbulent shear flows over undulating beds and formation of sand waves. *Physical Review E, 80*(3), 036304-1–036304-9.

Hutter, K., Wang, Y., & Chubarenko, I. P. (2014). Sediment transport in alluvial systems (Chap. 32). In *Physics of lakes*: *Methods of understanding lakes as components of the geophysical environment. Advances in Geophysical and Environmental Mechanics and Mathematics* (Vol. 3, pp. 487–579). Heidelberg: AGEM^2, Springer.

Iverson, R. M., & Ouyang, C. (2015). Entrainment of bed material by Earth-surface mass flows: Review and reformulation of depth-integrated theory. *Reviews of Geophysics*, *53*. doi:10.1002/2013RG000447.

Wu, W. (2008).*Computational river dynamics*. London, U.K: Taylor and Francis.

Author Index

© Springer International Publishing AG 2017

O. Castro-Orgaz and W.H. Hager, *Non-Hydrostatic Free Surface Flows*,
Advances in Geophysical and Environmental Mechanics and Mathematics
DOI 10.1007/978-3-319-47971-2

D

E

Subject Index

© Springer International Publishing AG 2017

O. Castro-Orgaz and W.H. Hager, *Non-Hydrostatic Free Surface Flows*,
Advances in Geophysical and Environmental Mechanics and Mathematics
DOI 10.1007/978-3-319-47971-2